The Dissertation Committee for Marcus Douglas Hilliard certifies that this is the approved version of the following dissertation:

A Predictive Thermodynamic Model for an Aqueous Blend of Potassium Carbonate, Piperazine, and Monoethanolamine for Carbon Dioxide Capture from Flue Gas

Committee:

____

Gary T. Rochelle, Supervisor

____

Benny D. Freeman

____

Isaac C. Sanchez

____

R. Bruce Eldridge

____

Hallvard Fjøsne Svendsen

A Predictive Thermodynamic Model for an Aqueous Blend of Potassium Carbonate, Piperazine, and Monoethanolamine for Carbon Dioxide Capture from Flue Gas

by

Marcus Douglas Hilliard, B.S.Ch.E.; M.S.E.

Dissertation

Presented to the Faculty of the Graduate School of

the University of Texas at Austin

in Partial Fulfillment

of the Requirements

for the Degree of

Doctor of Philosophy

The University of Texas at Austin

May, 2008

To my family

and especially to my partner,

James Shewbert

for his constant love and support that always kept me going.

In modeling there is no pressure, it’s all partial pressure…

James Shewbert and Marcus Hilliard

Acknowledgements

There have been so many people who have helped me throughout the years to make me into the person that I am today. I would first like to thank my parents, Mary Elizabeth and Gregg Hannah, who have been a constant force in my life, illuminating the way while putting up with all of my shenanigans.

I also want to thank my extended family and friends, Regina Sandoval, Linda Gregston, Nathanael Haddox, Frank Ramos, Jan and Doug Love, Jessica Bayless, Ken and Derenda Shewbert, Cheryl Paden, Bob Miller and Brian Jantz, Lindi Horton, Ron and Carol Barrett, Lizz and Christophe Restat, and Joy Herring. Thanks for always being there for me and nodding your head when I would tell ya'll what I was up to in school.

I would also like to give a special than you to Pat Knight for editing my dissertation and who taught me that literature and writing could be something that was cool. I would also like to thank some very special teachers at Texas Tech University, who taught me how to become an engineer: Dr. Ted Wiesner, Dr. Robert Bethea, Dr. Jeremy Leggoe, Dr. Uzi Mann, Dr. Sindee Simon, and Dr. Karlene Hoo.

Over the past six years while attending graduate school at The University of Texas at Austin, I have been very fortunate to work with so many talented and caring people. I would like to thank all of the students in Dr. Rochelle's group, Jody Lester, Kay Swift, Maeve Cooney, Randy Rife, Eduardo Ibarra, Randle Martin, Kevin Haynes, Butch Cunningham, Jim Smitherman, and especially T. Stockman. I could have never done this without your support.

I have also been very fortunate to have been given the opportunity to travel to Norway and study at The Norwegian University of Science and Technology under the supervision of Dr. Hallvard F. Svendsen. I would like to thank him for his kindness, hospitality, encouragement, and especially the advice he gave me during my stay in Trondheim. I would also like to thank Inna Kim, Jana Poplsteinova Jakobsen, Sholeh Ma'mun, Eirik de Silva, Hanna Knuutila, Karl A Hoff, Synnøve Hestnes, Andrew Tobiesen, Kristin Giske Lauritsen, Vishwas Dindore, and Arne Lindbrathe, for the kindness they showed and for the advice to bring extra woolen jumpers.

I would also like to thank the members of my committee, who have truly been some of the best teachers I have ever had the pleasure to learn from, thank you. I would also like to thank Dr. Gary T. Rochelle for dealing with my mayhem and foolishness over the past six years. He taught me how to think as a researcher and gave me the opportunity to study at The University of Texas at Austin after some persuading, and I am truly grateful. Thank you.

I would also like to thank Dr. Chau-Chyun Chen and Dr. Suphat Watanasiri from Aspen Technology. In addition, I want to thank Mark Nelson from GASMET-USA for helping me understand and optimize our FTIR analytical methods. Their support has been an integral part in this research and I am truly honored to have been able to work with them both on this project.

This work was made possible in part by the Separations Research Program, Luminant Carbon Management Program, the Industrial Associates Program for CO_2 Capture by Aqueous Absorption, and the Department of Energy (DE-FC26-02NT41440).

This work was prepared with the support of the U.S. Department of Energy, under Award No. DE-FC26-02NT41440. However, any opinions, findings, conclusions, or recommendations expressed herein are those of the authors and do not necessarily reflect the views of the DOE or other sponsors.

A Predictive Thermodynamic Model for an Aqueous Blend of Potassium Carbonate, Piperazine, and Monoethanolamine for Carbon Dioxide Capture from Flue Gas

Publication No. ___________

Marcus Douglas Hilliard, Ph.D.
The University of Texas at Austin, 2008

Supervisor: Gary T. Rochelle

The Electrolyte Nonrandom Two-Liquid Activity Coefficient model in Aspen Plus^{TM} 2006.5 was used to develop a rigorous and consistent thermodynamic representation for the base sub-component systems associated with aqueous combinations of K_2CO_3, $KHCO_3$, MEA, and piperazine (PZ) in a mixed-solvent electrolyte system for the application of CO_2 absorption/stripping from coal fired power plants.

We developed a new vapor-liquid equilibrium apparatus to measure CO_2, amine, and H_2O vapor pressures at 40 and 60 °C. We found that the volatility of MEA and PZ can be approximated at 50 and 20 ppm_v at 40 °C for any solvent composition studied in this work, over the CO_2 partial pressure range from 0.01 to 0.1 kPa. Very few solvent compositions exhibited a greater differential capacity than 7 m MEA at 60 °C; specifically 11 m MEA, 3.5

m MEA + 3.6 m PZ, 7 m MEA + 2 m PZ, 7 m MEA + 3.6 m PZ, and 5 m K^+ + 7 m MEA + 3.6 m PZ. Piperazine exhibited a possible maximum differential capacity of 2.21 mole CO_2/kg-H_2O at a concentration of 7.3 m.

At the Norwegian University of Science and Technology, Inna Kim determined the differential enthalpy of CO_2 absorption for aqueous combinations of K_2CO_3, $KHCO_3$, MEA, PZ, and CO_2, based on a consistent experimental method developed for MEA, from 40 to 120 ^oC for use in this work. In addition, we developed a consistent method to measure the specific heat capacity for a number of similar solvent combinations. We found that the enthalpy of CO_2 absorption increased with temperature because the apparent partial heat capacity of CO_2 may be considered small.

Finally, by using a differential scanning calorimeter, we determined the dissolution temperature for aqueous mixtures of unloaded piperazine, which inferred an effective operating range for solutions of concentrated piperazine, greater than 5 m PZ, over a loading range between 0.25 to 0.45 mole CO_2/2·mol PZ. Through unit cell x-ray diffraction, we were able to identify and characterize the presence of three solid phases ($PZ \cdot 6H_2O$, $KHCO_3$, and $K_2PZ(COO)_2$) in aqueous mixture combinations of K_2CO_3, $KHCO_3$, PZ, and CO_2.

CONTENTS

LIST OF TABLES

LIST OF FIGURES

CHAPTER I

General Introduction

1.1 Motivation

This research addresses the use of carbon capture technology from coal fired power plants to reduce possible factors contributing to global warming. Some of the current competitive technologies for post-combustion capture are: integrated gasification combined cycle (IGCC), oxycombustion, and aqueous absorption. Some of the disadvantages of IGCC and oxycombustion are that they are not tail-end processes which would require a significant capital investment to demonstrate and deploy the technology. In addition, IGCC and oxycombustion are relatively new technologies associated with carbon capture. As a result, this work focused on solvents for post-combustion capture utilizing aqueous absorption. Aqueous absorption is "capture ready" with conventional coal fired power plants for a lower capital investment. The technology is easy to develop and demonstrate.

For the absorption process, 30 weight percent monoethanolamine is considered the most promising solvent for CO_2 absorption [Aaron and Tsouris (2005)] and has been used in the acid gas scrubbing industry over the past 70 years. Our aim in this work is to understand the fundamental thermodynamic behavior associated with the chemical absorption process using a variety of aqueous salt/amine chemical solvents which have shown an increase in capacity, exhibited faster rates, and have demonstrated robustness to corrosion.

1.2 The Absorption Process

CO_2 removal by reactive absorption/stripping using aqueous monoethanolamine (MEA) and other blended amine solvents has been established as a mature CO_2 capture technology. Figure 1.2-1 shows a typical counter-current absorber/stripper. Flue gas entering the absorber is counter-currently contacted with an aqueous amine solvent. CO_2 is absorbed into the aqueous amine solvent through a reversible chemical reaction to form a rich or loaded solvent (with respect to CO_2). Alkanolamine/CO_2 reactions are known to occur within the liquid boundary layer. Under some conditions, the reactions are nearly instantaneous as the concentration of the amine becomes depleted at the gas-liquid interface. To correctly predict these rates, we will need an accurate equilibrium model to account for the complexities of the mass transfer with fast chemical reaction as well as the speciation of the amines in the solution. The rich amine solution is then sent through a counter-current heat exchanger, where the solution is pre-heated by the lean amine solution before entering the stripper. In the stripper, heat is provided in the reboiler in the form of steam to reverse the chemical equilibrium between the amine and CO_2. The liberated CO_2 and water vapor then leaves the stripper for downstream processing and storage. The optimal amine solvent would depend on the residual CO_2 specification and the stripping energy costs associated with the enthalpy of CO_2 absorption. The hot, lean amine solution is then sent back through the counter-current heat exchange where the solution is cooled before reaching the absorber.

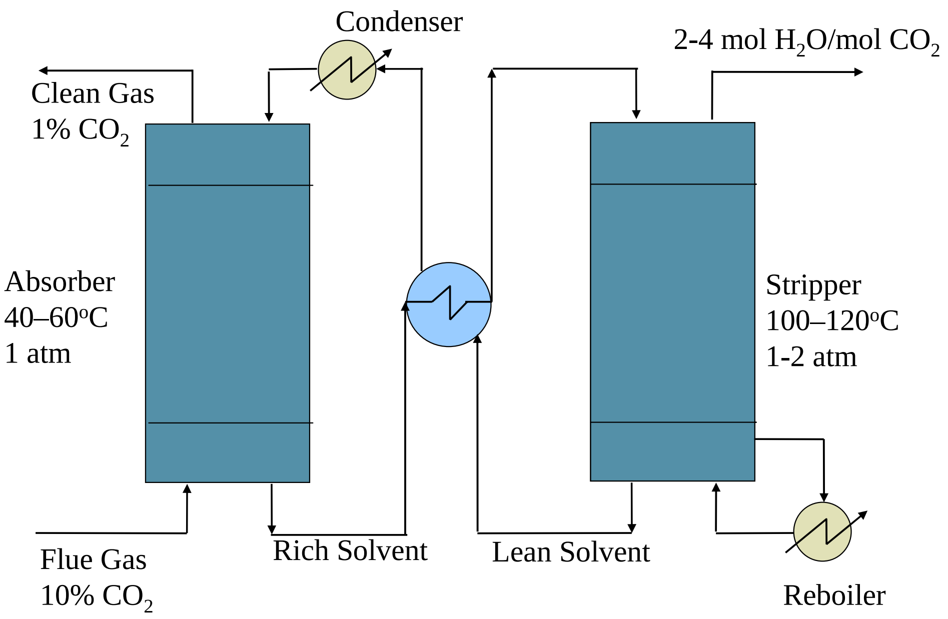

Figure 1.2-1. Absorption/Stripping System for Removal of CO_2 from Flue Gas using Aqueous Alkanolamine Solutions.

1.3 Thermodynamic Considerations

In this work, we have focused our efforts on addressing specific thermodynamic areas of interest associated with the absorption/stripping process as shown in Figure 1.3-1.

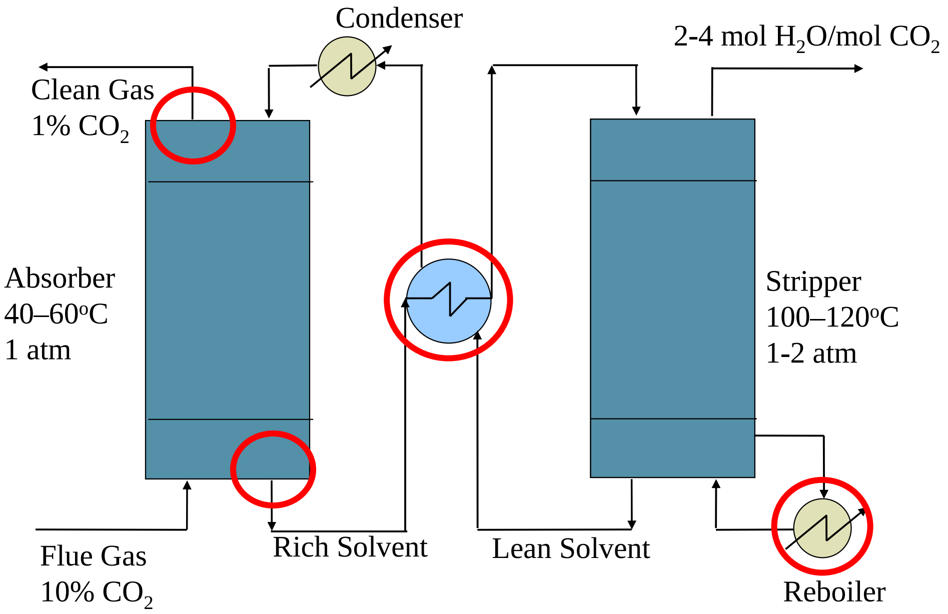

Figure 1.3-1. Thermodynamic Areas of Interest for the Absorption/Stripping Process.

Figure 1.3-1 illustrates four areas where additional thermodynamic research is needed and can be further sub-divided into two main areas associated with mass transfer and calorimetry effects. Separation driving forces in terms of mass transfer are associated with the ability to characterize the solvent with respect to the solvents affinity for CO_2, the capacity of the solvent, and losses of the solvent due to amine volatility. Calorimetry also plays an important role in the design and sizing of heat exchangers and affects the energy requirements associated with regeneration of the lean solvent.

This work has made a uniquely measured multiple independent data sets to address deficiencies in the framework of previous thermodynamic models. We then seamlessly combine all available data to create a rigorous and consistent model to describe the thermodynamics associated with the absorption/stripping process.

1.4 Related Research Activities

The quest to develop a new solvent to maximize CO_2 capacity can be very laborious. A tremendous amount of experimental work has been done over the years to characterize new solvents with respect to different properties (solubility, absorption, capacity, amine volatility, etc.). Alkanolamines are among several solvents that have been investigated and current research is focused on designing a chemically stable, less corrosive, solvent with fast reaction rates and high enthalpies of absorption to minimize energy requirements for regeneration of the solvent.

Recently, there has been an increased interest in the use of mixed amine solvents in gas-treating processes. Blends comprising of primary, secondary, or tertiary amines have been suggested for the industrial gas-treating processes (Mandal et al., 2003). Using different blends of amines, researchers can tailor solvent properties associated with each amine to meet specific acid gas removal requirements (high capacity, fast reaction rates, etc.).

While previous models have studied the rates of MEA blends [Dang and Rochelle (2003) and Okoye (2005)], to date, a rigorous thermodynamic model has not been developed for the MEA/PZ system. One motivation behind this work was to complete a comprehensive thermodynamic study for MEA/PZ where reliable data for the solubility of CO_2 in aqueous MEA/PZ at elevated temperatures between 80 and 120 °C could then serve as a standard for use in stripper modeling of vapor-liquid equilibrium in blended MEA/PZ solutions.

The development of new solvents involving potassium carbonate (K_2CO_3) and piperazine (PZ) has shown potential as a new CO_2 capture process [Cullinane (2005)].

Cullinane (2005) reported equilibrium partial pressure of CO_2 measured in a wetted-wall column in 0.6–3.6 m PZ and 2.5–6.2 m potassium ion (K^+) from 40 – 110 °C. Cullinane (2005) suggested that additional measurements be carried out at high temperatures (80 – 120 °C) to account for amine volatility and to verify current CO_2 solubility in aqueous PZ and K^+/PZ solutions.

Currently, little information is available in literature concerning the vapor pressure of alkanolamines in blended or aqueous binary systems. For example, Park and Lee (1997) reported isobaric VLE measurements for MEA and water from 100 – 170 °C at atmospheric pressure where compositions of the liquid and gas phases were determined by gas chromatography. Unfortunately, there are no useful binary VLE data for systems with PZ available in literature. Cullinane (2005) and Hilliard (2005) were able to represent the K^+/PZ VLE behavior using rigorous thermodynamic electrolyte-NRTL models, but there were apparent inconsistencies between the predictive capabilities for the vapor pressure of PZ due to a lack of available literature data.

The enthalpy of CO_2 absorption is an important physical property that is required in the design of acid gas removal plants. The enthalpy of CO_2 absorption is directly related to the energy requirements for the solvent regeneration, and it is desirable that the value be known as accurately as possible to avoid uneconomic over design. Although the enthalpy of CO_2 absorption may be estimated from a rigorous thermodynamic model using the Gibbs–Helmholtz equation to predict CO_2 solubility, the process of differentiation can magnify any errors in the solubility data and the resulting values are rarely more accurate than ± 20 %. For this reason direct calorimetric measurements for the enthalpy of CO_2 absorption in the solvent are preferred. Inna Kim, a doctoral student at NTNU, conducted experiments for this work using an isothermal heat flow calorimeter to measure the enthalpy of CO_2 absorption in a mixed solvent of K_2CO_3 + PZ + H_2O and in a mixed amine solution of MEA + PZ + H_2O.

Understanding the thermodynamics of amine and blended amine systems is essential to their use as part of a CO_2 capture methodology. This includes the understanding of amine vaporization losses, CO_2 solubility, and calorimetry, speciation, and solution phase behavior. This framework can then be applied to predict the thermodynamic characteristics of the H_2O-K_2CO_3-PZ-MEA-CO_2 system using a rigorous thermodynamic model.

Several thermodynamic models have been developed and applied to the thermodynamic modeling of aqueous amine solutions. Kent and Eisenberg (1976) were the first to create an equilibrium model based on pseudo-equilibrium constants and Henry's Law, but the result was a model with only two adjustable parameters that could not predict speciation. Edwards et al. (1975, 1978) developed a model for the capture of carbon dioxide, hydrogen sulfide, sulfur dioxide, and hydrogen cyanide using an aqueous ammonia solution. In their work, they assembled chemical equilibrium and Henry's constants in water as a function of temperature. Deshmukh and Mather (1981) developed a rigorous thermodynamic equilibrium model based on the extended Debye-Hückel theory where the activity coefficient equation had one term to account for electrostatic forces and the second adjustable term to account for short range interactions. More recently, Cullinane (2005) modified a stand-alone rigorous thermodynamic equilibrium/rate model for the H_2O-K_2CO_3-PZ-CO_2 system by utilizing the electrolyte-Nonrandom Two-Liquid (NRTL) theory developed by Chen and coworkers [Chen et al. (1979, 1982), Chen and Evans (1986), and Mock et al. (1986)] where the stand-alone FORTRAN code was first created by Austgen (1989) for the amine-water systems and then later modified by Bishnoi (2000), Dang (2000), and Freguia (2002).

In recent years, there has been a growing trend in aqueous electrolyte reactive system modeling to combine multiple independent data sets in terms of vapor-liquid equilibrium (VLE), solid-liquid equilibrium (SLE), and calorimetry into a rigorous consistent thermodynamic model. Thomsen and Rasmussen (1999) have focused their efforts in modeling reactive electrolyte systems containing ammonia and/or carbon dioxide in the presence of various salts through a combination of the extended UNIQUAC model for electrolytes an the Soave-Redlich-Kwong cubic equation of state. The model was evaluated on the basis of more than 7,000 experimental data points including VLE, SLE, and calorimetry. This direction in thermodynamic modeling for reactive aqueous electrolyte systems stems from governmental and industrial needs for increasingly accurate predictions in designing, optimizing, and in determining potential environmental impacts.

For this work, we have chosen the electrolyte-NRTL model available as a property package in Aspen Plus™. The framework of Aspen Plus™ was chosen for its wide use in process industries and academic institutions and; it provides a process environment framework for simulating multiple unit operations on a plant wide scale. Aspen Plus™ also facilitates collaborative engineering by allowing different engineering groups to work together more effectively through electronically sharing information and it contains accurate and up-to-date physical properties databanks. Also, Aspen Plus™ contains a built in data regression algorithm called the Data Regression System^{TM} (DRS). DRS allows for the simultaneous regression of multiple types of data sets to create a fundamental based thermodynamic model. The final reason for choosing the Aspen Plus^{TM} framework was the successful modeling of CO_2 capture technologies by utilizing the rigorous thermodynamic electrolyte-NRTL model within Aspen Plus^{TM} from previous authors [Austgen (1989) and Posey (1996)]. Based on the above reasons, we felt that the Aspen Plus^{TM} framework would be an ideal environment to further the thermodynamic understanding of the H_2O-K_2CO_3-PZ-MEA-CO_2 system as part of a synergistic CO_2 capture methodology.

1.5 Scope of Work

This project expands upon previous work in the area of modeling amines and amine blends for CO_2 capture by aqueous absorption/stripping where a rigorous electrolyte-NRTL thermodynamic model is required for quantitative analysis of the solvent to describe:

a. The driving forces for CO_2 mass transfer utilizing all available data types (e.g. CO_2 solubility, enthalpy of CO_2 absorption, and NMR liquid speciation)
b. Speciation of the liquid phase where complex kinetic contributes to mass transfer are enhanced by fast reactions
c. The driving forces for amine mass transfer in terms of volatilization
d. Heats of absorption/desorption
e. The effective liquid heat capacity to size counter-current heat exchanges affecting the energy requirements and vapor rates for the stripper

This project will focus on characterizing the base systems of chemical reactions at equilibrium to predict the solubility of CO_2 in the solvent, the enthalpy of CO_2 absorption, and the concentration of reactive species for aqueous H_2O-K_2CO_3-PZ-MEA-CO_2 from the respective sub-component systems as shown in Figure 1.5-1.

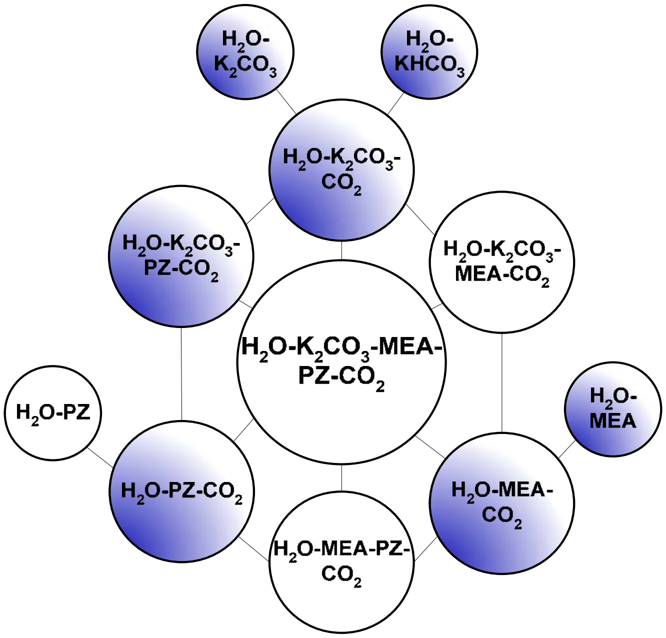

Figure 1.5-1. Thermodynamic Sub-Component System Tree. Shaded circles: Systems found in literature. Open circles: Systems proposed to study.

Part of this work has been a collaborative effort between The University of Texas at Austin (UT) and the Norges Teknish-Naturvitenshapelige Universitet (NTNU) in Trondheim, Norway, to generate data by independent methods and to confirm the enthalpy of CO_2 absorption and CO_2 solubility at stripper conditions involving mixtures of aqueous potassium carbonate, piperazine, and monoethanolamine to add additional thermodynamic data for the sub-component systems in the following areas:

Experimental Methods

a. Developed methods for quantifying solution and vapor speciation using acid-base titration and FT-IR analysis.
b. Investigated solid-liquid equilibrium in experimental solutions of potassium carbonate, piperazine, and monoethanolamine.

Experimental Measurements

a. Determined the CO_2 solubility and amine volatility through VLE measurements of the vapor phase utilizing an atmospheric pressure apparatus with unique Fourier-Transform infrared (FT-IR) analysis technique and through a high pressure VLE apparatus.

b. Measured the enthalpies of CO_2 absorption of potassium carbonate, piperazine, and monoethanolamine.

Thermodynamic Modeling

a. Predicted the thermodynamic characteristics of H_2O-K_2CO_3-PZ-MEA-CO_2 using a rigorous thermodynamic model of the base sub-component systems.

1.6 Outline of the dissertation

The dissertation is divided into four parts according to the development described above: part one describes the experimental methods used in this work while at The University of Texas at Austin in Austin, Texas, USA, and at the Norges Teknisk-Naturvitenshapelige Universitet in Trondheim, Norway. Part two describes the electrolyte nonrandom two-liquid model as part of the internal framework within Aspen Plus^{TM} 2006.5. Part three describes the thermodynamic modeling and data representation for the base sub-component systems. Finally, part four describes the predictive nature of the thermodynamic model for the H_2O-PZ-MEA-CO_2, H_2O-K_2CO_3-MEA-CO_2, and H_2O-K_2CO_3-PZ-MEA-CO_2 systems as compared to experimental data collected as part of this work.

PART I

Experimental

Methods

CHAPTER II

Vapor-Liquid Equilibrium Methods

2.1 Introduction

This chapter details the experimental methods used to measure CO_2 solubility and amine volatility of alkalonamine solutions used throughout this work. The chapter will be divided into two parts: part one describes the high temperature CO_2 solubility measurements (80 - 120 °C) performed at Norges Teknish-Naturvitenshapelige Universitet (NTNU) in Trondheim, Norway, and part two describes the low temperature CO_2 solubility and amine volatility measurements (40 - 60 °C) performed at The University of Texas at Austin (UT) in Austin, Texas, USA. The use of each apparatus has been documented by previous authors, Ma'mum et al. (2005) and Goff (2005), respectively; thus only a brief description on each apparatus will be given.

2.2 Literature Review

To describe the thermodynamics involved in the solubility of a gas into an aqueous solution, one has to be able to accurately determine and measure the properties of the solubility and the liquid state. Through experimental determination, the solubility of a gas can be determined through measurement of the vapor-liquid equilibrium under known conditions for temperature and pressure. By sampling both vapor and liquid phases, we can determine a reliable measurement of the equilibrium state.

To measure the solubility of a gas, Hefter and Tomkins (2003) reviewed several experimental methods for solubility measurements:

Method	Apparatus
Gas Bubbler	Direct bubbling of gas into a liquid.
Volumetric	Ostwald (1894)
Thin Film	Ben-Naim and Baer (1963)
	Benson et al. (1979)
High Pressure	Huang et al. (1985)
	Kennan and Pollack (1990)

Ostwald (1894) designed a volumetric apparatus consisting of a stirred and thermostated equilibrium cell, a pressure manometer, and multiple burets to measure the volume of either a dry or saturated gas. The solubility of the gas is then determined assuming ideal gas behavior and Henry's law for the dissolved gas.

Ben-Naim and Baer (1963) and Benson et al. (1979) designed a closed-loop equilibrium apparatus where a circulating liquid flows over a sphere producing a slow gentle film in contact with an initial amount of 1 bar of dry gas. The liquid continues to circulate until equilibrium is reached where the liquid and gas phases are analyzed.

For high pressure measurements, each apparatus is somewhat unique to the investigator. Huang et al. (1985) described an equilibrium cell charged with known amounts of each component. The temperature and pressure are monitored by a calibrated iron-constantan thermocouple and a calibrated pressure transducer. During an experiment, the temperature is set and the pressure is adjusted by moving an internal piston. The entire apparatus is rocked to achieve equilibrium between the two phases. At equilibrium, samples of both phases are taken and analyzed by gas chromatography.

In absorption rate measurements, the solubility of a gas could be determined as reported by Mshewa (1995) through the use of a wetted-wall column. During an experiment, liquid flows over a stainless steel tube with a known area producing a gentle flowing thin film. The liquid film contacts a saturated gas stream of carbon dioxide and nitrogen at absorption and desorption conditions. During the experiment, the gas phase is analyzed by a CO_2 analyzer after the gas stream passes through a condenser. The liquid phase is analyzed for total CO_2 concentration by total inorganic carbon analysis. The equilibrium gas solubility is determined where the flux of CO_2 between the liquid and gas phases is equal to zero.

In this work, we focused on accurately measuring the vapor-liquid equilibrium for the systems involving water (H_2O), monoethanolamine (MEA), piperazine (PZ), potassium carbonate (K_2CO_3) and carbon dioxide (CO_2). A number of investigators have measured the vapor-liquid equilibrium and CO_2 solubility for the above systems based on a variety of methods. In this work, we developed a closed-loop reactor utilizing a unique Fourier Transform Infrared (FT-IR) analyzer to determine the total H_2O, CO_2, and amine concentrations in the gas phase without the need to condense the vapor phase prior to the vapor phase analysis between 40 and 60 °C.

2.3 Chemicals

The chemicals used at NTNU included carbon dioxide (CO_2) (AGA, ≥ 99.99 % pure); nitrogen (N_2) (AGA, ≥ 99.999 % pure); monoethanolamine (MEA) (Acros Organics, 99 % pure); piperazine (PZ) (Fluka Chemie GmbH, ≥ 98.0 % pure); potassium carbonate (K_2CO_3) (Fluka Chemie GmbH, ≥ 99.0 % pure); and potassium bicarbonate ($KHCO_3$) (Sigma-Aldrich Inc., ≥ 99.5 % pure). All chemicals were used without any further purification.

Chemicals used at UT included CO_2 (Matheson Tri-Gas, ≥ 99.99 % pure); N_2 (Cryogenics Laboratory at The University of Texas at Austin, ≥ 99. % pure); MEA (Acros Organics, 99 % pure); PZ (Fluka Chemie GmbH, ≥ 98.0 % pure); K_2CO_3 (Fluka Chemie GmbH, ≥ 99.0 % pure); and $KHCO_3$ (Sigma-Aldrich Inc., ≥ 99.5 % pure). All chemicals were used without any further purification.

2.3.1 *Experimental Design*

In this work, we focused on accurately assembling a database of high quality and consistent vapor-liquid equilibrium data for the systems involving H_2O, MEA, PZ, K_2CO_3, and CO_2. Figure 2.3-1 illustrates the systems where CO_2 solubility and amine volatility were collected based on vapor-liquid equilibrium (VLE) experimental methods in this chapter. A detailed overview of our experimental design is given in Table 2.3-1.

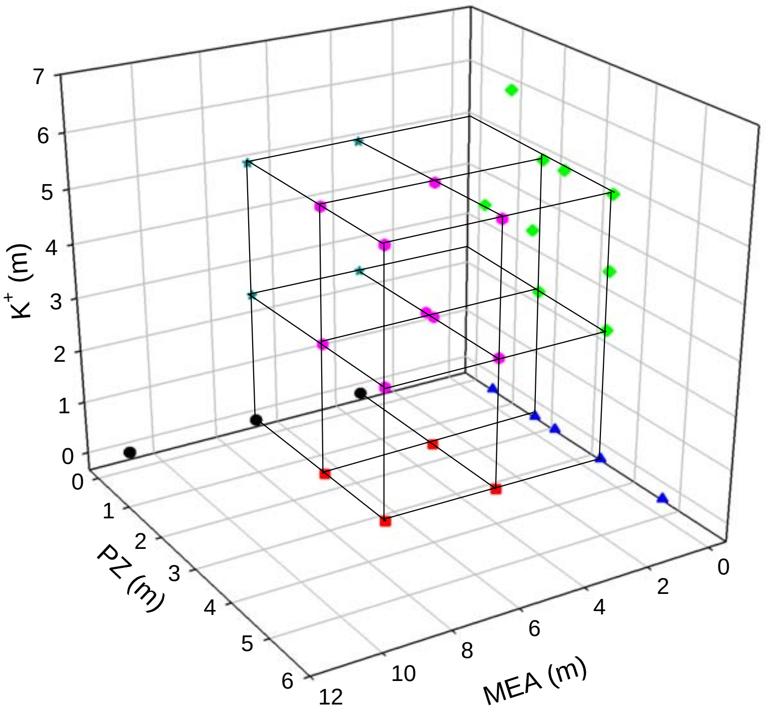

Figure 2.3-1. VLE Experimental Design for Loaded Solutions. Points: ●, H_2O-MEA-CO_2, ▲, H_2O-PZ-CO_2, ■, H_2O-MEA-PZ-CO_2, ♦, H_2O-K_2CO_3-PZ-CO_2, *, H_2O-K_2CO_3-MEA-CO_2, ●, H_2O-K_2CO_3-MEA-PZ-CO_2.

Table 2.3-1. VLE Experimental Design for Systems Studied in This Work.

MEA (m)	PZ (m)	K^+ (m)	MEA (m)	PZ (m)	K^+ (m)	MEA (m)	PZ (m)	K^+ (m)
7	0	0	0	2.5	5	7	0	2.5
3.5	0	0	0	2	2.5	7	0	5
11	0	0	0	3.6	2.5	7	3.6	5
0	0.9	0	0	1.2	6	7	2	5
0	2	0	0	2	5	3.5	1.8	2.5
0	2.5	0	3.5	3.6	0	3.5	3.6	5
0	3.6	0	3.5	2	0	3.5	2	5
0	5	0	7	3.6	0	7	3.6	2.5
0	0.6	3.6	7	2	0	7	2	2.5
0	1.8	3.6	3.5	0	5	3.5	3.6	2.5
0	3.6	3.6	3.5	0	2.5	3.5	2	2.5
0	3.6	5						

2.3.2 *Solution Preparation*

All solutions were prepared gravimetrically from deionized water (NTNU) or from ultra pure deionized water (UT). Amine solutions were loaded with CO_2 by slowly sparging pure CO_2 (~0.1 gm/10 sec) through a submerged fritted disk in the solution as shown in Figure 2.3-1. The CO_2 loader was placed on a top-loading scale (± 0.1 gm). As CO_2 reacted with the amine solution, the amount of CO_2 absorbed into the solution would then be displayed on the scale and would continue until the desired loading was reached. Amine solutions loaded with this technique produced CO_2 loadings within ± 5.0 % based on an analytical analysis of the loaded solution. Liquid samples containing bound CO_2 were analyzed for total CO_2 by the barium chloride method (NTNU) or by acidic evolution method (UT), respectively. The total alkalinity of the solution was determined by a standard monotonic endpoint sulfuric acid/sodium hydroxide titration analysis. Please refer to Appendix B and C for more information.

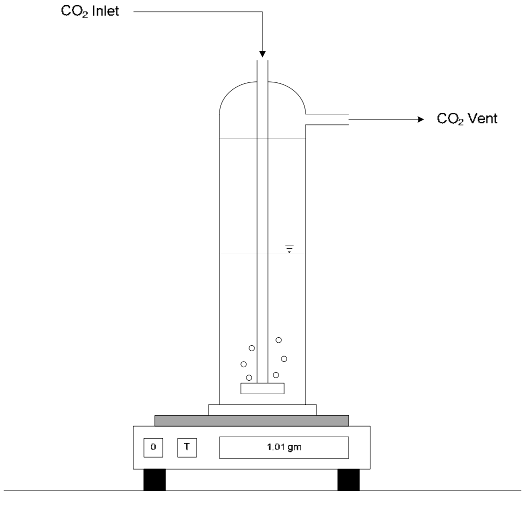

Figure 2.3-2. CO_2 Loading Apparatus.

Initial Experimental Solution Preparation

Cullinane (2005) reported solid-liquid equilibrium (SLE) for mixtures of potassium carbonate with piperazine and potassium bicarbonate with piperazine at 25 and 40 °C and theorized as to the composition of the solid phase, but did not investigate the solubility of loaded potassium carbonate, potassium bicarbonate, and piperazine mixtures. In this work, we were able to characterize the solid phase in loaded potassium-piperazine mixtures through x-ray diffraction, described in Chapter III, as potassium piperazine dicarbamate. To produce a homogenous solution of potassium and piperazine, all three components must be present in the initial "unloaded" mixture. Cullinane (2005) reported a criterion for precipitation of either potassium carbonate or potassium bicarbonate salt as the following:

$$0.5 < \frac{K_2CO_3(m) + KHCO_3(m)}{\left[2 \cdot K_2CO_3(m) + KHCO_3(m)\right] = K^+(m)} < 1.0 \qquad \text{2-1}$$

where if Equation 2-1 is near 0.5 the solid phase is likely potassium carbonate and if Equation 2-1 is near 1.0 the solid phase is likely potassium bicarbonate. Thus, possible experimental values to Equation 2-1 are described to produce a homogenous solution with respect to mixtures of potassium carbonate, potassium bicarbonate and/or piperazine, and monoethanolamine as described in Table 2.3-2, Table 2.3-3, and Table 2.3-4.

Table 2.3-2. Lean Homogenous Solution Compositions for MEA+K^+ (mole/kg-H_2O basis) Mixtures.

MEA (m)	K_2CO_3 (m)	$KHCO_3$ (m)	K^+ (m)	Equation 2-1
3.50	0.82	0.86	2.50	0.672
3.50	2.03	0.95	5.00	0.595
7.00	0.82	0.86	2.50	0.672
7.00	1.64	1.72	5.00	0.672

Table 2.3-3. Lean Homogenous Solution Compositions for MEA+PZ+K^+ (mole/kg-H_2O basis) Mixtures.

MEA (m)	PZ (m)	K_2CO_3 (m)	$KHCO_3$ (m)	K^+ (m)	Equation 2-1
3.50	1.80	0.36	1.79	2.50	0.857
3.50	2.00	0.75	1.00	2.50	0.700
3.50	2.00	1.50	2.00	5.00	0.700
3.50	3.60	0.30	1.89	2.50	0.879
7.00	2.00	0.75	1.00	2.50	0.700
3.50	3.60	0.61	3.79	5.00	0.879
7.00	2.00	0.61	3.79	5.00	0.879
7.00	3.60	0.29	1.92	2.50	0.885
7.00	3.60	0.58	3.85	5.00	0.885

Table 2.3-4. Lean Homogenous Solution Compositions for PZ+K^+ (mole/kg-H_2O basis) Mixtures.

PZ (m)	K_2CO_3 (m)	$KHCO_3$ (m)	K^+ (m)	Equation 2-1
0.60	1.58	0.43	3.60	0.560
2.00	0.34	1.82	2.50	0.864
1.80	1.01	1.58	3.60	0.720
1.20	2.54	0.91	6.00	0.576
2.00	1.64	1.72	5.00	0.672
3.60	0.37	1.77	2.50	0.854
2.50	1.62	1.75	5.00	0.675
3.60	0.72	2.16	3.60	0.800
3.60	0.87	3.26	5.00	0.826

It should be noted that the above solution compositions are only a small fraction of the total number of possible industrial combinations. We would recommend more work be taken to fully describe the solution behavior with respect to identifying where the phase splitting boundaries occur into possible salt-organic and salt-aqueous phases. Figure 2.3-3, Figure 2.3-4, and Figure 2.3-5 graphically illustrate the possible experimental values given in the above tables.

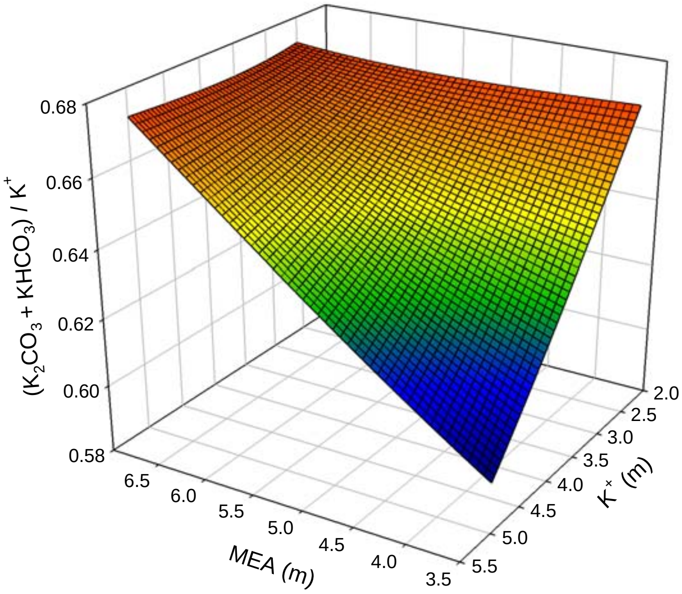

Figure 2.3-3. Lean Homogenous Solution Composition Surface for MEA+K$^+$ Mixtures.

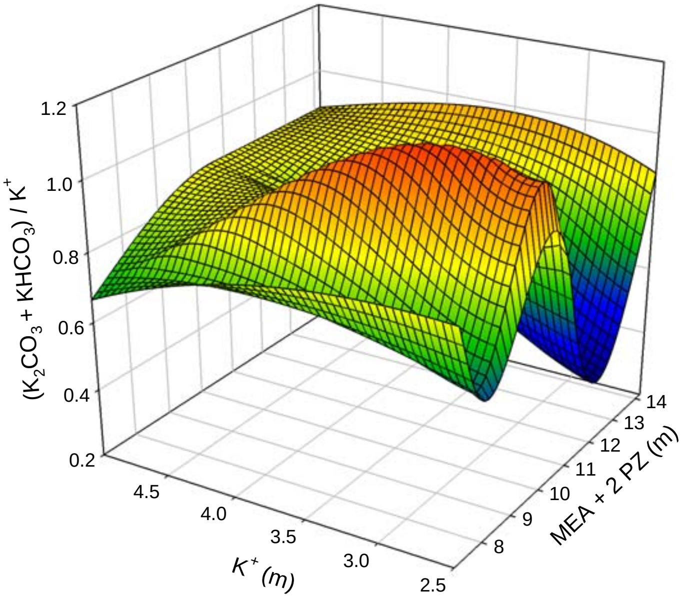

Figure 2.3-4. Lean Homogenous Solution Composition Surface for MEA+PZ+K$^+$ Mixtures.

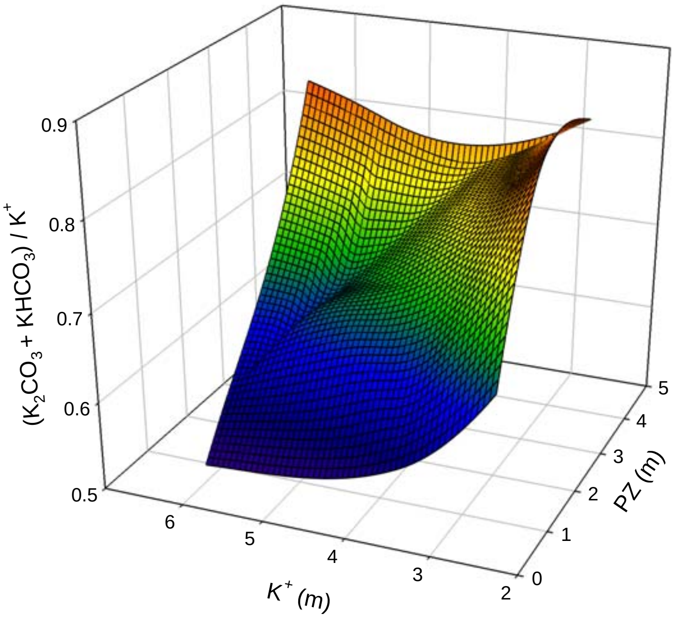

Figure 2.3-5. Lean Homogenous Solution Composition Surface for PZ+K⁺ Mixtures.

— Part One —

2.3.3 *High Temperature Apparatus (NTNU)*

The vapor-liquid equilibrium (VLE) apparatus consisted of three 300 cm^3 stainless steel cylinders containing the liquid solution operating in series with a circulating gas phase at a pressure of ~ 7 bar using N_2 as a diluent as shown in Figure 2.3-6 and Figure 2.3-7. A Fisher-Rosemount CO_2 IR analyzer determined continuously the total CO_2 concentration in the gas phase. A FieldPoint FP-1000 and FP-AI-110 data acquisition system recorded all operating conditions as a function of time.

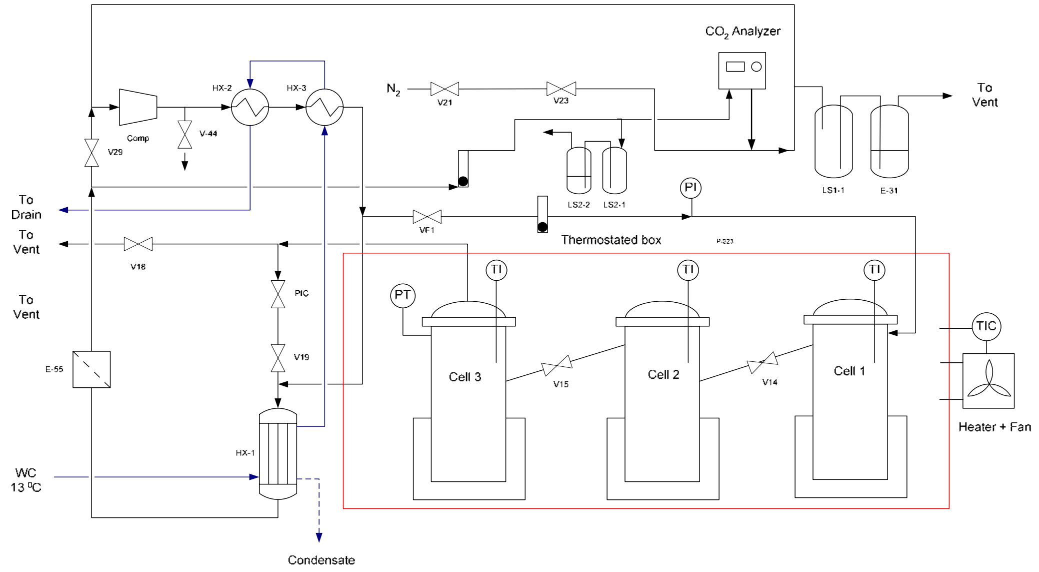

Figure 2.3-6. Process Flow Diagram for High Temperature Experiments, Vapor Phase.

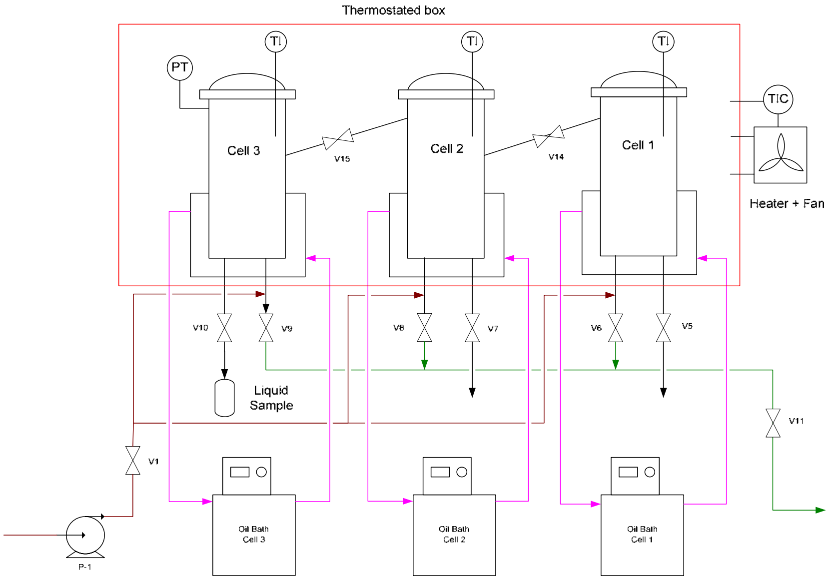

Figure 2.3-7. Process Flow Diagram for High Temperature Experiments, Liquid Phase.

Experimental Uncertainty

Experimental solubility data for CO_2 were measured from 80 to 120 °C with an expanded uncertainty of ± 0.5 °C. CO_2 loading was determined in two parallel liquid samples as described in Appendix B. The relative standard uncertainty in the loading estimated from the standard deviation of the loading measurements was ± 2.0 %. The CO_2 partial pressure was measured online with an IR analyzer, as mentioned previously, where the analyzer was calibrated at the start of everyday using AGA calibration gases of 0.5, 1.0, 2.5, 5.0, 10.0, 20.0, and 35.0 mole percent of CO_2/N_2 balanced with a relative standard uncertainty of ± 2.0 %. The calibration gases were then used to create a polynomial correlation between the IR voltage (mV) versus the precent CO_2 concentration and was then input into the FieldPoint data acquisition system for online CO_2 analysis. An example CO_2 calibration curve is shown in Figure 2.3-8. The estimated relative expanded uncertainty in the CO_2 partial pressure was then estimated to be ± 2.0 %.

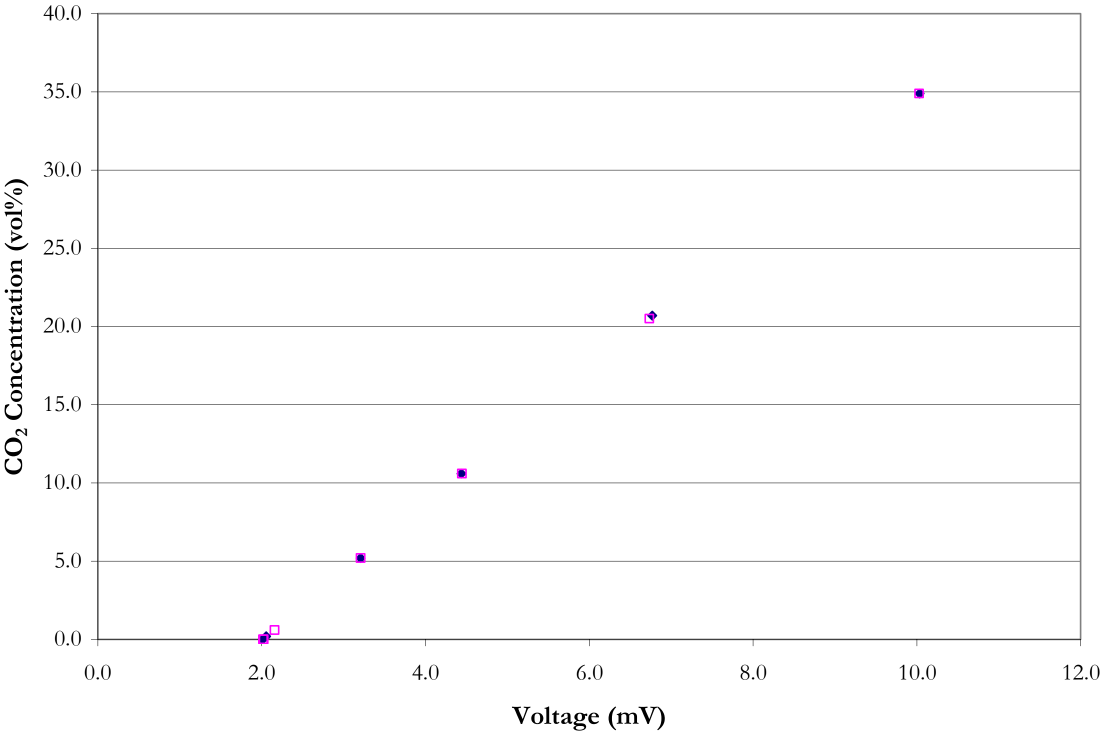

Figure 2.3-8. Example CO_2 Calibration Curves for 04/27/2005 - 06/17/2005. Points: ♦, 04/27/2005, □, 06/17/2005.

Experimental Procedure

During an experiment, three 300 cm^3 stainless steel cylinders (equilibrium cells 1, 2, and 3) containing 200/150/150 cm^3, respectively, were filled with a known amount of preloaded sample solution. The cells were located within a thermostated box where the temperature of each cell was measured within ±0.1 °C and controlled through the use of three separate oil baths. Initially, the cells were pressurized to 300 kPa to minimize vaporization of the loaded solution during the initial heating of the apparatus. When the experimental temperature was reached (approximately two to three hours), the system was then pressurized to 700 kPa and the vapor phase was allowed to circulate. Equilibrium was obtained when the temperature, CO_2 concentration in the vapor phase, and the equilibrium pressure were constant. This process normally took fifteen to thirty minutes. When equilibrium was achieved, a 75 cm^3 liquid sample was withdrawn from cell 3 into an evacuated sampling cylinder and then allowed to cool to ambient temperature before the sample was removed and analyzed. The CO_2 loading analysis was performed by using two parallel liquid samples each titrated for CO_2 and total alkalinity, using barium carbonate precipitation and a standard monotonic endpoint titration with 0.1 N sulfuric acid, respectively. The relative standard uncertainty in the loading was ± 2 %. Please refer to Appendix B for more information.

During the experiment, the circulating vapor was dried prior to CO_2 analysis by condensing both water and then amine. Through liquid analysis, it was found that the water condensate collected from the vapor bleed stream during the experiment did contain trace amounts of dissolved CO_2 and amine. This implied CO_2 was absorbing into the aqueous amine condensate as the gas stream passed over the condensing coils during the experiment and all of the CO_2 was not entering into the CO_2 analyzer, thus adding a systematic error to the solubility measurements. Through a mass balance around the condenser, it was found that this systematic error would only have a significant effect on measurements that exhibited a low partial pressure of CO_2 (<0.01 bar).

For solutions containing piperazine plus potassium carbonate, the loading of the CO_2 in the water condensate to the "dry" partial pressure of CO_2 was represented in this work by the following equation:

$$Ldg^{cond}\left(\frac{\text{mol CO}_2}{\text{mol PZ}}\right)=0.6913+0.0498\cdot\ln\left(P_{CO_2}^{dry}\right)-0.0163\cdot\left(\frac{\text{mol K}^+}{\text{mol PZ}}\right) \qquad 2\text{-}2$$

Where
Ldg^{cond} is the loading of the water condensate, mole CO_2/mole PZ,
$P_{CO_2}^{dry}$ is the experimental "dry" partial pressure of CO_2, kPa,
mol K^+/mol PZ is the ratio of the nominal molality of potassium and piperazine in the experimental solution.

With the determination of Equation 2-2, we could then calculate the actual CO_2 concentration before the vapor was dried and apply this systematic correction to our measurements where the partial pressure of CO_2 was less than 0.01 bar.

For solutions containing monoethanolamine plus piperazine, a similar correlation to Equation 2-2 was not possible. Therefore, in this work, experimental data points from the NTNU high temperature VLE apparatus with partial pressures of CO_2 below 0.01 bar should be treated with caution or excluded.

– Part Two –

2.3.4 *Low Temperature Apparatus (UT)*

The vapor-liquid equilibrium (VLE) apparatus consisted of a 1000 cm^3 jacketed glass reactor containing the liquid solution with a circulating gas phase at atmospheric pressure using N_2 as a diluent as shown in Figure 2.3-9. A portable Temet Gasmet Dx-4000 Fourier Transform Infrared (FT-IR) analyzer determined continuously the total H_2O, CO_2, and amine concentrations in the gas phase. CALCMET^{TM} and PicoLog data acquisition systems recorded all operating conditions as a function of time.

Experimental Uncertainty

For each experiment, a 1000 cm^3 jacketed glass reactor was filled with approximately 500 cm^3 of a known amount of preloaded sample solution. The reactor was insulated to minimize heat losses to the environment and the temperature of the reactor was controlled within ±0.1 °C by circulating di-methyl silicone oil 200/50 cS purchased from Krayden Inc. as the thermostatting liquid. The system continuously measured the vapor phase compositions and the reactor temperature and pressure, respectively. All operating conditions as a function of time were recorded using CALCMET^{TM} (v4.48) and PicoLog Recorder (v5.10.7). The pressure in the reactor was measured by a PTX-610 pressure transducer (Druck Inc.) with a working range from zero to eight bar with an accuracy of ± 0.08 % of full scale.

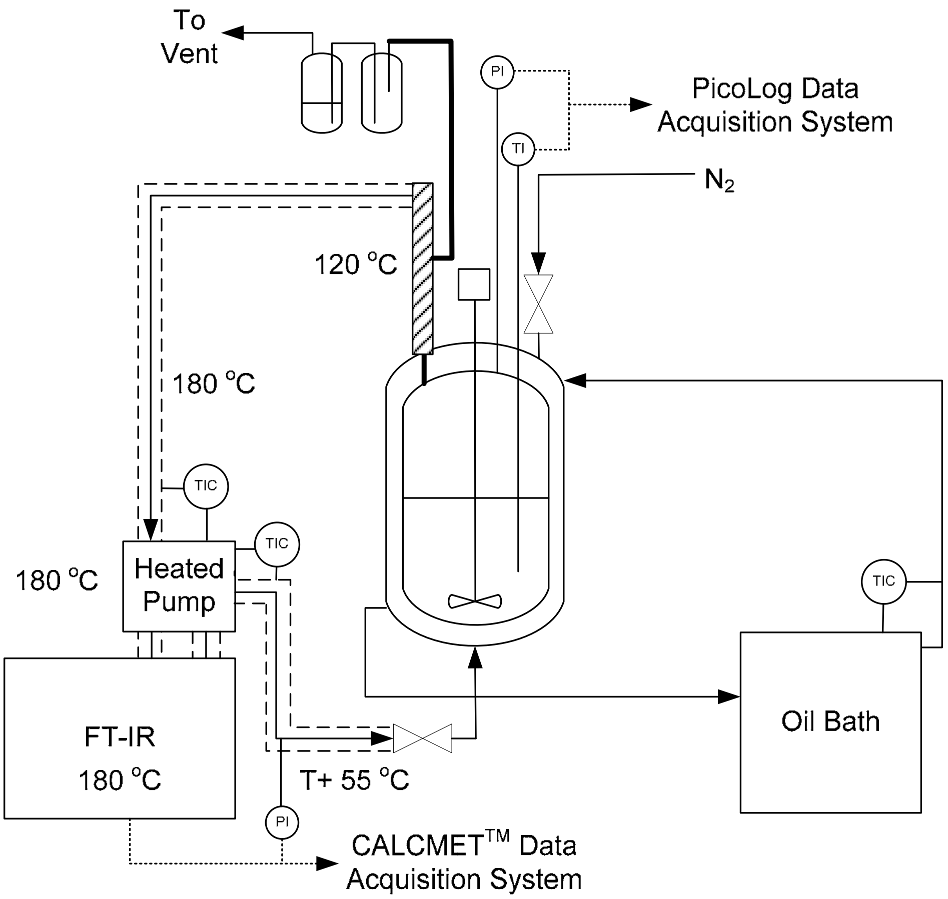

Figure 2.3-9. Process Flow Diagram for Low Temperature Experiments.

The temperature inside the reactor was measured with a platinum resistance thermometer with an accuracy of ± 0.01 °C. The temperature in the sample feed line was operated at 180 °C and the temperature in the sample return line was operated at the system temperature of interest plus 55 °C. Gas phase analysis was performed using a DX-4000 portable Temet Gasmet FT-IR spectrometer with a ten meter gas cell path length operated at 180 °C with a working pressure range from zero to two bar with a measured accuracy of ± 3.0 % of full scale. The vapor phase concentrations were measured online with an FT-IR analyzer, as mentioned previously, where the calibration of the analyzer has been described previously by

Goff (2005) – Section 3.3.1.3. Goff (2005) estimated relative expanded uncertainty in the vapor phase concentration to be ± 2.0 %. For liquid samples, the CO_2 loading was determined in two parallel liquid samples as described in Appendix C. The relative standard uncertainty in the loading estimated from the standard deviation of the loading measurements was ± 2.0 %.

Experimental Procedure

Before starting the experiment, N_2 was flushed through the apparatus to purge the air within the heated samples lines and the FT-IR. Then, the solution reservoir was filled with the experimental solution and approximately 500 grams of the experimental solution was transferred to the reactor. The heated samples lines were then connected to the apparatus and the apparatus was sealed. The solution reservoir was weighed to determine the exact amount of solution transfer. The reactor is equipped with an agitator comprised of a ten millimeter stainless steel stir shaft with a single five centimeter propeller. The nominal agitation rate during the experiments was 350 ± 5 rpm. N_2 was introduced into the system and the system was allowed to circulate. The N_2 was then turned off after approximately forty seconds. Equilibrium was obtained in approximately one and a half to two hours which was determined by observing when the temperature measurement had stabilized to within 0.05 °C. When equilibrium was achieved, a 30 cm^3 liquid sample was withdrawn from the reactor into a sample vial and then allowed to cool to ambient temperature before a sample of the experimental solution was removed and analyzed. CO_2 loading was performed by using two parallel liquid samples each titrated for CO_2 and total alkalinity, using acidic evolution and a standard monotonic endpoint titration with 0.1 N sulfuric acid, respectively.

The relative standard uncertainty in the loadings was ± 2 %. Please refer to Appendix C for more information.

2.3.5 *Multiple Component Analysis*

To determine the composition of a gas stream vis-à-vis FT-IR analysis, each compound (e.g. CO_2) must exhibit a net dipole moment which allows the compound to undergo a transition in its vibrational or rotational energy levels when exposed to IR radiation. Homo-nuclear diatomic compounds (e.g. N_2) which do not exhibit a net dipole moment are said to be IR inactive since the compounds do not absorb IR radiation over the entire IR region. N_2 was used in this work as a carrier gas or as a diluent due to its IR inactive nature.

The Temet Gasmet FT-IR analyzer utilizes a software package called CALCMET to quantitatively determine the concentration of each compound using the Beer-Lambert law to transform the transmittance spectrum from the FT-IR to an absorbance spectrum. A multiple least squares algorithm, based on the work of Saarinen and Kauppinen (1991), was used to solve for the unknown absorbance spectra based on reference spectra over a range of specific concentrations for each compound in the unknown spectra. In 2005, Goff (2005) created a method for analyzing multiple compounds in a vapor stream to quantify oxidative degradation in aqueous monoethanolamine solutions. Goff (2005) quantified vapor phase concentrations between 0.15 to 1.0 volume percent of CO_2 while in the presence of the following possible compounds: H_2O, carbon monoxide, nitrous oxide, nitrogen monoxide, nitrogen dioxide, ammonia, formaldehyde, acetaldehyde, MEA, PZ, methanol, methylamine, and methane.

In this work, we utilized the base method of Goff (2005) and optimized for a range of CO_2 and MEA concentrations by creating three unique analysis methods: for low concentrations of CO_2 (50 ppm_v to 15,000 ppm_v), medium concentrations of CO_2 (15,000 ppm_v to 30,000 ppm_v), and high concentrations of CO_2 (3.0 – 50 vol%). Figure 2.3-10 illustrates the possible analysis region for CO_2.

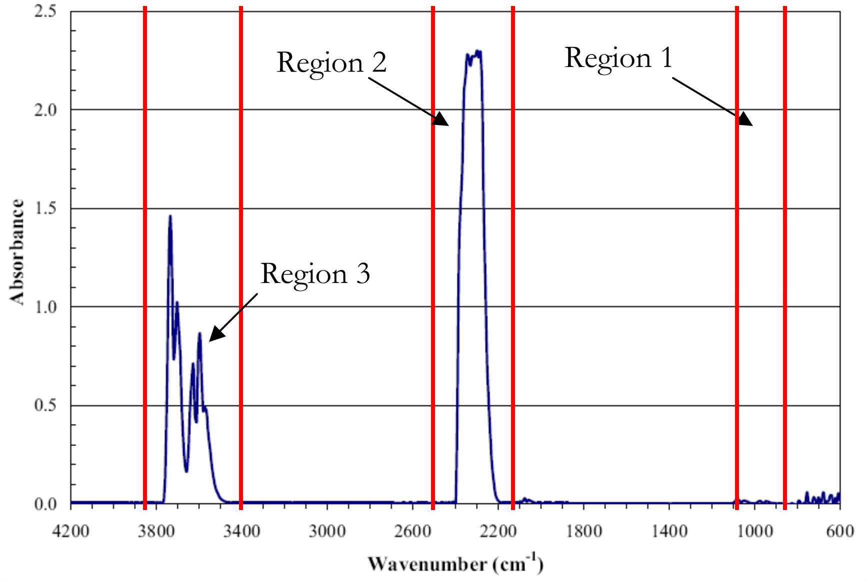

Figure 2.3-10. CO_2 Reference Spectrum (3.0 volume % or 30,000 ppm_v) as Presented by Goff (2005).

Region 1 described the symmetric stretch of a CO_2 molecule due to absorbance of IR radiation. Region 2 describes the asymmetric stretch and Region 3 describes the unresolved symmetric stretch. At low CO_2 concentrations, only Regions 2 and 3 contain enough information to be included in the analysis method. Region 3, due to the nonlinear absorbance nature of the unresolved symmetric stretch makes the analysis region difficult to optimize above CO_2 concentrations of 15,000 ppm_v. In addition, above 15,000 ppm_v Region 3 starts to saturate the IR detector (absorbance $\geq$ one). As the CO_2 concentration increases to levels above 15,000 ppm$_v$, Region 1 absorbs enough IR radiation to aid in the analysis method, but for concentrations above 30,000 ppm$_v$ Region 2 starts to saturate the IR detector and Region 1 becomes the main source of information.

To properly resolve the concentration of CO_2, different analysis areas or wavenumber regions were optimized for each method. Table 2.3-5 gives the analysis areas used in this work for the determination of CO_2. Please note: CO_2 was the only compound that required multiple methods over the entire range of concentrations. Please refer to Appendix D for more information on each method with respect to other compounds.

Table 2.3-5. Analysis Regions for Low, Medium, and High CO_2 Concentrations.

Concentration Range	Region One		Region Two		Region Three		Num. Of References
50 - 15,000 ppm$_v$	-	-	1984	2169	2207	2501	9
15,000 - 30,000 ppm$_v$	910	1019	1984	2169	-	-	9
3.0 – 50 vol%	910	1019	1984	2169	-	-	10

Based on calibration procedures reported by Geoff (2005), additional MEA reference spectra were included in the analysis methods to properly resolve the concentrations of MEA measured in this work. Analysis regions determined by Geoff (2005) for MEA [Region One: 980-119 cm^{-1}, Region Two: 2624-3150 cm^{-1}] did not require further optimization. Table 2.3-6 gives additional MEA reference spectra used in this work to supplement the base analysis method created by Geoff (2005).

Table 2.3-6. MEA Reference Spectra Required for Proper MEA Resolution.

Source	MEA Reference Spectra (ppm$_v$)
Geoff (2005)	500
This work	100, 500, 1,000, 2,000, 5,000, 10,000, 15,000

Analysis regions and reference spectra determined by Geoff (2005) for PZ [Region One: 1096-1380 cm^{-1}, Region Two: 1810-2223 cm^{-1}, Region Three: 2550-3095 cm^{-1}] did not require further optimization. Table 2.3-7 gives PZ reference spectra used in this work to base on analysis method created by Geoff (2005).

Table 2.3-7. PZ Reference Spectra Required for Proper PZ Resolution.

Source	PZ Reference Spectra (ppm_v)
Geoff (2005)	2, 40, 105, 188, 407, 471

2.3.6 *Low Temperature Apparatus Benchmarking*

Benchmarking the low temperature apparatus, in terms of validating the experimental vapor pressures against key literature sources, was completed in two phases: phase one: pure component vapor pressures for H_2O and MEA against pure component DIPPR correlations, and phase two: comparison of CO_2 solubility measurements for 7 m (mole/kg-H_2O) MEA and 2 m PZ against Jou et al. (1995) and Ermatchkov et al. (2006), respectively. Within each phase, the analysis method was optimized due to interferences between additional compounds present in the vapor phase. Overall, the reported methods in Appendix D adequately represent experimental vapor phase compositions for the H_2O-MEA-PZ-K_2CO_3-CO_2 system and all sub-systems tested in this work.

2.4 Experimental Results

2.4.1 *Pure H_2O System*

We chose water as the first system to be testing in the Low Temperature VLE Apparatus (UT) due to the large volume of literature reporting the pure component vapor pressure. We chose to benchmark our results against correlations from the DIPPR Physical and Thermodynamic Properties database [Rowley et al. (1994)] as shown in Figure 2.4-1.

Figure 2.4-1 illustrates experimental results from this work as compared to accepted literature values reported by Kell et al. (1984). Kell et al. (1984) reported a relative standard uncertainty in the vapor pressure equal to < 0.2 %. Overall, the low temperature VLE apparatus (UT) represents the vapor pressure of water within an average absolute relative deviation (AARD) of ± 4.40 % with the exception of a few outliers.

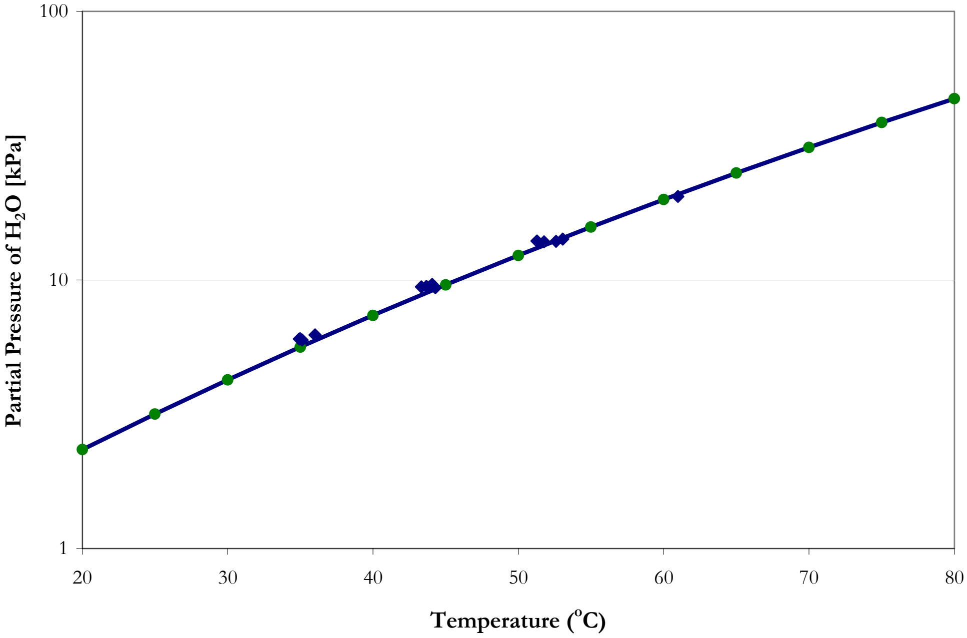

Figure 2.4-1. Vapor Pressure of Water. Points: ●, Kell et al. (1984), ♦, this work. Lines: DIPPR Correlation.

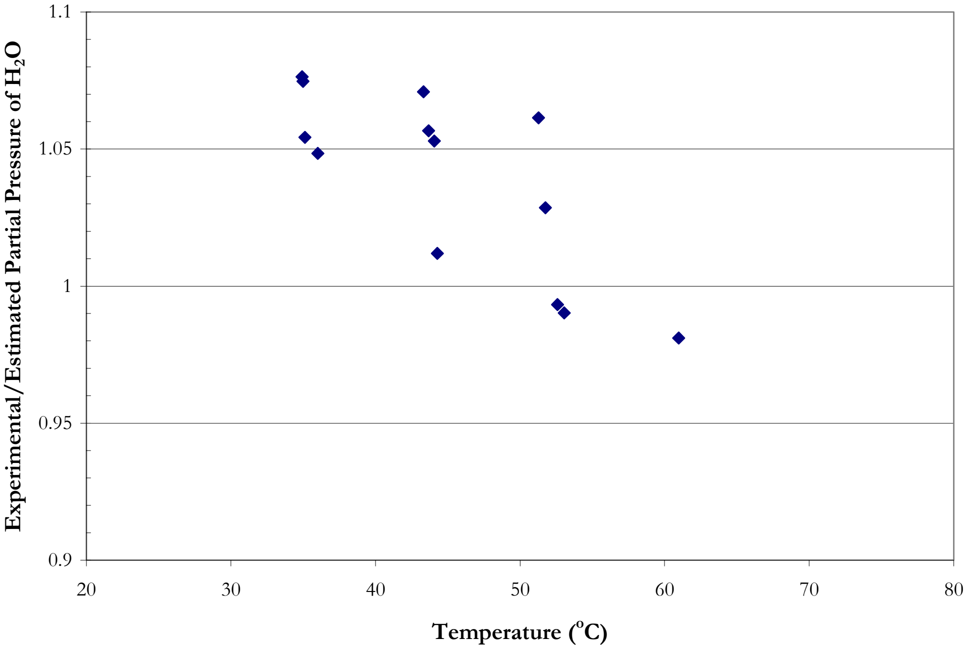

Figure 2.4-2. Comparison of Experimental Vapor Pressure Measurements To Predictions from DIPPR Correlations Based on the work of Kell et al. (1984).

Since the uncertainty associated with low temperature vapor pressure analysis is ± 2.0 %; we felt that an experimental AARD of ± 4.40 % was acceptable as compared to estimated predictions from the DIPPR correlation based on the work of Kell et al. (1984) as shown in Figure 2.4-2.

2.4.2 *Pure MEA System*

We chose MEA as the second system to be tested in the Low Temperature VLE Apparatus (UT) due in addition to the large volume of literature information available for the pure component vapor pressure. We chose to benchmark our results against correlations from the DIPPR Physical and Thermodynamic Properties database [Rowley et al. (1994)] as shown in Figure 2.4-3.

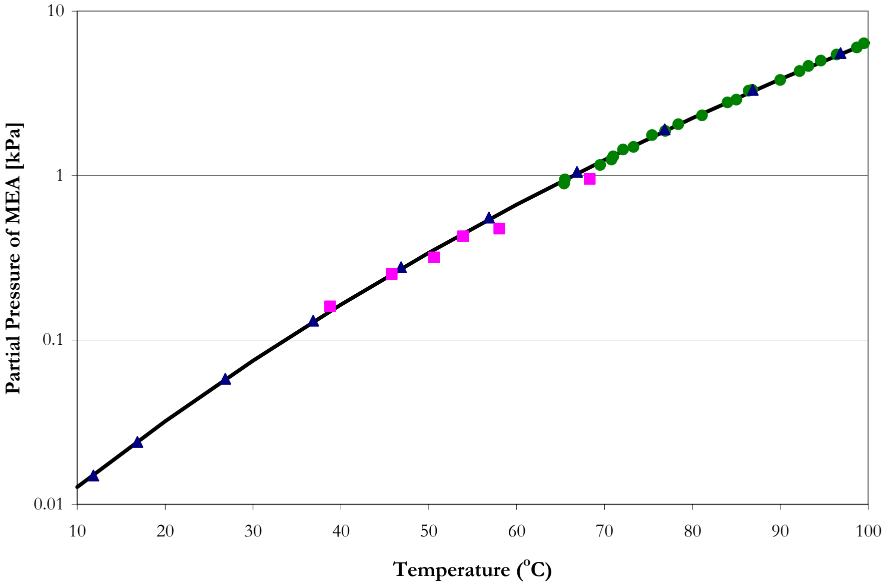

Figure 2.4-3. Vapor Pressure of MEA. Points: ●, Matthews et al. (1950), ♦, Engineering Sciences Data (1979), ■,this work. Lines: DIPPR Correlation.

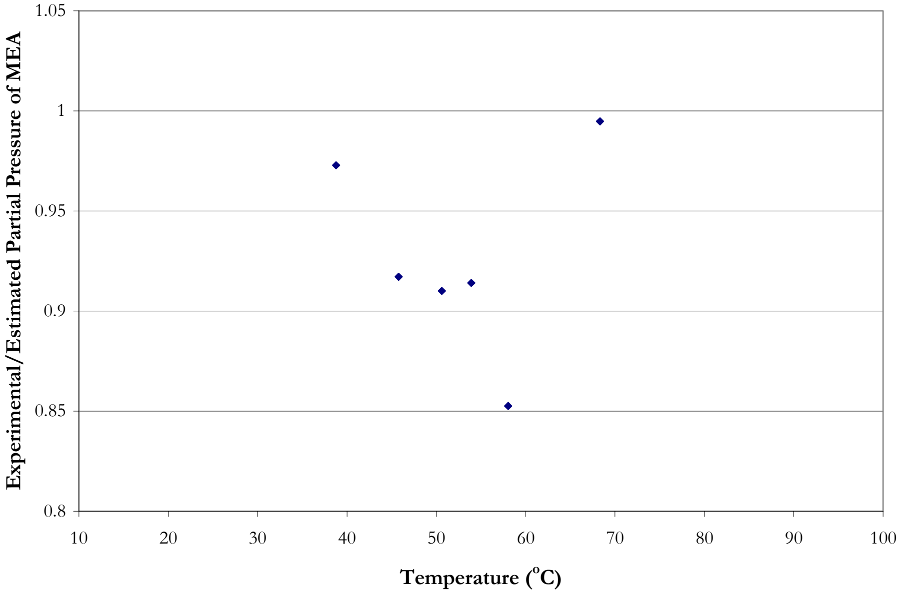

Figure 2.4-4. Comparison of Experimental Vapor Pressure Measurements To Predictions from DIPPR Correlations Based on the work of Matthews et al. (1950) and Engineering Sciences Data (1979).

Figure 2.4-3 and Figure 2.4-4 illustrate experimental results from this work as compared to accepted literature values reported by Matthews et al. (1950) and Engineering Sciences Data (1979). DIPPR reports a relative standard uncertainty in the vapor pressure correlation to < 10.0 % error. Overall, the low temperature VLE apparatus (UT) represents an adequate measurement of the vapor pressure of MEA within an AARD of ± 7.31 % with the exception of a few outliers.

2.4.3 *H_2O-MEA-CO_2 Systems*

For systems involving the measurement of CO_2 solubility, we chose H_2O-MEA-CO_2 for comparison in the Low Temperature VLE Apparatus (UT) against literature data from Jou et al. (1995) for 7 m or 30 wt% MEA as shown in Figure 2.4-5.

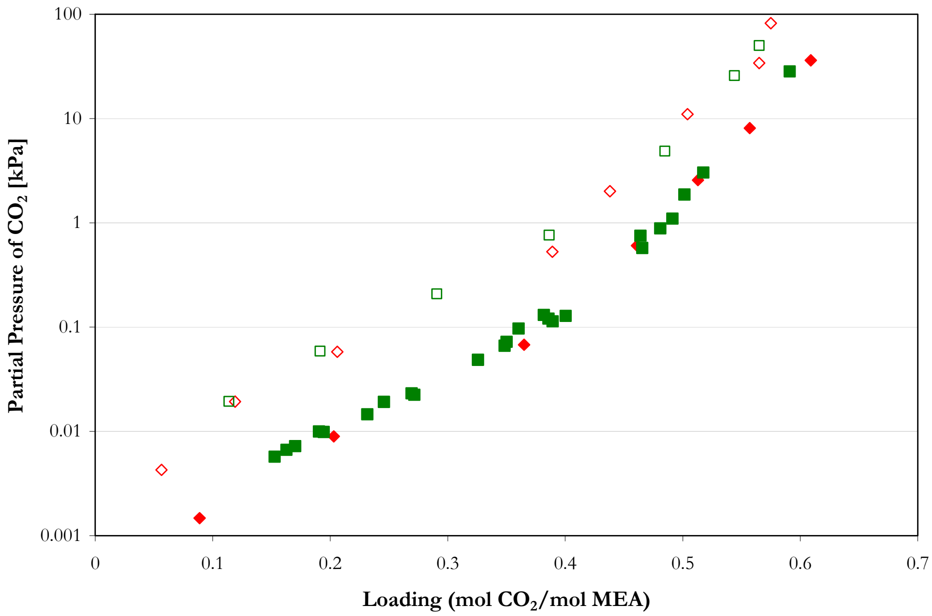

Figure 2.4-5. CO_2 Solubility Comparison in 7 m MEA at 40 and 60 °C. Solid Points - 40 °C: ♦, Jou et al. (1995), ■, this work. Open Points – 60 °C: ◊, Jou et al. (1995), □, this work.

Figure 2.4-5 illustrates that experimental results from this work are consistent with reported CO_2 solubility measurements from Jou et al. (1995) at 40 and 60 °C with respect to the experimental loading and partial pressure of CO_2.

2.4.4 *H_2O-PZ-CO_2 Systems*

We chose H_2O-PZ-CO_2 as our next system tested in the Low Temperature VLE Apparatus (UT) against CO_2 solubility data from Ermatchkov et al. (2006) for 2 m PZ as shown in Figure 2.4-6. However, Bishnoi and Rochelle (2000), Aroua and Mohd (2003), and Derks et al. (2005) have reported CO_2 solubility in aqueous solutions of PZ at low concentrations from 0.2 and 0.6 kmol/m^3, but were too low for industrial applications studied in this work.

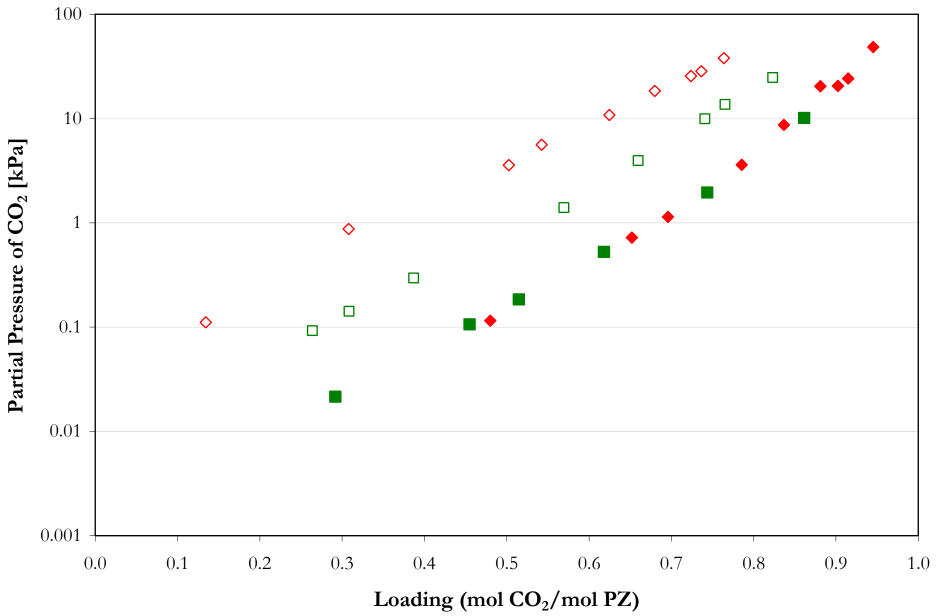

Figure 2.4-6. CO_2 Solubility Comparison in 2 m PZ at 40, 60, and 80 °C. Solid Points - 40 °C: ♦, Ermatchkov et al. (2006), ■, this work. Open Points: ◊, Ermatchkov et al. (2006) at 80 °C, □, this work at 60 °C.

Figure 2.4-6 illustrates experimental results from this work are consistent with reported CO_2 solubility measurements from Ermatchkov et al. (2006) at 40 °C with respect to the experimental loading and partial pressure of CO_2.

2.5 Conclusions

To sum up, in this work we have developed a new vapor-liquid equilibrium apparatus to measure vapor phase speciation at low temperatures. We have shown that experimental results are consistent and agree with key literature data. In addition we have been able to demonstrate a possible procedure to develop homogenous solutions with respect to mixtures of potassium carbonate, potassium bicarbonate and/or piperazine and monoethanolamine. We recommend that more work should be done to fully understand and describe the solution behavior with respect to identifying where the phase splitting boundaries occur for these solutions. Overall, the presented vapor-liquid equilibrium methods provide an opportunity for future work to contribute a deeper understanding into the composition of vapor phase speciation for several aqueous phase solutions.

CHAPTER III

Liquid Phase Speciation - NMR Methods

3.1 Introduction

This chapter details the experimental methods used to measure liquid phase speciation of alkanolamine solutions utilizing nuclear magnetic resonance (NMR) spectroscopy. The chapter will describe the low temperature NMR spectroscopy measurements (27 - 60 ^{o}C) performed at The University of Texas at Austin in Austin, Texas, USA. The experiments were carried out by Willian and Sorey (2007). NMR spectroscopy provides a glimpse into the solution composition vis-à-vis speciation at a unique moment where the "composition" of the solution can determined while refining the understanding of solution thermodynamics.

3.2 Literature Review

To describe the thermodynamics taking place in the liquid phase would require the ability to study the individual species present in a solution. NMR spectroscopy does not allow the individual species concentrations to be determined but does allow specific combinations of ionic and molecular species to be determined. Several previous investigations have been performed to understand solution speciation in loaded alkanolamine solutions:

Systems	NMR Method	Source
MEA, MAE, EAE, BEA, and MDEA	^{13}C	Suda et al. (1996)
DEA, DGA, and DIPA	^{13}C	Barth et al. (1984)
PZ	^{1}H and ^{13}C	Bishnoi and Rochelle (2000)
MEA	^{1}H	Wang (2001)
PZ	^{1}H	Ermatchkov et al. (2003)
BEA, MEA, and MDEA	^{13}C	Poplsteinova (2004)
PZ and K_2CO_3	^{1}H	Cullinane (2005)

where MAE: 2-methylamino-ethanol, EAE: 2-ethylamino-ethanol, BEA: buthylethanolamine, MDEA: N-methyldiethanolamine, DEA: Diethanolamine, DGA: Diglycolamine, and DIPA: Diisopropanolamine.

Several of the above investigations utilized NMR to verify or determine thermodynamic properties associated with specific systems. Suda et al. (1996) and Bishnoi and Rochelle (2000) identified peaks associated with the carbamate, carbonate/bicarbonate, and free/protonated amine within the NMR spectra and the areas of each peak were utilized in the determination of a carbamate stability constant. Wang (2001), Ermatchkov et al. (2003), Poplsteinova (2004), and Cullinane (2005) reported liquid phase NMR speciation data based on a broad range of concentrations and temperatures.

In this work, we focused on accurately measuring and verifying the NMR speciation for systems involving water (H_2O), monoethanolamine (MEA), piperazine (PZ), and carbon dioxide (CO_2). We also conducted a sensitivity analysis on the concentration of 1,4-dioxane as an internal standard and on the concentration of deuterium oxide (D_2O) as an NMR resonance lock for field stabilization to prevent the NMR signal of the sample from being swamped by that of the solvent.

3.3 Chemicals

The chemicals employed: carbon 13 (C^{13}) carbon dioxide (CO_2) (Cambridge Isotopes, ≥ 99.99% pure), ethanolamine (MEA) (Acros Organics, 99% pure), piperazine (PZ) (Fluka Chemie GmbH, ≥ 98.0% pure), and 1,4-dioxane (Fisher, ≥ 99.9% pure, CAS#: 123-91-1) were used without any further purification. The amine solutions were prepared from ultra pure deionized water and deuterium oxide (D_2O) (Cambridge Isotopes, ≥ 99.99% pure) by weight.

3.4 Sample Preparation

All solutions were prepared gravimetrically from ultra pure deionized water. Amine solutions were loaded with CO_2 by slowly sparging C^{13} CO_2 through a submerged fritted disk in the solution as shown in Figure 3.4-1. The CO_2 loader (~5 ml capacity) was custom made by Ronalter (2007). The empty CO_2 loader was placed on an analytical scale (± 10 μg) and weighed and approximately 5 ml of solution was then transferred to the loader where the entire apparatus was weighed again to determine the exact amount of solution in the CO_2

loader. The CO_2 loader was then attached to a C^{13} CO_2 cylinder and the gas was allowed to react with the amine solution for approximately 2 minutes. The apparatus was weighed again to determine the amount of CO_2 absorbed into the solution by difference. This procedure would then be repeated until the desired loading was reached.

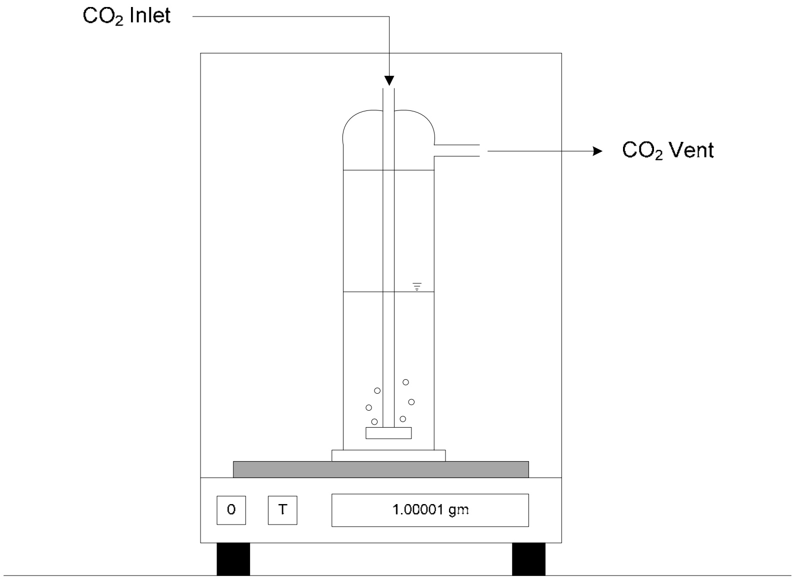

Figure 3.4-1. CO_2 Loading Apparatus.

3.5 Molecular Structures and Active Nuclei

In NMR the structure and functional groups of a molecule contribute to the way the molecule will behave when placed in a magnetic field. Each type of active nuclei depends upon the environment the nuclei are exposed to in terms of the solvent or the presence of other species within a magnetic field. When a molecule is placed in a magnetic field with active nuclei, distinct magnetic energy levels are formed by the absorption of energy by varying the magnetic field at a constant frequency. An NMR spectrum is then a plot of the absorbance energy by a molecule as a function of the frequency. This frequency has units of

PPM relative to the operating frequency of the NMR spectrometer and is commonly referred to as the chemical shift, δ. In this section, the molecular structures for each species that are present in this study have been identified and the active nuclei (proton or carbon) for each molecule have been labeled accordingly.

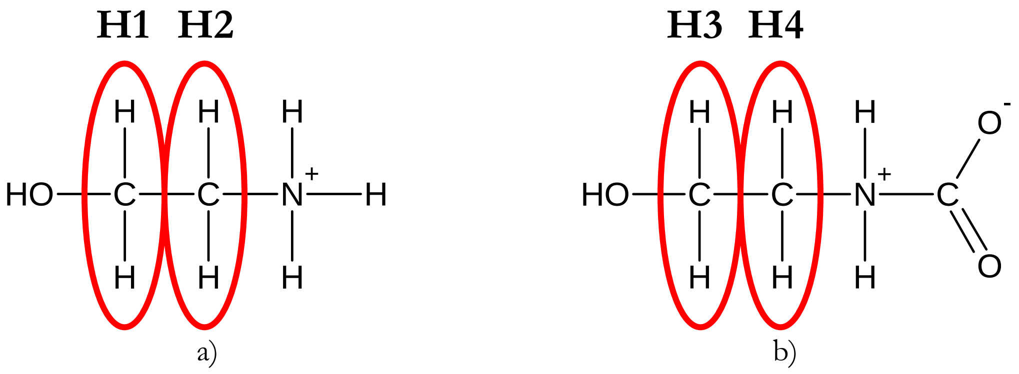

a) b)

Figure 3.5-1. Molecular structure and active nuclei of protons associated with a) MEA and $MEAH^+$ and b) $MEACOO^{-1}$.

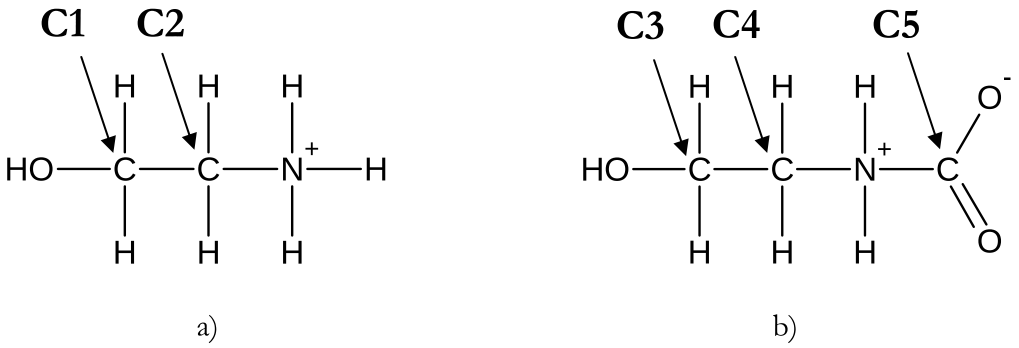

a) b)

Figure 3.5-2 Molecular structure and active nuclei of carbons associated with a) MEA and $MEAH^+$ and b) $MEACOO^{-1}$.

Figure 3.5-1 and Figure 3.5-2 illustrate the molecular structures of MEA, protonated monoethanolamine ($MEAH^+$), and monoethanolamine carbamate ($MEACOO^{-1}$). Protons and carbons associated with MEA and $MEAH^+$ cannot be separated due to time constant associated with the protonation chemical reaction of MEA, but the protons not involved in the chemical reaction (H1 and H2) and the carbons associated (C1 and C2) can be distinguished due to the deshielding effects by the hydroxyl group causing the active nuclei to absorb at higher frequencies. Typical substituent groups in order of increasing field effects (i.e. smaller δ values) are:

$$-OR > -OH > -NR_2 > -NHR > -NH_2$$

Protons (H3 and H4) and carbons (C3 and C4) associated with $MEACOO^{-1}$ differ from chemical shifts associated with $MEA/MEAH^+$ due to the deactivating effect that the carboxyl group attached to the nitrogen has on alpha carbons and beta protons.

With respect to piperazine species, Figure 3.5-3 through Figure 3.5-8 illustrate the molecular structures of PZ, protonated piperazine (PZH^{+1}), piperazine carbamate ($PZCOO^{-1}$), piperazine dicarbamate ($PZ(COO^{-1})_2$), and protonated piperazine carbamate (H^+PZCOO^{-1}). Protons and carbons associated with PZ and PZH^+ can not be separated due to time constant associated with the protonation chemical reaction of PZ, but the protons not involved in the chemical reaction (H5) and the carbons associated (C6) can be distinguished as a single peak. Protons (H6 and H7) and carbons (C7 and C8) associated with $PZCOO^{-1}$ differ from chemical shifts associated with PZ/PZH^+ due to the deactivating effect that the carboxyl group attached to the nitrogen has on the alpha carbon and beta protons, resulting in two distinguishable peaks.

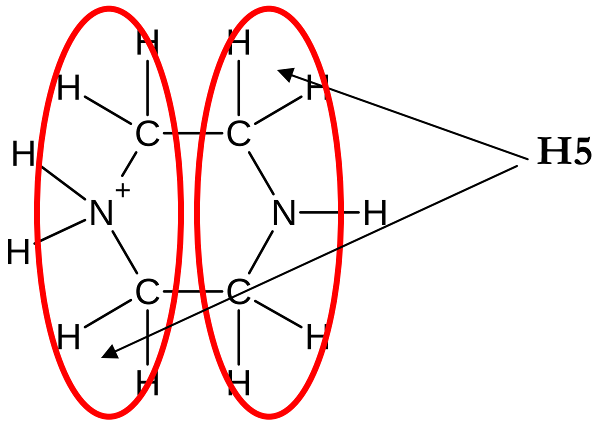

Figure 3.5-3 Molecular structure and active nuclei of protons associated with a) PZ and PZH^+.

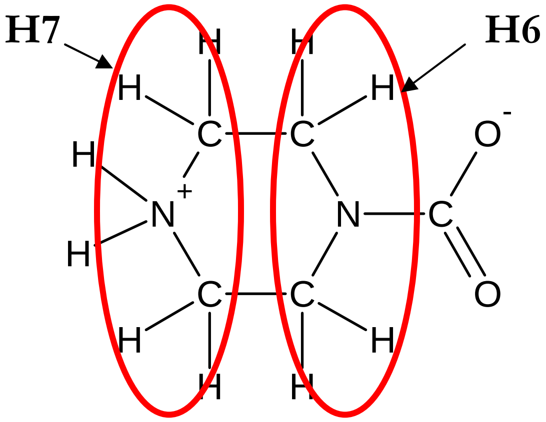

Figure 3.5-4 Molecular structure and active nuclei of protons associated with $PZCOO^-$ and H^+PZCOO^{-1}.

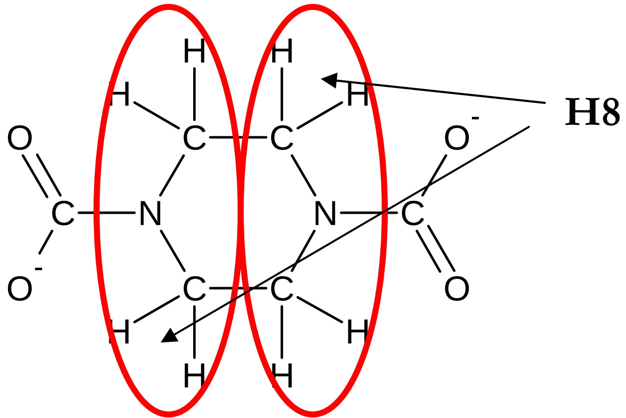

Figure 3.5-5 Molecular structure and active nuclei of protons associated with $PZ(COO^-)_2$.

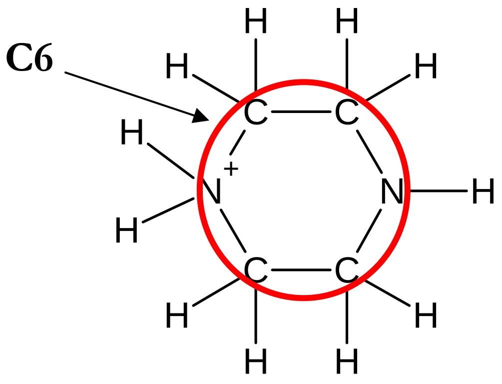

Figure 3.5-6 Molecular structure and active nuclei of carbons associated with PZ and PZH$^+$.

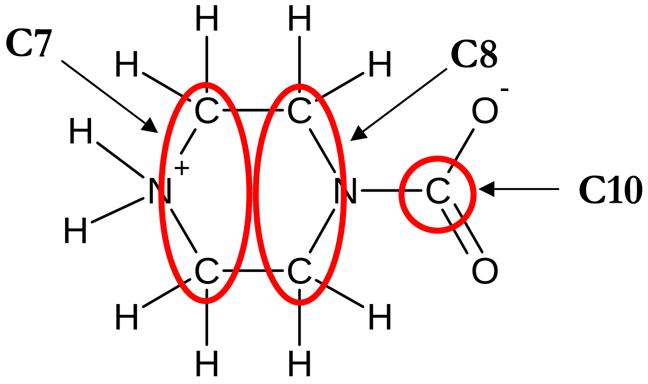

Figure 3.5-7 Molecular structure and active nuclei of carbons associated with PZCOO$^-$ and H$^+$PZCOO^{-1}.

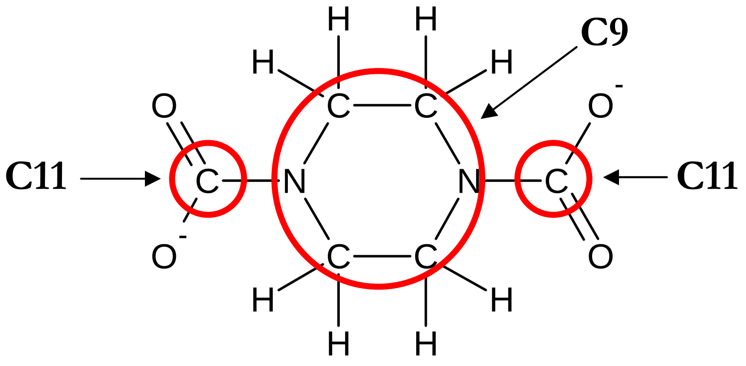

Figure 3.5-8 Molecular structure and active nuclei of carbons associated with PZ(COO$^-$)$_2$.

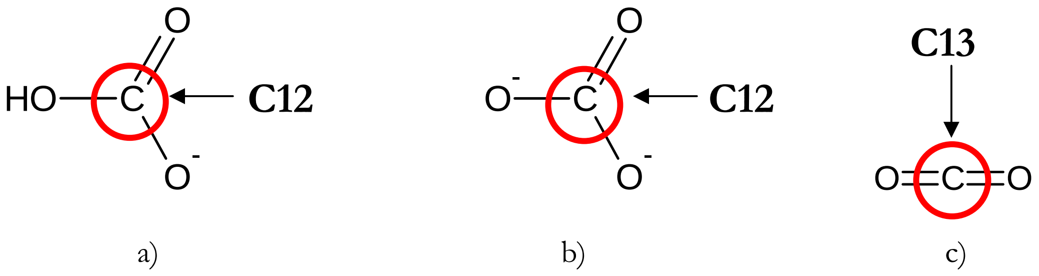

a) b) c)

Figure 3.5-9 Molecular structure and active nuclei of carbons associated with a) HCO_3^-, b) CO_3^{2-}, and CO_2.

Protons (H8) and carbons (C9) associated with piperazine dicarbamate are distinguished as a single peak due to the deactivating effect of the two carboxyl groups attached to each the nitrogen has on the alpha carbons and beta protons.

All carbons involved in a chemical reaction (i.e. C5, C10, C11, C12, and C13) will appear at a low field frequency (high chemical shift) due to the double bond to oxygen. In this work, carbons associated with CO_2 (C13) could not be distinguished in the experimental NMR spectra because the peak intensity is within the intensity of the background noise.

3.6 Spectrometer

In this work, experimental samples were placed into 5.0 mm O.D. x 0.77 mm I.D. x 7 in. length, 300 mHz, yellow top NMR sample tubes by WILMAD Labglass. Approximately 500 μl of C^{13} CO_2 loaded solution was filled in each tube. The tubes were then sealed by Ronalter (2007) before the samples were submitted for analysis to the NMR laboratory at the Department of Chemistry and Biochemistry, The University of Texas at Austin in Austin, Texas, USA.

All spectra acquisitions were performed by Willian and Sorey (2007) on a Varian INOVA 500 MHz NMR Spectrometer with variable temperature control. Samples at 40 and 60 °C were conditioned by heating for at least one hour at the requested temperature in a water bath prior to spectra acquisition.

3.7 Experiments with Loaded Samples

In this work, we focused on accurately measuring the liquid phase speciation for the systems involving water (H_2O), monoethanolamine (MEA), piperazine (PZ), and carbon dioxide (CO_2). A number of investigators have measured the liquid phase speciation for H_2O-MEA-CO_2 and H_2O-PZ-CO_2 which were used as experimental benchmarks in this work for determining the liquid phase speciation for H_2O-MEA-PZ-CO_2 systems.

3.8 Evaluation of Spectra

Spectra in this work were evaluated based on the proton and carbon assignment of Bishnoi (2000) and Poplsteinova (2004) for H_2O-PZ-CO_2 and H_2O-MEA-CO_2 systems, respectively. Examples of evaluated spectra for 7 m MEA, 2 m PZ, and 7 m MEA plus 3.6 m PZ are presented and peaks associated with protons and carbons labeled in Figure 3.5-1 through Figure 3.5-9 are assigned.

For consistency between previous works, loading in this chapter is defined as mole of CO_2 per mole of MEA or mole of PZ or mole MEA + 2 mole PZ, respectively.

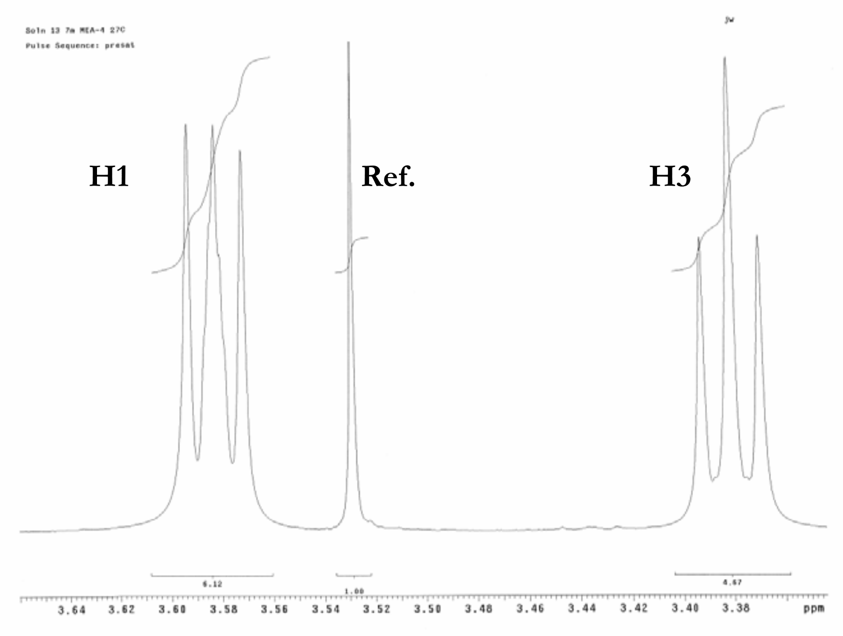

Figure 3.8-1. Expanded Medium Field ^1H Spectra at 27 ^oC for 7m MEA with 10% D_2O and 1% Dioxane at Loading = 0.55.

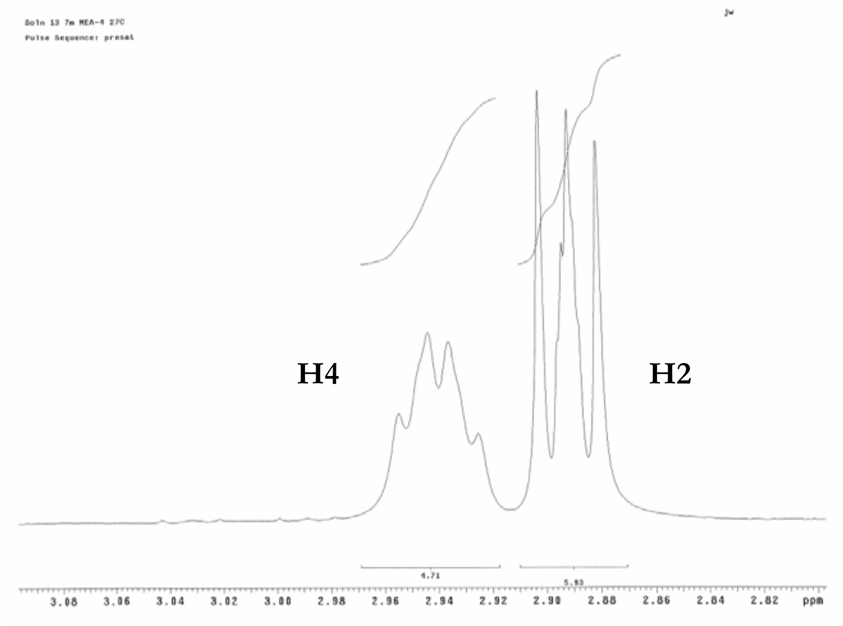

Figure 3.8-2. Expanded High Field ^1H Spectra at 27 ^oC for 7m MEA with 10% D_2O and 1% Dioxane at Loading = 0.55.

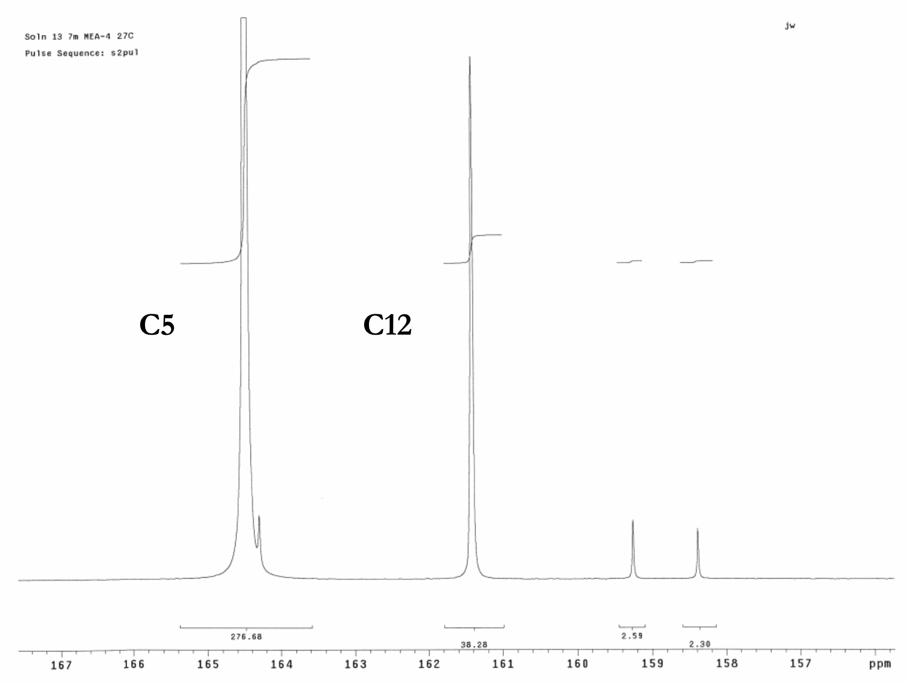

Figure 3.8-3. Expanded Low Field ^{13}C Spectra at 27 °C for 7m MEA with 10% D_2O and 1% Dioxane at Loading = 0.55.

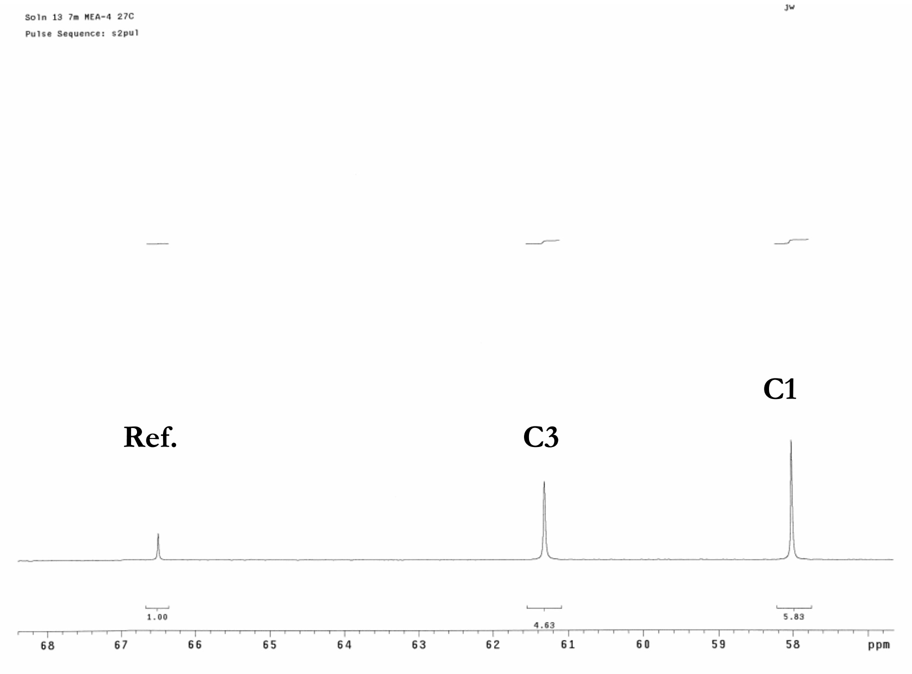

Figure 3.8-4. Expanded Medium Field ^{13}C Spectra at 27 °C for 7m MEA with 10% D_2O and 1% Dioxane at Loading = 0.55.

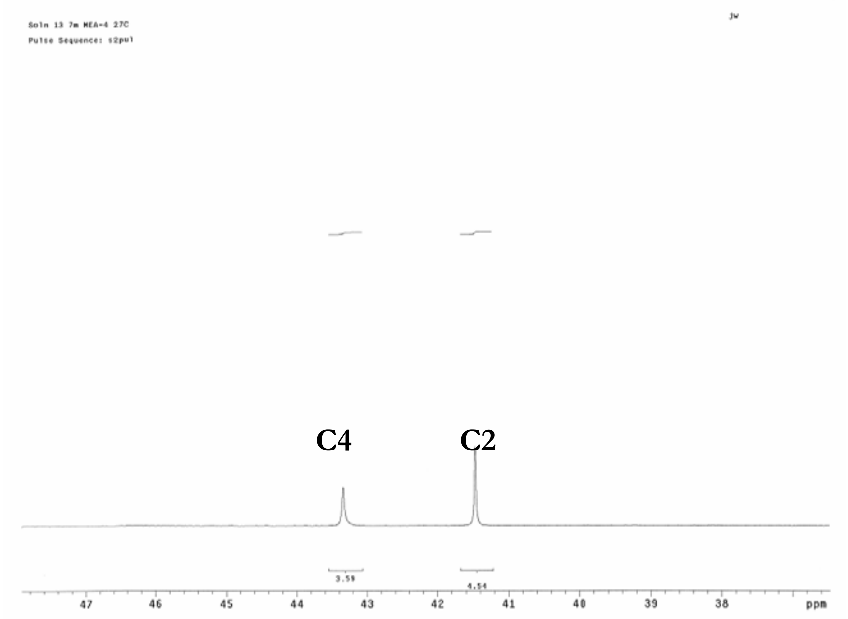

Figure 3.8-5. Expanded High Field ^{13}C Spectra at 27 ^{o}C for 7m MEA with 10% D_2O and 1% Dioxane at Loading = 0.55.

Spectra of CO_2 in Aqueous Piperazine Solutions

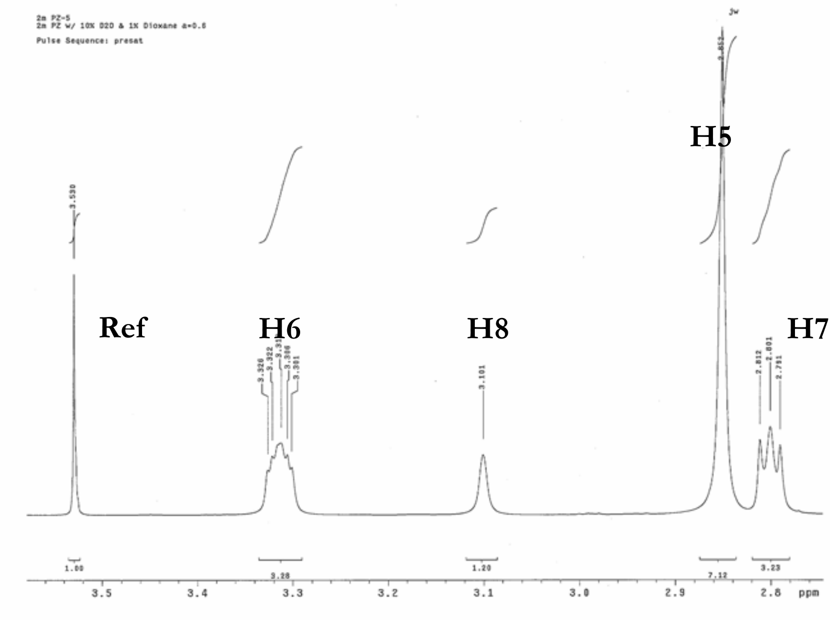

Figure 3.8-6. Expanded High Field ^{1}H Spectra at 27 ^{o}C for 2 m PZ with 10% D_2O and 1% Dioxane at Loading = 0.64.

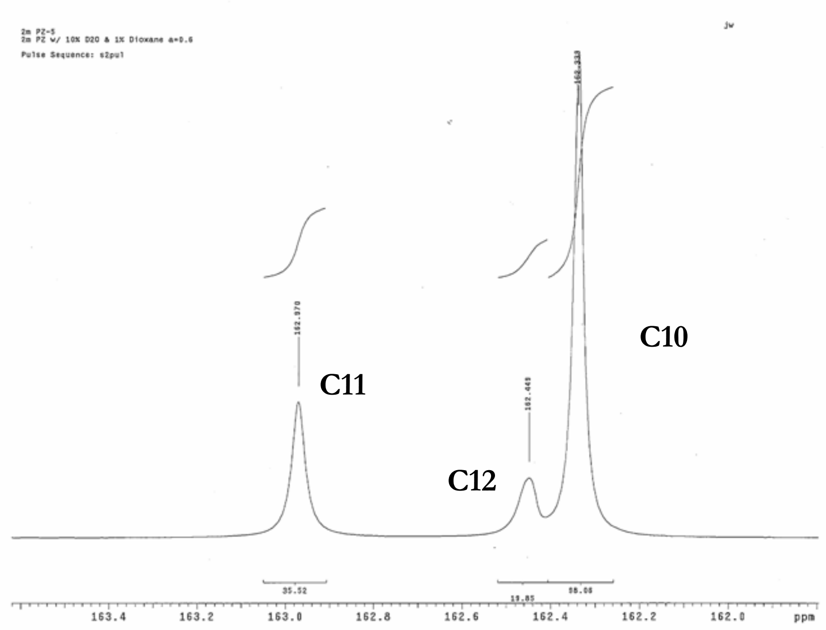

Figure 3.8-7 Expanded Low Field C^{13} Spectra at 27 °C for 2m PZ w/ 10% D_2O & 1% Dioxane at Loading = 0.64.

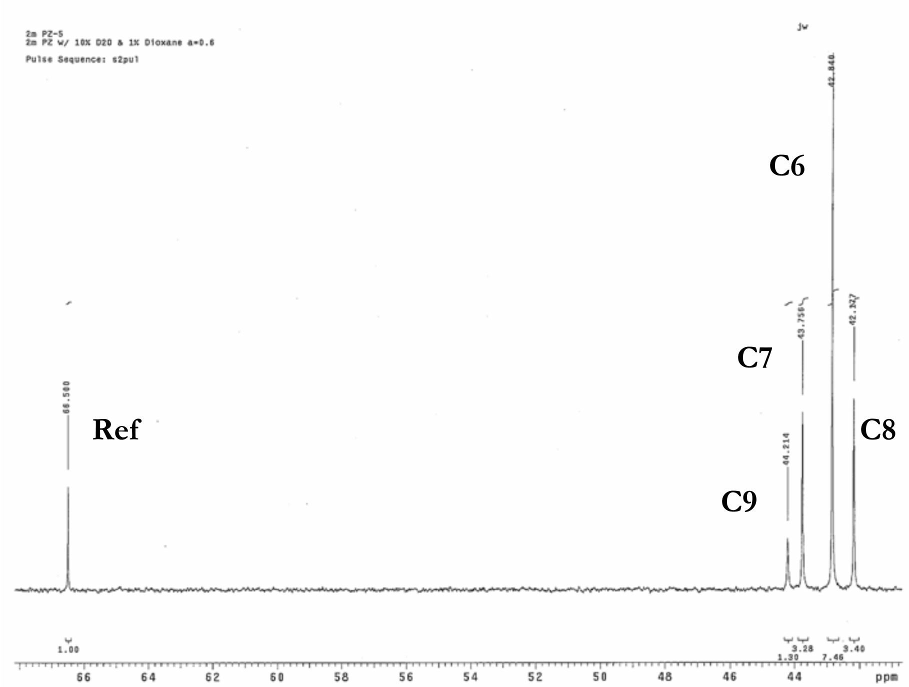

Figure 3.8-8 Expanded Low Field C^{13} Spectra at 27 °C for 2m PZ w/ 10% D_2O & 1% Dioxane at Loading = 0.64.

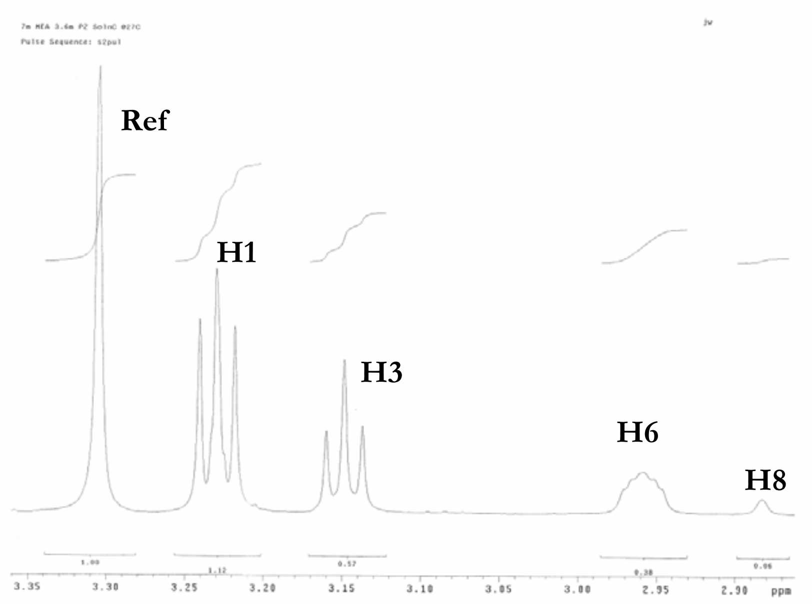

Figure 3.8-9. Expanded Medium Field ^1H Spectra at 27 ^oC for 7m MEA + 3.6 m PZ with 10% D_2O and 1% Dioxane at Loading = 0.24.

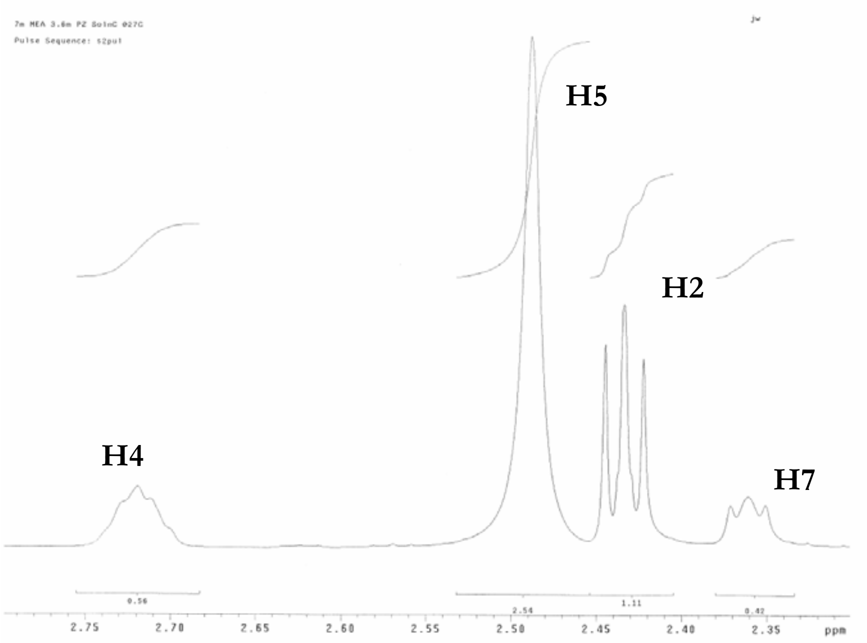

Figure 3.8-10. Expanded High Field ^1H Spectra at 27 ^oC for 7m MEA + 3.6 m PZ with 10% D_2O and 1% Dioxane at Loading = 0.24.

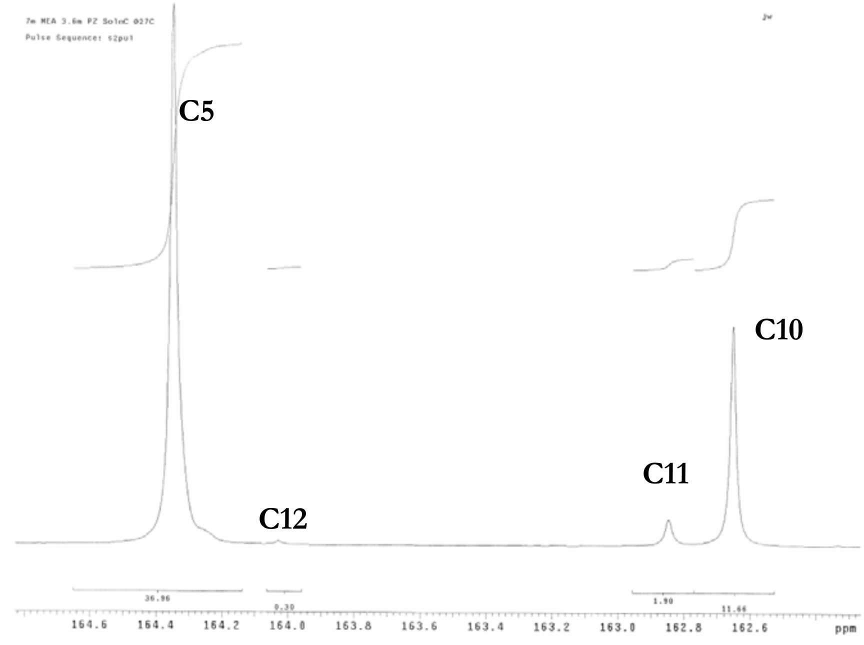

Figure 3.8-11. Expanded Low Field C^{13} Spectra at 27 °C for 7 m MEA + 3.6 m PZ w/ 10% D_2O & 1% Dioxane at Loading = 0.24.

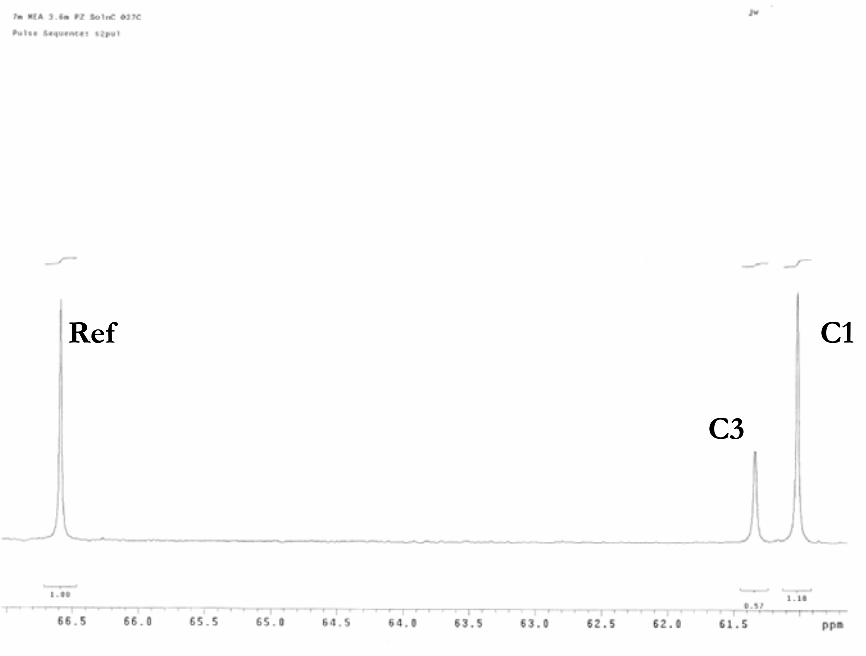

Figure 3.8-12. Expanded Medium Field C^{13} Spectra at 27 °C for 7 m MEA + 3.6 m PZ w/ 10% D_2O & 1% Dioxane at Loading = 0.24.

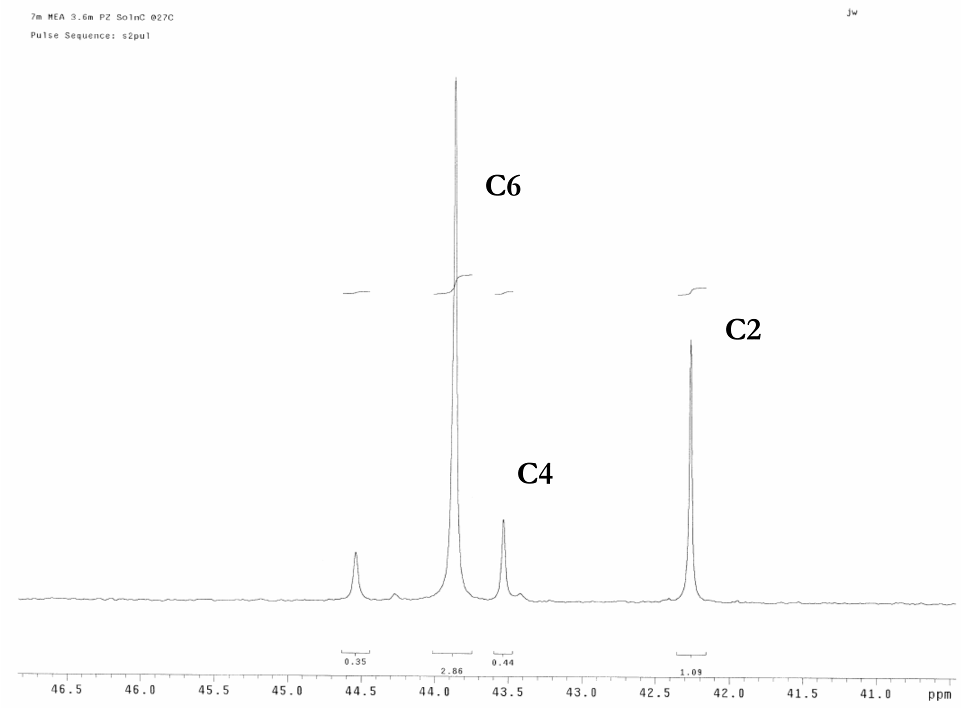

Figure 3.8-13. Expanded High Field C^{13} Spectra at 27 °C for 7 m MEA + 3.6 m PZ w/ 10% D_2O & 1% Dioxane at Loading = 0.24.

3.9 Spectra with Varying CO_2 Loading

As mentioned previously, a change in the environment will cause a shift in the chemical frequency. In this case, a change in the pH of the solution due to an increase in loading will cause the chemical shift of each species to vary somewhat. Figures 3.9-1 through 3.9-6 illustrate the variations in the spectra in terms of the central peak position associated with each species and functional group. The figures show that as loading increases the peaks for CO_3^{-2} + HCO_3^{-1} and MEACOO^{-1} shift toward lower frequencies. Poplsteinova (2004) also documented similar variations for the H_2O-MEA-CO_2 system and comparisons to her work adequately agree. One major problem in this work was the identification and assignment of peak location due to peak overlap as can been seen within the peak treads.

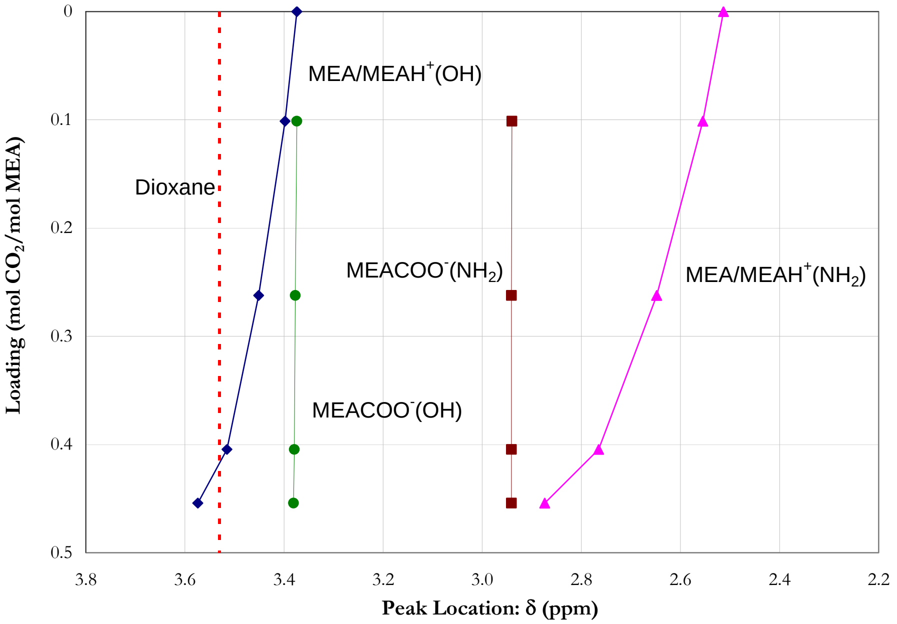

Figure 3.9-1. ^{1}H Chemical Shifts for 7 m MEA at 27 °C with Varying CO_2 Loading.

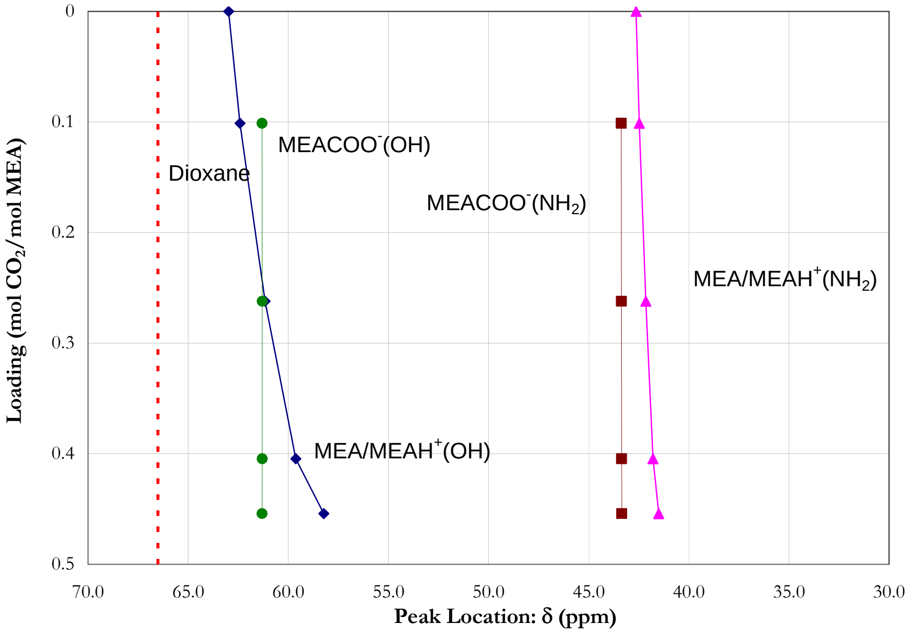

Figure 3.9-2. High Field ^{13}C Chemical Shifts for 7 m MEA at 27 °C with Varying CO_2 Loading.

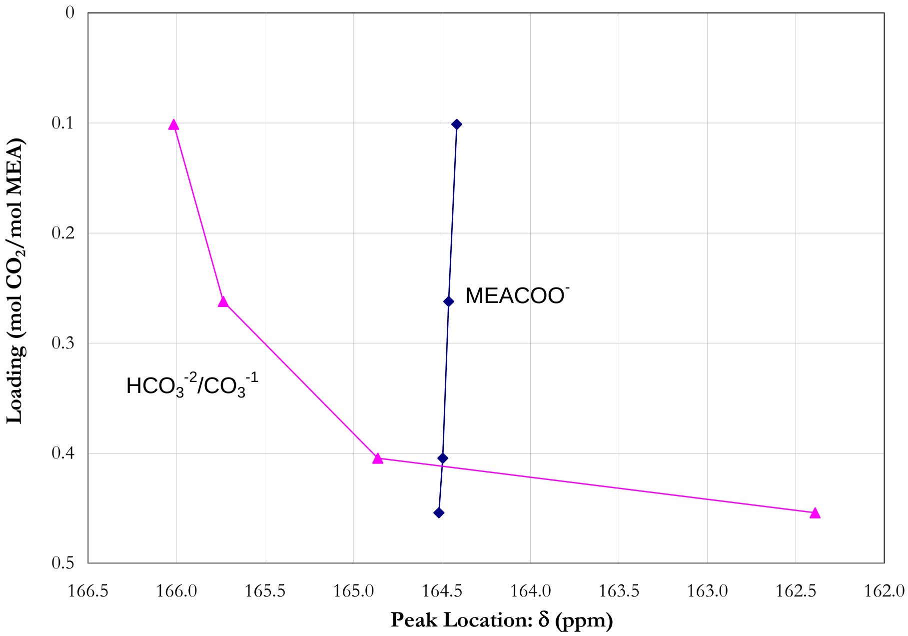

Figure 3.9-3. Low Field ^{13}C Chemical Shifts for 7 m MEA at 27 °C with Varying CO_2 Loading.

Spectra of CO_2 in Aqueous Piperazine Solutions

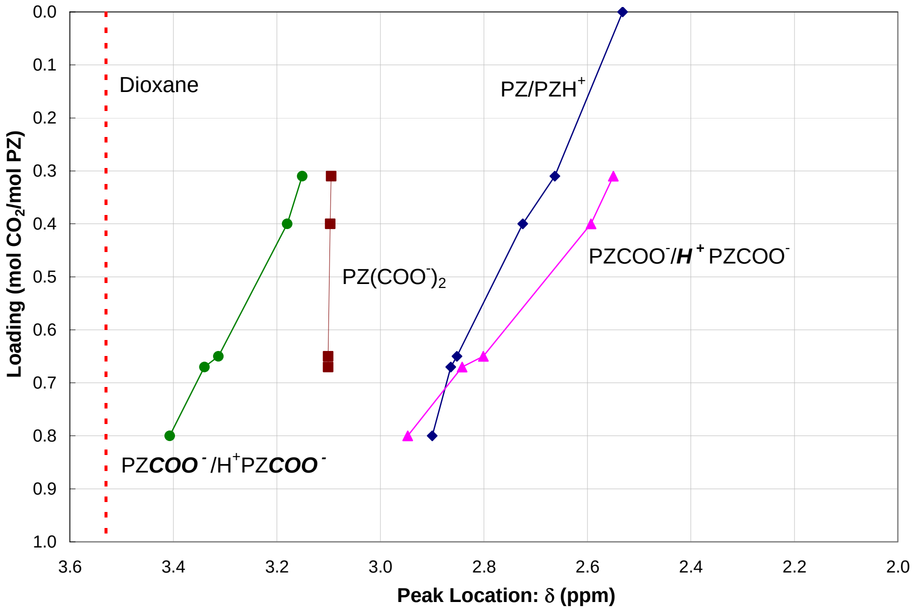

Figure 3.9-4. ^{1}H Chemical Shifts for 2 m PZ at 27 °C with Varying CO_2 Loading.

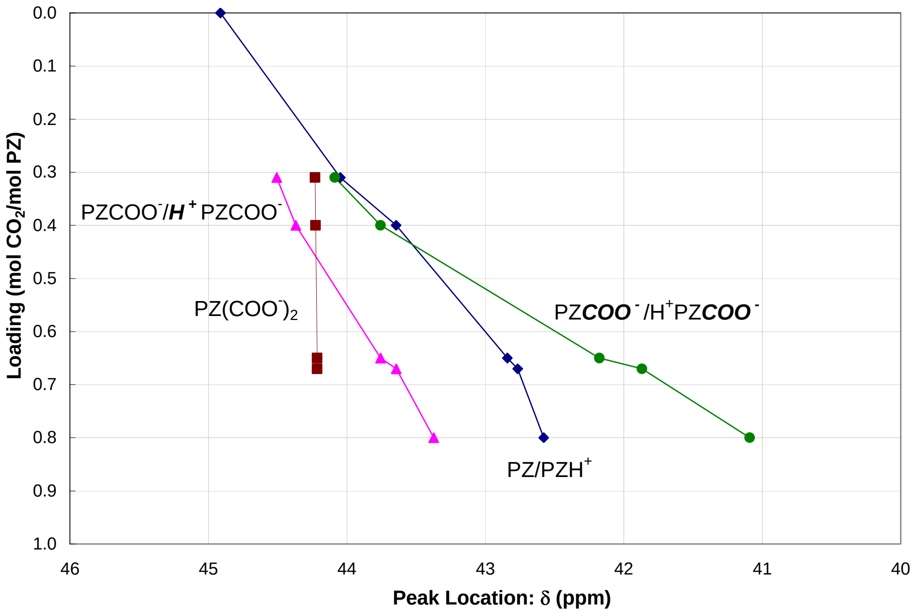

Figure 3.9-5. High Field ^{13}C Chemical Shifts for 2 m PZ at 27 °C with Varying CO_2 Loading.

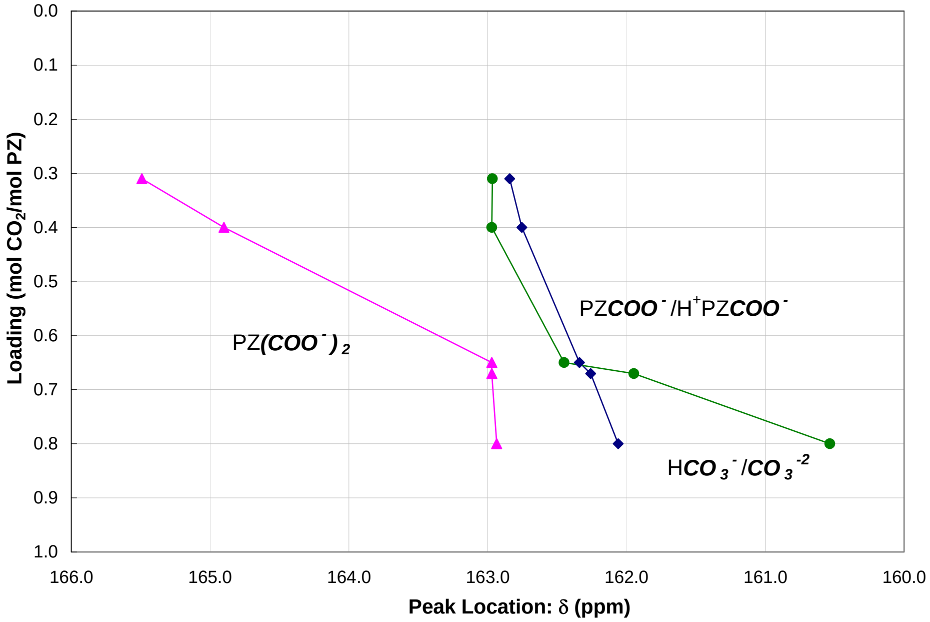

Figure 3.9-6. Low Field ^{13}C Chemical Shifts for 2 m PZ at 27 °C with Varying CO_2 Loading.

3.10 Apparent Speciation Calculation

The following equations can be used to represent the liquid phase equilibrium for the NMR speciation data from this work:

$$n^*_{MEA} = n_{MEA} + n_{MEAH^+} \tag{3-1}$$

$$n^*_{MEACOO^{-1}} = n_{MEACOO^{-1}} \tag{3-2}$$

$$n^*_{PZ} = n_{PZ} + n_{PZH^+} + n_{PZH^{+2}} \tag{3-3}$$

$$n^*_{PZ(COO)_2^{-2}} = n_{PZ(COO)_2^{-2}} \tag{3-4}$$

$$n^*_{H^+/PZCOO^{-1}} = n_{H^+PZCOO^{-1}} + n_{PZCOO^{-1}} \tag{3-5}$$

$$n^*_{CO_2} = n_{CO_2} + n_{CO_3^{-2}} + n_{HCO_3^{-1}} \tag{3-6}$$

Where
n_i is the true number of moles for each component per kilogram of water corresponding to the relative proton and or carbon NMR peak areas,
n_i^* is the pseudo-component quantity based on experimental NMR data.

In this work, the measured peak areas or intensities for the corresponding carbons and or protons associated with each molecule(s) relative to an internal standard (1,4-dioxane) allowed for a quantitative analysis of the NMR data based on the following equation:

$$R_b = \frac{\varphi \cdot n_{ref}}{A_{ref}} \tag{3-7}$$

Where
R_b is the number of moles of dioxane/kg-H_2O per unit area,
φ is the number of active protons or carbons in dioxane, 8 - ^{1}H and 4 - ^{13}C,
n_{ref} is the experimental dioxane molality based on the batch solution, mole/kg-H_2O,
A_{ref} is th experimental integrated area for the dioxane reference peak.

Based on Equation 3-7, the number of moles/kg-H_2O for the other species can then be determined by the following equation:

$$n_i = \frac{A_i \cdot R_b}{\varphi_i} \qquad 3\text{-}8$$

Where
A_i is the experimental integrated area for species *i*,
φ is the number of active protons or carbons in species *i*.

For species with multiple proton or carbon types, the number of moles was obtained by taking the average of the corresponding results on a proton or ^{12}C basis. From the apparent species compositions, mole fractions were calculated based on 1 kg of H_2O.

3.11 Experimental Results

1,4-Dioxane Study

In this work, the measured peak areas or intensities for the corresponding carbons and or protons associated with each molecule(s) were evaluated relative to an internal standard of 1,4-dioxane (dioxane) which allowed for a quantitative analysis of the NMR data. Suda et al. (1996) and Poplsteinova (2004) choose a concentration of 5 wt% dioxane, but did not perform a sensitivity analysis on the minimal amount of dioxane that would be required for an accurate determination for liquid phase speciation analysis. In this work, we choose to vary the concentration of dioxane from 1,000 to 50,000 ppm_w to test our quantitative analysis against a gravimetrically prepared solution of 7 m MEA submitted for NMR analysis at 27 °C as shown in Figure 3.11-1.

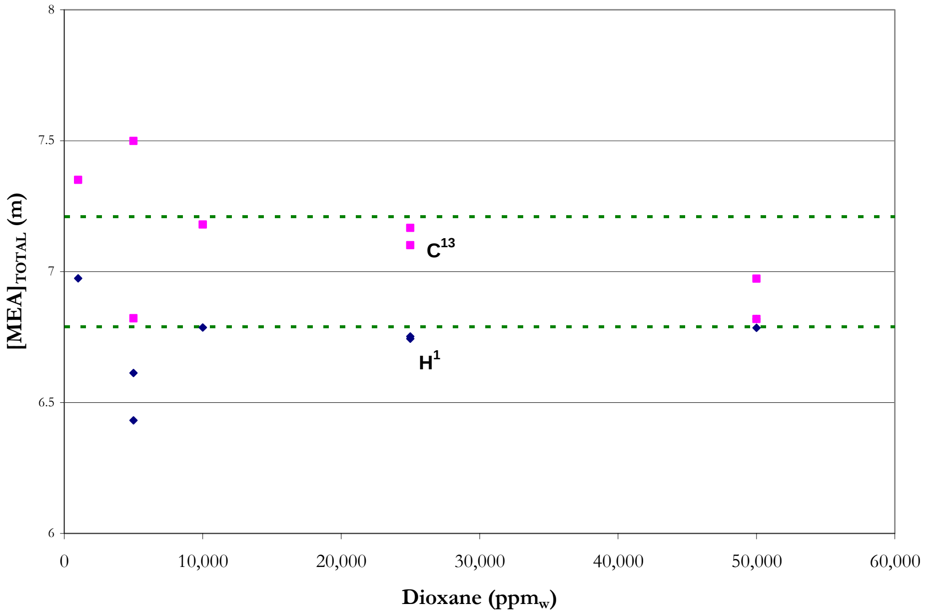

Figure 3.11-1. Comparison of H^1 and C^{13} Analysis in 7 m MEA with Varying Levels of Dioxane for Use as an Internal Standard at 27 °C. Points: ♦, H^1 Results, ■, C^{13} Results. Dash Lines: ± 3.0 percent error bounds.

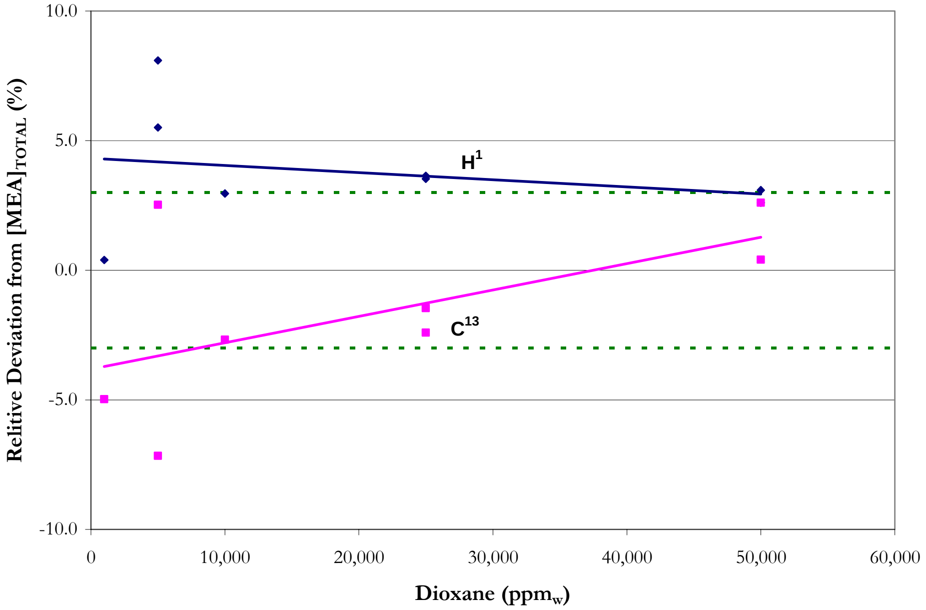

Figure 3.11-2. Relative Deviation of H^1 and C^{13} Analysis in 7 m MEA with Varying Levels of Dioxane for Use as an Internal Standard at 27 °C. Points: ♦, H^1 Results, ■, C^{13} Results. Dash Lines: ± 3.0 percent error bounds.

Figure 3.11-2 illustrates that for a dioxane concentration between 1 and 5 weight percent the use of dioxane as an internal standard should give an adequate representation of the liquid phase concentration. For C^{13} NMR analysis, Figure 3.11-2 illustrates for a value of approximately 3.82 weight percent dioxane may yield a possible optimum concentration for quantitative analysis of NMR data. For samples containing C^{13} CO_2, we have observed a slight improvement in the quality of the NMR analysis using 5 weight percent dioxane as compared to 1 weight percent, but due to scatter in the carbonate/bicarbonate concentrations, varying the concentration did not drastically improve the overall analysis. For dioxane concentrations less than 1 weight percent, Figure 3.11-2 illustrate an average absolute relative error of approximately ± 5.0 percent was observed for both proton and carbon NMR analysis.

H_2O-MEA-CO_2 System

We chose 7 m MEA as the first system to benchmark our methods and compare the results against literature data from Poplsteinova (2004) at 40 °C as shown in Figure 3.11-3. Poplsteinova (2004) additionally measured speciation at 20 °C, but due to temperature laminations we were unable to reproduce this data set.

Figure 3.11-3 illustrates that experimental results from this work are consistent with reported liquid phase speciation from Poplsteinova (2004) at 40 °C with respect to the experimental concentrations and solution loading trends. In terms of the CO_3^{-2}/HCO_3^{-1} species, experimental results from this work underpredict Poplsteinova (2004). This discrepancy could be due to the relative nature of the measurement since the concentration of the CO_3^{-2}/HCO_3^{-1} species is on the order of 0.01 to 0.1 mole/kg-H_2O.

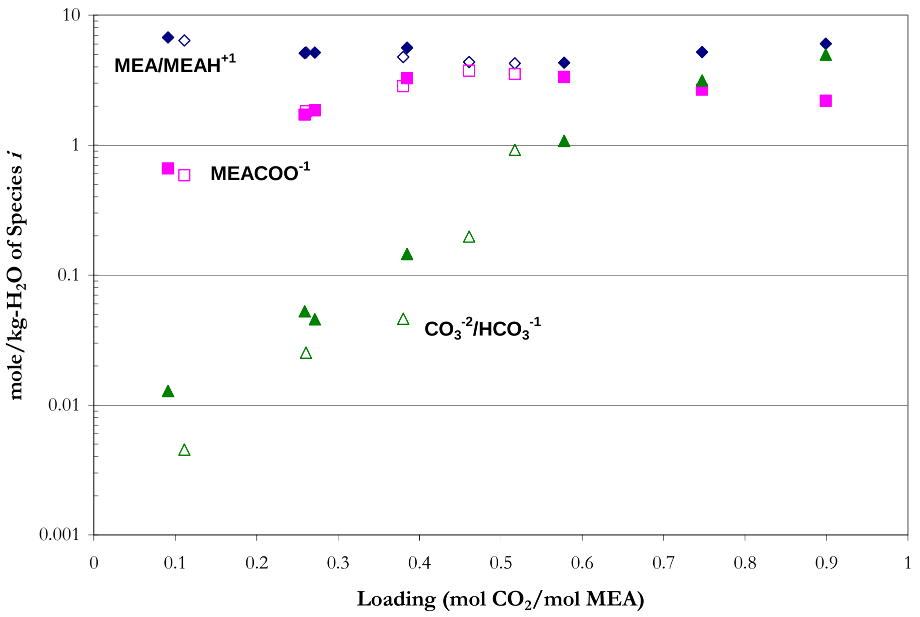

Figure 3.11-3. C^{13} NMR Liquid Phase Speciation for 7 m MEA at 27 °C. Close Points: Poplsteinova (2004). Open Points: This work.

H_2O-PZ-CO_2 System

We chose 1 m PZ as the final system to benchmark our methods and compare our results against literature data from Ermatchkov et al. (2003) at 27 °C as shown in Figure 3.11-4. Ermatchkov et al. (2003) additionally measured speciation at 40 and 60 °C, but due to equipment time limitations we were unable to reproduce these data sets. In addition, Ermatchkov et al. (2003) measured liquid phase speciation through ^{1}H NMR which did not allow for the determination of the CO_3^{-2}/HCO_3^{-1} species. Thus, we have then excluded this data from Figure 3.11-4 for a direct comparison.

Figure 3.11-4 illustrates that experimental results from this work are consistent with reported liquid phase speciation from Ermatchkov et al. (2003) at 27 °C with respect to the experimental concentrations and solution loading trends.

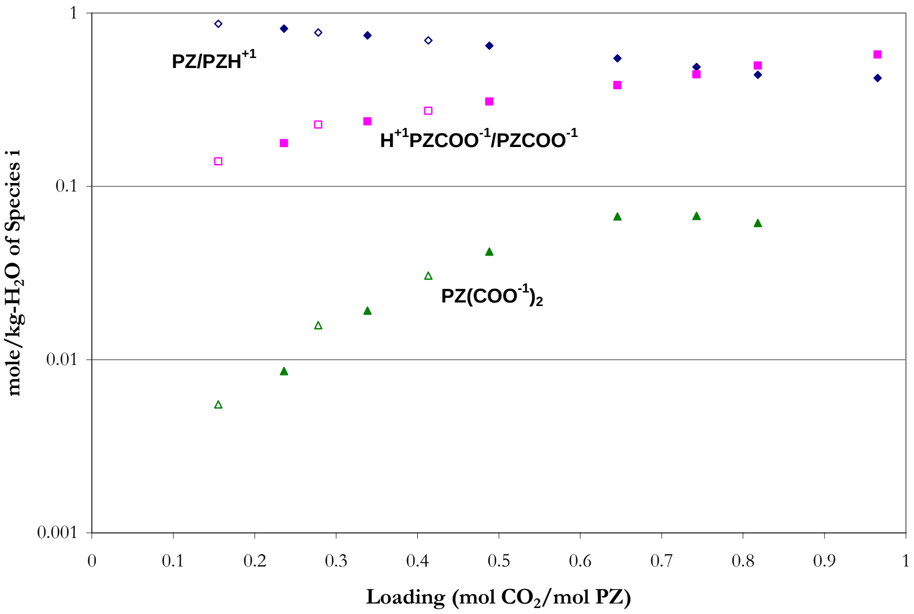

Figure 3.11-4. H^1 NMR Liquid Phase Speciation for 1 m PZ at 27 °C. Close Points: Ermatchkov et al. (2003). Open Points: This work.

3.12 Conclusions

In conclusion, in this work we have developed consistent liquid phase speciation methods using NMR spectroscopy. We have shown that experimental results are consistent and agree well with key literature data. In addition, we have been able to demonstrate the effect of CO_2 loading on the chemical shift of each species. We would recommend that more work be done at high concentrations of PZ to create a data base of high quality and consistent data for the H_2O-PZ-CO_2 system since the extensive database of liquid phase speciation by Ermatchkov et al. (2003) is limited to concentrations up to 1.5 m PZ. Overall, the presented liquid phase NMR speciation method may provide an opportunity for future work to contribute a deeper understanding of solution thermodynamics for several aqueous phase solutions.

CHAPTER IV

Specific Heat Capacity Methods

4.1 Introduction

This chapter details the experimental methods used to measure liquid phase specific heat capacity of alkanolamine solutions utilizing a differential scanning calorimeter (DSC). The chapter will describe liquid specific heat capacity measurements (40 – 120 ºC) performed at The University of Texas at Austin in Austin, Texas, USA. These experiments were carried out with the help of Syed Shah and Humara Rafique, Undergraduate Research Assistants at the Department of Chemical Engineering, The University of Texas at Austin, Austin, Texas, USA. Calorimetry plays an important role in the design of acid gas removal plants and in terms of developing a rigorous and consistent thermodynamic model that has the ability to adequately predict heat effects associated with the complexities of mass transfer with fast chemical reactions during the absorption/stripping process.

4.2 Literature Review

To describe the thermodynamics taking place in the liquid phase would require the ability to study the heat effects associated with the specific heat capacity (C_P) in a solution. Differential scanning calorimetry is a thermoanalytical technique where the difference in the amount of heat required to increase the temperature of a sample and reference are measured as a function of temperature. Several earlier calorimetric investigations of alkanolamines in terms of monoethanolamine (MEA) and piperazine (PZ) in aqueous and pure liquid and crystalline states are listed below:

Systems	C_P Method	Source
MEA	BC	Swanson and Chueh (1973)
	N/A	The Dow Chemical Company (1981)
	DSC	Chiu et al. (1999)
PZ	DSC	Steele et al. (1997)
H_2O-MEA	FMC	Pagé et al. (1993)
	BC	Weiland et al. (1997)
	DSC	Chiu and Li (1999)
H_2O-MEA-CO_2	BC	Weiland et al. (1997)

where BC: Batch calorimeter, HFMC: Flow microcalorimeter, DSC: Differential scanning calorimeter, N/A: Not available.

Swanson and Chueh (1973) and Weiland et al. (1997) most likely utilized a batch calorimeter, given the equipment descriptions, where the heat capacity of a sample was determined by measuring the temperature rise of a known mass of sample and recording the response to a known electrical energy input.

Pagé et al. (1993) utilized a flow densimeter and a flow microcalorimeter to measure solutions densities and the isobaric volumetric heat capacities by following the methods described by Picker et al. (1968) and Picker et al. (1971). The isobaric specific heat capacities were then calculated by dividing the isobaric volumetric heat capacities from the measured densities.

Chiu et al. (1999), Steele et al. (1997), Chiu and Li (1999), and this work utilized a differential scanning calorimeter (DSC) to measure the specific heat capacity. Specific heat capacity, also known simply as specific heat, is the measure of the heat energy required to increase the temperature of a unit quantity of a substance by a certain temperature interval. Heat capacity, as distinct from specific heat capacity, is the measure of the heat energy required to increase the temperature of an object by a certain temperature interval.

As mentioned previously, a DSC is a thermoanalytical technique where the difference in the amount of heat required to increase the temperature of a sample and reference are measured as a function of temperature. During an experiment both the sample and reference pans are maintained at nearly the same temperature throughout the experiment. When a material within the sample pan undergoes a physical transformation such as phase transitions, more (or less) heat will be required to flow to the sample pan than into the reference pan in order to maintain both pans at the same temperature. By observing the difference in heat flow between the sample and reference pans, differential scanning calorimeters are able to measure the amount of heat absorbed or released during such transitions.

In this work, we have focused on accurately measuring and verifying the specific heat capacity for systems involving water (H_2O), monoethanolamine (MEA), piperazine (PZ), potassium carbonate (K_2CO_3), potassium bicarbonate ($KHCO_3$), and carbon dioxide (CO_2).

4.3 Chemicals

Chemicals used in this work included: CO_2 (Matheson Tri-Gas, ≥ 99.99 % pure), N_2 (Cryogenics Laboratory at The University of Texas at Austin, ≥ 99. % pure), MEA (Acros Organics, 99 % pure), PZ (Fluka Chemie GmbH, ≥ 98.0 % pure), K_2CO_3 (Fluka Chemie GmbH, ≥ 99.0 % pure), and $KHCO_3$ (Sigma-Aldrich Inc., ≥ 99.5 % pure). All chemicals were used without any further purification.

4.4 Sample Preparation

All solutions were prepared gravimetrically from ultra pure deionized water. Amine solutions were loaded with CO_2 by slowly sparging CO_2 through a submerged fritted disk in the solution as shown in Figure 4.4-1. The CO_2 loader (~5 ml capacity) was custom made by Ronalter (2007). The empty CO_2 loader was placed on an analytical scale (± 10 μg) and weighed and approximately 5 ml of solution was transferred to the loader and weighed again to determine the exact amount of solution in the CO_2 loader. The CO_2 loader was then attached to a CO_2 cylinder and the gas was allowed to react with the amine solution for approximately 2 minutes. The apparatus was weighed again to determine the amount of CO_2 absorbed into the solution by difference. This procedure would then be repeated until the desired loading was reached.

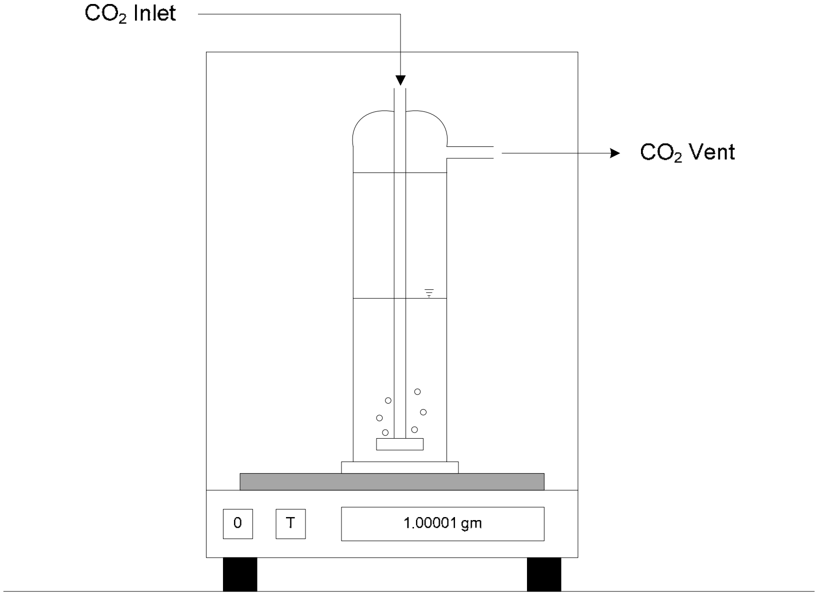

Figure 4.4-1. CO_2 Loading Apparatus.

4.5 Differential Scanning Calorimeter

The differential scanning calorimeter used in this work consisted of a DSC-Q100 calorimeter and a thermal analysis controller from TA Instruments located and maintained in the research laboratories of Dr. Benny D. Freeman, Department of Chemical Engineering at The University of Texas at Austin, Austin, Texas, USA. The DSC operating range is from -90 to 400 °C and operates with a temperature repeatability of ± 0.05 °C and a calorimetric sensitivity of ± 10 μW. Nitrogen was used as a purge gas with a flowrate of 40 ml/min.

Large volume 304 stainless steel (SS) sample pans used in this work were purchased from Perkin Elmer (#03190218). The sample pan and lids were joined together by a Perkin Elmer Quick Press (#0990-8467). When the pans are properly assembled an o-ring, placed inside the lid of the sample pan, forms a seal able to withstand an internal pressure of 150 bar and has an internal volume of approximately 60 mm^3. Figure 4.5-1 illustrates a cross section of a properly sealed sample pan.

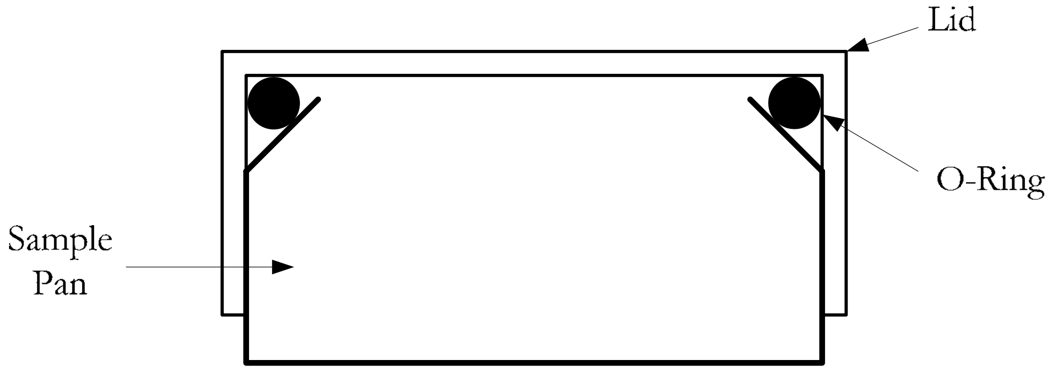

Figure 4.5-1. Cross Section of a Properly Sealed Sample Pan.

Figure 4.5-2. DSC-Q100 Sample Cell. Disks: red, reference sapphire disk, colorless, sample sapphire disk.

4.5.1 *DSC Calibration*

To obtain accurate results, a TZero baseline calibration was performed periodically by Scott Matteucci, a Senior Graduate Researcher at The University of Texas at Austin, Austin, Texas, USA. The TZero baseline is used to compensate for subtle differences in the thermal resistance and capacitance between the reference and sample platforms in the DSC sensor. The calibration is based on two experiments: one experiment with an empty cell and a second experiment with equal weight sapphire disks on the sample and reference platforms as shown in Figure 4.5-2.

The cell constant and temperature calibration were obtained by heating pure indium (~5 mg) in a sealed 304 SS sample pan used in this work, through its melting point (156.5895 °C). The cell constant is used as a calibration factor to adjust for subtle differences in the calorimetric response of the DSC cell whereas the temperature calibration ensures that the sample thermocouple reading is correct under experimental conditions. These calibrations were verified at the beginning of every experiment by running the calibration sample in standard mode on the DSC. When the difference between the calibrated heat flow and standard heat flow of the indium sample differed by more than 0.3 percent, the indium calibration procedures were performed. An example of a typical heat flow curve during the cell constant and temperature calibration for indium is shown in Figure 4.5-3.

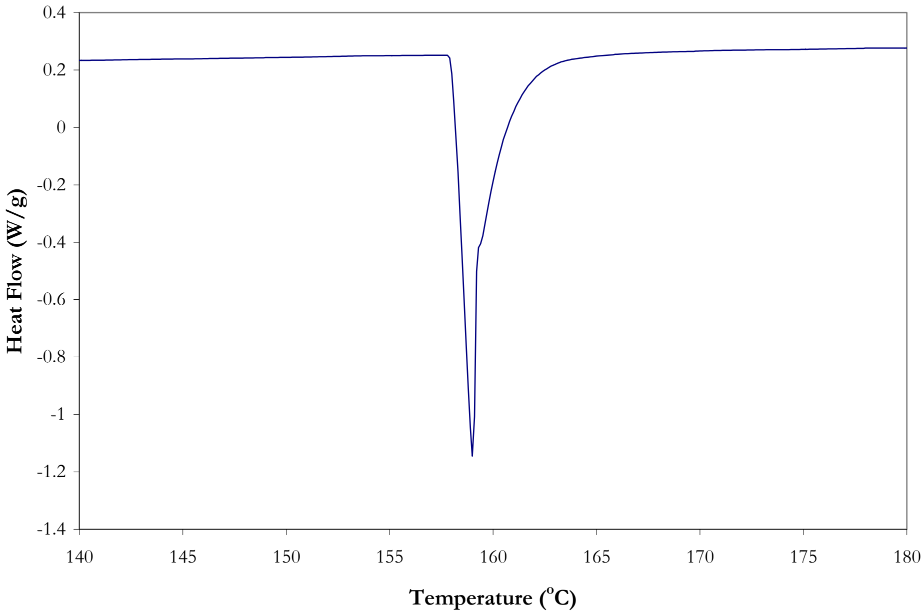

Figure 4.5-3. Typical Heat Flow Calibration Curve using ~ 5 mg of Indium.

4.6 Specific Heat Capacity Procedure

In this work, we utilized the ASTM International (www.astm.org), originally known as the American Society for Testing and Materials (ASTM), standard test method for determining the specific heat capacity by differential scanning calorimetry under the designation of E 1269-05.

During an experiment, an empty reference pan and a sample pan were placed on the sample platforms inside the DSC cell. After the DSC cover was lowered into position, a method created to cool the sample pans to 25 °C and isothermally hold the samples at 25 °C for ten minutes would ensure that the specimen inside the sample pan reached an equilibrium starting condition. After ten minutes, the DSC would then ramp up the temperature at a constant rate of 5 °C/min until the temperature reached 125.0 °C. The

DSC would then cool the samples at a rate of 10 °C/min to 40 °C where the sample would then be safely removed.

The specific heat capacity of a substance could then be determined by creating a baseline profile (empty sample pan), a standard sample profile, and a sample profile under identical conditions to those described previously. The baseline would then be subtracted from each thermal profile using software provided by TA. Figure 4.6-1 illustrates typical thermal profiles observed in this work.

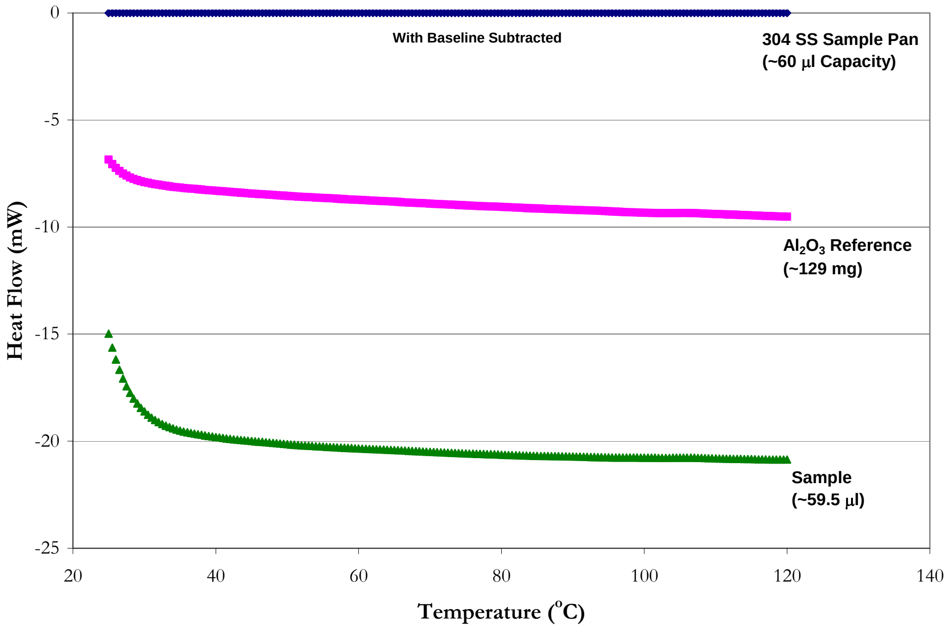

Figure 4.6-1. Typical DSC Curves for Specific Heat Capacity Measurements.

In this work, the specific heat capacity for an unknown sample was referenced to the known heat capacity of aluminum oxide (Al_2O3) (Acros Organics, #40 sieve, 99.98 – 99.99 % pure) as described by Ditmars et al. (1985) and Archer et al. (1993) as shown in Figure 4.6-2.

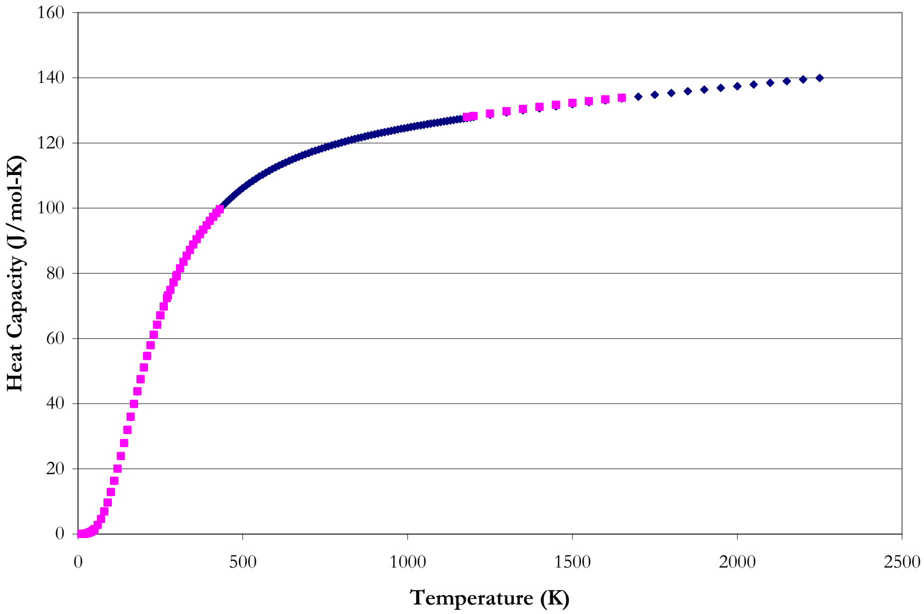

Figure 4.6-2. Heat Capacity of Al_2O_3. Points: ♦, Archer et al. (1993), ■, Ditmars et al. (1981)

The specific heat capacity of a sample could then be determined by the difference in the y-axis displacement between the sample and blank curves at any desired temperature. The specific heat capacity of a sample could then be calculated using the following equation:

$$C_P\left(s\right)=\left[\frac{60\cdot E\cdot D_s}{W_s\cdot b}\right]-\left[\frac{\Delta W\cdot C_P^{pan}}{W_s}\right] \qquad 4\text{-}1$$

Where
$C_P(s)$ is the specific heat capacity of the sample, kJ/kg-K,
E is the calorimetric sensitivity of the DSC apparatus,
B is the heat rate, 5 °C/min,
D_s is the vertical displacement between the empty sample pan and the sample DSC thermal curves at a given temperature, mW,
W_s is the mass of the sample, mg,
ΔW, is the difference in mass between the reference pan and the sample pan, and
C_P^{pan} is the specific heat capacity of the 304 stainless steel pans.

The calorimetric sensitivity constant was based on the known heat capacity of Al_2O_3 and was determined using the following equation:

$$E = \left[\frac{b}{60 * D_{st}} \right] \left[W_{st} \cdot C_P^{Al_2O_3} + \Delta W \cdot C_P^{pan} \right] \qquad 4\text{-}2$$

Where
D_{st} is the vertical displacement between the empty sample pan and the Al_2O_3 DSC thermal curves at a given temperature,
W_{st} the mass of Al_2O_3 sample, mg, and
$C_P^{Al_2O_3}$ is the specific heat capacity of Al_2O_3.

In this work, the specific heat capacity for 304 stainless steel was described by Dobrosavljevic and Maglic (1992) using pulse calorimetry as shown in Figure 4.6-3.

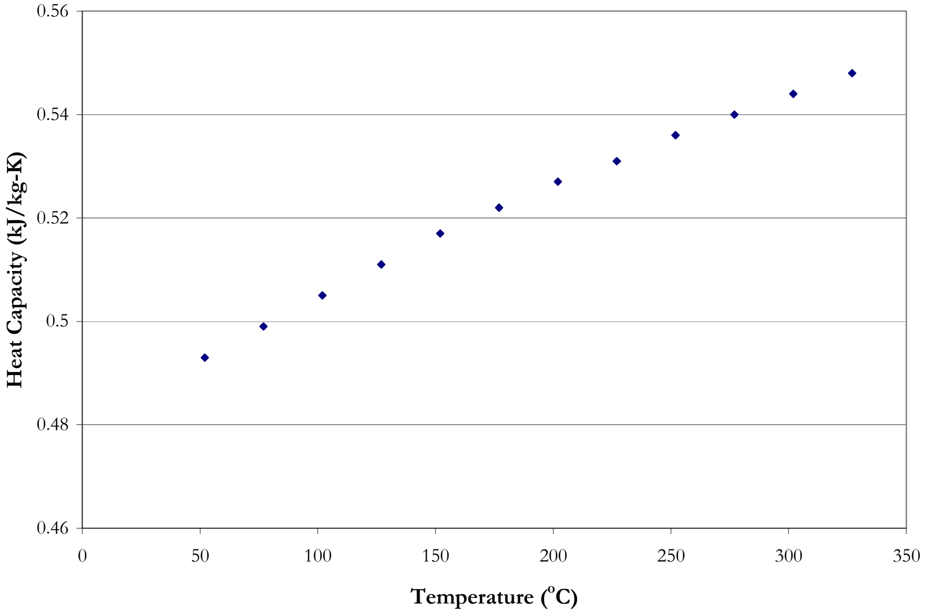

Figure 4.6-3. Specific Heat Capacity of 304 Stainless Steel from Dobrosavljevic and Maglic (1992).

For each sample an average of four runs was used to determine the specific heat capacity of the sample. The reproducibility of the experimental method is illustrated in Figure 4.6-4 for water. The accuracy and reproducibility of the specific heat capacity measurements were estimated to be ± 2.0 and 1.0 percent, respectively, based on benchmarking the experimental method to the specific heat capacity of water.

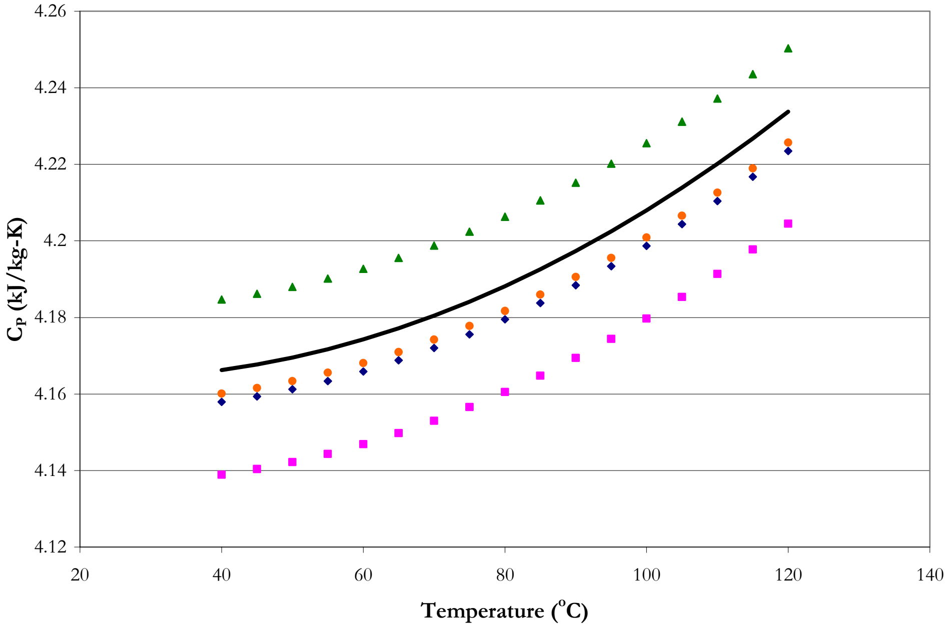

Figure 4.6-4. Reproducibility of the Specific Heat Capacity Experiments for H_2O. Points: ♦, Sample 1, ■, Sample 2, ▲, Sample 3, ●, Sample 4. Line: ━, Average.

4.7 Experimental Results

4.7.1 *Pure H_2O System*

We chose water as the first system to test in order to benchmark our results against the large volume of literature information reporting the pure component heat capacity of water as shown in Figure 4.7-1 and Figure 4.7-2.

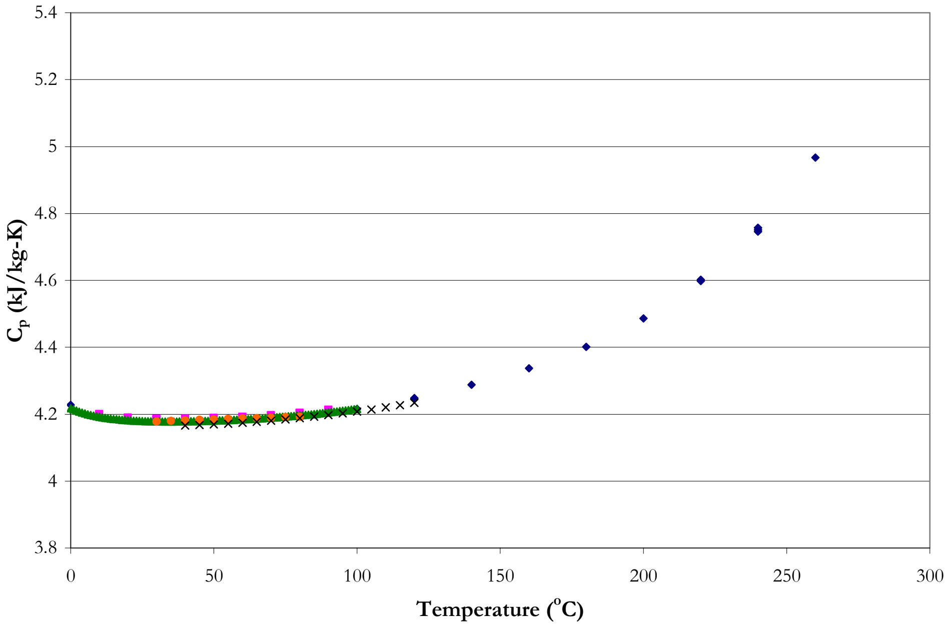

Figure 4.7-1. Specific Heat Capacity of Water. Points: ♦, Kell et al. (1984), ■, Engineering Sciences Data (1966), ▲, Osborne et al. (1939), ●, Chiu et al. (1999), and ×, from this work.

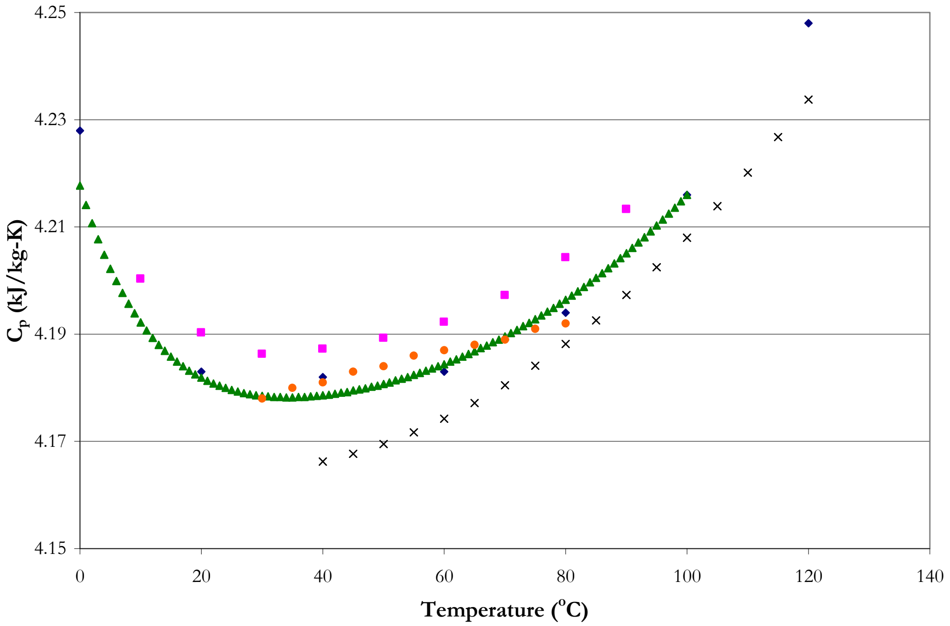

Figure 4.7-2. Enlargement of Figure 4.7-2 for the Specific Heat Capacity of Water. Points: ♦, Kell et al. (1984), ■, Engineering Sciences Data (1966), ▲, Osborne et al. (1939), ●, Chiu et al. (1999), and ×, from this work.

Figure 4.7-2 illustrates experimental results from this work as compared to accepted literature values. Overall, experimental specific heat capacity measurements from this work are within ± 0.4 percent of the average specific heat capacity of water even though, experimental results from this work tend to underestimate published literature data. Due to this discrepancy, we gave a conservative estimate for the accuracy of the specific heat capacity measurements of ± 2.0 percent.

4.7.2 *Pure MEA System*

We chose MEA as the second system to be tested due to the large volume of literature information available for the pure component specific heat capacity. A comparison of the experimental literature data and measurements from this work are shown in Figure 4.7-3.

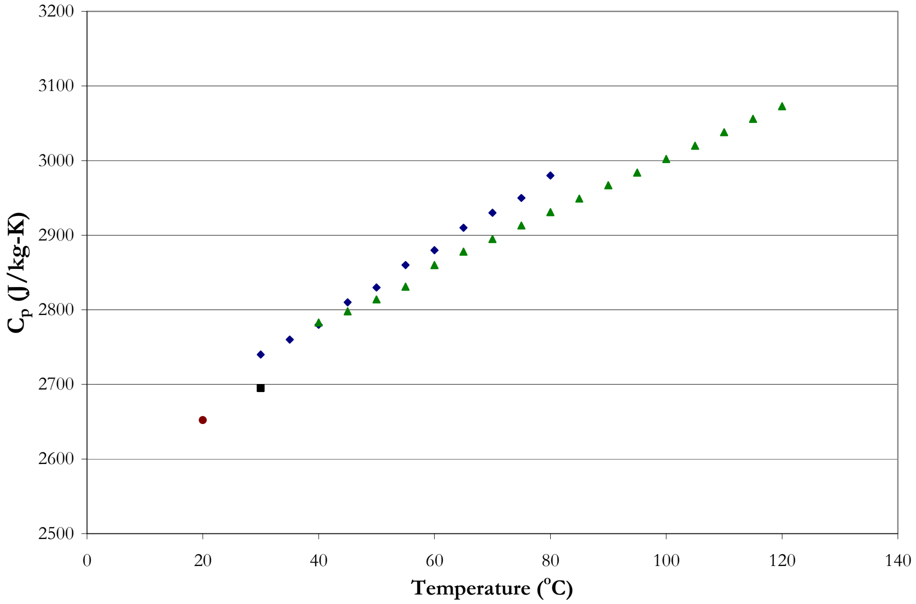

Figure 4.7-3. Specific Heat Capacity of MEA. Points: ■, The Dow Chemical Company (1981), ●, Swanson and Chueh (1973), ♦, Chiu et al. (1999) and ▲, from this work.

Figure 4.7-3 illustrates that experimental specific heat capacity from this work agree with published literature data within ± 2.0 percent of the average specific heat capacity. Experimental results from this work illustrate a similar trend in the temperature dependence as compared to experimental results from The Dow Chemical Company (1981) and Swanson and Chueh (1973).

4.7.3 *H_2O-MEA System*

For the binary system, H_2O-MEA, we chose to compare experimental specific heat capacity measurements for 3.5 and 7 m MEA against literature data from Page et al. (1993), and Chiu and Li (1999) at 40, 60, and 80 °C as shown in Figure 4.7-4 through Figure 4.7-6.

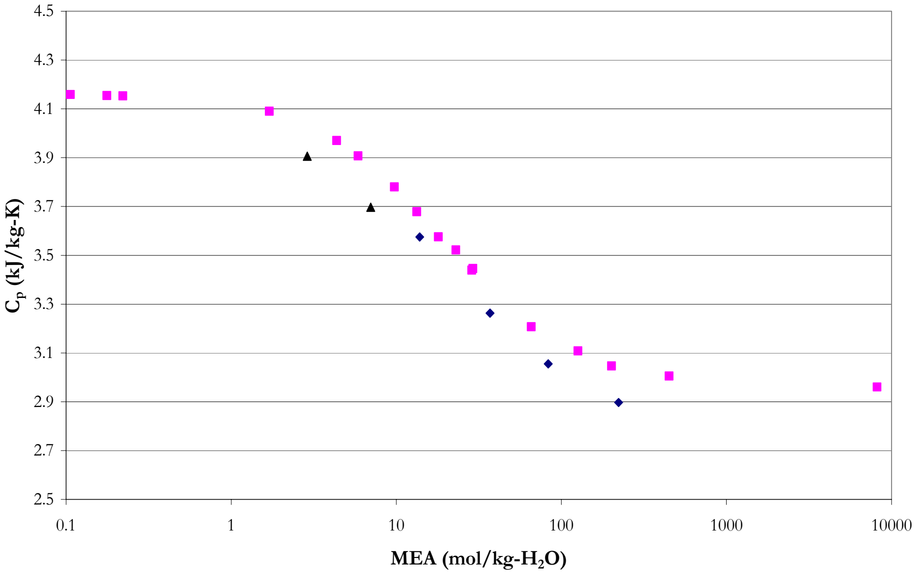

Figure 4.7-4. Specific Heat Capacity for Mixtures of H_2O-MEA at 40 °C. Points: ■, Pagé et al. (1993), ♦, Chiu and Li (1999), and ▲, from this work.

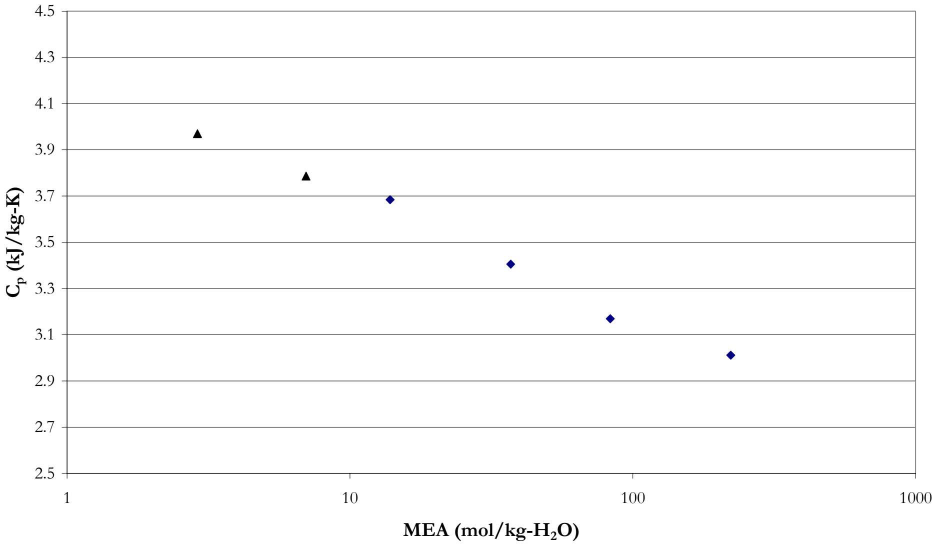

Figure 4.7-5. Specific Heat Capacity for Mixtures of H_2O-MEA at 60 °C. Points: ♦, Chiu and Li (1999), and ▲, from this work.

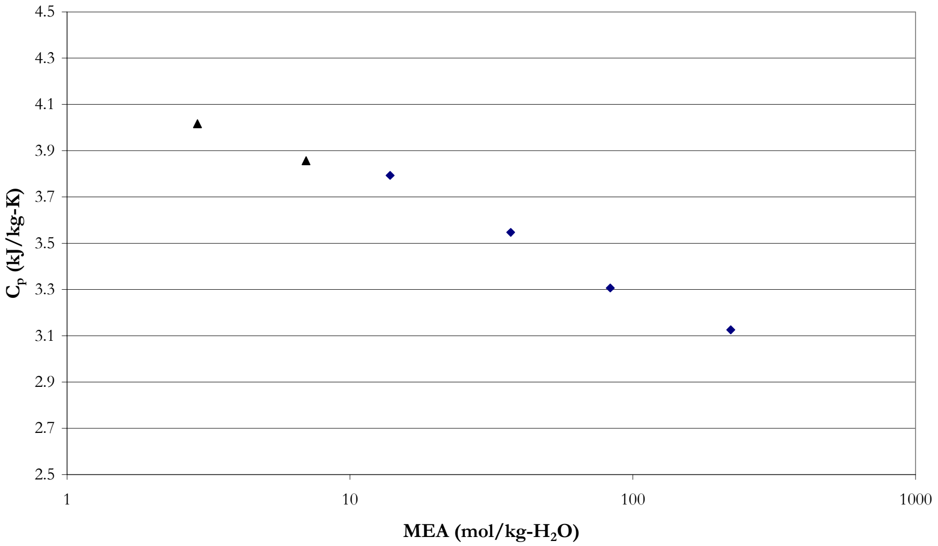

Figure 4.7-6. Specific Heat Capacity for Mixtures of H_2O-MEA at 80 °C. Points: ♦, Chiu and Li (1999), and ▲, from this work.

Figure 4.7-4 through 4.7-6 illustrates that experimental results from this work are consistent with reported specific heat capacity measurements from Page et al. (1993), and Chiu and Li (1999) over the entire temperature and concentration range.

4.8 Conclusions

In conclusion, in this work we have developed a consistent method, based on the ASTM standard, to measure specific heat capacity of alkanolamine solutions. The experimental results are consistent and agree well with key literature data. We are confident in the method to measure the specific heat capacity of loaded alkanolamine solutions, but we would like to recommend that more work be done in this area to verify experimental results reported in this work and to expand the experimental database for specific heat capacity measurements. Overall, the presented specific heat capacity method provides an opportunity for future work to contribute to the understanding of calorimetric heat effects associated with aqueous alkanolamine solutions.

CHAPTER V

Solid-Liquid Equilibrium Methods and Solid Phase Characterization

5.1 Introduction

In the carbon capture processes, the deposition of a salt within the process could cause premature equipment fouling or seizing and should be avoided for systems not designed for salt precipitation. Thus, for carbon capture process utilizing a salt and/or amine for the chemical solvent, knowledge about the range of conditions where salt precipitation is possible is very important. In this work, we have investigated possible methods to describe the solid solubility of salt precipitation in a binary system of H_2O-PZ and solid solubility in the H_2O-K_2CO_3-PZ-CO_2 system.

In addition, Cullinane (2005) reported solid-liquid equilibrium (SLE) for mixtures of potassium carbonate with piperazine and potassium bicarbonate with piperazine at 25 and 40 °C and theorized as to the composition of the solid phase, but did not investigate the solubility of loaded potassium carbonate, potassium bicarbonate, and piperazine mixtures. In this work, we were able to characterize the solid phase in loaded potassium-piperazine mixtures through x-ray diffraction as potassium piperazine dicarbamate ($K_2PZ(COO)_2$).

For mixtures of loaded potassium-piperazine-monoethanolamine mixtures, we were able to observe the precipitation of a solid phase and determine through powder x-ray diffraction that the solid phase was the combination of two salts, $KHCO_3$ and $K_2PZ(COO)_2$.

This chapter will be divided into three parts: part one describes solid solubility measurements for the H_2O-PZ system utilizing results from differential scanning calorimetry (DSC), part two describes solid solubility utilizing visual observations to determine the salt dissolution temperature for mixtures in the H_2O-K_2CO_3-PZ-CO_2 system, and part three describes solid phase characterization utilizing unit cell x-ray diffraction and powder x-ray diffraction. X-ray diffraction experiments were conducted by Lynch (2007).

5.2 Chemicals

Chemicals used in this work included: CO_2 (Matheson Tri-Gas, $\geq$ 99.99 % pure), MEA (Acros Organics, 99 % pure), PZ (Fluka Chemie GmbH, $\geq$ 98.0 % pure), K_2CO_3 (Fluka Chemie GmbH, $\geq$ 99.0 % pure), and $KHCO_3$ (Sigma-Aldrich Inc., $\geq$ 99.5 % pure). All chemicals were used without any further purification.

5.2.1 *Solution Preparation*

All solutions were prepared gravimetrically from ultra pure deionized water. Potassium-piperazine solutions were loaded with CO_2 by slowly sparging pure CO_2 (~0.1 gm/10 sec) through a submerged fritted disk in the solution as shown in Figure 5.2-1. The CO_2 loader was placed on a top-loading scale (± 0.1 gm). As CO_2 reacted with the amine solution, the amount of CO_2 absorbed into the solution would then be displayed on the scale and would continue until the desired loading was reached. Potassium-piperazine solutions loaded with this technique produced CO_2 loadings within ± 5.0 % based on an analytical analysis of the loaded solution. Liquid samples containing bound CO_2 were analyzed for total CO_2 by acidic evolution method. The total alkalinity of the solution was determined by a standard monotonic endpoint sulfuric acid/sodium hydroxide titration analysis. Please refer to Appendix C for more information.

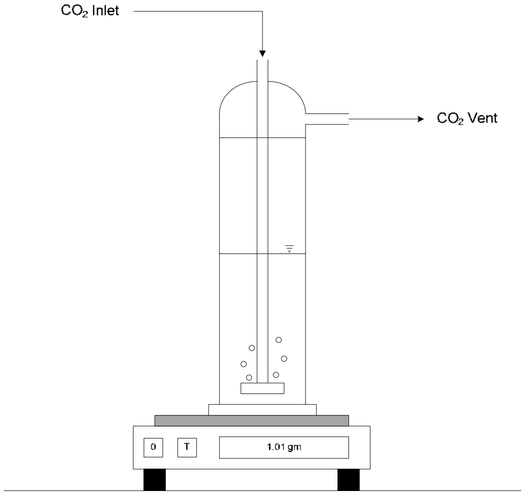

Figure 5.2-1. CO_2 Loading Apparatus.

– Part One –

5.3 H_2O-PZ Solid Solubility

The solid solubility for mixtures of H_2O-PZ was determined utilizing a differential scanning calorimeter and a thermal analysis controller from TA Instruments as previously described in Chapter IV, where the difference in the amount of heat required to increase the temperature of a sample and reference is measured as a function of temperature. During an experiment both the sample and reference pans are maintained at nearly the same temperature throughout the experiment. When a material within the sample pan undergoes a physical transformation such as a phase transition, more (or less) heat will be required to flow to the sample pan than into the reference pan in order to maintain both pans at the same temperature. By observing the difference in heat flow between the sample and reference pans, a DSC is able to measure the amount of heat absorbed or released during such transitions. In this work, we utilized the DSC to determine the dissolution temperature of the solid phase, vis-à-vis synthetic method, as function of concentration and temperature. This technique has been previously described by Nibu and Inoue (1998) for the determination of the solid-liquid phase behavior for binary mixtures of tetraethylene glycol decyl ether and water. In this work, we were able to infer the dissolution temperature based on experimental DSC thermal profiles to determine temperature dependent equilibrium constants for the following reactions as described in Chapter IX.

$$PZ \cdot 6H_2O \leftrightarrow PZ + 6H_2O \tag{5-1}$$

$$PZ_{anh} \leftrightarrow PZ \qquad (5\text{-}2)$$

Where
$PZ \cdot 6H_2O$ is piperazine hexahydrate,
PZ_{anh} is anhydrous piperazine.

Mixtures of water and piperazine were gravimetrically prepared for piperazine concentrations between 0 to 40 m (mole/kg-H_2O). For each piperazine concentration, a fifty gram batch solution was prepared and approximately 59.5 mg of the experimental solution was placed inside two sample pans for analysis.

During an experiment, an empty reference pan and a sample pan were placed on the sample platforms inside the DSC cell. After the DSC cover was lowered into position, a method was created to pre-melt the sample by equilibrating the sample at 150 ^{o}C. This would ensure that the experimental sample covered the bottom of the sample pan. The sample was then slowly cooled to -20 ^{o}C and isothermally held at -20 ^{o}C for ten minutes to ensure that the specimen inside the sample pan reached an equilibrium starting condition. After ten minutes, the DSC would then ramp up the temperature at a constant rate of 5 ^{o}C/min until the temperature reached 125.0 ^{o}C. The DSC would then cool the samples at a rate of 10 ^{o}C/min to 40 ^{o}C where the sample would then be safely removed.

The dissolution temperature was then assigned to the maximum peak height for each phase transition. Figure 5.3-1 and Figure 5.3-2 illustrates typical thermal profiles observed in this work.

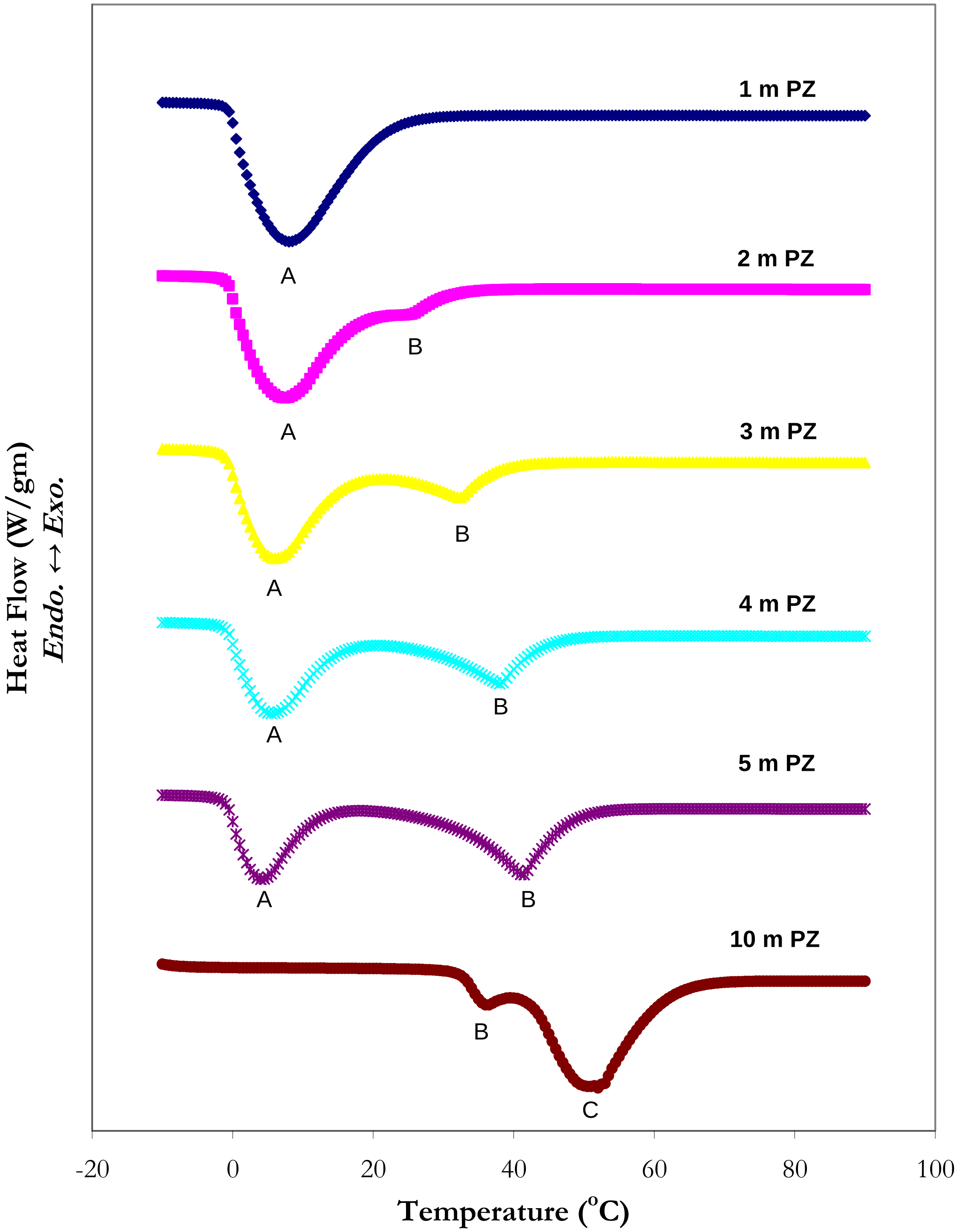

Figure 5.3-1. DSC Thermal Profiles for Mixtures of 1 to 10 m PZ.

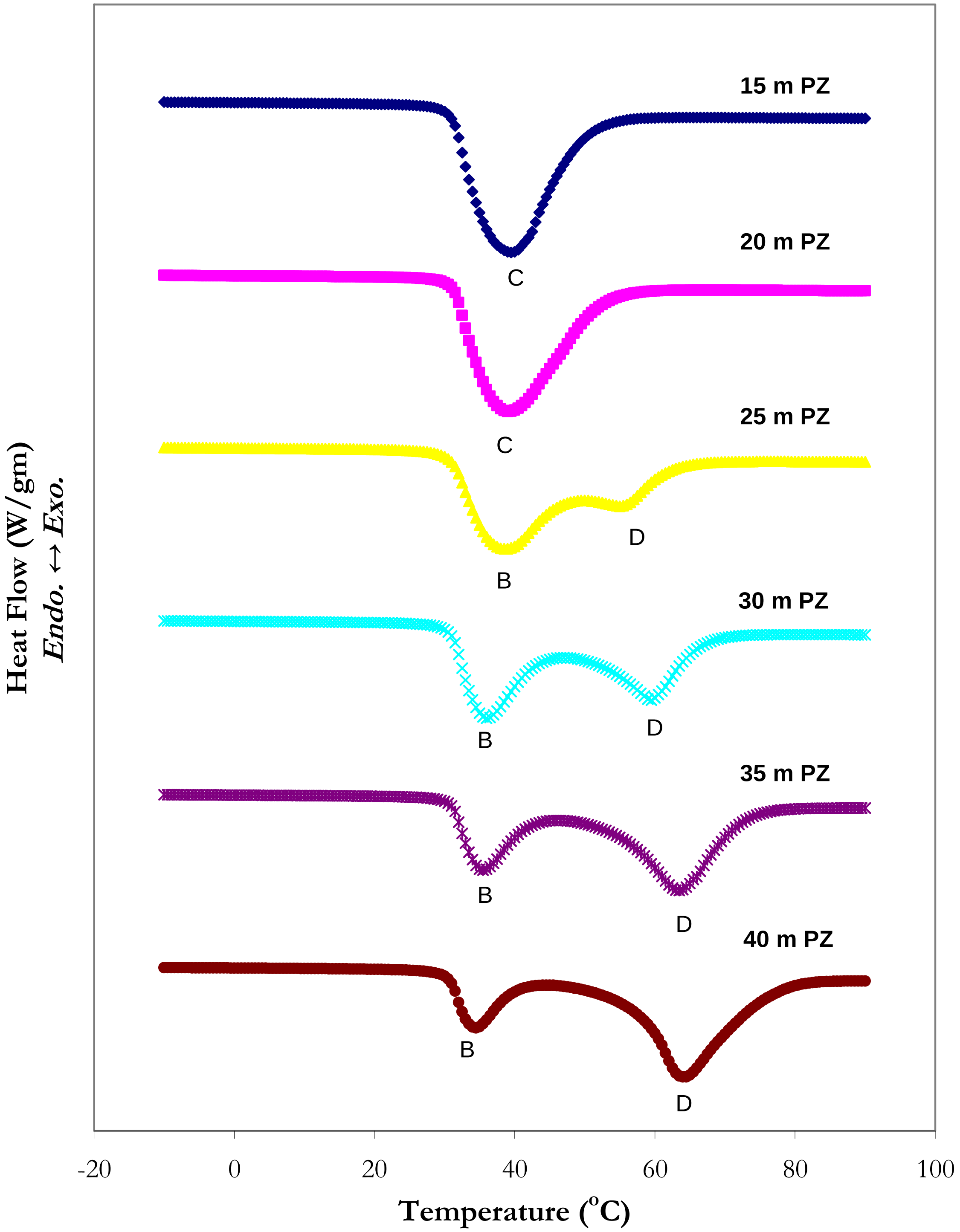

Figure 5.3-2. DSC Thermal Profiles for Mixtures of 15 to 40 m PZ.

Figure 5.3-1 and Figure 5.3-2 illustrate typical DSC thermal profiles obtained by heating various mixtures of water and piperazine from -20 to 125 °C. The endothermic peak (A) was assigned to the melting of water in the form of ice in the presence of piperazine. As the concentration of piperazine is increased, the presence of the endothermic peak (B) was assigned to the melting of piperazine hexahydrate. From 10 to 20 m PZ, the formation of a eutectic mixture of piperazine hexahydrate and anhydrous piperazine was assigned to the endothermic peak (C). Beyond 20 m PZ, formation of anhydrous piperazine was assigned to the endothermic peak (D).

With the determination of the dissolution temperature for each piperazine concentration, a T-X phase diagram for the mixture can be constructed based on the DSC results. Figure 5.3-3 illustrates a possible phase diagram for water-piperazine mixtures obtained by plotting the peak temperatures from the DSC thermal profiles against the weight fraction of piperazine in the mixture as compared to experimental solid solubility measurements from Bishnoi (2002).

Figure 5.3-3 illustrates the start of solidification from a homogeneous liquid state (U) and then by cooling the sample the mixture will pass through the liquidius and then finally solidus lines. At each end of the liquidius line are the pure component melting points for water (F_1) and piperazine (F_2). Points E_1 and E_2 may be considered eutectic points. A eutectic or eutectic mixture is a mixture where all the constituents crystallize simultaneously and form a molten liquid solution. This type of simultaneous crystallization of a eutectic mixture is known as a eutectic reaction where the composition and temperature at which the eutectic reaction takes place is called the eutectic point. A eutectic point is commonly exhibited at the bottom of the "V" formed by two liquidius lines.

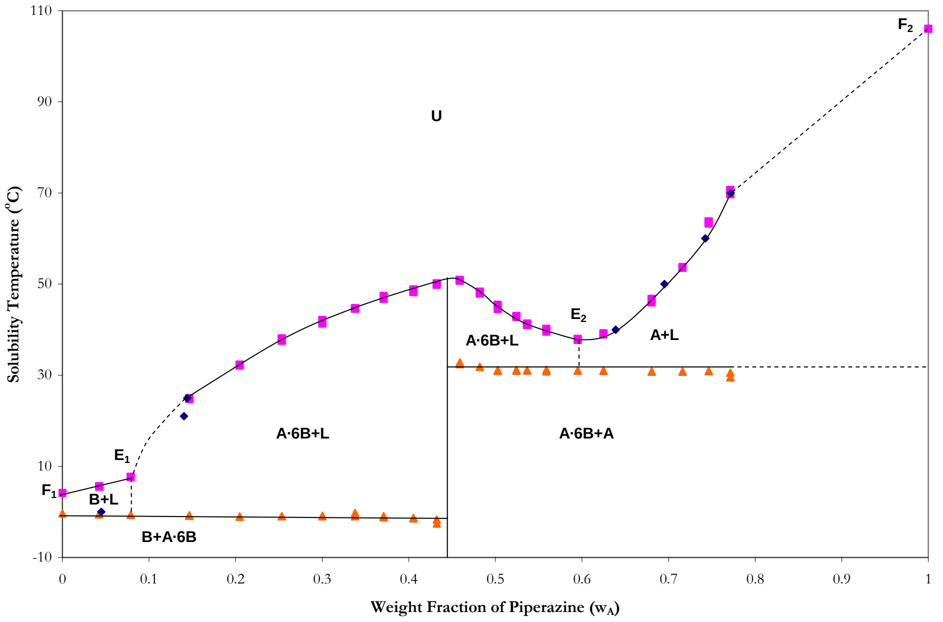

Figure 5.3-3. T-X Phase Diagram for Mixtures of H_2O-PZ. Points: ◆, Bishnoi (2002), ■, liquidius ▲, solidus. Solid lines: Best Fit Approximations, Dash lines: Extrapolations. Abbreviations: U: Homogenous Liquid, L: Metaphase Liquid, F: Pure Component Melting Points, E: Eutectic Point, A: Piperazine, and B: Water.

Based on the above solid solubility for mixtures of H_2O-PZ, we chose not to describe the anhydrous precipitation in our final model because conditions where anhydrous piperazine ($w_{PZ} > 0.6$) would precipitate from an aqueous solution are well beyond the salt concentrations of interest in connection with carbon capture processes and its modifications. Experimental solubility from Bishnoi et al. (2002) and from this work, describing liquidius phase transitions between 9 and 45 weight percent of piperazine, were used to determine coefficients for the temperature dependent equilibrium constant for Equation 5-1 through optimum model predictions for the H_2O-PZ system as described in Chapter IX, Section 9.2.4.

In this work, we did not investigate solid solubility for the H_2O-PZ-CO_2 system. As described in Chapter XIV, we were able to use the optimum model as a predictive tool to illustrate the possible effects of loading on the solid solubility in the H_2O-PZ-CO_2 system over the concentration range from 1 to 5 m PZ. We would recommend that future work should verify predictions from this work to create a rigorous and consistent thermodynamic model for predicting vapor-liquid and solid-liquid equilibrium for the H_2O-PZ-CO_2 system.

– Part Two –

5.4 Solid Solubility Visual Observations

Visual observations of the solid solubility for the H_2O-K_2CO_3-PZ-CO_2 system were conducted in this work utilizing the synthetic method by Marshall et al. (1954) where we prepared loaded solutions of known liquid phase compositions and then visually determined the temperature at which a phase transition occurred. The solution was sealed in a 30 ml media sample bottle containing a micro-stir bar for agitation. The sample bottles were placed in a water bath (± 0.1 °C) and then on top of a magnetic stir plate and allowed to equilibrate over a period of 24 hours before a visual observation as to the presence of a solid phase was made. The water bath temperature would then be raised 0.5 °C where the sample bottle would again be allowed to equilibrate. This process would continue until all of the solutions represented a clear and homogenous solution. The dissolution temperature was then determined as the average temperature between the visual observation of a solid phase and that of a clear and homogenous solution. In this work, only solution compositions of 5 m K^+ + 2.5 m PZ, 6 m K^+ + 1.2 m PZ, and 5 m K^+ + 3.6 m PZ demonstrated the possibility for the precipitation of a solid phase. The accuracy of the measurements depended on the ability to detect the last trace of a dissolving solid or the first appearance of a precipitating solid. We would recommend that future work verify the dissolution temperatures reported in this work and utilize a more sophisticated and accurate method than that presented in this investigation.

5.3.1 ***Experimental Results***

Figure 5.4-1 through Figure 5.4-4 illustrate visual observations conducted in this work to determine the dissolution temperature for mixtures in the H_2O-K_2CO_3-PZ-CO_2 system. Figure 5.4-4 illustrates a three dimensional representation of the determined dissolution temperatures associated with mixtures of 5 m K^+ + 2.5 m PZ (K^+/PZ = 2), 6 m K^+ + 1.2 m PZ (K^+/PZ = 5), and 5 m K^+ + 3.6 m PZ (K^+/PZ = 1.39) where the potassium to piperazine ratio was utilized to differentiate the solution compositions.

Figure 5.4-1 through Figure 5.4-3 illustrates the precipitation of $KHCO_3$ and $K_2PZ(COO)_2$ for mixtures in the H_2O-K_2CO_3-PZ-CO_2 system and were verified through unit cell x-ray diffraction preformed by Lynch (2007). Please refer to section 5.3.2 for more information about the determination of the $K_2PZ(COO)_2$ salt.

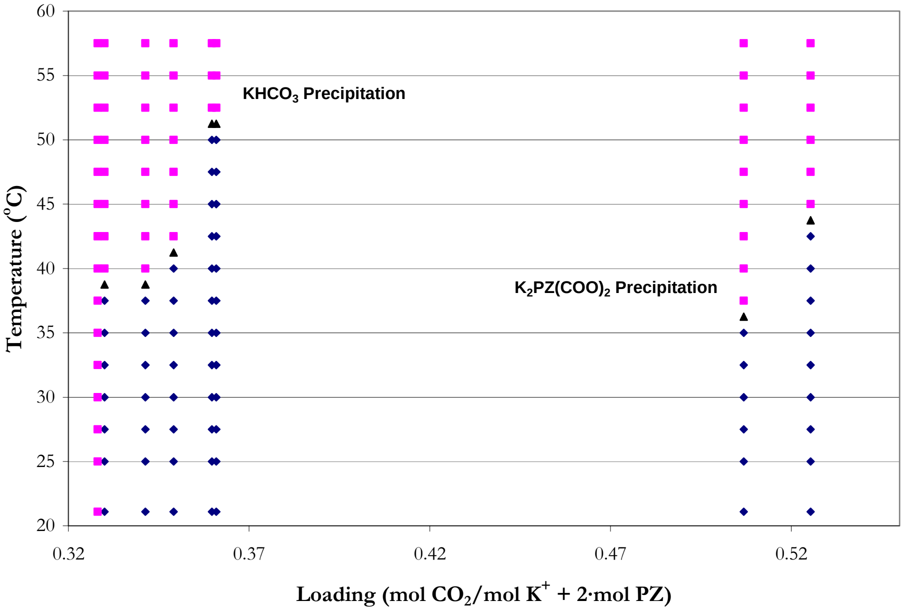

Figure 5.4-1. Visual Observations in Determining the Dissolution Temperature for Mixtures of 5 m K$^+$ + 3.6 m PZ. Points: ♦, Presence of a Solid Phase, ■, Presence of a Clear and Homogenous Solution, ▲, Temperature of Dissolution.

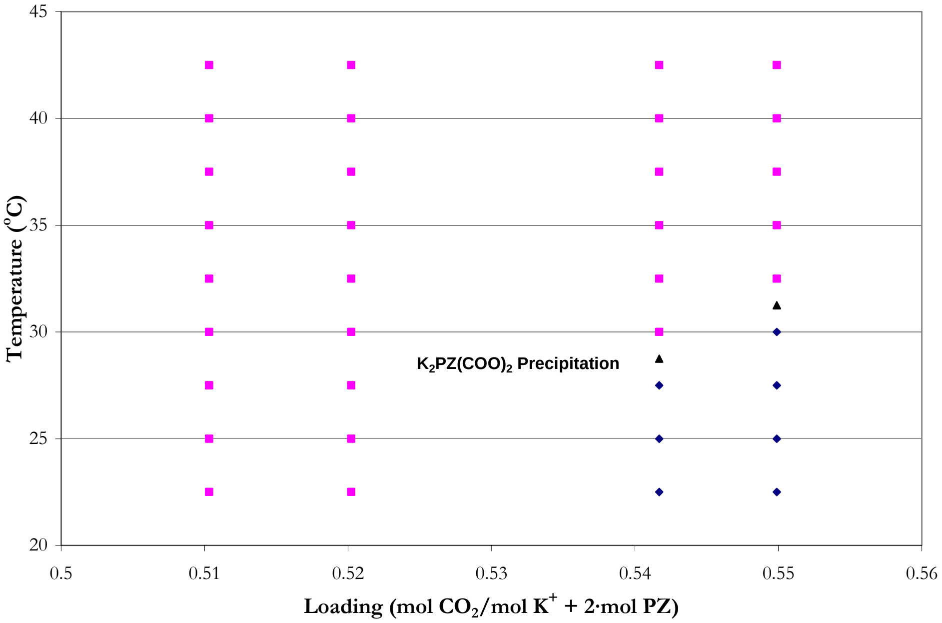

Figure 5.4-2. Visual Observations in Determining the Dissolution Temperature for Mixtures of 5 m K$^+$ + 2.5 m PZ. Points: ♦, Presence of a Solid Phase, ■, Presence of a Clear and Homogenous Solution, ▲, Temperature of Dissolution.

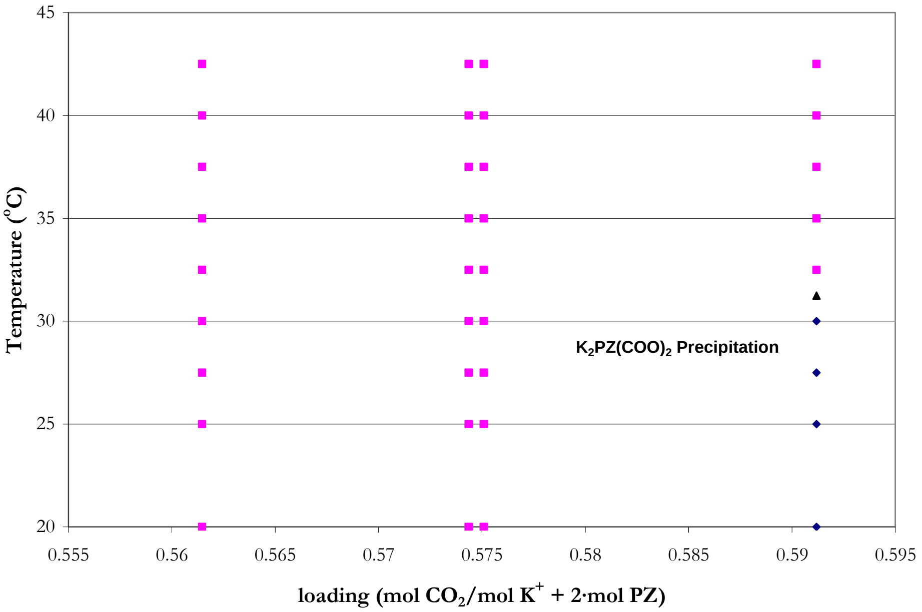

Figure 5.4-3. Visual Observations in Determining the Dissolution Temperature for Mixtures of 6 m K^+ + 1.2 m PZ. Points: ♦, Presence of a Solid Phase, ■, Presence of a Clear and Homogenous Solution, ▲, Temperature of Dissolution.

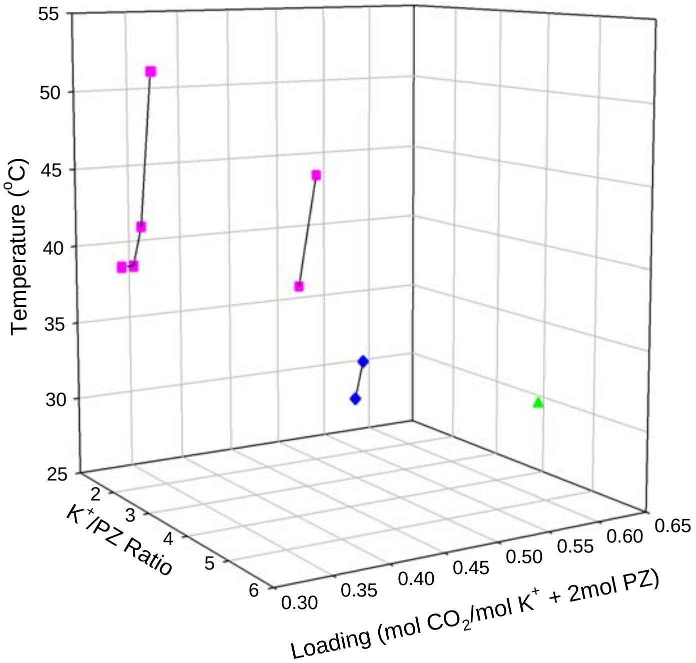

Figure 5.4-4. Visual Observations in Determining the Dissolution Temperature for Mixtures in the H_2O-K_2CO_3-PZ-CO_2 System. Points: ♦, 5 m K^+ + 3.6 m PZ, ■, 5 m K^+ + 2.5 m PZ, ▲, 6 m K^+ + 1.2 m PZ.

Using vacuum filtration, we were able to separate the $K_2PZ(COO)_2$ solid phase from the mother liquor in a solution of 5 m K^+ + 3.6 m PZ. The solid phase was then dried in a vacuum over the course of 24 hours. The crystals were then documented using a scanning electron microscope and a digital camera as shown in Figure 5.4-5 and Figure 5.4-6.

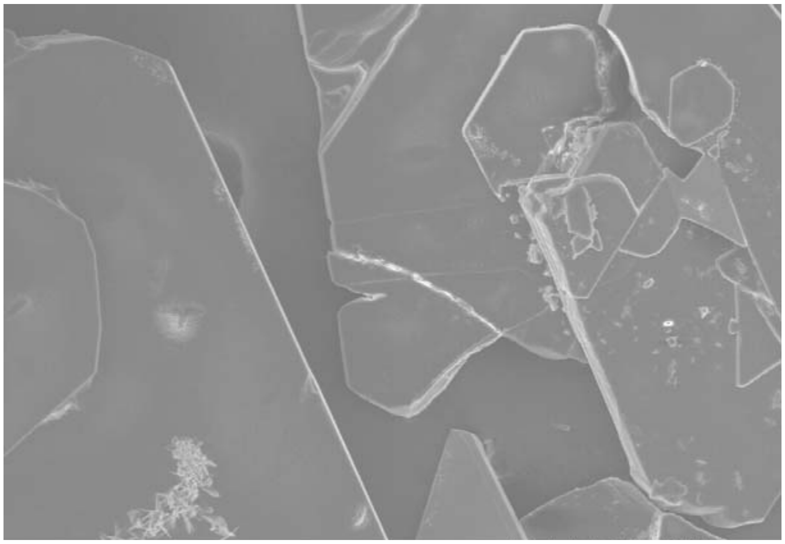

Figure 5.4-5. Scanning Electron Microscope Image of $K_2PZ(COO)_2$ salt at a Magnification of 120 μm.

Figure 5.4-6. Digital Image of $K_2PZ(COO)_2$ salt.

— Part Three —

5.5 Solid Phase Characterization

Solid phase characterization in this work was performed in two phases: phase one described the determination of the potassium piperazine dicarbamate ($K_2PZ(COO)_2$) through unit cell x-ray diffraction preformed by Lynch (2007), and phase two describes powder x-ray diffraction for the characterization of the solid phase present in mixtures of loaded potassium-piperazine-monoethanolamine mixtures.

5.3.2 *Unit Cell X-ray Diffraction*

In this work, Lynch (2007) performed unit cell x-ray diffraction on samples of 5 m K^+ + 2.5 m PZ, 6 m K^+ + 1.2 m PZ, and 5 m K^+ + 3.6 m PZ to determine the structure of the present solid phase. Low loading samples contained a $KHCO_3$ salt and were verified through the comparison of the unit cell structure to the known unit cell powder diffraction file based on Thomas et al. (1974). High loading samples were found to contain a $K_2PZ(COO)_2$ salt based on the structure of the unit cell as described by the following experimental description as prepared by Lynch (2007) for inclusion in this work.

X-ray Diffraction Experiment for $K_2PZ(COO)_2$

Crystals grew as large, colorless prisms by slow cooling from water. The data crystal was cut from a much larger crystal and had approximate dimensions of 0.43 x 0.33 x 0.08 mm. The data were collected on a Nonius Kappa CCD diffractometer using a graphite monochromator with MoKα radiation (λ = 0.71073Å). A total of 133 frames of data were collected using ω-scans with a scan range of 2° and a counting time of 70 seconds per frame. The data were collected at 153 K using an Oxford Cryostream low temperature device. Details of crystal data, data collection, and structure refinement are listed in Table 5.5-1.

Table 5.5-1. Crystal Data for $K_2PZ(COO)_2$ salt.

Empirical formula	$C_6 H_8 K_2 N_2 O_4$	
Formula weight	250.34	
Temperature	153(2) K	
Wavelength	0.71073 Å	
Crystal system	Monoclinic	
Space group	P21/c	
Unit cell dimensions	a = 10.0350(4) Å	α= 90°.
	b = 3.9900(2) Å	β= 106.766(3)°.
	c = 11.5470(5) Å	γ = 90°.
Volume	442.68(3) $Å^3$	
Z	2	
Density (calculated)	1.878 Mg/m^3	
Absorption coefficient	1.059 mm^{-1}	
F(000)	256	
Crystal size	0.43 x 0.33 x 0.08 mm	
Theta range for data collection	2.12 to 27.45°.	
Index ranges	-13<=h<=13, -5<=k<=5, -14<=l<=14	
Reflections collected	982	
Completeness to theta = 27.45°	97.2 %	
Absorption correction	None	
Refinement method	Full-matrix least-squares on F^2	
Data / restraints / parameters	982 / 0 / 66	
Goodness-of-fit on F^2	1.122	
Final R indices [I>2sigma(I)]	R1 = 0.0302, wR2 = 0.0919	
R indices (all data)	R1 = 0.0328, wR2 = 0.0943	
Extinction coefficient	9.9(15)x10^{-5}	
Largest diff. peak and hole0.493 and -0.510 e.$Å^{-3}$		

Data reduction were performed using DENZO-SMN (1997). The structure was solved by direct methods using SIR97 (1999) and refined by full-matrix least-squares on F^2 with anisotropic displacement parameters for the non-H atoms using SHELXL-97 [Sheldrick (1994)]. The hydrogen atoms on carbon were calculated in ideal positions with isotropic displacement parameters set to 1.2xUeq of the attached atom (1.5xUeq for methyl hydrogen atoms).

The crystal was twinned. The twin law was determined using the TwinRotMat utility in Platon98 [Spek (1998)]. The twin law was (-1, 0, ½; 0, -1, 0; 0, 0, 1) about the 0, 0, -1, direct axis direction. The twin fraction refined to 0.642(5). Platon98 was used as incorporated in WinGX (1999).

The following function was minimized

$$\sum w\left(|F_o|^2-|F_c|^2\right)^2 \qquad 5\text{-}3$$

Where

$$w=\frac{1}{\left(\sigma F_o\right)^2+\left(0.0451P\right)^2+0.3484P} \qquad 5\text{-}4$$

$$P=\frac{|F_o|^2+2|F_c|^2}{3} \qquad 5\text{-}5$$

The square of the weighted residual $\left(R_w\left(F^2\right)\right)$ was refined to 0.0943 with a residual $\left(R\left(F\right)\right)$ equal to 0.0302 and a goodness of fit equal to 1.12. Definitions used for calculating $R\left(F\right)$, $R_w\left(F^2\right)$, and the goodness of fit, S, are given by Equation 5-6 through 5-8.

$$R_w\left(F^2\right)=\left[\frac{\sum w\left(|F_o|^2-|F_c|^2\right)^2}{\sum w|F_o|^4}\right]^{1/2} \qquad 5\text{-}6$$

Where
W is the weight given for each reflection.

$$R(F) = \frac{\sum(|F_o| - |F_c|)}{\sum|F_o|} \quad 5\text{-}7$$

Where
$F_o > 4(\sigma F_o)$

$$S = \left[\frac{\sum w\left(|F_o|^2 - |F_c|^2\right)^2}{n - p} \right]^{1/2} \quad 5\text{-}8$$

Where
n is the number of reflections, and
p is the number of refined parameters.

The data were corrected for secondary extinction effects based on the following form:

$$F_{corr} = \left[\frac{kF_c}{1 + 9.9\left(15\times10^{-5}\right)\frac{F_c^2\lambda^3}{\sin 2\theta}} \right]^{0.25} \quad 5\text{-}9$$

Where
k is the overall scale factor.

Neutral atom scattering factors and values used to calculate the linear absorption coefficient are from the International Tables for X-ray Crystallography (1992). All figures illustrating the crystalline structure were generated using SHELXTL/PC [Sheldrick (1994)]. Tables of positional and thermal parameters, bond lengths and angles, torsion angles, figures, and lists of observed and calculated structure factors are located in Tables 5.5-2 through 5.5-8, respectively.

Table 5.5-2. Fractional Coordinates and Equivalent Isotropic Thermal Parameters (Å2) for the non-hydrogen atoms for $K_2PZ(COO)_2$.

	x	y	z	U(eq)
K1	-1035(1)	7577(1)	3493(1)	12(1)
O1	1631(4)	7491(4)	5124(3)	14(1)
O2	1632(4)	7600(4)	3178(3)	13(1)
N1	3584(2)	5960(5)	4649(2)	10(1)
C1	2202(2)	7047(5)	4304(4)	9(1)
C2	4219(3)	4632(7)	5861(2)	10(1)
C3	4215(3)	4694(7)	3747(2)	11(1)

Table 5.5-3. Bond Lengths (Å) and Angles (°) for the Non-hydrogen Atoms for $K_2PZ(COO)_2$.

K1-O1#1	2.708(3)	O2-K1#3	2.712(2)
K1-O2#2	2.712(2)	O2-K1#2	2.726(3)
K1-O2#3	2.726(3)	N1-C1	1.396(2)
K1-O1#4	2.748(3)	N1-C3	1.457(3)
K1-O1	2.793(3)	N1-C2	1.460(3)
K1-O2	2.803(3)	C2-C3#5	1.529(3)
K1-C1	3.1179(19)	C2-H2A	0.96
O1-C1	1.252(5)	C2-H2B	0.96
O1-K1#1	2.708(3)	C3-C2#5	1.529(3)
O1-K1#4	2.748(3)	C3-H3A	0.96
O2-C1	1.280(5)	C3-H3B	0.96
O1#1-K1-O2#2	155.58(4)	O1#1-K1-O2	117.11(10)
O1#1-K1-O2#3	80.94(5)	O2#2-K1-O2	86.18(9)
O2#2-K1-O2#3	94.39(9)	O2#3-K1-O2	85.92(9)
O1#1-K1-O1#4	93.99(10)	O1#4-K1-O2	116.99(9)
O2#2-K1-O1#4	80.47(5)	O1-K1-O2	47.35(4)
O2#3-K1-O1#4	155.83(4)	O1#1-K1-C1	105.09(10)
O1#1-K1-O1	86.72(9)	O2#2-K1-C1	99.28(9)
O2#2-K1-O1	116.27(9)	O2#3-K1-C1	105.06(9)
O2#3-K1-O1	117.28(9)	O1#4-K1-C1	99.09(9)
O1#4-K1-O1	85.75(9)	O1-K1-C1	23.64(10)

Table 5.5-4. Bond Lengths (Å) and Angles (^{o}) for the Non-hydrogen Atoms for $K_2PZ(COO)_2$, Continued.

O2-K1-C1	24.22(10)	C1-O2-K1	91.82(18)
C1-O1-K1#1	140.89(16)	K1#3-O2-K1	94.10(9)
C1-O1-K1#4	123.98(14)	K1#2-O2-K1	93.80(9)
K1#1-O1-K1#4	93.99(10)	C1-N1-C3	120.3(3)
C1-O1-K1	92.88(19)	C1-N1-C2	120.6(3)
K1#1-O1-K1	93.28(9)	C3-N1-C2	113.56(16)
K1#4-O1-K1	94.25(9)	O1-C1-O2	125.12(18)
C1-O2-K1#3	142.30(16)	O1-C1-N1	117.5(3)
C1-O2-K1#2	122.33(14)	O2-C1-N1	117.3(3)
K1#3-O2-K1#2	94.39(9)	O1-C1-K1	63.47(17)
O2-C1-K1	63.96(17)	H2A-C2-H2B	108.1
N1-C1-K1	165.81(13)	N1-C3-C2#5	110.4(2)
N1-C2-C3#5	110.3(2)	N1-C3-H3A	109.1
N1-C2-H2A	109.6	C2#5-C3-H3A	109.3
C3#5-C2-H2A	109.7	N1-C3-H3B	110.1
N1-C2-H2B	109.6	C2#5-C3-H3B	109.7
C3#5-C2-H2B	109.5	H3A-C3-H3B	108.1

Symmetry transformations used to generate equivalent atoms:

#1: -x,-y+2,-z+1, #2: -x,y-1/2,-z+1/2, #3: -x,y+1/2,-z+1/2, #4: -x,-y+1,-z+1, #5: -x+1,-y+1,-z+1

Table 5.5-5. Anisotropic Thermal Parameters for the Non-hydrogen Atoms for $K_2PZ(COO)_2$.

	U^{11}	U^{22}	U^{33}	U^{23}	U^{13}	U^{12}
K1	12(1)	12(1)	11(1)	0(1)	4(1)	0(1)
O1	12(1)	17(2)	13(1)	0(1)	6(1)	2(1)
O2	12(1)	15(1)	10(1)	2(1)	2(1)	3(1)
N1	11(1)	14(1)	6(1)	0(1)	3(1)	2(1)
C1	11(1)	3(1)	11(1)	0(1)	2(1)	0(1)
C2	13(1)	11(1)	8(1)	0(1)	4(1)	2(1)
C3	14(1)	11(1)	7(1)	-1(1)	3(1)	2(1)

Table 5.5-6. Fractional Coordinates and Isotropic Thermal Parameters (Å²) for the Hydrogen Atoms for $K_2PZ(COO)_2$.

	x	y	z	U(eq)
H2A	4053	2264	5867	12
H2B	3803	5671	6422	12
H3A	3798	5792	2989	13
H3B	4048	2331	3633	13

Table 5.5-7. Observed and Calculated Structure Factor Amplitudes for $K_2PZ(COO)_2$.

h	k	l	10Fo	10Fc	10s
1	0	0	252	256	5
2	0	0	78	72	1
3	0	0	580	607	11
5	0	0	47	30	1
6	0	0	171	170	1
7	0	0	60	65	1
8	0	0	62	60	1
9	0	0	174	176	3
10	0	0	138	137	3
11	0	0	121	123	3
12	0	0	149	141	5
1	1	0	298	288	3
2	1	0	95	108	1
3	1	0	625	620	8
4	1	0	542	527	9
-5	-1	0	286	286	2
6	1	0	354	347	3
7	1	0	484	490	5
8	1	0	309	311	3
9	1	0	204	200	2
10	1	0	146	142	2
11	1	0	249	250	5
12	1	0	239	231	7
2	2	0	207	201	1
3	2	0	516	523	5
4	2	0	338	337	2
5	2	0	299	304	2
6	2	0	38	36	1
7	2	0	61	59	1
8	2	0	125	129	1
9	2	0	105	101	1
10	2	0	151	151	2
11	2	0	156	150	3
1	3	0	12	12	1
2	3	0	75	78	1
3	3	0	297	292	3
4	3	0	415	417	5
5	3	0	16	18	1
6	3	0	132	129	1
7	3	0	329	321	4
8	3	0	344	349	5
9	3	0	6	9	6
10	3	0	5	15	5
0	4	0	447	445	5
1	4	0	234	235	3
2	4	0	30	31	1
3	4	0	272	272	3
-4	-4	0	235	237	5
-5	-4	0	122	119	2
7	4	0	97	100	2
-1	-5	0	60	64	1
-2	-5	0	50	46	1
-3	-5	0	240	245	8
12	-1	-1	13	13	4
11	-1	-1	14	14	3
10	-1	-1	21	26	2
9	-1	-1	20	26	1
8	-1	-1	0	2	1
7	-1	-1	20	23	1
6	-1	-1	56	54	1
5	-1	-1	110	105	3
4	-1	-1	104	96	2
3	-1	-1	33	36	1
2	-1	-1	59	66	1
1	-1	-1	202	265	3
0	-1	-1	281	297	8
1	1	1	138	172	1
2	1	1	7	8	1
3	1	1	88	89	1
4	1	1	97	86	2
5	1	1	108	98	3
6	1	1	34	36	1
7	1	1	6	8	2
8	1	1	19	26	1
9	1	1	13	21	1
10	1	1	14	8	2
11	1	1	3	11	3
11	-2	-1	8	7	8
10	-2	-1	24	28	2
9	-2	-1	50	50	2
8	-2	-1	68	63	2
7	-2	-1	30	34	1
6	-2	-1	69	62	2
5	-2	-1	30	31	1
4	-2	-1	55	61	1
3	-2	-1	18	15	1
2	-2	-1	43	41	1
1	-2	-1	54	52	1
0	-2	-1	8	1	2
1	2	1	113	111	2
2	2	1	10	5	1
3	2	1	28	32	1
4	2	1	28	27	1
5	2	1	77	74	1
6	2	1	45	44	1
7	2	1	3	3	3
8	2	1	78	70	2
9	2	1	41	41	1
10	2	1	3	2	2
11	2	1	21	22	2
10	-3	-1	23	24	2
9	-3	-1	9	4	6
8	-3	-1	69	67	2
7	-3	-1	32	40	1
6	-3	-1	43	41	1
5	-3	-1	5	7	1
4	-3	-1	22	25	1
3	-3	-1	7	4	1
1	-3	-1	19	16	1
0	-3	-1	36	34	1
1	3	1	54	50	1
3	3	1	12	10	1
4	3	1	64	60	1
5	3	1	7	7	2
6	3	1	37	41	1
7	3	1	91	87	3
8	3	1	9	3	5
9	3	1	0	2	1
8	-4	-1	12	7	8
7	-4	-1	37	39	1
6	-4	-1	9	10	7
5	-4	-1	86	86	4
4	-4	-1	17	14	1
3	-4	-1	23	24	1
2	-4	-1	10	2	2
1	-4	-1	20	18	1
0	4	1	24	21	1
1	4	1	57	57	1
-2	-4	-1	24	28	2
-3	-4	-1	11	14	4
-4	-4	-1	78	83	2
-5	-4	-1	27	29	2
6	4	1	0	5	1
7	4	1	28	29	2
3	-5	-1	46	43	2
2	-5	-1	29	35	2
1	-5	-1	31	27	2
0	-5	-1	5	3	4
-1	-5	-1	15	9	3
-2	-5	-1	18	8	2
-12	0	2	217	213	6
-11	0	2	162	159	3
-10	0	2	78	80	1
-9	0	2	197	193	3
-8	0	2	270	284	4
-7	0	2	423	429	5
-6	0	2	215	215	2
-5	0	2	346	344	4
-4	0	2	424	436	6
-3	0	2	568	643	19
-2	0	2	294	296	2
-1	0	2	314	313	3
0	0	2	325	313	6
1	0	2	291	296	3
3	0	2	412	436	5
4	0	2	339	344	4
5	0	2	214	216	2
6	0	2	417	429	5
7	0	2	279	285	4
8	0	2	199	193	2
9	0	2	79	79	1
10	0	2	160	159	3
11	0	2	215	215	6
12	-1	-2	69	73	1
11	-1	-2	170	168	3
10	-1	-2	213	209	3
9	-1	-2	243	240	3
8	-1	-2	6	5	2
7	-1	-2	172	171	1
6	-1	-2	195	196	1
5	-1	-2	417	404	5
4	-1	-2	404	399	3
3	-1	-2	224	229	1
2	-1	-2	177	176	1
1	1	2	171	178	1
2	1	2	227	231	2
3	1	2	413	400	3
4	1	2	415	403	3
5	1	2	194	198	1
6	1	2	175	169	1
7	1	2	4	4	4
8	1	2	242	241	2
9	1	2	209	210	3
10	1	2	176	168	2
11	1	2	70	74	2
11	-2	-2	94	96	2
10	-2	-2	21	21	1
9	-2	-2	164	177	2
8	-2	-2	277	277	3
7	-2	-2	316	308	3
6	-2	-2	140	137	1
5	-2	-2	130	127	1
4	-2	-2	449	444	3
3	-2	-2	382	372	3
2	-2	-2	132	139	1
1	-2	-2	104	103	1
0	-2	-2	105	103	1
1	2	2	132	139	1
2	2	2	376	373	3
3	2	2	461	444	4
4	2	2	125	129	1
5	2	2	138	138	1
6	2	2	317	310	2
7	2	2	282	277	3
8	2	2	172	178	2
9	2	2	23	20	1
10	2	2	94	96	2
10	-3	-2	239	235	5
9	-3	-2	95	95	2
8	-3	-2	54	54	1
7	-3	-2	83	83	1
6	-3	-2	253	256	2
5	-3	-2	175	175	1
4	-3	-2	262	260	3
3	-3	-2	155	156	1
2	-3	-2	203	221	2
1	-3	-2	388	380	4
0	-3	-2	386	383	4
1	3	2	219	217	2
-2	-3	-2	154	155	2
-3	-3	-2	264	261	4
4	3	2	175	176	2
5	3	2	258	252	2
6	3	2	81	85	1
7	3	2	55	57	1
8	3	2	96	93	2
9	3	2	238	236	5
8	-4	-2	240	241	7
7	-4	-2	158	156	3
6	-4	-2	107	109	2
5	-4	-2	66	71	1
4	-4	-2	255	254	3
3	-4	-2	193	195	2
2	-4	-2	141	138	2
1	-4	-2	62	63	1
0	4	2	61	61	1
-1	-4	-2	139	140	2
-2	-4	-2	196	193	4
-3	-4	-2	254	257	5
-4	-4	-2	71	69	2
-5	-4	-2	106	108	2
-6	-4	-2	158	157	4
7	4	2	230	243	4
3	-5	-2	51	56	2
2	-5	-2	112	111	2
1	-5	-2	208	213	4
0	-5	-2	210	210	3
-1	-5	-2	106	112	2
-2	-5	-2	52	58	1
12	-1	-3	26	26	2
11	-1	-3	25	30	2
10	-1	-3	9	11	3
9	-1	-3	21	19	1
8	-1	-3	85	75	3
7	-1	-3	66	65	1
6	-1	-3	22	23	1
5	-1	-3	0	1	1
4	-1	-3	59	54	1
3	-1	-3	54	57	1
2	-1	-3	42	48	1
1	-1	-3	6	7	1
0	1	3	18	18	1
1	1	3	96	91	5
2	1	3	54	56	1
4	1	3	5	6	2
5	1	3	58	56	1
6	1	3	77	75	2
7	1	3	57	55	2
8	1	3	7	0	4
9	1	3	22	27	3
10	1	3	27	24	2
11	1	3	33	34	2
11	-2	-3	17	25	3
10	-2	-3	19	19	2
9	-2	-3	38	42	2
8	-2	-3	8	7	4
7	-2	-3	16	18	1
6	-2	-3	44	46	1
5	-2	-3	4	5	4
4	-2	-3	23	24	1
3	-2	-3	16	18	1
2	-2	-3	114	100	1
1	-2	-3	17	19	1
0	2	3	83	72	1
1	2	3	89	74	1
2	2	3	23	26	1
3	2	3	10	10	1
4	2	3	8	10	1
5	2	3	56	61	1
6	2	3	27	30	1
7	2	3	48	47	1
8	2	3	8	7	7
9	2	3	5	4	5
10	2	3	0	8	1
10	-3	-3	0	7	1
9	-3	-3	20	26	3
8	-3	-3	18	25	2
7	-3	-3	20	20	1
6	-3	-3	57	54	1
5	-3	-3	3	5	3
4	-3	-3	14	16	1
3	-3	-3	13	11	1
2	-3	-3	8	1	2
1	-3	-3	50	50	1
0	3	3	85	85	1
-1	-3	-3	46	45	1
-2	-3	-3	13	13	3
-3	-3	-3	26	25	1
4	3	3	59	58	1
5	3	3	15	21	1
6	3	3	0	4	1
7	3	3	0	7	1
8	3	3	22	27	2
9	3	3	14	11	3
8	-4	-3	16	18	3
7	-4	-3	11	9	5
6	-4	-3	15	9	2
5	-4	-3	28	27	1
4	-4	-3	20	22	1
3	-4	-3	92	80	1
2	-4	-3	18	20	1
1	-4	-3	4	3	4
0	4	3	0	3	1
-1	-4	-3	54	36	2
-2	-4	-3	63	50	1
-3	-4	-3	28	26	2
-4	-4	-3	59	60	2
-5	-4	-3	16	19	4
-6	-4	-3	19	16	4
2	-5	-3	41	41	1
1	-5	-3	29	24	2
0	-5	-3	0	14	1
1	5	3	74	73	1
-13	0	4	174	168	6
-12	0	4	179	168	5
-11	0	4	245	236	5
-10	0	4	396	389	9
-9	0	4	304	303	7
-8	0	4	421	412	8
-7	0	4	268	271	4
-6	0	4	545	533	6
-5	0	4	181	180	2
-4	0	4	216	193	2
-3	0	4	22	19	1
-2	0	4	457	456	4
-1	0	4	196	220	2
0	0	4	463	460	8
1	0	4	25	17	1
2	0	4	216	193	2
3	0	4	183	184	1
4	0	4	539	536	6
5	0	4	264	271	2
6	0	4	414	409	5
7	0	4	313	304	4
8	0	4	397	390	8
9	0	4	237	237	5
10	0	4	180	166	5
11	0	4	179	167	7
12	-1	-4	73	77	2
-11	1	4	67	68	2
10	-1	-4	89	89	1
9	-1	-4	65	63	1
8	-1	-4	150	148	1
7	-1	-4	358	358	2
6	-1	-4	236	236	1
5	-1	-4	100	103	1
4	-1	-4	424	424	3
2	-1	-4	353	341	2
1	-1	-4	10	7	1
0	1	4	351	344	2
2	1	4	429	422	3
3	1	4	98	102	1
4	1	4	236	236	1
5	1	4	362	356	2
6	1	4	147	149	1
7	1	4	67	64	1
8	1	4	89	90	1
9	1	4	68	68	1
10	1	4	75	78	2
-12	2	4	0	17	1
11	-2	-4	301	295	6
10	-2	-4	325	360	6
9	-2	-4	86	86	1
8	-2	-4	58	59	1
7	-2	-4	490	479	5
6	-2	-4	265	262	2
5	-2	-4	157	156	1
4	-2	-4	31	28	1
3	-2	-4	212	210	1
2	-2	-4	125	129	1
1	-2	-4	357	353	3
0	2	4	125	132	1
1	2	4	215	210	2
2	2	4	33	28	1
3	2	4	156	159	1
4	2	4	267	264	1
5	2	4	489	478	4
6	2	4	58	59	1
7	2	4	88	89	1
8	2	4	367	360	5
9	2	4	302	295	6
10	2	4	18	17	5
10	-3	-4	59	62	1
9	-3	-4	81	80	1
8	-3	-4	160	160	2
7	-3	-4	184	181	2
6	-3	-4	175	180	2
5	-3	-4	48	47	1
4	-3	-4	400	398	3
3	-3	-4	283	277	3
2	-3	-4	344	343	3
1	-3	-4	7	4	1
0	3	4	346	344	4
1	3	4	279	277	4
-3	-3	-4	49	46	1
4	3	4	179	179	2
5	3	4	181	182	2
6	3	4	162	159	2
7	3	4	81	81	1
8	3	4	63	62	1
8	-4	-4	104	109	3
7	-4	-4	198	196	3
6	-4	-4	279	277	5
5	-4	-4	68	66	1
4	-4	-4	34	36	1
3	-4	-4	56	53	1
2	-4	-4	224	227	3
1	-4	-4	64	62	1
0	4	4	224	227	2
-1	-4	-4	54	55	1
-2	-4	-4	31	37	2
-3	-4	-4	67	66	1
-4	-4	-4	279	278	7
-5	-4	-4	198	196	5
-6	-4	-4	103	108	3

Table 5.5-8. Observed and Calculated Structure Factor Amplitudes for $K_2PZ(COO)_2$, Continued.

h	k	l	10Fo	10Fc	10s	h	k	l	10Fo	10Fc	10s	h	k	l	10Fo	10Fc	10s	h	k	l	10Fo	10Fc	10s	h	k	l	10Fo	10Fc	10s
12	-1	-5	35	38	2	3	0	6	124	123	1	4	-1	-7	37	33	1	5	-1	-8	369	360	2	2	2	9	29	26	1
11	-1	-5	21	27	2	4	0	6	222	221	2	3	-1	-7	9	10	1	4	-1	-8	293	286	2	3	2	9	51	49	2
10	-1	-5	15	20	2	5	0	6	400	393	3	2	-1	-7	69	60	1	3	-1	-8	77	79	1	4	2	9	20	21	3
9	-1	-5	95	85	4	6	0	6	54	53	1	1	-1	-7	44	50	1	2	-1	-8	8	6	1	5	2	9	10	3	10
8	-1	-5	121	108	5	7	0	6	106	108	3	0	1	7	27	24	1	1	-1	-8	79	79	1	6	2	9	49	59	3
7	-1	-5	100	94	2	8	0	6	114	110	2	1	1	7	30	28	1	0	1	8	295	287	2	9	-3	-9	42	47	1
6	-1	-5	14	16	1	9	0	6	52	52	2	2	1	7	34	36	1	1	1	8	369	359	3	8	-3	-9	33	38	1
5	-1	-5	23	21	1	12	-1	-6	173	174	5	3	1	7	23	28	1	2	1	8	184	190	1	7	-3	-9	2	3	2
4	-1	-5	76	63	1	11	-1	-6	354	345	6	4	1	7	18	21	1	3	1	8	8	9	1	6	-3	-9	29	29	1
3	-1	-5	117	111	1	-10	1	6	315	315	7	5	1	7	30	34	1	4	1	8	268	264	2	5	-3	-9	0	6	1
2	-1	-5	34	37	1	9	-1	-6	19	15	1	6	1	7	36	36	1	5	1	8	264	262	3	4	-3	-9	91	74	2
1	-1	-5	27	30	1	8	-1	-6	365	362	5	7	1	7	0	2	1	6	1	8	140	141	2	3	-3	-9	12	9	3
0	1	5	75	79	1	7	-1	-6	367	363	3	8	1	7	23	26	1	7	1	8	123	122	2	2	-3	-9	37	35	1
1	1	5	96	86	2	6	-1	-6	263	262	1	9	1	7	8	12	7	11	-2	-8	176	176	3	1	-3	-9	57	51	1
2	1	5	56	54	1	5	-1	-6	62	64	1	11	-2	-7	11	17	10	10	-2	-8	116	116	2	0	3	9	29	23	1
3	1	5	7	10	1	4	-1	-6	206	196	1	10	-2	-7	33	36	2	9	-2	-8	96	96	1	-1	-3	-9	19	12	1
4	1	5	49	46	1	3	-1	-6	62	73	1	9	-2	-7	0	0	1	8	-2	-8	137	135	1	2	3	9	41	42	1
5	1	5	118	109	3	2	-1	-6	280	281	2	8	-2	-7	29	32	1	7	-2	-8	245	244	2	3	3	9	6	11	5
6	1	5	124	113	4	1	-1	-6	279	285	2	7	-2	-7	53	52	1	6	-2	-8	175	171	1	4	3	9	29	36	3
7	1	5	41	43	1	0	1	6	64	76	1	6	-2	-7	8	9	2	5	-2	-8	171	174	1	4	-4	-9	16	13	2
8	1	5	0	2	1	1	1	6	204	198	1	5	-2	-7	5	5	2	4	-2	-8	16	17	1	3	-4	-9	14	17	3
9	1	5	40	39	1	2	1	6	63	67	1	4	-2	-7	13	12	1	3	-2	-8	335	331	2	2	-4	-9	9	4	3
10	1	5	45	51	2	3	1	6	262	267	2	3	-2	-7	104	94	1	2	-2	-8	308	304	2	1	-4	-9	44	44	1
11	-2	-5	5	2	5	4	1	6	370	364	3	2	-2	-7	9	5	1	1	-2	-8	331	330	2	0	4	9	8	13	5
10	-2	-5	0	3	1	5	1	6	357	361	4	1	-2	-7	46	51	1	0	2	8	19	16	1	-11	0	10	145	150	5
9	-2	-5	25	28	1	6	1	6	15	11	1	0	2	7	44	37	1	1	2	8	171	177	1	-10	0	10	322	318	8
8	-2	-5	26	30	1	7	1	6	318	316	4	1	2	7	30	30	1	2	2	8	176	172	1	-9	0	10	221	227	5
7	-2	-5	53	55	1	8	1	6	354	346	6	2	2	7	10	12	1	3	2	8	246	245	3	-8	0	10	149	157	2
6	-2	-5	12	11	1	9	1	6	175	174	4	3	2	7	8	9	1	4	2	8	137	136	1	-7	0	10	316	323	4
5	-2	-5	18	18	1	11	-2	-6	55	61	1	4	2	7	40	44	1	5	2	8	95	94	1	-6	0	10	249	244	2
4	-2	-5	59	60	1	10	-2	-6	16	18	2	5	2	7	22	24	1	6	2	8	119	117	2	-5	0	10	216	215	2
3	-2	-5	84	81	1	9	-2	-6	163	161	2	6	2	7	34	39	1	7	2	8	181	177	5	-4	0	10	126	124	1
2	-2	-5	85	84	1	8	-2	-6	120	119	1	7	2	7	20	23	1	9	-3	-8	197	195	4	-3	0	10	231	232	2
1	-2	-5	15	14	1	7	-2	-6	327	320	3	8	2	7	12	13	4	8	-3	-8	132	132	2	-2	0	10	234	234	3
0	2	5	122	127	1	6	-2	-6	69	71	1	10	-3	-7	24	28	2	7	-3	-8	94	93	1	-1	0	10	125	124	1
1	2	5	41	44	1	5	-2	-6	254	253	2	9	-3	-7	33	36	1	6	-3	-8	212	212	2	0	0	10	218	218	3
2	2	5	47	44	1	4	-2	-6	410	404	3	8	-3	-7	12	8	2	5	-3	-8	244	245	3	1	0	10	250	248	3
3	2	5	31	34	1	3	-2	-6	487	475	6	7	-3	-7	46	45	1	4	-3	-8	175	174	2	2	0	10	314	322	5
4	2	5	44	46	1	2	-2	-6	117	123	1	6	-3	-7	23	22	1	3	-3	-8	121	120	1	3	0	10	152	159	3
5	2	5	29	30	1	1	-2	-6	121	127	1	5	-3	-7	4	4	3	2	-3	-8	3	1	2	4	0	10	226	232	4
6	2	5	12	10	1	0	2	6	483	478	5	4	-3	-7	11	13	2	1	-3	-8	121	123	1	5	0	10	327	322	9
7	2	5	19	22	1	1	2	6	407	400	3	3	-3	-7	11	7	2	0	3	8	175	174	1	6	0	10	144	149	4
8	2	5	3	4	2	2	2	6	248	251	2	2	-3	-7	37	31	1	-1	-3	-8	248	245	3	11	-1	-10	141	140	4
9	2	5	26	26	2	3	2	6	70	72	1	1	-3	-7	34	30	1	-2	-3	-8	214	212	4	10	-1	-10	11	5	3
10	-3	-5	19	30	3	4	2	6	320	319	3	0	-3	-7	53	48	1	3	3	8	92	95	1	9	-1	-10	47	48	1
9	-3	-5	11	14	6	5	2	6	120	118	1	-1	-3	-7	15	13	2	4	3	8	134	132	2	8	-1	-10	62	60	1
8	-3	-5	36	37	1	6	2	6	163	161	2	-2	-3	-7	10	9	5	5	3	8	196	197	4	7	-1	-10	266	259	2
7	-3	-5	39	38	1	7	2	6	19	19	1	3	3	7	34	32	1	6	-4	-8	138	137	3	6	-1	-10	273	277	2
6	-3	-5	76	74	1	8	2	6	59	62	1	4	3	7	2	5	2	5	-4	-8	132	136	2	5	-1	-10	197	198	1
5	-3	-5	0	5	1	10	-3	-6	212	209	5	5	3	7	0	0	1	4	-4	-8	48	53	1	4	-1	-10	119	120	1
-4	3	5	23	32	1	9	-3	-6	0	4	1	6	3	7	23	25	2	3	-4	-8	167	163	2	3	-1	-10	489	476	5
3	-3	-5	16	21	1	8	-3	-6	196	198	2	7	-4	-7	11	0	6	2	-4	-8	246	246	4	2	-1	-10	486	474	5
-2	3	5	102	96	1	7	-3	-6	336	331	4	6	-4	-7	52	52	1	1	-4	-8	164	164	2	1	-1	-10	117	116	1
1	-3	-5	104	93	1	6	-3	-6	175	177	2	5	-4	-7	18	19	2	0	4	8	49	51	1	0	1	10	202	202	1
0	-3	-5	40	29	1	5	-3	-6	10	7	1	4	-4	-7	74	68	2	1	4	8	136	135	2	1	1	10	275	278	3
1	3	5	15	15	1	4	-3	-6	39	43	1	3	-4	-7	37	34	1	-2	-4	-8	136	140	2	2	1	10	266	257	3
2	3	5	0	1	1	3	-3	-6	231	229	2	2	-4	-7	22	20	1	11	-1	-9	24	28	2	3	1	10	60	59	1
-3	-3	-5	12	9	2	2	-3	-6	132	133	1	1	-4	-7	16	15	2	10	-1	-9	14	14	2	4	1	10	45	46	2
5	3	5	39	38	1	1	-3	-6	134	130	1	0	4	7	42	36	1	9	-1	-9	26	27	1	5	1	10	4	4	3
6	3	5	5	2	5	0	3	6	228	233	2	-1	-4	-7	18	19	2	8	-1	-9	43	44	1	6	1	10	142	139	5
7	3	5	47	50	1	1	3	6	36	43	1	-2	-4	-7	16	11	2	7	-1	-9	61	65	1	10	-2	-10	209	212	3
7	-4	-5	19	21	1	-2	-3	-6	10	8	4	-12	0	8	167	167	4	6	-1	-9	30	38	1	9	-2	-10	297	300	4
6	-4	-5	31	32	1	-3	-3	-6	184	178	3	-11	0	8	257	247	8	5	-1	-9	4	7	4	8	-2	-10	7	9	6
5	-4	-5	41	44	1	4	3	6	335	334	4	-10	0	8	97	98	2	4	-1	-9	29	28	1	7	-2	-10	115	112	1
4	-4	-5	69	71	1	5	3	6	201	195	2	-9	0	8	80	82	1	3	-1	-9	127	112	2	6	-2	-10	309	316	3
3	-4	-5	74	69	1	6	3	6	5	3	5	-8	0	8	227	224	4	2	-1	-9	127	114	2	5	-2	-10	208	205	2
2	-4	-5	4	2	3	7	3	6	215	212	7	-7	0	8	156	149	1	1	-1	-9	79	71	1	4	-2	-10	43	46	1
1	-4	-5	16	15	1	7	-4	-6	121	122	2	-6	0	8	340	348	3	0	1	9	17	19	1	3	-2	-10	90	94	1
0	4	5	16	12	2	6	-4	-6	84	89	1	-5	0	8	128	131	1	1	1	9	34	38	1	2	-2	-10	88	93	1
-1	-4	-5	130	111	2	5	-4	-6	186	190	3	-4	0	8	34	35	1	2	1	9	40	47	1	1	-2	-10	42	45	1
-2	-4	-5	66	58	2	4	-4	-6	268	266	4	-3	0	8	175	177	1	3	1	9	61	63	1	0	2	10	213	208	2
-3	-4	-5	19	19	2	3	-4	-6	212	215	3	-1	0	8	170	177	2	4	1	9	40	41	1	1	2	10	317	318	6
-4	-4	-5	28	23	2	2	-4	-6	181	181	2	0	0	8	33	34	1	5	1	9	13	11	3	2	2	10	114	114	2
-5	-4	-5	8	7	7	1	-4	-6	184	184	2	1	0	8	128	133	2	6	1	9	23	27	3	3	2	10	0	7	1
-12	0	6	54	51	2	0	4	6	218	214	2	2	0	8	346	349	6	7	1	9	18	22	5	4	2	10	313	304	9
-11	0	6	110	110	2	-1	-4	-6	267	267	4	3	0	8	158	151	1	10	-2	-9	50	54	1	5	2	10	215	215	6
-10	0	6	106	107	2	-2	-4	-6	184	185	5	4	0	8	228	223	2	9	-2	-9	18	17	1	-8	3	10	160	158	3
-9	0	6	51	54	1	-3	-4	-6	84	88	2	5	0	8	82	81	1	8	-2	-9	45	49	2	7	-3	-10	101	100	2
-8	0	6	405	394	7	-4	-4	-6	118	123	3	6	0	8	97	99	1	7	-2	-9	17	16	1	6	-3	-10	280	275	5
-7	0	6	223	223	2	12	-1	-7	16	23	3	7	0	8	246	248	8	6	-2	-9	47	43	1	5	-3	-10	120	124	2
-6	0	6	123	121	1	11	-1	-7	7	7	7	12	-1	-8	39	43	2	5	-2	-9	10	12	1	4	-3	-10	124	127	2
-5	0	6	162	175	1	10	-1	-7	0	3	1	11	-1	-8	124	124	3	4	-2	-9	15	16	1	3	-3	-10	325	324	3
-3	0	6	511	503	8	9	-1	-7	46	49	2	10	-1	-8	140	138	2	3	-2	-9	24	23	1	2	-3	-10	328	324	4
-2	0	6	224	222	2	8	-1	-7	34	35	1	9	-1	-8	255	261	3	2	-2	-9	0	1	1	1	-3	-10	122	123	2
-1	0	6	226	229	3	7	-1	-7	15	16	1	8	-1	-8	264	262	2	1	-2	-9	46	43	1	0	3	10	123	125	2
0	0	6	521	503	9	6	-1	-7	16	20	1	7	-1	-8	12	9	1	0	2	9	13	14	1	1	3	10	284	276	5
2	0	6	160	170	1	5	-1	-7	43	42	1	6	-1	-8	185	191	1	1	2	9	25	22	1	2	3	10	104	101	2

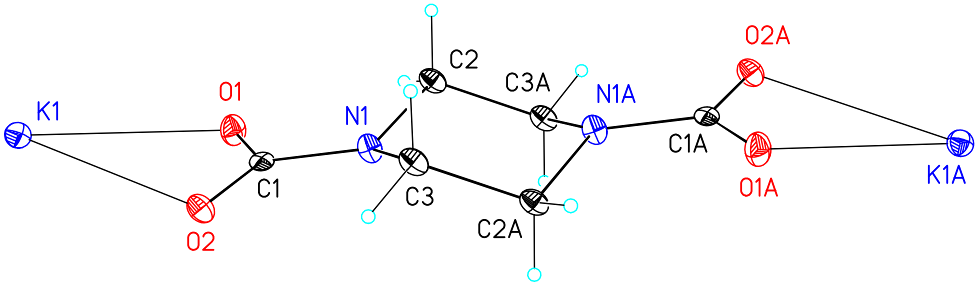

Figure 5.5-1. View of $K_2PZ(COO)_2$ showing the Atom Labeling Scheme. Displacement Ellipsoids are Scaled to the 50 % Probability Level. The Complex Lies on a Crystallographic Inversion Center at ½, ½, ½. Atoms with Labels Appended by an "A" are Related by 1-x, 1-y, and 1-z.

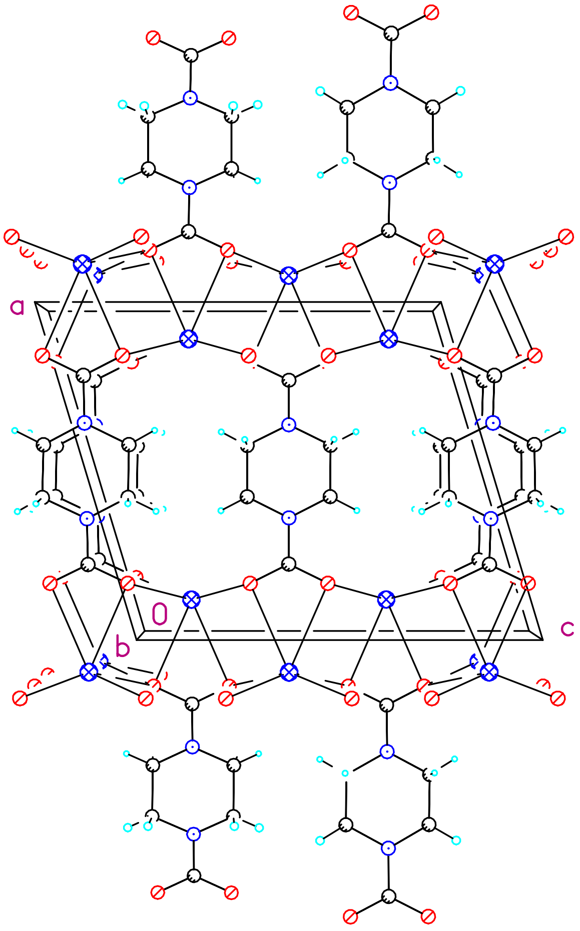

Figure 5.5-2. Unit Cell Packing Diagram for $K_2PZ(COO)_2$. The View is Approximately Down the "B" Axis.

5.3.3 *Powder X-ray Diffraction*

In this work, we utilized powder x-ray diffraction for mixtures of loaded potassium-piperazine-monoethanolamine mixtures to determine the relative amounts of $KHCO_3$ and $K_2PZ(COO)_2$ present in experimental samples through the method of standard additions. Standard additions is a technique where samples are measured using powder x-ray diffraction with known concentrations of each component. From the resulting diffraction pattern, the most intense peaks for each component are then correlated with the known phase impurity to build a calibration curve. The most intense peaks associated with an unknown sample are then compared to the calibration curve to determine the relative amount of each component in the unknown sample.

Figure 5.5-3 and Figure 5.5-4 illustrates the diffraction patterns measured in this work for the pure component samples of $KHCO_3$ and $K_2PZ(COO)_2$, respectively, and Table 5.5-9 documents the most intense peaks associated with each sample in the calibration curve presented in Figure 5.5-5.

Table 5.5-9. Pure Component Measured Intensities for $KHCO_3$ and $K_2PZ(COO)_2$.

Sample	Angle (°)	Intensity (counts/sec)
$KHCO_3$	24.246	889
20 wt%	27.827	894
40 wt%	27.808	1551
60 wt%	27.839	1639
80 wt%	37.414	2998
$K_2PZ(COO)_2$	27.824	1474

Weight percent is in terms of $K_2PZ(COO)_2$.

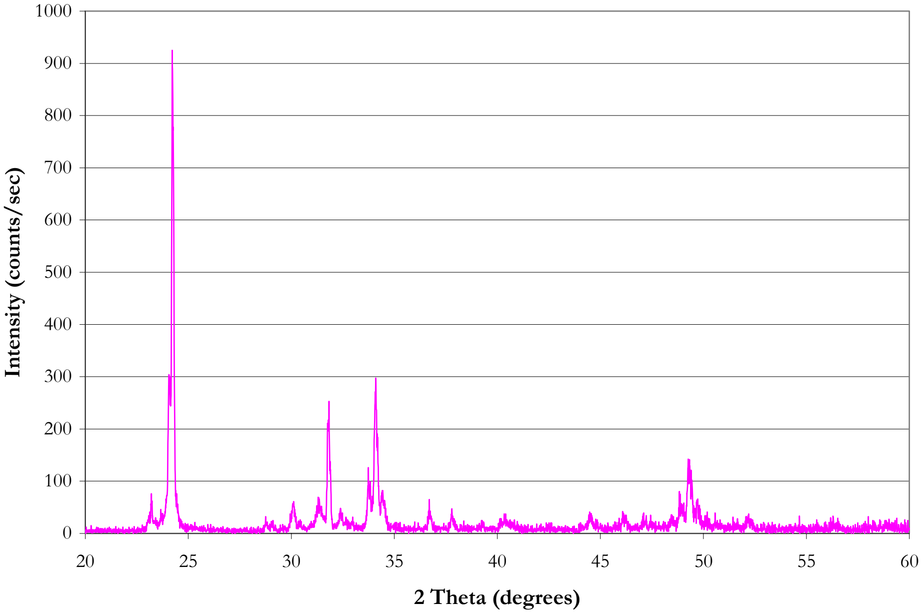

Figure 5.5-3. Powder Diffraction Pattern of Pure $KHCO_3$.

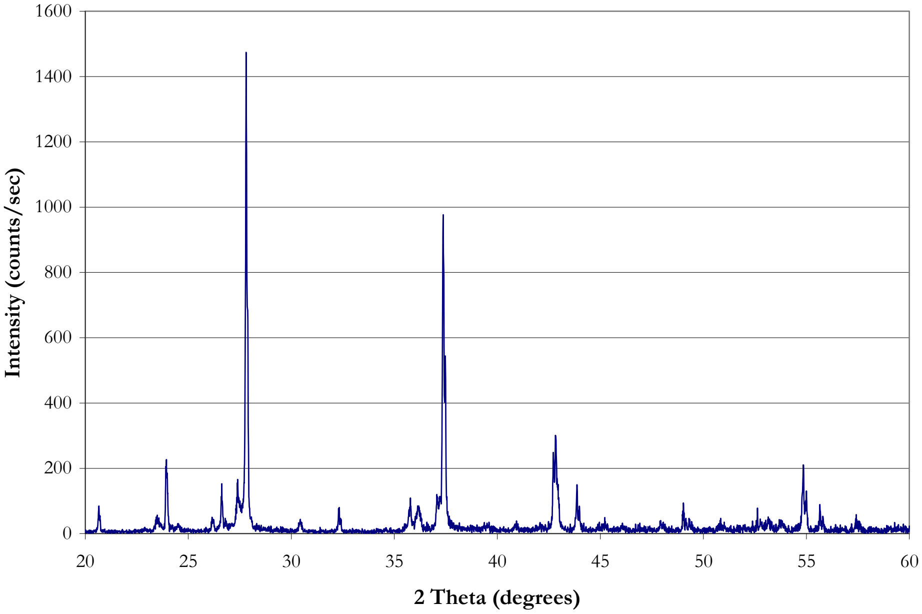

Figure 5.5-4. Powder Diffraction Pattern of Pure $K_2PZ(COO)_2$.

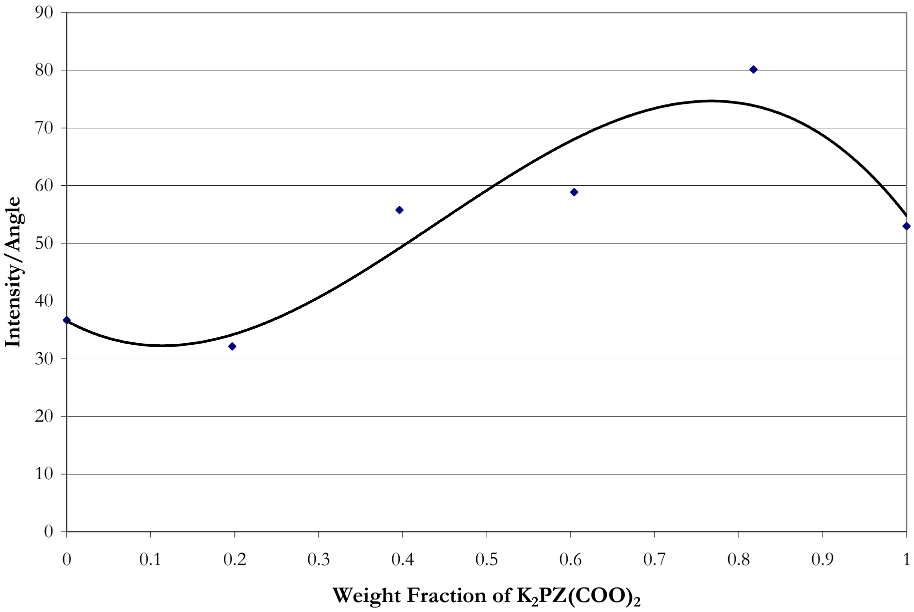

Figure 5.5-5. Calibration Curve for Determining the Relative Amounts of $KHCO_3$ and $K_2PZ(COO)_2$ Presented in Potassium + Piperazine + Monoethanolamine Mixtures.

In this work, we analyzed two samples within the experimental design in mixtures of loaded potassium + piperazine + monoethanolamine for 5 m K^+ + 3.6 m PZ + 7 m MEA and 5 m K^+ + 2 m PZ + 7 m MEA to determine the relative amount of each salt present. Please note that the method presented in this work was intended to be a first order analysis and should not be considered a rigorous analysis method. We were interested in illustrating possible trends in solid solubility presented in two samples for mixtures of loaded potassium + piperazine + monoethanolamine.

Based on the calibration curve illustrated in Figure 5.5-5, Table 5.5-10 gives the relative amounts of $KHCO_3$ and $K_2PZ(COO)_2$ that were found in samples of 5 m K^+ + 3.6 m PZ + 7 m MEA and 5 m K^+ + 2 m PZ + 7 m MEA.

Table 5.5-10. Relative Amounts for $KHCO_3$ and $K_2PZ(COO)_2$ in Mixtures of Loaded Potassium + Piperazine + Monoethanolamine.

Sample	$KHCO_3$ (wt%)	$K_2PZ(COO)_2$ (wt%)
5 m K^+ + 3.6 m PZ + 7 m MEA	23	77
5 m K^+ + 2 m PZ + 7 m MEA	78	22

Table 5.5-10 illustrates that for the sample of 5 m K^+ + 3.6 m PZ + 7 m MEA the majority of the solid phase was the $K_2PZ(COO)_2$ salt and for the sample of 5 m K^+ + 2 m PZ + 7 m MEA the majority of the solid phase was the $KHCO_3$ salt. This illustrates a possible trend that with the increase in the piperazine concentration from 2 to 3.6 m, there may be an increase in the possibility of precipitation for the $K_2PZ(COO)_2$ salt. These results would need to be verified in future work to determine the solid solubility for the H_2O-K_2CO_3-MEA-PZ-CO_2 system as a function of concentration, temperature, and loading. Results presented in this work illustrate a small fraction of the possible combinations that would need to be examined to build a consistent solid solubility phase diagram for the H_2O-K_2CO_3-MEA-PZ-CO_2 system.

5.6 Conclusions

In conclusion, in this work we were able to determine the dissolution temperature by analyzing DSC thermal profiles obtained by heating various mixtures of water and piperazine from -20 to 125 °C and construct a possible phase diagram for water-piperazine mixtures as compared to experimental sold solubility measurements from Bishnoi (2002). In this work, we did not investigate solid solubility for the H_2O-PZ-CO_2 system, but would recommend that future work should verify predictions from this work to create a rigorous and consistent thermodynamic model for predicting vapor-liquid and solid-liquid equilibrium for the H_2O-PZ-CO_2 system.

In addition, we were able to characterize the solid phase in the H_2O-K_2CO_3-PZ-CO_2 system as potassium piperazine dicarbamate ($K_2PZ(COO)_2$) through unit cell x-ray diffraction analysis preformed by Vince Lynch.

Using powder x-ray diffraction for the characterization of the solid phase present in mixtures of loaded potassium-piperazine-monoethanolamine mixtures, we were able to determine that for a sample of 5 m K^+ + 3.6 m PZ + 7 m MEA, the majority of the solid phase present was the $K_2PZ(COO)_2$ salt and for a sample of 5 m K^+ + 2 m PZ + 7 m MEA, the majority of the solid phase present was the $KHCO_3$ salt. In this work, we were able illustrate a possible trend indicating that with the increase in the piperazine concentration from 2 to 3.6 m, there may be an increase in the possibility of precipitation for the $K_2PZ(COO)_2$ salt. We feel that these results should be verified for future work to determine the solid solubility for the H_2O-K_2CO_3-MEA-PZ-CO_2 system as a function of concentration, temperature, and loading. Results presented in this work illustrate a small fraction of the possible combinations that would need to be examined to build a consistent solid solubility phase diagram for the H_2O-K_2CO_3-MEA-PZ-CO_2 system.

PART II

Thermodynamic

Modeling

Framework

CHAPTER VI

Electrolyte Nonrandom Two-Liquid Model

6.1 Introduction

George E.P. Box once said, “All models are wrong, but some models are useful.” Implications of this statement underscore that models are really crude approximations and must be wrong. An effective model is itself an abstraction of the real world with the ability to capture enough detail to be realistic. Hence, models can be useful and powerful tools; an indispensable aid to research and a corner stone to industrial project applications.

This chapter describes the electrolyte nonrandom two-liquid model (elecNRTL) and serves to document the constants and equations used in this work. The first section discusses the basic scalar physical properties for molecular, ionic, and molecular solute species. Temperature dependent relationships (i.e. Henry’s constant, heat capacity, Antoine equations, dielectric constants, etc.) are provided and discussed.

The discussion then turns to the structure of the elecNRTL model. A basic overview of the theory is given and each ingredient of the model is discussed. The vapor phase non-idealities were modeled by the Redlich-Kwong-Soave (SRK) equation of state [Soave (1972)] where liquid phase non-idealities in terms of the activity coefficients were modeled by the elecNRTL model [Chen et al. (1979, 1982), Chen and Evans (1986), and Mock et al. (1986)]. The elecNRTL model contains three terms: a Debye-Huckel term, Born correction for mixed solvents, and the local interactions term governed by the NRTL equations. Equations for each part of the elecNRTL model are given and details on parameters and their structure are discussed within the framework of Aspen Plus^{TM} 2006.5.

6.2 Physical Properties

In this work, we discovered that the foundations of the NRTL model and the elecNRTL within Aspen Plus^{TM} are not transparent with respect to each other, where the calculation routes and scalar pure component proprieties are different between each model. In theory, as the concentration of ions in an electrolyte solution approaches zero, elecNRTL model reduces to the NRTL model of Renon and Prausnitz (1968). We discovered that calculation routes for physical properties between the NRTL and the elecNRTL property models are different. In the end, we will use the elecNRTL property model package with consistent scalar and temperature dependent parameters as compared to the DIPPR database for all future chapters to describe molecular and ionic interactions.

6.2.1 *Scalar Properties*

Table 6.2-1 lists the differences for the molecular component critical constants used by the NRTL and elecNRTL physical property models within Aspen Plus™ as compared to the DIPPR database.

Table 6.2-1. Scalar Physical Properties for H_2O, MEA, and PZ as given in the DIPPR database and within NRTL and elecNRTL models within Aspen Plus™.

		NRTL			elecNRTL Model			DIPPR		
Parameters	Units	H_2O	MEA	PZ	H_2O	MEA	PZ	H_2O	MEA	PZ
API		10	7.5	80.4899	10	7.5	80.4899	10	7.5	80.4899
DGFORM	kcal/mol	*-54.5978*	-24.6728	40.6038	*-54.64*	-24.6728	40.6038	-54.6343	-24.6893	40.6310
DGSFRM	kcal/mol	-56.5492			-56.5492			-56.5492		
DHFORM	kcal/mol	*-57.7563*	*-49.3694*	3.917073	*-57.8*	*-50.2037*	3.917073	-57.7949	-49.4025	3.91969
DHSFRM	kcal/mol	-69.9627			-69.9627			-69.9627		
DHVLB	kcal/mol	*9.744507*	*11.88812*	9.999355	*9.717*	*12.21599*	9.999355	9.744507	11.88812	9.999355
FREEZEPT	°C	*0*	*10.5*	106	*0.05*	*10.31*	106	0.0	10.5	106
HCOM	kcal/mol	0	*-325.547*	-653.96	0	*-325.564*	-653.96	0.0	-325.765	-654.398
MUP	debye	*1.849724*	*0.776462*	1.470001	*1.8*	*2.6*	1.470001	1.84972	0.77646	1.47000
MW		18.01528	61.08372	86.13688	18.01528	61.08372	86.13688	18.01528	61.08308	86.1356
OMEGA		*0.344861*	*0.446737*	0.41376	*0.344*	*0.83505*	0.41376	0.344861	0.446737	0.41376
PC	bar	*220.64*	*71.24*	55.3	*220.4832*	*44.68*	55.3	220.64	71.24	55.3
RKTZRA		0.243172	*0.24764*		0.243172	*0.19852*		0.243172	0.24764	
SG		1	1.0179	0.667485	1	1.0179	0.667485	1	1.0179	0.667485
TB	°C	*100*	*170*	146	*100.05*	*170.5*	146	100.0	170	146
TC	°C	*373.946*	*405.05*	364.85	*374.15*	*341.3*	364.85	373.946	405.05	364.85
VB	cc/mol	*18.8311*	*68.6673*	134.772	*19.63607*	*75.00305*	134.772	18.8311	68.6673	134.772
VC	cc/mol	*55.9472*	*225*	310	*55.89534*	*196*	310	55.9472	225	310
VLSTD	cc/mol	*18.05*	*60.0161*	129.371	*18.04999*	*60.016116*	129.371	18.0691	60.3415	129.371
ZC		0.229	*0.284*	0.323	0.229	*0.1714*	0.323	0.229	0.284	0.323

For a complete list of scalar parameter nomenclature, please refer to Appendix N for more information. Table 6.2-2 lists the critical constants for molecular salts, potassium carbonate (K_2CO_3) and potassium bicarbonate ($KHCO_3$). For precipitating species, K_2CO_3(s), $KHCO_3$(s), piperazine hexahydrate ($PZ{\cdot}6H_2O$), and dipotassium piperazine dicarbamate ($K_2PZ(COO)_2$), the solid phase was described by the base pure component species where the molecular weight and melting point (if known) were adjusted to match the precipitating species due to the limited thermodynamic information available in literature to accurately describe the solid phase within Aspen Plus^{TM}.

Table 6.2-2. Pure Component Properties for Salt Species.

Parameters	Units	K_2CO_3	$KHCO_3$
DGFORM	kcal/mol	0	0
DGSFRM	kcal/mol	-254.013	-206.243
DHFORM	kcal/mol	0	0
DHSFRM	kcal/mol	-274.916	-230.056
FREEZEPT	C	900.85	
MW		138.2058	100.1154
OMEGA		0	0
PC	bar	50	50
TC	C	1726.85	1726.85
VC	cc/mol	100	100
ZC		0.2	0.2

Table 6.2-2 lists the critical constants for molecular solutes, CO_2.

Table 6.2-3. Pure Component Properties for Molecule Solutes.

Parameters	Units	CO_2
API		340
DGFORM	kcal/mol	-94.26000048
DHFORM	kcal/mol	-94.0511
DHVLB	kcal/mol	4.1
FREEZEPT	C	-56.57
HCOM	kcal/mol	0
MUP	debye	0
MW		44.0095
OMEGA		0.225
PC	bar	73.83
RKTZRA		0.2736149
SG		0.3
TB	C	-78.45
TC	C	31.05
VB	cc/mol	35.637394
VC	cc/mol	94
VLSTD	cc/mol	61.6782
ZC		0.274
RGYR	meter	1.04E-10
CHARGE		0
DGAQFM	J/kmol	-385980000
DGAQHG	J/kmol	-386232300
DHAQFM	J/kmol	-413800000
DHAQHG	J/kmol	-414074520
IONTYP		0
OMEGHG	J/kmol	-8373600
S25HG	J/kmol-K	117649.08
S025C	J/kmol-K	117600
S025E	J/kmol-K	210887.4

Table 6.2-4 and Table 6.2-5 give the critical constants for ionic species. Pre-defined ionic species within the Aspen PlusTM database are shown in Table 6.2-4. For user defined ionic species associated with MEA and PZ, DGAQFM and DHAQFM were calculated as described in Chapters VIII, IX, XIII, and XIV, as shown in Table 6.2-5.

Table 6.2-4. Pure Component Properties for Ionic Species.

Parameters	Units	K^{+1}	OH^{-1}	H^{+1}	HCO_3^{-1}	CO_3^{-2}
MW		39.09775	17.00789	1.00739	61.01769	60.0103
CHARGE		1	-1	1	-1	-2
DGAQFM	J/kmol	-283270000	-157244000	0	-587370182.1	-538355662.9
DGAQHG	J/kmol	-282650870	-157402750	0	-587332680	-528336480
DHAQFM	J/kmol	-252380000	-229994000	0	-690767961	-677140000
DHAQHG	J/kmol	-252338440	-230177700	0	-690394950	-675686720
IONRDL	cc/mol	-6.500429923	18	-7.799656062	-14.30008598	-6.500429923
IONTYP		1	2	1	4	3
OMEGHG	J/kmol	80679636	722055528	0	533105244	1419911350
S25HG	J/kmol-K	101111.22	-10718.208	0	98515.404	-50032.26
S025C	J/kmol-K	102500	-10750	0	91200	-56900
S025E	J/kmol-K	-670	233253.5	0	444140.9	444140.9

Table 6.2-5. Pure Component Properties for Ionic Species Continued.

Parameters	Units	$MEAH^{+1}$	$MEACOO^{-1}$	PZH^{+1}	PZH^{+2}	$PZCOO^{-1}$
MW		62.09111	104.08613	87.14299	88.1504	129.13771
CHARGE		1	-1	1	2	-1
DGAQFM	J/kmol	-171023632	-492922520	102408575	91897612.25	-216402690
DHAQFM	J/kmol	-336961728.8	-707209080	-91542774.38	-122665214.9	-482028620

Parameters	Units	$PZ(COO^{-1})_2$	$H^{+1}PZCOO^{-1}$
MW		172.14	130.145
CHARGE		-2	1.00E-05
DGAQFM	J/kmol	-576616170	-273454210
DHAQFM	J/kmol	-860671110	-522383060

6.2.2 *Temperature Dependent Properties*

Extended Vapor Pressure Correlation

Table 6.2-6 gives the Antoine equations for molecular species from the DIPPR database [Rowley et al. (1994)] based on the following expression:

$$\ln P_i^0\left(\frac{N}{m^2}\right)=A+\frac{B}{T\left(K\right)+C}+DT\left(K\right)+E\ln T\left(K\right)+FT\left(K\right)^G \qquad 6\text{-}1$$

Ionic species are defined as non-volatile species and vapor pressure correlations for ionic species reflect this definition.

Table 6.2-6. Pure Component Antoine Equations.

Components	H_2O	PZ	CO_2	Ions
A	72.55	70.50	72.83	-1.00E+20
B	-7207	-7915	-3403	0
C	0	0	0	0
D	0	0	9.49E-03	0
E	-7.139	-6.646	-8.560	0
F	4.046E-06	5.21E-18	2.91E-16	0
G	2	6	6	0

$$\ln P_i^0\left(\frac{N}{m^2}\right)=A+\frac{B}{T\left(K\right)+C}+DT\left(K\right)+E\ln T\left(K\right)+FT\left(K\right)^G$$

Dielectric Constant

The dielectric constant relates a component's ability to stabilize an ionic solution. As the dielectric constant increases, the tendency for ions to form and remain as ionic species also increases. According to Atkins and de Paula (2002), the dielectric constant is related to the square of the refractive index. Nevertheless, given the lack of substantial data, the dielectric constant for piperazine was assumed to be the same as piperidine and was obtained from the CRC (2004) and corrected to the one experimental data point for piperazine. The dielectric constant for water and monoethanolamine were obtained from the CRC (2004). The temperature dependence for water, monoethanolamine, and piperazine dielectric constants are represented in this work by the following functions:

$$D_{H_2O} = 78.65 + 31989\left(\frac{1}{T(K)} - \frac{1}{T^{ref}}\right) \tag{6-2}$$

$$D_{MEA} = 31.07 + 15128\left(\frac{1}{T(K)} - \frac{1}{T^{ref}}\right) \tag{6-3}$$

$$D_{PZ} = 4.25 + 1532\left(\frac{1}{T(K)} - \frac{1}{T^{ref}}\right) \tag{6-4}$$

Where
T^{ref} is the reference temperature at 298.15 K.

For the mixed solvent, the dielectric constant is calculated based on the following expression:

$$D_m = \sum_i w_{m_i}^{sf} D_i \tag{6-5}$$

Where
$w_{m_i}^{sf}$ is the solute free, solvent mass fraction.

Henry's Constant

Henry's constants are an important part for the vapor-liquid equilibrium of supercritical gases. The Henry's constant model is used when Henry's Law to is applied to molecular solutes in enthalpy and aqueous chemistry algorithms within Aspen Plus™. Aspen Plus™ utilizes a volume weighted mixing rule for the Henry's solubility of CO_2 in mixed solvent. In this work, reference state for the activity coefficient of molecular solutes (i.e. CO_2) within Aspen Plus^{TM} 2006.5 allows the user to choose between infinite dilution in mixed solvent or infinite dilution in aqueous solvent. In the former, Aspen Plus^{TM} utilizes a volume weighted mixing rule to describe the Henry's constant of CO_2 in mixed solvent as shown below.

$$\ln\left(\frac{H_i}{\gamma_i^\infty}\right) = \sum_A w_A \ln\left(\frac{H_{i,A}}{\gamma_{i,A}^\infty}\right) \tag{6-6}$$

This convention normalizes the reference state of CO_2 to infinite dilution in solution, but in loaded alkanolamine solutions the reference state for the activity coefficient of CO_2 at infinite dilution is not zero; therefore to account for this, Aspen Plus^{TM} defines the asymmetric activity coefficient:

$$\gamma_i^* = \frac{\gamma_i}{\gamma_i^\infty} \tag{6-7}$$

Thus, Aspen Plus^{TM} calculates γ_i^∞ at any loading by setting the CO_2 concentration to zero while allowing all of the other ionic species to remain at the loaded concentration values. This results in a floating reference state for CO_2 and for other CO_2-related species as a function of loading.

In this work, we chose to describe the reference state of molecular solutes in infinite dilution in water to be consistent with the ionic component reference state. This distinction implies that only a correlation describing the Henry's constant for CO_2 in water is required within the elecNRTL model. The Henry's constant for CO_2 in water can be described by the following expression within Aspen Plus^{TM}.

$$\ln H_i\left(T, P_{H_2O}^0\right) = C_1 + \frac{C_2}{T\left(K\right)} + C_3 \ln T\left(K\right) + C_4 T\left(K\right) + \frac{C_5}{T\left(K\right)^2} \qquad \text{6-8}$$

Where
H_i is the Henry's constant for CO_2 in H_2O at the system temperature and saturation pressure of water, $P_{H_2O}^0$.

Table 6.2-7 gives the coefficients used in this work for the Henry's constant for CO_2 in H_2O given by Chen et al. (1979) based on Equation 6-8.

Table 6.2-7. Coefficients for the Henry's Constant of CO_2 in H_2O (Pa/mole fraction).

C_1	C_2	C_3	C_4	C_5
170.7126	-8477.711	-21.95743	0.005781	0.0

$\ln H = C_1 + C_2/T(K) + C_3 \cdot \ln T(K) + C_4 \cdot T(K) + C_5/T(K)^2$

In this work, we chose to describe the solubility of CO_2 in water using the Chen et al. (1979) correlation for the Henry's constant for CO_2 in H_2O. Chen et al. (1979) developed their correlation based on the experimental work of Ellis and Golding (1963).

Standard Enthalpy of Vaporization

According to Atkins and de Paula (2002) the standard enthalpy of vaporization, also known as the heat of vaporization, is the energy required to transform a given quantity of a substance into a gas. Aspen Plus^{TM} relates the specific heat capacity to the ideal gas enthalpy and the heat of vaporization to eliminate errors associated with accurate thermal properties of both phases by the following method:

$$H_i^l - H_i^l\left(T^{ref}\right) = \int_{T^{ref}}^{T} C_{p,i}^l dT \qquad \text{6-9}$$

$$H_i^l\left(T^{ref}\right) = H_i^{ig} + \left(H_i^v - H_i^{ig}\right) - \Delta H_i^{vap} \qquad \text{6-10}$$

Where

$H_i^l\left(T^{ref}\right)$ is the reference enthalpy of component i at $T^{ref} = 298.15K$,

H_i^{ig} is the ideal gas enthalpy of component i,

$H_i^v - H_i^{ig}$ is the vapor enthalpy departure of component i,

ΔH_i^{vap} is the heat of vaporization of component i.

The Watson heat of vaporization equation for H_2O and MEA used in Aspen Plus™ is based on the following expression:

$$\Delta H_i\left(T\right) = \Delta H_i\left(T_1\right)\left(\frac{1-T/T_{ci}}{1-T_1/T_{ci}}\right)^{a_i+b_i\left(1-T/T_{ci}\right)} \qquad \text{6-11}$$

Where

T_{ci} is the critical temperature of component i,

T is the temperature, °C.

The Watson equation estimates the heat of vaporization of a pure liquid component at any temperature from the known value at a single temperature $\left(\Delta H_i\left(T_1\right)\right)$. Table 6.2-8 gives the coefficients for the Watson heat of vaporization equation for H_2O and MEA used in the elecNRTL model within Aspen Plus™ based on equation 6-11.

Table 6.2-8. Watson Heat of Vaporization Default Coefficients for H_2O and MEA in the elecNRTL model [J/kmol].

Parameter	Symbol	H2O	MEA
DHVLWT-1	$\Delta H_1(T_1)$	40655000	54835800
DHVLWT -2	T_1	100.0	126.67
DHVLWT -3	a_i	0.3106	0.3288
DHVLWT -4	b_i	0	-0.0857

For PZ, the DIPPR heat of vaporization equation is used within Aspen Plus™ and is based on the following expression:

$$\Delta H_i^{vap}\left(\frac{J}{kmol}\right) = C_{1i}\left(1-T_{ri}\right)^{\left(C_{2i}+C_{3i}T+C_{4i}T^2\right)} \qquad \text{6-12}$$

Where

T_{ri} is the reduced temperature, T/T_{ci},

T_{ci} is the critical temperature of component i,

T is the temperature, °C.

Table 6.2-9 gives the coefficients for the DIPPR heat of vaporization equation for PZ used in the elecNRTL model within Aspen Plus™ based on equation 6-12.

Table 6.2-9. DIPPR Heat of Vaporization Default Coefficients for PZ in the elecNRTL model [J/kmol].

Parameter	Symbol	PZ
DHVLPD-1	C_1	6.5323E+7
DHVLDP-2	C_2	0.4158
DHVLDP-3	C_3	0.0
DHVLDP-4	C_4	0.0

Specific Heat Capacity

Aspen Plus™ calculates the liquid phase heat capacity of a *mixture* (CPMX) by taking the derivative of the liquid enthalpy at constant pressure:

$$H_m^l(T+\Delta T)-H_m^l(T)=\int_T^{T+\Delta T} C_{p,m}^l dT \qquad 6\text{-}13$$

where the liquid enthalpy of a mixture is calculated by the following equation:

$$H_m^l(T)=\sum_i x_i H_i+\sum_k x_k H_k^\infty + H_m^E \qquad 6\text{-}14$$

for solvents:

$$H_i(T)=\Delta H_f^{ig}\left(T^{ref}\right)+\int_{T^{ref}}^{T} C_p^{ig} dT+\left[H_i(T,p)-H_i^{ig}(T,p)\right] \qquad 6\text{-}15$$

for molecular solutes (CO_2):

$$H_i(T)=H_i^{ig}(T)+RT\ln\left(\frac{H_{i,H_2O}}{P^{ref}}\right) \qquad 6\text{-}16$$

for cations or anions:

$$H_k^\infty(T) = \Delta H_{f,k}^\infty\left(T^{ref}\right) + \int_{T^{ref}}^{T} C_{p,k}^\infty dT \qquad \text{6-17}$$

Where

ΔT is the perturbation in temperature from *T*,

H_m^E is the excess enthalpy of the mixture,

$\Delta H_f^{ig}\left(T^{ref}\right)$ is the standard enthalpy of formation of component i at T^{ref},

T^{ref} is the reference temperature, 25.0 °C,

C_p^{ig} is the ideal gas heat capacity of component i,

H_i^{ig} is the ideal gas enthalpy of component i,

H_k^∞ is the infinite dilution aqueous phase enthalpy of component k,

$\Delta H_{f,k}^\infty\left(T^{ref}\right)$ is the infinite dilution aqueous phase standard enthalpy of formation of component k at T^{ref},

$C_{p,k}^\infty$ is the infinite dilution aqueous phase heat capacity polynomial of component k.

Table 6.2-10 gives the coefficients for the infinite dilution aqueous phase heat capacity used in Aspen Plus™ based on the following expression:

$$C_{p,k}^\infty\left(\frac{J}{kmol \cdot K}\right) = C_1 + C_2 T(K) + C_3\left(T(K)\right)^2 + \frac{C_4}{T(K)} \qquad \text{6-18}$$

For user defined ionic species associated with MEA and PZ, coefficients for the infinite dilution aqueous phase heat capacity polynomial were regressed as described in Chapters VIII, IX, XIII, and XIV, shown in Table 6.2-11.

Table 6.2-10. Infinite Dilution Aqueous Phase Heat Capacity Default Coefficients.

Parameter	Symbol	H^+	OH^-	K^+	HCO_3^{-1}	CO_3^{-2}
CPAQ0-1	C_1	0.0	0.0	19886	211387	1334017
CPAQ0-2	C_2	0.0	-497.9	72.80	-882	-5565
CPAQ0-3	C_3	0.0	0.0	0.0	0.875	5.19
CPAQ0-4	C_4	0.0	0.0	0.0	-1.9E+07	-1.2E+08

Table 6.2-11. Infinite Dilution Aqueous Phase Heat Capacity Default Coefficients.

Parameter	Symbol	$MEAH^{+1}$	$MEACOO^{-1}$	PZH^{+1}	PZH^{+2}	$PZCOO^{-1}$	$PZ(COO^{-1})_2$	$H^{+1}PZCOO^{-1}$
CPAQ0-1	C_1	-1700443	-2408071	603662.9	1228464	-6853709	-881654	4189850
CPAQ0-2	C_2	7093	17268	-2518	-5125	23209	-18936	-13614
CPAQ0-3	C_3	-8.49	-26.0	4.17	7.09	4.90	80.1	5.19
CPAQ0-4	C_4	1.51E+08	0.0	-5.4E+07	-1.1E+08	0.0	0.0	0.0

6.2.3 *Aqueous Phase Chemistry*

The chemical equilibrium constant for j reactions are expressed in Aspen Plus™ in terms of the activity of component i as given by the following relationship.

$$K_j = \prod_i a_i^{\nu_{i,j}} \qquad \text{6-19}$$

Where
K_j is the chemical equilibrium constant,
$\nu_{i,j}$ is the reaction stoichiometric coefficient of component i,
a_i is the activity of component i.

In this work, we did not define the chemical equilibrium constants as linear temperature dependent functions, but rather in terms of the reference state Gibbs free energy of the system:

$$\ln K_j = -\frac{\Delta G^o_{i,j}}{RT} \qquad \text{6-20}$$

Where
$\Delta G^o_{i,j}$ is the standard free energy of formation of component i.

The previous framework allows our rigorous thermodynamic model to be internally consistent with respect to governing thermodynamic definitions. Equation 6-20 relates the chemical equilibrium constant to the standard Gibbs free energy change of j reaction.

$$\frac{\Delta G^o}{RT} = -\ln K \tag{6-21}$$

Where the standard property changes of reaction (e.g. Gibbs free energy and enthalpy) are defined as the difference between the standard property change of the products and reactants, weighted by their stoichiometric coefficients.

$$\Delta M^o = \sum_i \nu_i M_i^o \tag{6-22}$$

For molecular solutes (e.g. CO_2), the standard Gibbs free energy is described based on the ideal gas reference state by following equation:

$$G_{CO_2}^o(T) = G_{CO_2}^{ig}(T) + RT\ln\frac{H_{CO_2}(T)}{P^{ref}} \tag{6-23}$$

Where
$G_{CO_2}^{ig}$ is the ideal gas Gibbs free energy, J/kmol,
H_{CO_2} is the Henry's Constant for CO_2 in H_2O (Chen et al. 1979), atm,
P^{ref} is the reference pressure, 1 atm.

For a given temperature, a starting point for a rigorous development starts with the following equation:

$$\Delta G_m^o = \Delta H_m^o - T\Delta S_m^o \tag{6-24}$$

Equation 6-24 is from the definition of the molar Gibbs free energy applied to each component in a chemical reaction evaluated at the standard state. Applying Equation 6-22 to Equation 6-24 yields

$$\sum_i \nu_i G_{m,i}^o = \sum_i \nu_i H_{m,i}^o - T\sum_i \nu_i S_{m,i}^o \tag{6-25}$$

where the standard molar heat of reaction and standard molar entropy change of reaction are related to temperature by the following expressions

$$\Delta H_m^o = \Delta H_{0,m}^o + R\int_{T_0}^{T} \frac{\Delta C_{p,m}^o}{R} dT \qquad \text{6-26}$$

$$\Delta S_m^o = \Delta S_{0,m}^o + R\int_{T_0}^{T} \frac{\Delta C_{p,m}^o}{R}\frac{dT}{T} \qquad \text{6-27}$$

Equations 6-24, 6-26, and 6-27 are combined to yield

$$\Delta G_m^o = \Delta H_{0,m}^o + R\int_{T_0}^{T} \frac{\Delta C_{p,m}^o}{R} dT - T\Delta S_{0,m}^o - RT\int_{T_0}^{T} \frac{\Delta C_{p,m}^o}{R}\frac{dT}{T} \qquad \text{6-28}$$

However,

$$\Delta S_{0,m}^o = \frac{\Delta H_{0,m}^o - \Delta G_{0,m}^o}{T_0} \qquad \text{6-29}$$

hence

$$\Delta G_m^o = \Delta H_{0,m}^o - \frac{T}{T_0}\left(\Delta H_{0,m}^o - \Delta G_{0,m}^o\right) + R\int_{T_0}^{T} \frac{\Delta C_{p,m}^o}{R} dT - RT\int_{T_0}^{T} \frac{\Delta C_{p,m}^o}{R}\frac{dT}{T} \qquad \text{6-30}$$

Finally, division by RT yields

$$-\ln K_i = \frac{\Delta G_m^o}{RT} = \frac{\Delta G_{0,m}^o - \Delta H_{0,m}^o}{RT_0} + \frac{\Delta H_{0,m}^o}{RT} + \frac{1}{T}\int_{T_0}^{T} \frac{\Delta C_{p,m}^o}{R} dT - \int_{T_0}^{T} \frac{\Delta C_{p,m}^o}{R}\frac{dT}{T} \qquad \text{6-31}$$

Chemical equilibrium constants calculated within Aspen Plus$^{\text{TM}}$ following the above convention are on a molality basis. In addition, chemical equilibria reported in literature are normally referenced to infinite dilution in water (molality based), treating monoethanolamine and piperazine as solutes. Solutes and ionic activity coefficients are described by the asymmetric reference state convention which states that as the activity coefficient approaches one, the mole fraction of the species approaches zero in pure water.

Due to the asymmetric reference state convention, the chemical equilibrium constant of monoethanolamine or piperazine requires an additional conversion to the symmetric reference state convention since all subsequent monoethanolamine or piperazine based ionic equilibrium constants are determined based on the asymmetric reference state convention referenced to infinite dilution in monoethanolamine or piperazine. These two reference state conventions are related by the following expression:

$$\frac{\gamma_{Amine}}{\gamma^{*}_{Amine}} = \lim_{x_{Amine}\to 0} \gamma_{Amine} = \gamma^{\infty}_{Amine} \qquad 6\text{-}32$$

Where
γ_{Amine} is the symmetric activity coefficient for the amine,
γ^{*}_{Amine} is the asymmetric activity coefficient for the amine as the solution approaches its pure solute reference state.

Thus, the chemical equilibrium constant of monoethanolamine and piperazine referenced to the symmetric reference state convention used in this work is related by the following expression:

$$\ln K^{*} = \ln K + \ln\left(\frac{1000}{MW_w}\right)\sum_{i\neq w} \nu_i + \ln \gamma^{\infty}_{Amine} \qquad 6\text{-}33$$

Where
MW_w is the molecular weight of H_2O, 18.01528 gm/mole,
K is the symmetric chemical equilibrium constant (mole fraction based).

The infinite dilution activity coefficient of monoethanolamine and piperazine is calculated from the binary interaction parameters for the water-amine system using the elecNRTL model. The resulting values were then re-regressed to the standard temperature dependent form of the chemical equilibrium constant used in Equation 6-33 for this conversion. This modified chemical equilibrium constant for the amine was then utilized in the elecNRTL model within Aspen Plus^{TM} to specify the infinite dilution standard state free energy and enthalpy of formation, respectively, for ionic amine species. Therefore, chemical equilibrium constants reported in this work must be corrected for the infinite dilution activity coefficient for the amine prior to comparison with other work.

6.3 Vapor Phase Model

Soave's (1972) modification of the Redlich-Kwong [Redlich and Kwong (1949)] equation of state is used to represent the vapor phase equilibrium. Soave changed the temperature dependence term $a / T^{0.5}$ by making the constant "a" a function of temperature and the accentric factor (ω). The Soave-Redlich-Kwong equation of state is given by the following expression:

$$P = \frac{RT}{V_m - b} - \frac{a}{V_m\left(V_m - b\right)} \qquad \text{6-34}$$

Where

$$a = \sum_i \sum_j x_i x_j \left(a_i a_j\right)^{0.5} \left(1 - k_{ij}\right) \qquad \text{6-35}$$

$$b = \sum_i x_i b_i \qquad \text{6-36}$$

$$k_{ij} = k_{ji} \qquad \text{6-37}$$

$$b_i = 0.08664 \frac{RT_{c_i}}{P_{c_i}} \qquad \text{6-38}$$

$$a_i = \alpha_i 0.42747 \frac{R^2 T_{c_i}^2}{P_{c_i}} \qquad \text{6-39}$$

$$\alpha_i = \left[1 + m_i\left(1 - T_{r_i}^{0.5}\right)\right]^2 \tag{6-40}$$

$$m_i = 0.48 + 1.57\omega_i - 0.176\omega_i^2 \tag{6-41}$$

6.4 Activity Coefficient Model

The molar Gibbs free energy within the elecNRTL model is given by the following form:

$$G_m^* = x_w \mu_w^* + \sum_k x_k \mu_k^\infty + \sum_j x_j \ln x_j + G_m^{*E} \tag{6-42}$$

where the excess Gibbs free energy associated with the elecNRTL model is given by the following form:

$$\frac{G_m^{*E}}{RT} = \frac{G_m^{*E,PDH}}{RT} + \frac{G_m^{*E,Born}}{RT} + \frac{G_m^{*E,lc}}{RT} \tag{6-43}$$

Where
PDH is the Pitzer-Debije-Hückel contribution for long range ion-ion interactions,
Born is the Born Correction for change in mixed solvent reference state, and
lc is the local contribution for short range interactions.

The molar Gibbs free energy and the molar excess Gibbs free energy are defined with the asymmetrical references state as infinite dilute in pure solvent. The reference state for ionic and molecular solutes follows the unsymmetrical convention defined as infinite dilution in water. The ideal mixing terms is calculated where j refers to any component and the molar Gibbs free energy of pure water is calculated from the ideal gas contribution. The aqueous infinite dilution chemical potential is calculated from the infinite dilution aqueous phase heat capacity polynomial model, where the subscript k refers to any ions or molecular solute.

$$\mu_k^{\infty} = \Delta_f H_k^{\infty,aq} + \int_{T_0}^{T} \frac{C_{p,k}^{\infty,aq}}{T} dT - T\left(\frac{\Delta_f H_k^{\infty,aq} - \Delta_f G_k^{\infty,aq}}{T_0} + \int_{T_0}^{T} \frac{C_{p,k}^{\infty,aq}}{T} dT \right) + RT \ln\left(\frac{1000}{MW_w} \right) \quad 6\text{-}44$$

Where $\Delta_f H_k^{\infty,aq}$ and $\Delta_f G_k^{\infty,aq}$ are based on a molality scale and μ_k^{∞} is based on a mole fraction scale, the last term is added for the conversion.

For molecular solutes, the aqueous infinite dilution chemical potential is calculated from Henry's law:

$$\mu_k^{\infty} = \mu_k^{\infty,ig} + RT \ln\left(\frac{H_{k,w}}{P^{ref}} \right) \quad 6\text{-}45$$

Where
T_0 is the reference temperature, 298.15 K,
P^{ref} is the reference pressure, 1 atm.

Thus, when the derivative of the Gibbs free energy at constant temperature and pressure reaches a minimum for closed homogeneous system the system has satisfied the condition for thermodynamic equilibrium.

With ions in an electrolyte solution, the elecNRTL model is a versatile model for the calculation of activity coefficients. The model is based on two fundamental assumptions:

1. The like-ion repulsion assumption: the local composition of cations around cations is zero (and likewise for anions around anions) since repulsive forces between ions of like charge are extremely large and repulsive forces between ions of the same sign are very strong for neighboring species.
2. The local electroneutrality assumption: the distribution of cations and anions around a central molecular species is such that the net local ionic charge is zero.

Chen et al. (1982) proposed an excess Gibbs energy expression which contains two contributions: one contribution for the long-range ion-ion interactions and the other related to the local interactions that exist around any central species. The unsymmetric Pitzer-Debije-Hückel (PDH) model and the Born equation are used to represent the contribution of the long-range ion-ion interactions, and the NRTL theory was used to represent the local interactions (lc). The local interactions model was developed as a symmetric model with a reference state based on pure solvent and pure completely dissociated liquid electrolyte. Infinite dilution activity coefficients are then normalized by the model to obtain an un-symmetric model. The NRTL expression for the local interactions, the Pitzer-Debije-Hückel expression, and the Born equation are added to give Equation 6-43 for the excess Gibbs energy.

For the elecNRTL model to calculate activity coefficients, the excess Gibbs free energy is related to the activity coefficient by the following thermodynamic relationship.

$$\ln \gamma_i = \frac{G_m^{*E}}{RT} = \left[\frac{\delta\left(nG_m^{*E} / RT\right)}{\delta n_i} \right] \qquad 6\text{-}46$$

Applying Equation 6-46 to Equation 6-43 yields,

$$\ln \gamma_i^* = \ln \gamma_i^{*,PDH} + \ln \gamma_i^{*,Born} + \ln \gamma_i^{*,lc} \qquad 6\text{-}47$$

Notice that in the absence of ions Equation 6-43 reduces to the original NRTL expression for nonelectrolyte systems.

6.4.1 *Long-Range Contribution*

The first term in Equation 6-43 accounts for the Pitzer-Debije-Hückel long range ion-ion interactions that occur at low ionic strengths.

$$\frac{G_m^{*E,PDH}}{RT} = -\sum_k x_k \left(\frac{1000}{M_s}\right)^{0.5} \left(\frac{4A_\phi I_x}{\rho}\right) \ln\left(1+\rho I_x^{0.5}\right) \qquad 6\text{-}48$$

Where
M_s is the molecular weight of the solvent,
ρ is the "Closest approach" parameter,
I_x is the ionic strength on a mole fraction basis,

$$I_x = 0.5\sum_i x_i z_i^2 \qquad 6\text{-}49$$

x_i is the mole fraction of component *i*,
z_i is the charge of component,
A_ϕ is the Debije-Hückel parameter,

$$A_\phi = \frac{1}{3}\left(\frac{2\pi N_o d}{1000}\right)^{0.5} \left(\frac{e^2}{D_w kT}\right)^{1.5} \qquad 6\text{-}50$$

N_o is Avogadro's number,
d is the solvent density,
e is the charge of an electron,
D_w is the dielectric constant for water,
T is temperature, K,
k is the Boltzmann constant.

6.4.2 *Born Correction*

The Born correction term accounts for the change in reference state given by the difference in the dielectric constants.

$$\frac{G_m^{*E,Born}}{RT}=\left(\frac{e^2}{2kT}\right)\left(\frac{1}{D_m}-\frac{1}{D_w}\right)\frac{\sum_i x_i z_i^2}{r_i}10^{-2} \qquad 6\text{-}51$$

Where

r_i is the Born radius,

D_m is the Dielectric constant of the mixed solvent.

6.4.3 *Local Contribution*

The NRTL model accounts for sort range interactions between the molecules. These could be considered the most important interactions, because contributions from the previous two terms are only analytical in nature. Contributions from the NRTL model are regressed to fit system requirements. Subscripts m, c, and a, represent molecules, cations, and anions, respectively.

$$\begin{aligned}\frac{G_m^{*E,lc}}{RT}&=\sum_m X_m\frac{\sum_j X_j G_{jm}\tau_{jm}}{\sum_k X_k G_{km}}+\sum_c X_c\sum_{a'}\left(\frac{X_{a'}}{\sum_{a''}X_{a''}}\right)\frac{\sum_j G_{jc,a'c}\tau_{jc,a'c}}{\sum_k X_k G_{kc,a'c}}+\dots\\&\dots+\sum_a X_a\sum_{c'}\left(\frac{X_{c'}}{\sum_{c''}X_{c''}}\right)\frac{\sum_j G_{ja,a'c}\tau_{ja,a'c}}{\sum_k X_k G_{ka,a'c}}\end{aligned} \qquad 6\text{-}52$$

Where

$$G_{cm}=\frac{\sum_a X_a G_{ca,m}}{\sum_{a'}X_{a'}}, \qquad G_{am}=\frac{\sum_c X_c G_{ca,m}}{\sum_{c'}X_{c'}},$$

$$\alpha_{cm}=\frac{\sum_a X_a \alpha_{ca,m}}{\sum_{a'}X_{a'}}, \qquad \alpha_{am}=\frac{\sum_c X_c G_{ca,m}}{\sum_{c'}X_{c'}},$$

$$G_{jc,a'c}=\exp\left(-\alpha_{jc,a'c}\tau_{jc,a'c}\right), \qquad G_{ja,c'a}=\exp\left(-\alpha_{ja,c'a}\tau_{ja,c'a}\right),$$

$$G_{im}=\exp\left(-\alpha_{im}\tau_{im}\right), \qquad G_{ca,m}=\exp\left(-\alpha_{ca,m}\tau_{ca,m}\right),$$

$$\tau_{ma,ca} = \tau_{am} - \tau_{ca,m} + \tau_{m,ca}, \qquad \tau_{mc,ac} = \tau_{cm} - \tau_{ca,m} + \tau_{m,ca},$$

$X_j = x_j C_j$ ($C_j = Z_j$ for ions and C_j = unity for molecule),
α is the nonrandomness parameter,
τ is the binary energy interaction parameter.

Specific information concerning the temperature dependent nature of τ can be found in subsequent chapters.

6.5 Vapor-Liquid Equilibrium Calculations

When the activity coefficients are calculated, the equilibrium between the vapor and liquid phases can be determined. From thermodynamics we know that the fugacity of the liquid and fugacity of the vapor must be equal. We can then write the following expression describing the vapor-liquid equilibrium for non supercritical species:

$$y_i \hat{\phi}_i^v P = x_i \gamma_i \hat{\phi}_i^0 P_i^0 \exp\left[\frac{V_i^l \left(P - P_i^0\right)}{RT}\right] \tag{6-53}$$

and the vapor-liquid equilibrium for supercritical components (e.g. CO_2) is given by

$$y_i \hat{\phi}_i^v P = x_i \gamma_i \left(\frac{H_i}{\gamma_i^{\infty,aq}}\right) \exp\left[\frac{V_i^{\infty,aq} \left(P - P_{H_2O}^0\right)}{RT}\right] \tag{6-54}$$

Where
P_i^0 is the saturation pressure of component i at the system temperature,
$\gamma_i^{\infty,aq}$ is the infinite dilution activity coefficient for CO_2 in H_2O at the system temperature,
V_i^l is the molar volume of the pure solvent at the system temperature and saturation pressure,
$V_i^{\infty,aq}$ is the Brelvi-O'Connell partial molar volume for CO_2 at infinite dilution in H_2O at system temperature and $P_{H_2O}^0$,
y_i is the true mole fraction in the vapor phase of component i, and,
x_i is the true mole fraction in the liquid phase of component i.

PART III

Parameter Regression

and

Data Interpretation

CHAPTER VII

Pure Component Systems: MEA, PZ, and H_2O

Preface for the User

We start this chapter with a warning to the end user: The foundations of the NRTL model and the electrolyte-NRTL (elecNRTL) within Aspen Plus^{TM} are not transparent with respect to each other; the calculation methods and scalar pure component properties (as stated in Chapter VI) are different between each model. This chapter has been segmented into two parts: part one describes the heat of vaporization corrections to the NRTL model to predict the specific heat capacity of the pure component. Part two describes corrections to the elecNRTL model to predict the specific heat capacity of the pure component.

In the end, we will be using the elecNRTL property model for all future chapters to describe molecular and ionic interactions. Therefore, part one of this chapter will not be included in the final elecNRTL code and is included as a supplement to the end user.

— Part One —

7.1 NRTL Introduction

The development of any thermodynamic model starts with the basic scalar and temperature dependant physical properties of the molecular components. At this point in the model development, we are building the foundation of our model, which represents the values of the basic properties used in Aspen Plus^{TM}. This chapter describes the data regression and model predictions to correct the specific heat capacity (heat capacity) of monoethanolamine (MEA), piperazine (PZ), and water (H_2O) based on previous literature data and experimental results from this work. Coefficients for the heat of vaporization and solid heat capacity polynomial associated with these systems are then regressed in the NRTL model. Overall, the new parameters adequately describe the specific heat capacity of MEA, PZ, and H_2O within an average absolute relative error of ± 0.41, 0.83, and 0.39 percent, respectively.

7.2 Specific Heat Capacity of MEA

As stated in Chapter VI, Aspen Plus^{TM} calculates the liquid phase heat capacity of a *pure component* by taking the derivative of the liquid enthalpy departure, which is a function of the ideal gas enthalpy and the heat of vaporization. Six data sets have been regressed with the NRTL model to correct the liquid phase heat capacity of MEA. Coefficients of the DIPPR heat of vaporization equation were adjusted to account for the heat of vaporization [Clapeyron (1834) and Riddick and Bunger (1970)] and liquid heat capacity [The Dow

Chemical Company (1981), Swanson and Chueh (1973), Chiu et al. (1999), and this work] of pure MEA.

7.2.1 *Standard Enthalpy of Vaporization*

According to Atkins and de Paula (2002) the standard enthalpy of vaporization, also known as the heat of vaporization, is the energy required to transform a given quantity of a substance into a gas. Aspen Plus^{TM} relates the specific heat capacity to the ideal gas enthalpy and the heat of vaporization to eliminate errors associated with accurate thermal properties of both phases by the following method:

$$H_i^l - H_i^l\left(T^{ref}\right) = \int_{T^{ref}}^{T} C_{p,i}^l dT \qquad 7\text{-}1$$

$$H_i^l\left(T^{ref}\right) = H_i^{ig} + \left(H_i^v - H_i^{ig}\right) - \Delta H_i^{vap} \qquad 7\text{-}2$$

Where

$H_i^l\left(T^{ref}\right)$ is the reference enthalpy of component i at $T^{ref} = 298.15K$,

H_i^{ig} is the ideal gas enthalpy of component i,

$H_i^v - H_i^{ig}$ is the vapor enthalpy departure of component i,

ΔH_i^{vap} is the heat of vaporization of component i.

Table 7.2-1 gives the coefficients for the DIPPR heat of vaporization equation for MEA used in Aspen Plus^{TM} based on the following expression:

$$\Delta H_i^{vap}\left(\frac{J}{kmol}\right) = C_{1i}\left(1 - T_{ri}\right)^{\left(C_{2i} + C_{3i}T + C_{4i}T^2\right)} \qquad 7\text{-}3$$

Where

T_{ri} is the reduced temperature, T / T_{ci},

T_{ci} is the critical temperature of component i,

T is the temperature, °C.

Table 7.2-1. DIPPR Heat of Vaporization Default Coefficients for MEA from 10.5 – 405.05 °C.

Parameter	Symbol	Default value
DHVLPD-1	C_1	8.5465E+7
DHVLDP-2	C_2	0.5102
DHVLDP-3	C_3	0.0
DHVLDP-4	C_4	0.0

Experimental heat of vaporization data used in this work from the above two sources is shown in Figure 7.2-1.

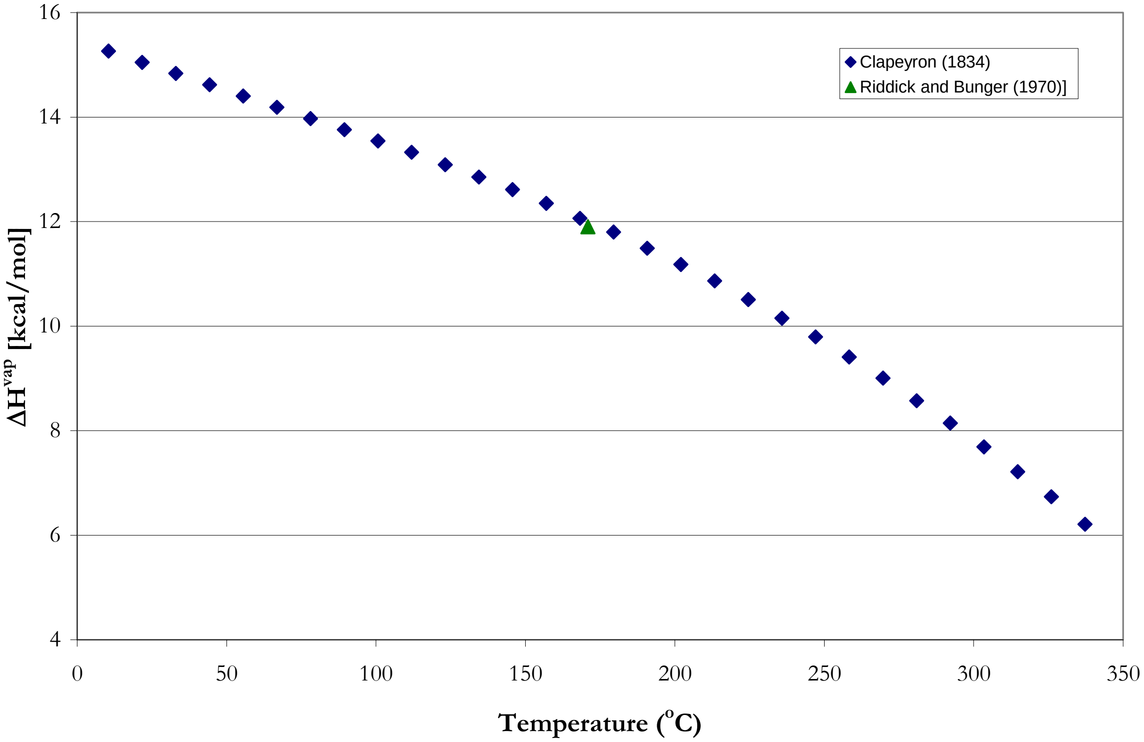

Figure 7.2-1. Heat of Vaporization of MEA.

We decided to limit the heat of vaporization data to values under 171 °C to capture successfully the experimental specific heat capacity trends within the current work.

Using the Clausius-Clapeyron equation, we can verify the consistency between the DIPPR Heat of Vaporization Equation given for MEA versus the DIPPR Extended Antoine Vapor Pressure Equation based on the following expression:

$$\ln P_i^{*,l}\left(kPa\right) = C_{1i} + \frac{C_{2i}}{T\left(K\right)+C_{3i}} + C_{4i}T\left(K\right) + C_{5i}\ln T\left(K\right) + C_{6i}T\left(K\right)^{C_{7i}} \qquad 7\text{-}4$$

where coefficients for MEA are given in Table 7.2-2.

Table 7.2-2. DIPPR Extended Antoine Vapor Pressure Default Coefficients for MEA from 10.0 – 365.0 °C.

Parameter	Symbol	Default value
PLXANT-1	C_1	165.87
PLXANT-2	C_2	-13492
PLXANT-3	C_3	0.0
PLXANT-4	C_4	0.0
PLXANT-5	C_5	-21.9
PLXANT-6	C_6	1.38E-05
PLXANT-7	C_7	2.00

The Clausius-Clapeyron equation, relates the heat of vaporization directly to the vapor pressure curve based on the following equation:

$$\Delta H_i^{vap} = -R\frac{d\ln P_i^{*,l}}{d\left(1/T\right)} \qquad 7\text{-}5$$

and valid only at low pressures, approximately below 2 atm. Using Equation 7-5, Equation 7-4 yields

$$\Delta H_i^{vap} = -R\left\{\left(\frac{-T\left(K\right)}{\left(T\left(K\right)+C_{3i}\right)^2}\right)\left[\begin{array}{l} C_{6i}C_{7i}\left(T\left(K\right)+C_{3i}\right)^2 T\left(K\right)^{C_{7i}} + \\ C_{4i}T\left(K\right)^3 + \left(2C_{3i}C_{4i}+C_{5i}\right)T\left(K\right)^2 - \\ \left(C_{2i}-C_{3i}\left(C_{3i}C_{4i}+2C_{5i}\right)\right)T\left(K\right) + \\ C_{3i}^2 C_{5i} \end{array}\right]\right\} \qquad 7\text{-}6$$

Since C_{3i} = 0.0 for MEA, we can simplify Equation 7-6 to yield

$$\Delta H_i^{vap} = R\left(C_{6i}C_{7i}T(K)^{C_{7i}+1} + C_{4i}T(K)^2 + C_{5i}T(K) - C_{2i}\right) \qquad 7\text{-}7$$

Based on Equation 7-7, we can compare the coefficients for the DIPPR Extended Antoine Vapor Pressure for MEA given in Table 7.2-2 to literature heat of vaporization as shown in Figure 7.2-2. Deviations at high pressures appear above 200 °C between cited and predicted values due to the approximate linear nature of the Clausius-Clapeyron equation.

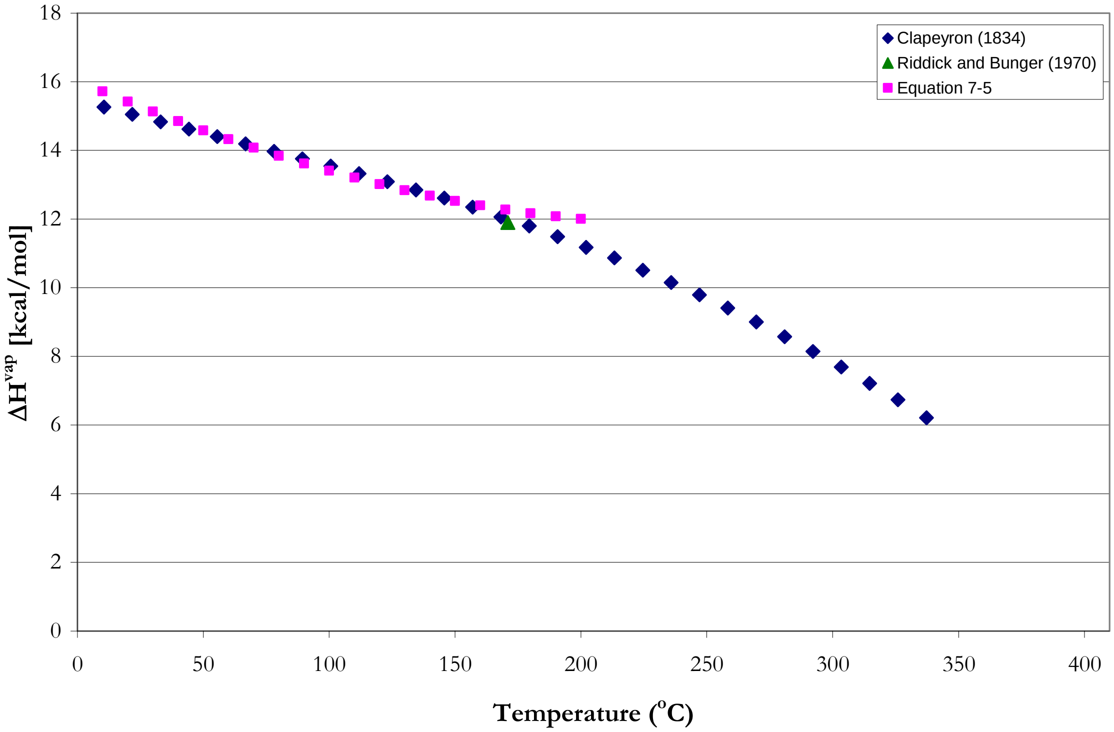

Figure 7.2-2. Comparison of the Heat of Vaporization based on Equation 7-5 to Literature Values for MEA.

7.2.2 *Data Regression*

Through simultaneous regression, the coefficients for the DIPPR heat of vaporization equation were determined by DRS in Aspen Plus utilizing the maximum likelihood principle of Britt and Luecke (1973) through the minimization of the following objective function:

$$f = \sum_{k=1}^{n} W_{U_k} \left(\frac{\left(U_{k,adj} - U_{k,obs} \right)^2}{\sigma_{U_k}^2} \right) + \sum_{k=1}^{n} W_{P_k} \left(\frac{\left(P_{k,adj} - P_{k,obs} \right)^2}{\sigma_{P_k}^2} \right) \qquad 7\text{-}8$$

where the measurable variables, U_k (e.g. state variables: T, P, x, y), and property variables, P_k (e.g. heat of vaporization and heat capacity) are weighted by their standard error, σ. The objective function is then minimized using Lagrange multipliers to adjust the measurable variables and the model parameters within parameter bounds. A list of the pure component data sets that were examine in this work is given in Figure 7.2-3. The column labels σ_T, σ_{DHVL}, σ_{CPL-M} gives standard error associated with the temperature, heat of vaporization, and the heat capacity, respectively, with each data set.

Table 7.2-3. Experimental data used in the regression of Heat of Vaporization Coefficients for MEA.

	Obs.	T (ºC)	σ_T	σ_{DHVL}	Source
ΔH^{vap}	1	170.95	0.1	1%	Riddick and Bunger (1970)
	15	10.50 – 337.23	0.1	1%	Clapeyron (1834)

	Obs.	T (ºC)	σ_T	σ_{CPL-M}	Source
C_p	1	30.0	0.1	1%	The Dow Chemical Company (1981)
	1	20.0	0.1	1%	Swanson and Chueh (1973)
	11	30.0 – 80.0	0.1	1%	Chiu et al. (1999)
	17	40.0 – 120.0	0.1	1%	This work

Table 7.2-4 shows the following regression summary statistics output for estimates of the heat of vaporization coefficients after performing a nonlinear regression for the full

model using DRS. To account for the temperature dependant nature of heat capacity in the heat of vaporization equation, we include the third term into the full model regression.

Table 7.2-4. DRS Regression Output for Full MEA Model.

Parameter	Estimate	σ wrt Estimate
DHVLPD-1	8.8033E+07	8.2460E+09
DHVLDP-2	0.7078	0.0055
DHVLDP-3	-0.2813	0.0058

Residual Sum of Squares: 29.2382
Residual Root Mean Square: 3.707

Recall that the standard error of an estimate is the estimated standard deviation of that statistic. Notice that all of the estimates are large relative to their standard errors with the exception of the first coefficient. A complete description of the variability of the coefficient estimates requires examining the correlations between the estimates is shown in Table 7.2-5.

Table 7.2-5. Correlation Matrix of the Coefficient Estimates for the Full MEA Model.

Parameter	1	2	3
1	1.00		
2	0.00	1.00	
3	0.00	-0.98	1.00

Each correlation coefficient is a summary statistic for a 2D scatterplot of the variables used in the correlation and is a measure of the linear relationship between the variables. The correlation coefficient is a unitless number that always falls between -1 and 1. If the correlation coefficient equals 1 or -1, then the parameters can be described by a linear line with either a positive or negative slope. If the correlation coefficient equals 0, then the parameters are said to be uncorrelated and independent. The correlation matrix is symmetric because the covariance between parameters $\hat{\eta}_j$ and $\hat{\eta}_k$ is the same as the covariance between parameters $\hat{\eta}_k$ and $\hat{\eta}_j$.

Table 7.2-5 shows a high negative correlation between $\hat{\eta}_{3\rightarrow 2}$ for the third parameter, but the correlation between $\hat{\eta}_{3\rightarrow 1}$ and $\hat{\eta}_{2\rightarrow 1}$ is independent due to the non-linear nature of Equation 7-3. Table 7.2-5 suggests that the third parameter might be usefully removed from the model without significant loss of information.

7.2.3 *Full MEA Model Results*

With the determination of the estimates for the heat of vaporization parameters known for the full model, a simple Aspen Plus^{TM} Flash model was used to test the predictive capability of the MEA model against literature data. For each data point, the deviation between the experimental and estimated values is expressed in terms of the absolute average relative deviation (AARD), as given by the following equation:

$$AARD(\%) = \frac{100}{N}\sum_i \frac{\left|\exp_i - \mathrm{est}_i\right|}{\exp_i} \qquad 7\text{-}9$$

Where
N is the number of experimental data points.

Table 7.2-6 gives the AARD and the maximum AARD for the model predictions.

Overall, the model adequately describes the MEA property data listed above within an average absolute relative error of ±0.41 percent, with the exception of a few outliers.

We found that parameters regressed for the above two systems with heat of vaporization data above 171 °C did not accurately describe significant systematic trends presented in the specific heat capacity data.

Table 7.2-6. Absolute Percent Relative Error for the MEA Full Model.

		AARD(%)	Max. AARD
ΔH^{vap}	Riddick and Bunger (1970)	1.22	-
	Clapeyron (1834)	0.16	0.37
C_p	The Dow Chemical Company (1981)	2.10	-
	Swanson and Chueh (1973)	2.62	-
	Chiu et al. (1999)	0.87	1.80
	This work	0.20	0.60
Overall		**0.41**	**1.80**

7.2.4 *MEA Model Predictions*

With the determination of the estimates for the heat of vaporization coefficients known for the full model, a simple Aspen Plus^{TM} Flash model was used to test the predictive capability of the MEA heat of vaporization coefficients against literature data. Figure 7.2-3 compares estimated and experimental heat of vaporization from Riddick and Bunger (1970) and Clapeyron (1834) for MEA from 10.50 to 337.23 °C. The full model over estimates the heat of vaporization above 202.03 °C with a maximum error of 17.0 % at 337.23 °C. However, this error is well beyond the operating range of present carbon capture technology and is negligible overall since the full model is consistent with the critical temperature of MEA (405.05 °C).

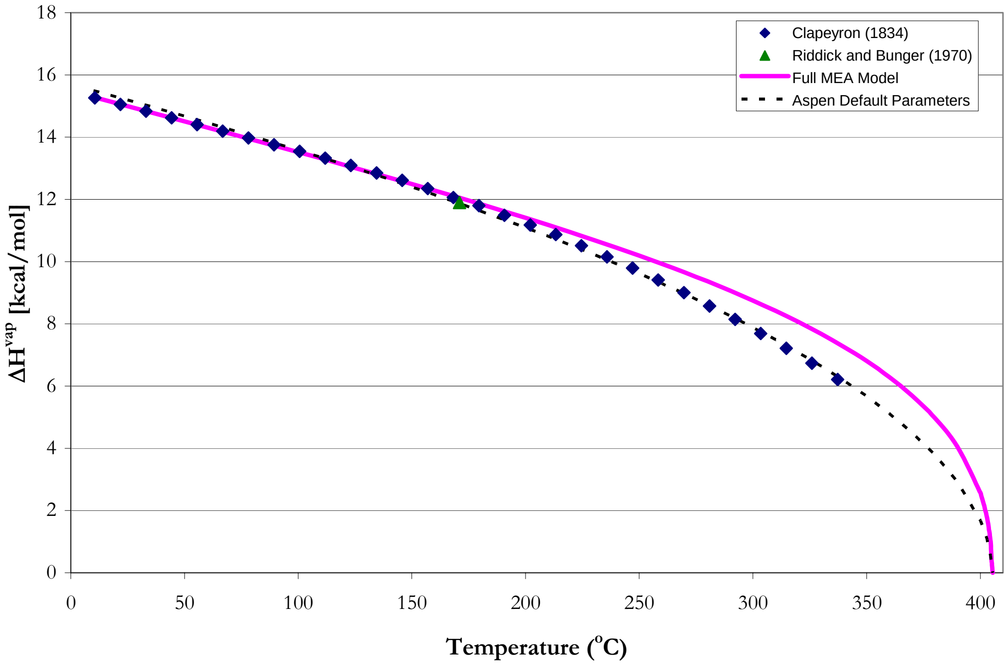

Figure 7.2-3. Comparison of Model Predictions with Experimental Data from Riddick and Bunger (1970) and Clapeyron (1834) for the ΔH^{vap} of MEA from 10.50-337.23 °C.

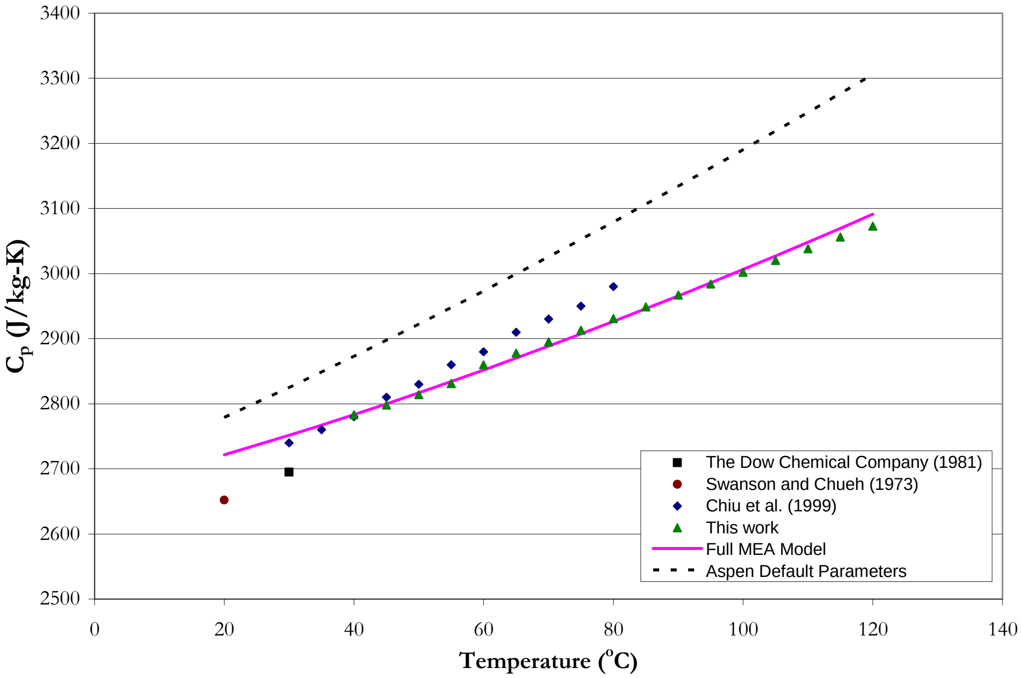

Figure 7.2-4. Comparison of Model Predictions with Experimental Data for the Specific Heat Capacity of MEA from 20 – 120 °C

Figure 7.2-4 compares estimated and experimental specific heat capacity from The Dow Chemical Company (1981), Swanson and Chueh (1973), Chiu et al. (1999) and from this work for pure MEA from 20 – 120 ^{o}C. The full model overestimates the specific heat capacity at low temperatures as compared to Swanson and Chueh (1973) and The Dow Chemical Company (1981), even though all of the predictions for the model were within an AARD of ± 0.59 %. Figure 7.2-4 illustrates a 5.19 % decrease for the prediction of the specific heat capacity as compared to Aspen default parameters.

7.3 Specific Heat Capacity of PZ

Two data sets have been regressed with the NRTL model to correct the liquid phase heat capacity of PZ. Coefficients of the DIPPR heat of vaporization equation were adjusted to account for the heat of vaporization [Clapeyron (1834)] and liquid heat capacity [Swanson and Chueh (1973)] of pure PZ. Coefficients for the solid heat capacity equation were not adjusted since predictions from the Aspen default parameters accurately described literature data from Steele et al. (1997) and from this work with an AARD of ± 0.54 and 1.28 %, respectively.

7.3.1 *Standard Enthalpy of Vaporization*

As stated in section 7.2, Aspen Plus^{TM} relates the liquid phase specific heat capacity to the ideal gas enthalpy and the heat of vaporization through equations 7-1 to 7-3. Table 7.3-1 gives the coefficients for the DIPPR heat of vaporization equation for PZ used in Aspen Plus^{TM} based on equation 7-3:

Table 7.3-1. DIPPR Heat of Vaporization Default Coefficients for PZ from 106 – 364.85 °C.

Parameter	Symbol	Default value
DHVLPD-1	C_1	6.5323E+7
DHVLDP-2	C_2	0.4158
DHVLDP-3	C_3	0.0
DHVLDP-4	C_4	0.0

Experimental heat of vaporization data used in this work from Clapeyron (1834) is shown in Figure 7.3-1.

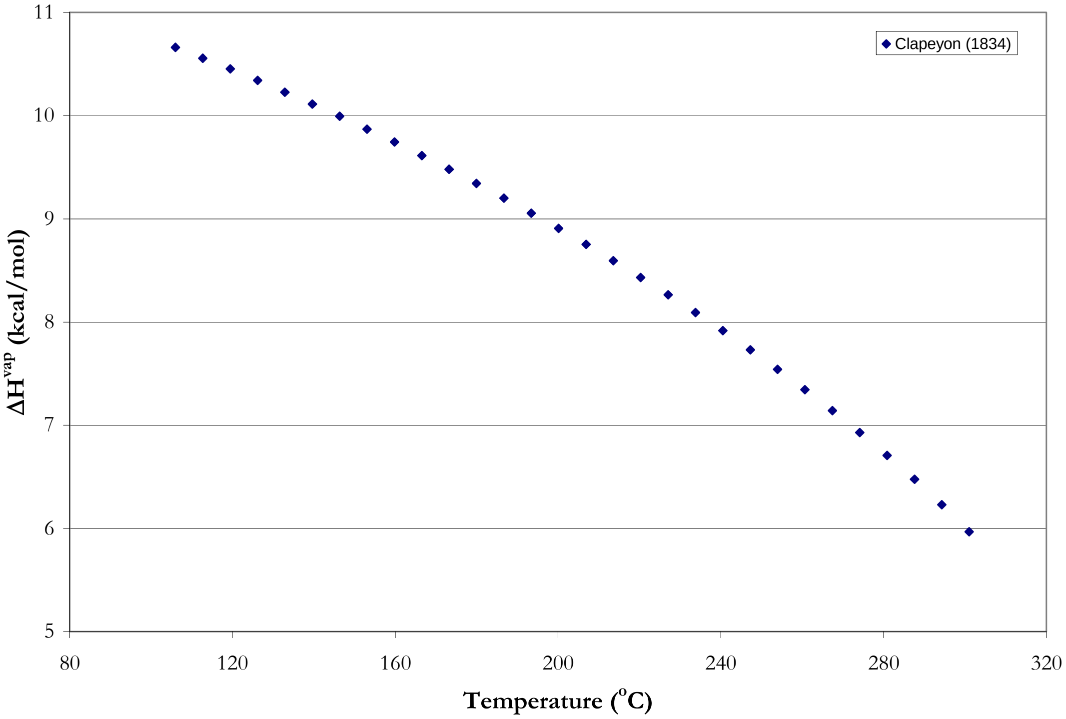

Figure 7.3-1. Heat of Vaporization of PZ.

Using the Clausius-Clapeyron equation, we can verify the consistency between the DIPPR Heat of Vaporization Equation given for PZ versus the DIPPR Extended Antoine Vapor Pressure Equation based on Equation 7-4 and Table 7.3-2.

Table 7.3-2. DIPPR Extended Antoine Vapor Pressure Default Coefficients for PZ from 106 – 364.85 °C.

Parameter	Symbol	Default value
PLXANT-1	C_1	63.60
PLXANT-2	C_2	-7915
PLXANT-3	C_3	0.0
PLXANT-4	C_4	0.0
PLXANT-5	C_5	-6.65
PLXANT-6	C_6	5.21E-18
PLXANT-7	C_7	6.00

Based on Equation 7-7, we can compare the coefficients for the DIPPR Extended Antoine Vapor Pressure for PZ given in Table 7.3-2 to literature heat of vaporization as shown in Figure 7.3-2. Deviations at high pressures appear above 150 °C between cited and predicted values due to the approximate linear nature of the Clausius-Clapeyron equation.

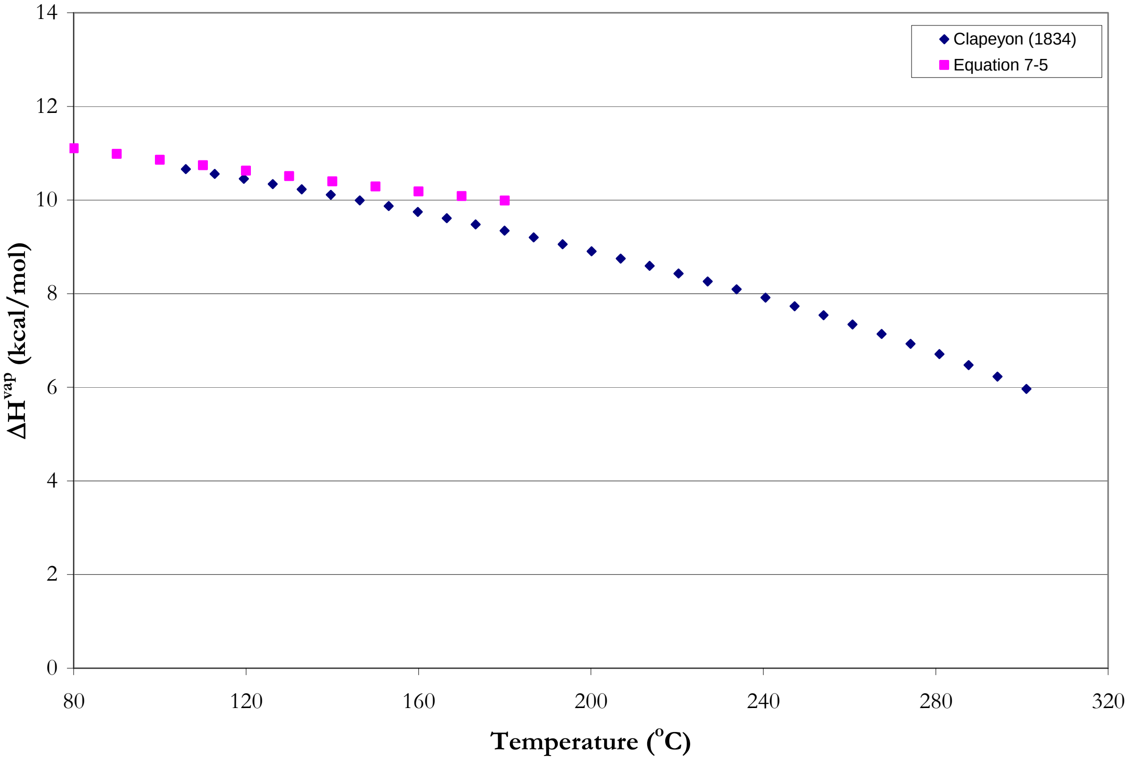

Figure 7.3-2. Comparison of the Heat of Vaporization based on Equation 7-5 to Literature Values for PZ.

7.3.2 *Solid Specific Heat Capacity*

Aspen Plus^{TM} calculates the solid phase specific heat capacity for PZ by the DIPPR solid heat capacity equation based on the following expression:

$$C_{p,i}^{s}\left(\frac{J}{kmol-K}\right)=C_{1i}+C_{2i}T \qquad 7\text{-}10$$

Where
T is the temperature, K.

Parameters for equation 7-6 are given in Table 7.3-3.

Table 7.3-3. DIPPR Solid Heat Capacity Default Coefficients for PZ from 21.85 – 106.0 °C

Parameter	Symbol	Default value
CPSDIP-1	C_1	-46900.0
CPSDIP-2	C_2	542.0

Experimental solid phase specific heat capacity data, based on equation 7-6, from Swanson and Chueh (1973) is shown in Figure 7.3-3. Note that the solid phase specific heat capacity from this work was not regressed.

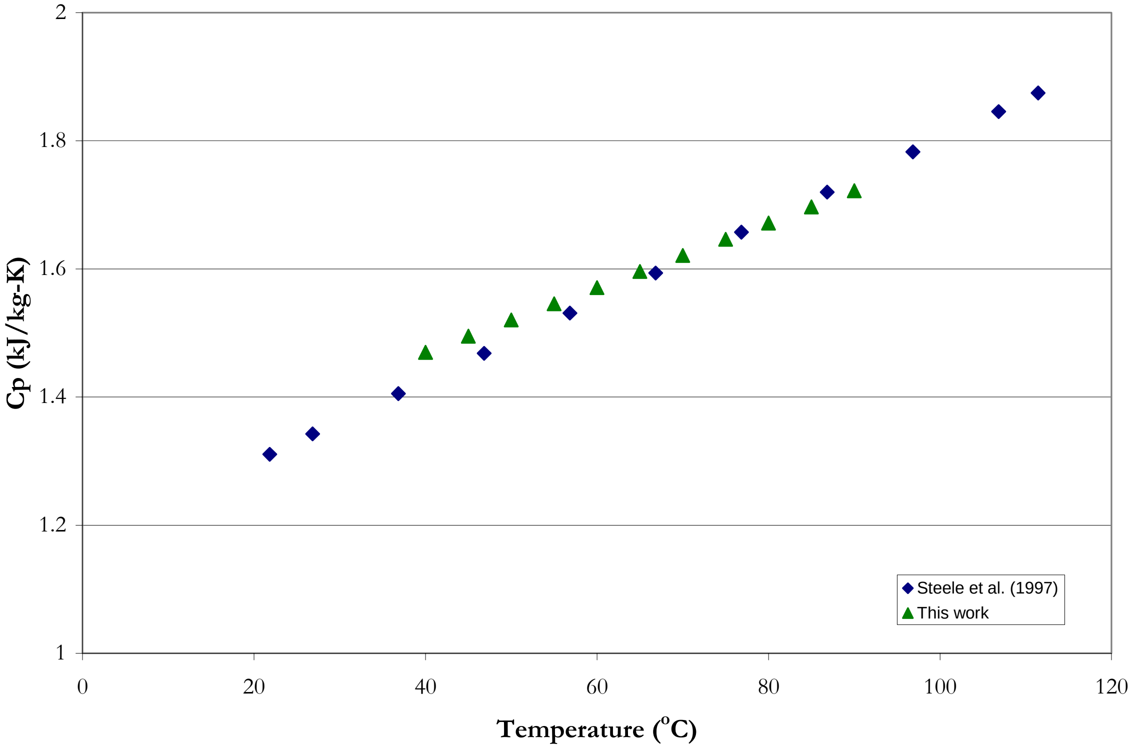

Figure 7.3-3. Solid Phase Specific Heat Capacity of PZ.

7.3.3 *Data Regression*

Through simultaneous regression, the coefficients for the DIPPR heat of vaporization equation were obtained through the regression of the heat of vaporization [Clapeyron (1834)] and liquid heat capacity [Swanson and Chueh (1973)] of pure PZ as determined by DRS in Aspen Plus™. A list of the pure component data sets that were examine in this work is given in Table 7.3-4.

Table 7.3-4. Experimental data used in the regression of Heat of Vaporization Coefficients for PZ.

	Obs.	T (°C)	σ_T	σ_{DHVL}	Source
ΔH^{vap}	30	106 – 301.05	0.1	1%	Clapeyron (1834)

	Obs.	T (°C)	σ_T	$\sigma_{CPL\text{-}M}$	Source
C_p (l)	7	105.85 – 195.85	0.1	1%	Swanson and Chueh (1973)

Table 7.3-5 shows the following regression summary statistics output for estimates of the heat of vaporization coefficients after performing a nonlinear regression for the full model using DRS. As stated in section 7.2.2, we also include an additional term into the full model regression to account for the temperature dependant of the liquid phase specific heat capacity within the heat of vaporization equation.

Table 7.3-5. DRS Regression Output for Full PZ Model.

Parameter	Estimate	σ wrt Estimate
DHVLPD-1	6.4715E+07	1.8074E+06
DHVLDP-2	0.4673	0.0727
DHVLDP-3	-0.0734	0.0693

Residual Sum of Squares: 83.8909
Residual Root Mean Square: 1.5708

Notice that all of the estimates are large relative to their standard errors. A complete description of the variability of the coefficient estimates requires examining the correlations between the estimates as shown in Table 7.3-6.

Table 7.3-6. Correlation Matrix of the Coefficient Estimates for the Full PZ Model.

Parameter	1	2	3
1	1.00		
2	0.99	1.00	
3	-0.99	-1.00	1.00

Table 7.3-6 shows highly negative and positive correlations between all of the parameters. This suggests that some of the parameters might be usefully removed from the model without significant loss of information.

7.3.4 *Full PZ Model Results*

With the determination of the estimates for the heat of vaporization parameters known for the full model, a simple Aspen Plus™ Flash model was used to test the predictive capability of the PZ model against literature data. Table 7.3-7 gives the deviation between the experimental values and model predictions expressed in terms of the absolute average relative deviation (AARD) and the maximum AARD.

Table 7.3-7. Absolute Percent Relative Error for the PZ Full Model.

		AARD(%)	Max. AARD
ΔH^{vap}	Clapeyron (1834)	1.05	2.74
C_p (l)	Swanson and Chueh (1973)	0.95	2.39
C_p (s)	Steele et al. (1997)	0.05	0.08
	This work	1.28	3.09
TOTAL		**0.83**	**3.09**

Overall, the model adequately describes the PZ property data listed above within an average absolute relative error of ± 0.83 percent, with the exception of a few outliers.

7.3.5 *PZ Model Predictions*

With the determination of the estimates for the heat of vaporization coefficients known for the full model, a simple Aspen Plus^{TM} Flash model was used to test the predictive capability of the PZ heat of vaporization coefficients against literature data. Figure 7.3-4 compares estimated and experimental heat of vaporization from Clapeyron (1834) for PZ from 106 to 301.05 ^{o}C. The full model accurately predicts the heat of vaporization over the full temperature range. In addition, the full model demonstrates its consistency with the critical temperature of PZ (364.85 ^{o}C).

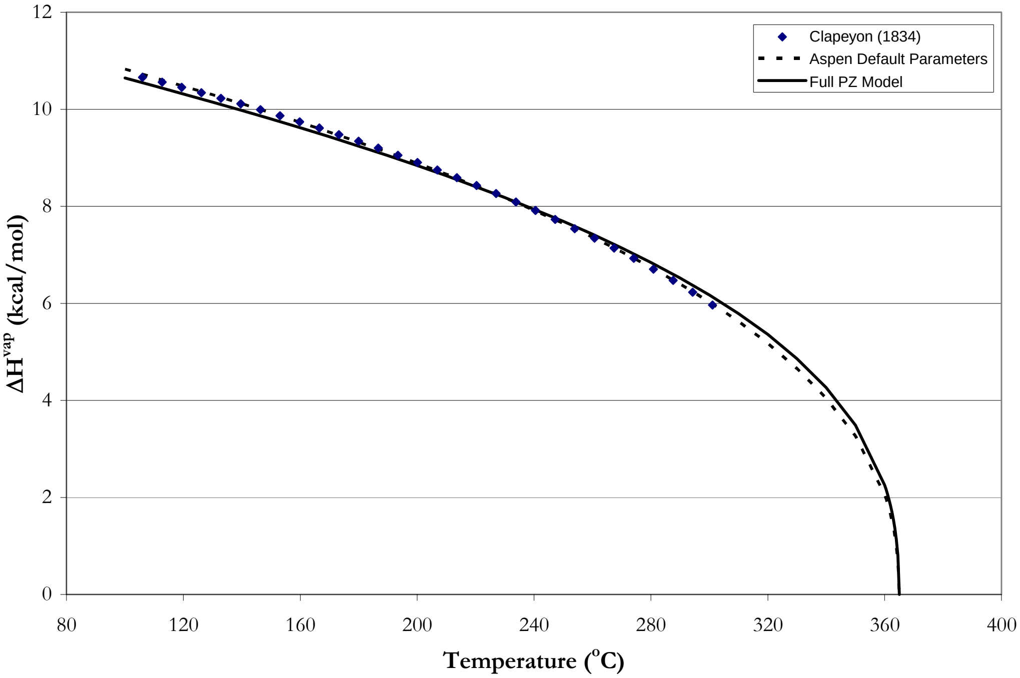

Figure 7.3-4. Comparison of Model Predictions with Experimental Data from Clapeyron (1834) for the Heat of Vaporization of PZ from 106 – 301.05 ^{o}C

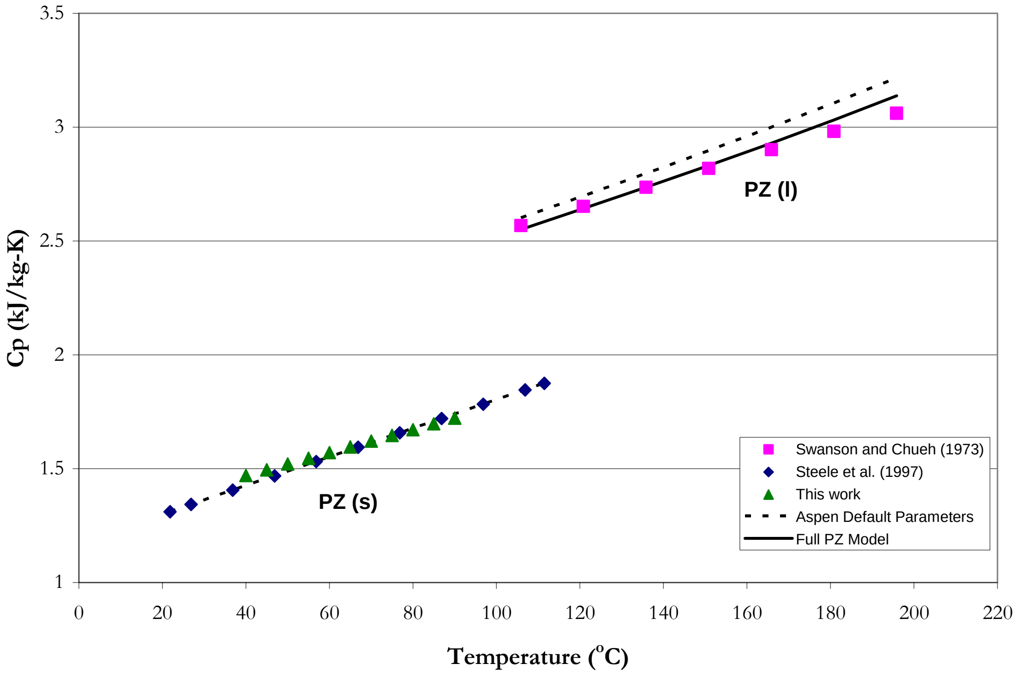

Figure 7.3-5. Comparison of Model Predictions with Experimental Data for the Specific Heat Capacity of PZ from 20 – 200 °C.

Figure 7.3-5 compares estimated and experimental specific heat capacity from Swanson and Chueh (1973), Steele et al. (1997) and from this work for pure PZ from 20 – 200 °C. The full model overestimates the specific heat capacity at high temperatures (> 200 °C) as compared to Swanson and Chueh (1973) even though all of the predictions for the model were within an AARD of ± 0.95 %. Figure Figure 7.3-5 illustrates an AARD of ± 1.28 % for the predictions of the solid phase specific heat capacity as compared to this work.

7.4 Specific Heat Capacity of H_2O

Four data sets have been regressed with the NRTL model to correct the liquid phase heat capacity of H_2O. Coefficients of the DIPPR heat of vaporization equation were adjusted to account for the heat of vaporization [Moore et al. (1969) and Kell et al. (1984)] and liquid heat capacity [Osborne et al. (1939) and Kell et al. (1984)] of pure H_2O.

7.4.1 *Standard Enthalpy of Vaporization*

As stated in section 7.2, Aspen Plus^{TM} relates the liquid phase specific heat capacity to the ideal gas enthalpy and the heat of vaporization through equations 7-1 to 7-3. Table 7.4-1 gives the coefficients for the DIPPR heat of vaporization equation for H_2O used in Aspen Plus^{TM} based on equation 7-3:

Table 7.4-1. DIPPR Heat of Vaporization Default Coefficients for H_2O from 0.01 – 373.95 °C.

Parameter	Symbol	Default value
DHVLPD-1	C_1	5.2053E+07
DHVLDP-2	C_2	0.3199
DHVLDP-3	C_3	-0.2120
DHVLDP-4	C_4	0.2580

Experimental heat of vaporization data used in this work from Moore et al. (1969) and Kell et al. (1984) is shown in Figure 7.4-1.

We decided not to include the work by Clapeyron (1834) due to deviations at high temperatures as compared to previous authors. In addition, we decided to limit the heat of vaporization data to values under 200 °C to capture successfully the experimental specific heat capacity trends within the current work.

Using the Clausius-Clapeyron equation, we can verify the consistency between the DIPPR Heat of Vaporization Equation given for H_2O versus the DIPPR Extended Antoine Vapor Pressure Equation based on Equation 7-4 and Table 7.4-2.

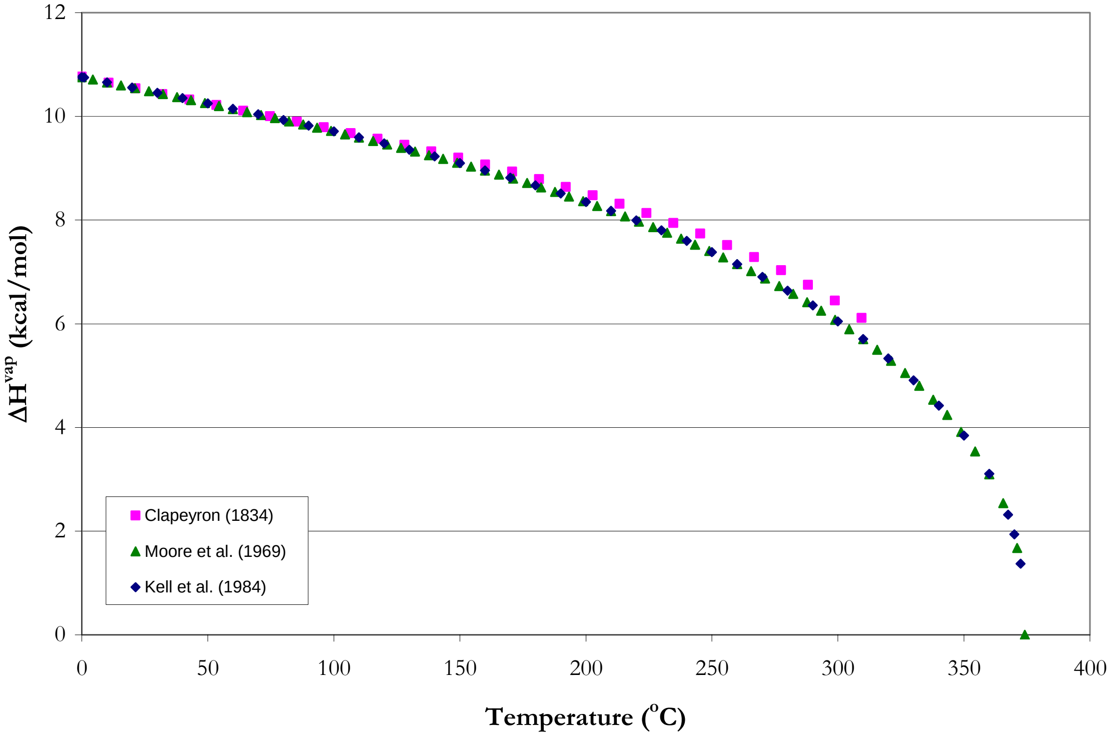

Figure 7.4-1. Heat of Vaporization of H_2O.

Table 7.4-2. DIPPR Extended Antoine Vapor Pressure Default Coefficients for H_2O from 0.01 – 373.95 °C.

Parameter	Symbol	Default value
PLXANT-1	C_1	65.64
PLXANT-2	C_2	-7207
PLXANT-3	C_3	0.0
PLXANT-4	C_4	0.0
PLXANT-5	C_5	-7.14
PLXANT-6	C_6	4.05E-06
PLXANT-7	C_7	2.00

Based on Equation 7-7, we can compare the coefficients for the DIPPR Extended Antoine Vapor Pressure for H_2O given in Table 7.4-2 to literature heat of vaporization as shown in Figure 7.4-2. Deviations at high pressures appear above 130 °C between cited and predicted values due to the approximate linear nature of the Clausius-Clapeyron equation.

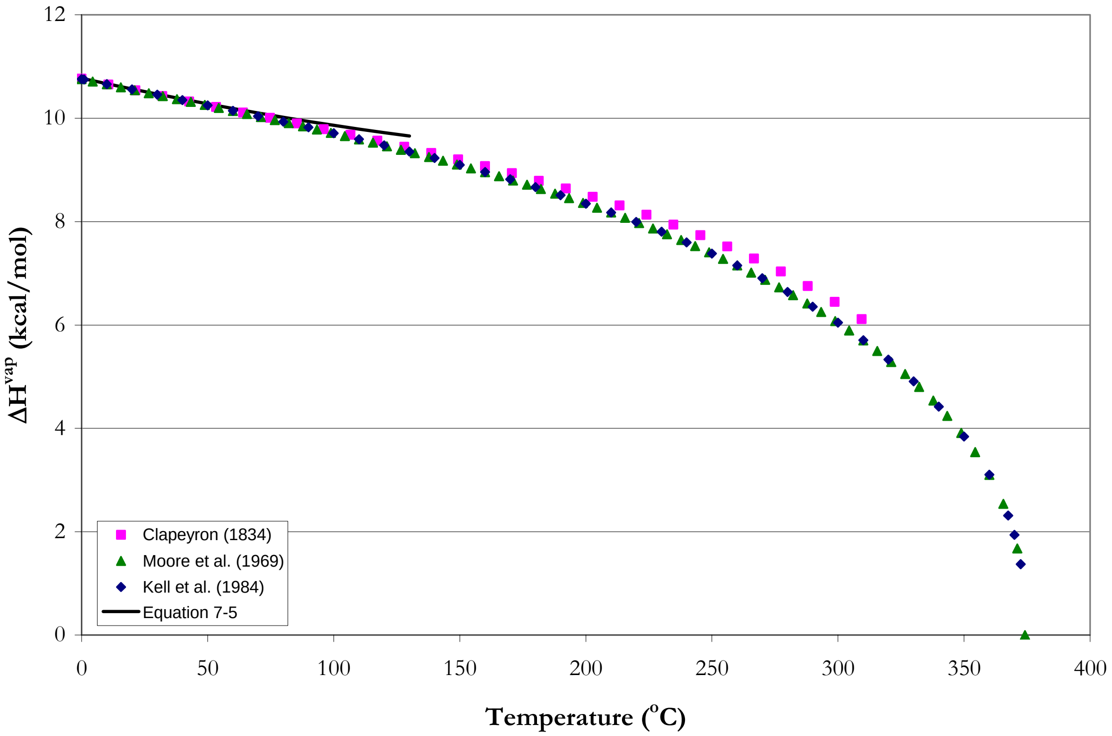

Figure 7.4-2. Comparison of the Heat of Vaporization based on Equation 7-5 to Literature Values for H_2O.

7.4.2 *Data Regression*

Through simultaneous regression, the coefficients for the DIPPR heat of vaporization equation were obtained through the regression of the heat of vaporization [Moore et al. (1969) and Kell et al. (1984)] and liquid heat capacity [Osborne et al. (1939) and Kell et al. (1984)] of pure H_2O as determined by DRS in Aspen Plus™. A list of the pure component data sets that were examine in this work is given in Table 7.4-3.

Table 7.4-3. Experimental data used in the regression of Heat of Vaporization Coefficients for H_2O.

	Obs.	T (ºC)	σ_T	σ_{DHVL}	Source
ΔH^{vap}	37	0.01 – 198.89	0.1	1%	Moore et al. (1969)
	22	0.01 – 200.00	0.1	1%	Kell et al. (1984)

	Obs.	T (ºC)	σ_T	$\sigma_{CPL\text{-}M}$	Source
C_p (l)	101	0.0 – 100.0	0.1	0.5%	Osborne et al. (1939)
	17	0.0 – 260.0	0.1	0.5%	Kell et al. (1984)

Table 7.4-4 shows the following regression summary statistics output for estimates of the heat of vaporization coefficients after performing a nonlinear regression for the full model using DRS.

Table 7.4-4. DRS Regression Output for Full H_2O Model.

Parameter	Estimate	σ wrt Estimate
DHVLPD-1	5.9101E+07	5.0137E+09
DHVLDP-2	0.7687	0.0024
DHVLDP-3	-0.7479	0.0045
DHVLDP-4	0.3079	0.0027

Residual Sum of Squares:	43.4867
Residual Root Mean Square:	0.5014

Notice that all of the estimates are large relative to their standard errors with the exception for the first coefficient. A complete description of the variability of the coefficient estimates requires examining the correlations between the estimates as shown in Table 7.4-5.

Table 7.4-5. Correlation Matrix of the Coefficient Estimates for the Full H_2O Model.

Parameter	1	2	3	4
1	1.00			
2	0.00	1.00		
3	0.00	-0.98	1.00	
4	0.00	0.91	-0.97	1.00

Table 7.4-5 shows both highly positive and highly negative correlations between $\hat{\eta}_{3\to2}$, $\hat{\eta}_{4\to2}$, and $\hat{\eta}_{4\to3}$ for the second and third parameters, but the correlations between $\hat{\eta}_{4\to1}$, $\hat{\eta}_{3\to1}$, and $\hat{\eta}_{2\to1}$ are independent due to the non-linear nature of Equation 7-3. Table 7.4-5 suggests that the fourth parameter might be usefully removed from the model without significant loss of information.

7.4.3 *Full H_2O Model Results*

With the determination of the estimates for the heat of vaporization parameters known for the full model, a simple Aspen Plus™ Flash model was used to test the predictive capability of the H_2O model against literature data. Table 7.4-6 gives the deviation between the experimental values and model predictions expressed in terms of the absolute average relative deviation (AARD) and the maximum AARD.

Table 7.4-6. Absolute Percent Relative Error for the H_2O Full Model.

		AARD(%)	Max. AARD
ΔH^{vap}	Moore et al. (1969)	0.59	1.77
	Kell et al. (1984)	0.63	1.78
C_p (l)	Osborne et al. (1939)	0.06	0.37
	Kell et al. (1984)	0.28	1.11
TOTAL		**0.39**	**1.78**

Overall, the model adequately describes the H_2O property data listed above within an average absolute relative error of ± 0.39 percent, with the exception of a few outliers.

7.4.4 *H_2O Model Predictions*

With the determination of the estimates for the heat of vaporization coefficients known for the full model, a simple Aspen Plus™ Flash model was used to test the predictive capability of the H_2O heat of vaporization coefficients against literature data. Figure 7.4-3 compares estimated and experimental heat of vaporization from Moore et al. (1969), Kell et al. (1984) and Clapeyron (1834) for H_2O from 0.01 to 373.95 °C. The full model over predicts the heat of vaporization above 204.44 °C with a maximum error of 21.7 % at 348.98 °C. However, this error is well beyond the operating range of present carbon capture technology and is negligible overall since the full model is consistent with the critical temperature of H_2O (373.95 °C).

Figures 7.4-3 and 7.4-4 compares estimated and experimental specific heat capacity from Osborne et al. (1939), Engineering Sciences Data (1966), Kell et al. (1984), Chiu et al. (1999) and from this work for pure H_2O from 0 – 260 °C. The full model underestimates the specific heat capacity as compared to Kell et al. (1984) even though all of the predictions for the model were within an AARD of ± 0.17 %. Figure 7.4-5 illustrates a 0.27 % difference for the prediction of the specific heat capacity from this work as compared to the Full H_2O Model.

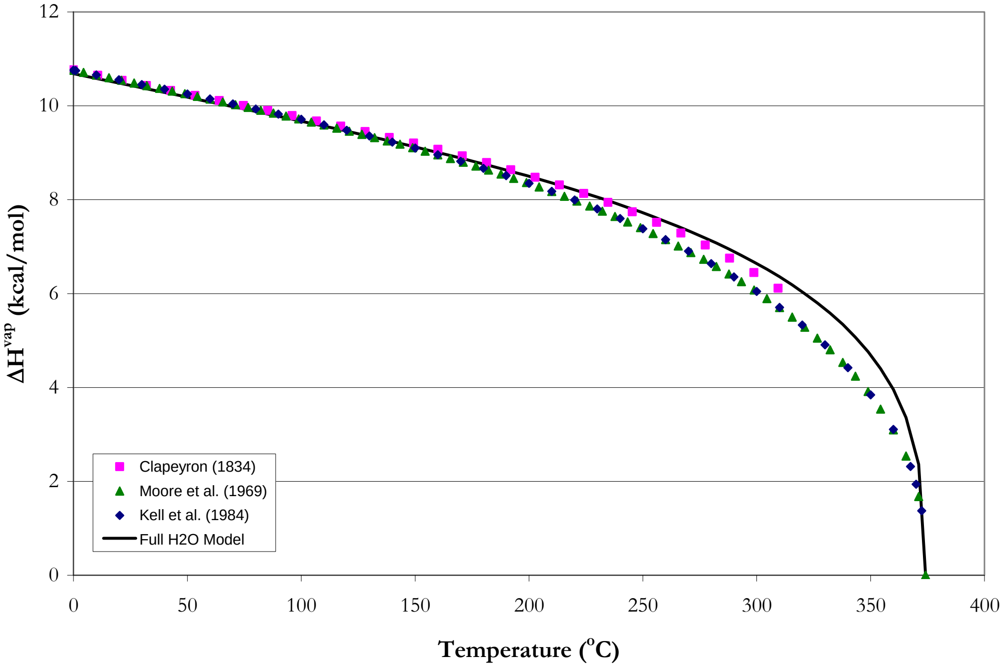

Figure 7.4-3. Comparison of Model Predictions with Experimental Data for the Heat of Vaporization of H_2O from 0.01 – 373.95 °C.

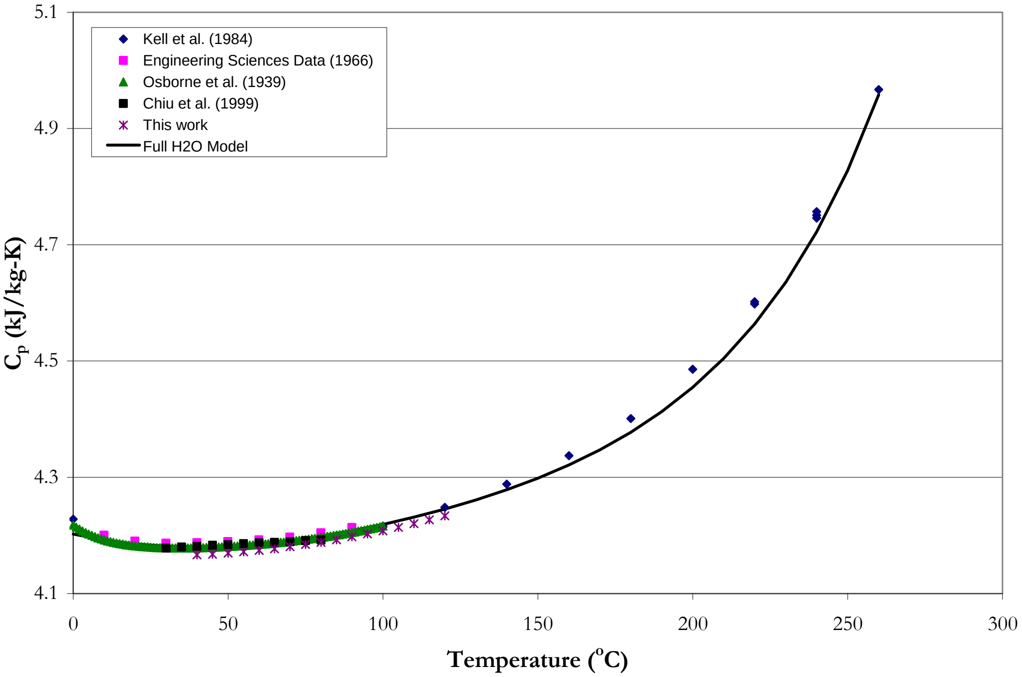

Figure 7.4-4. Comparison of Model Predictions with Experimental Data for the Specific Heat Capacity of H_2O from 0 – 260 °C.

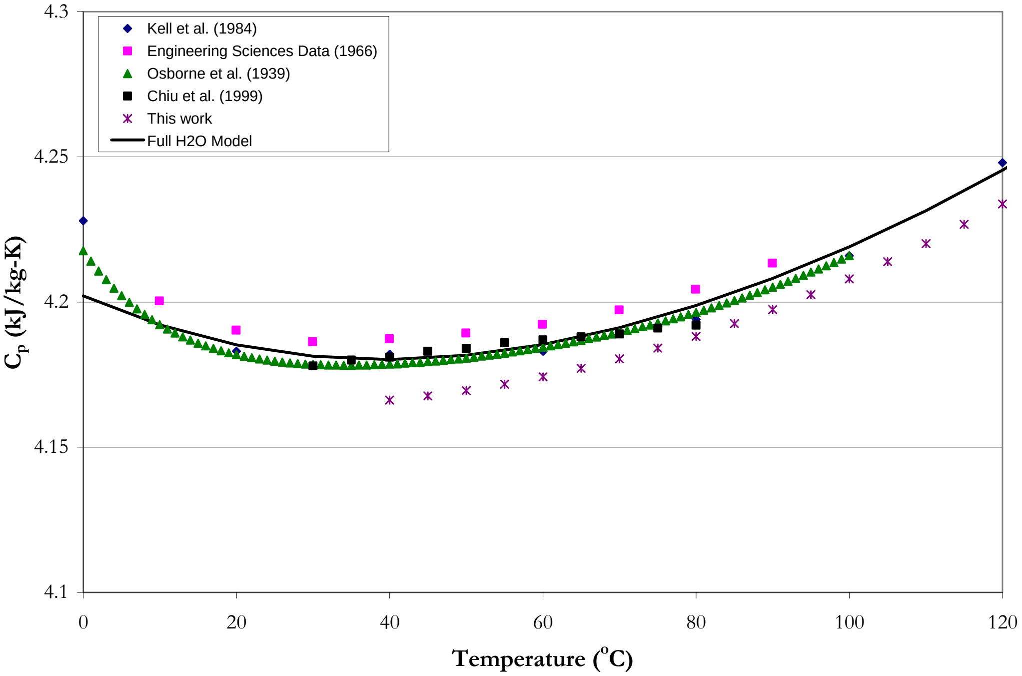

Figure 7.4-5. Expansion of Figure 7.4-3 from 0 – 120 °C for the Comparison of Model Predictions with Experimental Data for the Specific Heat Capacity of H_2O.

7.5 NRTL Conclusions

Results presented above indicate that the NRTL model, through simultaneous regression gave a set of heat of vaporization coefficients to describe liquid phase specific heat capacity for MEA, PZ, and H_2O. In addition, the model adequately represents the solid phase specific heat capacity for pure PZ.

— Part Two —

7.6 elecNRTL Introduction

Within the NRTL model, Aspen Plus calculates the liquid phase specific heat capacity for a pure component (CP) based on the heat of vaporization as stated in Section 7.2.1. Predictions for the liquid phase heat capacity of a *mixture* (CPMX), based on the derivative of the liquid enthalpy at constant pressure and are consistent with values for CP for the pure component. On the contrary, predictive values for CP and CPMX within the elecNRTL model are inconsistent with respect to one other. This chapter explains the calculation method for CP and CPMX with respect to H_2O, MEA and PZ associated with the elecNRTL model. In addition, we will try to improve upon existing parameters in order to agree with literature data.

7.7 Specific Heat Capacity for a Mixture (CPMX)

The elecNRTL model, within Aspen Plus™, calculates the liquid phase heat capacity of a *mixture* (CPMX) by taking the derivative of the liquid enthalpy at constant pressure as shown by the following expression:

$$H_i^l\left(T+\Delta T\right)-H_i^l\left(T\right)=\int_T^{T+\Delta T} C_{p,i}^l dT \qquad 7\text{-}11$$

where the liquid enthalpy of a mixture is calculated by the following equation:

$$H_i^l\left(T\right)=\sum_i x_i H_i + H_i^E \qquad 7\text{-}12$$

$$H_i\left(T\right)=\Delta H_{f,i}^{ig}\left(T^{ref}\right)+\int_{T^{ref}}^{T} C_{p,i}^{ig} dT+\left[H_i\left(T,p\right)-H_i^{ig}\left(T,p\right)\right] \qquad 7\text{-}13$$

Where
ΔT is the perturbation in temperature from T,
H_i^E is the excess enthalpy of component i,
$\Delta H_f^{ig}\left(T^{ref}\right)$ is the standard enthalpy of formation of component i at T^{ref},
T^{ref} is the reference temperature, 25.0 °C,
C_p^{ig} is the ideal gas heat capacity of component i,
H_i^{ig} is the ideal gas enthalpy of component i.

Liquid solutions are often described through properties that measure their deviations from ideal-solution behavior and not from ideal behavior.

$$M^E = M - M^{id} \tag{7-14}$$

Thus, an excess property (e.g. excess enthalpy) is defined as the difference between the value of the actual property of a solution and the value the property would have as an ideal solution at the same temperature, pressure, and composition. However, excess properties have no physical meaning for pure components, because there is no deviation. Thus, equations 7-8 and 7-9 would reduce to the following functional form.

$$H_i^l\left(T\right) = \Delta H_{f,i}^{ig}\left(T^{ref}\right) + \int_{T^{ref}}^{T} C_{p,i}^{ig} dT + \left[H_i\left(T,p\right) - H_i^{ig}\left(T,p\right)\right] \tag{7-15}$$

7.8 Specific Heat Capacity of H_2O

For H_2O, Aspen Plus^{TM} calculates CP through equations 7-1 and 7-2, but the heat of vaporization for H_2O is based on the Watson equation.

$$\Delta H_i\left(T\right) = \Delta H_i\left(T_1\right)\left(\frac{1-T/T_{ci}}{1-T_1/T_{ci}}\right)^{a_i+b_i\left(1-T/T_{ci}\right)} \tag{7-16}$$

where the Watson equation can estimate the heat of vaporization of a pure liquid component at any temperature from the known value at a single temperature $\left(\Delta H_i\left(T_1\right)\right)$. Table 7.8-1 gives the coefficients for the Watson heat of vaporization equation for H_2O in the elecNRTL model within Aspen Plus^{TM} based on equation 7-12.

Table 7.8-1. Watson Heat of Vaporization Default Coefficients for H_2O in the elecNRTL model from 0.05 – 373.95 °C [J/kmol].

Parameter	Symbol	Default value
DHVLWT-1	$\Delta H_1(T_1)$	40655000
DHVLWT -2	T_1	100.0
DHVLWT -3	a_i	0.3106
DHVLWT -4	b_i	0

Figure 7.8-1 illustrates the prediction of the heat of vaporization for H_2O from equation 7-12 within the elecNRTL model. Note, one of the deficiencies of a two parameter heat of vaporization model, vis-à-vis Watson equation, is apparent with the prediction of CP for H_2O as shown in Figure 7.8-2. Figure 7.8-2 demonstrates a known issue within the elecNRTL model where the liquid phase specific heat capacity of H_2O is calculated from the Watson heat of vaporization equation for CP and from the ASME Steam Table (1967) Equation-of-State for CPMX.

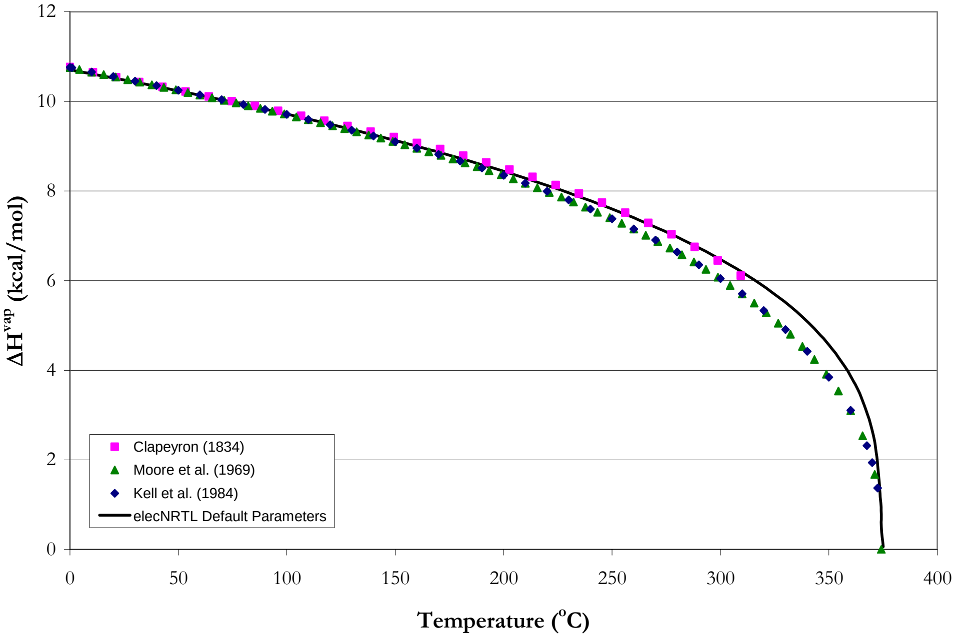

Figure 7.8-1. Predictions for the Watson Heat of Vaporization for H_2O from default values in the elecNRTL model.

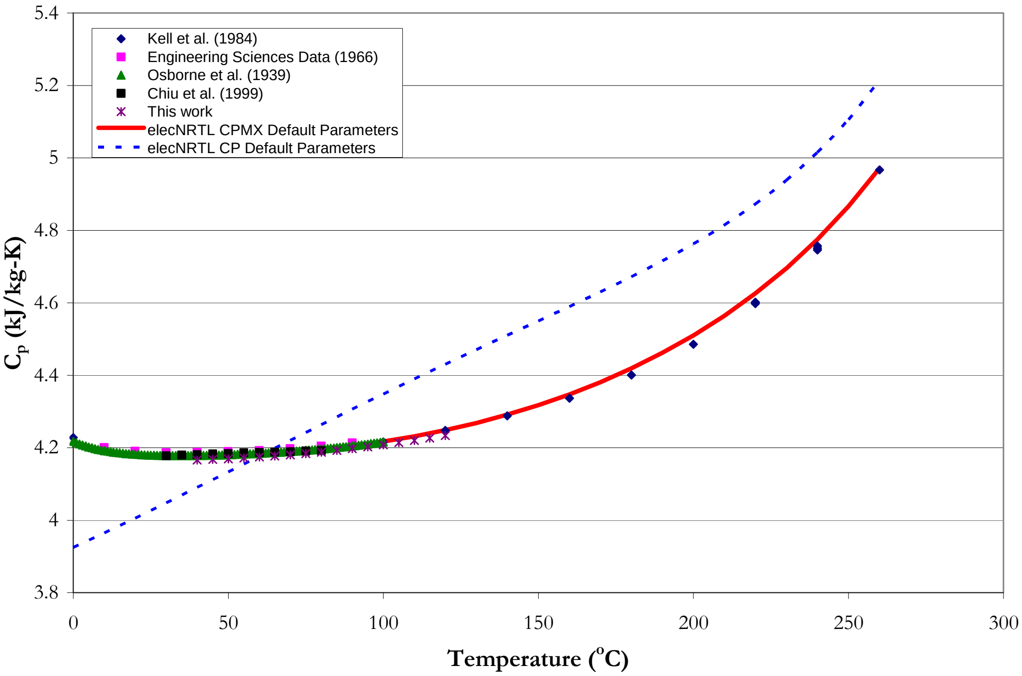

Figure 7.8-2. Predictions for CP and CPMX for H_2O from default values in the elecNRTL model.

Due to the large deviations between CP and CPMX for H_2O, we attempted to adjust the a and b terms of equation 7-12 implementing a similar procedure as described in section 7.4.2, but we were only able to improve the fit slightly as shown in Figure 7.8-3.

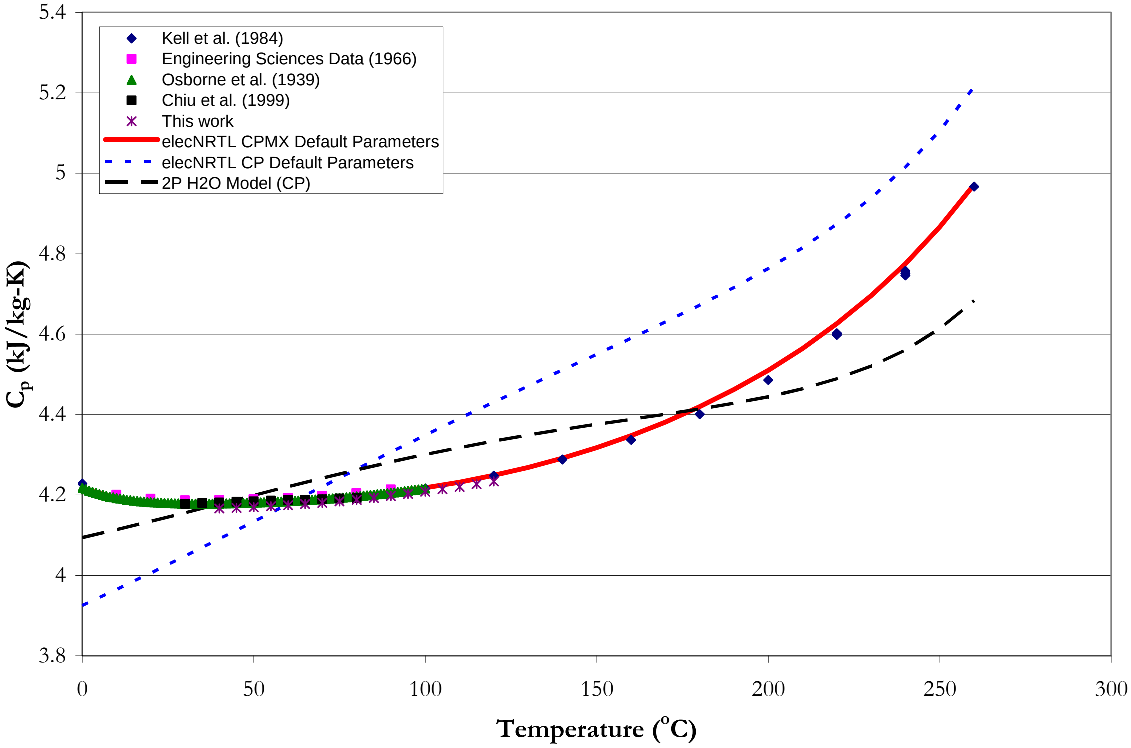

Figure 7.8-3. Comparison of elecNRTL Model Predictions (v3) with Experimental Data for the Specific Heat Capacity of H_2O from 0 – 260 °C.

Resulting in the following regression summary statistics output for estimates of the heat of vaporization coefficients as shown in Table 7.8-2.

Table 7.8-2. DRS Regression Output for 2P H_2O Model for CP.

Parameter	Estimate	σ wrt Estimate
DHVLWT -3	0.2662	0.0019
DHVLWT -4	0.0911	0.0036

Figure 7.8-4 compares estimated and experimental heat of vaporization based on parameters in Table 7.8-2 to literature data from Moore et al. (1969), Kell et al. (1984) and Clapeyron (1834) for H_2O from 0.01 to 373.95 °C. The two parameter (2P) model over predicts the heat of vaporization above 254.44 °C with a maximum error of 30.2 % at 348.98

°C. However, this error is well beyond the operating range of present carbon capture technology and is negligible overall since the full model is consistent with the critical temperature of H_2O (373.95 °C).

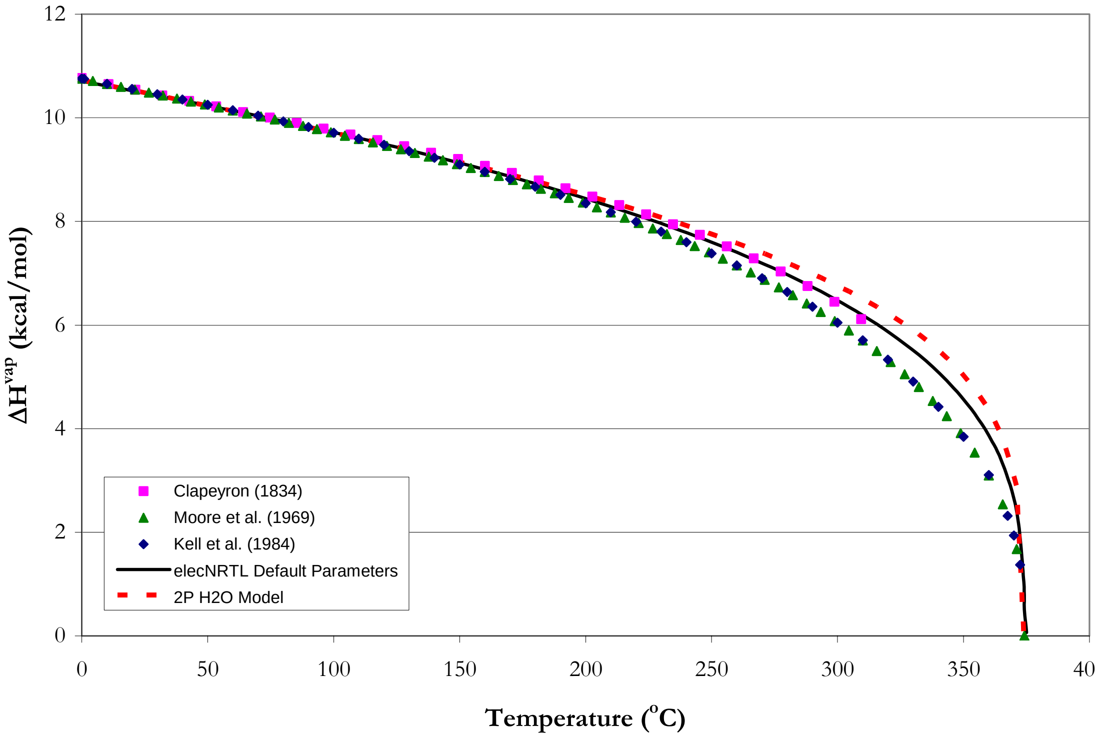

Figure 7.8-4. Comparison of Model Predictions (v3) with Experimental Data for the Heat of Vaporization of H_2O from 0.01 – 373.95 °C.

The above results attempted to improve upon the correlation for the specific heat capacity by adjusting the heat of vaporization of H_2O, but were unable to achieve satisfactory results as previously discussed in section 7.4.4. In solution mixtures, the elecNRTL model will use the ASME Steam Table (1967) Equation-of-State for H_2O in the calculation of CPMX and hence, the CP value will not affect future calculations, but we do not feel this to be a satisfactory solution. We will then recommend to AspenTech to change the calculation structure within the elecNRTL model to reflect the heat of vaporization of H_2O based on the DIPPR equation and results as described in section 7.4.2.

7.9 Specific Heat Capacity of MEA

Table 7.9-1 gives the coefficients for the Watson heat of vaporization equation for MEA in the elecNRTL model within Aspen Plus^{TM} based on equation 7-12.

Table 7.9-1. Watson Heat of Vaporization Default Coefficients for MEA in the elecNRTL model from 10.5 – 405.05 °C [J/kmol].

Parameter	Symbol	Default value
DHVLWT-1	$\Delta H_1(T_1)$	54835800
DHVLWT -2	T_1	126.67
DHVLWT -3	a_i	0.3288
DHVLWT -4	b_i	-0.0857

Figure 7.9-1 illustrates the prediction of the heat of vaporization for MEA from equation 7-12 within the elecNRTL model. Figure 7.9-1 demonstrates an issue between the NRTL and the elecNRTL model where the critical temperature of MEA reported in the elecNRTL model is from the work by Austgen (1989). The liquid phase specific heat capacity of MEA is calculated from the Watson heat of vaporization equation for CP and CPMX, but there is a 1 % deviation between CP and CPMX for temperatures above 120 °C as shown in Figure 7.9-2. Even though there is a minimum AARD of 5 % at 140 °C between predictions from the elecNRTL model and current literature data.

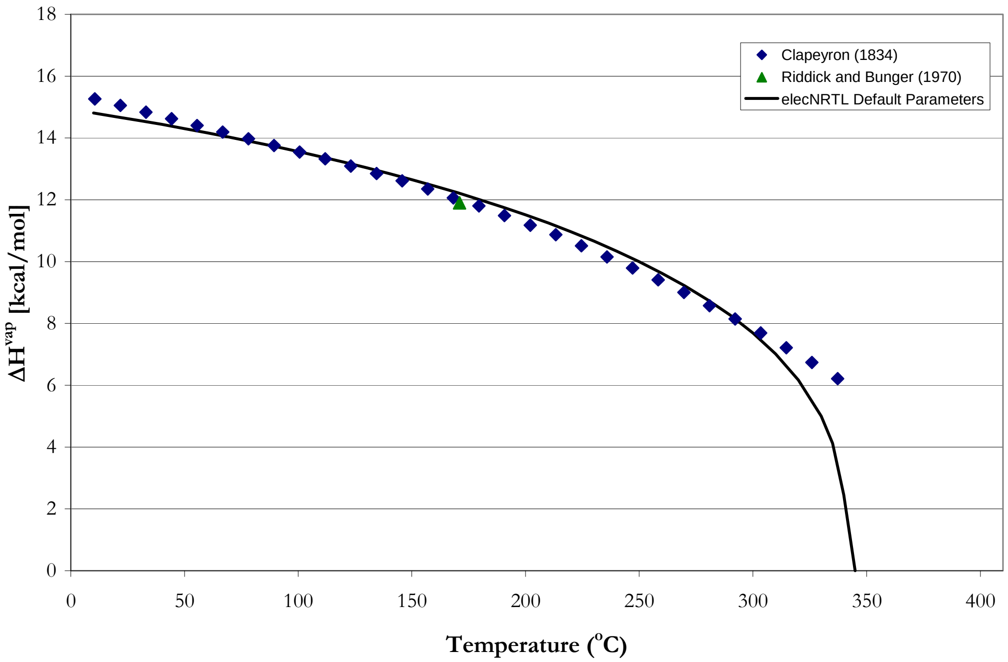

Figure 7.9-1. Predictions for the Watson Heat of Vaporization for MEA from default values in the elecNRTL model.

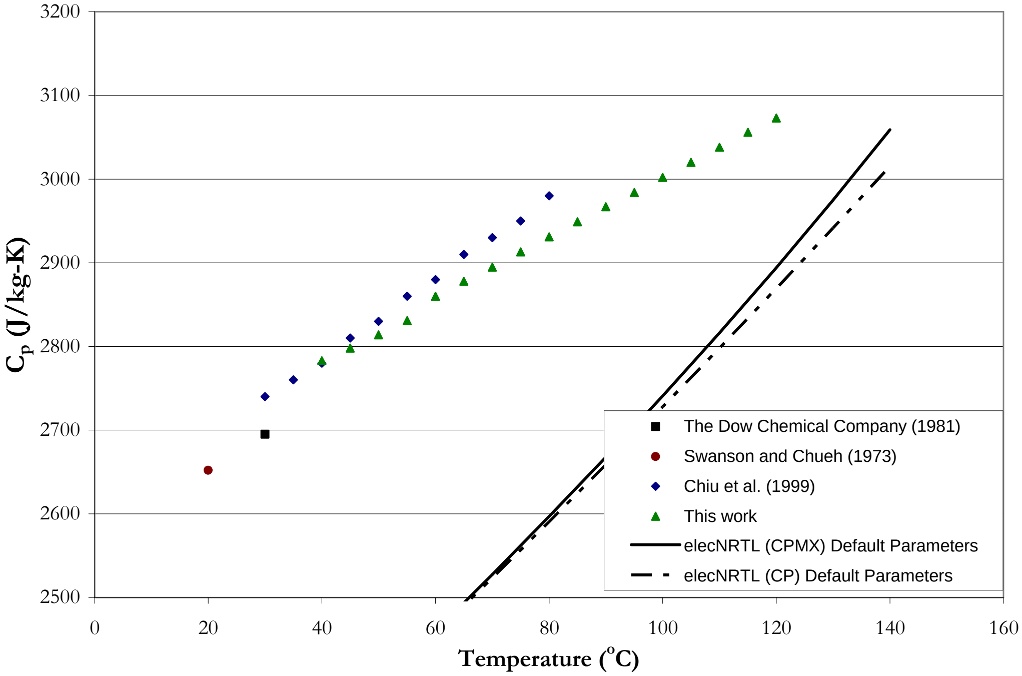

Figure 7.9-2. Predictions for CP and CPMX for MEA from default values in the elecNRTL model.

Due to the large deviations between predictions from the elecNRTL model and current literature data, we also regressed the a and b terms of equation 7-12 implementing a similar procedure as described in section 7.2.2, however in this case, we successfully matched the specific heat capacity for MEA (AARD = 0.6 %) as shown in Figure 7.9-3. Even though, the liquid phase specific heat capacity of MEA calculated from the regressed parameters of the Watson heat of vaporization equation displays approximately 1 % deviation between CP and CPMX for temperatures above 130 °C.

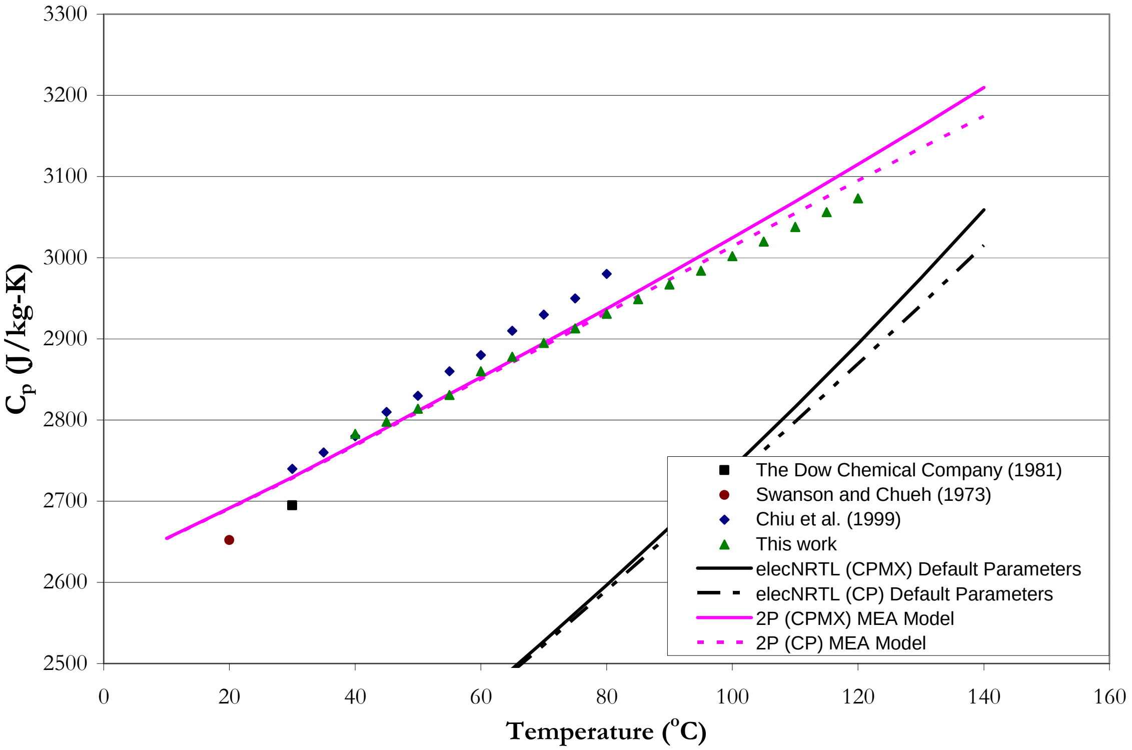

Figure 7.9-3. Comparison of elecNRTL Model Predictions (v4) with Experimental Data for the Specific Heat Capacity of MEA from 20 – 140 °C

Resulting in the following regression summary statistics output for estimates of the heat of vaporization coefficients as shown in Table 7.9-2.

Table 7.9-2. DRS Regression Output for 2P MEA Model for CP.

Parameter	Estimate	σ wrt Estimate
DHVLWT -3	0.4041	0.0077
DHVLWT -4	0.1101	0.0138

Figure 7.9-4 compares estimated and experimental heat of vaporization based on parameters in Table 7.9-2 to literature data from Riddick and Bunger (1970) and Clapeyron (1834) for MEA from 10.50 to 337.23 °C. The two parameter (2P) model over estimates the heat of vaporization above 213.30 °C with a maximum error of 15.0 % at 337.23 °C. However, this error is well beyond the operating range of present carbon capture technology and is negligible overall since the full model is now consistent with the critical temperature of MEA (405.05 °C).

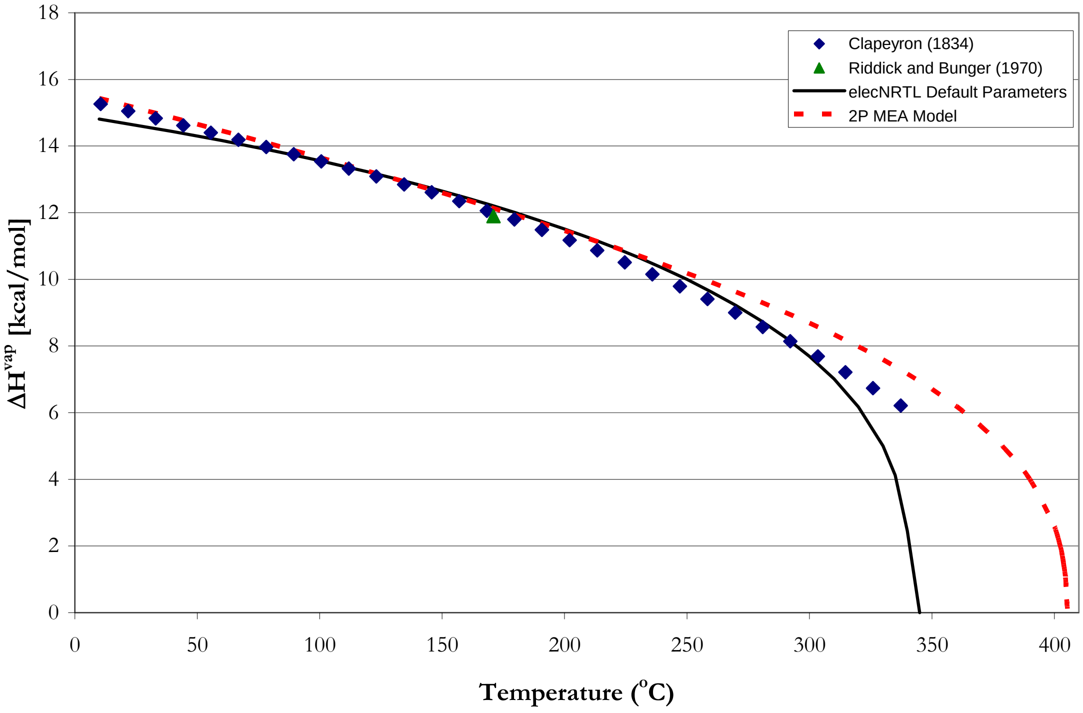

Figure 7.9-4. Comparison of Model Predictions (v4) with Experimental Data for the Heat of Vaporization of MEA from 10.5 – 405.05 °C.

The above results indicate an improvement upon the default elecNRTL parameters for the Watson heat of vaporization equation to predict the specific heat capacity of MEA. Critical properties in the elecNRTL model were adjusted to match correctly the critical temperature of MEA and to improve the heat of vaporization correlation between predicted values and current literature data.

7.10 Specific Heat Capacity of PZ

In section 7.3, we were able to illustrate that predictions for the liquid phase specific heat capacity of PZ could improve by adjusting the coefficients of the DIPPR heat of vaporization equation. In the elecNRTL model, Aspen Plus™ calculates the solid and liquid phase specific heat capacity by the same method as described in section 7.3, however, as shown in Figure 7.10-2, there is an AARD of ±2.58 % between predictions of CP and CPMX for the liquid phase specific heat capacity of PZ.

Due to deviations between the predictions from the elecNRTL model and current literature data, we regressed coefficients for the heat of vaporization of PZ implementing a similar procedure as described in section 7.3.3. In this case, we successfully matched the pure and mixture specific heat capacities for PZ (AARD = 0.0 and 0.0 %, respectively) as shown in Figures 7.10-3 and 7.10-4. Resulting in the following regression summary statistics output for estimates of the heat of vaporization coefficients as shown in Table 7.10-1.

Table 7.10-1. DRS Regression Output for 3P PZ Model for CP.

Parameter	Estimate	σ wrt Estimate
DHVLPD-1	64355423	263643
DHVLDP-2	0.3857	0.0107
DHVLDP-3	0.0257	0.0102

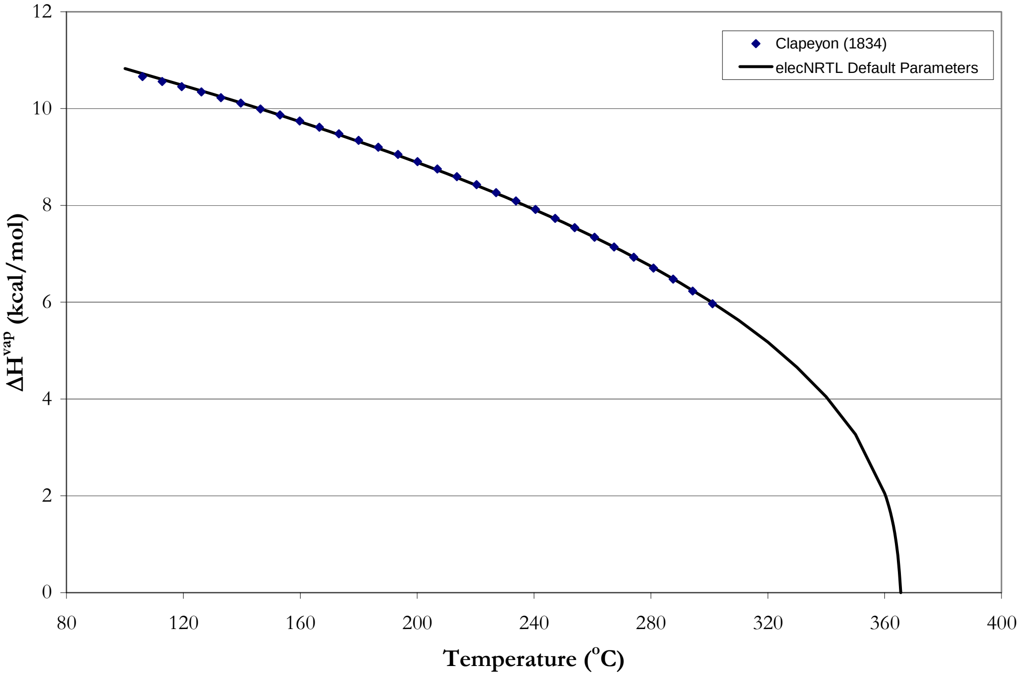

Figure 7.10-1. Comparison of elecNRTL Model Predictions with Experimental Data from Clapeyron (1834) for the Heat of Vaporization of PZ from 106 – 301.05 °C.

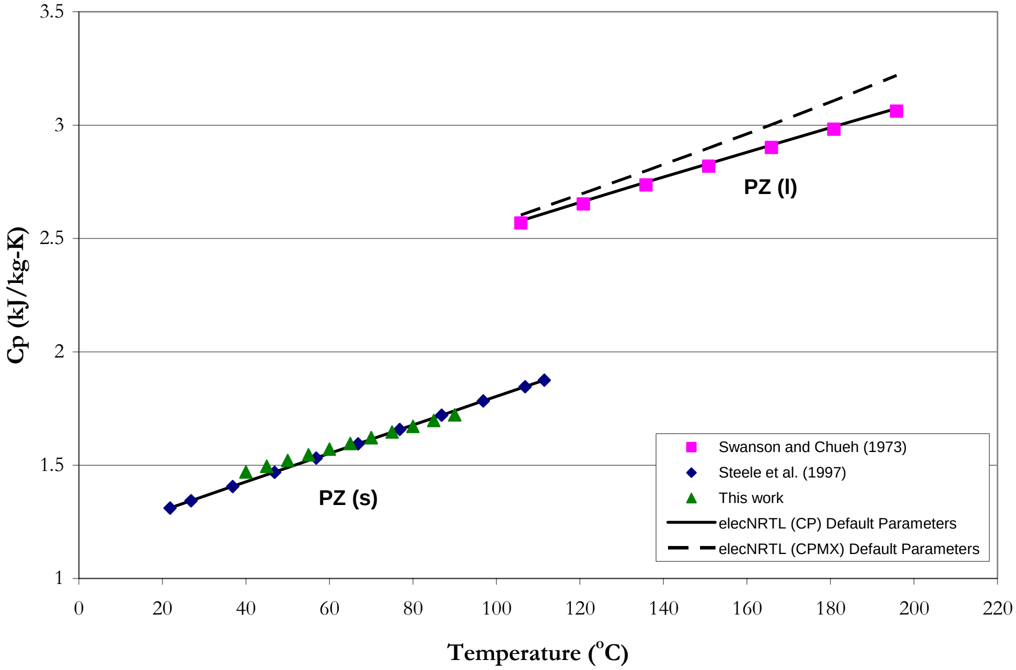

Figure 7.10-2. Comparison of elecNRTL model Predictions with Experimental Data for the Specific Heat Capacity of PZ from 20 to 200 °C.

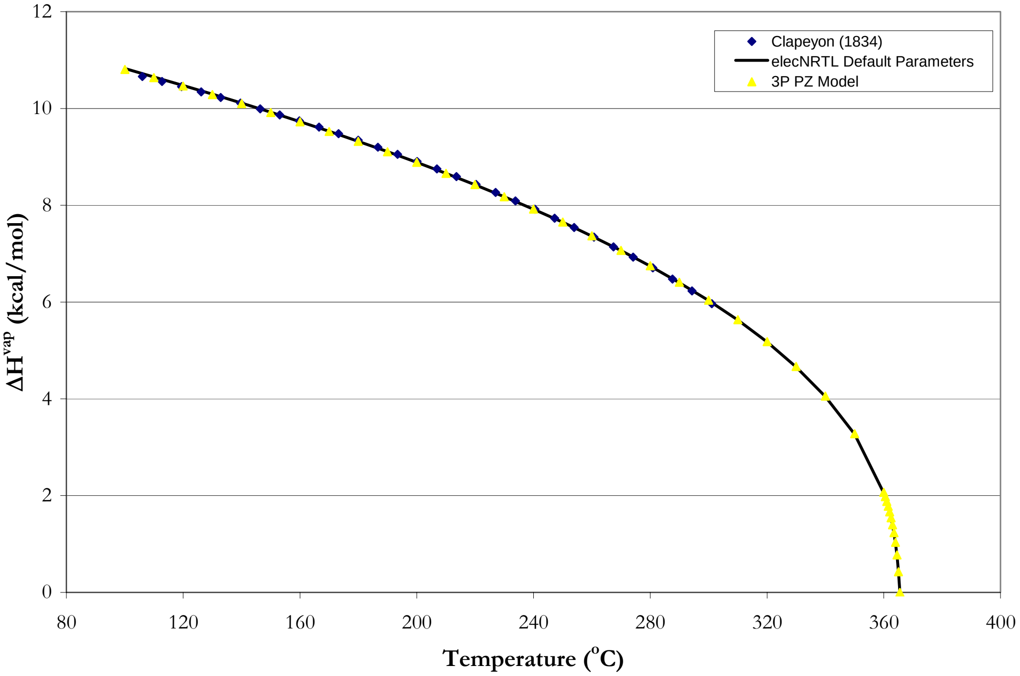

Figure 7.10-3. Comparison of Model Predictions (v2) with Experimental Data from Clapeyron (1834) for the Heat of Vaporization of PZ from 106 – 301.05 °C.

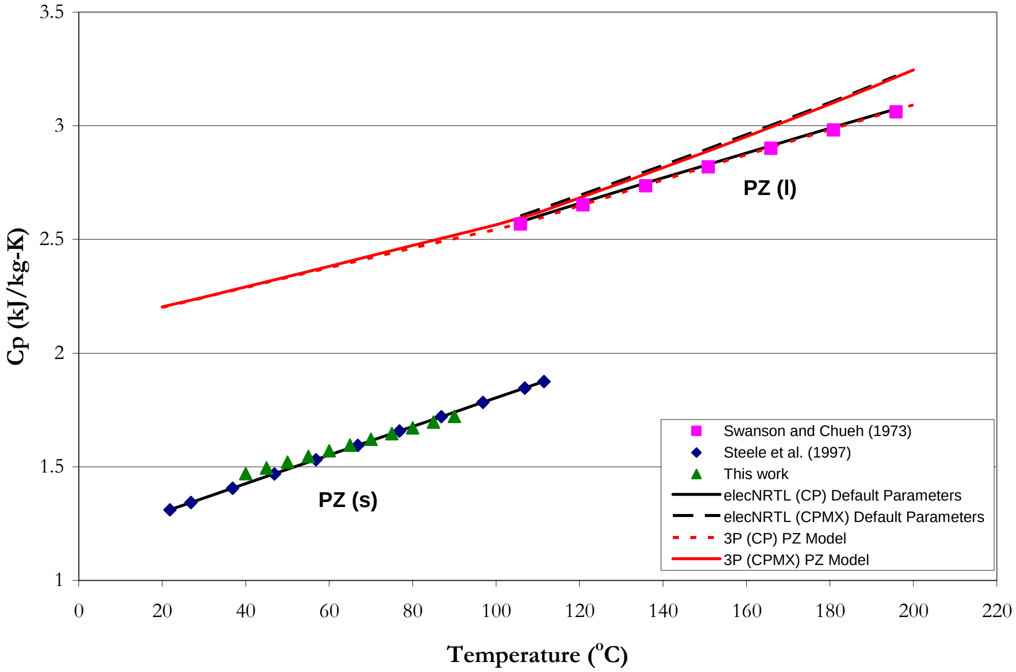

Figure 7.10-4. Comparison of elecNRTL Model Predictions (v2) with Experimental Data for the Specific Heat Capacity of PZ from 20 to 200 °C.

By adjusting the coefficients of the DIPPR heat of vaporization equation, we were unable to decrease the deviation between the prediction of CP and CPMX. As shown in Figure 7.10-4, there is an AARD of ±2.69 % between predictions of CPMX and Swanson and Chueh (1973) for the liquid phase specific heat capacity of PZ. Due to this relatively small error between CP and CPMX and the slight improvement for the prediction of the heat of vaporization based on the 3P PZ model, the above analysis is satisfactory given the lack of documentation from Aspen Plus^{TM} to describe the calculation methods of CP and CPMX for PZ. We will then recommend limiting predictions for the specific heat capacity of pure PZ to temperatures below 140 ^{o}C.

7.11 Abridged elecNRTL Predictive Correlations

To anticipate installation difficulties with the implementation of our model on future platforms, we have developed specific correlations based on predictive results from our rigorous thermodynamic model for the liquid phase specific heat capacity of H_2O, MEA, and PZ. We chose to relate the liquid phase specific heat capacity by the following relation:

$$C_{p,i}^{l,*}\left(\frac{kJ}{kg\cdot K}\right)=C_{1i}+C_{2i}T+C_{3i}T^2+C_{4i}T^3+C_{5i}T^4 \qquad 7\text{-}17$$

Where
$C_{p,i}^{l,*}$ is the predictive liquid phase specific heat capacity for component i,
T is the temperature, ^{o}C.

In this case of H_2O, we successfully matched the liquid phase specific heat capacity (CPMX) (AARD = 0.04 %) as shown in Figure 7.11-1. Resulting in the following regression

summary statistics output for estimates of the abridged model correlation coefficients as shown in Table 7.11-1.

Table 7.11-1. DRS Regression Output for the Abridged Model Correlation for H_2O.

Parameter	Estimate	σ wrt Estimate
C_1	4.2107	0.0020
C_2	-1.696E-03	1.0874E-04
C_3	2.568E-05	1.7486E-06
C_4	-1.095E-07	1.0198E-08
C_5	3.038E-10	1.9449E-11

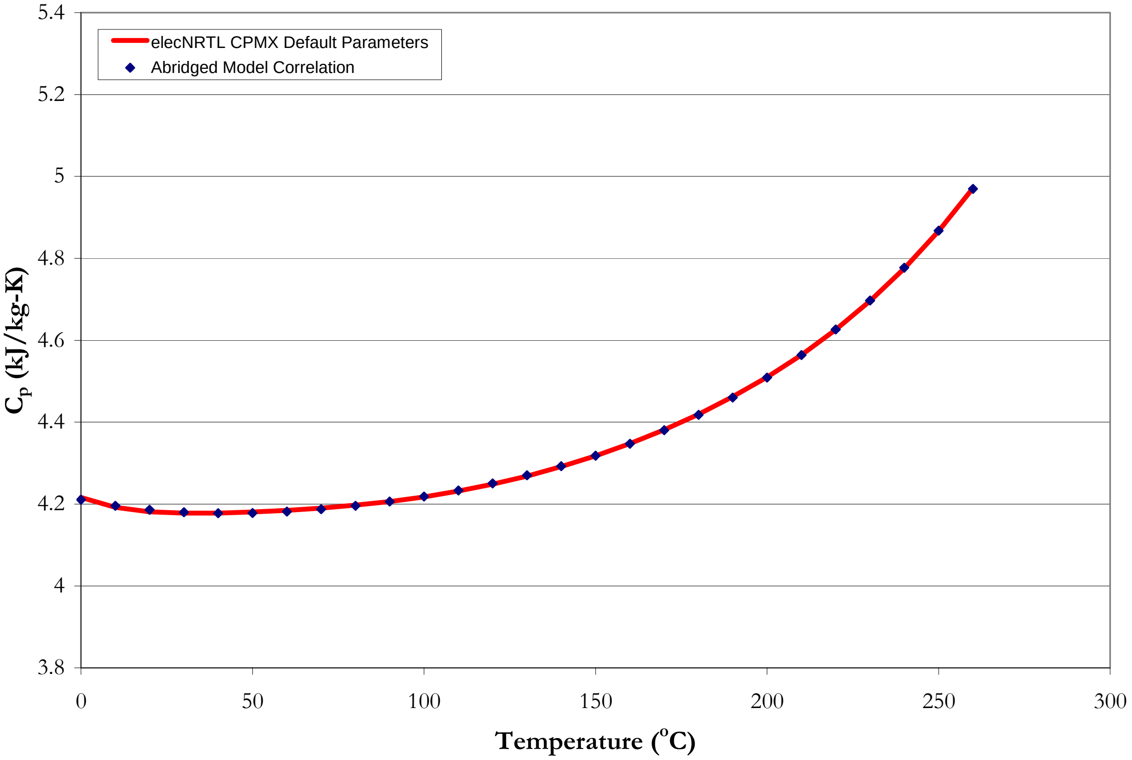

Figure 7.11-1. Comparison of elecNRTL model Predictions with the Abridged Model Correlation for the Specific Heat Capacity of H_2O from 0 to 260 °C.

For MEA, we successfully matched the liquid phase specific heat capacity (CPMX) (AARD = 0.02 %) as shown in Figure 7.11-2. Resulting in the following regression

summary statistics output for estimates of the abridged model correlation coefficients as shown in Table 7.11-2.

Table 7.11-2. DRS Regression Output for the Abridged Model Correlation for MEA.

Parameter	Estimate	σ wrt Estimate
C_1	2.6161	0.0006
C_2	3.706E-03	1.8487E-05
C_3	3.787E-06	1.1989E-07
C_4	0.0	-
C_5	0.0	-

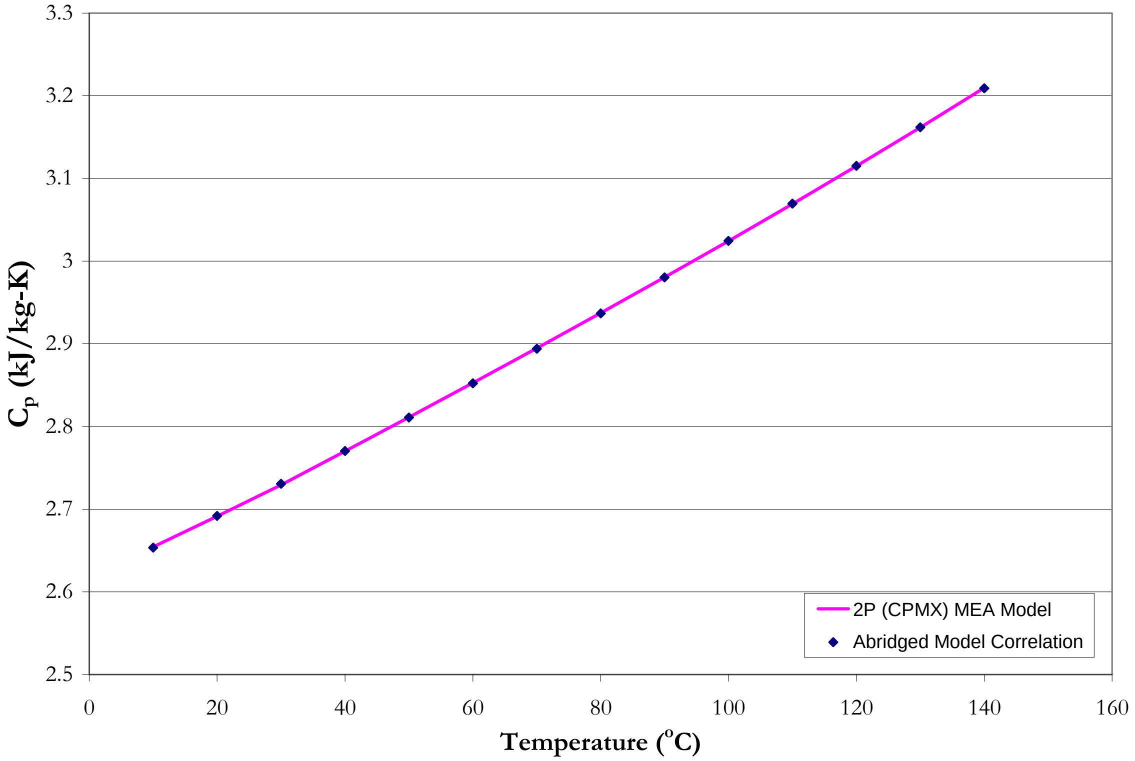

Figure 7.11-2. Comparison of elecNRTL model Predictions with the Abridged Model Correlation for the Specific Heat Capacity of MEA from 10 to 140 °C.

In this case of PZ, we successfully matched the liquid phase specific heat capacity (CPMX) (AARD = 0.23 %) as shown in Figure 7.11-3. Resulting in the following regression

summary statistics output for estimates of the abridged model correlation coefficients as shown in Table 7.11-3.

Table 7.11-3. DRS Regression Output for the Abridged Model Correlation for PZ.

Parameter	Estimate	σ wrt Estimate
C_1	2.1470	0.0061
C_2	3.038E-03	1.2548E-04
C_3	1.234E-05	5.5684E-07
C_4	0.0	-
C_5	0.0	-

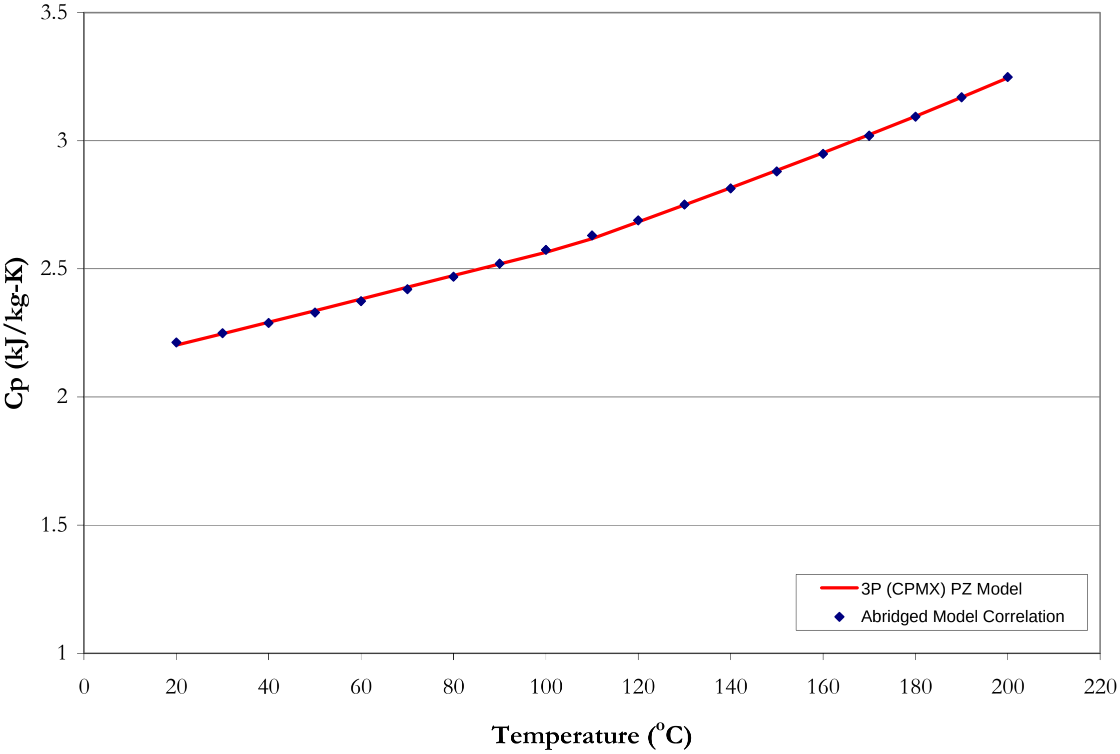

Figure 7.11-3. Comparison of elecNRTL model Predictions with the Abridged Model Correlation for the Specific Heat Capacity of PZ from 20 to 200 °C.

7.12 elecNRTL Conclusions

With reference to H_2O, the above results attempted to improve upon the correlation for the specific heat capacity by adjusting the heat of vaporization of H_2O, but were unable to achieve satisfactory results as previously discussed in section 7.4.4. In solution mixtures, the elecNRTL model will use the ASME Steam Table (1967) Equation-of-State for H_2O in the calculation of CPMX and hence, the CP value will not affect future calculations, but we do not feel this to be a satisfactory solution. We will then recommend to AspenTech to change the calculation structure within the elecNRTL model to reflect the heat of vaporization of H_2O based on the DIPPR equation and results as described in section 7.4.2.

With reference to MEA, the above results indicate an improvement upon the default elecNRTL parameters for the Watson heat of vaporization equation to predict the specific heat capacity of MEA. Critical properties in the elecNRTL model were adjusted to correctly match the critical temperature of MEA and to improve the heat of vaporization correlation between predicted values and current literature data.

With reference to PZ, we were unable to decrease the deviation between the prediction of CP and CPMX by adjusting the coefficients of the DIPPR heat of vaporization equation. As shown in Figure 7.10-4, there is an AARD of ±2.69 % between predictions of CPMX and Swanson and Chueh (1973) for the liquid phase specific heat capacity of PZ. Due to this relatively small error between CP and CPMX and the slight improvement for the prediction of the heat of vaporization based on the 3P PZ model, the above analysis is satisfactory given the lack of documentation from Aspen Plus^{TM} to describe the calculation methods of CP and CPMX for PZ. We will then recommend to limit predictions for the specific heat capacity of pure PZ to temperatures below 140 °C.

Using an abridged model correlation, we were successful in matching the liquid phase specific heat capacity for H_2O, MEA, and PZ over the respective temperature ranges for each component.

Overall, results presented above indicate that the elecNRTL model, through simultaneous regression gave a set of heat of vaporization coefficients to describe liquid phase specific heat capacity for MEA, PZ, and H_2O. In addition, the model adequately represents the solid phase specific heat capacity for pure PZ as compared to the NRTL model and current literature data.

CHAPTER VIII

Binary Systems: H_2O-MEA

8.1 Introduction

We continue the thermodynamic model development by describing the molecule-molecule interactions between water and monoethanolamine. Interactions between water and piperazine will be addressed in Chapter IX. This chapter describes the data regression and model predictions for the H_2O-Monoethanolamine (MEA) system based on previous literature data and experimental results from this work. The results for the binary interaction parameters for the electrolyte-NRTL (elecNRTL) model in Aspen Plus^{TM} are then presented; showing good statistical fit to the literature data with an average absolute relative error of ± 2.62 % with the exception of a few outliers.

8.2 H_2O-MEA System

Recall from Chapter VI that as the concentration of ions in an electrolyte solution approaches zero, the elecNRTL model reduces in theory to the NRTL Model of Renon and Prausnitz (1968). As shown in Chapter VII, the calculation routes for physical properties between the NRTL and the elecNRTL property models are different. In this section, we present background on the NRTL model for clarification purposes only since we will be using the elecNRTL property model for all future chapters to describe molecular and ionic interactions.

The NRTL model is an excess Gibbs energy model given by the following form for a binary system:

$$\frac{G^{ex}}{RT} = x_1 x_2 \left(\frac{\tau_{21} G_{21}}{x_1 + x_2 G_{21}} + \frac{\tau_{12} G_{12}}{x_2 + x_1 G_{12}} \right) \qquad \text{8-1}$$

Where
i is the species index, 1: H_2O and 2: MEA,
j is the species index, 1: H_2O and 2: MEA,
x_i is the liquid mole fraction of component i,
τ_{ij} is the binary interaction parameter between component i and j,
α_{ij} is the molecule-molecule nonrandomness factor, 0.2,
$G_{12} = e^{-\alpha_{12}\tau_{12}}$,
$G_{21} = e^{-\alpha_{21}\tau_{21}}$.

The molecule-molecule binary interaction parameters were assumed to be temperature dependent and were fitted to the following function of temperature:

$$\tau_{12} = A_{12} + \frac{B_{12}}{T} + C_{12}\ln(T) + D_{12}T \qquad \text{8-2}$$

$$\tau_{21} = A_{21} + \frac{B_{21}}{T} + C_{21}\ln(T) + D_{21}T \tag{8-3}$$

Taking the appropriate derivative of Equation 8-1, an expression for the activity coefficient of MEA can then be derived from thermodynamic relationships.

$$\ln\gamma_i = \left[\frac{\delta\left(nG^{ex}/RT\right)}{\delta n_i}\right] \tag{8-4}$$

$$\ln\gamma_2 = x_1^2\left[\tau_{12}\left(\frac{G_{12}}{x_2 + x_1G_{12}}\right)^2 + \frac{\tau_{21}G_{21}}{\left(x_1 + x_2G_{21}\right)^2}\right] \tag{8-5}$$

By taking the limit as the mole fraction of MEA$\left(x_2\right)$ approaches zero, we get an explicit form of Equation 8-5 for the infinite dilution activity coefficient of MEA as given below:

$$\ln\gamma_2^{\infty} = \tau_{12} + \tau_{21}e^{-\alpha_{12}\tau_{21}} \tag{8-6}$$

Where
γ_2^{∞} is the infinite dilution activity coefficient for monoethanolamine.

From Equation 8-6, we can see how excess Gibbs energy and activity coefficients are related through model parameters. The creation of the H_2O-MEA model begins with the regression of literature data. Twelve data sets have been regressed with the elecNRTL model to represent the phase equilibrium of a single solvent system through regression of total vapor pressure [Nath and Bender (1983) and Touhara et al. (1982)], vapor-liquid equilibrium [Park and Lee (1997), Tochigi et al. (1999), Cai et al. (1996), and from this work], specific heat capacity [Pagé et al. (1993), Chiu and Li (1999), Weiland et al. (1997), and from this work], and freezing point depression [Chang et al. (1993)] data over monoethanolamine solutions. The elecNRTL model was never designed to regress excess enthalpy data thus we will reserve literature data from Touhara et al. (1982) and Posey (1996) until a comparison can be made from predictions based on an optimum set of binary interaction parameters. For more information, please refer to Section 8.4.5.

The following stoichiometric chemical equilibrium expression (Equation 8-7) for the dissociation of monoethanolamine is given below:

$$MEAH^{+} \leftrightarrow MEA(l) + H^{+} \tag{8-7}$$

Equation 8-7 describes the dissociation of protonated monoethanolamine $\left(MEAH^{+}\right)$ ion to aqueous monoethanolamine and proton $\left(H^{+}\right)$ ion. The chemical equilibrium constant for the above reaction was determined analytically from pKa data reported by Bates and Pinching (1951) and corrected, based on the optimum binary interaction model parameters, for the symmetric reference state for the activity coefficient of monoethanolamine from infinite dilution in water to infinite dilution in amine solvent. We were then able to determine the following standard state properties: the infinite dilution aqueous phase free energy of formation $\left(\Delta G_f^{\infty,aq}\right)$ and the infinite dilution aqueous phase enthalpy of formation $\left(\Delta H_f^{\infty,aq}\right)$ for protonated monoethanolamine.

The following section describes the different types of data used in the creation of the binary H_2O-MEA elecNRTL model.

8.2.1 *Total Vapor Pressure*

Data in the form of total vapor pressure from aqueous monoethanolamine solutions as a function of concentration and temperature was used to adjust the activity coefficients of monoethanolamine and water through the simultaneous regression of the binary interaction parameters in the elecNRTL model. For the binary system, the following equation can be used to represent the equilibrium for the total vapor pressure data.

$$P = x_{MEA}\gamma_{MEA}P_{MEA}^{0} + x_{H_2O}\gamma_{H_2O}P_{H_2O}^{0} \qquad 8\text{-}8$$

Where
P is the total pressure of the system,
x_i is the apparent mole fraction of component i,
γ_i is the symmetric activity coefficient of component i,
P_i^0 is the Extended Antoine pure vapor pressure of component i.

Note, total vapor pressure data does not allow for the direct calculation of individual component activity coefficients or extrapolation to infinite dilution. Therefore, activity coefficients regressed from total pressure data cannot be accurately determined. An example of the experimental total vapor pressure data used in this work by Nath and Bender (1983) and Touhara et al. (1982) from 333 – 393 K at 2 m PZ and from 353 – 393 K at 4 m PZ are shown in Figures 8.2-1 and 8.2-2, respectively.

8.2.2 *Vapor-Liquid Equilibrium*

Data in the form of vapor-liquid equilibrium (VLE), which measures the vapor and liquid compositions in aqueous monoethanolamine solutions, as a function of concentration and temperature were also used to adjust the activity coefficients of monoethanolamine and water through the simultaneous regression of the binary interaction parameters in the NRTL model. For the binary system, Equation 8-9 can be used to represent the vapor-liquid equilibrium data.

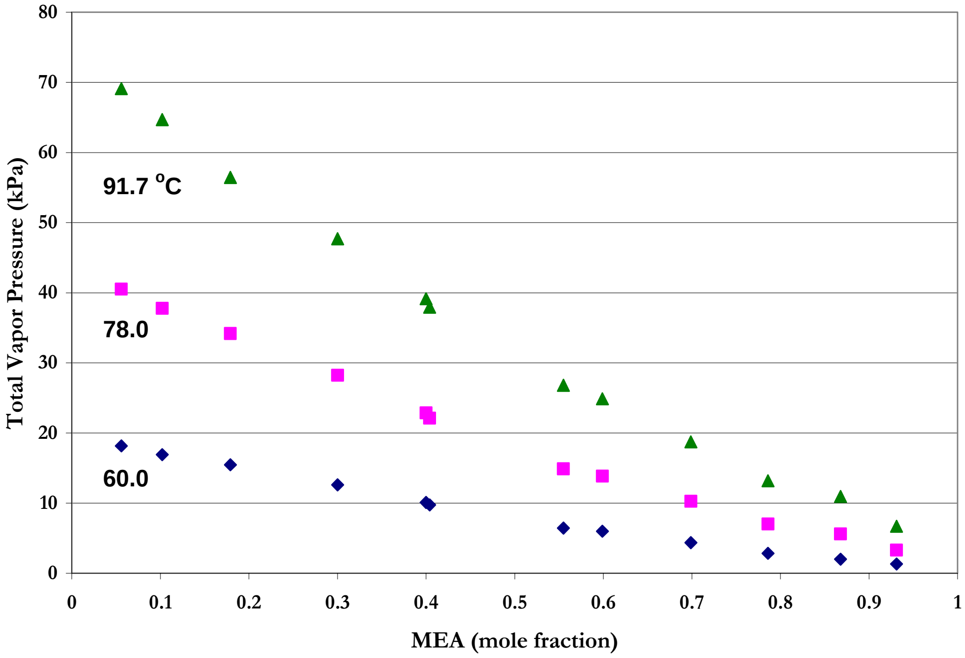

Figure 8.2-1. Total Vapor Pressure at 60, 78, and 91.7 °C. Points: Nath and Bender (1983).

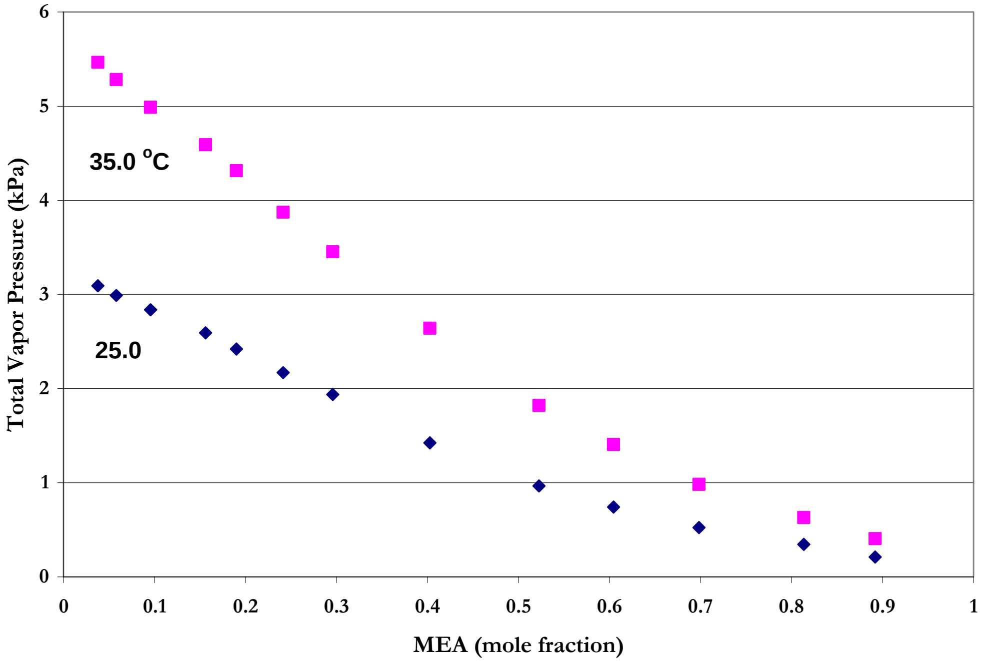

Figure 8.2-2. Total Vapor Pressure at 25.0 and 35.0 °C. Points: Touhara et al. (1982).

$$y_i P = x_i \gamma_i P_i^0 \qquad \text{8-9}$$

Where

y_i is the vapor mole fraction of component i,

P is the total pressure of the system,

x_i is the liquid mole fraction of component i,

γ_i is the symmetric activity coefficient of component i,

P_i^0 is the Extended Antoine pure vapor pressure of component i.

Examples of experimental isobaric vapor-liquid equilibrium used in this work from Park and Lee (1997) and Cai et al. (1996) are shown in Figure 8.2-3 and for isothermal vapor-liquid equilibrium from Tochigi et al. (1999) in Figure 8.2-4. As previously shown in Chapter II, amine volatility from this work between 3.5 and 23.8 m MEA is presented in Figure 8.2-5. Please note: we did not include the measured vapor pressure of H_2O data as part of this work within experimental database given in Table 8.3-1.

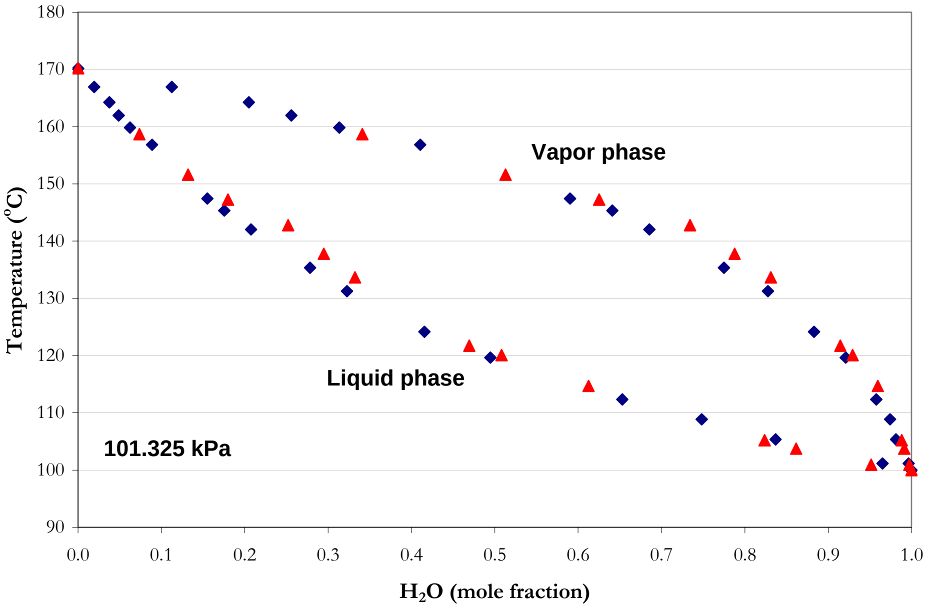

Figure 8.2-3. Isobaric VLE at 101.325 kPa. Points: ◆, Park and Lee (1997) and ▲, Cai et al. (1996).

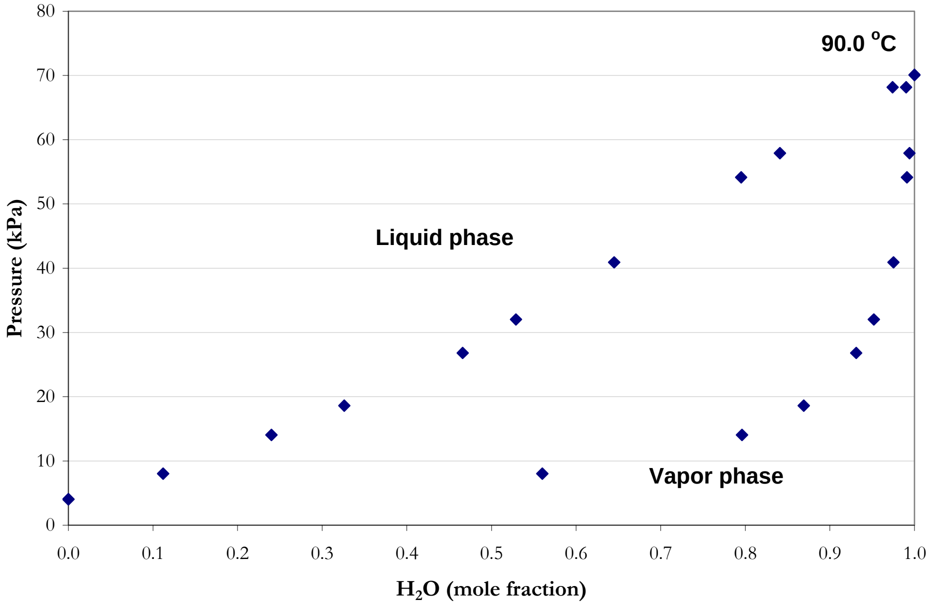

Figure 8.2-4. Isothermal VLE at 90.0 °C. Points: ◆,Tochigi et al. (1999).

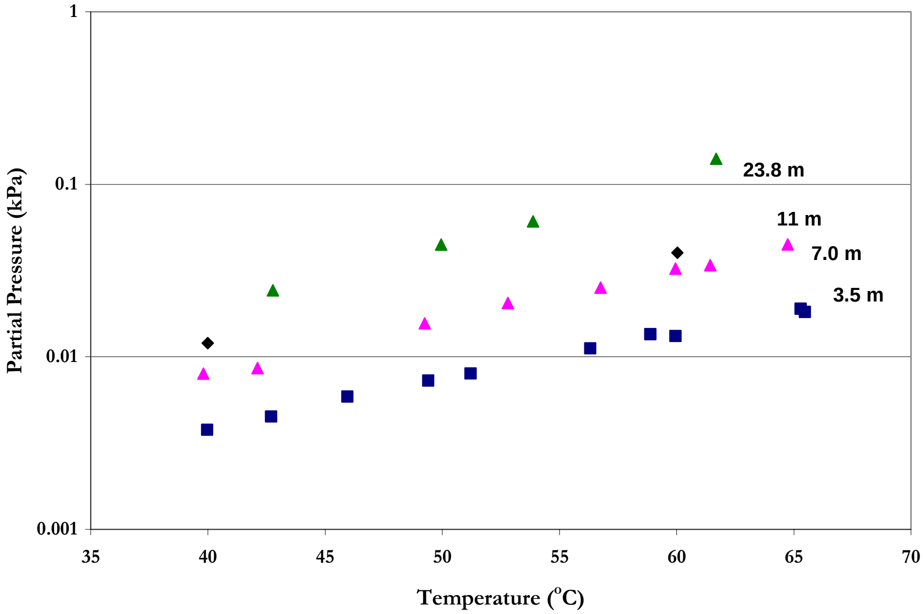

Figure 8.2-5. Amine Volatility for 3.5, 7, 11, and 23.8 m MEA from this work.

8.2.3 *Specific Heat Capacity*

As stated in Chapter VI, Aspen Plus^{TM} calculates the liquid phase heat capacity of a *mixture* (CPMX) by taking the derivative of the liquid enthalpy at constant pressure:

$$H_i^l\left(T+\Delta T\right)-H_i^l\left(T\right)=\int_T^{T+\Delta T} C_{p,i}^l dT \qquad \text{8-10}$$

where the liquid enthalpy of a mixture is calculated by the following equation:

$$H_i^l\left(T\right)=\sum_i x_i H_i + H_i^E \qquad \text{8-11}$$

$$H_i\left(T\right)=\Delta H_f^{ig}\left(T^{ref}\right)+\int_{T^{ref}}^{T} C_p^{ig} dT+\left[H_i\left(T,p\right)-H_i^{ig}\left(T,p\right)\right] \qquad \text{8-12}$$

Where
ΔT is the perturbation in temperature from *T*,
H_i^E is the excess enthalpy of component i,
$\Delta H_f^{ig}\left(T^{ref}\right)$ is the standard enthalpy of formation of component i at T^{ref},
T^{ref} is the reference temperature, 25.0 °C,
C_p^{ig} is the ideal gas heat capacity of component i,
H_i^{ig} is the ideal gas enthalpy of component i.

Data in the form of specific heat capacity of a mixture as a function of concentration and temperature were used to adjust the activity coefficients of monoethanolamine and water through the simultaneous regression of the binary interaction parameters by taking the derivative of the NRTL model, vis-à-vis excess enthalpy. Thus, specific heat capacity effects are limited only to the second and third terms of Equations 8-2 and 8-3. Examples of experimental specific heat capacity used in this work are from: Pagé et al. (1993) and Weiland et al. (1997) at 25 °C, Pagé et al. (1993), Chiu and Li (1999), and from this work at

40 °C, and from Chiu and Li (1999) and from this work at 60 °C, as shown in Figures 8.2-6, 8.2-7, and 8.2-8, respectively.

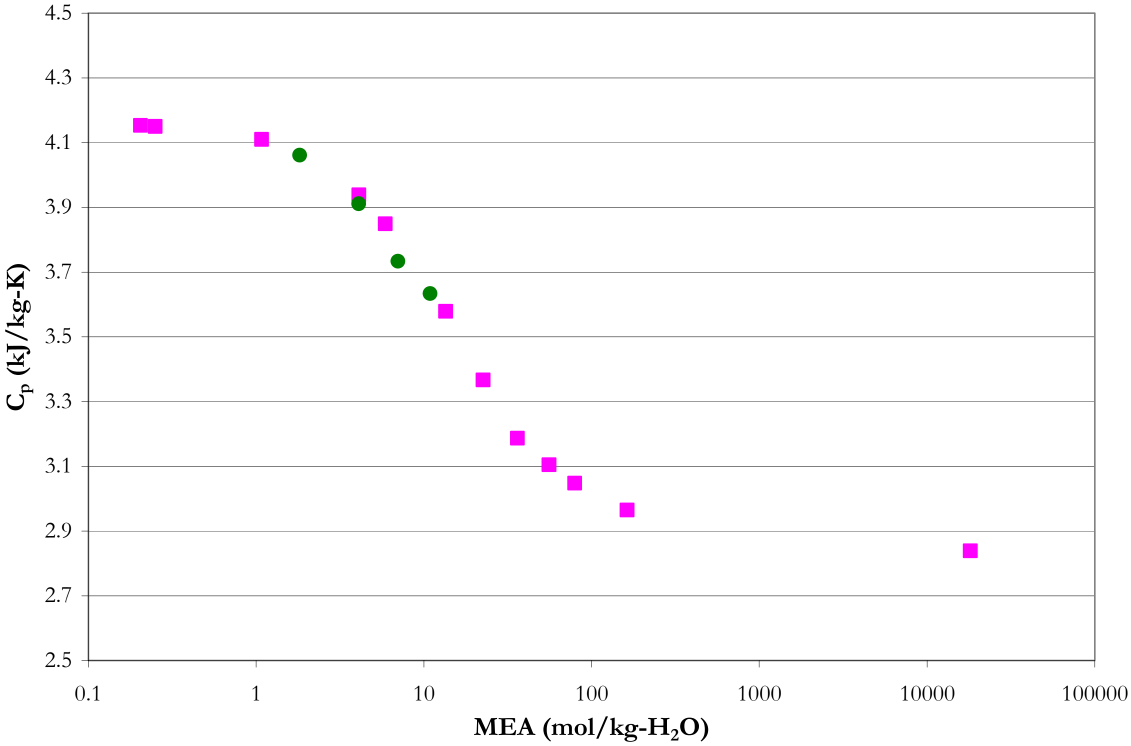

Figure 8.2-6. Specific Heat Capacity at 25.0 °C. Points: ■, Pagé et al. (1993) and ●, Weiland et al. (1997).

8.2.4 *Excess Enthalpy*

Prausnitz et al. (1999) noted that the behavior of a real binary mixture is frequently described using excess properties. In the electrolyte-NRTL model, one of the main goals is the ability to describe the excess Gibbs energy of a system, including temperature derivatives, to accurately represent deviations from ideal solution behavior. In this case, the excess enthalpy of mixing is referred to more commonly as the heat of mixing through Equation 8-13.

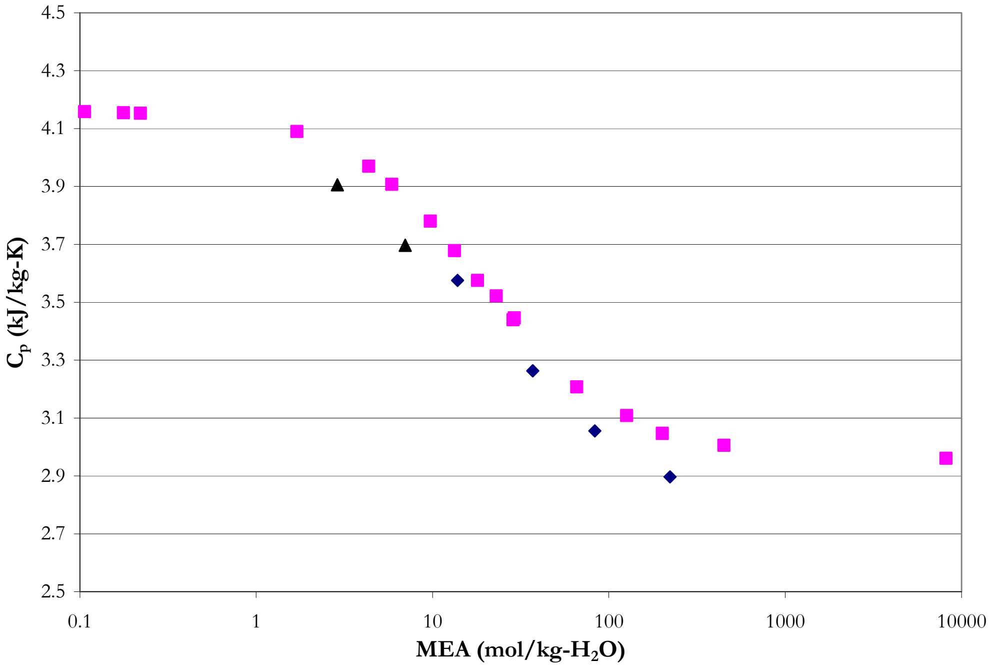

Figure 8.2-7. Specific Heat Capacity at 40.0 °C. Points: ■, Pagé et al. (1993), ♦, Chiu and Li (1999), and ▲, this work.

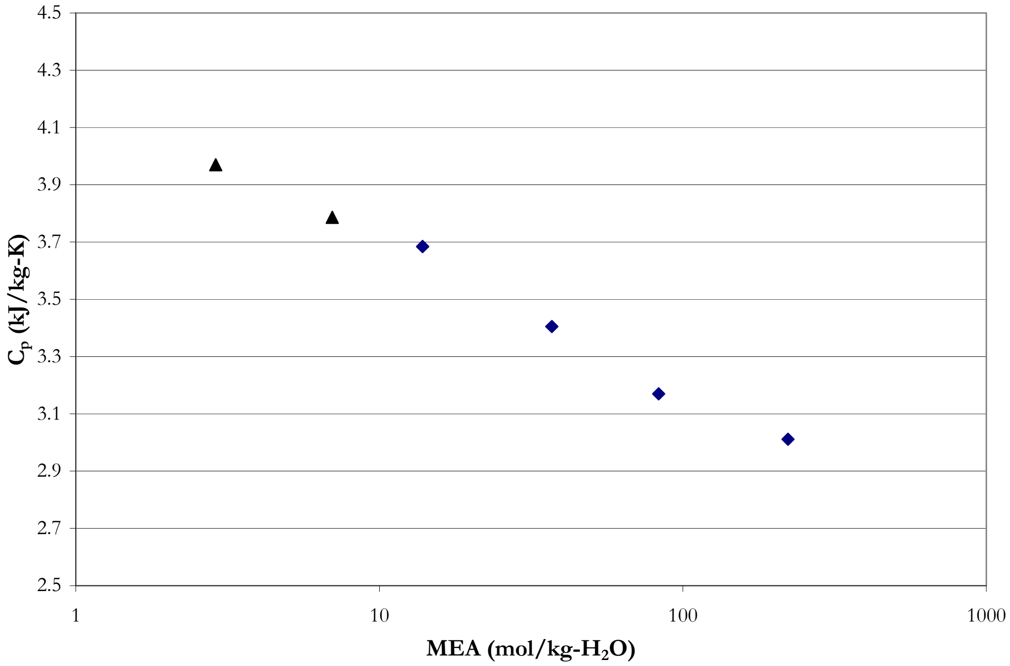

Figure 8.2-8. Specific Heat Capacity at 60.0 °C. Points: ♦, Chiu and Li (1999) and ▲, this work.

$$-\frac{H_i^E}{RT^2} = \left(\frac{\partial G_i^E / RT}{\partial T} \right)_{P,x_i} \qquad 8\text{-}13$$

By apply the partial molar property to Equation 8-13, an expression describing the relationship between the temperature dependence of the activity coefficient and the excess Gibbs energy is given by Equation 8-14.

$$\left(\frac{\partial \ln \gamma_i}{\partial T} \right)_{P,x} = -\frac{H_i^E}{RT^2} \qquad 8\text{-}14$$

For a binary mixture, the molar excess enthalpy can be described by the following expression:

$$H_m^{E,l} = -RT^2 \sum_i x_i \left(\frac{\partial \ln \gamma_i}{\partial T} \right) \qquad 8\text{-}15$$

Where

$H_m^{E,l}$ is the liquid molar excess enthalpy of the mixture,

x_i is the mole fraction of component i,

γ_i is the symmetric activity coefficient of component i.

An example of experimental excess enthalpy data from Touhara et al. (1982) and Posey (1996) at 25 and 70 °C is shown in Figure 8.2-9.

8.2.5 *Freezing Point Depression*

Freezing point depression of aqueous MEA mixtures from Chang et al. (1993) were transformed to represent the partial pressure of water, P^{H_2O}. Harned and Owen (1950) related the activity of water to the freezing point depression of water through Equation 8-16.

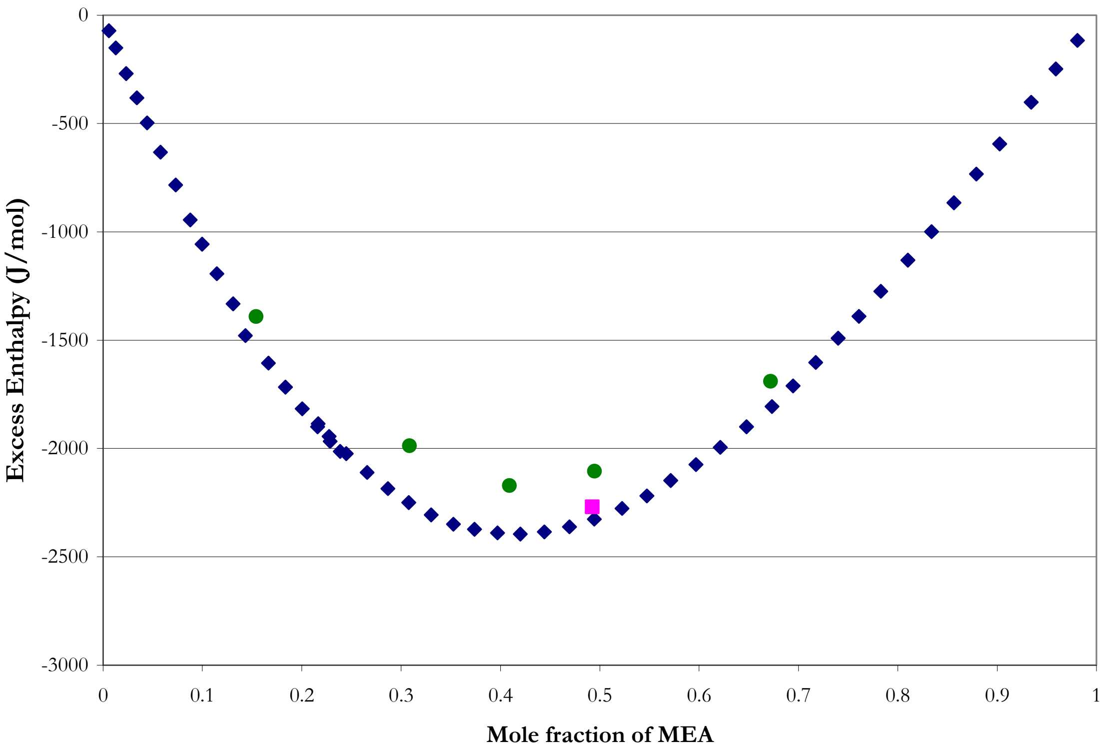

Figure 8.2-9. Excess Enthalpy at 25.0 and 70.0 °C. Points: ◆, Touhara et al. (1982), ■, Posey (1996) at 25 °C, and ●,Posey (1996) at 75 °C.

$$-\ln(a_w) = \Delta T_f \left(\frac{\Delta H_f}{R \cdot T_o^2}\right) + \frac{\Delta T_f^2}{T_o^2}\left(\frac{\Delta H_f}{R \cdot T_o} - \frac{\Delta C_p}{2 \cdot R}\right) \tag{8-16}$$

simplifying and substituting Equation 8-16 into Equation 8-9, an expression for the partial pressure of water as a function of the freezing point depression vis-à-vis activity of water, is given below

$$P_{H_2O} = \exp\left(\frac{-0.018 \cdot \Delta T_f}{1.858}\right) P_{H_2O}^o \tag{8-17}$$

Where

a_w is the activity of water,

R is the universal gas constant, 8.314 J/mole-K,

T_o is the melting point of ice, 0.0 °C,
ΔT_f is the freezing point depression, $T_o - T_f$,
T_f is the mixture freezing point, °C,
ΔH_f is the heat of fusion of water, -6.008 kJ/mole,
ΔC_p is the heat capacity difference between water and ice, 37.6 J/mole-K.

Freezing point depression in the form of vapor pressure of water, as a function of molality and temperature, was used to adjust the activity coefficient of water for the H_2O-MEA system through the simultaneous regression of the binary interaction parameters in the electrolyte NRTL model.

An example of the vapor pressure of water based on Equation 8-17 from literature of Chang et al. (1993) is shown in Figure 8.2-10 from -20.0 to -5.0 °C.

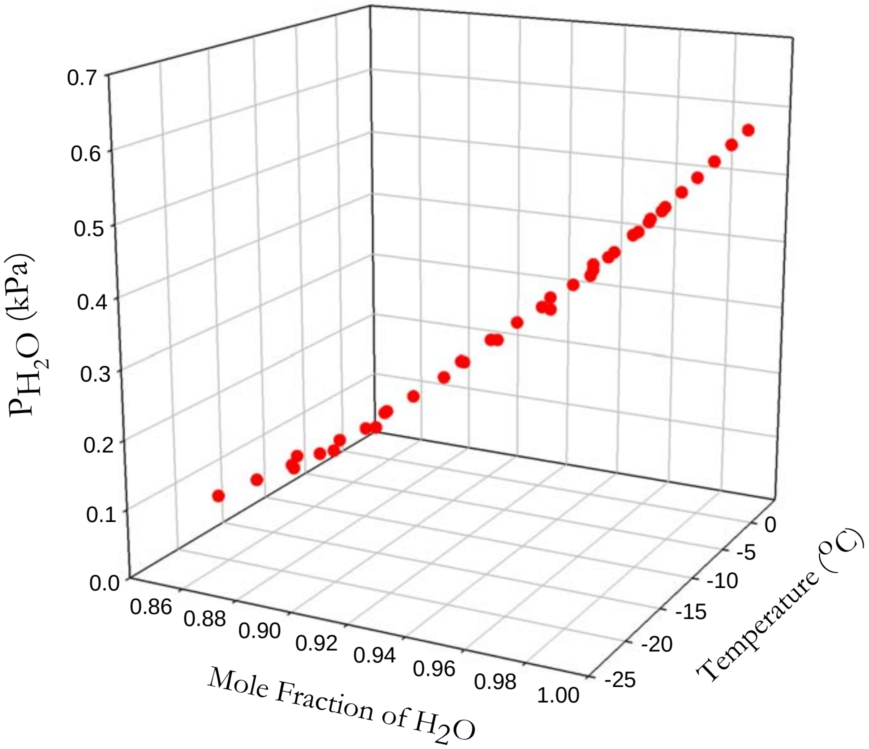

Figure 8.2-10. Partial Pressure of H_2O based on Equation 8-17 from Freezing Point Depression Data by Chang et al. (1993) from -20.0 to -5.0 °C.

8.2.6 *Dissociation Constant of Monoethanolamine*

Recall from Chapter VII that the chemical equilibrium or dissociation constant for Equation 8-7 in terms of the activity is given by the following relationship:

$$K^* = \frac{a_{MEA} \cdot a_{H^+}}{a_{MEAH^+}} \qquad \text{8-18}$$

where the thermodynamic equilibrium constant can be defined as

$$\ln K^* = \left(\frac{-\Delta G_m^o}{RT} \right) \qquad \text{8-19}$$

$$\Delta G_m^o = \sum_i \nu_i \mu_i^o \qquad \text{8-20}$$

Where

K^* is the asymmetric chemical equilibrium constant for Equation 8-7 (molality based),
a_i is the activity of component i,
ΔG_m^o is the standard molar Gibbs free energy change for Equation 8-7,
ν_i is the stoichiometric coefficient of component i,
μ_i^o is the reference chemical potential for component i.

The chemical equilibrium constant vis-à-vis component activities provides the connection between the standard Gibbs free energy change of reaction to the standard (reference) states of the individual species activities in a given reaction. In this work, H_2O and MEA were regarded as solvents and the solution was treated as a mixed-solvent system and described by the symmetric reference state convention where the activity coefficient approaches one as the mole fraction of the species approaches its pure liquid state.

Experimental pKa data from Bates and Pinching (1951) (Figure 8.2-11) were used analytically, to determine the chemical equilibrium constant for Equation 8-7 for the dissociation constant of monoethanolamine. We were then able to determine the following standard state infinite dilution aqueous phase properties: the free energy of formation $\left(\Delta G_f^{\infty,aq}\right)$, the enthalpy of formation $\left(\Delta H_f^{\infty,aq}\right)$, and coefficients for the temperature dependent heat capacity $\left(\Delta C_p^{\infty,aq}\right)$ of protonated monoethanolamine.

Chemical equilibria reported in literature are normally referenced to infinite dilution in water (molality based), treating monoethamine as a solute. Solute and ionic activity coefficients are described by the asymmetric reference state convention which states that as the activity coefficient approaches one, the mole fraction of the species approaches zero in pure water.

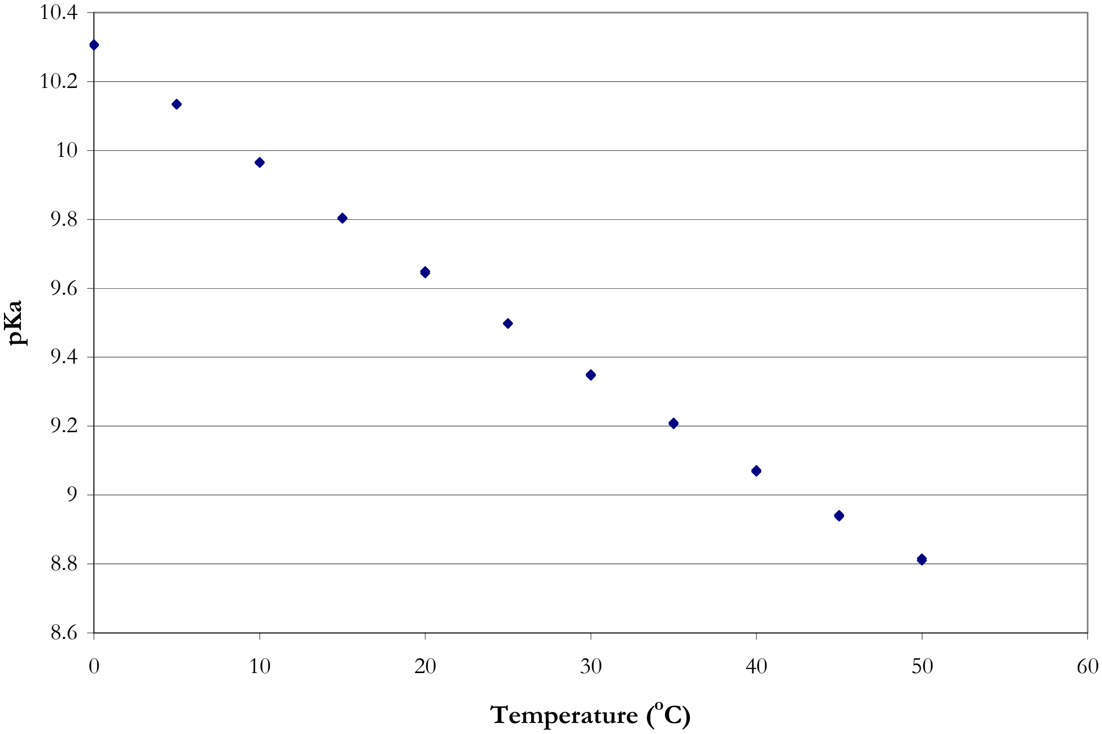

Figure 8.2-11. Experimental pKa from Bates and Pinching (1951) for the Dissociation Constant of Monoethanolamine (molality based) from 0 to 50 °C.

Bates and Pinching (1951) found it helpful to express the chemical equilibrium as a p-function where the p-function is the negative logarithm (base 10) of the number as given by the following expression:

$$pK = -\log_{10}\left(K\right) \tag{8-21}$$

Where
p is the p-function of a numerical datum.

In this work, chemical equilibrium constants are defined in terms of mole fractions; therefore the chemical equilibrium constant reported by Bates and Pinching (1951) has to be converted. However, due to the asymmetric reference state convention, the chemical equilibrium constant of monoethanolamine requires an additional conversion to the symmetric reference state convention since all subsequent monoethanolamine based ionic equilibrium constants are determined based on the asymmetric reference state convention referenced to infinite dilution in monoethanolamine. These two reference state conventions are related for monoethanolamine by the following expression:

$$\frac{\gamma_{MEA}}{\gamma_{MEA}^{*}} = \lim_{x_{MEA}\to 0}\gamma_{MEA} = \gamma_{MEA}^{\infty} \tag{8-22}$$

Where
γ_{MEA} is the symmetric activity coefficient for monoethanolamine,
γ_{MEA}^{*} is the asymmetric activity coefficient for monoethanolamine as the solution approaches its pure solute reference state.

Thus, the chemical equilibrium constant of monoethanolamine (Equation 8-7) referenced to the symmetric reference state convention used in this work is related by the following expression:

$$\ln K^{*} = \ln K + \ln\left(\frac{1000}{MW_w}\right)\sum_{i\neq w}\nu_i + \ln \gamma_{MEA}^{\infty} \qquad 8\text{-}23$$

Where
MW_w is the molecular weight of H_2O, 18.01528 gm/mole,
K is the symmetric chemical equilibrium constant (mole fraction based).

The infinite dilution activity coefficient of monoethanolamine is calculated from the binary interaction parameters for the water-monoethanolamine system using the elecNRTL model. The resulting values were then re-regressed to the standard temperature dependent form of the chemical equilibrium constant given in Chapter VI and compared to Equation 8-6. This modified chemical equilibrium constant for monoethanolamine was then utilized in the elecNRTL model within Aspen Plus^{TM} to specify the infinite dilution standard state free energy and enthalpy of formation, respectively, for protonated monoethanolamine. Therefore, chemical equilibrium constants reported in this work must be corrected for the infinite dilution activity coefficient of monoethanolamine prior to comparison with other work.

8.3 Data Regression

For the elecNRTL model, binary interaction parameters for molecule-molecule interactions were given a default value of zero.

Through simultaneous regression, the molecule-molecule binary interaction parameters for the H_2O-MEA system were obtained through the regression of total vapor pressure [Nath and Bender (1983) and Touhara et al. (1982)], vapor-liquid equilibrium [Park and Lee (1997), Tochigi et al. (1999), Cai et al. (1996), and from this work], specific heat capacity [Pagé et al. (1993), Chiu and Li (1999), Weiland et al. (1997), and from this work], and freezing point depression [Chang et al. (1993)] data over monoethanolamine solutions.

A list of the aqueous electrolyte data sets that were examined in this work is given in Table 8.3-1. The column labels σ_T , σ_P , σ_{Cp} ,σ_{x_i} , σ_{y_i} , give standard error associated with the temperature, pressure, specific heat capacity, liquid mole fraction, and the vapor mole fraction, respectively, with each data set. DRS suggested standard error default values were assigned unless otherwise stated by the author.

Table 8.3-1. Experimental data used in the regression of the H_2O-MEA system.

	Obs.	T (^{o}C)	σ_T	σ_P	σ_x	σ_y	Source
TP	36	60.0 – 91.7	0.05	0.25%	0.1%	10%	Nath and Bender (1983)
	26	25.0 – 35.0	0.01	0.25%	0.1%	10%	Touhara et al. (1982)

	Obs.	T (^{o}C)	σ_T	σ_P	σ_x	σ_y	Source
VLE	16	101.2 – 167.0	0.1	0.1%	0.5%	0.5%	Park and Lee (1997)
	9	90.0	0.01	0.03	0.7%	0.7%	Tochigi et al. (1999)
	25	89.7 – 158.7	0.01	0.133	0.1%	0.1%	Cai et al. (1996)
	25	39.8 – 72.7	0.01	0.1%	0.1%	0	This work

	Obs.	T (^{o}C)	σ_T	σ_x	σ_{Cp}	Source
Cp	48	10.0 – 40.0	0.01	0.1%	0.1%	Pagé et al. (1993)
	44	30.0 – 80.0	0.01	0.1%	0.1%	Chiu and Li (1999)
	4	25.0	0.01	0.1%	0.1%	Weiland et al. (1997)
	34	40.0 – 120.0	0.01	0.1%	0.1%	This work

	Obs.	T (^{o}C)	σ_T	σ_P	σ_x	σ_y	Source
P^{H2O}	40	-20.5 – (-0.5)	0.01	2.0%	0.1%	0	Chang et al. (1993)

After performing a nonlinear regression for the full model using DRS, the following regression summary statistics output for estimates of the adjustable binary parameter coefficients are shown in Table 8.3-2.

Table 8.3-2. DRS Regression Output for Full H_2O-MEA System Model.

Parameter	Interacting Species i	 j	Estimate	σ wrt Estimate
1-$A_{m,m}$	H_2O	MEA	-434	23.1
2-$B_{m,m}$	H_2O	MEA	11272	778
3-$C_{m,m}$	H_2O	MEA	75.8	3.97
4-$D_{m,m}$	H_2O	MEA	-0.1111	0.0069
5-$A_{m,m}$	MEA	H_2O	115	12.1
6-$B_{m,m}$	MEA	H_2O	-3483	406
7-$C_{m,m}$	MEA	H_2O	-20.2	2.04
8-$D_{m,m}$	MEA	H_2O	0.0308	0.0031

Residual Sum of Squares:	724,121
Residual Root Mean Square:	49.294
Degree of Freedom:	299

Recall that the standard error of an estimate is the estimated standard deviation of that statistic. Notice that all of the estimates are large relative to their standard errors. A complete description of the variability of the coefficient estimates requires examining the correlations between the estimates as shown in Table 8.3-3.

Table 8.3-3. Correlation Matrix of the Coefficient Estimates, for the Full H_2O-MEA Model.

Parameter	1	2	3	4	5	6	7	8
1	1.00							
2	-0.87	1.00						
3	*-0.99*	0.82	1.00					
4	0.83	-0.47	-0.88	1.00				
5	-0.79	0.77	0.76	-0.57	1.00			
6	0.68	-0.86	-0.61	0.26	*-0.91*	1.00		
7	0.80	-0.74	-0.78	0.62	*-1.00*	0.86	1.00	
8	-0.77	0.50	0.79	-0.84	0.86	-0.57	*-0.90*	1.00

Table 8.3-3 shows a high negative correlation between $\hat{\eta}_{3\to 1}$ for the first energy parameter estimate, $\tau_{H_2O/MEA}$, but the correlation between other coefficients is relatively small, suggesting that $\hat{\eta}_3$ might be usefully removed from the model without significant loss

of information. On the other hand, Table 8.3-3 shows three highly correlated coefficients for τ_{MEA/H_2O} where a submodel containing fewer coefficients for the τ_{MEA/H_2O} expression might be useful without a significant loss of information.

After performing backward elimination using DRS, the following optimum model regression summary statistics output for estimates of the adjustable binary parameter coefficients are shown in Table 8.3-4. Please refer to Appendix O for more information about the backward elimination procedure to determine the optimal set of binary interaction parameters for the H_2O-MEA system.

Table 8.3-4. DRS Regression Output for Optimum H_2O-MEA Model.

	Interacting Species			
Parameter	i	j	Estimate	σ wrt Estimate
1-$A_{m,m}$	H_2O	MEA	-123	9.65
2-$B_{m,m}$	H_2O	MEA	2575	306
3-$C_{m,m}$	H_2O	MEA	22.1	1.65
4-$D_{m,m}$	H_2O	MEA	-0.0297	0.0022
5-$A_{m,m}$	MEA	H_2O	-1.71	0.149
6-$B_{m,m}$	MEA	H_2O	-214	66.3

Residual Sum of Squares:	740,215
Residual Root Mean Square:	49.673
Degree of Freedom:	301

Notice that all of the estimates are larger relative to their standard errors. Comparing the estimates from the full model to the optimum model, there was relatively little difference between the estimated values. The proposed optimum model provides the following correlations between the estimates as shown in Table 8.3-5.

Table 8.3-5. Correlation Matrix of the Coefficient Estimates, for the Optimum H_2O-MEA Model.

Parameter	1	2	3	4	5	6
1	1.00					
2	*-0.96*	1.00				
3	*-1.00*	*0.96*	1.00			
4	*0.99*	*-0.95*	*-0.99*	1.00		
5	-0.14	0.34	0.13	-0.10	1.00	
6	0.26	-0.46	-0.25	0.19	*-0.91*	1.00

Table 8.3-5 again shows highly negative correlations between all of the $\tau_{H_2O/MEA}$ parameters suggesting that some of the remaining parameters might be usefully removed from the model without significant loss of information.

Results from the previous section show that dropping a term from the full model may provide a submodel that may have a decrease in the correlation between the estimate coefficients and improve the reliability of the model. Testing whether any subset of the regression estimate coefficients may be zero plays an important role in many analyses which leads to the following hypotheses:

NH: $3C_{m,m} = 7C_{m,m} = 0$ Submodel function applies
AH: At lease one $3C_{m,m}, 7C_{m,m} \neq 0$ Full model function applies

We can perform an F-Test to compare the purposed submodel with the full model. Significance levels for this test are obtained by comparing the observed value of F to the $F_{df_{NH}-df_{AH},df_{AH}}$ distribution. The p-value is then computed as an upper-tail test and gives the probability associated with evidence to reject the null hypothesis which will then be compared to the results given by the submodel.

If we were to remove the highly correlated parameters from the full model, the following submodel regression summary statistics output for estimates of the adjustable binary parameter coefficients is shown in Table 8.3-6.

Table 8.3-6. DRS Regression Output for H_2O-MEA Submodel.

Parameter	Interacting Species i	j	Estimate	σ wrt Estimate
1-$A_{m,m}$	H_2O	MEA	-4.46	0.67
2-$B_{m,m}$	H_2O	MEA	-85.3	174
3-$D_{m,m}$	H_2O	MEA	0.0149	0.0011
4-$A_{m,m}$	MEA	H_2O	2.90	0.72
5-$B_{m,m}$	MEA	H_2O	-456	190
6-$D_{m,m}$	MEA	H_2O	-0.0079	0.0007

Residual Sum of Squares:	831,795
Residual Root Mean Square:	52.656
Degree of Freedom:	301

Notice that only one of the estimates is smaller relative to the standard error. Comparing the estimates from the submodel to the full model, there was large difference between the estimated values with respect to the order of magnitude. The residual sum of squares and the standard errors for the submodel have increased as compared to the full model. The proposed submodel provides the following estimated covariances between the estimates as shown in Table 8.3-7.

Table 8.3-7 shows parameter $\left(2B_{m,m}\right)$ is highly correlated to the first coefficient, $\left(1A_{m,m}\right)$, suggesting that $\hat{\eta}_2$ might be usefully removed from the model without significant loss of information.

Table 8.3-7. Correlation Matrix of the Coefficient Estimates for the H_2O-MEA Submodel.

Parameter	1	2	3	4	5	6
1	1.00					
2	*-0.91*	1.00				
3	-0.86	0.77	1.00			
4	-0.82	0.80	0.50	1.00		
5	0.79	*-0.91*	-0.60	*-0.91*	1.00	
6	*0.90*	-0.79	-0.61	*-0.97*	0.83	1.00

The two models were then compared using the test statistic F applied to the null hypothesis versus the alternative:

$$\frac{\left[\dfrac{831795-724121}{301-299}\right]}{\left[\dfrac{724121}{299}\right]} \sim 22.4355(2,299)$$

We can then calculate the probability for a F-distribution, df = 2, 299, upper-tail.

F dist. with (2, 299) df, value = 22.4355, upper-tail probability = 8.35122e-10

The finding of $p \approx 0$ provides strong evidence against the null hypothesis that $3C_{m,m} = 7C_{m,m} = 0$. Since a value of F this strong would be observed 0 times out of a hundred if the null hypothesis were true, the submodel will not give an adequate description of the data over the range of temperatures and concentration available in the data.

8.3.1 *Optimum Model Results*

With the determination of the estimates for the binary interaction parameters known for the optimum model, a simple Aspen Plus™ Flash model was used to test the predictive capability of the H_2O-MEA model against literature data. For each data point, the deviation between the experimental and estimated values is expressed in terms of the average absolute relative deviation (AARD). Table 8.3-8 gives the percent AARD and the maximum percent AARD for the model predictions.

Table 8.3-8. Absolute Percent Relative Error for the H_2O-MEA Optimum Model.

		AARD(%)	Max. AARD
TP	Nath and Bender (1983)	2.01	6.94
	Touhara et al. (1982)	2.40	11.78
VLE	Park and Lee (1997)	6.99	11.79
	Tochigi et al. (1999)	5.49	11.59
	Cai et al. (1996)	4.81	11.27
	This work	4.28	7.02
C_p	Pagé et al. (1993)	1.95	6.26
	Chiu and Li (1999)	1.20	2.51
	Weiland et al. (1997)	2.20	2.79
	This work	0.16	0.48
P^{H2O}	Chang et al. (1993)	0.35	0.67
Overall		**2.62**	**11.79**

Overall, the model adequately describes the H_2O-MEA property data listed above within an average absolute relative error of ± 2.62 percent, with the exception of a few outliers.

8.3.2 *Chemical Equilibrium Constant*

With the determination of the estimates for the binary interaction parameters known for the optimum model, we can directly evaluate the infinite dilution activity coefficient of monoethanolamine (Equation 8-6) as given by the following expression:

$$\ln \gamma_{MEA}^{\infty} = \left(-123 + \frac{2575}{T(K)} + 22.1 \ln T(K) - 0.0297 T(K) \right) + \left(-1.71 - \frac{214}{T(K)} \right) e^{-0.2\left(-1.71 - \frac{214}{T(K)} \right)} \qquad \text{8-24}$$

Previous authors chose to linearize the above expression into the temperature dependent form used for the chemical equilibrium constants as given by the following expression from the ARC (2004) summary statistics output for estimates of the temperature dependent coefficients shown in Table 8.3-9:

$$\ln \gamma_{MEA}^{\infty} = -8.95 - \frac{1296}{T\left(K\right)} + 2.016 \ln T\left(K\right) \tag{8-25}$$

Table 8.3-9. ARC Regression Output for the Infinite Dilution Activity Coefficient for Monoethanolamine.

```
Data set = Dataset, Name of Fit = L1
Normal Regression
Kernel mean function = Identity
Response      = LNMEA
Terms         = (1T LNT)
Coefficient Estimates
Label         Estimate      Std. Error     t-value        p-value
Constant      -8.95461      0.735950       -12.137        0.0000
1T            -1295.89      35.7499        -36.725        0.0000
LNT           2.01628       0.108184       18.689         0.0000

R Squared:                  0.999995
Sigma hat:                  0.00108305
Number of cases:            17
Degrees of freedom:         14

Summary Analysis of Variance Table
Source        df     SS             MS              F              p-value
Regression    2      3.32927        1.66464         1419139.54     0.0000
Residual      14     0.0000164219   1.172989E-6
```

We can then compare the two expressions as shown in Table 8.3-10. Table 8.3-10 illustrates how linearization of Equation 8-24 may cause minor errors at elevated temperatures. In this work, we chose to use Equation 8-24 to represent the infinite dilution activity coefficient of monoethanolamine due to the small variations between Equation 8-24 and Equation 8-25.

Table 8.3-10. Comparison between Equations 8-24 and 8-25 for the Natural Log Infinite Dilution Activity Coefficient for Monoethanolamine in Water.

LN Infinite Dilution Activity Coefficient for MEA			
Temp (°C)	Equation 8-24	Equation 8-25	AARD(%)
25	-1.8128	-1.8131	0.02
30	-1.7085	-1.7079	0.04
35	-1.6066	-1.6056	0.07
40	-1.5072	-1.5060	0.08
45	-1.4100	-1.4090	0.07
50	-1.3152	-1.3145	0.05
55	-1.2227	-1.2225	0.02
60	-1.1325	-1.1327	0.02
65	-1.0445	-1.0451	0.06
70	-0.9588	-0.9597	0.10
75	-0.8752	-0.8763	0.13
80	-0.7937	-0.7949	0.14
Overall			**0.07**

Since there are only minor differences between Equation 8-24 and 8-25, we can illustrate thermal effects of the solution equivalent to the infinite dilution excess enthalpy given by the following equation for MEA:

$$-\frac{\Delta H^{E}}{R} = \frac{d \ln \gamma_{MEA}^{\infty}}{d1/T} = -1296 + 2.016 \cdot T\left(K\right) \qquad \text{8-26}$$

At 25 and 80 °C, the infinite dilution excess enthalpy (kJ/mol) is -12.46 and -11.34, respectively. Figure 8.3-1 illustrates experimental [Touhara et al. (1982) and Kim et al. (1987)] and predicted [Austgen et al. (1991), Posey (1996), and this work] values for the infinite dilution excess enthalpy for MEA from 20 to 100 °C.

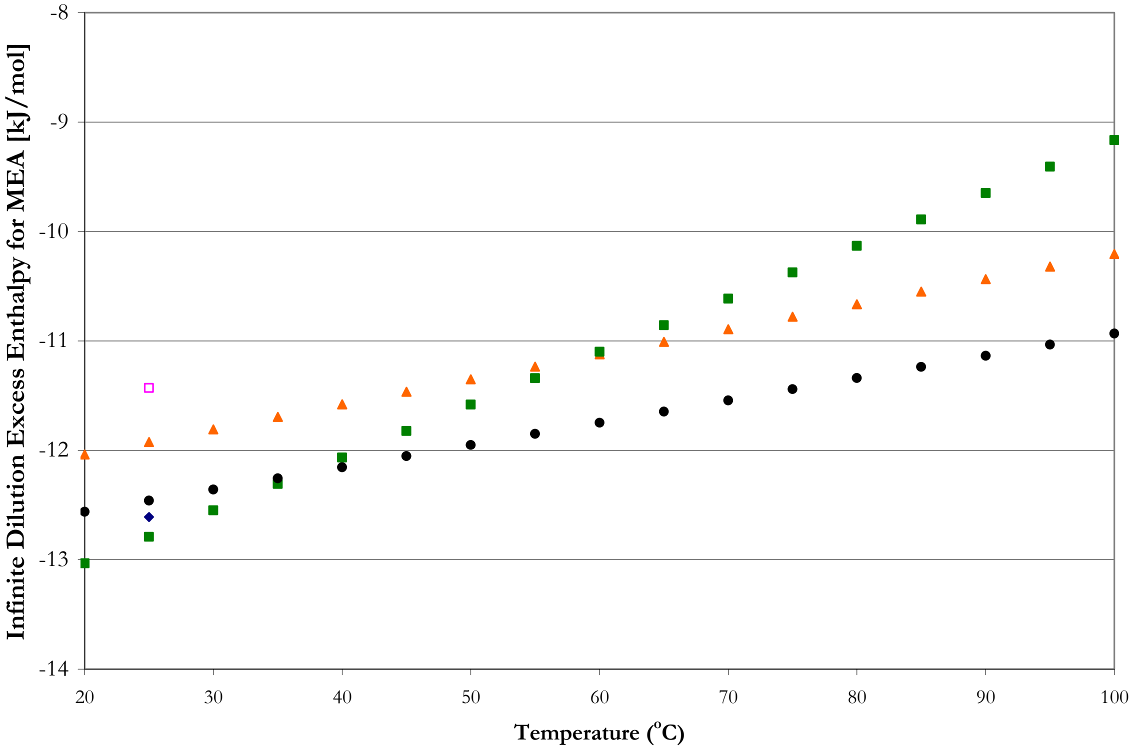

Figure 8.3-1. Infinite Dilution Excess Enthalpy for MEA from 20 to 100 °C. Points: ♦, Touhara et al. (1982), □, Kim et al. (1987), ▲, Austgen et al. (1991), ■, Posey (1996), an ●, this work.

Experimental values for the infinite dilution excess enthalpy for MEA from Touhara et al. (1982) and Kim et al. (1987) differ by ± 10% from one another. As compared to model predictions from Posey (1996) and from this work, differ by ± 2% from Touhara et al. (1982), whereas, Austgen et al. (1991) differs from Kim et al. (1997) by ± 5%. One striking feature of Figure 8.3-1 is the temperature dependence of the infinite dilution excess enthalpy. This difference is a magnification of the temperature effect on the infinite dilution activity coefficient of MEA as shown in Figure 8.3-2.

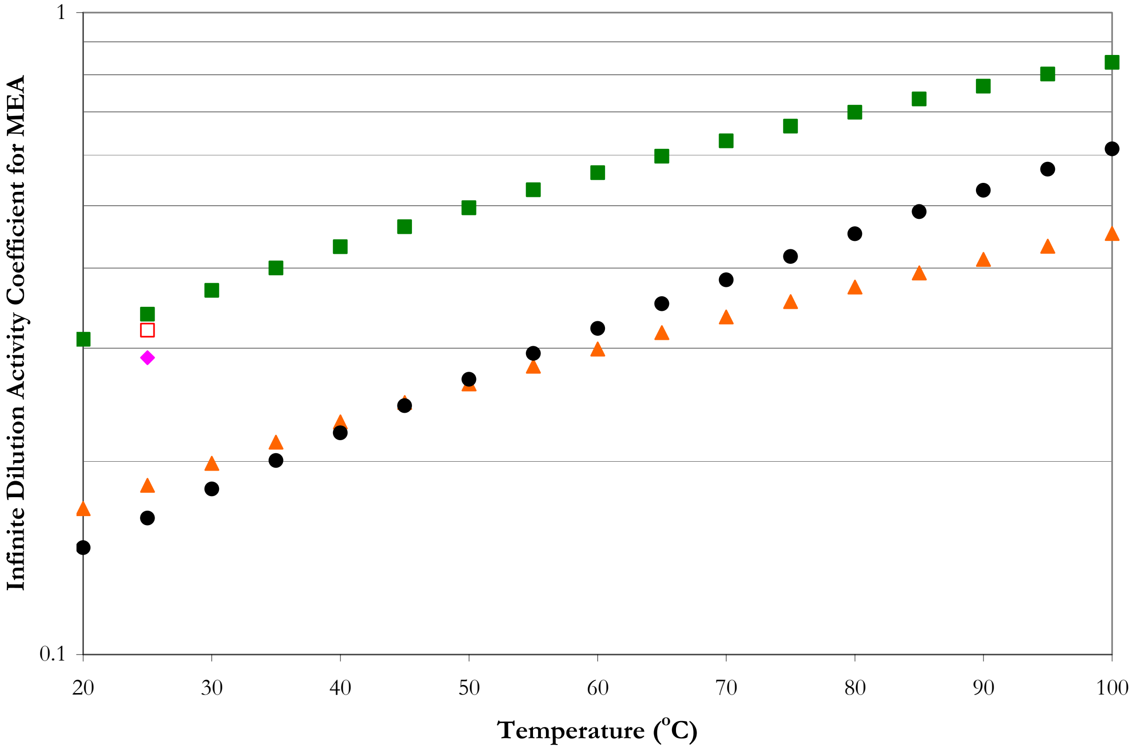

Figure 8.3-2. Infinite Dilution Activity Coefficient for MEA from 20 to 100 °C. Points: ▲, Austgen et al. (1991), □, Lee (1996), ■, Posey (1996),◆, Poplsteinova (2004), and ●, this work.

For most activity coefficient models, the reference state for solutes is defined as infinite dilution in pure solvent; at 25 °C we can see that there is a large degree of scatter even at this temperature. The optimum model parameters were fitted to a more extensive database than previous authors, thus infinite dilution activity coefficients predicted with the optimum model may give more realistic activity coefficients as a function of temperature and composition as compared to data found in the literature.

With the determination of the Equation 8-25 known, we can then regress Equation 8-23 to the standard temperature dependent form of the chemical equilibrium constant given in Chapter VI based on experimental data reported by Bates and Pinching (1951) using ARC (2004) as shown in Table 8.3-11.

Table 8.3-11. Estimates for the Chemical Equilibrium Coefficients for the H_2O-MEA System.

Reference State	Concentration Basis	A	σ_A	B	σ_B	C	σ_C	D	σ_D
Asymmetric	Molality	3.17	6.33	-6286	281	-0.694	0.946	0.0	-
Asymmetric	Mole Fraction	-0.844	6.33	-6286	281	-0.694	0.946	0.0	-
Symmetric	Mole Fraction	-22.82	6.46	-6997	286	3.26	0.965	0.0	-

Data Reference: Bates and Pinching (1951)
$\ln K = A + B/T(K) + C\cdot\ln T(K) + D\cdot T(K)$

We can now compare our linear equilibrium constant expression for the dissociation of MEA to coefficients reported by Austgen et al. (1989) as shown in Figure 8.3-3.

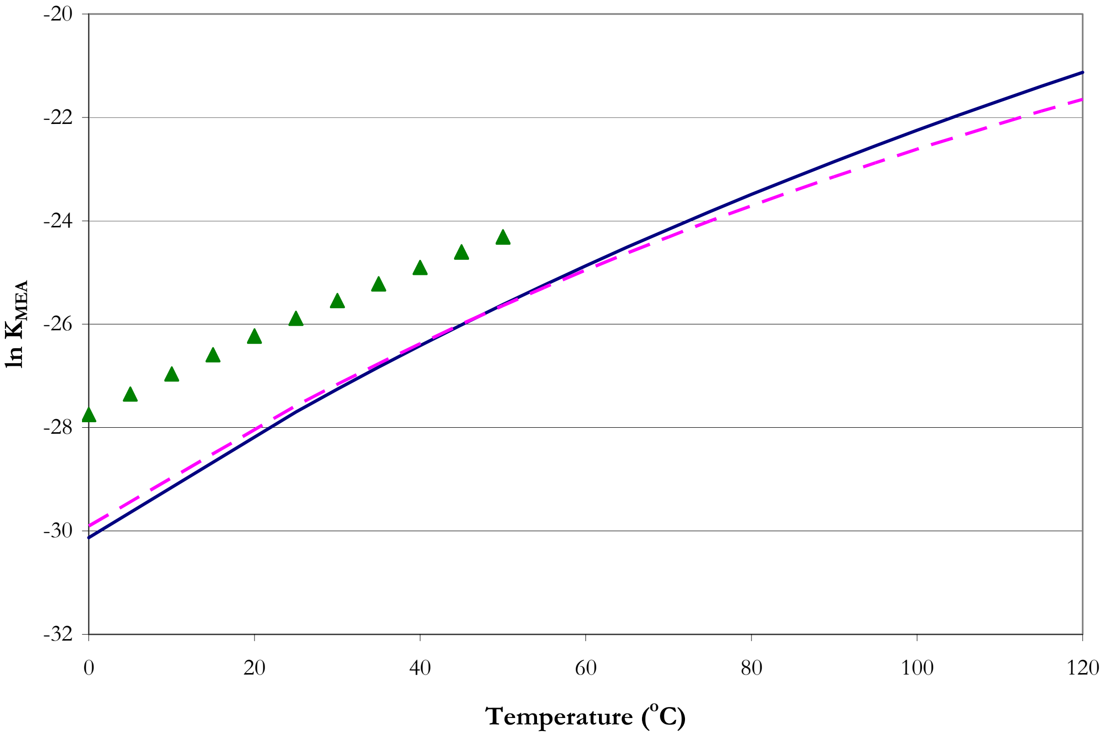

Figure 8.3-3. Comparison of the Dissociation Equilibrium Constant for MEA (mole fraction based) from 0 – 120 °C. Points: ▲, Bates and Pinching (1951). Lines: – –, Austgen et al. (1989), ▬, this work.

Figure 8.3-3 illustrates similar trends presented in Figure 8.3-2 where predictions for the infinite dilution activity coefficient for MEA reported by Austgen et al. (1989) as compared to predictions from this work crossed at 45 ºC. Since both works utilized Bates and Pinching (1951) to describe the dissociation of MEA, the only differences between the two reported K-values would be in the treatment of the infinite dilution activity coefficient of MEA applied to the linearization of the chemical equilibrium constant to the temperature dependent functional form. Over the range (0 – 50 ºC) where the experimental data are valid, the two expressions adequately describe similar trends but tend to diverge at high temperatures.

As stated previously, Equation 8-19 relates the equilibrium constant for the dissociation of MEA to the standard Gibbs free energy change of reaction.

$$\frac{\Delta G^o}{RT} = -\ln K \tag{8-27}$$

$$\frac{\Delta G^o}{RT} = -\left(A + \frac{B}{T(K)} + C \cdot \ln T(K) + D \cdot T(K) \right) \tag{8-28}$$

By taking the partial derivative of Equation 8-28 with respect to temperature; Equation 8-29 relates the standard enthalpy of reaction to the standard Gibbs free energy.

$$-\frac{\Delta H^o}{RT} = \frac{d\left(\Delta G^o / RT\right)}{dT} \tag{8-29}$$

$$\Delta H^o = RT^2 \frac{d \ln K}{dT} = RT^2 \frac{d}{dT}\left(A + \frac{B}{T(K)} + C \cdot \ln T(K) + D \cdot T(K) \right) \tag{8-30}$$

$$\Delta H^o = RT^2 \left(-\frac{B}{T(K)^2} + \frac{C}{T(K)} + D \right) \tag{8-31}$$

$$\Delta H^{o}=R\left(-B+C\cdot T\left(K\right)+D\cdot T\left(K\right)^{2}\right) \tag{8-32}$$

Where the standard property changes of reaction (e.g. Gibbs free energy and enthalpy) are defined as the difference between the standard property change of the products and reactants, weighted by their stoichiometric coefficients.

$$\Delta M^{o}=\sum_{i}\nu_{i}M_{i}^{o} \tag{8-33}$$

For ionic species the aqueous phase infinite dilution molar heat capacity is described by the following equation:

$$C_{p,i}^{\infty,aq}\left(\frac{J}{kmol\cdot K}\right)=C_{1,i}+C_{2,i}T\left(K\right)+C_{3,i}T\left(K\right)^{2}+\frac{C_{4,i}}{T\left(K\right)} \tag{8-34}$$

The molar heat capacity of MEA was described in Chapter VIII by the following equation:

$$C_{p,MEA}^{l,*}\left(\frac{J}{kmol\cdot K}\right)=115228+99.98\cdot T\left(K\right)+0.231\cdot T\left(K\right)^{2} \tag{8-35}$$

Based on Equations 8-27 to 8-32, Table 8.3-12 reports the standard property changes of formation as compare to literature values and Table 8.3-13 reports the coefficients for the aqueous phase infinite dilution heat capacity for a proton.

Table 8.3-12. Standard Property Changes of Formation at 298.15 K for Molecular and Ionic Components.

		This work.		DIPPR Literature*	
Component	v_i	ΔG° (kcal/mol)	ΔH° (kcal/mol)	ΔG° (kcal/mol)	ΔH° (kcal/mol)
$MEAH^+$	-1	-43.2255†	-80.4807†	-30.2103*	-65.5999*
MEA	1	-29.2059‡	-64.5427‡		
H^+	1	0.0	0.0		

*Rowley et al. (2004) – DIPPR: Model Predictions.
†Calculated based on Equation 8-23.
‡Based on Chapter VIII.

Table 8.3-13. Coefficients for the Aqueous Phase Infinite Dilution Heat Capacity (J/kmol·K).

Component	C_1	C_2	C_3	C_4
H^+	0.0	0.0	0.0	0.0

For a given temperature, the molar aqueous phase infinite dilution heat capacity of $MEAH^+$ can then be determined analytically. A starting point for a rigorous development starts with the following equation:

$$\Delta G_m^o = \Delta H_m^o - T\Delta S_m^o \qquad \text{8-36}$$

Equation 8-36 is from the definition of the molar Gibbs free energy applied to each component in a chemical reaction evaluated at the standard state. By applying Equation 8-33 to Equation 8-36 yields

$$\sum_i \nu_i G_{m,i}^o = \sum_i \nu_i H_{m,i}^o - T\sum_i \nu_i S_{m,i}^o \qquad \text{8-37}$$

where the standard molar heat of reaction and standard molar entropy change of reaction are related to temperature by the following expressions

$$\Delta H_m^o = \Delta H_{0,m}^o + R\int_{T_0}^{T} \frac{\Delta C_{p,m}^o}{R} dT \qquad \text{8-38}$$

$$\Delta S_m^o = \Delta S_{0,m}^o + R\int_{T_0}^{T} \frac{\Delta C_{p,m}^o}{R} \frac{dT}{T} \qquad \text{8-39}$$

Equations 8-36, 8-38, and 8-39 are combined to yield

$$\Delta G_m^o = \Delta H_{0,m}^o + R\int_{T_0}^{T} \frac{\Delta C_{p,m}^o}{R} dT - T\Delta S_{0,m}^o - RT\int_{T_0}^{T} \frac{\Delta C_{p,m}^o}{R} \frac{dT}{T} \qquad \text{8-40}$$

However,

$$\Delta S_{0,m}^o = \frac{\Delta H_{0,m}^o - \Delta G_{0,m}^o}{T_0} \qquad \text{8-41}$$

hence

$$\Delta G_m^o = \Delta H_{0,m}^o - \frac{T}{T_0}\left(\Delta H_{0,m}^o - \Delta G_{0,m}^o\right) + R\int_{T_0}^{T} \frac{\Delta C_{p,m}^o}{R} dT - RT\int_{T_0}^{T} \frac{\Delta C_{p,m}^o}{R}\frac{dT}{T} \qquad 8\text{-}42$$

Finally, division by RT yields

$$-\ln K_i = \frac{\Delta G_m^o}{RT} = \frac{\Delta G_{0,m}^o - \Delta H_{0,m}^o}{RT_0} + \frac{\Delta H_{0,m}^o}{RT} + \frac{1}{T}\int_{T_0}^{T} \frac{\Delta C_{p,m}^o}{R} dT - \int_{T_0}^{T} \frac{\Delta C_{p,m}^o}{R}\frac{dT}{T} \qquad 8\text{-}43$$

The change in heat capacity for the mixture can be expressed as

$$\Delta C_p^o\left(\frac{J}{kmol \cdot K}\right) = \Delta A + \Delta B \cdot T\left(K\right) + \Delta C \cdot T\left(K\right)^2 + \Delta D \cdot T\left(K\right)^3 + \Delta E \cdot T\left(K\right)^4 \qquad 8\text{-}44$$

with

$$\Delta A = \sum_i v_i A_i \qquad 8\text{-}45$$

With analogous definitions for ΔB, ΔC, ΔD, and ΔE. Using Equation 8-43 and the coefficients for the chemical equilibrium constant given in Table 8.3-11, we can determine the coefficients for the aqueous phase infinite dilution molar heat capacity of MEAH$^+$.

Table 8.3-14. Coefficients for the Aqueous Phase Infinite Dilution Heat Capacity (J/kmol·K) of MEAH$^+$ from 0 – 200 ^{o}C based on Equation 8-44.

Coefficient	Estimate
C_1	0.0001
C_2	0.0256
C_3	4.5343
C_4	-0.0089

Coefficients for the aqueous phase infinite dilution molar heat capacity of MEAH$^+$ were adjusted to match the form of Equation 8-34.

Table 8.3-15. Coefficients for the Aqueous Phase Infinite Dilution Heat Capacity (J/kmol·K) of MEAH$^+$ from 0 – 200 ^{o}C based on Equation 8-34.

Coefficient	Estimate	Aspen Plus Default Estimate
C_1	-1710760	0.0
C_2	7136	295.12
C_3	-8.547	0.0
C_4	1.5206E+08	0.0

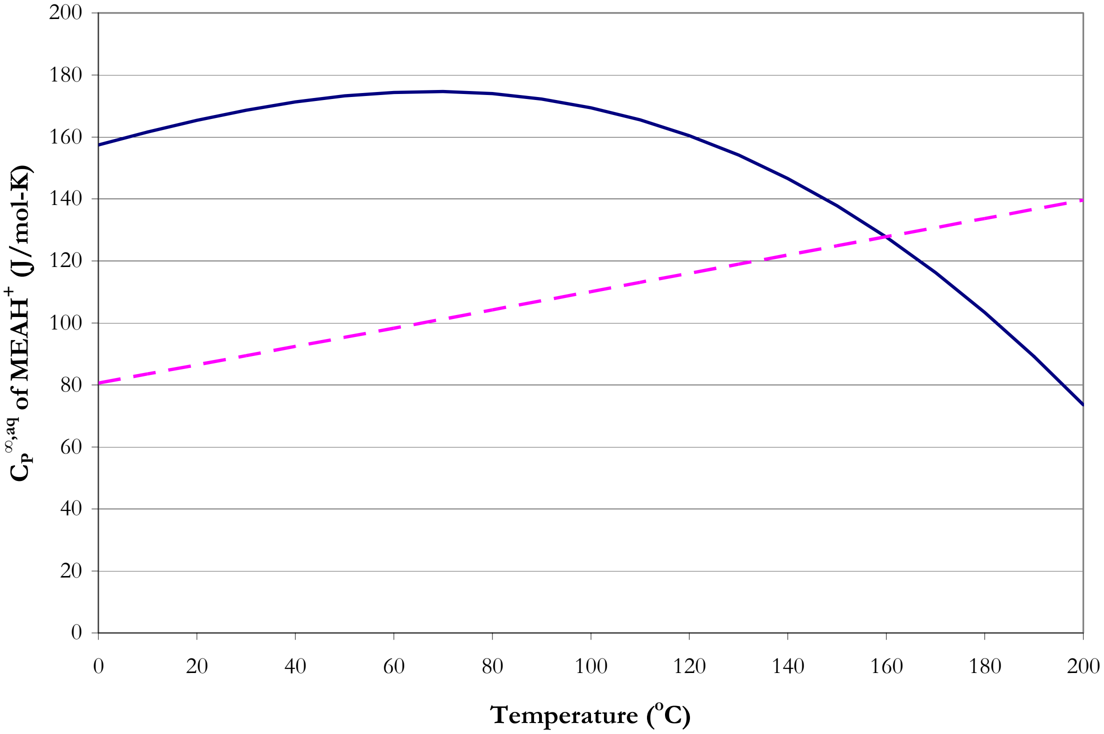

Figure 8.3-4. Comparison of the Coefficients for the Aqueous Phase Infinite Dilution Heat Capacity (J/kmol·K) of MEAH$^+$ from 0 – 200 ^{o}C based on Equation 8-34 to Aspen Plus™ Default Parameters. Lines: ▬, This work, – –, Aspen Plus™ Default Parameters.

Aspen Tech does not provide source documentation for the coefficients assigned to MEAH$^+$, but does reference Austgen et al. (1989), even though Austgen et al. (1989) did not provide documentation. In this work, we have compiled a consistent database for experimental H_2O-MEA data as compared to the work by Austgen et al. (1989). The difference between the two predictions for the aqueous phase infinite dilution heat capacity of $MEAH^+$ accounts for differences is in the model framework. Austgen et al. (1989) chose to describe the liquid phase chemical equilibrium through linear temperature dependent functions. In this work, we chose not to provide the chemical equilibrium constants, but rather determine the chemical equilibrium from the reference state free energy of the system. Thus, Austgen et al. (1989) was never required to fully describe the standard property changes for each ionic species because Aspen Plus™ would rely on the provided chemical equilibrium constants for the necessary ionic information (e.g. ΔG, ΔH, ΔC_p) as shown in Figure 8.3-5.

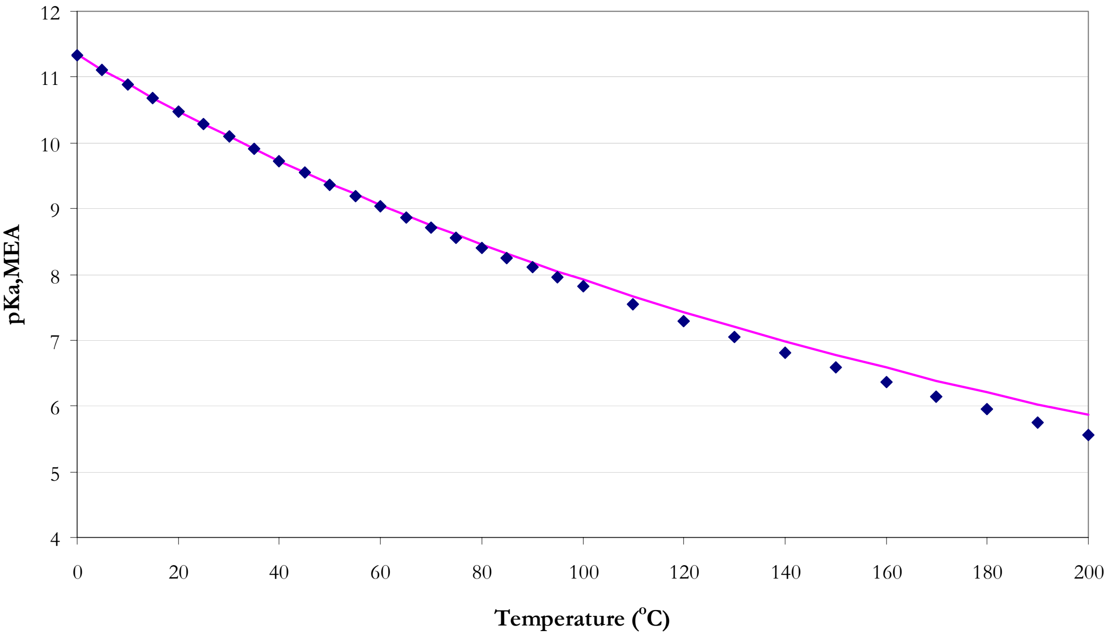

Figure 8.3-5. Comparison of the Dissociation Equilibrium Constant for MEA (mole fraction based) from 0 – 200 °C. Points: ◆, Austgen et al. (1989). Lines: ▬, Corrected Bates and Pinching (1951) based on Table 8.3-11.

By determining the coefficients for the aqueous phase infinite dilution molar heat capacity of $MEAH^+$ analytically, this work is thermodynamically consistent with published literature for the dissociation constant of MEA as shown in Figure 8.3-6.

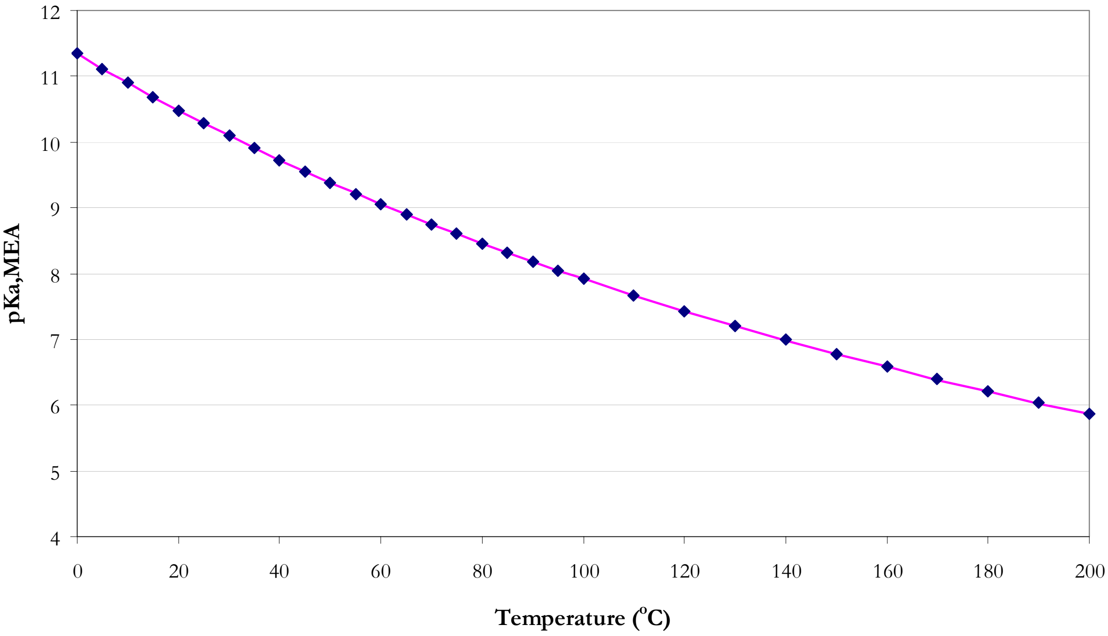

Figure 8.3-6. Comparison of the Dissociation Equilibrium Constant for MEA (mole fraction based) from 0 – 200 °C. Points: ◆, This work. Lines: ▬, Corrected Bates and Pinching (1951) based on Table 8.3-11.

8.4 Optimum Model Predictions

In this work, we have compiled a large database of consistent high quality data needed to obtain a unique set of binary interaction parameters to describe the H_2O-MEA system. The remainder of this chapter will be devoted to using our model as a predictive tool as described in the subsequent sections.

8.4.1 *Total Vapor Pressure*

With the determination of the estimates for the energy parameter coefficients known for the optimum model, a simple Aspen Plus^{TM} Flash model was used to test the predictive capability of the H_2O-MEA energy parameter coefficients against literature data. Figures 8.4-1 and 8.4-2 compare estimated and experimental total pressure measurements from Nath and Bender (1983) and Touhara et al. (1982), for aqueous MEA mixtures from 25.0 – 91.7 °C. The optimum model exhibits systematic error and under predicts the total vapor pressure with a maximum error of ± 6.99 % for concentrations less than 40 mole percent of MEA even though all the predictions of the model were within an AARD of ± 2.01 %, with the exception of a few outliers. Figure 8.4-1 and Figure 8.4-2 illustrates the departure from an ideal solution behavior vis-à-vis Raoult's Law as compared to predictions from the elecNRTL model. Over the temperature range from 25 to 91.7 °C, Raoult's Law moderately describes the vapor pressure of H_2O-MEA mixtures below $x_{MEA} = 0.1$, but as the concentration of MEA increases so does the importance of including activities to describe the vapor-liquid equilibrium.

Overall, the optimum model adequately describes the total vapor pressure data in MEA mixtures within an average absolute relative error of ± 2.21 percent.

8.4.2 *Vapor-Liquid Equilibrium*

Figure 8.4-3 gives the results of fit for experimental isobaric (*Txy*) vapor-liquid equilibrium (VLE) data from Park and Lee (1997) and Cai et al. (1996) versus the concentration of water at 101.325 kPa. To describe the *Txy* behavior of H_2O-MEA mixtures at atmospheric pressure given the degree of scatter between Park and Lee (1997) and Cai et al. (1996) allows Raoult's Law and the elecNRTL model to describe systematic trends presented in both data sets adequately. Overall, the optimum model adequately describes the *Txy* data within an average absolute relative error of ± 2.82 percent.

Figure 8.4-4 compares estimated and experimental isothermal (*Pxy*) VLE data from Tochigi et al. (1999) versus the concentration of water at 90.0 °C. To describe the liquid phase we see from Figure 8.4-4 the extent of this departure from an ideal solution to a real solution as illustrated by predictions from the elecNRTL model.

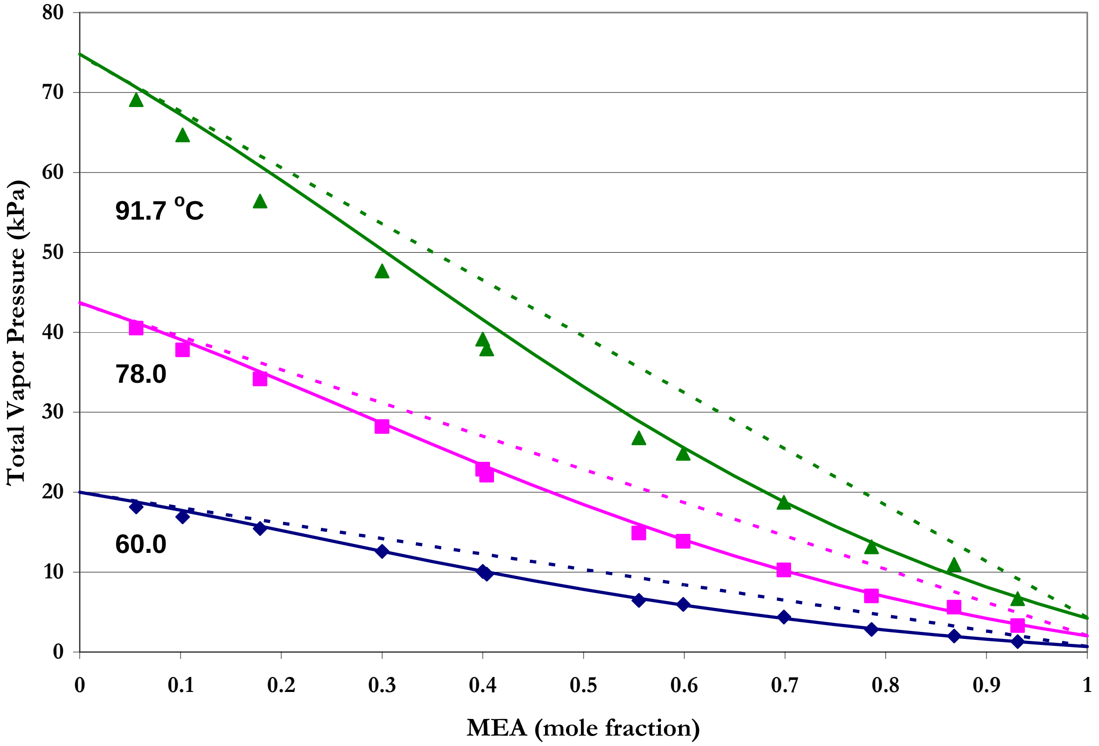

Figure 8.4-1. Comparison of Nath and Bender (1983) Total Pressure data to elecNRTL Model Predictions from 60.0 – 91.7 °C. Lines: ▬, elecNRTL Predictions, - - - , Raoult's Law.

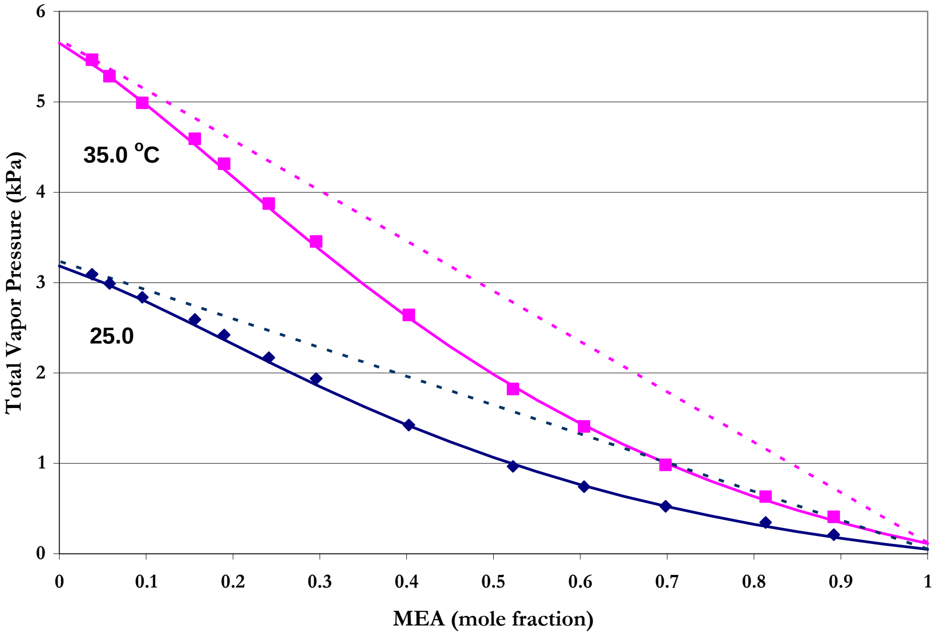

Figure 8.4-2. Comparison of Touhara (1982) Total Pressure data to elecNRTL Model Predictions from 25.0 – 35.0 °C. Lines: ▬, elecNRTL Predictions, - - - , Raoult's Law.

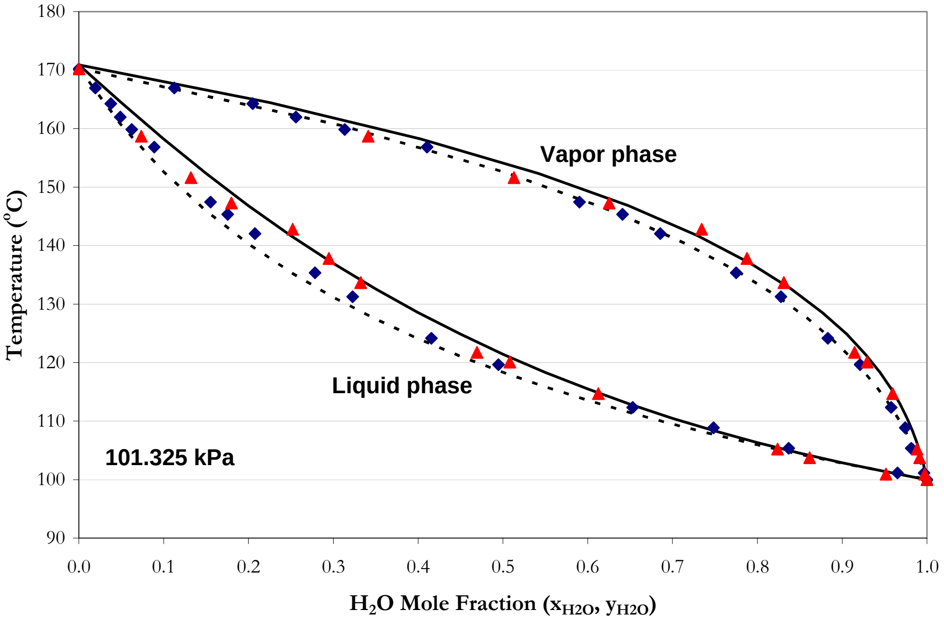

Figure 8.4-3. Comparison of Park and Lee (1997) and Cai et al. (1996) Isobaric *Txy* data to elecNRTL Model Predictions at 101.325 kPa. Points: ◆, Park and Lee (1997) and ▲, Cai et al. (1996). Lines: ▬, elecNRTL Predictions, - - - , Raoult's Law.

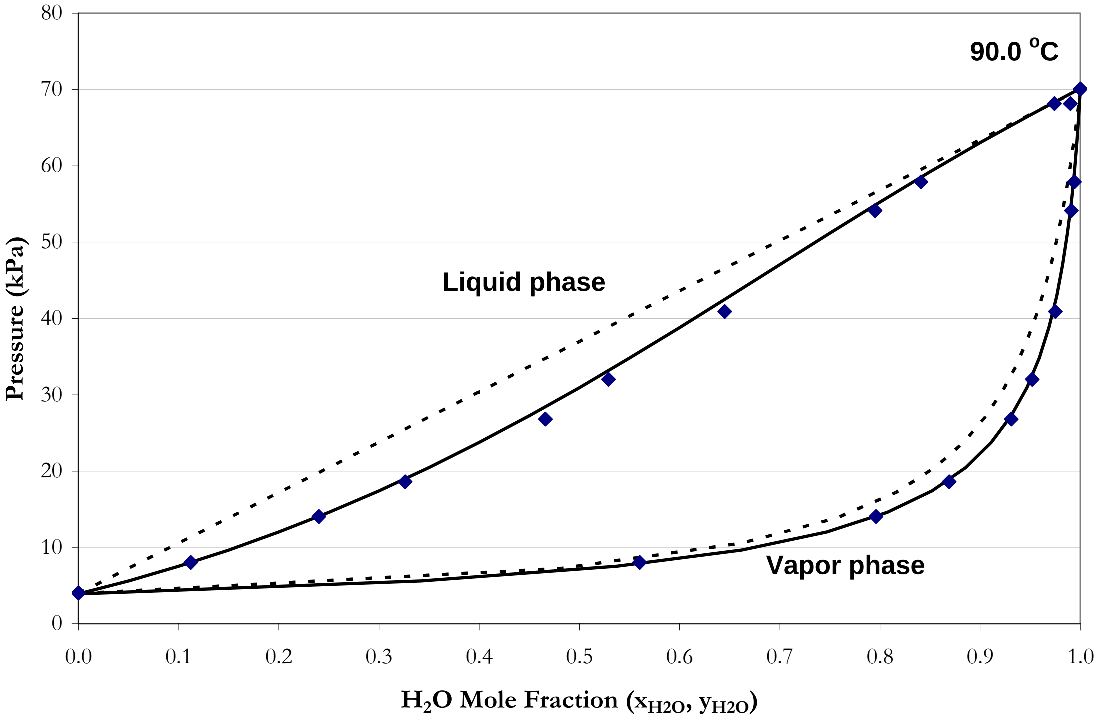

Figure 8.4-4. Comparison of Tochigi et al. (1999) Isothermal *Pxy* data to elecNRTL Model Predictions at 90.0 °C. Points: ◆,Tochigi et al. (1999). Lines: ▬, elecNRTL Predictions, - - - , Raoult's Law.

Overall, the optimum model adequately describes the *Pxy* data within an average absolute relative error of ± 4.81 percent.

One of the main goals of this work was to describe the amine volatility at absorber and stripper conditions. Figure 8.4-5 and Figure 8.4-6 compares estimated and experimental amine volatility data from this work to predictions from the elecNRTL model up to 120 °C.

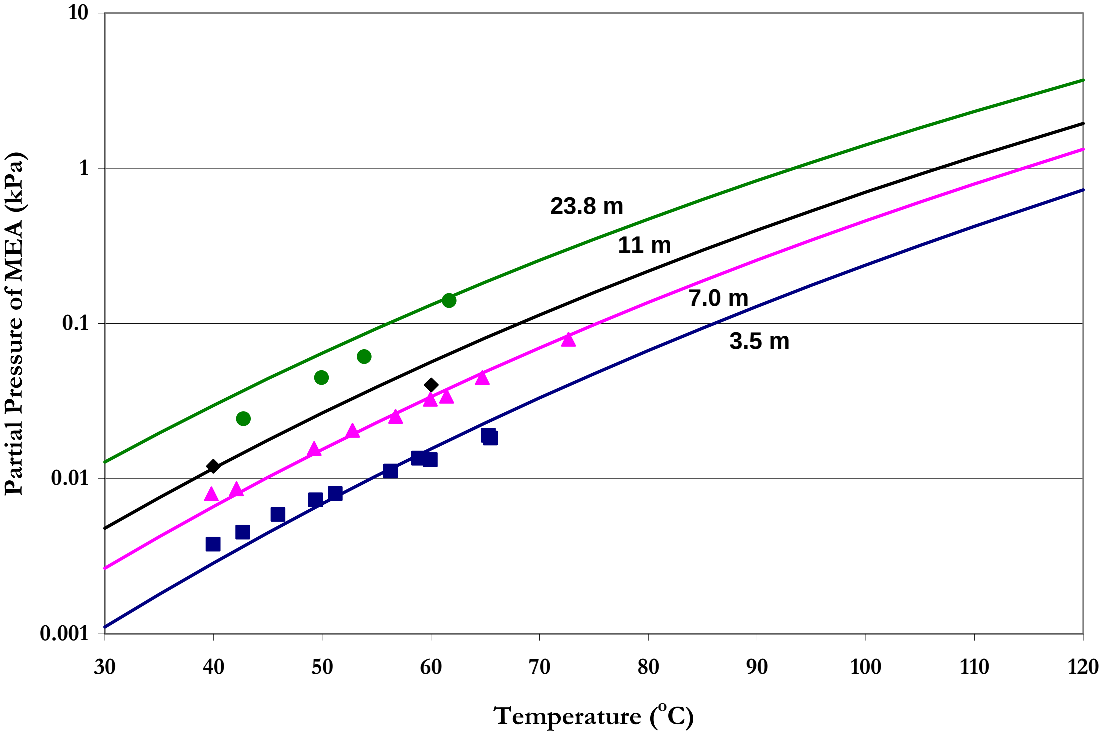

Figure 8.4-5. Comparison of Amine Volatility (e.g. Partial Pressure of MEA) from this work to elecNRTL Model Predictions from 30 – 120 ^{o}C. Points: experimental data from this work ■, 3.5 m (mole/kg-H_2O), ▲, 7 m, ♦, 11 m, ●, 23.8 m. Lines: ▬, elecNRTL Predictions.

We chose to concentrate our modeling efforts to describe the partial pressure of MEA between 3.5 and 7.0 m MEA due to limited data at 11.0 and 23.8 m MEA. Overall, the optimum model adequately describes the partial pressure of MEA within an average absolute relative error of ± 4.28 percent, with the exception of a few outliers. In addition, the optimum model adequately described the partial pressure of water within an average absolute relative error of ± 6.64 percent, with the exception of a few outliers. We would recommend that future work should endeavor to describe the binary system at stripper conditions (e.g. temperatures between 80 - 120 ^{o}C) to complete this analysis. Modifications to the reactor used in this work would need the ability to perform at high temperatures and high pressures to obtain high quality data.

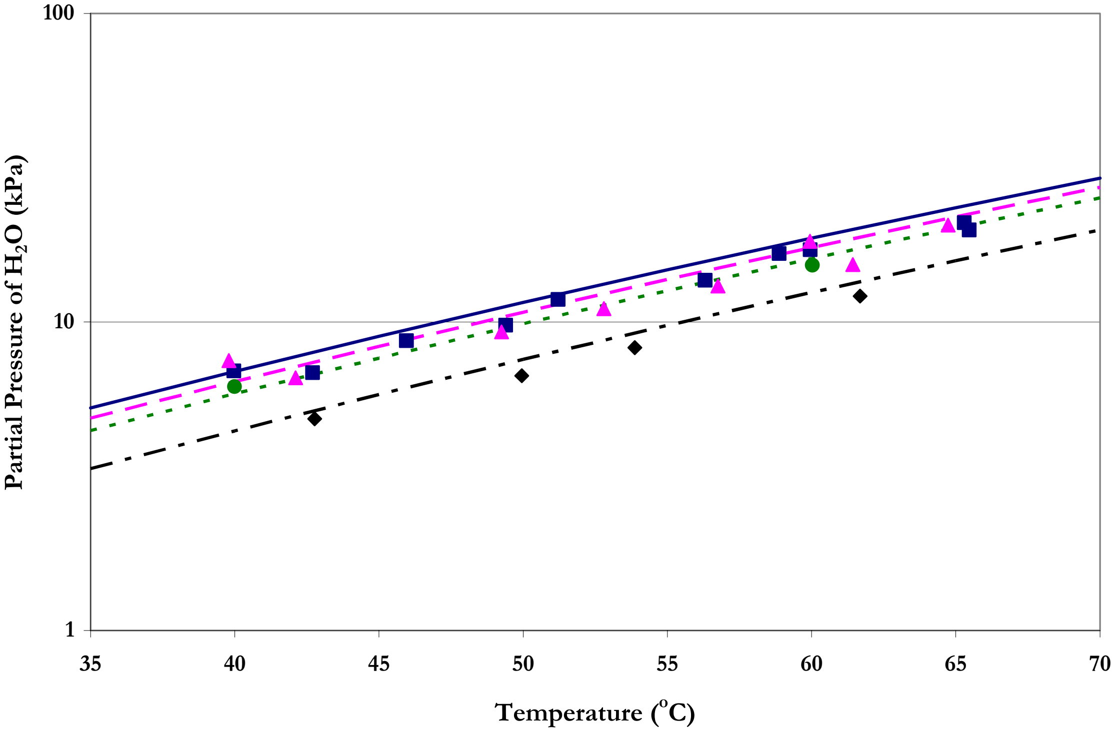

Figure 8.4-6. Comparison of Amine Volatility (e.g. Partial Pressure of Water) from this work to elecNRTL Model Predictions from 30 – 120 ^oC. Points: experimental data from this work ■, 3.5 m (mole/kg-H_2O), ▲, 7 m, ●, 11 m, ◆, 23.8 m. Lines: —, 3.5 m (mole/kg-H_2O) elecNRTL Predictions, – –, 7 m, - - -, 11 m, — ·, 23.8 m.

8.4.3 *Specific Heat Capacity*

To describe the specific heat capacity of H_2O-MEA solutions, we chose to concentrate our modeling efforts to describe the specific heat capacity from Chiu and Li (1999) and from this work due to the agreement between the two sources where specific heat capacity from Pagé et al. (1993) and Weiland et al. (1997) were limited to temperatures below 40 °C.

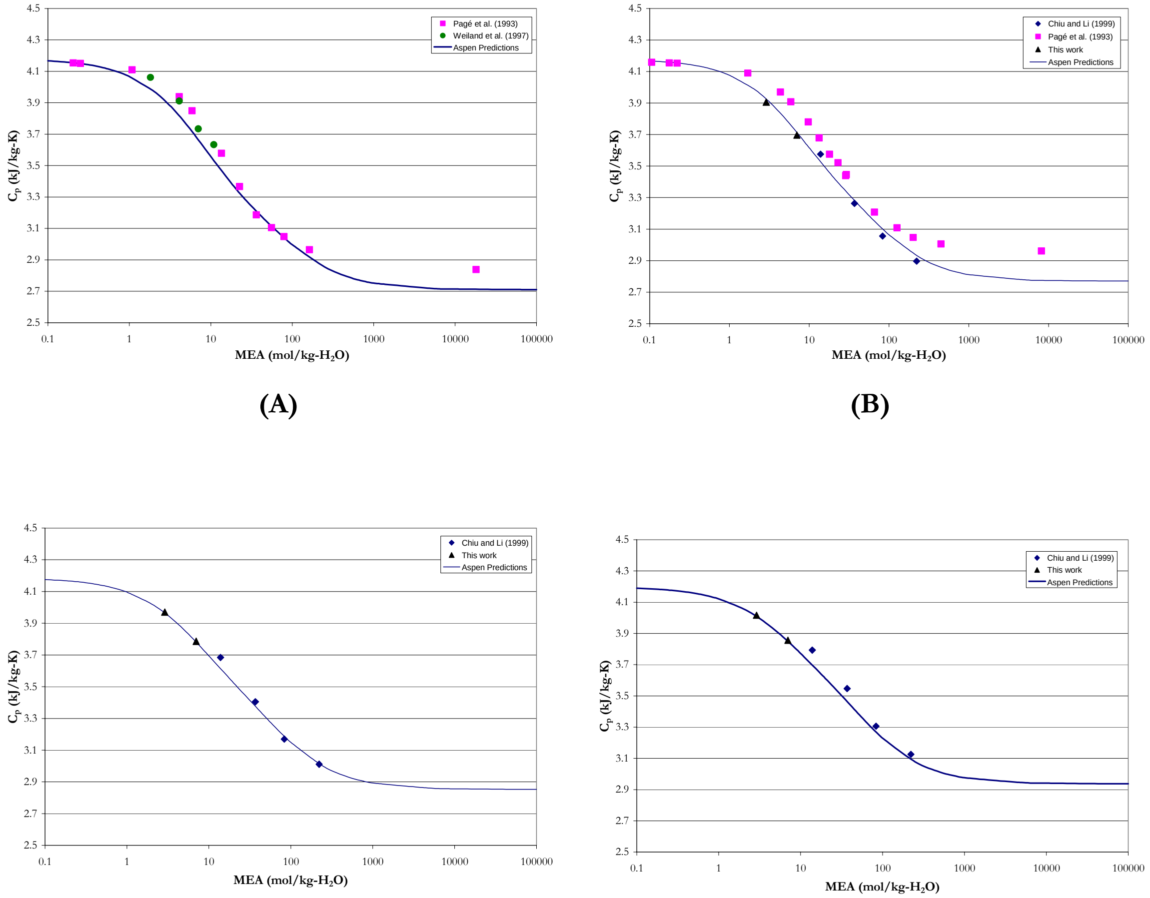

(A)

(B)

(C)

(D)

Figure 8.4-7. Comparison of Specific Heat Capacity from Pagé et al. (1993), Chiu and Li (1999), Weiland et al. (1997), and from this work to elecNRTL Model Predictions at 25.0 (A), 40.0 (B), 60.0 (C), and 80.0 °C (D).

Figure 8.4-7 compares estimated and experimental specific heat capacities from 25 to 80 °C over the full range of concentrations. Figure 8.4-7 also illustrates that the optimum model is consistent with the pure component specific heat capacities as discussed in Chapter VII. To use the H_2O and MEA parameters for an NRTL property model, please refer to

Chapter VII for more information on the pure component parameters. Otherwise, the specific heat capacity for the mixture will not have the correct pure component specific heat capacity for water as shown in Figure 8.4-8.

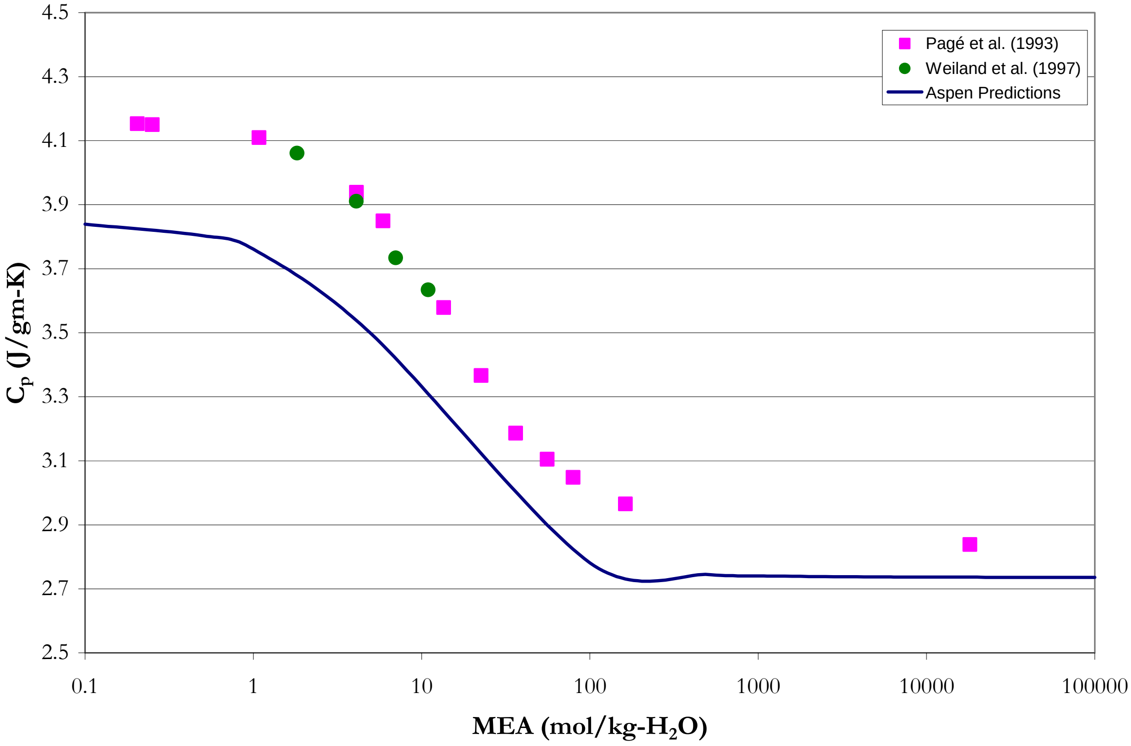

Figure 8.4-8. Comparison of Specific Heat Capacity from Pagé et al. (1993) and Weiland et al. (1997) to NRTL Model Predictions at 25.0 °C based on the default parameters for the DIPPR Heat of Vaporization Equation for H_2O.

Specific heat capacity predictions from this work are shown in Figure 8.4-9. Overall, the optimum model adequately describes the specific heat capacity for aqueous mixtures of MEA within an average absolute relative error of ± 1.38 percent, with the exception of a few outliers.

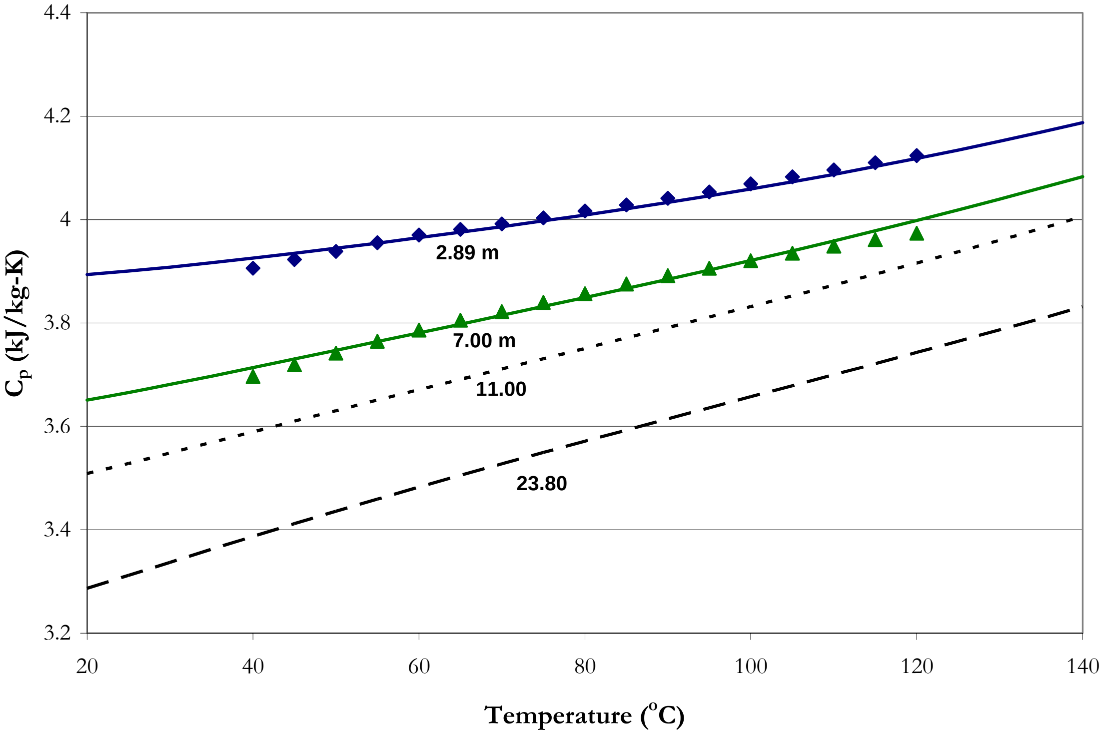

Figure 8.4-9. Comparison of Specific Heat Capacity from this work to elecNRTL Model Predictions for 2.89 – 23.80 m MEA.

8.4.4 *Freezing Point Depression*

Figure 8.4-10 compares estimated and experimental freezing point depression vis-à-vis vapor pressure of water from Chang et al. (1993) for aqueous MEA mixtures over the concentration range 0.86 – 0.995 mole fraction of H_2O from -20.5 to -0.5 °C. The optimum model reproduces the vapor pressure of water within an AARD of ± 0.35 percent.

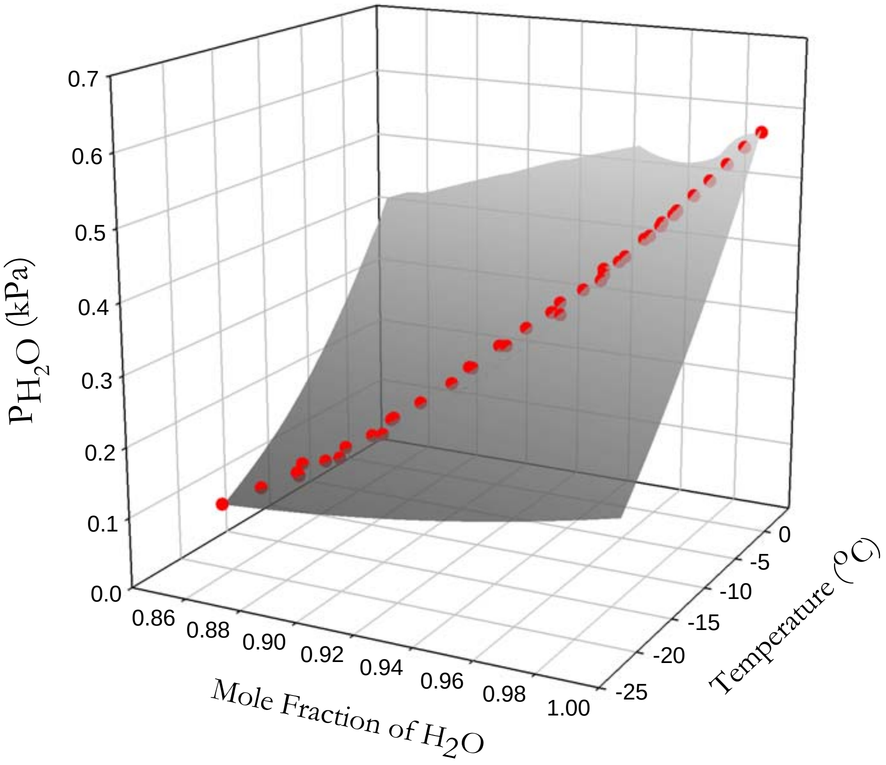

Figure 8.4-10. Comparison of Model Predictions with Experimental Data for Chang et al. (1993) Vapor Pressure Depression from - 20.5 to -0.5 °C.

8.4.5 *Excess Enthalpy Predictions for H_2O-MEA*

As stated at the beginning of this chapter, the elecNRTL model was never designed to regress excess enthalpy data thus we were required to reserve literature data from Touhara et al. (1982) and Posey (1996) until a comparison can be made from predictions based on an optimum set of binary interaction parameters. Thus, using the optimum model as a purely predictive model, the excess enthalpy for aqueous MEA mixtures were calculated based on Equation 8-15. On the other hand, Aspen Plus™ gives the following equation as an alternative procedure to calculate the excess enthalpy. Results based on the two methods are presented in Figures 8.4-11 and 8.4-12.

$$H_m^{E,l} = H_m^l - \sum_i x_i H_i^{*,l} \tag{8-46}$$

Where

$H_m^{E,l}$ is the liquid molar excess enthalpy of the mixture,

H_m^l is the liquid molar enthalpy of the mixture,

x_i is the mole fraction of component i,

$H_m^{*,l}$ is the pure liquid molar enthalpy of component i.

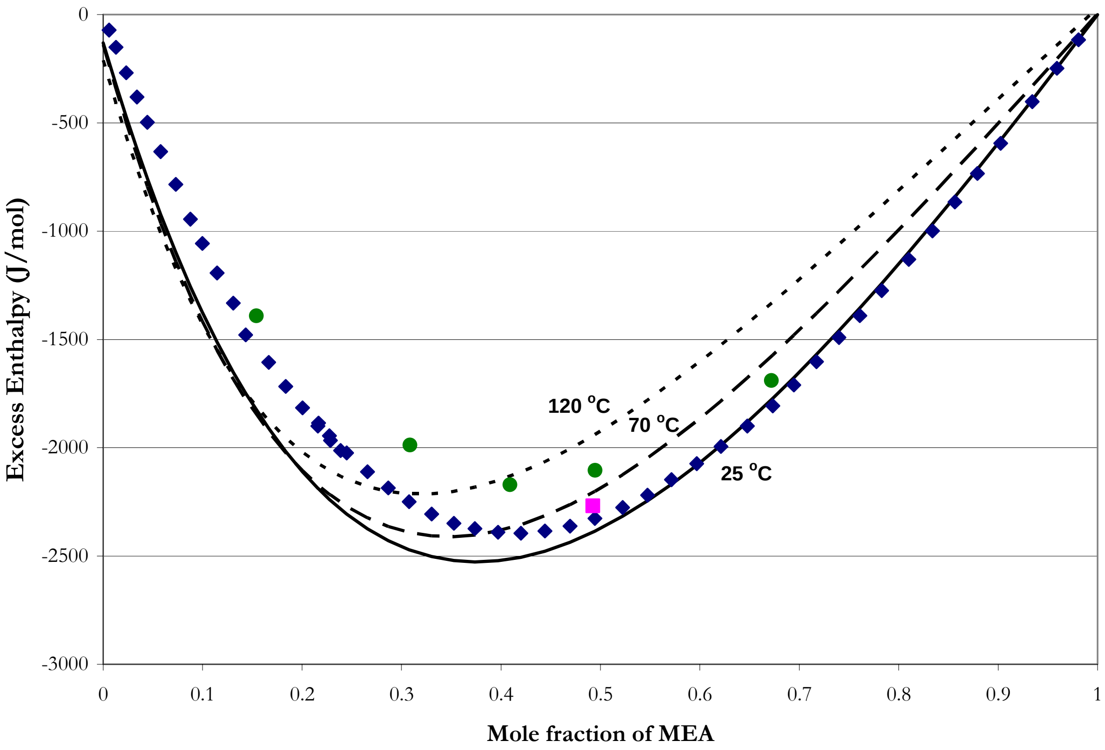

Figure 8.4-11. Comparison of Model Predictions with Experimental Excess Enthalpy Data for Touhara et al. (1982) and Posey (1996) at 25 and 70 °C Based on Equation 8-23. Points: ◆, Touhara et al. (1982) and ■, Posey (1996) at 25 °C, ●, Posey (1996) at 70 °C.

Figure 8.4-11 illustrates two important issues: one, the model was unable to predict the liquid enthalpy of pure water; two, the model does under predict the temperature dependence of the activity coefficients for MEA and H_2O. The above results would then contradict the previous discussion, vis-à-vis the representation of the optimum model to adequately represents the regressed literature data. Figure 8.4-12 validates previous work by demonstrating Equation 8-15 to calculate the excess enthalpy.

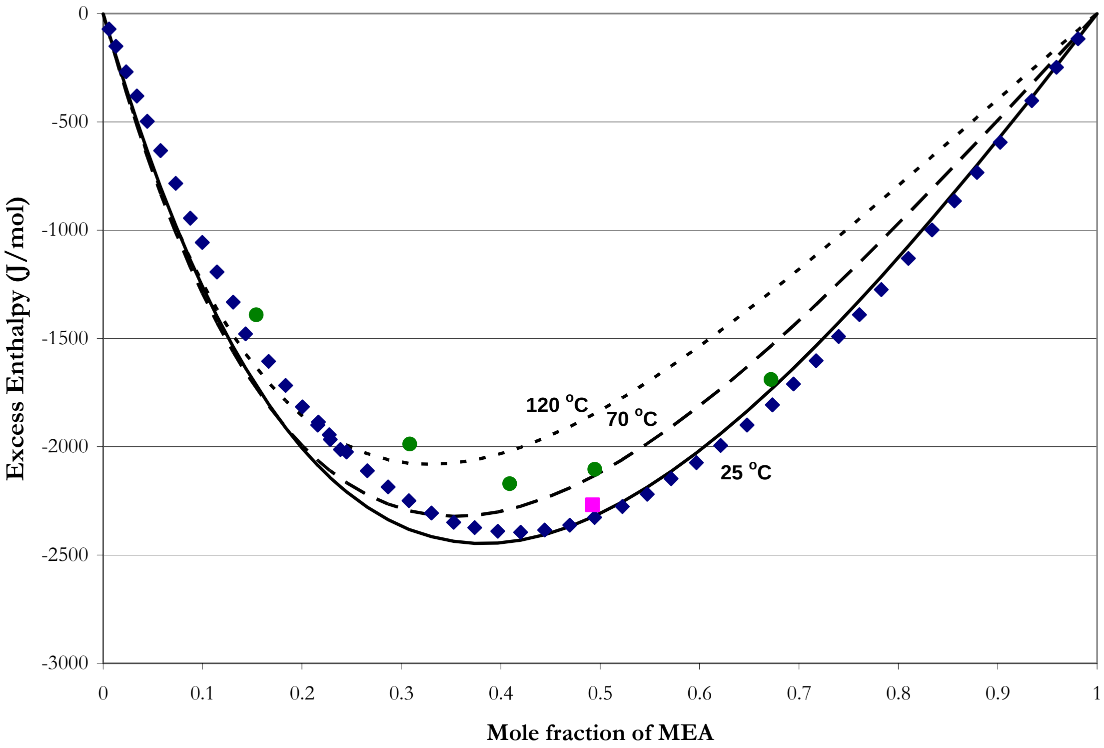

Figure 8.4-12. Comparison of Model Predictions with Experimental Excess Enthalpy Data for Touhara et al. (1982) and Posey (1996) at 25 and 70 °C Based on Equation 8-15. Points: ♦, Touhara et al. (1982) and ■, Posey (1996) at 25 °C, ●, Posey (1996) at 70 °C.

Even though the optimum model does not capture the excess enthalpy temperature dependence, the model does characterize the experimental data within an average absolute relative error of ± 9.17 percent. We would then recommend to Aspen Plus™ to include the excess enthalpy calculation route, based on equation 8-15, as part of the simulation package in the elecNRTL model.

8.4.6 *Activity Coefficient Predictions for H_2O-MEA*

Several authors have presented activity-based models to calculate the activity coefficient of MEA in aqueous MEA mixtures. Works include:

Author	Model
Deshmukh and Mather (1981)	Applying Guggenheim extension of the Debye-Hückel theory
Austgen et al. (1989)	Electrolyte-NRTL (Aspen Plus)
Weiland et al. (1993)	Applying Deshmukh-Mather Model
Li and Mather (1994)	Pitzer Equation
Lee (1996)	UNIFAC Group Contribution Method
Posey (1996)	Electrolyte-NRTL (Aspen Plus)
Kaewsichan et al. (2001)	Electrolyte-UNIQUAC Model
Poplsteinova (2004)	UNIFAC Group Contribution Method

All of the above authors had a limited database of experimental literature data to describe interactions between H_2O and MEA. In this work, we have compiled an extensive database of consistent high quality literature data. Thus, the subsequent discussion on predicting the activity coefficients for MEA in aqueous MEA mixtures will provide the most realistic values to date. Figure 8.4-13 compares activity coefficient predictions based on the works by Lee (1996), Prausnitz et al. (1999), and Poplsteinove (2004) described by the UNIFAC Group Contribution Method and the Wilson Equation as presented by Poplsteinove (2004).

Poplsteinove (2004) described predictions from Lee (1996) as producing a concentration dependent minimum with respect to the activity coefficient of MEA indicating an "azeotropic behavior." Lee (1996) based his work on excess enthalpy [Touhara et al. (1982) and Posey (1996)], vapor-liquid equilibrium [The Dow Chemical Company (1981)], and total pressure [Nath and Bender (1983) and Touhara et al. (1982)] data. In this work, we have increased the amount of literature data by including additional vapor-liquid equilibrium, amine volatility, specific heat capacity, and water vapor pressure depression data. In the end, Poplsteinove (2004) decided to adopt parameters from Lee (1996) into her work based on the agreement with predictions from his model to data found in the literature.

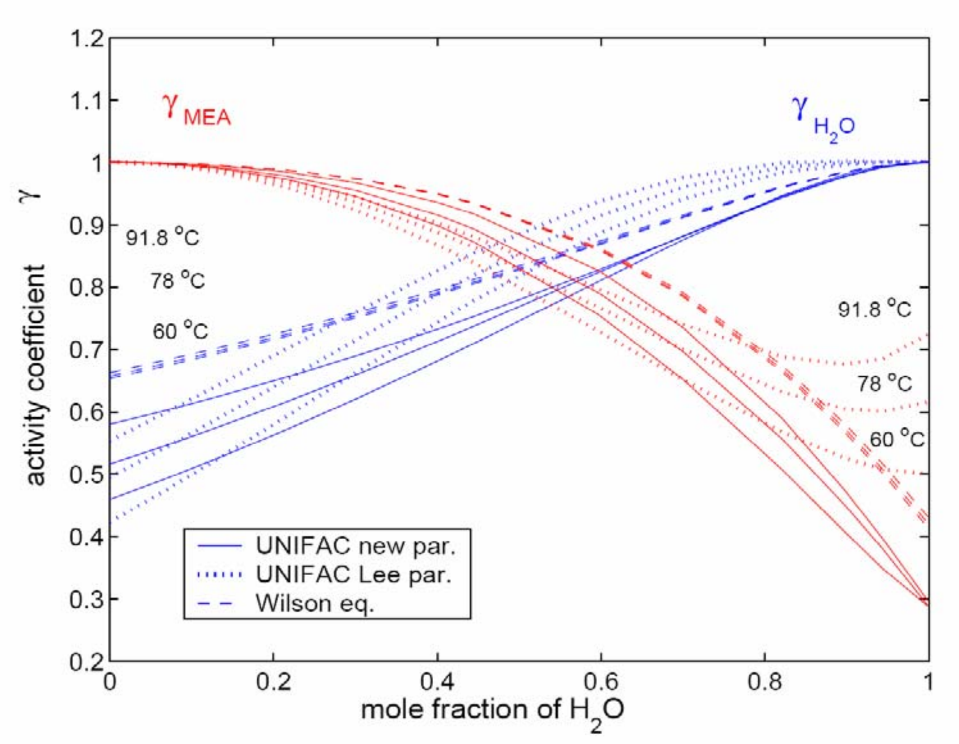

Figure 8.4-13. Predictions of Activity Coefficients for MEA and H2O as Presented by Poplsteinove (2004).

In this work, the optimum model also predicted a minimum value for the activity coefficient of MEA (x_{H2O} = 0.86, T = 120 °C) as shown in Figure 8.4-14, but the phase diagram at this temperature does not indicate the presence of an azeotrope (Figure 8.4-15). If we vary the temperature or pressure, results do not indicate the presence of an azeotropic state. Thus, the azeotropic behavior for the activity coefficient of MEA, as reported in Poplsteinove (2004), may not adequately describe this situation.

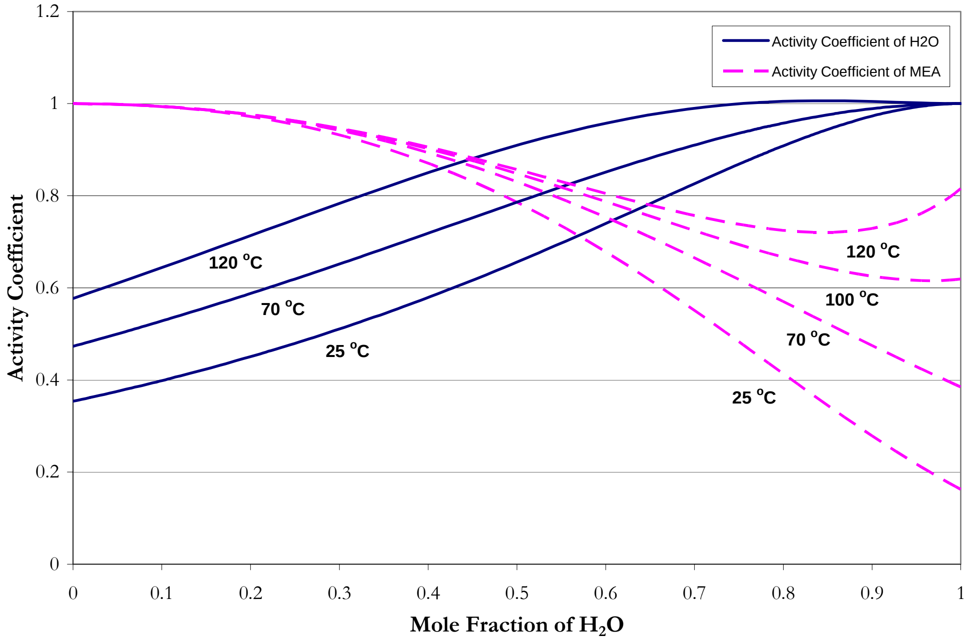

Figure 8.4-14. Model Predictions for the Activity Coefficient of Water and Monoethanolamine at 25, 70 and 120 °C.

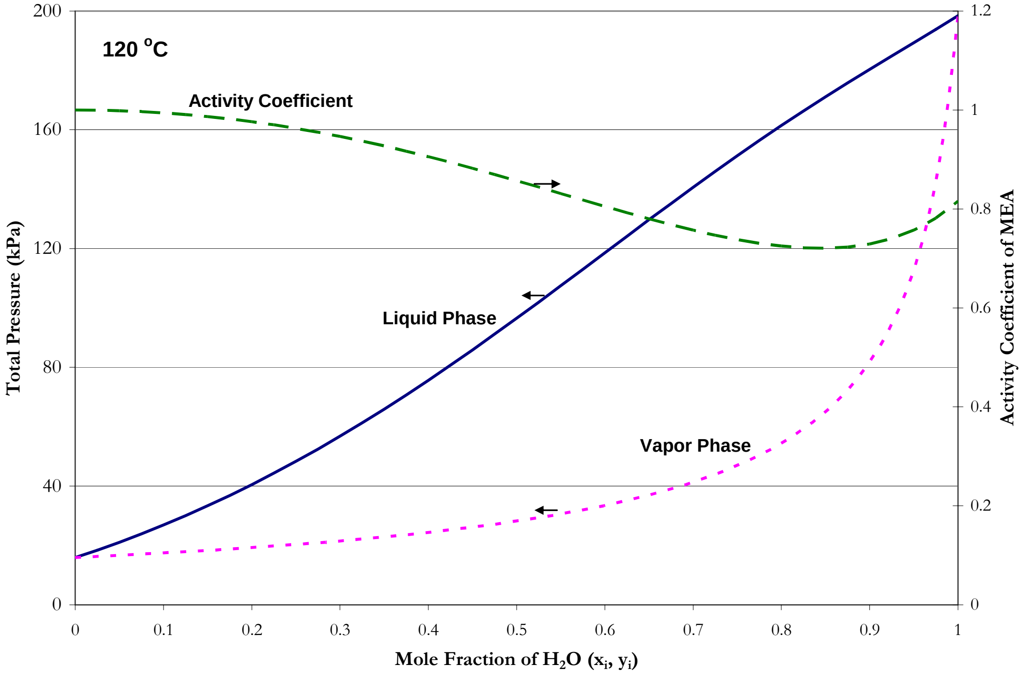

Figure 8.4-15. Pxy Diagram at 120 °C for H_2O-MEA mixtures based on the elecNRTL Model.

8.5 Abridged elecNRTL Predictive Correlations

To anticipate installation difficulties with the implementation of our model on future platforms, we have developed specific correlations based on predictive results from our rigorous thermodynamic model for the partial pressure of MEA and liquid phase specific heat capacity of H_2O-MEA based on experimental results from this work.

Correlations for the Partial Pressure of MEA

Predictions for the partial pressure of MEA for 3.5, 7, 11, and 23.8 m MEA based on the elecNRTL model, as shown in Figure 8.4-5, where related to the natural logarithm of the partial pressure of MEA by the following relation for two predictors:

$$\ln P_{MEA} = C_1 + \frac{C_2}{T} + C_3 \ln\left(T\right) + C_4 T + \frac{C_5}{\left[MEA\right]} + C_6 \ln\left(\left[MEA\right]\right) + C_7\left[MEA\right] + C_8\left[MEA\right]T \qquad \text{8-47}$$

Where
T is the temperature, K,
$\left[MEA\right]$ is the concentration of MEA, m (mole/kg-H_2O).

Equation 8-47 allows for nonlinearity in the temperature and concentration dependence. The interaction term $\left(\left[MEA\right]T\right)$ allows for twisting of the predictive surface versus the two predictors. Predictions from the elecNRTL model for the partial pressure of MEA are tabulated in Table 8.5-1.

Performing ordinary least squares (OLS) regression for the full model using ARC (2004), the following regression summary statistics output for coefficient estimates in Equation 8-47 are shown in Table 8.5-2.

Table 8.5-1. Tabulated Predictions for the P_{MEA} (kPa) from the elecNRTL Model.

	MEA Concentration (mole/kg-H_2O)			
Temperature (°C)	3.5	7	11	23.8
30	0.00111	0.002649	0.00479	0.0128
35	0.00180	0.004225	0.00754	0.0196
40	0.00286	0.006617	0.0117	0.0297
45	0.00448	0.0102	0.0177	0.0440
50	0.00689	0.0154	0.0264	0.0644
55	0.0104	0.0230	0.0389	0.0927
60	0.0156	0.0337	0.0564	0.13
65	0.0229	0.0488	0.0805	0.18
70	0.0331	0.0696	0.11	0.26
75	0.0474	0.0981	0.16	0.35
80	0.0669	0.14	0.22	0.47
85	0.0935	0.19	0.30	0.63
90	0.13	0.26	0.40	0.83
95	0.18	0.34	0.53	1.09
100	0.24	0.46	0.70	1.42
105	0.32	0.61	0.92	1.82
110	0.42	0.79	1.19	2.33
120	0.72	1.33	1.95	3.70

Table 8.5-2. ARC Regression Output for the Predictive Full P_{MEA} Correlation.

Parameter	Estimate	σ wrt Estimate
C_1	222	258
C_2	-15856	7607
C_3	-33.0	24.2
C_4	0.0346	0.0239
C_5	0.447	0.548
C_6	1.193	0.139
C_7	0.138	0.00826
C_8	-0.000420	0.000014

Residual Sum of Squares:	0.0385
Degree of Freedom:	64

Recall that the standard error of an estimate is the estimated standard deviation of that statistic. Notice that only one of the estimates (C_5) is smaller relative to the standard error. This term might be usefully removed from the model without significant loss of information. A complete description of the variability of the coefficient estimates requires examining the correlations between the estimates as shown in Table 8.5-3.

Table 8.5-3. Correlation Matrix of the Coefficient Estimates, for the Full P_{MEA} Model.

Parameter	1	2	3	4	5	6	7	8
1	1.00							
2	-0.97	1.00						
3	-0.97	*0.99*	1.00					
4	0.96	-0.97	*-0.99*	1.00				
5	-0.24	0.00	0.00	0.00	1.00			
6	-0.24	0.00	0.00	0.00	*0.99*	1.00		
7	0.23	0.00	0.00	0.01	-0.97	-0.98	1.00	
8	0.01	0.00	0.00	-0.07	0.00	0.00	-0.15	1.00

Table 8.5-3 shows three highly correlated coefficients between parameter estimates, $\hat{\eta}_{3\rightarrow 2}$, $\hat{\eta}_{3\rightarrow 2}$, and $\hat{\eta}_{3\rightarrow 2}$, but the correlation between other coefficients is relatively small, suggesting that C_3, C_4, and C_6, might be usefully removed from the model without significant loss of information. Using the Full Model as our base case, we can perform backward elimination using ARD to determine the optimum model as shown in Table 8.5-4.

From Table 8.5-4, the deletion of parameter C_5 from the Full Model gives the smallest change in the residual sum of squares (RRS) as compared to the other regression cases. We then chose Case 1 as the optimum model; the regression summary statistics output for coefficient estimates in Equation 8-47 based on Case 1 are shown in Table 8.5-4.

Table 8.5-4. P_{MEA} Backward Elimination Case Summary Results.

FULL MODEL	RSS	0.039

Case	Current terms: (C_2 C_3 C_4 C_5 C_6 C_7 C_8)				
			df	RSS	AARD (%)
1	Delete:	C_5	65	0.039	1.0
2	Delete:	C_7	65	0.045	17.9
3	Delete:	C_4	65	0.076	98.5
4	Delete:	C_6	65	0.081	111.0
5	Delete:	C_2	65	0.087	124.7
6	Delete:	C_3	65	0.189	390.4
7	Delete:	C_8	65	0.561	1356.1

Case	Current terms: (C_2 C_3 C_4 C_6 C_7 C_8)				
			df	RSS	AARD (%)
8	Delete:	C_4	66	0.077	99.5
9	Delete:	C_2	66	0.087	125.7
10	Delete:	C_3	66	0.189	391.4
11	Delete:	C_7	66	0.209	441.5
12	Delete:	C_8	66	0.561	1357.1
13	Delete:	C_6	66	3.194	8195.6

Case	Current terms: (C_2 C_3 C_6 C_7 C_8)				
			df	RSS	AARD (%)
14	Delete:	C_7	67	0.240	524.1
15	Delete:	C_8	67	0.583	1413.4
16	Delete:	C_2	67	2.691	6890.2
17	Delete:	C_6	67	3.232	8294.1
18	Delete:	C_3	67	17.390	45065.6

Case	Current terms: (C_2 C_3 C_6 C_8)				
			df	RSS	AARD (%)
19	Delete:	C_8	68	0.584	1416.6
20	Delete:	C_2	68	2.716	6953.9
21	Delete:	C_6	68	10.644	27545.5
22	Delete:	C_3	68	18.057	46798.4

Case	Current terms: (C_2 C_3 C_6)				
			df	RSS	AARD (%)
23	Delete:	C_2	69	2.789	7143.9
24	Delete:	C_3	69	19.375	50219.7
25	Delete:	C_6	69	39.844	103383.1

Table 8.5-5. ARC Regression Output for the Predictive Optimum P_{MEA} Correlation.

Parameter	Estimate	σ wrt Estimate
C_1	222	157
C_2	-15856	7587
C_3	-33.0	24.1
C_4	0.0346	0.0238
C_6	1.0804	0.0146
C_7	0.143	0.00501
C_8	-0.000420	0.0000140

Residual Sum of Squares: 0.0388
Degree of Freedom: 65

Notice that all of the estimates are larger relative to their standard errors. Comparing the estimates from the full model to the optimum model, there was relatively little difference between the estimated values. The proposed optimum model provides the following correlations between the estimates as shown in Table 8.3-5.

Table 8.5-6. Correlation Matrix of the Coefficient Estimates, for the Optimum P_{MEA} Model.

Parameter	1	2	3	4	5	6	7
1	1.00						
2	*-1.00*	1.00					
3	*-1.00*	*0.99*	1.00				
4	*0.99*	*-0.97*	*-0.99*	1.00			
5	-0.01	0.00	0.00	0.00	1.00		
6	0.00	0.00	0.00	0.04	-0.76	1.00	
7	0.01	0.00	0.00	-0.07	0.00	-0.61	1.00

Table 8.5-6 shows highly negative correlations between all of the temperature dependent parameters suggesting that some of the remaining parameters might be usefully removed from the model without significant loss of information. From Table 8.5-4 illustrated the point with further parameter elimination the deviation between the submodel and the full model increases beyond an adequate level for the predictive correlation to describe systematic trends in the smoothed data. Figure 8.5-1 demonstrates the predictive

quality of Equation 8-44 based on coefficients from Table 8.5-5 for the optimum model. The functional form of Equation 8-45 adequately describes the predictions from the elecNRTL model within an average absolute relative error of ± 1.83 percent., presented in Figure 8.5 1.

$$\ln P_{MEA}(kPa) = 222 - \frac{15856}{T(K)} - 33.0 \ln T(K) + 0.0346T(K) + 1.08 \ln([MEA]) + \ldots \qquad \text{8-48}$$
$$\ldots + 0.143[MEA] - 0.000420[MEA]T(K)$$

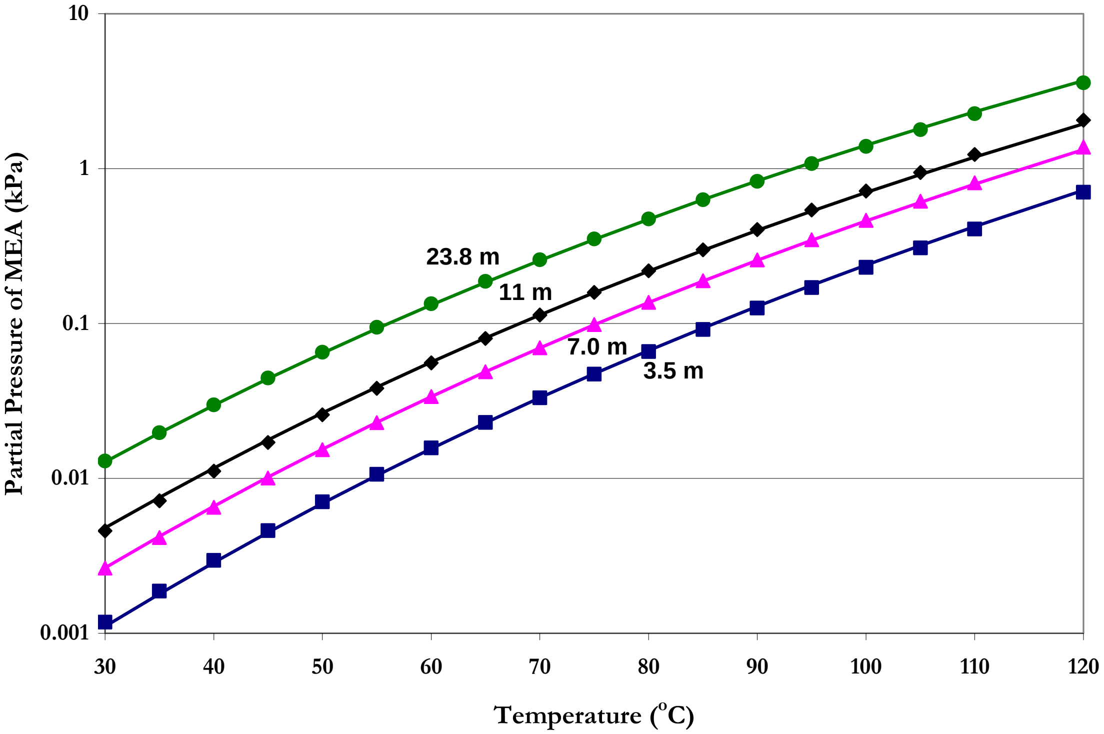

Figure 8.5-1. Comparison of Amine Volatility Predictions from Equation 8-45 to elecNRTL Model Predictions from 30 – 120 °C. Points: Smooth Prediction at ■, 3.5 m (mole/kg-H_2O), ▲, 7 m, ♦, 11 m, ●, 23.8 m. Lines: ▬, original elecNRTL Predictions.

Since there are only minor differences between Equation 8-45 and the predictions from the elecNRTL model, we can illustrate thermal effects of the solution equivalent to the effective heat of vaporization of MEA from water given by the following equation:

$$-\frac{\Delta H}{R}=\frac{d\ln P_{MEA}}{d1/T} \tag{8-49}$$

Substituting Equation 8-45 into Equation 8-46 and evaluating the derivative gives the following relationship for the effective heat of vaporization of MEA from water.

$$-\frac{\Delta H}{R}=\frac{d\ln P_{MEA}}{d1/T}=-15856+33.0T\left(K\right)-\left(0.0346+0.000420\left[MEA\right]\right)T\left(K\right)^{2} \tag{8-50}$$

Over absorber and stripper conditions, the effective heat of vaporization of MEA from water (kJ/mol) at 3.5, 7, 11, and 23.8 m MEA is given in Table 8.5-7.

Table 8.5-7. Effective Heat of Vaporization of MEA from H_2O (kJ/mol-MEA).

	MEA Concentration (mole/kg-H_2O)			
Temperature (°C)	3.5	7	11	23.8
40	-73.01	-71.81	-70.44	-66.04
80	-69.40	-67.88	-66.13	-60.55
120	-66.68	-64.79	-62.63	-55.71

The effective heat of vaporization of MEA from H_2O given in Table 8.5-7 reflects a relatively high heat of solution associated with strong interactions between H_2O and MEA. Thus, to evolve MEA from the liquid phase requires the heat of vaporization of pure MEA plus the effective heat of vaporization of MEA from H_2O. Recovery of MEA in industrial applications (i.e. absorber water washing) would require an additional parameter, in this case temperature, to design an effective process.

Correlations for the Specific Heat Capacity

Predictions for the specific heat capacity for 2.89, 7, 11, and 23.8 m MEA based on the elecNRTL model, as shown in Figure 8.4-9, where related to the following relation for two predictors:

$$C_p^l\left(\frac{kJ}{kg\cdot K}\right)=C_1+C_2T+C_3T^2+C_4\left[MEA\right]+C_5\left[MEA\right]^2+C_6\left[MEA\right]T \qquad 8\text{-}51$$

Where
T is the temperature, °C,
$\left[MEA\right]$ is the concentration of MEA, m (mole/kg-H_2O).

Equation 8-51 allows for nonlinearity in the temperature and concentration dependence. The interaction term $\left(\left[MEA\right]T\right)$ allows for twisting of the predictive surface versus the two predictors. Predictions from the elecNRTL model for the partial pressure of MEA are tabulated in Table 8.5-8.

Table 8.5-8. Specific Heat Capacity Predictions (kJ/kg-K) from the elecNRTL model.

	MEA Concentration (mole/kg-H_2O)			
Temperature (°C)	2.89	7.0	11.0	23.8
40	3.926	3.714	3.589	3.387
50	3.945	3.747	3.630	3.436
60	3.965	3.781	3.671	3.482
70	3.986	3.815	3.711	3.527
80	4.009	3.849	3.751	3.571
90	4.033	3.885	3.791	3.614
100	4.059	3.921	3.832	3.657
110	4.088	3.959	3.873	3.700
120	4.118	3.998	3.916	3.743

Performing ordinary least squares (OLS) regression for the full model using ARC (2004), the following regression summary statistics output for coefficient estimates in Equation 8-51 are shown in Table 8.5-9.

Table 8.5-9. ARC Regression Output for the Predictive Full CPMX Correlation.

Parameter	Estimate	σ wrt Estimate
C_1	3.93	0.0188
C_2	0.00229	0.000455
C_3	0.000002	0.000003
C_4	-0.0519	0.00114
C_5	0.000904	0.000034
C_6	0.000084	0.000008

Residual Sum of Squares: 0.0092
Degree of Freedom: 62

Recall that the standard error of an estimate is the estimated standard deviation of that statistic. Notice that only one of the estimates (C_3) is smaller relative to the standard error. This term might be usefully removed from the model without significant loss of information. A complete description of the variability of the coefficient estimates requires examining the correlations between the estimates as shown in Table 8.5-3.

Table 8.5-10. Correlation Matrix of the Coefficient Estimates, for the Full P_{MEA} Model.

Parameter	1	2	3	4	5	6
1	1.00					
2	-0.93	1.00				
3	0.85	-0.97	1.00			
4	-0.40	0.10	*0.00*	1.00		
5	0.23	*0.00*	*0.00*	-0.83	1.00	
6	0.37	-0.19	*0.00*	-0.54	*0.00*	1.00

Table 8.5-3 shows five independent coefficients between parameter estimates, $\hat{\eta}_{4\to3}$, $\hat{\eta}_{5\to2}$, $\hat{\eta}_{5\to3}$, $\hat{\eta}_{6\to3}$, and $\hat{\eta}_{6\to5}$, but the correlation between other coefficients is relatively small, suggesting that C_3 and C_5, might be usefully removed from the model without significant loss of information. Using the Full Model as our base case, we can perform

backward elimination using ARC (2004) to determine the optimum model as shown in Table 8.5-11.

With the deletion of parameter C_3 from the Full Model gives the smallest change in the RRS as compared to the other regression cases. We then chose Case 1 as the optimum model; Table 8.5-12 gives the regression summary statistics output for coefficient estimates in Equation 8-51 based on Case 1.

Table 8.5-11. CPMX Backward Elimination Case Summary Results.

FULL MODEL RSS 0.0092

Case	Current terms: (C_2 C_3 C_4 C_5 C_6)		df	RSS	AARD (%)
1	Delete:	C_3	63	0.0093	1.2
2	Delete:	C_2	63	0.0130	40.9
3	Delete:	C_6	63	0.0267	190.0
4	Delete:	C_5	63	0.1162	1162.3
4	Delete:	C_4	63	0.3165	3339.9

Case	Current terms: (C_2 C_4 C_5 C_6)		df	RSS	AARD (%)
6	Delete:	C_6	64	0.0268	191.1
7	Delete:	C_2	64	0.1048	1039.4
8	Delete:	C_5	64	0.1163	1163.4
9	Delete:	C_4	64	0.3166	3341.1

Case	Current terms: (C_2 C_4 C_5)		df	RSS	AARD (%)
10	Delete:	C_5	65	0.1337	1353.4
11	Delete:	C_4	65	0.3561	3769.8
12	Delete:	C_2	65	0.5552	5933.7

Case	Current terms: (C_2 C_4)		df	RSS	AARD (%)
13	Delete:	C_2	66	0.6622	7096.0
14	Delete:	C_4	66	1.7944	19401.0

Table 8.5-12. ARC Regression Output for the Predictive Optimum CPMX Correlation.

Parameter	Estimate	σ wrt Estimate
C_1	3.92	0.010
C_2	0.00267	0.000105
C_4	-0.0519	0.00114
C_5	0.000904	0.000034
C_6	0.000084	0.000008

Residual Sum of Squares: 0.0093
Degree of Freedom: 63

Notice that all of the estimates are larger relative to their standard errors. Comparing the estimates from the full model to the optimum model, there was relatively little difference between the estimated values. The proposed optimum model provides the following correlations between the estimates as shown in Table 8.5-6.

Table 8.5-13. Correlation Matrix of the Coefficient Estimates, for the Optimum P_{MEA} Model.

Parameter	1	2	3	4	5
1	1.00				
2	-0.86	1.00			
3	-0.78	0.44	1.00		
4	0.43	*0.00*	-0.83	1.00	
5	0.71	-0.82	-0.54	*0.00*	1.00

Table 8.5-6 shows only two independent correlations between all of the parameter estimates suggesting that some of the remaining parameters might be usefully removed from the model without significant loss of information. Table 8.5-5 demonstrated that with further elimination of parameters, the deviation between the possible submodels and the full model increases beyond an adequate level for the predictive correlation to describe systematic trends in the smoothed data.

Figure 8.5-2 demonstrates the predictive quality of Equation 8-48 based on coefficients from Table 8.5-12 for the optimum model. The functional form of Equation 8-

48 adequately describes the predictions from the elecNRTL model within an average absolute relative error of ± 0.25 percent.

Since there are only minor differences between Equation 8-48 and the predictions from the elecNRTL model, we can illustrate nonideality of the solution equivalent to the excess specific heat capacity using the Redlich-Kister equation to represent the concentration dependence as shown in Equation 8-49.

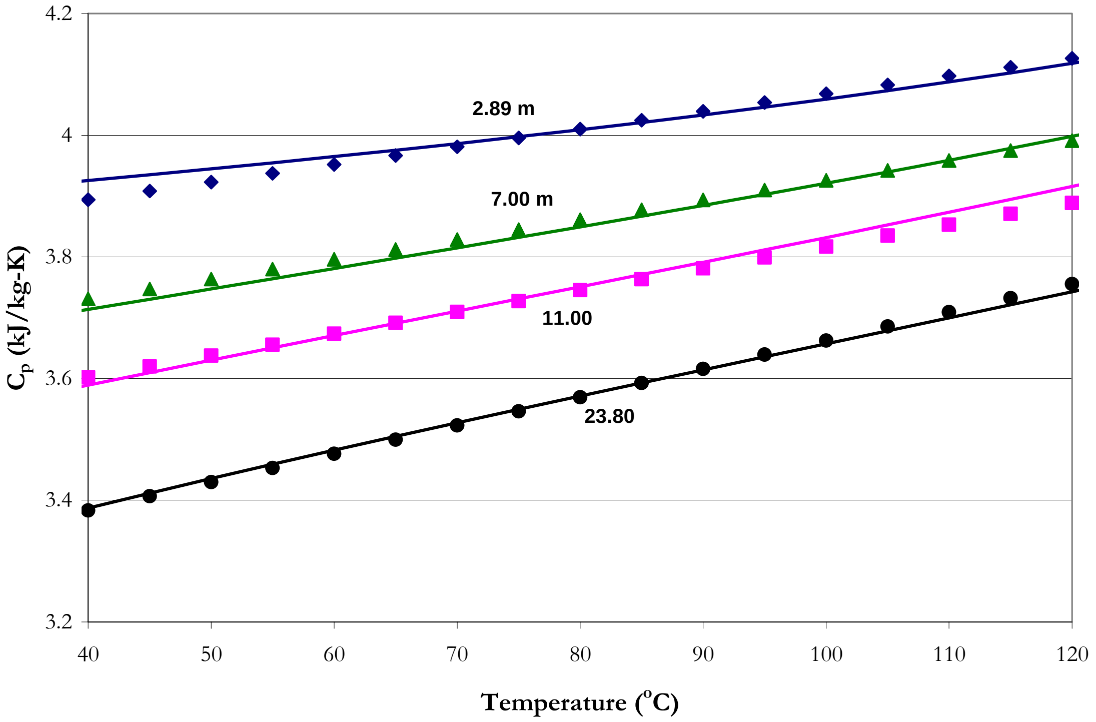

Figure 8.5-2. Comparison of Specific Heat Capacity Predictions from Equation 8-48 to elecNRTL Model Predictions from 40 – 120 °C. Points: Smooth Prediction at ♦, 2.89 m (mole/kg-H_2O), ▲, 7 m, ■, 11 m, ●, 23.8 m. Lines: —, original elecNRTL Predictions.

$$C_p^E = C_p^l - \left(x_{H_2O}C^*_{p,H_2O} - x_{MEA}C^*_{p,MEA}\right) \tag{8-52}$$

Where

C_p^E is the excess specific heat capacity, kJ/kmol-K,

C_p^l is the molar heat capacity of the mixture, Equation 8-48,
x_i is the mole fraction of component i,
$C_{p,i}^*$ is the pure component molar heat capacity (ref. Chapter VII).

In general, the value of the excess specific heat capacity will indicate the degree of nonideality of the binary mixture; as the value of the excess specific heat capacity decreases, the closer the binary mixture will approach an ideal solution. Figure 8.5-3 illustrates the departure from ideal behavior as compared to predictions from the elecNRTL model.

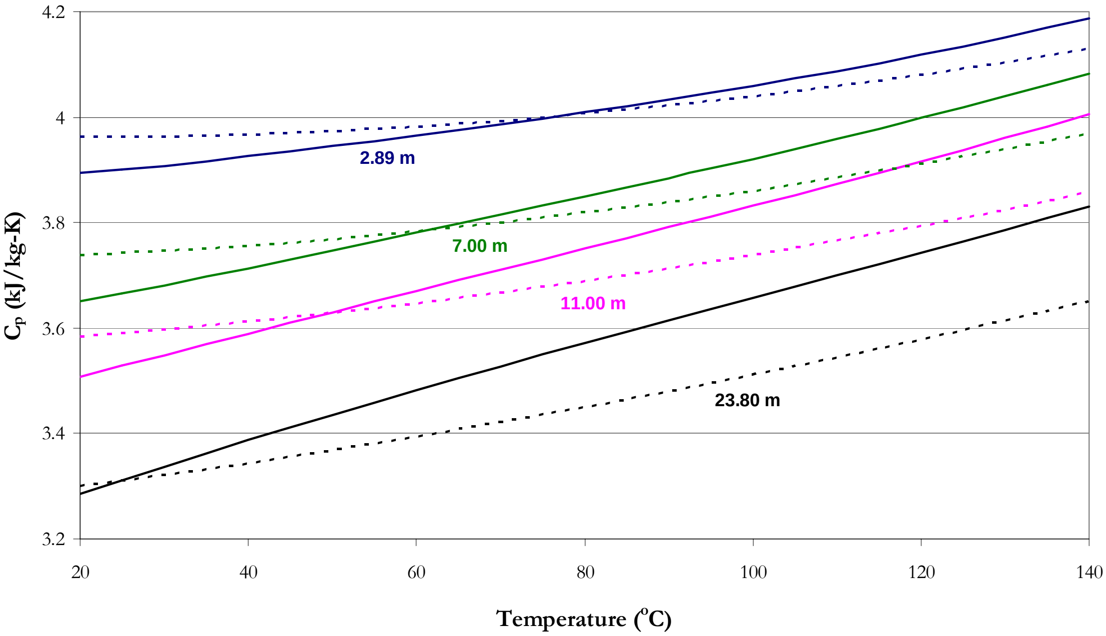

Figure 8.5-3. Comparison of elecNRTL Model Predictions of Ideal and Solution Specific Heat Capacity from 20 – 140 °C. Lines: - - -, Ideal Behavior, ▬, Solution Behavior.

Figure 8.5-3 demonstrates that as the concentration of MEA increases, the nonideality of the solution also increases. An ideal solution can adequately describe the specific heat capacity for 2.89 m MEA within ± 1.0 %, but for concentrations greater than 7 m MEA, this ability breaks down. As far as the degree of nonideality, the ratio of the excess specific heat capacity to the solution specific heat capacity has been shown to be a suitable replacement factor for the absolute value of the excess heat capacity (Chiu and Li (1999)).

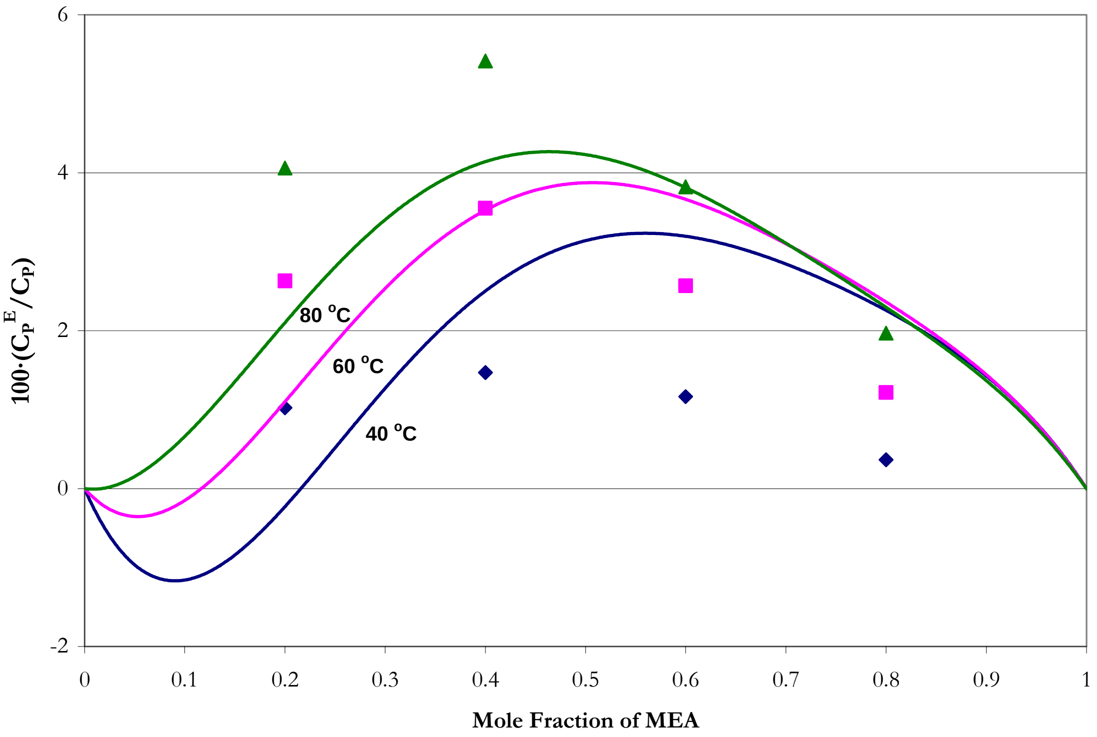

Figure 8.5-4. The Ratio of the Excess Specific Heat Capacity to the Mixture Specific Heat Capacity based on Predictions from the elecNRTL Model as compared to Chiu and Li (1999) at 40, 60, and 80 °C. Points: Chiu and Li (1999) ◆, 40 °C, , ■, 60 °C, and ▲, 80 °C. Lines: —, elecNRTL Predictions.

Figure 8.5-4 illustrates the differences between the two authors to describe the ideal solution since we have already shown the elecNRTL model to match the specific heat capacity of the solution within ± 1.37 %. As shown in Chapter XIII, Chiu and Li (1999) over predicted the specific heat capacity of H_2O and MEA as compared to previous authors. This discrepancy would explain the difference shown in Figure 8.5-4 in addition to the behavior shown in Figure 8.5-3. Chiu and Li (1999) described the excess specific heat capacity with a Redlich-Kister expansion taking into account concentration and temperature dependences. Chiu and Li (1999) noted a 60 % AARD between the model predictions and calculated results for the excess specific heat capacity, but concluded the calculated values looked reasonable.

Using the elecNRTL model, we can extend the description of the behavior of excess properties of liquid H_2O-MEA mixtures. Those of primary interest are the excess Gibbs free energy $\left(G^E / RT\right)$ in addition to the excess enthalpy or heat of mixing $\left(H^E / RT\right)$ which is related to the temperature derivative of the excess Gibbs free energy, where the excess entropy is normally calculated from the following equation

$$G^E = H^E - TS^E \qquad 8\text{-}53$$

Figure 8.5-5 demonstrates the composition dependence of G^E, H^E, TS^E, and C_P^E for H_2O-MEA mixtures at 40 °C. Even though the system exhibits a diverse behavior, we can note some common features for excess properties:

1. All excess properties are zero for each pure component.
2. G^E may exhibit a parabolic shape, the structure of H^E and TS^E predictions are concentration dependent.

Figure 8.5-5 exhibits only one sign for the value of the excess properties, but the relative magnitudes of these quantities are useful for describing the solution behavior, in particular, the behavior of G^E in relation to H^E contributions. Abbott et al. (1994) presented a visual scheme to identify patterns in different mixture types based on a dimensionless form of Equation 8-50

$$\frac{G^E}{RT} = \frac{H^E}{RT} - \frac{S^E}{R} \tag{8-54}$$

where each contribution for the three excess properties defined a region on a plot of G^E/RT versus H^E/RT.

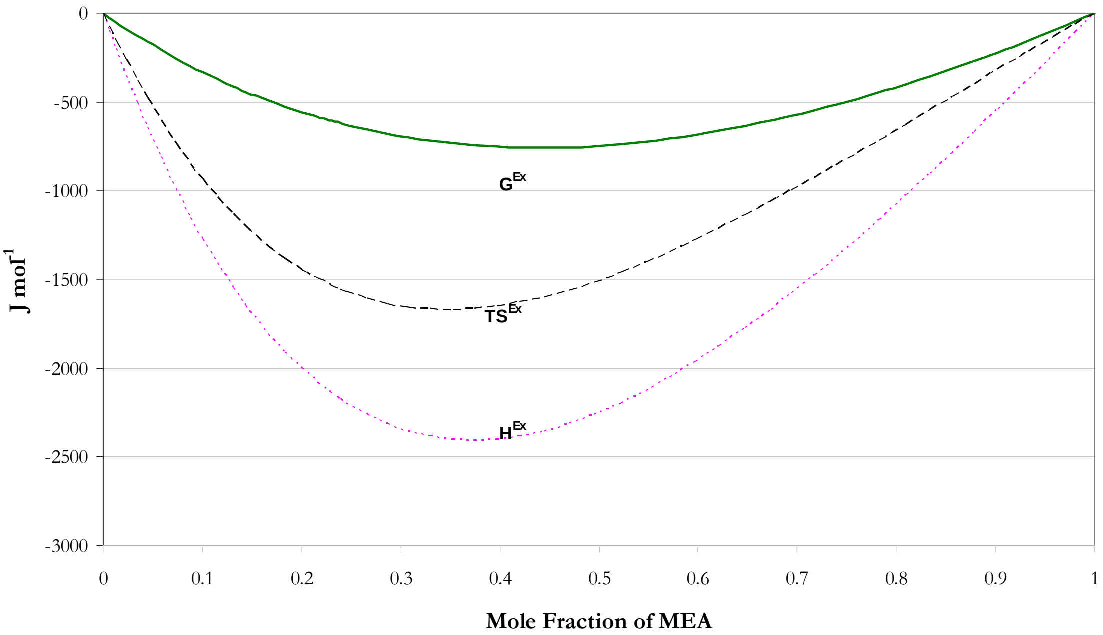

Figure 8.5-5. Excess Properties for H_2O-MEA Mixtures at 40 °C. Lines: —, G^{Ex}, — —, TS^{Ex}, and - - -, H^{Ex}.

For mixtures of H_2O-MEA, Figure 8.5-6 illustrates the enthalpy dominates the solution behavior over the absorption and regeneration temperature range because, mixtures of H_2O-MEA offer a variety of opportunities for hydrogen-bonded dimers by either solvation or by association with respect to the molecular functional groups.

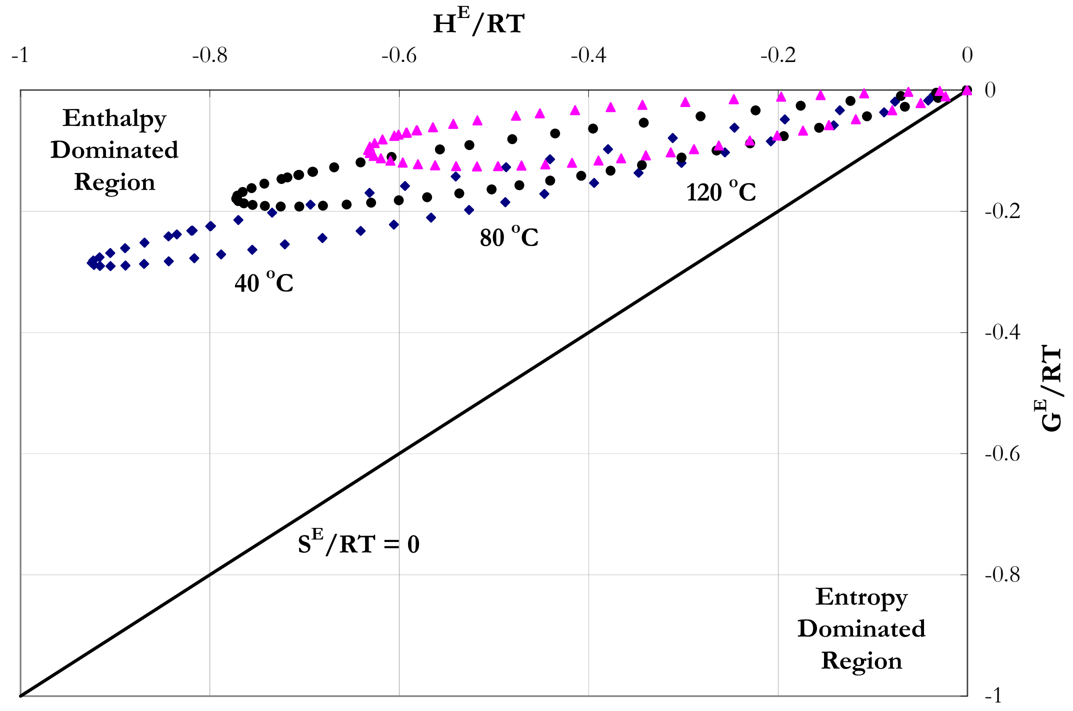

Figure 8.5-6. Equimolar Excess Properties for H_2O-MEA Mixtures at 40, 80 and 120 °C.

8.6 Conclusions

To sum up, in this work we chose to use Equation 8-24 to represent the infinite dilution activity coefficient of monoethanolamine due to the small variations between Equation 8-24 and Equation 8-25. Based on the optimum model, parameters were fitted to a more extensive database than previous authors, thus infinite dilution activity coefficients predicted with the optimum model may give more realistic activity coefficients as a function of temperature and composition as compared to data found in the literature.

We saw that Figure 8.3-3 illustrated similar trends presented in Figure 8.3-2 where predictions for the infinite dilution activity coefficient for MEA reported by Austgen et al. (1989) as compared to predictions from this work crossed at 45 °C. Since both works used

Bates and Pinching (1951) to describe the dissociation of MEA, the only differences between the two reported K-values would be in the treatment of the infinite dilution activity coefficient of MEA applied to the linearization of the chemical equilibrium constant to the temperature dependent functional form.

In addition, the difference between the two predictions for the aqueous phase infinite dilution heat capacity of $MEAH^+$ accounted for differences is in the treatment of the activity coefficient of MEA at infinite dilution as shown in Figure 8.3-2 and in the linearization of the equilibrium constant for MEA.

Figure 8.4-1 and Figure 8.4-2 illustrated the departure from an ideal solution behavior vis-à-vis Raoult's Law as compared to predictions from the elecNRTL model. Over the temperature range from 25 to 91.7 °C, Raoult's Law adequately described the vapor pressure of H_2O-MEA mixtures below $x_{MEA} = 0.1$, but as the concentration of MEA increases so does the importance of including activities to describe the vapor-liquid equilibrium.

Figure 8.4-3 gave the results of fit for experimental isobaric (*Txy*) vapor-liquid equilibrium (VLE) data from Park and Lee (1997) and Cai et al. (1996) versus the concentration of water at 101.325 kPa. Given the degree of scatter between Park and Lee (1997) and Cai et al. (1996) to describe *Txy* behavior of H_2O-MEA mixtures at atmospheric pressure allowed Raoult's Law and the elecNRTL model to describes systematic trends presented in both data sets adequately. Overall, the optimum model adequately describes the *Txy* data within an average absolute relative error of ± 2.82 percent.

We chose to concentrate our modeling efforts to describe the partial pressure of MEA (amine volatility) between 3.5 and 7.0 m MEA due to limited data at 11.0 and 23.8 m MEA. Overall, the optimum model adequately describes the partial pressure of MEA within an average absolute relative error of ± 4.28 percent, with the exception of a few outliers. In addition, the optimum model adequately described the partial pressure of water within an average absolute relative error of ± 6.64 percent, with the exception of a few outliers. We would recommend that future work should endeavor to describe the binary system at stripper conditions (e.g. temperatures between 80 - 120 °C) to complete this analysis.

In terms of excess enthalpy, Figure 8.4-11 illustrated two important issues: one, the proposed Aspen method was unable to predict the liquid enthalpy of pure water; two, the method under predicted the temperature dependence of the activity coefficients for MEA and H_2O. The above results would then contradict the previous discussion, vis-à-vis the representation of the optimum model to adequately represent the regressed literature data. Figure 8.4-12 validated previous work by demonstrating Equation 8-15's ability to calculate the excess enthalpy. Even though the optimum model does not capture the excess enthalpy temperature dependence, the model does characterize the experimental data within an average absolute relative error of ± 9.17 percent.

In this work, the optimum model predicted a minimum value for the activity coefficient of MEA (x_{H2O} = 0.86, T = 120 °C) as shown in Figure 8.4-14, but the phase diagram at this temperature did not indicate the presence of an azeotrope (Figure 8.4-15). If we vary the temperature or pressure, results do not indicate the presence of an azeotropic state. Thus, the azeotropic behavior for the activity coefficient of MEA, as reported in Poplsteinove (2004), may not adequately describe this situation.

The effective heat of vaporization of MEA from H_2O given in Table 8.5-7 reflects a relatively high heat of solution associated with strong interactions between H_2O and MEA. Thus, to evolve MEA from the liquid phase requires the heat of vaporization of pure MEA plus the effective heat of vaporization of MEA from H_2O. Recovery of MEA in industrial applications (i.e. absorber water washing) would require an additional parameter, in this case temperature, to design an effective process.

Figure 8.5-4 illustrated the differences between Chiu and Li (1999) and this work to describe the ideal. As shown in Chapter XIII, Chiu and Li (1999) over predicted the specific heat capacity of H_2O and MEA as compared to previous authors. This discrepancy would explain the difference shown in Figure 8.5-4 in addition to the behavior shown in Figure 8.5-3. Chiu and Li (1999) described the excess specific heat capacity with a Redlich-Kister expansion taking into account concentration and temperature dependences, but noted a 60 % AARD between the model predictions and calculated results for the excess specific heat capacity. They concluded the calculated values looked reasonable.

For mixtures of H_2O-MEA, Figure 8.5-6 illustrated that as compared to the excess Gibbs free energy the enthalpy dominates the solution behavior over the absorption and regeneration temperature range because, mixtures of H_2O-MEA offer a variety of opportunities for hydrogen-bonded dimers by either solvation or by association.

Overall, the results presented above indicate that the elecNRTL model, through simultaneous regression gave a set of optimum binary interaction parameters for the H_2O-

MEA system. The optimum model adequately represents the literature data for aqueous MEA mixtures.

CHAPTER IX

Binary Systems: H_2O-PZ

9.1 Introduction

We continue the thermodynamic model development by describing the second binary system with molecule-molecule interactions between water and piperazine (PZ). This chapter describes the data regression and model predictions for the H_2O-PZ system based on previous literature data and experimental results from this work. The results for the binary interaction parameters for the electrolyte-NRTL (elecNRTL) model in Aspen Plus™ are then presented, showing good statistical fit to the literature data with an average absolute relative error of ± 5.84 % with the exception of a few outliers.

9.2 H_2O-PZ System

Recall from Chapter VI that as the concentration of ions in an electrolyte solution approaches zero, the elecNRTL model reduces in theory to the NRTL Model of Renon and Prausnitz (1968). As shown in Chapter VII, the calculation routes for physical properties between the NRTL and the elecNRTL property models are different. In this section we present background on the NRTL model for clarification purposes only since we will be using the elecNRTL property model for all future chapters to describe molecular and ionic interactions.

The NRTL model is an excess Gibbs energy model given by the following form for a binary system:

$$\frac{G^{ex}}{RT} = x_1 x_2 \left(\frac{\tau_{21} G_{21}}{x_1 + x_2 G_{21}} + \frac{\tau_{12} G_{12}}{x_2 + x_1 G_{12}} \right) \qquad 9\text{-}1$$

Where
i is the species index, 1: H_2O and 2: PZ,
j is the species index, 1: H_2O and 2: PZ,
x_i is the liquid mole fraction of component i,
τ_{ij} is the binary interaction parameter between component i and j,
α_{ij} is the molecule-molecule nonrandomness factor, 0.2,
$G_{12} = e^{-\alpha_{12}\tau_{12}}$,
$G_{21} = e^{-\alpha_{21}\tau_{21}}$.

The molecule-molecule binary interaction parameters were assumed to be temperature dependent and were fitted to the following function of temperature:

$$\tau_{12} = A_{12} + \frac{B_{12}}{T} + C_{12}\ln(T) + D_{12}T \qquad 9\text{-}2$$

$$\tau_{21} = A_{21} + \frac{B_{21}}{T} + C_{21}\ln(T) + D_{21}T \tag{9-3}$$

Taking the appropriate derivative of Equation 9-1, an expression for the activity coefficient of PZ can then be derived from thermodynamic relationships.

$$\ln\gamma_i = \left[\frac{\delta\left(nG^{ex}/RT\right)}{\delta n_i}\right] \tag{9-4}$$

$$\ln\gamma_2 = x_1^2\left[\tau_{12}\left(\frac{G_{12}}{x_2 + x_1G_{12}}\right)^2 + \frac{\tau_{21}G_{21}}{\left(x_1 + x_2G_{21}\right)^2}\right] \tag{9-5}$$

By taking the limit as the mole fraction of PZ$\left(x_2\right)$ approaches zero, we get an explicit form of Equation 9-1 for the infinite dilution activity coefficient of PZ as given below:

$$\ln\gamma_2^\infty = \tau_{12} + \tau_{21}e^{-\alpha_{12}\tau_{21}} \tag{9-6}$$

Where
γ_2^∞ is the infinite dilution activity coefficient for piperazine.

From Equation 9-6, we can see how excess Gibbs energy and activity coefficients are related through model parameters. The creation of the H_2O-PZ model begins with the regression of literature data. Four data sets have been regressed with the elecNRTL model to represent the phase equilibrium of a single solvent system through regression of total vapor pressure [Wilson and Wilding (1994) and Xia et al. (2003)], vapor-liquid equilibrium [this work], specific heat capacity [this work], and PZ solid solubility [Bishnoi et al. (2002) and from this work] data over piperazine solutions. We will reserve piperazine solid solubility literature data from Bishnoi et al. (2002) and this work until a comparison can be

---

made from predictions based on an optimum set of binary interaction parameters. For more information, please refer to Section 9.4.1.

The following stoichiometric chemical equilibrium expressions for the dissociation of piperazine are given below:

$$PZ^{+} \leftrightarrow PZ\left(l\right) + H^{+} \tag{9-7}$$

$$PZ^{+2} \leftrightarrow PZ^{+} + H^{+} \tag{9-8}$$

Equation 9-7 describes the dissociation of protonated piperazine $\left(PZ^{+}\right)$ ion to aqueous piperazine and proton $\left(H^{+}\right)$ ion. Equation 9-8 describes the dissociation of diprotonated piperazine $\left(PZ^{+2}\right)$ ion to aqueous protonated piperazine and proton ion. The chemical equilibrium constants for the above reactions were determined analytically from pKa data reported by Hetzer et al. (1968) and corrected, based on the optimum binary interaction model parameters for the symmetric reference state for the activity coefficient of piperazine from infinite dilution in water to infinite dilution in amine solvent. We were then able to determine the following standard state properties: the infinite dilution aqueous phase free energy of formation $\left(\Delta G_f^{\infty,aq}\right)$ and the infinite dilution aqueous phase enthalpy of formation $\left(\Delta H_f^{\infty,aq}\right)$ for protonated and diprotonated piperazine.

The following section describes the different types of data used in the creation of the binary H_2O-PZ elecNRTL model.

9.2.1 *Total Vapor Pressure*

Data in the form of total vapor pressure from aqueous piperazine solutions as a function of concentration and temperature was used to adjust the activity coefficients of piperazine and water through the simultaneous regression of the binary interaction parameters in the elecNRTL model. For the binary system, the following equation can be used to represent the equilibrium for the total vapor pressure data.

$$P = x_{PZ}\gamma_{PZ}P_{PZ}^{0} + x_{H_2O}\gamma_{H_2O}P_{H_2O}^{0} \tag{9-9}$$

Where
P is the total pressure of the system,
x_i is the apparent mole fraction of component i,
γ_i is the symmetric activity coefficient of component i,
P_i^0 is the Extended Antoine pure vapor pressure of component i.

Note, total vapor pressure data does not allow for the direct calculation of individual component activity coefficients or extrapolation to infinite dilution. Therefore, activity coefficients regressed from total pressure data cannot be accurately determined. An example of the experimental total vapor pressure data used in this work by Wilson and Wilding (1994) and Xia et al. (2003) from 113 – 199 °C are shown in Figure 9.2-1.

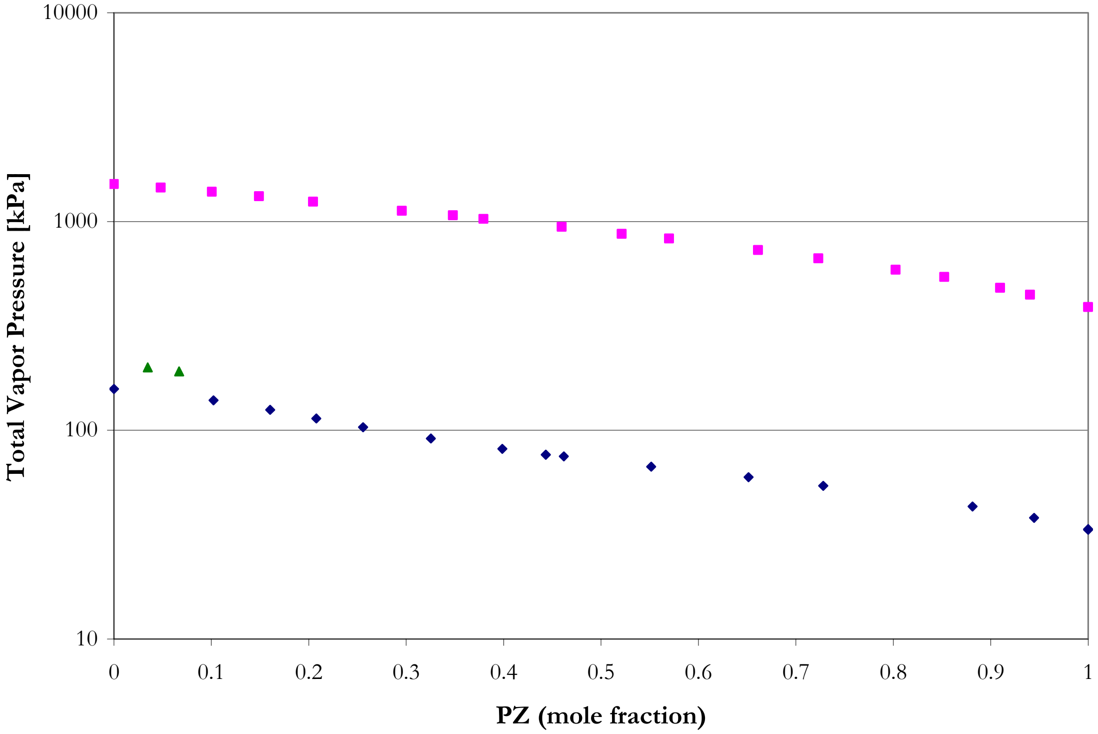

Figure 9.2-1. Total Vapor Pressure at 113, 120, and 199 °C. Points: ♦,■, Wilson and Wilding (1994) at 113 and 199 °C, respectively; ▲, Xia et al. (2003) at 120 °C.

9.2.2 *Vapor-Liquid Equilibrium*

Data in the form of vapor-liquid equilibrium (VLE), which measures the vapor and liquid compositions in aqueous piperazine solutions, as a function of concentration and temperature were also used to adjust the activity coefficients of monoethanolamine and water through the simultaneous regression of the binary interaction parameters in the NRTL model. For the binary system, Equation 9-10 can be used to represent the vapor-liquid equilibrium data.

$$y_i P = x_i \gamma_i P_i^0 \qquad 9\text{-}10$$

Where

y_i is the vapor mole fraction of component i,
P is the total pressure of the system,
x_i is the liquid mole fraction of component i,
γ_i is the symmetric activity coefficient of component i,
P_i^0 is the Extended Antoine pure vapor pressure of component i.

Examples of vapor-liquid equilibrium, as amine volatility, from this work between 0.9 and 5.0 m (mole/kg-H_2O) PZ is presented in Figure 9.2-2.

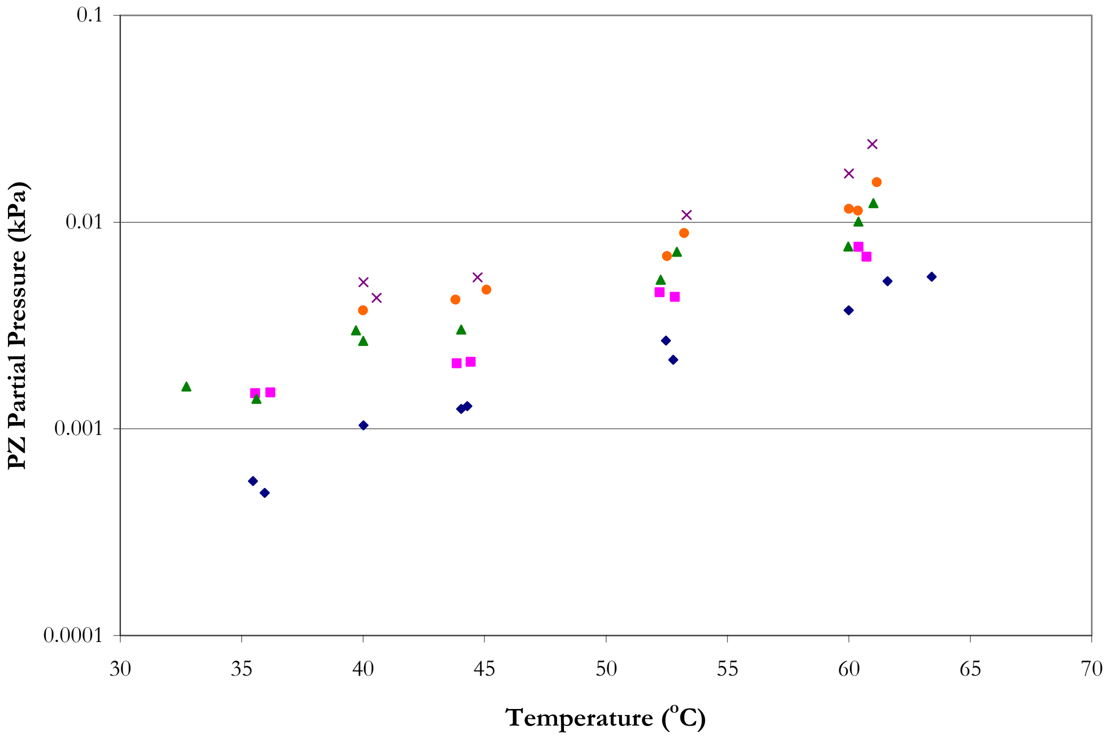

Figure 9.2-2. Amine Volatility from 0.9 – 5.0 m PZ from this work. Points: ♦, 0.9 m PZ, ■, 1.8 m PZ, ▲, 2.5 m PZ, ●, 3.6 m PZ, and ×, 5.0 m PZ.

9.2.3 *Specific Heat Capacity*

As stated in Chapter VI, Aspen Plus™ calculates the liquid phase heat capacity of a *mixture* (CPMX) by taking the derivative of the liquid enthalpy at constant pressure:

$$H_i^l\left(T+\Delta T\right)-H_i^l\left(T\right)=\int_T^{T+\Delta T} C_{p,i}^l dT \qquad \text{9-11}$$

where the liquid enthalpy of a mixture is calculated by the following equation:

$$H_i^l\left(T\right)=\sum_i x_i H_i + H_i^E \qquad \text{9-12}$$

$$H_i\left(T\right)=\Delta H_f^{ig}\left(T^{ref}\right)+\int_{T^{ref}}^{T} C_p^{ig} dT + \left[H_i\left(T,p\right)-H_i^{ig}\left(T,p\right)\right] \qquad \text{9-13}$$

Where
ΔT is the perturbation in temperature from *T*,
H_i^E is the excess enthalpy of component i,
$\Delta H_f^{ig}\left(T^{ref}\right)$ is the standard enthalpy of formation of component i at T^{ref},
T^{ref} is the reference temperature, 25.0 °C,
C_p^{ig} is the ideal gas heat capacity of component i,
H_i^{ig} is the ideal gas enthalpy of component i.

Data in the form of specific heat capacity of a mixture as a function of concentration and temperature were used to adjust the activity coefficients of piperazine and water through the simultaneous regression of the binary interaction parameters by taking the derivative of the NRTL model, vis-à-vis excess enthalpy. Thus, specific heat capacity effects are limited only to the second and third terms of Equations 9-2 and 9-3. Examples of experimental specific heat capacity from this work at 2.0 and 3.6 m PZ from 40 – 120 °C are shown in Figure 9.2-3.

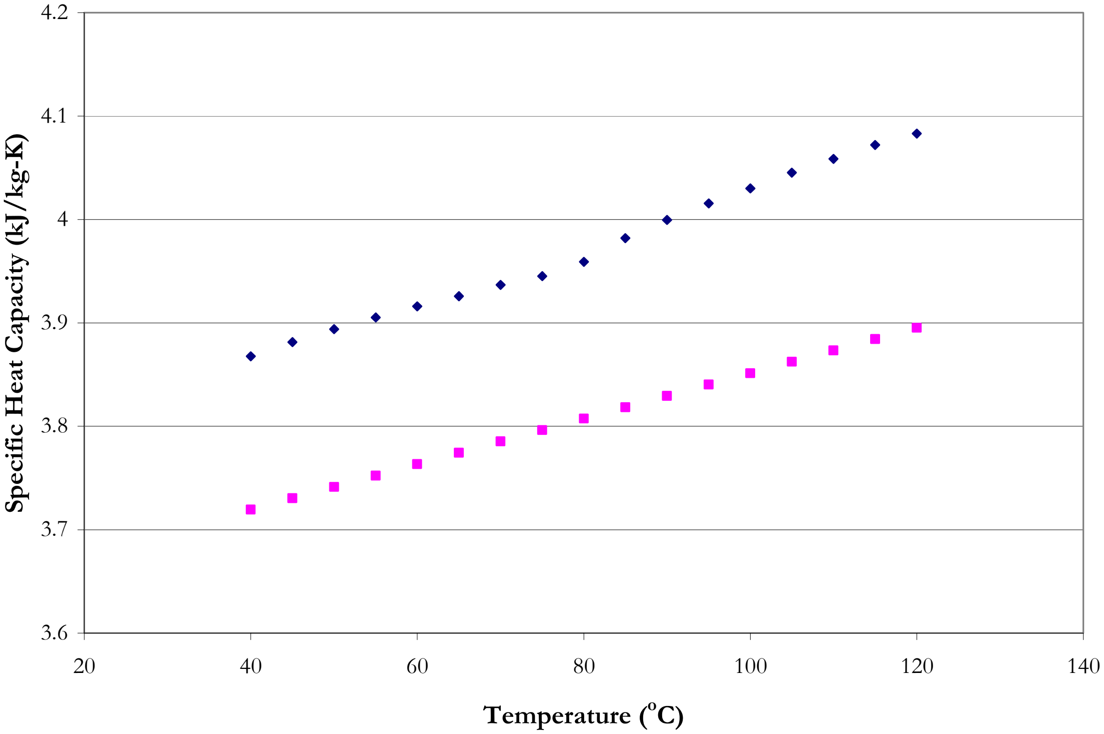

Figure 9.2-3. Specific Heat Capacity in 2.0 and 3.6 m PZ from this work. Points: ◆, 2.0 m PZ and ■, 3.6 m PZ.

9.2.4 *Solid Solubility*

Data in the form of solid solubility, which measures the dissolution temperature of the solid phase, vis-à-vis synthetic method, as function of concentration and temperature, was used to adjust the temperature dependent equilibrium constants for the following reactions:

$$PZ \cdot 6H_2O \leftrightarrow PZ + 6H_2O \qquad 9\text{-}14$$

$$PZ_{anh} \leftrightarrow PZ \qquad 9\text{-}15$$

Where

$PZ \cdot 6H_2O$ is piperazine hexahydrate,

PZ_{anh} is anhydrous piperazine.

We chose not to include the anhydrous precipitation reaction in our model because conditions where anhydrous piperazine (w_{PZ}>0.6) would precipitate from an aqueous solution are well beyond the salt concentrations of interest in connection with carbon capture processes and its modifications. Experimental solubility from Bishnoi et al. (2002) and from this work were used to regress coefficients in Equation 9-14 through optimum model predictions for the H_2O-PZ system.

An example of the experimental solid solubility used in this work from Bishnoi et al. (2002) and from this work for aqueous piperazine mixtures is shown in Figure 9.2-4.

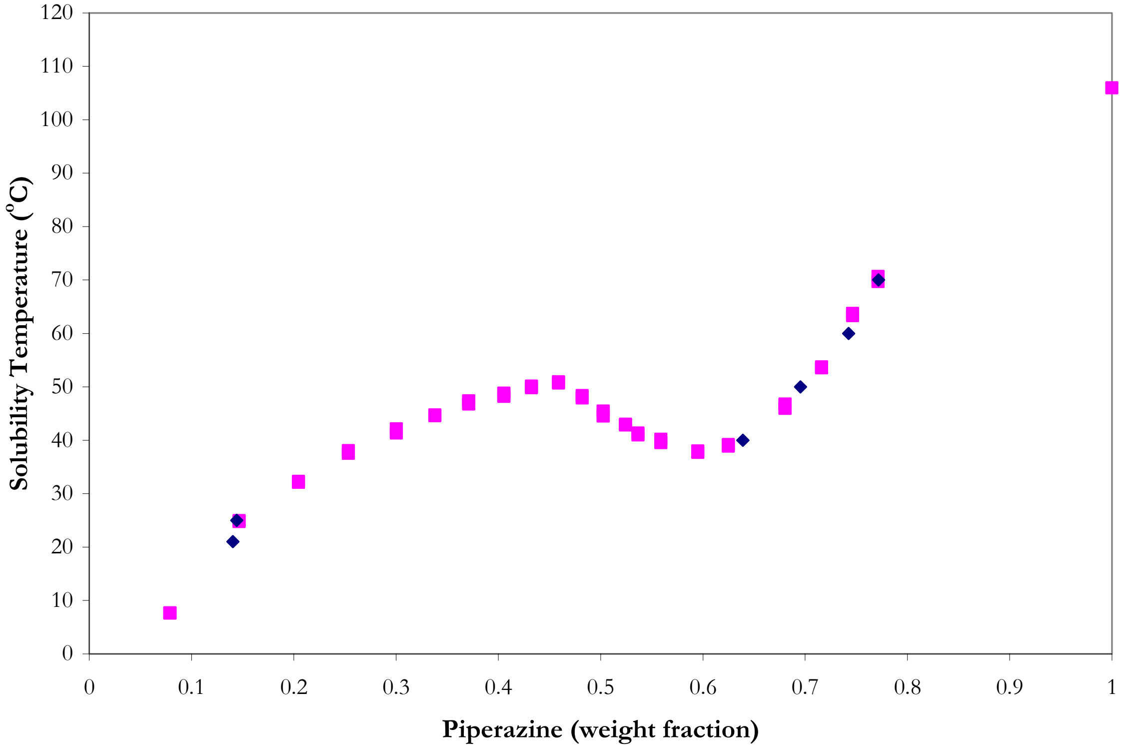

Figure 9.2-4. Solid Solubility of Aqueous PZ mixtures. Points: ♦, Bishnoi et al. (2002), ■, this work.

9.2.5 *Dissociation Constant of Piperazine*

Recall from Chapter VI that the chemical equilibrium or dissociation constant for Equations 9-7 and 9-8 in terms of the activity are given by the following relationships:

$$K^* = \frac{a_{PZ} \cdot a_{H^+}}{a_{PZH^+}} \qquad 9\text{-}16$$

$$K^* = \frac{a_{PZH^+} \cdot a_{H^+}}{a_{PZH^{+2}}} \qquad 9\text{-}17$$

where the thermodynamic equilibrium constant can be defined as

$$\ln K^* = \left(\frac{-\Delta G_m^o}{RT} \right) \qquad 9\text{-}18$$

$$\Delta G_m^o = \sum_i \nu_i \mu_i^o \qquad 9\text{-}19$$

Where
K^* is the asymmetric chemical equilibrium constant for Equations 9-7 and 9-8 (molality based),
a_i is the activity of component i,
ΔG_m^o is the standard molar Gibbs free energy change for Equations 9-7 and 9-8,
ν_i is the stoichiometric coefficient of component i,
μ_i^o is the reference chemical potential for component i.

The chemical equilibrium constant vis-à-vis component activities provides the connection between the standard Gibbs free energy change of reaction to the standard (reference) states of the individual species activities in a given reaction. In this work, H_2O and PZ were regarded as solvents and the solution was treated as a mixed-solvent system and described by the symmetric reference state convention where the activity coefficient approaches one as the mole fraction of the species approaches its pure liquid state.

Experimental pKa data from Hetzer et al. (1968) (Figure 9.2-5) were used analytically to determine the chemical equilibrium constant for Equations 9-7 and 9-8 for the dissociation constant of piperazine and protonated piperazine. We were then able to determine the following standard state infinite dilution aqueous phase properties: the free energy of formation $\left(\Delta G_f^{\infty,aq}\right)$, the enthalpy of formation $\left(\Delta H_f^{\infty,aq}\right)$, and coefficients for the temperature dependent heat capacity $\left(\Delta C_p^{\infty,aq}\right)$ of protonated and diprotonated piperazine.

Chemical equilibria reported in literature are normally referenced to infinite dilution in water (molality based), treating piperazine as a solute. Solute and ionic activity coefficients are described by the asymmetric reference state convention which states that as the activity coefficient approaches one, the mole fraction of the species approaches zero in pure water.

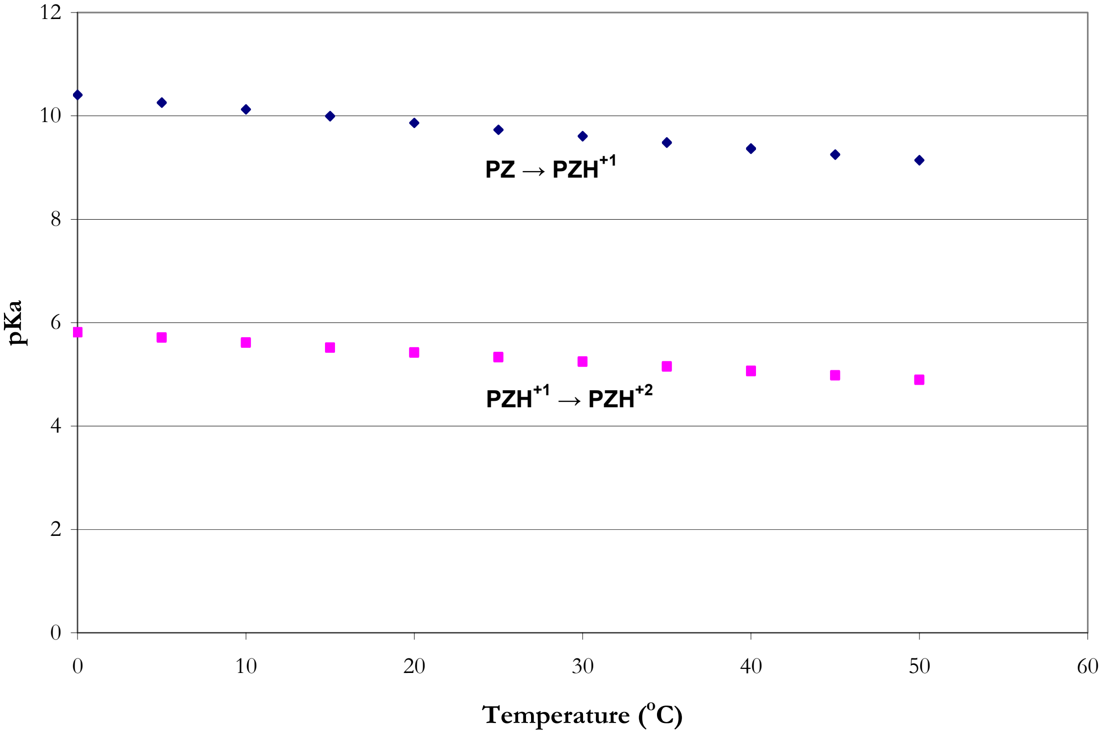

Figure 9.2-5. Experimental pKa for the First and Second Dissociation Constant of Piperazine (molality based) from Hetzer et al. (1968).

Hetzer et al. (1968) found it helpful to express the chemical equilibrium as a p-function where the p-function is the negative logarithm (base 10) of the number as given by the following expression:

$$pK = -\log_{10}\left(K\right) \tag{9-20}$$

Where
p is the p-function of a numerical datum.

In this work, chemical equilibrium constants are defined in terms of mole fractions; therefore the chemical equilibrium constant reported by Hetzer et al. (1968) has to be converted. However, due to the asymmetric reference state convention, the chemical equilibrium constant of piperazine requires an additional conversion to the symmetric reference state convention since all subsequent piperazine based ionic equilibrium constants are determined based on the asymmetric reference state convention referenced to infinite dilution in piperazine. These two reference state conventions are related for piperazine by the following expression:

$$\frac{\gamma_{PZ}}{\gamma_{PZ}^{*}} = \lim_{x_{PZ}\to 0}\gamma_{PZ} = \gamma_{PZ}^{\infty} \tag{9-21}$$

Where
γ_{MEA} is the symmetric activity coefficient for piperazine,
γ_{MEA}^{*} is the asymmetric activity coefficient for piperazine as the solution approaches its pure solute reference state.

Thus, the chemical equilibrium constant of piperazine (Equations 9-7 and 9-8) referenced to the symmetric reference state convention used in this work is related by the following expression:

$$\ln K^{*} = \ln K + \ln\left(\frac{1000}{MW_w}\right)\sum_{i \neq w} \nu_i + \ln \gamma_{PZ}^{\infty} \qquad 9\text{-}22$$

Where
MW_w is the molecular weight of H_2O, 18.01528 gm/mole,
K is the symmetric chemical equilibrium constant (mole fraction based).

The infinite dilution activity coefficient of piperazine is calculated from the binary interaction parameters for the water-piperazine system using the elecNRTL model. The resulting values were then re-regressed to the standard temperature dependent form of the chemical equilibrium constant given in Chapter VI and compared to Equation 9-6. This modified chemical equilibrium constant for piperazine was then utilized in the elecNRTL model within Aspen Plus^{TM} to specify the infinite dilution standard state free energy and enthalpy of formation, respectively, for protonated and diprotonated piperazine. Therefore, chemical equilibrium constants reported in this work must be corrected for the infinite dilution activity coefficient of piperazine prior to comparison with other work.

9.3 Data Regression

For the elecNRTL model, binary interaction parameters for molecule-molecule interactions were given a default value of zero.

Through simultaneous regression, the molecule-molecule binary interaction parameters for the H_2O-PZ system were obtained through the regression of total vapor pressure [Wilson and Wilding (1994) and Xia et al. (2003)], vapor-liquid equilibrium [this work], and specific heat capacity [this work] data over piperazine solutions. A list of the aqueous electrolyte data sets that were examined in this work is given in Table 9.3-1. The column labels σ_T , σ_P , σ_{Cp} ,σ_{x_i} , σ_{y_i} , give standard error associated with the temperature, pressure, specific heat capacity, liquid mole fraction, and the vapor mole fraction, respectively, with each data set. DRS suggested standard error default values were assigned unless otherwise stated by the author.

Table 9.3-1. Experimental data used in the regression of the H_2O-PZ system.

	Obs.	T (°C)	σ_T	σ_P	σ_x	σ_y	Source
TP	29	113.0 – 199.0	0.01	5%	0.1%	10%	Wilson and Wilding (1994)
	2	120.0	0.01	5%	0.1%	10%	Xia et al. (2003),

	Obs.	T (°C)	σ_T	σ_P	σ_x	σ_y	Source
VLE	48	101.2 – 167.0	0.01	0.1%	0.1%	0	This work

	Obs.	T (°C)	σ_T	σ_x	σ_{Cp}	Source
Cp	34	40.0 – 120.0	0.01	0.1%	0.1%	This work

After performing a nonlinear regression for the full model using DRS, the following regression summary statistics output for estimates of the adjustable binary parameter coefficients is shown in Table 9.3-2.

Table 9.3-2. DRS Regression Output for Full H_2O-PZ System Model.

	Interacting Species			
Parameter	i	j	Estimate	σ wrt Estimate
1-$A_{m,m}$	H_2O	PZ	-0.395	56.3
2-$B_{m,m}$	H_2O	PZ	-1935	9281
3-$C_{m,m}$	H_2O	PZ	0.318	6.76
4-$D_{m,m}$	H_2O	PZ	-0.000138	0.0423
5-$A_{m,m}$	PZ	H_2O	-1.86	133
6-$B_{m,m}$	PZ	H_2O	228	8141
7-$C_{m,m}$	PZ	H_2O	-0.227	23.0
8-$D_{m,m}$	PZ	H_2O	0.0155	0.0530

Residual Sum of Squares: 272,103
Residual Root Mean Square: 51.398
Degree of Freedom: 105

Recall that the standard error of an estimate is the estimated standard deviation of that statistic. Notice that all of the estimates are smaller relative to their standard errors. A complete description of the variability of the coefficient estimates requires examining the correlations between the estimates as shown in Table 9.3-3.

Table 9.3-3. Correlation Matrix of the Coefficient Estimates for the Full H_2O-PZ Model.

Parameter	1	2	3	4	5	6	7	8
1	1.00							
2	-0.87	1.00						
3	*-0.99*	0.82	1.00					
4	0.83	-0.47	-0.88	1.00				
5	-0.79	0.77	0.76	-0.57	1.00			
6	0.68	-0.86	-0.61	0.26	*-0.91*	1.00		
7	0.80	-0.74	-0.78	0.62	*-1.00*	0.86	1.00	
8	-0.77	0.50	0.79	-0.84	0.86	-0.57	*-0.90*	1.00

Table 9.3-3 shows a high negative correlation between $\hat{\eta}_{3\to1}$ for the first energy parameter estimate, $\tau_{H_2O/PZ}$, but the correlation between other coefficients is relatively small, suggesting that $\hat{\eta}_3$ might be usefully removed from the model without significant loss of information. On the other hand, Table 9.3-3 shows three highly correlated coefficients for τ_{PZ/H_2O} where a submodel containing fewer coefficients for the τ_{PZ/H_2O} expression might be useful without a significant loss of information.

After performing backward elimination using DRS, the following optimum model regression summary statistics output for estimates of the adjustable binary parameter coefficients is shown in Table 9.3-4.

Table 9.3-4. DRS Regression Output for Optimum H_2O-PZ Model.

Parameter	Interacting Species i	j	Estimate	σ wrt Estimate
1-$A_{m,m}$	H_2O	PZ	-7.68	1.44
2-$D_{m,m}$	H_2O	PZ	0.0107	0.00343
3-$A_{m,m}$	PZ	H_2O	-6.42	0.685
4-$D_{m,m}$	PZ	H_2O	0.0249	0.00373

Residual Sum of Squares:	740,215
Residual Root Mean Square:	49.673
Degree of Freedom:	301

Notice that all of the estimates are larger relative to their standard errors. Comparing the estimates from the full model to the optimum model, there was relatively little difference between the estimated values. The proposed optimum model provides the following correlations between the estimates as shown in Table 9.3-5.

Table 9.3-5. Correlation Matrix of the Coefficient Estimates for the Optimum H_2O-PZ Model

Parameter	1	2	3	4
1	1.00			
2	*-0.97*	1.00		
3	0.62	-0.77	1.00	
4	*-0.98*	*0.95*	-0.64	1.00

Table 9.3-5 again shows highly negative correlations between two of the $\tau_{H_2O/PZ}$ parameters suggesting that some of the remaining parameters might be usefully removed from the model without significant loss of information.

9.3.1 *Optimum Model Results*

With the determination of the estimates for the binary interaction parameters known for the optimum model, a simple Aspen Plus™ Flash model was used to test the predictive capability of the H_2O-PZ model against literature data. For each data point, the deviation between the experimental and estimated values is expressed in terms of the average absolute relative deviation (AARD). Table 9.3-6 gives the percent AARD and the maximum percent AARD for the model predictions.

Table 9.3-6. Absolute Percent Relative Error for the H_2O-PZ Optimum Model

		AARD(%)	Max. AARD
TP	Wilson and Wilding (1994)	11.85	45.95
	Xia et al. (2003)	3.84	4.21
VLE	This work	13.03	29.43
C_p	This work	0.25	0.53
Overall		**5.84**	**45.95**

Overall, the model adequately describes the H_2O-PZ property data listed above within an average absolute relative error of ± 5.84 percent, with the exception of a few outliers.

9.3.2 *Chemical Equilibrium Constant*

With the determination of the estimates for the binary interaction parameters known for the optimum model, we can directly evaluate the infinite dilution activity coefficient of piperazine (Equation 9-6) as given by the following expression:

$$\ln \gamma_{PZ}^{\infty} = \left(-7.68 + 0.0107T(K)\right) + \left(-6.42 + 0.0249T(K)\right)e^{-0.2\left(-6.42+0.0249T(K)\right)} \qquad 9\text{-}23$$

Previous authors chose to linearize the above expression into the temperature dependent form used for the chemical equilibrium constants as given by the following expression:

$$\ln\gamma_{PZ}^{\infty}=12.76-\frac{2782}{T(K)}-1.25\ln T(K) \tag{9-24}$$

Using Equation 9-24, we can illustrate thermal effects of the solution equivalent to the infinite dilution excess enthalpy given by the following equation for PZ:

$$-\frac{\Delta H^{E}}{R}=\frac{d\ln\gamma_{PZ}^{\infty}}{d1/T}=-2782+1.25\cdot T(K) \tag{9-25}$$

At 25 and 80 °C, the infinite dilution excess enthalpy (kJ/mol) is -20.04 and -19.47, respectively. Figure 9.3-1 illustrates experimental values for the phase change of PZ between the heat of dissolution and the heat of fusion, vis-à-vis the heat of solution, reported by Steele et al. (1997) and Enea and Berthon (1973) and predicted [Hilliard (2005)] UNIFAC values for the infinite dilution excess enthalpy for PZ from 20 to 160 °C. Experimental values for the infinite dilution excess enthalpy for PZ from Steele et al. (1997) and Enea and Berthon (1973) are the difference between the maximum and minimum reported values at 25 and 111 °C. Hilliard (2005) predicted the activity coefficient of PZ from the UNIFAC [Dortmund Modified (DMD)] Method [Weidlich and Gmehling (1987) and Gmehling et al. (1993)], where the activity coefficients were predicted from group contributions and were assumed accurate due to the lack of experimental information. The modified UNIFAC model treated cyclic PZ as an aliphatic molecule with respect to predicating the effect of substituent groups to the amine's structure, thereby affecting how the molecule will interact in an aqueous environment with increasing temperature.

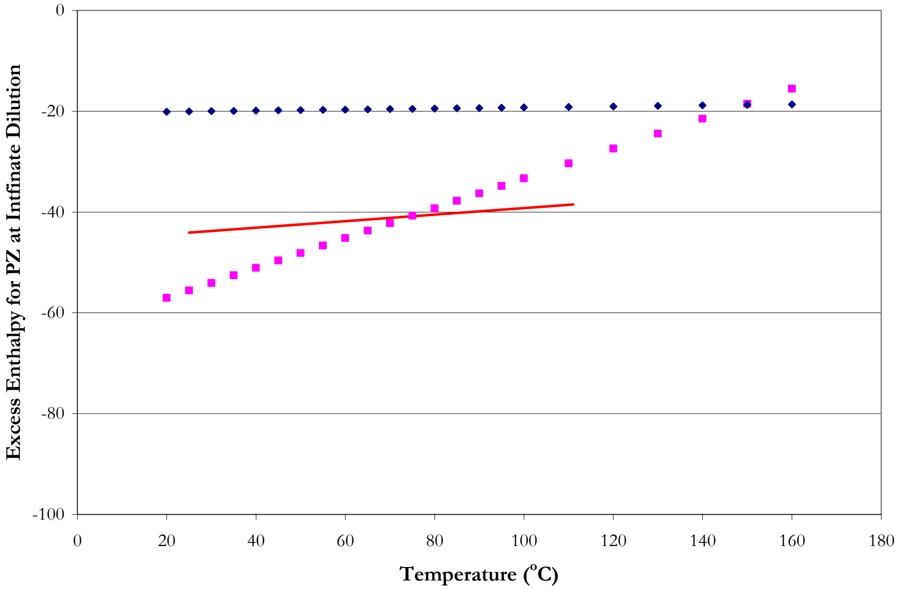

Figure 9.3-1. Infinite Dilution Excess Enthalpy for PZ from 20 to 160 °C. Points: ■, Hilliard (2005), ♦, this work. Line: Difference between the ΔH_{dis} and the ΔH_{fus} from Steele et al. (1997) and Enea and Berthon (1973).

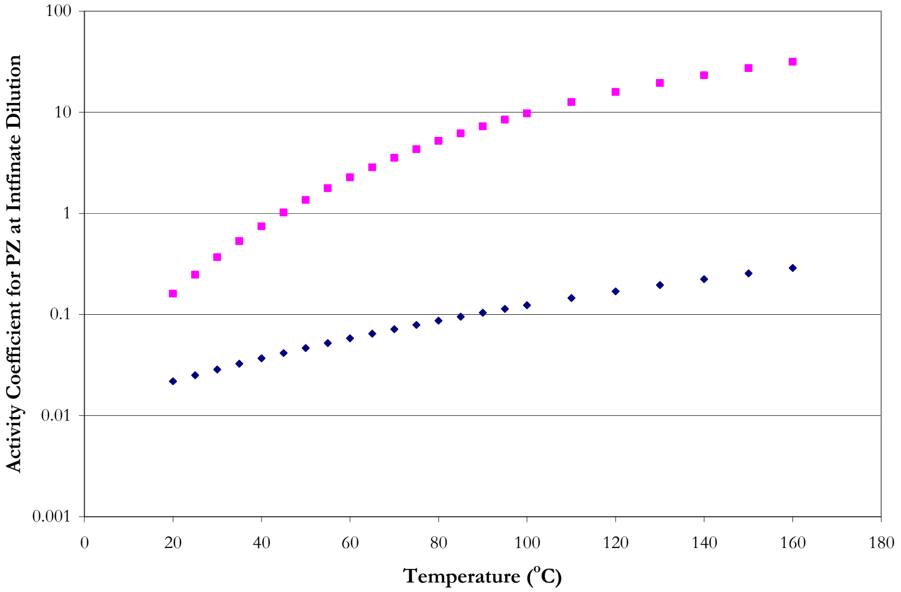

Figure 9.3-2. Infinite Dilution Activity Coefficient for PZ from 20 to 160 °C. Points: ■, Hilliard (2005), ♦, this work.

One striking feature of Figure 9.3-1 is the temperature dependence of the infinite dilution excess enthalpy. This difference is a magnification of the temperature effect on the infinite dilution activity coefficient of PZ as shown in Figure 9.3-2.

For most activity coefficient models, the reference state for solutes is defined as infinite dilution in pure solvent; at 25 °C we can see that there is a large difference even at this temperature. The optimum model parameters were fitted to a more extensive database than the previous author; thus infinite dilution activity coefficients predicted with the optimum model may give more realistic activity coefficients as a function of temperature and composition as compared to data found in the literature.

With the determination of Equation 9-24 known, we can then regress Equation 9-22 to the standard temperature dependent form of the chemical equilibrium constant given in Chapter VI based on experimental data reported by Hetzer et al. (1968) as shown in Table 9.3-7.

Table 9.3-7. Estimates for the Chemical Equilibrium Coefficients for the H_2O-PZ System (mole fraction basis).

Equation Number	A	σ_A	B	σ_B	C	σ_C	D	σ_D
9-16	-64.4	18.5	-4899	821	8.90	2.76	0.0	-
9-17	-67.8	17.5	-3091	775	10.2	2.61	0.0	-

Data Reference: Hetzer et al. (1968)
$\ln K = A + B/T(K) + C \cdot \ln T(K) + D \cdot T(K)$

As stated previously, Equation 9-18 relates the equilibrium constant for the dissociation of PZ to the standard Gibbs free energy change of reaction.

$$\frac{\Delta G^o}{RT} = -\ln K \qquad 9\text{-}26$$

$$\frac{\Delta G^o}{RT} = -\left(A + \frac{B}{T(K)} + C \cdot \ln T(K) + D \cdot T(K) \right) \qquad 9\text{-}27$$

By taking the partial derivative of Equation 9-27 with respect to temperature, Equation 9-28 relates the standard enthalpy of reaction to the standard Gibbs free energy.

$$-\frac{\Delta H^o}{RT} = \frac{d\left(\Delta G^o / RT\right)}{dT} \qquad 9\text{-}28$$

$$\Delta H^o = RT^2 \frac{d \ln K}{dT} = RT^2 \frac{d}{dT}\left(A + \frac{B}{T(K)} + C \cdot \ln T(K) + D \cdot T(K) \right) \qquad 9\text{-}29$$

$$\Delta H^o = RT^2 \left(-\frac{B}{T(K)^2} + \frac{C}{T(K)} + D \right) \qquad 9\text{-}30$$

$$\Delta H^o = R\left(-B + C \cdot T(K) + D \cdot T(K)^2 \right) \qquad 9\text{-}31$$

Where the standard property changes of reaction (e.g. Gibbs free energy and enthalpy) are defined as the difference between the standard property change of the products and reactants, weighted by their stoichiometric coefficients.

$$\Delta M^o = \sum_i \nu_i M_i^o \qquad 9\text{-}32$$

For ionic species the aqueous phase infinite dilution molar heat capacity is described by the following equation:

$$C_{p,i}^{\infty,aq}\left(\frac{J}{kmol \cdot K} \right) = C_{1,i} + C_{2,i} T(K) + C_{3,i} T(K)^2 + \frac{C_{4,i}}{T(K)} \qquad 9\text{-}33$$

The molar heat capacity of PZ was described in Chapter VII by the following equation:

$$C_{p,PZ}^{l,*}\left(\frac{J}{kmol \cdot K} \right) = 115228 + 99.98 \cdot T(K) + 0.231 \cdot T(K)^2 \qquad 9\text{-}34$$

Based on Equations 9-26 to 9-31, Table 9.3-8 reports the standard property changes of formation as compared to literature values, and Table 9.3-9 reports the coefficients for the aqueous phase infinite dilution heat capacity for a proton.

Table 9.3-8. Standard Property Changes of Formation at 298.15 K for Molecular and Ionic Components.

	This work.		DIPPR Literature[*]	
Component	ΔG^o (kcal/mol)	ΔH^o (kcal/mol)	ΔG^o (kcal/mol)	ΔH^o (kcal/mol)
PZH_2^{+2}	17.3889[†]	-34.0497[†]		
PZH^+	24.4600[†]	-21.8646[†]		
PZ(l)	37.5332[‡]	-8.1589[‡]	39.6006[*]	-10.8914[*]
H^+	0.0	0.0		

[*] Rowley et al. (2004) – DIPPR: Model Predictions.
[†] Calculated based on Equation 9-22.
[‡] Based on Chapter VII.

Table 9.3-9. Coefficients for the Aqueous Phase Infinite Dilution Heat Capacity (J/kmol·K).

Component	C_1	C_2	C_3	C_4
H^+	0.0	0.0	0.0	0.0

For a given temperature, the molar aqueous phase infinite dilution heat capacity of PZ^{+2} and PZH^+ can then be determined analytically. A starting point for a rigorous development starts with the following equation:

$$\Delta G_m^o = \Delta H_m^o - T\Delta S_m^o \tag{9-35}$$

Equation 9-35 is from the definition of the molar Gibbs free energy applied to each component in a chemical reaction evaluated at the standard state. Applying Equation 9-32 to Equation 9-35 yields

$$\sum_i \nu_i G_{m,i}^o = \sum_i \nu_i H_{m,i}^o - T\sum_i \nu_i S_{m,i}^o \tag{9-36}$$

where the standard molar heat of reaction and standard molar entropy change of reaction are related to temperature by the following expressions:

$$\Delta H_m^o = \Delta H_{0,m}^o + R\int_{T_0}^{T} \frac{\Delta C_{p,m}^o}{R} dT \qquad 9\text{-}37$$

$$\Delta S_m^o = \Delta S_{0,m}^o + R\int_{T_0}^{T} \frac{\Delta C_{p,m}^o}{R} \frac{dT}{T} \qquad 9\text{-}38$$

Equations 9-35, 9-37, and 9-38 are combined to yield

$$\Delta G_m^o = \Delta H_{0,m}^o + R\int_{T_0}^{T} \frac{\Delta C_{p,m}^o}{R} dT - T\Delta S_{0,m}^o - RT\int_{T_0}^{T} \frac{\Delta C_{p,m}^o}{R} \frac{dT}{T} \qquad 9\text{-}39$$

However,

$$\Delta S_{0,m}^o = \frac{\Delta H_{0,m}^o - \Delta G_{0,m}^o}{T_0} \qquad 9\text{-}40$$

hence

$$\Delta G_m^o = \Delta H_{0,m}^o - \frac{T}{T_0}\left(\Delta H_{0,m}^o - \Delta G_{0,m}^o\right) + R\int_{T_0}^{T} \frac{\Delta C_{p,m}^o}{R} dT - RT\int_{T_0}^{T} \frac{\Delta C_{p,m}^o}{R} \frac{dT}{T} \qquad 9\text{-}41$$

Finally, division by RT yields

$$-\ln K_i = \frac{\Delta G_m^o}{RT} = \frac{\Delta G_{0,m}^o - \Delta H_{0,m}^o}{RT_0} + \frac{\Delta H_{0,m}^o}{RT} + \frac{1}{T}\int_{T_0}^{T} \frac{\Delta C_{p,m}^o}{R} dT - \int_{T_0}^{T} \frac{\Delta C_{p,m}^o}{R} \frac{dT}{T} \qquad 9\text{-}42$$

The change in heat capacity for the mixture can be expressed as

$$\Delta C_p^o\left(\frac{J}{kmol \cdot K}\right) = \Delta A + \Delta B \cdot T\left(K\right) + \Delta C \cdot T\left(K\right)^2 + \Delta D \cdot T\left(K\right)^3 + \Delta E \cdot T\left(K\right)^4 \qquad 9\text{-}43$$

with

$$\Delta A = \sum_i v_i A_i \qquad 9\text{-}44$$

with analogous definitions for ΔB, ΔC, ΔD, and ΔE. Using Equation 9-42 and the coefficients for the chemical equilibrium constant given in Table 9.3-10, we can determine the coefficients for the aqueous phase infinite dilution molar heat capacity of PZH_2^{+2} and PZH^+.

Table 9.3-10. Coefficients for the Aqueous Phase Infinite Dilution Heat Capacity (J/kmol·K) of PZH_2^{+2} amd PZH^+ from 0 – 200 °C based on Equation 9-43.

Coefficient	PZH_2^{+2}	PZH^+
C1	-9.929E-05	-5.440E-05
C2	-1.415E-02	-3.460E-03
C3	-2.287E+00	-4.499E-01
C4	6.361E-03	3.137E-03

Coefficients for the aqueous phase infinite dilution molar heat capacity of $MEAH^+$ were adjusted to match the form of Equation 9-33.

Table 9.3-11. Coefficients for the Aqueous Phase Infinite Dilution Heat Capacity (J/kmol·K) of PZH_2^{+2} amd PZH^+ from 0 – 200 °C based on Equation 9-33.

Coefficient	PZH_2^{+2}	PZH^+
C_1	1.224E+06	6.035E+05
C_2	-5.105E+03	-2.517E+03
C_3	7.071E+00	4.165E+00
C_4	-1.088E+08	-5.364E+07

Hilliard (2005) did not provide source documentation for the coefficients assigned to PZH_2^{+2} or PZH^+. In this work, we have compiled a consistent database for experimental H_2O-PZ data as compared to the work by Hilliard (2005). The difference between the two predictions for the aqueous phase infinite dilution heat capacity of PZH_2^{+2} and PZH^+ accounts for differences is in the model framework. Hilliard (2005) chose to describe the liquid phase chemical equilibrium through linear temperature dependent functions. In this work, we chose not to provide the chemical equilibrium constants, but rather to determine the chemical equilibrium from the reference state free energy of the system. Thus, Hilliard (2005) was never required to fully describe the standard property changes for each ionic species because Aspen Plus™ would rely on the provided chemical equilibrium constants for the necessary ionic information (e.g. ΔG, ΔH, ΔC_p). By determining the coefficients for the aqueous phase infinite dilution molar heat capacity of PZH_2^{+2} and PZH^+ analytically, this work is thermodynamically consistent with published literature for the dissociation constant of PZ as shown in Figure 9.3-3.

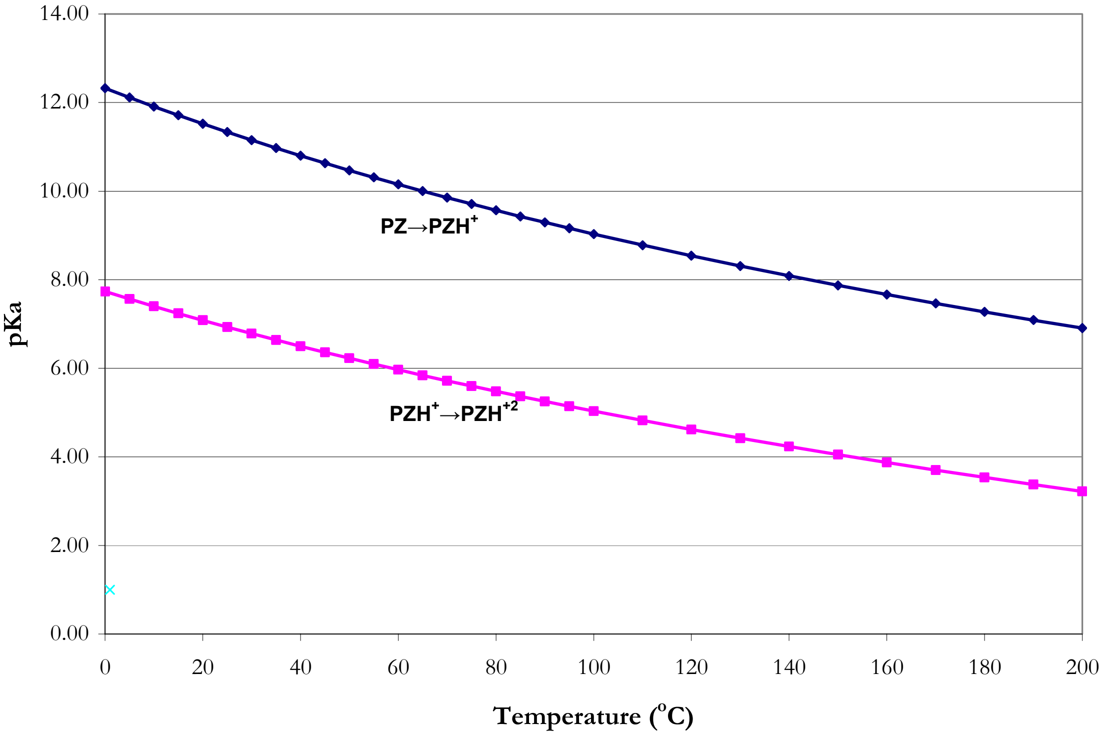

Figure 9.3-3. Comparison of the Dissociation Equilibrium Constant for PZ (mole fraction based) from 0 – 200 °C. Points: ♦ and ■, This work. Lines: ▬, Corrected Hetzer (1968) based on Table 9.3-11.

9.4 Optimum Model Predictions

In this work, we have compiled a large database of consistent high quality data needed to obtain a unique set of binary interaction parameters to describe the H_2O-PZ system. The remainder of this chapter will be devoted to using our model as a predictive tool as described in the subsequent sections.

9.4.1 *Solid Solubility*

In this work, we have compiled a database to describe experimental solid solubility data for precipitating salts, vis-à-vis piperazine hexahydrate and anhydrous piperazine. We chose not to include the precipitation of anhydrous piperazine because for concentrations were anhydrous piperazine would precipitate from an aqueous solution are well beyond the piperazine concentrations of interest in connection with the carbon capture processes and its modifications.

To describe the salt chemical equilibrium constant for Equations 9-14 and 9-15, predictions from the optimum model were used to express the activity of component i as given by the following relationship:

$$K_j = \prod_i a_i^{\nu_{i,j}} \qquad 9\text{-}45$$

Where
K_j is the chemical equilibrium constant,
$\nu_{i,j}$ is the reaction stoichiometric coefficient of component i,
a_i is the activity of component i.

In this work, for Equations 9-14 and 9-15, we chose to define the chemical equilibrium constants as linear temperature dependent functions due to the limited thermodynamic information associated with the precipitation of the solid phase.

$$\ln K_i = A + \frac{B}{T(K)} + C \ln T(K) + D \cdot T(K) \qquad 9\text{-}46$$

We have included coefficients for the anhydrous piperazine precipitation equilibrium reaction for inclusion by the end user as shown in Table 9.4-1.

Table 9.4-1. Chemical Equilibrium Coefficients for the Salt Precipitation of Piperazine Hexahydrate and Anhydrous Piperazine Based on Equation 9-45 (mole fraction basis).

Equation Number	A	B	C	D
9-15	-291	0.0	56.5	-0.128
9-16	316	0.0	-69.9	0.261

Data Reference: Bishnoi et al. (2002) and from this work
ln K = A + B/T(K) + C·lnT(K) + D·T(K)

Figure 9.4-1 illustrates the calculated chemical equilibrium salt precipitation reactions for piperazine hexahydrate and anhydrous piperazine as compared to model predictions for experimental solid solubility data from Bishnoi et al. (2002) and from this work within Regions 1, 2, and 4 as shown in Figure 9.4-2.

Experimental solid solubility data were separated into different regions according to experimental VLE boundary (Region 1), formation of piperazine hexahydrate as a single salt (Region 2), formation of double salts (Region 3), and formation of piperazine anhydrous as a single salt (Region 4). Predictions for anhydrous piperazine were included in Figure 9.4-2 but were not included as a feature in the optimum model and left to the discretion of the end user.

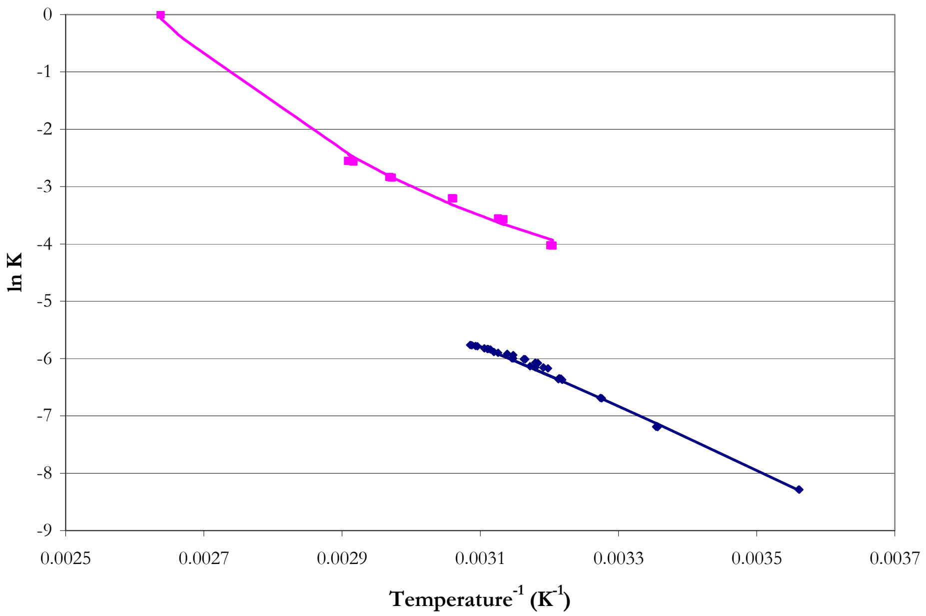

Figure 9.4-1. Chemical Equilibrium Salt Precipitation Reactions for Piperazine Hexahydrate (♦) and Anhydrous Piperazine (■) to elecNRTL Model Predictions.

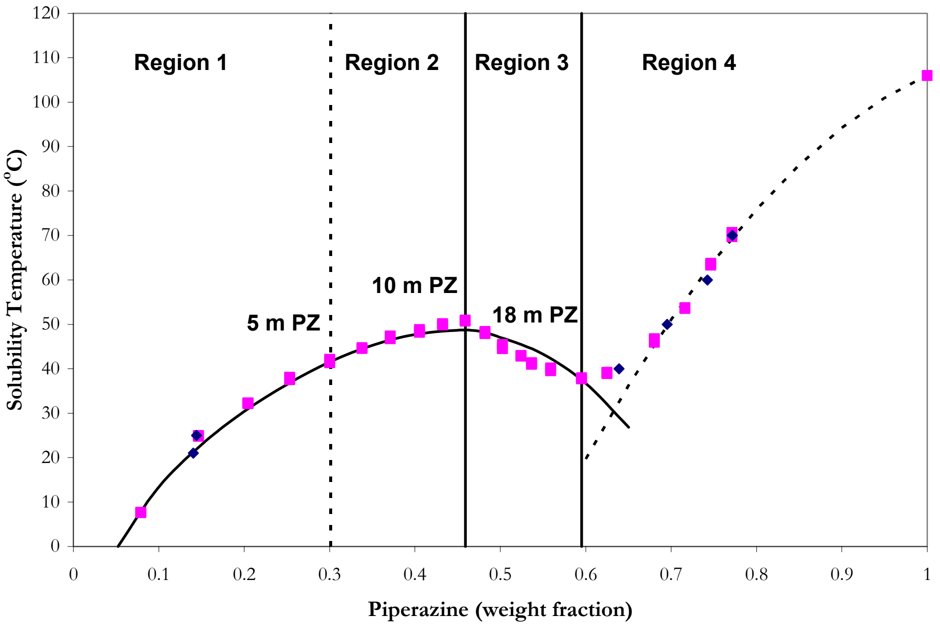

Figure 9.4-2. Solubility Product Predictions of Piperazine Hexahydrate and Anhydrous Piperazine in Water. Points: ♦, Bishnoi et al. (2002), ■, this work. Lines: elecNRTL Model Predictions.

9.4.2 *Total Vapor Pressure*

With the determination of the estimates for the energy parameter coefficients known for the optimum model, a simple Aspen Plus™ Flash model was used to test the predictive capability of the H_2O-PZ energy parameter coefficients against literature data. Figure 9.4-3 compares estimated and experimental total pressure measurements from Wilson and Wilding (1994) and Xia et al. (2003) for aqueous PZ mixtures from 113 – 199 °C.

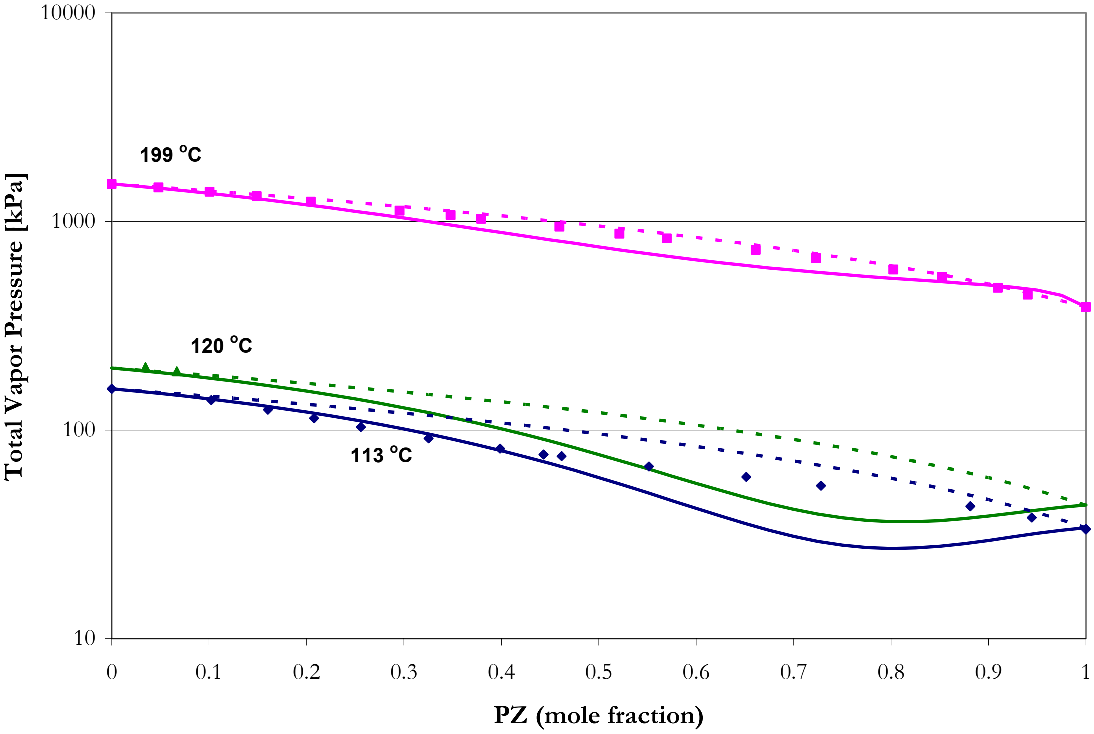

Figure 9.4-3. Comparison of Wilson and Wilding (1994) and Xia et al. (2003) Total Pressure data to elecNRTL Model Predictions from 113 to 199 °C. Points: ♦ and ■, Wilson and Wilding (1994), ▲, Xia et al. (2003). Lines: ▬, elecNRTL Predictions, - - -, Raoult's Law.

The optimum model exhibits systematic error and under predicts the total vapor pressure with a maximum error of ± 45.95 % for concentrations greater than 50 mole percent of PZ from 113 and 120 °C even though all the predictions of the model were within an AARD of ± 11.95 %, with the exception of a few outliers. Figure 9.4-3 illustrates the departure from an ideal solution behavior vis-à-vis Raoult's Law as compared to predictions from the elecNRTL model. Over the temperature range from 113 and 120 °C, Raoult's Law adequately describes the vapor pressure of H_2O-PZ mixtures below $x_{PZ} = 0.2$, but as the concentration of PZ increases so does the importance of including activities to describe the vapor-liquid equilibrium. Overall, the optimum model adequately describes the total vapor pressure data in PZ mixtures within an average absolute relative error of ± 7.85 percent.

9.4.3 *Vapor-Liquid Equilibrium*

One of the main goals of this work was to describe the amine volatility at absorber and stripper conditions. Figure 9.4-4 through Figure 9.4-10 compares estimated and experimental amine volatility data from this work to predictions from the elecNRTL model. We have included salt precipitation effects on piperazine volatility as described by the dashed lines. From the figures, the volatility of piperazine increases with increasing temperature and concentration.

Figure 9.4-10 illustrates predictions from the optimum model for piperazine concentrations from 0.5 to 10 m and over a temperature range from 20 to 120 °C. Volatility of 10 m PZ illustrates an interesting point: where below 50 °C, the predicted partial pressure occurs over a saturated salt solution and thereby increased the amine volatility. As the temperature increases, the precipitated salt melts and the solution becomes a homogenous liquid phase.

In addition, Figure 9.4-4 through Figure 9.4-10 illustrates the departure from an ideal solution behavior vis-à-vis Raoult's Law as compared to predictions from the elecNRTL model. Over the temperature range from 20 to 80 °C, Raoult's Law overestimates the vapor pressure of PZ in binary mixtures of H_2O-PZ by a factor of 20 as shown in Table 9.4-2.

Table 9.4-2. Comparison of PZ Volatility Based on Predictions from the elecNRTL Model and Raoult's Law at 40 °C.

	P^{PZ} (ppm$_v$)	
PZ (m)	elecNRTL	Raoult's Law
0.9	8	180
1.8	16	354
2.0	18	392
2.5	22	486
3.6	33	687
5.0	39	932

Overall, the optimum model adequately describes the partial pressure PZ within an average absolute relative error of ± 13.03 percent with the exception of a few outliers. We would recommend that future work should endeavor to describe the binary system at stripper conditions (e.g. temperatures between 80 – 120 °C) to complete this analysis.

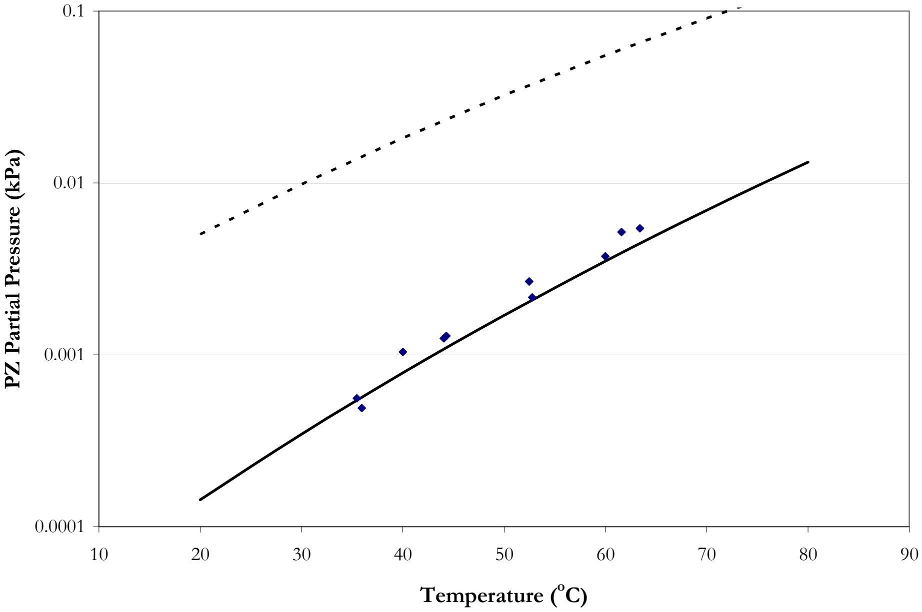

Figure 9.4-4. Comparison of Amine Volatility in 0.9 m PZ. Solid line: —, elecNRTL Predictions. Dash line: Raoult's Law Approximations.

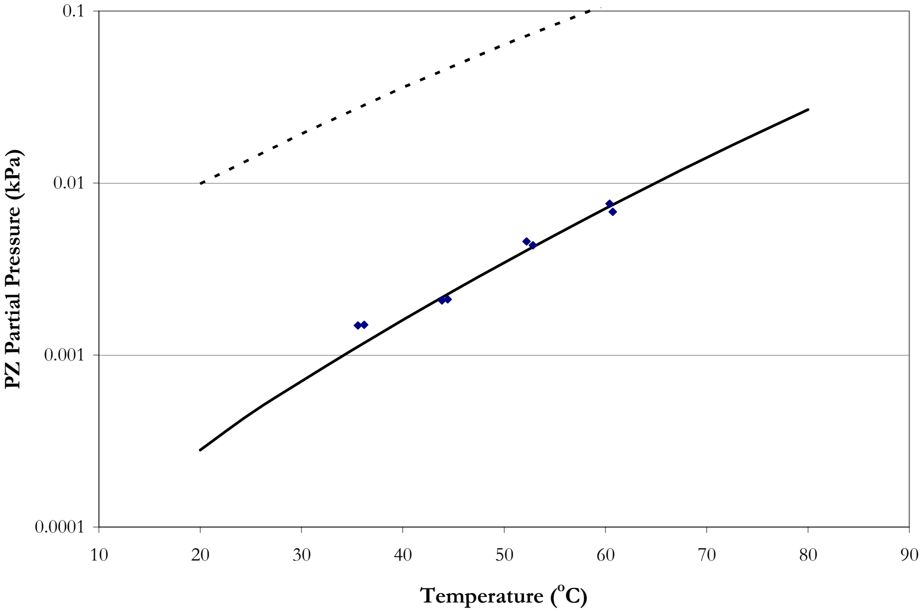

Figure 9.4-5. Comparison of Amine Volatility in 1.8 m PZ. Solid line: —, elecNRTL Predictions. Dash line: Raoult's Law Approximations.

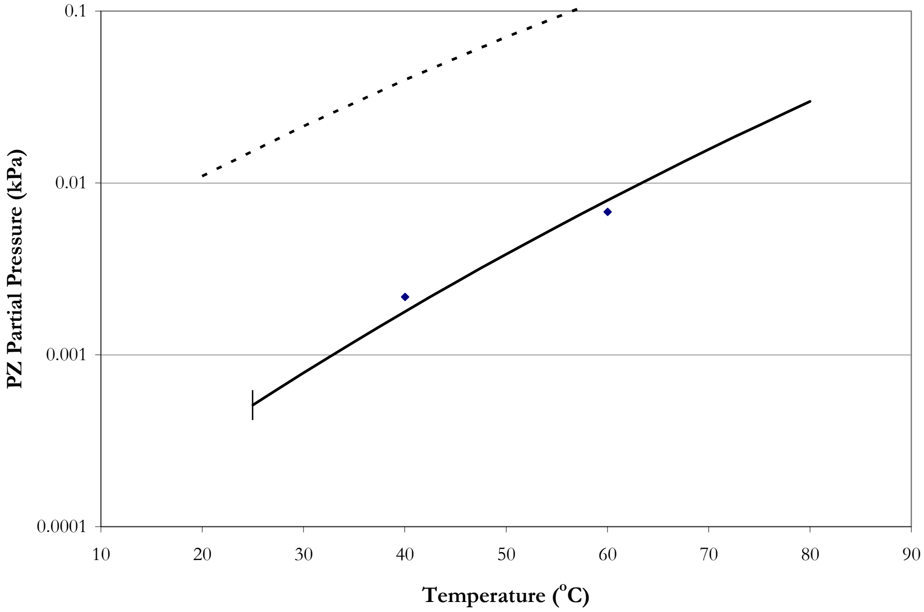

Figure 9.4-6. Comparison of Amine Volatility in 2.0 m PZ. Solid line: ▬, elecNRTL Predictions. Dash line: Raoult's Law Approximations. Vertical line: Solid Solubility Boundary.

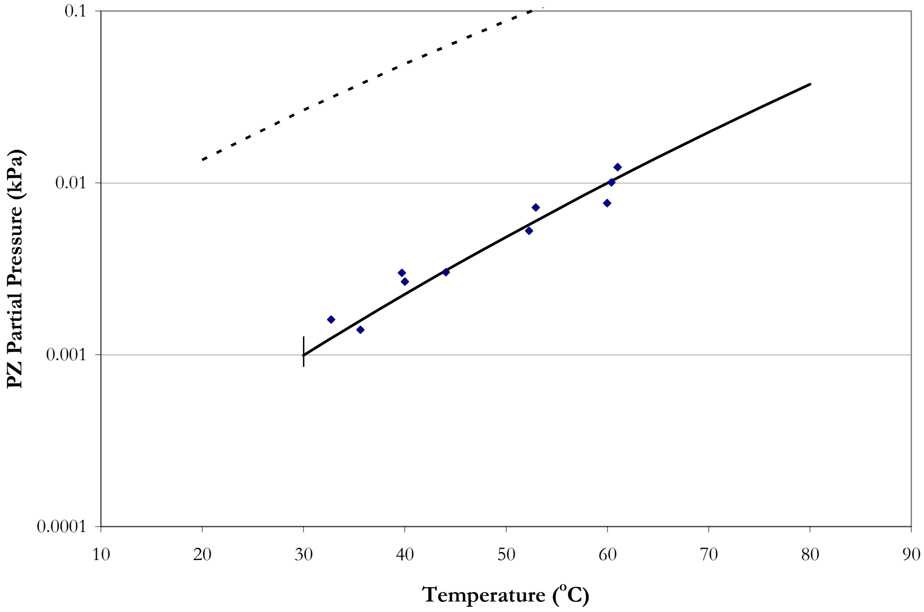

Figure 9.4-7. Comparison of Amine Volatility in 2.5 m PZ. Solid line: ▬, elecNRTL Predictions. Dash line: Raoult's Law Approximations. Vertical line: Solid Solubility Boundary.

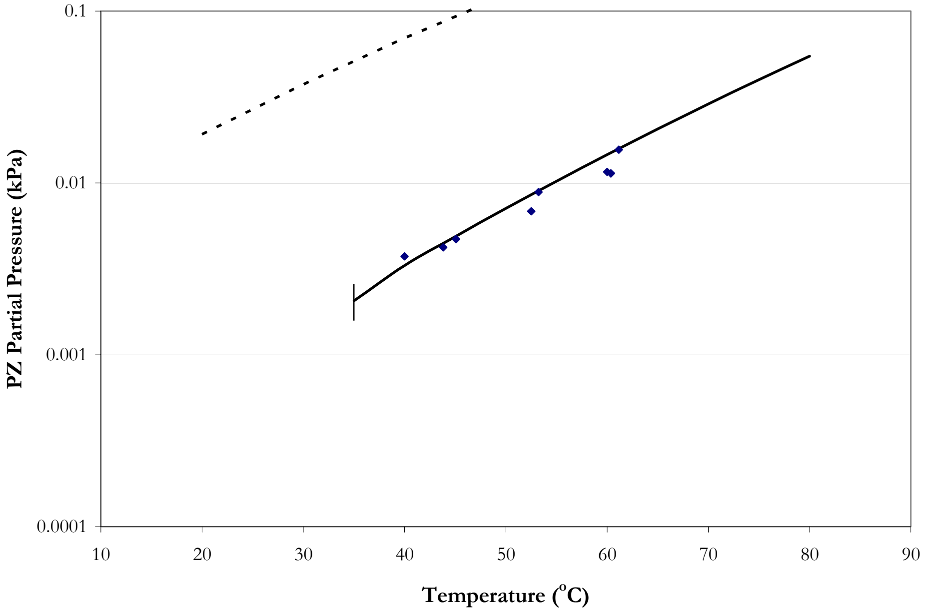

Figure 9.4-8. Comparison of Amine Volatility in 3.6 m PZ. Solid line: —, elecNRTL Predictions. Dash line: Raoult's Law Approximations. Vertical line: Solid Solubility Boundary.

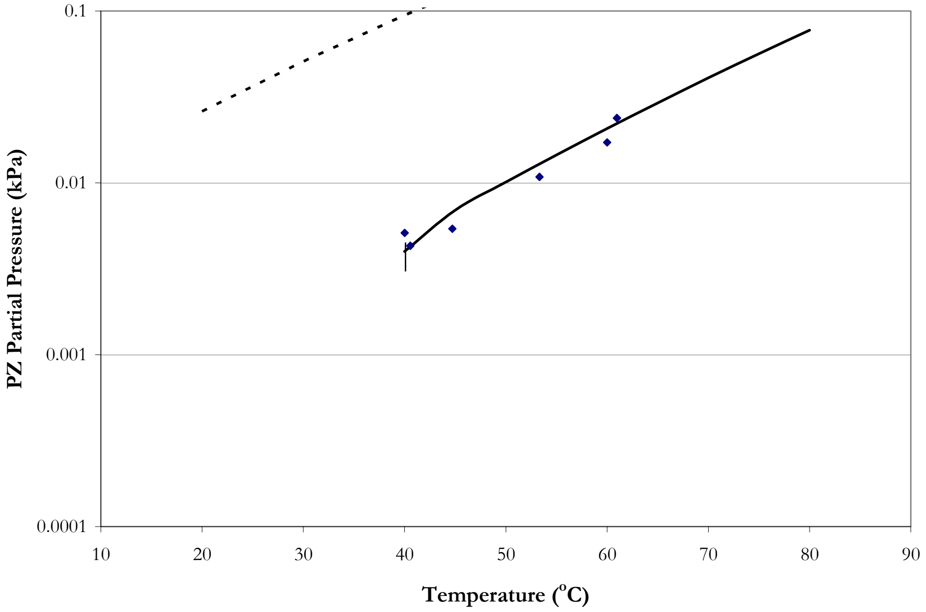

Figure 9.4-9. Comparison of Amine Volatility in 5.0 m PZ. Solid line: —, elecNRTL Predictions. Dash line: Raoult's Law Approximations. Vertical line: Solid Solubility Boundary.

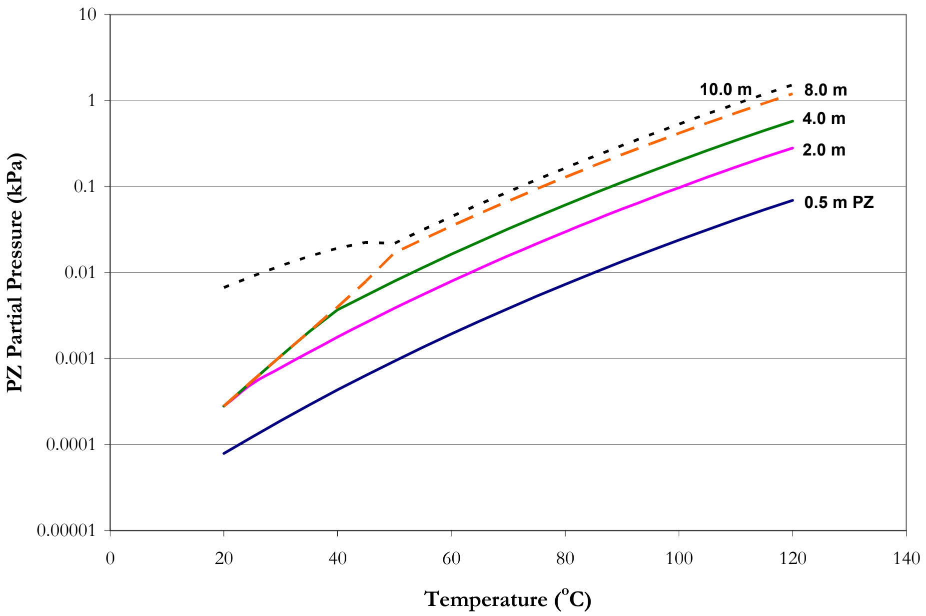

Figure 9.4-10. Predictions of Amine Volatility from the elecNRTL model of 0.5 to 10 m PZ from 20 to 120 °C with Salt Precipitation Effects.

9.4.4 *Specific Heat Capacity*

To describe the specific heat capacity of H_2O-PZ solutions, Figure 9.4-11 compares estimated and experimental specific heat capacities from 25 to 120 °C for 2 and 3.6 m PZ. Specific heat capacity for 2.0 m PZ above 80 °C were excluded from the optimum model regression due to an inconsistent trend in the overall specific heat capacity data but were included in Figure 9.4-11 for clarification. Figure 9.4-11 also illustrates optimum model predictions for 1.0 and 5.0 m PZ. Overall, the optimum model adequately describes the specific heat capacity for aqueous mixtures of PZ within an average absolute relative error of ± 0.25 percent, with the exception of a few outliers.

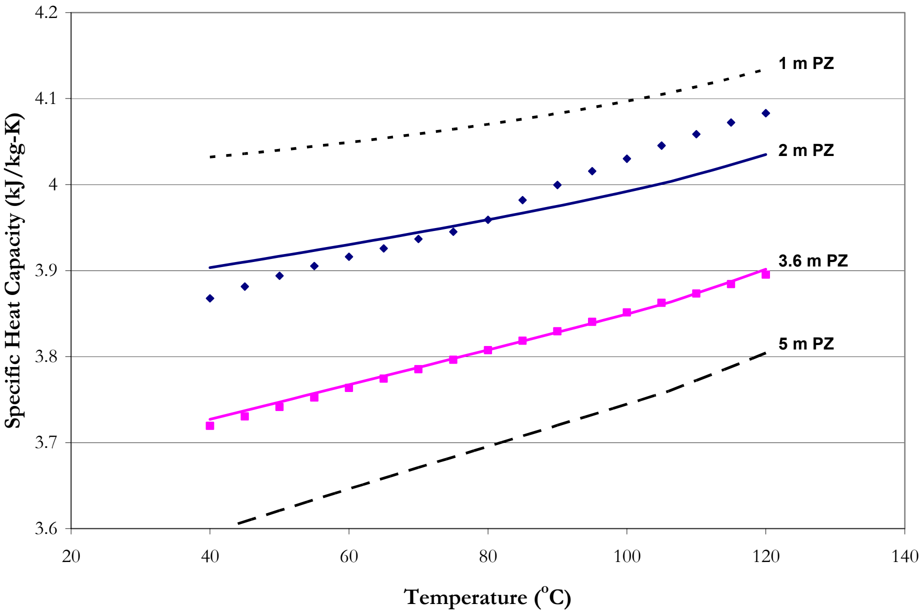

Figure 9.4-11. Comparison of Specific Heat Capacity from this work to elecNRTL Model Predictions for 2.0 and 3.6 m PZ. Points: ♦, 2.0 m PZ, ■, 3.6 m PZ. Lines: elecNRTL Model Predictions.

9.4.5 *Activity Coefficient Predictions for H_2O-PZ*

Several authors have presented activity-based models to calculate the activity coefficient of PZ in aqueous PZ mixtures. Works include:

Author	Model	H_2O-PZ Activity Coefficients
Bishnoi et al. (2002)	Electrolyte-NRTL	Predicted from UNIFAC (DMD)
Aroua and Salleh (2004)	Kent-Eisenberg	Neglected
Kamps et al. (2003)	Pitzer Equation	Neglected
Cullinane (2005)	Electrolyte-NRTL	Predicted from UNIFAC (DMD)
Derks et al. (2005)	Electrolyte EoS	Predicted from UNIFAC (DMD)
Hilliard (2005)	Electrolyte-NRTL (Aspen Plus)	Predicted from UNIFAC (DMD)
Ermatchkov et al. (2006)	Pitzer Equation	Neglected

All of the above authors chose to neglect interactions between PZ and water or to predict the activity coefficients based on the UNIFAC (DMD) Model due to a limited experimental date. In this work, we have compiled an extensive database of consistent high quality literature data. Thus, the subsequent discussion on predicting the activity coefficients for PZ in aqueous PZ mixtures will provide the most realistic values to date. Figure 9.4-12 compares activity coefficient predictions based on UNIFAC (DMD) predictions by Hilliard (2005) to this work.

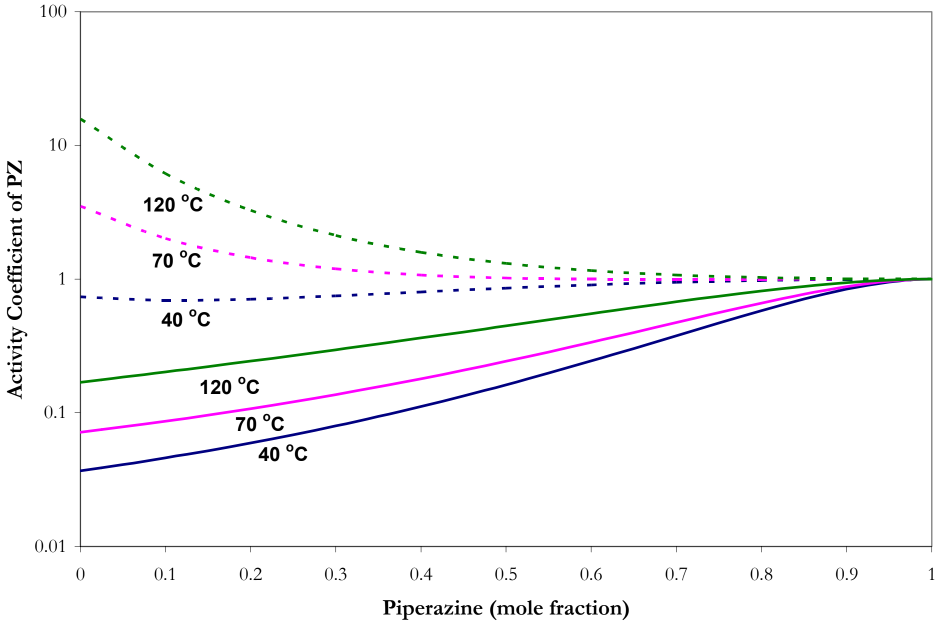

Figure 9.4-12. Predictions for the Activity Coefficient of PZ from Hilliard (2005) to this work at 40, 70, and 120 °C. Lines: dashed, Hilliard (2005); solid, this work.

As stated previously, Hilliard (2005) predicted the activity coefficient of PZ from the UNIFAC [Dortmund Modified (DMD)] Method [Weidlich and Gmehling (1987) and Gmehling et al. (1993)], where the activity coefficients were predicted from group contributions and were assumed accurate due to the lack of experimental information. The modified UNIFAC model treated cyclic PZ as an aliphatic molecule with respect to predicating the effect of substituent groups to the amine's structure, thereby affecting how the molecule will interact in an aqueous environment with increasing temperature as shown in Figure 9.4-12 as compared to this work.

Smith et al. (1996) noted for a binary system to remain stable (single phase) and not split into two phases the change in the Gibbs free energy at constant temperature and pressure and the first and second derivatives must be continuous functions with respect to concentration. Smith et al. (1996) gave the following criterion of the stability for a single phase in a binary system:

$$\frac{d^2\left(\Delta G / RT\right)}{dx_1^2} > 0 \tag{9-47}$$

This criterion can then be applied to an excess Gibbs energy expression for a binary system as given by the following expression:

$$\frac{d^2\left(G^{Ex} / RT\right)}{dx_1^2} > -\frac{1}{x_1 x_2} \tag{9-48}$$

Where for a binary system,

$$\frac{G^{Ex}}{RT} = x_1 \ln x_1 + x_2 \ln x_2 \tag{9-49}$$

Equation 9-48 combined with Equation 9-47 yields

$$\frac{d^2\left(G^{Ex} / RT\right)}{dx_1^2} = \frac{d \ln \gamma_1}{dx_1} - \frac{d \ln \gamma_2}{dx_2} \tag{9-50}$$

Applying the Gibbs-Duhem equation to Equation 9-50 results in the following criterion in terms of the activity coefficient of component i.

$$\frac{d\ln\gamma_i}{dx_i} > -\frac{1}{x_i} \tag{9-51}$$

Figure 9.4-13 illustrates predictions for the single phase stability of aqueous PZ mixtures at 40 and 120 °C from the optimum model binary interaction parameters. Figure 9.4-13 shows that a second phase will not appear over the operating range considered in this work.

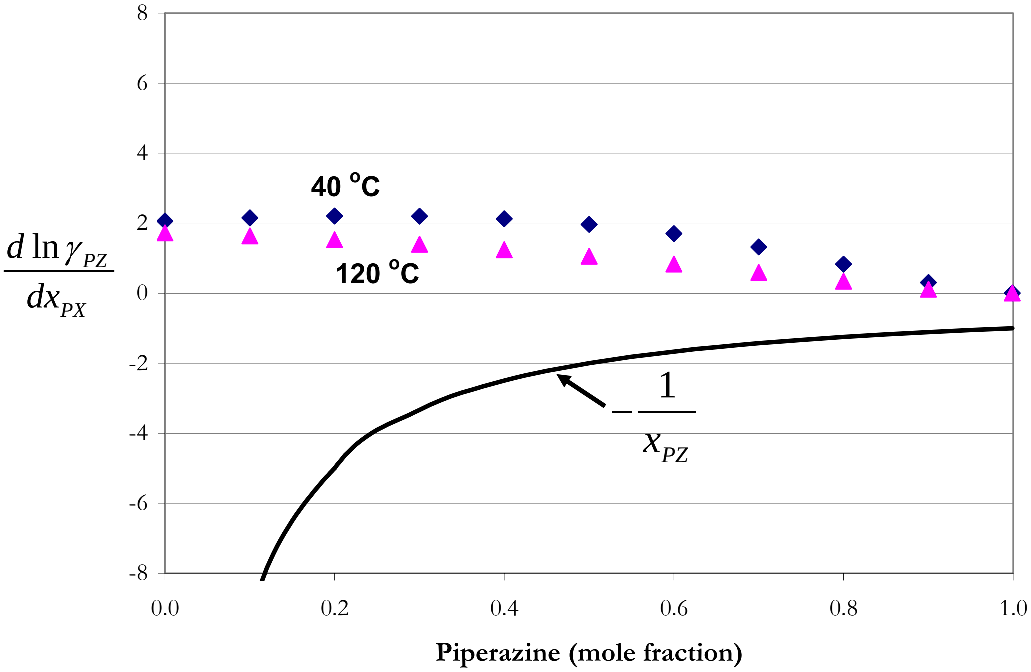

Figure 9.4-13. Model Predictions for the Phase Stability Criterion for Aqueous PZ Mixtures at 40 and 120 °C.

9.5 Conclusions

In conclusion, parameters for the H_2O-PZ system were fitted to a more extensive database than previous authors; thus infinite dilution activity coefficients predicted with the optimum model may give more realistic activity coefficients as a function of temperature and composition as compared to data found in the literature.

For total vapor pressure, the optimum model exhibited a systematic error and under predicted the total vapor pressure with a maximum error of ± 45.95 % for concentrations greater than 50 mole percent of PZ from 113 and 120 °C even though all the predictions of the model were within an AARD of ± 11.95 %, with the exception of a few outliers. Figure 9.4-3 illustrated the departure from an ideal solution behavior vis-à-vis Raoult's Law as compared to predictions from the elecNRTL model. Over the temperature range from 113 and 120 °C, it was shown that Raoult's Law adequately described the vapor pressure of H_2O-PZ mixtures below $x_{PZ} = 0.2$, but as the concentration of PZ increases so did the importance of including activities to describe the vapor-liquid equilibrium. Overall, the optimum model adequately described the total vapor pressure data in PZ mixtures within an average absolute relative error of ± 7.85 percent.

One of the main goals of this work was to describe the amine volatility at absorber and stripper conditions. Figure 9.4-4 through Figure 9.4-10 compared estimated and experimental amine volatility data from this work to predictions from the elecNRTL model. We chose to include salt precipitation effects on piperazine volatility. It was shown that the volatility of piperazine increased with increasing temperature and concentration. In addition,

Figure 9.4-4 through Figure 9.4-10 illustrated the departure from an ideal solution behavior vis-à-vis Raoult's Law as compared to predictions from the elecNRTL model. Over the temperature range from 20 to 80 °C, Raoult's Law overestimated the vapor pressure of PZ in binary mixtures of H_2O-PZ by a factor of 20 as shown in Table 9.4-2. Figure 9.4-10 illustrated predictions from the optimum model for piperazine concentrations from 0.5 to 10 m and over a temperature range from 20 to 120 °C. Overall, the optimum model adequately described the partial pressure PZ within an average absolute relative error of ± 13.03 percent, with the exception of a few outliers. We also recommend that future work should describe the binary system at stripper conditions (e.g. temperatures between 80 – 120 °C) to complete this analysis.

In terms of activity coefficients, previous authors chose to either neglect interactions between PZ and water or to predict the activity coefficients based on the UNIFAC (DMD) Model due to limited experimental data. In this work we have compiled an extensive database of consistent high quality literature data. Thus, predictions of the activity coefficients for PZ in aqueous PZ mixtures will provide the most realistic values to date. For instance, the infinite dilution activity coefficient for PZ was illustrated in Figure 9.3-2 to vary from 0.0219 – 0.288 over the temperature range from 20 to 160 °C as compared to predictions from the Hilliard (2005) model which varied from 0.161 – 31.6.

Overall, the results presented above indicate that the elecNRTL model, through simultaneous regression, gave a set of optimum binary interaction parameters for the H_2O-PZ system. The optimum model adequately represents the literature data for aqueous PZ mixtures.

CHAPTER X

Ternary Systems: H_2O-MEA-PZ

10.1 Introduction

Chapter VIII and IX described the molecule-molecule interactions between water (H_2O) and monoethanolamine (MEA) and piperazine (PZ), respectively. In this chapter, we continue the thermodynamic model development by describing the binary interactions associated when two binary systems are combined. This chapter describes the data regression and model predictions for the unreactive H_2O-MEA-PZ system based on data from this work. The results for the binary interaction parameters for the electrolyte-NRTL (elecNRTL) model in Aspen Plus^{TM} are then presented; showing good statistical fit to the data with an average absolute relative error of ± 9.32 % with the exception of a few outliers.

10.2 H_2O-MEA-PZ System

Up to this point for the H_2O-MEA-PZ system, we have been able to describe the molecule-molecule interactions between H_2O-MEA and H_2O-PZ given in Chapters VIII and IX. Molecular interactions between MEA and PZ in the presence of H_2O will be described by the elecNRTL model which reduces in theory to the NRTL Model of Renon and Prausnitz (1968) when the concentration of ions in an electrolyte solution approaches zero within Aspen Plus. In this section, we present background on the NRTL model for clarification purposes only since we will be using the elecNRTL property model for all future chapters to describe molecular and ionic interactions.

The NRTL model is an excess Gibbs energy model given by the following form after taking the partial derivative of the excess Gibbs energy to describe the activity coefficients for n components:

$$\ln \gamma_i = \frac{\sum_j x_j \tau_{ji} G_{ji}}{\sum_k x_k G_{ki}} + \sum_j \frac{x_j G_{jj}}{\sum_k x_k G_{kj}} \left(\tau_{ij} - \frac{\sum_m x_m \tau_{mj} G_{mj}}{\sum_k x_k G_{kj}} \right) \qquad \text{10-1}$$

Where
i, j, k are the species indices, 1: H_2O, 2: MEA, 3: PZ,
x_i is the liquid mole fraction of component i,
τ_{ij} is the binary interaction parameter between component i and j,
α_{ij} is the molecule-molecule nonrandomness factor, 0.2,
$G_{ij} = e^{-\alpha_{ij}\tau_{ij}}$.

The molecule-molecule binary interaction parameters were assumed to be temperature dependent and were fitted to the following function of temperature:

$$\tau_{ij} = A_{ij} + \frac{B_{ij}}{T} + C_{ij}\ln(T) + D_{ij}T \qquad 10\text{-}2$$

Interactions parameters for H_2O-MEA and H_2O-PZ were given in Chapters VIII and IX as shown in Table 10.2-1.

Table 10.2-1. Binary Interaction Parameters for H_2O-MEA and H_2O-PZ Systems.

	Interaction Species		
Parameter	i	j	Estimate
1-$A_{m,m}$	H_2O	MEA	-4.46
2-$B_{m,m}$	H_2O	MEA	-85.3
3-$D_{m,m}$	H_2O	MEA	0.0149
4-$A_{m,m}$	MEA	H_2O	2.90
5-$B_{m,m}$	MEA	H_2O	-456
6-$D_{m,m}$	MEA	H_2O	-0.0079
7-$A_{m,m}$	H_2O	PZ	-7.68
8-$D_{m,m}$	H_2O	PZ	0.0107
9-$A_{m,m}$	PZ	H_2O	-6.42
10-$D_{m,m}$	PZ	H_2O	0.0249

The above set of binary interaction parameters represents two unique sets for describing each system separately. In this chapter we will compare experimental data for the H_2O-MEA-PZ system to model predictions based on the combination of the binary systems and from additional binary interaction parameters for MEA-PZ regressed from experimental data.

The creation of the H_2O-MEA-PZ model begins with the regression of experimental data from this work. Two data sets have been regressed with the elecNRTL model to represent the phase equilibrium through regression of vapor-liquid equilibrium and specific heat capacity data over monoethanolamine plus piperazine solutions. The following section describes the different types of data used in the creation of the ternary H_2O-MEA-PZ model.

10.2.1 *Vapor-Liquid Equilibrium*

Data in the form of vapor-liquid equilibrium (VLE), which measures the vapor and liquid compositions in aqueous MEA plus piperazine solutions, as a function of concentration and temperature, were used to adjust the activity coefficients of MEA, PZ, and H_2O through simultaneous regression of binary interaction parameters in the NRTL model. For the ternary system, Equation 10-3 can be used to represent the vapor-liquid equilibrium data.

$$y_i \hat{\phi}_i^v P = x_i \gamma_i \hat{\phi}_i^0 P_i^0 \exp\left[\frac{V_i^l \left(P - P_i^0\right)}{RT}\right] \qquad 10\text{-}3$$

Where
$\hat{\phi}_i$ is the fugacity coefficient of component i,
P si the total pressure of the system,
P_i^0 is the Extended Antoine pure vapor pressure of component i,
γ_i is the symmetric activity coefficient of component i,
V_i^l is the Brelvi-O'Connel molar volume of the pure component at the system temperature and saturation pressure, and,
y_i and x_i are the true mole fractions in the vapor and liquid phases of component i.

Examples of experimental amine volatility from this work between 3.5 m MEA plus 1.8 m PZ and 7 m MEA plus 3.6 m PZ are shown in Figures 10.2-1 through 10.2-4 as compared to predictions from the binary system models.

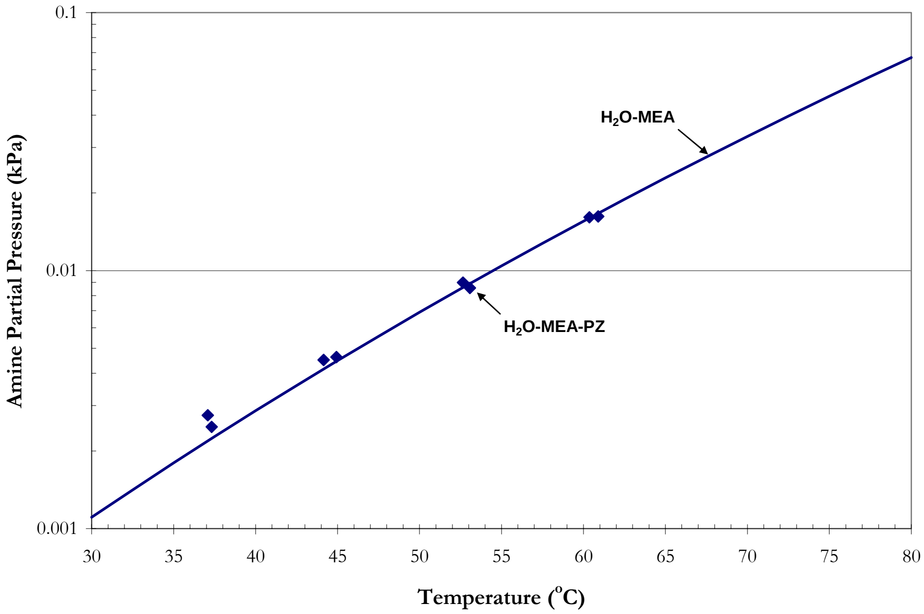

Figure 10.2-1. Comparison of Experimental MEA Volatility in 3.5 m MEA + 1.8 m PZ to 3.5 m MEA Binary elecNRTL Model Predictions.

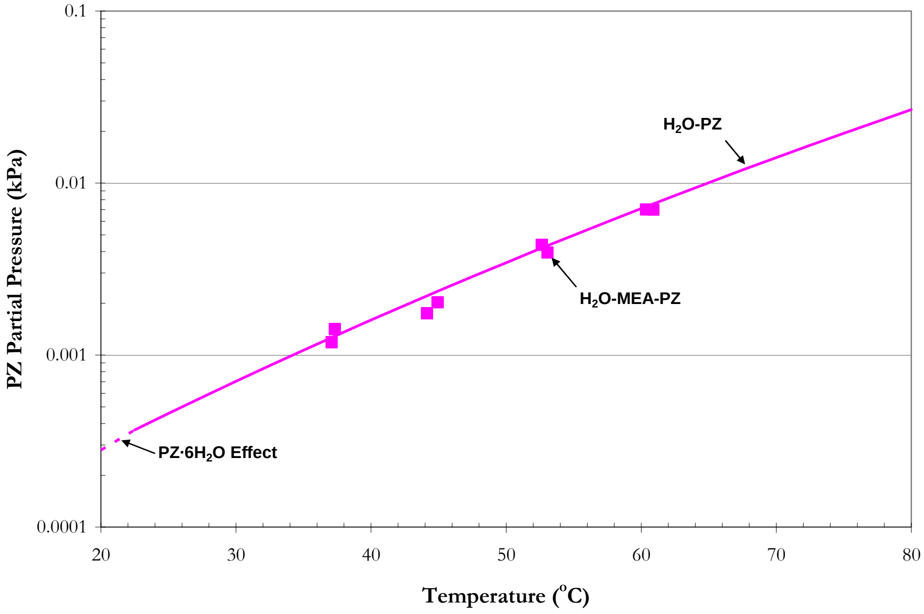

Figure 10.2-2. Comparison of Experimental PZ Volatility in 3.5 m MEA + 1.8 m PZ to 1.8 m PZ Binary elecNRTL Model Predictions.

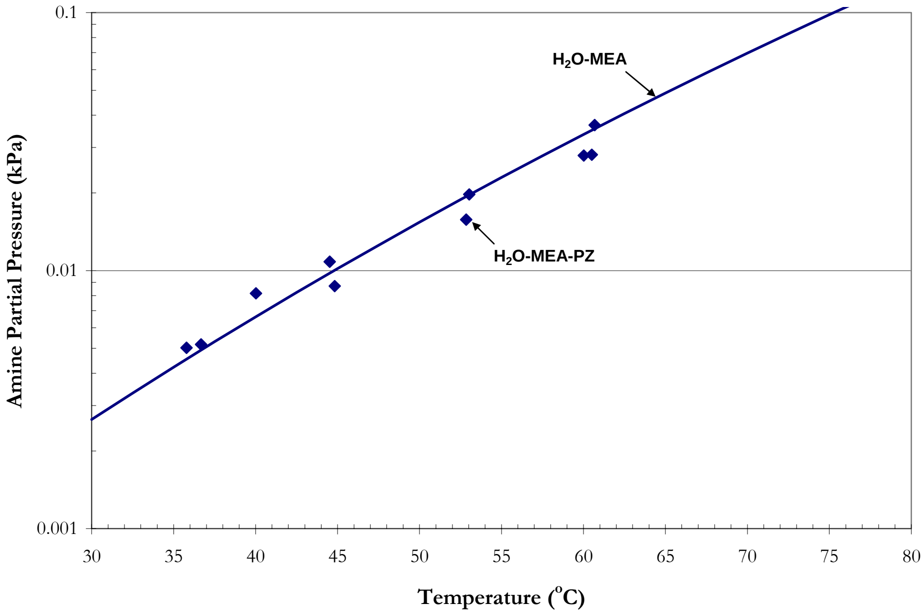

Figure 10.2-3. Comparison of Experimental MEA Volatility in 7 m MEA + 3.6 m PZ to 7 m MEA Binary elecNRTL Model Predictions.

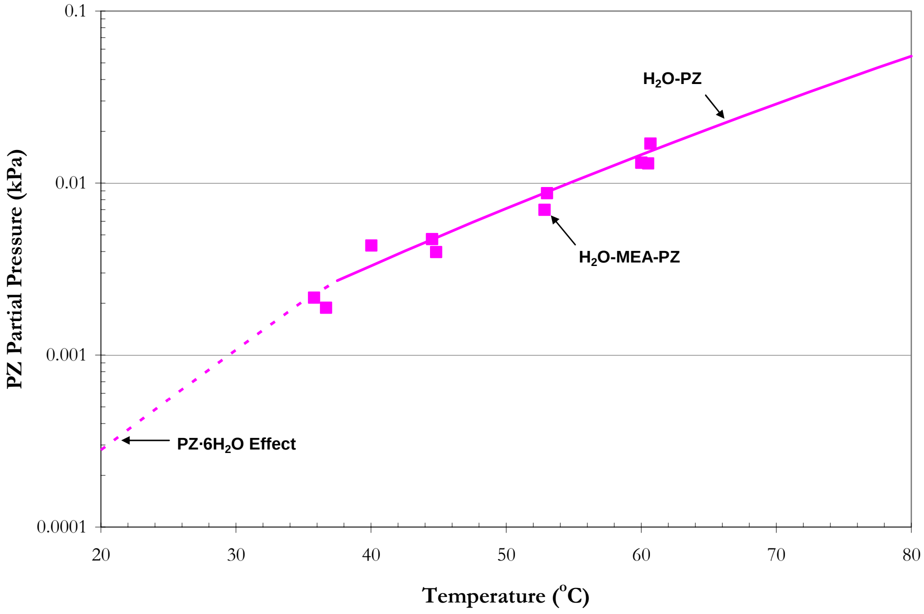

Figure 10.2-4. Comparison of Experimental PZ Volatility in 7 m MEA + 3.6 m PZ to 3.6 m PZ Binary elecNRTL Model Predictions.

The above figures illustrate that the binary models adequately describe the volatility of each amine in the mixture of MEA plus PZ between 40 and 70 °C. The amine volatility of the mixtures indicates that MEA and PZ have approximately the same volatility as compared to the same concentration associated with a binary mixture. Figure 10.2-4 illustrates an effect due to hydrogen bonding association of PZ with the addition of 7 m MEA. In the ternary mixture, the solubility of PZ is enhanced and does not precipitate to piperazine hexahydrate ($PZ \cdot 6H_2O$) as in the binary solution.

Overall, for each data point, the deviation between experimental and estimated values based on binary model predictions is expressed in terms of the average absolute relative deviation (AARD). Table 10.2-2 and Table 10.2-3 give the percent AARD and the maximum percent AARD for the binary model predictions.

Table 10.2-2. Absolute Percent Relative Error for Experimental MEA Volatility Data.

		AARD (%)	Max. AARD
P^{MEA}	3.5 m MEA + 1.8 m PZ	2.76	7.52
	3.5 m MEA + 2.0 m PZ	6.85	12.56
	3.5 m MEA + 3.6 m PZ	5.56	10.54
	7.0 m MEA + 1.8 m PZ	2.82	8.48
	7.0 m MEA + 2.0 m PZ	4.59	4.70
	7.0 m MEA + 3.6 m PZ	3.81	6.69
	Overall	4.40	12.56

Table 10.2-3. Absolute Percent Relative Error for Experimental PZ Volatility Data.

		AARD (%)	Max. AARD
P^{PZ}	3.5 m MEA + 1.8 m PZ	3.48	8.39
	3.5 m MEA + 2.0 m PZ	10.48	11.70
	3.5 m MEA + 3.6 m PZ	4.25	7.42
	7.0 m MEA + 1.8 m PZ	3.74	7.07
	7.0 m MEA + 2.0 m PZ	7.65	12.07
	7.0 m MEA + 3.6 m PZ	4.52	13.34
	Overall	5.69	13.34

Overall, separate binary model predictions adequately describes the MEA and PZ volatility data listed above within an average absolute relative error of ± 4.40 and 5.69 percent, respectively, with the exception of a few outliers. This would suggest there may not be a need for additional parameters to describe the ternary mixture.

10.2.2 *Specific Heat Capacity*

As stated in Chapter VI, Aspen Plus calculates the liquid phase heat capacity of a molecular mixture by taking the derivative of the liquid enthalpy at constant pressure:

$$H_i^l\left(T+\Delta T\right)-H_i^l\left(T\right)=\int_T^{T+\Delta T} C_{p,i}^l dT \qquad 10\text{-}4$$

where the liquid enthalpy of a mixture is calculated by the following equation:

$$H_i^l\left(T\right)=\sum_i x_i H_i + H_i^E \qquad 10\text{-}5$$

$$H_i\left(T\right) = \Delta H_f^{ig}\left(T^{ref}\right) + \int_{T^{ref}}^{T} C_p^{ig} dT + \left[H_i\left(T,p\right) - H_i^{ig}\left(T,p\right)\right] \qquad 10\text{-}6$$

Where
ΔT is the perturbation in temperature from *T*,
H_i^E is the excess enthalpy of component i,
$\Delta H_f^{ig}\left(T^{ref}\right)$ is the standard enthalpy of formation of component i at T^{ref},
T^{ref} is the reference temperature, 25.0 °C,
C_p^{ig} is the ideal gas heat capacity of component i,
H_i^{ig} is the ideal gas enthalpy of component i.

Data in the form of specific heat capacity of a mixture as a function of concentration and temperature were used to adjust the activity coefficients of monoethanolamine, piperazine, and water through the simultaneous regression of the binary interaction parameters by taking the derivative of the NRTL model, vis-à-vis excess enthalpy. Thus, specific heat capacity effects are limited only to the second and third terms of Equation 10-2. Examples of experimental specific heat capacity used in this work for 3.5 m MEA plus 2 m PZ and 7 m MEA plus 2 m PZ are shown in Figure 10.2-5 and Figure 10.2-6, respectively, as compared to the specific heat capacity for the binary mixtures.

Figure 10.2-5 illustrates that the experimental specific heat capacity may be similar to the combination of the specific heat capacity of the binary mixtures. The experimental specific heat capacity is lower than predictions for the binary mixtures, but is still within the accuracy of the data quality, vis-à-vis ± 1.0 % error. Figure 10.2-6 shows that the experimental specific heat capacity for 7 m MEA plus 2 m PZ may not be similar to the combination of the binary mixtures which may be due to error in the experimental measurement or a difference in the excess enthalpy of the ternary mixture.

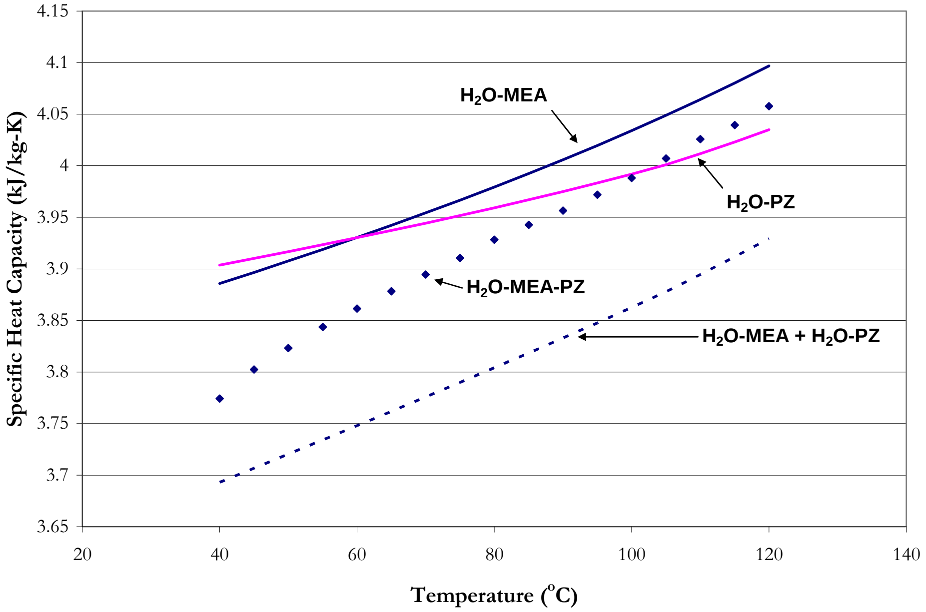

Figure 10.2-5. Comparison of 3.5 m MEA plus 2 m PZ Experimental Specific Heat Capacity from this work to elecNRTL Binary Mixture Predictions.

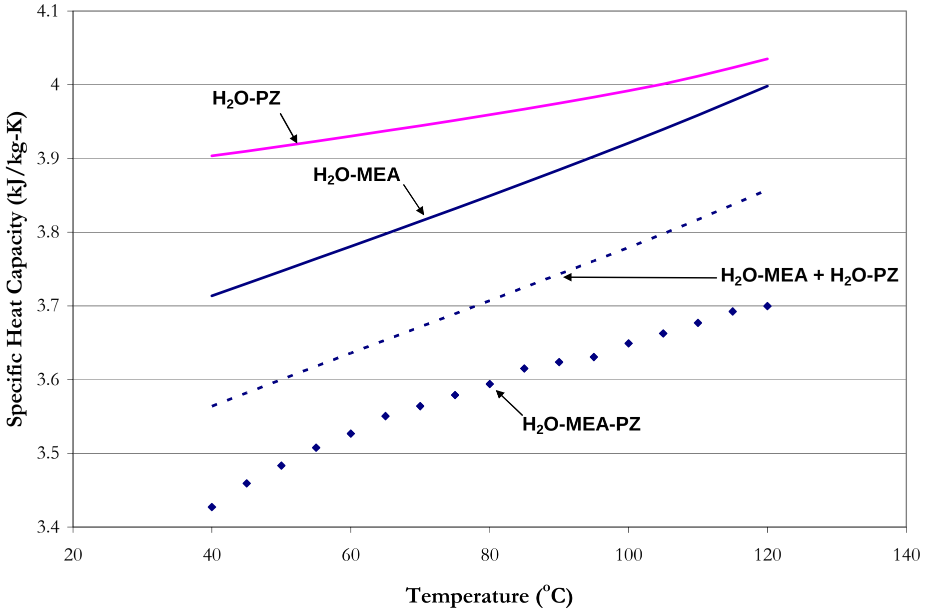

Figure 10.2-6. Comparison of 7 m MEA plus 2 m PZ Experimental Specific Heat Capacity from this work to elecNRTL Binary Mixture Predictions.

Figure 10.2-5 and 10.2-6 also illustrate the combined binary model predictions for the specific heat capacity without the regression of additional binary interaction parameters. The figure illustrates that the combined binary model adequately predicts the specific heat capacity of 3.5 m MEA plus 2 m PZ and 7 m MEA plus 2 m PZ within ± 3.16 and 3.14 percent, respectively. This error may be resolved if all three models were regressed simultaneously or the quality of the data may be subject to interpretation and additional verification.

10.3 Data Regression

For the elecNRTL model, binary interaction parameters for molecule-molecule interactions were given a default value of zero.

Through simultaneous regression, the molecule-molecule binary interaction parameters for the H_2O-MEA-PZ system were obtained through the regression of vapor-liquid equilibrium and specific heat capacity data from this work over monoethanolamine plus piperazine solutions.

A list of the aqueous electrolyte data sets that were examined in this work is given in Table 10.3-1. The column labels σ_T, σ_P, σ_{Cp}, σ_{x_i}, σ_{y_i}, give standard error associated with the temperature, pressure, specific heat capacity, liquid mole fraction, and the vapor mole fraction, respectively, with each data set. DRS suggested standard error default values were assigned unless otherwise stated by the author.

Table 10.3-1. Experimental data used in the regression of the H_2O-MEA-PZ system.

	Obs.	T (°C)	σ_T	σ_P	σ_x	σ_y	Source
VLE	80	31.5 – 61.4	0.1	2.0%	0.1%	0	This work

	Obs.	T (°C)	σ_T	σ_x	σ_{Cp}	Source
Cp	34	40.0 – 120.0	0.01	0.1%	0.1%	This work

After performing a nonlinear regression for the full model using DRS, the following regression summary statistics output for estimates of the adjustable binary parameters coefficients are shown in Table 10.3-2.

Table 10.3-2. DRS Regression Output for Full H_2O-MEA-PZ System Model.

	Interacting Species			
Parameter	i	j	Estimate	σ wrt Estimate
1-$A_{m,m}$	MEA	PZ	53.4	1054
2-$B_{m,m}$	MEA	PZ	1004	180873
3-$C_{m,m}$	MEA	PZ	8.74	249
4-$D_{m,m}$	MEA	PZ	-0.259	1.54
5-$A_{m,m}$	PZ	MEA	7.21	706
6-$B_{m,m}$	PZ	MEA	-2592	26014
7-$C_{m,m}$	PZ	MEA	2.60	124
8-$D_{m,m}$	PZ	MEA	-0.0377	0.244

Residual Sum of Squares:	33,774
Residual Root Mean Square:	17.850
Degree of Freedom:	106

Recall that the standard error of an estimate is the estimated standard deviation of that statistic. Notice that all of the estimates are smaller relative to their standard errors. A complete description of the variability of the coefficient estimates requires examining the correlations between the estimates as shown in Table 10.3-3.

Table 10.3-3. Correlation Matrix of the Coefficient Estimates for the Full H_2O-MEA-PZ Model.

Parameter	1	2	3	4	5	6	7	8
1	1.00							
2	-0.18	1.00						
3	-0.71	-0.56	1.00					
4	0.15	0.94	-0.80	1.00				
5	0.00	-0.23	0.16	-0.21	1.00			
6	0.00	-0.07	0.05	-0.06	-0.76	1.00		
7	0.00	0.28	-0.19	0.26	-0.99	0.65	1.00	
8	0.00	-0.45	0.30	-0.42	0.77	-0.17	-0.85	1.00

Table 10.3-3 shows two high negative correlations, but the correlation between other coefficients is relatively small, suggesting that $\hat{\eta}_4$ and/or $\hat{\eta}_7$ might be usefully removed from the model without significant loss of information.

After performing backward elimination using DRS, the following optimum model regression summary statistics output for estimates of the adjustable binary parameter coefficients are shown in Table 10.3-4. Please refer to Appendix O for more information about the backward elimination procedure to determine the optimal set of binary interaction parameters for the H_2O-MEA-PZ system.

Table 10.3-4. DRS Regression Output for the Optimum H_2O-MEA-PZ Model.

	Interacting Species			
Parameter	i	j	Estimate	σ wrt Estimate
1-$A_{m,m}$	MEA	PZ	61.8	14.0
2-$D_{m,m}$	MEA	PZ	-0.138	0.0369
3-$A_{m,m}$	PZ	MEA	1.64	0.540

Residual Sum of Squares:	35,762
Residual Root Mean Square:	17.949
Degree of Freedom:	111

Notice that all of the estimates are larger relative to their standard errors. Comparing the estimates from the full model to the optimum model, there was relatively little difference between the estimated values. The proposed optimum model provides the following correlations between the estimates as shown in Table 10.3-5.

Table 10.3-5. Correlation Matrix of the Coefficient Estimates for the Optimum H_2O-MEA-PZ Model.

Parameter	1	2	3
1	1.00		
2	-0.98	1.00	
3	0.14	-0.10	1.00

Table again shows a highly negative correlation between the temperature dependent parameter suggesting that some of the remaining parameters might be usefully removed from the model without significant loss of information.

10.3.1 *Optimum Model Results*

With the determination of the estimates for the binary interaction parameters known for the optimum model, a simple Aspen Plus™ Flash model was used to test the predictive capability of the H_2O-MEA-PZ model against literature data. For each data point, the deviation between the experimental and estimated values is expressed in terms of the average absolute relative deviation (AARD). Table 10.3-6 gives the percent AARD and the maximum percent AARD for the model predictions.

Table 10.3-6. Absolute Percent Relative Error for the H_2O-MEA-PZ Optimum Model.

		AARD(%)	Max. AARD
P^{MEA}	This work	11.84	34.59
P^{PZ}	This work	13.29	37.31
C_p	This work	2.84	3.93
Overall		**9.32**	**37.31**

Overall, the model adequately describes the H_2O-MEA property data listed above within an average absolute relative error of ± 9.32 percent, with the exception of a few outliers. For this reason, we chose not to include the optimum binary interaction parameters from this regression into future models due an increased in the relative error associated with the additional binary interaction parameters. The rest of the chapter will illustrate VLE predictions based on the combined binary models for H_2O-MEA and H_2O-PZ for all of the experimental amine volatility data.

10.3.2 *Vapor-Liquid Equilibrium*

One of the main goals of this work was to describe the amine volatility at absorber and stripper conditions. Figures 10.3-7 through 10.3-12 compare estimated and experimental amine volatility from this work to predictions from the elecNRTL binary and combined binary models.

As mentioned previously, the combined binary model adequately predicts the amine volatility in MEA plus PZ mixtures. Figures 10.3-9 and 10.3-12 illustrates an effect due to hydrogen bonding association of PZ with the addition of 3.5 and 7 m MEA, respectively. In the ternary mixture, the solubility of PZ is enhanced and does not precipitate to piperazine hexahydrate ($PZ \cdot 6H_2O$) as in the binary solution.

In terms of amine volatility and the effect of MEA and PZ with varying levels and the departure from an ideal solution behavior vis-à-vis Raoult's Law; Figure 10.3-13 illustrates the effect of 7 m MEA on 1.8 to 5.0 m PZ from 20 – 120 °C based on combined binary model predictions.

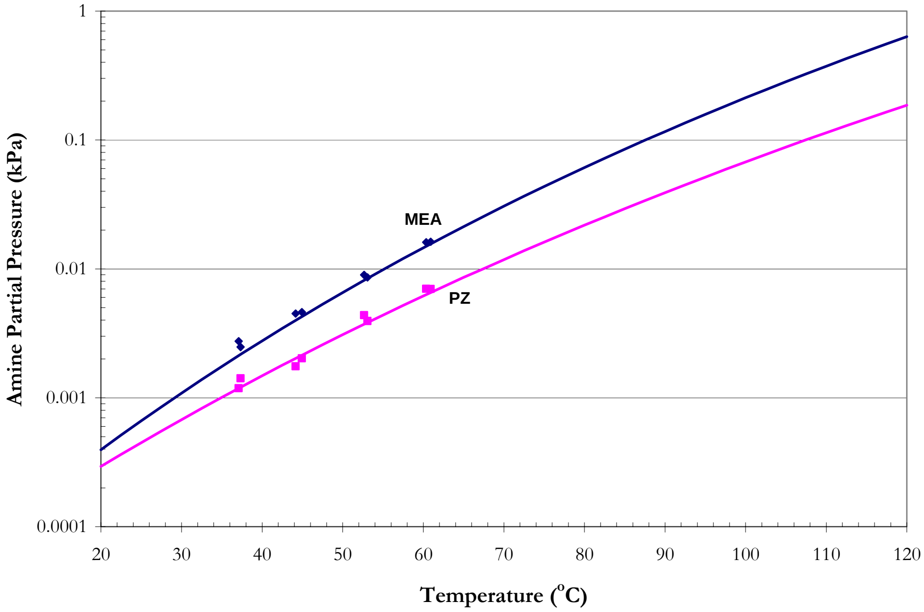

Table 10.3-7. Comparison of Experimental Amine Volatility in 3.5 m MEA Plus 1.8 m PZ to elecNRTL Combined Binary Model Predictions.

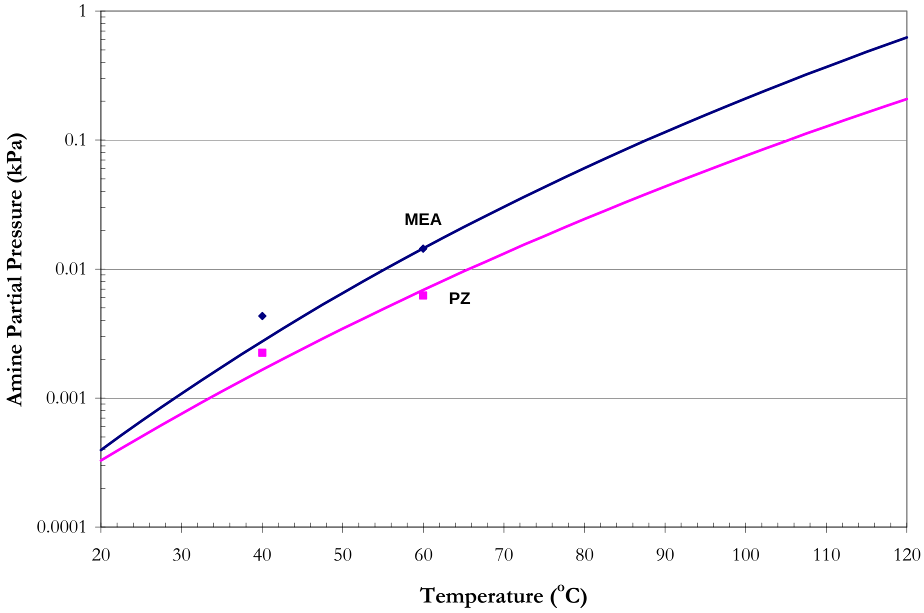

Table 10.3-8. Comparison of Experimental Amine Volatility in 3.5 m MEA Plus 2.0 m PZ to elecNRTL Combined Binary Model Predictions.

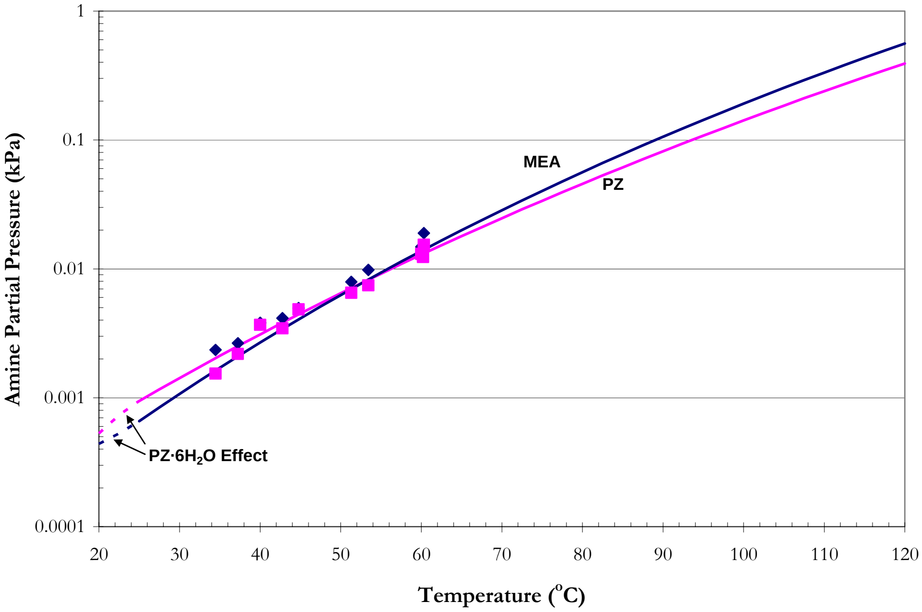

Table 10.3-9. Comparison of Experimental Amine Volatility in 3.5 m MEA Plus 3.6 m PZ to elecNRTL Combined Binary Model Predictions.

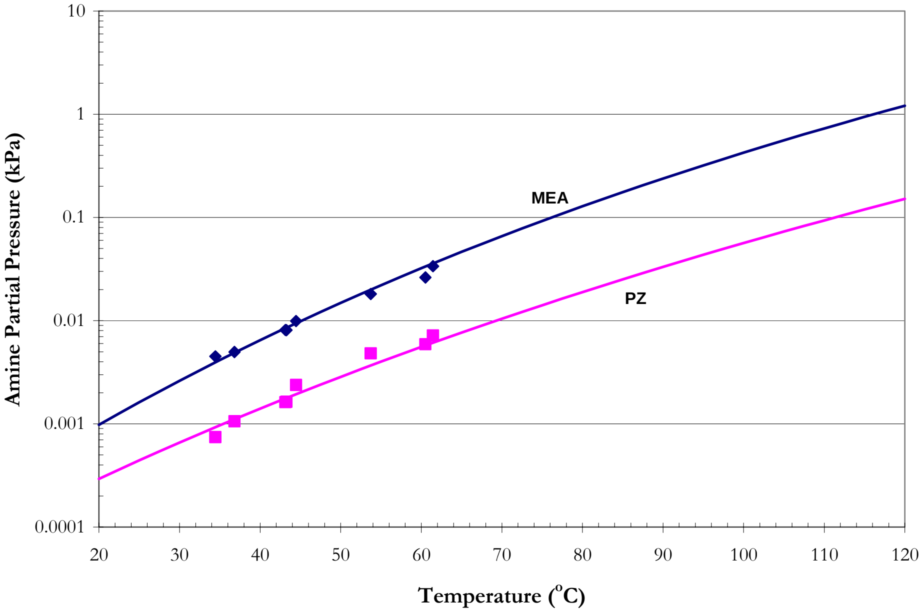

Table 10.3-10. Comparison of Experimental Amine Volatility in 7.0 m MEA Plus 1.8 m PZ to elecNRTL Combined Binary Model Predictions.

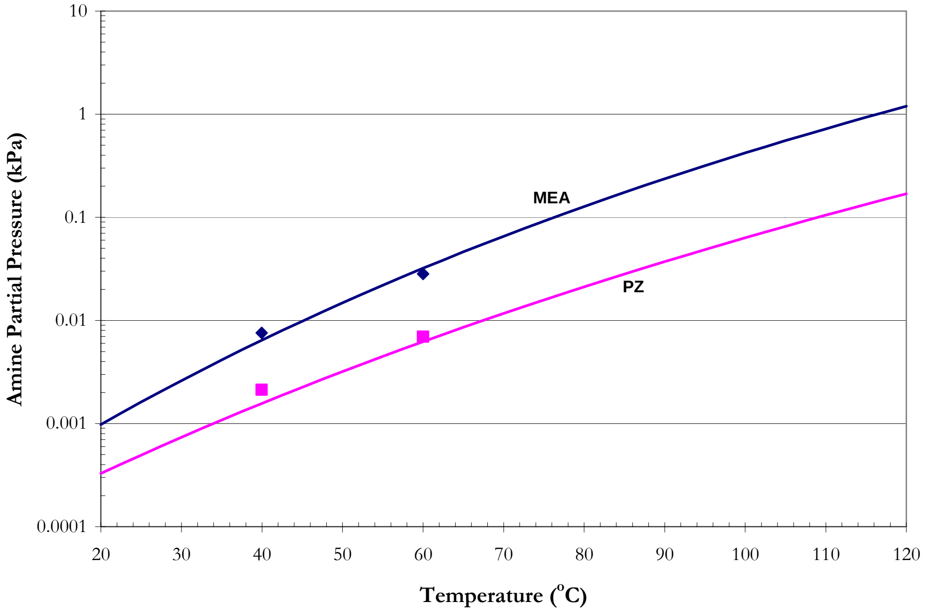

Table 10.3-11. Comparison of Experimental Amine Volatility in 7.0 m MEA Plus 2.0 m PZ to elecNRTL Combined Binary Model Predictions.

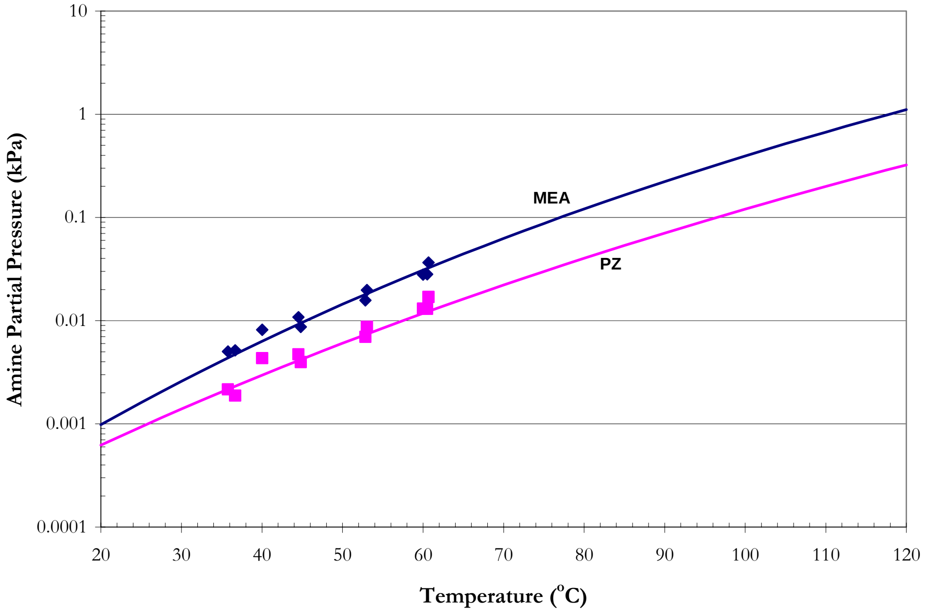

Table 10.3-12. Comparison of Experimental Amine Volatility in 7.0 m MEA Plus 3.6 m PZ to elecNRTL Combined Binary Model Predictions.

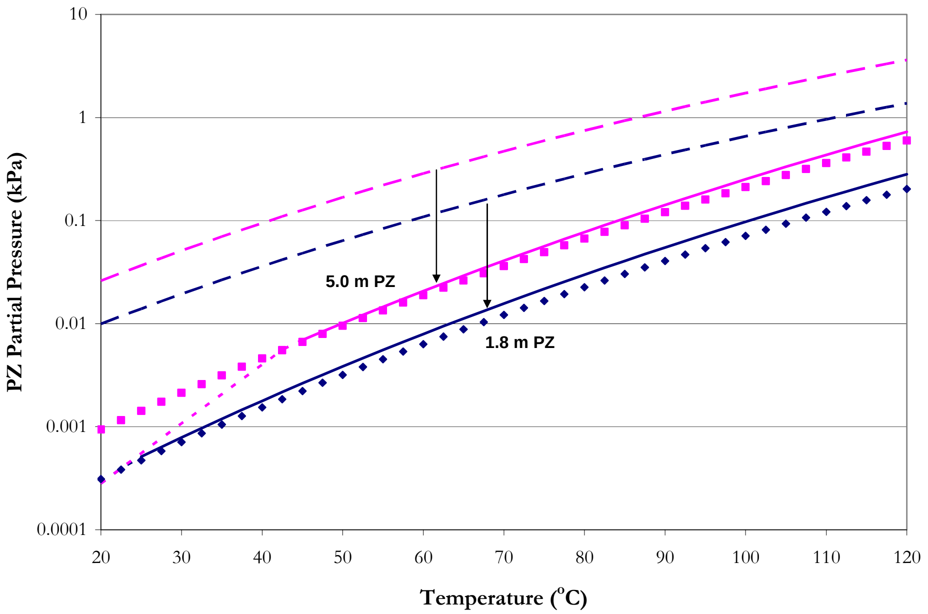

Table 10.3-13. Comparison of Predicted Amine Volatility in 7.0 m MEA Plus 1.8 – 5.0 m PZ to elecNRTL Combined Binary Model Predictions and the Deviation from Raoult's Law. Points: Combined Model Predictions. Solid lines: Binary Model Predictions. Dash lines: Raoult's Law Approximations.

Figure 10.3-14 illustrates the effect of 2 m PZ on 3.5 to 23.8 m MEA from 20 – 120 ^oC based on combined binary model predictions. Figure 10.3-13 shows a small effect of MEA on the volatility of PZ and could be contributed in a decreased in the activity coefficient of PZ, whereas the effect of PZ on MEA as shown in Figure 10.3-14 showed little or no effect due to the small concentration of PZ in the system. In terms of the departure of an ideal solution behavior, the effect of the activity coefficient on the partial pressure of PZ is shown in Figure 10.3-13. Predictions based on Raoult's Law do not adequately describe the vapor pressure of PZ and over estimates on the order of 1000 ppm_v.

On the other hand, predictions for MEA volatility based on Raoult's Law are adequate but may not be advisable at low concentrations of MEA.

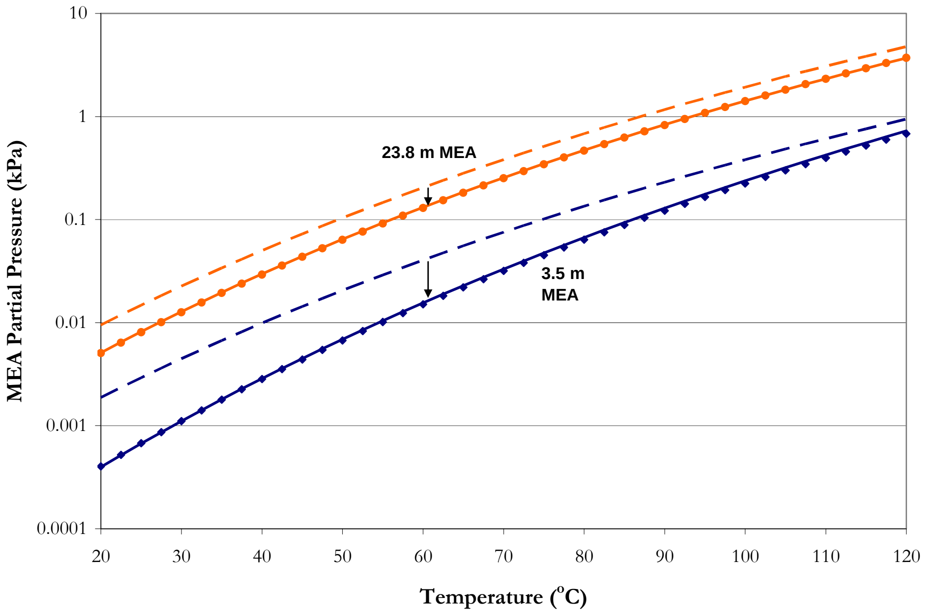

Table 10.3-14. Comparison of Predicted Amine Volatility in 2.0 m PZ Plus 3.5 – 23.8 m MEA to elecNRTL Combined Binary Model Predictions and the Deviation from Raoult's Law. Points: Combined Model Predictions. Solid lines: Binary Model Predictions. Dash lines: Raoult's Law Approximations.

10.4 Conclusions

In conclusion, binary models were shown to adequately describe the volatility of each amine in mixtures of MEA plus PZ between 40 and 70 °C. The amine volatility of the mixtures indicates that MEA and PZ have approximately the same volatility as compared to the same concentration associated with a binary mixture.

In terms of the solubility of PZ, Figure 10.2-4 illustrated the effect of hydrogen bonding of PZ with the addition of 7 m MEA where in the ternary mixture, the solubility of

PZ is enhanced and does not precipitate to piperazine hexahydrate ($PZ \cdot 6H_2O$) as in the binary solution.

Figure 10.2-5 illustrated that experimental specific heat capacity may be similar to the combination of the specific heat capacity of the binary mixtures at low concentrations. Even though the combined binary model was unable to adequately describe the experimental specific heat capacity data, this error may be resolved if all three models were regressed simultaneously. On the other hand, the quality of the data may be subject to interpretation and verification of the experimental specific heat capacity is recommended.

In terms of the departure of an ideal solution behavior, the effect of the activity coefficient on the partial pressure of PZ was shown in Figure 10.3-13. Predictions based on Raoult's Law were unable to adequately describe the vapor pressure of PZ and over estimated on the order of 1000 ppm. On the other hand, predictions for MEA volatility based on Raoult's Law are adequate but may not be advisable at low concentrations of MEA.

Overall, the results presented above indicate that the elecNRTL model, through combination of the binary models adequately represents experimental amine volatility and specific heat capacity from this work for aqueous MEA plus PZ mixtures.

CHAPTER XI

Ternary Systems: H_2O-MEA-N_2O

11.1 Introduction

We continue the thermodynamic model development by describing the molecule-molecule interactions between monoethanolamine (MEA) and carbon dioxide (CO_2) utilizing the CO_2-N_2O analogy. Interactions between piperazine and carbon dioxide will be addressed in Chapter XII. This chapter describes the data regression and model predictions for the unreacted H_2O-MEA-CO_2 system based on previous literature data. The results for the binary interaction parameters for the electrolyte-NRTL (elecNRTL) model in Aspen Plus^{TM} are then presented, showing good statistical fit to the literature data with an average absolute relative error of ± 3.48 % with the exception of a few outliers.

11.2 H_2O-MEA-N_2O System

Up to this point for the H_2O-MEA-N_2O system, we have been able to describe the molecule-molecule interactions between H_2O and MEA given in Chapter IX. Molecular interactions between H_2O and CO_2 are described by the Henry's constant for CO_2 in H_2O as reported by Chen et al. (1979), but interactions between MEA and CO_2 can not be directly measured. To account for molecule-molecule interactions between MEA and CO_2, Clarke (1964) proposed the CO_2-N_2O analogy method. Clarke proposed that if CO_2 reacts with a solvent, H_2O or MEA, the true solubility of CO_2 in the solvent can be determined by the proportionality to the solubility of a similar unreactive gas as in this case N_2O. N_2O is very similar to CO_2 in terms of their molecular weights, configurations, volumes, structures, and Lennard-Jones potentials. Plus, N_2O is unreactive to alkanolamines such as MEA and PZ. To describe molecular interactions between MEA and CO_2, N_2O solubility data in aqueous MEA mixtures were used to adjust the binary interaction parameters by using the CO_2-N_2O analogy method in the form of the Henry's constant.

$$H_{CO_2-MEA} = H_{CO_2-H_2O} \frac{H_{N_2O-MEA}}{H_{N_2O-H_2O}} \tag{11-1}$$

Where
H_{N_2O} is the solubility of N_2O in MEA and aqueous solutions as reported by Versteeg and van Swaaij (1988).

Recall from Chapter VI the representation of the solvent (e.g. H_2O or MEA) vapor-liquid equilibrium is given by the following equation.

$$y_i\hat{\phi}_i^v P = x_i\gamma_i\hat{\phi}_i^0 P_i^0 \exp\left[\frac{V_i^l\left(P-P_i^0\right)}{RT}\right] \tag{11-2}$$

and the vapor-liquid equilibrium for supercritical components (e.g. CO_2) is given by

$$y_i\hat{\phi}_i^v P = x_i\gamma_i\left(\frac{H_i}{\gamma_i^{\infty,aq}}\right)\exp\left[\frac{V_i^{\infty,aq}\left(P-P_{H_2O}^0\right)}{RT}\right] \tag{11-3}$$

and

$$\ln H_i\left(T,P_{H_2O}^0\right) = C_1 + \frac{C_2}{T(K)} + C_3\ln T(K) + C_4 T(K) + \frac{C_5}{T(K)^2} \tag{11-4}$$

Where

H_i is the Henry's constant for CO_2 in H_2O at the system temperature and saturation pressure of water, $P_{H_2O}^0$,

$\gamma_i^{\infty,aq}$ is the infinite dilution activity coefficient for CO_2 in H_2O at the system temperature,

V_i^l is the molar volume of the pure solvent at the system temperature and saturation pressure,

$V_i^{\infty,aq}$ is the Brelvi-O'Connell partial molar volume for CO_2 at infinite dilution in H_2O at system temperature and $P_{H_2O}^0$, and,

x_i is the true mole fraction in the liquid phase of component i.

Table 11.2-1 gives the coefficients used in this work for the Henry's constant for CO_2 in H_2O given by Chen et al. (1979) based on Equation 11-4.

Table 11.2-1. Coefficients for the Henry's Constant of CO_2 in H_2O (Pa/mole fraction).

C_1	C_2	C_3	C_4	C_5
170.7126	-8477.711	-21.95743	0.005781	0.0

$\ln H = C_1 + C_2/T(K) + C_3 \cdot \ln T(K) + C_4 \cdot T(K) + C_5/T(K)^2$

In this work, we chose to describe the solubility of CO_2 in water using the Chen et al. (1979) correlation for the Henry's constant for CO_2 in H_2O. Chen et al. (1979) developed their correlation based on the experimental work of Ellis and Golding (1963). In the literature, another key author, Edwards et al. (1978), developed a correlation for the Henry's constant for CO_2 in H_2O. Edwards et al. (1978) based their correlation on the work of Houghton et al. (1957), Stewart and Munjal (1970), Malinin (1959), and Malinin (1975). The two correlations adequately describe the solubility of CO_2 in H_2O as shown in Figure 11.2-1, even though the two correlations start to diverge above 120 °C, due to extrapolation differences.

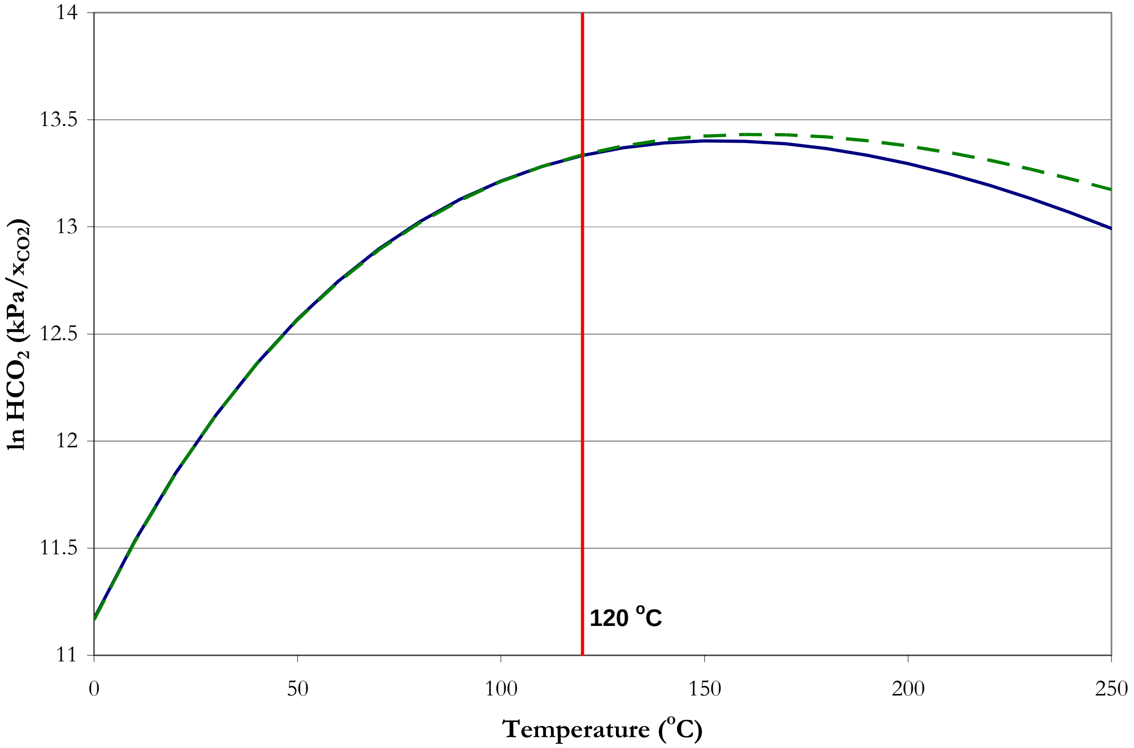

Figure 11.2-1. Solubility of CO_2 in H_2O as a Function of Temperature. Lines: – –, Chen et al. (1979) and —, Edwards et al. (1978).

In this work, Aspen Plus™ 2006.5 allowed for the user to choose the infinite dilution reference state of CO_2 as either infinite dilution in aqueous solvent or infinite dilution in mixed solvent. In the latter, Aspen Plus^{TM} utilized a volume weighted mixing rule to describe the Henry's constant of CO_2 in mixed solvent as shown below.

$$\ln\left(\frac{H_i}{\gamma_i^\infty}\right) = \sum_A w_A \ln\left(\frac{H_{i,A}}{\gamma_{i,A}^\infty}\right) \qquad 11\text{-}5$$

This convention normalizes the reference state of CO_2 to infinite dilution in solution, but in loaded alkanolamine solutions the reference state for the activity coefficient of CO_2 at infinite dilution is not zero; therefore to account for this, Aspen Plus^{TM} defines the asymmetric activity coefficient:

$$\gamma_i^* = \frac{\gamma_i}{\gamma_i^\infty} \qquad 11\text{-}6$$

Thus, Aspen Plus^{TM} calculates γ_i^∞ at any loading by setting the CO_2 concentration to zero while allowing all of the other ionic species to remain at the loaded concentration values. This results in a floating reference state for CO_2 and for other CO_2-related species as a function of loading.

The following section describes the different types of data used in the creation of the ternary H_2O-MEA-CO_2 elecNRTL model.

11.2.1 ***N_2O Solubility***

Data in the form of N_2O solubility in aqueous monoethanolamine solutions as a function of concentration and temperature was used to adjust the activity coefficients of monoethanolamine and carbon dioxide through the simultaneous regression of the molecule-molecule binary interaction parameters in the elecNRTL model based on the CO_2-N_2O analogy method. Recall from Chapter VI that as the concentration of ions in an electrolyte solution approaches zero, the elecNRTL model reduces in theory to the NRTL Model of Renon and Prausnitz (1968). In this section, we present background on the NRTL model for clarification purposes only since we will be using the elecNRTL property model for all future chapters to describe molecular and ionic interactions

The NRTL model is an excess Gibbs energy model given by the following form after taking the partial derivative of the excess Gibbs energy to describe the activity coefficient for n components:

$$\ln \gamma_i = \frac{\sum_j x_j \tau_{ji} G_{ji}}{\sum_k x_k G_{ki}} + \sum_j \frac{x_j G_{jj}}{\sum_k x_k G_{kj}} \left(\tau_{ij} - \frac{\sum_m x_m \tau_{mj} G_{mj}}{\sum_k x_k G_{kj}} \right) \qquad 11\text{-}7$$

Where
i, j, k are the species indices, 1: H_2O, 2: MEA, 3: CO_2,
x_i is the liquid mole fraction of component i,
τ_{ij} is the binary interaction parameter between component i and j,
α_{ij} is the molecule-molecule nonrandomness factor, 0.2,
$G_{ij} = e^{-\alpha_{ij}\tau_{ij}}$.

The molecule-molecule binary interaction parameters were assumed to be temperature dependent and were fitted to the following function of temperature:

$$\tau_{ij} = A_{ij} + \frac{B_{ij}}{T} + C_{ij} \ln(T) + D_{ij} T \qquad 11\text{-}8$$

The creation of the H_2O-MEA-CO_2 model begins with the regression of literature data. Five data sets have been regressed with the elecNRTL model to represent the phase equilibrium of a single solvent system through regression of N_2O solubility [Sada and Kito (1972), Little et al. (1992), Li and Lai (1995), Tsai et al. (2000), and Mandal et al. (2005)]data over monoethanolamine solutions.

From the experimental N_2O solubility data over monoethanolamine solutions, we assumed a partial pressure of CO_2 equal to 10.1325 kPa to determine the concentration of CO_2 in the liquid phase based on Equation 11-1 and the following expression for the partial pressure of CO_2 over monoethanolamine solutions:

$$P_{CO_2} = c_{CO_2} H_{CO_2} \qquad 11\text{-}9$$

Solving for the concentration of CO_2 yields

$$c_{CO_2} = P_{CO_2} \left(H_{CO_2-H_2O} \frac{H_{N_2O-MEA}}{H_{N_2O-H_2O}} \right)^{-1} \qquad 11\text{-}10$$

Where
c_{CO_2} is the concentration of CO_2 in the liquid phase, kmole/m^3,
P_{CO_2} is the partial pressure of CO_2, kPa.

The molar concentrations of CO_2 and MEA were then converted to mole fractions by assuming the density of the original H_2O-MEA-N_2O solution to be equivalent to an H_2O-MEA solution based on the work by Hsu and Li (1997).

An example of the experimental N_2O solubility data used in this work from Sada and Kito (1972), Little et al. (1992), Tsai et al. (2000), and Mandal et al. (2005) from 15 to 60 °C is shown in Figure 11.2-2. N_2O solubility reported from Li and Lai (1995) were excluded from the data regression due to inconstancies between the experimental data as compared to other works.

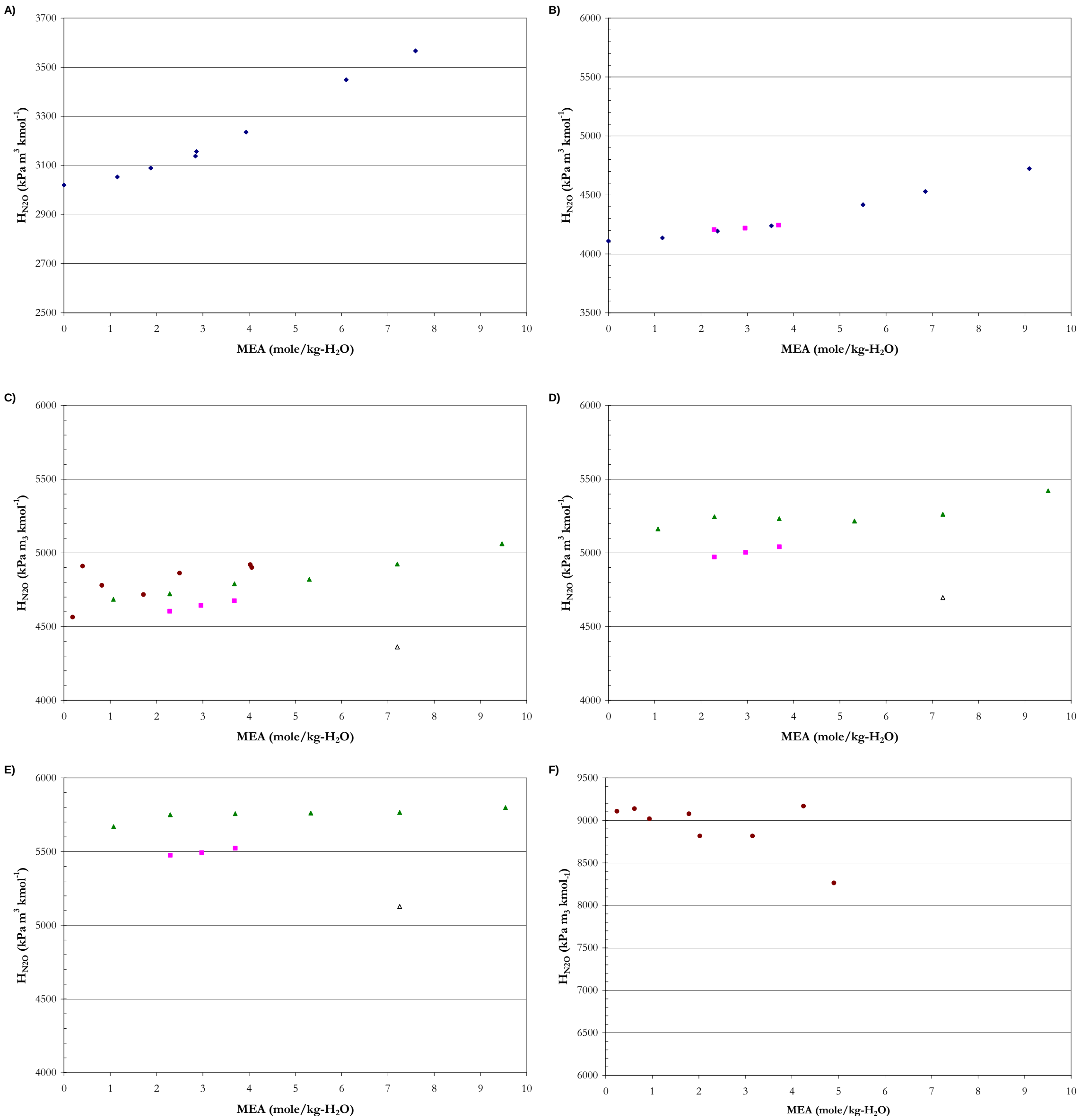

Figure 11.2-2. Solubility of N_2O in MEA Solutions as a Function of Concentration. Temperature: A) 15 °C, B) 25 °C, C) 30 °C, D) 35 °C, E) 40 °C, and F) 60 °C. Points: ◆, Sada and Kito (1972), ●, Little et al. (1992), Δ,Li and Lai (1995), ▲,Tsai et al. (2000), and, ■, Mandal et al. (2005).

11.3 Data Regression

For the elecNRTL model, binary interaction parameters for molecule-molecule interactions were given a default value equal to the molecule-molecule interactions between H_2O and CO_2.

Table 11.3-1. Aspen Plus™ Default Binary Interaction Parameters between H_2O and CO_2.

	Interacting Species		
Parameter	i	j	Estimate
1-$A_{m,m}$	H_2O	CO_2	10.064
2-$B_{m,m}$	H_2O	CO_2	-3268.14
3-$C_{m,m}$	H_2O	CO_2	0.0
4-$D_{m,m}$	H_2O	CO_2	0.0
5-$A_{m,m}$	CO_2	H_2O	10.064
6-$B_{m,m}$	CO_2	H_2O	-3268.14
7-$C_{m,m}$	CO_2	H_2O	0.0
8-$D_{m,m}$	CO_2	H_2O	0.0

A list of the aqueous electrolyte data sets that were examined in this work is given in Table 11.3-2. The column labels σ_T , σ_P , σ_{x_i} , σ_{y_i} , give standard error associated with the temperature, pressure, liquid mole fraction, and the vapor mole fraction, respectively, with each data set. DRS suggested standard error default values were assigned unless otherwise stated by the author.

Table 11.3-2. Experimental data used in the regression of the Unreacted H_2O-MEA-CO_2 system.

	Obs.	T (°C)	σ_T	σ_P	σ_x	σ_y	Source
P^{CO2}	15	15 & 25	0.01	0	0.1%	0	Sada and Kito (1972)
	15	30 & 60	0.01	0	0.1%	0	Little et al. (1992)
	18	30, 35, & 40	0.01	0	0.1%	0	Tsai et al. (2000)
	15	20.0 – 40.0	0.01	0	0.1%	0	Mandal et al. (2005)

Table 11.3-3 shows the following regression summary statistics output for estimates of the adjustable binary parameter coefficients after performing a nonlinear regression for the full model using DRS

Table 11.3-3. DRS Regression Output for Full Unreacted H_2O-MEA-CO_2 System Model.

	Interacting Species			
Parameter	i	j	Estimate	σ wrt Estimate
1-$A_{m,m}$	MEA	CO_2	-1.79	17.8
2-$B_{m,m}$	MEA	CO_2	-828	6061
3-$C_{m,m}$	MEA	CO_2	-2.03	3.06
4-$D_{m,m}$	MEA	CO_2	0.0375	0.0503
5-$A_{m,m}$	CO_2	MEA	10.2	870
6-$B_{m,m}$	CO_2	MEA	-1753	75239
7-$C_{m,m}$	CO_2	MEA	-0.0421	89.5
8-$D_{m,m}$	CO_2	MEA	0.00182	1.77

Residual Sum of Squares:	13,952
Residual Root Mean Square:	15.927
Degree of Freedom:	55

Recall that the standard error of an estimate is the estimated standard deviation of that statistic. Notice that all of the estimates are small relative to their standard errors. A complete description of the variability of the coefficient estimates requires examining the correlations between the estimates as shown in Table 11.3-4.

Table 11.3-4. Correlation Matrix of the Coefficient Estimates, for the Full Unreacted H_2O-MEA-CO_2 Model.

Parameter	1	2	3	4	5	6	7	8
1	1.00							
2	-0.58	1.00						
3	-0.07	-0.48	1.00					
4	-0.36	-0.03	-0.46	1.00				
5	0.01	-0.49	0.01	0.57	1.00			
6	0.15	0.29	0.15	-0.68	-0.84	1.00		
7	-0.02	-0.03	-0.02	0.08	-0.49	0.05	1.00	
8	-0.06	0.67	-0.06	-0.70	-0.75	0.82	-0.18	1.00

Table 11.3-4 does not show either highly positive or negative correlations between any of the energy parameter estimates, but correlations between some of the other coefficients are relatively small, suggesting that some of the energy parameter estimates might be usefully removed from the model without significant loss of information.

After performing backward elimination using DRS, the following optimum model regression summary statistics output for estimates of the adjustable binary parameter coefficients are shown in Table 11.3-5.

Table 11.3-5. DRS Regression Output for Optimum Unreacted H_2O-MEA-CO_2 Model.

	Interacting Species			
Parameter	i	j	Estimate	σ wrt Estimate
1-$A_{m,m}$	MEA	CO_2	8.22	8.22
2-$A_{m,m}$	CO_2	MEA	0.756	0.00227
3-$B_{m,m}$	CO_2	MEA	181	0.544

Residual Sum of Squares: 14,891
Residual Root Mean Square: 15.754
Degree of Freedom: 60

Notice that all of the estimates are larger relative to their standard errors. Comparing the estimates from the full model to the optimum model, there was a noticeable difference between the estimated values. The proposed optimum model provides the following correlations between the estimates as shown in Table 11.3-6.

Table 11.3-6. Correlation Matrix of the Coefficient Estimates, for the Optimum Unreacted H_2O-MEA-CO_2 Model.

Parameter	1	2	3
1	1.00		
2	0.76	1.00	
3	-0.55	*-0.96*	1.00

Table 11.3-6 shows a highly negative correlation between the $\tau_{CO_2/MEA}$ parameters suggesting that some of the remaining parameters might be usefully removed from the model without significant loss of information.

Results from the previous section show that dropping a term from the optimum model may provide a submodel that may have a decrease in the correlation between the estimate coefficients and improve the reliability of the model. Testing whether any subset of the regression estimate coefficients may be zero plays an important role in many analyses which leads to the following hypotheses:

NH: $3C_{m,m} = 0$ Submodel function applies
AH: At lease one $3C_{m,m} \neq 0$ Optimum model function applies

We can perform an F-Test to compare the purposed submodel with the optimum model. Significance levels for this test are obtained by comparing the observed value of F to the $F_{df_{NH}-df_{AH},df_{AH}}$ distribution. The p-value is then computed as an upper-tail test and gives the probability associated with evidence to reject the null hypothesis which will then be compared to the results given by the submodel.

If we were to remove the highly correlated parameters from the optimum model, the following submodel regression summary statistics output for estimates of the adjustable binary parameter coefficients is shown in Table 11.3-7.

Table 11.3-7. DRS Regression Output for Unreacted H_2O-MEA-CO_2 Submodel.

	Interacting Species			
Parameter	i	j	Estimate	σ wrt Estimate
1-$A_{m,m}$	MEA	CO_2	104	1.24E+09
2-$A_{m,m}$	CO_2	MEA	113	3.68E+09

Residual Sum of Squares: 2,729,433
Residual Root Mean Square: 211.530
Degree of Freedom: 61

Notice that all of the estimates are smaller relative to the standard errors. Comparing the estimates from the submodel to the optimum model, there was large difference between the estimated values with respect to the order of magnitude. The residual sum of squares and the standard errors for the submodel have increased as compared to the optimum model. The proposed submodel provides the following estimated covariances between the estimates as shown in Table 11.3-8.

Table 11.3-8. Correlation Matrix of the Coefficient Estimates for the Unreacted H_2O-MEA-CO_2 Submodel.

Parameter	1	2
1	1.00	
2	*-1.00*	1.00

Table 11.3-8 shows parameter $\left(2A_{m,m}\right)$ is highly correlated to the first coefficient, $\left(1A_{m,m}\right)$, suggesting that $\hat{\eta}_2$ might be usefully removed from the model without significant loss of information.

The two models were then compared using the test statistic F applied to the null hypothesis versus the alternative:

$$\frac{\left[\frac{2729433-14891}{61-60}\right]}{\left[\frac{14891}{60}\right]} \sim 10937.65(1,60)$$

We can then calculate the probability for a F-distribution, df = 1, 60, upper-tail.

F dist. with (1, 60) df, value = 10937.65, upper-tail probability = 0

The finding of $p=0$ provides strong evidence against the null hypothesis that $3C_{m,m}=0$. Since a value of F this strong would be observed zero times out of a hundred if the null hypothesis were true, the submodel will not give an adequate description of the data over the range of temperatures and concentration available in the data.

11.3.1 *Optimum Model Results*

With the determination of the estimates for the binary interaction parameters known for the optimum model, a simple Aspen Plus^{TM} Flash model was used to test the predictive capability of the unreacted H_2O-MEA-CO_2 model against literature data. For each data point, the deviation between the experimental and estimated values is expressed in terms of the average absolute relative deviation (AARD). Table 11.3-9 gives the percent AARD and the maximum percent AARD for the model predictions.

Table 11.3-9. Absolute Percent Relative Error for the Unreacted H_2O-MEA-CO_2 Optimum Model.

		AARD(%)	Max. AARD
P^{CO2}	Sada and Kito (1972)	3.65	11.77
	Little et al. (1992)	2.74	8.18
	Tsai et al. (2000)	2.09	4.39
	Mandal et al. (2005)	5.42	11.17
Overall		**3.48**	**11.77**

Overall, the model adequately describes the unreacted H_2O-MEA-CO_2 property data listed above within an average absolute relative error of ± 3.48 percent, with the exception of a few outliers.

From the optimum model interaction parameters listed in Table 11.3-5, we can evaluate the interaction parameters, τ, as a function of temperature using Equation 11-8 as shown in Figure 11.3-1 and Figure 11.3-2.

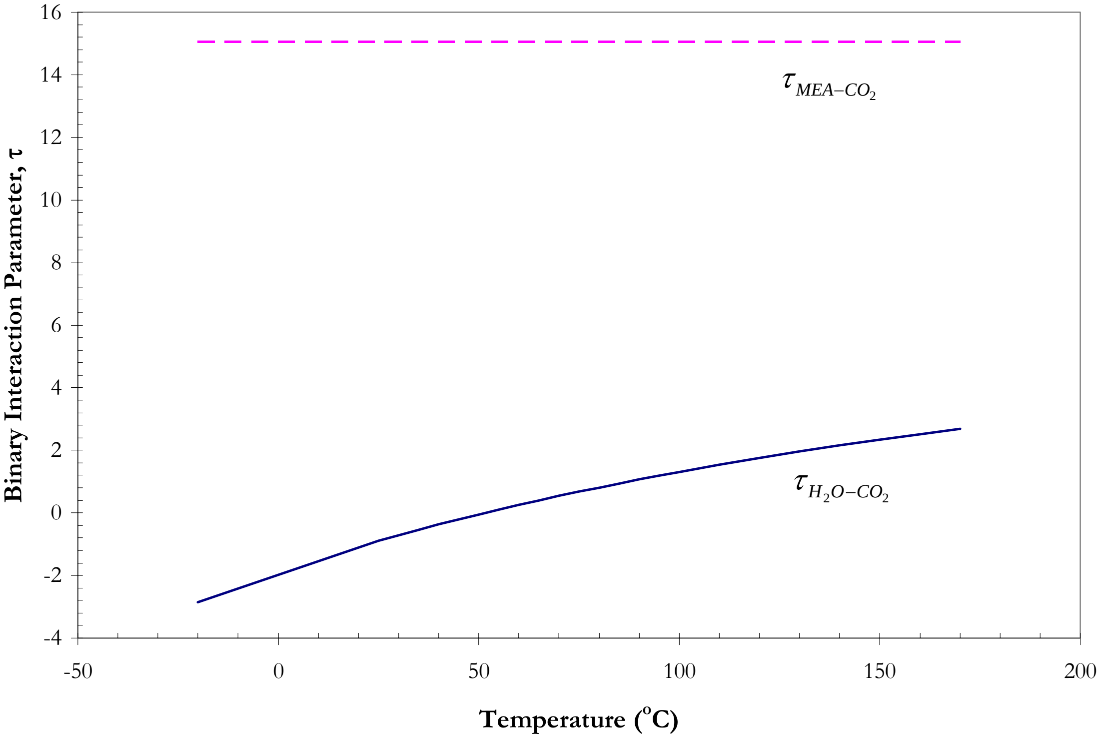

Figure 11.3-1. Evaluated Binary Interaction Parameters Between H_2O-CO_2 and MEA-CO_2. Lines: elecNRTL Model Predictions.

Figure 11.3-1 shows a large difference between the tau parameters for H_2O-CO_2 and MEA-CO_2. For interactions between H_2O and CO_2, the average value of tau is 0.69, from -

20.0 °C to 170.0 °C, but interactions between MEA-CO_2 were found not to exhibit a temperature dependence in the optimum model.

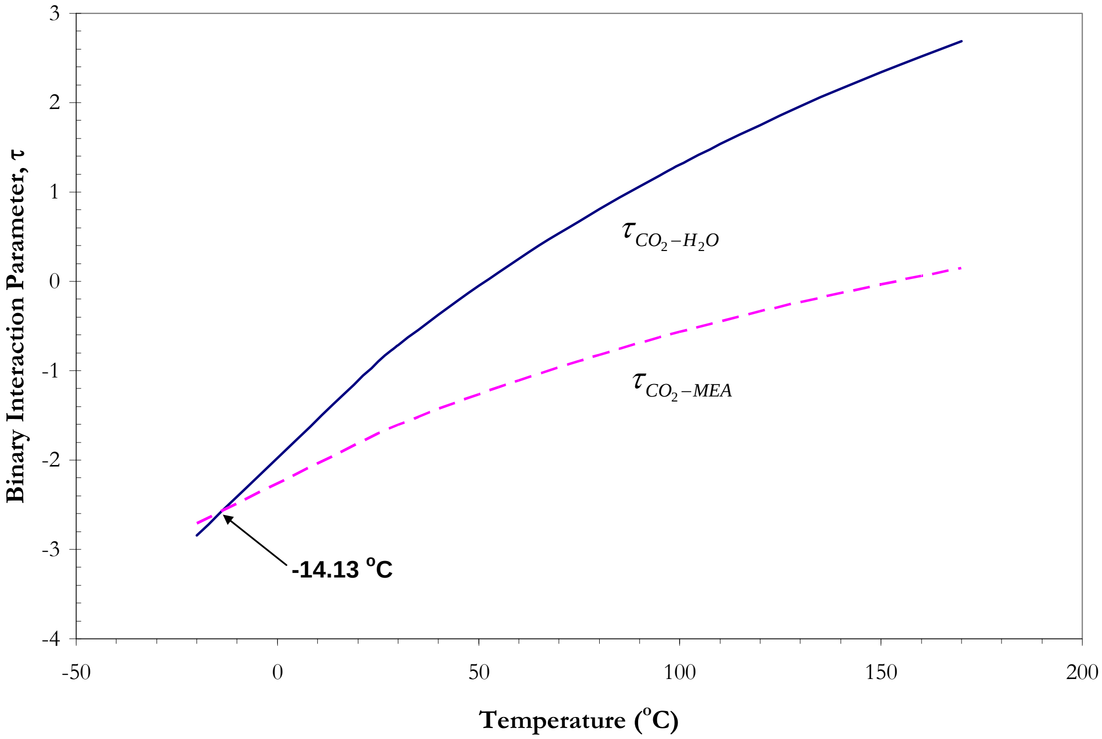

Figure 11.3-2. Evaluated Binary Interaction Parameters Between CO_2-H_2O and CO_2-MEA. Lines: elecNRTL Model Predictions.

Figure 11.3-2 shows the temperature dependency of the binary interaction parameters between CO_2-H_2O and CO_2-MEA where the two functions cross at -14.13 °C. Figure 11.3-3 demonstrates that there is a sufficient difference between the two interaction parameters to warrant the inclusion of the CO_2-MEA interactions. Previous authors assumed that the Henry's constant for CO_2 in MEA would be the same as the Henry's constant for CO_2 in H_2O vis-à-vis the binary interaction parameters. This assumption may affect the final model because interaction parameters associated with the activity coefficient in Equation 11-3 would be adjusted on the basis of CO_2 only interacting with H_2O. This would affect the activity coefficients of H_2O and MEA, the partial pressure of the two species, and this effect would increase as the concentration of MEA increases.

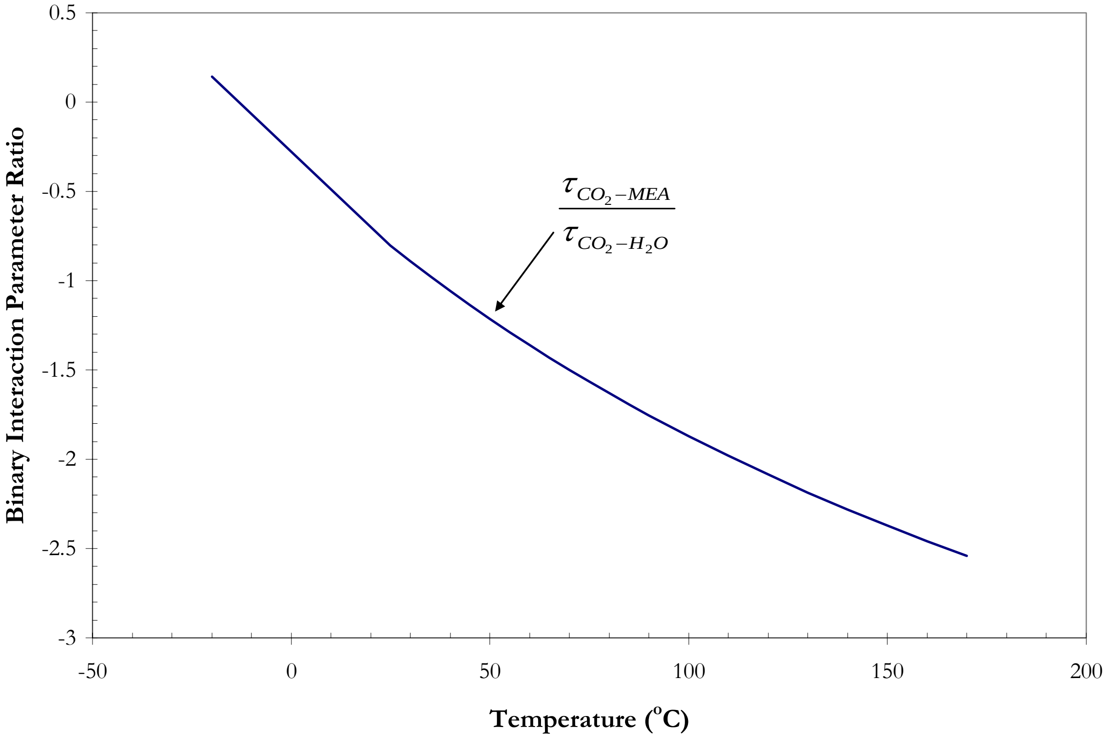

Figure 11.3-3. Evaluated Binary Interaction Parameter Ratio Between CO_2-MEA and CO_2-H_2O. Lines: elecNRTL Model Predictions.

11.4 Optimum Model Predictions

In this work, we have compiled all available literature data into a database of consistent high quality data needed to obtain a unique set of binary interaction parameters to describe the unreacted H_2O-MEA-CO_2 system. The remainder of this chapter will be devoted to using our model as a predictive tool as described in the subsequent sections.

11.4.1 *N_2O Solubility*

With the determination of the estimates for the energy parameter coefficients known for the optimum model, a simple Aspen Plus^{TM} Flash model was used to test the predictive capability of the MEA-CO_2 energy parameter coefficients against literature data. Figure 11.4-1 to Figure 11.4-6 compares estimated and experimental N_2O solubility measurements from Sada and Kito (1972), Little et al. (1992), Li and Lai (1995), Tsai et al. (2000), and Mandal et al. (2005), in terms of the Henry's constant of N_2O in aqueous MEA mixtures from 15.0 – 60.0 °C. The optimum model exhibits systematic error and under predicts the N_2O solubility with a maximum error of ± 11.77 % as compared to experimental N_2O solubility from Mandal et al. (2005) at 35.0 and 40.0 °C due to a high degree of scatter within the data sets. All the predictions of the model were within an AARD of ± 3.48 %, with the exception of a few outliers.

In Table 11.4-1, we can compare our model predictions to Tsai et al. (2000), who used a semiemprical model proposed by Wang et al. (1992) to represent the solubility of N_2O in aqueous MEA solutions. Overall both models adequately describe the systematic trends presented in the available literature data.

Table 11.4-1. Comparison Between the Model of Tsai et al. (2000) to This Work based on the Percent Average Absolute Relative Deviation (AARD) Between Experimental Literature Data and Model Predictions.

	This Work.	Tsai et al. (2000)
Sada and Kito (1972)	3.65	2.6
Little et al. (1992)	2.74	6.6
Tsai et al. (2000)	2.09	1.5
Overall	**2.82**	**3.57**

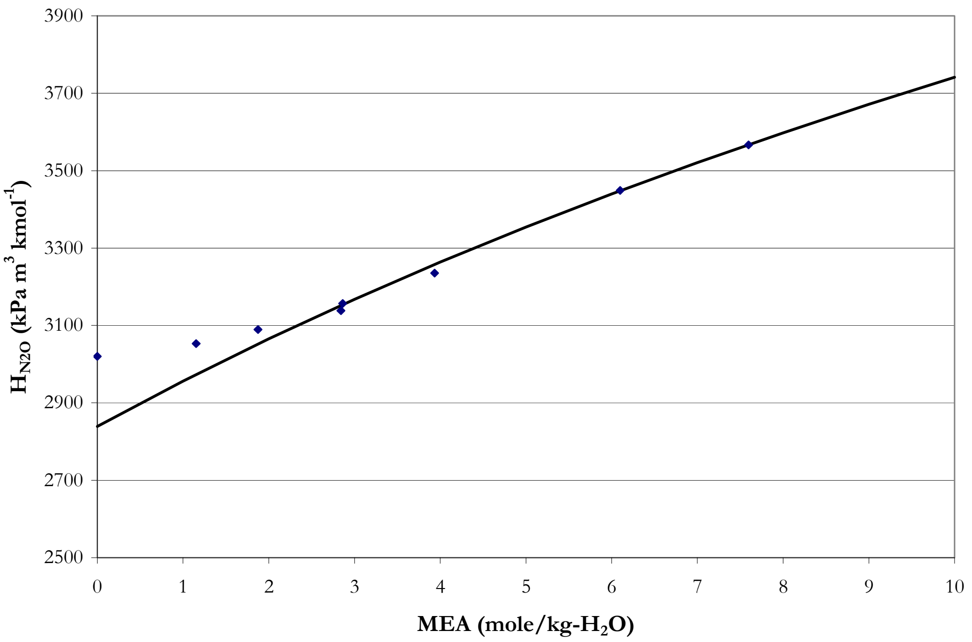

Figure 11.4-1. Experimental N_2O Solubility in MEA Solutions as Compared to elecNRTL Model Predictions at 15 °C. Points: ◆, Sada and Kito (1972). Lines: —, elecNRTL Model.

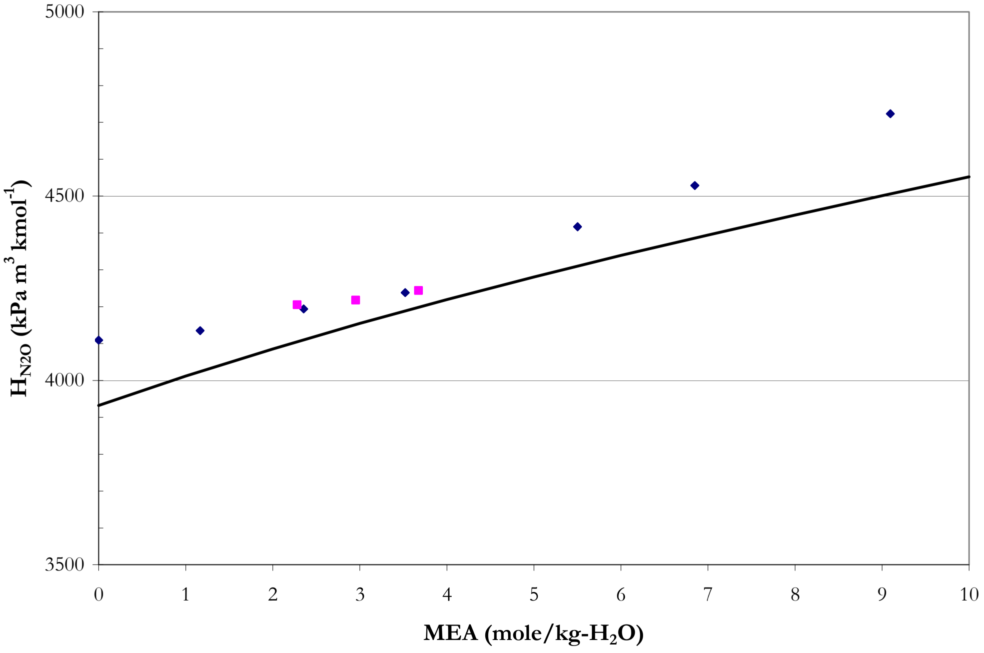

Figure 11.4-2. Experimental N_2O Solubility in MEA Solutions as Compared to elecNRTL Model Predictions at 25 °C. Points: ◆, Sada and Kito (1972) and ■, Mandal et al. (2005). Lines: —, elecNRTL Model.

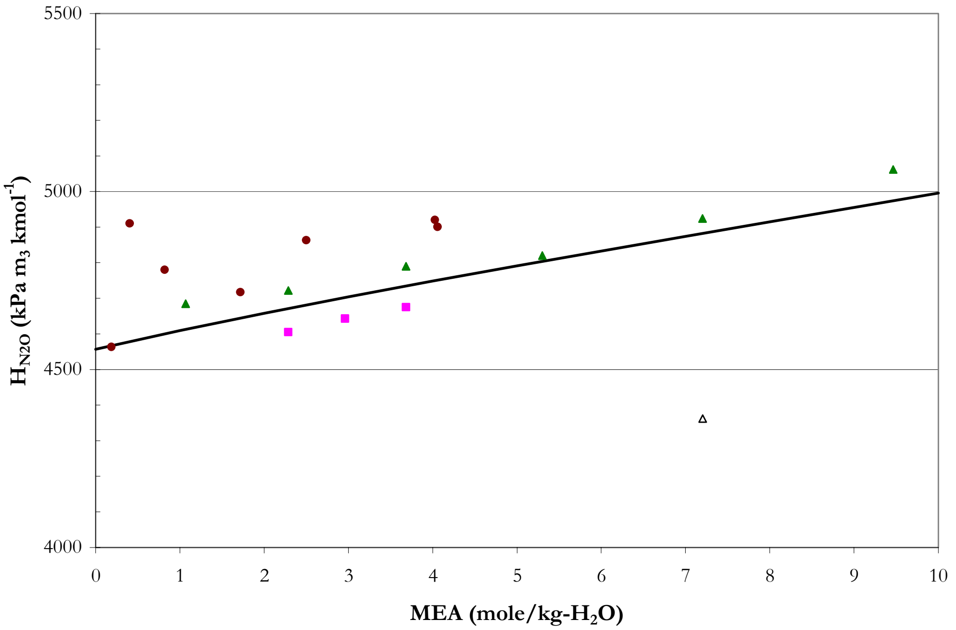

Figure 11.4-3. Experimental N_2O Solubility in MEA Solutions as Compared to elecNRTL Model Predictions at 30 ^{o}C. Points: ●, Little et al. (1992), Δ,Li and Lai (1995), ▲,Tsai et al. (2000), and ■, Mandal et al. (2005). Lines: —, elecNRTL Model.

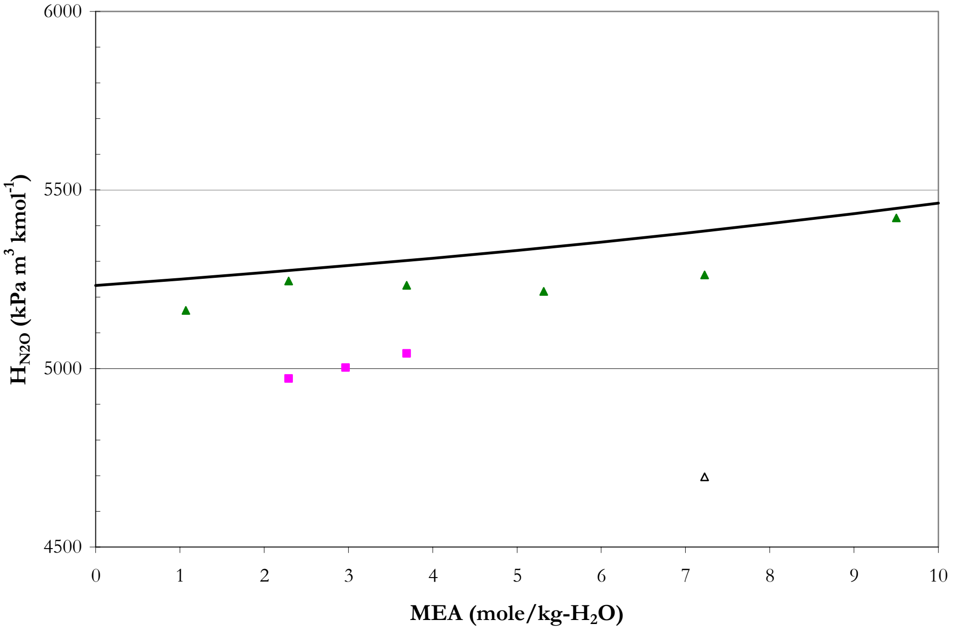

Figure 11.4-4. Experimental N_2O Solubility in MEA Solutions as Compared to elecNRTL Model Predictions at 35 ^{o}C. Points: Δ,Li and Lai (1995), ▲,Tsai et al. (2000), and ■, Mandal et al. (2005). Lines: —, elecNRTL Model

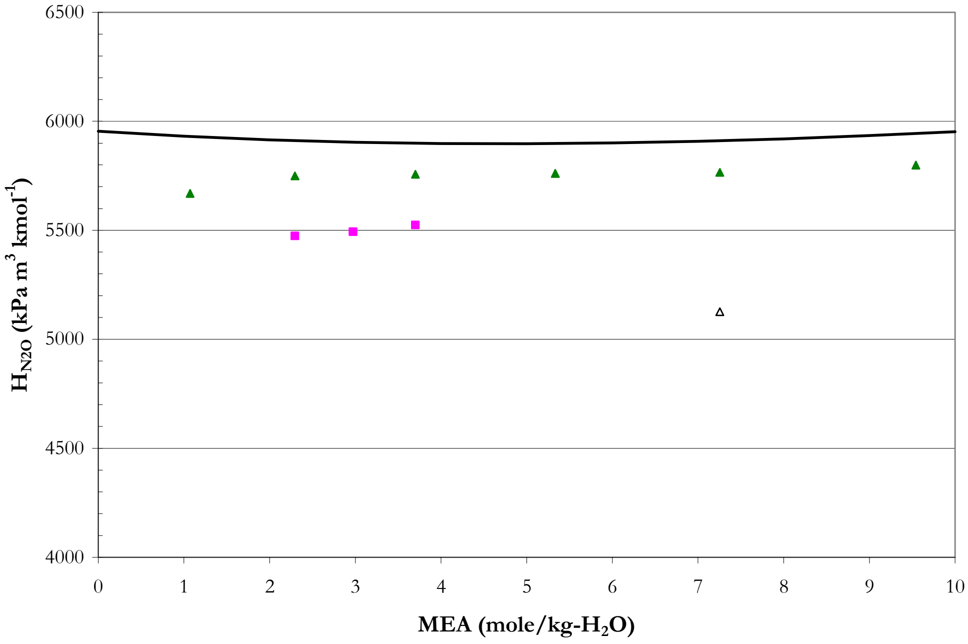

Figure 11.4-5. Experimental N_2O Solubility in MEA Solutions as Compared to elecNRTL Model Predictions at 40 °C. Points: Δ,Li and Lai (1995), ▲,Tsai et al. (2000), and ■, Mandal et al. (2005). Lines: ▬, elecNRTL Model

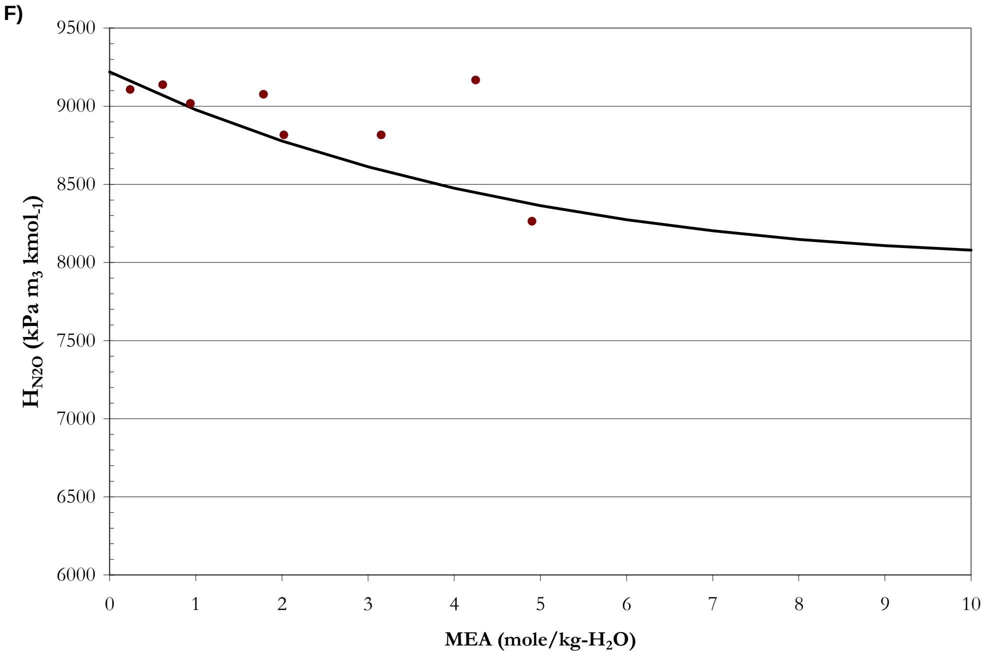

Figure 11.4-6. Experimental N_2O Solubility in MEA Solutions as Compared to elecNRTL Model Predictions at 60 °C. Points: ●, Little et al. (1992). Lines: ▬, elecNRTL Model

11.5 Conclusions

.

In conclusion, Figure 11.3-3 demonstrates, there is a sufficient difference between the two interaction parameters to warrant the inclusion of the CO_2-MEA interactions. Previous authors assumed that the Henry's constant for CO_2 in MEA would be the same as the Henry's constant for CO_2 in H_2O vis-à-vis the binary interaction parameters. This assumption may affect the final model because interaction parameters associated with the activity coefficient in Equation 11-3 would be adjusted on the basis of CO_2 only interacting with H_2O. This would affect the activity coefficients of H_2O and MEA, the partial pressure of the two species, and this effect would increase as the concentration of MEA increases.

Overall, the results presented above indicate that the elecNRTL model, through simultaneous regression, gave a set of optimum binary interaction parameters for the unreacted H_2O-MEA-CO_2 system. The optimum model adequately represents the solubility of N_2O for aqueous MEA mixtures.

CHAPTER XII

Ternary Systems: H_2O-K_2CO_3-CO_2

12.1 Introduction

To this point in the thermodynamic model development, we described only molecule-molecule interactions. For an electrolyte system, there are interactions between molecules and electrolytes, as between water and ionic species, and interactions between electrolytes, or between two different salts. This chapter describes the data regression and model predictions for the ternary {H_2O-Potassium carbonate (K_2CO_3)-Carbon dioxide (CO_2)} and binary {H_2O-K_2CO_3 and H_2O-Potassium bicarbonate ($KHCO_3$)} systems based on previous literature data. The results for the binary interaction parameters for the electrolyte-NRTL (elecNRTL) model within Aspen Plus^{TM} are then presented, showing good statistical fit to the literature data with an average absolute relative error of ± 3.85 %, with the exception of a few outliers.

12.2 H_2O-K_2CO_3 System

The creation of the H_2O-K_2CO_3-CO_2 model begins with the regression of H_2O-K_2CO_3 literature data. Three data sets have been regressed with the elecNRTL model to represent the phase equilibrium of a single solvent system through regression of mean ionic activity coefficient [Aseyev and Zaytsev (1996)], water vapor pressure depression [Aseyev (1999) and Puchkov and Kurochkina (1970)], and specific heat capacity [Aseyev and Zaytsev (1996)] over potassium carbonate solutions. The data provides a wide range of both temperature and concentration from 25 to 130 °C and 0.014 to 50 weight percent (wt%) or approximately 0.001 to 7.5 moles K_2CO_3 per kg water (m) respectively. Potassium carbonate was assumed to completely dissociate in an aqueous solution resulting in the formation of two potassium ions, K^+, and one carbonate ion, CO_3^{-2}, given by the following aqueous dissociation reaction.

$$K_2CO_3 \rightarrow 2K^+ + CO_3^{-2} \qquad \text{12-1}$$

In this work, the concentrations of K_2CO_3 studied did warrant the inclusion of the salt precipitation equilibrium reaction. Two data sets [Linke and Seidell (1965) and Moore et al. (1997)] were regressed with the elecNRTL model to describe the solid-liquid equilibrium associated with the temperature dependant equilibrium constant for the formation of hydrated potassium carbonate ($K_2CO_3 \cdot 1.5H_2O$).

$$K_2CO_3 \cdot 1\frac{1}{2}H_2O(s) \leftrightarrow 2K^+ + CO_3^{-2} + 1\frac{1}{2}H_2O \qquad \text{12-2}$$

12.3 H_2O-$KHCO_3$ System

The next step in the creation of the H_2O-K_2CO_3-CO_2 model continues with the regression of H_2O-$KHCO_3$ literature data. Two data sets have been regressed with the elecNRTL model to represent the phase equilibrium of a single solvent system through regression of vapor pressure depression [Aseyev (1999)] and specific heat capacity [Aseyev and Zaytsev (1996)] over potassium bicarbonate solutions. The data provide a wide range of both temperature and concentration from 5 to 130 ºC and 2 to 20 wt% or approximately 0.2 to 2.5 m of $KHCO_3$, respectively. Potassium bicarbonate was assumed to completely dissociate in an aqueous solution resulting in the formation of one potassium ion, K^+, and one bicarbonate ion, HCO_3^{-1}, given by the following aqueous dissociation reaction.

$$KHCO_3 \rightarrow K^+ + HCO_3^{-1} \tag{12-3}$$

In this work, the concentrations of $KHCO_3$ studied did warrant the inclusion of the salt precipitation equilibrium reaction. Literature data from Linke and Seidell (1965) was regressed with the elecNRTL model to describe the solid-liquid equilibrium associated with the temperature dependant equilibrium constant for the formation of potassium bicarbonate.

$$KHCO_3\left(s\right) \leftrightarrow K^+ + HCO_3^{-1} \tag{12-4}$$

12.4 H_2O-K_2CO_3-CO_2 System

For the completion of the H_2O-K_2CO_3-CO_2 model, CO_2 solubility in potassium carbonate as reported by Tosh et al. (1959) was regressed with the electrolyte NRTL model to represent the phase equilibrium of H_2O-K_2CO_3-$KHCO_3$ mixtures through the regression of the equilibrium partial pressure of CO_2, P_{CO_2}. The data provide a wide range of both temperature and concentration from 69 to 140 °C and 20 to 40 % equivalent concentration of K_2CO_3 or approximately 0.33 to 9.12 m K_2CO_3, respectively, at various fractional conversions (loadings) to $KHCO_3$ from approximately 0.1 to 0.9 mol CO_2^{tot}/mol K_2CO_3. "Equivalent concentration of K_2CO_3" refers to a solution where only K_2CO_3 and H_2O are present. For example, a 20 % equivalent solution contains 20 grams (gm) of K_2CO_3 and 80 gm of H_2O if all of the bicarbonate in the system was converted back to carbonate.

The following stoichiometric chemical equilibrium expression for the absorption of carbon dioxide by an aqueous solution of K_2CO_3 is given below:

$$K_2CO_3 + CO_2 + H_2O \leftrightarrow 2KHCO_3 \qquad 12\text{-}5$$

12.5 Chemical and Vapor-liquid Equilibrium of K_2CO_3

Figure 12.5-1 illustrates the proposed system to correlate/predict the solubility of CO_2 in aqueous solutions of K_2CO_3.

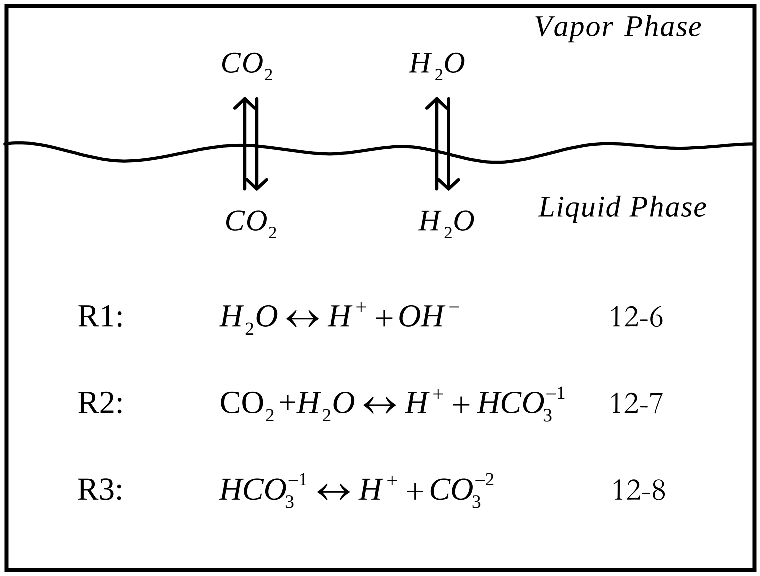

R1: $H_2O \leftrightarrow H^+ + OH^-$ 12-6

R2: $CO_2 + H_2O \leftrightarrow H^+ + HCO_3^{-1}$ 12-7

R3: $HCO_3^{-1} \leftrightarrow H^+ + CO_3^{-2}$ 12-8

Figure 12.5-1. Chemical and Vapor-liquid Equilibrium of K_2CO_3.

Reaction 12-6 describes the ionization of water to proton $\left(H^{+}\right)$ and hydroxide ions $\left(OH^{-}\right)$; Reaction 12-7 describes the hydrolysis and ionization of dissolved CO_2 to H^+ and bicarbonate $\left(HCO_3^{-}\right)$ ions; Reaction 12-8 describes the dissociation of HCO_3^- to H^+ and carbonate $\left(CO_3^{-2}\right)$ ions. The chemical equilibrium constant for the above j equations are expressed in Aspen Plus™ in terms of the activity of component i as given by the following relationship:

$$K_j = \prod_i a_i^{\nu_{i,j}} \qquad 12\text{-}9$$

Where
K_j is the chemical equilibrium constant,
$\nu_{i,j}$ is the reaction stoichiometric coefficient of component i,
a_i is the activity of component i.

In this work, for Reactions 12-6 to 12-8 we did not define the chemical equilibrium constants as linear temperature dependent functions, but rather in terms of the reference state free energy of the system:

$$\ln K_j = -\frac{\Delta G^o}{RT} \qquad 12\text{-}10$$

Where
$G^o_{i,j}$ is the standard free energy of formation of component i.

The previous framework allows our rigorous thermodynamic model to be internally consistent with respect to governing thermodynamic definitions. Table 12.5-1 reports standard state conditions at 25 °C associated with the species in Reactions 12-6 to 12-8. Standard state conditions are consistent with published literature by Edwards et al. (1978).

Table 12.5-1. Standard State Property Values for Reactions 12-6 to 12-8 at 25 °C.

Species	G_f^o (kcal/mole)	H_f^o (kcal/mole)
H_2O(l)	-56.6828	-68.2755
H^+(aq)	0.0	0.0
OH^-(aq)	-37.5571	-54.9331
CO_2(aq)	-92.18974	-98.83443
CO_3^{-2}(aq)	-128.584	-161.7321
HCO_3^{-1}(aq)	-140.291	-164.9871

Table 12.5-2. Chemical Equilibrium Coefficients for the H_2O-K_2CO_3-CO_2 System reported by Edwards et al. (1978) (mole fraction basis).

Equation #	A	B	C	D
14-6	132.8989	-13445.9	-22.4773	0.0
14-7	231.4654	-12092.1	-36.7816	0.0
14-8	216.0504	-12431.7	-35.4819	0.0

ln K = A + B/T(K) + C·lnT(K) + D·T(K)

As stated previously, Equation 12-10 relates the chemical equilibrium constant to the standard Gibbs free energy change of reaction.

$$\frac{\Delta G^o}{RT} = -\ln K \qquad 12\text{-}11$$

Where the standard property changes of reaction (e.g. Gibbs free energy and enthalpy) are defined as the difference between the standard property change of the products and reactants, weighted by their stoichiometric coefficients.

$$\Delta M^o = \sum_i \nu_i M_i^o \qquad 12\text{-}12$$

For molecular solutes (e.g. CO_2), the standard Gibbs free energy is described based on the ideal gas reference state by following equation:

$$G^o_{CO_2}\left(T\right)=G^{ig}_{CO_2}\left(T\right)+RT\ln\frac{H_{CO_2}\left(T\right)}{P^{ref}} \qquad 12\text{-}13$$

Where

$G^{ig}_{CO_2}$ is the ideal gas Gibbs free energy, J/kmol,

H_{CO_2} is the Henry's Constant for CO_2 in H_2O (Chen et al. 1979), atm,

P^{ref} is the reference pressure, 1 atm.

For ionic species the aqueous phase infinite dilution molar heat capacity is described by the following equation:

$$C^{\infty,aq}_{p,i}\left(\frac{J}{kmol\cdot K}\right)=C_{1,i}+C_{2,i}T\left(K\right)+C_{3,i}T\left(K\right)^2+\frac{C_{4,i}}{T\left(K\right)} \qquad 12\text{-}14$$

The molar heat capacity of H_2O was described in Chapter VII by the following equation:

$$\begin{aligned}C^{l,*}_{p,H_2O}\left(\frac{J}{kmol\cdot K}\right)&=189366-1171\cdot T\left(K\right)+4.53\cdot T\left(K\right)^2-\ldots\\&\ldots-0.00795\cdot T\left(K\right)^3+5.4723\times10^{-6}\cdot T\left(K\right)^4\end{aligned} \qquad 12\text{-}15$$

For a given temperature, the molar aqueous phase infinite dilution heat capacity of bicarbonate and carbonate can then be determined analytically. A starting point for a rigorous development starts with the following equation:

$$\Delta G^o_m=\Delta H^o_m-T\Delta S^o_m \qquad 12\text{-}16$$

Equation 12-16 is from the definition of the molar Gibbs free energy applied to each component in a chemical reaction evaluated at the standard state. Applying Equation 12-12 to Equation 12-16 yields

$$\sum_i \nu_i G^o_{m,i}=\sum_i \nu_i H^o_{m,i}-T\sum_i \nu_i S^o_{m,i} \qquad 12\text{-}17$$

where the standard molar heat of reaction and standard molar entropy change of reaction are related to temperature by the following expressions

$$\Delta H_m^o = \Delta H_{0,m}^o + R\int_{T_0}^{T} \frac{\Delta C_{p,m}^o}{R} dT \qquad 12\text{-}18$$

$$\Delta S_m^o = \Delta S_{0,m}^o + R\int_{T_0}^{T} \frac{\Delta C_{p,m}^o}{R} \frac{dT}{T} \qquad 12\text{-}19$$

Equations 12-16, 12-18, and 12-19 are combined to yield

$$\Delta G_m^o = \Delta H_{0,m}^o + R\int_{T_0}^{T} \frac{\Delta C_{p,m}^o}{R} dT - T\Delta S_{0,m}^o - RT\int_{T_0}^{T} \frac{\Delta C_{p,m}^o}{R} \frac{dT}{T} \qquad 12\text{-}20$$

However,

$$\Delta S_{0,m}^o = \frac{\Delta H_{0,m}^o - \Delta G_{0,m}^o}{T_0} \qquad 12\text{-}21$$

hence

$$\Delta G_m^o = \Delta H_{0,m}^o - \frac{T}{T_0}\left(\Delta H_{0,m}^o - \Delta G_{0,m}^o\right) + R\int_{T_0}^{T} \frac{\Delta C_{p,m}^o}{R} dT - RT\int_{T_0}^{T} \frac{\Delta C_{p,m}^o}{R} \frac{dT}{T} \qquad 12\text{-}22$$

Finally, division by RT yields

$$-\ln K_i = \frac{\Delta G_m^o}{RT} = \frac{\Delta G_{0,m}^o - \Delta H_{0,m}^o}{RT_0} + \frac{\Delta H_{0,m}^o}{RT} + \frac{1}{T}\int_{T_0}^{T} \frac{\Delta C_{p,m}^o}{R} dT - \int_{T_0}^{T} \frac{\Delta C_{p,m}^o}{R} \frac{dT}{T} \qquad 12\text{-}23$$

The change in heat capacity for the mixture can be expressed as

$$\Delta C_p^o\left(\frac{J}{kmol \cdot K}\right) = \Delta A + \Delta B \cdot T\left(K\right) + \Delta C \cdot T\left(K\right)^2 + \Delta D \cdot T\left(K\right)^3 + \Delta E \cdot T\left(K\right)^4 \qquad 12\text{-}24$$

with

$$\Delta A = \sum_i v_i A_i \qquad 12\text{-}25$$

with analogous definitions for ΔB, ΔC, ΔD, and ΔE. Using Equation 12-24 and the coefficients for the chemical equilibrium constant given in Table 12.5-2, we can determine the coefficients for the aqueous phase infinite dilution molar heat capacity of bicarbonate and carbonate ion.

Table 12.5-3. Coefficients for the Aqueous Phase Infinite Dilution Heat Capacity (J/kmol·K) of bicarbonate and carbonate from 0 – 200 °C based on Equation 12-24.

	Estimate	
Coefficient	HCO_3^{-1}	CO_3^{-2}
C_1	-0.0000232	-0.00013
C_2	-0.00454	-0.0288
C_3	-0.742	-5.01
C_4	0.00110	0.00693

Coefficients for the aqueous phase infinite dilution molar heat capacity of bicarbonate and carbonate were adjusted to match the form of Equation 12-14.

Table 12.5-4. Coefficients for the Aqueous Phase Infinite Dilution Heat Capacity (J/kmol·K) of bicarbonate and carbonate from 0 – 200 °C based on Equation 12-14.

	Estimate	
Coefficient	HCO_3^{-1}	CO_3^{-2}
C_1	211387	1334017
C_2	-882	-5565
C_3	0.875	5.19
C_4	-1.9E+07	-1.2E+08

Aspen Tech does not provide source documentation for the coefficients assigned to bicarbonate and carbonate, but does reference Austgen et al. (1989), even though Austgen et al. (1989) did not provide documentation. In this work, we have compiled a consistent database for experimental H_2O-K_2CO_3-CO_2 data as compared to the work by Austgen et al. (1989). The difference between the two predictions for the aqueous phase infinite dilution heat capacity of bicarbonate and carbonate accounts for differences in the model framework. Austgen et al. (1989) chose to describe the liquid phase chemical equilibrium through linear temperature dependent functions. In this work, we chose not to provide the chemical equilibrium constants, but rather determine the chemical equilibrium from the reference state free energy of the system. Thus, Austgen et al. (1989) was never required to fully describe the standard property changes for each ionic species because Aspen Plus™ would rely on the provided chemical equilibrium constants for the necessary ionic information (e.g. ΔG, ΔH, ΔC_p) as shown in Figure 12.5-2.

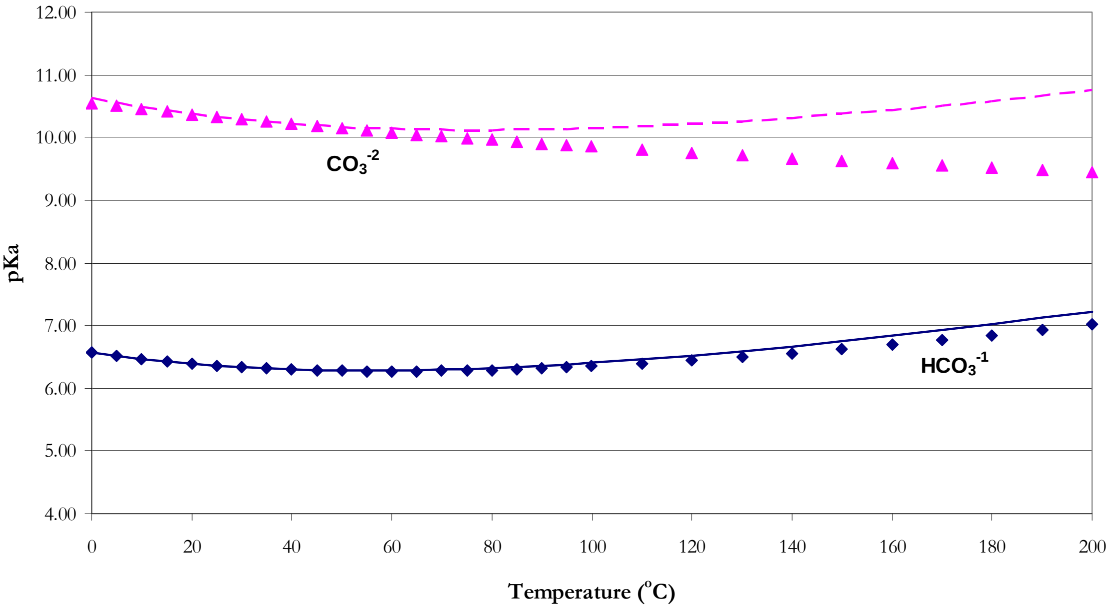

Figure 12.5-2. Comparison of the Dissociation Equilibrium Constant for HCO_3^{-1} and CO_3^{-2} (mole fraction based) from 0 – 200 °C. Points: ◆ and ▲, Austgen et al. (1989). Lines: ━, Edwards et al. (1978) based on Table 12.5-2.

By analytically determining the coefficients for the aqueous phase infinite dilution molar heat capacity of bicarbonate and carbonate, this work is thermodynamically consistent with Edwards et al. (1978) as shown in Figure 12.5-3.

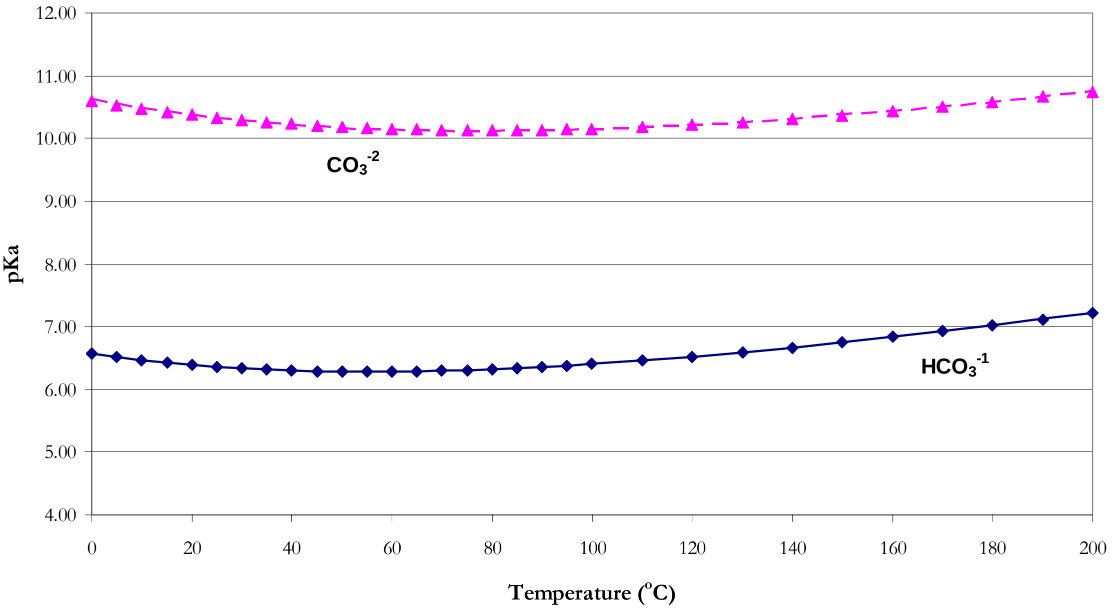

Figure 12.5-3. Comparison of the Dissociation Equilibrium Constant for HCO_3^{-1} and CO_3^{-2} (mole fraction based) from 0 – 200 °C. Points: ◆ and ▲, This work. Lines: ▬, Edwards et al. (1978) based on Table 12.5-2.

In the carbon capture processes, the deposition of a salt in the process needs to be avoided. Thus, for carbon capture process utilizing a salt and/or amine for the chemical solvent, knowledge about the range of conditions where salt precipitation is possible is very important. For salt precipitation reactions 12-2 and 12-4, we chose to describe the salt precipitation equilibrium reactions as temperature dependent linear functions due to the limited thermodynamic information associated with the precipitating solid phase through simultaneous regressions with binary interaction parameters in the elecNRTL model for the H_2O-K_2CO_3-CO_2 system.

$$\ln K_i = A + \frac{B}{T(K)} + C \ln T(K) + D \cdot T(K) \qquad 12\text{-}26$$

We chose to neglect the influence of pressure on Equation 12-26. If the activity product for each system is below the solubility product, potassium carbonate or potassium bicarbonate will not precipitate from the liquid mixture.

Hill (1930) and Lyudkovskaya et al. (1965) reported a third stable solid phase: $K_2CO_3 \cdot 2KHCO_3 \cdot 1.5H_2O$, between 5 – 50 °C, 49.48 – 50.90 wt % K_2CO_3, and 1.72 – 7.10 wt% $KHCO_3$. We chose not to include this third solid phase in our model, but have included coefficients for the salt precipitation equilibrium reaction, Equation 12-27, based on our optimum model in Section 12.8.5 for inclusion by the end user.

$$K_2CO_3 \cdot 2KHCO_3 \cdot 1\frac{1}{2}H_2O(s) \leftrightarrow 4K^+ + CO_3^{-2} + 2HCO_3^{-1} + 1\frac{1}{2}H_2O \qquad 12\text{-}27$$

12.6 Data Types

12.6.1 *Vapor Pressure Depression*

Data in the form of vapor pressure depression which measures the partial pressure of water, P_{H_2O}, as a function of molality and temperature was used to adjust the activity coefficient of water for the H_2O-K_2CO_3 and H_2O-$KHCO_3$ systems through the simultaneous regression of the binary interaction parameters in the elecNRTL model for the H_2O-K_2CO_3-CO_2 system.

An example of the experimental vapor pressure depression data used in this work from two literature sources, Aseyev (1999) and Puchkov and Kurochkina (1970) from 40 to 80 °C, is shown in Figure 12.6-1. Apelbat (1992) and Sarbar et al. (1982) reported vapor pressures of water over aqueous potassium carbonate solutions, but systematic deviations

(Δ_{max}~5.8 %) from Aseyev (1999) and Puchkov and Kurochkina (1970) required the exclusion of these two data sets from this work.

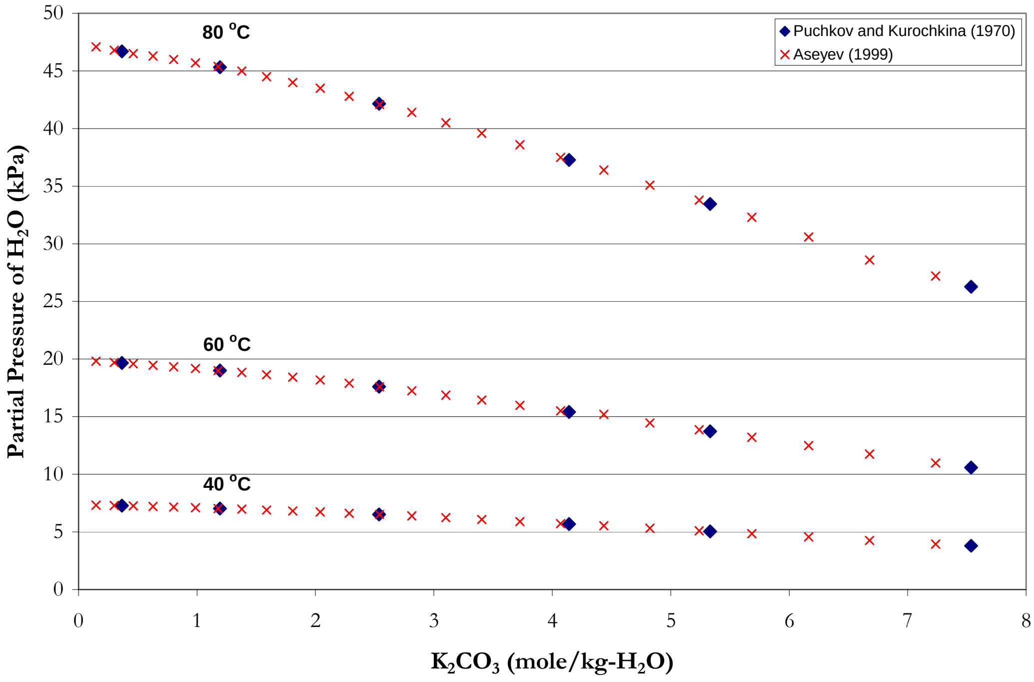

Figure 12.6-1. Vapor Pressure of Water in Aqueous Potassium Carbonate Mixtures at 40, 60, and 80 °C.

12.6.2 *Mean Ionic Activity Coefficient*

Data in the form of the mean ionic activity coefficient, $\gamma_{\pm}$, which relates the ionic activity coefficients to the mean activity coefficient for a single salt solution as a function of molality, was used to adjust the ionic activity coefficients of K^{+} and CO_3^{-2} in the H_2O-K_2CO_3 system through the simultaneous regression of the binary interaction parameters in the elecNRTL model for the H_2O-K_2CO_3-CO_2 system.

In general, mean ionic activity coefficient is given by the following equation

$$\gamma_{\pm} = \left(\gamma_{+}^{\nu_1}\gamma_{-}^{\nu_2}\right)^{\nu} \qquad 12\text{-}28$$

Where

γ_{+} and γ_{-} are the individual ionic activity coefficients, unitless,

ν_1 and ν_2 are the charge numbers of the respective ions, unitless,

ν is the sum of the respective ions charge numbers, [=] $\nu_1 + \nu_2$.

An example of the experimental mean ionic activity coefficient data used in this work from Aseyev and Zaytsev (1996) at 25 °C is shown in Figure 12.6-2.

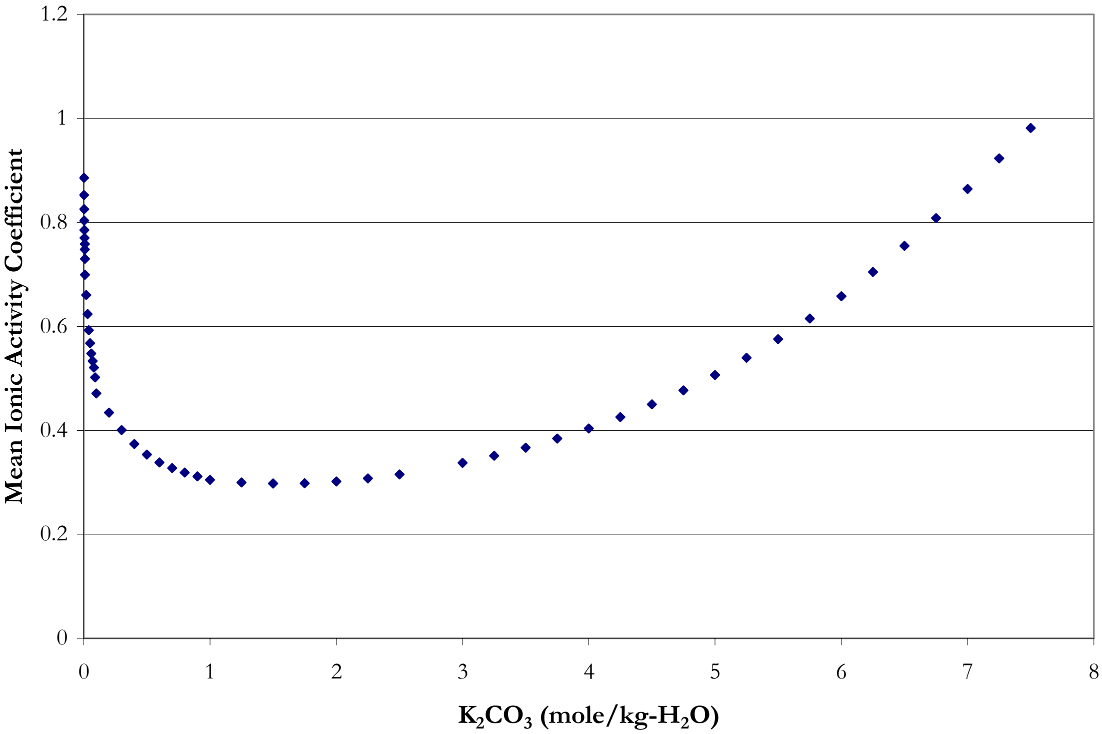

Figure 12.6-2. Mean Ionic Activity Coefficient from Aseyev and Zaytsev (1996) in Aqueous Potassium Carbonate Mixtures at 25 °C.

12.6.3 *Specific Heat Capacity*

As stated in Chapter VI, Aspen Plus™ calculates the liquid phase heat capacity of a *mixture* (CPMX) by taking the derivative of the liquid enthalpy at constant pressure:

$$H_m^l\left(T+\Delta T\right)-H_m^l\left(T\right)=\int_T^{T+\Delta T} C_{p,m}^l dT \tag{12-29}$$

where the liquid enthalpy of a mixture is calculated by the following equation:

$$H_m^l\left(T\right)=\sum_i x_i H_i+\sum_k x_k H_k^\infty+H_m^E \tag{12-30}$$

for solvents:

$$H_i\left(T\right)=\Delta H_f^{ig}\left(T^{ref}\right)+\int_{T^{ref}}^{T} C_p^{ig} dT+\left[H_i\left(T,p\right)-H_i^{ig}\left(T,p\right)\right] \tag{12-31}$$

for molecular solutes, cations, or anions:

$$H_k^\infty\left(T\right)=\Delta H_{f,k}^\infty\left(T^{ref}\right)+\int_{T^{ref}}^{T} C_{p,k}^\infty dT \tag{12-32}$$

Where
ΔT is the perturbation in temperature from T,
H_m^E is the excess enthalpy of the mixture,
$\Delta H_f^{ig}\left(T^{ref}\right)$ is the standard enthalpy of formation of component i at T^{ref},
T^{ref} is the reference temperature, 25.0 °C,
C_p^{ig} is the ideal gas heat capacity of component i,
H_i^{ig} is the ideal gas enthalpy of component i,
H_k^∞ is the infinite dilution aqueous enthalpy of component k,
$\Delta H_{f,k}^\infty\left(T^{ref}\right)$ is the infinite dilution aqueous phase standard enthalpy of formation of component k at T^{ref},
$C_{p,k}^\infty$ is the infinite dilution aqueous phase heat capacity polynomial of component k.

Table 12.6-1 gives the coefficients for the infinite dilution aqueous phase heat capacity used in Aspen Plus^{TM} based on the following expression:

$$C_{p,k}^{\infty}\left(\frac{J}{kmol \cdot K}\right)=C_1+C_2T\left(K\right)+C_3T\left(K\right)^2+\frac{C_4}{T\left(K\right)} \qquad 12\text{-}33$$

Table 12.6-1. Infinite Dilution Aqueous Phase Heat Capacity Default Coefficients.

Parameter	Symbol	H^+	OH^-	K^+	HCO_3^{-1}	CO_3^{-2}
CPAQ0-1	C_1	0.0	0.0	19886	211387	1334017
CPAQ0-2	C_2	0.0	-497.9	72.80	-882	-5565
CPAQ0-3	C_3	0.0	0.0	0.0	0.875	5.19
CPAQ0-4	C_4	0.0	0.0	0.0	-1.9E+07	-1.2E+08

Data in the form of specific heat capacity of a mixture as a function of molality and temperature were used to adjust the coefficients for the binary interaction parameters of the elecNRTL model. An example of the experimental specific heat capacity used in this work from Aseyev and Zaytsev (1996) from 40 to 120 °C for H_2O-K_2CO_3 and H_2O-$KHCO_3$ systems is shown in Figures 12.6-2 and 12.6-3, respectively.

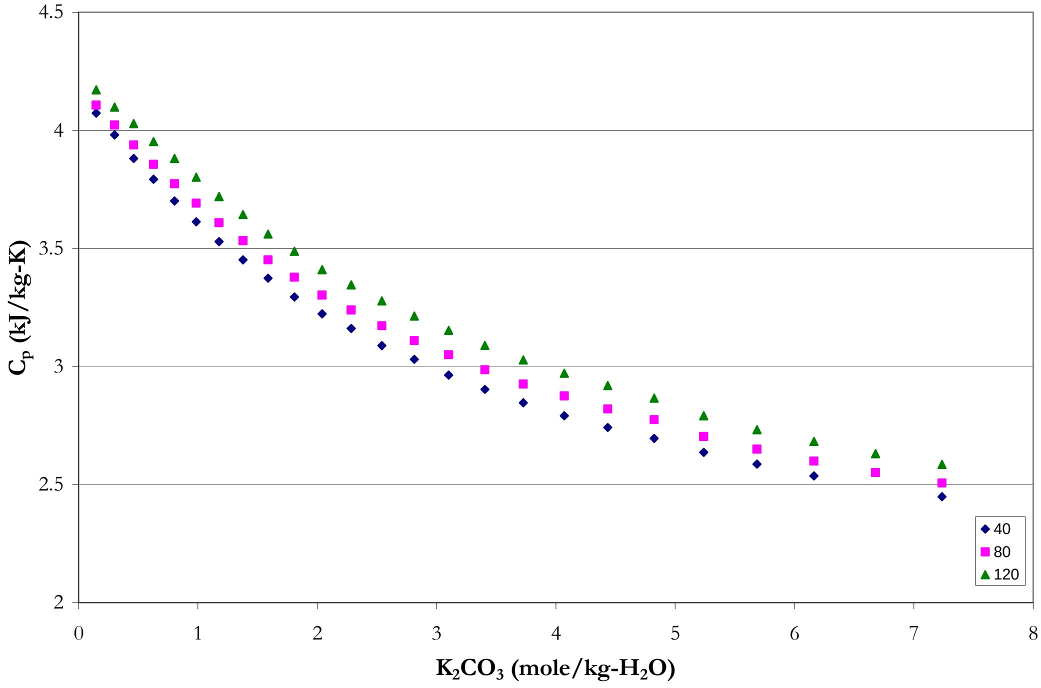

Table 12.6-2. Specific Heat Capacity in Aqueous K_2CO_3 Mixtures from 40 to 120 °C.

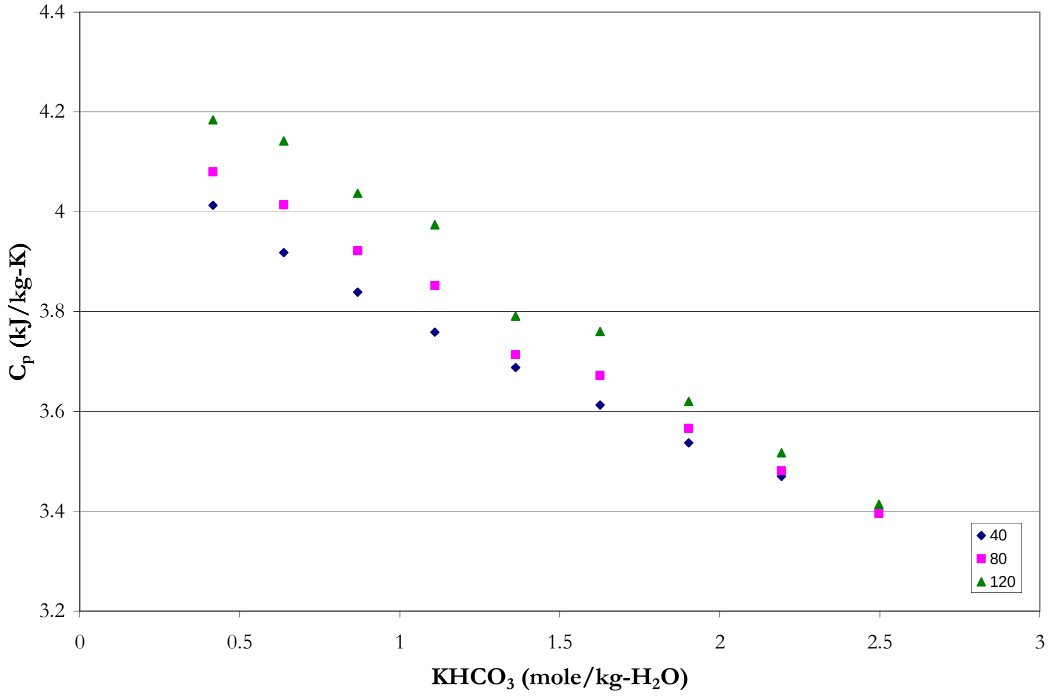

Table 12.6-3. Specific Heat Capacity in Aqueous $KHCO_3$ Mixtures from 40 to 120 °C.

12.6.4 *CO_2 Solubility*

Data in the form of CO_2 solubility, which measures the partial pressure of CO_2 over aqueous potassium carbonate/bicarbonate solutions, P_{CO_2}, as a function of the fractional conversion (loading) of K_2CO_3 to $KHCO_3$ and temperature were used to adjust the partial pressure of CO_2 for the H_2O-K_2CO_3-CO_2 system through the simultaneous regression of the binary interaction parameters in the elecNRTL model for the H_2O-K_2CO_3-CO_2 system.

Tosh et al. (1959) reported the equilibrium total pressure and the partial pressure of CO_2 and H_2O, where the volume percent of CO_2 and H_2O was determined by mass spectroscopy; thus the vapor fraction of CO_2 and H_2O were used to calculate the partial pressure of the respective species by the following relation:

$$P_i = y_i P \qquad 12\text{-}34$$

Where
P_i is the partial pressure of species i, kPa,
y_i is the vapor fraction of species i, unitless,
P is the equilibrium total pressure of the system, kPa.

Examples of the experimental CO_2 solubility used in this work from Tosh et al. (1959) at 20, 30, and 40 % equivalent concentration of K_2CO_3, are shown in Figures 12.6-3, 12.6-4, and 12.6-5. Perez-Salado Kamps et al. (2007) reported total vapor pressures over loaded (α = 1 - 4 mol CO_2/mol K_2CO_3) potassium carbonate solutions over the concentration and temperature rage of 0.43 to 1.7 m K_2CO_3 and from 40 to 120 °C, respectively. Total vapor pressure reported by Perez-Salado Kamps et al. (2007) were excluded due to the high CO_2 loadings that were beyond the range of interest in this work.

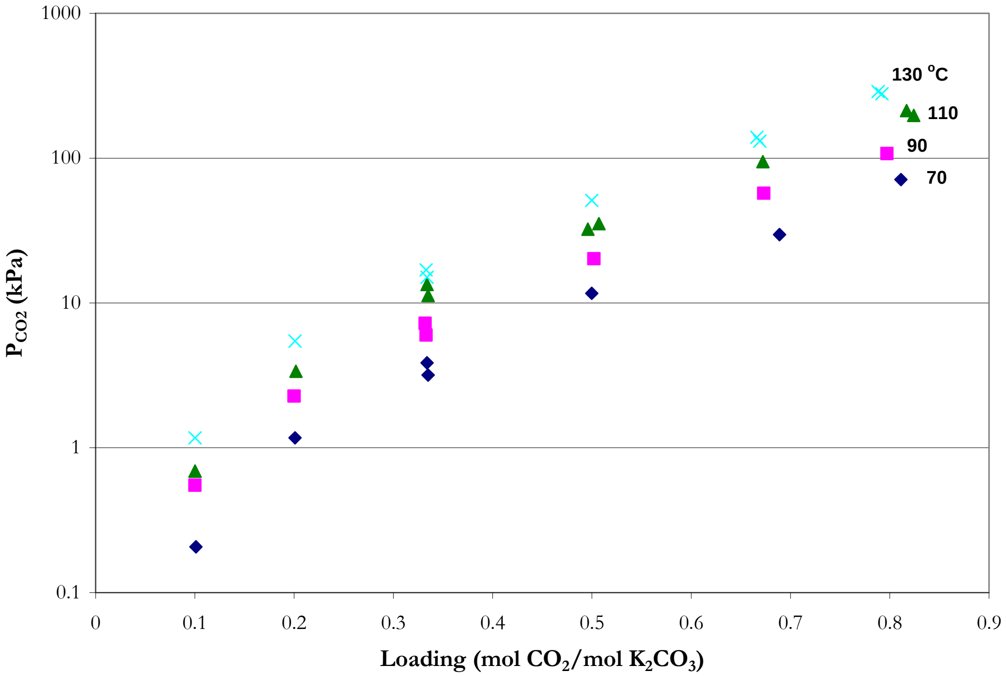

Figure 12.6-3. CO_2 Solubility in a 20 % equivalent concentration of aqueous solution of K_2CO_3.

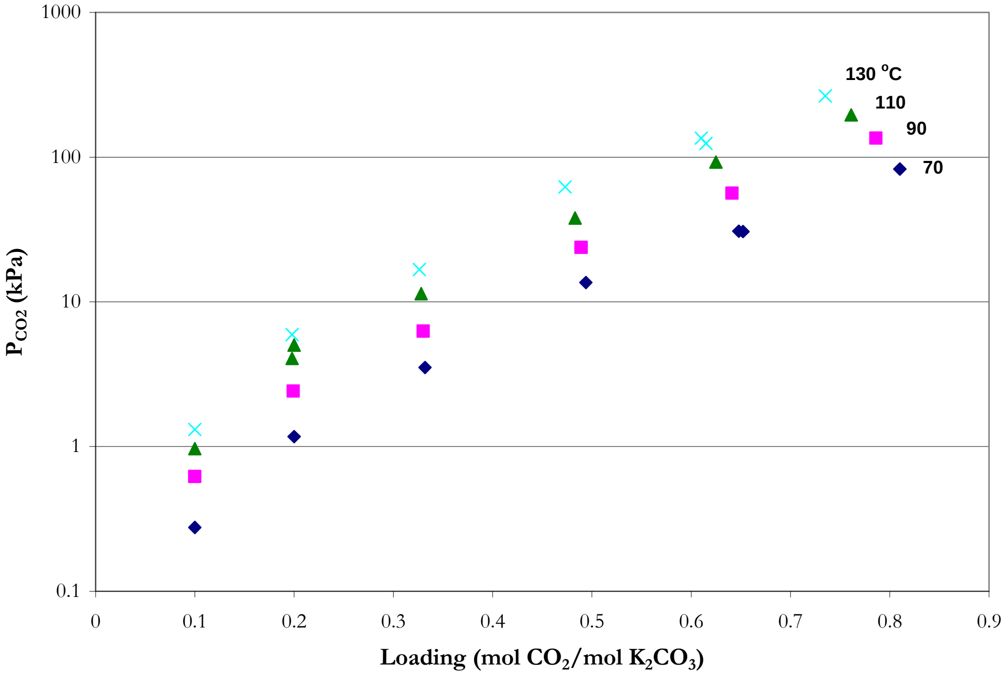

Figure 12.6-4. CO_2 Solubility in a 30 % equivalent concentration of aqueous solution of K_2CO_3.

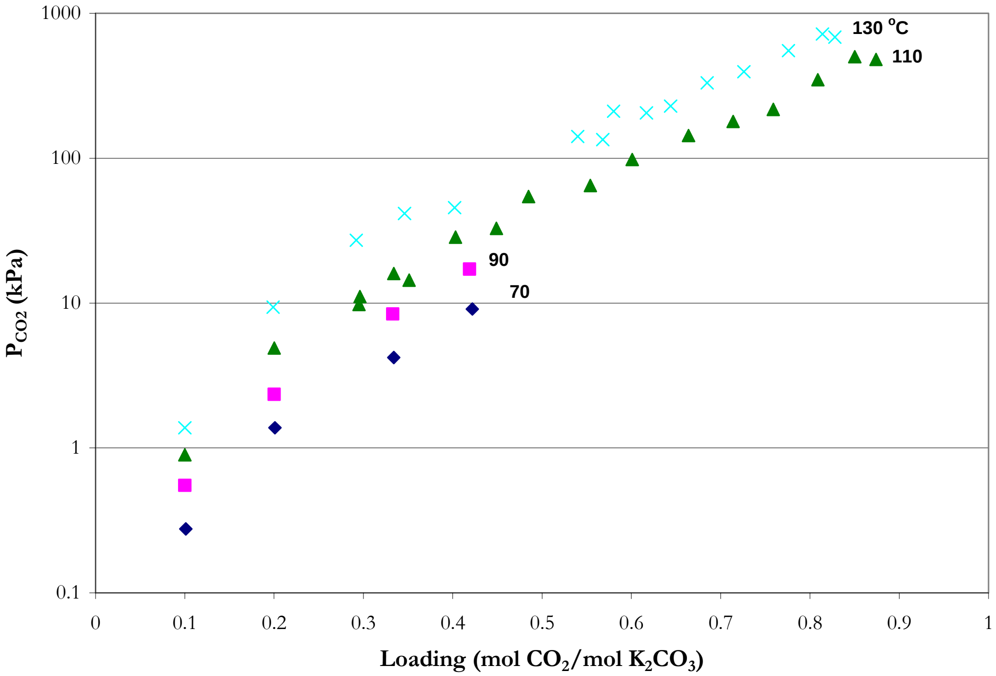

Figure 12.6-5. CO_2 Solubility in a 40 % equivalent concentration of aqueous solution of K_2CO_3.

12.6.5 *Solid Solubility*

Data in the form of solid solubility, which measures the dissolution temperature of the solid phase, vis-à-vis synthetic method, as function of molality and temperature, was used to adjust the temperature dependent equilibrium constants for Reactions 12-2 and 12-4. Experimental solid solubility data from Linke and Seidell (1965) and Moore et al. (1997) for H_2O-K_2CO_3, H_2O-$KHCO_3$, and H_2O-K_2CO_3-$KHCO_3$ systems were used in the regression for coefficients in Equation 12-26 through the simultaneous regression with the binary interaction parameters in the elecNRTL model for the H_2O-K_2CO_3-CO_2 system.

Examples of the experimental solid solubility used in this work from Linke and Seidell (1965) and Moore et al. (1997) for aqueous K_2CO_3 and $KHCO_3$ mixtures are shown in Figure 12.6-6. In this work, we have concentrated our efforts to describe SLV for 1.8 m < K_2CO_3 < 5 m in loaded solutions, where the major solid phase is $KHCO_3$(s) as shown in Figure 12.6-6.

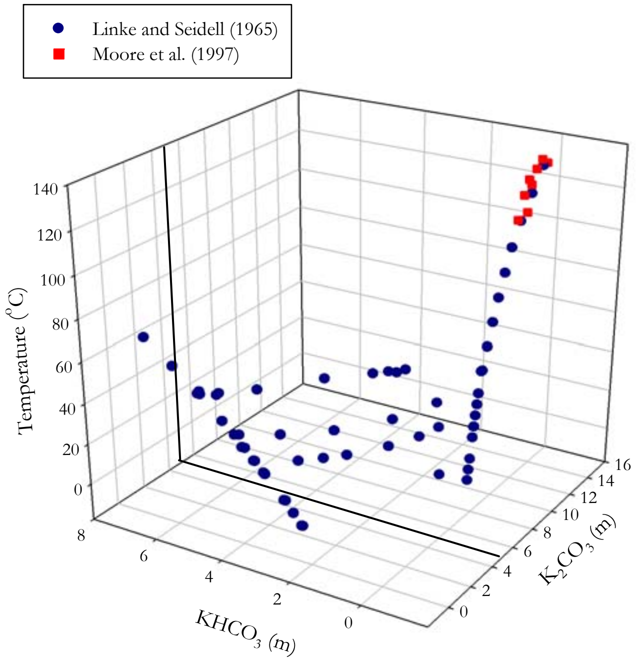

Figure 12.6-6. Solid Solubility of Aqueous K_2CO_3 and $KHCO_3$ Mixtures.

12.7 Data Regression

Recall from Chapter VI that there are three types of binary interaction parameters in the elecNRTL model: molecule-molecule, $\tau_{m,m'}$ and $\tau_{m',m}$; molecule-electrolyte, $\tau_{m,ca}$ and $\tau_{ca,m}$; electrolyte-electrolyte (with a common cation or anion) $\tau_{ca,ca'}$ and $\tau_{ca',ca}$ or $\tau_{ca,c'a}$ and $\tau_{c'a,ca}$; and the molecule-electrolyte nonrandomness factor, $\alpha_{ca,m}$. Chen and Evans (1986) noted that in their regression attempts it was not always possible to obtain statistically significant results for all four types of binary interaction parameters. In this work, the molecule-electrolyte nonrandomness parameter was set to an arbitrary value of $\alpha_{ca,m} = 0.2$ for all correlations involving electrolyte systems as suggested by Chen and Evans (1986). In this work, the electrolyte – electrolyte parameters are generally negligible and were assumed to be zero.

For the elecNRTL model, default values given for molecule-electrolyte and electrolyte-molecule interactions are given in Table 12.7-1.

Table 12.7-1. Default Binary Interaction Parameters for the elecNRTL Model in Aspen Plus™.

Binary Interaction Pairs	τ
Molecule-electrolyte	10
Electrolyte-molecule	-2
Water-electrolyte	8
Electrolyte-water	-4

The energy parameters are adjusted to provide the best fit to the data. The binary interaction parameters were assumed to be temperature dependent and were fitted to the following function of temperature:

$$\tau_{m,ca} = A_{m,ca} + \frac{B_{m,ca}}{T} + C_{m,ca}\left[\frac{\left(T^{ref} - T\right)}{T} + \ln\left(\frac{T}{T^{ref}}\right)\right] \qquad 12\text{-}35$$

$$\tau_{ca,m} = A_{ca,m} + \frac{B_{ca,m}}{T} + C_{ca,m}\left[\frac{\left(T^{ref} - T\right)}{T} + \ln\left(\frac{T}{T^{ref}}\right)\right] \qquad 12\text{-}36$$

where electrolyte-electrolyte interactions follow a similar form as given above.

A list of the aqueous electrolyte data sets that were examined in this work is given in Table 12.7-2. The column labels σ_T, σ_P, $\sigma_{\gamma\pm}$, σ_{PH2O}, σ_{PCO2}, σ_{x_i}, σ_{y_i}, σ_{Cp}, give standard error associated with the temperature, pressure, mean ionic activity coefficient, partial pressure of water, partial pressure of CO_2, liquid mole fraction, vapor mole fraction, the specific heat capacity, and solid solubility, respectively, with each data set. DRS suggested standard error default values were assigned unless otherwise stated by the author.

Table 12.7-2. Experimental data used for regression of the H_2O-K_2CO_3-CO_2 systems.

H_2O-K_2CO_3 System

	Obs.	T (^{o}C)	σ_T	σ_P	σ_x	$\sigma_{\gamma\pm}$	Source
$\gamma_{\pm}$	53	25.0	0.1	0.1%	0.1%	1.0%	Aseyev and Zaytsev (1996)

	Obs.	T (^{o}C)	σ_T	σ_{PH2O}	σ_x	σ_y	Source
P^{H2O}	543	25.0 – 130.0	0.1	0.5%	0.1%	0	Aseyev (1999)
	42	25.0 – 90.0	0.1	0.6%	0.1%	0	Puchkov and Kurochkina (1970)

	Obs.	T (^{o}C)	σ_T	σ_x	σ_{Cp}	Source
Cp	298	10.0 – 130.0	0.1	0.1%	0.5%	Aseyev and Zaytsev (1996)

	Obs.	T (^{o}C)	σ_T	σ_x	Source
Salt	19	0.0 – 130.0	0.1	0.1%	Linke and Seidell (1965)
	8	111.0 – 133.0	0.1	0.1%	Moore et al. (1997)

H_2O-$KHCO_3$ System

	Obs.	T (^{o}C)	σ_T	σ_{PH2O}	σ_x	σ_y	Source
P^{H2O}	10	25.0	0.1	0.5%	0.1%	0	Aseyev (1999)

	Obs.	T (^{o}C)	σ_T	σ_x	σ_{Cp}	Source
Cp	214	5.0 – 130.0	0.1	0.1%	0.5%	Aseyev and Zaytsev (1996)

	Obs.	T (^{o}C)	σ_T	σ_x	Source
Salt	17	0.0 – 70.0	0.1	0.1%	Linke and Seidell (1965)

H_2O-K_2CO_3-CO_2 System

	Obs.	T (^{o}C)	σ_T	σ_{PCO2}	σ_x	σ_y	Source
P^{CO2}	113	70.0 – 130.0	0.01	5.0%	0.1%	0	Tosh et al. (1959)

	Obs.	T (^{o}C)	σ_T	σ_x	Source
Salt	21	5.0 – 50.0	0.1	0.1%	Linke and Seidell (1965)

Overall, 1,338 experimental data points were included in the model regression. Over the course of the model regression, three attempts were made to determine an optimum set of model parameters to adequately describe the H_2O-K_2CO_3-CO_2 system. The following discussion outlines each regression case.

In Case I, coefficients for the infinite dilution aqueous phase heat capacity polynomial of HCO_3^{-1} and CO_3^{-2} and molecule-electrolyte and electrolyte-molecule binary interaction parameters were regressed to the experimental database outlined in Table 14.7-2. Electrolyte-electrolyte binary interaction parameters were set to zero. In this case, what we found was that even though the model was able to predict the correct CO_2 solubility and specific heat capacity, etc., the model was inconsistent with published pKa data for the dissociation of bicarbonate and the formation of carbonate at infinite dilution. Since this information was never a part of the database, the model was unbounded and allowed to wander off even though at 25 °C the ΔG_f and ΔH_f of bicarbonate and carbonate were consistent with Edwards et al. (1978).

In Case II, coefficients for the infinite dilution aqueous phase heat capacity polynomial of HCO_3^{-1} and CO_3^{-2} were adjusted to match pKa predictions by Edwards et al. (1978) and were fixed through the regressions (ref. Section 12.5). Molecule-electrolyte and electrolyte-molecule binary interaction parameters were regressed to the experimental database outlined in Table 12.7-2. Electrolyte-electrolyte binary interaction parameters were set to zero. In Case II, we found that the model was unable to adequately describe systematic trends in the CO_2 solubility data from Tosh et al. (1959) even though predictions for H_2O-K_2CO_3 system data were acceptable.

In our final and successful attempt, Case III, coefficients for the infinite dilution aqueous phase heat capacity polynomial of HCO_3^{-1} and CO_3^{-2} were fixed through the regressions as described in Case II. Molecule-electrolyte, electrolyte-molecule, and electrolyte-electrolyte binary interaction parameters were regressed to the experimental database outlined in Table 12.7-2, resulting in a very reasonable description of the experimental data.

Throughout the above three regression cases, solid solubility measurements were regressed simultaneously in the DRS data regression case. We found that chemical equilibrium constants describing K_2CO_3 and $KHCO_3$ salt precipitation sequentially regressed did not accurately describe systematic trends presented in the data. Hilliard (2005) reported parameters sequentially regressed for H_2O-K_2CO_3 and H_2O-$KHCO_3$ systems did not accurately describe CO_2 solubility data from Tosh et al. (1959); nor did parameters regressed by Aspen Plus^{TM} for the H_2O-K_2CO_3-CO_2 system were unable to capture systematic temperature trends apart of the CO_2 solubility data from Tosh et al. (1959).

With a reliable regression methodology determined, Table 12.7-3 shows the regression summary statistics output for estimates of the adjustable binary parameter coefficients after performing a nonlinear regression, Case III, for the full model using DRS in Aspen Plus^{TM}.

Table 12.7-3. DRS Regression Output for Full H_2O-K_2CO_3-CO_2 System Model.

	Interacting Species				
Parameter	i	j	k	Estimate	σ wrt Estimate
1-$A_{ca,m}$	K^+	CO_3^{-2}	H_2O	-4.49	0.123
2-$B_{ca,m}$	K^+	CO_3^{-2}	H_2O	-32.3	37.8
3-$C_{ca,m}$	K^+	CO_3^{-2}	H_2O	0.296	0.241
4-$A_{m,ca}$	H_2O	K^+	CO_3^{-2}	10.71	0.615
5-$B_{m,ca}$	H_2O	K^+	CO_3^{-2}	-447	186
6-$C_{m,ca}$	H_2O	K^+	CO_3^{-2}	4.12	0.814
7-$A_{ca,m}$	K^+	HCO_3^{-1}	H_2O	-5.42	0.647
8-$B_{ca,m}$	K^+	HCO_3^{-1}	H_2O	158	214
9-$C_{ca,m}$	K^+	HCO_3^{-1}	H_2O	4.51	3.15
10-$A_{m,ca}$	H_2O	K^+	HCO_3^{-1}	11.9	1.45
11-$B_{m,ca}$	H_2O	K^+	HCO_3^{-1}	-269	488
12-$C_{m,ca}$	H_2O	K^+	HCO_3^{-1}	-8.94	5.70
13-$A_{ca,ca}$	K^+ CO_3^{-2}	K^+ HCO_3^{-1}		12.17	2.22
14-$B_{ca,ca}$	K^+ CO_3^{-2}	K^+ HCO_3^{-1}		-3182	737
15-$C_{ca,ca}$	K^+ CO_3^{-2}	K^+ HCO_3^{-1}		-37.8	8.31
16-$A_{ca,ca}$	K^+ HCO_3^{-1}	K^+ CO_3^{-2}		0.202	0.566
17-$B_{ca,ca}$	K^+ HCO_3^{-1}	K^+ CO_3^{-2}		-636	183
18-$C_{ca,ca}$	K^+ HCO_3^{-1}	K^+ CO_3^{-2}		-8.61	3.50
19-K_{sp}-A	$K_2CO_3(s)$			1.59	5.84
20-K_{sp}-B	$K_2CO_3(s)$			-779	479
21-K_{sp}-C	$K_2CO_3(s)$			1.25	1.08
22-K_{sp}-D	$K_2CO_3(s)$			-0.0411	0.00344
23-K_{sp}-A	$KHCO_3(s)$			-80.3	6.06
24-K_{sp}-B	$KHCO_3(s)$			5432	987
25-K_{sp}-C	$KHCO_3(s)$			4.89	1.68
26-K_{sp}-D	$KHCO_3(s)$			0.0852	0.0142

Residual Sum of Squares:	79,331
Residual Root Mean Square:	7.860
Degree of Freedom:	1,312

Recall that the standard error of an estimate is the estimated standard deviation of that statistic. Notice that all but five of the estimates are large relative to their standard errors. Table 12.7-4 gives a complete description of the variability of the coefficient estimates requires examining the correlations between the estimates.

Table 12.7-4. Correlation Matrix of the Coefficient Estimates for the Full H_2O-K_2CO_3-CO_2 System Model

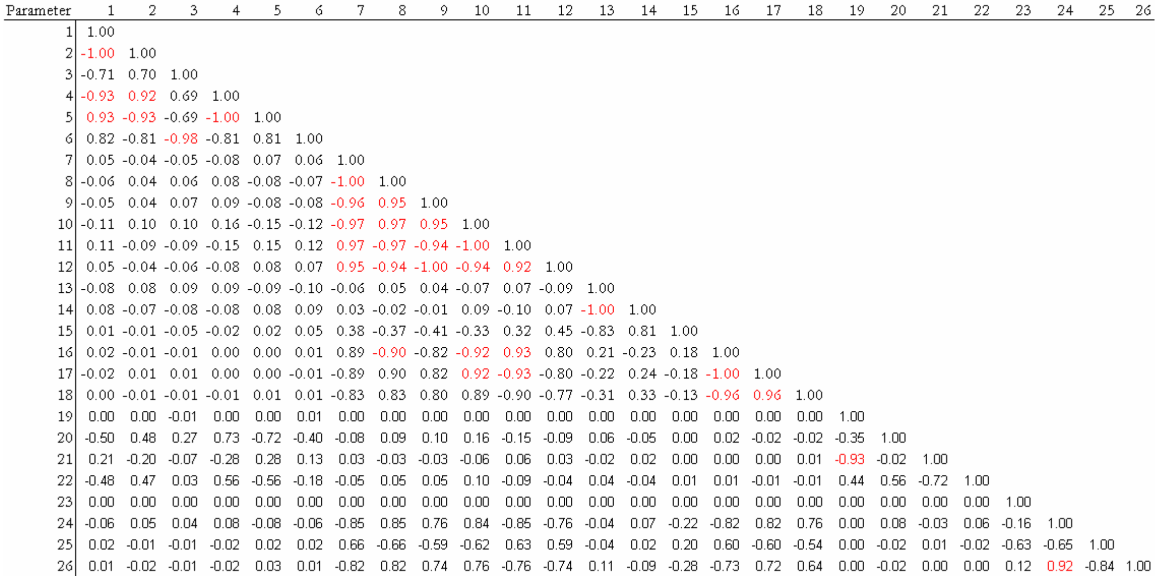

Parameter	1	2	3	4	5	6	7	8	9	10	11	12	13	14	15	16	17	18	19	20	21	22	23	24	25	26
1	1.00																									
2	-1.00	1.00																								
3	-0.71	0.70	1.00																							
4	-0.93	0.92	0.69	1.00																						
5	0.93	-0.93	-0.69	-1.00	1.00																					
6	0.82	-0.81	-0.98	-0.81	0.81	1.00																				
7	0.05	-0.04	-0.05	-0.08	0.07	0.06	1.00																			
8	-0.06	0.04	0.06	0.08	-0.08	-0.07	-1.00	1.00																		
9	-0.05	0.04	0.07	0.09	-0.08	-0.08	-0.96	0.95	1.00																	
10	-0.11	0.10	0.10	0.16	-0.15	-0.12	-0.97	0.97	0.95	1.00																
11	0.11	-0.09	-0.09	-0.15	0.15	0.12	0.97	-0.97	-0.94	-1.00	1.00															
12	0.05	-0.04	-0.06	-0.08	0.08	0.07	0.95	-0.94	-1.00	-0.94	0.92	1.00														
13	-0.08	0.08	0.09	0.09	-0.09	-0.10	-0.06	0.05	0.04	-0.07	0.07	-0.09	1.00													
14	0.08	-0.07	-0.08	-0.08	0.08	0.09	0.03	-0.02	-0.01	0.09	-0.10	0.07	-1.00	1.00												
15	0.01	-0.01	-0.05	-0.02	0.02	0.05	0.38	-0.37	-0.41	-0.33	0.32	0.45	-0.83	0.81	1.00											
16	0.02	-0.01	-0.01	0.00	0.00	0.01	0.89	-0.90	-0.82	-0.92	0.93	0.80	0.21	-0.23	0.18	1.00										
17	-0.02	0.01	0.01	0.00	0.00	-0.01	-0.89	0.90	0.82	0.92	-0.93	-0.80	-0.22	0.24	-0.18	-1.00	1.00									
18	0.00	-0.01	-0.01	-0.01	0.01	0.01	-0.83	0.83	0.80	0.89	-0.90	-0.77	-0.31	0.33	-0.13	-0.96	0.96	1.00								
19	0.00	0.00	-0.01	0.00	0.00	0.01	0.00	0.00	0.00	0.00	0.00	0.00	0.00	0.00	0.00	0.00	0.00	0.00	1.00							
20	-0.50	0.48	0.27	0.73	-0.72	-0.40	-0.08	0.09	0.10	0.16	-0.15	-0.09	0.06	-0.05	0.00	0.02	-0.02	-0.02	-0.35	1.00						
21	0.21	-0.20	-0.07	-0.28	0.28	0.13	0.03	-0.03	-0.03	-0.06	0.06	0.03	-0.02	0.02	0.00	0.00	0.00	0.01	-0.93	-0.02	1.00					
22	-0.48	0.47	0.03	0.56	-0.56	-0.18	-0.05	0.05	0.05	0.10	-0.09	-0.04	0.04	-0.04	0.01	0.01	-0.01	-0.01	0.44	0.56	-0.72	1.00				
23	0.00	0.00	0.00	0.00	0.00	0.00	0.00	0.00	0.00	0.00	0.00	0.00	0.00	0.00	0.00	0.00	0.00	0.00	0.00	0.00	0.00	0.00	1.00			
24	-0.06	0.05	0.04	0.08	-0.08	-0.06	-0.85	0.85	0.76	0.84	-0.85	-0.76	-0.04	0.07	-0.22	-0.82	0.82	0.76	0.00	0.08	-0.03	0.06	-0.16	1.00		
25	0.02	-0.01	-0.01	-0.02	0.02	0.02	0.66	-0.66	-0.59	-0.62	0.63	0.59	-0.04	0.02	0.20	0.60	-0.60	-0.54	0.00	-0.02	0.01	-0.02	-0.63	-0.65	1.00	
26	0.01	-0.02	-0.01	-0.02	0.03	0.01	-0.82	0.82	0.74	0.76	-0.76	-0.74	0.11	-0.09	-0.28	-0.73	0.72	0.64	0.00	-0.02	0.00	0.00	0.12	0.92	-0.84	1.00

Table 12.7-4 shows 33 highly negative and positive correlations out of a possible 351. The highly correlated parameters are between the temperature dependent coefficients and the respective constant for each energy parameter estimate, but the correlation between other coefficients is relatively small, suggesting the amount of temperature dependant parameters might be usefully removed from the model without significant loss of information.

After performing backward elimination using DRS, the following optimum model regression summary statistics output for estimates of the adjustable binary parameter coefficients are shown in Table 12.7-5.

Table 12.7-5. DRS Regression Output for Optimum H_2O-K_2CO_3-CO_2 Model.

	Interacting Species				
Parameter	i	j	k	Estimate	σ wrt Estimate
1-$A_{ca,m}$	K^+	CO_3^{-2}	H_2O	-4.42	0.0851
2-$B_{ca,m}$	K^+	CO_3^{-2}	H_2O	-54.2	26.6
3-$A_{m,ca}$	H_2O	K^+	CO_3^{-2}	10.4	0.419
4-$B_{m,ca}$	H_2O	K^+	CO_3^{-2}	-365	127
5-$C_{m,ca}$	H_2O	K^+	CO_3^{-2}	5.01	0.157
6-$A_{ca,m}$	K^+	HCO_3^{-1}	H_2O	-4.94	0.0274
7-$C_{ca,m}$	K^+	HCO_3^{-1}	H_2O	2.47	0.971
8-$A_{m,ca}$	H_2O	K^+	HCO_3^{-1}	11.1	0.0645
9-$B_{m,ca}$	H_2O	K^+	HCO_3^{-1}	-5.23	1.89
10-$A_{ca,ca}$	K^+ CO_3^{-2}	K^+ HCO_3^{-1}		11.3	1.88
11-$B_{ca,ca}$	K^+ CO_3^{-2}	K^+ HCO_3^{-1}		-2908	624
12-$C_{ca,ca}$	K^+ CO_3^{-2}	K^+ HCO_3^{-1}		-35.47	7.66
13-$A_{ca,ca}$	K^+ HCO_3^{-1}	K^+ CO_3^{-2}		0.490	0.199
14-$B_{ca,ca}$	K^+ HCO_3^{-1}	K^+ CO_3^{-2}		-726	63.5
15-$C_{ca,ca}$	K^+ HCO_3^{-1}	K^+ CO_3^{-2}		-9.69	1.35
16-K_{sp}-A	$K_2CO_3(s)$			-70.3	6.17
17-K_{sp}-B	$K_2CO_3(s)$			1361	493
18-K_{sp}-C	$K_2CO_3(s)$			13.5	0.991
19-K_{sp}-D	$K_2CO_3(s)$			-0.0582	0.00286
20-K_{sp}-A	$KHCO_3(s)$			-1421	6.25
21-K_{sp}-B	$KHCO_3(s)$			40191	511
22-K_{sp}-C	$KHCO_3(s)$			241	1.29
23-K_{sp}-D	$KHCO_3(s)$			-0.3145	0.00770

Residual Sum of Squares:	79,427
Residual Root Mean Square:	7.856
Degree of Freedom:	1,315

Notice that all of the estimates in Table 12.7-5 are larger relative to their standard errors. In comparing the estimates from the full model to the optimum model, there was relatively little difference between the estimated values. The proposed optimum model provides the following correlations between the estimates as shown in Table 12.7-6.

Table 12.7-6. Correlation Matrix of the Coefficient Estimates for the Optimum H_2O-K_2CO_3-CO_2 Model.

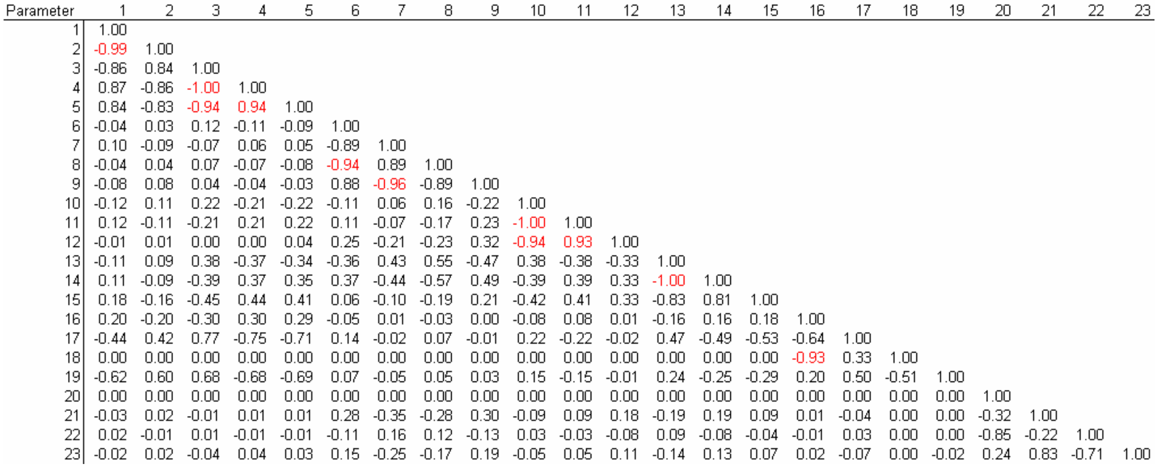

Parameter	1	2	3	4	5	6	7	8	9	10	11	12	13	14	15	16	17	18	19	20	21	22	23
1	1.00																						
2	-0.99	1.00																					
3	-0.86	0.84	1.00																				
4	0.87	-0.86	-1.00	1.00																			
5	0.84	-0.83	-0.94	0.94	1.00																		
6	-0.04	0.03	0.12	-0.11	-0.09	1.00																	
7	0.10	-0.09	-0.07	0.06	0.05	-0.89	1.00																
8	-0.04	0.04	0.07	-0.07	-0.08	-0.94	0.89	1.00															
9	-0.08	0.08	0.04	-0.04	-0.03	0.88	-0.96	-0.89	1.00														
10	-0.12	0.11	0.22	-0.21	-0.22	-0.11	0.06	0.16	-0.22	1.00													
11	0.12	-0.11	-0.21	0.21	0.22	0.11	-0.07	-0.17	0.23	-1.00	1.00												
12	-0.01	0.01	0.00	0.00	0.04	0.25	-0.21	-0.23	0.32	-0.94	0.93	1.00											
13	-0.11	0.09	0.38	-0.37	-0.34	-0.36	0.43	0.55	-0.47	0.38	-0.38	-0.33	1.00										
14	0.11	-0.09	-0.39	0.37	0.35	0.37	-0.44	-0.57	0.49	-0.39	0.39	0.33	-1.00	1.00									
15	0.18	-0.16	-0.45	0.44	0.41	0.06	-0.10	-0.19	0.21	-0.42	0.41	0.33	-0.83	0.81	1.00								
16	0.20	-0.20	-0.30	0.30	0.29	-0.05	0.01	-0.03	0.00	-0.08	0.08	0.01	-0.16	0.16	0.18	1.00							
17	-0.44	0.42	0.77	-0.75	-0.71	0.14	-0.02	0.07	-0.01	0.22	-0.22	-0.02	0.47	-0.49	-0.53	-0.64	1.00						
18	0.00	0.00	0.00	0.00	0.00	0.00	0.00	0.00	0.00	0.00	0.00	0.00	0.00	0.00	0.00	-0.93	0.33	1.00					
19	-0.62	0.60	0.68	-0.68	-0.69	0.07	-0.05	0.05	0.03	0.15	-0.15	-0.01	0.24	-0.25	-0.29	0.20	0.50	-0.51	1.00				
20	0.00	0.00	0.00	0.00	0.00	0.00	0.00	0.00	0.00	0.00	0.00	0.00	0.00	0.00	0.00	0.00	0.00	0.00	0.00	1.00			
21	-0.03	0.02	-0.01	0.01	0.01	0.28	-0.35	-0.28	0.30	-0.09	0.09	0.18	-0.19	0.19	0.09	0.01	-0.04	0.00	0.00	-0.32	1.00		
22	0.02	-0.01	0.01	-0.01	-0.01	-0.11	0.16	0.12	-0.13	0.03	-0.03	-0.08	0.09	-0.08	-0.04	-0.01	0.03	0.00	0.00	-0.85	-0.22	1.00	
23	-0.02	0.02	-0.04	0.04	0.03	0.15	-0.25	-0.17	0.19	-0.05	0.05	0.11	-0.14	0.13	0.07	0.02	-0.07	0.00	-0.02	0.24	0.83	-0.71	1.00

Table 12.7-6 again shows highly negative and positive correlations between some of the temperature dependant parameters, but the correlation between other coefficients is relatively small suggesting the amount of temperature dependant parameters might be usefully removed from the model without significant loss of information.

Results from the previous section show that dropping a term from the optimum model may provide a submodel that may have a decrease in the correlation between the estimate coefficients and improve the reliability of the model. Testing whether any subset of the regression estimate coefficients may be zero plays an important role in many analyses which leads to the following hypotheses:

NH: $2 = 4 = 5 = 8 = 9 = 11 = 12 = 14 = 18 = 0$ Submodel function applies
AH: At lease one $2 = 4 = 5 = 8 = 9 = 11 = 12 = 14 = 18 \neq 0$ Optimum model function applies

We can perform an F-Test to compare the purposed submodel with the optimum model. Significance levels for this test are obtained by comparing the observed value of F to the $F_{df_{NH}-df_{AH},df_{AH}}$ distribution. The p-value is then computed as an upper-tail test and gives the probability associated with evidence to reject the null hypothesis which will then be compared to the results given by the submodel.

If we were to remove the highly correlated parameters from the optimum model, the following submodel regression summary statistics output for estimates of the adjustable binary parameter coefficients is shown in Table 12.7-7.

Table 12.7-7. DRS Regression Output for H_2O-K_2CO_3-CO_2 Submodel.

	Interacting Species				
Parameter	i	j	k	Estimate	σ wrt Estimate
1-$A_{ca,m}$	K^+	CO_3^{-2}	H_2O	-4.55	0.0268
2-$A_{m,ca}$	H_2O	K^+	CO_3^{-2}	9.02	0.0867
3-$A_{ca,m}$	K^+	HCO_3^{-1}	H_2O	-3.64	0.0286
4-$C_{ca,m}$	K^+	HCO_3^{-1}	H_2O	-10.7	0.843
5-$A_{ca,ca}$	K^+ CO_3^{-2}	K^+ HCO_3^{-1}		4.69	0.465
6-$A_{ca,ca}$	K^+ HCO_3^{-1}	K^+ CO_3^{-2}		-1.34	0.0292
7-$C_{ca,ca}$	K^+ HCO_3^{-1}	K^+ CO_3^{-2}		-20.4	2.18
8-K_{sp}-A	$K_2CO_3(s)$			-1.06	3.45
9-K_{sp}-B	$K_2CO_3(s)$			-791	583
10-K_{sp}-D	$K_2CO_3(s)$			-0.00788	0.00503
11-K_{sp}-A	$KHCO_3(s)$			6115	11.9
12-K_{sp}-B	$KHCO_3(s)$			-158885	1169
13-K_{sp}-C	$KHCO_3(s)$			-1078	2.61
14-K_{sp}-D	$KHCO_3(s)$			1.84	0.0177

Residual Sum of Squares:	1,080,253
Residual Root Mean Square:	28.871
Degree of Freedom:	1,324

Notice that all but one of the estimates are larger relative to their standard errors. Comparing the estimates from the submodel to the optimum model, there was large difference between the estimated values with respect to the order of magnitude. The residual sum of squares and the standard errors for the submodel have increased as compared to the optimum model. The proposed submodel provides the following estimated covariances between the estimates as shown in Table 12.7-8.

Table 12.7-8. Correlation Matrix of the Coefficient Estimates for the H_2O-K_2CO_3-CO_2 Submodel.

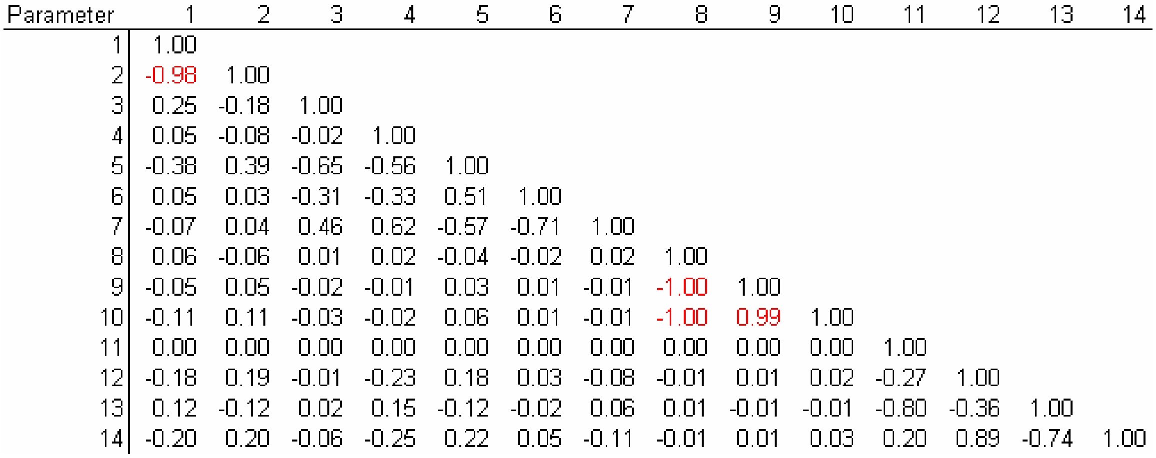

Parameter	1	2	3	4	5	6	7	8	9	10	11	12	13	14
1	1.00													
2	-0.98	1.00												
3	0.25	-0.18	1.00											
4	0.05	-0.08	-0.02	1.00										
5	-0.38	0.39	-0.65	-0.56	1.00									
6	0.05	0.03	-0.31	-0.33	0.51	1.00								
7	-0.07	0.04	0.46	0.62	-0.57	-0.71	1.00							
8	0.06	-0.06	0.01	0.02	-0.04	-0.02	0.02	1.00						
9	-0.05	0.05	-0.02	-0.01	0.03	0.01	-0.01	-1.00	1.00					
10	-0.11	0.11	-0.03	-0.02	0.06	0.01	-0.01	-1.00	0.99	1.00				
11	0.00	0.00	0.00	0.00	0.00	0.00	0.00	0.00	0.00	0.00	1.00			
12	-0.18	0.19	-0.01	-0.23	0.18	0.03	-0.08	-0.01	0.01	0.02	-0.27	1.00		
13	0.12	-0.12	0.02	0.15	-0.12	-0.02	0.06	0.01	-0.01	-0.01	-0.80	-0.36	1.00	
14	-0.20	0.20	-0.06	-0.25	0.22	0.05	-0.11	-0.01	0.01	0.03	0.20	0.89	-0.74	1.00

Table 12.7-8 shows that parameters describing the temperature dependence are highly correlated. The two models were then compared using the test statistic F applied to the null hypothesis versus the alternative:

$$\frac{\left[\dfrac{1,080,253-79,427}{1,324-1,315}\right]}{\left[\dfrac{79,427}{1,315}\right]} \sim 1841.08\left(9,1,315\right)$$

We can then calculate the probability for a F-distribution, df = 9, 1315, upper-tail.

F dist. with (9, 1315) df, value = 1841.08, upper-tail probability = 0

The finding of $p=0$ provides strong evidence against the null hypothesis that $2=4=5=8=9=11=12=14=18=0$. Since a value of F this strong would be observed 0 times out of a hundred if the null hypothesis were true, the submodel will not give an adequate description of the data over the range of temperatures and concentration available in the data.

12.7.1 *Optimum Model Results*

With the determination of the estimates for the binary interaction parameters known for the optimum model, a simple Aspen Plus™ Flash model was used to test the predictive capability of the H_2O-K_2CO_3-CO_2 model against literature data. For each data point, the deviation between the experimental and estimated values is expressed in terms of the average absolute relative deviation (AARD). Table 12.7-9 gives the percent AARD and the maximum percent AARD for the model predictions.

Table 12.7-9. Absolute Percent Relative Error for the H_2O-K_2CO_3-CO_2 Optimum Model.

H_2O-K_2CO_3 System		AARD(%)	Max. AARD
$\gamma_\pm$	Aseyev and Zaytsev (1996)	8.23	22.73
P^{H2O}	Aseyev (1999)	1.13	3.59
	Puchkov and Kurochkina (1970)	1.69	7.58
C_p	Aseyev and Zaytsev (1996)	1.10	4.28
Salt	Linke and Seidell (1965)	0.29	0.81
	Moore et al. (1997)	0.99	1.59
H_2O-$KHCO_3$ System		AARD(%)	Max. AARD
P^{H2O}	Aseyev (1999)	0.30	0.42
C_p	Aseyev and Zaytsev (1996)	1.04	3.59
Salt	Linke and Seidell (1965)	2.39	5.85
H_2O-K_2CO_3-CO_2 System		AARD(%)	Max. AARD
P^{CO2}	Tosh et al. (1959)	10.80	32.99
Salt	Linke and Seidell (1965)	3.17	10.42
Overall		**3.85**	**32.99**

Overall, the model adequately describes the H_2O-K_2CO_2-CO_2 property data listed above within an average absolute relative error of ± 3.85 percent with the exception of a few outliers.

12.8 Optimum Model Predictions

In this work, we have compiled a large database of consistent high quality data needed to obtain a unique set of binary interaction parameters to describe the H_2O-K_2CO_3-CO_2 system. The remainder of this chapter will be devoted to using our model as a predictive tool as described in the subsequent sections.

Figure 12.8-1 illustrates hierarchical interactions based on the types of data included in the optimum model (presented as shaded areas) and allows accurate model predictions within the bounds of the literature data. The open areas represent predictions by the optimum model and should be regarded as an extrapolation. Previous experience has revealed that model predictions outside the model bounds should be regarded with caution and with the intentions to illustrate possible temperature and concentration trends only.

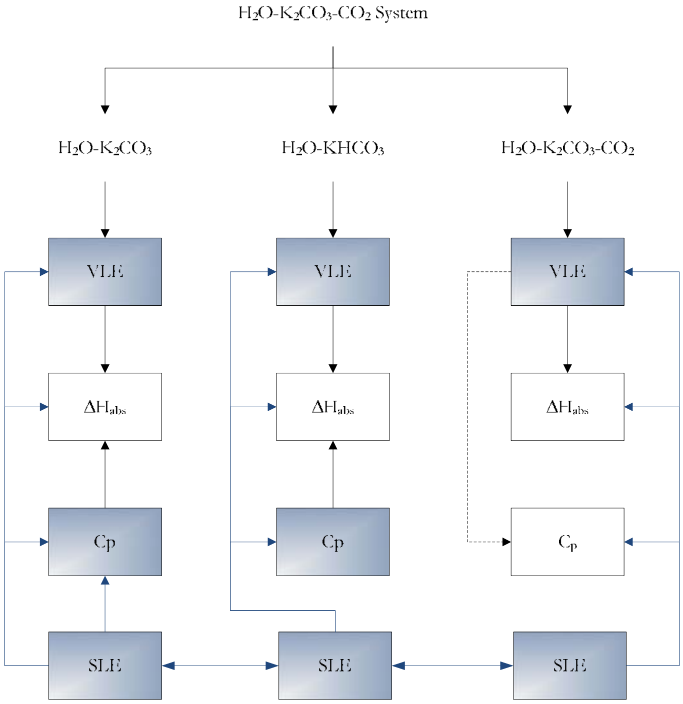

Figure 12.8-1. Optimum Model Data Type Representation for Model Predictions and Extrapolations. Shaded Area: Model Predictions. Open Area: Model Extrapolations.

12.8.1 *Vapor Pressure Depression*

With the determination of the estimates for the energy parameter coefficients known for the optimum model, a simple Aspen Plus™ Flash model was used to test the predictive capability of the H_2O-K_2CO_3-CO_2 energy parameter coefficients against literature data. Figure 12.8-2 and Figure 12.8-3 compare estimated and experimental vapor pressure measurements from Aseyev (1999) and Puchkov and Kurochkina (1970), for H_2O-K_2CO_3 and H_2O-$KHCO_3$ mixtures from 25.0 – 80.0 °C.

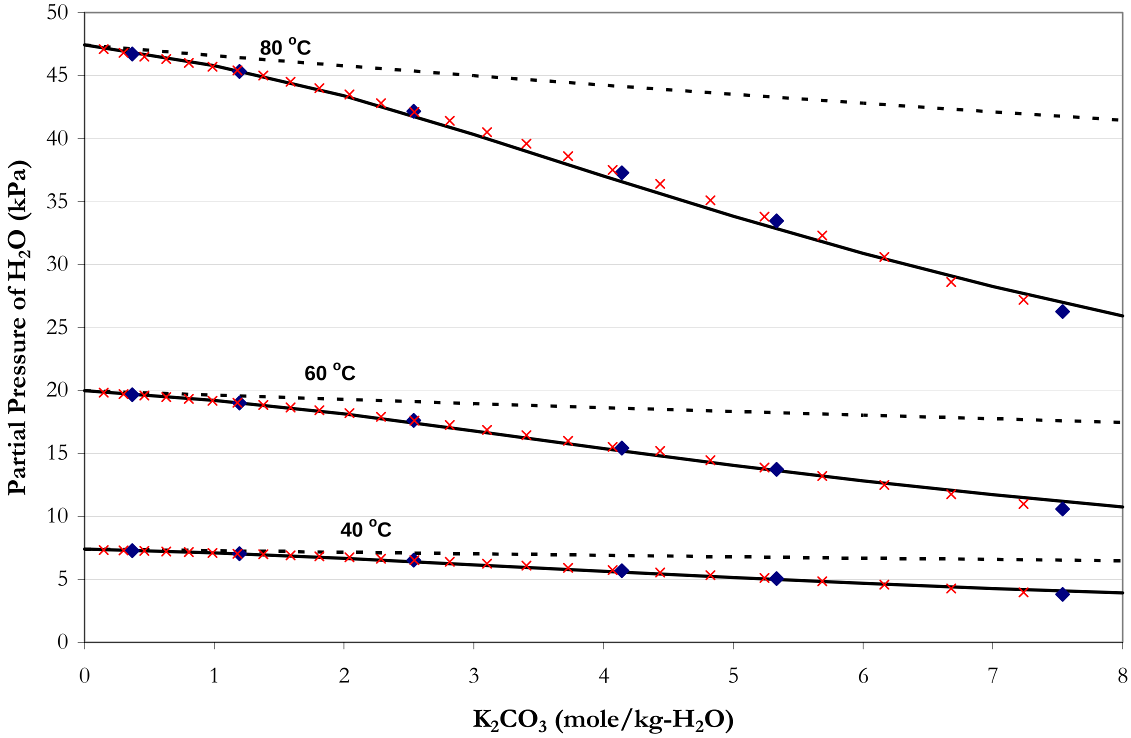

Figure 12.8-2. Comparison of the Partial Pressure of H_2O from Aseyev (1999) and Puchkov and Kurochkina (1970) to elecNRTL Model Predictions from 40 – 80 °C. Points: ■, Puchkov and Kurochkina (1970), ×, Aseyev (1999). Lines: ▬, elecNRTL Predictions, - - -, elecNRTL Ideal Solution Predictions.

The optimum model, as shown in Figure 12.8-2, predicts the partial pressure of H_2O from Aseyev (1999) and Puchkov and Kurochkina (1970) adequately.

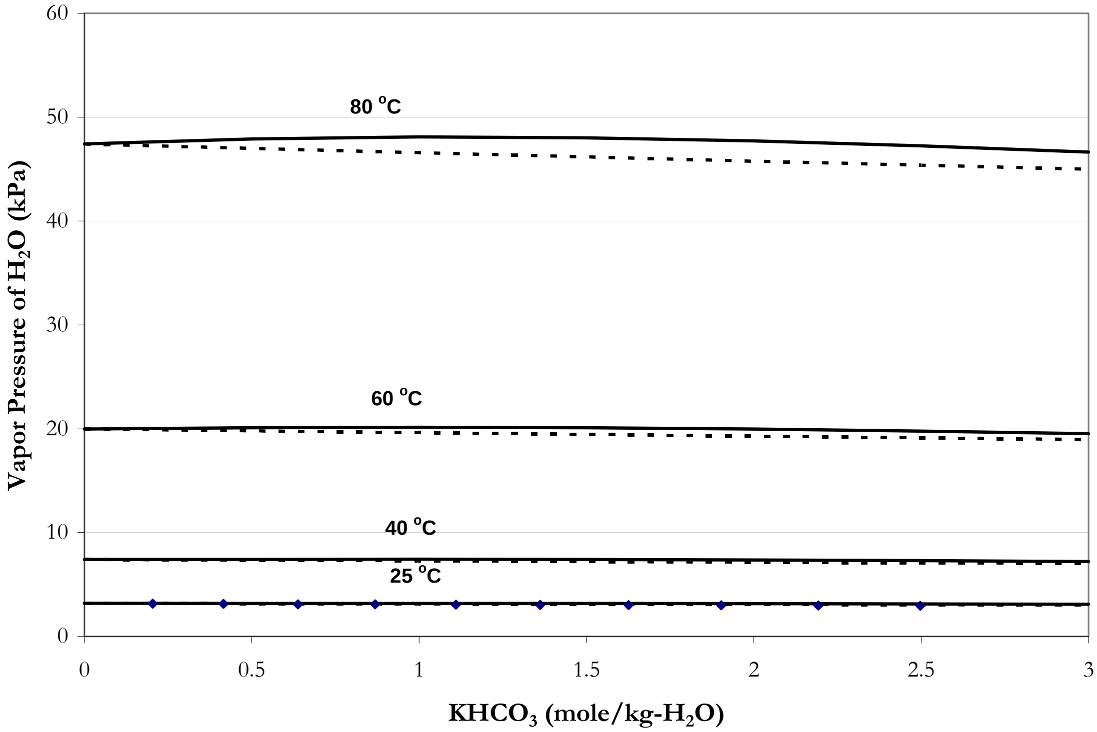

Figure 12.8-3. Comparison of the Partial Pressure of H_2O from Aseyev (1999) to elecNRTL Model Predictions from 25 – 80 °C. Points: ■, Aseyev (1999). Lines: ▬, elecNRTL Predictions, - - -, elecNRTL Ideal Solution Predictions.

Figure 12.8-2 and Figure 12.8-3 illustrate the departure from an ideal solution behavior vis-à-vis Raoult's Law as compared to predictions from the elecNRTL model. For H_2O-K_2CO_3 system, Raoult's Law adequately describes the vapor pressure of H_2O below 1 m K_2CO_3 over the temperature range between 40 and 80 °C, but as the concentration of K_2CO_3 increases so does the importance of including activities to describe the vapor-liquid equilibrium. On the other hand, Raoult's Law adequately describes the vapor pressure of H_2O over the entire $KHCO_3$ concentration range included in this work. There are slight deviations at 60 and 80 °C, but Raoult's Law does provide an adequate estimate for the vapor pressure of water.

Overall, the optimum model adequately predicts the partial pressure of H_2O over aqueous potassium carbonate and aqueous potassium bicarbonate mixtures within an AARD of 1.32 and 0.30 %, respectively with the exception of a few outliers.

12.8.2 *Mean Ionic Activity Coefficient*

Figure 12.8-4 shows the comparison between experimental and predicted mean ionic activity coefficient data at 25 °C. The optimum model provides an adequate representation of the data, but the optimum model overestimates the mean ionic activity coefficient between 2 and 5.8 m K_2CO_3 and under estimates the mean ionic activity coefficient between 6 and 7.5 m K_2CO_3.

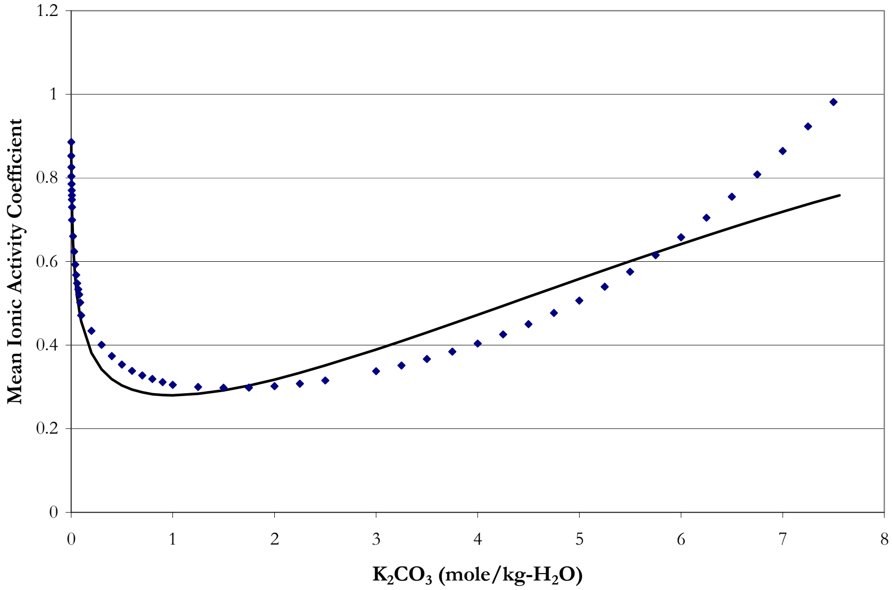

Figure 12.8-4. Comparison of Model Predictions with Experimental Data for K_2CO_3 Mean Ionic Activity Coefficient at 25 °C. Points: ■, Aseyev and Zaytsev (1999). Lines: ▬, elecNRTL Predictions.

Overall, the optimum model adequately describes the mean ionic activity coefficient data in aqueous K_2CO_3 mixtures within an average absolute relative error of ± 8.23 %.

12.8.3 *Specific Heat Capacity*

Figure 12.8-5 compares estimated and experimental specific heat capacities from 40 to 120 °C over the full range of concentrations of K_2CO_3 and $KHCO_3$.

Figure 12.8-5 also illustrates that the optimum model is consistent with the pure component specific heat capacities as discussed in Chapter VII, even though the optimum model tends to diverge at high salt concentrations. Overall, the optimum model adequately describes the specific heat capacity for H_2O-K_2CO_3 and H_2O-$KHCO_3$ systems within an average absolute relative error of ± 1.10 and 1.04 % error, respectively.

To describe the departure from an ideal solution behavior, Figure 12.8-6 separates the molar heat capacity of the solution into the weighted molar heat capacity of each contributing species with respect to the components reference state (i.e. Solvent: pure liquid; Ionic and Molecular Solutes: Infinite Dilution). Deviations between the molar heat capacity of the solution from the ideal molar heat capacity are accounted for by the excess molar heat capacity. Figure 12.8-6 illustrates that the solution molar heat capacity may be estimated by the weighted molar heat capacity of water to a first approximation.

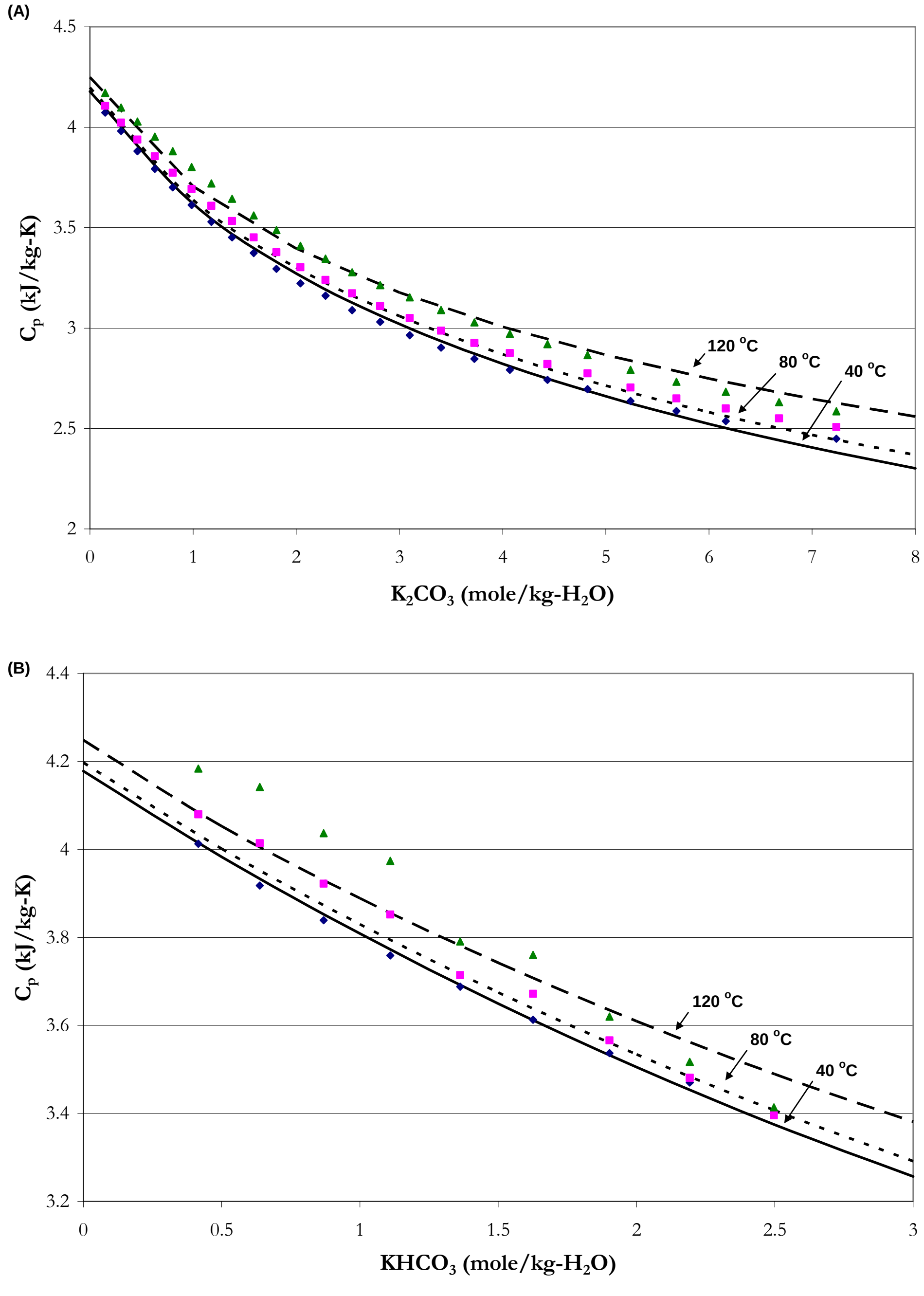

Figure 12.8-5. Comparison of Specific Heat Capacity from Aseyev and Zaytsev (1996) to H_2O-K_2CO_3 (A) and H_2O-$KHCO_3$ (B) elecNRTL Model Predictions from 40 to 120 °C. Points: ◆, 40 °C, ■, 80 °C, ▲, 120 °C.

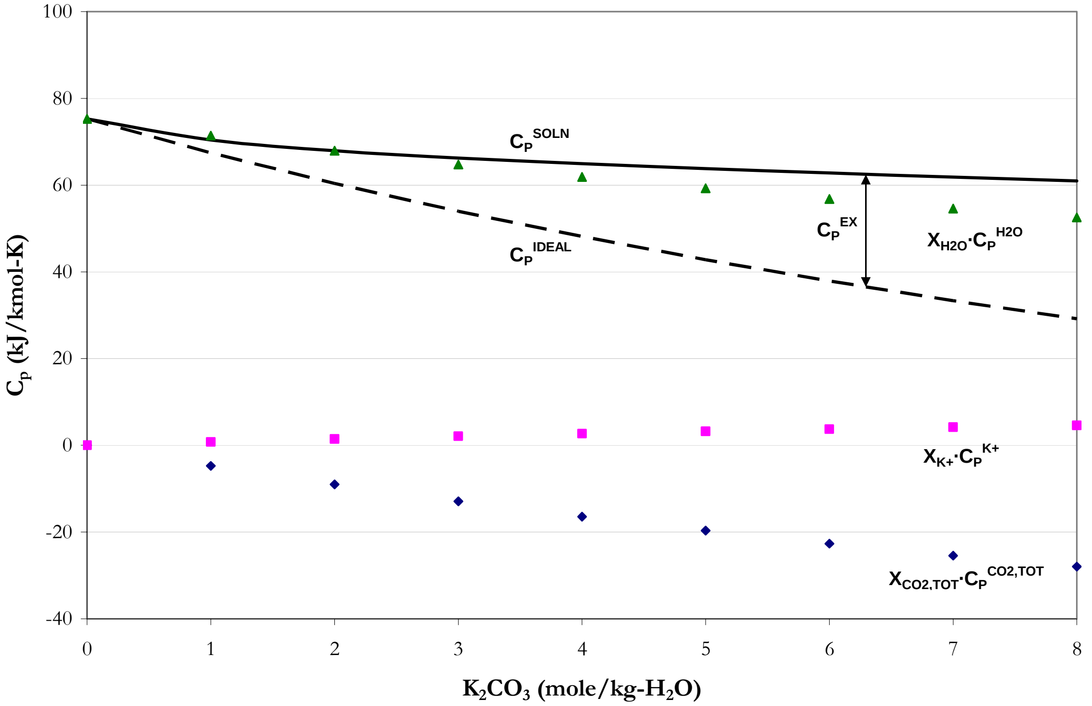

Figure 12.8-6. Comparison of the Molar Heat Capacity Predictions for H_2O-K_2CO_3 Mixtures at 40 °C from the elecNRTL Model to the Ideal Molar Heat Capacity based on the Constituent Components.

The molar heat capacity of the solution can be described by the following equation:

$$C_p = x_{H_2O}C_p^{*,l} + x_{K^+}C_p^{\infty,aq} + x_{CO_2}C_p^{\infty,aq} + x_{CO_3^{-2}}C_p^{\infty,aq} + x_{HCO_3^{-1}}C_p^{\infty,aq} + C_p^{Ex} \qquad 12\text{-}37$$

where

$$x_{CO_2TOT}C_p^{CO_2TOT} = x_{CO_2}C_p^{\infty,aq} + x_{CO_3^{-2}}C_p^{\infty,aq} + x_{HCO_3^{-1}}C_p^{\infty,aq} \qquad 12\text{-}38$$

$$x_{K_2CO_3}C_p^{K_2CO_3} = x_{K^+}C_p^{\infty,aq} + x_{CO_2TOT}C_p^{CO_2TOT} \qquad 12\text{-}39$$

and simplifying Equation 12-37 yields,

$$C_p = x_{H_2O}C_p^{*,l} + x_{K_2CO_3}C_p^{K_2CO_3} + C_p^{Ex} \qquad 12\text{-}40$$

We can now determine a criterion for estimating the solution molar heat capacity by the weighted molar heat capacity of water given by the following function.

$$\frac{C_p - x_{H_2O} C_p^{*,l}}{x_{K_2CO_3}} = C_p^{K_2CO_3} + \frac{C_p^{Ex}}{x_{K_2CO_3}} \qquad 12\text{-}41$$

When the order of magnitude of Equation 12-41 is equivalent to the magnitude of the molar heat capacity of water, our first order estimation will no longer be adequate (~6 m K_2CO_3) to estimate the molar heat capacity of the solution as shown by Figure 12.8-7.

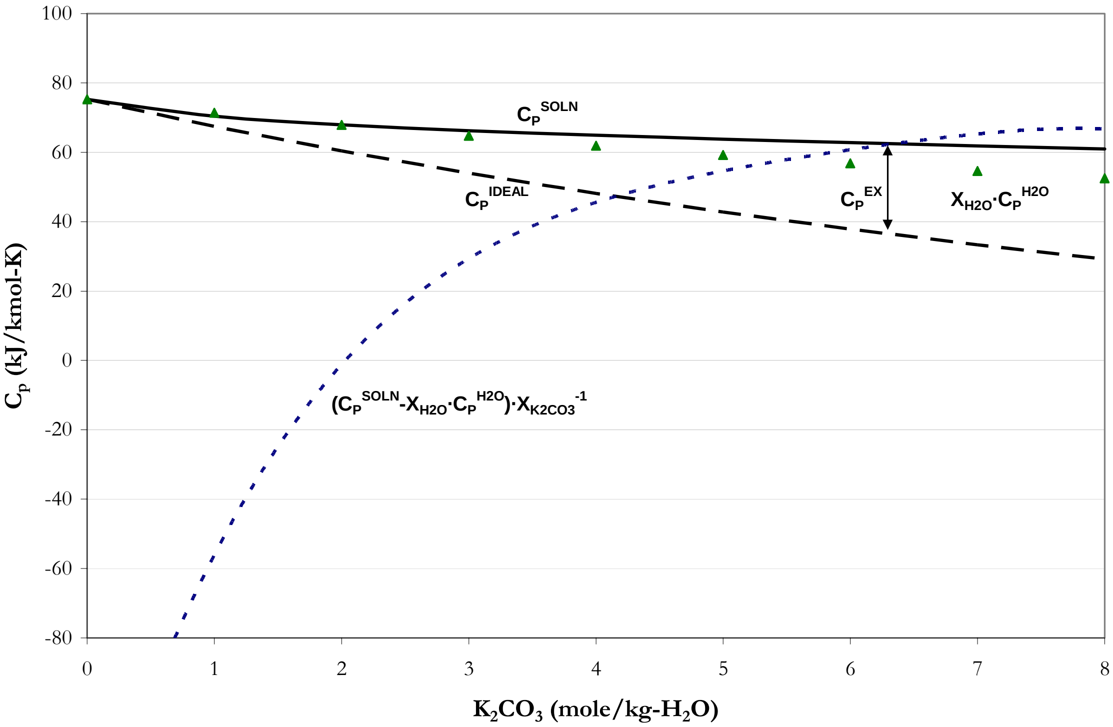

Figure 12.8-7. Comparison of the Molar Heat Capacity Predictions for H_2O-K_2CO_3 Mixtures at 40 °C from the elecNRTL Model to the Ideal Molar Heat Capacity based on the Constituent Components and Equation 12-41.

A similar methodology can describe mixtures of H_2O-$KHCO_3$ as

$$\frac{C_p - x_{H_2O} C_p^{*,l}}{x_{KHCO_3}} = C_p^{KHCO_3} + \frac{C_p^{Ex}}{x_{KHCO_3}} \qquad 12\text{-}42$$

Similarly, since the order of magnitude of Equation 12-42 is equivalent to the magnitude of the molar heat capacity of water, our first order estimation will no longer be adequate to estimate the molar heat capacity of the solution as shown by Figure 12.8-8 and Figure 12.8-9. In this case, the weighted molar heat capacity of water can adequately describe the molar heat capacity of H_2O-$KHCO_3$ mixtures over the entire range of concentrations used in this work.

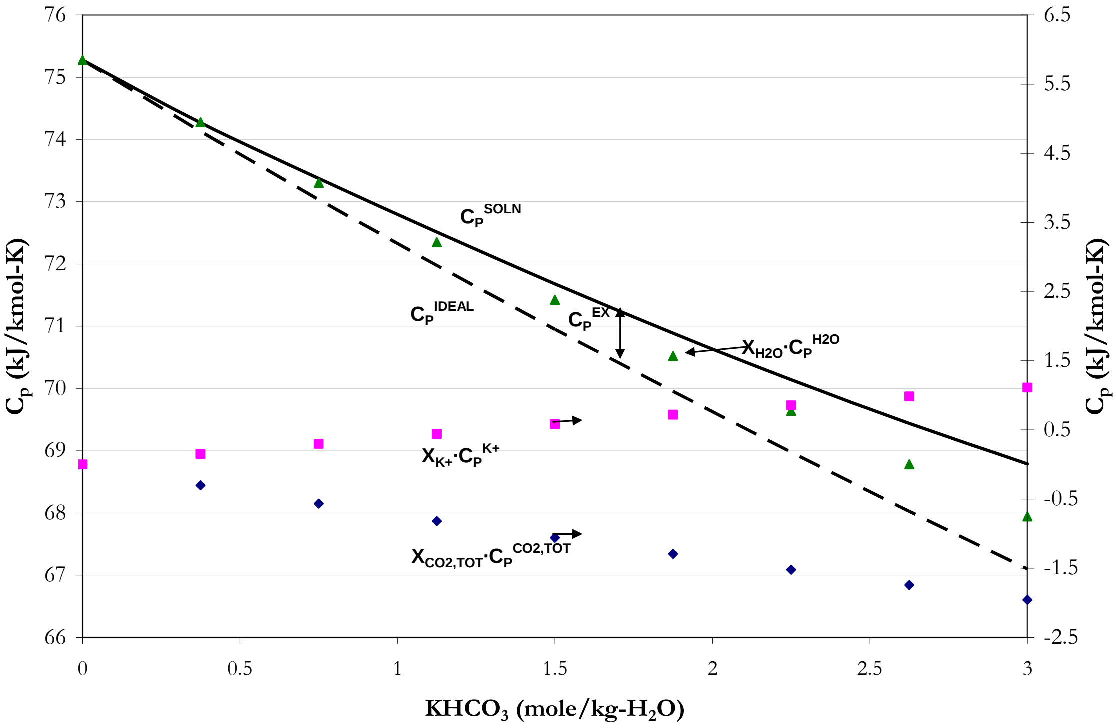

Figure 12.8-8. Comparison of the Molar Heat Capacity Predictions for H_2O-$KHCO_3$ mixtures at 40 °C from the elecNRTL Model to the Ideal Molar Heat Capacity based on the Constituent Components.

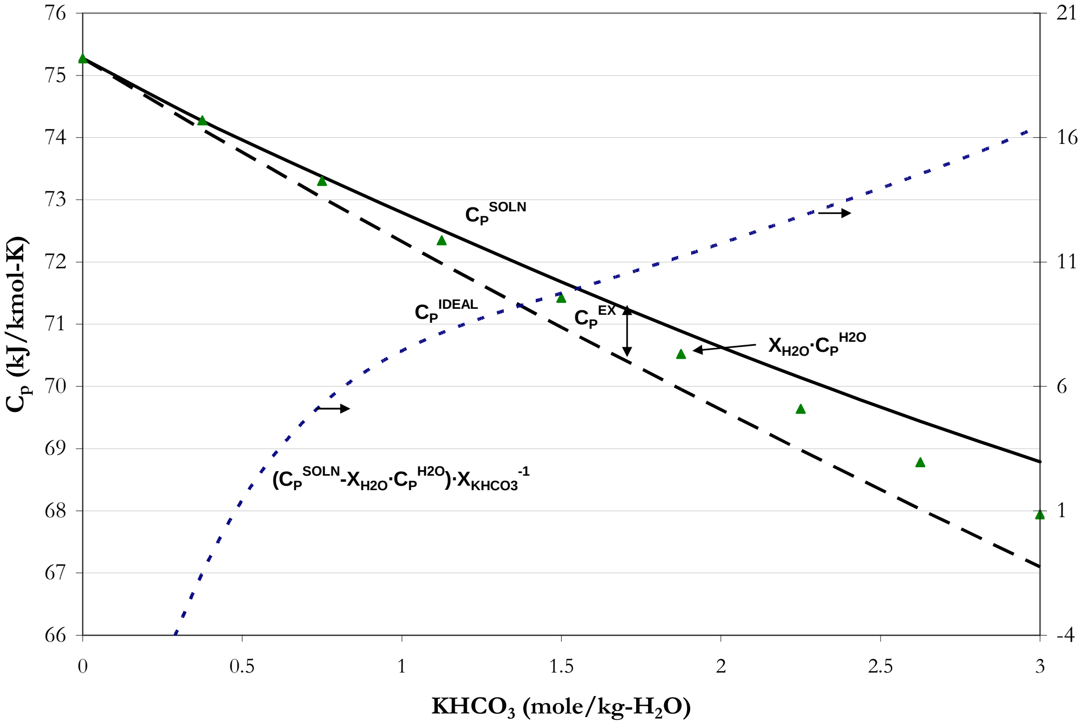

Figure 12.8-9. Comparison of the Molar Heat Capacity Predictions for H_2O-$KHCO_3$ Mixtures at 40 °C from the elecNRTL Model to the Ideal Molar Heat Capacity based on the Constituent Components and Equation 12-42.

12.8.4 *CO_2 Solubility*

Figure 12.8-10, Figure 12.8-12, and Figure 12.8-14 give the results of fit for the experimental CO_2 Solubility at 20, 30 and 40 wt % equivalent concentration of K_2CO_3 per loading squared versus the solution loading from 40 – 175 °C. This type of representation is analogous to a semi-log plot, where small deviations are exaggerated. Overall, the optimum model adequately describes the CO_2 solubility data at 20, 30 and 40 wt % equivalent concentration of K_2CO_3 within an average absolute relative error of ± 10.8 percent.

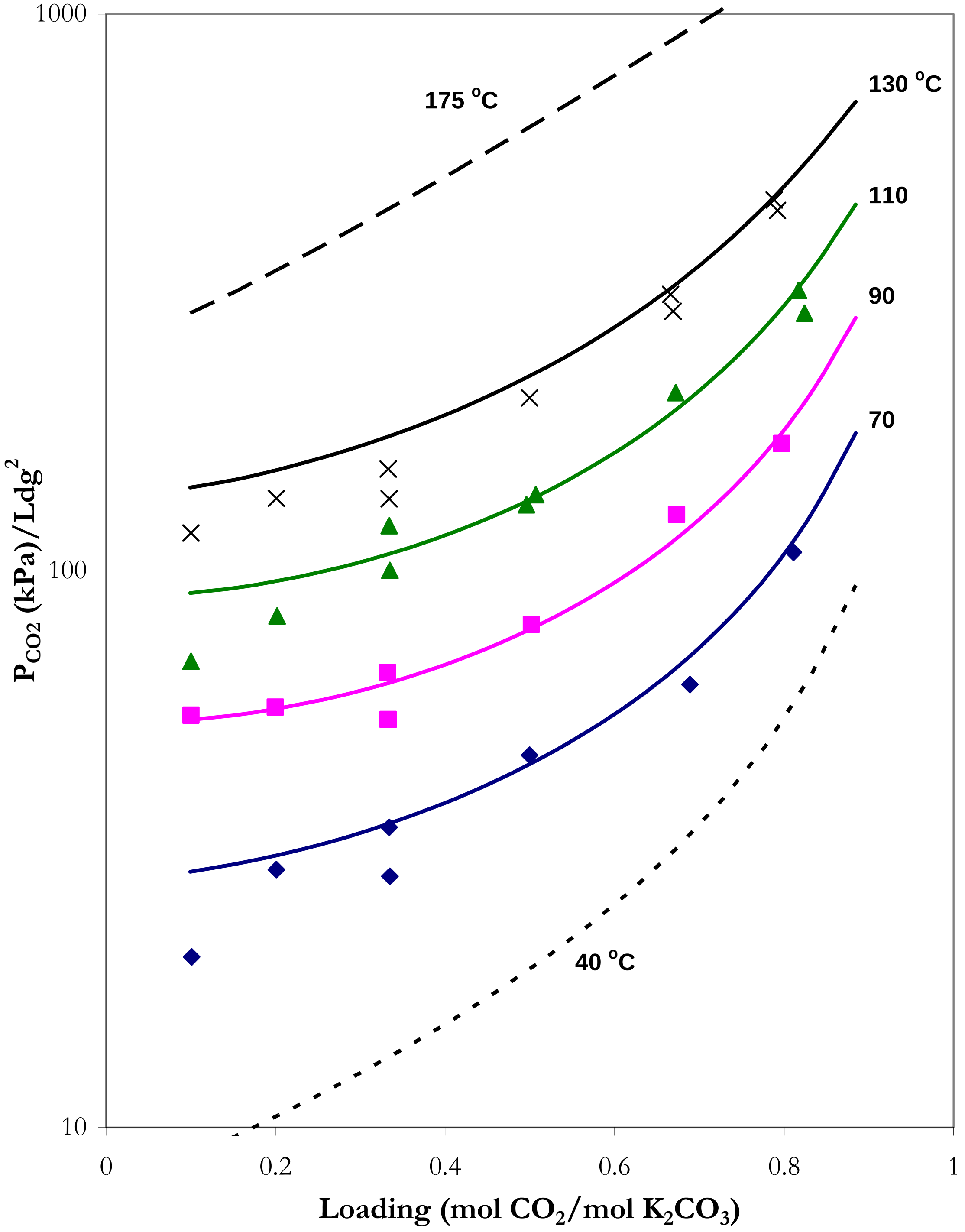

Figure 12.8-10. **Exaggerated CO_2 Solubility in a 20 wt % Equivalent Concentration of Aqueous K_2CO_3.**

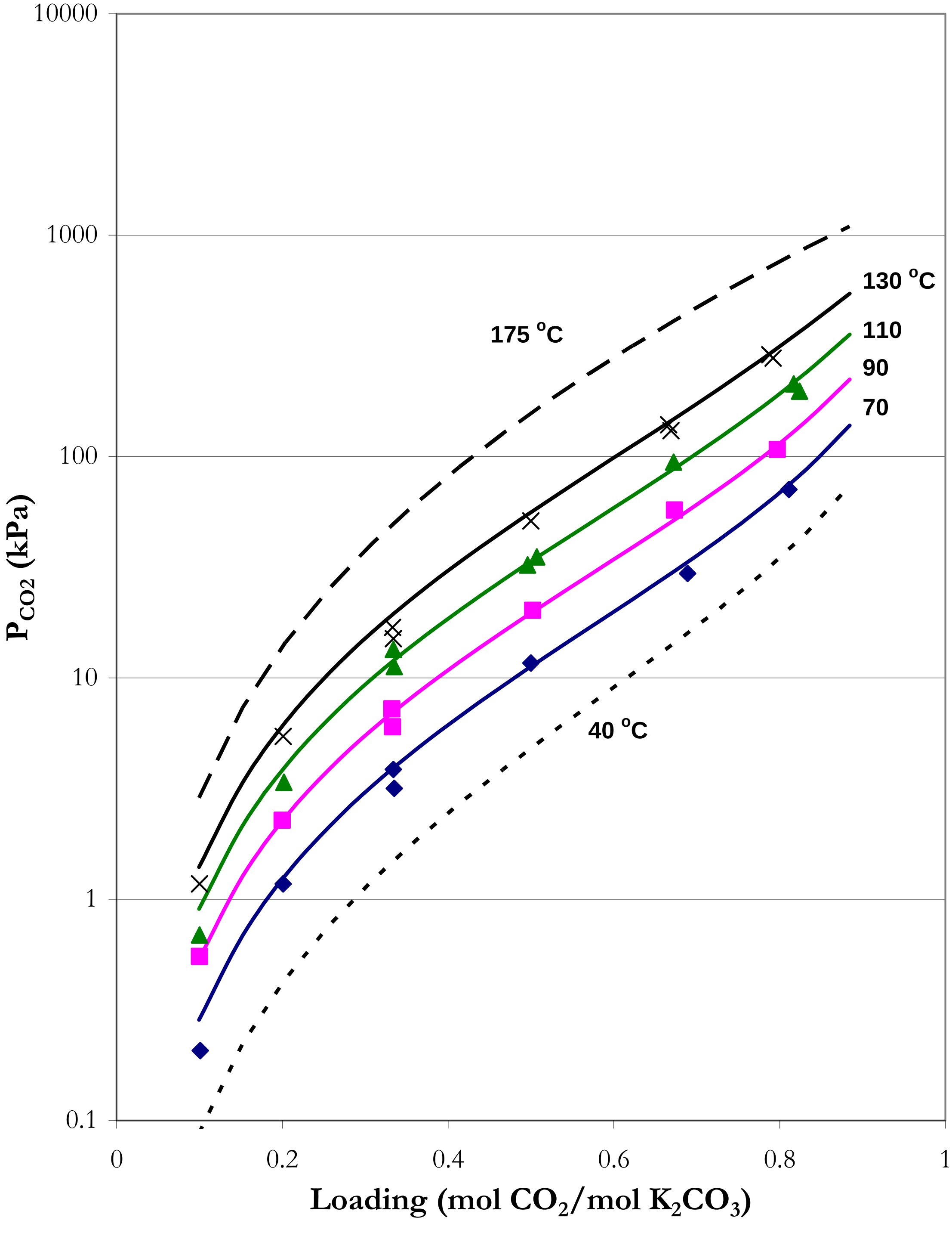

Figure 12.8-11. CO_2 Solubility in a 20 wt % Equivalent Concentration of Aqueous K_2CO_3.

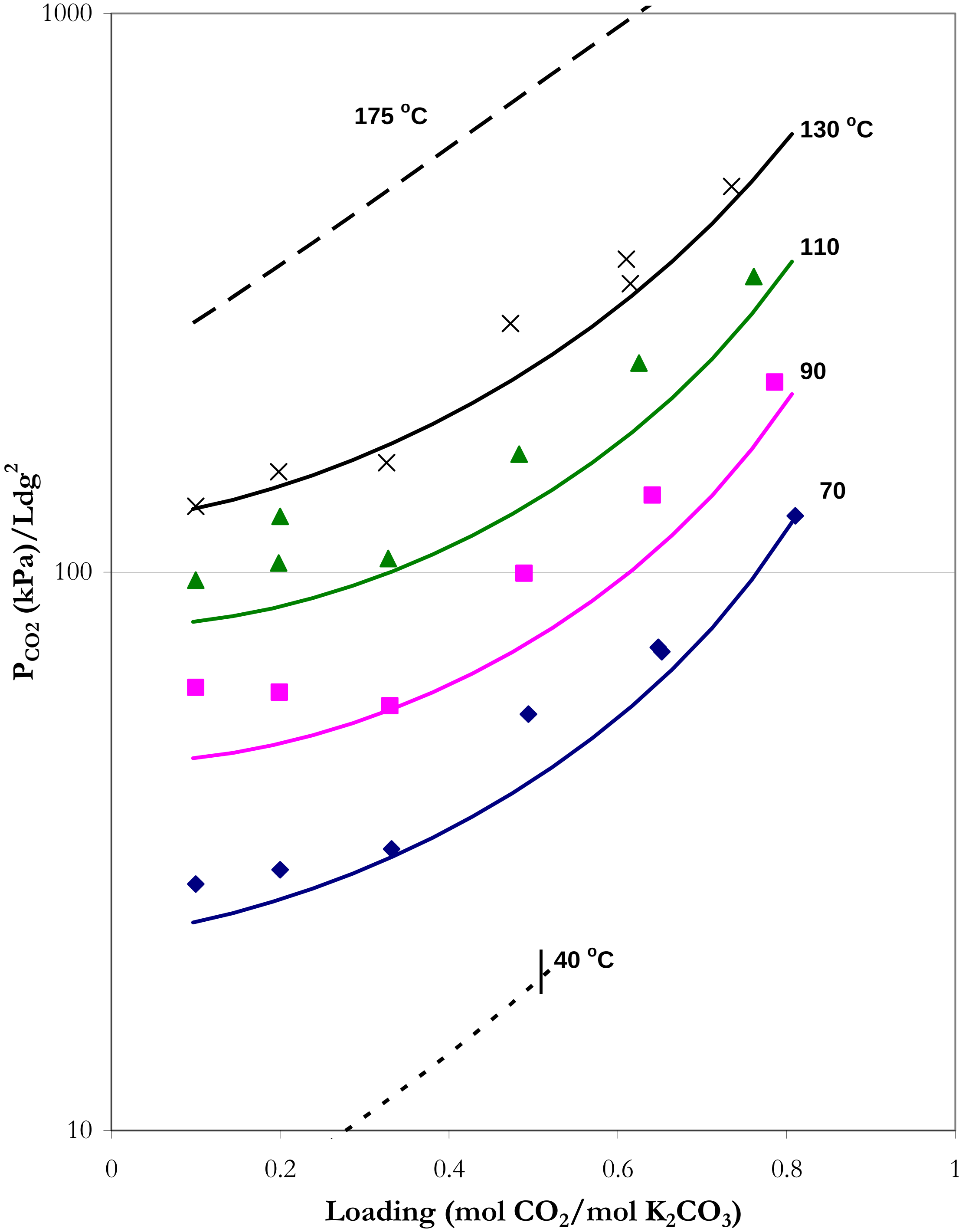

Figure 12.8-12. Exaggerated CO_2 Solubility in a 30 wt % Equivalent Concentration of Aqueous K_2CO_3. Vertical bar: Saturation Limit of the Solution.

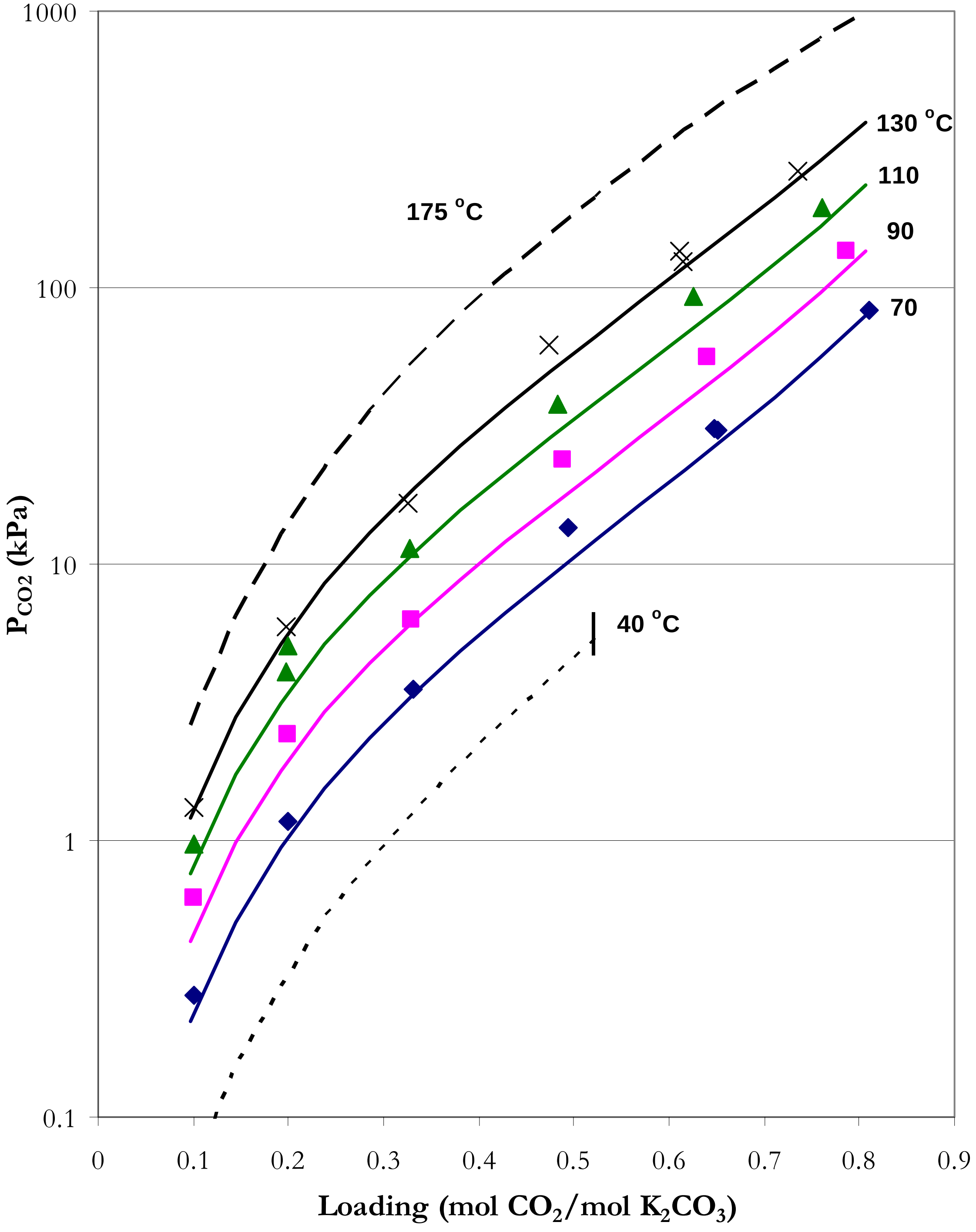

Figure 12.8-13. CO_2 Solubility in a 30 wt % Equivalent Concentration of Aqueous K_2CO_3. Vertical bar: Saturation Limit of the Solution.

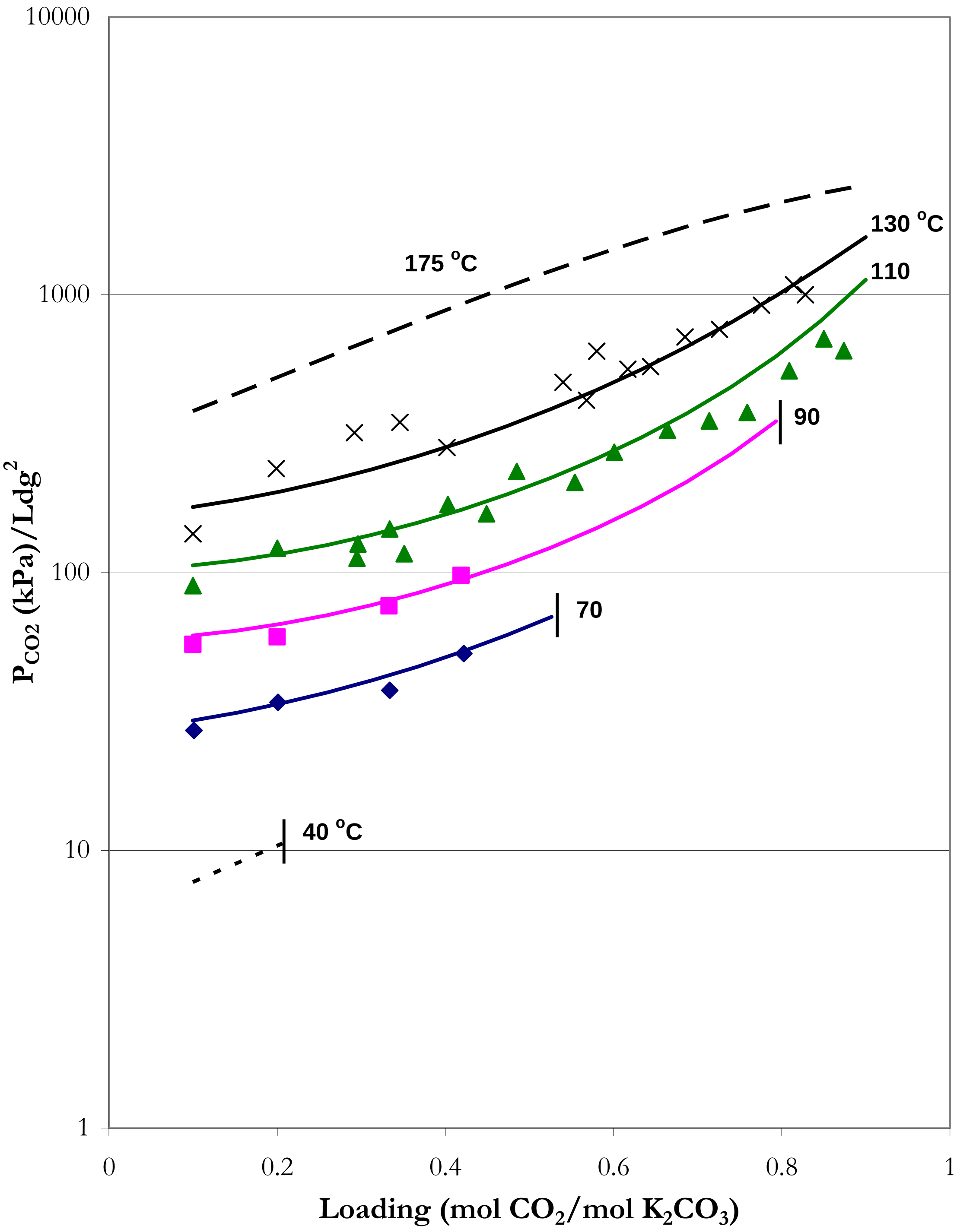

Figure 12.8-14. Exaggerated CO_2 Solubility in a 40 wt % Equivalent Concentration of Aqueous K_2CO_3. Vertical bars: Saturation Limit of the Solution.

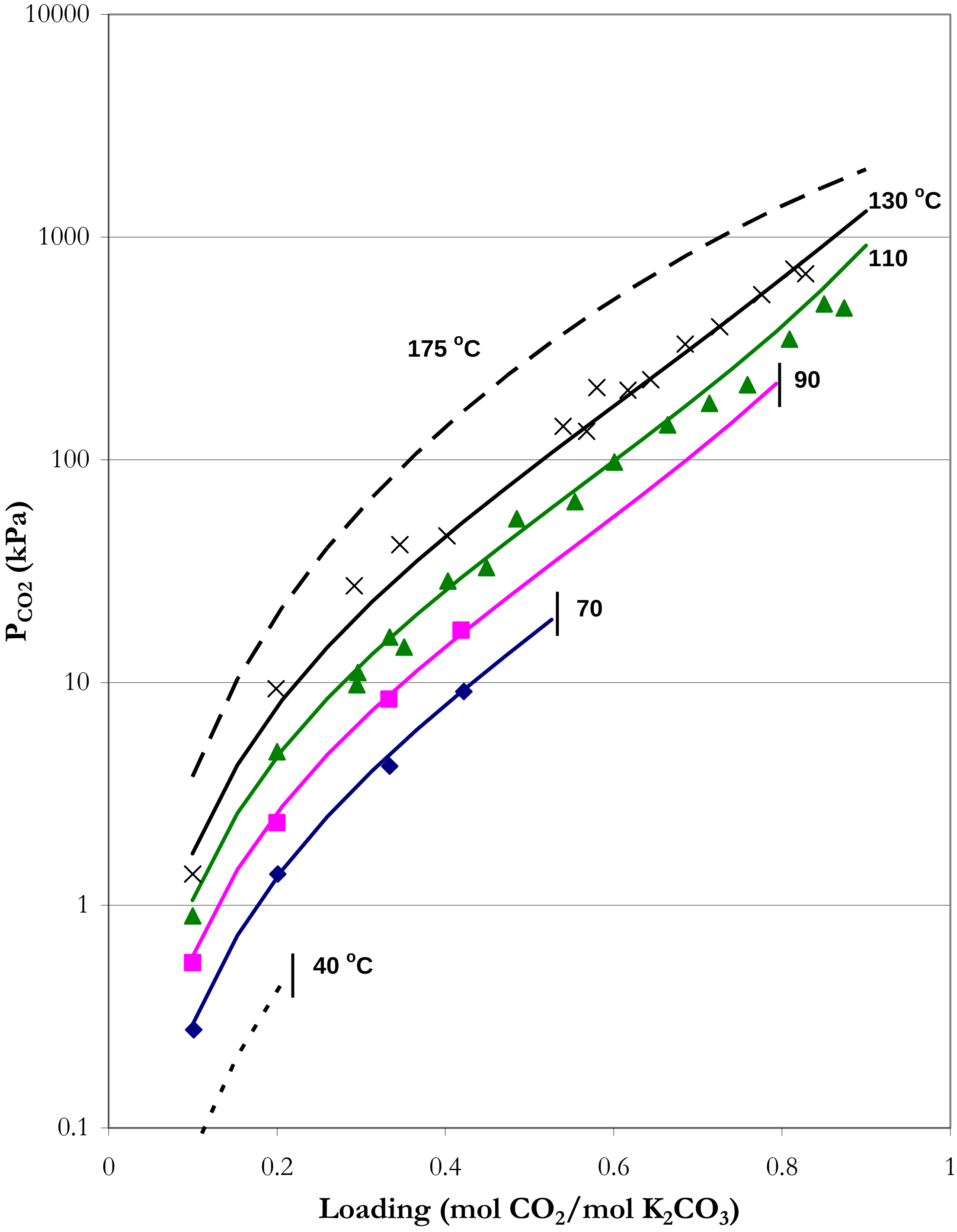

Figure 12.8-15. CO_2 Solubility in a 40 wt % Equivalent Concentration of Aqueous K_2CO_3. Vertical bar: Saturation Limit of the Solution.

Recently, Pérez-Salado Kamps et al. (2007) reported interaction parameters based on a Pitzer's molality scale based equation for the Gibbs excess energy of the aqueous phase through simultaneous regression of similar VLE and SLE data, but chose not to include calorimetry effects into their model. Predictions for CO_2 solubility data from Tosh et al. (1959) were reported with an average absolute relative deviation of ± 12.2 %. In this work, we were able to increase the amount of literature data and predict CO_2 solubility data from Tosh et al. (1959) within average absolute relative deviation of ± 10.8 %. Thus, we feel predictions from our optimum model will provide the most realistic values to date.

In this work, we have concentrated our efforts to describe CO_2 solubility below a loading (mol CO_2/mol K_2CO_3) equal to one. Below a solution loading of one, carbon dioxide is more or less converted to bicarbonate resulting in a negligible amount of free CO_2 in solution. Predictions above a solution loading of one should be perceived as an extrapolation by the optimum model beyond the bounds of the regression data. In future work, we would recommend extending the model beyond a CO_2 loading equal to one. Parameters describing the interactions between CO_2 and electrolytes, specifically interactions for $CO_2/K^+,HCO_3$, and $K^+,HCO_3/CO_2$, would need to be included in the final model to account for physical absorption of CO_2 into the aqueous phase.

12.8.5 *Solid Solubility*

In this work, we have compiled a database to describe experimental solid solubility data for precipitating salts vis-à-vis hydrated potassium carbonate and potassium bicarbonate. We chose not to describe the precipitation of the hydrated double salt

($K_2CO_3{\cdot}2KHCO_3{\cdot}1.5H_2O$,) because conditions where $K_2CO_3{\cdot}2KHCO_3{\cdot}1.5H_2O$ would precipitate from an aqueous solution are well beyond the salt concentrations of interest in connection with carbon capture processes and its modifications. We have included coefficients for the salt precipitation equilibrium reaction, Equation 12-27, based on solid solubility data of Hill (1930) and Lyudkovskaya et al. (1955) from optimum model predictions for the chemical equilibrium salt precipitation reaction for inclusion by the end user as shown in Table 12.8-1.

Table 12.8-1. Chemical Equilibrium Coefficients for the Salt Precipitation of $K_2CO_3{\cdot}2KHCO_3{\cdot}1.5H_2O$ Based on Equation 14-27 (mole fraction basis).

Equation #	A	B	C	D
14-27	-1530.94	63429.08	227.1714	0.0

$\ln K = A + B/T(K) + C{\cdot}\ln T(K) + D{\cdot}T(K)$

Figure 12.8-16 and Figure 12.8-17 gives the results for the calculated chemical equilibrium salt precipitation reaction for hydrated K_2CO_3 and $KHCO_3$ as compared to Aspen Plus^{TM} default values and Pérez-Salado Kamps et al. (2007).

Figure 12.8-16 and Figure 12.8-17 illustrates an important point: even though each author successfully regressed solid solubility data for each system, predictions for the calculated chemical equilibrium salt precipitation reaction are different. This discrepancy is due to the thermodynamic foundations for each model. Each model would describe the activity coefficients of potassium, carbonate, and bicarbonate ions differently based on the regression methodology employed, the type of thermodynamic model used, and the types of thermodynamic data used in the regression. To illustrate this point, predictions for the chemical equilibrium salt precipitation reaction for $KHCO_3$ based on sequential model predictions for the activity product of potassium and bicarbonate was inversed even though the model adequately predicted VLE and calorimetric data.

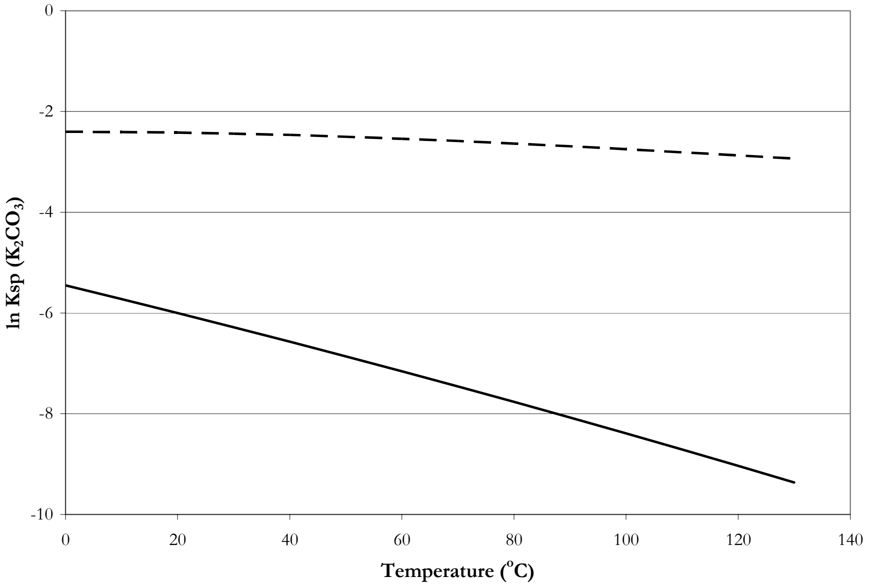

Figure 12.8-16. Comparison of the Chemical Equilibrium Salt Precipitation Reaction for Hydrated K_2CO_3. Lines: ▬, elecNRTL Model, — —, Aspen Plus™ Default Values.

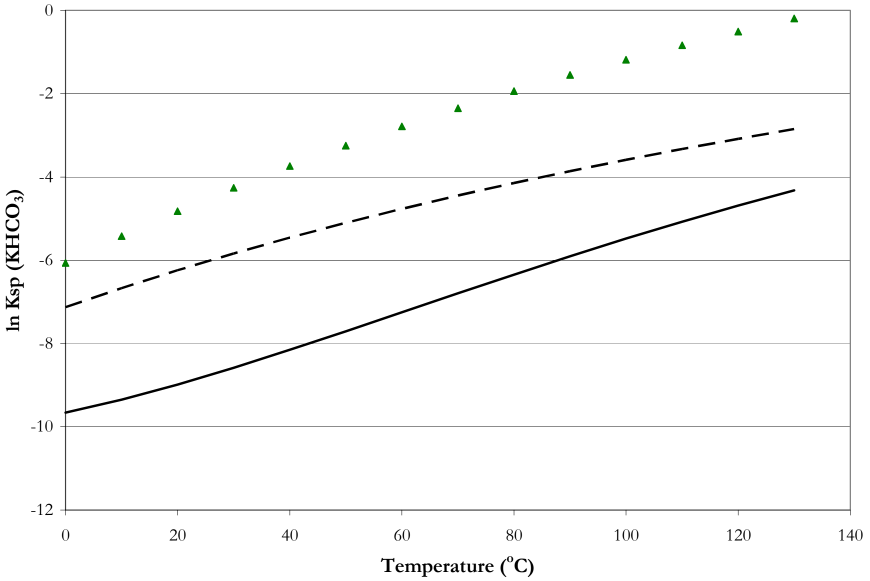

Figure 12.8-17. Comparison of the Chemical Equilibrium Salt Precipitation Reaction for Hydrated $KHCO_3$. Points: ▲, Pérez-Salado Kamps et al. (2007). Lines: ▬, elecNRTL Model, — —, Aspen Plus™ Default Values.

In terms of solubility data, Figure 12.8-18 and Figure 12.8-19 give predictions for solid solubility for the binary systems (H_2O-K_2CO_3 and H_2O-$KHCO_3$) based on literature from Linke and Seidell (1965) and Moore et al. (1997) for hydrated K_2CO_3 and Linke and Seidell (1965) for $KHCO_3$.

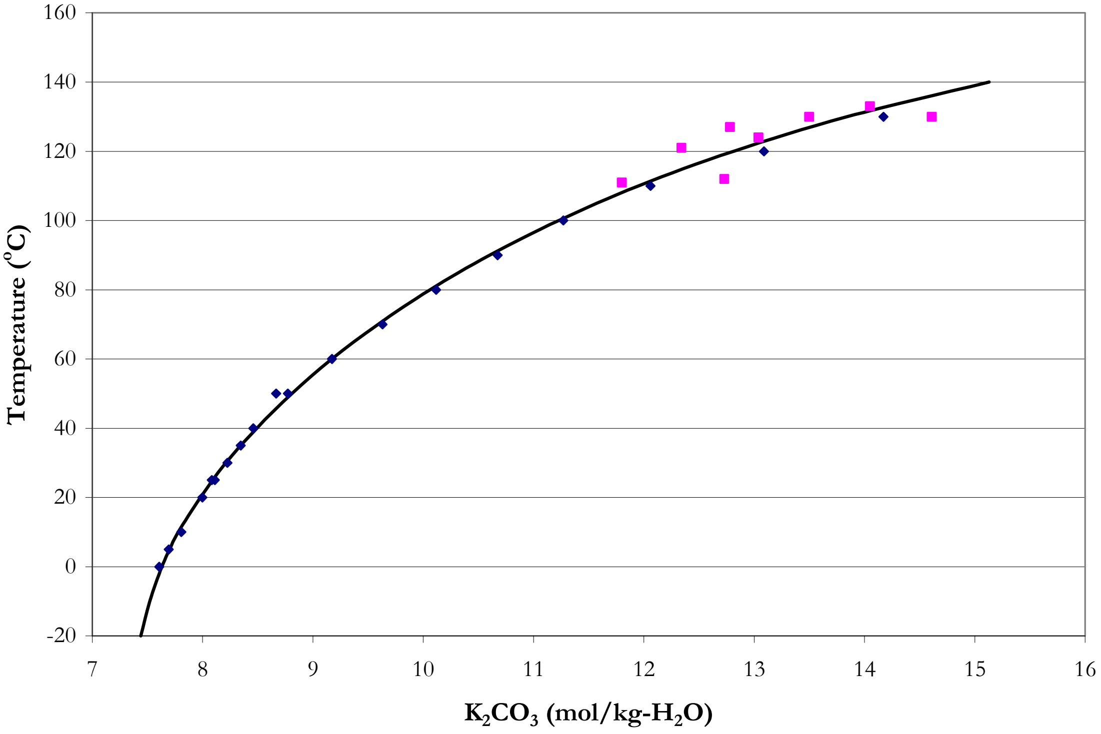

Figure 12.8-18. Solubility Product of Hydrated Potassium Carbonate in Water. Points: ◆, Linke and Seidell (1965), ■, Moore et al. (1997). Lines: —, elecNRTL Model Predictions.

Predictions for solid solubility of $KHCO_3$ for the ternary system (H_2O-K_2CO_3-$KHCO_3$) based on literature from Linke and Seidell (1965) is shown in Figure 12.8-20 in terms of the saturation temperature deviation.

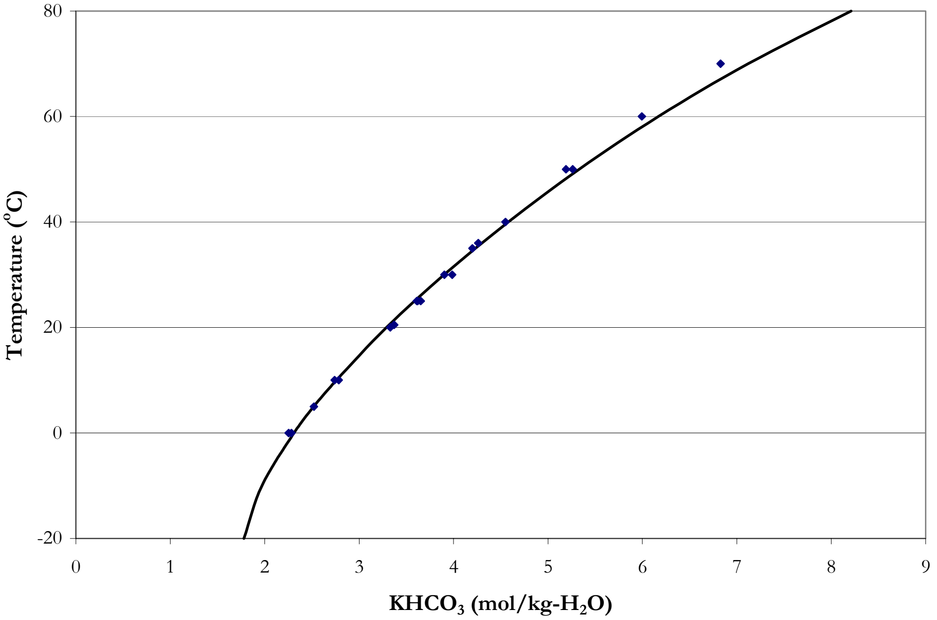

Figure 12.8-19. Solubility Product of Potassium Bicarbonate in Water. Points: ◆, Linke and Seidell (1965). Lines: ▬, elecNRTL Model Predictions.

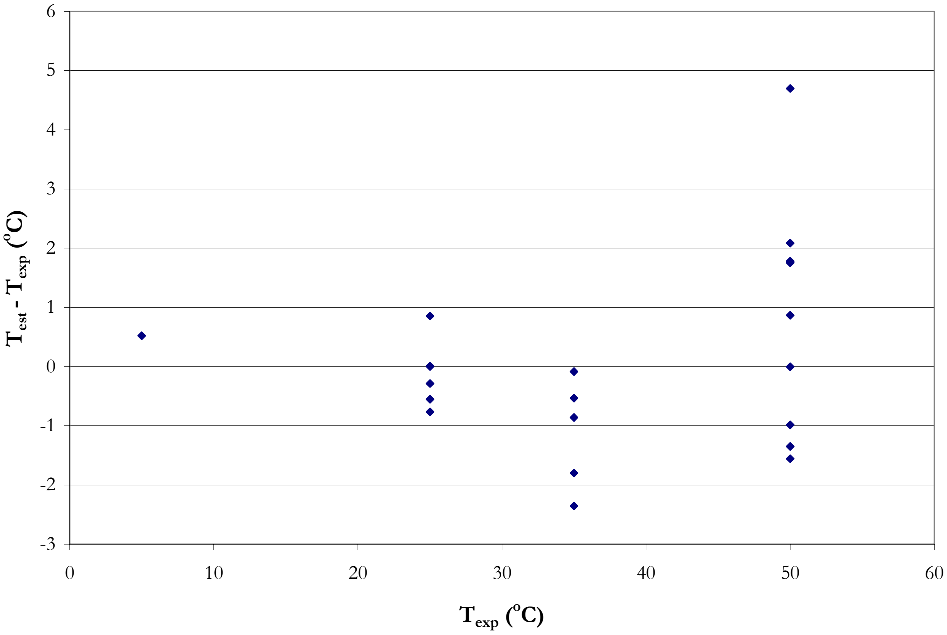

Figure 12.8-20. Solubility Product of Potassium Bicarbonate in Water-Potassium Carbonate-Potassium Bicarbonate. Points: ◆, Linke and Seidell (1965). Lines: ▬, elecNRTL Model Predictions.

Over the entire range of conditions for the H_2O-K_2CO_3-$KHCO_3$ system, the average absolute deviation between the experimental and estimated solubility temperature is within ± 1.13 °C.

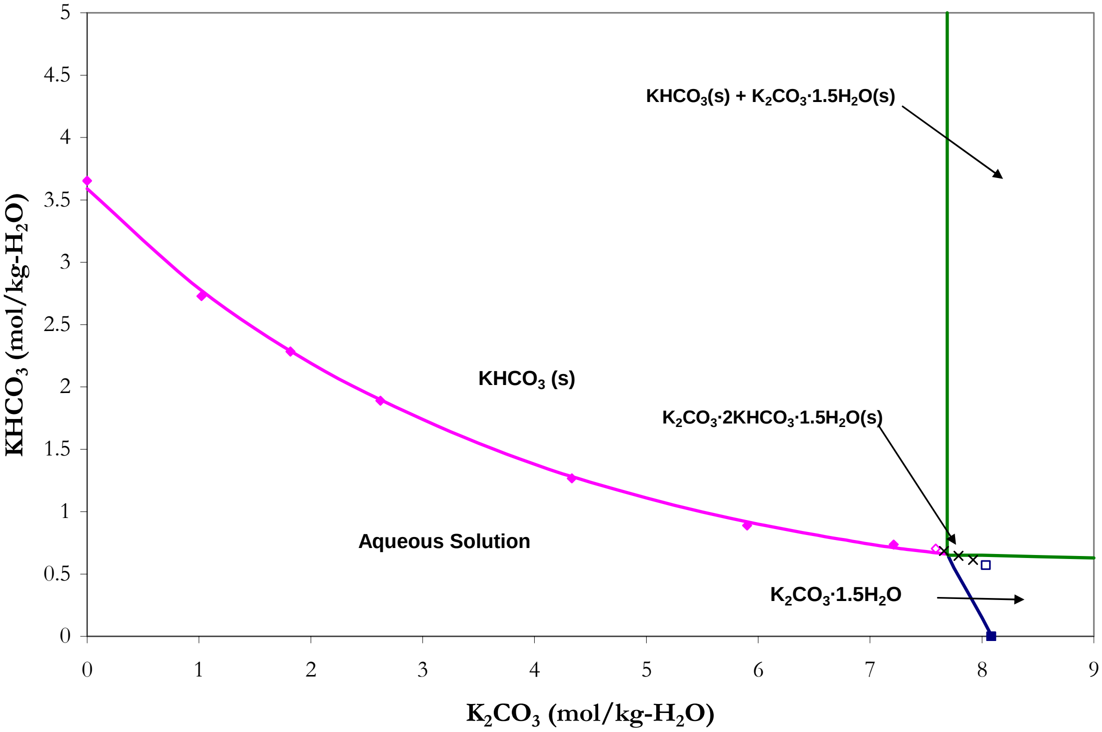

Figure 12.8-21. Isothermal Phase Diagram at 25 °C for the Formation of Hydrated K_2CO_3, $KHCO_3$, and Predictions for the Formation of Hydrated K_2CO_3+$KHCO_3$. Solid Points: Linke and Seidell (1965). Open Points: Hill (1930).

For two solid solutes + water, there are many possible types of phase behavior that may be encountered. In this work, we chose not to describe the hydrated double salt formation ($K_2CO_3 \cdot 2KHCO_3 \cdot 1.5H_2O$,) even though the model does predict the formation of two dissolved solutes in solution. Construction of isothermal phase diagrams at 25, 50, 75 and 100 °C are shown in Figure 12.8-21, Figure 12.8-22, and Figure 12.8-23, respectively. At

25 and 50 °C, literature data for the formation of the hydrated double salt from Hill (1930) and Lyudkovskaya et al. (1955) are shown as "×," the formation of the hydrated double salt + $KHCO_3$ are shown as "◊," and the formation of the hydrated double salt + hydrated K_2CO_3 are shown as "□." The optimum model does fail to capture of temperature dependence of the hydrated double salt formation at 50 °C, but the model does an adequate representation of capturing the formation effects at 25 °C.

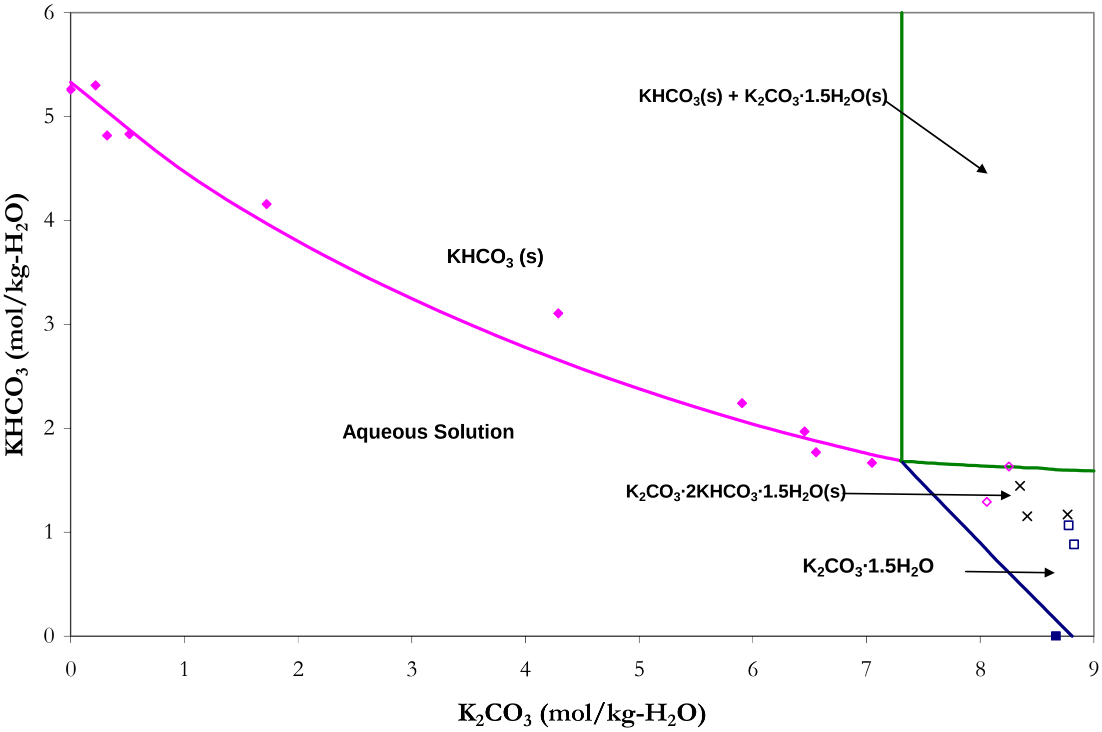

Figure 12.8-22. Isothermal Phase Diagram at 50 °C for the Formation of Hydrated K_2CO_3, $KHCO_3$, and Predictions for the Formation of Hydrated K_2CO_3+$KHCO_3$. Solid Points: Linke and Seidell (1965). Open Points: Lyudkovskaya et al. (1955).

The intersection of the four curves is a triple point, representing the temperature at which hydrated potassium carbonate and potassium bicarbonate can coexist in stable equilibrium. Each triple point corresponds to a slurry containing $K_2CO_3 \cdot 1.5H_2O$ + $KHCO_3$.

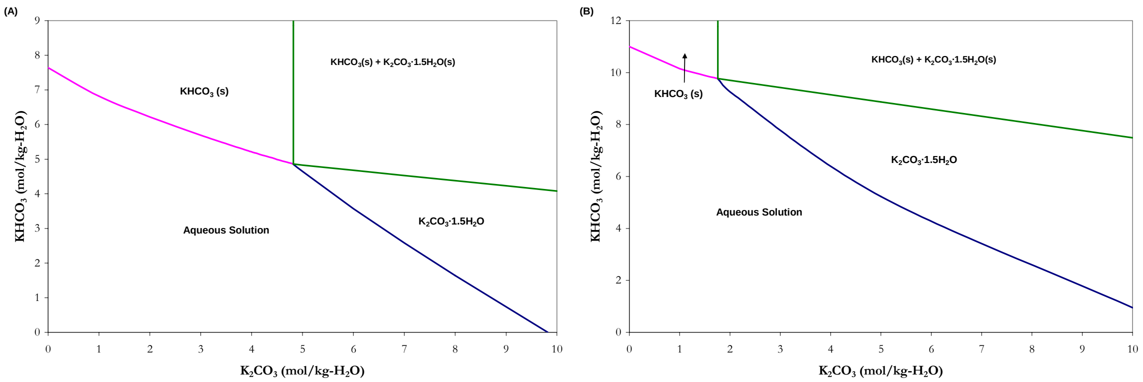

Figure 12.8-23. Isothermal Phase Diagram at 75 °C (A) and 100 °C (B) for the Formation of Hydrated K_2CO_3, $KHCO_3$, and Predictions for the Formation of Hydrated K_2CO_3+$KHCO_3$.

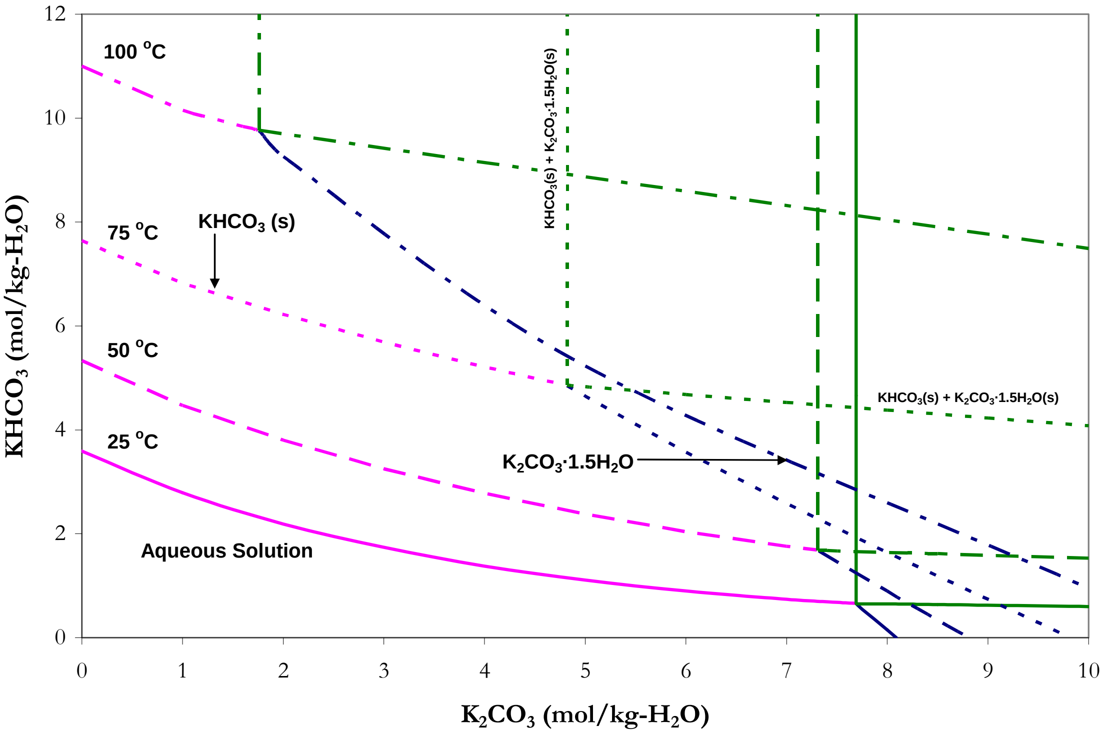

Figure 12.8-24. Isothermal Overlay Phase Diagram at 25, 50, 75, and 100 °C for the Formation of Hydrated K_2CO_3, $KHCO_3$, and Predictions for the Formation of Hydrated K_2CO_3+$KHCO_3$.

The CO_2 solubility over a saturated solution of $K_2CO_3 \cdot 1.5H_2O$ + $KHCO_3$ can be predicted from the optimum model as shown in Figure 12.8-25. Figure 12.8-26 illustrates the partial pressure of CO_2 divided by loading squared versus the solution loading from 25 – 100 °C. This type of representation is analogous to a simi-log plot, where small deviations are exaggerated. A vertical bar designates the triple point at each temperature.

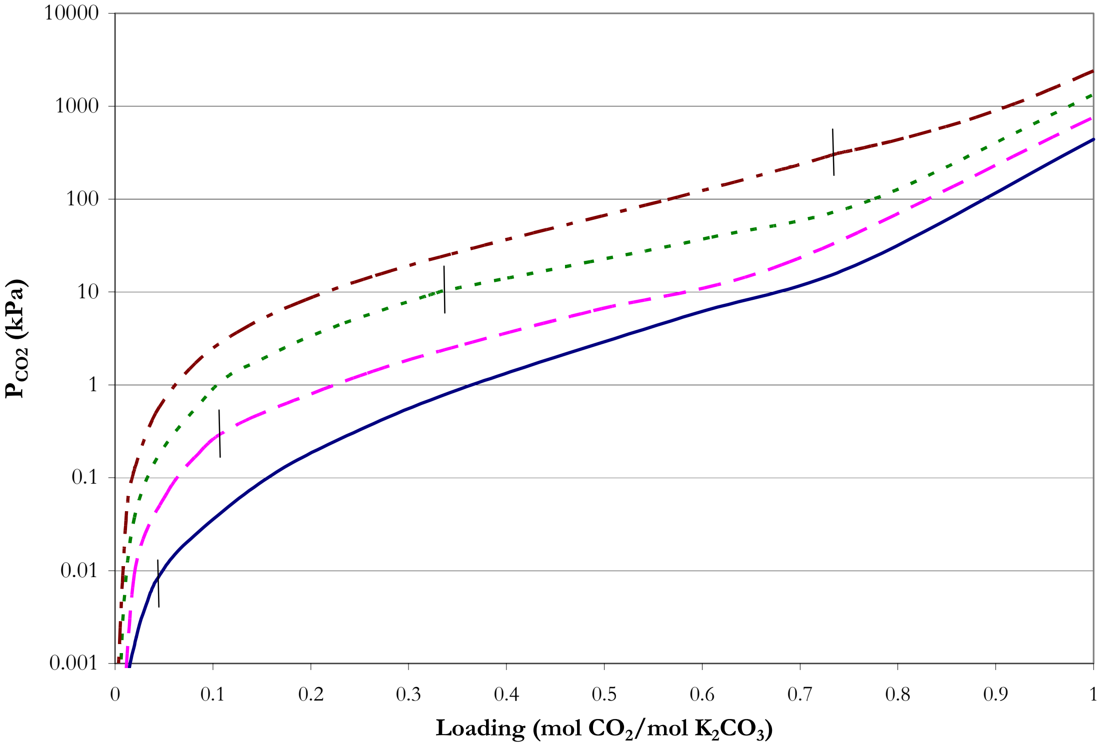

Figure 12.8-25. Partial Pressure of CO_2 over a Saturated Solution of Hydrated K_2CO_3 and $KHCO_3$ from 25 to 100 °C. Lines: ━, 25 °C, — —, 50 °C, - - -, 75 °C, — · —, 100 °C.

Figure 12.8-26 exaggerated the discontinuity between precipitation of hydrated K_2CO_3, which occurs to the left of the vertical bar, and precipitation of $KHCO_3$, which occurs to the right of the vertical bar.

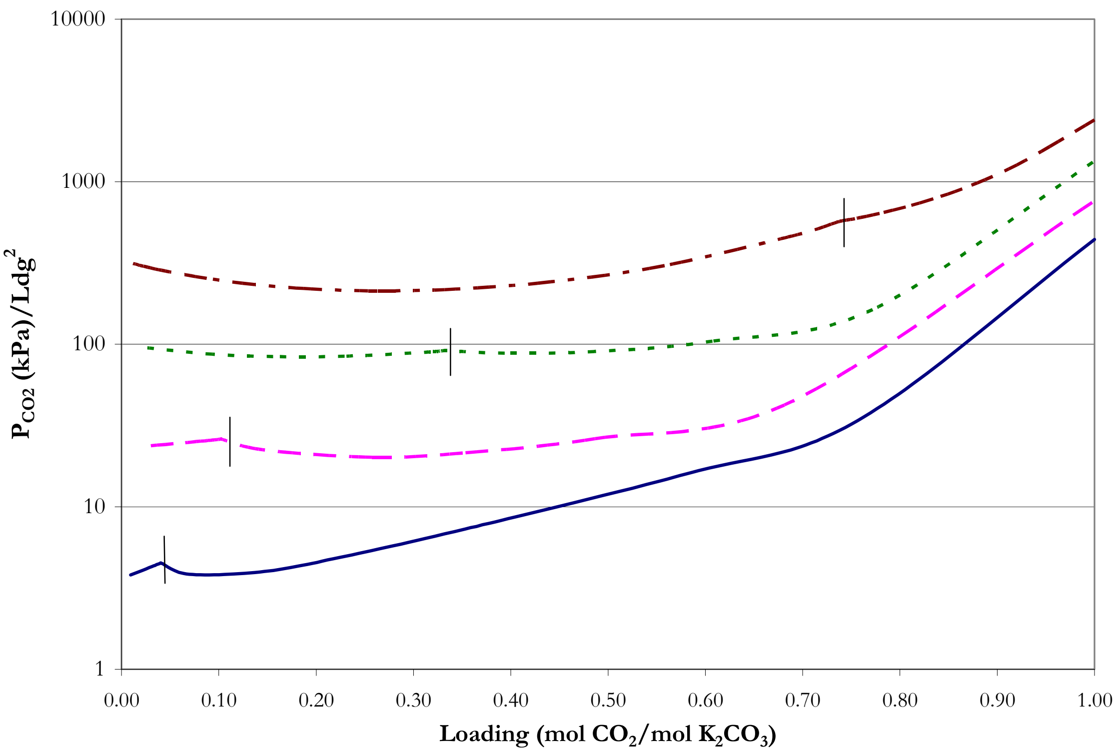

Figure 12.8-26. Exaggerated Partial Pressure of CO_2 over a Saturated Solution of Hydrated K_2CO_3 and $KHCO_3$ from 25 to 100 °C. Lines: ▬, 25 °C, – – –, 50 °C, - - -, 75 °C, —·—, 100 °C

To illustrate thermal effects of the solution at the triple point, we can describe the partial pressure of CO_2 at the triple point versus reciprocal absolute temperature (as shown in Figure 12.8-27) based on the following linear function:

$$\ln P_{CO_2} = -463.7 + \frac{9208}{T(K)} + 75.10 \ln T(K) \qquad 12\text{-}43$$

By employing the Gibbs-Helmholtz equation, we can determine the enthalpy of CO_2 absorption in a slurry of hydrated K_2CO_3 and $KHCO_3$ based on the vapor phase fugacity of CO_2 as shown by Equation 12-44.

$$-\frac{\Delta H_{abs}}{R} = \left(\frac{d\, f_{CO_2}}{d(1/T)}\right)_{x_{CO_2}} \qquad 12\text{-}44$$

Where

f_{CO_2} is the vapor phase fugacity of CO_2, $f_{CO_2} = \phi_{CO_2} P_{CO_2}$,

ϕ_{CO_2} is the vapor phase fugacity coefficient of CO_2.

We can approximate the vapor phase fugacity of CO_2 by taking the derivative of the partial pressure of CO_2.

$$-\frac{\Delta H_{abs}}{R} \approx \left(\frac{d\ P_{CO_2}}{d\left(1/T\right)} \right)_{x_{CO_2}} \qquad 12\text{-}45$$

Substituting Equation 12-43 in Equation 12-45 and evaluating the derivative gives the following relationship for the enthalpy of CO_2 absorption in a slurry of hydrated K_2CO_3 and $KHCO_3$.

$$-\frac{\Delta H_{abs}}{R} \approx \left(\frac{d\ P_{CO_2}}{d\left(1/T\right)} \right)_{x_{CO_2}} = 9208 - 75.10T\left(K\right) \qquad 12\text{-}46$$

Over absorber and stripper conditions, the enthalpy of CO_2 absorption (kcal/mol-CO_2) in a slurry of hydrated K_2CO_3 and $KHCO_3$ is given in Table 12.8-2.

Table 12.8-2. Enthalpy of CO_2 Absorption in a Slurry of Hydrated K_2CO_3 and $KHCO_3$ (kcal/mol-CO_2).

Temperature (°C)	ΔH_{abs}
40	-28.43
80	-34.40
120	-40.37

In comparison, the latent heat of steam required to regenerate the solvent in an aqueous H_2O-K_2CO_3–CO_2 capture process is approximately -50 kcal/mol-CO_2.

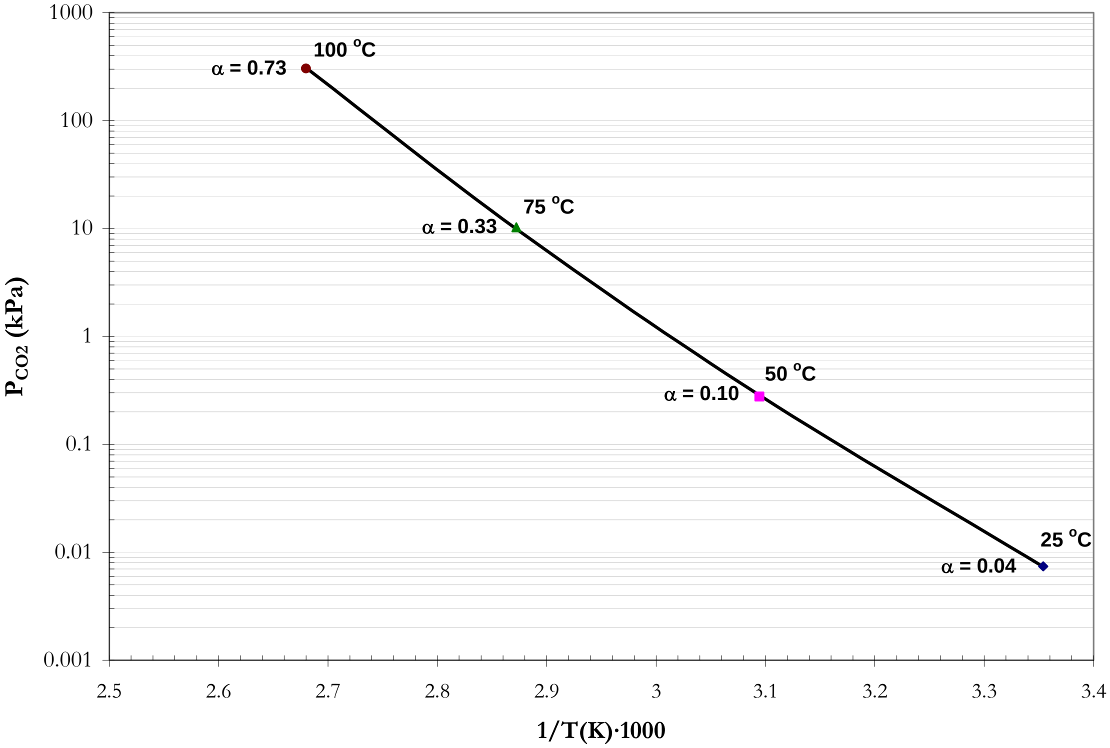

Figure 12.8-27. Partial Pressure of CO_2 at the Triple Point versus Reciprocal Absolute Temperature. Line: Equation 12-43.

12.8.6 *Total Pressure Predictions for H_2O-K_2CO_3-CO_2*

Using the optimum elecNRTL model as a purely predictive model, the total pressure for aqueous H_2O-K_2CO_3-CO_2 mixtures were compared to experimental total pressure data from Pérez-Salado Kamps et al. (2007) for 5 and 20 wt % equivalent concentration of K_2CO_3 versus the solution loading at 40, 80, and 120 °C as shown in Figure 12.8-28 and Figure 12.8-29, respectively. The optimum model in Figure 12.8-28 adequately predicts the total pressure trends from 40 to 100 °C, but seems to overestimate the total pressure at high loadings. In Figure 12.8-29, the optimum model does not capture the temperature dependence at high loadings, but adequately predicts the total pressure below loadings of 1.

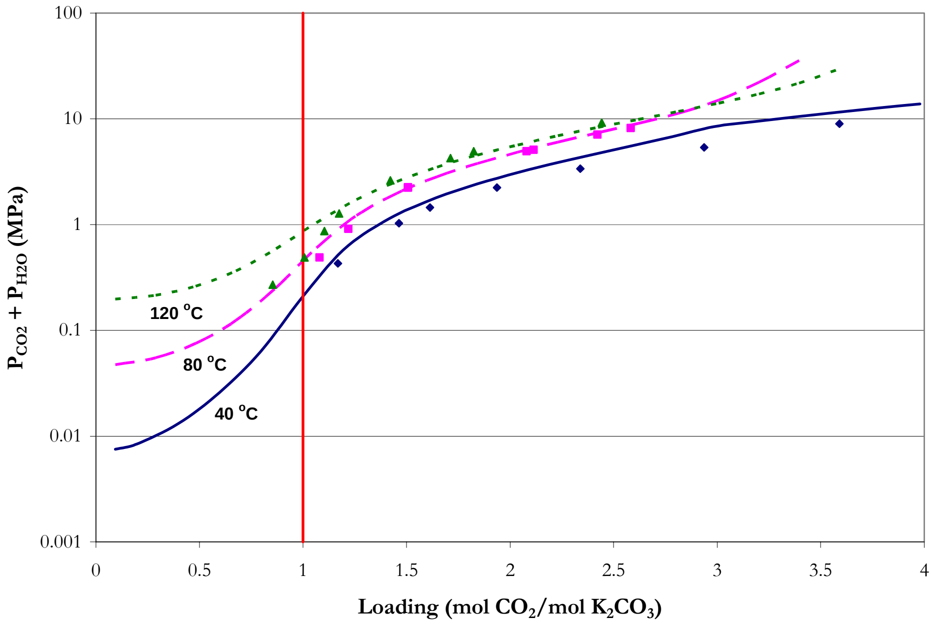

Figure 12.8-28. Total Pressure in a 5 wt % Equivalent Concentration of Aqueous H_2O-K_2CO_3-CO_2 Solution. Points: ◆, 40°C, ■, 80 °C, ▲, 120 °C. Lines: —, elecNRTL Model Predictions.

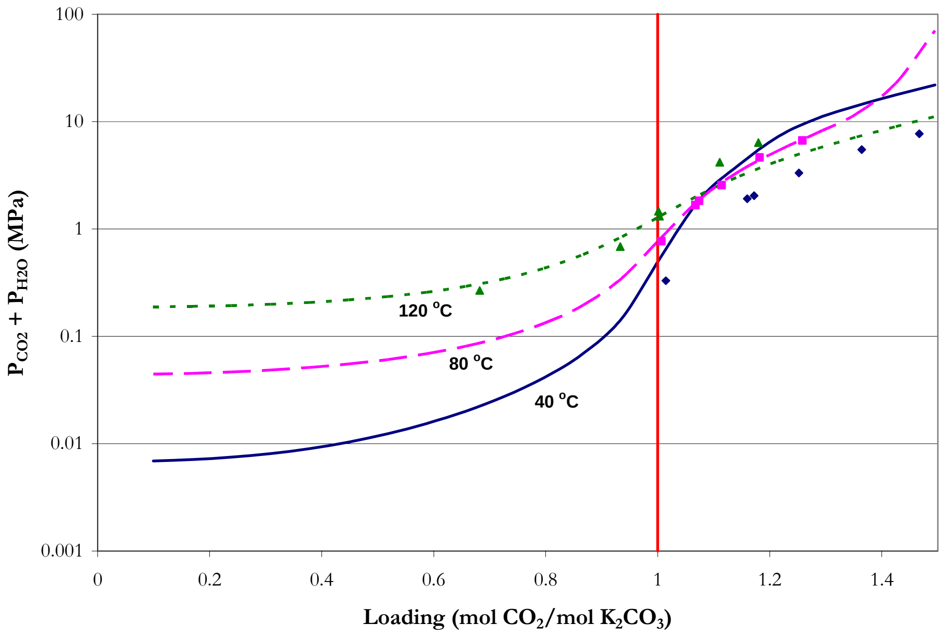

Figure 12.8-29. Total Pressure in a 20 wt % Equivalent Concentration of Aqueous H_2O-K_2CO_3-CO_2 Solution. Points: ◆, 40°C, ■, 80 °C, ▲, 120 °C. Lines: —, elecNRTL Model Predictions.

In this work, we have concentrated our efforts to describe CO_2 solubility below a loading (mol CO_2/mol K_2CO_3) equal to one. Below a solution loading of one, carbon dioxide is more or less converted to bicarbonate resulting in a negligible amount free CO_2 in solution. Predictions above a solution loading of one should be perceived as an extrapolation by the optimum model beyond the bounds of the regression data. In future work, we would recommend extending the model beyond a CO_2 loading equal to one. Parameters describing the interactions between CO_2 and electrolytes, specifically interactions for CO_2/K^+,HCO_3, and K^+,HCO_3/CO_2, would need to be included in the final model to account for physical absorption of CO_2 into the aqueous phase.

12.8.7 *Enthalpy of CO_2 Absorption Predictions for H_2O-K_2CO_3-CO_2*

Using the optimum elecNRTL model as a purely predictive model, the enthalpy of CO_2 absorption for aqueous H_2O-K_2CO_3-CO_2 mixtures was calculated based on the Gibbs-Helmholtz equation (Equation 12-44) which relates to the enthalpy change when CO_2 is dissolved in a liquid and chemically reacts. The heat released can be measured by direct calorimetry or estimated from CO_2 solubility data. The enthalpy of CO_2 absorption is an important qualification in solvent selection for the CO_2 capture process and aids in determining the amount of energy required to regenerate the solvent after aqueous absorption.

Figure 12.8-30, Figure 12.8-31, Figure 12.8-32, Figure 12.8-33, and Figure 12.8-34 illustrate the predictive capabilities of the elecNRTL model for the differential enthalpy of CO_2 absorption for 40 wt % K_2CO_3 mixtures from 40 – 130 °C.

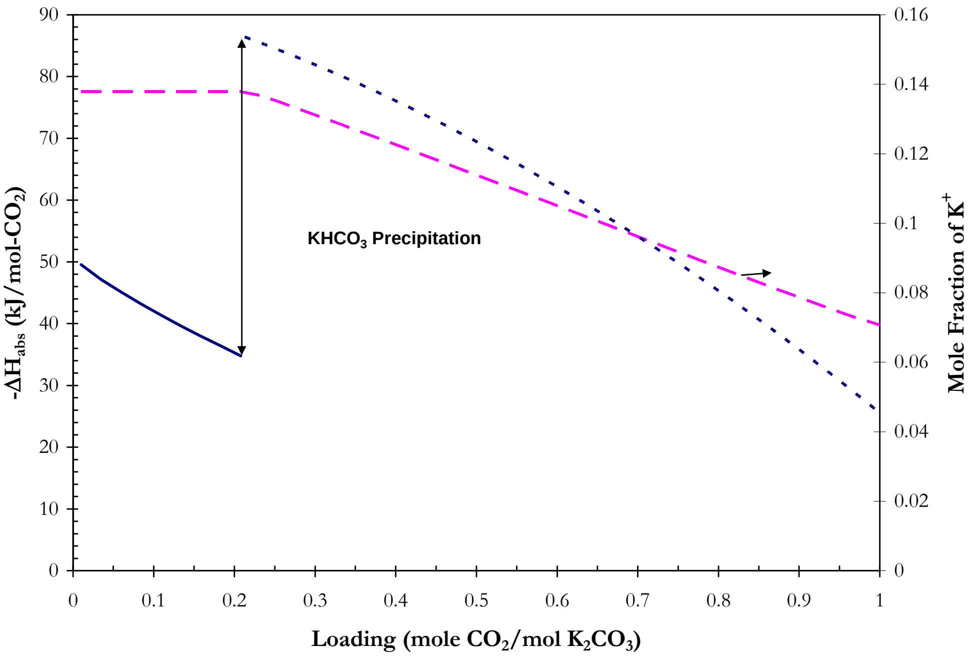

Figure 12.8-30. Predictions for the Differential Enthalpy of CO_2 Absorption from the elecNRTL Model in 40 wt % K_2CO_3 solutions at 40 °C.

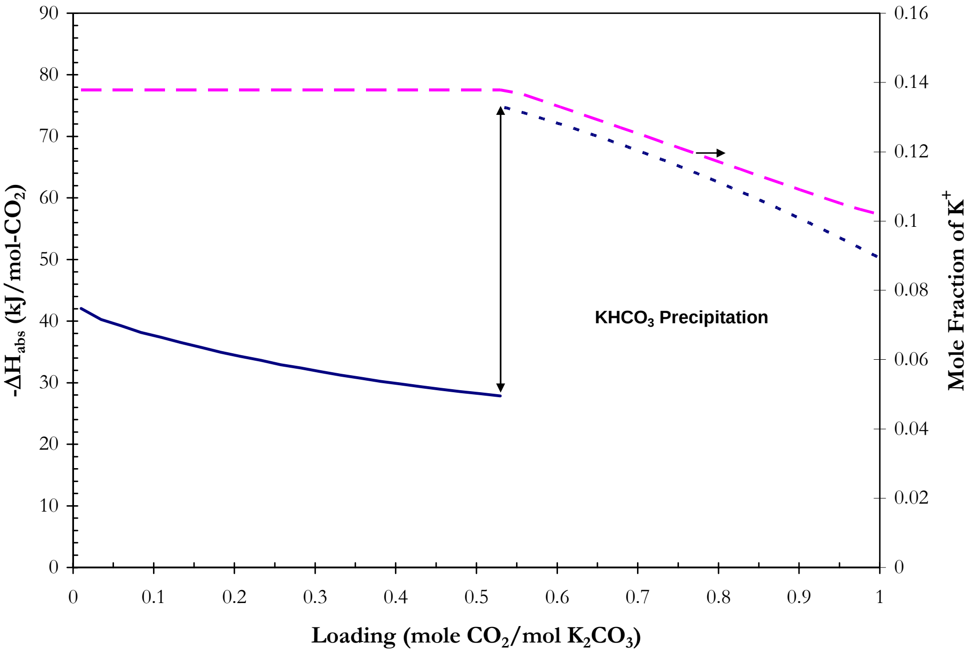

Figure 12.8-31. Predictions for the Differential Enthalpy of CO_2 Absorption from the elecNRTL Model in 40 wt % K_2CO_3 solutions at 70 °C.

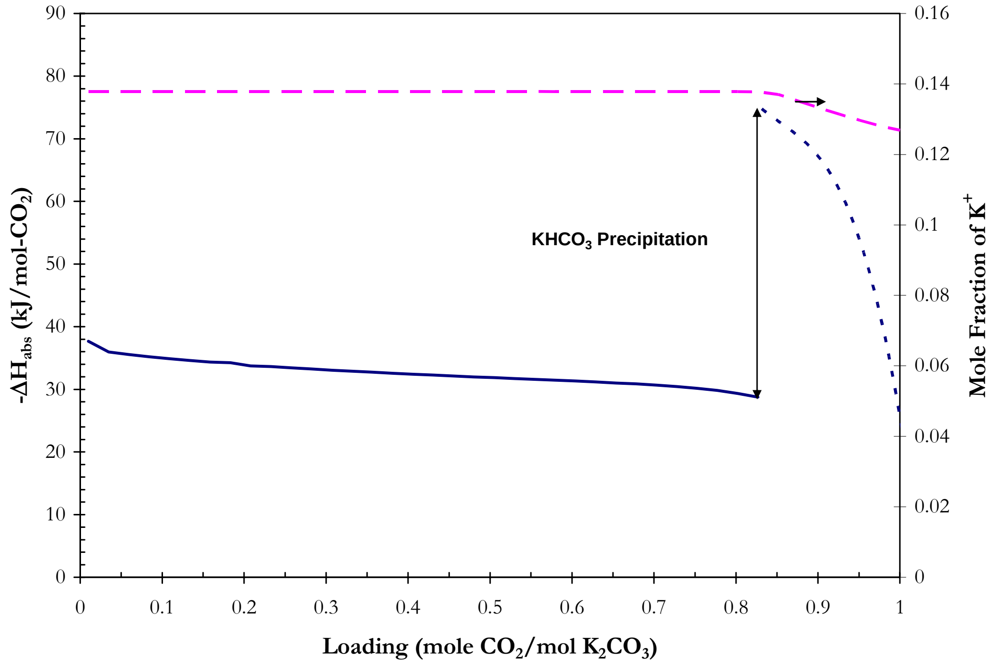

Figure 12.8-32. Predictions for the Differential Enthalpy of CO_2 Absorption from the elecNRTL Model in 40 wt % K_2CO_3 solutions at 90 °C.

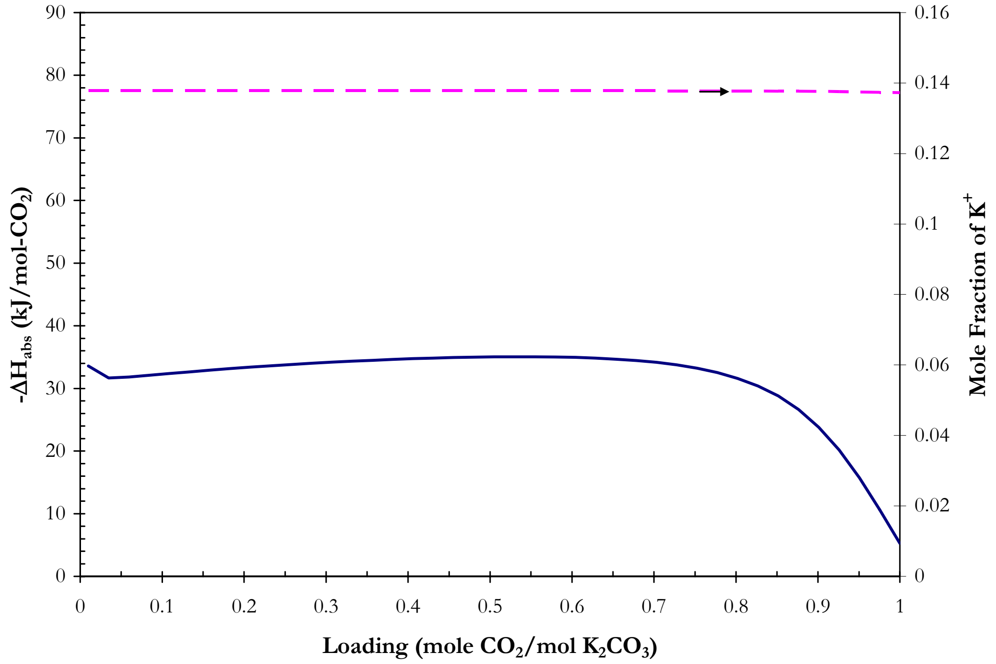

Figure 12.8-33. Predictions for the Differential Enthalpy of CO_2 Absorption from the elecNRTL Model in 40 wt % K_2CO_3 solutions at 110 °C.

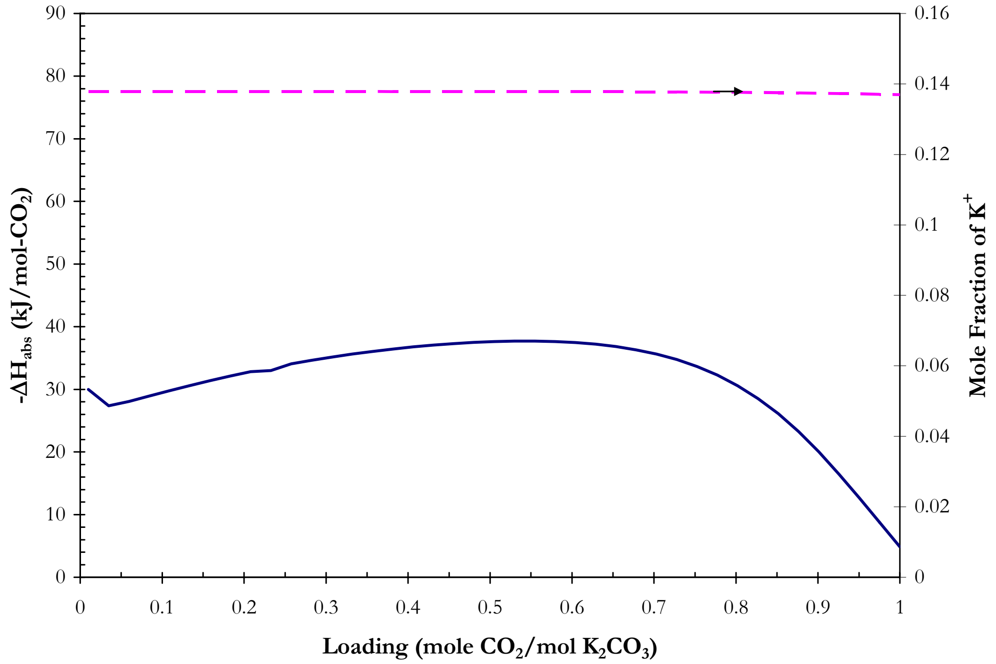

Figure 12.8-34. Predictions for the Differential Enthalpy of CO$_2$ Absorption from the elecNRTL Model in 40 wt % K$_2$CO$_3$ solutions at 130 °C.

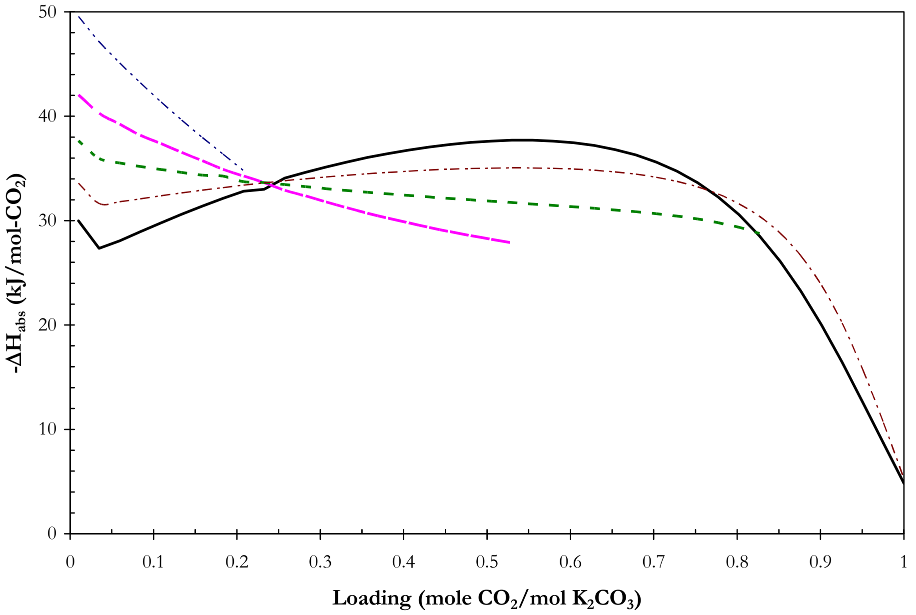

Figure 12.8-35. Overlay Predictions for the Differential Enthalpy of CO$_2$ Absorption from the elecNRTL Model in 40 wt % K$_2$CO$_3$ solutions from 40 to 130 °C. Lines: —··—, 40 °C, — —, 70 °C, · · ·, 90 °C, —·—, 110 °C, and —, 130 °C.

Figure 12.8-30, Figure 12.8-31, and Figure 12.8-32 illustrate $KHCO_3$ precipitation effects on the enthalpy of CO_2 absorption, which is also evident based on the discontinuity of the mole fraction of potassium ion. As the amount of free potassium decreases, due to $KHCO_3$ precipitation, the relative solution composition of K_2CO_3 decreases from the nominal amount. Figure 12.8-35 demonstrates the temperature effects on the enthalpy of CO_2 absorption. At low loadings, we see a shift in the dominate reaction mechanism from Equation 12-8 to Equation 12-7 based on the discontinuity in the enthalpy of CO_2 absorption. Overall, predictions for the enthalpy of CO_2 absorption in 40 wt % K_2CO_3 solutions provide a realistic estimate for future design considerations. Since the enthalpy of CO_2 absorption, in this case, is a purely predictive quantity, gathering experimental data for the enthalpy of CO_2 absorption and specific heat capacity for solutions at various loadings will help to validate model predictions from various authors.

12.8.8 *Specific Heat Capacity Predictions for H_2O-K_2CO_3-CO_2*

Using the optimum elecNRTL model as a purely predictive model, the specific heat capacity for aqueous H_2O-K_2CO_3-CO_2 mixtures was calculated based on Equation 12-29. Figure 12.8-36 illustrates the predictive capabilities of the elecNRTL model for the specific heat capacity for 40 wt % K_2CO_3 mixtures from 40 – 130 °C.

Figure 12.8-36 demonstrates the effect of temperature on the specific heat capacity, where predictions for the specific heat capacity of aqueous H_2O-K_2CO_3-CO_2 mixtures are base on CO_2 solubility and salt solubility data, since literature data for the specific heat capacity of aqueous H_2O-K_2CO_3-CO_2 mixtures have not yet been quantified.

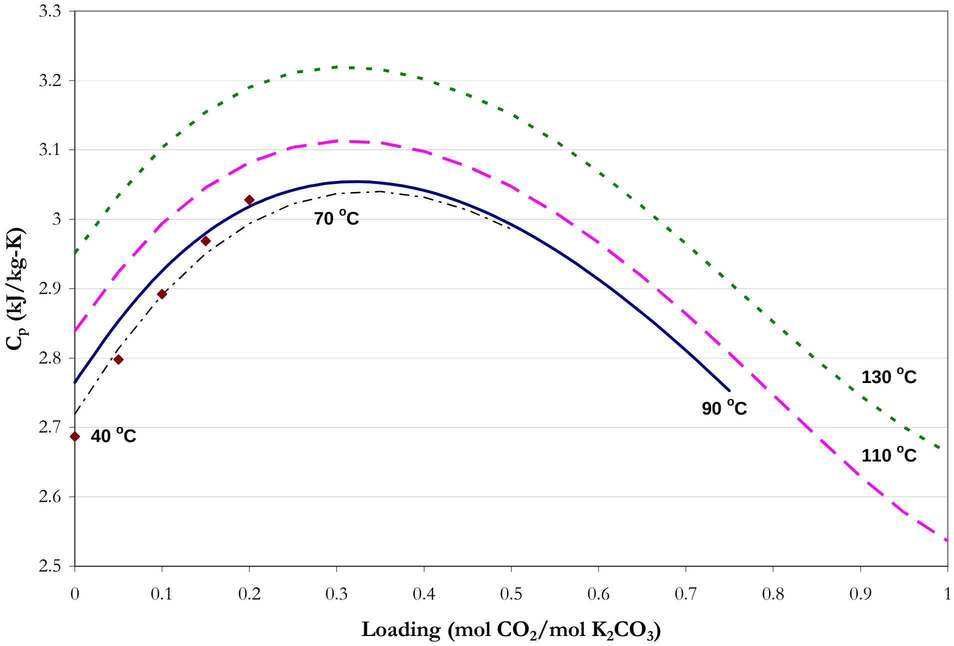

Figure 12.8-36. Specific Heat Capacity of a 40 wt % K_2CO_3 mixtures from 40 – 130 °C.

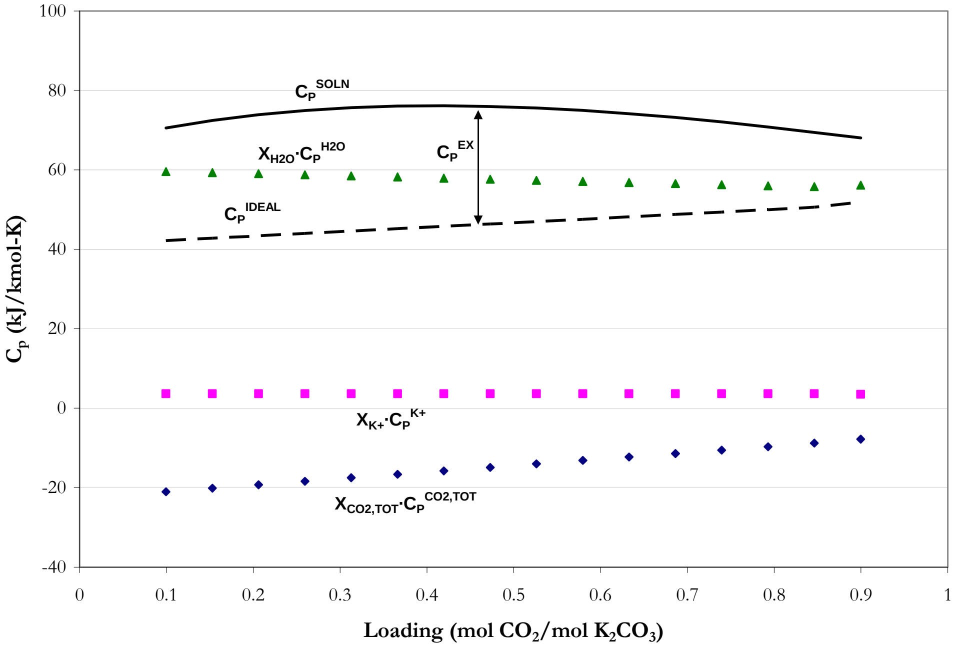

Figure 12.8-37. Comparison of the Molar Heat Capacity Predictions for 40 wt % K2CO3 mixtures at 90 °C from the elecNRTL Model to the Ideal Molar Heat Capacity based on the Constituent Components.

To describe the departure from an ideal solution behavior, Figure 12.8-37 separates the molar heat capacity of the solution into the weighted molar heat capacity of each contributing species with respect to the components reference state (i.e. Solvent: pure liquid; Ionic and Molecular Solutes: Infinite Dilution). Deviations between the molar heat capacity of the solution from the ideal molar heat capacity are accounted by the excess molar heat capacity. Figure 12.8-37 illustrates the solution molar heat capacity may not be estimated by the weighted molar heat capacity of water to a first approximation. In addition, the weighted molar heat capacity of CO_2^{TOT} decreases (approaching zero) as loading increases, even though the weighted molar heat capacity of CO_2^{TOT} increases (becoming more negative) in binary solutions of K_2CO_3 and $KHCO_3$. All the while, the weighted molar heat capacity of potassium ion is approximately constant versus increasing loading for all of the systems.

12.9 Conclusions

In conclusion, in this work we have shown in Figure 12.8-2 and Figure 12.8-3 the departure nature from an ideal solution behavior vis-à-vis Raoult's Law as compared to predictions from the elecNRTL model. For H_2O-K_2CO_3 system, Raoult's Law adequately describes the vapor pressure of H_2O below 1 m K_2CO_3 over the temperature range between 40 and 80 °C, but as the concentration of K_2CO_3 increases so does the importance of including activities to describe the vapor-liquid equilibrium. On the other hand, Raoult's Law adequately describes the vapor pressure of H_2O over the entire $KHCO_3$ concentration ranged included in this work. There are slight deviations at 60 and 80 °C, but Raoult's Law does provide an adequate estimate for the vapor pressure of water.

In terms of H_2O-K_2CO_3 and H_2O-$KHCO_3$ molar heat capacity, the weighted molar heat capacity of water can adequately describe the molar heat capacity of H_2O-$KHCO_3$ mixtures over the entire range of concentrations used in this work, whereas the weighted molar heat capacity of water can adequately describe the molar heat capacity of H_2O-K_2CO_3 mixtures for concentrations less than 6 m K_2CO_3.

Pérez-Salado Kamps et al. (2007) reported interaction parameters based on a Pitzer's molality based equation for the Gibbs excess energy of the aqueous phase through simultaneous regression of similar VLE and SLE data, but chose not to include Calorimetry effects into their model. Predictions for CO_2 solubility data from Tosh et al. (1959) were reported with an average absolute relative deviation of ± 12.2 %. In this work, we were able to increase the amount of literature data and predict CO_2 solubility data from Tosh et al. (1959) within average absolute relative deviation of ± 10.8 %. Thus, we feel predictions from our optimum model will provide the most realistic values to date.

In addition, we have concentrated our efforts to describe CO_2 solubility below a loading (mol CO_2/mol K_2CO_3) equal to one. Below a solution loading of one, carbon dioxide is more or less converted to bicarbonate resulting in a negligible amount free CO_2 in solution. Predictions above a solution loading of one should be perceived as an extrapolation by the optimum model beyond the bounds of the regression data. In future work, we would recommend extending the model beyond a CO_2 loading equal to one. Parameters describing the interactions between CO_2 and electrolytes, specifically interactions for $CO_2/K^+,HCO_3$, and $K^+,HCO_3/CO_2$, would need to be included in the final model to account for physical absorption of CO_2 into the aqueous phase.

Figure 12.8-16 and Figure 12.8-17 illustrates an important point: even though each author successfully regressed solid solubility data for each system, predictions for the calculated chemical equilibrium salt precipitation reaction are different. This discrepancy is due to the thermodynamic foundations for each model. Each model would describe the activity coefficients of potassium, carbonate, and bicarbonate ions differently based on the regression methodology employed, the type of thermodynamic model used, and the types of thermodynamic data used in the regression. To illustrate this point, predictions for the chemical equilibrium salt precipitation reaction for $KHCO_3$ based on sequential model predictions for the activity product of potassium and bicarbonate inversed even though, the model adequately predicted VLE and calorimetric data.

Over the entire range of conditions for the H_2O-K_2CO_3-$KHCO_3$ system, the average absolute deviation between the experimental and estimated salt solubility temperature is within $\pm$ 1.13 ^oC.

Overall, results presented above indicate that the elecNRTL model, through simultaneous regression gave a set of optimum binary interaction parameters for the H_2O-K_2CO_3-CO_2 system. The optimum model adequately represents the literature data for aqueous H_2O-K_2CO_3-CO_2 mixtures.

CHAPTER XIII

Ternary Systems: H_2O-MEA-CO_2

13.1 Introduction

To this point in the thermodynamic model development, we described only molecule-molecule interactions. For an electrolyte system, there are interactions between molecules and electrolytes, for example between water and ionic species, and interactions between electrolyte pairs with a common cation or anion. This chapter describes the data regression and model predictions for the ternary {H_2O-Monoethanolamine (MEA)-Carbon dioxide (CO_2)} system based on previous literature data and experimental results from this work. The results for the binary interaction parameters for the electrolyte-NRTL (elecNRTL) model within Aspen Plus^{TM} are then presented showing good statistical fit to the literature data with an average absolute relative error of ± 24.79 %, with the exception of a few outliers.

13.2 H_2O-MEA-CO_2 System

With ions in an electrolyte solution, the elecNRTL model accounts for contributions associated with long-range ion-ion interactions and local interactions which exist around any central species as proposed by Chen et al. (1982). In this section, we present background on the elecNRTL model for clarification purposes only.

The elecNRTL model is a molar Gibbs energy model given by the following form:

$$G_m^* = x_w \mu_w^* + \sum_k x_k \mu_k^\infty + \sum_j x_j \ln x_j + G_m^{*E} \tag{13-1}$$

where the excess Gibbs free energy model is given by the following form:

$$\frac{G_m^{*E}}{RT} = \frac{G_m^{*E,PDH}}{RT} + \frac{G_m^{*E,Born}}{RT} + \frac{G_m^{*E,lc}}{RT} \tag{13-2}$$

Where
PDH is the Pitzer-Debije-Hückel contribution for long range ion-ion interactions,
Born is the Born Correction for change in mixed solvent reference state, and
lc is the local contribution for short range interactions.

The molar Gibbs free energy and the molar excess Gibbs free energy are defined with the asymmetrical reference state as infinite dilute in pure solvent. The reference state for ionic and molecular solutes follows the unsymmetrical convention: defined as infinite dilution in water. The ideal mixing terms is calculated where j refers to any component and the molar Gibbs free energy of pure water is calculated from the ideal gas contribution. The aqueous infinite dilution chemical potential is calculated from the infinite dilution aqueous phase heat capacity polynomial model, where the subscript k refers to any ions or molecular solute.

$$\mu_k^{\infty} = \Delta_f H_k^{\infty,aq} + \int_{T_0}^{T} \frac{C_{p,k}^{\infty,aq}}{T} dT - T\left(\frac{\Delta_f H_k^{\infty,aq} - \Delta_f G_k^{\infty,aq}}{T_0} + \int_{T_0}^{T} \frac{C_{p,k}^{\infty,aq}}{T} dT \right) + RT \ln\left(\frac{1000}{MW_w} \right) \quad 13\text{-}3$$

Where $\Delta_f H_k^{\infty,aq}$ and $\Delta_f G_k^{\infty,aq}$ are based on a molality scale and μ_k^{∞} is based on a mole fraction scale, the last term is added for the conversion.

For molecular solutes, the aqueous infinite dilution chemical potential is calculated from Henry's law:

$$\mu_k^{\infty} = \mu_k^{\infty,ig} + RT \ln\left(\frac{H_{k,w}}{P^{ref}} \right) \quad 13\text{-}4$$

Where
T_0 is the reference temperature, 298.15 K,
P^{ref} is the reference pressure, 1 atm.

Thus, when the derivative of the Gibbs free energy at constant temperature and pressure reaches a minimum for a closed homogeneous system; the system has satisfied the condition for thermodynamic equilibrium.

For the elecNRTL model to calculate activity coefficients, the excess Gibbs free energy is related to the activity coefficient by the following thermodynamic relationship.

$$\ln \gamma_i = \frac{G_m^{*E}}{RT} = \left[\frac{\delta\left(nG_m^{*E} / RT \right)}{\delta n_i} \right] \quad 13\text{-}5$$

Please refer to Chapter VI for information relating to the specific contributions to the excess Gibbs energy model.

13.3 Chemical and Vapor-liquid Equilibrium of MEA

Figure 13.3-1 illustrates the proposed system to correlate/predict the solubility of CO_2 and MEA in aqueous solutions of MEA.

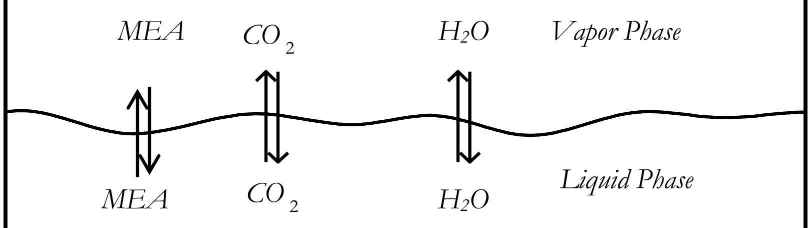

R1: $H_2O \leftrightarrow H^+ + OH^-$ 13-6

R2: $CO_2 + H_2O \leftrightarrow H^+ + HCO_3^{-1}$ 13-7

R3: $HCO_3^{-1} \leftrightarrow H^+ + CO_3^{-2}$ 13-8

R4: $MEAH^{+1} \leftrightarrow MEA + H^+$ 13-9

R5: $MEACOO^{-1} + H_2O \leftrightarrow MEA + HCO_3^{-1}$ 13-10

Figure 13.3-1. Chemical and Vapor-liquid Equilibrium of MEA.

Reaction 13-6 describes the ionization of water to proton (H^+) and hydroxide ions (OH^-); Reaction 13-7 describes the hydrolysis and ionization of dissolved CO_2 to H^+ and bicarbonate (HCO_3^-) ions; Reaction 13-8 describes the dissociation of HCO_3^- to H^+ and carbonate (CO_3^{-2}) ions; Reaction 13-9 describes the protonation of monoethanolamine (MEA) to protonated monoethanolamine $(MEAH^{+1})$; Reaction 13-10 describes the monoethanolamine carbamate formation $\left(MEACOO^{-1}\right)$. The chemical equilibrium constant for the above j equations are expressed in Aspen Plus™ in terms of the activity of component i as given by the following relationship.

$$K_j = \prod_i a_i^{\nu_{i,j}} \qquad 13\text{-}11$$

Where
K_j is the chemical equilibrium constant,
$\nu_{i,j}$ is the reaction stoichiometric coefficient of component i,
a_i is the activity of component i.

In this work, for Reactions 13-6 to 13-9, we did not define the chemical equilibrium constants as linear temperature dependent functions, but rather in terms of the reference state Gibbs free energy of the system:

$$\ln K_j = -\frac{\Delta G_{i,j}^o}{RT} \qquad 13\text{-}12$$

Where
$\Delta G_{i,j}^o$ is the standard free energy of formation of component i.

The previous framework allows our rigorous thermodynamic model to be internally consistent with respect to governing thermodynamic definitions. Table 8.3-12 and Table 12.5-1 reported the standard state conditions at 25 °C associated with the species in Reactions 13-6 to 13-9 where the standard state conditions are consistent with published literature by Bates and Pinching (1951) and Edwards et al. (1978) as shown in Chapter VIII and Chapter XII, respectively.

As stated previously, Equation 13-12 relates the chemical equilibrium constant to the standard Gibbs free energy change of reaction.

$$\frac{\Delta G^o}{RT} = -\ln K \qquad 13\text{-}13$$

Where the standard property changes of reaction (e.g. Gibbs free energy and enthalpy) are defined as the difference between the standard property change of the products and reactants, weighted by their stoichiometric coefficients.

$$\Delta M^o = \sum_i \nu_i M_i^o \qquad 13\text{-}14$$

For molecular solutes (e.g. CO_2), the standard Gibbs free energy is described based on the ideal gas reference state by following equation:

$$G_{CO_2}^o\left(T\right) = G_{CO_2}^{ig}\left(T\right) + RT \ln \frac{H_{CO_2}\left(T\right)}{P^{ref}} \qquad 13\text{-}15$$

Where

$G_{CO_2}^{ig}$ is the ideal gas Gibbs free energy, J/kmol,

H_{CO_2} is the Henry's Constant for CO_2 in H_2O (Chen et al. 1979), atm,

P^{ref} is the reference pressure, 1 atm.

For ionic species the aqueous phase infinite dilution molar heat capacity is described by the following equation:

$$C_{p,i}^{\infty,aq}\left(\frac{J}{kmol \cdot K}\right) = C_{1,i} + C_{2,i}T\left(K\right) + C_{3,i}T\left(K\right)^2 + \frac{C_{4,i}}{T\left(K\right)} \qquad 13\text{-}16$$

where coefficients for the aqueous phase infinite dilution molar heat capacity for carbonate, bicarbonate, and $MEAH^+$ were described previously in Chapter XII - Section 12.5 and Chapter VIII - Section 8.3, respectively.

The molar heat capacity of H_2O was described in Chapter VII by the following equation:

$$C_{p,H_2O}^{l,*}\left(\frac{J}{kmol\cdot K}\right)=189366-1171\cdot T\left(K\right)+4.53\cdot T\left(K\right)^2-\ldots$$
$$\ldots-0.00795\cdot T\left(K\right)^3+5.4723\times10^{-6}\cdot T\left(K\right)^4 \qquad \text{13-17}$$

For a given temperature, the molar aqueous phase infinite dilution heat capacity of monoethanolamine carbamate can then be determined analytically based on the simultaneously regressed infinite dilution aqueous phase free energy of formation $\left(\Delta G_f^{\infty,aq}\right)$, the infinite dilution aqueous phase enthalpy of formation $\left(\Delta H_f^{\infty,aq}\right)$, and the infinite dilution aqueous phase heat capacity polynomial $\left(C_p^{\infty,aq}\right)$ for monoethanolamine carbamate. A starting point for a rigorous development starts with the following equation:

$$\Delta G_m^o=\Delta H_m^o-T\Delta S_m^o \qquad \text{13-18}$$

Equation 13-18 is from the definition of the molar Gibbs free energy applied to each component in a chemical reaction evaluated at the standard state. Applying Equation 13-14 to Equation 13-18 yields

$$\sum_i \nu_i G_{m,i}^o=\sum_i \nu_i H_{m,i}^o-T\sum_i \nu_i S_{m,i}^o \qquad \text{13-19}$$

where the standard molar heat of reaction and standard molar entropy change of reaction are related to temperature by the following expressions

$$\Delta H_m^o=\Delta H_{0,m}^o+R\int_{T_0}^{T}\frac{\Delta C_{p,m}^o}{R}dT \qquad \text{13-20}$$

$$\Delta S_m^o=\Delta S_{0,m}^o+R\int_{T_0}^{T}\frac{\Delta C_{p,m}^o}{R}\frac{dT}{T} \qquad \text{13-21}$$

Equations 13-18, 13-20, and 13-21 are combined to yield

$$\Delta G_m^o = \Delta H_{0,m}^o + R\int_{T_0}^{T} \frac{\Delta C_{p,m}^o}{R} dT - T\Delta S_{0,m}^o - RT\int_{T_0}^{T} \frac{\Delta C_{p,m}^o}{R}\frac{dT}{T} \qquad 13\text{-}22$$

However,

$$\Delta S_{0,m}^o = \frac{\Delta H_{0,m}^o - \Delta G_{0,m}^o}{T_0} \qquad 13\text{-}23$$

hence

$$\Delta G_m^o = \Delta H_{0,m}^o - \frac{T}{T_0}\left(\Delta H_{0,m}^o - \Delta G_{0,m}^o\right) + R\int_{T_0}^{T} \frac{\Delta C_{p,m}^o}{R} dT - RT\int_{T_0}^{T} \frac{\Delta C_{p,m}^o}{R}\frac{dT}{T} \qquad 13\text{-}24$$

Finally, division by RT yields

$$-\ln K_i = \frac{\Delta G_m^o}{RT} = \frac{\Delta G_{0,m}^o - \Delta H_{0,m}^o}{RT_0} + \frac{\Delta H_{0,m}^o}{RT} + \frac{1}{T}\int_{T_0}^{T} \frac{\Delta C_{p,m}^o}{R} dT - \int_{T_0}^{T} \frac{\Delta C_{p,m}^o}{R}\frac{dT}{T} \qquad 13\text{-}25$$

The change in heat capacity for the mixture can be expressed as

$$\Delta C_p^o\left(\frac{J}{kmol \cdot K}\right) = \Delta A + \Delta B \cdot T(K) + \Delta C \cdot T(K)^2 + \Delta D \cdot T(K)^3 + \Delta E \cdot T(K)^4 \qquad 13\text{-}26$$

with

$$\Delta A = \sum_i v_i A_i \qquad 13\text{-}27$$

with analogous definitions for ΔB, ΔC, ΔD, and ΔE. Through simultaneous regression of CO_2 solubility, amine volatility, specific heat capacity, liquid phase speciation, and enthalpy of CO_2 absorption, we were able to determine the infinite dilution aqueous phase free energy of formation, the infinite dilution aqueous phase enthalpy of formation, and the infinite dilution aqueous phase heat capacity polynomial for monoethanolamine carbamate. Please refer to section 13.5.5 for more information.

Ten data sets have been regressed with the elecNRTL model to represent the phase equilibrium of a mixed solvent system through regression of CO_2 solubility [Goldman and Leibush (1959), Lawson and Garst (1976), Lee. et al. (1976), Jou et al. (1995), Ma'mun et al. (2005), and from this work], specific heat capacity [from this work], enthalpy of CO_2 absorption [Kim et al. (2007)], and NMR speciation [Poplsteinova (2004) and from this work] data over monoethanolamine solutions. The elecNRTL model was never designed to regress enthalpy of CO_2 absorption or NMR speciation data thus we created a fortran subroutine to link with the data regression system (DRS) in Aspen Plus^{TM}.

The following section describes the different types of data used in the creation of the binary H_2O-MEA-CO_2 elecNRTL model.

13.3.1 *CO_2 Solubility and Amine Volatility*

Data in the form of CO_2 solubility, which measures the partial pressure of CO_2 over aqueous MEA solutions, P_{CO_2} , as a function of loading (mole CO_2 per mole MEA) and temperature were used to adjust the partial pressure of CO_2 for the H_2O-MEA-CO_2 system through the simultaneous regression of the binary interaction parameters in the elecNRTL model for the H_2O-MEA-CO_2 system.

For our ternary system (H_2O, MEA, and CO_2), the following equation can be used to represent the equilibrium for CO_2 solubility data.

$$Py_{CO_2} = x_{CO_2}\gamma^*_{CO_2}H_{CO_2,H_2O} \qquad 13\text{-}28$$

Where

y_{CO_2} is the vapor mole fraction of CO_2,

$\gamma^*_{CO_2}$ is the unsymmetric activity coefficient of CO_2,

H_{CO_2,H_2O} is the Henry's Constant for CO_2 in H_2O.

Table 13.3-1 lists current literature data for CO_2 solubility in aqueous MEA solutions.

Table 13.3-1. Sources of CO_2 Solubility Data.

Author	Concentration/mass%	Temperature/°C	P_{CO2}/kPa
Mason and Dodge (1936)	3 12 30 56 74	0 25 50 75	1.3 - 100
Reed and Wood (1941)	15	100 120 140	138 - 1724
Lyudkovskaya and Leibush (1949)	3 12 30	25 50 75	254 - 4054
Atadan (1954)	15 30 45 59	30 50 70	1033 - 3447
Muhlbauer and Monaghan (1957)	15	25 100	< 133
Goldman and Leibush (1959)	6 12 15 30	75 100 120 140	0.3 - 467
Jones et al. (1959)	15	40 60 80 100 120 140	< 931
Murzin and Leites (1971)	3 6 12 15 21	30 40 50 60 70 80	< 93
Lee et al. (1974)	15 30	4 100	1.4 - 6620
Lawson and Garst (1976)	15	40 60 80 100 120 134 140	2.9 - 2786
Lawson and Garst (1976)	30	94	23 - 453
Lee et al. (1976)	6 15 23 30	25 40 60 80 100 120	0.2 - 6616
Nasir and Mather (1977)	15 30	60 80 100	0.001 - 1.3
Isaacs et al. (1980)	15	80 100	0.007 - 1.6
Austgen and Rochelle (1991)	15	40 80	0.09 - 229
Shen and Li (1992)	15 30	40 60 80 100	1.1 - 2550
Murrieta-Guevara et al. (1993)	15 30	30 50 100	1.5 - 2210
Robinson (1993)	20 30	40 70 100 120	0.003 - 6293
Jou et al. (1995)	30	0 25 40 60 80 100 120 150	0.0012 - 19954
Shong et al. (1996)	15	40	15.7 - 2550
Ma'mun et al. (2005)	30	120	7.4 - 192

In this work, we chose Goldman and Leibush (1959), Lawson and Garst (1976), Lee et al. (1976), Jou et al. (1995), and Ma'mun et al. (2005) as the key literature sources for CO_2 solubility data based on previous modeling works in the area. The data by Lee et al. (1976) were known to be biased due to an error in the liquid phase analysis as reported by Jou et al. (1995). The loading in this data set was then corrected by +0.04 mole CO_2 per mole MEA.

Examples of the experimental CO_2 solubility used in this work from Goldman and Leibush (1959), Lee. et al. (1976), Jou et al. (1995), and Ma'mun et al. (2005) and from this work in 7 m (mole/kg-H_2O) or 30 wt% MEA, are shown in Figure 13.3-2. In addition, examples of experimental CO_2 solubility used in this work from Lawson and Garst (1976), Lee et al. (1976) and from this work in 3.5 m or 15 wt% MEA are shown in Figure 13.3-3.

In this work, we used a unique Fourier-transform infrared (FT-IR) technique to measure the vapor phase speciation in aqueous alkanolamine systems as described in Chapter II Using this technique, we have been able to measure the vapor phase partial pressure of MEA over aqueous MEA solutions, P_{MEA}, as a function of loading (mole CO_2 per mole MEA) and temperature.

For our ternary system (H_2O, MEA, and CO_2), the following equation can be used to represent the equilibrium for MEA volatility data.

$$Py_{MEA} = x_{MEA}\gamma_{MEA}P^{o}_{MEA} \qquad 13\text{-}29$$

Where
y_{MEA} is the vapor mole fraction of MEA,
γ_{MEA} is the asymmetric activity coefficient of MEA,
P^{o}_{MEA} is the extended Antoine vapor pressure correlation for MEA given in Chapter VII.

Examples of the experimental MEA volatility from this work in 3.5, 7, and 11 m MEA, are shown in Figure 13.3-4, Figure 13.3-5, and Figure 13.3-6, respectively.

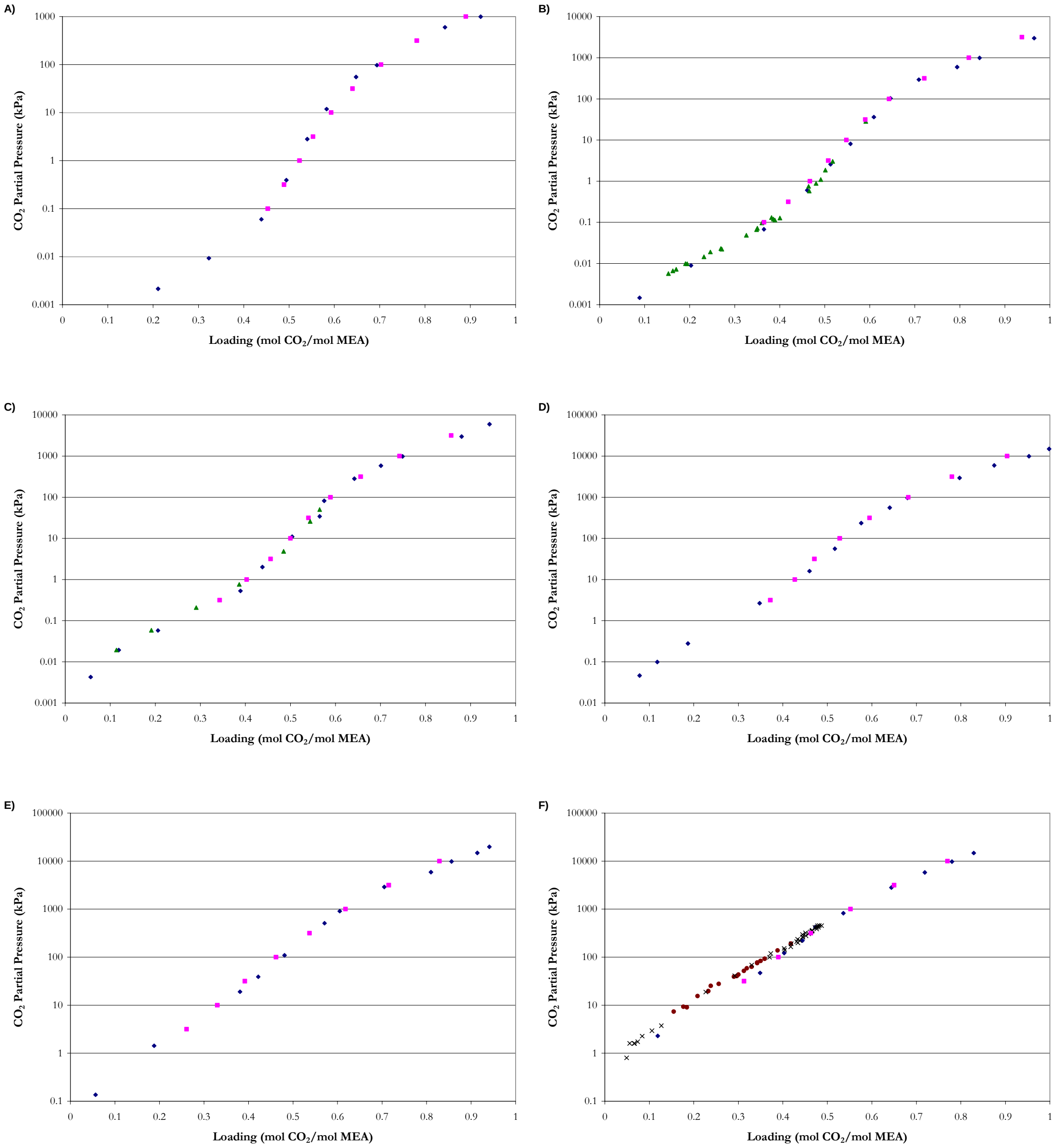

Figure 13.3-2. CO_2 Solubility in ~7 m MEA at 25 (A), 40 (B), 60 (C), 80 (D), 100 (E), and 120 °C (F). Points: ×, Goldman and Leibush (1959), ■, Lee et al. (1976), ◆, Jou et al. (1995),●,Ma'mum et al. (2005), ▲, this work.

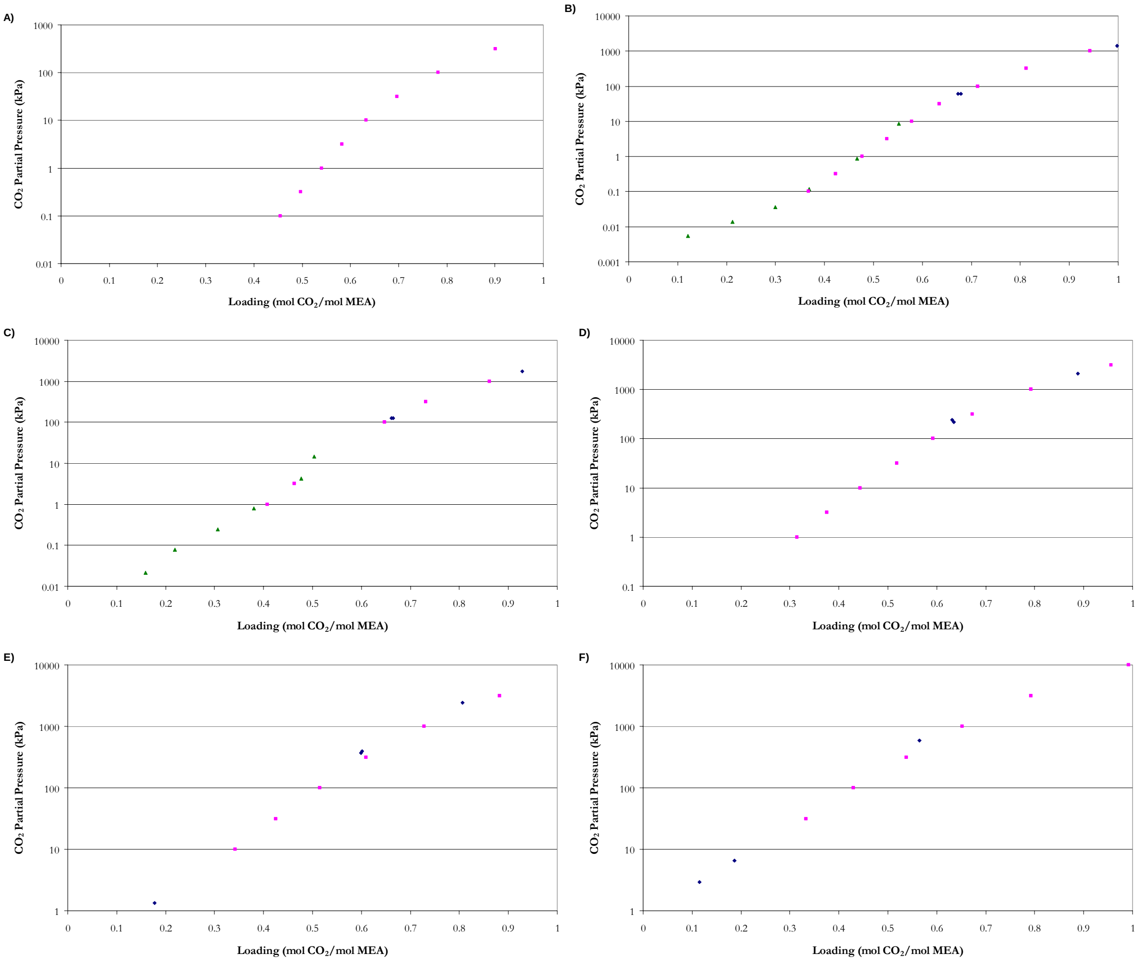

Figure 13.3-3. CO_2 Solubility in ~3.5 m MEA at 25 (A), 40 (B), 60 (C), 80 (D), 100 (E), and 120 ^{o}C (F). Points: ◆, Lawson and Garst (1976), ■, Lee et al. (1976), ▲, this work.

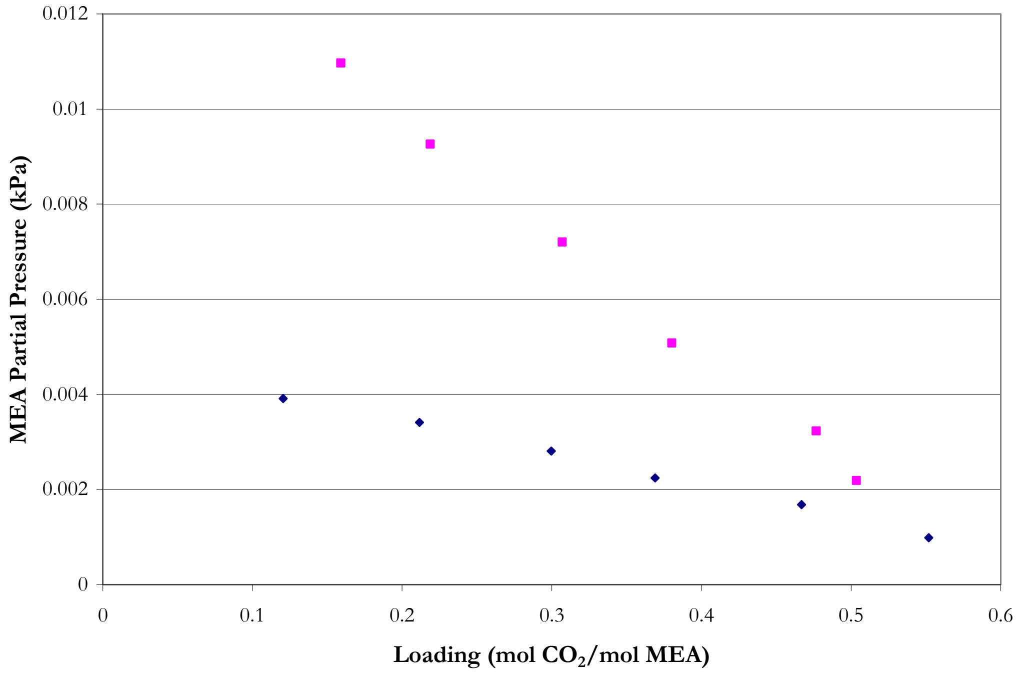

Figure 13.3-4. MEA Volatility for 3.5 m MEA from this work. Points: ◆, 40 °C, ■, 60 °C.

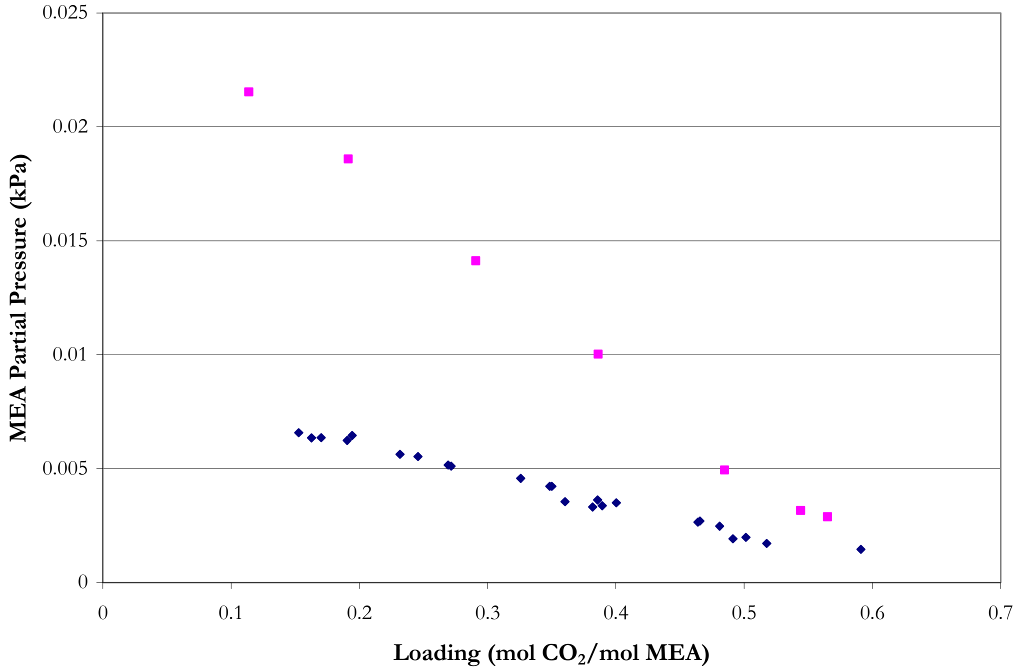

Figure 13.3-5. MEA Volatility for 7 m MEA from this work. Points: ◆, 40 °C, ■, 60 °C.

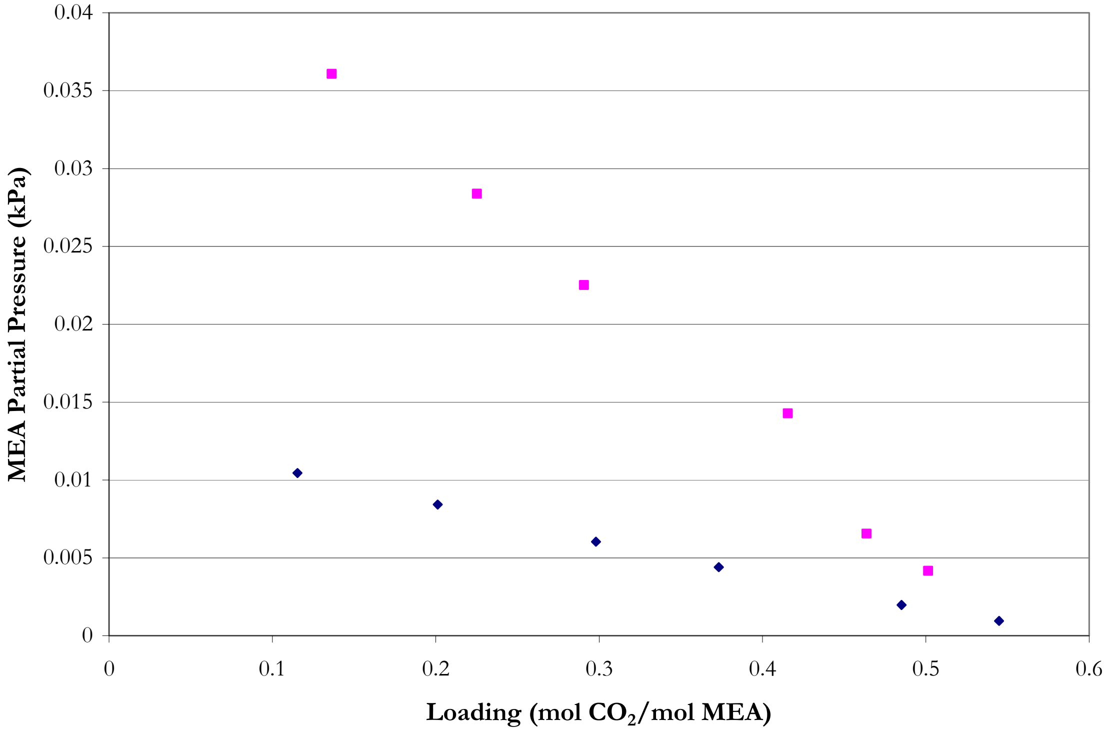

Figure 13.3-6. MEA Volatility for 11 m MEA from this work. Points: ◆, 40 ^{o}C, ■, 60 ^{o}C.

13.3.2 *Specific Heat Capacity*

As stated in Chapter VI, Aspen Plus^{TM} calculates the liquid phase heat capacity of a *mixture* (CPMX) by taking the derivative of the liquid enthalpy at constant pressure:

$$H_m^l\left(T+\Delta T\right)-H_m^l\left(T\right)=\int_T^{T+\Delta T} C_{p,m}^l dT \qquad 13\text{-}30$$

where the liquid enthalpy of a mixture is calculated by the following equation:

$$H_m^l\left(T\right)=\sum_i x_i H_i+\sum_k x_k H_k^\infty+H_m^E \qquad 13\text{-}31$$

for solvents:

$$H_i\left(T\right)=\Delta H_f^{ig}\left(T^{ref}\right)+\int_{T^{ref}}^{T} C_p^{ig}dT+\left[H_i\left(T,p\right)-H_i^{ig}\left(T,p\right)\right] \tag{13-32}$$

for molecular solutes (CO_2):

$$H_i\left(T\right)=H_i^{ig}\left(T\right)+RT\ln\left(\frac{H_{i,H_2O}}{P^{ref}}\right) \tag{13-33}$$

for cations or anions:

$$H_k^{\infty}\left(T\right)=\Delta H_{f,k}^{\infty}\left(T^{ref}\right)+\int_{T^{ref}}^{T} C_{p,k}^{\infty}dT \tag{13-34}$$

Where
ΔT is the perturbation in temperature from *T*,
H_m^E is the excess enthalpy of the mixture,
$\Delta H_f^{ig}\left(T^{ref}\right)$ is the standard enthalpy of formation of component i at T^{ref} ,
T^{ref} is the reference temperature, 25.0 °C,
C_p^{ig} is the ideal gas heat capacity of component i,
H_i^{ig} is the ideal gas enthalpy of component i,
H_k^{∞} is the infinite dilution aqueous enthalpy of component k,
$\Delta H_{f,k}^{\infty}\left(T^{ref}\right)$ is the infinite dilution aqueous phase standard enthalpy of formation of component k at T^{ref} ,
$C_{p,k}^{\infty}$ is the infinite dilution aqueous phase heat capacity polynomial of component k.

Table 13.3-2 gives the coefficients for the infinite dilution aqueous phase heat capacity used in Aspen Plus™ based on the following expression:

$$C_{p,k}^{\infty}\left(\frac{J}{kmol\cdot K}\right)=C_1+C_2T\left(K\right)+C_3\left(T\left(K\right)\right)^2+\frac{C_4}{T\left(K\right)} \tag{13-35}$$

Table 13.3-2. Infinite Dilution Aqueous Phase Heat Capacity Default Coefficients.

Parameter	Symbol	H^+	OH^-	HCO_3^{-1}	CO_3^{-2}	$MEAH^{+1}$
CPAQ0-1	C_1	0.0	0.0	211387	1334017	-1710760
CPAQ0-2	C_2	0.0	-497.9	-882	-5565	7136
CPAQ0-3	C_3	0.0	0.0	0.875	5.19	-8.54
CPAQ0-4	C_4	0.0	0.0	-1.9E+07	-1.2E+08	1.5E+08

Data in the form of specific heat capacity as a function of loading, molality, and temperature were used to adjust the coefficients for the binary interaction parameters of the elecNRTL model. An example of the experimental specific heat capacity from this work from 40 to 120 °C for 3.5 and 7 m MEA is shown in Figure 13.3-7and Figure 13.3-8, respectively. Points shown corresponding to a loading of zero were regressed as part of Chapter VIII. Please refer to Chapter VIII for more information.

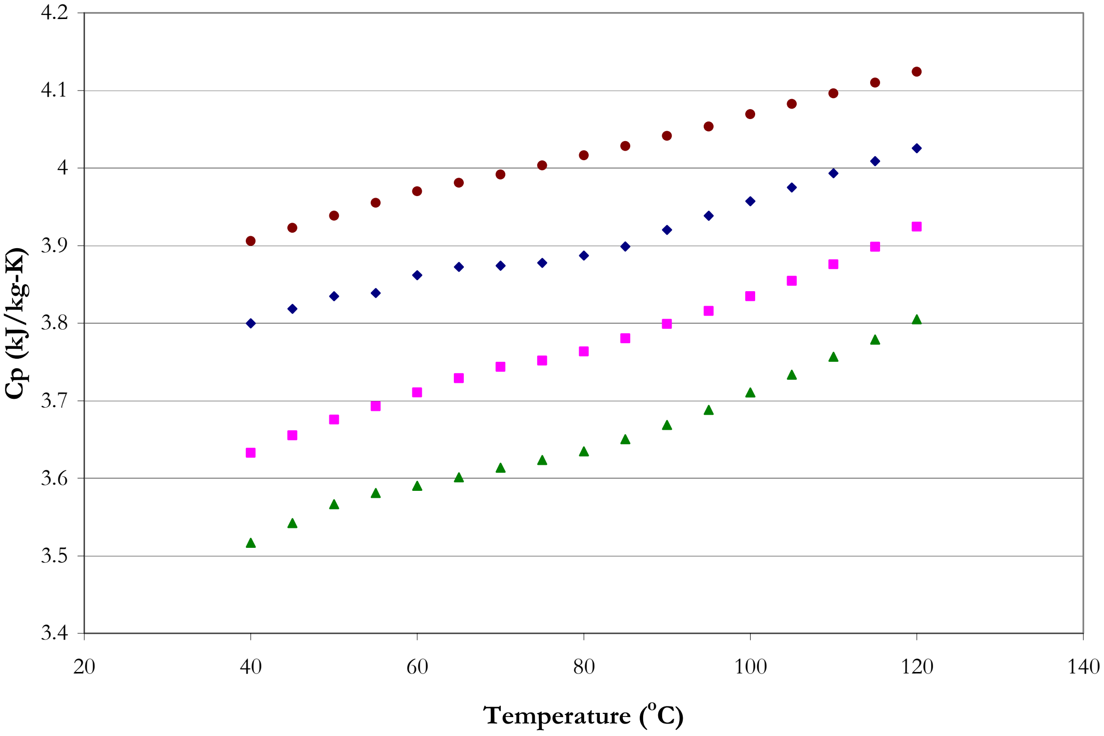

Figure 13.3-7. Specific Heat Capacity in Loaded 3.5 m MEA Solutions from this work. Points: ●, Ldg = 0.0, ♦, Ldg = 0.097, ■, Ldg = 0.375, ▲, Ldg = 0.583.

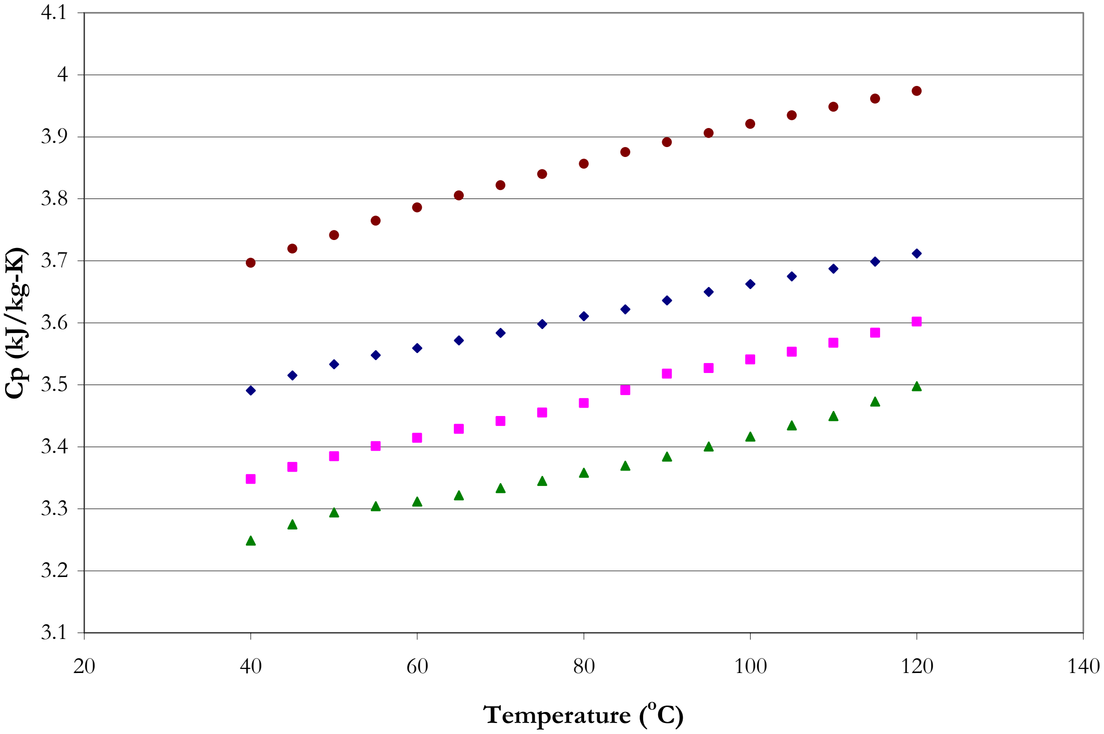

Figure 13.3-8. Specific Heat Capacity in Loaded 7 m MEA Solutions from this work. Points: ●, Ldg = 0.0, ◆, Ldg = 0.139, ■, Ldg = 0.358, ▲, Ldg = 0.541.

13.3.3 *Enthalpy of CO_2 Absorption*

Data in the form of the enthalpy of CO_2 absorption for aqueous monoethanolamine solutions, as a function of loading and temperature, were used to adjust the activity coefficients for each liquid phase component in the H_2O-MEA-CO_2 system through the simultaneous regression of the binary interaction parameters in the elecNRTL model.

For our true component ternary system (H_2O, MEA, and CO_2), the Gibbs-Helmholtz equation can be used to represent the differential enthalpy of CO_2 absorption:

$$-\frac{\Delta H_{abs}}{R} = \left(\frac{d\, f^{v}_{CO_2}}{d\left(1/T\right)} \right)_{x_{CO_2}} \tag{13-36}$$

The heat released can be measured by direct calorimetry or estimated from CO_2 solubility data. The latter has been shown to have a high degree of uncertainty on the order of ± 20 to 30 % as reported by Lee et al. (1974). However, if the loading span within one CO_2 addition can be kept rather low, the measurements gave enthalpy data close to differential values in loading rather than integral as shown by Kim et al. (2007) with respect to the total amount of heat released from zero loading to the experimental loading data point as shown by the following expression:

$$-\Delta H_{\text{int}} = -\int_0^{\alpha} \Delta H_{diff}\, \mathrm{d}\alpha \qquad 13\text{-}37$$

Where
α is the loading of the solution, mole CO_2/mole MEA.

In addition, only a limited amount of experimental data is available in the literature for aqueous monoethanolamine. Mathonat (1995) and Mathonat et al. (1998) reported integral enthalpy of CO_2 absorption in 30 wt% monoethanolamine solutions at 40, 80, and 120 °C and over the range of loading from 0 – 2 mol CO_2/mol MEA, but due to a high degree of scatter the data set was excluded for the data regression. Carson et al. (2000) also reported integral enthalpy of CO_2 absorption in 10, 20, and 30 wt% monoethanolamine at 25 °C and at low loading, < 0.1 mol CO_2/mol MEA. For this reason, this data set was excluded from the data regression. Finally, Kim et al. (2007) reported consistent experimental differential enthalpy of CO_2 absorption data in 30 wt% monoethanolamine solutions at 40, 80, and 120 °C and over the range of loading from 0 – 0.7 mol CO_2/mol MEA.

Aspen Plus™ was never designed to regress differential enthalpy of CO_2 absorption data; nevertheless, in this work we were able to develop a fortran subroutine to regress experimental differential enthalpy of CO_2 absorption data within DRS utilizing the following schema presented in Figure 13.3-9.

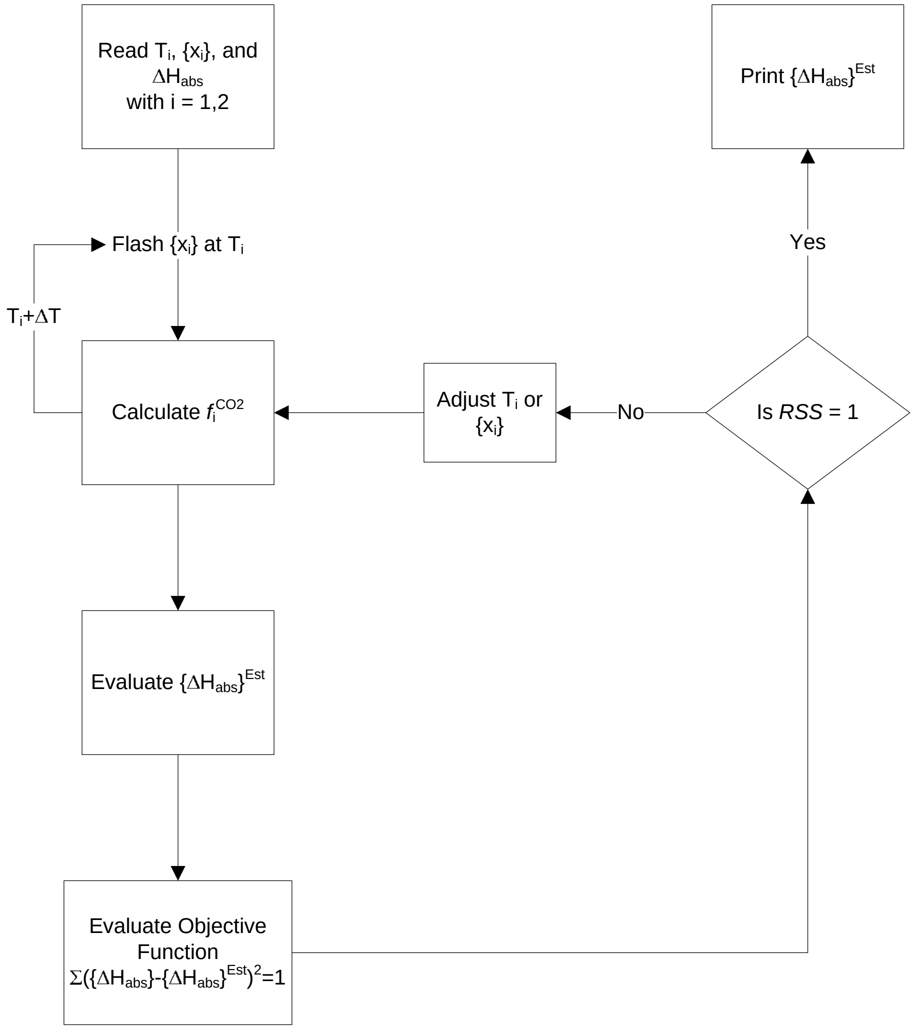

Figure 13.3-9. Differential Enthalpy of CO_2 Absorption Fortran Subroutine Schema Developed for Aspen Plus™.

Within DRS, the user inputs the temperature in Kelvin, the apparent liquid phase mole fractions for MEA, CO_2, and H_2O, and the differential enthalpy of CO_2 absorption. The fortran subroutine then calls a FLSH_FLASH subroutine within Aspen Plus^{TM} and performs a temperature-vapor fraction flash calculation. Once the FLASH subroutine converges, the fortran subroutine calculates the CO_2 vapor phase fugacity based on the estimated partial pressure and the vapor phase fugacity coefficient of CO_2, respectively. The fortran subtroutine then numerically differentiates the vapor phase fugacity of CO_2 at T and (T + 1 K) based on Equation 13-36.

Finally, the fortran subroutine exports the estimated enthalpy of CO_2 absorption to DRS. DRS then tries to minimize the difference between the estimated enthalpy of CO_2 absorption calculated from the fortran subroutine and the experimental value utilizing the Maximum Likelihood Method within Aspen Plus^{TM} to minimize the overall objective function while adjusting each property variable. For more information about the complete fortran subroutine code, please refer to Appendix K.

Examples of the experimental differential enthalpy of CO_2 absorption used in this work from Kim et al. (2007) at 40, 80, and 120 °C for 30 wt% monoethanolamine are shown in Figure 13.3-10, Figure 13.3-11, and Figure 13.3-12, respectively.

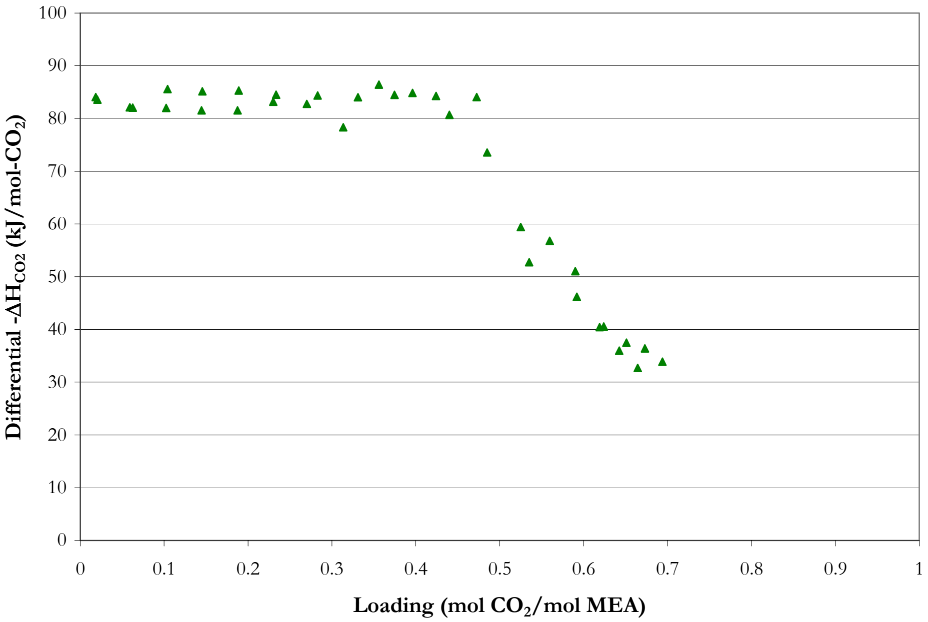

Figure 13.3-10. Negative Differential Enthalpy of CO_2 Absotption in 30 wt% MEA at 40 °C from Kim et al. (2007).

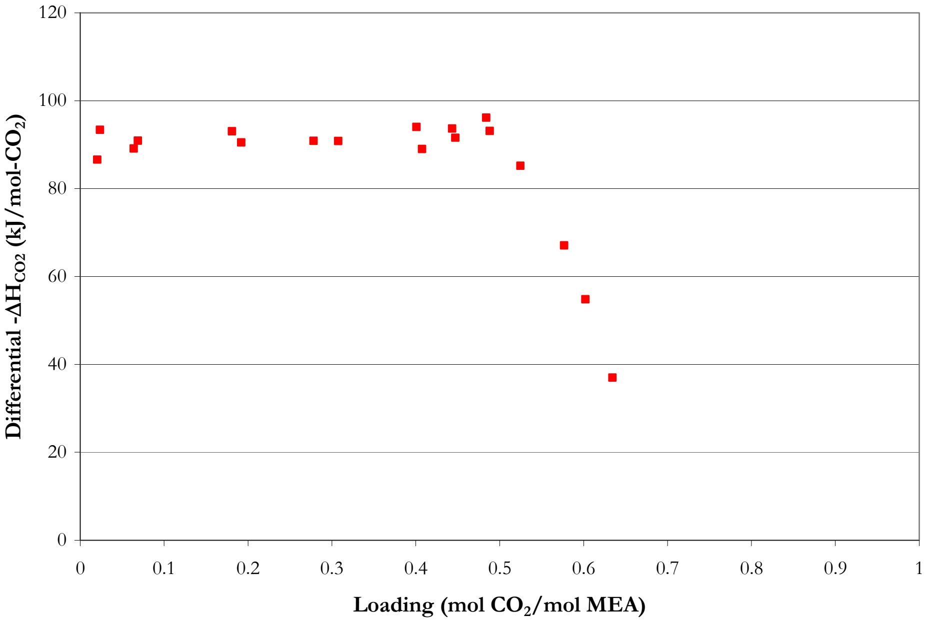

Figure 13.3-11. Negative Differential Enthalpy of CO_2 Absotption in 30 wt% MEA at 80 °C from Kim et al. (2007).

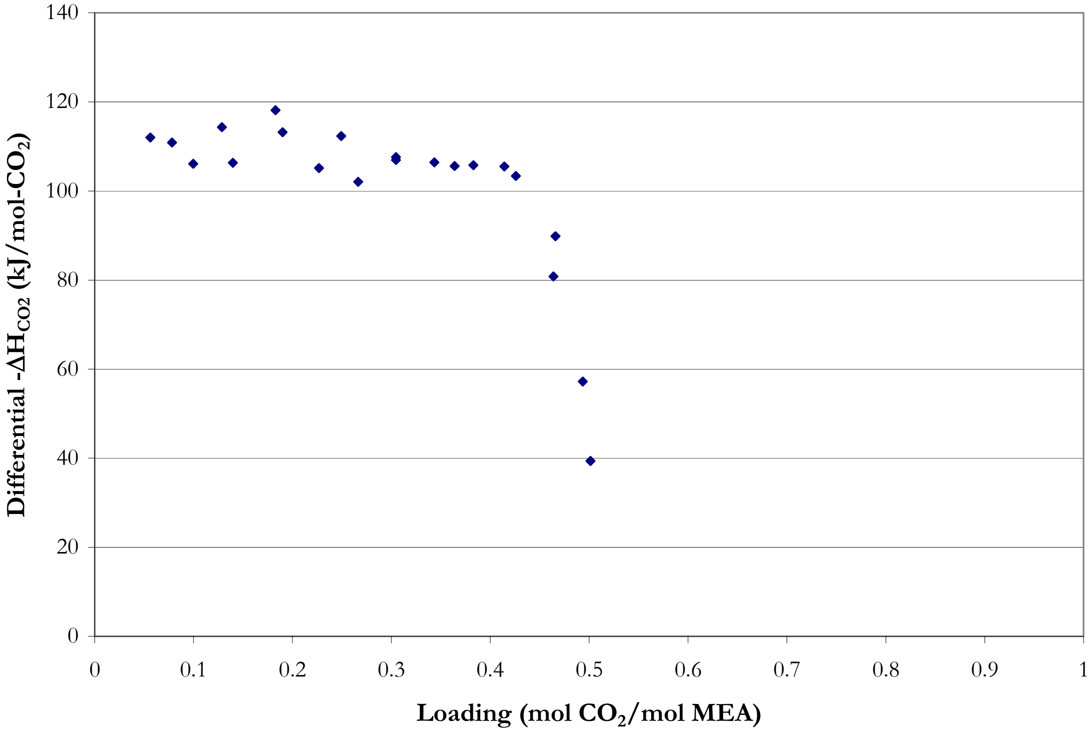

Figure 13.3-12. Negative Differential Enthalpy of CO_2 Absotption in 30 wt% MEA at 120 °C from Kim et al. (2007).

13.3.4 *NMR Speciation*

Data in the form of carbon13 NMR speciation for aqueous monoethanolamine solutions, as a function of loading, concentration, and temperature, were used to adjust the activity coefficients for each liquid phase component in the H_2O-MEA-CO_2 system through the simultaneous regression of the binary interaction parameters in the elecNRTL model.

For our true component ternary system (H_2O, MEA, and CO_2), the following equations can be used to represent the liquid phase equilibrium for the NMR speciation data as reported by Poplsteinova (2004) and from this work.

$$n^*_{MEA} = n_{MEA} + n_{MEAH^+} \qquad 13\text{-}38$$

$$n^*_{MEACOO^{-1}} = n_{MEACOO^{-1}} \qquad 13\text{-}39$$

$$n^*_{CO_2} = n_{CO_2} + n_{CO_3^{-2}} + n_{HCO_3^{-1}} \qquad 13\text{-}40$$

Where
n_i is the true number of moles for each component per kilogram of water corresponding to the relative proton/carbon NMR peak areas,
ni* is the pseudo-component quantity based on experimental NMR data.

Poplsteinova (2004) and this work measured the peak areas or intensities for the corresponding carbons associated with each molecule(s) relative to an internal standard (dioxane) which allowed for a quantitative analysis of the NMR data. Please refer to Chapter III for more information about experimental NMR speciation methods.

Aspen Plus^{TM} was never designed to regress NMR speciation data; nevertheless, in this work we were able to develop a fortran subroutine to regress experimental NMR speciation data within DRS utilizing the schema presented in Figure 13.3-13. Within DRS, the user inputs the temperature in Kelvin, and the pseudo-component mole fractions for MEA, $MEACOO^{-1}$, CO_2, and H_2O. The fortran subtroutine then calculates the apparent component mole fractions based on the following expressions:

$$x^A_{MEA} = x^*_{MEA} + x^*_{MEACOO^{-1}} \qquad 13\text{-}41$$

$$x^A_{CO_2} = x^*_{CO_2} + x^*_{MEACOO^{-1}} \qquad 13\text{-}42$$

The fortran subroutine then calls a FLSH_FLASH subroutine within Aspen Plus^{TM} and performs a temperature-vapor fraction flash calculation. Once the FLASH subroutine converges, the fortran subroutine calls a PPSTUB_GETTRU subroutine within Aspen Plus^{TM} and extracts the true species mole fractions from the converged flash calculation.

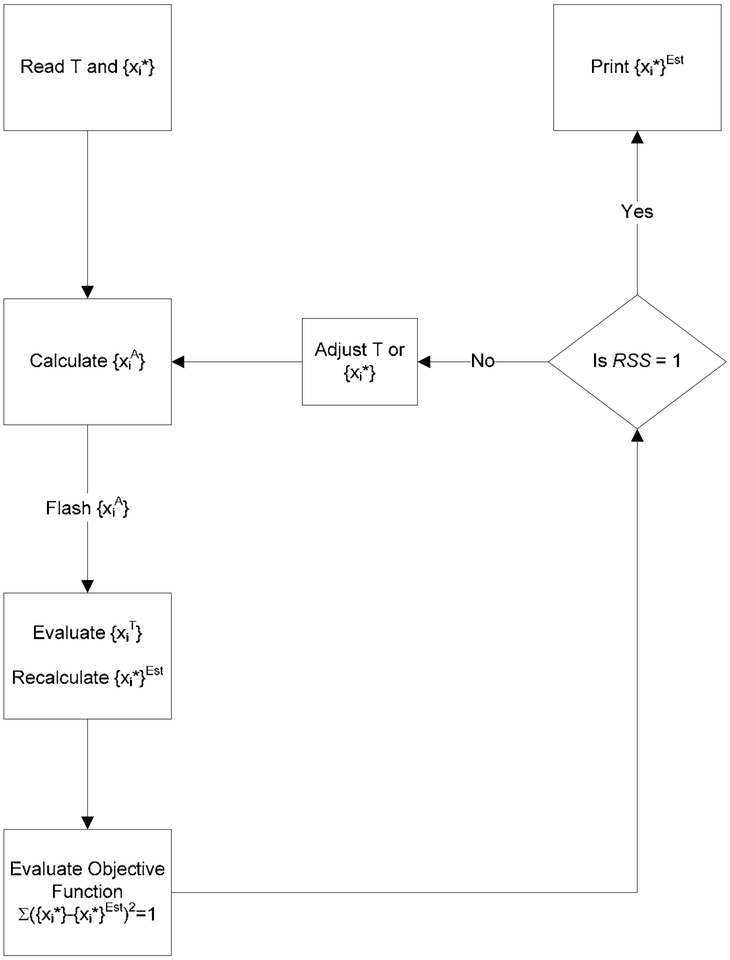

Figure 13.3-13. NMR Speciation Fortran Subroutine Schema Developed for Aspen Plus™.

The fortran subroutine then takes the true species mole fractions and calculates the estimated pseudo-component mole fractions based on the following expressions:

$$x_{MEA}^{*,est} = x_{MEA} + x_{MEAH^{+}} \qquad 13\text{-}43$$

$$x_{MEACOO^{-1}}^{*,est} = x_{MEACOO^{-1}} \qquad 13\text{-}44$$

$$x_{CO_2}^{*,est} = x_{CO_2} + x_{CO_3^{-2}} + x_{HCO_3^{-1}} \qquad 13\text{-}45$$

Finally, the fortran subroutine compares the estimated pseudo-component mole fractions to the experimental pseudo-component mole factions and calculates one minus the residual sum of squares (RSS). DRS then tries to minimize the difference between the RSS calculated from the fortran subroutine and the user property supplied to DRS by the user, a value of one, while DRS utilizes the Maximum Likelihood Method within Aspen Plus™ to minimize the overall objective function while adjusting each property variable. For more information about the complete fortran subroutine code, please refer to Appendix K for more information.

Examples of the experimental NMR speciation used in this work from Poplsteinova (2004) and this work for 7 m monoethanolamine solutions at 27, 40, and 60 °C are shown in Figure 13.3-14, Figure 13.3-15, and Figure 13.3-16, respectively.

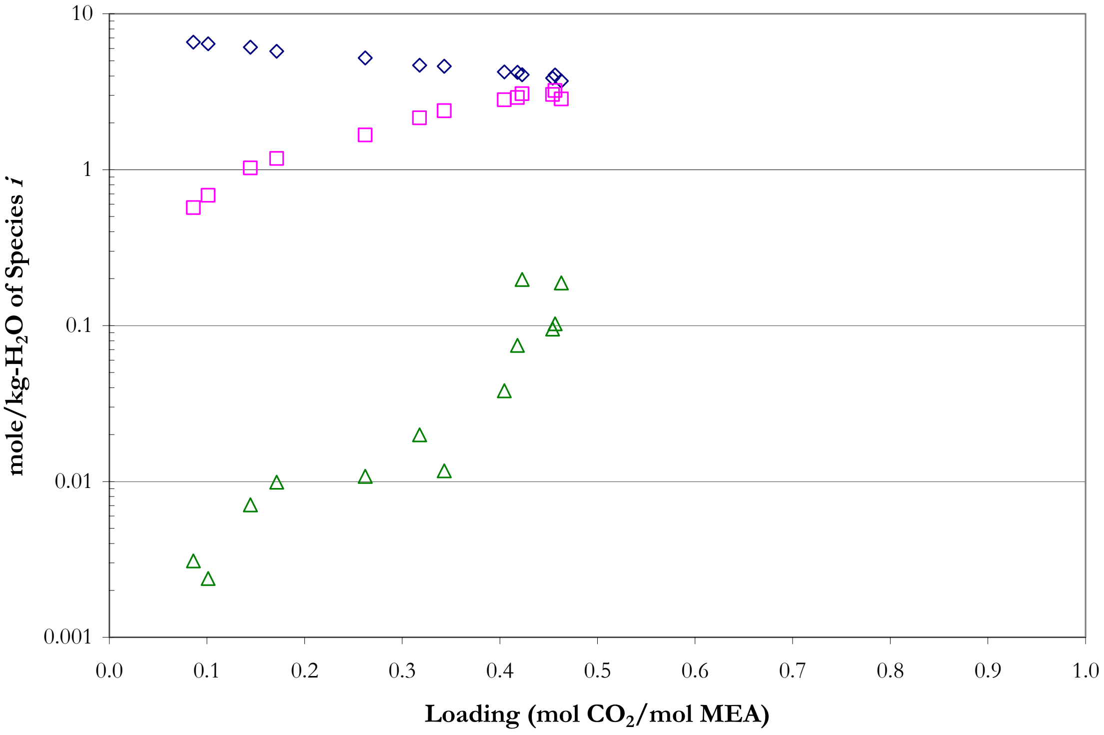

Figure 13.3-14. Liquid Phase Speciation from C^{13} NMR at 27 °C. Points: ◊, MEA+$MEAH^+$, □, $MEACOO^{-1}$, △, CO_3^{-2}+HCO_3^{-1}, from this work.

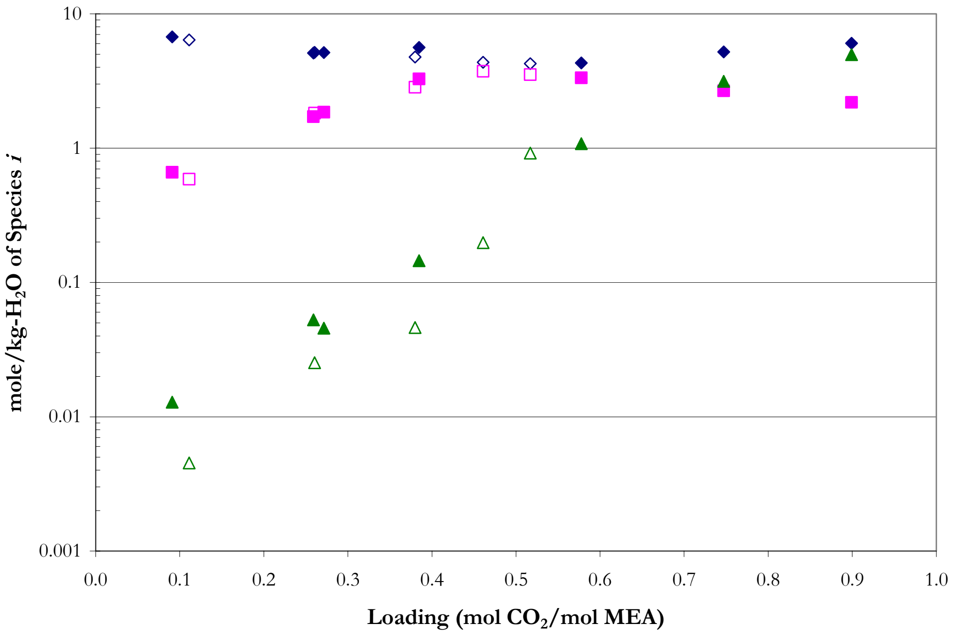

Figure 13.3-15. Liquid Phase Speciation from C^{13} NMR at 40 °C. Points: ♦, MEA+$MEAH^+$, ■, $MEACOO^{-1}$, ▲, CO_2+CO_3^{-2}+HCO_3^{-1}, from Poplsteinova (2004); ◊, MEA+$MEAH^+$, □, $MEACOO^{-1}$, Δ, CO_3^{-2}+HCO_3^{-1}, from this work.

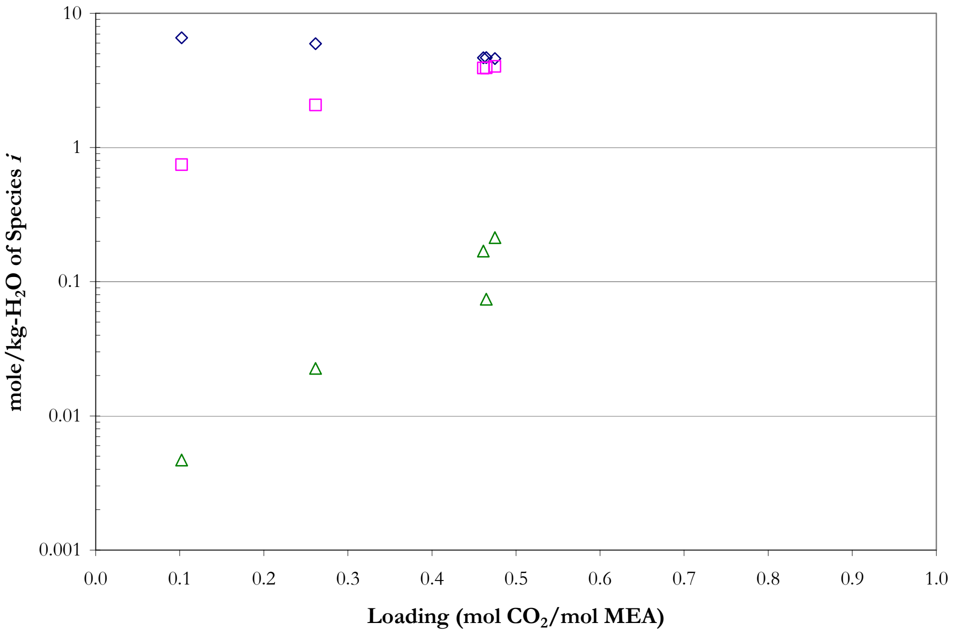

Figure 13.3-16. Liquid Phase Speciation from C^{13} NMR at 60 °C. Points: ◊, MEA+$MEAH^+$, □, $MEACOO^{-1}$, Δ, CO_3^{-2}+HCO_3^{-1}, from this work.

13.4 Data Regression

There are three types of binary interaction parameters in the elecNRTL model: molecule-molecule, $\tau_{m,m'}$ and $\tau_{m',m}$; molecule-electrolyte, $\tau_{m,ca}$ and $\tau_{ca,m}$; electrolyte-electrolyte (with a common cation or anion) $\tau_{ca,ca'}$ and $\tau_{ca',ca}$ or $\tau_{ca,c'a}$ and $\tau_{c'a,ca}$; and the molecule-electrolyte nonrandomness factor, $\alpha_{ca,m}$. Chen and Evans (1986) noted that in their regression attempts it was not always possible to obtain statistically significant results for all four types of binary interaction parameters. In this work, the molecule-electrolyte nonrandomness parameter was set to an arbitrary value of $\alpha_{ca,m} = 0.2$ for all correlations involving electrolyte systems as suggested by Chen and Evans (1986). In this work, the electrolyte – electrolyte parameters are generally negligible and were assumed to be zero.

For the elecNRTL model, default values for molecule-electrolyte and electrolyte-molecule interactions are given in Table 13.4-1.

Table 13.4-1. Default Binary Interaction Parameters for the elecNRTL Model in Aspen Plus™.

Binary Interaction Pairs	τ
Molecule-electrolyte	10
Electrolyte-molecule	-2
Water-electrolyte	8
Electrolyte-water	-4

The energy parameters are adjusted to provide the best fit to the data. The binary interaction parameters were assumed to be temperature dependent and were fitted to the following function of temperature:

$$\tau_{m,ca} = A_{m,ca} + \frac{B_{m,ca}}{T} + C_{m,ca}\left[\frac{\left(T^{ref} - T\right)}{T} + \ln\left(\frac{T}{T^{ref}}\right)\right] \tag{13-46}$$

$$\tau_{ca,m} = A_{ca,m} + \frac{B_{ca,m}}{T} + C_{ca,m}\left[\frac{\left(T^{ref} - T\right)}{T} + \ln\left(\frac{T}{T^{ref}}\right)\right] \tag{13-47}$$

where T^{ref} is defined as 298.15 K and electrolyte-electrolyte interactions follow a similar form as given above. A list of the aqueous electrolyte data sets that were examined in this work is given in Table 13.4-2.

Table 13.4-2. Experimental data used for regression of the H_2O-MEA-CO_2 systems.

	Obs.	T (°C)	σ_T	σ_{PCO2}	σ_{MEA}	σ_{CO2}	σ_y	Source
P_{CO2}	38	120.0	0.01	2.0%	0.1%	0.2%	0	Goldman and Leibush (1959)
	93	25.0 – 120.0	0.01	2.0%	0.1%	0.2%	0	Lee et al. (1976)
	16	40.0 – 120.0	0.01	2.0%	0.1%	0.2%	0	Lawson and Garst (1976)
	70	25.0 – 120.0	0.01	2.0%	0.1%	0.2%	0	Jou et al. (1995)
	19	120.0	0.01	2.0%	0.1%	0.2%	0	Ma'mun et al. (2005)
	55	40.0 – 120.0	0.01	2.0%	0.1%	0.2%	0	This work

	Obs.	T (°C)	σ_T	σ_{PMEA}	σ_{MEA}	σ_{CO2}	σ_y	Source
P_{MEA}	55	40.0 – 120.0	0.01	2.0%	0.1%	0.2%	0	This work

	Obs.	T (°C)	σ_T	σ_{MEA}	σ_{CO2}	σ_{Cp}	Source
Cp	102	40.0 – 120.0	0.1	0.1%	0.2%	2.0%	This work

	Obs.	T (°C)	σ_T	σ_{MEA}	σ_{CO2}	$\sigma_{\Delta H}$	Source
ΔH_{abs}	53	40.0 – 120.0	0.01	0.1%	0.2%	2.0%	Kim et al. (2007)

	Obs.	T (°C)	σ_T	σ_x	Source
NMR	23	20.0 – 40.0	0.01	1.0%	Poplsteinova (2004)
	53	27.0 – 60.0	0.01	1.0%	This work

The column labels σ_T , σ_{PCO2} , σ_{PMEA} , σ_{x_i} , σ_{y_i} , σ_{Cp} , $\sigma_{\Delta H}$, give the standard error associated with the temperature, partial pressure of CO_2, partial pressure of MEA, liquid mole fraction, vapor mole fraction, the specific heat capacity, and the enthalpy of CO_2

absorption, respectively, with each data set. DRS suggested standard error default values were assigned unless otherwise stated by the author. Overall, 577 experimental data points were included in the model regression..

Table 13.4-3 shows the regression summary statistics output for estimates of the adjustable binary parameter coefficients, the infinite dilution aqueous phase free energy of formation, the infinite dilution aqueous phase enthalpy of formation, and the infinite dilution aqueous phase heat capacity polynomial for monoethanolamine carbamate after performing a nonlinear regression for the full model using DRS in Aspen Plus^{TM}.

Table 13.4-3. DRS Regression Output for Full H_2O-MEA-CO_2 System Model.

	Interacting Species				
	i	j	k	Estimate	σ wrt Estimate
1	ΔG_{MEACOO}			-492922521	614438
2	ΔH_{MEACOO}			-707209084	10666596
3-CP-A	$MEACOO^{-1}$			-2408071	4943171
4-CP-B	$MEACOO^{-1}$			17268	29480
5-CP-C	$MEACOO^{-1}$			-26.0	43.3
6-$A_{m,ca}$	H_2O	$MEAH^+$	HCO_3^{-1}	12.8	2.66
7-$B_{m,ca}$	H_2O	$MEAH^+$	HCO_3^{-1}	156	824
8-$C_{m,ca}$	H_2O	$MEAH^+$	HCO_3^{-1}	24.6	17.8
9-$A_{ca,m}$	$MEAH^+$	HCO_3^{-1}	H_2O	-3.81	1.125
10-$B_{ca,m}$	$MEAH^+$	HCO_3^{-1}	H_2O	-215	348
11-$C_{ca,m}$	$MEAH^+$	HCO_3^{-1}	H_2O	-5.89	8.00
12-$A_{m,ca}$	H_2O	$MEAH^+$	$MEACOO^{-1}$	19.0	2.38
13-$B_{m,ca}$	H_2O	$MEAH^+$	$MEACOO^{-1}$	-790	740
14-$C_{m,ca}$	H_2O	$MEAH^+$	$MEACOO^{-1}$	-19.7	16.8
15-$A_{ca,m}$	$MEAH^+$	$MEACOO^{-1}$	H_2O	-7.39	0.523
16-$B_{ca,m}$	$MEAH^+$	$MEACOO^{-1}$	H_2O	432	167
17-$C_{ca,m}$	$MEAH^+$	$MEACOO^{-1}$	H_2O	1.76	3.03

	Interacting Species				
	i	j	k	Estimate	σ wrt Estimate
18-$A_{m,ca}$	MEA	$MEAH^+$	HCO_3^{-1}	1.79	88.1
19-$B_{m,ca}$	MEA	$MEAH^+$	HCO_3^{-1}	3129	28486
20-$C_{m,ca}$	MEA	$MEAH^+$	HCO_3^{-1}	66.0	514
21-$A_{ca,m}$	$MEAH^+$	HCO_3^{-1}	MEA	-30.8	38.0
22-$B_{ca,m}$	$MEAH^+$	HCO_3^{-1}	MEA	6982	12102
23-$C_{ca,m}$	$MEAH^+$	HCO_3^{-1}	MEA	440	359
24-$A_{m,ca}$	MEA	$MEAH^+$	$MEACOO^{-1}$	16.9	3.76
25-$B_{m,ca}$	MEA	$MEAH^+$	$MEACOO^{-1}$	-2810	1236
26-$C_{m,ca}$	MEA	$MEAH^+$	$MEACOO^{-1}$	22.4	15.9
27-$A_{ca,m}$	$MEAH^+$	$MEACOO^{-1}$	MEA	-13.6	5.40
28-$B_{ca,m}$	$MEAH^+$	$MEACOO^{-1}$	MEA	1865	1770
29-$C_{ca,m}$	$MEAH^+$	$MEACOO^{-1}$	MEA	16.5	16.3
30-$A_{m,ca}$	CO_2	$MEAH^+$	HCO_3^{-1}	49.2	287
31-$B_{m,ca}$	CO_2	$MEAH^+$	HCO_3^{-1}	430	81739
32-$C_{m,ca}$	CO_2	$MEAH^+$	HCO_3^{-1}	2263	10709
33-$A_{ca,m}$	$MEAH^+$	HCO_3^{-1}	CO_2	-5.89	1277
34-$B_{ca,m}$	$MEAH^+$	HCO_3^{-1}	CO_2	14445	406897
35-$C_{ca,m}$	$MEAH^+$	HCO_3^{-1}	CO_2	659	14857

Residual Sum of Squares: 298,712
Residual Root Mean Square: 24.869
Degree of Freedom: 542

Recall that the standard error of an estimate is the estimated standard deviation of that statistic. Notice that eighteen of the estimates are smaller relative to their standard errors. Table 13.4-4 gives a complete description of the variability of the coefficient estimates by examining the correlations between the estimates.

Table 13.4-4. Correlation Matrix of the Coefficient Estimates for the Full H_2O-MEA-CO_2 System Model

Parameter	1	2	3	4	5	6	7	8	9	10	11	12	13	14	15	16	17	18	19	20	21	22	23	24	25	26	27	28	29	30	31	32	33	34	35
1	1.00																																		
2	0.60	1.00																																	
3	-0.20	-0.40	1.00																																
4	0.15	0.31	-0.99	1.00																															
5	-0.10	-0.21	0.97	-0.99	1.00																														
6	-0.48	-0.67	0.28	-0.23	0.16	1.00																													
7	0.50	0.65	-0.28	0.22	-0.15	-1.00	1.00																												
8	0.22	0.17	-0.32	0.33	-0.32	-0.61	0.61	1.00																											
9	0.43	0.51	-0.18	0.13	-0.07	-0.92	0.91	0.68	1.00																										
10	-0.45	-0.52	0.18	-0.13	0.08	0.92	-0.92	-0.69	-0.99	1.00																									
11	-0.15	0.17	0.03	-0.05	0.06	0.15	-0.15	-0.73	-0.43	0.41	1.00																								
12	-0.19	-0.43	0.53	-0.50	0.45	0.33	-0.31	-0.28	-0.09	0.07	-0.15	1.00																							
13	0.21	0.43	-0.53	0.50	-0.45	-0.33	0.31	0.28	0.09	-0.07	0.14	-1.00	1.00																						
14	-0.02	0.05	-0.45	0.48	-0.51	-0.04	0.03	0.22	-0.17	0.18	0.14	-0.84	0.83	1.00																					
15	-0.47	-0.59	-0.11	0.17	-0.24	0.44	-0.44	-0.09	-0.58	0.59	0.17	-0.41	0.41	0.68	1.00																				
16	0.50	0.58	0.11	-0.17	0.24	-0.44	0.44	0.10	0.58	-0.59	-0.18	0.40	-0.41	-0.67	-1.00	1.00																			
17	0.32	0.41	0.07	-0.11	0.16	-0.31	0.31	0.05	0.49	-0.51	-0.24	0.57	-0.57	-0.81	-0.93	0.92	1.00																		
18	-0.26	-0.55	0.35	-0.30	0.24	0.54	-0.50	-0.23	-0.32	0.29	-0.22	0.60	-0.59	-0.33	0.00	0.00	0.14	1.00																	
19	0.28	0.54	-0.35	0.31	-0.25	-0.53	0.49	0.23	0.31	-0.28	0.22	-0.60	0.60	0.34	0.01	-0.02	-0.15	-1.00	1.00																
20	-0.03	0.19	-0.21	0.19	-0.17	-0.06	0.06	-0.05	-0.18	0.17	0.38	-0.38	0.36	0.26	0.23	-0.23	-0.30	-0.63	0.61	1.00															
21	-0.04	-0.41	0.00	0.06	-0.12	0.26	-0.23	0.15	-0.11	0.09	-0.33	0.27	-0.25	-0.05	0.11	-0.11	0.02	0.57	-0.54	-0.68	1.00														
22	0.07	0.41	0.00	-0.05	0.12	-0.26	0.23	-0.14	0.12	-0.10	0.32	-0.28	0.25	0.05	-0.12	0.12	-0.02	-0.59	0.56	0.66	-1.00	1.00													
23	-0.11	0.05	0.03	-0.03	0.03	-0.15	0.14	0.31	0.11	-0.10	-0.16	-0.22	0.21	0.25	0.14	-0.14	-0.22	-0.25	0.23	0.27	-0.46	0.44	1.00												
24	0.11	0.34	0.05	-0.10	0.15	-0.35	0.34	0.14	0.30	-0.31	0.03	-0.15	0.14	-0.09	-0.25	0.25	0.14	-0.31	0.30	0.26	-0.47	0.46	0.29	1.00											
25	-0.18	-0.09	-0.09	0.11	-0.13	0.15	-0.17	-0.10	-0.17	0.19	0.07	-0.03	0.02	0.12	0.17	-0.18	-0.11	0.06	-0.07	-0.06	0.12	-0.12	-0.06	-0.87	1.00										
26	0.23	0.01	-0.09	0.09	-0.08	0.11	-0.10	-0.26	-0.12	0.12	0.15	0.07	-0.06	-0.12	-0.05	0.06	0.09	0.07	-0.04	-0.07	0.22	-0.21	-0.70	-0.27	-0.01	1.00									
27	0.45	0.52	-0.40	0.36	-0.30	-0.41	0.42	0.34	0.26	-0.27	-0.02	-0.65	0.66	0.40	0.00	0.01	-0.13	-0.49	0.51	0.04	0.17	-0.16	-0.09	0.19	-0.22	0.20	1.00								
28	-0.48	-0.45	0.38	-0.34	0.30	0.36	-0.37	-0.32	-0.22	0.23	0.05	0.59	-0.61	-0.38	-0.02	0.01	0.13	0.41	-0.44	0.02	-0.26	0.25	0.14	-0.15	0.24	-0.27	-0.99	1.00							
29	-0.12	-0.17	0.51	-0.53	0.53	0.16	-0.16	-0.32	0.05	-0.04	-0.09	0.73	-0.73	-0.75	-0.48	0.47	0.56	0.46	-0.48	-0.27	-0.19	0.19	-0.09	0.01	0.02	0.00	-0.77	0.76	1.00						
30	-0.01	-0.07	0.00	0.00	-0.01	0.06	-0.06	0.01	-0.02	0.02	-0.10	0.01	0.00	0.00	0.04	-0.04	-0.02	0.11	-0.11	0.01	-0.02	0.01	-0.02	-0.03	-0.03	0.14	-0.04	0.02	0.04	1.00					
31	-0.07	0.04	-0.02	0.02	-0.02	-0.02	0.01	-0.04	-0.04	0.04	0.13	-0.04	0.04	0.05	0.04	-0.05	-0.04	-0.12	0.12	0.00	0.03	-0.02	0.02	0.00	0.07	-0.17	0.03	-0.02	-0.07	-0.97	1.00				
32	0.12	0.25	-0.02	-0.02	0.06	-0.19	0.19	0.01	0.15	-0.16	0.09	-0.02	0.01	-0.15	-0.24	0.24	0.19	-0.14	0.13	0.11	-0.17	0.17	0.01	0.21	-0.12	-0.05	0.10	-0.08	0.06	-0.40	0.29	1.00			
33	-0.22	-0.17	-0.14	0.16	-0.19	0.01	-0.01	0.11	-0.02	0.03	-0.06	-0.16	0.17	0.25	0.32	-0.33	-0.26	0.02	-0.01	-0.06	0.11	-0.12	0.05	-0.08	0.08	-0.12	0.01	-0.01	-0.18	0.37	-0.20	-0.31	1.00		
34	0.22	0.17	0.14	-0.17	0.19	0.00	0.00	-0.12	0.01	-0.02	0.05	0.16	-0.17	-0.25	-0.31	0.32	0.25	-0.03	0.02	0.05	-0.11	0.12	-0.05	0.07	-0.07	0.13	-0.02	0.02	0.18	-0.36	0.20	0.30	-1.00	1.00	
35	0.18	0.34	-0.01	-0.03	0.09	-0.22	0.23	-0.03	0.16	-0.18	0.15	-0.04	0.03	-0.19	-0.31	0.31	0.24	-0.21	0.20	0.22	-0.28	0.28	0.00	0.24	-0.13	0.02	0.12	-0.09	0.08	-0.32	0.18	0.85	-0.67	0.66	1.00

Table 13.4-4 shows 18 highly negative and positive correlations out of a possible 630. The highly correlated parameters are between the temperature dependent coefficients and the respective constant for the each energy parameter estimate, but the correlation between other coefficients is relatively small, suggesting the amount of temperature dependent parameters might be usefully removed from the model without significant loss of information.

After performing backward elimination using DRS, the following "optimum" model regression summary statistics output for estimates of the adjustable binary parameter coefficients are shown in Table 13.4-5.

Table 13.4-5. DRS Regression Output for Optimum H_2O-MEA-CO_2 System Model.

	Interacting Species				
	i	j	k	Estimate	σ wrt Estimate
1	ΔG_{MEACOO}			-492410636	527668
2	ΔH_{MEACOO}			-723540100	5262527
3-CP-A	$MEACOO^{-1}$			5332580	5220248
4-CP-B	$MEACOO^{-1}$			-28100	29167
5-CP-C	$MEACOO^{-1}$			39.9	40.7
6-$A_{m,ca}$	H_2O	$MEAH^+$	HCO_3^{-1}	3.35	3.17
7-$B_{m,ca}$	H_2O	$MEAH^+$	HCO_3^{-1}	3060	957
8-$C_{m,ca}$	H_2O	$MEAH^+$	HCO_3^{-1}	59.9	23.7
9-$A_{ca,m}$	$MEAH^+$	HCO_3^{-1}	H_2O	0.0843	1.670
10-$B_{ca,m}$	$MEAH^+$	HCO_3^{-1}	H_2O	-1416	506
11-$C_{ca,m}$	$MEAH^+$	HCO_3^{-1}	H_2O	-26.5	12.9
12-$A_{m,ca}$	H_2O	$MEAH^+$	$MEACOO^{-1}$	15.8	1.10
13-$B_{m,ca}$	H_2O	$MEAH^+$	$MEACOO^{-1}$	368	359
14-$C_{m,ca}$	H_2O	$MEAH^+$	$MEACOO^{-1}$	0.0	-
15-$A_{ca,m}$	$MEAH^+$	$MEACOO^{-1}$	H_2O	-4.28	0.380
16-$B_{ca,m}$	$MEAH^+$	$MEACOO^{-1}$	H_2O	-575	124
17-$C_{ca,m}$	$MEAH^+$	$MEACOO^{-1}$	H_2O	-11.9	1.17
18-$A_{m,ca}$	MEA	$MEAH^+$	HCO_3^{-1}	-102	43.0
19-$B_{m,ca}$	MEA	$MEAH^+$	HCO_3^{-1}	32855	13529
20-$C_{m,ca}$	MEA	$MEAH^+$	HCO_3^{-1}	2004	409
21-$A_{ca,m}$	$MEAH^+$	HCO_3^{-1}	MEA	25.3	19.9
22-$B_{ca,m}$	$MEAH^+$	HCO_3^{-1}	MEA	-8743	6240
23-$C_{ca,m}$	$MEAH^+$	HCO_3^{-1}	MEA	960	249
24-$A_{m,ca}$	MEA	$MEAH^+$	$MEACOO^{-1}$	20.1	1.69
25-$B_{m,ca}$	MEA	$MEAH^+$	$MEACOO^{-1}$	-4254	496
26-$C_{m,ca}$	MEA	$MEAH^+$	$MEACOO^{-1}$	90.0	23.2
27-$A_{ca,m}$	$MEAH^+$	$MEACOO^{-1}$	MEA	-35.3	5.17
28-$B_{ca,m}$	$MEAH^+$	$MEACOO^{-1}$	MEA	9202	1706
29-$C_{ca,m}$	$MEAH^+$	$MEACOO^{-1}$	MEA	59.3	15.4
30-$A_{m,ca}$	CO_2	$MEAH^+$	HCO_3^{-1}	-189	411
31-$B_{m,ca}$	CO_2	$MEAH^+$	HCO_3^{-1}	62022	130433
32-$C_{m,ca}$	CO_2	$MEAH^+$	HCO_3^{-1}	1710	3189
33-$A_{ca,m}$	$MEAH^+$	HCO_3^{-1}	CO_2	-174	264
34-$B_{ca,m}$	$MEAH^+$	HCO_3^{-1}	CO_2	55673	87032
35-$C_{ca,m}$	$MEAH^+$	HCO_3^{-1}	CO_2	775	1370

Residual Sum of Squares: 286,715
Residual Root Mean Square: 24.343
Degree of Freedom: 541

Notice that nine of the estimates are smaller relative to their standard errors. Comparing the estimates from the full model to the "optimum" model, there was relatively little difference between the estimated values. With the elimination of one parameter, the optimum model was unable to provide adequate predictions to the experimental data even though the sum of squares decreased by 4.01 percent. Furthermore, none of the other possible submodels proposed by backward elimination were able to provide adequate predictions and capture systematic trends with the data sets. **In this work, we chose the full model to describe the interactions in the H_2O-MEA-CO_2 system.**

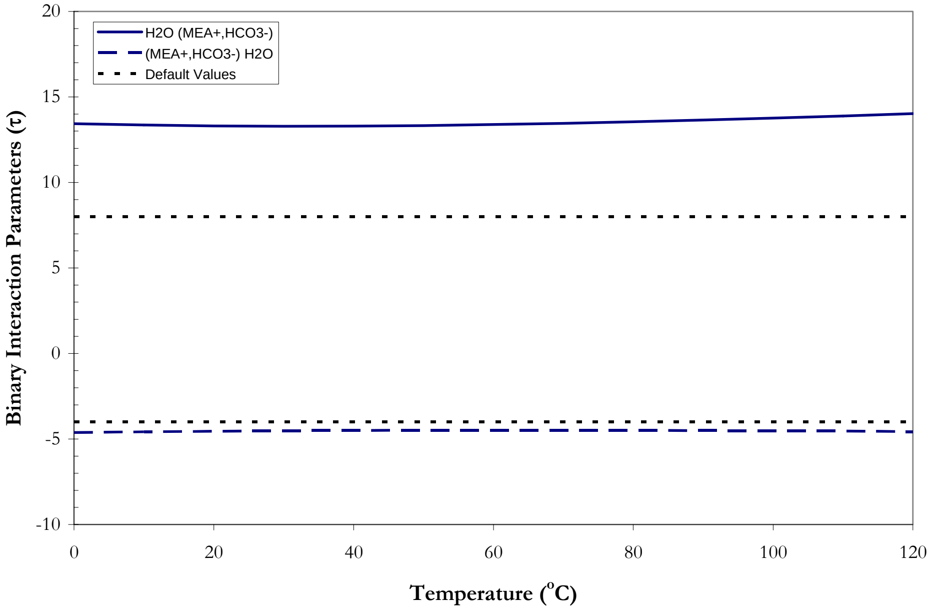

Figure 13.4-1. Binary Interaction Parameters for H_2O,$MEAH^+$/HCO_3^{-1}.

Estimated Binary Interaction Parameters

With the determination of the estimates for the binary interaction parameters known for the full model, we can use Equation 13-47 and Equation 13-48 to illustrate the temperature dependence of the molecule-electrolyte, electrolyte-molecule, water-electrolyte, and electrolyte-water energy parameters as shown in Figure 13.4-1 through Figure 13.4-5.

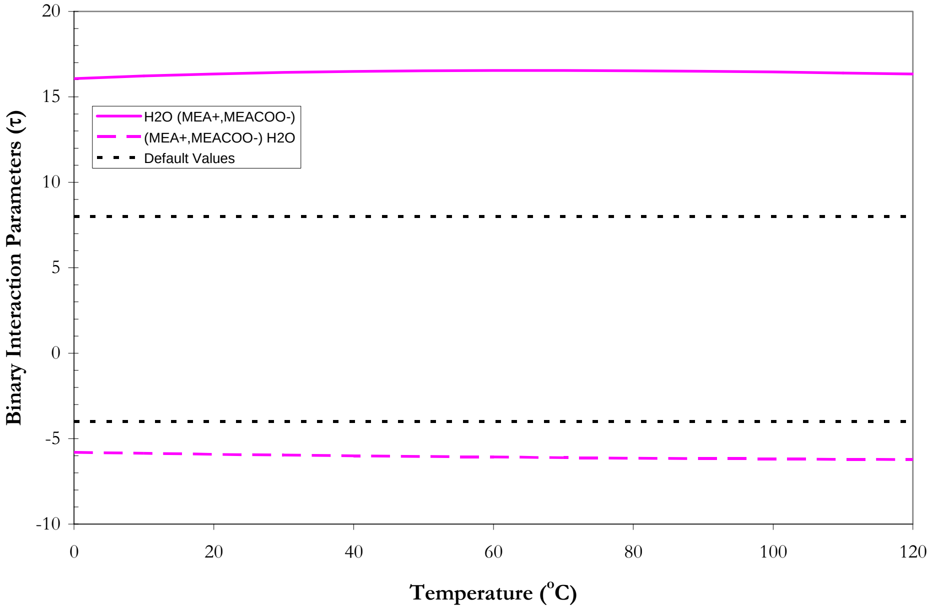

Figure 13.4-2. Binary Interaction Parameters for H_2O,$MEAH^+$/$MEACOO^{-1}$.

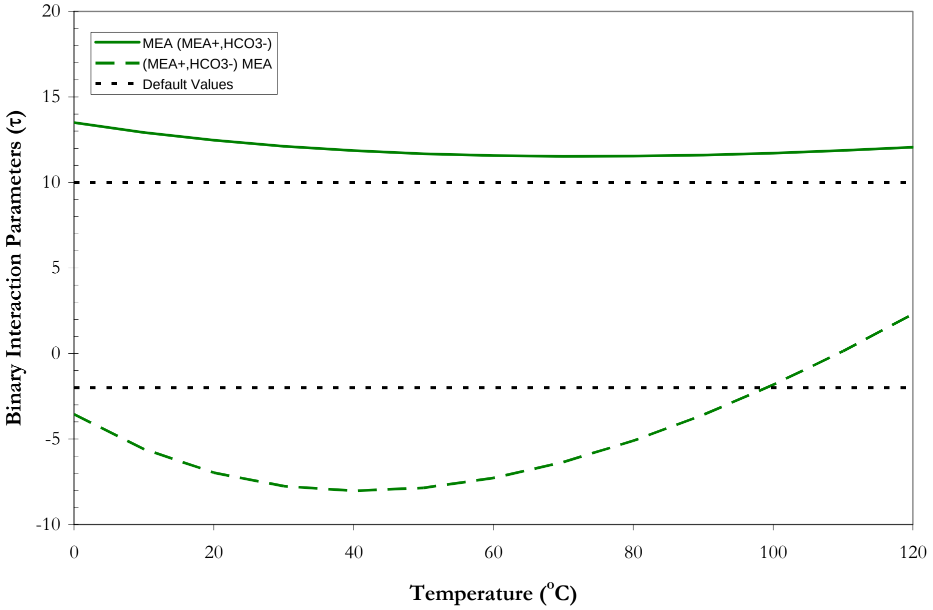

Figure 13.4-3. Binary Interaction Parameters for MEA,$MEAH^+$/HCO_3^{-1}.

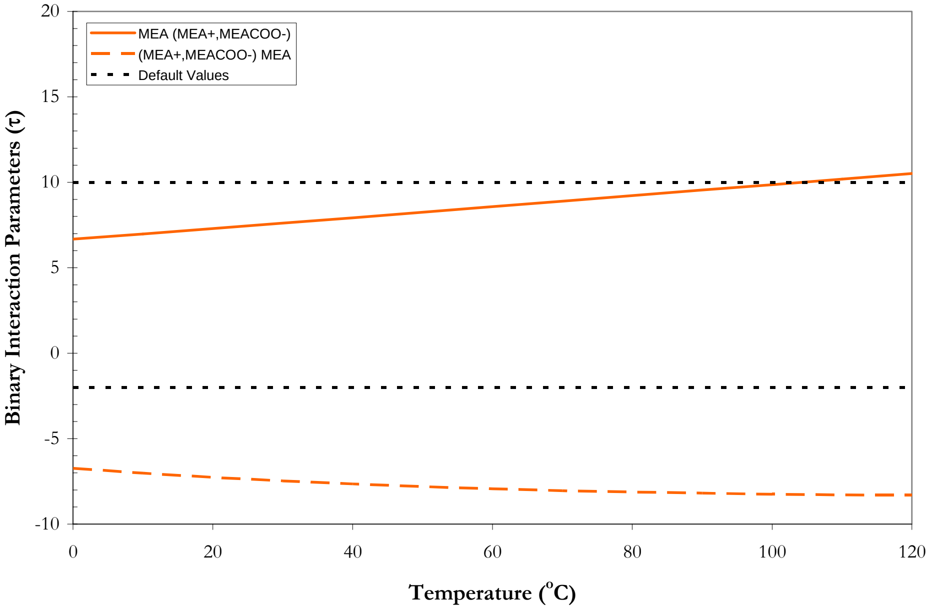

Figure 13.4-4. Binary Interaction Parameters for MEA,$MEAH^{+}/MEACOO^{-1}$.

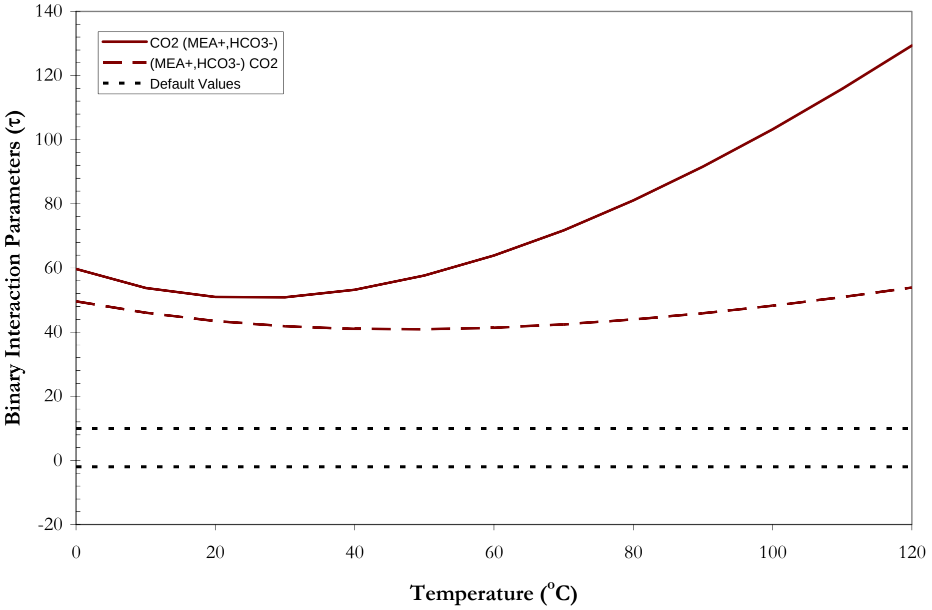

Figure 13.4-5. Binary Interaction Parameters for CO_2,$MEAH^{+}/HCO_3^{-1}$.

13.4.1 *Full Model Results*

With the determination of the estimates for the binary interaction parameters known for the full model, a simple Aspen PlusTM Flash model was used to test the predictive capability of the H_2O-MEA-CO_2 model against literature data. For each data point, the deviation between the experimental and estimated values is expressed in terms of the average absolute relative deviation (AARD) given in Table 13.4-6 and Table 13.4-7. Overall, the model adequately describes the H_2O-MEA-CO_2 property data listed above within an average absolute relative error of ± 24.79 percent, with the exception of a few outliers.

Table 13.4-6. Absolute Percent Relative Error for the H_2O-MEA-CO_2 Full Model.

CO_2 Solubility	**P^{CO2} AARD**	**Loading AARD**
This work	30.01	2.06
Lee et al. (1976)	21.67	0.84
Lawson and Garst (1976)	67.99	1.85
Jou et al. (1995)	13.55	0.52
Goldman and Leibush (1959)	13.93	0.86
Ma'mun et al. (2005)	27.06	1.60
MEA Solubility	**P^{MEA}**	**Loading**
This work	35.22	2.22
Enthalpy of CO_2 Abs.	**ΔH_{ABS}**	**Loading**
Kim et al. (2007)	12.91	0.57
Specific Heat Capacity	**C_P**	**Loading**
This work	0.79	0.037
Overall	**24.79**	**1.17**

Table 13.4-7. Absolute Percent Relative Error for the H_2O-MEA-CO_2 Full Model Speciation.

NMR Speciation	$MEA+MEAH^{+}$ AARD	$MEACOO^{-1}$ AARD	$CO_2+CO_3^{-2}+HCO_3^{-1}$ AARD	Loading AARD
This work	7.25	4.84	0.04	8.30
Poplsteinova (2004)	9.13	5.62	1.07	10.57

13.5 Full Model Predictions

In this work, we have compiled a large database of consistent high quality data needed to obtain a unique set of binary interactions parameters to describe the H_2O-MEA-CO_2 system. The remainder of this chapter will be devoted to using our model as a predictive tool as described in the subsequent sections.

13.5.1 *CO_2 Solubility and Amine Volatility*

Figure 13.5-1 through Figure 13.5-15 gives the results of fit for the experimental CO_2 solubility at 3.5, 7 and 11 m MEA versus loading from 25 – 120 °C. Overall, the full model adequately describes the CO_2 solubility data within an average absolute relative error of ± 27.19 percent.

CO_2 Solubility Predictions for 3.5 m MEA

Thoughout Figure 13.5-1 through Figure 13.5-6, the full model overestimates the solubility of CO_2 by a factor of 3. This error is due to full model over estimating the liquid phase speciation as shown in Figure 13.5-44, implying that an error may exist within either the experimental NMR speciation data or the experimental CO_2 solubility data. On the other hand, since this system lies at the boundary of the chosen experimental data, the error could be a result of the regression analysis.

Model predictions based on the current Aspen Plus model by Austgen (1989) are compared to predictions from this work. Overall, predictions from Austgen (1989) accurately estimate the CO_2 solubility at low loading from 25 to 120 ^oC, but overestimate the CO_2 solubility at moderate to high loading. Austgen (1989) chose to regress only CO_2 solubility data from Lee et al. (1976), Isaacs et al. (1980), Lawson and Garst (1976), Jones et al. (1959), and Muhlbauer and Monaghan (1957) by regressing binary interaction parameters and coefficients for the temperature dependent chemical equilibrium constant for the monoethanolamine carbamate. Over the course of eighteen years, previous works have found inconsistencies within several of the above mentioned data sets and an error in loading analysis of Lee et al. (1976). However, the Austgen (1989) model has served as a cornerstone in thermodynamic model comparisons for the H_2O-MEA-CO_2 system because the model adequately predicts the solubility of CO_2 over a large range in concentration, loading, and temperature.

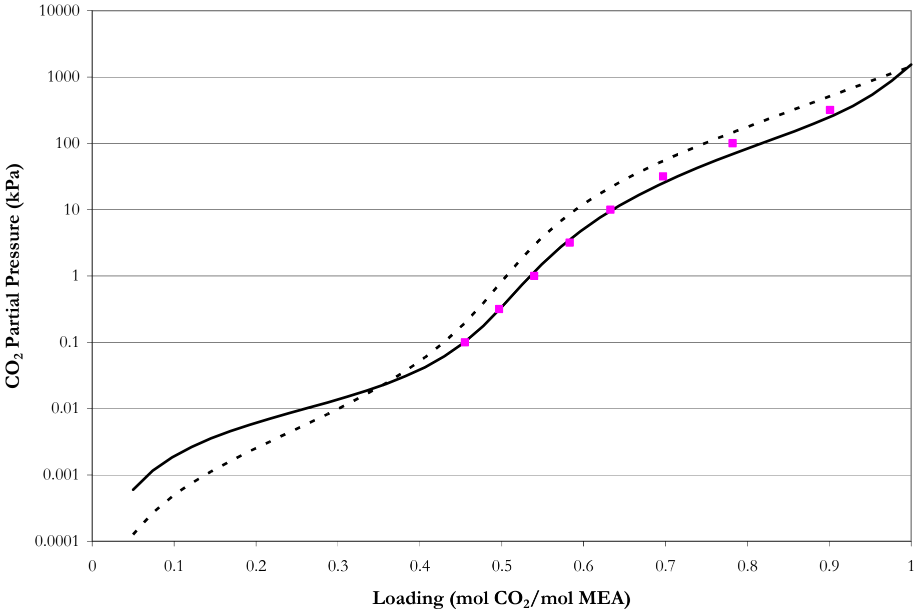

Figure 13.5-1. Comparison between Experimental and Predicted CO_2 Solubility in ~3.5 m MEA at 25 °C. Points: ♦, Lawson and Garst (1976), ■, Lee et al. (1976). Lines: · · ·, Austgen (1989), —, this work.

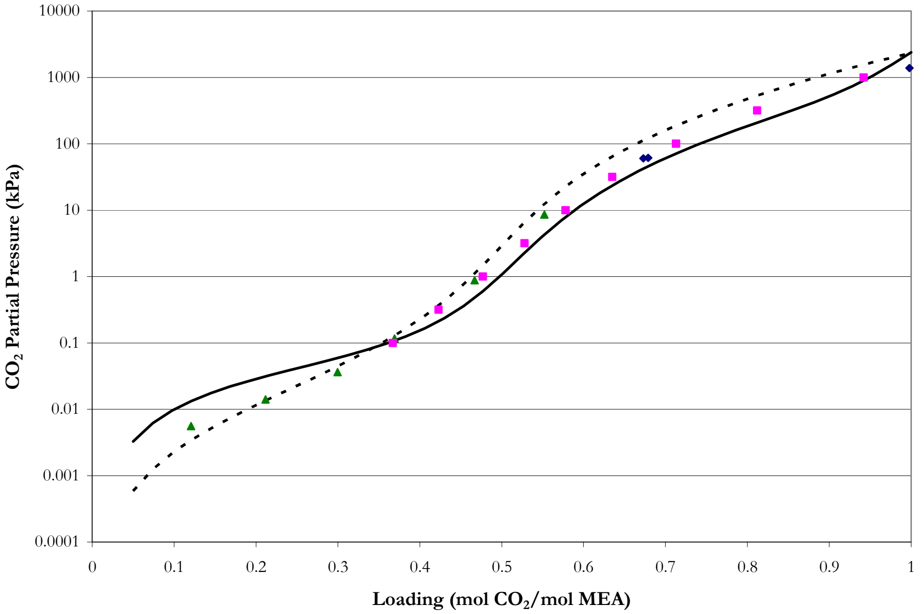

Figure 13.5-2. Comparison between Experimental and Predicted CO_2 Solubility in ~3.5 m MEA at 40 °C. Points: ♦, Lawson and Garst (1976), ■, Lee et al. (1976), ▲, this work. Lines: · · ·, Austgen (1989), —, this work.

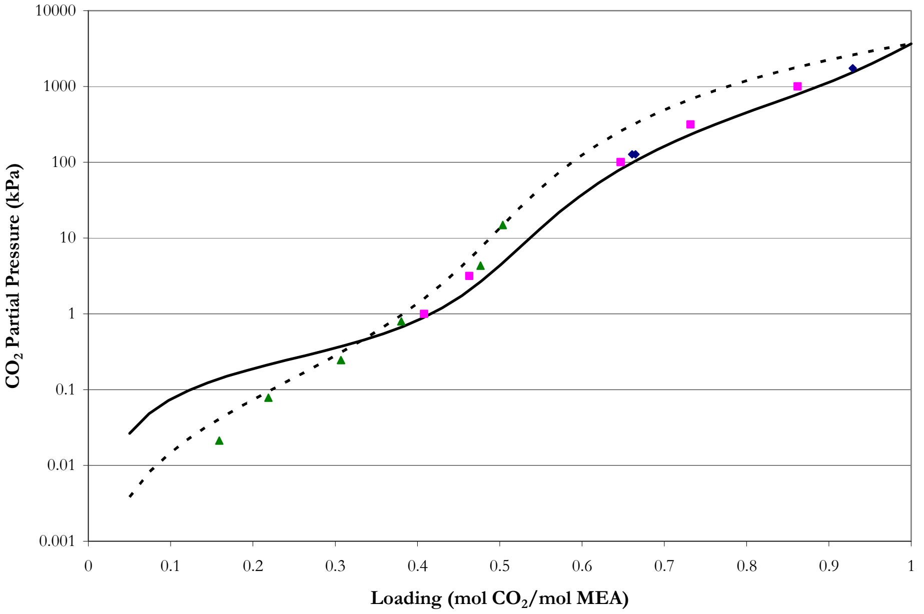

Figure 13.5-3. Comparison between Experimental and Predicted CO$_2$ Solubility in ~3.5 m MEA at 60 °C. Points: ♦, Lawson and Garst (1976), ■, Lee et al. (1976), ▲, this work. Lines: · · ·, Austgen (1989), —, this work.

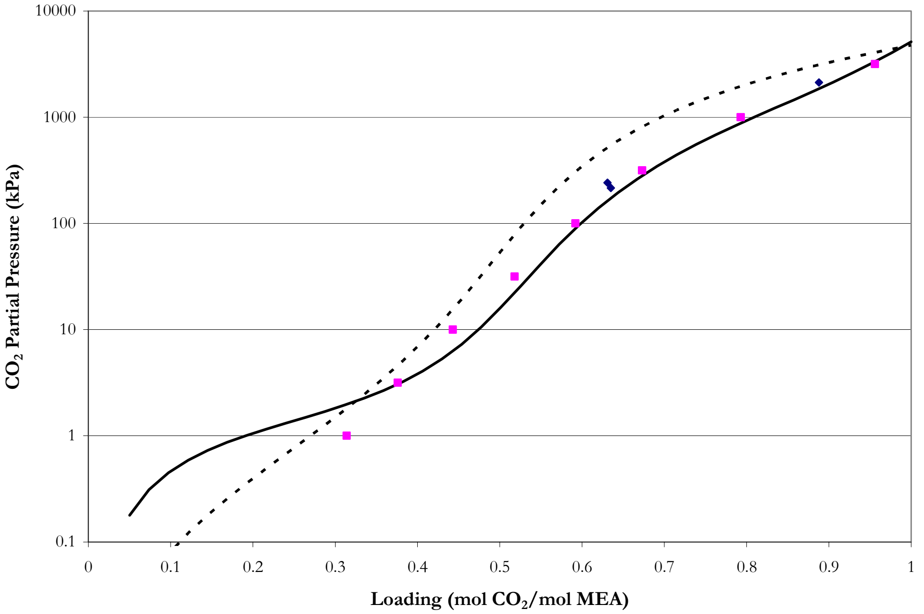

Figure 13.5-4. Comparison between Experimental and Predicted CO$_2$ Solubility in ~3.5 m MEA at 80 °C. Points: ♦, Lawson and Garst (1976), ■, Lee et al. (1976). Lines: · · ·, Austgen (1989), —, this work.

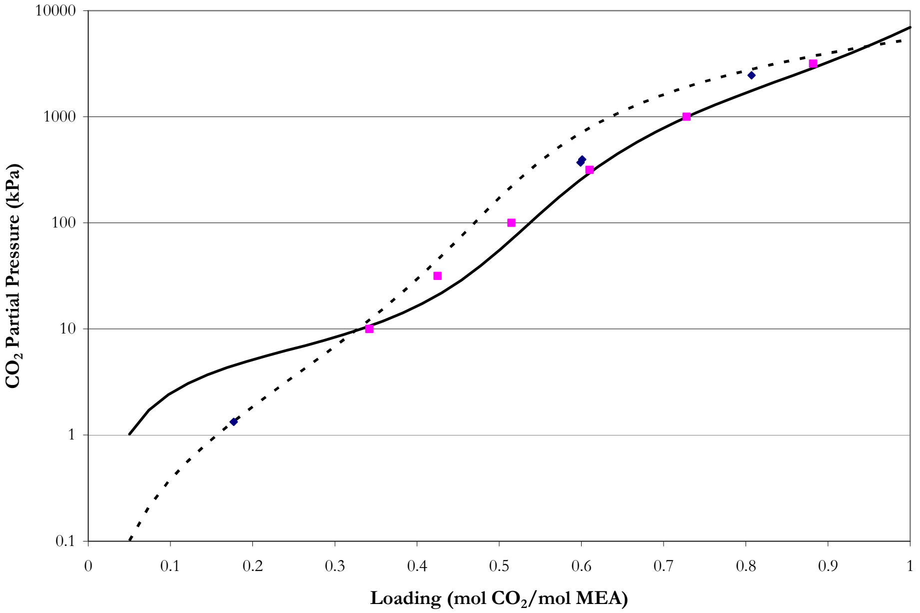

Figure 13.5-5. Comparison between Experimental and Predicted CO$_2$ Solubility in ~3.5 m MEA at 100 °C. Points: ♦, Lawson and Garst (1976), ■, Lee et al. (1976). Lines: · · ·, Austgen (1989), —, this work.

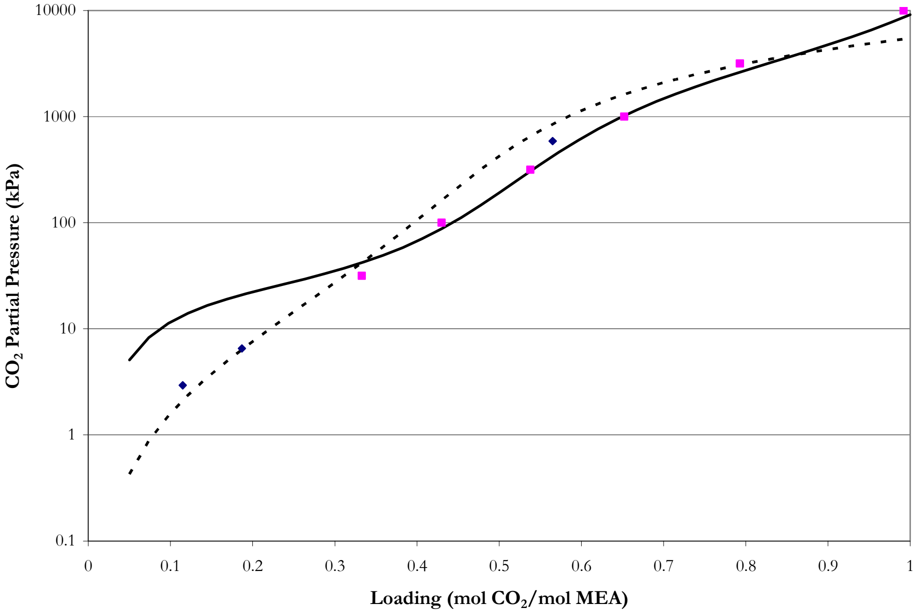

Figure 13.5-6. Comparison between Experimental and Predicted CO$_2$ Solubility in ~3.5 m MEA at 120 °C. Points: ♦, Lawson and Garst (1976), ■, Lee et al. (1976). Lines: · · ·, Austgen (1989), —, this work.

CO_2 Solubility Predictions for 7 m MEA

In Figure 13.5-7 through Figure 13.5-12 the full model adequately predicts the solubility of CO_2 over the entire range of loading and temperature. Model predictions from Austgen (1989) are compared to predictions from this work. Overall, predictions from Austgen (1989) overestimate the CO_2 solubility as compared to the experimental data. In 1995, Jou et al. (1995) reported an 0.04 error in loading within the work by Lee et al. (1976). After 1995, most works have made this correction before regressing the Lee et al. (1976) data set. The overestimation in the Austgen (1989) model is due to this reason since the Lee et al. (1976) data set was a major part of the model regression.

Model predictions based on the work by Freguia (2002) are also compared to predictions from this work. Freguia (2002) reproduced the model by Austgen (1989) and included interaction parameters to match the CO_2 solubility data by Jou et al. (1995) over the range in loading from 0.1 to 0.5 mole of CO_2 per mole of MEA. In addition, Freguia (2002) included heat stable salts (i.e. formate) effects by assigning the same interaction parameters associated with $MEACOO^{-1}$. Heat stable salts are a bi-product of MEA reacting with a strong acid to form formate or sulfate, thus altering the chemical equilibrium by increasing the partial pressure of CO_2 at a given loading. In this work, we chose not to include heat stable salt effects. We would recommend that in future work, the effects of heat stable salts be included in a rigorous thermodynamic model to accurately represent industrial chemical equilibrium.

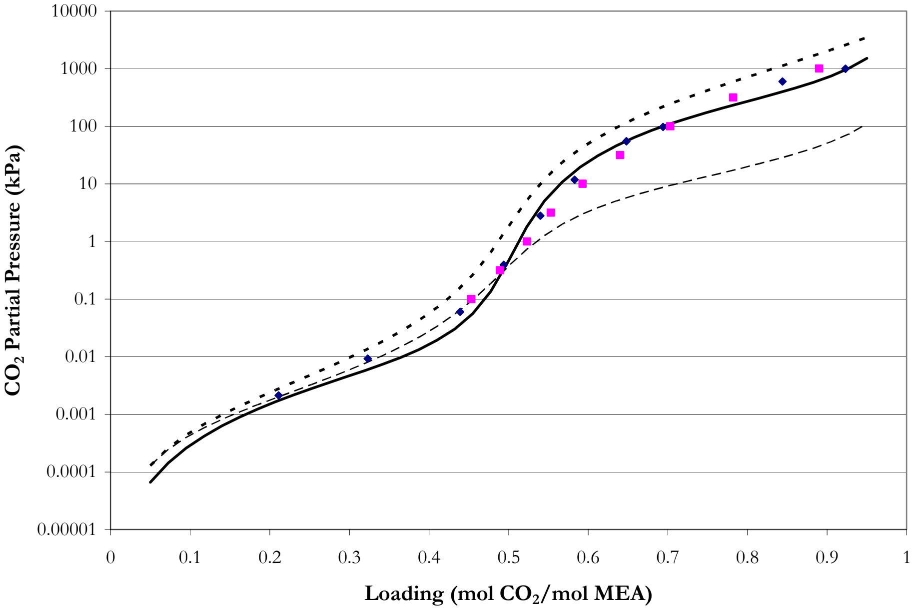

Figure 13.5-7. Comparison between Experimental and Predicted CO_2 Solubility in ~7 m MEA at 25 °C. Points: ■, Lee et al. (1976), ♦, Jou et al. (1995). Lines: · · ·, Austgen (1989), — —, Freguia (2002), —, this work.

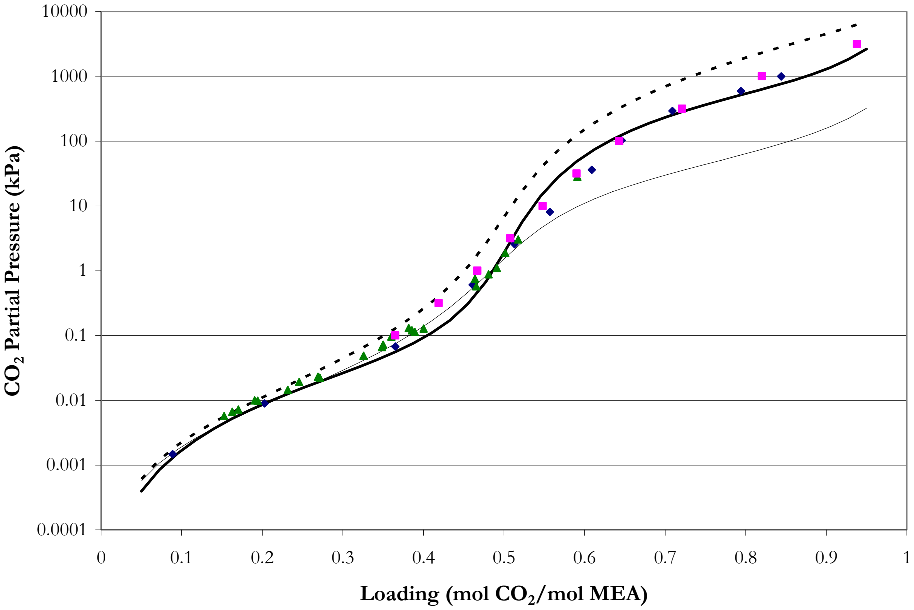

Figure 13.5-8. Comparison between Experimental and Predicted CO_2 Solubility in ~7 m MEA at 40 °C. Points: ■, Lee et al. (1976), ♦, Jou et al. (1995), ▲, this work. Lines: · · ·, Austgen (1989), — —, Freguia (2002), —, this work.

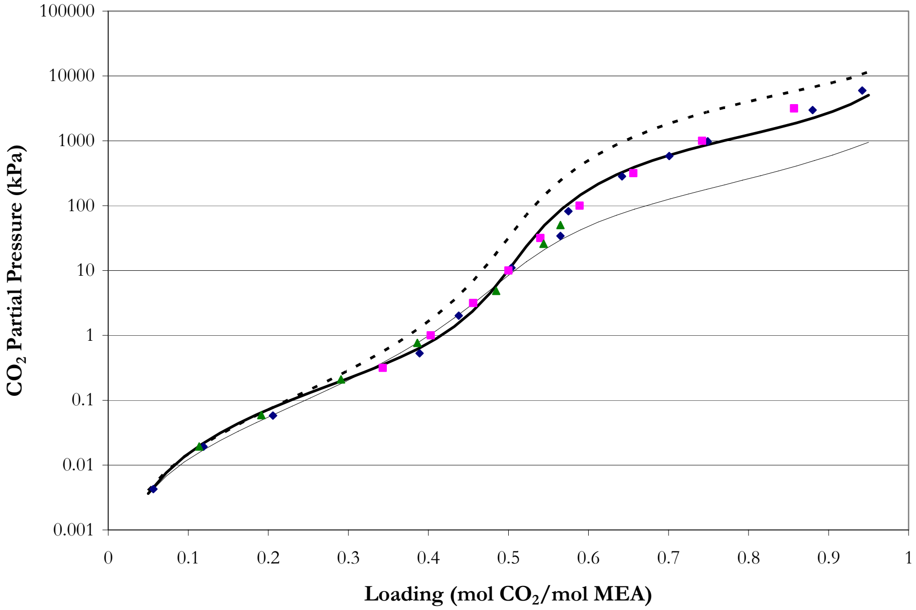

Figure 13.5-9. Comparison between Experimental and Predicted CO$_2$ Solubility in ~7 m MEA at 60 °C. Points: ■, Lee et al. (1976), ♦, Jou et al. (1995), ▲, this work. Lines: · · ·, Austgen (1989), — —, Freguia (2002), —, this work.

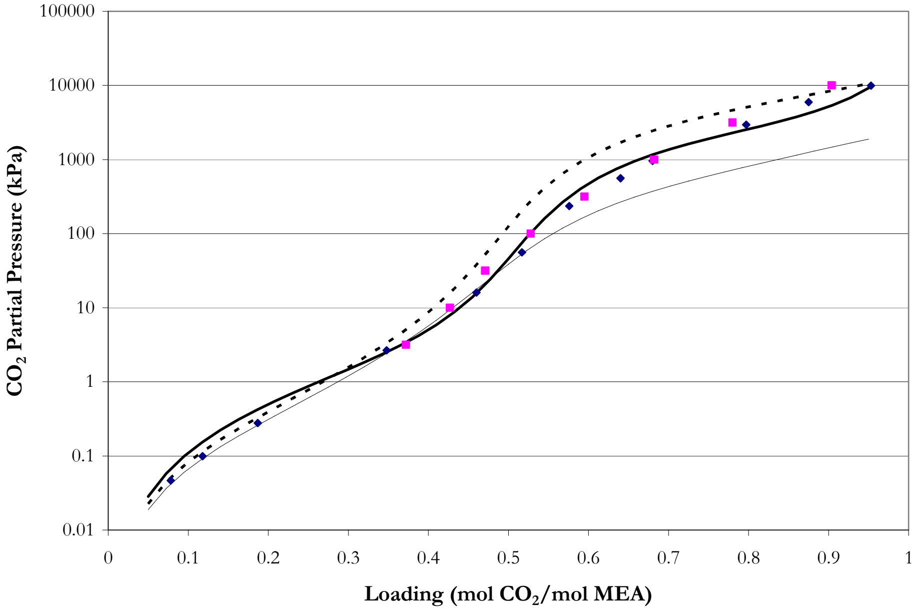

Figure 13.5-10. Comparison between Experimental and Predicted CO$_2$ Solubility in ~7 m MEA at 80 °C. Points: ■, Lee et al. (1976), ♦, Jou et al. (1995). Lines: · · ·, Austgen (1989), — —, Freguia (2002), —, this work.

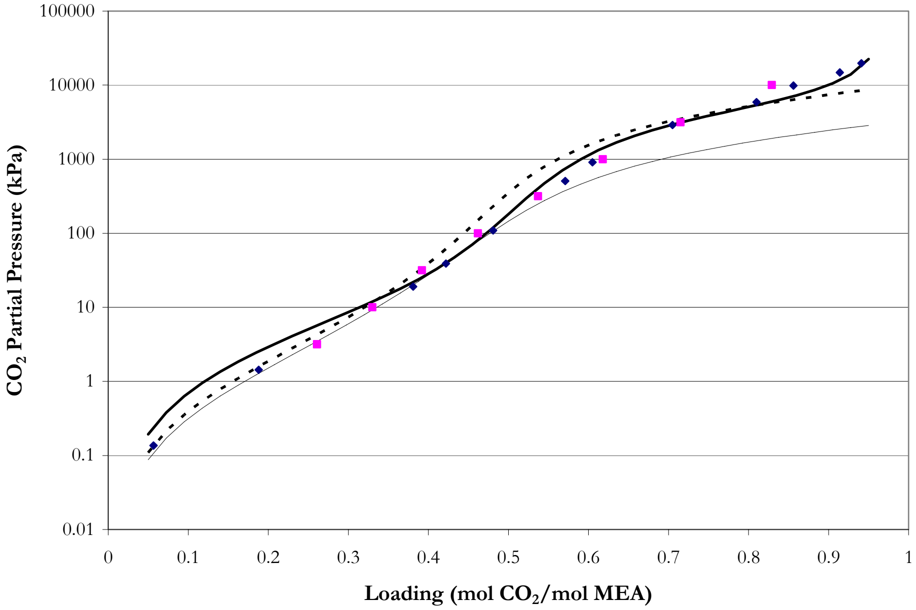

Figure 13.5-11. Comparison between Experimental and Predicted CO_2 Solubility in ~7 m MEA at 100 °C. Points: ■, Lee et al. (1976), ♦, Jou et al. (1995). Lines: · · ·, Austgen (1989), — —, Freguia (2002), —, this work.

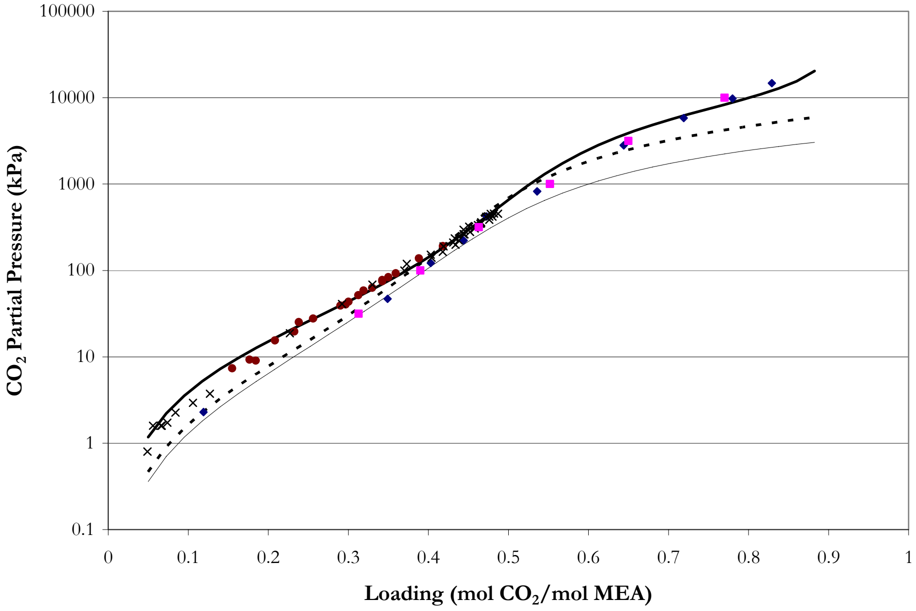

Figure 13.5-12. Comparison between Experimental and Predicted CO_2 Solubility in ~7 m MEA at 120 °C. Points: ×, Goldman and Leibush (1959), ■, Lee et al. (1976), ♦, Jou et al. (1995), ●, Ma'mum et al. (2005). Lines: · · ·, Austgen (1989), — —, Freguia (2002), —, this work.

CO_2 Capture Implications

For industrial CO_2 capture applications such as aqueous absorption/stripping from coal fired power plants, one of the critical regions for an adequate representation of experimental VLE data is within the absorber column where CO_2 chemically reacts with an aqueous amine solvent reducing the amount of CO_2 released into the atmosphere. Figure 13.5-13 illustrates a parity plot for the prediction of CO_2 partial pressure based on predictions from Austgen (1989), Freguia (2002), and this work to the experimental work by Jou et al. (1995). In the figure, the loading region from 0.2 to 0.5 mol CO_2/mol MEA indicates the nominal aqueous absorption operating region between 40 and 60 °C. The figure illustrates that predictions from this work and from Freguia (2002) adequately predicts the partial pressure of CO_2 within this region.

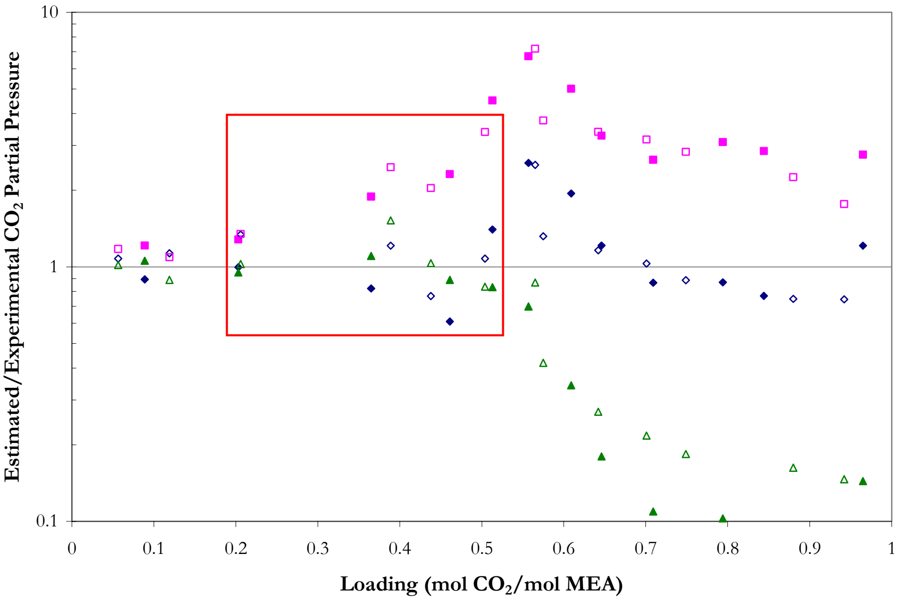

Figure 13.5-13. Comparison the CO_2 Partial Pressure Between Experimental Measurements in 7 m MEA by Jou et al. (1995) and Model Predictions by Austgen (1989), Freguia (2002) and this work. Solid/Open Points at 40/60 °C: ■,□, Austgen (1989), ▲,Δ, Freguia (2002), ♦,◊, this work.

CO_2 Solubility Predictions for 11 m MEA

In Figure 13.5-14 and Figure 13.5-15, the full model overestimates the solubility of CO_2 by a factor of 2. This error may be due to full model overestimating the liquid phase speciation as shown in Figure 13.5-60, implying that an error may exist within either the experimental NMR speciation data or the experimental CO_2 solubility data. On the other hand, since this system lies at the boundary of the chosen experimental data, the error could be a result of the regression analysis.

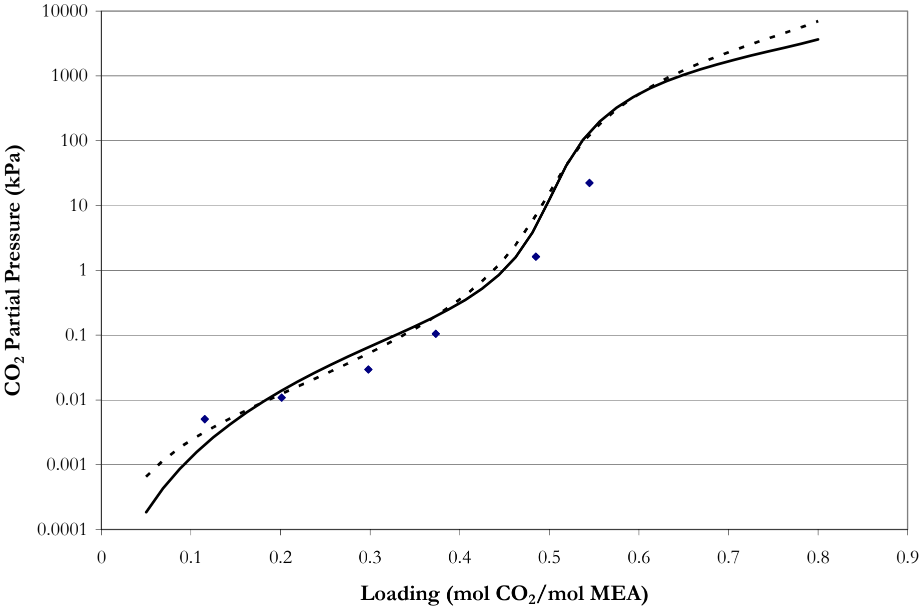

Figure 13.5-14. Comparison between Experimental and Predicted CO_2 Solubility in ~11 m MEA at 40 °C. Points: ♦, this work. Lines: · · ·, Austgen (1989), —, this work.

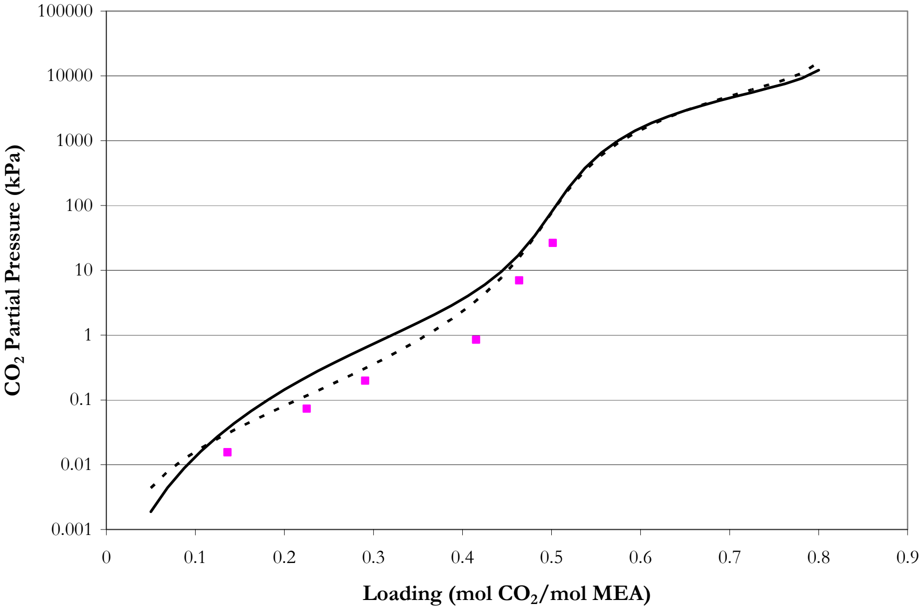

Figure 13.5-15. Comparison between Experimental and Predicted CO_2 Solubility in ~11 m MEA at 60 °C. Points: ■, this work. Lines: · · ·, Austgen (1989), —, this work.

MEA Volatility Predictions for 3.5, 7 and 11 m MEA

As shown in Chapter VIII, Figure 13.5-16 compares estimated model predictions to experimental partial pressure of MEA in solutions of H_2O-MEA. The model adequately predicts the partial pressure of MEA but fails to predict the correct partial pressure at 40 and 60 °C. Since this error is the initial boundary of MEA volatility, subsequent volatility predictions will be subjected to this estimation as shown by the circled region in Figure 13.5-17 through Figure 13.5-22. Overall, the full model gives an adequate fit to the experimental volatility data.

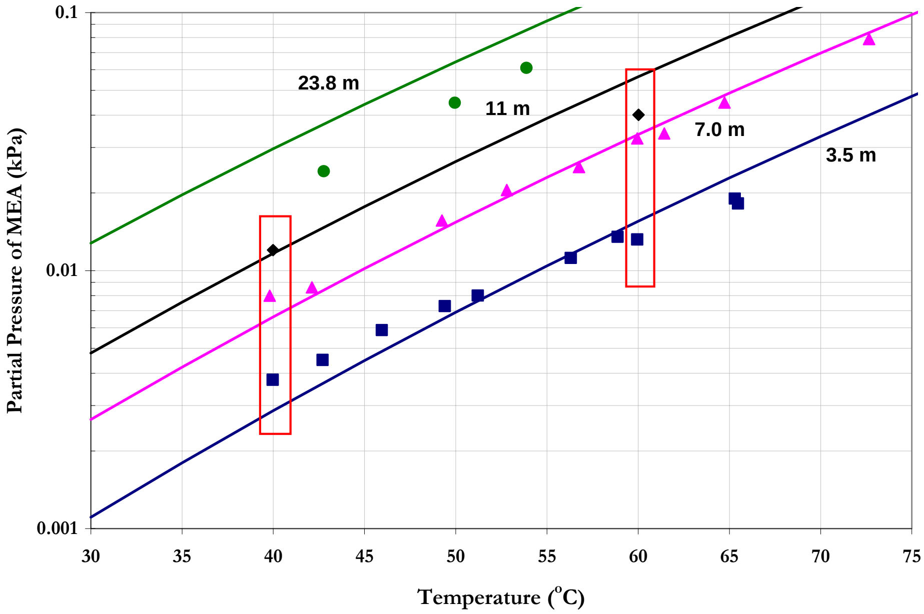

Figure 13.5-16. Comparison of Amine Volatility from this work to elecNRTL Model Predictions from 30 – 120 °C. Points: experimental data from this work ■, 3.5 m (mole/kg-H_2O), ▲, 7 m, ◆, 11 m, ●, 23.8 m. Lines: —, elecNRTL Predictions.

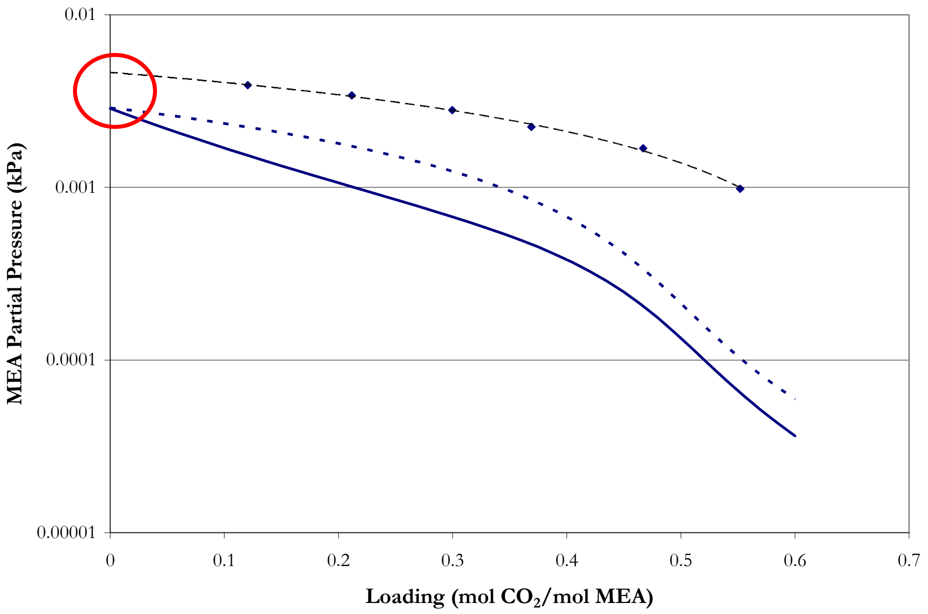

Figure 13.5-17. Comparison between Experimental and Predicted MEA Volatility in ~3.5 m MEA at 40 °C. Points: this work. Lines: · · ·, Austgen (1989), — —, OLS Approximation, —, this work.

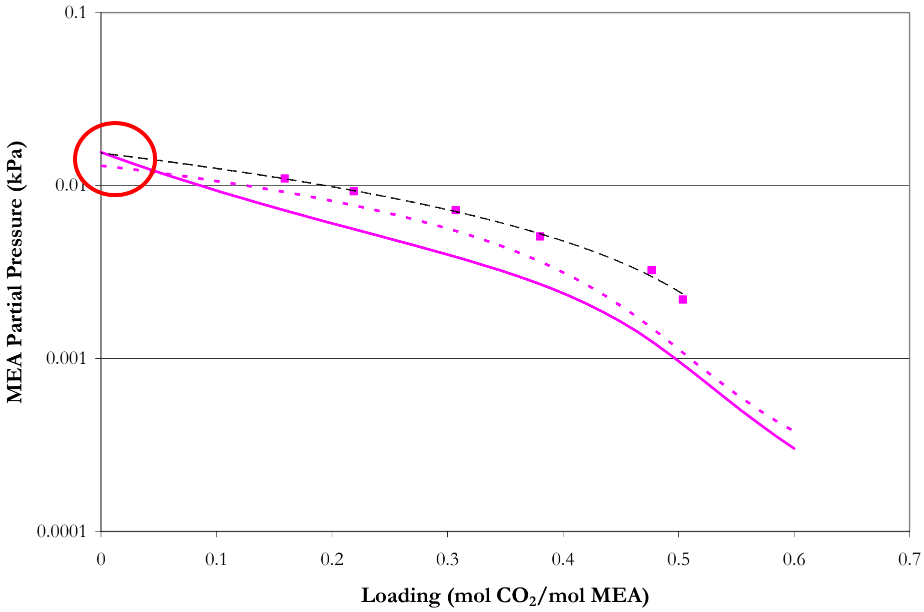

Figure 13.5-18. Comparison between Experimental and Predicted MEA Volatility in ~3.5 m MEA at 60 °C. Points: this work. Lines: · · ·, Austgen (1989), — —, OLS Approximation, ▬, this work.

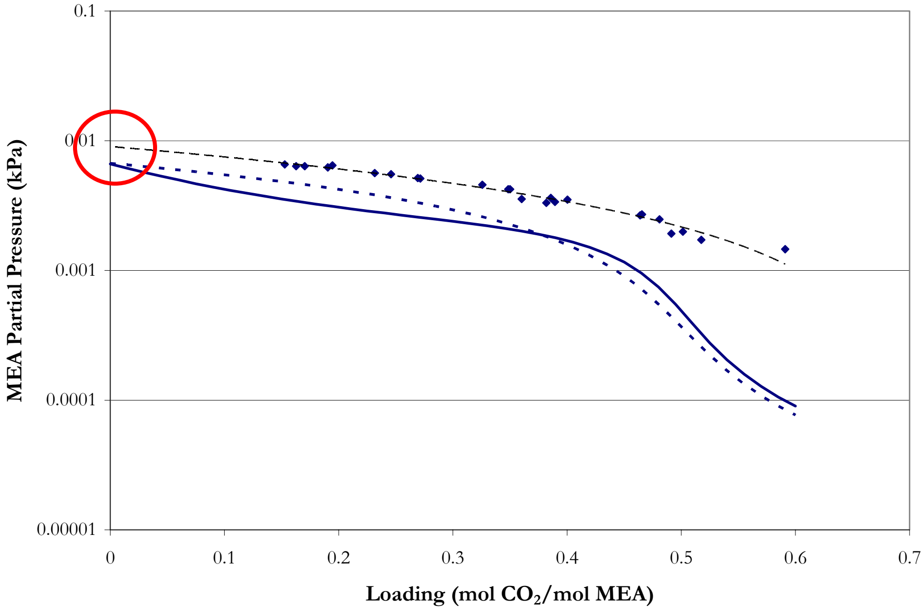

Figure 13.5-19. Comparison between Experimental and Predicted MEA Volatility in ~7 m MEA at 40 °C. Points: this work. Lines: · · ·, Austgen (1989), — —, OLS Approximation, ▬, this work.

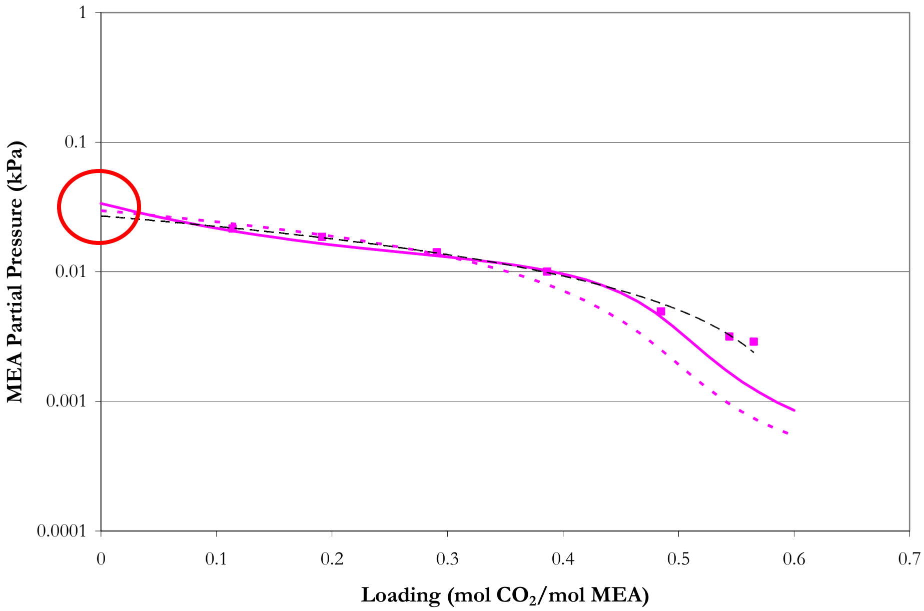

Figure 13.5-20. Comparison between Experimental and Predicted MEA Volatility in ~7 m MEA at 60 °C. Points: this work. Lines: · · ·, Austgen (1989), — —, OLS Approximation, ▬, this work.

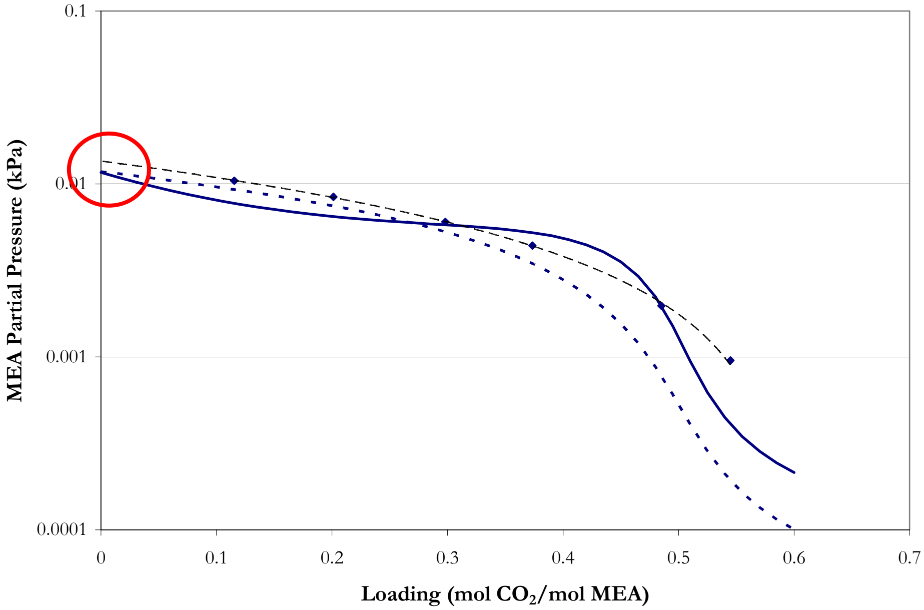

Figure 13.5-21. Comparison between Experimental and Predicted MEA Volatility in ~11 m MEA at 40 °C. Points: this work. Lines: · · ·, Austgen (1989), — —, OLS Approximation, ▬, this work.

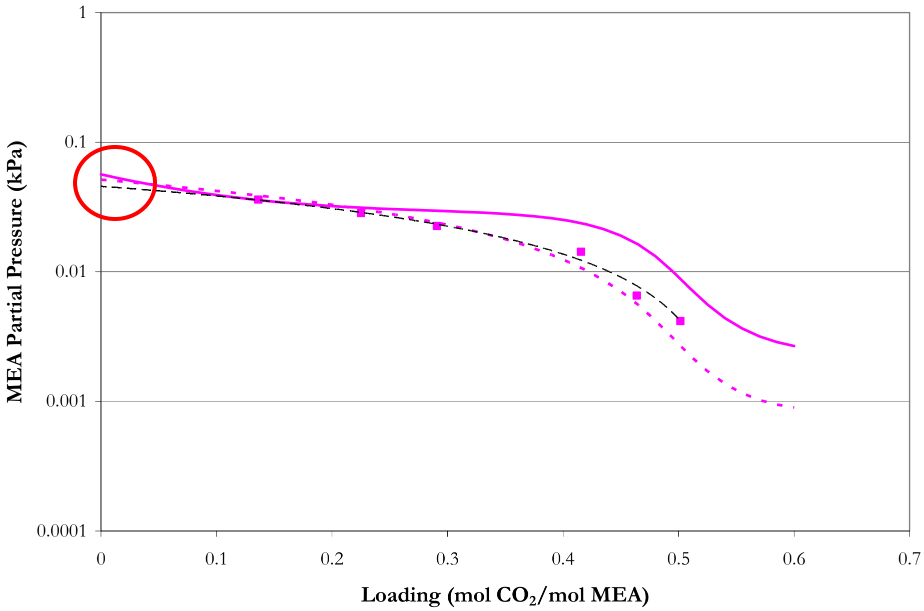

Figure 13.5-22. Comparison between Experimental and Predicted MEA Volatility in ~11 m MEA at 60 °C. Points: this work. Lines: · · ·, Austgen (1989), — —, OLS Approximation, ▬, this work.

Predictions of the Partial Pressure of MEA as a Function of Temperature

Using the full model as a purely predictive tool, Figure 13.5-23 through 13.5-25 illustrates the partial pressure of MEA in 3.5, 7, and 11 m solutions. In Figure 13.5-24, the main effects on the partial pressure of MEA, in a 7 m solution, to decrease from a loading between 0 and 0.3 mol CO_2/mol MEA are due to changes in the activity coefficient of MEA and solution speciation. Within the loading range of 0.3 to 0.6, the main effects are now contributions of the chemical equilibrium constant for monoethanolamine carbamate and the solution speciation, vis-à-vis the concentration of free amine in the liquid phase, where beyond a loading of 0.6, the concentration of free amine can be considered negligible as shown in Figure 13.5-53.

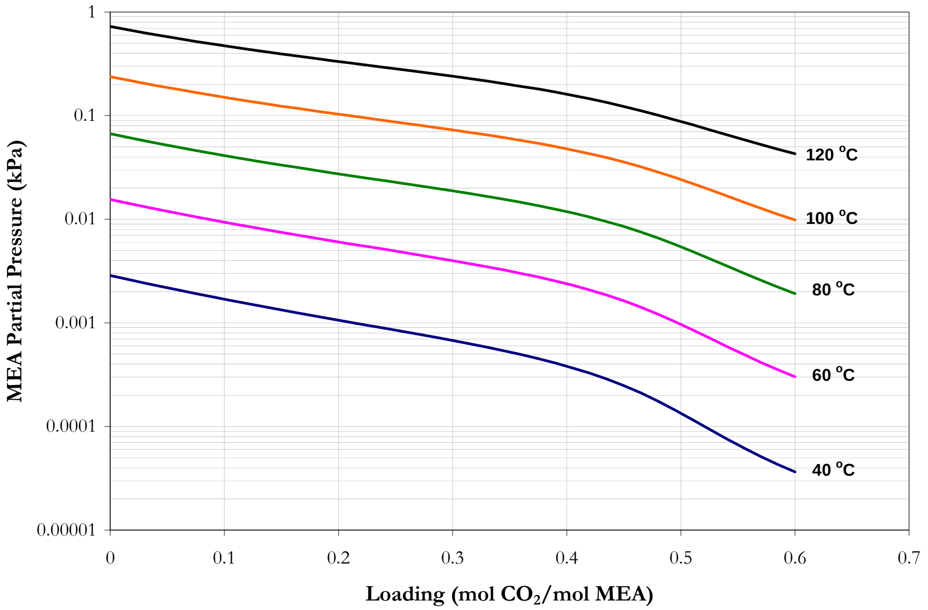

Figure 13.5-23. Predictions for Amine Volatility in 3.5 m MEA from this work.

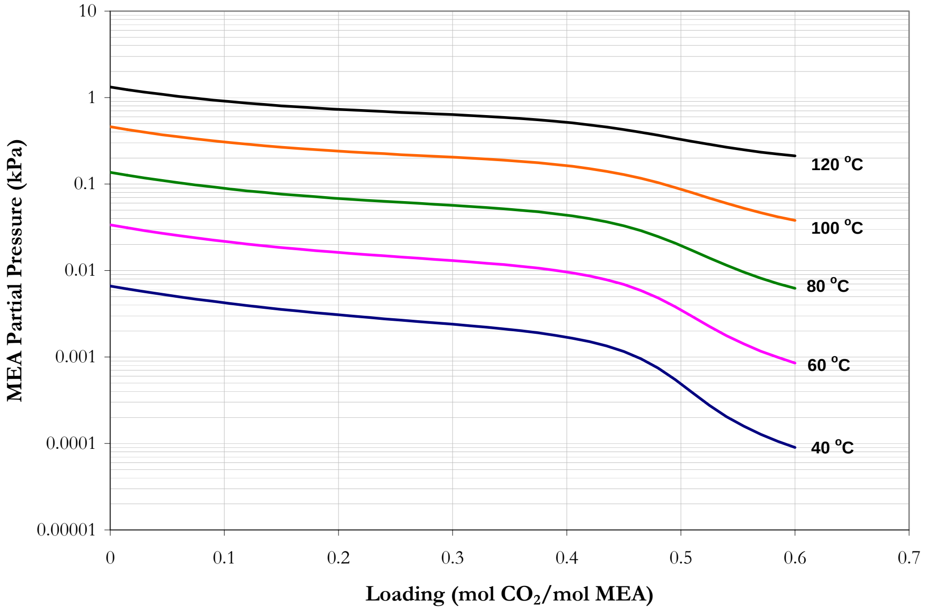

Figure 13.5-24. Predictions for Amine Volatility in 7 m MEA from this work.

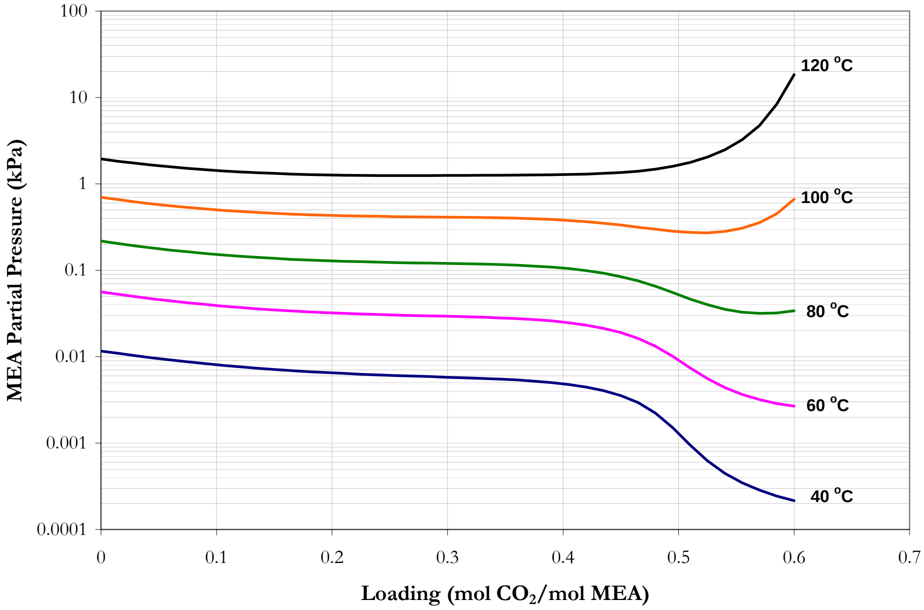

Figure 13.5-25. Predictions for Amine Volatility in 11 m MEA from this work.

13.5.2 *Specific Heat Capacity*

Figure 13.5-26 through Figure 13.5-29 compare experimental specific heat capacity measurements from this work to predictions from Austgen (1989), Freguia (2002), and to this work. Model predictions from Austgen (1989) and Freguia (2002) over estimate the specific heat capacity over the range in loading. On the other hand, Austgen (1989) and Freguia (2002) did not include calometric measurements as part of their original regression analysis, but we chose to illustrate the possible enthalpy differences as compared to purely CO_2 solubility based thermodynamic models. Overall, the full model adequately predicts the specific heat capacity for 3.5 and 7 m MEA mixtures within an average absolute relative error of ± 0.79 percent.

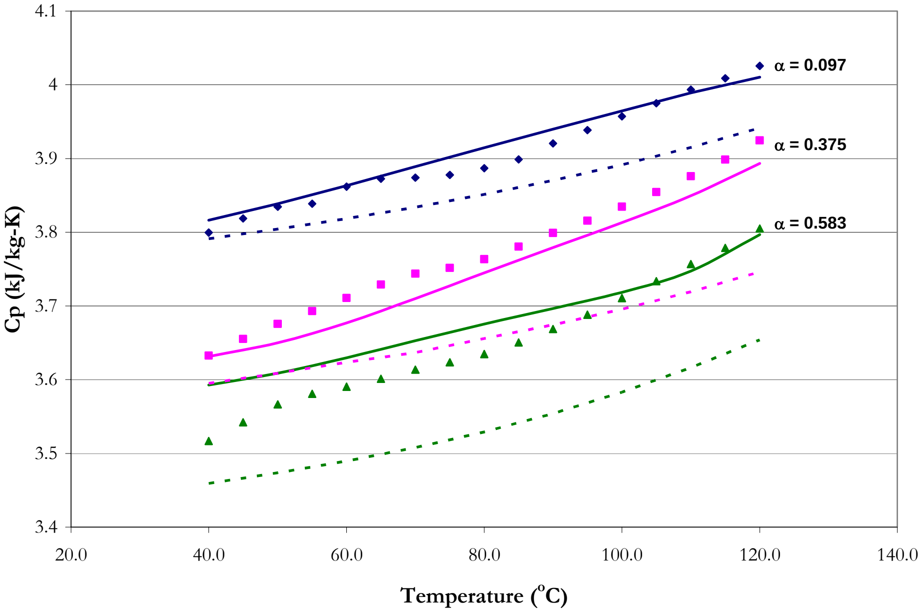

Figure 13.5-26. Comparison of Experimental Specific Heat Capacity in loaded (α) 3.5 m MEA Mixtures from 40 to 120 °C. Points: ♦, α = 0.097, ■, α = 0.375, ▲, α = 0.583 from this work. Lines: - - -, Austgen (1989), ▬, this work.

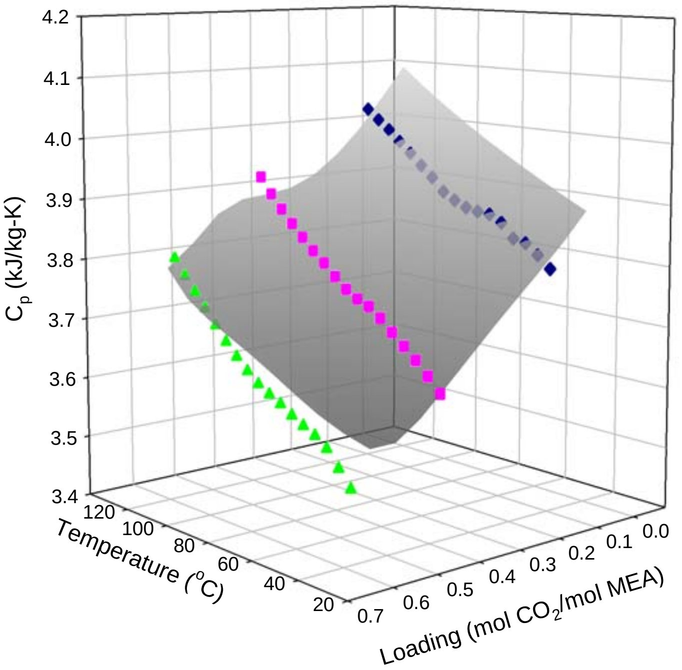

Figure 13.5-27. Surface Comparison of Experimental Specific Heat Capacity in loaded (α) 3.5 m MEA Mixtures from 40 to 120 °C. Points: ♦, α = 0.097, ■, α = 0.375, ▲, α = 0.583 from this work. Surface: this work.

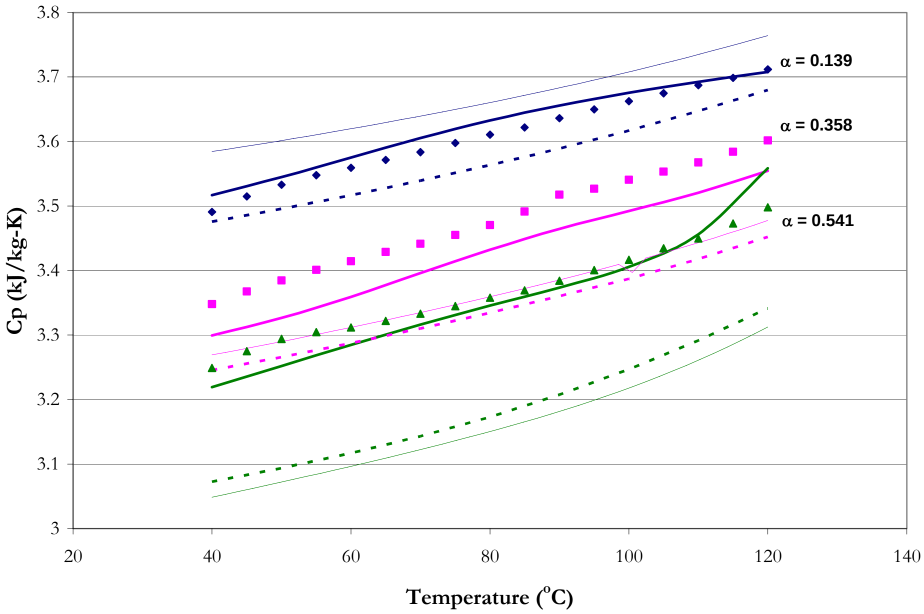

Figure 13.5-28. Comparison of Experimental Specific Heat Capacity in loaded (α) 7 m MEA Mixtures from 40 to 120 °C. Points: ♦, α = 0.139, ■, α = 0.358, ▲, α = 0.541 from this work. Lines: - - -, Austgen (1989), — —, Freguia (2002), ▬, this work.

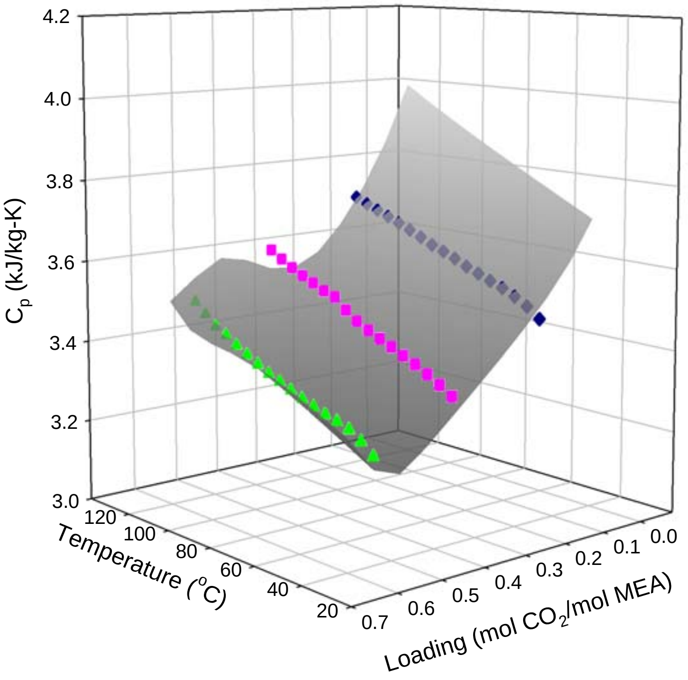

Figure 13.5-29. SurfaceComparison of Experimental Specific Heat Capacity in loaded (α) 7 m MEA Mixtures from 40 to 120 °C. Points: ♦, α = 0.139, ■, α = 0.358, ▲, α = 0.541 from this work. Surface: this work.

To describe the departure from an ideal solution behavior, Figure 13.5-30 illustrates the proposed molar infinite dilution aqueous phase heat capacity for ionic and molecular solute species in the H_2O-MEA-CO_2 system where the molar infinite dilution aqueous phase heat capacity for CO_3^{-2} and HCO_3^{-1}, and $MEAH^{+1}$ were described in Chapters XII and VIII, respectively.

By differentiating Equation 13-33 with respect to temperature, the molar infinite dilution aqueous phase heat capacity for CO_2 can be determined as shown in Figure 13.5-30. From Table 13.4-3, coefficients for the molar infinite dilution aqueous phase heat capacity of $MEACOO^{-1}$ were determined through simultaneous regression as described in Section 13.4

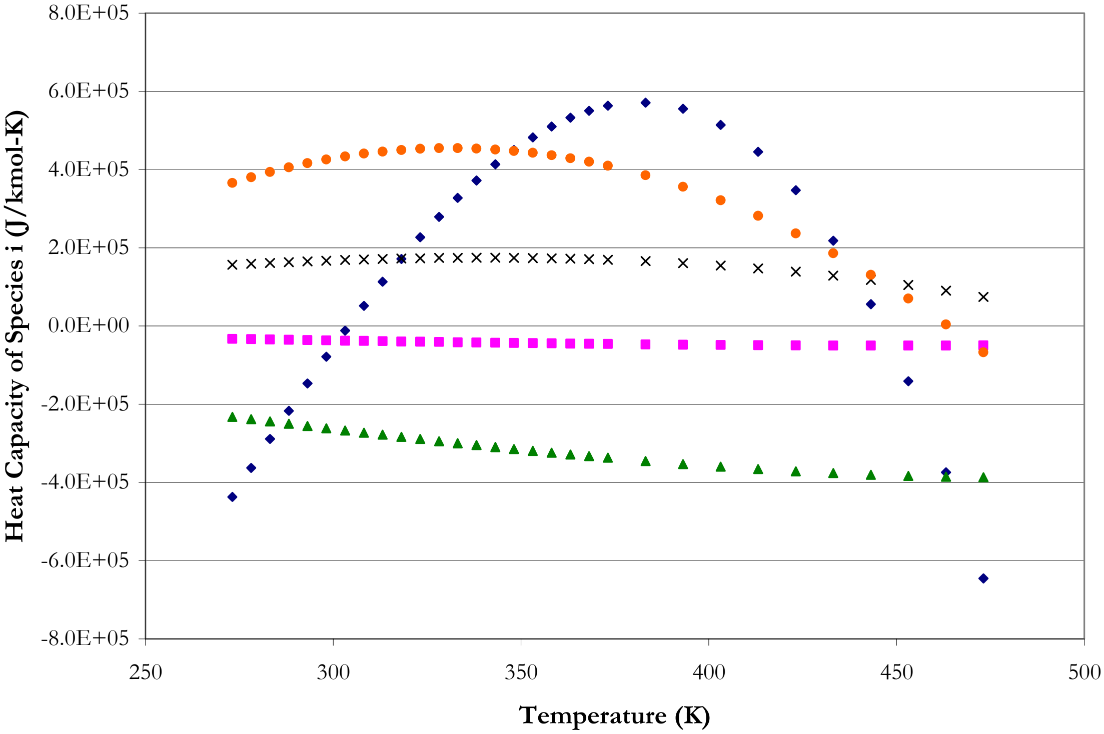

Figure 13.5-30. Molar Infinite Dilution Aqueous Phase Heat Capacity for Ionic and Molecular Solute Species in the H_2O-MEA-CO_2 System. Points: ◆, CO_2, ■, HCO_3^{-1}, ▲, CO_3^{-2}, ×, $MEAH^{+1}$, ●, $MEACOO^{-1}$.

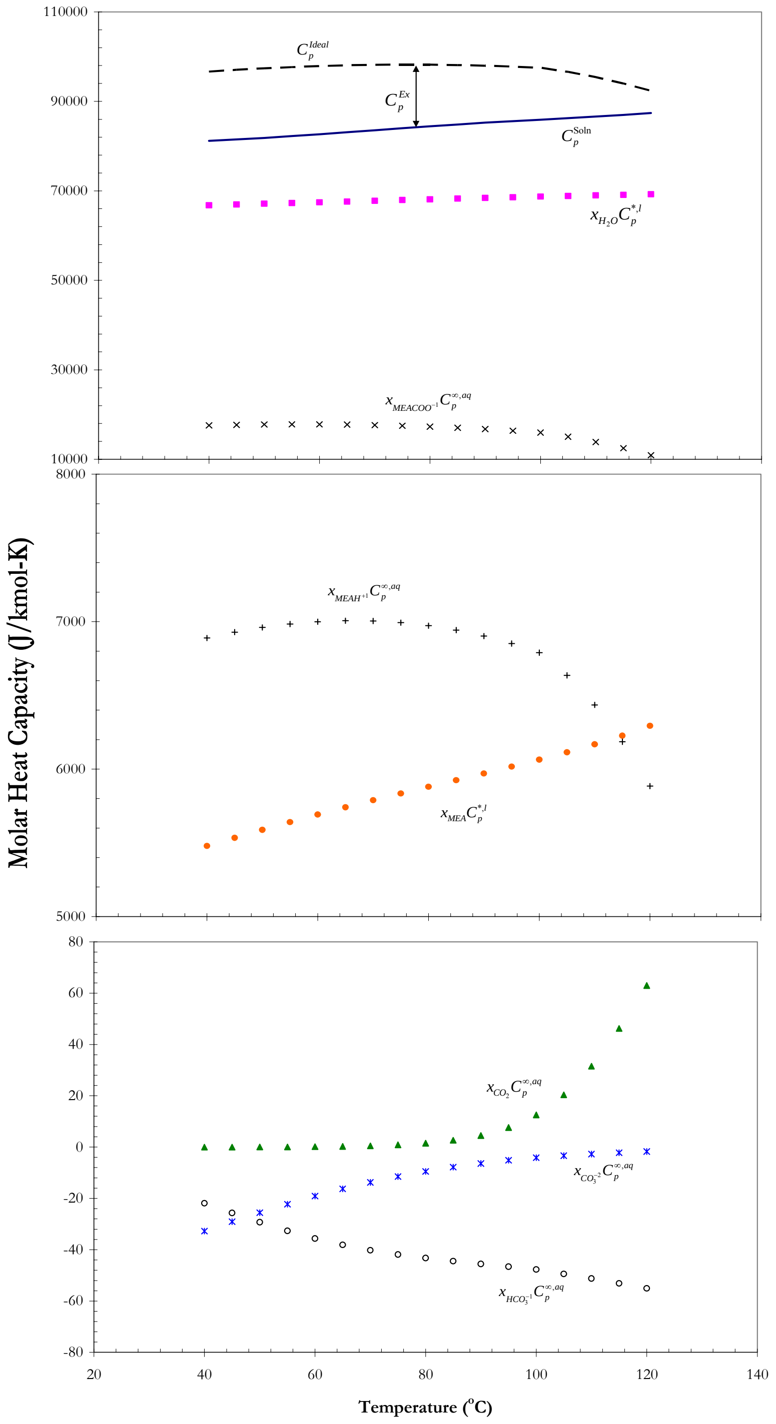

Figure 13.5-31. Comparison of the Molar Heat Capacity for 7 m MEA at a loading = 0.358 mol CO_2/mol MEA from this work to the Ideal Molar Heat Capacity based on the Constituent Components.

Figure 13.5-31 separates the molar heat capacity in 7 m MEA at a loading of 0.358 into the weighted molar heat capacity of each contributing species with respect to the components reference state (i.e. Solvents: pure liquid; Ionic and Molecular Solutes: infinite dilution in water). By describing the molar heat capacity of the solution by the following equation:

$$\begin{aligned} C_p = {} & x_{H_2O} C_p^{*,l} + x_{MEA} C_p^{*,l} + x_{CO_2} C_p^{\infty,aq} + x_{CO_3^{-2}} C_p^{\infty,aq} \\ & + x_{HCO_3^{-1}} C_p^{\infty,aq} + x_{MEAH^{+1}} C_p^{\infty,aq} + x_{MEACOO^{-1}} C_p^{\infty,aq} + C_p^{Ex} \end{aligned} \qquad 13\text{-}48$$

deviations between the molar heat capacity of the solution from the ideal molar heat capacity are accounted by the excess molar heat capacity. The excess molar heat capacity also accounts for the heat of reaction associated with any change in speciation with temperature.

We can now account for the molar heat capacity of the apparent MEA and CO_2 species from Equation 13-48 by the following equations:

$$x_{MEATOT} C_p^{MEA,TOT} = x_{MEA} C_p^{*,l} + x_{MEAH^{+1}} C_p^{\infty,aq} + x_{MEACOO^{-1}} C_p^{\infty,aq} \qquad 13\text{-}49$$

$$x_{CO_2TOT} C_p^{CO_2TOT} = x_{CO_2} C_p^{\infty,aq} + x_{CO_3^{-2}} C_p^{\infty,aq} + x_{HCO_3^{-1}} C_p^{\infty,aq} + x_{MEACOO^{-1}} C_p^{\infty,aq} \qquad 13\text{-}50$$

To satisfy the material balance, the molar heat capacity of $MEACOO^{-1}$ has to contribute to both equations. We can separate the effect of each functional group by subtracting the amine group from the carbonate group.

$$C_p^{-COO^{-1}} = \gamma_{MEA}^{\infty} C_p^{MEA} - C_p^{MEACOO^{-1}} \qquad 13\text{-}51$$

where the infinite dilution activity coefficient for MEA converts the molar heat capacity of MEA from a pure liquid reference state to a reference state at infinite dilution in pure water.

Thus, the amine effect would then be the molar heat capacity of MEA times the infinite dilution activity coefficient of MEA. Subsituting the amine effect into Equation 13-49 yields

$$x_{MEATOT} C_p^{MEA,TOT} = x_{MEA} C_p^{*,l} + x_{MEAH^{+1}} C_p^{\infty,aq} + x_{MEACOO^{-1}} \left(\gamma_{MEA}^{\infty} C_p^{MEA} \right) \qquad 13\text{-}52$$

Now substituting Equation 13-52 into Equation 13-48 yields

$$C_p = x_{H_2O} C_p^{*,l} + x_{MEATOT} C_p^{MEATOT} + x_{CO_2TOT} C_p^{CO_2TOT} + C_p^{Ex} \qquad 13\text{-}53$$

Solving for the apparent molar heat capacity of CO_2 gives:

$$\frac{C_p - x_{H_2O} C_p^{*,l} - x_{MEATOT} C_p^{MEATOT}}{x_{CO_2TOT}} = C_p^{CO_2TOT} + \frac{C_p^{Ex}}{x_{CO_2TOT}} \qquad 13\text{-}54$$

Figure 13.5-32 illustrates the magnitude of the apparent molar heat capacity of CO_2.

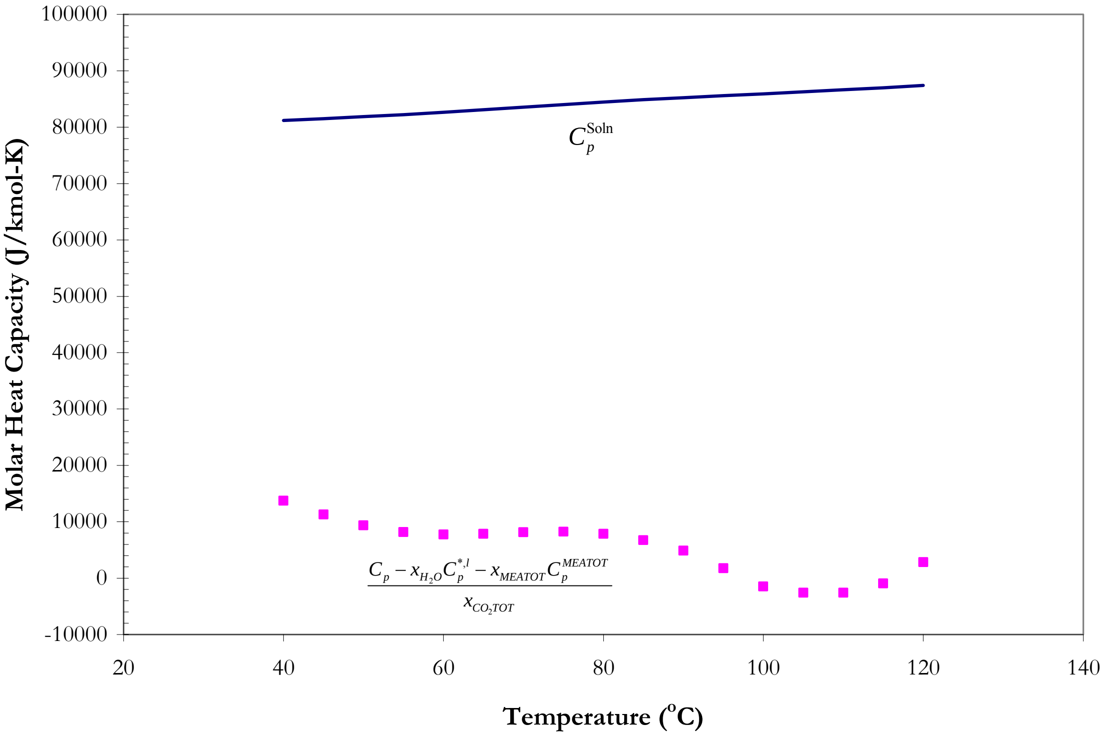

Figure 13.5-32. Comparison of the Molar Heat Capacity Predictions for 7 m MEA at a loading of 0.358 based on the Constituent Components and Equation 15-54.

Another approach based on an ideal solution methodology to create an empirical criterion for the magnitude of the molar heat capacity of apparent CO$_2$ at a given condition is represented by the following equation:

$$C_p = x_{H_2O} C_p^{*,l} + C_p^{MEA} \sum_{i=1}^{3} x_i^{MEA^*} + C_p^{CO_2^*} \sum_{j=1}^{4} x_j^{CO_2^*} \qquad 13\text{-}55$$

Where

$\sum_{i=1}^{3} x_i^{MEA^*}$ is the summation of the MEA constituent components,

$\sum_{j=1}^{4} x_j^{CO_2^*}$ is the summation of the CO$_2$ constituent components.

Solving for the apparent CO$_2$ molar heat capacity yields,

$$C_p^{CO_2^*} \sum_{j=1}^{4} x_j^{CO_2^*} = C_p - x_{H_2O} C_p^{*,l} - C_p^{MEA} \sum_{i=1}^{3} x_i^{MEA^*} \qquad 13\text{-}56$$

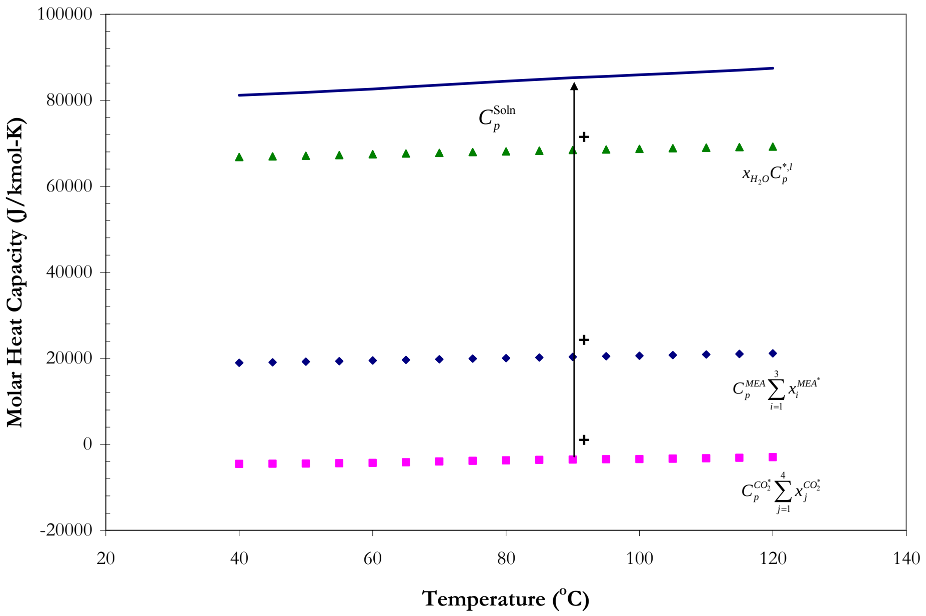

Figure 13.5-33. Comparison of the Molar Heat Capacity Predictions for 7 m MEA at a loading of 0.358 based on the Ideal Constituent Components and Equation 15-56.

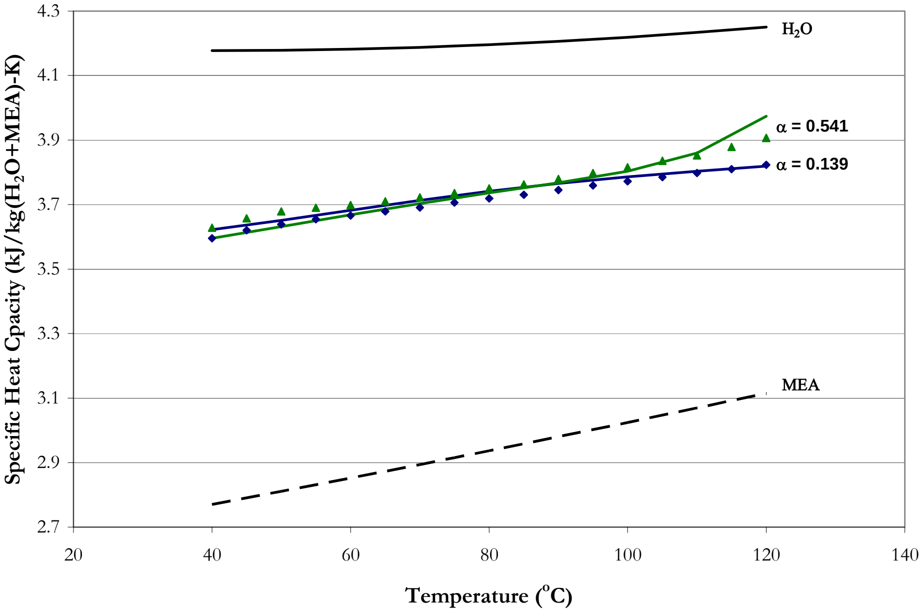

Figure 13.5-34. Apparent Partial Specific Heat Capacity for loaded 7 m MEA.

From the above analysis and based on Figure 13.5-34, the contribution of the molar heat capacity of apparent CO_2 species may be considered a constant (~3812 J/kmol-K) over the temperature range from 40 to 120 °C.

13.5.3 *Enthalpy of CO_2 Absorption*

Figure 13.5-35 through Figure 13.5-37 compares experimental differential enthalpy of CO_2 absorption measurements from Kim et al. (2007) to predictions based on Equation 13-36 (Gibbs-Helmholtz) from Austgen (1989), Freguia (2002), and this work. Model predictions from Austgen (1989) and Freguia (2002) underestimate the enthalpy of CO_2 absorption at high temperatures over the range in loading. On the other hand, Austgen (1989) and Freguia (2002) did not include calorimetric measurements as part of their original regression analysis, but we chose to illustrate the possible enthalpy differences as compared to purely CO_2 solubility based thermodynamic models.

Figure 13.5-35 through Figure 13.5-37 illustrates that the full model overestimates the enthalpy of CO_2 absorption at low loading. This error may be due to an error in the liquid phase speciation at low loading, since the concentration of the liquid phase drives the prediction for the fugacity of CO_2 in the vapor phase. Or this error may be due to the regression method itself. Within DRS, each variable is given a standard deviation according to the error associated with the measurement. During a regression, DRS attempts to satisfy the model constraints while simultaneously adjusting the measured variables (i.e. T, P, x_i, y_i, etc.) to minimize the objective function.

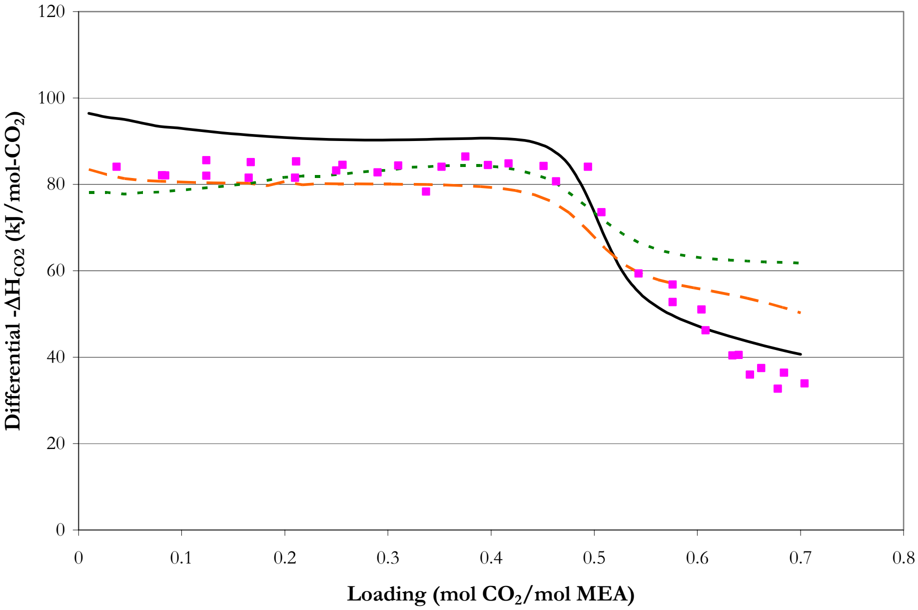

Figure 13.5-35. Comparison of the Enthalpy of CO_2 Absorption in 7 m MEA at 40 °C. Points: ■, Kim et al. (2007). Lines: — —, Austgen (1989), - - -, Freguia (2002), ▬, this work.

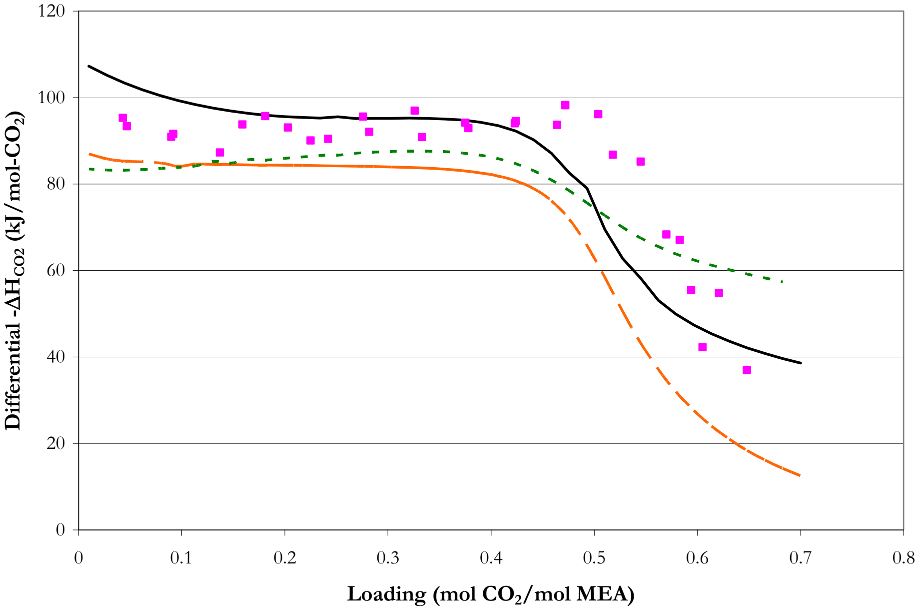

Figure 13.5-36. Comparison of the Enthalpy of CO_2 Absorption in 7 m MEA at 80 °C. Points: ■, Kim et al. (2007). Lines: — —, Austgen (1989), - - -, Freguia (2002), ▬, this work.

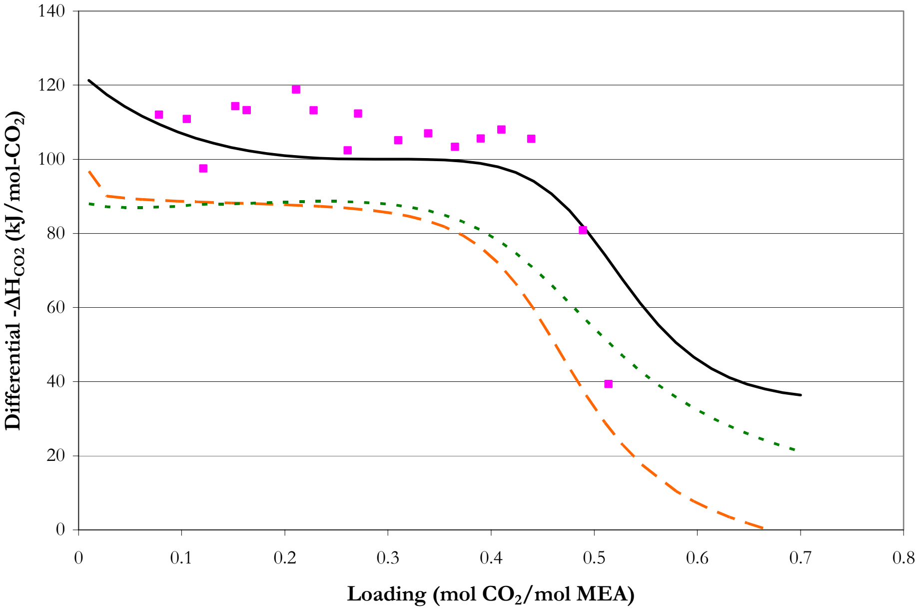

Figure 13.5-37. Comparison of the Enthalpy of CO_2 Absorption in 7 m MEA at 120 °C. Points: ■, Kim et al. (2007). Lines: — —, Austgen (1989), - - -, Freguia (2002), ▬, this work.

Enthalpy of CO_2 Absorption as Compared to the Predicted Heat Duty

In Figure 13.5-38 through 13.5-40 the differential enthalpy of CO_2 absorption from 40 to 120 °C from Kim et al. (2007) is compared to predictions from this work based on the Gibbs-Helmholtz Equation (Equ. 13-36) and the calculated heat duty from a flash block within Aspen Plus^{TM}. The figures illustrate a discrepancy between the enthalpy and solution chemistry algorithms within Aspen Plus^{TM}. This discrepancy has been known to exist and was one of the main motivations behind this work to describe the vapor-liquid equilibrium and calometric effects through a consistent thermodynamic framework. Since both calometric and vapor-liquid equilibrium were simultaneously regressed within DRS, both algorithms should have been satisfied. Thus, the error may still be due to a discrepancy within the software of Aspen Plus^{TM}.

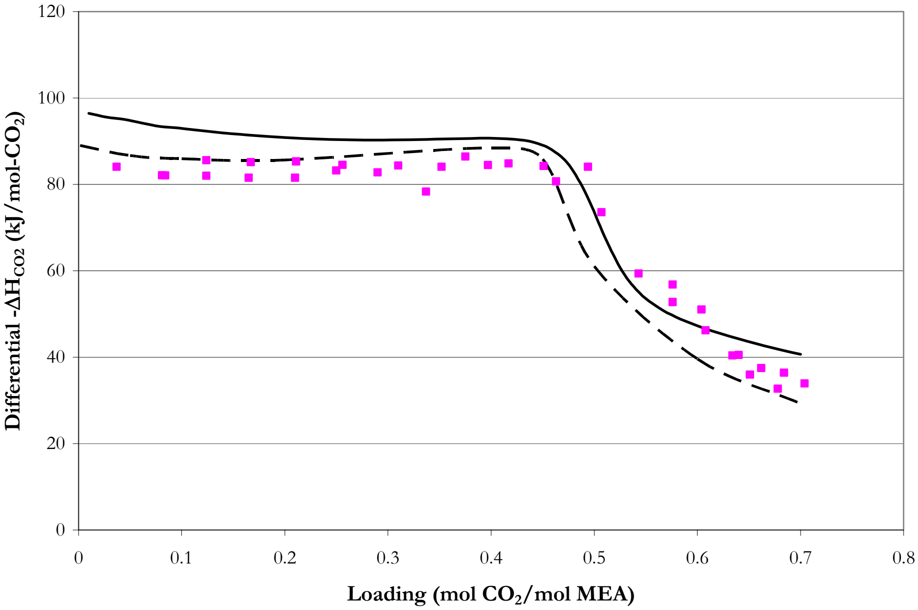

Figure 13.5-38. Comparison of the Enthalpy of CO_2 Absorption at 40 °C to Predictions from the Gibbs-Helmholtz Equation and the Calculated Heat Duty from a Flash Block based on this work. Points: ■, Kim et al. (2007). Lines: ▬, Predicted Gibbs-Helmholtz Equation, — —, Predicted Heat Duty.

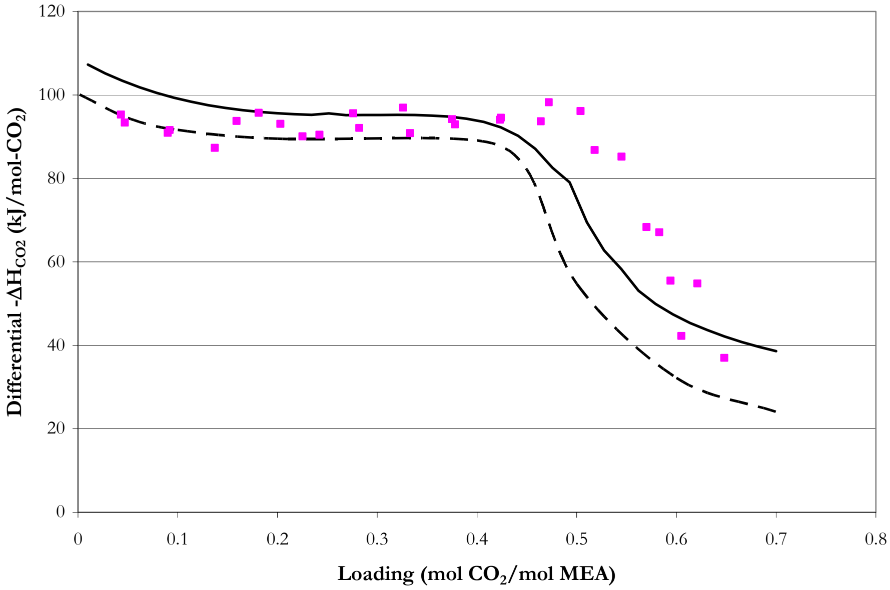

Figure 13.5-39. **Comparison of the Enthalpy of CO_2 Absorption at 80 °C to Predictions from the Gibbs-Helmholtz Equation and the Calculated Heat Duty from a Flash Block based on this work. Points: ■, Kim et al. (2007). Lines: ▬, Predicted Gibbs-Helmholtz Equation, — —, Predicted Heat Duty.**

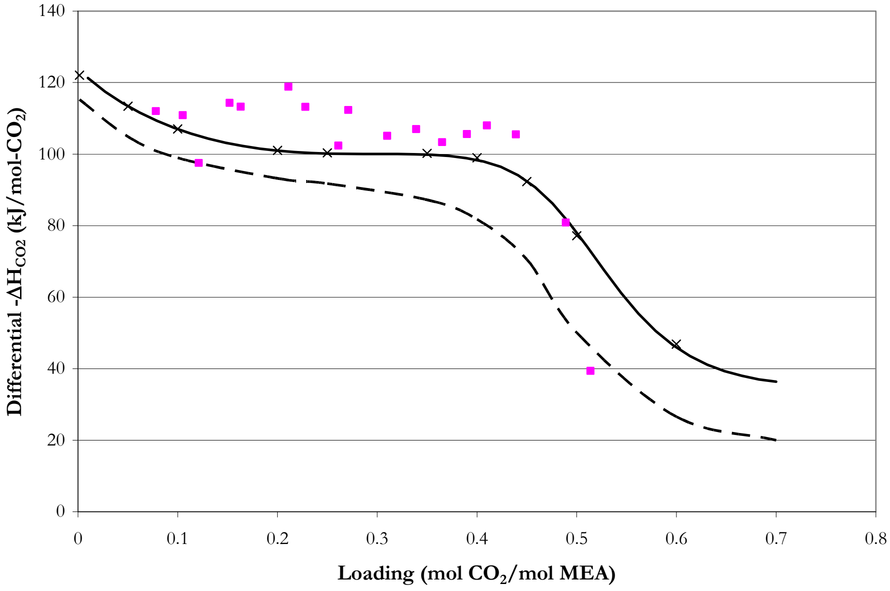

Figure 13.5-40. **Comparison of the Enthalpy of CO_2 Absorption at 120 °C to Predictions from the Gibbs-Helmholtz Equation and the Calculated Heat Duty from a Flash Block based on this work. Points: ■, Kim et al. (2007). Lines: ▬, Predicted Gibbs-Helmholtz Equation, — —, Predicted Heat Duty.**

Enthalpy of CO_2 Absorption as a Function of Temperature

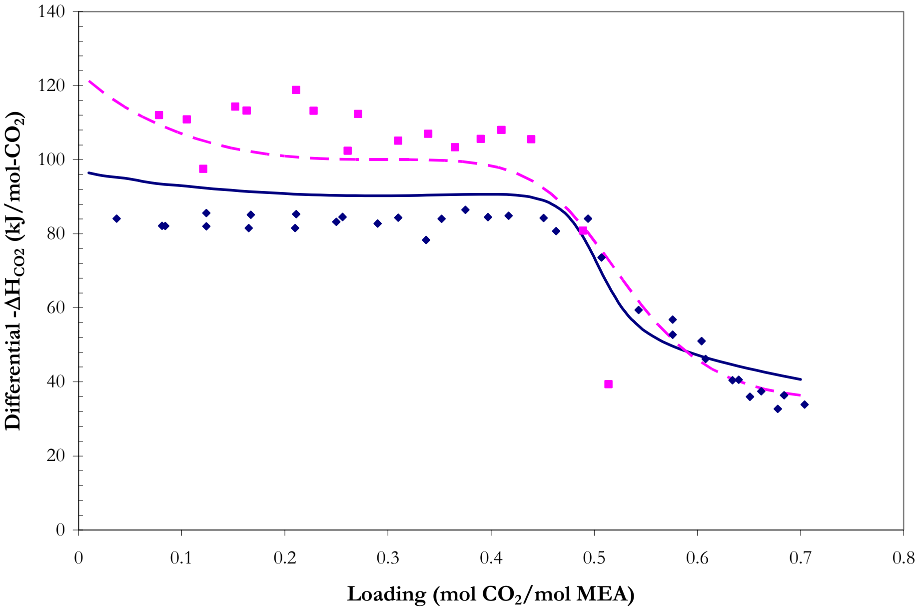

Figure 13.5-41. Comparision of Predictions for the Enthalpy of CO_2 Absorption in 7 m MEA from 40 to 120 °C from this work. Points: Kim et al. (2007) ♦, 40 °C, ■, 120 °C. Lines: —, 40 °C, — —, 120 °C.

Figure 13.5-41 compares experimental enthalpy of CO_2 absorption from Kim et al. (2007) to model predictions from this work illustrating the model's ability to adequately predict systematic trends in terms of the temperature and loading dependence presented in the experimental enthalpy of CO_2 absorption data within an average absolute relative error of ± 12.91 percent.

13.5.4 *NMR Speciation*

Figure 13.5-42 through Figure 13.5-63 compare experimental liquid phase NMR speciation measurements from Poplsteinova (2004) and this work to predictions from Austgen (1989) and to this work. Model predictions from Austgen (1989) overestimate the

CO_3^{-2} + HCO_3^{-1} concentration at low loadings and the $MEACOO^{-1}$ concentration at high loadings over the range in temperature studied in this work. On the other hand, Austgen (1989) did not include NMR speciation measurements as part of his original regression analysis, but we chose to illustrate the possible liquid phase speciation differences as compared to purely CO_2 solubility based thermodynamic models. Overall, the full model adequately predicts the liquid phase NMR speciation for 3.5, 7, and 11 m MEA mixtures within an average absolute relative error of ± 4.66 percent.

As mentioned in Section 13.5.1, the full model overestimated the solubility of CO_2 at low loading in 3.5 m MEA. This error may have been due to full model overestimating the liquid phase speciation in terms of the calculated activity coefficients for MEA, $MEAH^{+1}$, and $MEACOO^{-1}$, because the partial pressure of CO_2 at low loading can be described by the following equation:

$$P_{CO_2} = K_{MEACOO^{-1}} \left(\frac{x_{MEA}\gamma_{MEA} \cdot x_{MEAH^{+1}}\gamma_{MEAH^{+1}}}{x_{MEACOO^{-1}}\gamma_{MEACOO^{-1}}} \right) \qquad 13\text{-}57$$

As shown in following liquid phase speciation predictions from Austgen (1989) and from this work, the two models adequately describe the concentrations of MEA, $MEAH^{+1}$, and $MEACOO^{-1}$ over a range of amine concentrations and temperature at low loading, but predicted activity coefficients based on the two model predictions are unexpected.

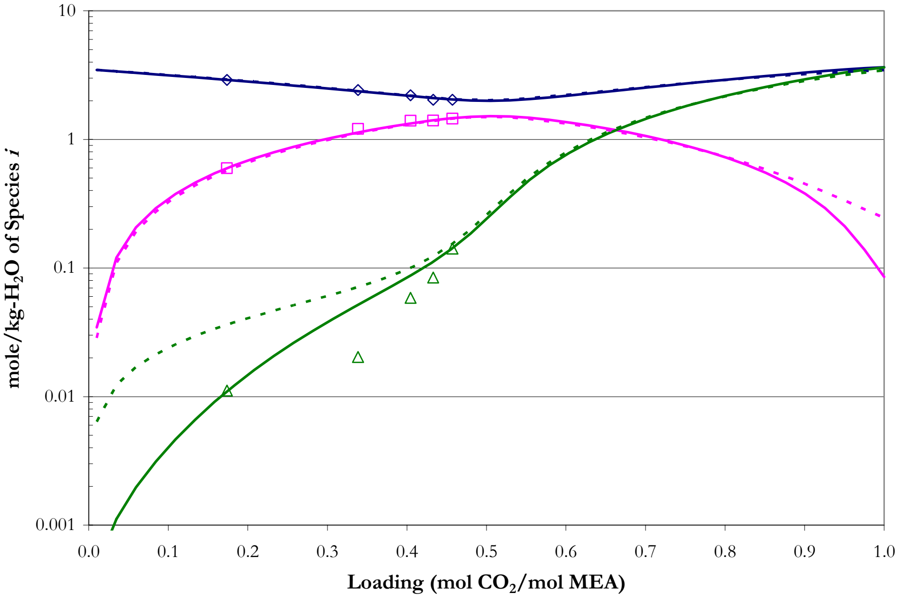

Figure 13.5-42. Comparison of Liquid Phase NMR Speciation in 3.5 m MEA at 27 °C to Model Predictions. Points: ◊, MEA+$MEAH^+$, □, $MEACOO^{-1}$, △, $CO_2+CO_3^{-2}+HCO_3^{-1}$, from this work. Lines: - - -, Austgen (1989), ▬, this work.

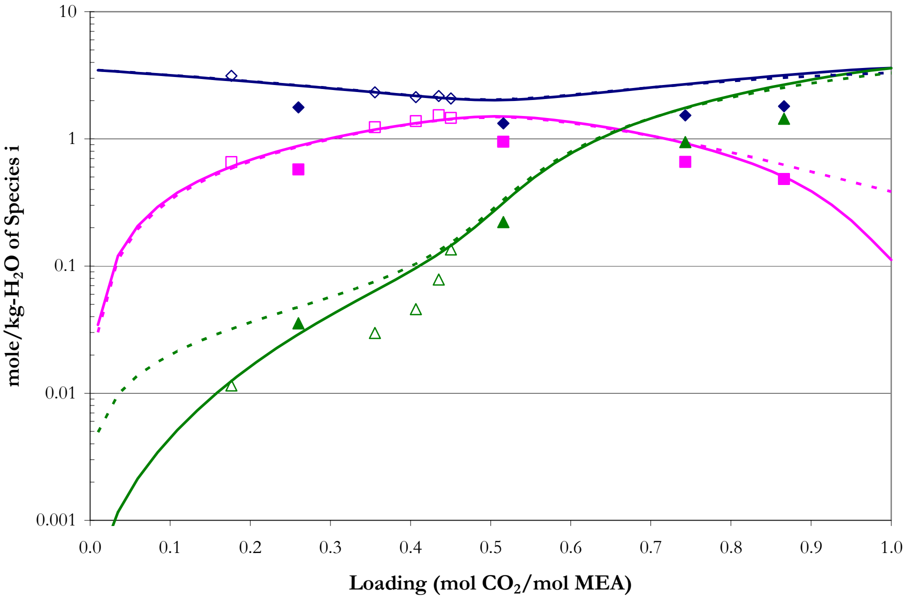

Figure 13.5-43. Comparison of Liquid Phase NMR Speciation in 3.5 m MEA at 40 °C to Model Predictions. Points: ♦, MEA+$MEAH^+$, ■, $MEACOO^{-1}$, ▲, $CO_2+CO_3^{-2}+HCO_3^{-1}$, from Poplsteinova (2004); ◊, MEA+$MEAH^+$, □, $MEACOO^{-1}$, △, $CO_2+CO_3^{-2}+HCO_3^{-1}$, from this work. Lines: - - -, Austgen (1989), ▬, this work.

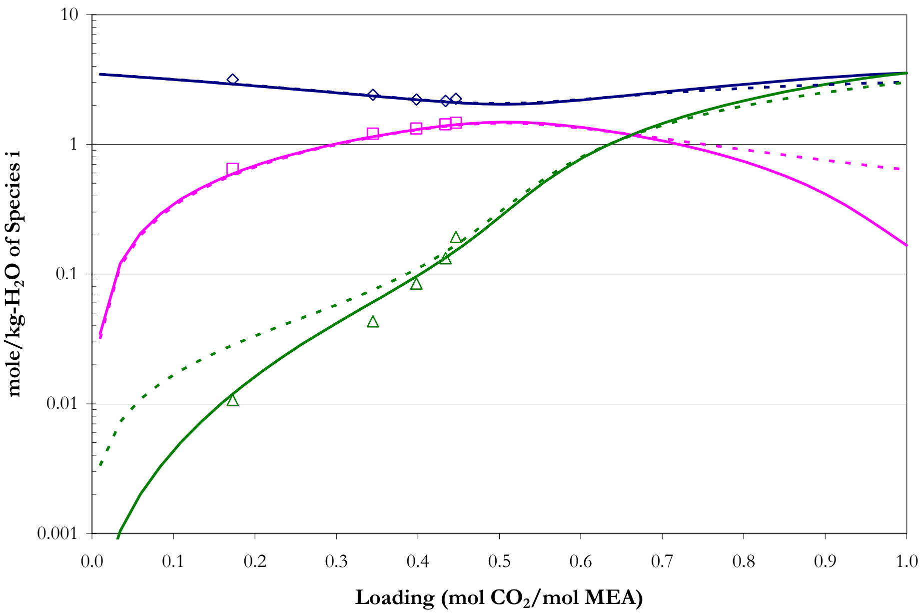

Figure 13.5-44. Comparison of Liquid Phase NMR Speciation in 3.5 m MEA at 60 °C to Model Predictions. Points: ◊, MEA+MEAH$^+$, □, MEACOO^{-1}, △, CO_2+CO_3^{-2}+HCO_3^{-1}, from this work. Lines: - - -, Austgen (1989), ▬, this work.

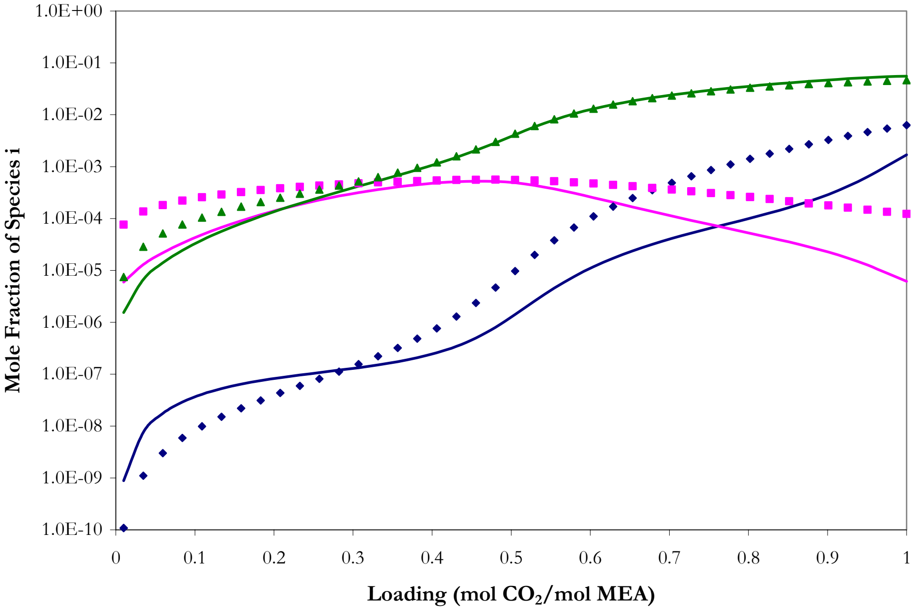

Figure 13.5-45. Comparison of Liquid Phase Speciation in 3.5 m MEA at 40 °C based on Model Predictions. Points: ◆, CO_2, ■, CO_3^{-2}, ▲, HCO_3^{-1} from Austgen (1989). Lines: this work.

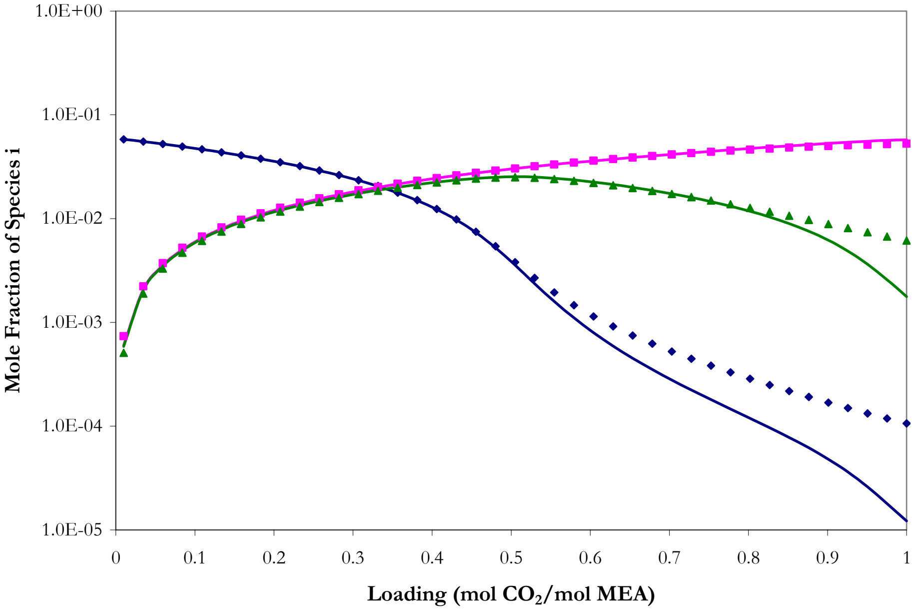

Figure 13.5-46. Comparison of Liquid Phase Speciation in 3.5 m MEA at 40 °C based on Model Predictions. Points: ♦, MEA, ■, MEAH^{+1}, ▲, MEACOO^{-1} from Austgen (1989). Lines: this work.

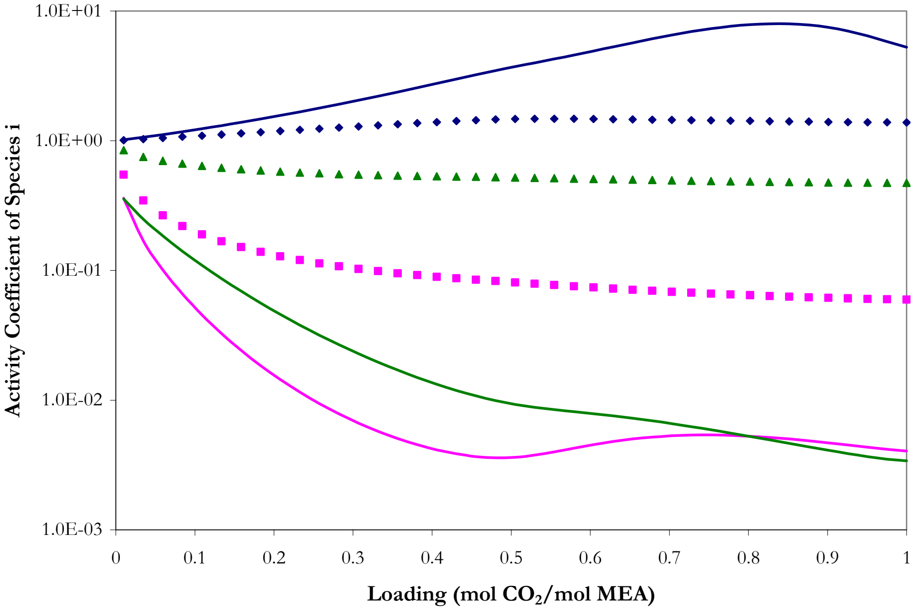

Figure 13.5-47. Comparison of Liquid Phase Activity Coefficients in 3.5 m MEA at 40 °C based on Model Predictions. Points: ♦, CO_2, ■, CO_3^{-2}, ▲, HCO_3^{-1} from Austgen (1989). Lines: this work.

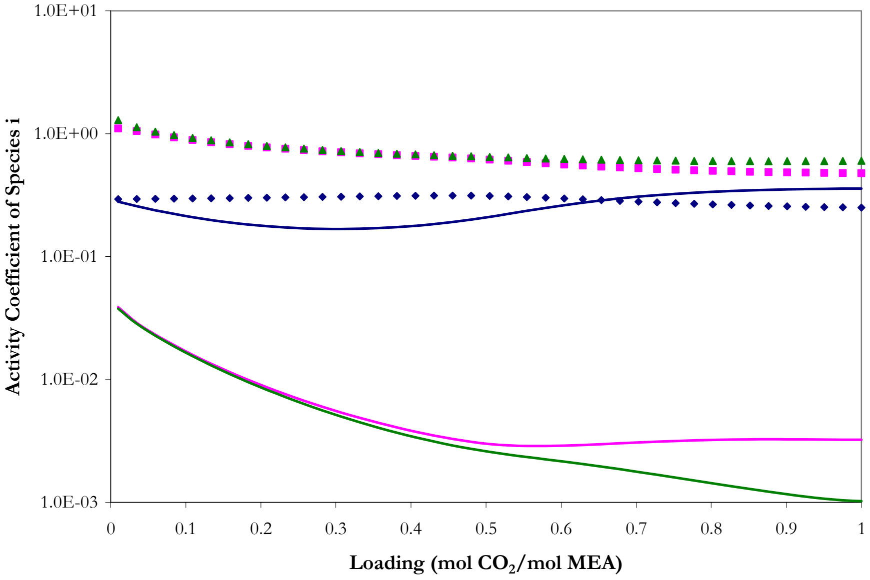

Figure 13.5-48. Comparison of Liquid Phase Activity Coefficients in 3.5 m MEA at 40 °C based on Model Predictions. Points: ♦, MEA, ■, $MEAH^{+1}$, ▲, $MEACOO^{-1}$ from Austgen (1989). Lines: this work.

Liquid Phase Speciation Predictions for 7 m MEA

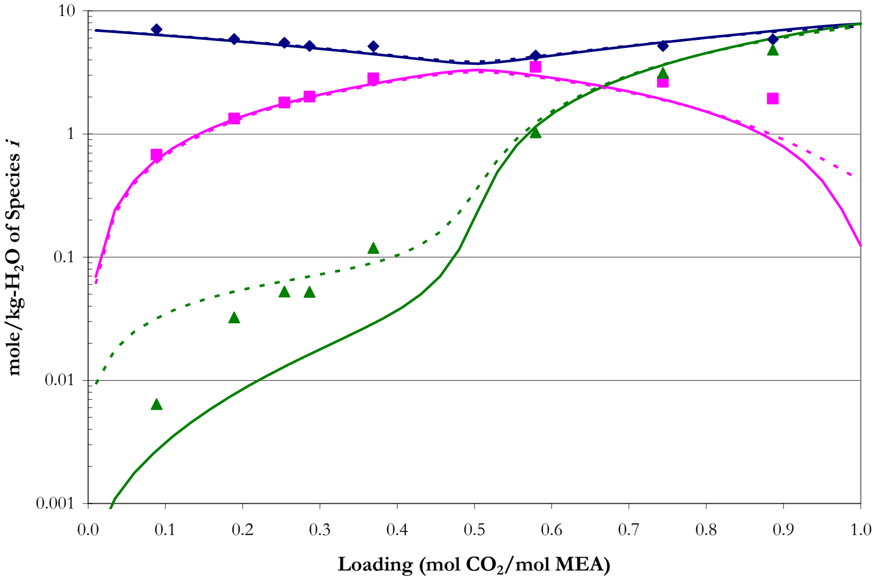

Figure 13.5-49. Comparison of Liquid Phase NMR Speciation in 7 m MEA at 20 °C to Model Predictions. Points: ♦, MEA+$MEAH^+$, ■, $MEACOO^{-1}$, ▲, CO_2+CO_3^{-2}+HCO_3^{-1}, from Poplsteinova (2004). Lines: - - -, Austgen (1989), ▬, this work.

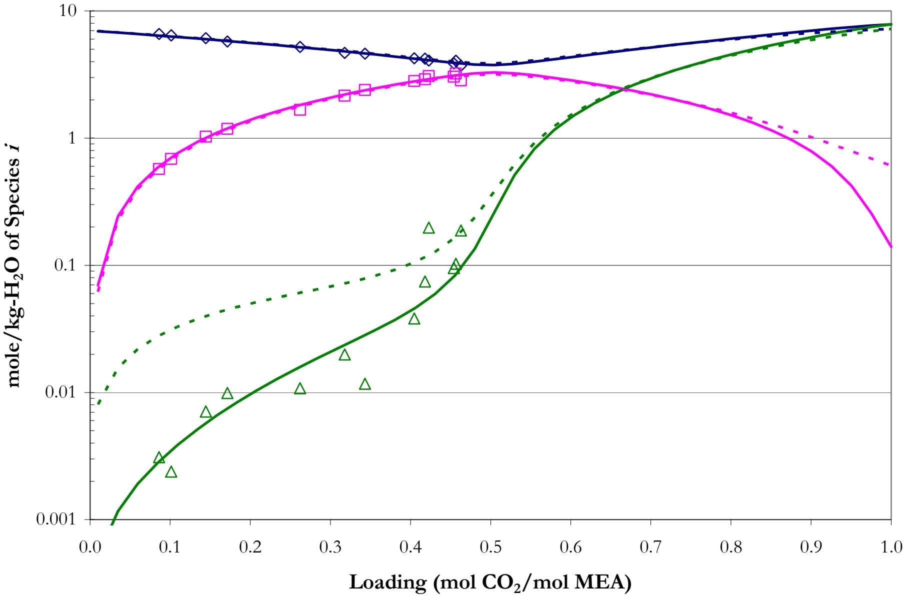

Figure 13.5-50. Comparison of Liquid Phase NMR Speciation in 7 m MEA at 27 °C to Model Predictions. Points: ◊, MEA+MEAH$^+$, □, MEACOO^{-1}, Δ, CO_2+CO_3^{-2}+HCO_3^{-1}, from this work. Lines: - - -, Austgen (1989), ▬, this work.

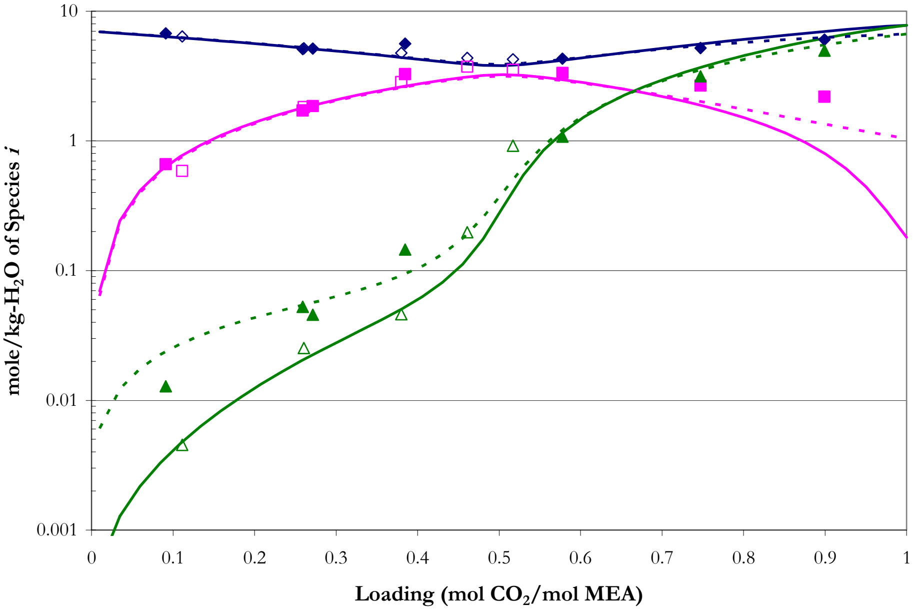

Figure 13.5-51. Comparison of Liquid Phase NMR Speciation in 7 m MEA at 40 °C to Model Predictions. Points: ♦, MEA+MEAH$^+$, ■, MEACOO^{-1}, ▲, CO_2+CO_3^{-2}+HCO_3^{-1}, from Poplsteinova (2004); ◊, MEA+MEAH$^+$, □, MEACOO^{-1}, Δ, CO_2+CO_3^{-2}+HCO_3^{-1}, from this work. Lines: - - -, Austgen (1989), ▬, this work.

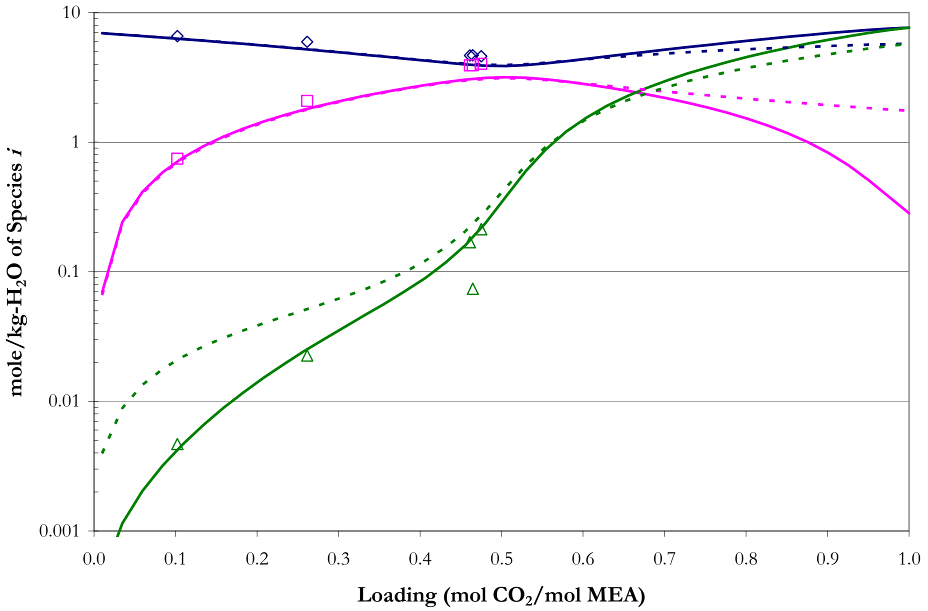

Figure 13.5-52. Comparison of Liquid Phase NMR Speciation in 7 m MEA at 60 °C to Model Predictions. Points: ◊, MEA+MEAH⁺, □, MEACOO⁻¹, Δ, CO_2+CO_3^{-2}+HCO_3^{-1}, from this work. Lines: - - -, Austgen (1989), ▬, this work.

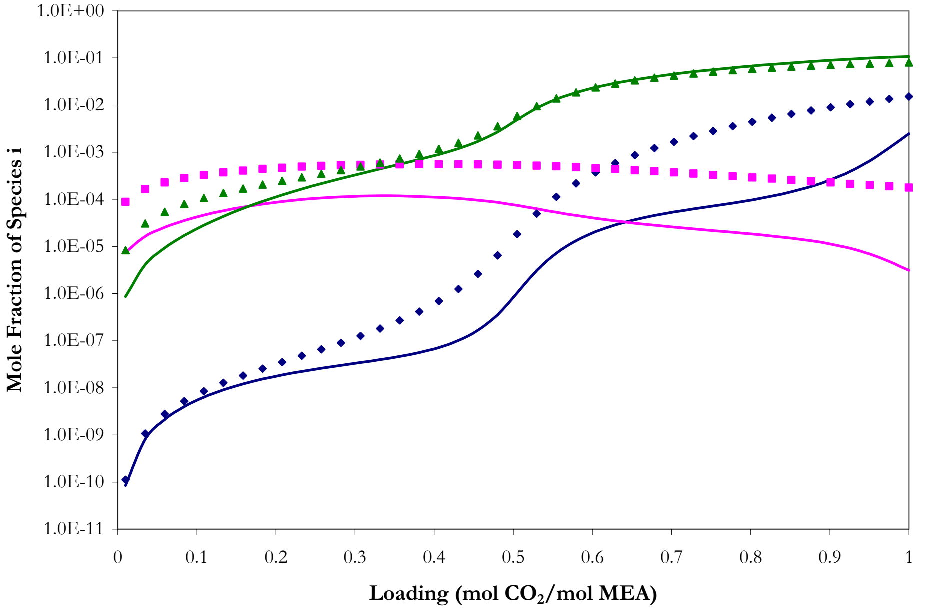

Figure 13.5-53. Comparison of Liquid Phase Speciation in 7 m MEA at 40 °C based on Model Predictions. Points: ♦, CO_2, ■, CO_3^{-2}, ▲, HCO_3^{-1} from Austgen (1989). Lines: this work.

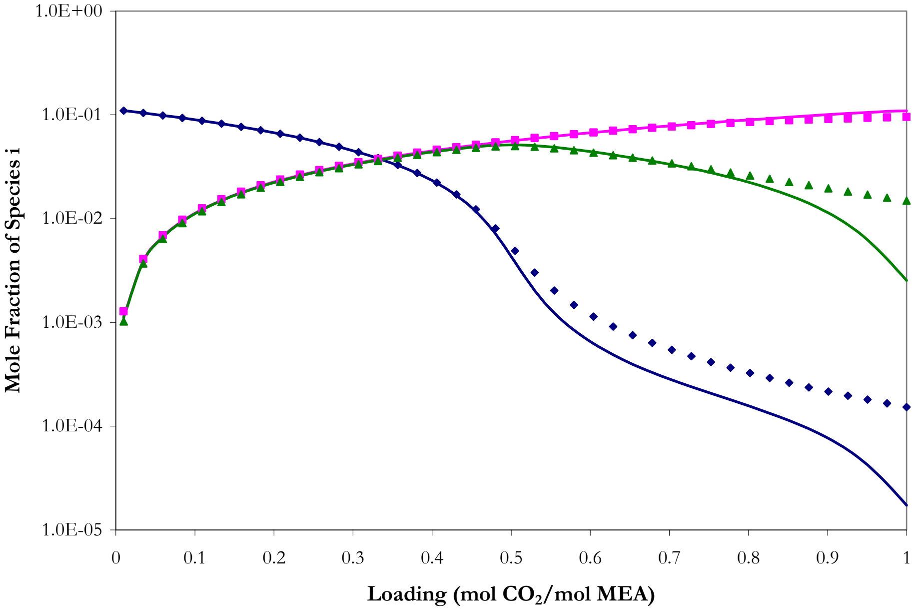

Figure 13.5-54. Comparison of Liquid Phase Speciation in 7 m MEA at 40 °C based on Model Predictions. Points: ♦, MEA, ■, MEAH^{+1}, ▲, MEACOO^{-1} from Austgen (1989). Lines: this work.

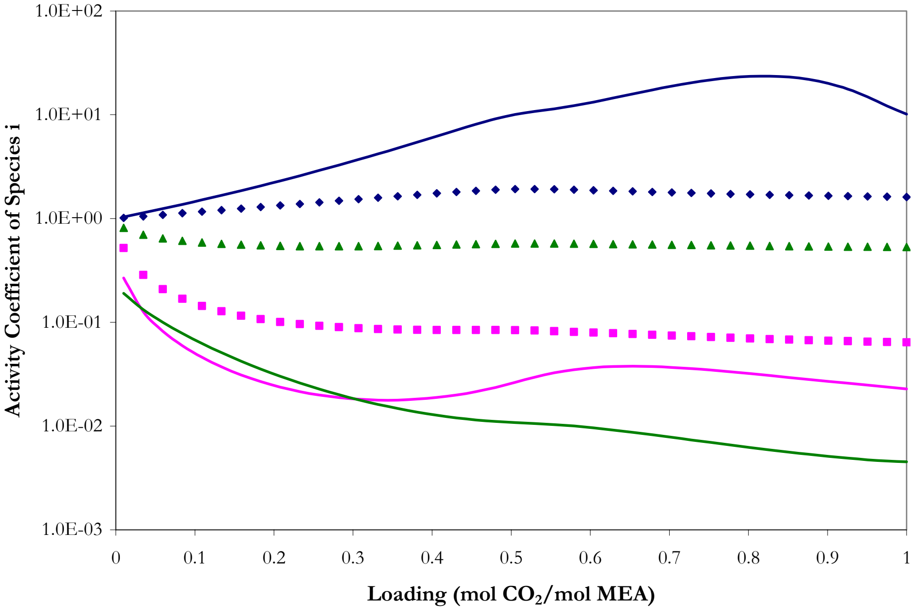

Figure 13.5-55. Comparison of Liquid Phase Activity Coefficients in 7 m MEA at 40 °C based on Model Predictions. Points: ♦, CO_2, ■, CO_3^{-2}, ▲, HCO_3^{-1} from Austgen (1989). Lines: this work.

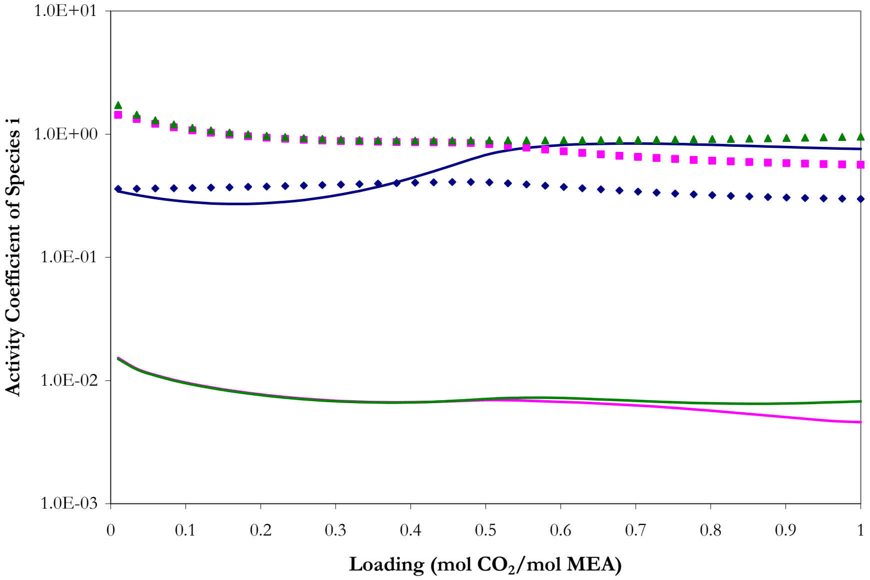

Figure 13.5-56. Comparison of Liquid Phase Activity Coefficients in 7 m MEA at 40 °C based on Model Predictions. Points: ♦, MEA, ■, $MEAH^{+1}$, ▲, $MEACOO^{-1}$ from Austgen (1989). Lines: this work.

Liquid Phase Speciation Predictions for 11 m MEA

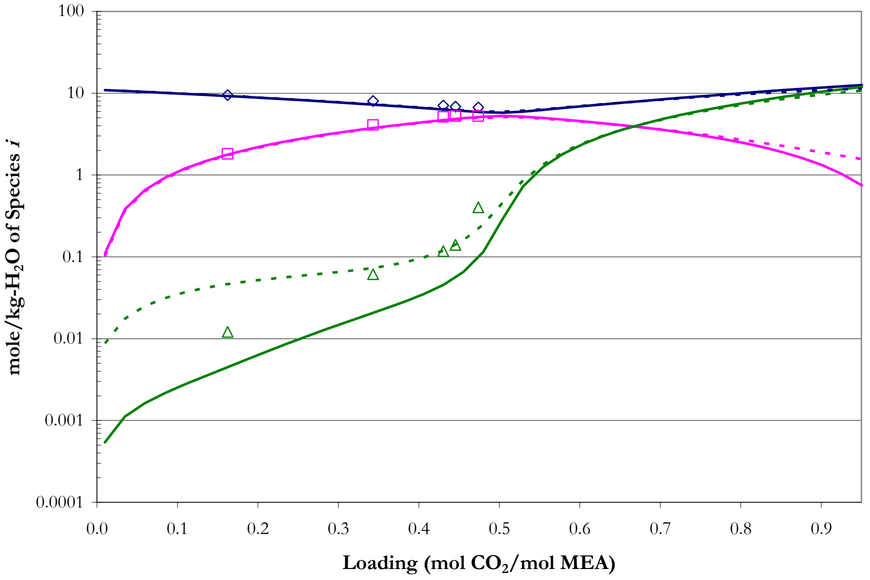

Figure 13.5-57. Comparison of Liquid Phase NMR Speciation in 11 m MEA at 27 °C to Model Predictions. Points: ♦, MEA+$MEAH^+$, ■, $MEACOO^{-1}$, ▲, CO_2+CO_3^{-2}+HCO_3^{-1}, from Poplsteinova (2004). Lines: - - -, Austgen (1989), ▬, this work.

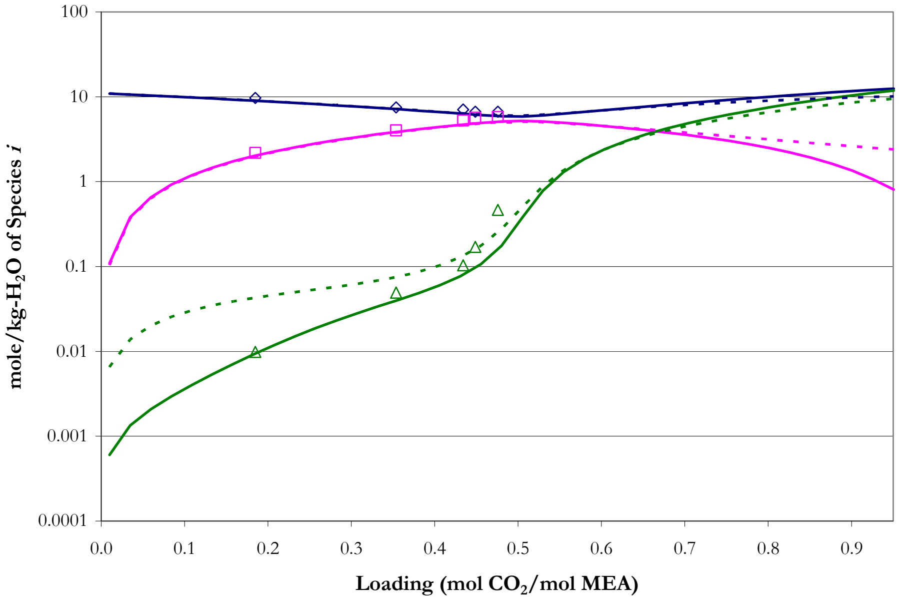

Figure 13.5-58. Comparison of Liquid Phase NMR Speciation in 11 m MEA at 40 °C to Model Predictions. Points: ♦, MEA+MEAH$^+$, ■, MEACOO^{-1}, ▲, CO_2+CO_3^{-2}+HCO_3^{-1}, from Poplsteinova (2004). Lines: - - -, Austgen (1989), ▬, this work.

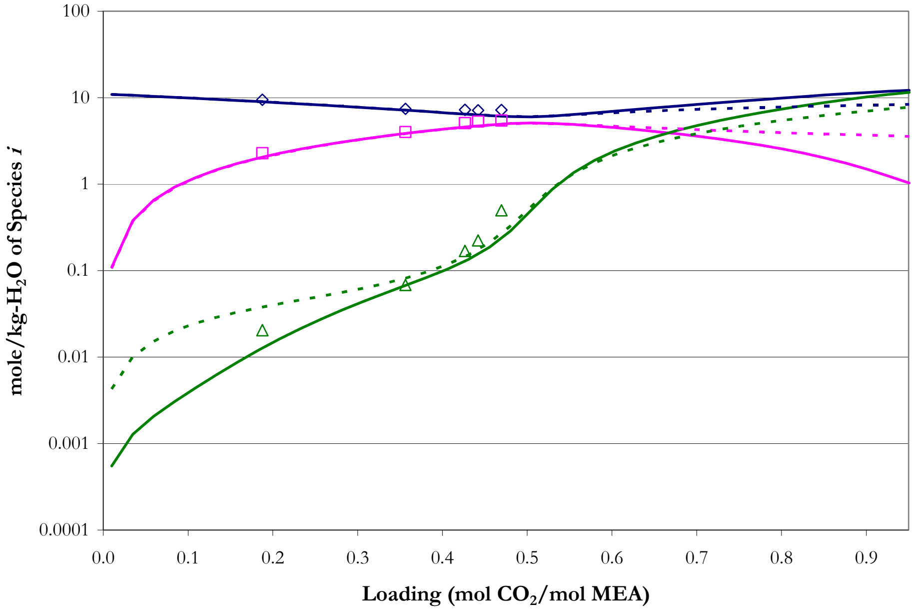

Figure 13.5-59. Comparison of Liquid Phase NMR Speciation in 11 m MEA at 60 °C to Model Predictions. Points: ♦, MEA+MEAH$^+$, ■, MEACOO^{-1}, ▲, CO_2+CO_3^{-2}+HCO_3^{-1}, from Poplsteinova (2004). Lines: - - -, Austgen (1989), ▬, this work.

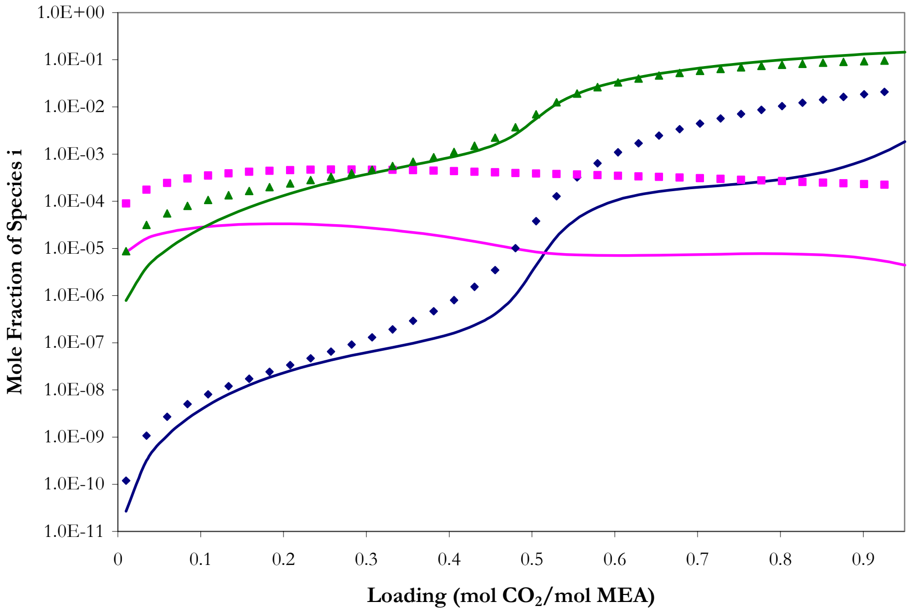

Figure 13.5-60. Comparison of Liquid Phase Speciation in 11 m MEA at 40 °C based on Model Predictions. Points: ♦, CO_2, ■, CO_3^{-2}, ▲, HCO_3^{-1} from Austgen (1989). Lines: this work.

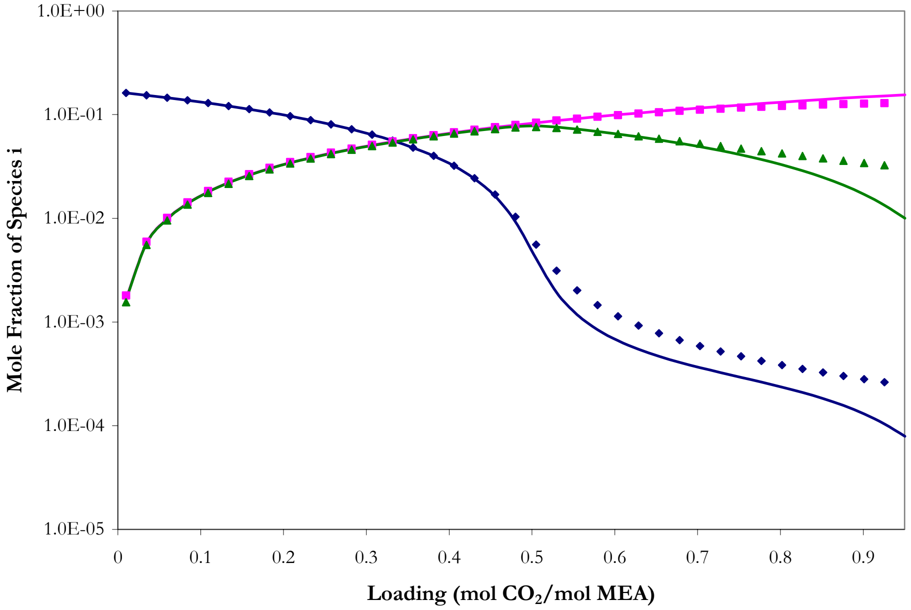

Figure 13.5-61. Comparison of Liquid Phase Speciation in 11 m MEA at 40 °C based on Model Predictions. Points: ♦, MEA, ■, $MEAH^{+1}$, ▲, $MEACOO^{-1}$ from Austgen (1989). Lines: this work.

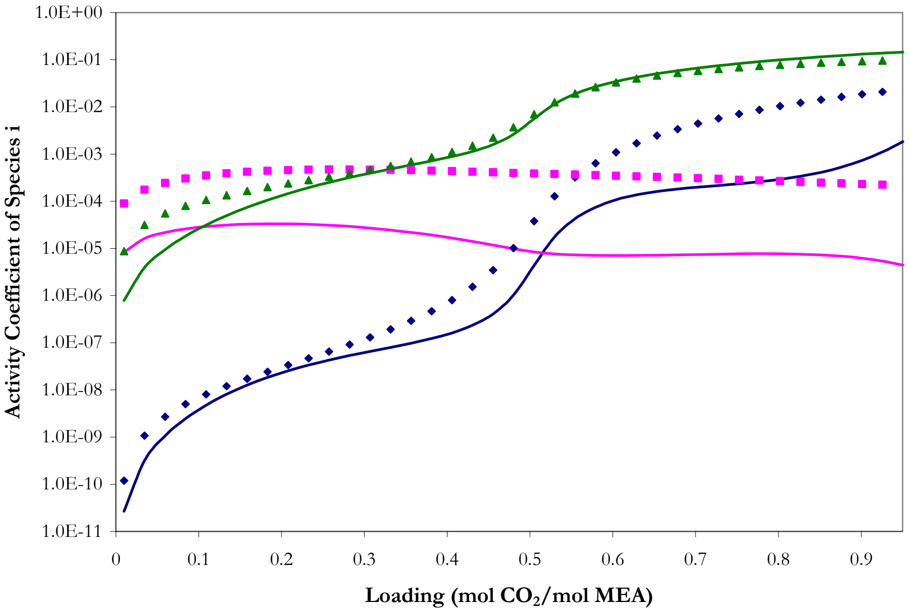

Figure 13.5-62. Comparison of Liquid Phase Activity Coefficients in 11 m MEA at 40 °C based on Model Predictions. Points: ♦, CO_2, ■, CO_3^{-2}, ▲, HCO_3^{-1} from Austgen (1989). Lines: this work.

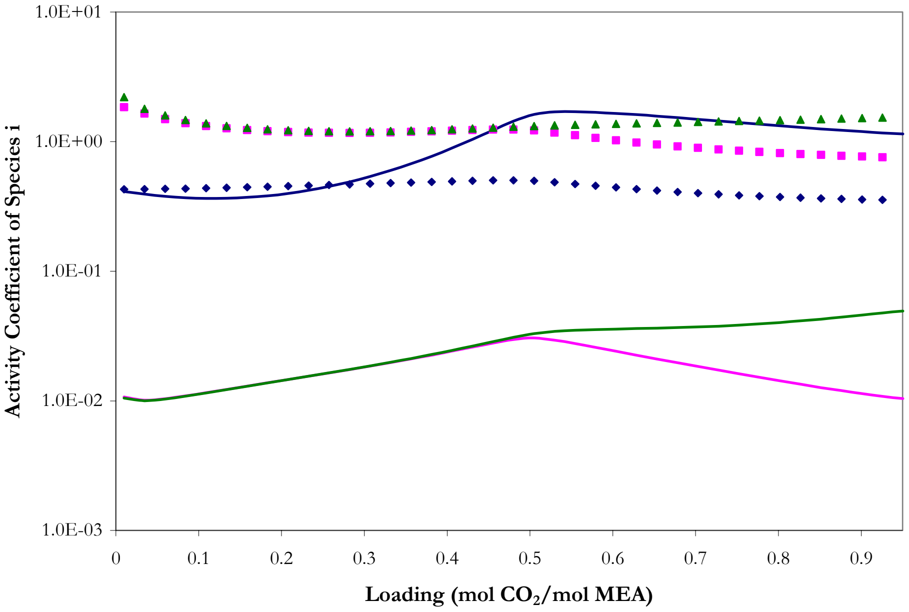

Figure 13.5-63. Comparison of Liquid Phase Activity Coefficients in 11 m MEA at 40 °C based on Model Predictions. Points: ♦, MEA, ■, $MEAH^{+1}$, ▲, $MEACOO^{-1}$ from Austgen (1989). Lines: this work.

13.5.5 *Carbamate Stability Constant*

Using Equations 13-25 and estimates for the infinite dilution aqueous phase free energy of formation, the infinite dilution aqueous phase enthalpy of formation, and the infinite dilution aqueous phase heat capacity polynomial for monoethanolamine carbamate from Table 13.4-3, we can then analytically determine the chemical equilibrium constant for monoethanolamine carbamate as illustrated in Figure 13.5-64 and given below as a temperature dependent linear function on a mole fraction basis based on Table 13.5-1.

Table 13.5-1. Estimates for the Chemical Equilibrium Constant Associated with the MEA Carbamate Formation (mole fraction basis).

Equation #	A	σ_A	B	σ_B	C	σ_C	D	σ_D
13-10	-222	0.25	-657	27	42.0	0.74	-0.108	0.0029

$\ln K = A + B/T(K) + C \cdot \ln T(K) + D \cdot T(K)$

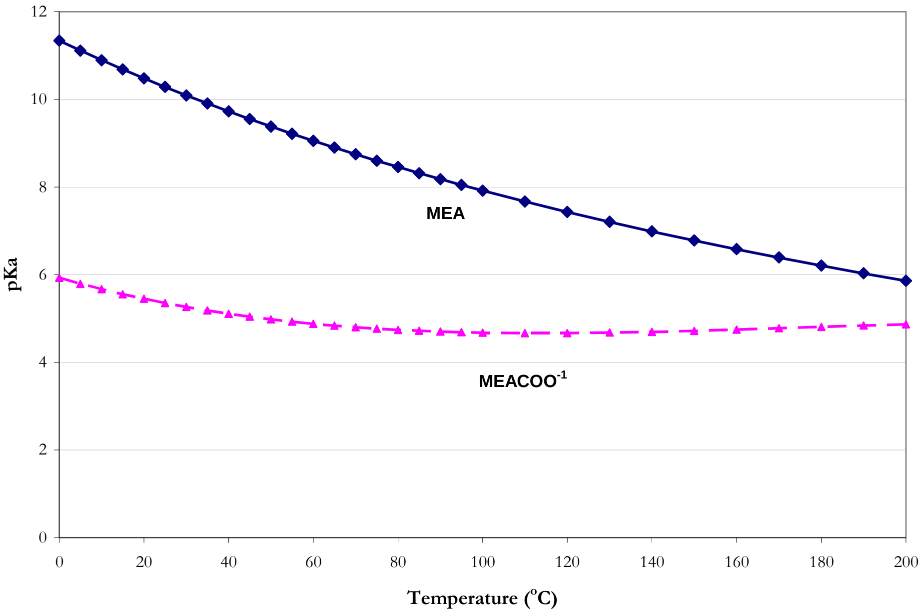

Figure 13.5-64. Mole Fraction Based Chemical Equilibrium Constants for Equations 13-9 and 13-10.

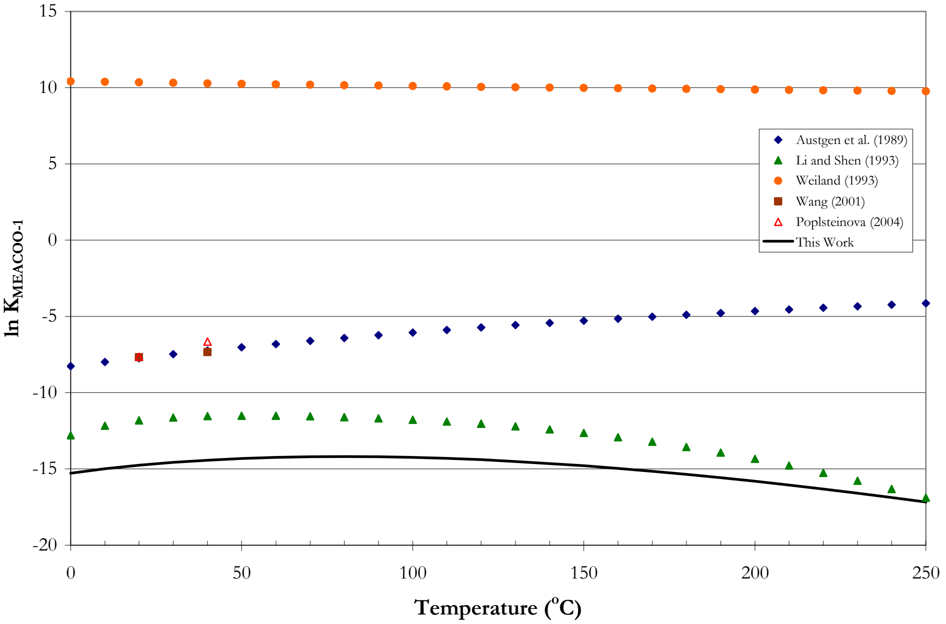

Figure 13.5-65. Comparison of Molality Based Carbamate Chemical Equilibrium Constant.

Figure 13.5-64 illustrates an important point; even though each author successfully regressed experimental data for the H_2O-MEA-CO_2 system, predictions for the calculated chemical equilibrium constant for monoethanolamine carbamate are different. This discrepancy is due to the thermodynamic foundations for each model. Each model would describe the activity coefficients differently based on the regression methodology they employed, the type of thermodynamic model they used, and the types of thermodynamic data that were used in the model regression. Overall, predictions for the chemical equilibrium constant for monoethanolamine carbamate are consistent with previous work given the range of scatter of the reported values.

13.6 Abridged elecNRTL Predictive Correlations

To anticipate installation difficulties with the implementation of our model on future platforms, we have developed specific correlations based on predictive results from our rigorous thermodynamic model for the liquid phase specific heat capacity of H_2O-MEA-CO_2 based on experimental predictions from this work.

Correlations for the Specific Heat Capacity

Predictions for the specific heat capacity for 3.5 and 7 m MEA in loaded solutions are based on the full model predictions, as shown in Figure 13.5-26 and Figure 13.5-28, where related to the following relations for three predictors:

$$\begin{aligned} C_p^l\left(\frac{kJ}{kg-K}\right) = {} & C_1 + C_2T + C_3T^2 + C_4\left[MEA\right] + C_5Ldg + \\ & C_6Ldg^2 + C_7\left[MEA\right]T + C_8\left[MEA\right]Ldg + \\ & C_9T\cdot Ldg + C_{10}\left[MEA\right]\cdot T\cdot Ldg \end{aligned} \qquad 13\text{-}58$$

Where
T is the temperature, °C,
$\left[MEA\right]$ is the concentration of MEA, m (mole/kg-H_2O),
Ldg is the loading of the solution, mol CO_2/mol MEA.

Equation 13-59 allows for nonlinearity in the temperature, concentration, and loading dependence. The interaction terms $\left(\left[MEA\right]\cdot T\right.$, $\left[MEA\right]\cdot Ldg$, $T\cdot Ldg$, $\left.\left[MEA\right]\cdot T\cdot Ldg\right)$ allows for twisting of the predictive surface versus the four predictors. Predictions from the full model for the specific heat capacity of MEA are tabulated in Table 13.6-1.

Performing ordinary least squares (OLS) regression for the full model using ARC, the following regression summary statistics output for coefficients estimates in Equation 13-59 are shown in Table 13.6-2.

Table 13.6-1. Specific Heat Capacity Predictions (kJ/kg-K) from the full model.

	MEA Concentration (mole/kg-H_2O)					
	3.5			7		
	Loading (mol CO_2/mol MEA)					
Temperature (°C)	0.097	0.375	0.583	0.139	0.358	0.541
40	3.816	3.631	3.593	3.517	3.299	3.219
50	3.839	3.650	3.609	3.545	3.327	3.252
60	3.863	3.677	3.630	3.575	3.359	3.285
70	3.889	3.710	3.653	3.605	3.396	3.316
80	3.915	3.745	3.675	3.633	3.432	3.346
90	3.940	3.779	3.697	3.656	3.465	3.374
100	3.964	3.813	3.719	3.676	3.492	3.406
110	3.989	3.849	3.747	3.693	3.521	3.456
120	4.010	3.893	3.797	3.708	3.555	3.558

Table 13.6-2. ARC Regression Output for the Predictive FULL CPMX Correlation.

Parameter	Estimate	σ wrt Estimate
C_1	4.008E+00	5.328E-02
C_2	2.474E-03	8.391E-04
C_3	5.907E-06	3.826E-06
C_4	-5.234E-02	9.110E-03
C_5	-5.575E-01	1.367E-01
C_6	7.671E-01	9.571E-02
C_7	-2.044E-04	1.083E-04
C_8	-1.283E-01	2.323E-02
C_9	-3.199E-03	1.440E-03
C_{10}	9.364E-04	2.764E-04

Residual Sum of Squares:	0.0119
Degree of Freedom:	44

Recall that the standard error of an estimate is the estimated standard deviation of that statistic. Notice that all of the estimates are smaller relative to the standard error. A complete description of the variability of the coefficient estimates requires examining the correlations between the estimates as shown in Table 13.6-3.

Table 13.6-3. Correlation Matrix of the Coefficient Estimates for the Full CPMX Model.

Parameter	1	2	3	4	5	6	7	8	9	10
1	1.00									
2	-0.89	1.00								
3	0.41	-0.73	1.00							
4	-0.85	0.61	0.00	1.00						
5	-0.75	0.51	0.00	0.72	1.00					
6	0.10	0.00	0.00	0.04	-0.46	1.00				
7	0.81	-0.65	0.00	-0.95	-0.71	0.00	1.00			
8	0.75	-0.54	0.00	-0.89	-0.83	-0.01	0.85	1.00		
9	0.76	-0.60	0.00	-0.80	-0.84	0.00	0.84	0.90	1.00	
10	-0.71	0.57	0.00	0.85	0.80	0.00	-0.89	-0.95	-0.94	1.00

Table 13.6-3 shows three highly correlated parameters and one independent parameter, but the correlation between other coefficients is relatively small, suggesting that C_3, C_8, or C_9 might be usefully removed from the model without significant loss of information.

After performing backward elimination using ARC, the following optimum model regression summary statistics output for estimates of the coefficients for Equation 13-59 are shown in Table 13.6-4.

Notice that all of the estimates are larger relative to their standard errors. Comparing the estimates from the full model to the optimum model, there was relatively little difference between the estimated values. Figure 13.6-1 and Figure 13.6-2 demonstrate the predictive quality of Equation 13-59 based on the coefficients from Table 13.6-4 for the optimum model.

Table 13.6-4. ARC Regression Output for the Predictive OPTIMUM CPMX Correlation.

Parameter	Estimate	σ wrt Estimate
C_1	3.974E+00	4.954E-02
C_2	3.429E-03	5.856E-04
C_4	-5.565E-01	1.395E-01
C_5	-5.225E-02	9.295E-03
C_6	7.648E-01	9.766E-02
C_7	-2.066E-04	1.105E-04
C_8	-1.283E-01	2.371E-02
C_9	-3.206E-03	1.469E-03
C_{10}	9.388E-04	2.820E-04

Residual Sum of Squares:	0.0127
Degree of Freedom:	45

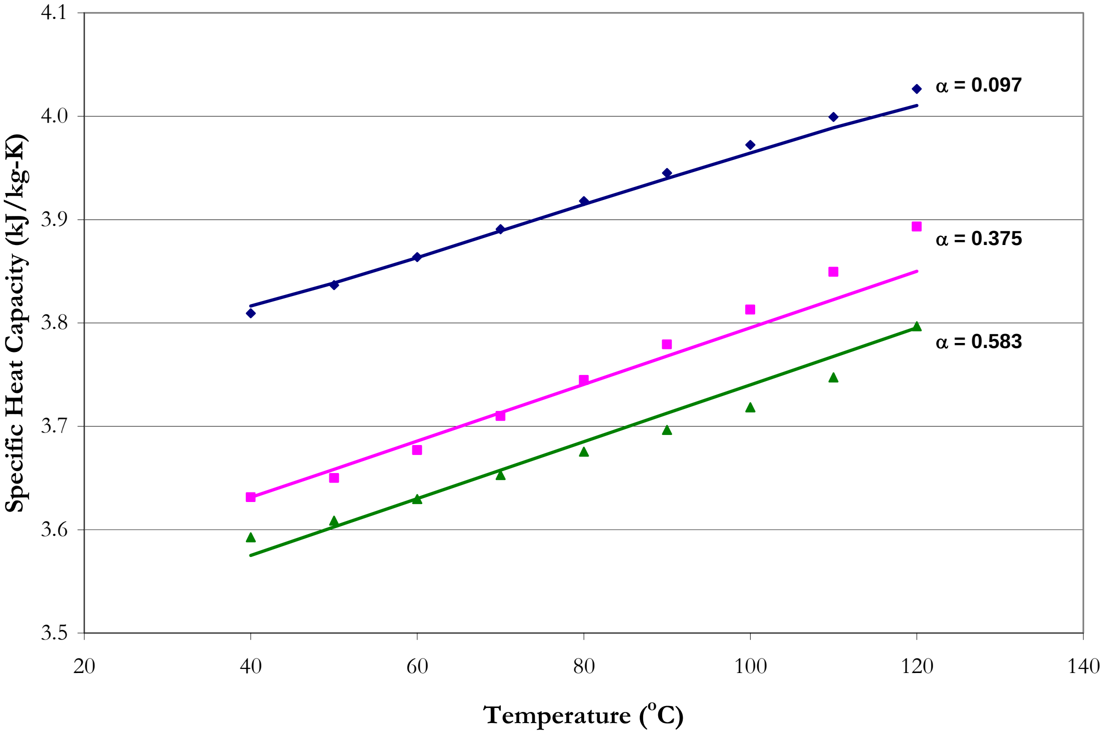

Figure 13.6-1. Comparison of the Specific Heat Capacity Predictions from Equation 15-59 to elecNRTL Model Predictions from 40 to 120 °C in loaded 3.5 m MEA solutions.

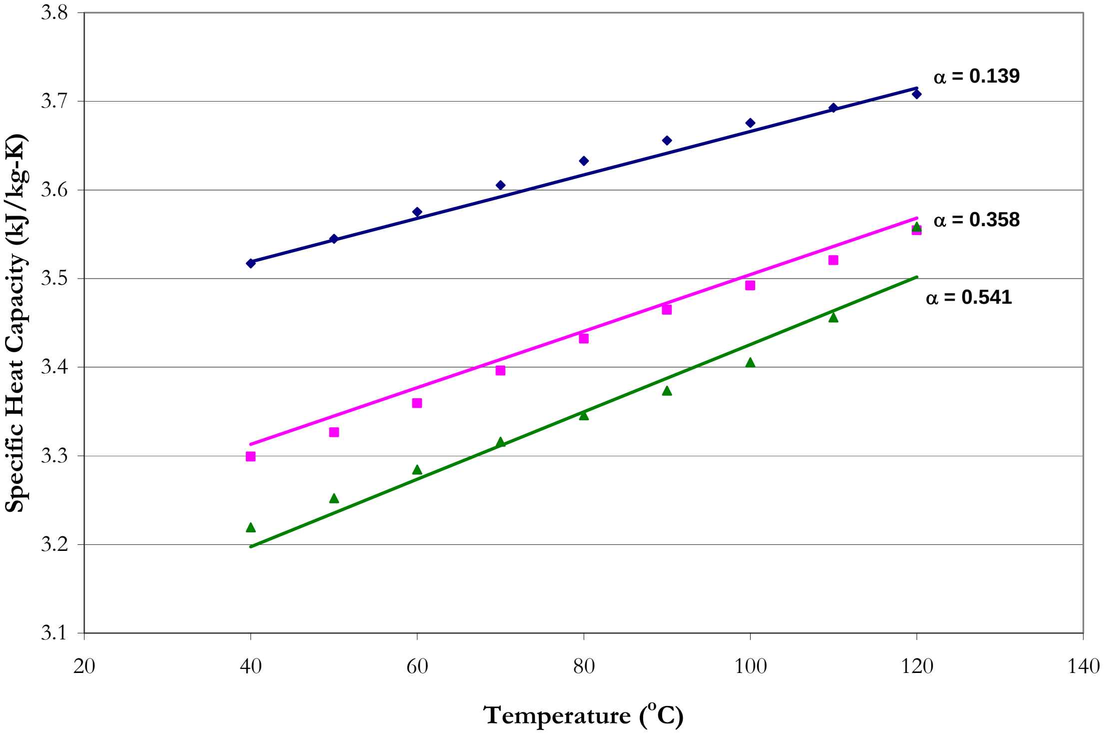

Figure 13.6-2. Comparison of the Specific Heat Capacity Predictions from Equation 15-59 to elecNRTL Model Predictions from 40 to 120 °C in loaded 7 m MEA solutions.

13.7 Conclusions

In conclusion, the full model adequately describes the CO_2 solubility data within an average absolute relative error of ± 27.19 percent even though the full model over estimates the solubility of CO_2 in 3.5 m MEA by a factor of 3. This error may be due to full model overestimating the liquid phase speciation as shown in Figure 13.5-45, implying an error may exist within either the experimental NMR speciation data or the experimental CO_2 solubility data. On the other hand, since this system lies at the boundary of the chosen experimental data, the error could be a result of the regression analysis.

The model was able to adequately predict the partial pressure of MEA. Due to an error in the estimation of the volatility in the binary system, subsequent volatility predictions were subjected to this estimation error as shown by the circled region in Figure 13.5-17 through Figure 13.5-22. Overall, the full model gave an adequate fit to the experimental volatility data.

In terms of CO_2 capture in industrial application, with a nominal loading between 0.2 to 0.5 mol CO_2/mol MEA between 40 and 60 °C, predictions from this work and from Freguia (2002) adequately predict the partial pressure of CO_2. In addition, experimental CO_2 solubility measurements from this work appear to agree with published literature data from Jou et al. (1995) at 40 and 60 °C.

We compared experimental specific heat capacity measurements from this work to predictions from Austgen (1989), Freguia (2002), and to this work. Model predictions from Austgen (1989) and Freguia (2002) overestimated the specific heat capacity over the range in loading. Even though the Austgen (1989) and Freguia (2002) models did not include calometric measurements as part of their original regression analysis, we chose to illustrate the possible enthalpy differences as compared to purely CO_2 solubility based thermodynamic models.

In addition, we were able to illustrate that the apparent partial heat capacity of total dissolved CO_2 may be considered small with a magnitude less than4 kJ/kmol-K. Overall, the full model adequately predicted the specific heat capacity for 3.5 and 7 m MEA mixtures within an average absolute relative error of ± 0.79 percent.

We also compared experimental differential enthalpy of CO_2 absorption measurements from Kim et al. (2007) to predictions based on Equation 13-36 from Austgen (1989), Freguia (2002), and to this work. Model predictions from Austgen (1989) and Freguia (2002) underestimate the enthalpy of CO_2 absorption at high temperatures over the range in loading. Figure 13.5-35 through Figure 13.5-37 illustrated that the full model over estimates the enthalpy of CO_2 absorption at low loading. We theorized that this error may be due to an error in the liquid phase speciation at low loading. Since the concentration of the liquid phase drives the prediction for the fugacity of CO_2 in the vapor phase. Or this error may be due to the regression method itself. Within DRS, each variable is given a standard deviation according to the error associated with the measurement. During a regression, DRS attempts to satisfy the model constraints while simultaneously adjusting the measured variables (i.e. T, P, x_i, y_i, etc.) to minimize the objective function. Overall, the full model adequately predicts the enthalpy of CO_2 absorption for 7 m MEA mixtures within an average absolute relative error of ± 12.91 percent with respect to the temperature and loading dependence of the experimental data.

The enthalpy of CO_2 absorption at a loading of 0.3 mol CO_2/mol MEA increased from 80 to110 kJ/mol-CO_2, because the apparent partial heat capacity of total dissolved CO_2 may be considered small.

In terms of NMR speation, we compared experimental liquid phase NMR speciation measurements from Poplsteinova (2004) and this work to predictions from Austgen (1989) and from this work. Model predictions from Austgen (1989) overestimated the apparent CO_3^{-2} + HCO_3^{-1} concentration at low loadings and the $MEACOO^{-1}$ concentration at high loadings over the range in temperature studied in this work. Overall, the full model adequately predicts the liquid phase NMR speciation for 3.5, 7, and 11 m MEA mixtures within an average absolute relative error of ± 4.66 percent.

We illustrated an important point in Figure 13.5-65; even though several authors successfully regressed experimental data for the H_2O-MEA-CO_2 system, predictions for the calculated chemical equilibrium constant for monoethanolamine carbamate varied. This discrepancy may be due to the thermodynamic foundations for each model where each model would describe the activity coefficients differently based on the regression methodology they employed, the type of thermodynamic model they used, and the types of thermodynamic data that were used in the model regression. Overall, predictions for the chemical equilibrium constant for monoethanolamine carbamate are consistent with previous work given the range of scatter of the reported values.

Overall, the results presented above indicate that the elecNRTL model, through simultaneous regression gave a set of optimum parameters for the H_2O-MEA-CO_2 system where the full model adequately represents the literature data for loaded MEA solution.

CHAPTER XIV

Ternary Systems: H_2O-PZ-CO_2

14.1 Introduction

At this point in the thermodynamic modeling development, we have described molecule-molecule and molecule-electrolyte interactions for previous systems. For the last ternary system, interactions between molecules and electrolytes and interactions between electrolyte pairs with a common cation or anion will be considered within the H_2O-PZ-CO_2 system. This chapter describes the data regression and model predictions for the ternary {H_2O-Piperazine (PZ)-Carbon dioxide (CO_2)} system based on previous literature data and experimental results from this work. The results for the binary interaction parameters for the electrolyte-NRTL (elecNRTL) model within Aspen Plus^{TM} are then presented, showing good statistical fit to the literature data with an average absolute relative error of ± 10.59 %, with the exception of a few outliers.

14.2 H_2O-PZ-CO_2

With ions in an electrolyte solution, the elecNRTL model accounts for contributions associated with long-range ion-ion interactions and local interactions which exist around any central species as proposed by Chen et al. (1982). In this section, we present background on the elecNRTL model for clarification purposes only.

The elecNRTL model is a molar Gibbs energy model given by the following form:

$$G_m^* = x_w \mu_w^* + \sum_k x_k \mu_k^\infty + \sum_j x_j \ln x_j + G_m^{*E} \qquad 14\text{-}1$$

where the excess Gibbs free energy model is given by the following form:

$$\frac{G_m^{*E}}{RT} = \frac{G_m^{*E,PDH}}{RT} + \frac{G_m^{*E,Born}}{RT} + \frac{G_m^{*E,lc}}{RT} \qquad 14\text{-}2$$

Where
PDH is the Pitzer-Debije-Hückel contribution for long range ion-ion interactions,
Born is the Born Correction for change in mixed solvent reference state, and
lc is the local contribution for short range interactions.

The molar Gibbs free energy and the molar excess Gibbs free energy are defined with the asymmetrical references state as infinite dilute in pure solvent. The reference state for ionic and molecular solutes follows the unsymmetrical convention defined as infinite dilution in water. The ideal mixing term is calculated where j refers to any component and the molar Gibbs free energy of pure water is calculated from the ideal gas contribution. The aqueous infinite dilution chemical potential is calculated from the infinite dilution aqueous phase heat capacity polynomial model, where the subscript k refers to any ions or molecular solute.

$$\mu_k^{\infty} = \Delta_f H_k^{\infty,aq} + \int_{T_0}^{T} \frac{C_{p,k}^{\infty,aq}}{T} dT - T\left(\frac{\Delta_f H_k^{\infty,aq} - \Delta_f G_k^{\infty,aq}}{T_0} + \int_{T_0}^{T} \frac{C_{p,k}^{\infty,aq}}{T} dT \right) + RT \ln\left(\frac{1000}{MW_w} \right) \quad 14\text{-}3$$

Where $\Delta_f H_k^{\infty,aq}$ and $\Delta_f G_k^{\infty,aq}$ are based on a molality scale and μ_k^{∞} is based on a mole fraction scale, the last term added for the conversion.

For molecular solutes, the aqueous infinite dilution chemical potential is calculated from Henry's law:

$$\mu_k^{\infty} = \mu_k^{\infty,ig} + RT \ln\left(\frac{H_{k,w}}{P^{ref}} \right) \quad 14\text{-}4$$

Where
T_0 is the reference temperature, 298.15 K,
P^{ref} is the reference pressure, 1 atm.

Thus, when the derivative of the Gibbs free energy at constant temperature and pressure reaches a minimum for a closed homogeneous system, the system has satisfied the condition for thermodynamic equilibrium.

For the elecNRTL model to calculate activity coefficients, the excess Gibbs free energy is related to the activity coefficient by the following thermodynamic relationship.

$$\ln \gamma_i = \frac{G_m^{*E}}{RT} = \left[\frac{\delta\left(nG_m^{*E} / RT \right)}{\delta n_i} \right] \quad 14\text{-}5$$

Please refer to Chapter VI for information relating to the specific contributions to the excess Gibbs energy model.

14.3 Chemical and Vapor-liquid Equilibrium of PZ

Figure 14.3-1 illustrates the proposed system to correlate/predict the solubility of CO_2 and PZ in aqueous solutions of PZ.

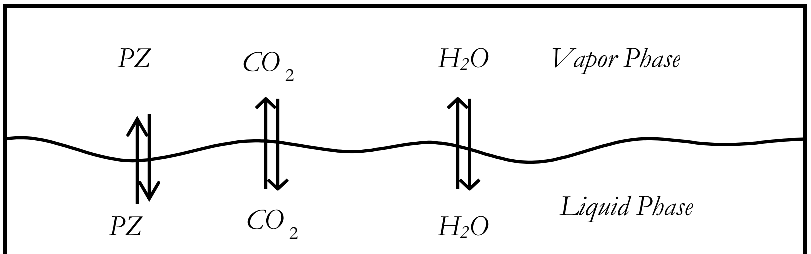

R1: $H_2O \leftrightarrow H^+ + OH^-$ 14-6

R2: $CO_2 + H_2O \leftrightarrow H^+ + HCO_3^{-1}$ 14-7

R3: $HCO_3^{-1} \leftrightarrow H^+ + CO_3^{-2}$ 14-8

R4: $PZH^{+1} \leftrightarrow PZ + H^+$ 14-9

R5: $PZH_2^{+2} \leftrightarrow PZH^{+1} + H^+$ 14-10

R6: $PZ + HCO_3^{-1} \leftrightarrow PZCOO^{-1} + H_2O$ 14-11

R7: $PZCOO^{-1} + HCO_3^{-1} \leftrightarrow PZ\left(COO^{-1}\right)_2 + H_2O$ 14-12

R8: $H^+PZCOO^{-1} \leftrightarrow PZCOO^{-1} + H^+$ 14-13

Figure 14.3-1. Chemical and Vapor-liquid Equilibrium of PZ.

Reaction 14-6 describes the ionization of water to proton $\left(H^{+}\right)$ and hydroxide ions $\left(OH^{-}\right)$; Reaction 14-7 describes the hydrolysis and ionization of dissolved CO_2 to H^+ and bicarbonate $\left(HCO_3^{-}\right)$ ions; Reaction 14-8 describes the dissociation of HCO_3^- to H^+ and carbonate $\left(CO_3^{-2}\right)$ ions; Reaction 14-9 describes the protonation of piperazine $\left(PZ\right)$ to protonated piperazine $\left(PZH^{+1}\right)$; Reaction 14-10 describes the protonation of protonated piperazine to diprotonated piperazine $\left(PZH_2^{+2}\right)$; Reaction 14-11 describes the piperazine carbamate formation $\left(PZCOO^{-1}\right)$; Reaction 14-12 describes the piperazine dicarbamate formation $\left(PZ\left(COO^{-1}\right)_2\right)$; Reaction 14-13 describes the protonated piperazine carbamate formation $\left(H^{+}PZCOO^{-1}\right)$. The chemical equilibrium constant for the above j equations is expressed in Aspen Plus™ in terms of the activity of component i as given by the following relationship.

$$K_j = \prod_i a_i^{\nu_{i,j}} \qquad 14\text{-}14$$

Where
K_j is the chemical equilibrium constant,
$\nu_{i,j}$ is the reaction stoichiometric coefficient of component i,
a_i is the activity of component i.

In this work, for Reactions 14-6 to 14-13, we did not define the chemical equilibrium constants as linear temperature dependent functions, but rather in terms of the reference state Gibbs free energy of the system:

$$\ln K_j = -\frac{\Delta G^o_{i,j}}{RT} \qquad \text{14-15}$$

Where

$\Delta G^o_{i,j}$ is the standard free energy of formation of component i.

The previous framework allows our rigorous thermodynamic model to be internally consistent with respect to governing thermodynamic definitions. Table 9.3-12 and Table 9.3-8 reported the standard state conditions at 25 °C associated with the species in Reactions 14-6 to 14-10 where the standard state conditions are consistent with published literature by Edwards et al. (1978) and Hetzer et al. (1968) as shown in Chapter XII and Chapter IX, respectively.

We chose to simplify the overall model by excluding Reaction 14-10 and diprotonated piperazine from the final model. This assumption is based on the second pKa of piperazine, as described in Chapter IX, where the relative concentration of diprotonated piperazine below a loading of 0.5 mol CO_2/2·mol PZ could be considered negligible. If in future work where the loading range is extended beyond a loading of 0.5, inclusion of the diprotonated piperazine reaction would need to be included.

For the precipitation of piperazine hexahydrate as described in Chapter IX, we chose to define the chemical equilibrium constant as linear temperature dependent function as given in Table 9-4-1 due to limited thermodynamic data available for the characterization of the solid phase.

As stated previously, Equation 14-15 relates the chemical equilibrium constant to the standard Gibbs free energy change of reaction.

$$\frac{\Delta G^o}{RT} = -\ln K \qquad 14\text{-}16$$

Where the standard property changes of reaction (e.g. Gibbs free energy and enthalpy) are defined as the difference between the standard property change of the products and reactants, weighted by their stoichiometric coefficients.

$$\Delta M^o = \sum_i \nu_i M_i^o \qquad 14\text{-}17$$

For molecular solutes (e.g. CO_2), the standard Gibbs free energy is described based on the ideal gas reference state by the following equation:

$$G_{CO_2}^o\left(T\right) = G_{CO_2}^{ig}\left(T\right) + RT\ln\frac{H_{CO_2}\left(T\right)}{P^{ref}} \qquad 14\text{-}18$$

Where
$G_{CO_2}^{ig}$ is the ideal gas Gibbs free energy, J/kmol,
H_{CO_2} is the Henry's Constant for CO_2 in H_2O (Chen et al. 1979), atm,
P^{ref} is the reference pressure, 1 atm.

For ionic species the aqueous phase infinite dilution molar heat capacity is described by the following equation:

$$C_{p,i}^{\infty,aq}\left(\frac{J}{kmol\cdot K}\right) = C_{1,i} + C_{2,i}T\left(K\right) + C_{3,i}T\left(K\right)^2 + \frac{C_{4,i}}{T\left(K\right)} \qquad 14\text{-}19$$

where coefficients for the aqueous phase infinite dilution molar heat capacity for carbonate, bicarbonate, and PZH^{+1} were described previously in Chapter XII - Section 12.5 and Chapter IX - Section 9.3, respectively.

The molar heat capacity of H_2O was described in Chapter VII by the following equation:

$$C_{p,H_2O}^{l,*}\left(\frac{J}{kmol\cdot K}\right)=189366-1171\cdot T\left(K\right)+4.53\cdot T\left(K\right)^2-\ldots$$
$$\ldots-0.00795\cdot T\left(K\right)^3+5.4723\times10^{-6}\cdot T\left(K\right)^4 \qquad 14\text{-}20$$

For a given temperature, the molar aqueous phase infinite dilution heat capacity of piperazine carbamate, piperazine dicarbamate, and protonated piperazine carbamate can then be determined analytically based on the simultaneously regressed infinite dilution aqueous phase free energy of formation $\left(\Delta G_f^{\infty,aq}\right)$, the infinite dilution aqueous phase enthalpy of formation $\left(\Delta H_f^{\infty,aq}\right)$, and the infinite dilution aqueous phase heat capacity polynomial $\left(C_p^{\infty,aq}\right)$ for piperazine carbamate, piperazine dicarbamate, and protonated piperazine carbamate. A starting point for a rigorous development starts with the following equation:

$$\Delta G_m^o=\Delta H_m^o-T\Delta S_m^o \qquad 14\text{-}21$$

Equation 14-21 is from the definition of the molar Gibbs free energy applied to each component in a chemical reaction evaluated at the standard state. Applying Equation 14-17 to Equation 14-21 yields

$$\sum_i \nu_i G_{m,i}^o=\sum_i \nu_i H_{m,i}^o-T\sum_i \nu_i S_{m,i}^o \qquad 14\text{-}22$$

where the standard molar heat of reaction and standard molar entropy change of reaction are related to temperature by the following expressions

$$\Delta H_m^o=\Delta H_{0,m}^o+R\int_{T_0}^{T}\frac{\Delta C_{p,m}^o}{R}dT \qquad 14\text{-}23$$

$$\Delta S_m^o = \Delta S_{0,m}^o + R\int_{T_0}^{T} \frac{\Delta C_{p,m}^o}{R}\frac{dT}{T} \qquad 14\text{-}24$$

Equations 14-21, 14-23, and 14-24 are combined to yield

$$\Delta G_m^o = \Delta H_{0,m}^o + R\int_{T_0}^{T} \frac{\Delta C_{p,m}^o}{R} dT - T\Delta S_{0,m}^o - RT\int_{T_0}^{T} \frac{\Delta C_{p,m}^o}{R}\frac{dT}{T} \qquad 14\text{-}25$$

However,

$$\Delta S_{0,m}^o = \frac{\Delta H_{0,m}^o - \Delta G_{0,m}^o}{T_0} \qquad 14\text{-}26$$

hence

$$\Delta G_m^o = \Delta H_{0,m}^o - \frac{T}{T_0}\left(\Delta H_{0,m}^o - \Delta G_{0,m}^o\right) + R\int_{T_0}^{T} \frac{\Delta C_{p,m}^o}{R} dT - RT\int_{T_0}^{T} \frac{\Delta C_{p,m}^o}{R}\frac{dT}{T} \qquad 14\text{-}27$$

Finally, division by RT yields

$$-\ln K_i = \frac{\Delta G_m^o}{RT} = \frac{\Delta G_{0,m}^o - \Delta H_{0,m}^o}{RT_0} + \frac{\Delta H_{0,m}^o}{RT} + \frac{1}{T}\int_{T_0}^{T} \frac{\Delta C_{p,m}^o}{R} dT - \int_{T_0}^{T} \frac{\Delta C_{p,m}^o}{R}\frac{dT}{T} \qquad 14\text{-}28$$

The change in heat capacity for the mixture can be expressed as

$$\Delta C_p^o\left(\frac{J}{kmol \cdot K}\right) = \Delta A + \Delta B \cdot T(K) + \Delta C \cdot T(K)^2 + \Delta D \cdot T(K)^3 + \Delta E \cdot T(K)^4 \qquad 14\text{-}29$$

with

$$\Delta A = \sum_i v_i A_i \qquad 14\text{-}30$$

with analogous definitions for ΔB, ΔC, ΔD, and ΔE. Through simultaneous regression of CO_2 solubility, amine volatility, specific heat capacity, liquid phase speciation, and enthalpy of CO_2 absorption, we were able to determine the infinite dilution aqueous phase free energy of formation, the infinite dilution aqueous phase enthalpy of formation, and the infinite dilution aqueous phase heat capacity polynomial for piperazine carbamate, piperazine dicarbamate, and protonated piperazine carbamate. Please refer to section 14.4 for more information.

In this work, we chose to describe the zwitterion (protonated piperazine carbamate) an ionic but net-neutral molecule, as a cation with a charge equal to $1e^{-5}$. Hilliard (2005) described the zwitterion as an ion with a neutral charge where the formation of protonated piperazine carbamate was described with a linear temperature dependent function for the chemical equilibrium constant. This framework allows a rather laissez-faire description of molecule/ionic characterization which circumvents potential problems associated with chemical equilibria. In this work, we chose to describe the chemical equilibrium in terms of the reference state Gibbs free energy of the system as given by Equation 14-29. By describing the zwitterion as an ion with a small charge within Aspen Plus^{TM}, the internal framework for ionic characterization remains rigorous and consistent throughout the simulation. We could have described the zwitterion as a non-volatile molecule under the current framework, but this process tended to open Pandora's Box to unforeseen complications with arbitrary molecule/ionic characterization.

Five data sets have been regressed with the elecNRTL model to represent the phase equilibrium of a mixed solvent system through regression of CO_2 solubility [Ermatchkov et al. (2006) and from this work], specific heat capacity [from this work], enthalpy of CO_2 absorption [Kim (2007)], and NMR speciation [Ermatchkov et al. (2003)] data over piperazine solutions. The elecNRTL model was never designed to regress enthalpy of CO_2

absorption or NMR speciation data; thus we created a fortran subroutine to link with the data regression system (DRS) in Aspen Plus^{TM}.

In this work, we concentrated our modeling efforts to describe aqueous piperazine mixtures from 1 to 5 m PZ. Reported CO_2 solubility measurements from Bishnoi (2000) and Derks et al. (2005) for mixtures of 0.2 and 0.6 M piperazine at 40 and 70 °C were excluded from the model regression. In addition, total pressure measurements from Pérez-Salado Kamps et al. (2003) for aqueous piperazine mixtures from 2 to 4 m PZ and later corrected by Ermatchkov et al. (2006) after applying a temperature correction were also excluded from this work. Total pressure data does not allow for the direct calculation of individual component activity coefficients or extrapolation to infinite dilution. Therefore, activity coefficients regressed from total pressure data cannot be accurately determined.

The following section describes the different types of data used in the creation of the binary H_2O-PZ-CO_2 elecNRTL model.

14.3.1 ***CO_2 Solubility and Amine Volatility***

Data in the form of CO_2 solubility, which measures the partial pressure of CO_2 over aqueous PZ solutions, P_{CO_2}, as a function of loading (mole CO_2 per 2·mole PZ) and temperature were used to adjust the partial pressure of CO_2 for the H_2O-PZ-CO_2 system through the simultaneous regression of the binary interaction parameters in the elecNRTL model for the H_2O-PZ-CO_2 system.

For our ternary system (H_2O, PZ, and CO_2), the following equation can be used to represent the equilibrium for CO_2 solubility data.

$$Py_{CO_2} = x_{CO_2}\gamma^*_{CO_2}H_{CO_2,H_2O} \tag{14-31}$$

Where

y_{CO_2} is the vapor mole fraction of CO_2,

$\gamma^*_{CO_2}$ is the unsymmetric activity coefficient of CO_2,

H_{CO_2,H_2O} is the Henry's Constant for CO_2 in H_2O.

An example of the experimental CO_2 solubility used in this work from Ermatchkov et al. (2006) and from this work in 2 m (mole/kg-H_2O) PZ is shown in Figure 14.3-2.

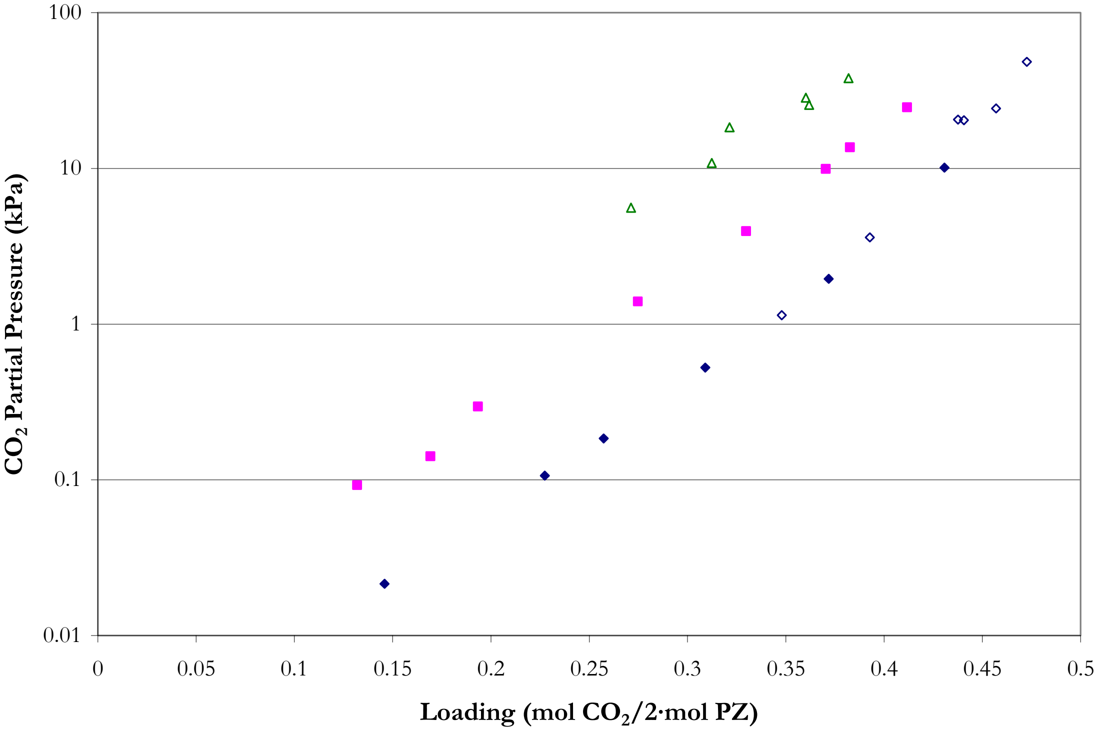

Figure 14.3-2. CO_2 Solubility in ~2 m PZ at 40, 60, and 80 °C. Points: ◊, 40 °C, △, 80 °C, Ermatchkov et al. (2006); ♦, 40 °C, ■, 60 °C, from this work.

In this work, we used a unique Fourier-transform infrared (FT-IR) technique to measure the vapor phase speciation in aqueous alkanolamine systems as described in Chapter II. Using this technique, we have been able to measure the vapor phase partial pressure of PZ over aqueous PZ solutions, P_{PZ} , as a function of loading (mole CO_2 per 2·mole PZ) and temperature.

For our ternary system (H_2O, PZ, and CO_2), the following equation can be used to represent the equilibrium for PZ volatility data.

$$Py_{PZ} = x_{PZ}\gamma_{PZ}P^o_{PZ} \qquad 14\text{-}32$$

Where
y_{PZ} is the vapor mole fraction of PZ,
γ_{PZ} is the asymmetric activity coefficient of PZ,
P^o_{PZ} is the extended Antoine vapor pressure correlation for PZ given in Chapter VI.

Examples of the experimental PZ volatility from this work in 0.9, 2.0, 2.5, 3.6, and 5.0 m PZ at 40 and 60 °C are shown in Figure 14.3-3 and Figure 14.3-4, respectively.

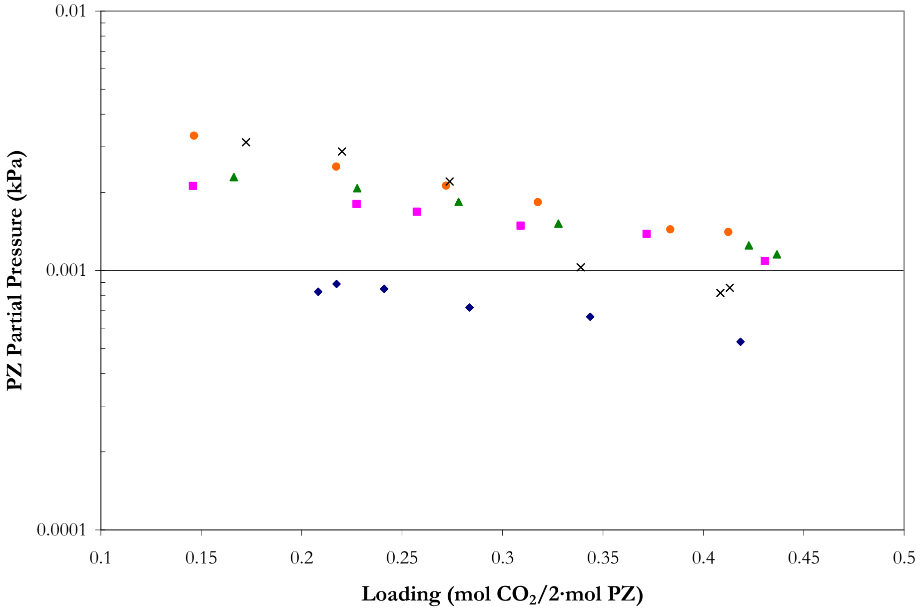

Figure 14.3-3. PZ Volatility for 0.9, 2.0, 2.5, 3.6, and 5.0 m PZ at 40 °C from this work. Points: ♦, 0.9 m PZ, ■, 2.0 m PZ, ▲, 2.5 m PZ, ●, 3.6 m PZ, and ×, 5.0 m PZ.

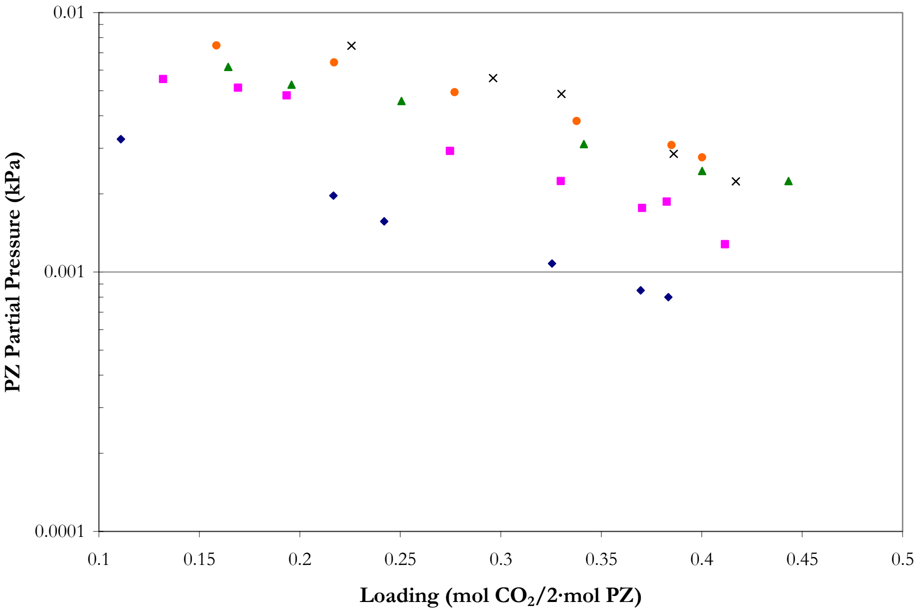

Figure 14.3-4. PZ Volatility for 0.9, 2.0, 2.5, 3.6, and 5.0 m PZ at 60 °C from this work. Points: ♦, 0.9 m PZ, ■, 2.0 m PZ, ▲, 2.5 m PZ, ●, 3.6 m PZ, and ×, 5.0 m PZ.

14.3.2 *Specific Heat Capacity*

As stated in Chapter VI, Aspen Plus™ calculates the liquid phase heat capacity of a *mixture* (CPMX) by taking the derivative of the liquid enthalpy at constant pressure:

$$H_m^l\left(T+\Delta T\right)-H_m^l\left(T\right)=\int_T^{T+\Delta T} C_{p,m}^l dT \qquad 14\text{-}33$$

where the liquid enthalpy of a mixture is calculated by the following equation:

$$H_m^l\left(T\right)=\sum_i x_i H_i+\sum_k x_k H_k^\infty+H_m^E \qquad 14\text{-}34$$

for solvents:

$$H_i\left(T\right)=\Delta H_f^{ig}\left(T^{ref}\right)+\int_{T^{ref}}^{T} C_p^{ig} dT+\left[H_i\left(T,p\right)-H_i^{ig}\left(T,p\right)\right] \qquad 14\text{-}35$$

for molecular solutes (CO_2):

$$H_i\left(T\right)=H_i^{ig}\left(T\right)+RT\ln\left(\frac{H_{i,H_2O}}{P^{ref}}\right) \tag{14-36}$$

for cations or anions:

$$H_k^{\infty}\left(T\right)=\Delta H_{f,k}^{\infty}\left(T^{ref}\right)+\int_{T^{ref}}^{T} C_{p,k}^{\infty}dT \tag{14-37}$$

Where
ΔT is the perturbation in temperature from T,
H_m^E is the excess enthalpy of the mixture,
$\Delta H_f^{ig}\left(T^{ref}\right)$ is the standard enthalpy of formation of component i at T^{ref},
T^{ref} is the reference temperature, 25.0 °C,
C_p^{ig} is the ideal gas heat capacity of component i,
H_i^{ig} is the ideal gas enthalpy of component i,
H_k^{∞} is the infinite dilution aqueous enthalpy of component k,
$\Delta H_{f,k}^{\infty}\left(T^{ref}\right)$ is the infinite dilution aqueous phase standard enthalpy of formation of component k at T^{ref},
$C_{p,k}^{\infty}$ is the infinite dilution aqueous phase heat capacity polynomial of component k.

Table 14.3-1 gives the coefficients for the infinite dilution aqueous phase heat capacity used in Aspen Plus™ based on the following expression:

$$C_{p,k}^{\infty}\left(\frac{J}{kmol\cdot K}\right)=C_1+C_2T\left(K\right)+C_3\left(T\left(K\right)\right)^2+\frac{C_4}{T\left(K\right)} \tag{14-38}$$

Table 14.3-1. Infinite Dilution Aqueous Phase Heat Capacity Default Coefficients.

Parameter	Symbol	H^+	OH^-	HCO_3^{-1}	CO_3^{-2}	PZH^{+1}
CPAQ0-1	C_1	0.0	0.0	211387	1334017	603662
CPAQ0-2	C_2	0.0	-497.9	-882	-5565	-2518
CPAQ0-3	C_3	0.0	0.0	0.875	5.19	4.16
CPAQ0-4	C_4	0.0	0.0	-1.9E+07	-1.2E+08	-5.4E+08

Data in the form of specific heat capacity as a function of loading, molality, and temperature were used to adjust the coefficients for the binary interaction parameters of the elecNRTL model. An example of the experimental specific heat capacity from this work from 40 to 120 °C for 2 and 3.6 m PZ is shown in Figure 14.3-5. Points shown corresponding to a loading of zero were regressed as part of Chapter IX. Please refer to Chapter IX for more information.

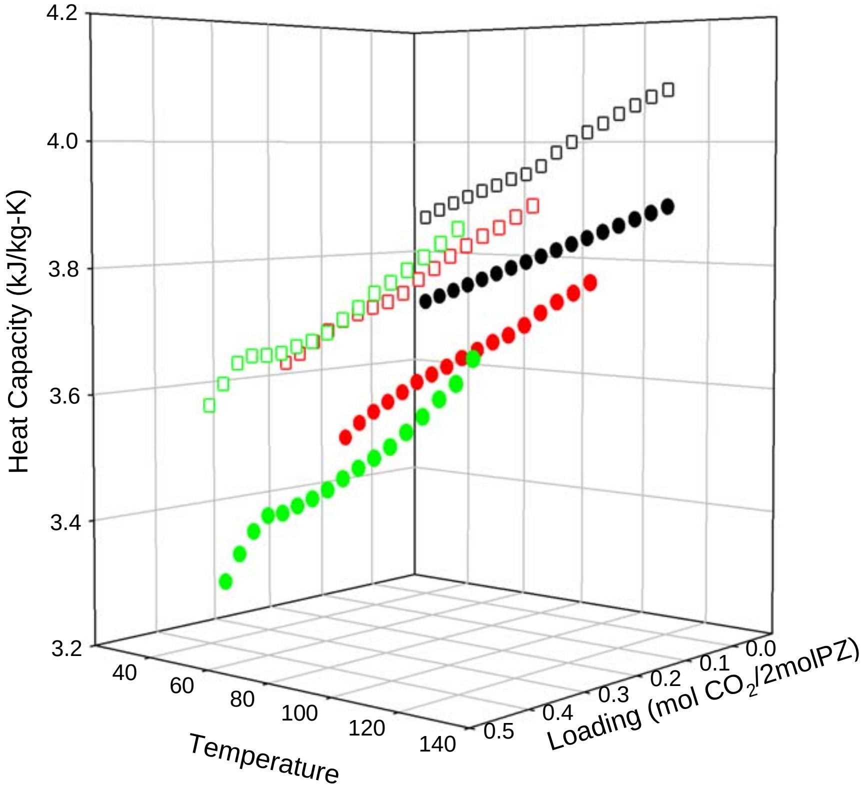

Figure 14.3-5. Specific Heat Capacity in Loaded 2.0 and 3.6 m PZ Solutions from this work. Points: □, Ldg = 0.0, □, Ldg = 0.16, □, Ldg = 0.27, ●, Ldg = 0.0, ●, Ldg = 0.16, ●, Ldg = 0.38.

14.3.3 *Enthalpy of CO_2 Absorption*

Data in the form of the enthalpy of CO_2 absorption for aqueous piperazine solutions, as a function of loading and temperature, were used to adjust the activity coefficients for each liquid phase component in the H_2O-PZ-CO_2 system through the simultaneous regression of the binary interaction parameters in the elecNRTL model.

For our true component ternary system (H_2O, PZ, and CO_2), the Gibbs-Helmholtz equation can be used to represent the differential enthalpy of CO_2 absorption:

$$-\frac{\Delta H_{abs}}{R} = \left(\frac{d\, f_{CO_2}^{v}}{d\left(1/T\right)} \right)_{x_{CO_2}} \qquad 14\text{-}39$$

The heat released can be measured by direct calorimetry or estimated from CO_2 solubility data. The later has been shown to have a high degree of uncertainty on the order of ± 20 to 30 % as reported by Lee et al. (1974). However, if the loading span within one CO_2 addition can be kept rather low, the measurements gave enthalpy data close to differential values in loading rather than integral as reported by Kim et al. (2007) with respect to the total amount of heat released from zero loading to the experimental loading data point as shown by the following expression:

$$-\Delta H_{\text{int}} = -\int_0^{\alpha} \Delta H_{diff}\, \mathrm{d}\alpha \qquad 14\text{-}40$$

Where

α is the loading of the solution, mole CO_2/2·mole PZ.

As part of an international collaboration between The University of Texas and the Norwegian University of Science and Technology, Kim (2007) determined the differential enthalpy of CO_2 absorption for 2.4 m PZ, based on a consistent experimental method developed for monoethanolamine [Kim et al. (2007)], at 40, 80, and 120 °C and over the range of loading from 0 – 0.5 mol CO_2/2·mol PZ for use in this work.

Aspen Plus™ was never designed to regress differential enthalpy of CO_2 absorption data; nevertheless in this work we were able to develop a fortran subroutine to regress experimental differential enthalpy of CO_2 absorption data within DRS utilizing the following schema presented in Figure 14.3-6.

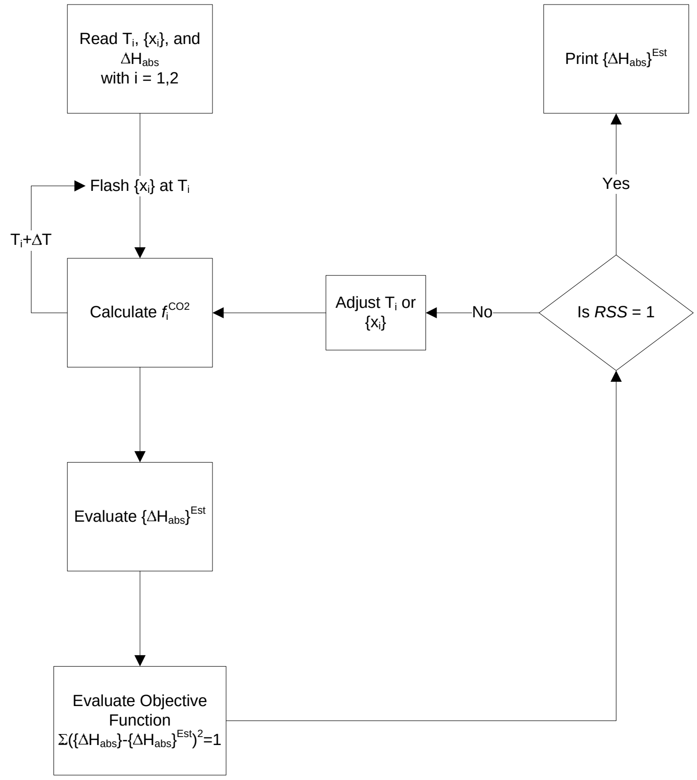

Figure 14.3-6. Differential Enthalpy of CO_2 Absorption Fortran Subroutine Schema Developed for Aspen Plus™.

Within DRS, the user inputs the temperature in Kelvin, the apparent liquid phase mole fractions for PZ, CO_2, and H_2O, and the differential enthalpy of CO_2 absorption. The fortran subroutine then calls a FLSH_FLASH subroutine within Aspen Plus^{TM} and performs a temperature-vapor fraction flash calculation. Once the FLASH subroutine converges, the fortran subroutine calculates the CO_2 vapor phase fugacity based on the estimated partial pressure and the vapor phase fugacity coefficient of CO_2, respectively. The fortran subroutine then numerically differentiates the vapor phase fugacity of CO_2 at T and (T + 1 K) based on Equation 14-39.

Finally, the fortran subroutine exports the estimated enthalpy of CO_2 absorption to DRS. DRS then tries to minimize the difference between the estimated enthalpy of CO_2 absorption calculated from the fortran subroutine and the experimental value utilizing the Maximum Likelihood Method within Aspen Plus^{TM} to minimize the overall objective function while adjusting each property variable. For more information about the complete fortran subroutine code, please refer to Appendix K.

An example of the experimental differential enthalpy of CO_2 absorption used in this work from Kim (2007) at 40, 80, and 120 °C for 2.4 m piperazine is shown in Figure 14.3-7, Figure 14.3-8, and Figure 14.3-9, respectively.

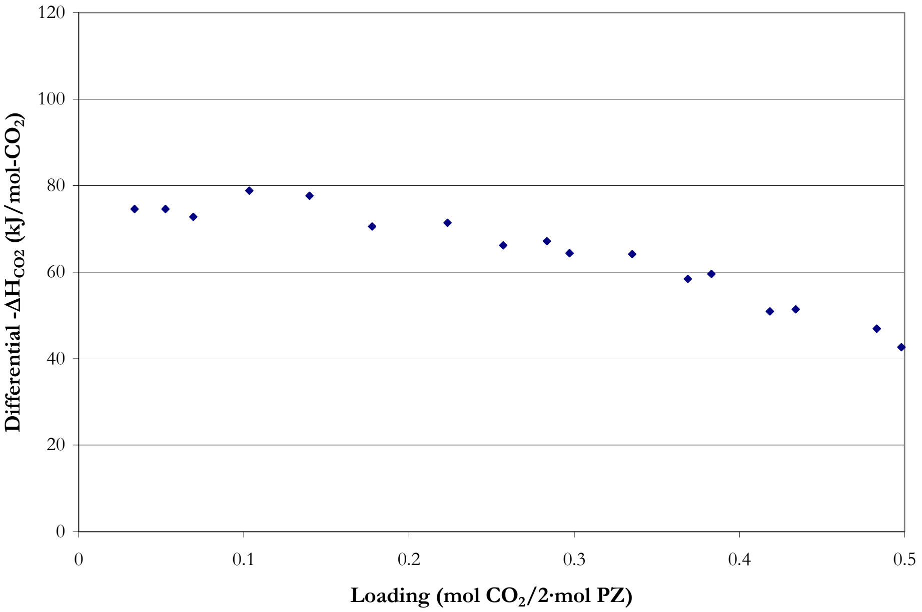

Figure 14.3-7. Negative Differential Enthalpy of CO_2 Absorption in 2.4 m PZ at 40 °C from Kim (2007).

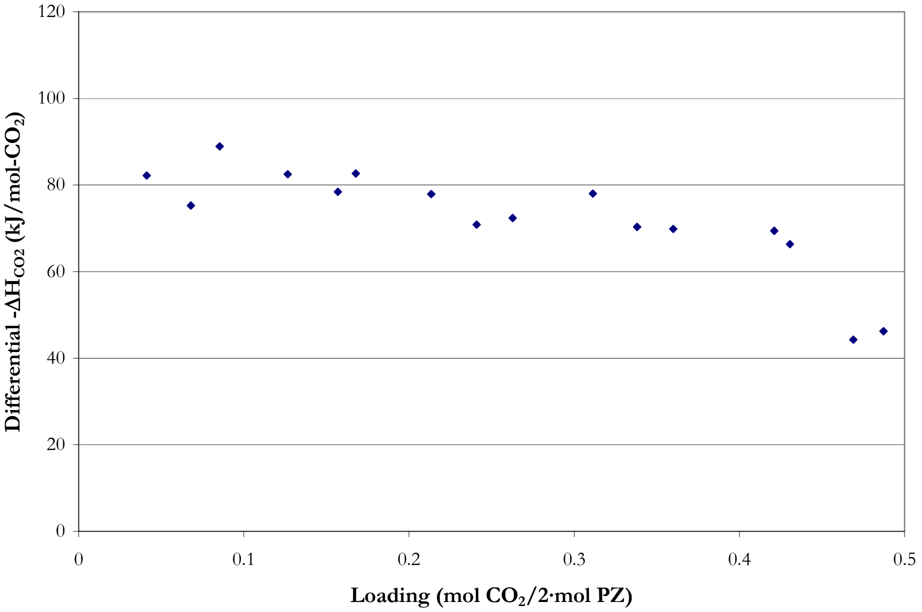

Figure 14.3-8. Negative Differential Enthalpy of CO_2 Absorption in 2.4 m PZ at 80 °C from Kim (2007).

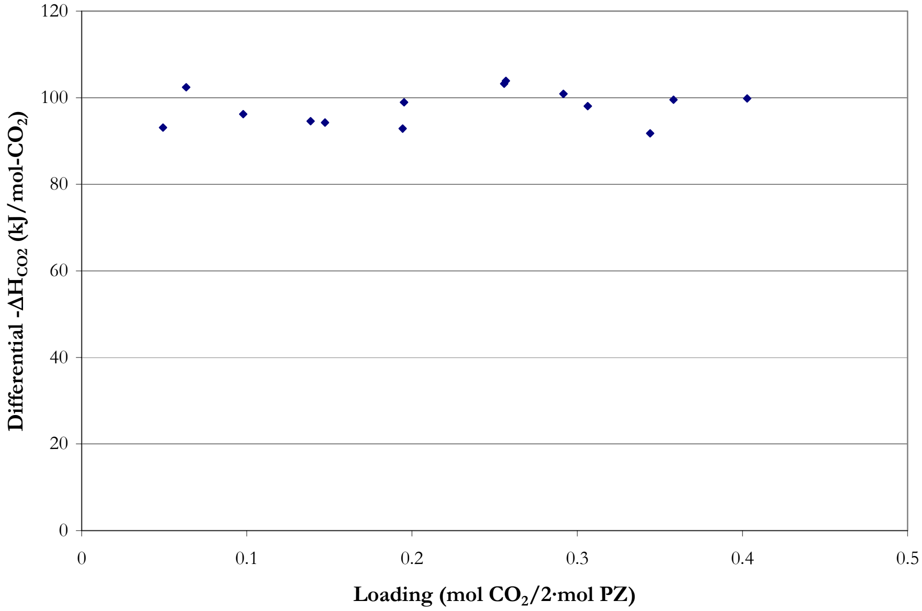

Figure 14.3-9. Negative Differential Enthalpy of CO_2 Absorption in 2.4 m PZ at 120 °C from Kim (2007).

14.3.4 *NMR Speciation*

Data in the form of proton H^1 NMR speciation for aqueous piperazine solutions, as a function of loading, concentration, and temperature were used to adjust the activity coefficients for each liquid phase component in the H_2O-PZ-CO_2 system through the simultaneous regression of the binary interaction parameters in the elecNRTL model.

For our true component ternary system (H_2O, PZ, and CO_2), the following equations can be used to represent the liquid phase equilibrium for the NMR speciation data as reported by Ermatchkov et al. (2003) and from this work.

$$n^*_{PZ} = n_{PZ} + n_{PZH^{+1}} \tag{14-41}$$

$$n^*_{H/PZCOO^{-1}} = n_{H^+PZCOO^{-1}} + n_{PZCOO^{-1}} \tag{14-42}$$

$$n^*_{PZ(COO^{-1})_2} = n_{PZ(COO^{-1})_2} \tag{14-43}$$

Where
n_i is the true number of moles for each component per kilogram of water corresponding to the relative proton NMR peak areas,
ni* is the pseudo-component quantity based on experimental NMR data.

Ermatchkov et al. (2003) measured the proton peak areas or intensities for the corresponding protons associated with each molecule(s). The main drawback with proton NMR speciation analysis is not having the ability to measure the loading of the solution as compared to carbon C^{13} NMR speciation described in Chapter XIII. The loading of the solution has to be determined a *priori* which may result in a discrepancy between the loading at the time of the NMR experiment and at the time of the CO_2 analysis. We would recommend that future work should concentrate on measuring carbon C^{13} NMR speciation for loaded piperazine solutions between 1 – 5 m PZ at 25, 40, and 60 ^{o}C to supplement the current database.

Aspen Plus^{TM} was never designed to regress NMR speciation data; nevertheless, in this work we were able to develop a fortran subroutine to regress experimental NMR speciation data within DRS utilizing the schema presented in Figure 14.3-10. Within DRS, the user inputs the temperature in Kelvin and the pseudo-component mole fractions for PZ, $H/PZCOO^{-1}$, $PZ(COO^{-1})_2$, CO_2, and H_2O. The fortran subroutine then calculates the apparent component mole fractions based on the following expressions:

$$x^A_{PZ} = x^*_{PZ} + x^*_{H/PZCOO^{-1}} + x^*_{PZ(COO^{-1})_2} \tag{14-44}$$

$$x^A_{CO_2} = x^*_{CO_2} + x^*_{H/PZCOO^{-1}} + 2 \cdot x^*_{PZ(COO^{-1})_2} \tag{14-45}$$

The fortran subroutine then calls a FLSH_FLASH subroutine within Aspen Plus™ and performs a temperature-vapor fraction flash calculation. Once the FLASH subroutine converges, the fortran subroutine calls a PPSTUB_GETTRU subroutine within Aspen Plus™ and extracts the true species mole fractions from the converged flash calculation.

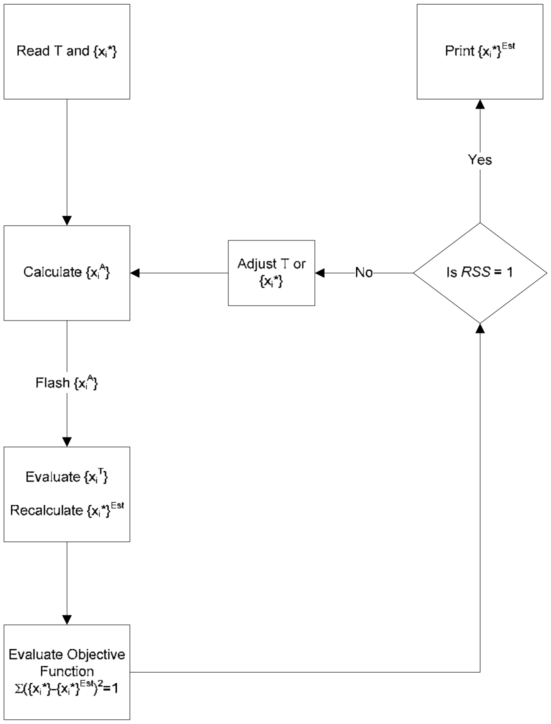

Figure 14.3-10. NMR Speciation Fortran Subroutine Schema Developed for Aspen Plus™.

The fortran subroutine then takes the true species mole fractions and calculates the estimated pseudo-component mole fractions based on the following expressions:

$$x_{PZ}^{*,est} = x_{PZ} + x_{PZH^{+1}} \tag{14-46}$$

$$x_{H/PZCOO^{-1}}^{*,est} = x_{H^{+}PZCOO^{-1}} + x_{PZCOO^{-1}} \tag{14-47}$$

$$x_{PZ\left(COO^{-1}\right)_2}^{*,est} = x_{PZ\left(COO^{-1}\right)_2} \tag{14-48}$$

$$x_{CO_2}^{*,est} = x_{CO_2} + x_{CO_3^{-2}} + x_{HCO_3^{-1}} \qquad 14\text{-}49$$

Finally, the fortran subroutine compares the estimated pseudo-component mole fractions to the experimental pseudo-component mole factions and calculates one minus the residual sum of squares (RSS). DRS then tries to minimize the difference between the RSS calculated from the fortran subroutine and the user property supplied to DRS by the user, a value of one, while DRS utilizes the Maximum Likelihood Method within Aspen Plus™ to minimize the overall objective function while adjusting each property variable. For more information about the complete fortran subroutine code, please refer to Appendix K.

An example of the experimental NMR speciation used in this work from Ermatchkov et al. (2003) and this work for 1 m piperazine solutions at 25, 40, and 60 °C is shown in Figure 15.3-14, Figure 15.3-15, and Figure 15.3-16, respectively.

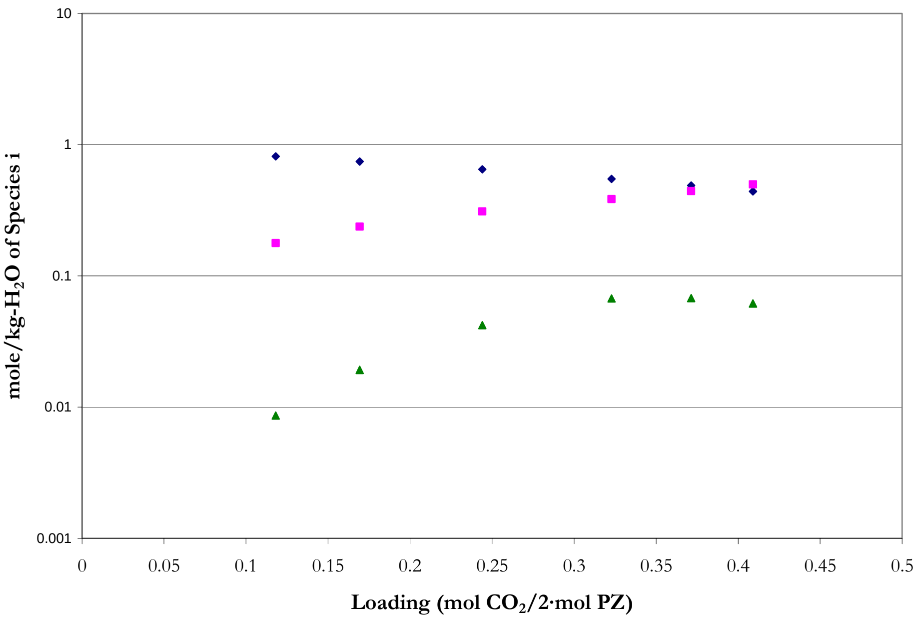

Figure 14.3-11. Liquid Phase Speciation from H^1 NMR at 25 °C from Ermatchkov et al. (2003). Points: ♦, PZ+PZH^{+1}, ■, H^+PZCOO^{-1}+$PZCOO^{-1}$, ▲, $PZ(COO^{-1})_2$.

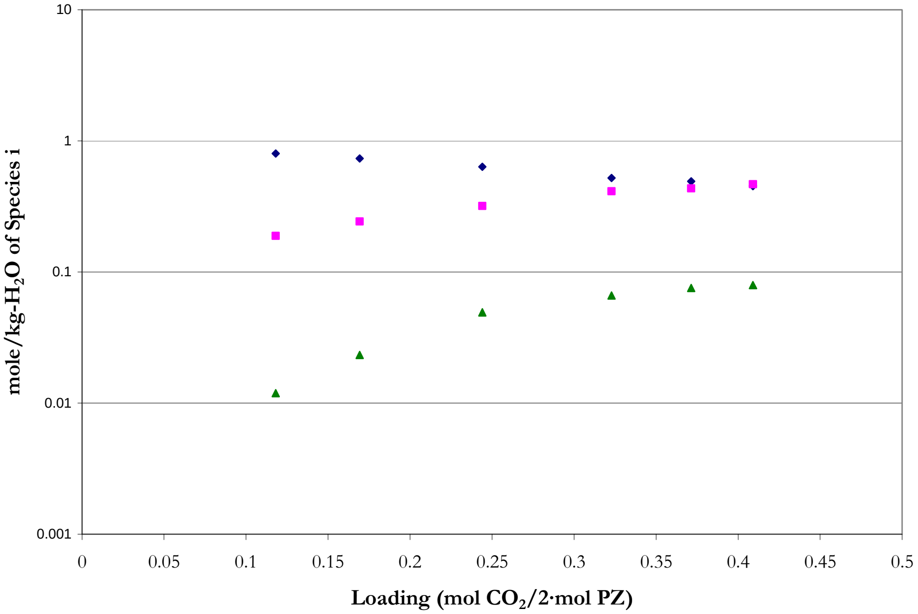

Figure 14.3-12. Liquid Phase Speciation from H^1 NMR at 40 °C from Ermatchkov et al. (2003). Points: ♦, $PZ+PZH^{+1}$, ■, $H^{+}PZCOO^{-1}+PZCOO^{-1}$, ▲, $PZ(COO^{-1})_2$.

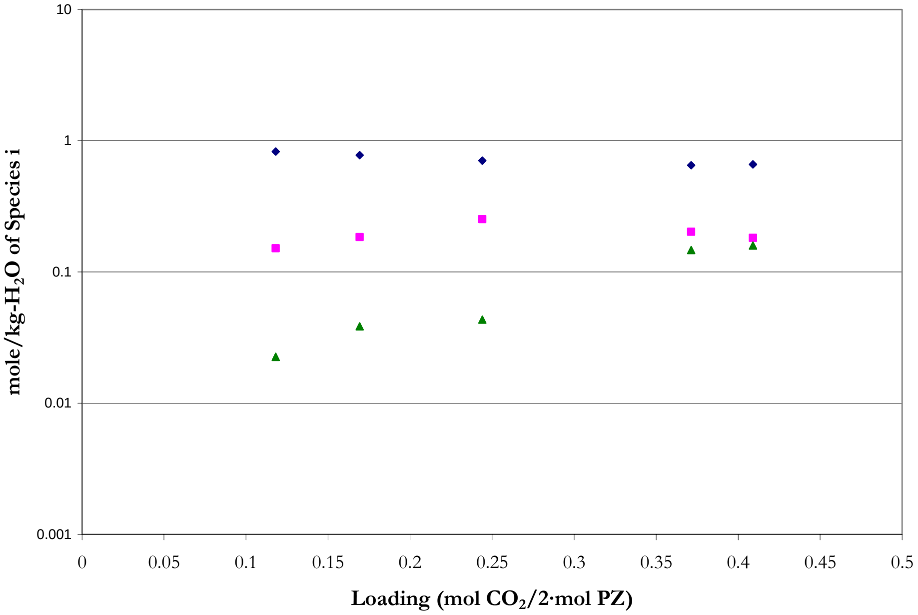

Figure 14.3-13. Liquid Phase Speciation from H^1 NMR at 60 °C from Ermatchkov et al. (2003). Points: ♦, $PZ+PZH^{+1}$, ■, $H^{+}PZCOO^{-1}+PZCOO^{-1}$, ▲, $PZ(COO^{-1})_2$.

14.4 Data Regression

There are three types of binary interaction parameters in the elecNRTL model: molecule-molecule, $\tau_{m,m'}$ and $\tau_{m',m}$; molecule-electrolyte, $\tau_{m,ca}$ and $\tau_{ca,m}$; electrolyte-electrolyte (with a common cation or anion) $\tau_{ca,ca'}$ and $\tau_{ca',ca}$ or $\tau_{ca,c'a}$ and $\tau_{c'a,ca}$; and the molecule-electrolyte nonrandomness factor, $\alpha_{ca,m}$. Chen and Evans (1986) noted that in their regression attempts it was not always possible to obtain statistically significant results for all four types of binary interaction parameters. In this work, the molecule-electrolyte nonrandomness parameter was set to an arbitrary value of $\alpha_{ca,m} = 0.2$ for all correlations involving electrolyte systems as suggested by Chen and Evans (1986). In this work, the electrolyte – electrolyte parameters are generally negligible and were assumed to be zero.

For the elecNRTL model, default values for molecule-electrolyte and electrolyte-molecule interactions are given in Table 14.4-1.

Table 14.4-1. Default Binary Interaction Parameters for the elecNRTL Model in Aspen Plus™.

Binary Interaction Pairs	τ
Molecule-electrolyte	10
Electrolyte-molecule	-2
Water-electrolyte	8
Electrolyte-water	-4

The energy parameters are adjusted to provide the best fit to the data. The binary interaction parameters were assumed to be temperature dependent and were fitted to the following function of temperature:

$$\tau_{m,ca} = A_{m,ca} + \frac{B_{m,ca}}{T} \tag{14-50}$$

$$\tau_{ca,m} = A_{ca,m} + \frac{B_{ca,m}}{T} \tag{14-51}$$

where electrolyte-electrolyte interactions follow a similar form as given above. A list of the aqueous electrolyte data sets that were examined in this work is given in Table 14.4-2.

Table 14.4-2. Experimental data used for regression of the H_2O-PZ-CO_2 systems.

	Obs.	T (°C)	σ_T	σ_{PCO2}	σ_{PZ}	σ_{CO2}	σ_y	Source
P^{CO2}	29	40.0 – 80.0	0.01	2.0%	0.1%	0.2%	0	Ermatchkov et al. (2006)
	62	40.0 – 60.0	0.01	2.0%	0.1%	0.2%	0	This work

	Obs.	T (°C)	σ_T	σ_{PPZ}	σ_{PZ}	σ_{CO2}	σ_y	Source
P^{PZ}	62	40.0 – 60.0	0.01	2.0%	0.1%	0.2%	0	This work

	Obs.	T (°C)	σ_T	σ_{PZ}	σ_{CO2}	σ_{Cp}	Source
Cp	200	40.0 – 120.0	0.1	0.1%	0.2%	2.0%	This work

	Obs.	T (°C)	σ_T	σ_{PZ}	σ_{CO2}	$\sigma_{\Delta H}$	Source
ΔH_{abs}	47	40.0 – 120.0	0.01	0.1%	0.2%	2.0%	Inna Kim(PC-2007)

	Obs.	T (°C)	σ_T	σ_x	Source
NMR	39	25.0 – 60.0	0.01	1.0%	Ermatchkov et al. (2003)

The column labels σ_T, σ_{PCO2}, σ_{PPZ}, σ_{x_i}, σ_{y_i}, σ_{Cp}, $\sigma_{\Delta H}$, give standard errors associated with the temperature, partial pressure of CO_2, partial pressure of PZ, liquid mole fraction, vapor mole fraction, the specific heat capacity, and the enthalpy of CO_2 absorption, respectively, with each data set. DRS suggested standard error default values were assigned unless otherwise stated by the author. Overall, 377 experimental data points were included in the model regression.

Table 14.4-3 shows the regression summary statistics output for estimates of the adjustable binary parameter coefficients, the infinite dilution aqueous phase free energy of formation, the infinite dilution aqueous phase enthalpy of formation, and the infinite dilution aqueous phase heat capacity polynomial for piperazine carbamate, piperazine dicarbamate, and protonated piperazine carbamate after performing a nonlinear regression for the full model using DRS in Aspen Plus^{TM}.

Table 14.4-3. DRS Regression Output for Full H_2O-PZ-CO_2 System Model.

	i	j	k	Estimate	σ wrt Estimate
1	ΔG_{PZCOO}			-216402689	145128
2	ΔH_{PZCOO}			-482028622	17478506
3-CP-A	$PZCOO^{-1}$			-6853709	8150363
4-CP-B	$PZCOO^{-1}$			23209	46387
5-CP-C	$PZCOO^{-1}$			4.90	73.8
6	ΔG_{PZCOO2}			-576616171	3365369
7	ΔH_{PZCOO2}			-860671113	66184501
8-CP-A	$PZ(COO^{-1})_2$			-881654	7547281
9-CP-B	$PZ(COO^{-1})_2$			-18936	23655
10-CP-C	$PZ(COO^{-1})_2$			80.1	60.4
11	ΔG_{HPZCOO}			-273454207	475040
12	ΔH_{HPZCOO}			-522383061	7367332
13-CP-A	H^+PZCOO^{-1}			4189850	9949541
14-CP-B	H^+PZCOO^{-1}			-13614	56496
15-CP-C	H^+PZCOO^{-1}			5.19	80.6
16-$A_{m,ca}$	H_2O	PZH^+	$PZCOO^{-1}$	-1.05	6.95
17-$B_{m,ca}$	H_2O	PZH^+	$PZCOO^{-1}$	3578	2226
18-$A_{ca,m}$	PZH^+	$PZCOO^{-1}$	H_2O	-104	46.2
19-$B_{ca,m}$	PZH^+	$PZCOO^{-1}$	H_2O	40581	18979
20-$A_{m,ca}$	H_2O	PZH^+	HCO_3^{-1}	4.44	3.56
21-$B_{m,ca}$	H_2O	PZH^+	HCO_3^{-1}	5973	1299
22-$A_{ca,m}$	PZH^+	HCO_3^{-1}	H_2O	-0.787	1.73
23-$B_{ca,m}$	PZH^+	HCO_3^{-1}	H_2O	-3071	587
24-$A_{m,ca}$	PZ	PZH^+	HCO_3^{-1}	7.04	0.555
25-$B_{m,ca}$	PZ	PZH^+	HCO_3^{-1}	0.0213	21.2
26-$A_{ca,m}$	PZH^+	HCO_3^{-1}	PZ	-5.75	5.48
27-$B_{ca,m}$	PZH^+	HCO_3^{-1}	PZ	0.0216	19.2
28-$A_{m,ca}$	PZ	PZH^+	$PZCOO^{-1}$	6.91	3.34
29-$B_{m,ca}$	PZ	PZH^+	$PZCOO^{-1}$	-0.0127	10.2
30-$A_{ca,m}$	PZH^+	$PZCOO^{-1}$	PZ	1.72	8.79
31-$B_{ca,m}$	PZH^+	$PZCOO^{-1}$	PZ	-0.0508	38.1
32-$A_{m,ca}$	CO_2	PZH^+	HCO_3^{-1}	10.5	11.7
33-$B_{m,ca}$	CO_2	PZH^+	HCO_3^{-1}	0.0139	13.5
34-$A_{ca,m}$	PZH^+	HCO_3^{-1}	CO_2	11.8	13.3
35-$B_{ca,m}$	PZH^+	HCO_3^{-1}	CO_2	-0.0133	12.6

Residual Sum of Squares:	15,073
Residual Root Mean Square:	9.0263
Degree of Freedom:	342

Recall that the standard error of an estimate is the estimated standard deviation of that statistic. Notice that eighteen of the estimates are smaller relative to their standard errors. Table 14.4-4 gives a complete description of the variability of the coefficient estimates which requires examining the correlations between the estimates.

Table 14.4-4. Correlation Matrix of the Coefficient Estimates for the Full H_2O-PZ-CO_2 System Model

Parameter	1	2	3	4	5	6	7	8	9	10	11	12	13	14	15	16	17	18	19	20	21	22	23	24	25	26	27	28	29	30	31	32	33	34	35
1	1.00																																		
2	0.60	1.00																																	
3	-0.20	-0.40	1.00																																
4	0.15	0.31	-0.99	1.00																															
5	-0.10	-0.21	0.97	-0.99	1.00																														
6	-0.48	-0.67	0.28	-0.23	0.16	1.00																													
7	0.50	0.65	-0.28	0.22	-0.15	-1.00	1.00																												
8	0.22	0.17	-0.32	0.33	-0.32	-0.61	0.61	1.00																											
9	0.43	0.51	-0.18	0.13	-0.07	-0.92	0.91	0.68	1.00																										
10	-0.45	-0.52	0.18	-0.13	0.08	0.92	-0.92	-0.69	-0.99	1.00																									
11	-0.15	0.17	0.03	-0.05	0.06	0.15	-0.15	-0.73	-0.43	0.41	1.00																								
12	-0.19	-0.43	0.53	-0.50	0.45	0.33	-0.31	-0.28	-0.09	0.07	-0.15	1.00																							
13	0.21	0.43	-0.53	0.50	-0.45	-0.33	0.31	0.28	0.09	-0.07	0.14	-1.00	1.00																						
14	-0.02	0.05	-0.45	0.48	-0.51	-0.04	0.03	0.22	-0.17	0.18	0.14	-0.84	0.83	1.00																					
15	-0.47	-0.59	-0.11	0.17	-0.24	0.44	-0.44	-0.09	-0.58	0.59	0.17	-0.41	0.41	0.68	1.00																				
16	0.50	0.58	0.11	-0.17	0.24	-0.44	0.44	0.10	0.58	-0.59	-0.18	0.40	-0.41	-0.67	-1.00	1.00																			
17	0.32	0.41	0.07	-0.11	0.16	-0.31	0.31	0.05	0.49	-0.51	-0.24	0.57	-0.57	-0.81	-0.93	0.92	1.00																		
18	-0.26	-0.55	0.35	-0.30	0.24	0.54	-0.50	-0.23	-0.32	0.29	-0.22	0.60	-0.59	-0.33	0.00	0.00	0.14	1.00																	
19	0.28	0.54	-0.35	0.31	-0.25	-0.53	0.49	0.23	0.31	-0.28	0.22	-0.60	0.60	0.34	0.01	-0.02	-0.15	-1.00	1.00																
20	-0.03	0.19	-0.21	0.19	-0.17	-0.06	0.06	-0.05	-0.18	0.17	0.38	-0.38	0.36	0.26	0.23	-0.23	-0.30	-0.63	0.61	1.00															
21	-0.04	-0.41	0.00	0.06	-0.12	0.26	-0.23	0.15	-0.11	0.09	-0.33	0.27	-0.25	-0.05	0.11	-0.11	0.02	0.57	-0.54	-0.68	1.00														
22	0.07	0.41	0.00	-0.05	0.12	-0.26	0.23	-0.14	0.12	-0.10	0.32	-0.28	0.25	0.05	-0.12	0.12	-0.02	-0.59	0.56	0.66	-1.00	1.00													
23	-0.11	0.05	0.03	-0.03	0.03	-0.15	0.14	0.31	0.11	-0.10	-0.16	-0.22	0.21	0.25	0.14	-0.14	-0.22	-0.25	0.23	0.27	-0.46	0.44	1.00												
24	0.11	0.34	0.05	-0.10	0.15	-0.35	0.34	0.14	0.30	-0.31	0.03	-0.15	0.14	-0.09	-0.25	0.25	0.14	-0.31	0.30	0.26	-0.47	0.46	0.29	1.00											
25	-0.18	-0.09	-0.09	0.11	-0.13	0.15	-0.17	-0.10	-0.17	0.19	0.07	-0.03	0.02	0.12	0.17	-0.18	-0.11	0.06	-0.07	-0.06	0.12	-0.12	-0.06	-0.87	1.00										
26	0.23	0.01	-0.09	0.09	-0.08	0.11	-0.10	-0.26	-0.12	0.12	0.15	0.07	-0.06	-0.12	-0.05	0.06	0.09	0.07	-0.04	-0.07	0.22	-0.21	-0.70	-0.27	-0.01	1.00									
27	0.45	0.52	-0.40	0.36	-0.30	-0.41	0.42	0.34	0.26	-0.27	-0.02	-0.65	0.66	0.40	0.00	0.01	-0.13	-0.49	0.51	0.04	0.17	-0.16	-0.09	0.19	-0.22	0.20	1.00								
28	-0.48	-0.45	0.38	-0.34	0.30	0.36	-0.37	-0.32	-0.22	0.23	0.05	0.59	-0.61	-0.38	-0.02	0.01	0.13	0.41	-0.44	0.02	-0.26	0.25	0.14	-0.15	0.24	-0.27	-0.99	1.00							
29	-0.12	-0.17	0.51	-0.53	0.53	0.16	-0.16	-0.32	0.05	-0.04	-0.09	0.73	-0.73	-0.75	-0.48	0.47	0.56	0.46	-0.48	-0.27	-0.19	0.19	-0.09	0.01	0.02	0.00	-0.77	0.76	1.00						
30	-0.01	-0.07	0.00	0.00	-0.01	0.06	-0.06	0.01	-0.02	0.02	-0.10	0.01	0.00	0.00	0.04	-0.04	-0.02	0.11	-0.11	0.01	-0.02	0.01	-0.02	-0.03	-0.03	0.14	-0.04	0.02	0.04	1.00					
31	-0.07	0.04	-0.02	0.02	-0.02	-0.02	0.01	-0.04	-0.04	0.04	0.13	-0.04	0.04	0.05	0.04	-0.05	-0.04	-0.12	0.12	0.00	0.03	-0.02	0.02	0.00	0.07	-0.17	0.03	-0.02	-0.07	-0.97	1.00				
32	0.12	0.25	-0.02	-0.02	0.06	-0.19	0.19	0.01	0.15	-0.16	0.09	-0.02	0.01	-0.15	-0.24	0.24	0.19	-0.14	0.13	0.11	-0.17	0.17	0.01	0.21	-0.12	-0.05	0.10	-0.08	0.06	-0.40	0.29	1.00			
33	-0.22	-0.17	-0.14	0.16	-0.19	0.01	-0.01	0.11	-0.02	0.03	-0.06	-0.16	0.17	0.25	0.32	-0.33	-0.26	0.02	-0.01	-0.06	0.11	-0.12	0.05	-0.08	0.08	-0.12	0.01	-0.01	-0.18	0.37	-0.20	-0.31	1.00		
34	0.22	0.17	0.14	-0.17	0.19	0.00	0.00	-0.12	0.01	-0.02	0.05	0.16	-0.17	-0.25	-0.31	0.32	0.25	-0.03	0.02	0.05	-0.11	0.12	-0.05	0.07	-0.07	0.13	-0.02	0.02	0.18	-0.36	0.20	0.30	-1.00	1.00	
35	0.18	0.34	-0.01	-0.03	0.09	-0.22	0.23	-0.03	0.16	-0.18	0.15	-0.04	0.03	-0.19	-0.31	0.31	0.24	-0.21	0.20	0.22	-0.28	0.28	0.00	0.24	-0.13	0.02	0.12	-0.09	0.08	-0.32	0.18	0.85	-0.67	0.66	1.00

Table 14.4-4 shows 18 highly negative and positive correlations out of a possible 630. The highly correlated parameters are between the temperature dependant coefficients and the respective constant for the each energy parameter estimate, but the correlation between other coefficients is relatively small, suggesting that the amount of temperature dependant parameters might be usefully removed from the model without significant loss of information.

After performing backward elimination using DRS, the following "optimum" model regression summary statistics output for estimates of the adjustable binary parameter coefficients is shown in Table 14.4-5.

Table 14.4-5. DRS Regression Output for Optimum H_2O-PZ-CO_2 System Model.

	i	j	k	Estimate	σ wrt Estimate
1	ΔG_{PZCOO}			-208605374	4324702
2	ΔH_{PZCOO}			-302202009	91895726
3-CP-A	$PZCOO^{-1}$			-20353192	13516014
4-CP-B	$PZCOO^{-1}$			-16379	15399
5-CP-C	$PZCOO^{-1}$			227	122
6	ΔG_{PZCOO2}			-577933128	1518873
7	ΔH_{PZCOO2}			-889198855	45841749
8-CP-A	$PZ(COO^{-1})_2$			3081046	12966463
9-CP-B	$PZ(COO^{-1})_2$			9895	103953
10-CP-C	$PZ(COO^{-1})_2$			-33.0	232
11	ΔG_{HPZCOO}			-273618109	1197501
12	ΔH_{HPZCOO}			-522578082	29488513
13-CP-A	H^+PZCOO^{-1}			4384726	21506173
14-CP-B	H^+PZCOO^{-1}			-18146	113054
15-CP-C	H^+PZCOO^{-1}			17.58	157
16-$A_{m,ca}$	H_2O	PZH^+	$PZCOO^{-1}$	-63.2	48.7
17-$B_{m,ca}$	H_2O	PZH^+	$PZCOO^{-1}$	23307	15187
18-$A_{ca,m}$	PZH^+	$PZCOO^{-1}$	H_2O	-89.3	732
19-$B_{ca,m}$	PZH^+	$PZCOO^{-1}$	H_2O	-149	51.7
20-$A_{m,ca}$	H_2O	PZH^+	HCO_3^{-1}	53010	17739
21-$B_{m,ca}$	H_2O	PZH^+	HCO_3^{-1}	320	224
22-$A_{ca,m}$	PZH^+	HCO_3^{-1}	H_2O	7.40	15.9
23-$B_{ca,m}$	PZH^+	HCO_3^{-1}	H_2O	5237	5020
24-$A_{m,ca}$	PZ	PZH^+	HCO_3^{-1}	123	107
25-$B_{m,ca}$	PZ	PZH^+	HCO_3^{-1}	-5.14	8.06
26-$A_{ca,m}$	PZH^+	HCO_3^{-1}	PZ	-1819	2529
27-$B_{ca,m}$	PZH^+	HCO_3^{-1}	PZ	-44.5	59.3
28-$A_{m,ca}$	PZ	PZH^+	$PZCOO^{-1}$	8.84	18.8
29-$B_{m,ca}$	PZ	PZH^+	$PZCOO^{-1}$	-111	6027
30-$A_{ca,m}$	PZH^+	$PZCOO^{-1}$	PZ	109	177
31-$B_{ca,m}$	PZH^+	$PZCOO^{-1}$	PZ	0.174	26.5
32-$A_{m,ca}$	CO_2	PZH^+	HCO_3^{-1}	18.3	4440
33-$B_{m,ca}$	CO_2	PZH^+	HCO_3^{-1}	102	714

Residual Sum of Squares: 14,771
Residual Root Mean Square: 8.8457
Degree of Freedom: 344

Notice that nine of the estimates are smaller relative to their standard errors. Comparing the estimates from the full model to the "optimum" model, there was relatively little difference between the estimated values. With the elimination of two parameters, the optimum model was unable to provide adequate predictions to the experimental data even though the sum of squares decreased by 2.05 percent. Furthermore, none of the other possible submodels proposed by backward elimination were able to provide adequate predictions and capture systematic trends with the data sets. **In this work, we chose the full model to describe the interactions in the H_2O-PZ-CO_2 system.**

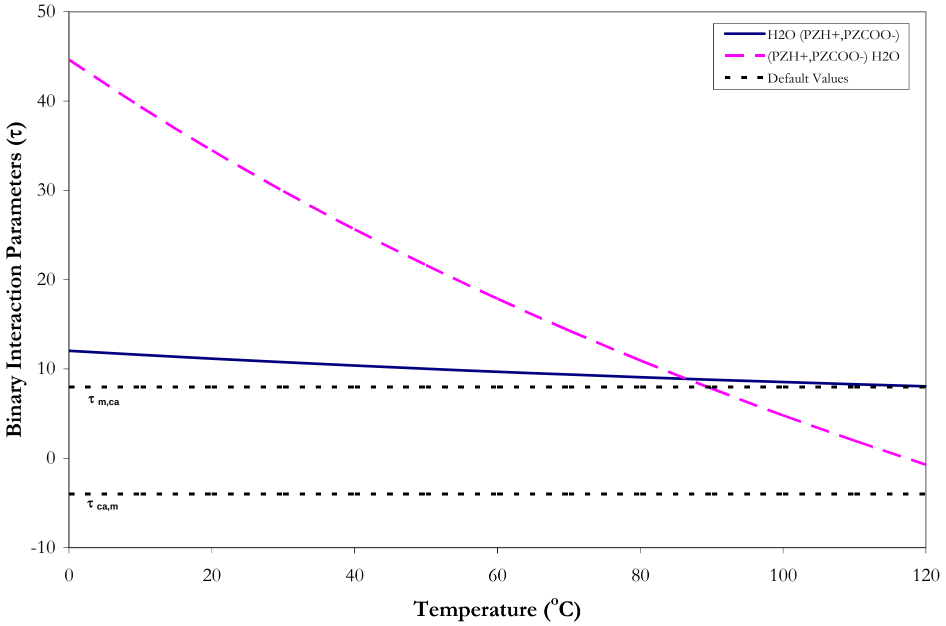

Figure 14.4-1. Binary Interaction Parameters for H_2O,PZH^{+1}/$PZCOO^{-1}$.

Estimated Binary Interaction Parameters

With the determination of the estimates for the binary interaction parameters known for the full model, we can use Equation 14-50 and Equation 14-51 to illustrate the temperature dependence of the molecule-electrolyte ($\tau_{m,ca}$), electrolyte-molecule ($\tau_{ca,m}$), water-electrolyte ($\tau_{m,ca}$), and electrolyte-water ($\tau_{ca,m}$) energy parameters as shown in Figure 14.4-1 through Figure 14.4-5.

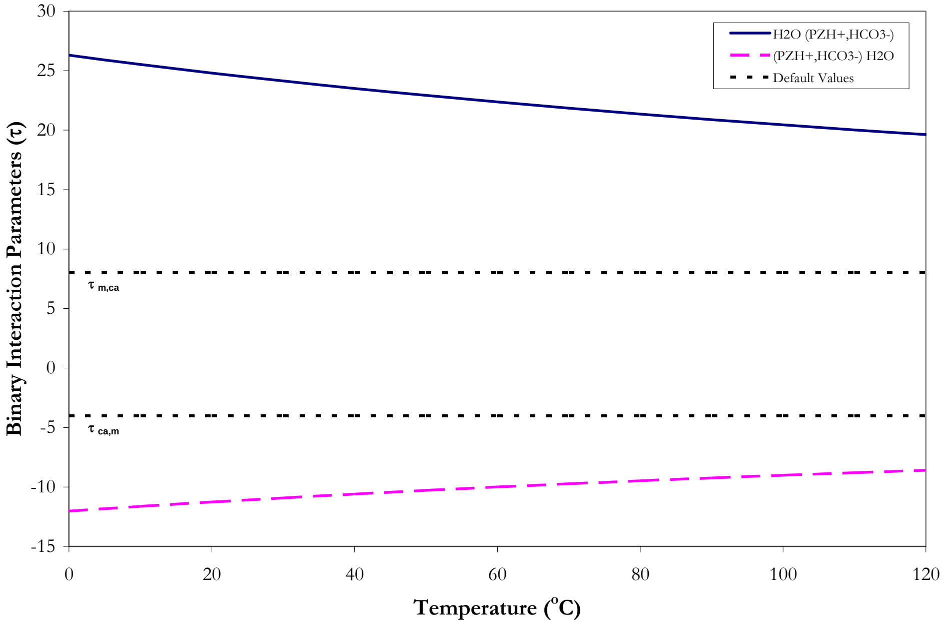

Figure 14.4-2. Binary Interaction Parameters for $H_2O,PZH^{+1}/ HCO_3^{-1}$.

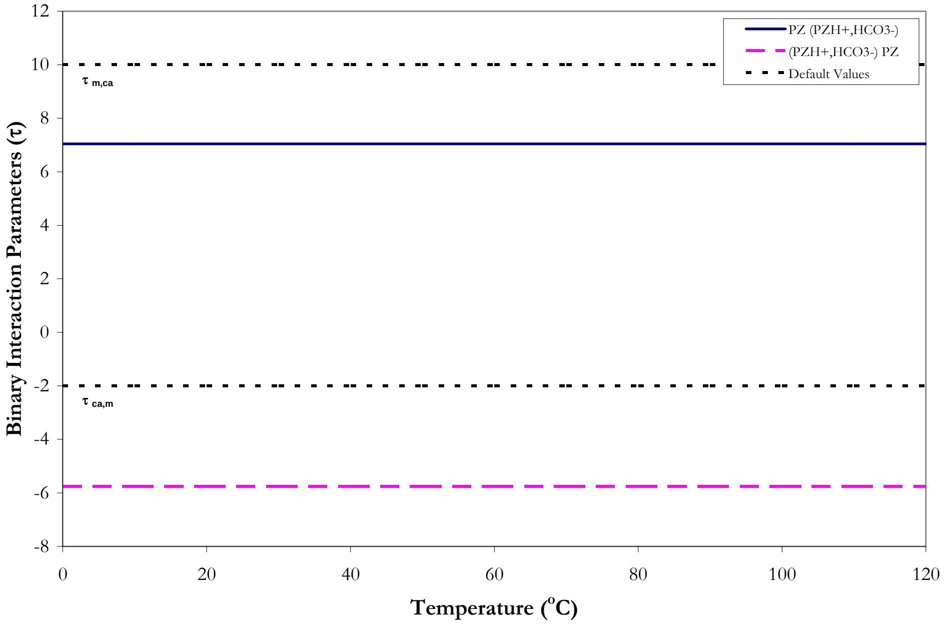

Figure 14.4-3. Binary Interaction Parameters for $PZ, PZH^{+1}/HCO_3^{-1}$.

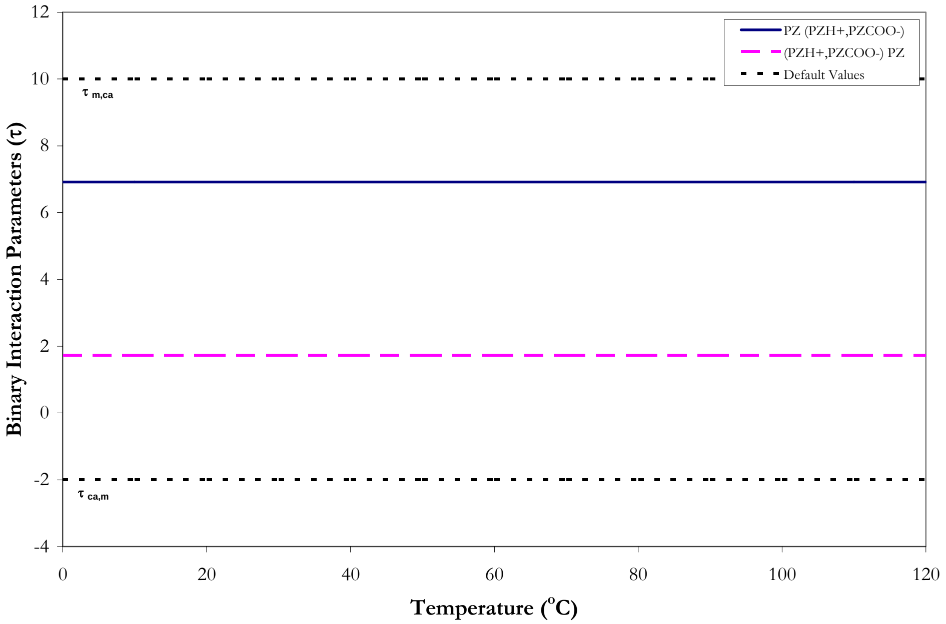

Figure 14.4-4. Binary Interaction Parameters for PZ, $PZH^{+1}/PZCOO^{-1}$.

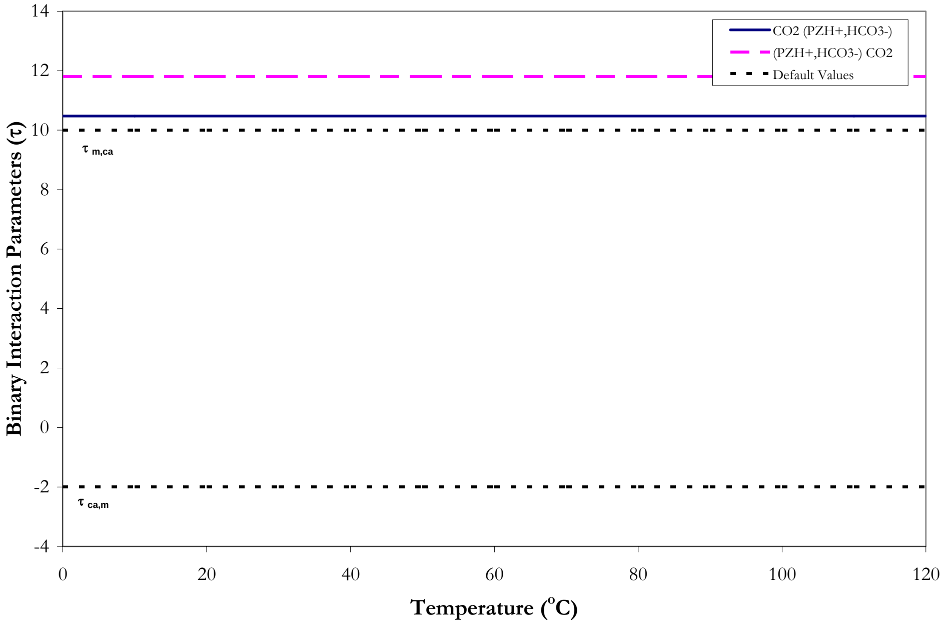

Figure 14.4-5. Binary Interaction Parameters for CO_2, PZH^{+1}/HCO_3^{-1}.

14.4.1 *Full Model Results*

With the determination of the estimates for the binary interaction parameters known for the full model, a simple Aspen Plus™ Flash model was used to test the predictive capability of the H_2O-PZ-CO_2 model against literature data. For each data point, the deviation between the experimental and estimated values is expressed in terms of the average absolute relative deviation (AARD) given in Table 14.4-6 and Table 14.4-7. Overall, the model adequately describes the H_2O-PZ-CO_2 property data listed above within an average absolute relative error of ± 10.59 percent, with the exception of a few outliers.

Table 14.4-6. Absolute Percent Relative Error for the H_2O-PZ-CO_2 Full Model.

CO_2 Solubility	**P^{CO2} AARD**	**Loading AARD**
This work	13.64	2.06
Ermatchkov et al. (2006)	7.12	1.6
PZ Solubility	**P^{PZ}**	**Loading**
This work	36.94	2.21
Enthalpy of CO_2 Abs.	**ΔH_{ABS}**	**Loading**
Inna Kim (PC-2007)	6.55	0.54
Specific Heat Capacity	**Cp**	**Loading**
This work	3.37	0.2
Overall	**10.59**	**1.50**

Table 14.4-7. Absolute Percent Relative Error for the H_2O-PZ-CO_2 Full Model Speciation.

NMR Speciation	$PZ+PZH^+$ AARD	$H^+PZCOO^-+PZCOO^-$ AARD	$PZ(COO^-)_2$ AARD	Loading AARD
Ermatchkov et al. (2003)	7.99	4.83	4.25	2.40

14.5 Full Model Predictions

In this work, we have compiled a large database of consistent high quality data needed to obtain a unique set of binary interactions parameters to describe the H_2O-PZ-CO_2 system. The remainder of this chapter will be devoted to using our model as a predictive tool as described in the subsequent sections.

14.5.1 *CO_2 Solubility and Amine Volatility*

Figure 14.5-1 through Figure 14.5-5 gives the results of fit for the experimental CO_2 solubility at 0.9, 2.0, 2.5, 3.6, and 5.0 m PZ versus loading at 40 and 60 °C from this work. Predictions from the Hilliard (2005) model are also compared to predictions from this work. As described in Chapter IX, Hilliard (2005) predicted activity coefficient of PZ from the UNIFAC [Dortmund Modified (DMD)] Method [Weidlich and Gmehling (1987) and Gmehling et al. (1993)] where the activity coefficients were predicted from group contributions and were assumed to be accurate due to the lack of experimental information. The modified UNIFAC model treated cyclic PZ as an aliphatic molecule with respect to the effect of substituent groups and amine's structure, whereby affecting how the molecule will interact in an aqueous environment with increasing temperature. This effect was demonstrated when a comparison of the activity coefficients from this work and those from Hilliard (2005) were made as described in Section 9.4-5. The Hilliard (2005) model was able to describe the CO_2 solubility in loaded piperazine solution, so a comparison between the two models is justified at this level.

Model predictions based on the Hilliard (2005) model tend to underestimate CO_2 vapor pressures at low loading and at low piperazine concentration and tend to overestimate at high loading over the entire range of piperazine concentrations studied in this work. In the Hilliard (2005) model, the available CO_2 solubility data at the time was 0.6 M PZ reported by Bishnoi (2000) at 40 and 70 °C and supplemented by total pressure data reported by Pérez-Salado Kamps et al. (2003) for aqueous piperazine mixtures from 2 to 4 m PZ. This could account for the overestimate at high loading since the range in loading reported by Bishnoi (2000) varied from 0.1 to 0.4 mol CO_2/2·mol PZ. In this work, we utilized the high loading CO_2 solubility data from Ermatchkov et al. (2006) at 40 and 80 °C to correct the loading dependence discrepancy as shown in the previous model.

Figure 14.5-6 compares experimental CO_2 solubility from Ermatchkov et al. (2006) at 40 and 80 °C to model predictions from this work. We chose to illustrate this comparison in a parity plot due to the numerous solution compositions reported by the author (e.g. 1.0, 1.2, 2.0, 2.1, 2.3, 4.0, and 4.2 m PZ) but over a selected range in loading.

Figures 14.5-7 and 14.5-8 illustrates an important point where over the range of piperazine concentrations studied in this work, the apparent CO_2 solubility is approximately independent of the piperazine concentration. Overall, the full model adequately described the CO_2 solubility data within an average absolute relative error of ± 10.4 percent.

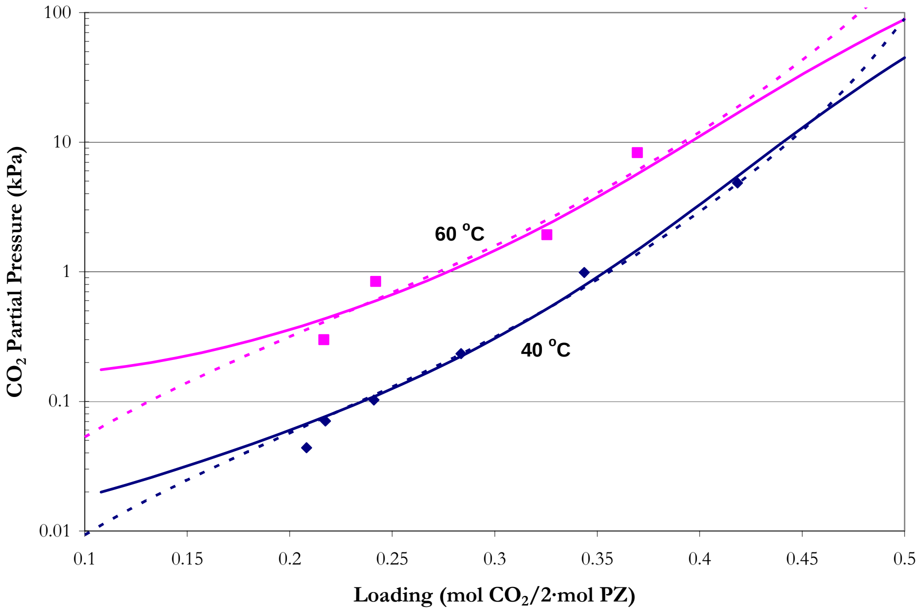

Figure 14.5-1. Comparison between Experimental and Predicted CO$_2$ Solubility in 0.9 m PZ at 40 and 60 °C. Points: ♦, 40 °C, ■, 60 °C, this work. Lines: - - -, Hilliard (2005), ▬, this work.

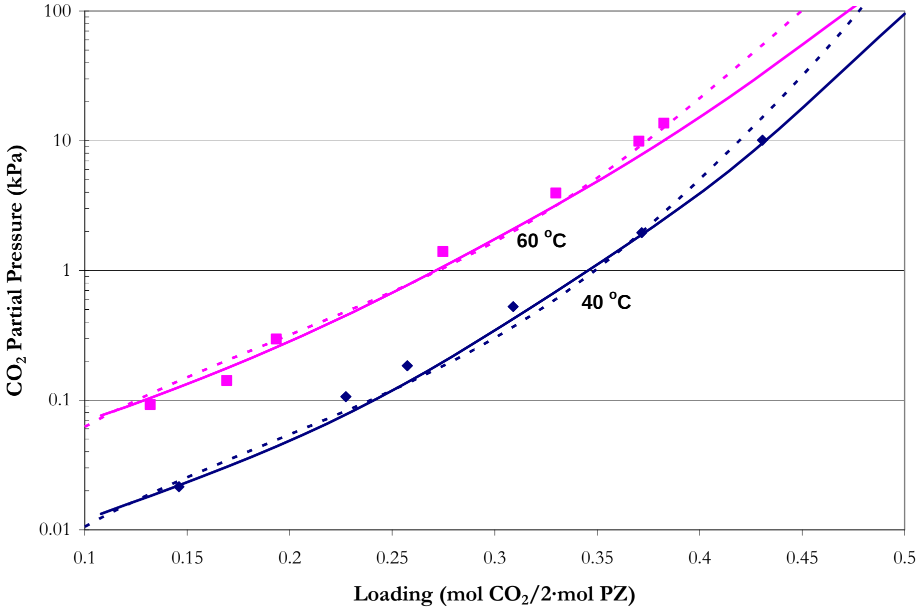

Figure 14.5-2. Comparison between Experimental and Predicted CO$_2$ Solubility in 2.0 m PZ at 40 and 60 °C. Points: ♦, 40 °C, ■, 60 °C, this work. Lines: - - -, Hilliard (2005), ▬, this work.

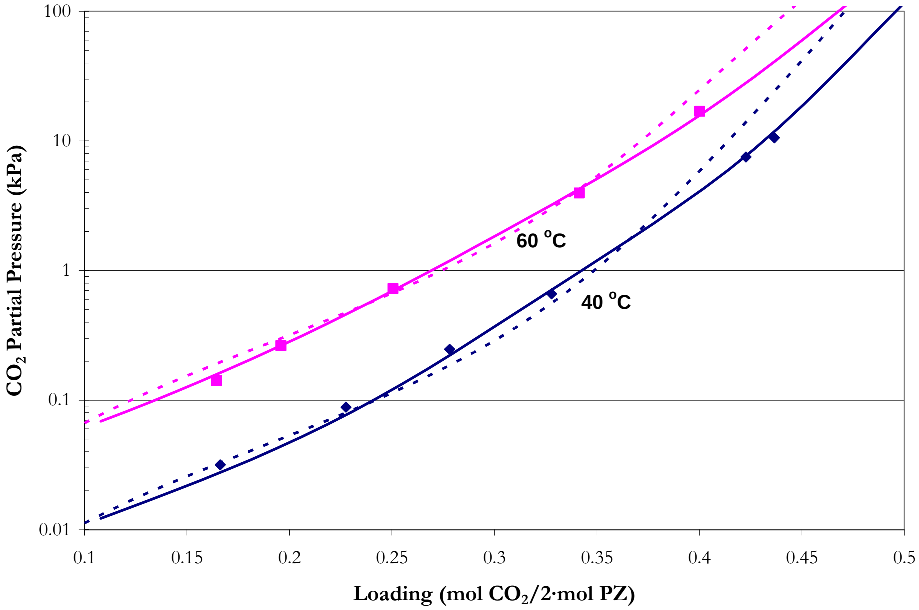

Figure 14.5-3. Comparison between Experimental and Predicted CO$_2$ Solubility in 2.5 m PZ at 40 and 60 °C. Points: ♦, 40 °C, ■, 60 °C, this work. Lines: - - -, Hilliard (2005), ▬, this work.

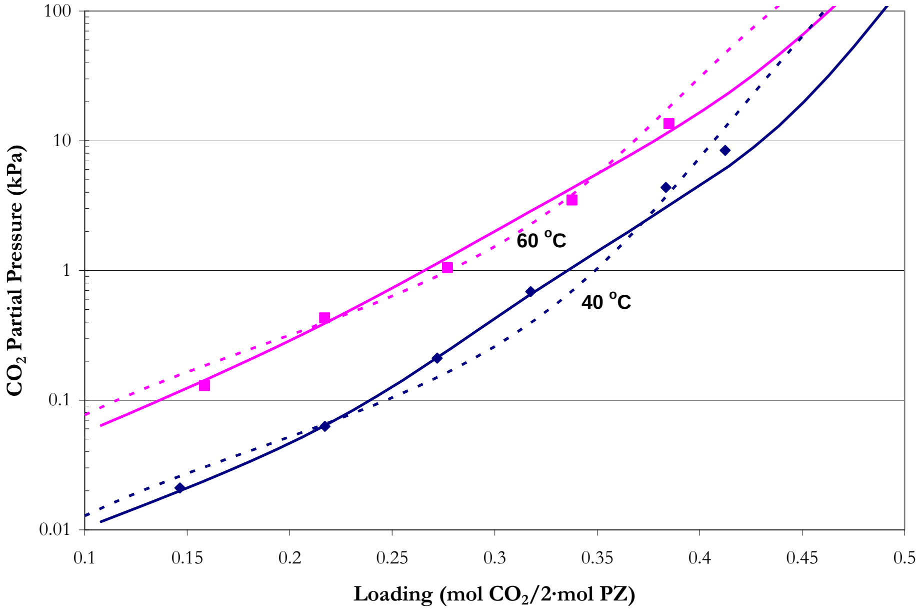

Figure 14.5-4. Comparison between Experimental and Predicted CO$_2$ Solubility in 3.6 m PZ at 40 and 60 °C. Points: ♦, 40 °C, ■, 60 °C, this work. Lines: - - -, Hilliard (2005), ▬, this work.

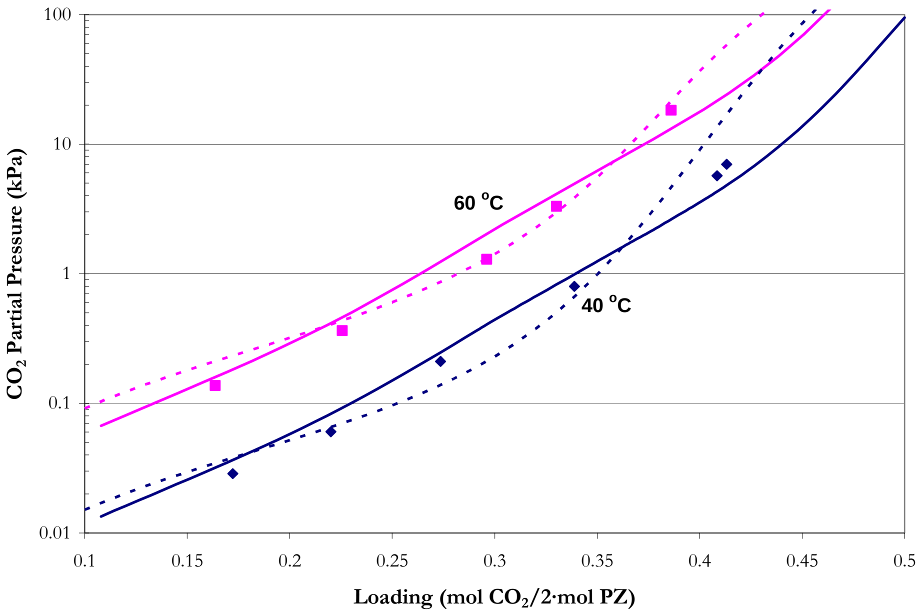

Figure 14.5-5. Comparison between Experimental and Predicted CO_2 Solubility in 5.0 m PZ at 40 and 60 °C. Points: ♦, 40 °C, ■, 60 °C, this work. Lines: - - -, Hilliard (2005), ▬, this work.

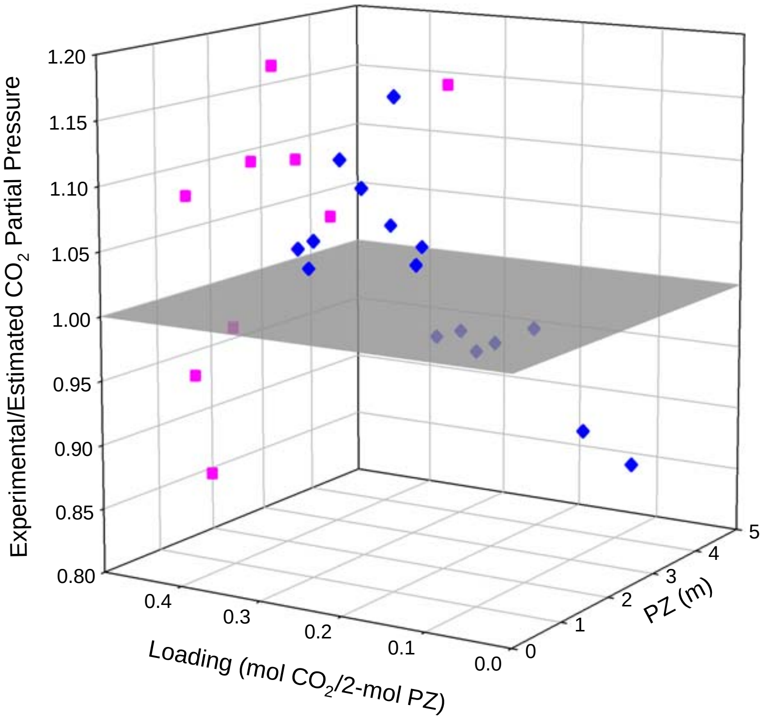

Figure 14.5-6. Comparison between Experimental CO_2 Solubility in 1 – 4 m PZ at 40 (♦) and 80 (■) °C from Ermatchkov et al. (2006) to Predictions from this work.

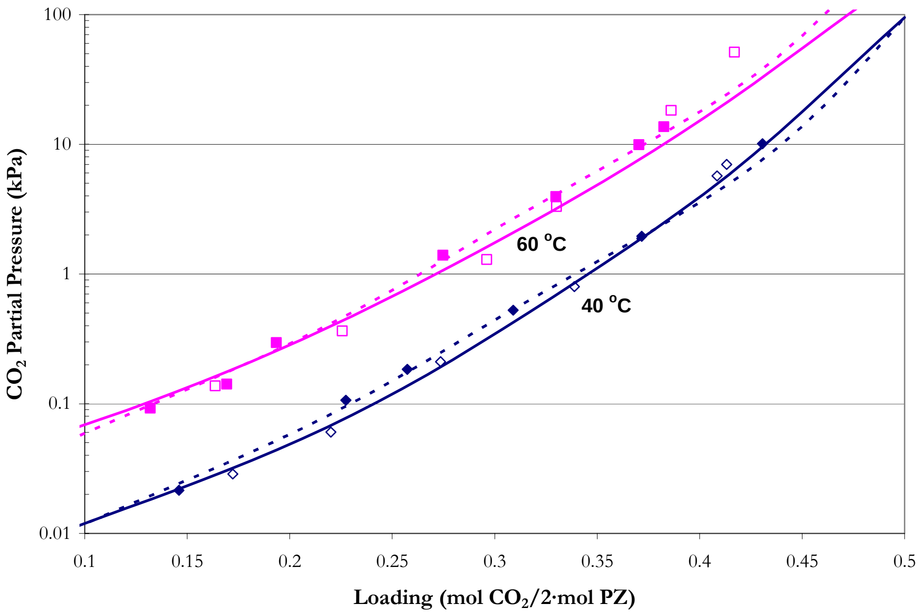

Figure 14.5-7. Comparison between Experimental and Predicted CO_2 Solubility in 2.0 and 5.0 m PZ at 40 and 60 °C from this work. Points: ♦, 40 °C, ■, 60 °C, 2.0 m PZ, ◊, 40 °C, □, 60 °C, 5.0 m PZ. Lines: 2.0 m PZ Predictions, 5.0 m PZ Predictions.

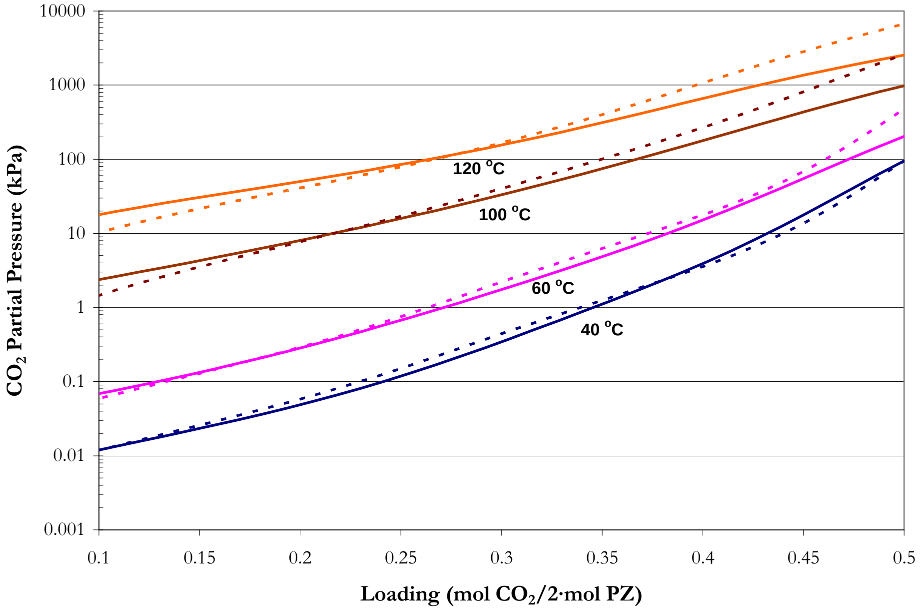

Figure 14.5-8. CO_2 Solubility Predictions for 2.0 and 5.0 m PZ from 40 to 120 °C. Solid lines: 2.0 m PZ. Dash lines: 5.0 m PZ.

CO_2 solubility Temperature Dependence

Figure 14.5-9 through 14.5-13 illustrates predictions for the temperature dependence of CO_2 solubility versus loading for 0.9 – 5 m PZ from 20 – 120 °C. Figure 14.5-9 through 14.5-13 demonstrates the limiting effect of piperazine hexahydrate precipitation on CO_2 solubility versus loading. In the carbon capture processes, the deposition of a salt in the process needs to be avoided. Thus, for carbon capture process utilizing salt and/or amines as a chemical solvent, knowledge about the range of conditions where salt precipitation may be possible is very important in addition in a laboratory environment where bench scale solubility measurements are performed.

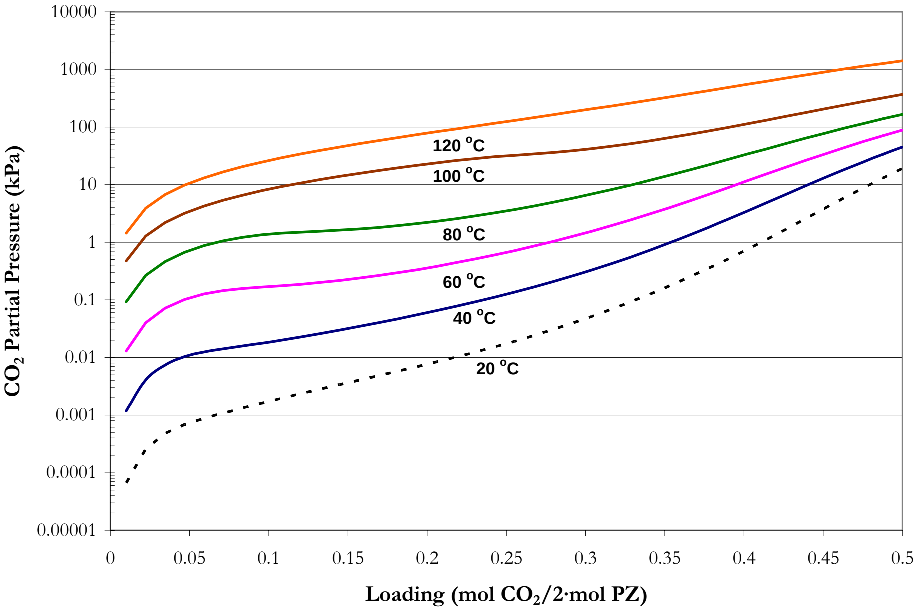

Figure 14.5-9. CO_2 Solubility Predictions for 0.9 m PZ from 20 to 120 °C.

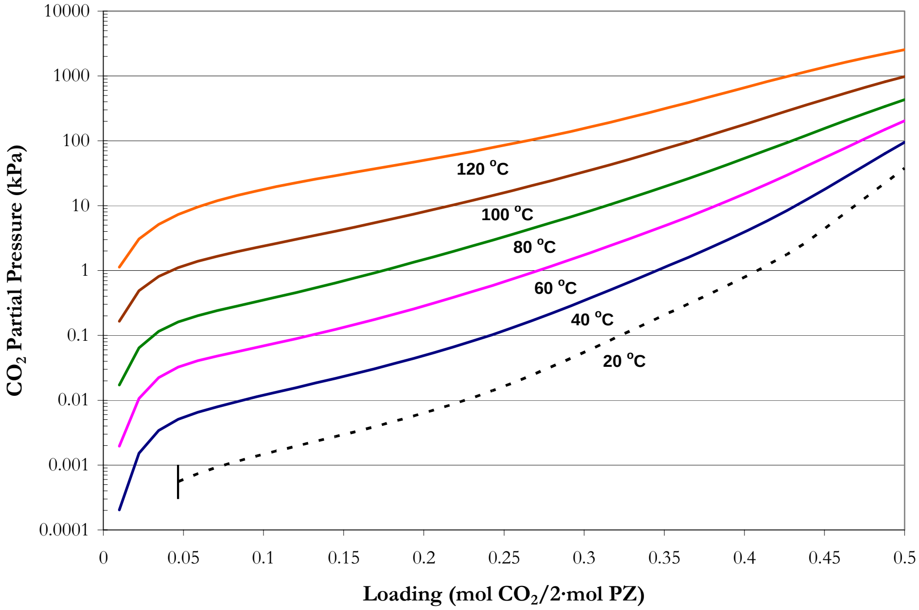

Figure 14.5-10. CO_2 Solubility Predictions for 2.0 m PZ from 20 to 120 °C.

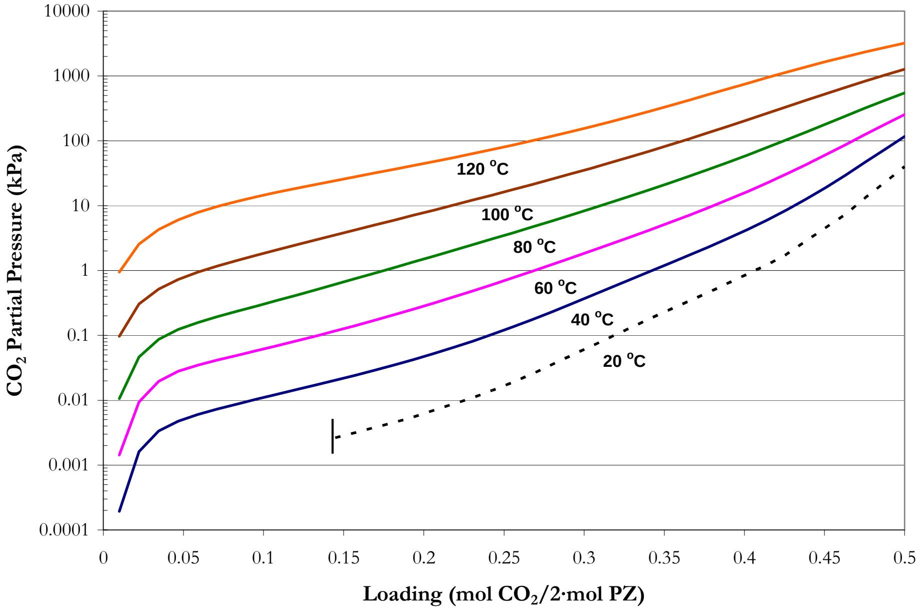

Figure 14.5-11. CO_2 Solubility Predictions for 2.5 m PZ from 20 to 120 °C.

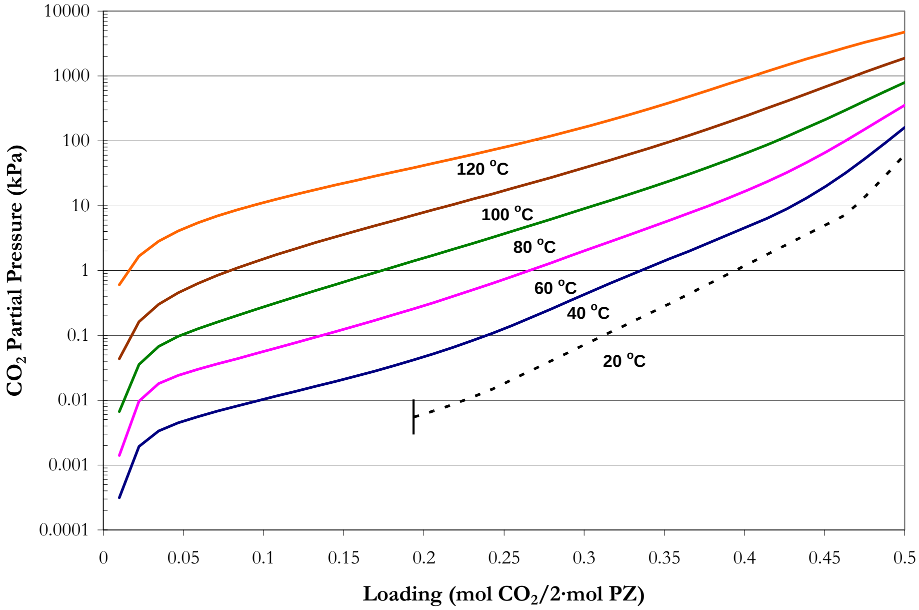

Figure 14.5-12. CO_2 Solubility Predictions for 3.6 m PZ from 20 to 120 °C.

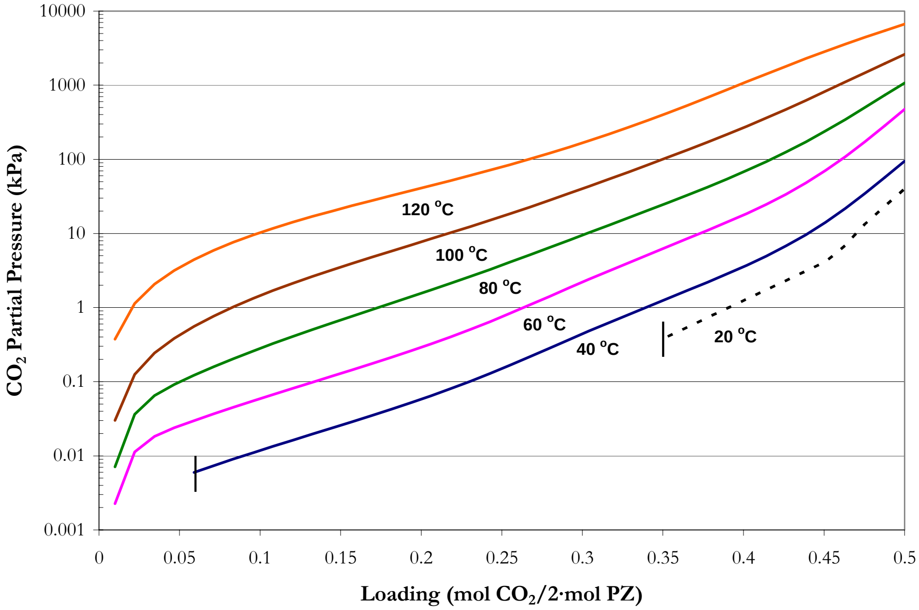

Figure 14.5-13. CO_2 Solubility Predictions for 5.0 m PZ from 20 to 120 °C.

PZ Volatility Predictions

As shown in Chapter IX, Figure 14.5-14 compares estimated model predictions to experimental partial pressure of PZ in solutions of H_2O-PZ. The model adequately predicts the partial pressure of PZ but fails to predict the correct partial pressure at 40 and 60 °C. Since this error is the initial boundary of PZ volatility, subsequent volatility predictions will be subjected to this estimation as shown by the dashed line based on an ordinary least squares (OLS) approximation in Figure 14.5-15 through Figure 14.5-19, illustrating the fit for the experimental PZ solubility at 0.9, 2.0, 2.5, 3.6, and 5.0 m PZ per loading at 40 and 60 °C as predicted from this work and compared to predictions from the Hilliard (2005) model.

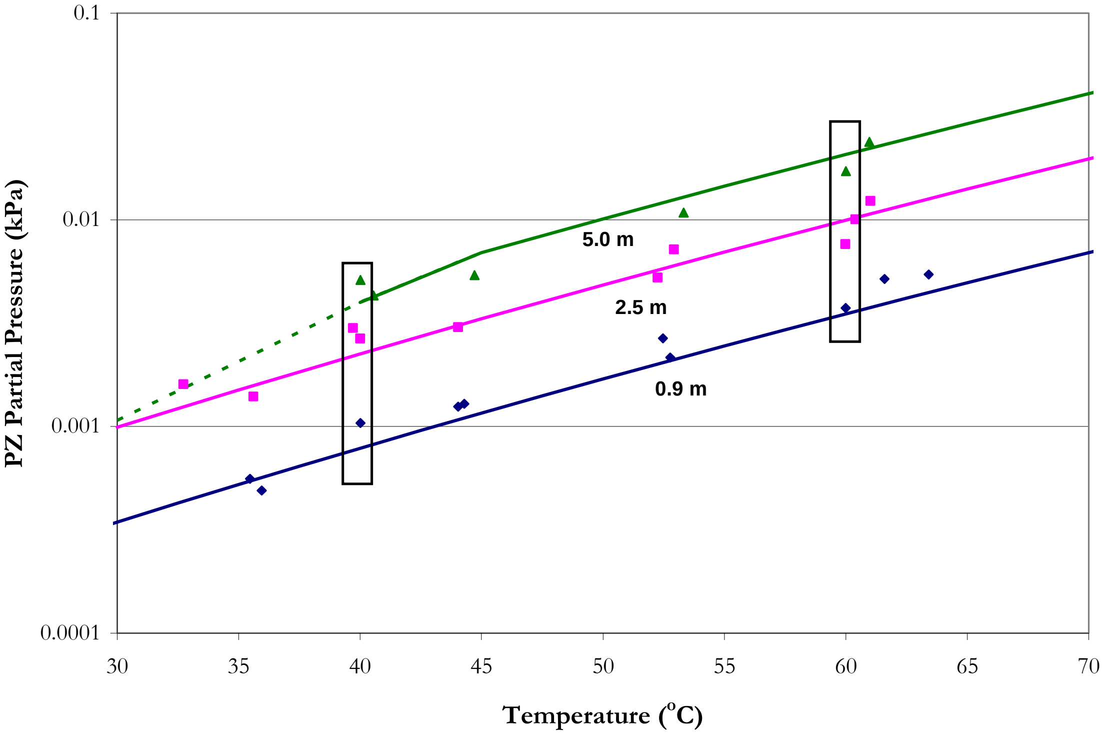

Figure 14.5-14. Comparison of Amine Volatility at Zero Loading from this work to elecNRTL Model Predictions from 30 – 120 °C. Points: experimental data from this work ♦, 0.9 m, ■, 2.5 m, ▲, 5.0 m. Lines: ▬, elecNRTL Predictions.

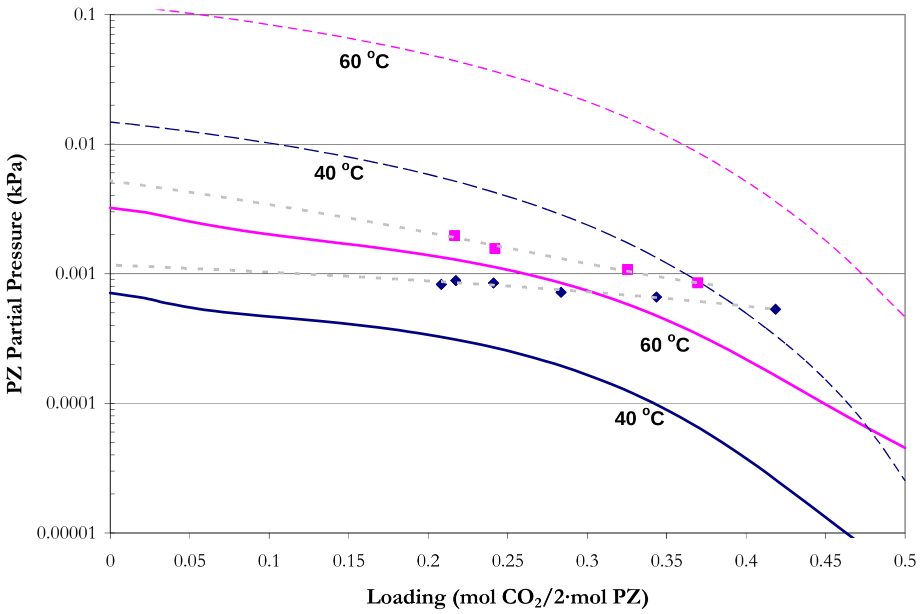

Figure 14.5-15. Comparison between Experimental and Predicted PZ Volatility in 0.9 m PZ at 40 and 60 °C. Points: ♦, 40 °C, ■, 60 °C, this work. Lines: — —, Hilliard (2005), - - -, OLS Approximation, ▬, this work.

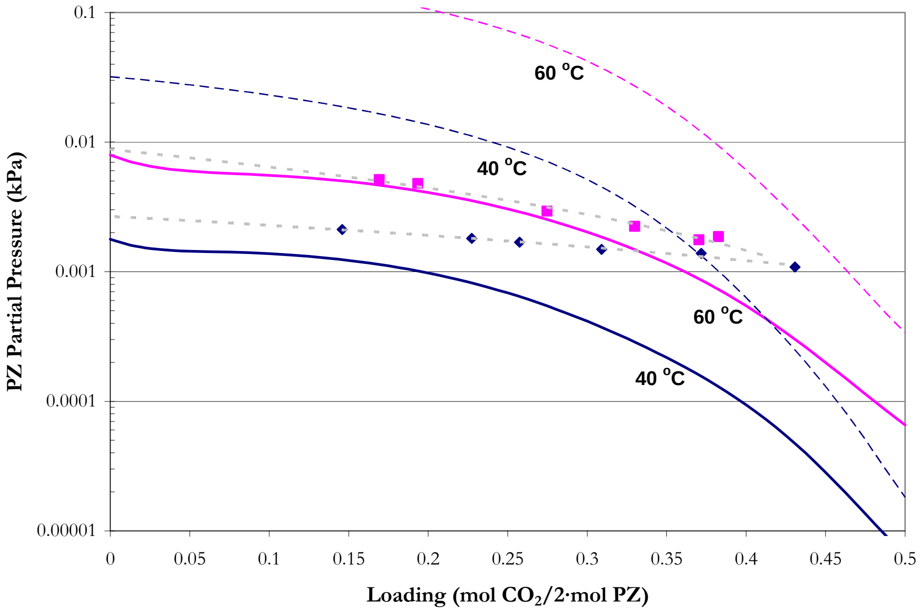

Figure 14.5-16. Comparison between Experimental and Predicted PZ Volatility in 2.0 m PZ at 40 and 60 °C. Points: ♦, 40 °C, ■, 60 °C, this work. Lines: — —, Hilliard (2005), - - -, OLS Approximation, ▬, this work.

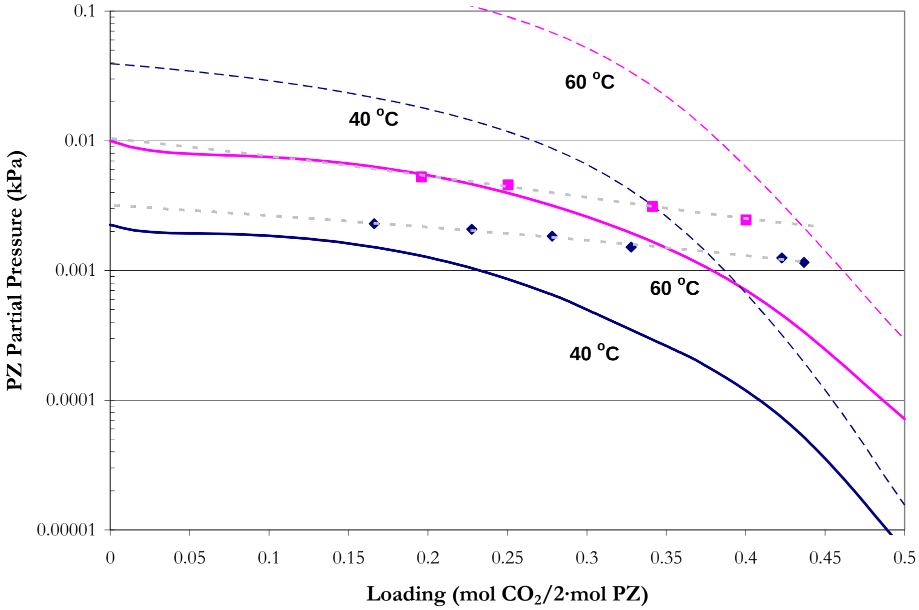

Figure 14.5-17. Comparison between Experimental and Predicted PZ Volatility in 2.5 m PZ at 40 and 60 °C. Points: ♦, 40 °C, ■, 60 °C, this work. Lines: — —, Hilliard (2005), - - -, OLS Approximation, ▬, this work.

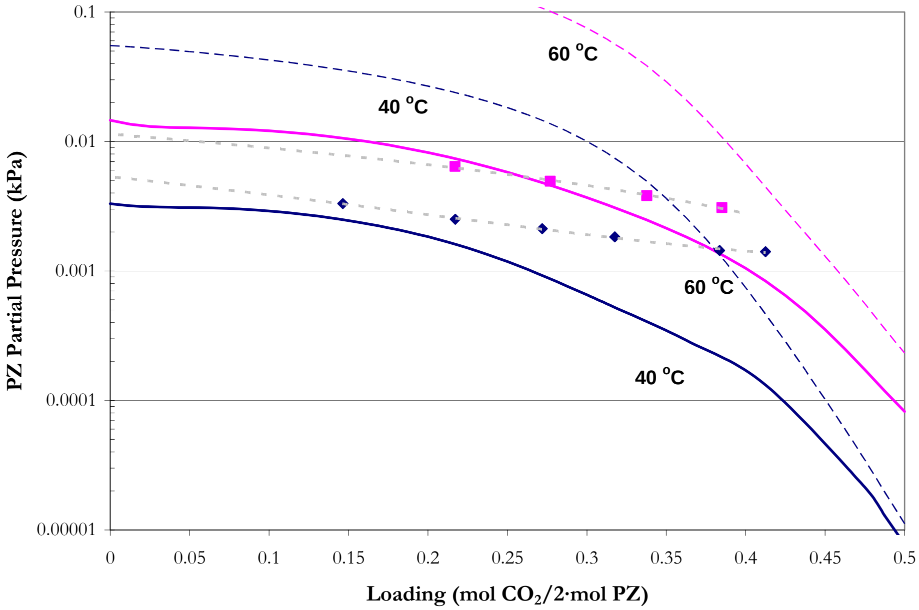

Figure 14.5-18. Comparison between Experimental and Predicted PZ Volatility in 3.6 m PZ at 40 and 60 °C. Points: ♦, 40 °C, ■, 60 °C, this work. Lines: — —, Hilliard (2005), - - -, OLS Approximation, ▬, this work.

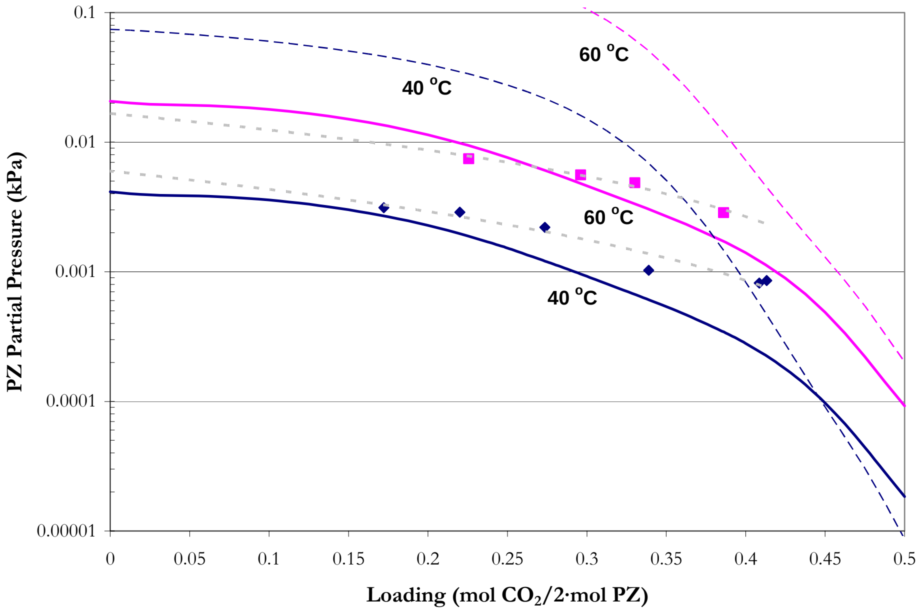

Figure 14.5-19. Comparison between Experimental and Predicted PZ Volatility in 5.0 m PZ at 40 and 60 °C. Points: ♦, 40 °C, ■, 60 °C, this work. Lines: — —, Hilliard (2005), - - -, OLS Approximation, ▬, this work.

As shown in Figure 14.5-15 through 14.5-19, the Hilliard (2005) model overestimates the PZ partial pressure over the entire range of conditions. The root cause to this overestimation was estimating the activity coefficient of PZ in H_2O-PZ by the UNIQUAC (DMD) model. We would recommend future works not to include predictions for the activity coefficient of PZ based on H2O-PZ systems into thermodynamic models. Thermodynamic models based on available experimental data are more likely to represent the correct activity coefficient behavior, but in reality may not be feasible due to the limited amount of binary information on unique amine systems.

PZ Volatility as a Function of Temperature

Using the full model as a purely predictive tool, Figure 14.5-20 through Figure 14.5-24 illustrates the partial pressure of PZ in 0.9, 2.0, 2.5, 3.6, and 5.0 m solutions. In Figure 14.5-22, the main effects that may affect the partial pressure of PZ in a 2.5 m solution to decrease from a loading between 0 and 0.25 mol CO_2/2mol PZ are due to changes in the activity coefficient of PZ and the solution loading. Within the loading range of 0.25 to 0.5, the main effects are now due to contributions of the chemical equilibrium constants and the solution speciation, vis-à-vis the concentration of free amine in the liquid phase where beyond a loading of 0.4, the concentration of free amine can be considered negligible as shown in Section 14.5.4.

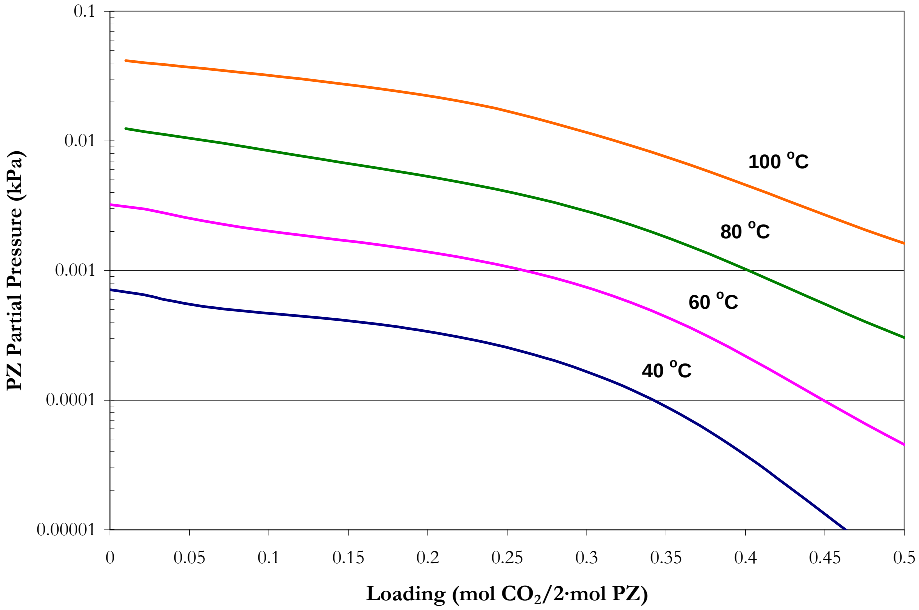

Figure 14.5-20. Predictions for Amine Volatility in 0.9 m PZ from this work.

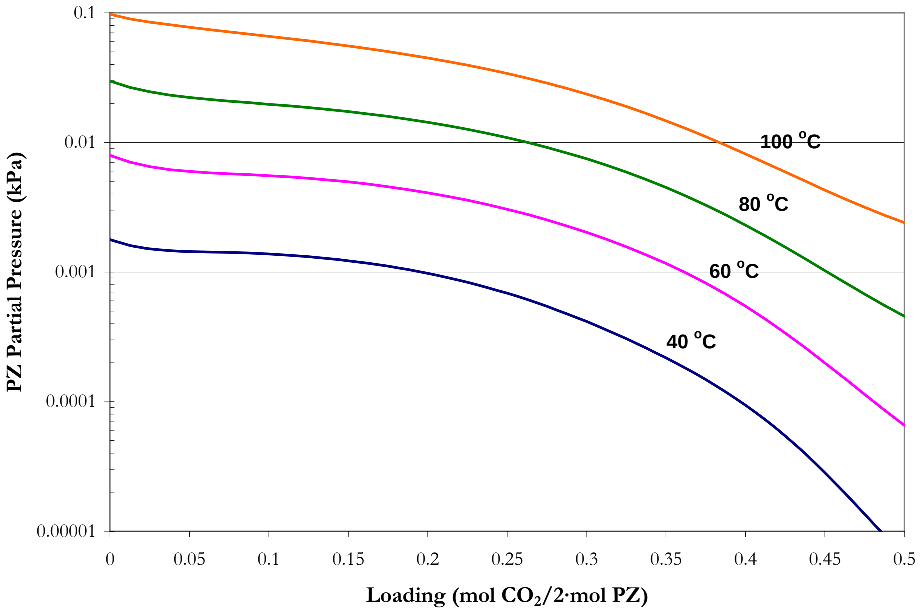

Figure 14.5-21. Predictions for Amine Volatility in 2.0 m PZ from this work.

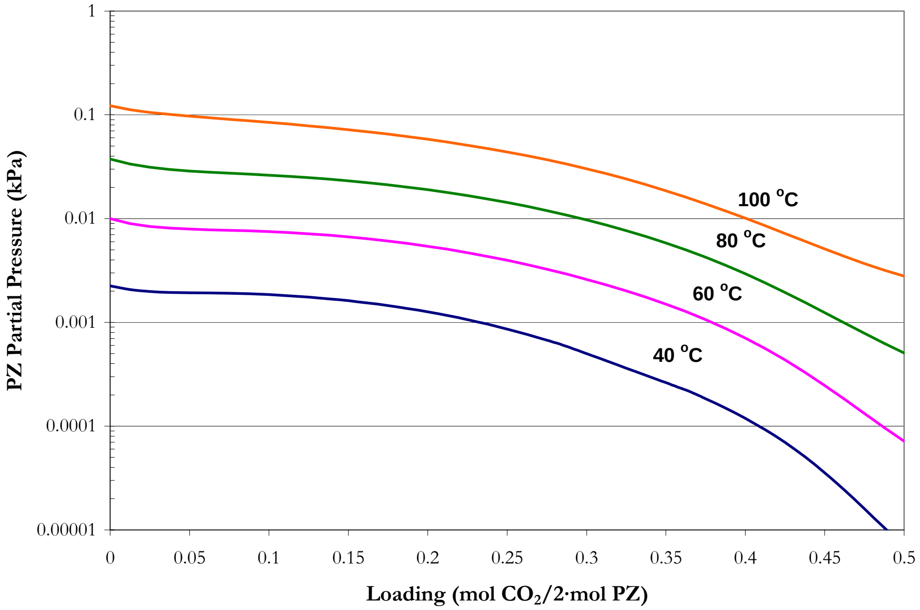

Figure 14.5-22. Predictions for Amine Volatility in 2.5 m PZ from this work.

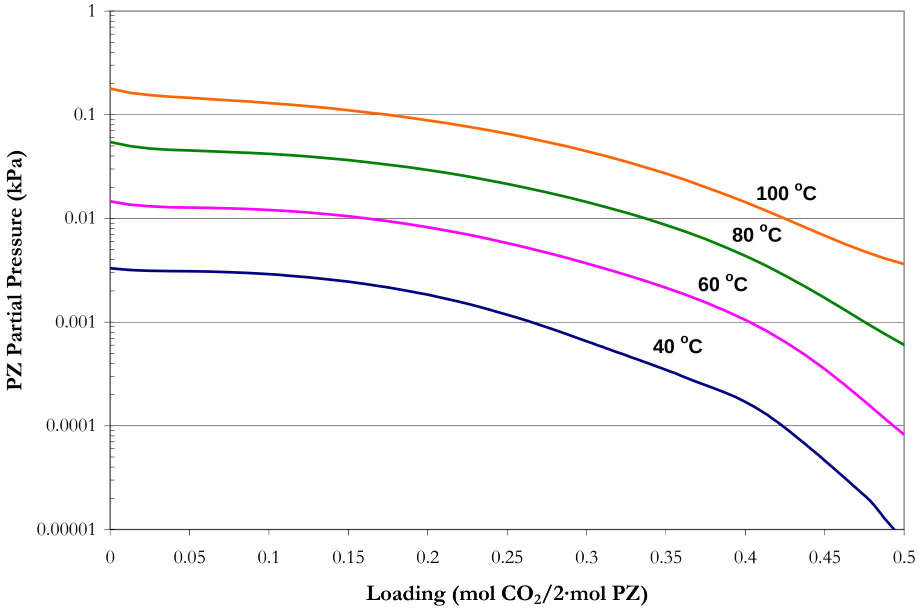

Figure 14.5-23. Predictions for Amine Volatility in 3.6 m PZ from this work.

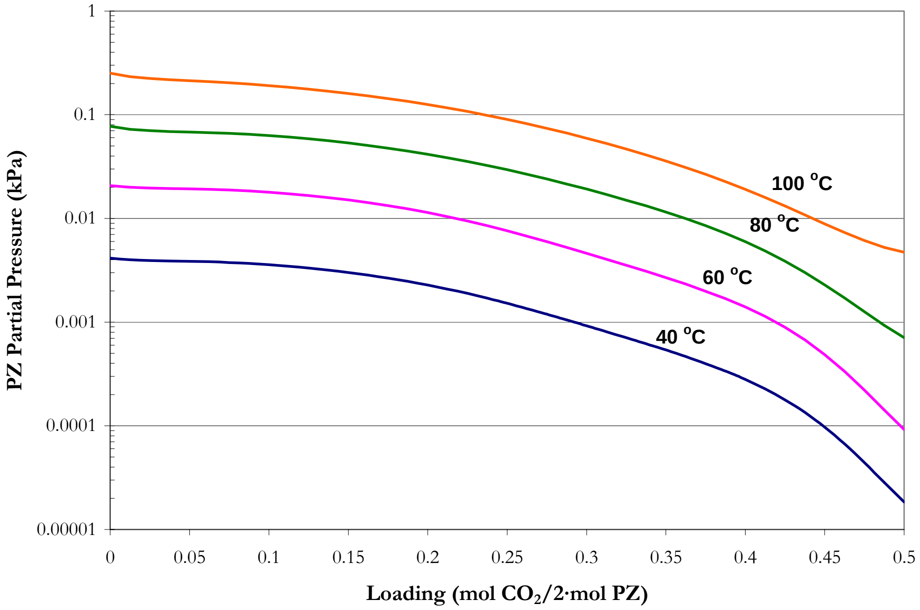

Figure 14.5-24. Predictions for Amine Volatility in 5.0 m PZ from this work.

14.5.2 *Enthalpy of CO_2 Absorption*

Figure 14.5-25 through Figure 14.5-27 compares experimental differential enthalpy of CO_2 absorption measurements from Kim (2007) to predictions based on Equation 14-39 (Gibbs-Helmholtz) from Hilliard (2005) and from this work.

Model predictions from Hilliard (2005) underestimate the enthalpy of CO_2 absorption at high temperatures over the range in loading and predict the wrong temperature dependence. The enthalpy data suggests that as the temperature increases so does the energy to release CO_2 from the solvent as shown in Figure 14.5-28.

On the other hand, the Hilliard (2005) model did not include calorimetric measurements as part of his original regression analysis, but we chose to illustrate the possible enthalpy differences as compared to a purely CO_2 solubility based thermodynamic model.

Figure 14.5-28 illustrates that at a loading of 0.2 mol CO_2/2·mol PZ, the enthalpy of CO_2 absorption increased from 70 to 90 kJ/mol-CO_2 as the temperature increased from 40 to 120 °C. Figure 14.5-29 illustrates an approximate 10 kJ/mol-CO_2 decrease in the enthalpy of CO_2 absorption in 2.4 m PZ at 40 °C as compared to 7 m MEA, but at 120 °C the enthalpy of CO_2 absorption is approximately equal over the range of CO_2 partial pressures from 10 to 1000 kPa.

Overall, the full model adequately predicts the enthalpy of CO_2 absorption for 2.4 m PZ mixtures within an average absolute relative error of ± 6.55 percent.

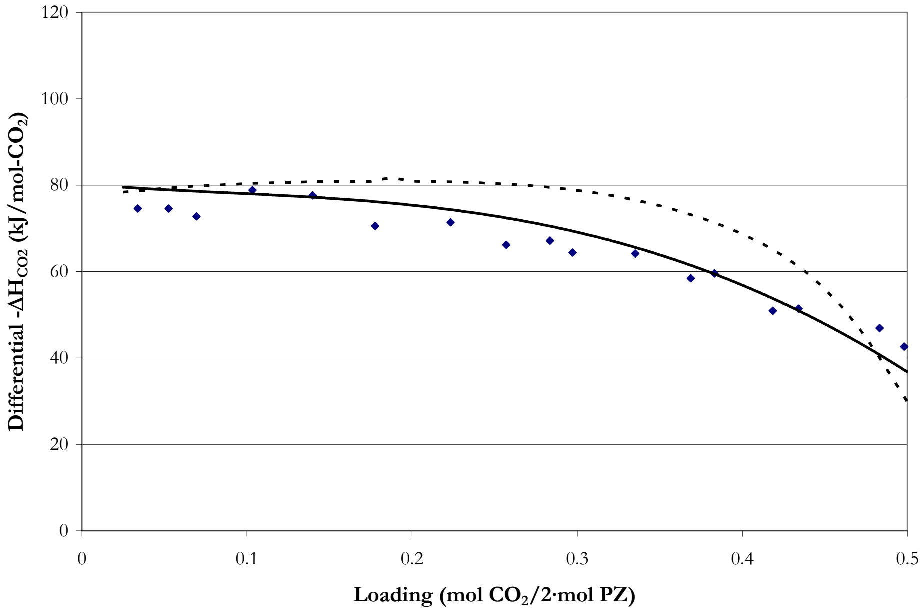

Figure 14.5-25. Comparison of the Enthalpy of CO_2 Absorption in 2.4 m PZ at 40 °C. Points: ♦, Kim (2007). Lines: - - -, Hilliard (2005), ▬, this work.

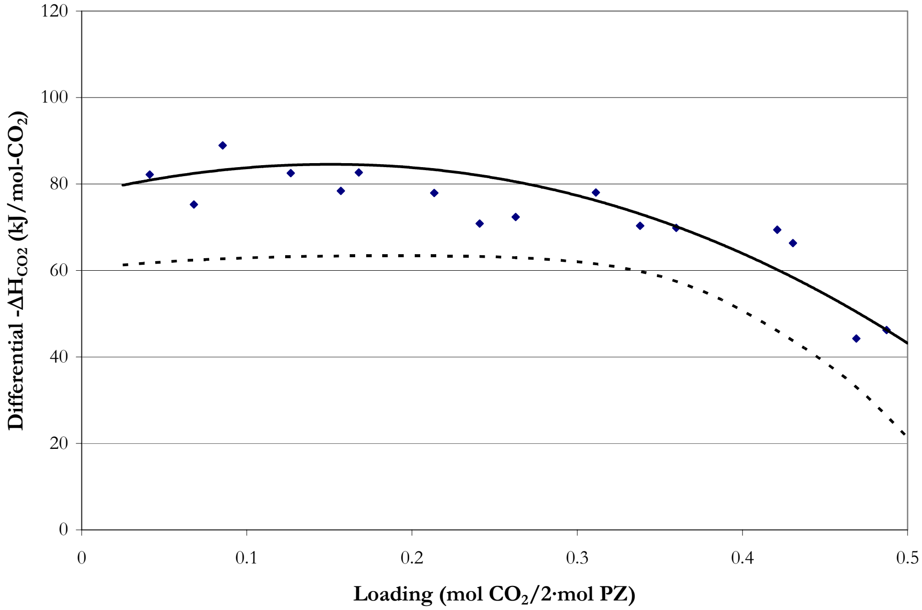

Figure 14.5-26. Comparison of the Enthalpy of CO_2 Absorption in 2.4 m PZ at 40 °C. Points: ♦, Kim (2007). Lines: - - -, Hilliard (2005), ▬, this work.

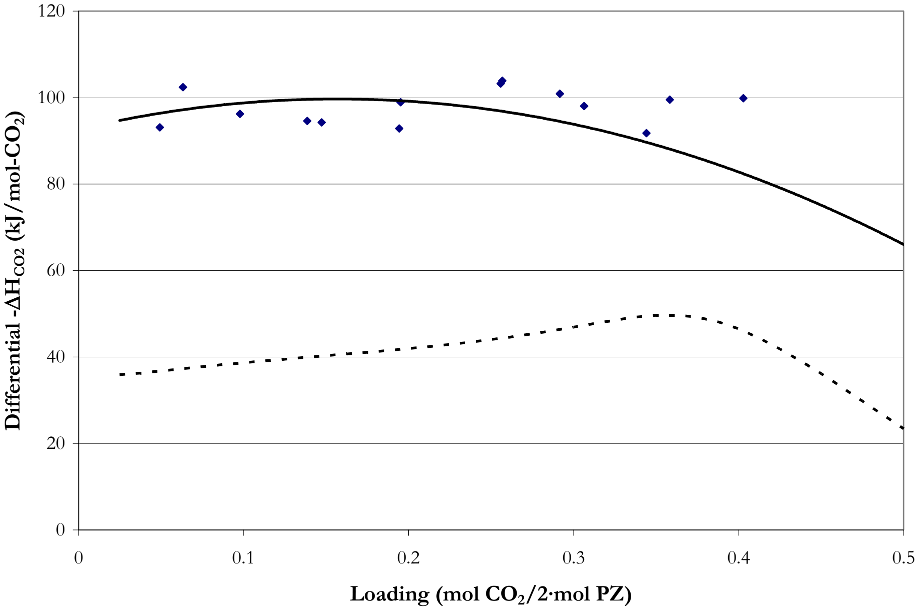

Figure 14.5-27. Comparison of the Enthalpy of CO_2 Absorption in 2.4 m PZ at 40 °C. Points: ♦, Kim (2007). Lines: - - -, Hilliard (2005), ▬, this work.

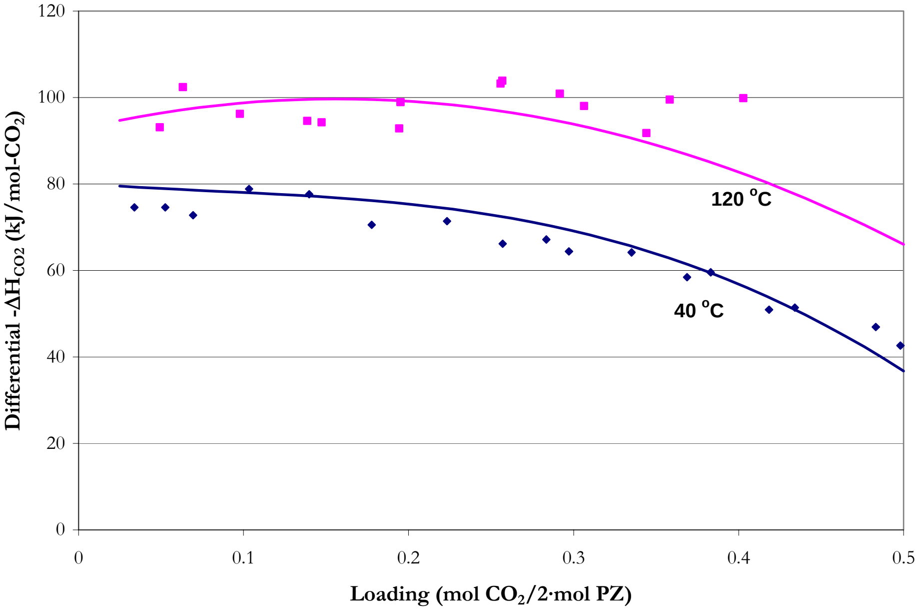

Figure 14.5-28. Comparison of the Enthalpy of CO_2 Absorption in 2.4 m PZ at 40 and 120 °C. Points: ♦, 40 °C, ■, 120 °C, Kim (2007). Lines: ▬, this work.

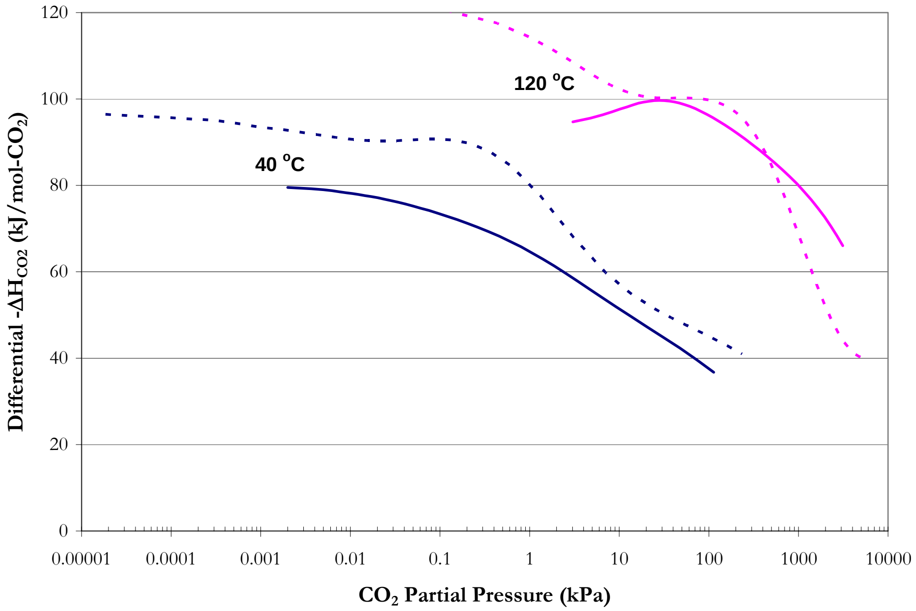

Figure 14.5-29. . Comparison of the Enthalpy of CO_2 Absorption Model Predictions from this work in Mixtures of H_2O-MEA-CO_2 and H_2O-PZ-CO_2 at 40 and 120 °C. Lines: ▬, 2.4 m PZ, - - -, 7 m MEA.

14.5.3 *Specific Heat Capacity*

Figure 14.5-30 through 14.5-37 compares experimental specific heat capacity measurements from this work to predictions from Hilliard (2005) and to this work. Model predictions from Hilliard (2005) were unable to capture trends in the specific heat capacity as a function of temperature as shown in Figure 14.5-33 through 14.5-37. On the other hand, Hilliard (2005) did not include calometric measurements as part of his original regression analysis, but we chose to illustrate the possibility enthalpy differences as compared to a purely CO_2 solubility based thermodynamic model.

Predictions from this work do capture the correct trends in the specific heat capacity as a function of temperature but falls short in predicting the correct specific heat capacity on the order of ± 5 percent. One possibility for this discrepancy may result from an inconsistency between the enthalpy of CO_2 absorption measurements from Kim (2007) and specific heat capacity from this work.

We can relate the liquid phase specific heat capacity measurements to the sensible liquid phase enthalpy of solution from 40 to 120 °C by integrating the specific heat capacity as a function of temperature through regression of the experimental specific heat capacity data to the following function:

$$\begin{aligned} C_p^l\left(\frac{kJ}{kg-K}\right) = {} & C_1 + C_2T + C_3\left[PZ\right] + C_4Ldg + \\ & C_5Ldg^2 + C_6\left[PZ\right]T + C_7\left[PZ\right]Ldg + \\ & C_8T\cdot Ldg + C_9\left[PZ\right]\cdot T\cdot Ldg \end{aligned} \tag{14-52}$$

Where
T is the temperature, °C,
$\left[PZ\right]$ is the concentration of PZ, m (mole/kg-H_2O),
Ldg is the loading of the solution, mol CO_2/2·mol PZ.

Equation 14-52 allows for nonlinearity in the temperature, concentration, and loading dependence. The interaction terms $\left(\left[PZ\right]\cdot T$, $\left[PZ\right]\cdot Ldg$, $T\cdot Ldg$, $\left[PZ\right]\cdot T\cdot Ldg\right)$ allow for twisting of the predictive surface versus the four predictors. Performing an ordinary least squares (OLS) regression on the experimental specific heat capacity measurements from this work using ARC gives the following coefficients estimates in Equation 14-52 as shown in Table 14.5.1.

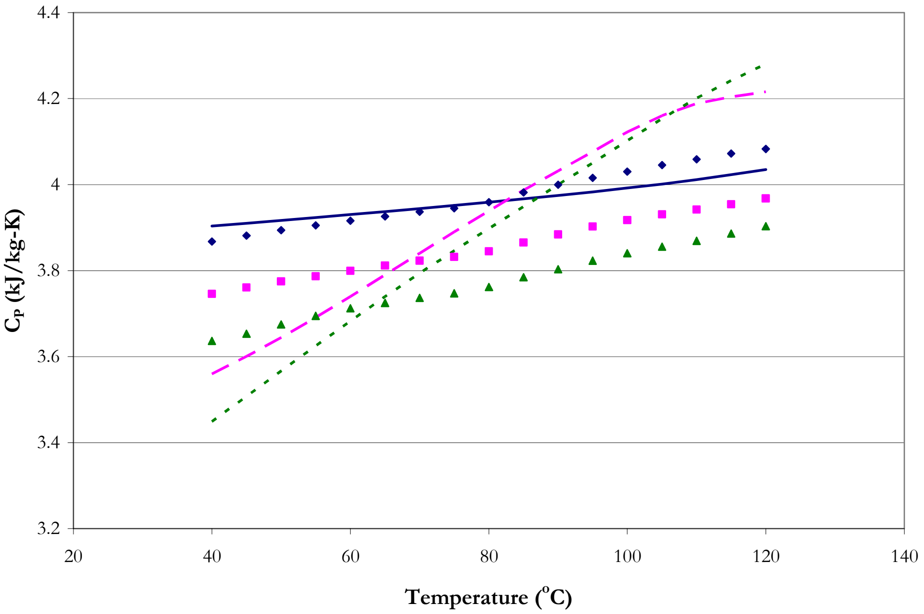

Figure 14.5-30. Comparison of Experimental Specific Heat Capacity in Loaded 2.0 m PZ Mixtures from 40 to 120 °C. Points: ♦, Ldg = 0.0, ■, Ldg = 0.16, ▲, Ldg = 0.27. Lines: —, Ldg = 0.0, — —, Ldg = 0.16, - - - , Ldg = 0.27, this work.

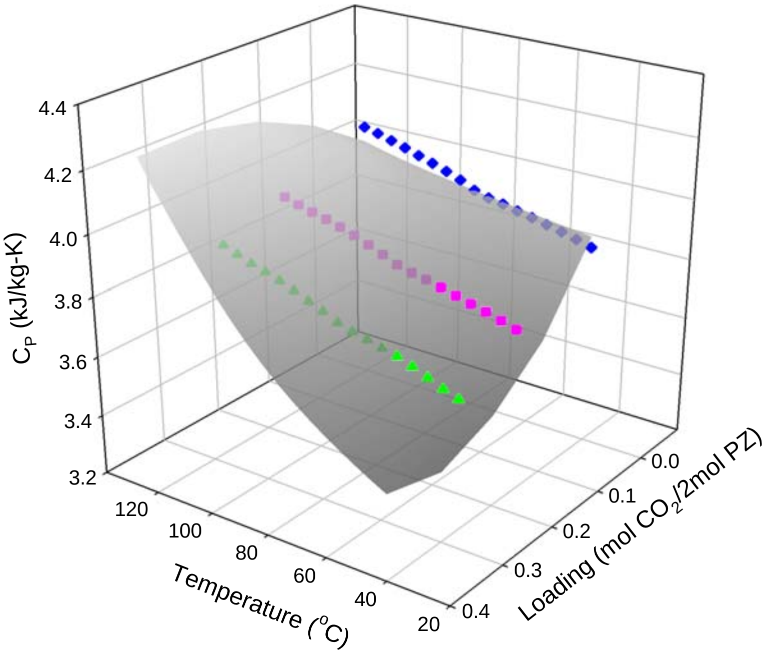

Figure 14.5-31. Surface Comparison of Experimental Specific Heat Capacity in Loaded 2.0 m PZ Mixtures from 40 to 120 °C. Points: ♦, Ldg = 0.0, ■, Ldg = 0.16, ▲, Ldg = 0.27. Surface: this work.

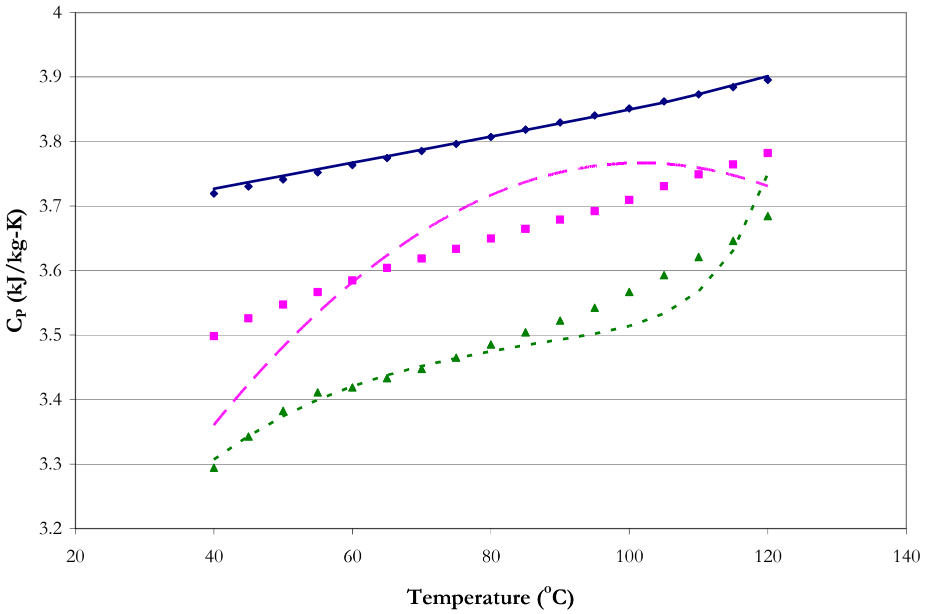

Figure 14.5-32. Comparison of Experimental Specific Heat Capacity in Loaded 3.6 m PZ Mixtures from 40 to 120 ^{o}C. Points: ♦, Ldg = 0.0, ■, Ldg = 0.16, ▲, Ldg = 0.38. Lines: —, Ldg = 0.0, — —, Ldg = 0.16, - - - , Ldg = 0.38, this work.

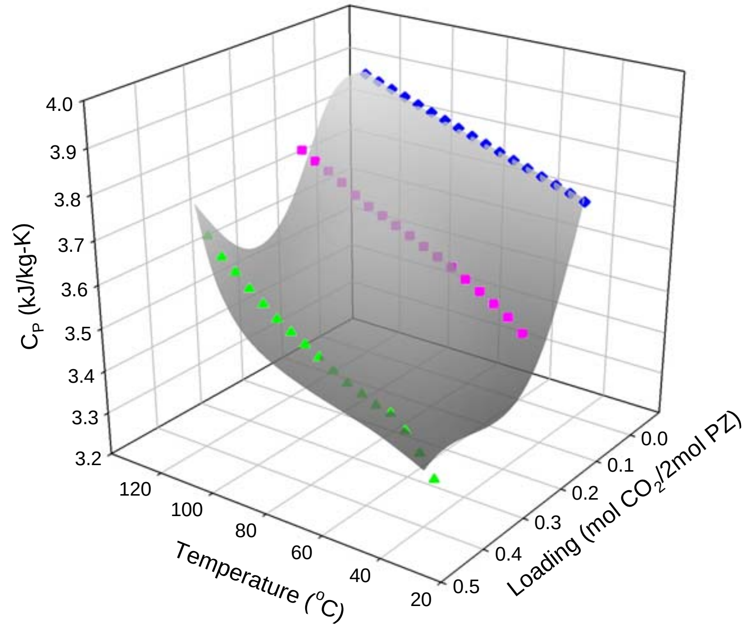

Figure 14.5-33. Surface Comparison of Experimental Specific Heat Capacity in Loaded 2.0 m PZ Mixtures from 40 to 120 ^{o}C. Points: ♦, Ldg = 0.0, ■, Ldg = 0.16, ▲, Ldg = 0.38. Surface: this work.

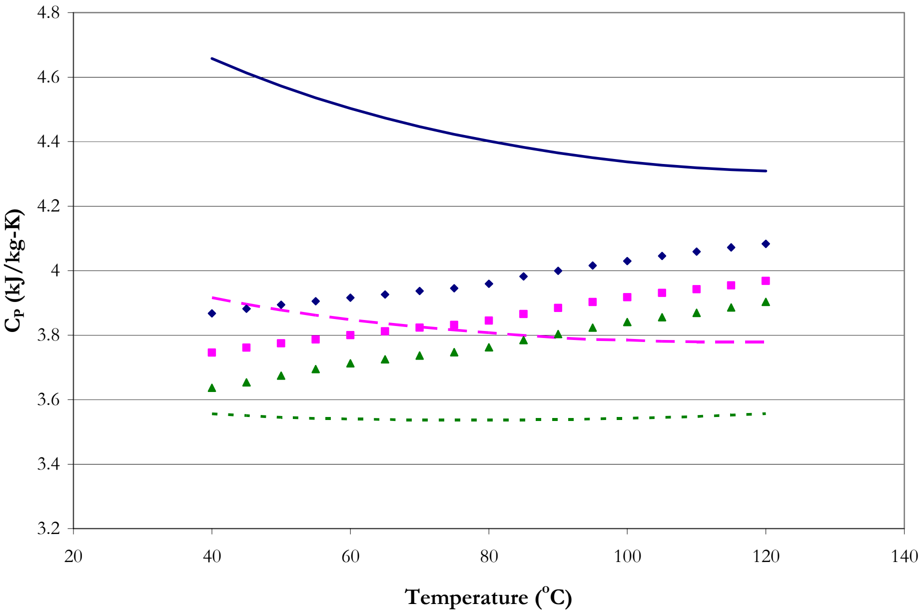

Figure 14.5-34. Comparison of Experimental Specific Heat Capacity in Loaded 2.0 m PZ Mixtures from 40 to 120 ^{o}C. Points: ♦, Ldg = 0.0, ■, Ldg = 0.16, ▲, Ldg = 0.27. Lines: —, Ldg = 0.0, — —, Ldg = 0.16, - - - , Ldg = 0.27, Hilliard (2005).

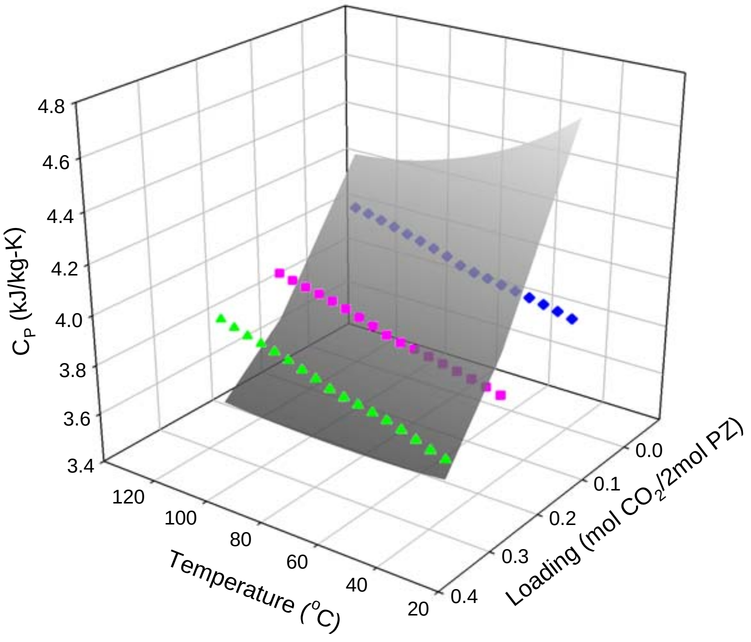

Figure 14.5-35. Surface Comparison of Experimental Specific Heat Capacity in Loaded 2.0 m PZ Mixtures from 40 to 120 ^{o}C. Points: ♦, Ldg = 0.0, ■, Ldg = 0.16, ▲, Ldg = 0.27. Surface: Hilliard (2005).

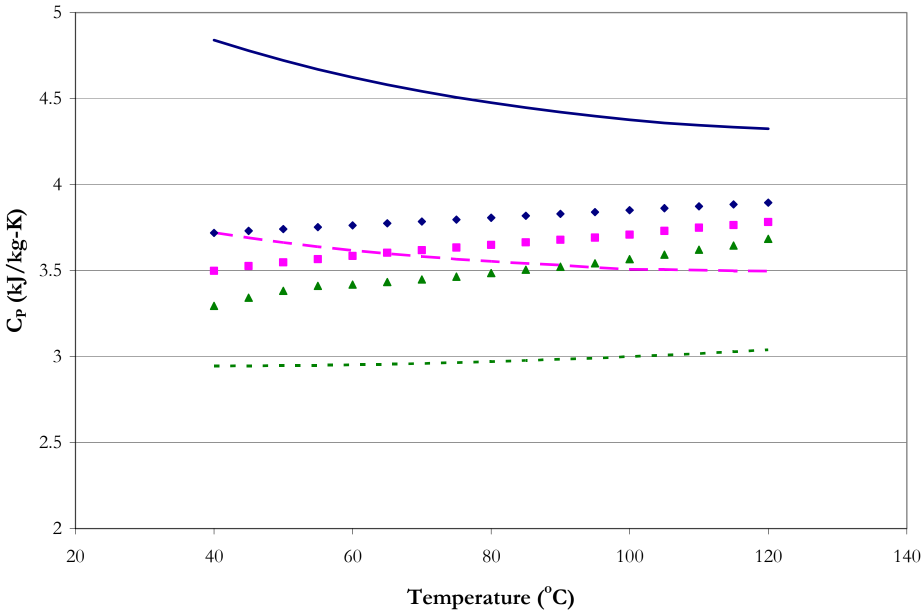

Figure 14.5-36. Comparison of Experimental Specific Heat Capacity in Loaded 3.6 m PZ Mixtures from 40 to 120 °C. Points: ♦, Ldg = 0.0, ■, Ldg = 0.16, ▲, Ldg = 0.38. Lines: ▬, Ldg = 0.0, — —, Ldg = 0.16, - - - , Ldg = 0.38, Hilliard (2005).

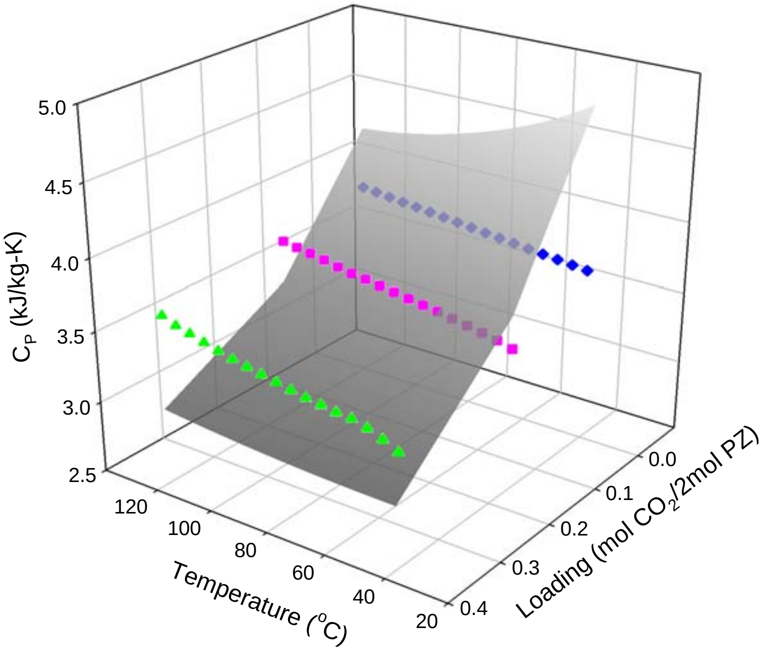

Figure 14.5-37. Comparison of Experimental Specific Heat Capacity in Loaded 3.6 m PZ Mixtures from 40 to 120 °C. Points: ♦, Ldg = 0.0, ■, Ldg = 0.16, ▲, Ldg = 0.38. Surface: Hilliard (2005).

Table 14.5-1. ARC Regression Output for Experimental Specific Heat Capacity Measurements from this work based on Equation 14-52.

Parameter	Estimate	σ wrt Estimate
C_1	3.92	0.0184
C_2	0.00323	0.000220
C_3	-0.0837	0.00636
C_4	-0.413	0.0770
C_5	0.767	0.0521
C_6	-2.54E-04	7.60E-05
C_7	-0.319	0.0261
C_8	-0.00329	0.000883
C_9	0.00242	0.000312

Residual Sum of Squares:	0.0109
Degree of Freedom:	110

Recall that the standard error of an estimate is the estimated standard deviation of that statistic. Notice that all of the estimates are smaller relative to the standard error. A complete description of the variability of the coefficient estimates requires examining the correlations between the estimates as shown in Table 14.5-2.

Table 14.5-2. Correlation Matrix of the Coefficient Estimates for the Full CPMX Model.

Parameter	1	2	3	4	5	6	7	8	9
1	1.00								
2	-0.89	1.00							
3	0.41	-0.73	1.00						
4	-0.85	0.61	0.00	1.00					
5	-0.75	0.51	0.00	0.72	1.00				
6	0.10	0.00	0.00	0.04	-0.46	1.00			
7	0.81	-0.65	0.00	-0.95	-0.71	0.00	1.00		
8	0.75	-0.54	0.00	-0.89	-0.83	-0.01	0.85	1.00	
9	0.76	-0.60	0.00	-0.80	-0.84	0.00	0.84	0.90	1.00

Table 14.5-3 shows three highly correlated parameters and one independent parameter, but the correlation between other coefficients is relatively small, suggesting that C_3, C_8, or C_9 might be usefully removed from the model without significant loss of information.

We can now evaluate the average experimental specific heat capacity over the temperature range from 40 to 120 °C and compare to the average specific heat capacity predictions based on the full model for 2 and 3.6 m PZ as shown in Table 14.5-3.

Table 14.5-3. Comparison of Average Specific Heat Capacity (kJ/kg-K) from 40 - 120 °C.

PZ (m)	Loading	Experimental	Full Model	AARD (%)
2	0.00	3.9716	3.9626	0.23
	0.16	3.8556	3.9224	1.73
	0.27	3.7711	3.8872	3.08
3.6	0.00	3.8074	3.8096	0.06
	0.16	3.6472	3.6874	1.10
	0.38	3.4919	3.4794	0.36

The average absolute relative error presented in Table 14.5-3 illustrates that the full model does predict the correct average specific heat capacity and in turn the sensible liquid phase enthalpy $\left(\bar{C}_p \Delta T\right)$ within the experimental accuracy of ± 2.0 percent error with the exception of 2 m PZ at a loading of 0.27 mol CO_2/2·mol PZ.

To describe the departure from an ideal solution behavior, Figure 14.5-38 and Figure 14.5-39 illustrate the proposed molar infinite dilution aqueous phase heat capacity for ionic, molecular solute, and molecular species in the H_2O-PZ-CO_2 system. The molar infinite dilution aqueous phase heat capacity for CO_3^{-2}, HCO_3^{-1}, and PZH^{+1} were given in Chapter XII and IX, respectively. By differentiating Equation 14-33 with respect to temperature, the molar infinite dilution aqueous phase heat capacity for CO_2 can be determined as shown in Figure 14.5-38. From Table 14.4-3, coefficients for the molar infinite dilution aqueous phase heat capacity of $PZCOO^{-1}$, $PZ(COO^{-1})_2$, and H^+PZCOO^{-1} were determined through simultaneous regression as described in Section 14.4.

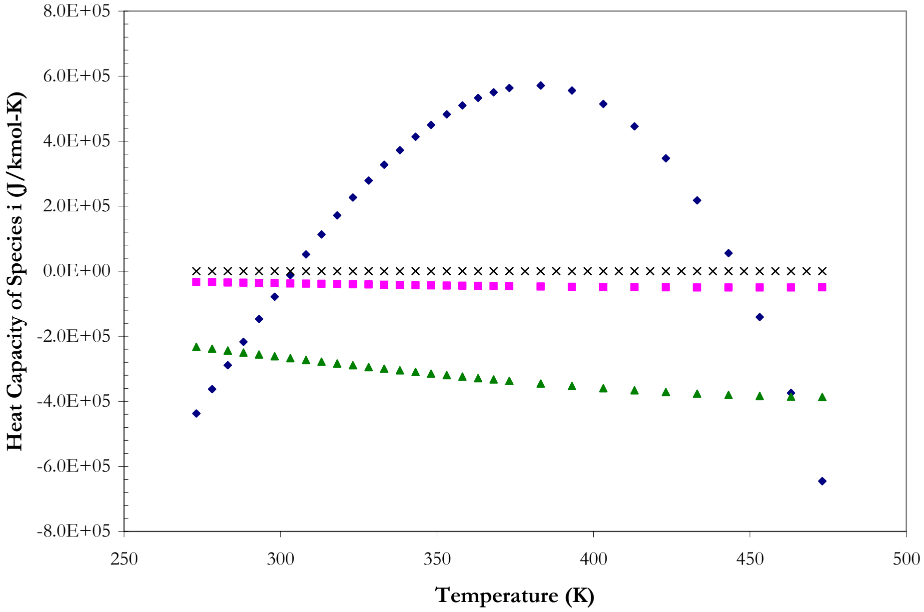

Figure 14.5-38. Molar Infinite Dilution Aqueous Phase Heat Capacity for Ionic, Molecular Solute, and Molecular Species in the H_2O-PZ-CO_2 System. Points: ♦,CO_2, ■,HCO_3^{-1}, ▲ CO_3^{-2}, ×H_2O.

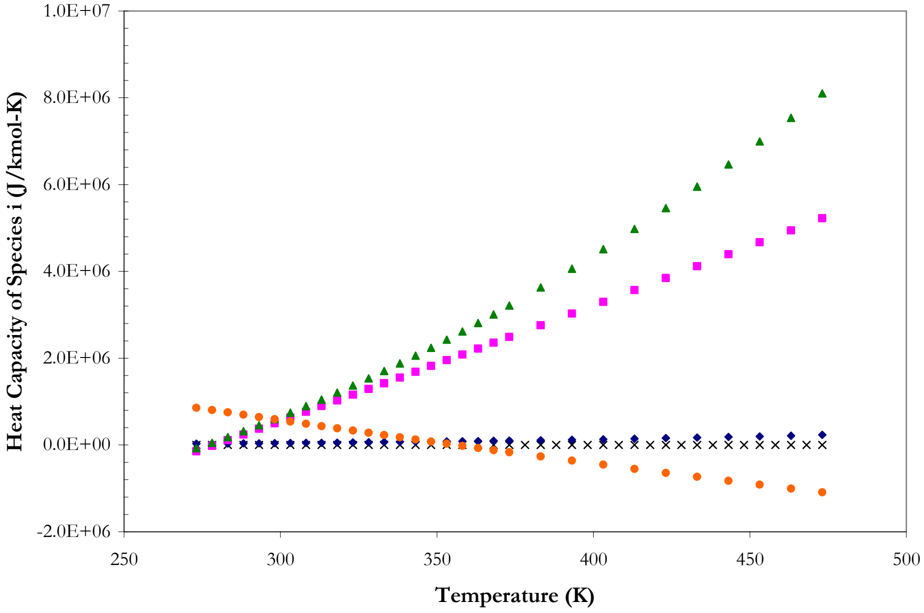

Figure 14.5-39. Molar Infinite Dilution Aqueous Phase Heat Capacity for Ionic, Molecular Solute, and Molecular Species in the H_2O-PZ-CO_2 System. Points: ♦, PZH^{+1}, ■, $PZCOO^{-1}$, ▲, $PZ(COO^{-1})_2$, ●, H^+PZCOO_{-1}, ×, PZ.

Figure 14.5-40 separates the molar heat capacity for 2 m PZ at a loading of 0.16 into weighted molar heat capacity of each contributing species with respect to the components reference state (i.e. Solvents: pure liquid, Ionic and Molecular Solutes: infinite dilution in water). By describing the molar heat capacity of the solution by the following equation:

$$\begin{aligned} C_p = {} & x_{H_2O} C_p^{*,l} + x_{PZ} C_p^{*,l} + x_{CO_2} C_p^{\infty,aq} + x_{CO_3^{-2}} C_p^{\infty,aq} + x_{HCO_3^{-1}} C_p^{\infty,aq} \\ & + x_{PZH^{+1}} C_p^{\infty,aq} + x_{PZCOO^{-1}} C_p^{\infty,aq} + x_{PZ\left(COO^{-1}\right)_2} C_p^{\infty,aq} + x_{H^+PZCOO^{-1}} C_p^{\infty,aq} + C_p^{Ex} \end{aligned} \qquad \text{14-53}$$

deviations between the molar heat capacity of the solution from the ideal molar heat capacity are accounted for by the excess molar heat capacity. The excess molar heat capacity also accounts for the heat of reaction associated with any change in speciation with temperature.

To investigate the effect of CO_2 loading on the liquid phase specific heat capacity, we can transform the specific heat capacity into an apparent heat capacity in terms of the mass of H_2O plus PZ in the experimental solution as shown in Figure 14.5-41.

Figure 14.5-41 illustrates how the experimental apparent heat capacity collapses into a surface, suggesting that contributions of the apparent heat capacity of apparent CO_2 species may be considered small with a magnitude less than 2 kJ/kmol-K due to the heat capacities of the piperazine carbamate and hydrated piperazine are approximately equal over a given temperature interval.

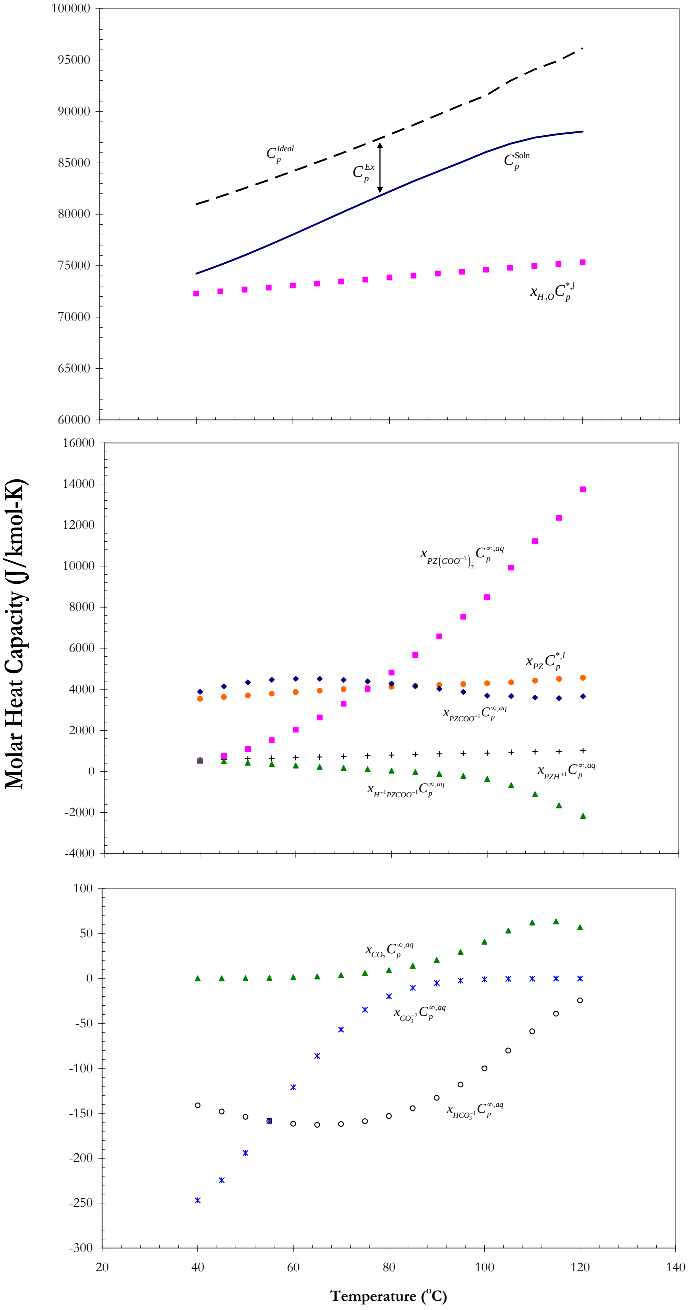

Figure 14.5-40. Comparison of the Molar Heat Capacity for 2 m PZ at a loading = 0.16 mol CO_2/2·mol PZ from this work to the Ideal Molar Heat Capacity based on the Constituent Components.

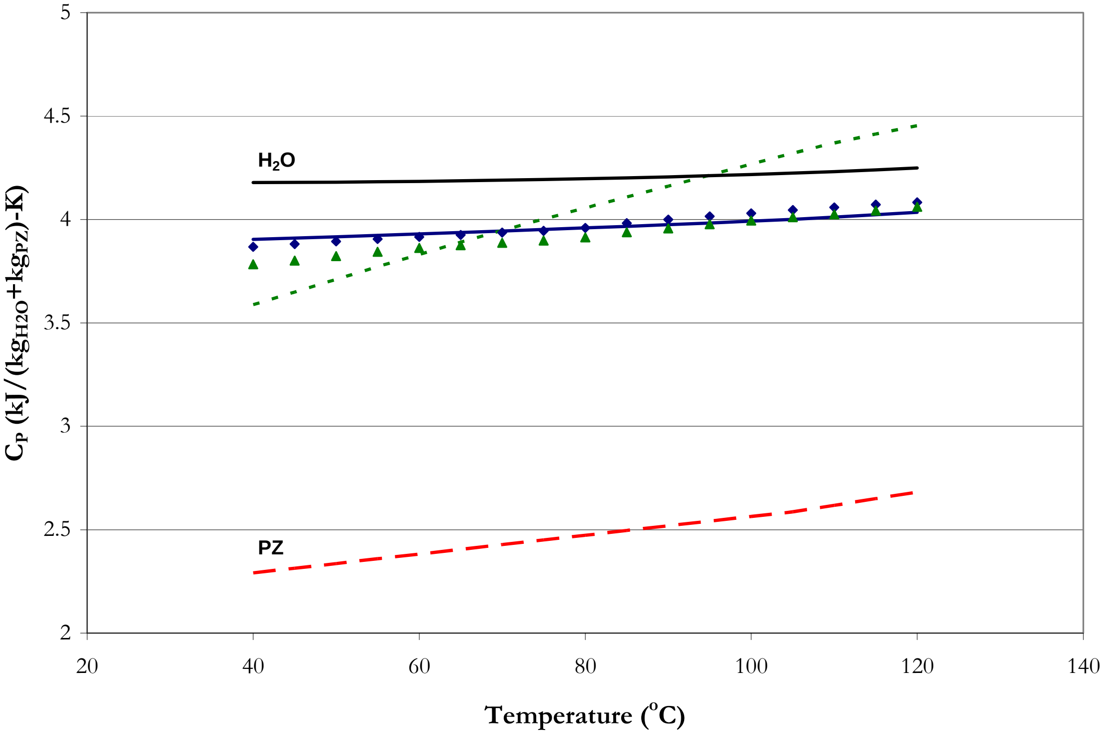

Figure 14.5-41. Comparison of the Experimental "Partial" Specific Heat Capacity for 2 m PZ to Predictions from the elecNRTL Model. Points: ♦, Ldg = 0.0, ▲, Ldg = 0.38. Lines: ▬, Ldg = 0.0, - - - , Ldg = 0.38, ▬, C_P (H_2O), — —, C_P (PZ).

14.5.4 *Liquid Phase Speciation*

Figure 14.5-42 through Figure 14.5-71 compare experimental liquid phase NMR speciation measurements from Ermatchkov et al. (2003) to predictions from Hilliard (2005) model and to this work. NMR speciation predictions from Hilliard (2005) were based on the regression of predictions for the "true" component speciation as predicted by the Cullinane (2005) model. In the Cullinane (2005) model, NMR speciation from Ermatchkov et al. (2003) was regressed based on a stand-alone rigorous thermodynamic equilibrium/rate model utilizing the Electrolyte NRTL model. The Fortran code was first created by Austgen (1989) for the amine-water systems and then later modified by Bishnoi (2000).

Model predictions from Hilliard (2005) adequately predict the liquid phase NMR speciation for 1.0 and 1.5 m PZ, but as previously shown, the Hilliard (2005) model does not adequately predict the piperazine volatility. Even though amine volatility is a concentration based measurement and NMR speciation allows the researcher to take a glimpse at the pseudo-component concentrations, when all of the data is poured into the electrolyte NRTL model, both pieces of information are affecting the adjustment of the activity coefficient of PZ.

In this work we were able to adequately predict the CO_2 solubility, amine volatility, enthalpy of CO_2 absorption and to some extent the liquid phase specific heat capacity, we feel that we have compiled an extensive database that gives a more realistic prediction for the liquid phase speciation. In this work, the full model was able to adequately predict the liquid phase NMR speciation for 1.0 and 1.5 m PZ mixtures within an average relative error of ± 5.69 percent.

Figure 14.5-72 through Figure 14.5-75 illustrate model predictions for liquid phase speciation and activity coefficient behavior in 5 m PZ at 40 ^{o}C. Since this concentration is outside the range of the regressed NMR speciation data reported from Ermatchkov et al. (2003); predictions are presented to illustrate possible trends associated with the solvent and should be treated with caution.

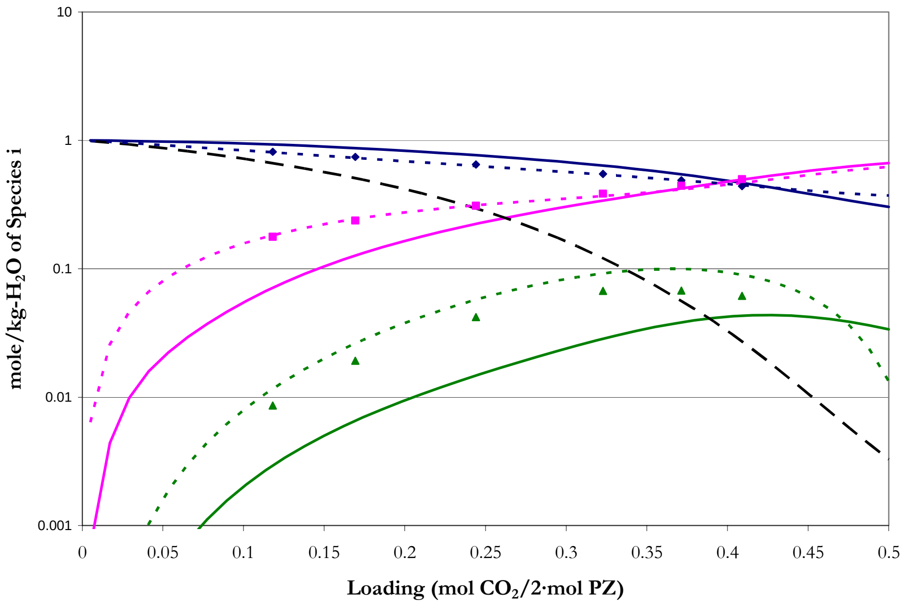

Figure 14.5-42. Comparison of Liquid Phase NMR Speciation in 1.0 m PZ at 25 °C to Model Predictions. Points: ♦, PZ+PZH^{+1}, ■, PZCOO^{-1}+H$^+$PZCOO^{-1}, ▲, PZ(COO^{-1})$_2$ from Ermatchkov et al. (2003). Lines: - - -, Hilliard (2005), ▬, this work, — —, Conc. Free PZ.

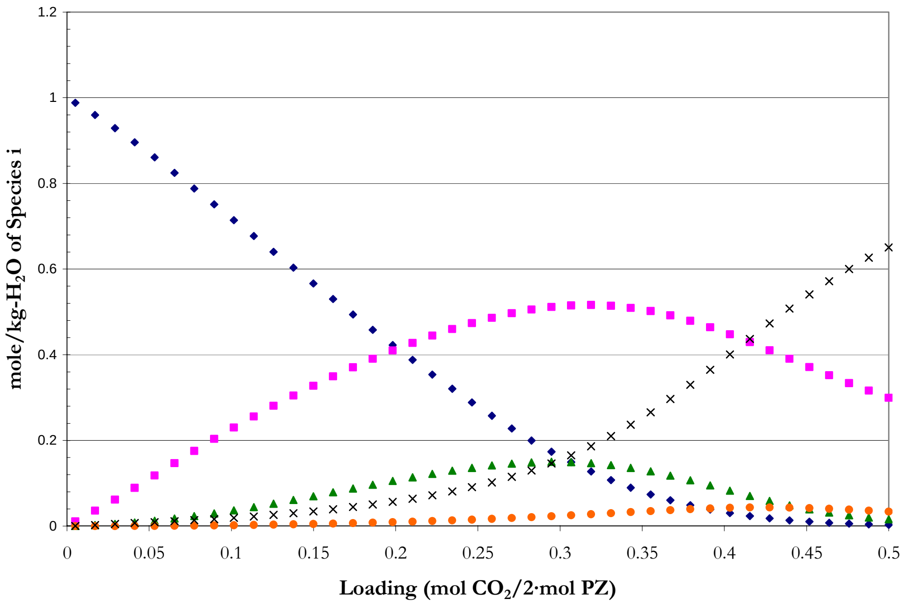

Figure 14.5-43. Predictions for the Liquid Phase Speciation in 1.0 m PZ at 25 °C from this work. Points: ♦, PZ, ■, PZH^{+1}, ▲, PZCOO^{-1}, ●, PZ(COO^{-1})$_2$, ×, H$^+$PZCOO^{-1}.

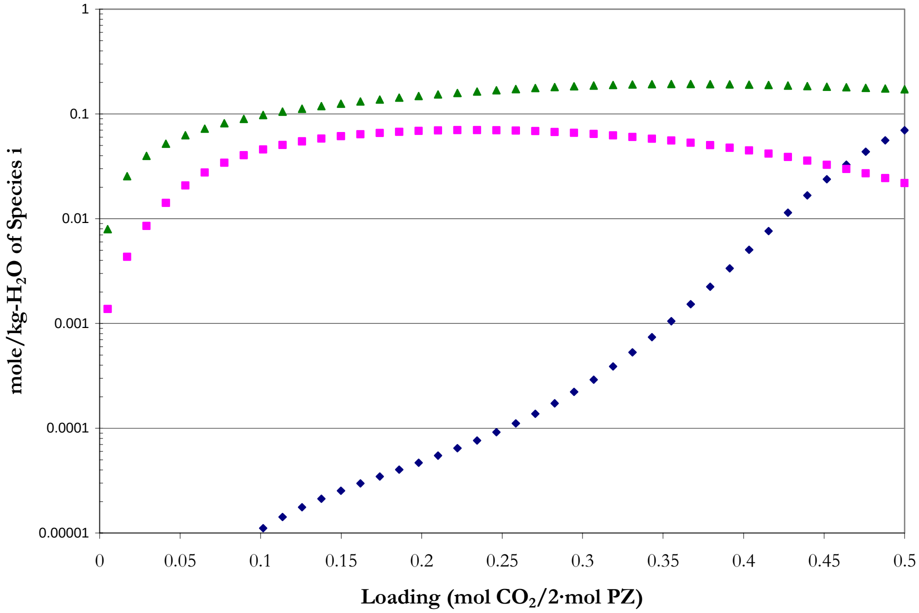

Figure 14.5-44. Predictions for the Liquid Phase Speciation in 1.0 m PZ at 25 °C from this work. Points: ♦, CO_2, ■, CO_3^{-2}, ▲, HCO_3^{-1}.

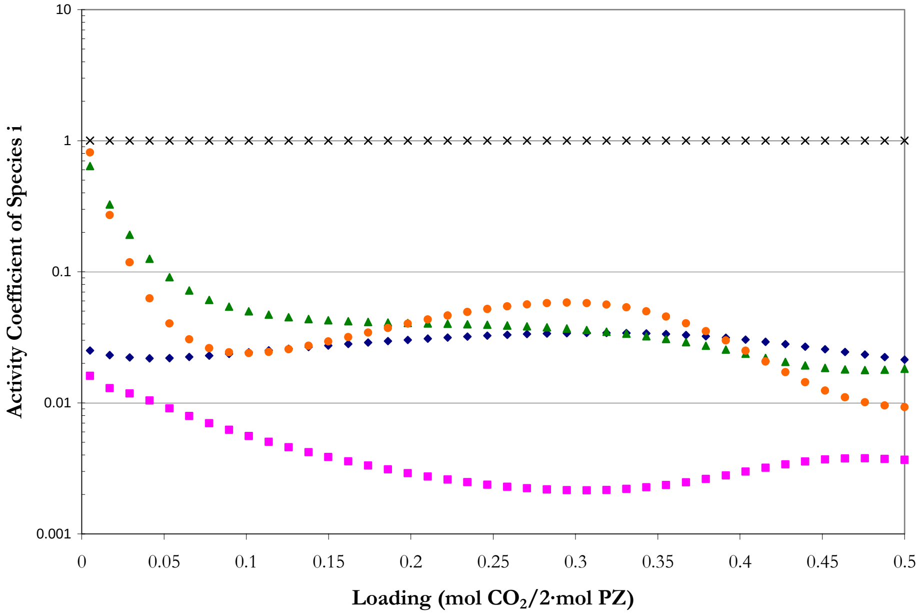

Figure 14.5-45. Predictions for the Liquid Phase Activity Coefficients in 1.0 m PZ at 25 °C from this work. Points: ♦, PZ, ■, PZH^{+1}, ▲, $PZCOO^{-1}$, ●, $PZ(COO^{-1})_2$, ×, H^+PZCOO^{-1}.

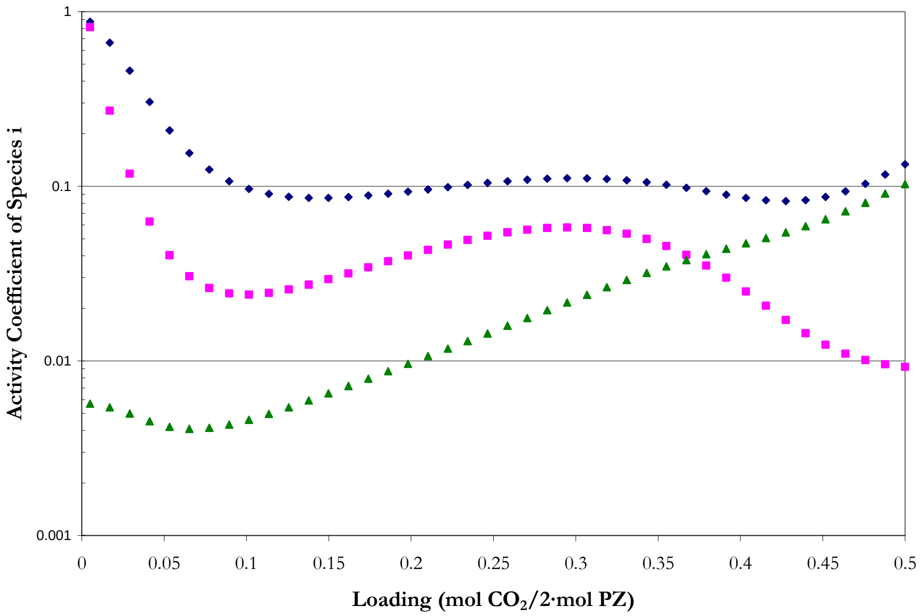

Figure 14.5-46. Predictions for the Liquid Phase Activity Coefficients in 1.0 m PZ at 25 °C from this work. Points: ♦, CO_2, ■, CO_3^{-2}, ▲, HCO_3^{-1}.

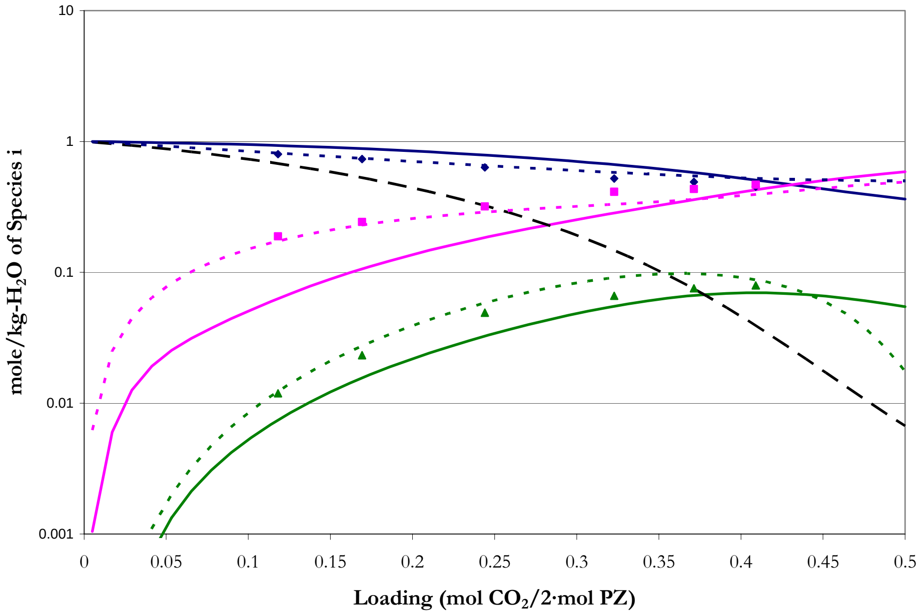

Figure 14.5-47. Comparison of Liquid Phase NMR Speciation in 1.0 m PZ at 40 °C to Model Predictions. Points: ♦, PZ+PZH^{+1}, ■, $PZCOO^{-1}$+H^+PZCOO^{-1}, ▲, $PZ(COO^{-1})_2$ from Ermatchkov et al. (2003). Lines: - - -, Hilliard (2005), ▬, this work, — —, Conc. Free PZ.

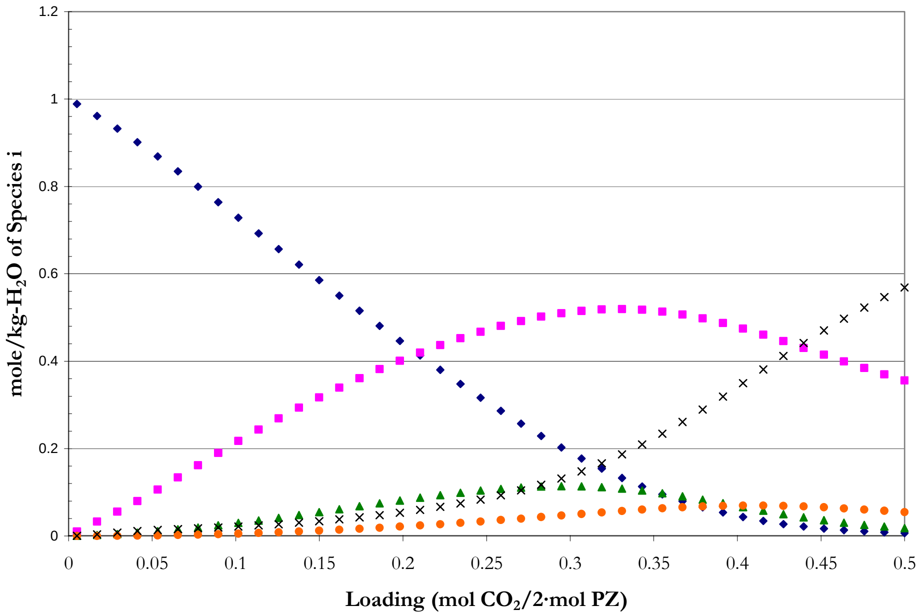

Figure 14.5-48. Predictions for the Liquid Phase Speciation in 1.0 m PZ at 40 °C from this work. Points: ♦, PZ, ■, PZH^{+1}, ▲, $PZCOO^{-1}$, ●, $PZ(COO^{-1})_2$, ×, H^+PZCOO^{-1}.

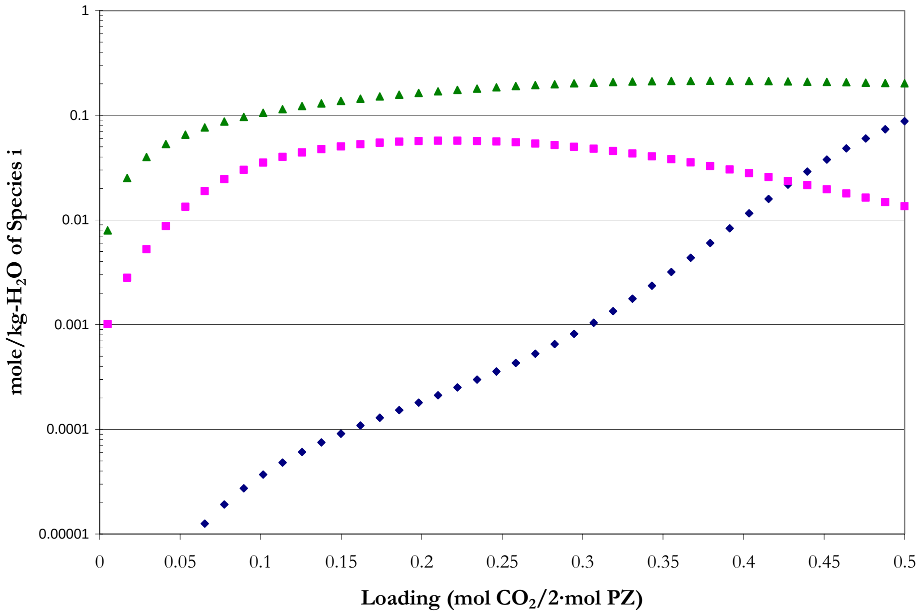

Figure 14.5-49. Predictions for the Liquid Phase Speciation in 1.0 m PZ at 40 °C from this work. Points: ♦, CO_2, ■, CO_3^{-2}, ▲, HCO_3^{-1}.

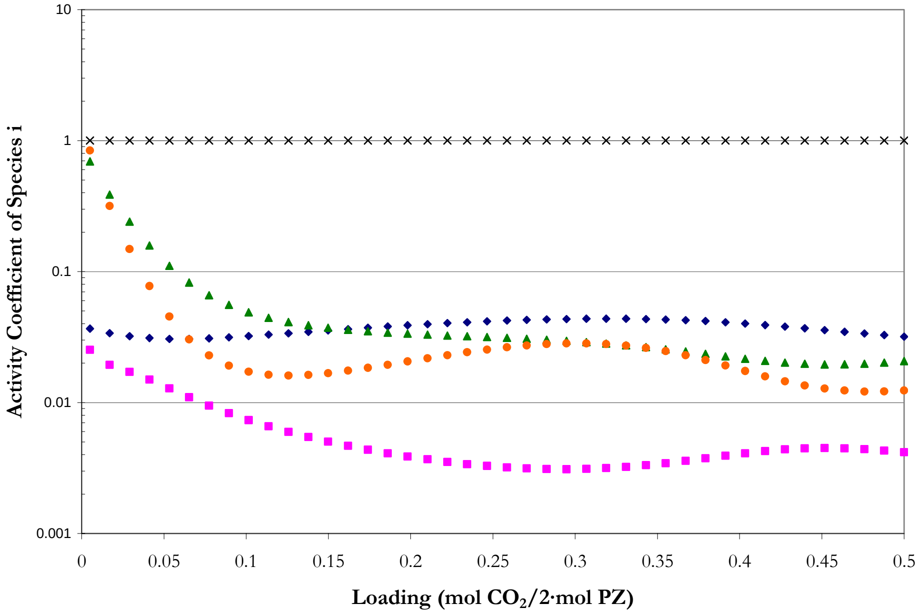

Figure 14.5-50. Predictions for the Liquid Phase Activity Coefficients in 1.0 m PZ at 40 °C from this work. Points: ◆, PZ, ■, PZH^{+1}, ▲, PZCOO^{-1}, ●, PZ(COO^{-1})$_2$, ×, H$^+$PZCOO^{-1}.

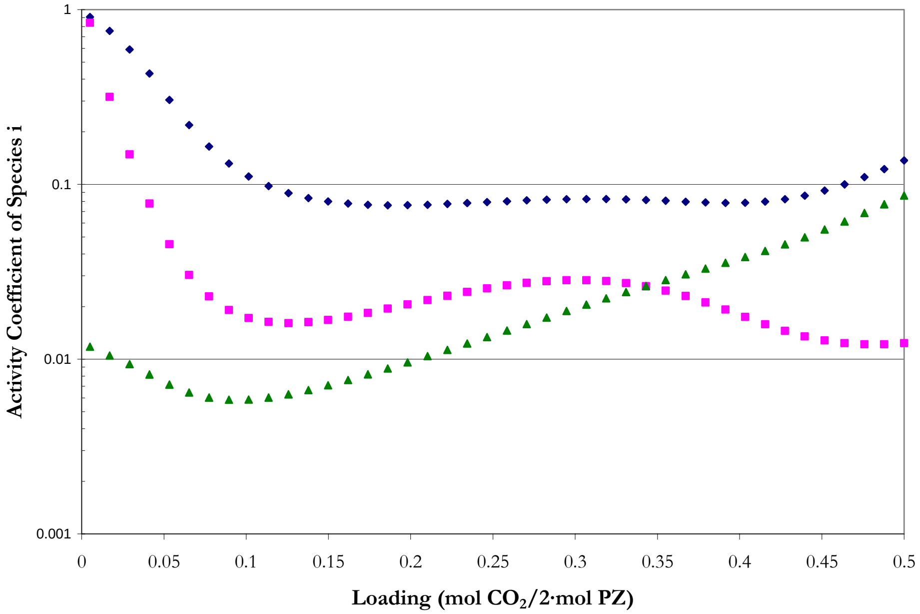

Figure 14.5-51. Predictions for the Liquid Phase Activity Coefficients in 1.0 m PZ at 40 °C from this work. Points: ◆, CO$_2$, ■, CO$_3^{-2}$, ▲, HCO$_3^{-1}$.

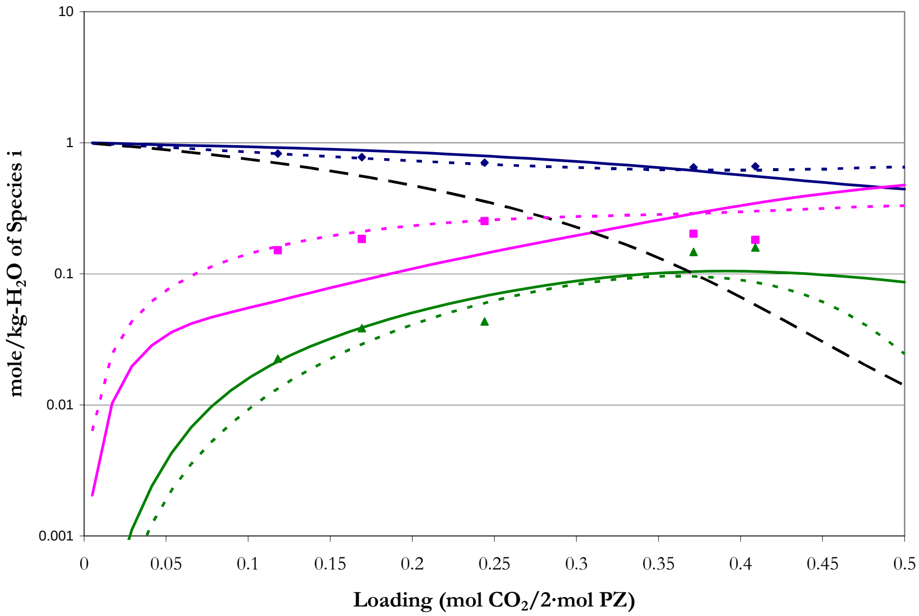

Figure 14.5-52. Comparison of Liquid Phase NMR Speciation in 1.0 m PZ at 60 °C to Model Predictions. Points: ♦, PZ+PZH^{+1}, ■, $PZCOO^{-1}$+$H^{+}PZCOO^{-1}$, ▲, $PZ(COO^{-1})_2$ from Ermatchkov et al. (2003). Lines: - - -, Hilliard (2005), ▬, this work, — —, Conc. Free PZ.

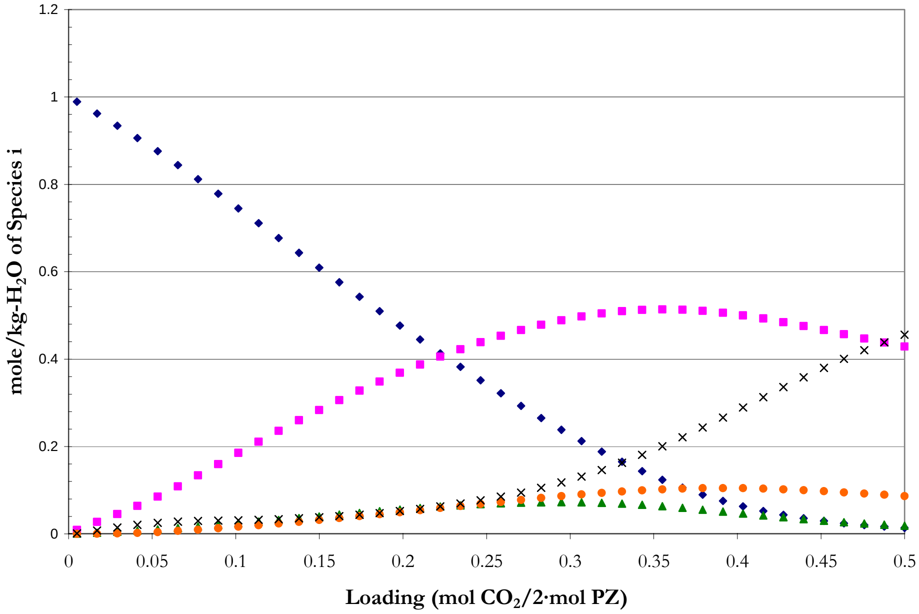

Figure 14.5-53. Predictions for the Liquid Phase Speciation in 1.0 m PZ at 60 °C from this work. Points: ♦, PZ, ■, PZH^{+1}, ▲, $PZCOO^{-1}$, ●, $PZ(COO^{-1})_2$, ×, $H^{+}PZCOO^{-1}$.

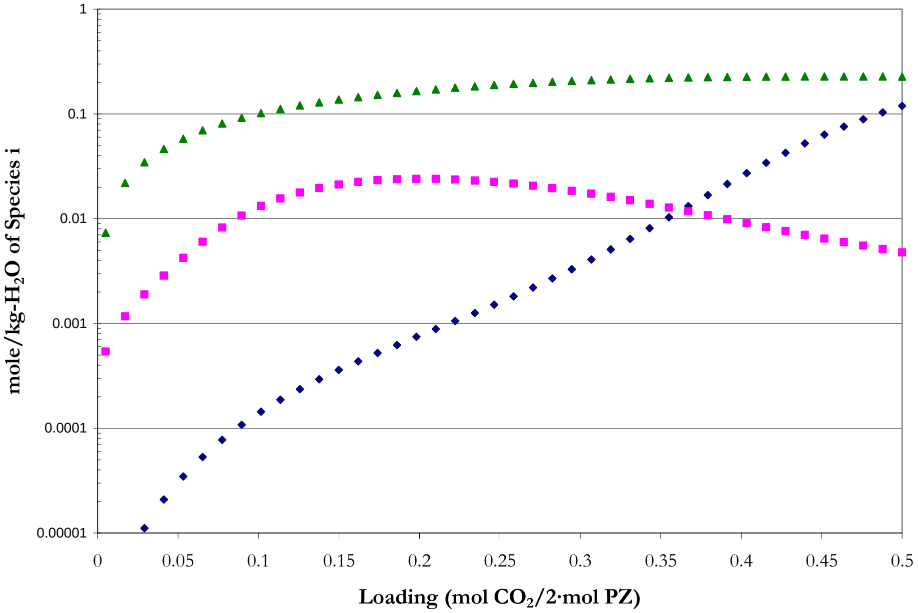

Figure 14.5-54. Predictions for the Liquid Phase Speciation in 1.0 m PZ at 60 °C from this work. Points: ♦, CO_2, ■, CO_3^{-2}, ▲, HCO_3^{-1}.

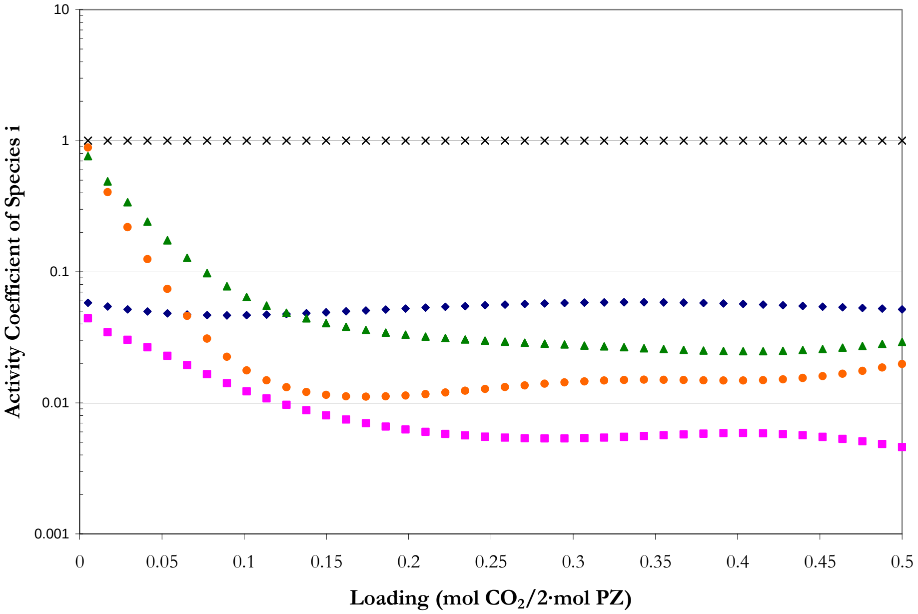

Figure 14.5-55. Predictions for the Liquid Phase Activity Coefficients in 1.0 m PZ at 60 °C from this work. Points: ♦, PZ, ■, PZH^{+1}, ▲, $PZCOO^{-1}$, ●, $PZ(COO^{-1})_2$, ×, H^+PZCOO^{-1}.

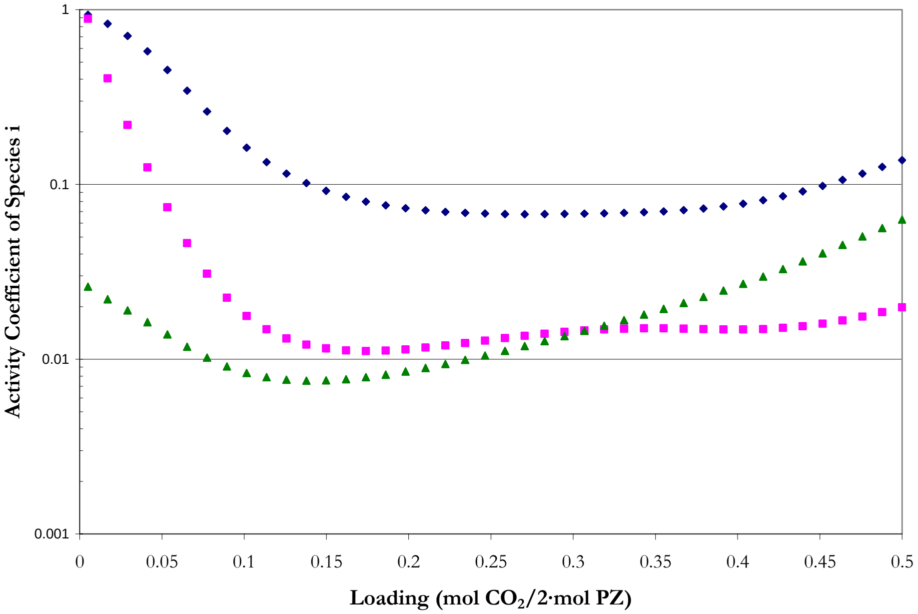

Figure 14.5-56. Predictions for the Liquid Phase Activity Coefficients in 1.0 m PZ at 60 °C from this work. Points: ♦, CO_2, ■, CO_3^{-2}, ▲, HCO_3^{-1}.

Liquid Phase Speciation for 1.5 m PZ

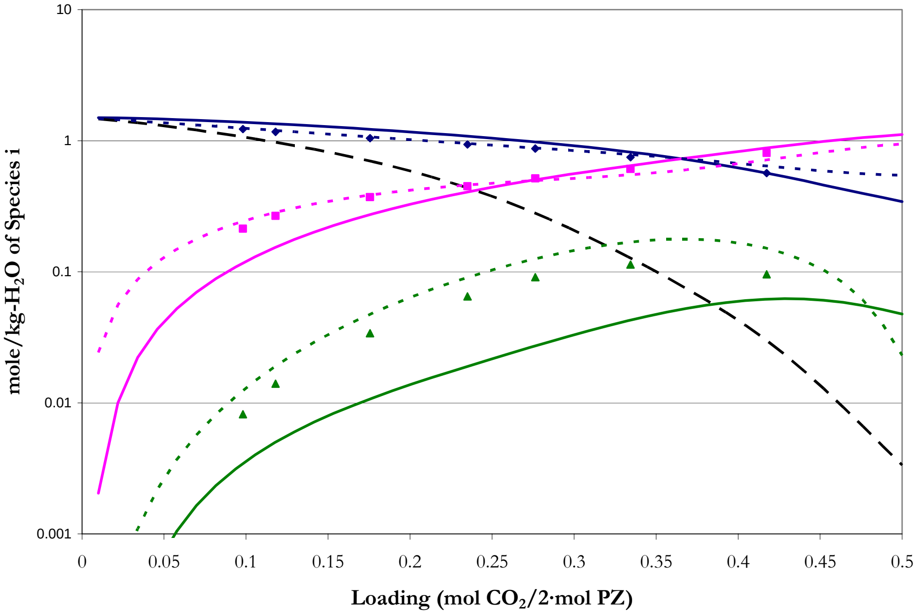

Figure 14.5-57. Comparison of Liquid Phase NMR Speciation in 1.5 m PZ at 25 °C to Model Predictions. Points: ♦, PZ+PZH^{+1}, ■, $PZCOO^{-1}$+H^+PZCOO^{-1}, ▲, $PZ(COO^{-1})_2$ from Ermatchkov et al. (2003). Lines: - - -, Hilliard (2005), ▬, this work, — —, Conc. Free PZ.

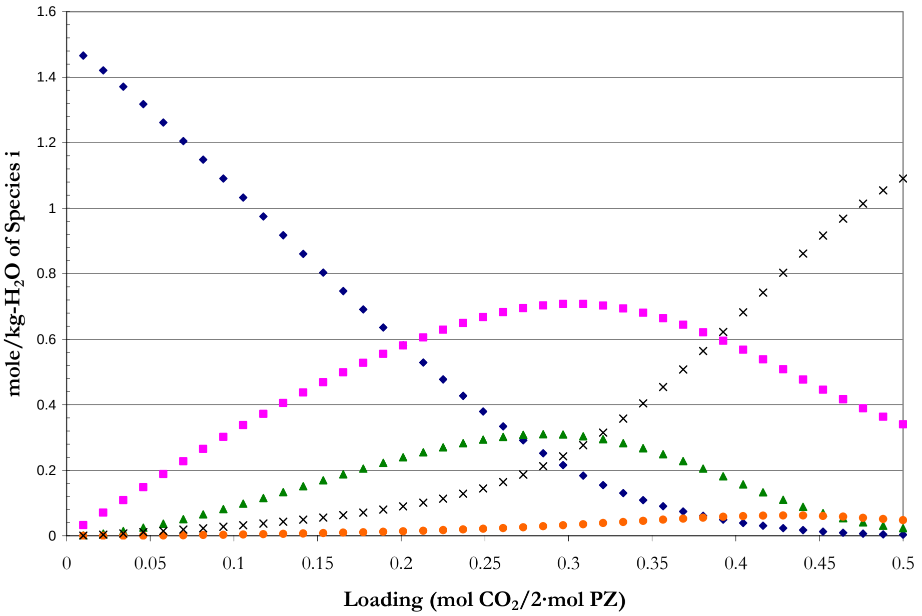

Figure 14.5-58. Predictions for the Liquid Phase Speciation in 1.5 m PZ at 25 °C from this work. Points: ♦, PZ, ■, PZH^{+1}, ▲, $PZCOO^{-1}$, ●, $PZ(COO^{-1})_2$, ×, H^+PZCOO^{-1}.

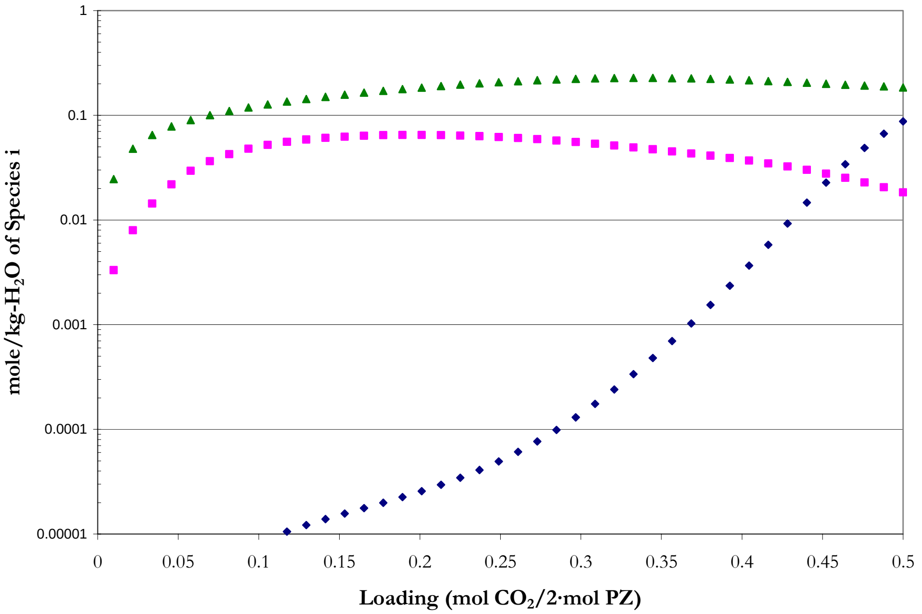

Figure 14.5-59. Predictions for the Liquid Phase Speciation in 1.5 m PZ at 25 °C from this work. Points: ♦, CO_2, ■, CO_3^{-2}, ▲, HCO_3^{-1}.

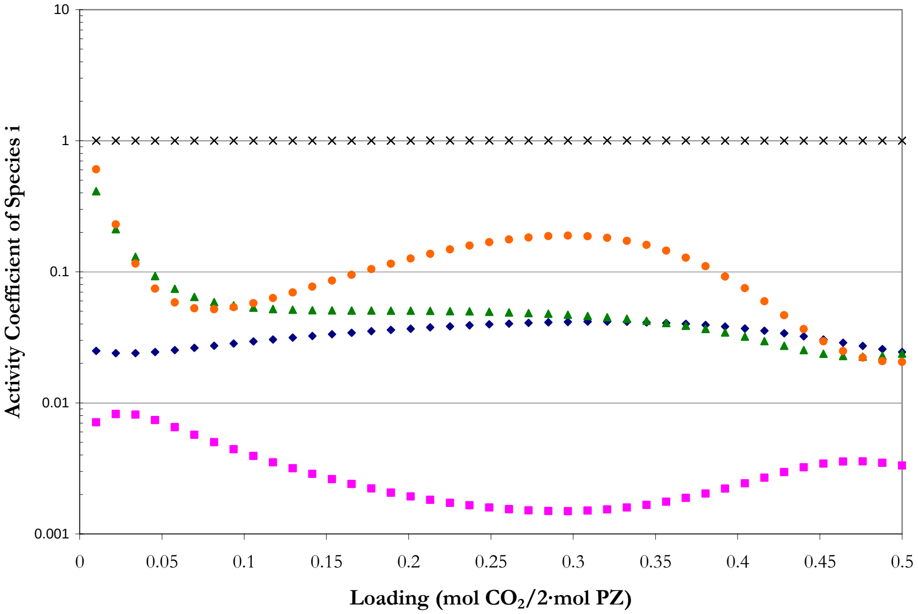

Figure 14.5-60. Predictions for the Liquid Phase Activity Coefficients in 1.5 m PZ at 25 °C from this work. Points: ♦, PZ, ■, PZH^{+1}, ▲, $PZCOO^{-1}$, ●, $PZ(COO^{-1})_2$, ×, H^+PZCOO^{-1}.

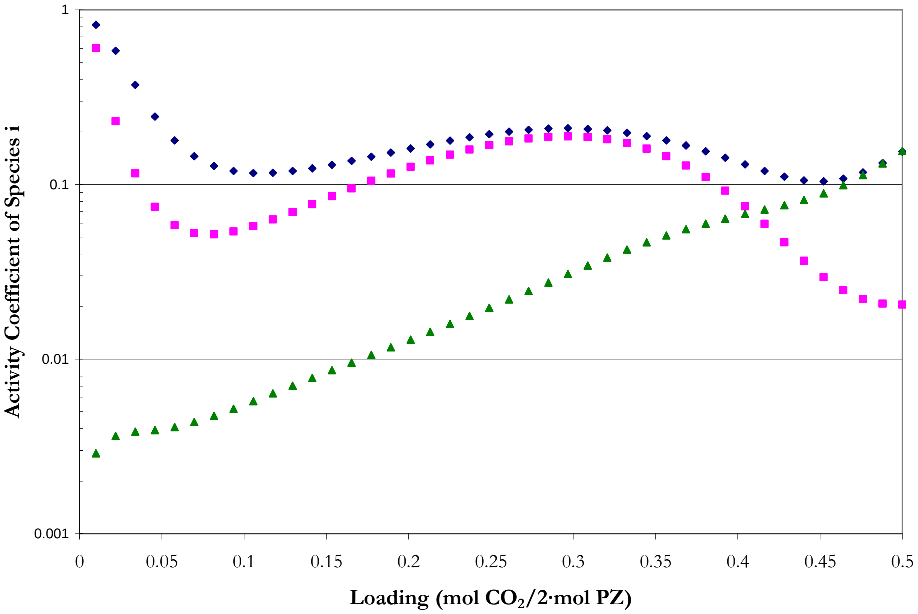

Figure 14.5-61. Predictions for the Liquid Phase Activity Coefficients in 1.5 m PZ at 25 °C from this work. Points: ♦, CO_2, ■, CO_3^{-2}, ▲, HCO_3^{-1}.

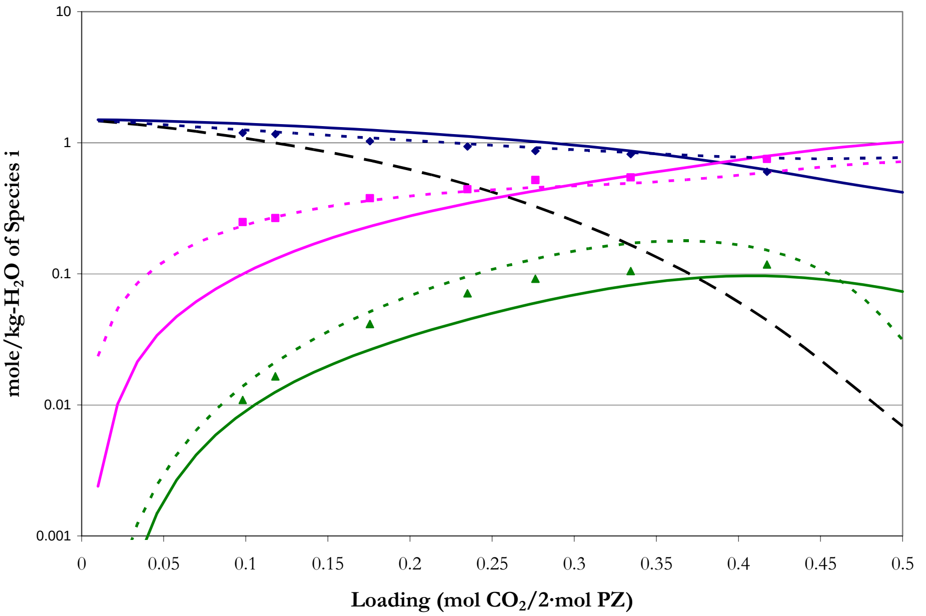

Figure 14.5-62. Comparison of Liquid Phase NMR Speciation in 1.5 m PZ at 40 °C to Model Predictions. Points: ♦, PZ+PZH^{+1}, ■, PZCOO^{-1}+H^{+}PZCOO^{-1}, ▲, PZ(COO^{-1})$_2$ from Ermatchkov et al. (2003). Lines: - - -, Hilliard (2005), ▬, this work, — —, Conc. Free PZ.

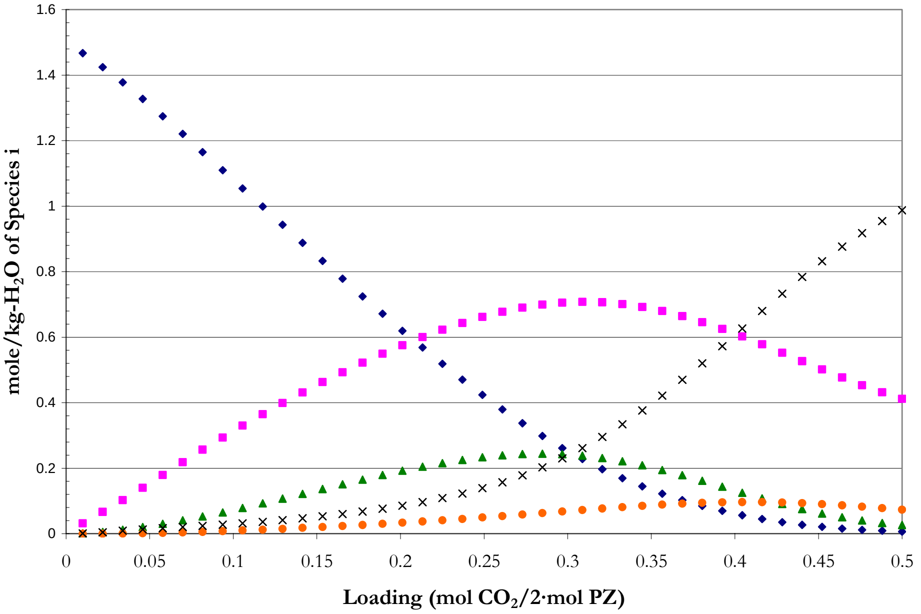

Figure 14.5-63. Predictions for the Liquid Phase Speciation in 1.5 m PZ at 40 °C from this work. Points: ♦, PZ, ■, PZH^{+1}, ▲, PZCOO^{-1}, ●, PZ(COO^{-1})$_2$, ×, H^{+}PZCOO^{-1}.

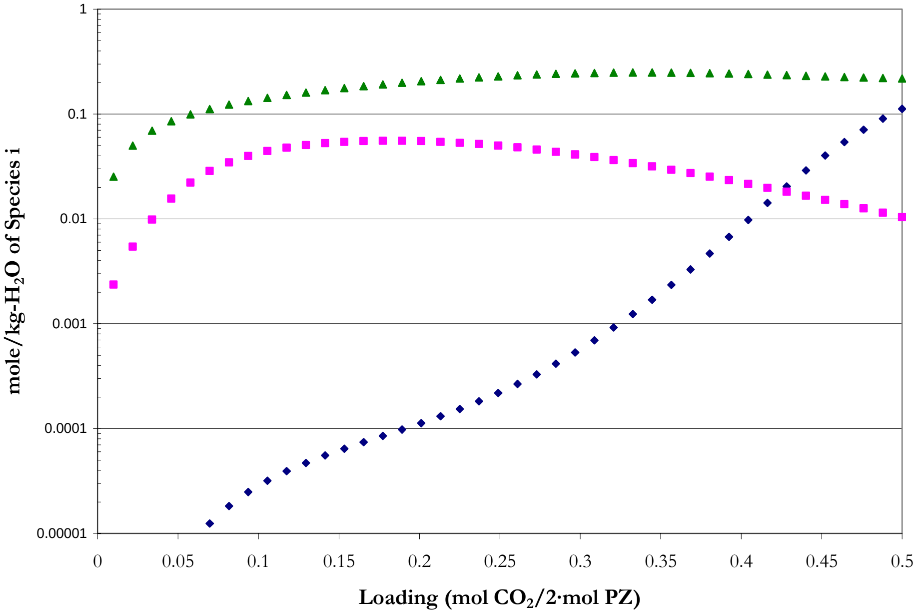

Figure 14.5-64. Predictions for the Liquid Phase Speciation in 1.5 m PZ at 40 °C from this work. Points: ♦, CO_2, ■, CO_3^{-2}, ▲, HCO_3^{-1}.

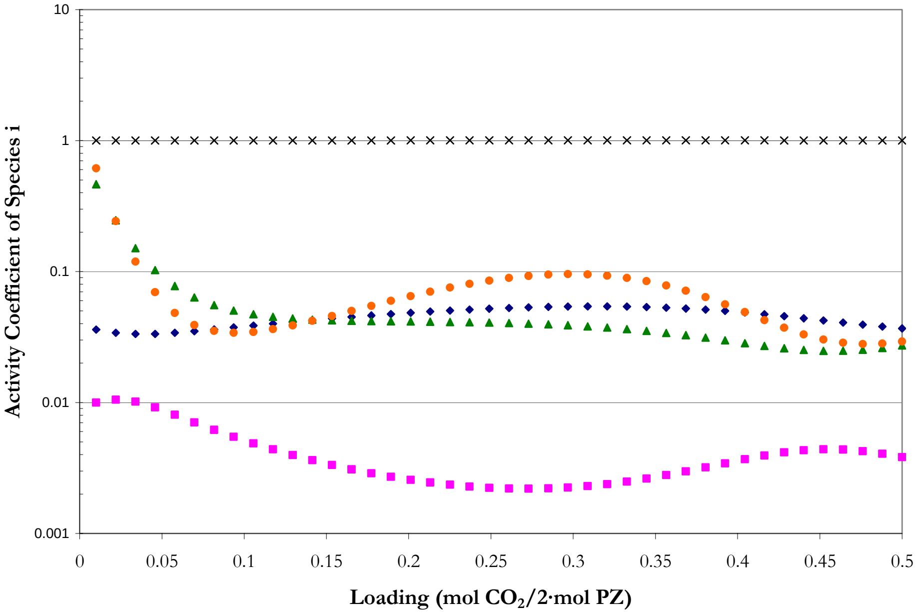

Figure 14.5-65. Predictions for the Liquid Phase Activity Coefficients in 1.5 m PZ at 40 °C from this work. Points: ♦, PZ, ■, PZH^{+1}, ▲, $PZCOO^{-1}$, ●, $PZ(COO^{-1})_2$, ×, H^+PZCOO^{-1}.

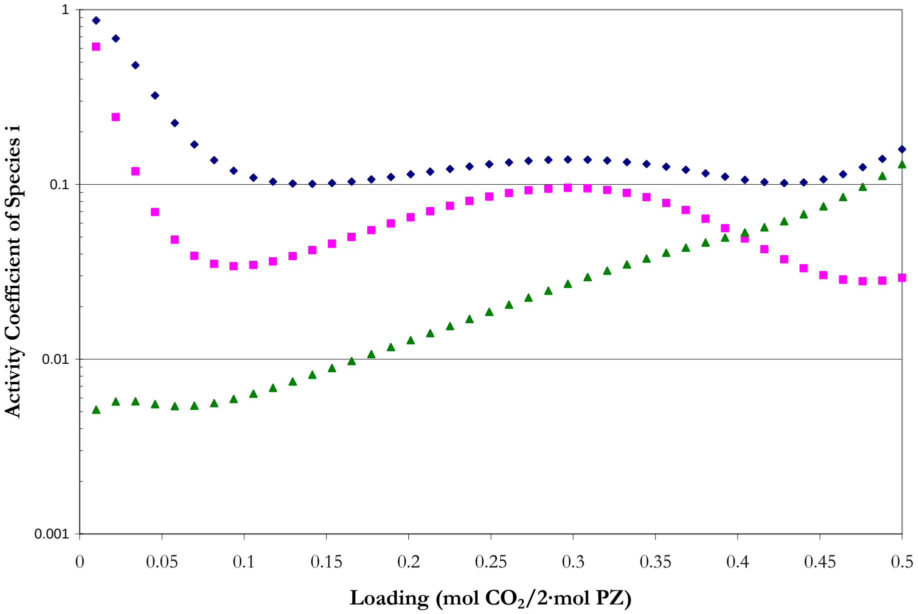

Figure 14.5-66. Predictions for the Liquid Phase Activity Coefficients in 1.5 m PZ at 40 °C from this work. Points: ♦, CO_2, ■, CO_3^{-2}, ▲, HCO_3^{-1}.

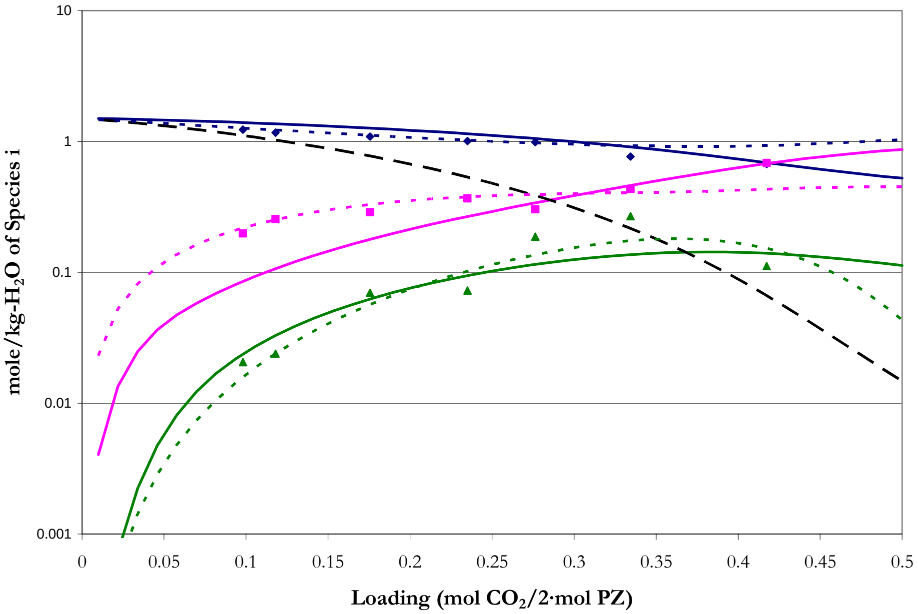

Figure 14.5-67. Comparison of Liquid Phase NMR Speciation in 1.5 m PZ at 60 °C to Model Predictions. Points: ♦, $PZ+PZH^{+1}$, ■, $PZCOO^{-1}+H^{+}PZCOO^{-1}$, ▲, $PZ(COO^{-1})_2$ from Ermatchkov et al. (2003). Lines: - - -, Hilliard (2005), ▬, this work, — —, Conc. Free PZ.

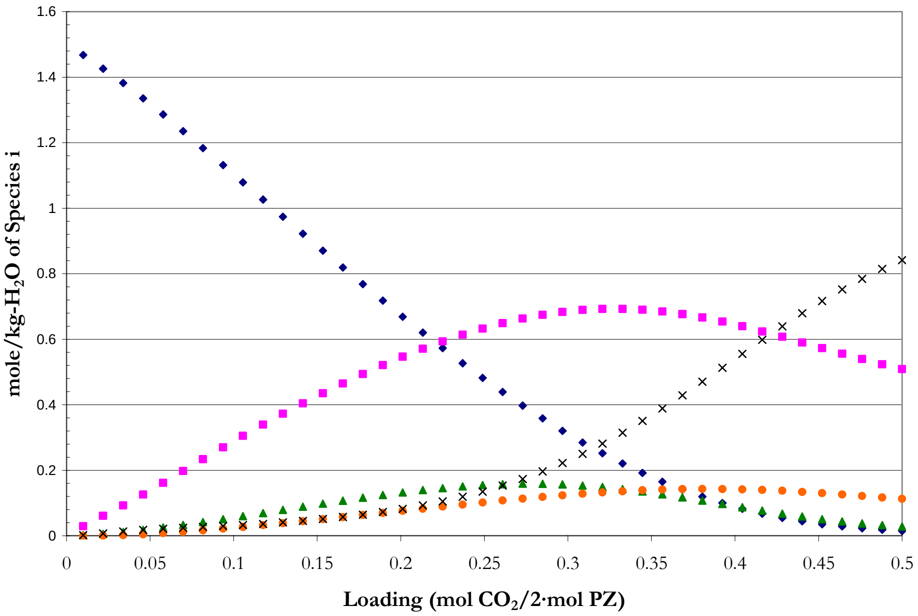

Figure 14.5-68. Predictions for the Liquid Phase Speciation in 1.5 m PZ at 60 °C from this work. Points: ♦, PZ, ■, PZH^{+1}, ▲, $PZCOO^{-1}$, ●, $PZ(COO^{-1})_2$, ×, H^+PZCOO^{-1}.

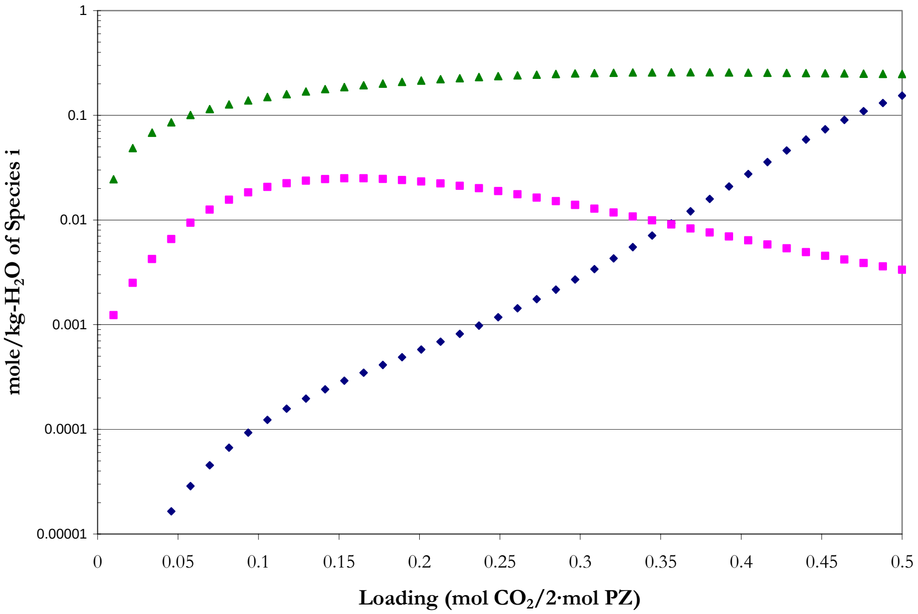

Figure 14.5-69. Predictions for the Liquid Phase Speciation in 1.5 m PZ at 60 °C from this work. Points: ♦, CO_2, ■, CO_3^{-2}, ▲, HCO_3^{-1}.

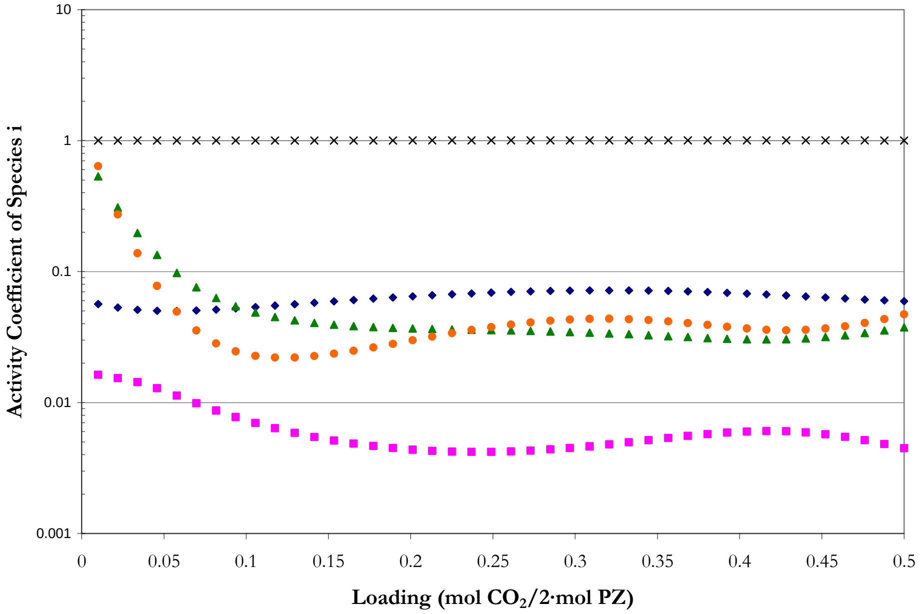

Figure 14.5-70. Predictions for the Liquid Phase Activity Coefficients in 1.5 m PZ at 60 °C from this work. Points: ♦, PZ, ■, PZH^{+1}, ▲, $PZCOO^{-1}$, ●, $PZ(COO^{-1})_2$, ×, H^+PZCOO^{-1}.

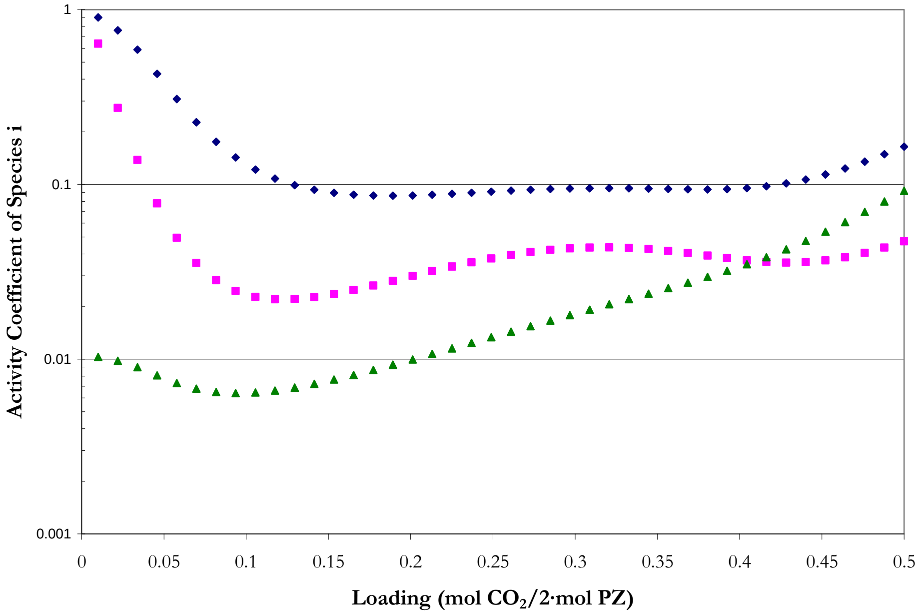

Figure 14.5-71. Predictions for the Liquid Phase Activity Coefficients in 1.5 m PZ at 60 °C from this work. Points: ♦, CO_2, ■, CO_3^{-2}, ▲, HCO_3^{-1}.

Liquid Phase Speciation for 5 m PZ

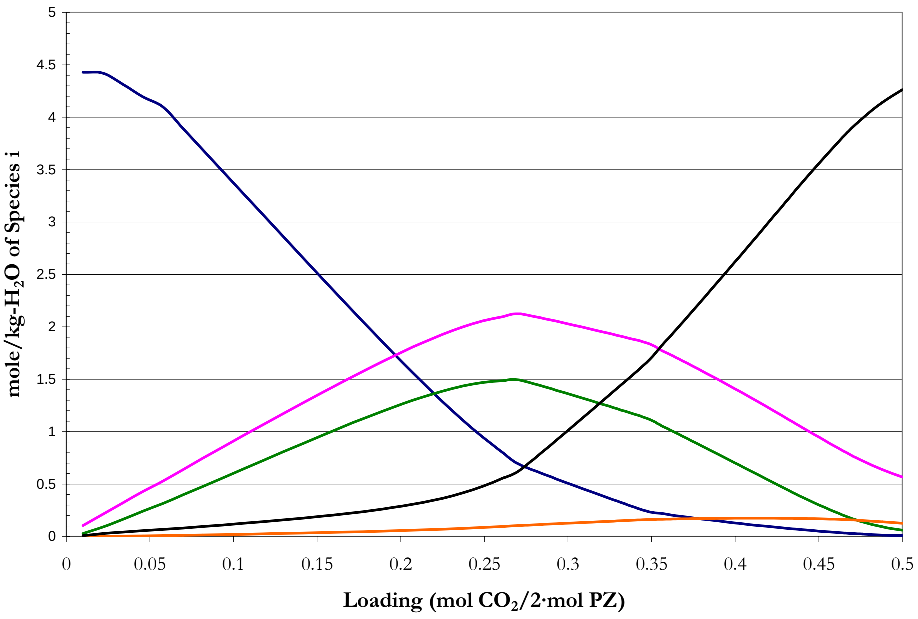

Figure 14.5-72. Predictions for the Liquid Phase Speciation in 5 m PZ at 40 °C from this work. Lines: ▬, PZ, ▬, PZH^{+1}, ▬, $PZCOO^{-1}$, ▬, $PZ(COO^{-1})_2$, ▬, H^+PZCOO^{-1}.

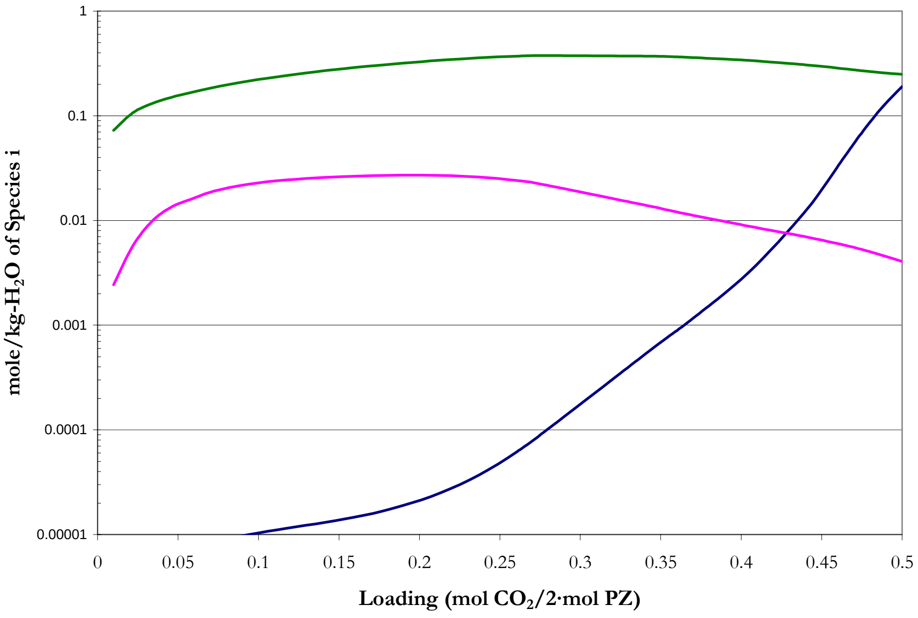

Figure 14.5-73. Predictions for the Liquid Phase Speciation in 5 m PZ at 40 °C from this work. Lines: ▬, CO_2, ▬, CO_3^{-2}, ▬, HCO_3^{-1}.

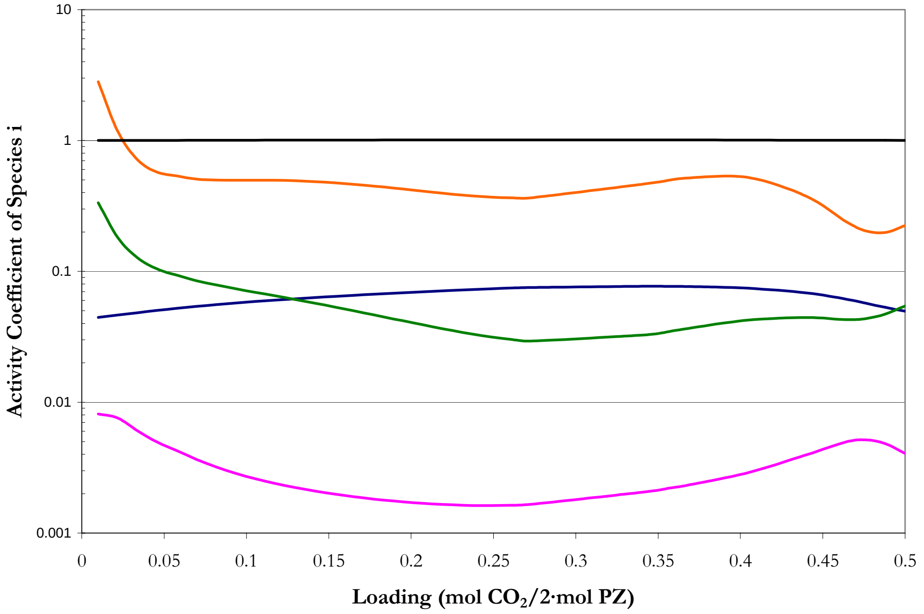

Figure 14.5-74. Predictions for the Liquid Phase Activity Coefficients in 5 m PZ at 40 °C from this work. Lines: ▬, PZ, ▬, PZH^{+1}, ▬, $PZCOO^{-1}$, ▬, $PZ(COO^{-1})_2$, ▬, H^+PZCOO^{-1}.

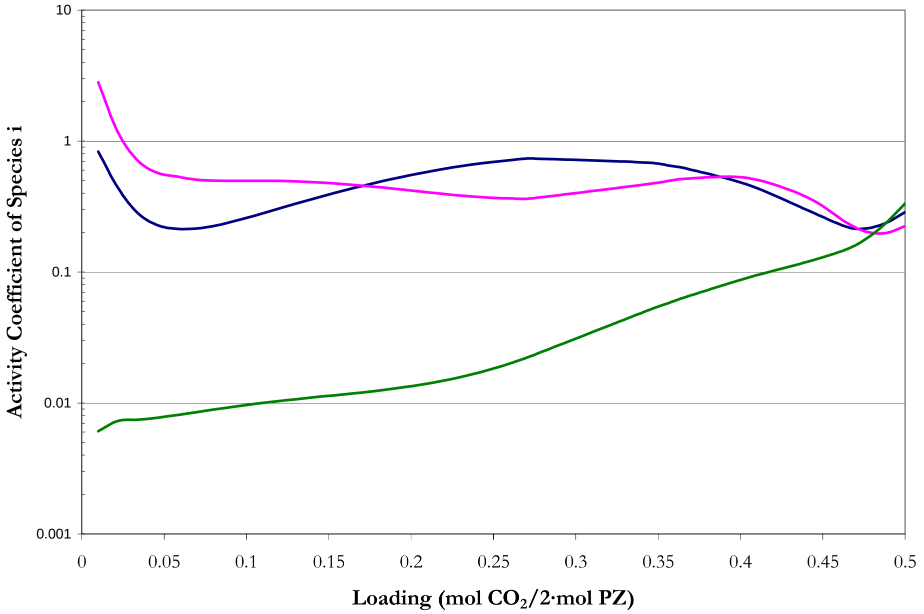

Figure 14.5-75. Predictions for the Liquid Phase Activity Coefficients in 5 m PZ at 40 °C from this work. Lines: ▬, CO_2, ▬, CO_3^{-2}, ▬, HCO_3^{-1}.

14.5.5 *Carbamate Stability Constant*

Using Equation 14-25 and estimates for the infinite dilution aqueous phase free energy of formation, the infinite dilution aqueous phase enthalpy of formation, and the infinite dilution aqueous phase heat capacity polynomial for piperazine carbamate, piperazine dicarbamate, and protonated piperazine carbamate, we can then analytically determine the chemical equilibrium constants as shown in Figure 14.5-76 through Figure 14.5-78 (molality infinite dilution in water basis), for the formation of $PZCOO^{-1}$, $PZ(COO^{-1})_2$, and H^+PZCOO^{-1} given by Equations 14-54 through 14-56. The chemical equilibrium constants for Equations 14-11, 14-12, and 14-13 are regressed into linear temperature dependent functions given in Table 14.5-4 on a mole fraction, infinite dilution in water basis.

Table 14.5-4. Chemical Equilibrium Coefficients for the H_2O-PZ-CO_2 System on a Mole Fraction, Infinite Dilution in Water Basis.

Equation #	A	σ_A	B	σ_B	C	σ_C	D	σ_D
14-11	1025	0.49	1606	13.9	-214	0.085	0.657	0.001
14-12	192	44.6	2029	1264	-44.7	7.69	0.200	0.012
14-13	668	1.96	3465	55.6	-156	0.338	0.594	0.001

$\ln K = A + B/T(K) + C \cdot \ln T(K) + D \cdot T(K)$

$$\mathrm{PZ} + CO_2 \leftrightarrow \mathrm{PZCOO}^{-1} + H^+ \qquad 14\text{-}54$$

$$\mathrm{PZCOO}^{-1} + CO_2 \leftrightarrow \mathrm{PZ}\left(\mathrm{COO}^{-1}\right)_2 + H^+ \qquad 14\text{-}55$$

$$H^+PZCOO^{-1} \leftrightarrow \mathrm{PZCOO}^{-1} + H^+ \qquad 14\text{-}56$$

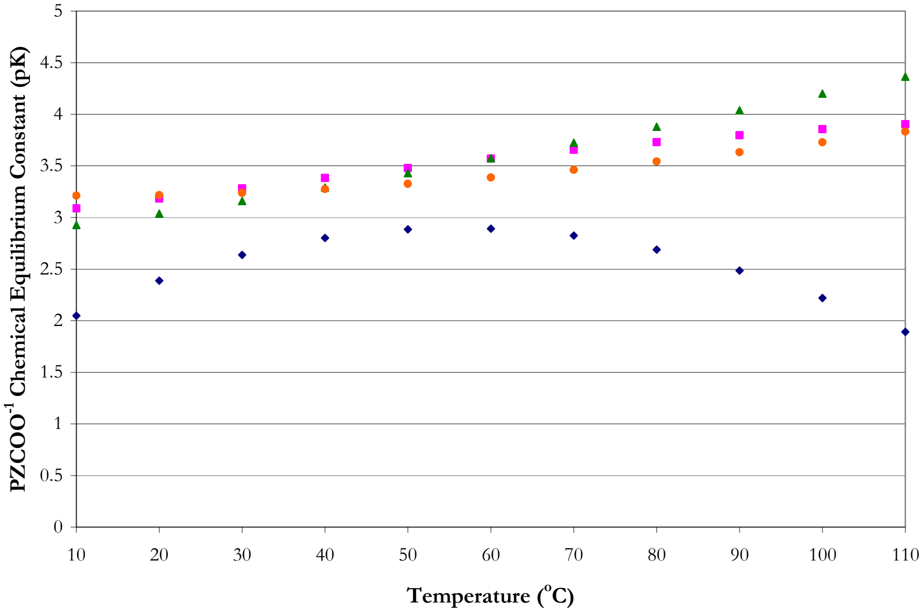

Figure 14.5-76. Comparison of the Chemical Equilibrium Constant of $PZCOO^{-1}$. Points: ●, Ermatchkov et al. (2003, ■, Cullinane (2005), ▲, Derks et al. (2005), ♦, this work.

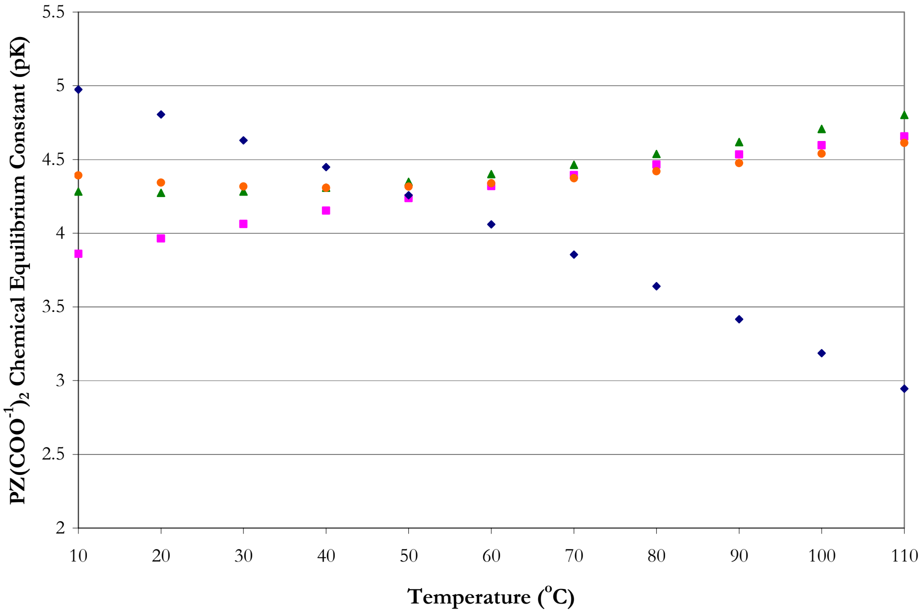

Figure 14.5-77. Comparison of the Chemical Equilibrium Constant of $PZ(COO^{-1})_2$. Points: ●, Ermatchkov et al. (2003, ■, Cullinane (2005), ▲, Derks et al. (2005), ♦, this work.

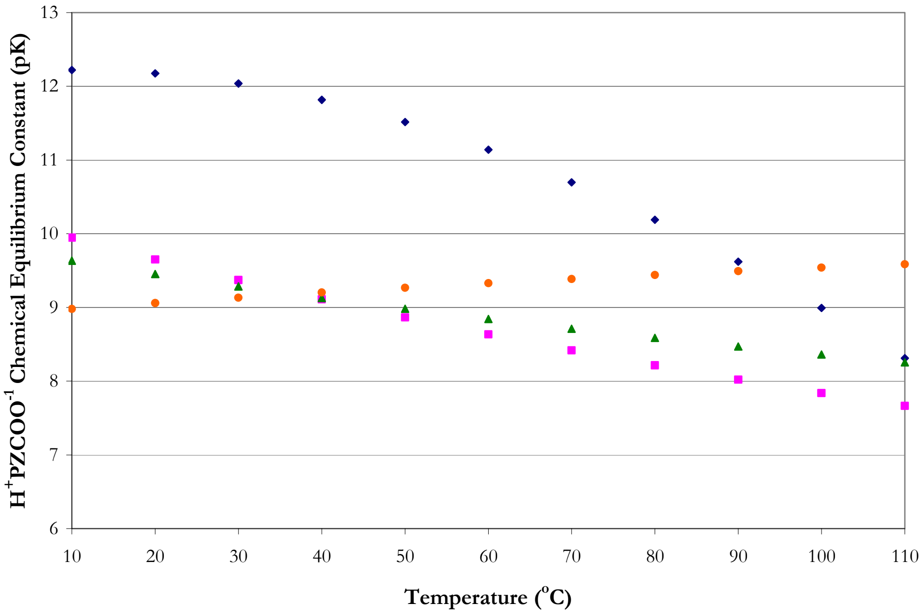

Figure 14.5-78. Comparison of the Chemical Equilibrium Constant of H^+PZCOO^{-1}. Points: ●, Ermatchkov et al. (2003), ■, Cullinane (2005), ▲, Derks et al. (2005), ♦, this work.

Figure 14.5-76 through Figure 14.5-78 illustrates an important point; even though each author successfully regressed experimental data for the H_2O-PZ-CO_2 system, predictions for the calculated chemical equilibrium constants differ. This discrepancy may be due to the thermodynamic foundations of each model framework. Each model would describe the activity coefficients differently based on the regression methodology each employed, the type of thermodynamic model used, and the types of thermodynamic data used in the model regression. In addition, the behavior for the activity coefficient of PZ as a function of temperature and concentration might also have the possibility of affecting the description of the chemical equilibrium environment. Overall, predictions for the chemical equilibrium constants appear to be consistent with previous work given the range of scatter of the reported values.

14.6 Solid Solubility Predictions

In this work we were able to use the full model as a predictive tool to illustrate the possible effects of loading on the solid solubility piperazine hexahydrate (PZ·6H_2O) in the H_2O-PZ-CO_2 system over the concentration range from 1 to 5 m PZ as shown in Figure 14.6-1 and as a surface prediction in Figure 14.6-2.

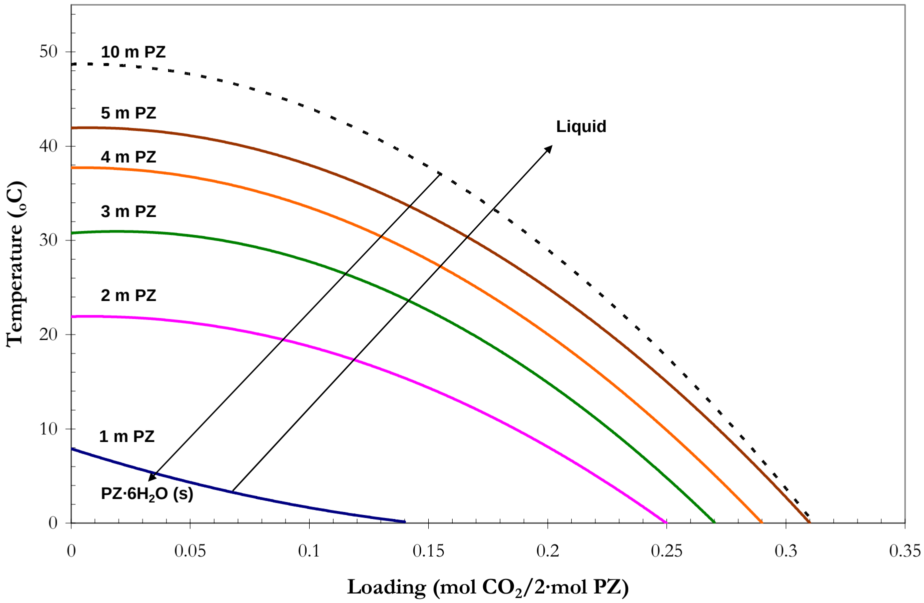

Figure 14.6-1. Predictive Solid Solubility for Aqueous Mixtures of Loaded Piperazine from 1 to 5 m PZ with an Extrapolation to 10 m PZ.

From Figure 14.6-3 we could recognize an effective operating range for solutions of concentrated piperazine, greater than 5 m PZ, over a loading range between 0.25 to 0.45 mole CO_2/2·mol PZ. We would recommend that future work should verify predictions from this work to create a rigorous and consistent thermodynamic model for predicting vapor-liquid and solid-liquid equilibrium for the H_2O-PZ-CO_2 system.

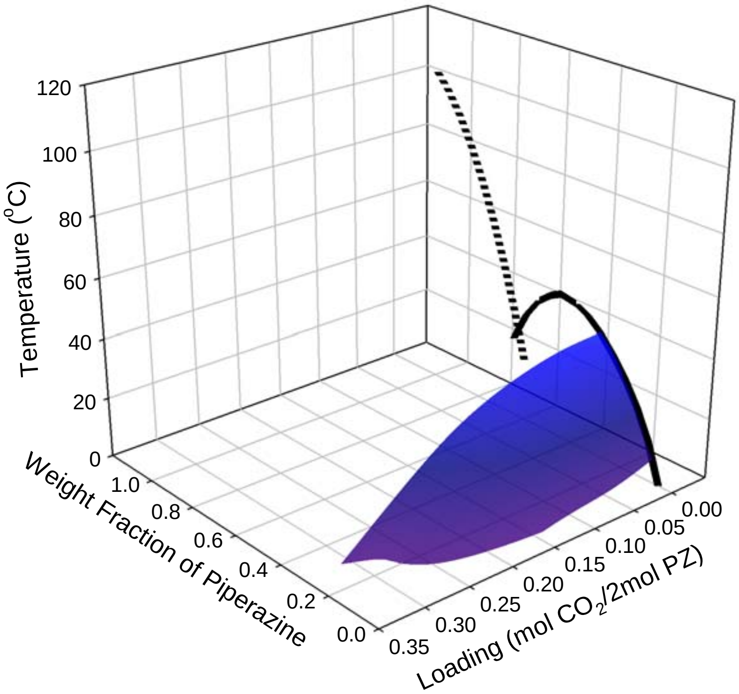

Figure 14.6-2. Predictive Solid Solubility Surface for Aqueous Mixtures of Loaded Piperazine from 1 to 5 m PZ.

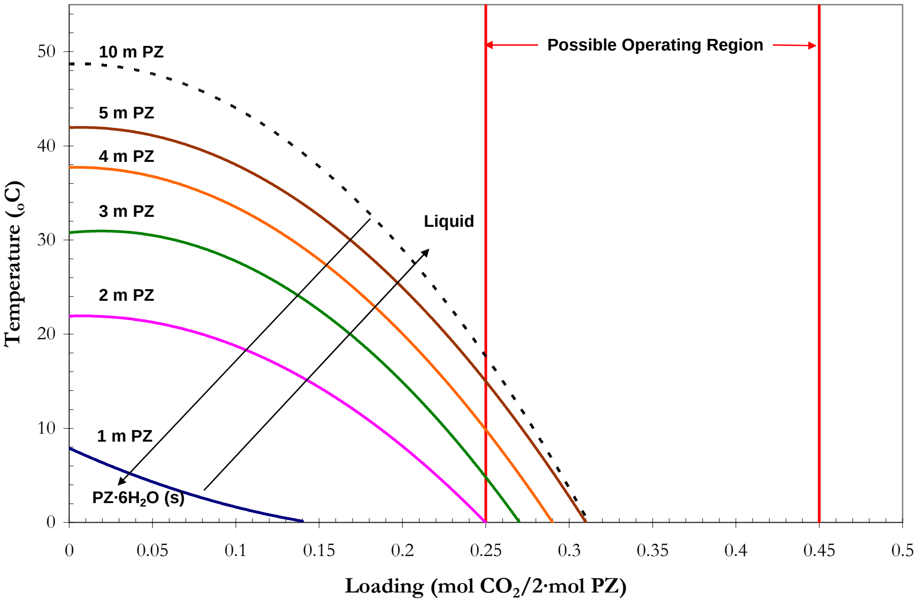

Figure 14.6-3. Possible Effective Operating Range for Concentrated Aqueous Mixtures of Loaded Piperazine from 1 to 5 m PZ with an Extrapolation to 10 m PZ.

14.7 Conclusions

In conclusion, we chose to describe the zwitterion (protonated piperazine carbamate) as an ionic but net-neutral molecule, as an ion with a charge equal to $1e^{-5}$. Previous work by Hilliard (2005) described the zwitterion as an ion with a neutral charge where the formation of protonated piperazine carbamate was described with a linear temperature dependent function for the chemical equilibrium constant. In this work, we chose to describe the chemical equilibrium in terms of the reference state Gibbs free energy of the system as given by Equation 14-29. By describing the zwitterion as an ion with a small charge within Aspen Plus^{TM}, the internal framework for ionic characterization remains rigorous and consistent throughout the simulation.

In terms of CO_2 solubility, Figure 14.5-1 through Figure 14.5-5 gave the results of fit for the experimental CO_2 solubility at 0.9, 2.0, 2.5, 3.6, and 5.0 m PZ per loading at 40 and 60 ^{o}C from this work. Predictions from the Hilliard (2005) model are also compared to predictions from this work. Model predictions based on the Hilliard (2005) model tend to underestimate the solubility of CO_2 at low loading and at low piperazine concentrations and tend to overestimate the solubility of CO_2 at high loading over the entire range of piperazine concentrations studied in this work. In the Hilliard (2005) model, the available CO_2 solubility data at the time was 0.6 M PZ reported by Bishnoi (2000) at 40 and 70 ^{o}C and supplemented by total pressure data reported by Pérez-Salado Kamps et al. (2003) for aqueous piperazine mixtures from 2 to 4 m PZ. This could account for the overestimation at high loading since the range in loading reported by Bishnoi (2000) varied from 0.1 to 0.4

mol CO_2/2·mol PZ. In this work, we were able to utilize the high loading CO_2 solubility data from Ermatchkov et al. (2006) at 40 and 80 °C to correct the loading dependence discrepancy as shown in the previous model. Overall, the full model adequately described the CO_2 solubility data within an average absolute relative error of ± 10.38 percent.

In terms of PZ volatility, Figure 14.5-15 through 14.5-19 illustrated that the Hilliard (2005) model overestimated the PZ partial pressure over the entire range of conditions. The root cause to this overestimation might have been in estimating the activity coefficient of PZ in H_2O-PZ by the UNIQUAC (DMD) model. We would recommend future works not to include predictions for the activity coefficient of PZ based on H_2O-PZ systems into thermodynamic models. Thermodynamic models based on available experimental data are more likely to represent the correct activity coefficient behavior, but in reality may not be feasible due to the limited amount of binary information on unique amine systems.

At a loading of 0.2 mol CO_2/2·mol PZ, piperazine volatility at 40 °C was shown to vary from 10 to 30 ppm_v for PZ concentrations from 0.9 to 5 m PZ.

Figure 14.5-25 through Figure 14.5-27 compared the experimental differential enthalpy of CO_2 absorption measurements from Kim (2007) to predictions based on Equation 14-39 (Gibbs-Helmholtz) from Hilliard (2005) and from this work. Figure 14.5-28 illustrated that at a loading of 0.2 mol CO_2/2·mol PZ, the enthalpy of CO_2 absorption increased from 70 to 90 kJ/mol-CO_2 as the temperature increased from 40 to 120 °C.

In addition, an approximate 10 kJ/mol-CO_2 decrease in the enthalpy of CO_2 absorption was observed in 2.4 m PZ at 40 °C as compared to 7 m MEA, but at 120 °C the enthalpy of CO_2 absorption was show to be approximately equal over the range of CO_2 partial pressures from 10 to 1000 kPa.

Model predictions from Hilliard (2005) model underestimated the enthalpy of CO_2 absorption at high temperatures over the range in loading and predicted the wrong temperature dependence. Granted, the Hilliard (2005) model did not include calometric measurements as part of his original regression analysis, but we chose to illustrate the possible enthalpy differences as compared to a purely CO_2 solubility based thermodynamic model. Overall, the full model adequately predicted the enthalpy of CO_2 absorption for 2.4 m PZ mixtures within an average absolute relative error of ± 6.55 percent.

Figure 14.5-30 through 14.5-37 compared the experimental specific heat capacity measurements from this work to predictions from Hilliard (2005) and to this work. Model predictions from Hilliard (2005) were unable to capture trends in the specific heat capacity as a function of temperature as shown in Figure 14.5-34 through 14.5-37. We did find that predictions from this work did capture the correct trends in the specific heat capacity as a function of temperature but failed in predicting the correct specific heat capacity on the order of ± 5 percent. One possibility for this discrepancy may result in an inconsistency between the enthalpy of CO_2 absorption measurements from Kim (2007) and specific heat capacity from this work. We were able to illustrate that the full model was able to predict the correct average specific heat capacity and in turn the sensible liquid phase enthalpy $\left(\bar{C}_p \Delta T\right)$ within the experimental accuracy of ± 2.0 percent error with the exception of 2 m PZ at a loading of 0.27 mol CO_2/2·mol PZ.

In addition, Figure 14.5-41 illustrated how the experimental apparent heat capacity suggested that contributions of the apparent heat capacity of apparent CO_2 species may be considered small with a magnitude less than 2 kJ/kmol-K.

Model predictions from Hilliard (2005) adequately predicted the liquid phase NMR speciation for 1.0 and 1.5 m PZ, but as previously shown, the Hilliard (2005) model did not adequately predict systematic trends in the piperazine volatility even though amine volatility is a concentration based measurement; NMR speciation does allow the researcher to take a glimpse at the pseudo-component concentrations. Using both pieces of information in the regression would effect the adjustment of the activity coefficient of PZ. Thus, we were able to adequately predict the CO_2 solubility, amine volatility, enthalpy of CO_2 absorption, and to some extent the liquid phase specific heat capacity. We feel that we have compiled an extensive database that gives a more realistic prediction for the liquid phase speciation. In this work, the full model was able to adequately predict the liquid phase NMR speciation for 1.0 and 1.5 m PZ mixtures within an average relative error of ± 5.69 percent.

Figure 14.5-72 through Figure 14.5-74 illustrated an important point in terms of chemical equilibrium constants even though different authors successfully regressed experimental data for the H_2O-PZ-CO_2 system, predictions for the chemical equilibrium constants differ. This discrepancy may be due to the thermodynamic foundations of each model framework. In addition, the behavior for the activity coefficient of PZ as a function of temperature and concentration might also have the possibility of affecting the description of the chemical equilibrium environment. Overall, predictions for the chemical equilibrium constants appear to be consistent with previous work given the range of scatter of the reported values.

In this work we were able to use the full model as a predictive tool to illustrate the possible effects of loading on the solid solubility piperazine hexahydrate (PZ·6H_2O) in the H_2O-PZ-CO_2 system over the concentration range from 1 to 5 m PZ as shown in Figure 14.6-1 and as a surface prediction in Figure 14.6-2. From Figure 14.6-3 we could recognize an effective operating range for solutions of concentrated piperazine, greater than 5 m PZ, over a loading range between 0.25 to 0.45 mole CO_2/2·mol PZ. We would recommend that future work should verify predictions from this work to create a rigorous and consistent thermodynamic model for predicting vapor-liquid and solid-liquid equilibrium for the H_2O-PZ-CO_2 system.

Overall, the results presented above indicate that the elecNRTL model, through simultaneous regression, gave a set of unique parameters for the H_2O-PZ-CO_2 system where the full model adequately represents the literature data for loaded PZ solutions.

CHAPTER XV

Quaternary Systems: H_2O-K_2CO_3-PZ-CO_2

15.1 Introduction

At this point in the thermodynamic modeling development, we have described the molecule-molecule and molecule-electrolyte interactions for previous systems. For the H_2O-K_2CO_3-PZ-CO_2 system, interactions between molecules and electrolytes and interactions between electrolyte pairs with a common cation or anion will be considered. This chapter describes the data regression and model predictions for the quaternary {H_2O-Potassium Carbonate (K_2CO_3)-Piperazine (PZ)-Carbon Dioxide (CO_2)} system based on previous literature data and experimental results from this work. The results from the binary interaction parameters for the electrolyte-NRTL (elecNRTL) model within Aspen Plus^{TM} are then presented, showing a good statistical fit to the literature data within an average absolute relative error of ± 15.48 %, with the exception of a few outliers.

15.2 H_2O-K_2CO_3-PZ-CO_2

With ions in an electrolyte solution, the elecNRTL model accounts for contributions associated with long-range ion-ion interactions and local interactions which exist around any central species as proposed by Chen et al. (1982). In this section, we present background on the elecNRTL model for clarification purposes only.

The elecNRTL model is a molar Gibbs energy model given by the following form:

$$G_m^* = x_w \mu_w^* + \sum_k x_k \mu_k^\infty + \sum_j x_j \ln x_j + G_m^{*E} \qquad \text{15-1}$$

where the excess Gibbs free energy model is given by the following form:

$$\frac{G_m^{*E}}{RT} = \frac{G_m^{*E,PDH}}{RT} + \frac{G_m^{*E,Born}}{RT} + \frac{G_m^{*E,lc}}{RT} \qquad \text{15-2}$$

Where
PDH is the Pitzer-Debije-Hückel contribution for long range ion-ion interactions,
Born is the Born Correction for change in mixed solvent reference state, and
lc is the local contribution for short range interactions.

The molar Gibbs free energy and the molar excess Gibbs free energy are defined with the asymmetrical references state as infinite dilute in pure solvent. The reference state for ionic and molecular solutes follows the unsymmetrical convention defined as infinite dilution in water. The ideal mixing term is calculated where j refers to any component and the molar Gibbs free energy of pure water is calculated from the ideal gas contribution. The aqueous infinite dilution chemical potential is calculated from the infinite dilution aqueous phase heat capacity polynomial model, where the subscript k refers to any ions or molecular solute.

$$\mu_k^\infty = \Delta_f H_k^{\infty,aq} + \int_{T_0}^{T} \frac{C_{p,k}^{\infty,aq}}{T} dT - T\left(\frac{\Delta_f H_k^{\infty,aq} - \Delta_f G_k^{\infty,aq}}{T_0} + \int_{T_0}^{T} \frac{C_{p,k}^{\infty,aq}}{T} dT \right) + RT \ln\left(\frac{1000}{MW_w}\right) \quad 15\text{-}3$$

Where $\Delta_f H_k^{\infty,aq}$ and $\Delta_f G_k^{\infty,aq}$ are based on a molality scale and μ_k^∞ is based on a mole fraction scale, the last term added for the conversion.

For molecular solutes, the aqueous infinite dilution chemical potential is calculated from Henry's law:

$$\mu_k^\infty = \mu_k^{\infty,ig} + RT \ln\left(\frac{H_{k,w}}{P^{ref}}\right) \quad 15\text{-}4$$

Where
T_0 is the reference temperature, 298.15 K,
P^{ref} is the reference pressure, 1 atm.

Thus, when the derivative of the Gibbs free energy at constant temperature and pressure reaches a minimum for a closed homogeneous system, the system has satisfied the condition for thermodynamic equilibrium.

For the elecNRTL model to calculate activity coefficients, the excess Gibbs free energy is related to the activity coefficient by the following thermodynamic relationship.

$$\ln \gamma_i = \frac{G_m^{*E}}{RT} = \left[\frac{\delta\left(nG_m^{*E} / RT\right)}{\delta n_i} \right] \quad 15\text{-}5$$

Please refer to Chapter VI for information relating to the specific contributions to the excess Gibbs energy model.

15.3 Chemical and Vapor-liquid Equilibrium of Potassium + PZ

Figure 15.3-1 illustrates the proposed system to correlate/predict the solubility of CO_2 and PZ in aqueous solutions of potassium (K^+) plus piperazine.

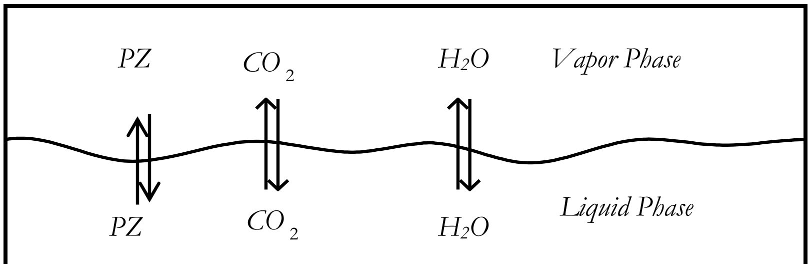

R1: $H_2O \leftrightarrow H^+ + OH^-$ 15-6

R2: $CO_2 + H_2O \leftrightarrow H^+ + HCO_3^{-1}$ 15-7

R3: $HCO_3^{-1} \leftrightarrow H^+ + CO_3^{-2}$ 15-8

R4: $PZH^{+1} \leftrightarrow PZ + H^+$ 15-9

R5: $PZH_2^{+2} \leftrightarrow PZH^{+1} + H^+$ 15-10

R6: $PZ + HCO_3^{-1} \leftrightarrow PZCOO^{-1} + H_2O$ 15-11

R7: $PZCOO^{-1} + HCO_3^{-1} \leftrightarrow PZ\left(COO^{-1}\right)_2 + H_2O$ 15-12

R8: $H^+PZCOO^{-1} \leftrightarrow PZCOO^{-1} + H^+$ 15-13

Figure 15.3-1. Chemical and Vapor-liquid Equilibrium of K^+ + PZ.

Reaction 15-6 describes the ionization of water to proton $\left(H^{+}\right)$ and hydroxide ions $\left(OH^{-}\right)$; Reaction 15-7 describes the hydrolysis and ionization of dissolved CO_2 to H^+ and bicarbonate $\left(HCO_3^{-}\right)$ ions; Reaction 15-8 describes the dissociation of HCO_3^- to H^+ and carbonate $\left(CO_3^{-2}\right)$ ions; Reaction 15-9 describes the protonation of piperazine $\left(PZ\right)$ to protonated piperazine $\left(PZH^{+1}\right)$; Reaction 15-10 describes the protonation of protonated piperazine to diprotonated piperazine $\left(PZH_2^{+2}\right)$; Reaction 15-11 describes the piperazine carbamate formation $\left(PZCOO^{-1}\right)$; Reaction 15-12 describes the piperazine dicarbamate formation $\left(PZ\left(COO^{-1}\right)_2\right)$; Reaction 15-13 describes the protonated piperazine carbamate formation $\left(H^{+}PZCOO^{-1}\right)$. The chemical equilibrium constant for the above j equations is expressed in Aspen Plus™ in terms of the activity of component i as given by the following relationship.

$$K_j = \prod_i a_i^{\nu_{i,j}} \qquad 15\text{-}14$$

Where
K_j is the chemical equilibrium constant,
$\nu_{i,j}$ is the reaction stoichiometric coefficient of component i,
a_i is the activity of component i.

In this work, for Reactions 15-6 to 15-13, we did not define the chemical equilibrium constants as linear temperature dependent functions, but rather in terms of the reference state Gibbs free energy of the system:

$$\ln K_j = -\frac{\Delta G^o_{i,j}}{RT} \qquad 15\text{-}15$$

Where

$\Delta G^o_{i,j}$ is the standard free energy of formation of component i.

The previous framework allows our rigorous thermodynamic model to be internally consistent with respect to governing thermodynamic definitions. Table 9.3-12 and Table 9.3-8 reported the standard state conditions at 25 °C associated with the species in Reactions 15-6 to 15-10 where the standard state conditions are consistent with published literature by Edwards et al. (1978) and Hetzer et al. (1968) as shown in Chapter XIV and Chapter IX, respectively.

We chose to simplify the overall model by excluding Reaction 15-10 from the final model. This assumption is based on the second pKa of piperazine, as described in Chapter IX, where the relative concentration of diprotonated piperazine below a loading of 0.5 mol CO_2/2·mol PZ could be considered negligible. If in future work the loading range is extended beyond a loading of 0.5, inclusion of the diprotonated piperazine reaction would need to be included.

For the precipitation of piperazine hexahydrate as described in Chapter IX, we chose to define the chemical equilibrium constant as a linear temperature dependent function as given in Table 9-4-1 due to limited thermodynamic data available for the characterization of the solid phase.

Dipotassium piperazine dicarbamate was observed to precipitate in a limited number of loaded solutions of potassium + piperazine as described in Chapter V. In this work, we chose to define the chemical equilibrium constant as linear temperature dependent function as given in section 15.5.5 due to limited thermodynamic data available for the characterization of the solid phase.

As stated previously, Equation 15-15 relates the chemical equilibrium constant to the standard Gibbs free energy change of reaction.

$$\frac{\Delta G^o}{RT} = -\ln K \tag{15-16}$$

Where the standard property changes of reaction (e.g. Gibbs free energy and enthalpy) are defined as the difference between the standard property change of the products and reactants, weighted by their stoichiometric coefficients.

$$\Delta M^o = \sum_i \nu_i M_i^o \tag{15-17}$$

For molecular solutes (e.g. CO_2), the standard Gibbs free energy is described based on the ideal gas reference state by the following equation:

$$G_{CO_2}^o\left(T\right) = G_{CO_2}^{ig}\left(T\right) + RT\ln\frac{H_{CO_2}\left(T\right)}{P^{ref}} \tag{15-18}$$

Where
$G_{CO_2}^{ig}$ is the ideal gas Gibbs free energy, J/kmol,
H_{CO_2} is the Henry's Constant for CO_2 in H_2O (Chen et al. 1979), atm,
P^{ref} is the reference pressure, 1 atm.

For ionic species the aqueous phase infinite dilution molar heat capacity is described by the following equation:

$$C_{p,i}^{\infty,aq}\left(\frac{J}{kmol\cdot K}\right) = C_{1,i} + C_{2,i}T\left(K\right) + C_{3,i}T\left(K\right)^2 + \frac{C_{4,i}}{T\left(K\right)} \tag{15-19}$$

where coefficients for the aqueous phase infinite dilution molar heat capacity for carbonate, bicarbonate, and PZH^{+1} were described previously in Chapter XII - Section 12.5 and Chapter IX - Section 9.3, respectively.

The molar heat capacity of H_2O was described in Chapter VII by the following equation:

$$C_{p,H_2O}^{l,*}\left(\frac{J}{kmol\cdot K}\right)=189366-1171\cdot T\left(K\right)+4.53\cdot T\left(K\right)^2 \\ -0.00795\cdot T\left(K\right)^3+5.4723\times10^{-6}\cdot T\left(K\right)^4 \qquad 15\text{-}20$$

For a given temperature, the molar aqueous phase infinite dilution heat capacity of piperazine carbamate, piperazine dicarbamate, and protonated piperazine carbamate can then be determined analytically based on the simultaneously regressed infinite dilution aqueous phase free energy of formation $\left(\Delta G_f^{\infty,aq}\right)$, the infinite dilution aqueous phase enthalpy of formation $\left(\Delta H_f^{\infty,aq}\right)$, and the infinite dilution aqueous phase heat capacity polynomial $\left(C_p^{\infty,aq}\right)$ for piperazine carbamate, piperazine dicarbamate, and protonated piperazine carbamate. A starting point for a rigorous development starts with the following equation:

$$\Delta G_m^o=\Delta H_m^o-T\Delta S_m^o \qquad 15\text{-}21$$

Equation 15-21 is from the definition of the molar Gibbs free energy applied to each component in a chemical reaction evaluated at the standard state. Applying Equation 15-17 to Equation 15-21 yields

$$\sum_i \nu_i G_{m,i}^o=\sum_i \nu_i H_{m,i}^o-T\sum_i \nu_i S_{m,i}^o \qquad 15\text{-}22$$

where the standard molar heat of reaction and standard molar entropy change of reaction are related to temperature by the following expressions

$$\Delta H_m^o = \Delta H_{0,m}^o + R\int_{T_0}^{T} \frac{\Delta C_{p,m}^o}{R} dT \qquad 15\text{-}23$$

$$\Delta S_m^o = \Delta S_{0,m}^o + R\int_{T_0}^{T} \frac{\Delta C_{p,m}^o}{R}\frac{dT}{T} \qquad 15\text{-}24$$

Equations 15-21, 15-23, and 15-24 are combined to yield

$$\Delta G_m^o = \Delta H_{0,m}^o + R\int_{T_0}^{T} \frac{\Delta C_{p,m}^o}{R} dT - T\Delta S_{0,m}^o - RT\int_{T_0}^{T} \frac{\Delta C_{p,m}^o}{R}\frac{dT}{T} \qquad 15\text{-}25$$

However,

$$\Delta S_{0,m}^o = \frac{\Delta H_{0,m}^o - \Delta G_{0,m}^o}{T_0} \qquad 15\text{-}26$$

hence

$$\Delta G_m^o = \Delta H_{0,m}^o - \frac{T}{T_0}\left(\Delta H_{0,m}^o - \Delta G_{0,m}^o\right) + R\int_{T_0}^{T} \frac{\Delta C_{p,m}^o}{R} dT - RT\int_{T_0}^{T} \frac{\Delta C_{p,m}^o}{R}\frac{dT}{T} \qquad 15\text{-}27$$

Finally, division by RT yields

$$-\ln K_i = \frac{\Delta G_m^o}{RT} = \frac{\Delta G_{0,m}^o - \Delta H_{0,m}^o}{RT_0} + \frac{\Delta H_{0,m}^o}{RT} + \frac{1}{T}\int_{T_0}^{T} \frac{\Delta C_{p,m}^o}{R} dT - \int_{T_0}^{T} \frac{\Delta C_{p,m}^o}{R}\frac{dT}{T} \qquad 15\text{-}28$$

The change in heat capacity for the mixture can be expressed as

$$\Delta C_p^o\left(\frac{J}{kmol\cdot K}\right) = \Delta A + \Delta B\cdot T\left(K\right) + \Delta C\cdot T\left(K\right)^2 + \Delta D\cdot T\left(K\right)^3 + \Delta E\cdot T\left(K\right)^4 \qquad 15\text{-}29$$

with

$$\Delta A = \sum_i v_i A_i \qquad 15\text{-}30$$

with analogous definitions for ΔB, ΔC, ΔD, and ΔE. Through simultaneous regression of CO_2 solubility, amine volatility, specific heat capacity, liquid phase speciation, and enthalpy of CO_2 absorption, we were able to determine the infinite dilution aqueous phase free energy of formation, the infinite dilution aqueous phase enthalpy of formation, and the infinite dilution aqueous phase heat capacity polynomial for piperazine carbamate, piperazine dicarbamate, and protonated piperazine carbamate. Please refer to section 15.4 for more information.

Five data sets have been regressed with the elecNRTL model to represent the phase equilibrium of a mixed solvent system through regression of CO_2 solubility [from this work], specific heat capacity [from this work], enthalpy of CO_2 absorption [Kim (2007)], and NMR speciation [Cullinane (2005)] data over potassium + piperazine solutions. The elecNRTL model was never designed to regress enthalpy of CO_2 absorption or NMR speciation data; thus we created a fortran subroutine to link with the data regression system (DRS) in Aspen Plus^{TM}.

The following section describes the different types of data used in the creation of the binary H_2O-PZ-CO_2 elecNRTL model.

15.3.1 *CO_2 Solubility and Amine Volatility*

Data in the form of CO_2 solubility, which measures the partial pressure of CO_2 over aqueous K^+ + PZ solutions, P_{CO_2}, as a function of loading (mole CO_2 per mole K^+ + 2·mole PZ) and temperature were used to adjust the partial pressure of CO_2 for the H_2O-K_2CO_3-PZ-CO_2 system through the simultaneous regression of the binary interaction parameters in the elecNRTL model for the H_2O- K_2CO_3-PZ-CO_2 system.

For our quaternary system (H_2O, K_2CO_3, PZ, and CO_2), the following equation can be used to represent the equilibrium for CO_2 solubility data.

$$P y_{CO_2} = x_{CO_2} \gamma^{*}_{CO_2} H_{CO_2,H_2O} \tag{15-31}$$

Where

y_{CO_2} is the vapor mole fraction of CO_2,

$\gamma^{*}_{CO_2}$ is the unsymmetric activity coefficient of CO_2,

H_{CO_2,H_2O} is the Henry's Constant for CO_2 in H_2O.

An example of the experimental CO_2 solubility from Cullinane (2005) and from this work in 5 m K^+ + 2.5 m (mole/kg-H_2O) PZ is shown in Figure 15.3-2. Ordinary least square (OLS) approximations were included for clarification.

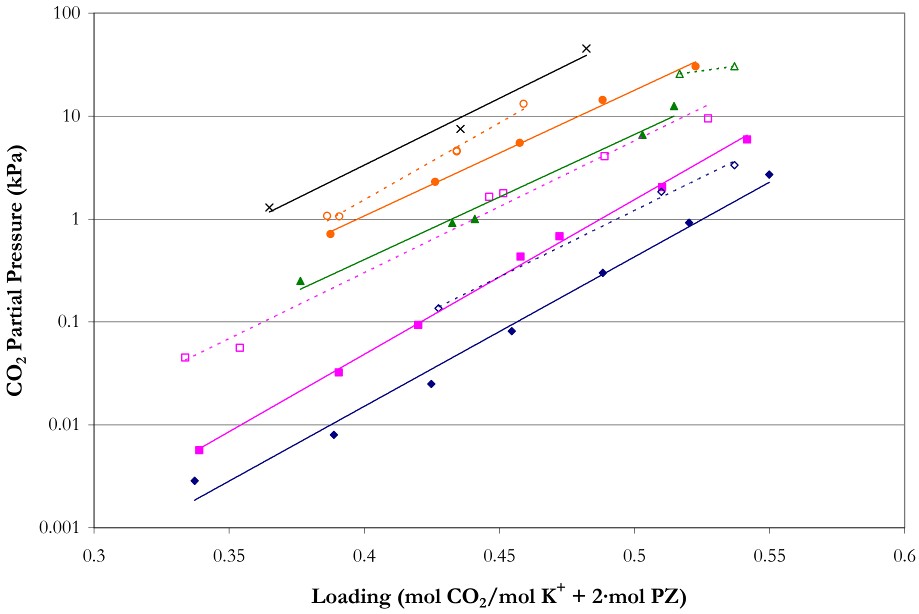

Figure 15.3-2. CO_2 Solubility in 5 m K^+ + 2.5 m PZ from 40 – 120 °C. Points: ◊, 40 °C, □, 60 °C, ○, 80 °C, Cullinane (2005); ♦, 40 °C, ■, 60 °C, ▲, 80 °C, ●, 100 °C, ×, 120 °C. Lines: OLS Approximations.

One of the main goals in this work was to verify experimental CO_2 solubility measurements reported by Cullinane (2005). Figure 15.3-2 illustrates a loading discrepancy for the solubility of CO_2 in mixtures of 5 m K^+ + 2.5 m PZ. Comparing experimental results from this work for other solvent combinations, similar trends are exhibited between the two data sets. Cullinane (2005) reported an experimental uncertainty between ± 5 to 10 percent for reported loading measurements based on a similar procedure for acidic evolution utilizing total inorganic carbon as described in Appendix B. In acidic evolution, an unknown sample containing a dissolved amount of CO_2 is injected into an evolution column containing an excess amount of phosphoric acid. During the analysis, nitrogen gas flows through the evolution column to strip the evolved CO_2 for analysis by a calibrated Horiba PIR 2000 carbon dioxide analyzer. The response signal is then integrated (trapezoid rule) and correlated to the response of known Na_2CO_3 standards as shown in Figure 15.3-3 and 15.3-4.

Cullinane (2005) chose not to integrate the response signal but instead to correlate the peak height to the response of known Na_2CO_3 standards by assuming that the peak height was proportional to the peak area. This alternative method is illustrated in Figure 15.3-4 as compared to the same calibration curve based on the integral of the peak area.

Figure 15.3-5 compares the response peak height to the integrated peak area for the known Na_2CO_3 standards against unknown 5 m K+ 2.5 m PZ 40 ^oC samples. The figure illustrates a small shift vis-à-vis peak broadening in the response between the standards and the unknowns. This shift may be due to the different rates of reaction where the amine

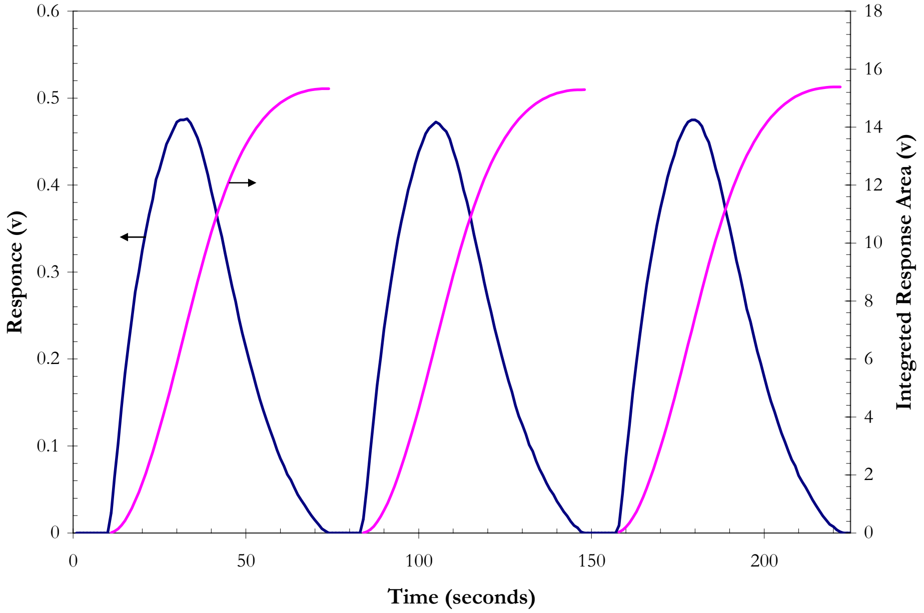

Figure 15.3-3. Response Signal for 100 ppm$_v$ Standard of Na_2CO_3 Solution on 02/13/07.

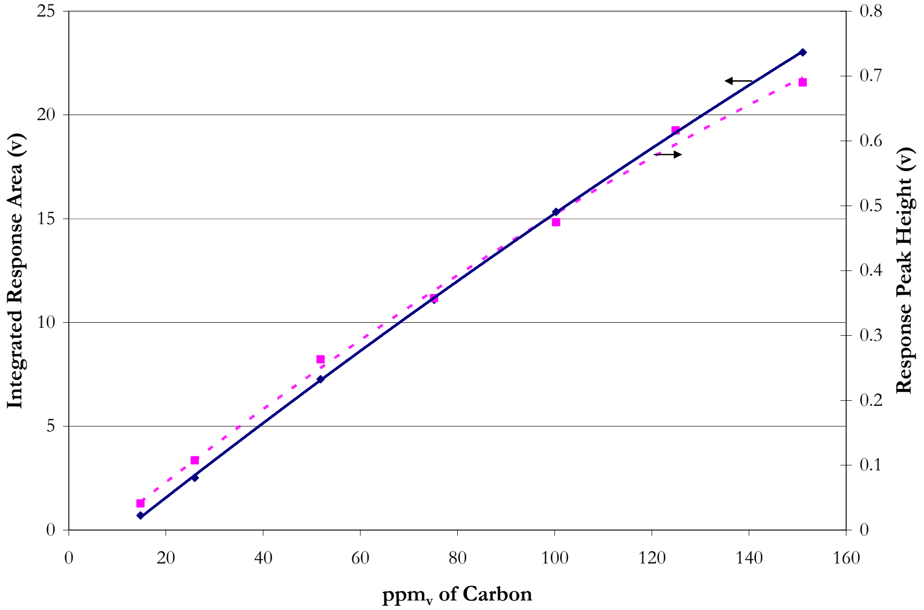

Figure 15.3-4. Acidic Evolution Calibration Curve for 02/13/07 based on Na_2CO_3 Standards. Points: ♦, Integrated Peak Area, ■, Peak Height. Lines: OLS Approximations.

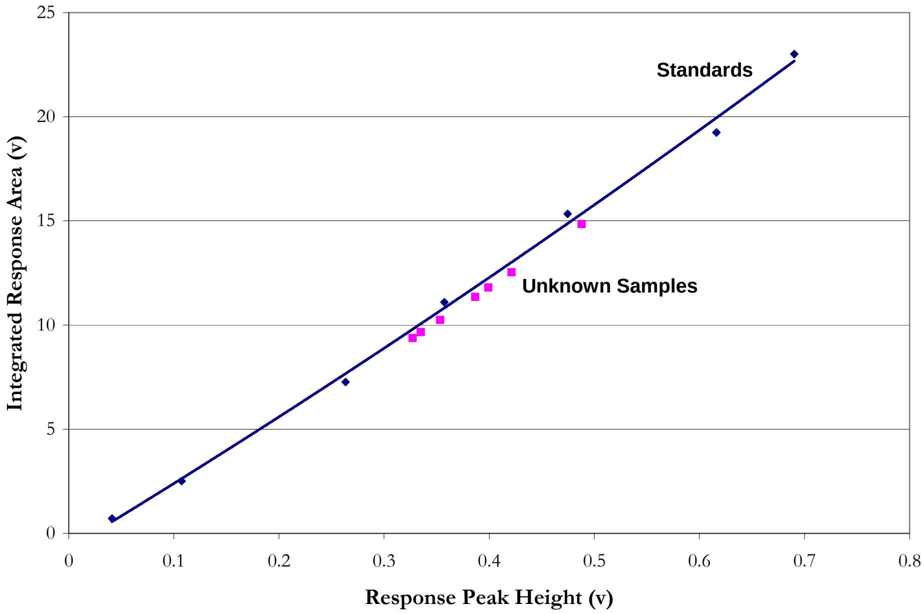

Figure 15.3-5. Acidic Evolution Calibration Curve based on Na_2CO_3 Standards and Unknown 5 m K^+ + 2.5 m PZ 40 ^oC Samples for 02/13/07. Points: ♦, Na_2CO_3 Standards, ■, 5 m K^+ + 2.5 m PZ Samples. Line: OLS Approximations.

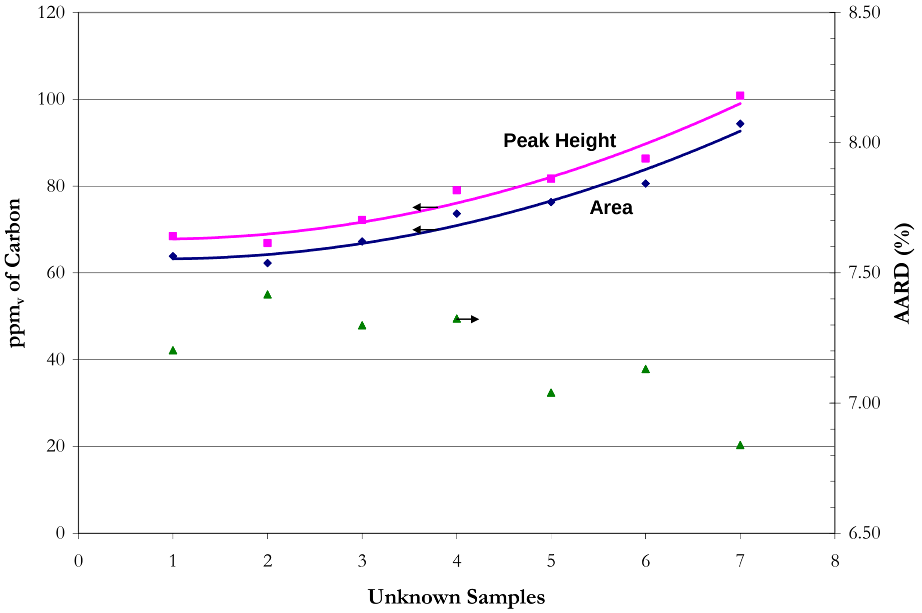

Figure 15.3-6. Acidic Evolution Analysis for Unknown 5 m K^+ + 2.5 m PZ 40 ^oC Samples on 02/13/07. Points: ♦, Peak Area, ■, Peak Height. Lines: OLS Approximations.

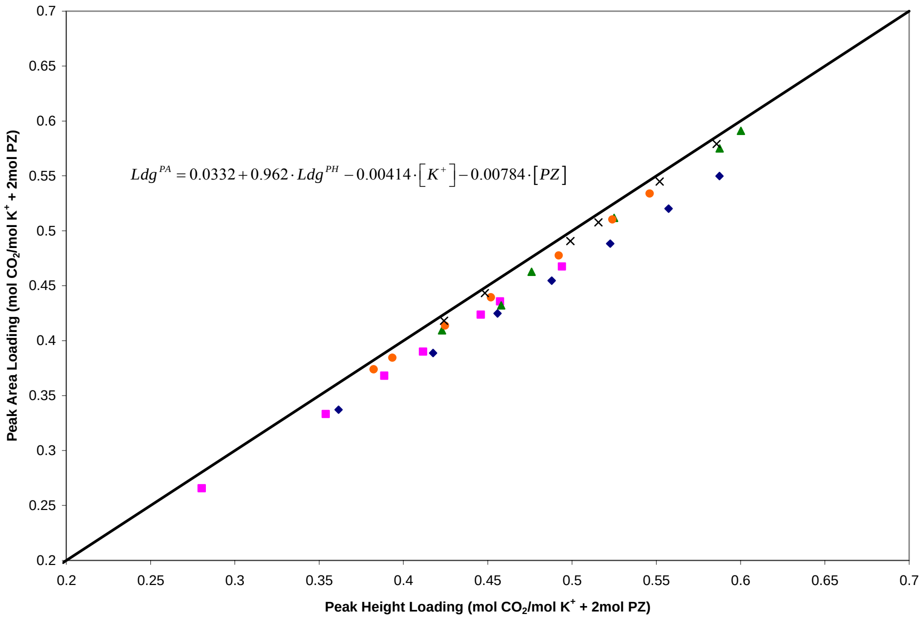

Figure 15.3-7. Acidic Evolution Loading Analysis Comparison based on Peak Height versus Peak Area for Unknown Samples from this work at 40 °C. Points: ♦, 5 m K^++2.5 m PZ, ■, 3.6 m K^++3.6 m PZ, ▲, 6 m K^++1.2 m PZ, ●, 3.6 m K^++1.8 m PZ, ×, 3.6 m K^++0.6 m PZ.

reaction rates are faster than the reaction rate of the Na_2CO_3 salt. Figure 15.3-6 illustrates the calculated concentration of CO_2 (ppm$_v$ of Carbon) in unknown 5 m K+ 2.5 m PZ 40 °C samples from this work. Concentrations calculated from the response peak height show a systematic overestimation for the concentration of CO_2 in the unknown samples. This may be due to the unsymmetric distribution of the response peak which is skew to the right and is not proportional to the peak height. Since Cullinane (2005) assumed that the peak height was proportional to the peak area, this overestimation may offer an exploration to discrepancy between the two data sets. The analysis can be extended to include a population of random unknown samples from five solvents examined in this work to create a possible correlation for loadings determined base on the response peak height versus the integrated peak area as shown in Figure 15.3-7 and Table 15.3-1.

Table 15.3-1. Selected Experimental Data Points for Acidic Evolution Loading Analysis Determined by Peak Area or Peak Height from this work.

K^+ (m)	PZ (m)	Loading^{PH}	Loading^{PA}	AARD (%)	Ave. (%)
5.0	2.5	0.362	0.337	7.20	7.18
		0.418	0.389	7.42	
		0.456	0.425	7.30	
		0.488	0.455	7.32	
		0.523	0.488	7.04	
		0.557	0.520	7.13	
		0.587	0.550	6.84	
3.6	3.6	0.280	0.266	5.50	5.53
		0.354	0.333	6.24	
		0.389	0.368	5.59	
		0.412	0.390	5.54	
		0.446	0.424	5.23	
		0.457	0.436	4.91	
		0.494	0.467	5.67	
6.0	1.2	0.423	0.409	3.30	3.07
		0.458	0.432	5.98	
		0.476	0.463	2.87	
		0.525	0.512	2.57	
		0.588	0.575	2.18	
		0.600	0.591	1.53	
3.6	0.6	0.424	0.418	1.39	1.37
		0.448	0.443	1.13	
		0.499	0.491	1.72	
		0.516	0.508	1.56	
		0.552	0.545	1.32	
		0.586	0.579	1.13	
3.6	1.8	0.382	0.374	2.22	2.56
		0.393	0.385	2.32	
		0.425	0.414	2.62	
		0.452	0.439	2.83	
		0.492	0.478	3.02	
		0.524	0.510	2.67	
		0.546	0.534	2.27	

Loading: mole CO_2/mole K^+ + 2·mole PZ, PH: Peak Height, PA: Peak Area.

Acidic evolution based on the response of the peak height as compared to the integrated response peak area may yield an average absolute relative error of ± 7.18 percent for unknown samples associated with 5 m K^+ + 2.5 m PZ solvent as determined in this work. Overall, an average absolute relative error of ± 3.94 percent would suggest the possibility of a systematic error associated with the CO_2 analysis procedure reported by Cullinane (2005) and would agree with the experimental uncertainty reported by Cullinane (2005) for reported loading measurements based on peak height.

These results may explain the discrepancy between reported CO_2 solubility measurements from Cullinane (2005) and from this work. In addition, Cullinane (2005) chose not to analyze the total alkalinity of the experimental solution which may pose an addition error within the reported experimental loading. Based on the above analysis, we chose to exclude reported CO_2 solubility from Cullinane (2005) due to an error in the loading analysis.

In addition, Cullinane (2005) also reported proton (H^1) NMR speciation for H_2O-K_2CO_3-PZ-CO_2 system. The main drawback with an H^1 NMR speciation analysis is not having the ability to measure the loading of the solution as compared to carbon C^{13} NMR speciation as described in Chapter XIII. In the H^1 NMR analysis the loading of the solution has to be determined *a prori* which may result in a discrepancy between the loading at the time of the NMR experiment and at the time of the CO_2 analysis since the loading for NMR solutions reported by Cullinane (2005) were completed in a similar manner as CO_2 solubility measurements, the uncertainty in loading for experimental NMR speciation data reported by

Cullinane (2005) was assigned a standard deviation of ± 10 % to account for the discrepancy in the loading analysis as compared to this work.

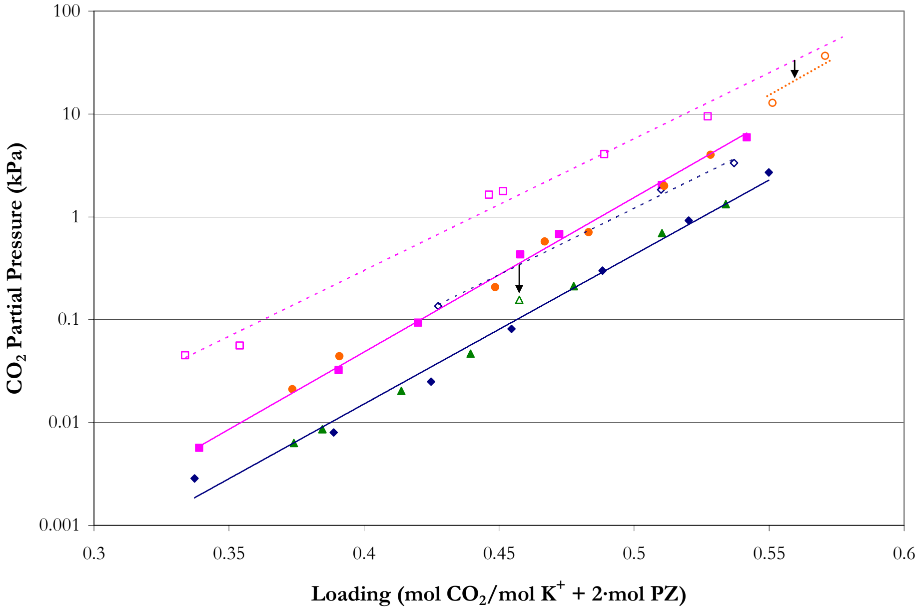

Figure 15.3-8. Comparison of Potassium to Piperazine Effect in 5 m K^+ + 2.5 m PZ and 3.6 m K^+ + 1.8 m PZ at 40 and 60 °C from Cullinane (2005) to this work. Points: ♦, 40 °C, ■, 60 °C, 5 m K^+ + 2.5 m PZ; ▲, 40 °C, ●, 60 °C, 3.6 m K^+ + 3.6 m PZ, from this work; ◊, 40 °C, □, 60 °C, 5 m K^+ + 2.5 m PZ; Δ, 40 °C, ○, 60 °C, 3.6 m K^+ + 3.6 m PZ, Cullinane (2005). Lines: OLS Approximations.

Furthermore, Cullinane (2005) observed that solvent concentrations with the same potassium to piperazine ratio may exhibit the same CO_2 solubility. Figure 15.3-8 illustrates the salt to amine effect for 5 m K^+ + 2.5 m PZ and 3.6 m K^+ + 1.8 m PZ at 40 and 60 °C where the potassium to piperazine ratio equals 2. Experimental solubility for the two solvents from this work demonstrates a similar CO_2 solubility. On the other hand, experimental results from Cullinane (2005) demonstrate that systematic trends in the experimental data are not internally consistent. We would conclude that the Cullinane

(2005) CO_2 solubility data set are not consistent with reported observations by Cullinane (2005) and should be treated with caution in future works.

In this work, we used a unique Fourier-transform infrared (FT-IR) technique to measure the vapor phase speciation in aqueous alkanolamine systems as described in Chapter II. Using this technique, we have been able to measure the vapor phase partial pressure of PZ over aqueous K^+ + PZ solutions, P_{PZ} , as a function of loading (mole CO_2 per mole K^+ + 2·mole PZ) and temperature.

For our quaternary system (H_2O, K_2CO_3, PZ, and CO_2), the following equation can be used to represent the equilibrium for PZ volatility data.

$$Py_{PZ} = x_{PZ}\gamma_{PZ}P_{PZ}^{o} \qquad 15\text{-}32$$

Where
y_{PZ} is the vapor mole fraction of PZ,
γ_{PZ} is the asymmetric activity coefficient of PZ,
P_{PZ}^{o} is the extended Antoine vapor pressure correlation for PZ given in Chapter VI.

Examples of the experimental PZ volatility from this work in 5 m K^+ + 2.5 m PZ and 3.6 m K^+ + 3.6 m PZ at 40 and 60 °C are shown in Figure 15.3-9 and Figure 15.3-10, respectively. Figure 15.3-11 illustrates that with the decrease in the salt concentration the relative volatility of piperazine has decreased by a factor of 2.3 even though the concentration of piperazine was increased by a factor of 1.5.

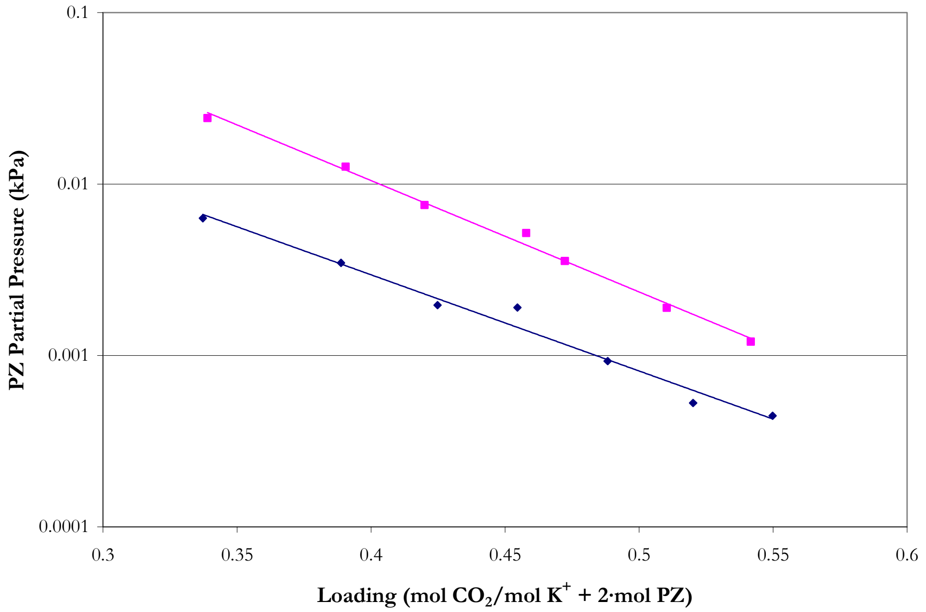

Figure 15.3-9. PZ Volatility in 5 m K⁺ + 2.5 m PZ at 40 and 60 °C from this work. Points: ♦, 40 °C, ■, 60 °C. Lines: OLS Approximations.

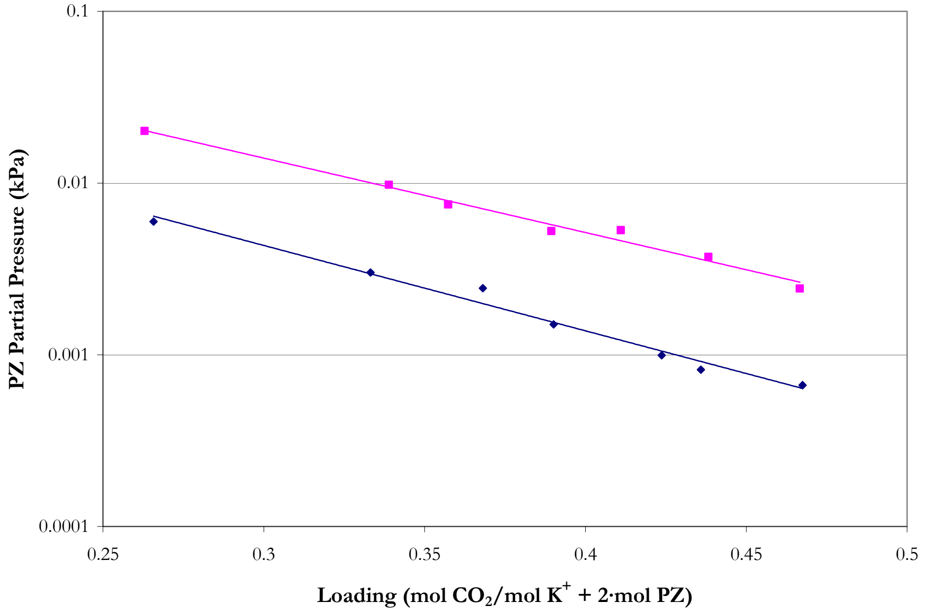

Figure 15.3-10. PZ Volatility in 3.6 m K⁺ + 3.6 m PZ at 40 and 60 °C from this work. Points: ♦, 40 °C, ■, 60 °C. Lines: OLS Approximations.

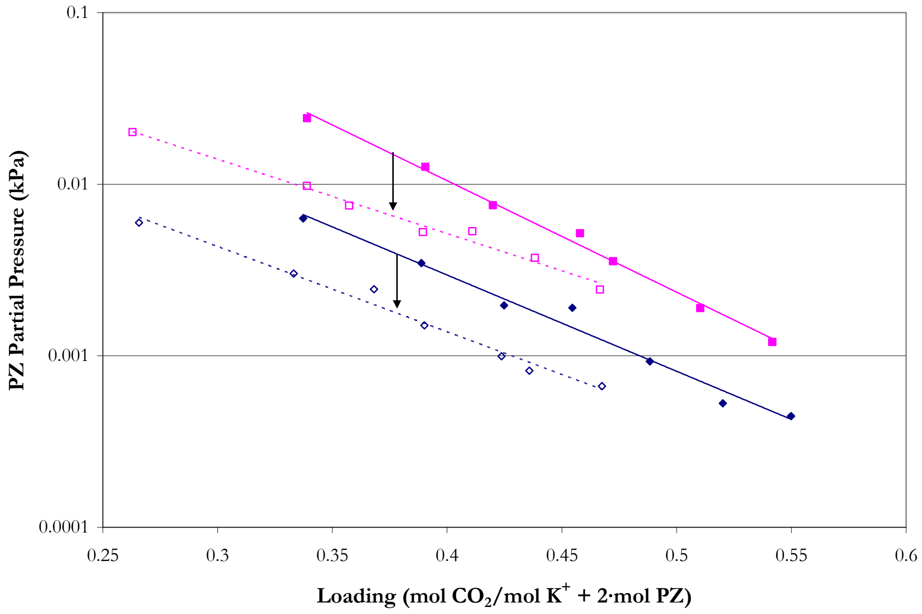

Figure 15.3-11. PZ Volatility in 5 m K$^+$ + 2.5 m PZ and 3.6 m K$^+$ + 3.6 m PZ at 40 and 60 °C from this work. Points: ♦, 40 °C, ■, 60 °C, 5 m K$^+$ + 2.5 m PZ; ◊, 40 °C, □, 60 °C, 3.6 m K$^+$ + 3.6 m PZ. Lines: OLS Approximations.

15.3.2 *Specific Heat Capacity*

As stated in Chapter VI, Aspen Plus™ calculates the liquid phase heat capacity of a *mixture* (CPMX) by taking the derivative of the liquid enthalpy at constant pressure:

$$H_m^l\left(T+\Delta T\right)-H_m^l\left(T\right)=\int_{T}^{T+\Delta T} C_{p,m}^l\,dT \tag{15-33}$$

where the liquid enthalpy of a mixture is calculated by the following equation:

$$H_m^l\left(T\right)=\sum_i x_i H_i+\sum_k x_k H_k^{\infty}+H_m^E \tag{15-34}$$

for solvents:

$$H_i\left(T\right)=\Delta H_f^{ig}\left(T^{ref}\right)+\int_{T^{ref}}^{T} C_p^{ig}\,dT+\left[H_i\left(T,p\right)-H_i^{ig}\left(T,p\right)\right] \tag{15-35}$$

for molecular solutes (CO_2):

$$H_i\left(T\right) = H_i^{ig}\left(T\right) + RT\ln\left(\frac{H_{i,H_2O}}{P^{ref}}\right) \tag{15-36}$$

for cations or anions:

$$H_k^{\infty}\left(T\right) = \Delta H_{f,k}^{\infty}\left(T^{ref}\right) + \int_{T^{ref}}^{T} C_{p,k}^{\infty} dT \tag{15-37}$$

Where
ΔT is the perturbation in temperature from T,
H_m^E is the excess enthalpy of the mixture,
$\Delta H_f^{ig}\left(T^{ref}\right)$ is the standard enthalpy of formation of component i at T^{ref},
T^{ref} is the reference temperature, 25.0 °C,
C_p^{ig} is the ideal gas heat capacity of component i,
H_i^{ig} is the ideal gas enthalpy of component i,
H_k^{∞} is the infinite dilution aqueous enthalpy of component k,
$\Delta H_{f,k}^{\infty}\left(T^{ref}\right)$ is the infinite dilution aqueous phase standard enthalpy of formation of component k at T^{ref},
$C_{p,k}^{\infty}$ is the infinite dilution aqueous phase heat capacity polynomial of component k.

Table 15.3-2 gives the coefficients for the infinite dilution aqueous phase heat capacity used in Aspen Plus™ based on the following expression:

$$C_{p,k}^{\infty}\left(\frac{J}{kmol \cdot K}\right) = C_1 + C_2 T\left(K\right) + C_3\left(T\left(K\right)\right)^2 + \frac{C_4}{T\left(K\right)} \tag{15-38}$$

Table 15.3-2. Infinite Dilution Aqueous Phase Heat Capacity Default Coefficients.

Parameter	Symbol	H^+	OH^-	HCO_3^{-1}	CO_3^{-2}	PZH^{+1}
CPAQ0-1	C_1	0.0	0.0	211387	1334017	603662
CPAQ0-2	C_2	0.0	-497.9	-882	-5565	-2518
CPAQ0-3	C_3	0.0	0.0	0.875	5.19	4.16
CPAQ0-4	C_4	0.0	0.0	-1.9E+07	-1.2E+08	-5.4E+08

Data in the form of specific heat capacity as a function of loading, molality, and temperature were used to adjust the coefficients for the binary interaction parameters of the elecNRTL model. An example of the experimental specific heat capacity from this work from 40 to 120 °C for 6 m K^+ + 1.2 m PZ and 3.6 m K^+ + 3.6 m PZ is shown in Figure 15.3-9 and Figure 15.3-10, respectively.

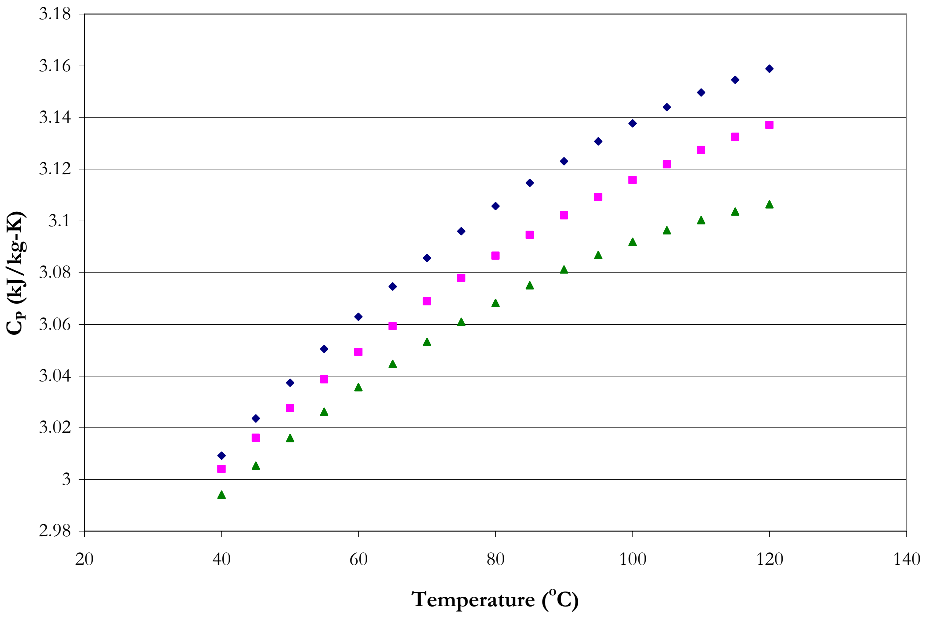

Figure 15.3-12. Specific Heat Capacity in Loaded (Ldg) 6 m K^+ + 1.2 m PZ Solutions from this work from 40 – 120 °C. Points: ♦, Ldg = 0.43, ■, Ldg = 0.53, ▲, Ldg = 0.57.

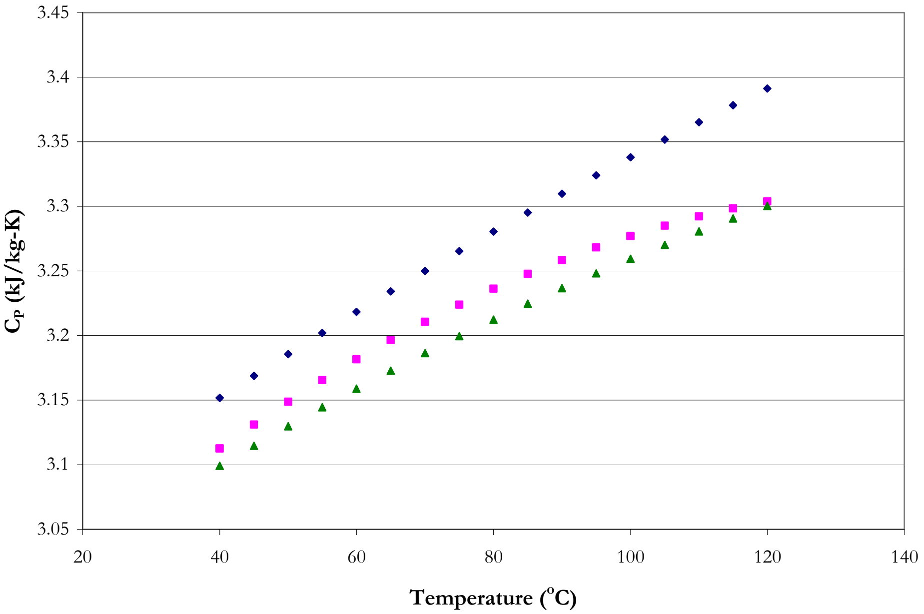

Figure 15.3-13. Specific Heat Capacity in Loaded (Ldg) 3.6 m K^+ + 3.6 m PZ Solutions from this work from 40 – 120 °C. Points: ♦, Ldg = 0.33, ■, Ldg = 0.42, ▲, Ldg = 0.47.

15.3.3 *Enthalpy of CO_2 Absorption*

Data in the form of the enthalpy of CO_2 absorption for aqueous potassium plus piperazine solutions as a function of loading and temperature were used to adjust the activity coefficients for each liquid phase component in the H_2O-K_2CO_3-PZ-CO_2 system through the simultaneous regression of the binary interaction parameters in the elecNRTL model.

For our true quaternary ternary system (H_2O, K_2CO_3, PZ, and CO_2), the Gibbs-Helmholtz equation can be used to represent the differential enthalpy of CO_2 absorption:

$$-\frac{\Delta H_{abs}}{R}=\left(\frac{d\, f^{v}_{CO_2}}{d\left(1/T\right)}\right)_{x_{CO_2}} \qquad 15\text{-}39$$

The heat released can be measured by direct calorimetry or estimated from CO_2 solubility data. The later has been shown to have a high degree of uncertainty on the order of ± 20 to 30 % as reported by Lee et al. (1974). However, if the loading span within one CO_2 addition can be kept rather low, the measurements give enthalpy data close to differential values in loading rather than integral as reported by Kim et al. (2007) with respect to the total amount of heat released from zero loading to the experimental loading data point as shown by the following expression:

$$-\Delta H_{\mathrm{int}} = -\int_0^{\alpha} \Delta H_{diff}\, \mathrm{d}\alpha \qquad 15\text{-}40$$

Where
α is the loading of the solution, mole CO_2/mole K^+ + 2·mole PZ.

In an international collaboration between The University of Texas and the Norwegian University of Science and Technology, Kim (2007) determined the differential enthalpy of CO_2 absorption for 5 m K^+ + 2.5 m PZ and 6 m K^+ + 1.2 m PZ, based on a consistent experimental method she developed for monoethanolamine [Kim et al. (2007)] at 40, 60/80, and 120 °C and over the range of loading from 0.4 – 0.6 mol CO_2/mol K^+ + 2·mol PZ for use in this work.

Aspen Plus^{TM} was never designed to regress differential enthalpy of CO_2 absorption data; nevertheless in this work we were able to develop a fortran subroutine to regress experimental differential enthalpy of CO_2 absorption data within DRS utilizing the following schema presented in Figure 15.3-14.

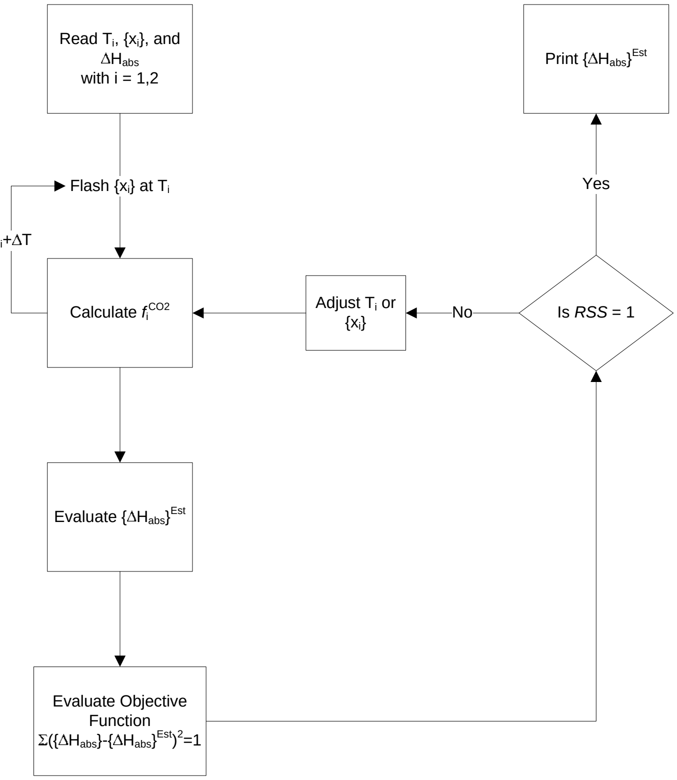

Figure 15.3-14. Differential Enthalpy of CO_2 Absorption Fortran Subroutine Schema Developed for Aspen Plus™.

Within DRS, the user inputs the temperature in Kelvin, the apparent liquid phase mole fractions for PZ, K_2CO_3, CO_2, and H_2O, and the differential enthalpy of CO_2 absorption. The fortran subroutine then calls a FLSH_FLASH subroutine within Aspen Plus™ and performs a temperature-vapor fraction flash calculation. Once the FLASH subroutine converges, the fortran subroutine calculates the CO_2 vapor phase fugacity based on the estimated partial pressure and the vapor phase fugacity coefficient of CO_2, respectively. The fortran subtroutine then numerically differentiates the vapor phase fugacity of CO_2 at T and (T + 1 K) based on Equation 15-39.

Finally, the fortran subroutine exports the estimated enthalpy of CO_2 absorption to DRS. DRS then tries to minimize the difference between the estimated enthalpy of CO_2

absorption calculated from the fortran subroutine and the experimental value utilizing the Maximum Likelihood Method within Aspen Plus™ to minimize the overall objective function while adjusting each property variable. For more information about the complete fortran subroutine code, please refer to Appendix K.

An example of the experimental differential enthalpy of CO_2 absorption used in this work from Kim (2007) at 40, 60, 80, and 120 °C for 5 m K^+ + 2.5 m piperazine is shown in Figure 14.3-15.

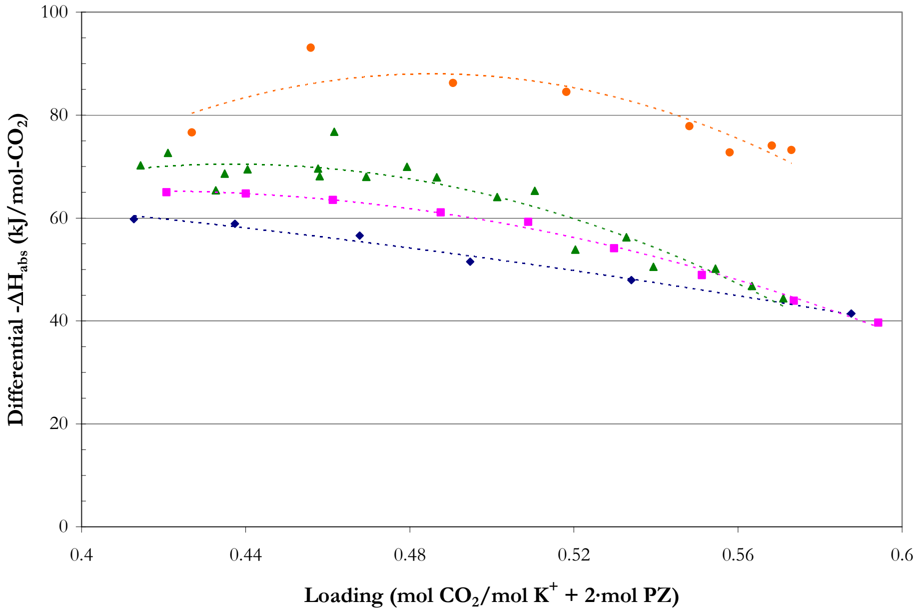

Figure 15.3-15. Negative Differential Enthalpy of CO_2 Absorption in 5 m K^+ + 2.5 m PZ at 40, 60, 80, and 120 °C from Kim (2007). Points: ♦, 40 °C, ■, 60 °C, ▲, 80 °C, ●, 120 °C. Lines: OLS Approximations.

Figure 15.3-15 illustrates that the enthalpy of CO_2 absorption increases as temperature increases and are similar to trends in other amine based systems (i.e. MEA and PZ). In this work, we decided to limit the enthalpy of CO_2 absorption data over the loading range from 0.4 to 0.6 mol CO_2/mol K^+ + 2·mol PZ for consistency with experimental CO_2

solubility measurements. Please refer to Appendix H for experimental enthalpy of CO_2 absorption measurements beyond a loading of 0.6.

15.3.4 ***NMR Speciation***

Data in the form of proton H^1 NMR speciation for aqueous potassium plus piperazine solutions as a function of loading, concentration and temperature, were used to adjust the activity coefficients for each liquid phase component in the H_2O-K_2CO_3-PZ-CO_2 system through the simultaneous regression of the binary interaction parameters in the elecNRTL model.

For our true component quaternary system (H_2O, K_2CO_3, PZ, and CO_2), the following equations can be used to represent the liquid phase equilibrium for the NMR speciation data as reported by Cullinane (2005).

$$n^*_{PZ} = n_{PZ} + n_{PZH^+} \qquad \text{15-41}$$

$$n^*_{H/PZCOO^{-1}} = n_{H^+PZCOO^{-1}} + n_{PZCOO^{-1}} \qquad \text{15-42}$$

$$n^*_{PZ\left(COO^{-1}\right)_2} = n_{PZ\left(COO^{-1}\right)_2} \qquad \text{15-43}$$

Where
n_i is the true number of moles for each component per kilogram of water corresponding to the relative proton NMR peak areas,
ni* is the pseudo-component quantity based on experimental NMR data.

Cullinane (2005) measured the proton peak areas or intensities for the corresponding protons associated with each molecule(s). The main drawback with proton NMR speciation analysis is not having the ability to measure the loading of the solution as compared to carbon C^{13} NMR speciation described in Chapter XIII. The loading of the solution has to be determined a *priori* which may result in a discrepancy between the loading at the time of the NMR experiment and at the time of the CO_2 analysis. We would recommend that future work should concentrate on validating the reported NMR speciation reported from Cullinane (2005) using carbon C^{13} NMR speciation for loaded potassium plus piperazine solutions due to the possible error in the liquid phase loading analysis as previously stated.

Aspen Plus™ was never designed to regress NMR speciation data; nevertheless, in this work we were able to develop a fortran subroutine to regress experimental NMR speciation data within DRS, utilizing the schema presented in Figure 15.3-16. Within DRS, the user inputs the temperature in Kelvin and the pseudo-component mole fractions for PZ, $H/PZCOO^{-1}$, $PZ(COO^{-1})_2$, K_2CO_3, CO_2, and H_2O. The fortran subroutine then calculates the apparent component mole fractions based on the following expressions:

$$x_{PZ}^{A} = x_{PZ}^{*} + x_{H/PZCOO^{-1}}^{*} + x_{PZ\left(COO^{-1}\right)_2}^{*} \qquad 15\text{-}44$$

$$x_{CO_2}^{A} = x_{CO_2}^{*} + x_{H/PZCOO^{-1}}^{*} + 2 \cdot x_{PZ\left(COO^{-1}\right)_2}^{*} \qquad 15\text{-}45$$

The fortran subroutine then calls a FLSH_FLASH subroutine within Aspen Plus™ and performs a temperature-vapor fraction flash calculation. Once the FLASH subroutine converges, the fortran subroutine calls a PPSTUB_GETTRU subroutine within Aspen Plus™ and extracts the true species mole fractions from the converged flash calculation.

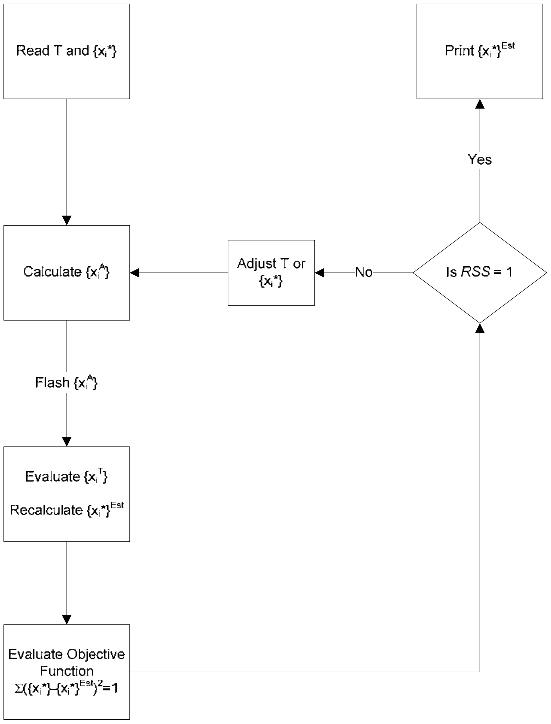

Figure 15.3-16. NMR Speciation Fortran Subroutine Schema Developed for Aspen Plus™.

The fortran subroutine then takes the true species mole fractions and calculates the estimated pseudo-component mole fractions based on the following expressions:

$$x_{PZ}^{*,est} = x_{PZ} + x_{PZH^+} \qquad 15\text{-}46$$

$$x_{H/PZCOO^{-1}}^{*,est} = x_{H^+PZCOO^{-1}} + x_{PZCOO^{-1}} \qquad 15\text{-}47$$

$$x_{PZ\left(COO^{-1}\right)_2}^{*,est} = x_{PZ\left(COO^{-1}\right)_2} \qquad 15\text{-}48$$

$$x_{K_2CO_3}^{*} = \frac{x_{K^{+1}}^{*}}{2} \qquad 15\text{-}49$$

$$x_{CO_2}^{*,est} = x_{CO_2} + x_{CO_3^{-2}} + x_{HCO_3^{-1}} - x_{K_2CO_3}^{*} \qquad 15\text{-}50$$

Finally, the fortran subroutine compares the estimated pseudo-component mole fractions to the experimental pseudo-component mole factions and calculates one minus the residual sum of squares (RSS). DRS then tries to minimize the difference between the RSS calculated from the fortran subroutine and the user property supplied to DRS by the user, a value of one, while DRS utilizes the Maximum Likelihood Method within Aspen Plus^{TM} to minimize the overall objective function while adjusting each property variable. For more information about the complete fortran subroutine code, please refer to Appendix K.

An example of the experimental NMR speciation used in this work from Cullinane (2005) for 5 m K^+ + 2.5 m piperazine solutions at 27, 40, and 60 °C is shown in Figure 15.3-17, Figure 15.3-18, and Figure 15.3-19, respectively.

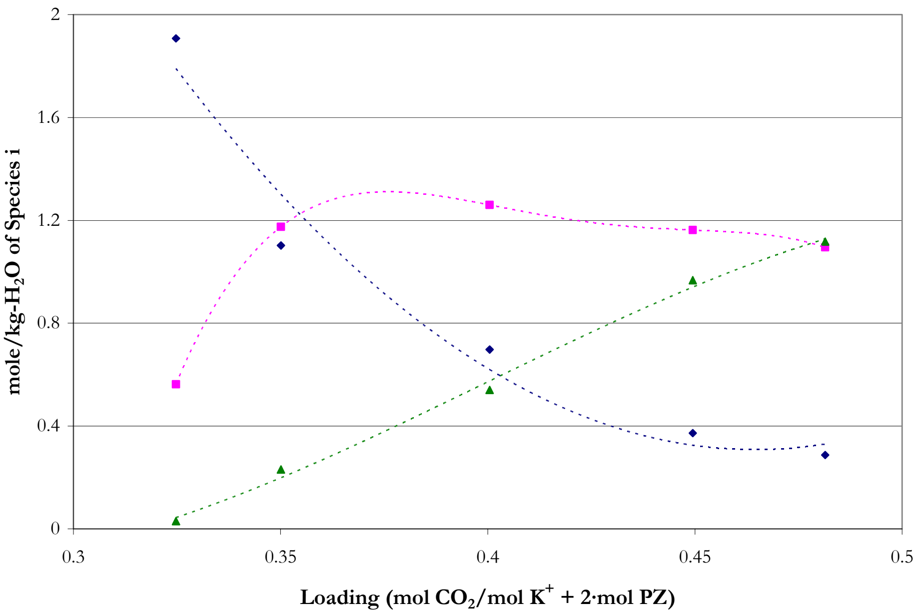

Figure 15.3-17. Liquid Phase Speciation from H1 NMR at 27 °C from Cullinane (2005). Points: ♦, PZ+PZH^{+1}, ■, H^+PZCOO^{-1}+$PZCOO^{-1}$, ▲, $PZ(COO^{-1})_2$. Lines: OLS Approximations.

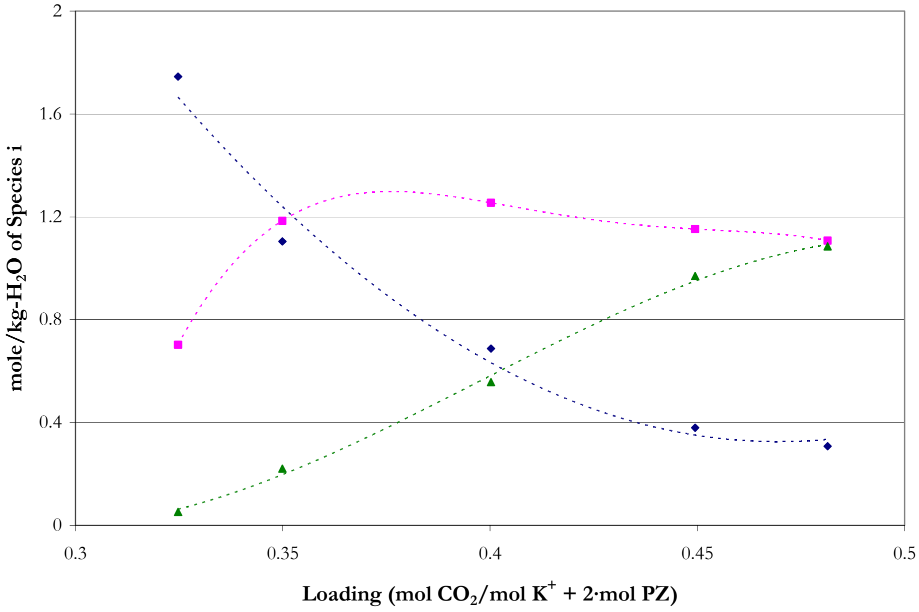

Figure 15.3-18. **Liquid Phase Speciation from H1 NMR at 40 °C from Cullinane (2005). Points: ♦, $PZ+PZH^{+1}$, ■, $H^+PZCOO^{-1}+PZCOO^{-1}$, ▲, $PZ(COO^{-1})_2$. Lines: OLS Approximations.**

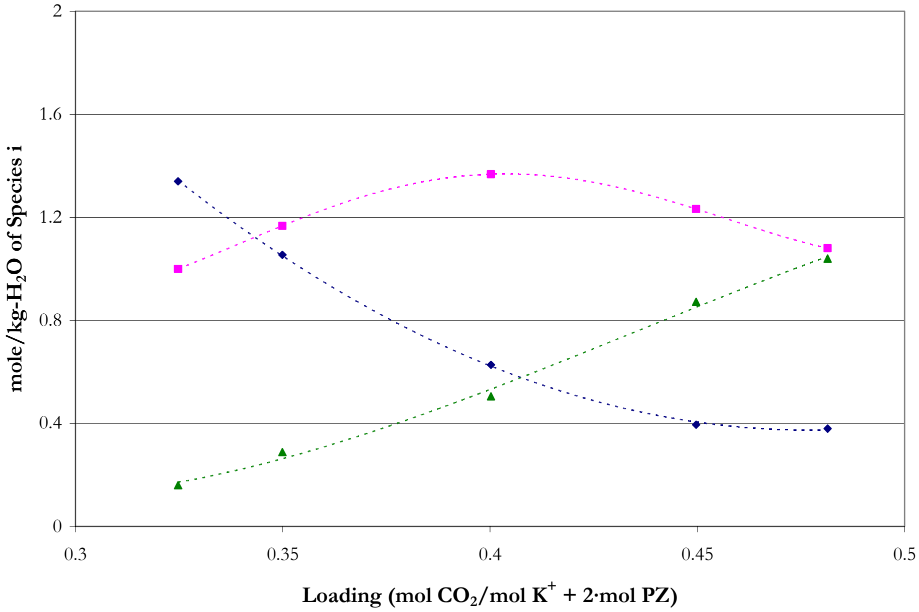

Figure 15.3-19. **Liquid Phase Speciation from H1 NMR at 60 °C from Cullinane (2005). Points: ♦, $PZ+PZH^{+1}$, ■, $H^+PZCOO^{-1}+PZCOO^{-1}$, ▲, $PZ(COO^{-1})_2$. Lines: OLS Approximations.**

15.3.5 *Solid Solubility*

Data in the form of solid solubility, which measures the dissolution temperature of the solid phase, vis-à-vis synthetic method, as a function of molality and temperature, was used to adjust the temperature dependent equilibrium constant for the following precipitation reaction of dipotassium piperazine dicarbamate as described in Chapter V.

$$K_2PZ\left(COO\right)_2\left(s\right)\leftrightarrow 2K^{+}+PZ\left(COO^{-1}\right)_2 \tag{15-51}$$

Experimental solid solubility visual observations from this work were used to regress coefficients to define the chemical equilibrium constant as a linear temperature dependent function due to the limited thermodynamic data available for the characterization of the solid phase.

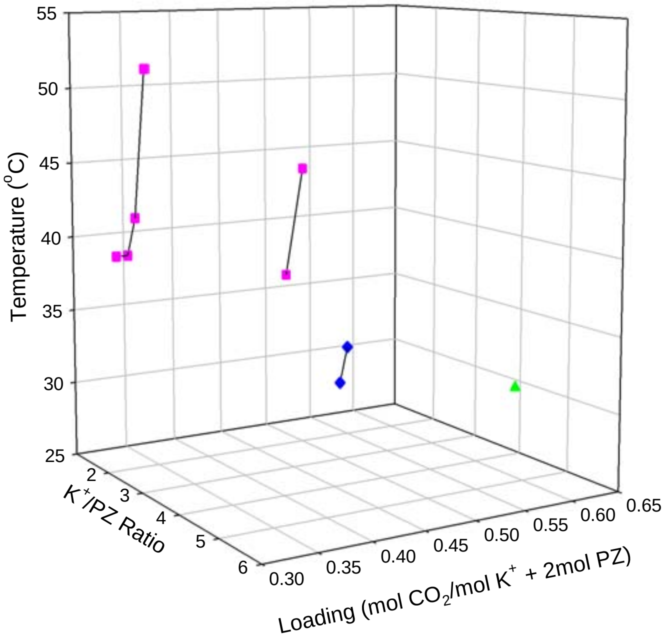

Figure 15.3-20. Solid Solubility of Aqueous K_2CO_3 Plus PZ Mixtures as Presented in Chapter V. Points: ♦, 5 m K^+ + 2.5 m PZ, ■, 5 m K^+ + 3.6 m PZ, ▲, 6 m K^+ + 1.2 m PZ.

15.4 Data Regression

There are three types of binary interaction parameters in the elecNRTL model: molecule-molecule, $\tau_{m,m'}$ and $\tau_{m',m}$; molecule-electrolyte, $\tau_{m,ca}$ and $\tau_{ca,m}$; electrolyte-electrolyte (with a common cation or anion) $\tau_{ca,ca'}$ and $\tau_{ca',ca}$ or $\tau_{ca,c'a}$ and $\tau_{c'a,ca}$; and the molecule-electrolyte nonrandomness factor, $\alpha_{ca,m}$. Chen and Evans (1986) noted that in their regression attempts it was not always possible to obtain statistically significant results for all four types of binary interaction parameters. In this work, the molecule-electrolyte nonrandomness parameter was set to an arbitrary value of $\alpha_{ca,m} = 0.2$ for all correlations involving electrolyte systems as suggested by Chen and Evans (1986). In this work, the electrolyte – electrolyte parameters are generally negligible and were assumed to be zero.

For the elecNRTL model, default values for molecule-electrolyte and electrolyte-molecule interactions are given in Table 15.4-1.

Table 15.4-1. Default Binary Interaction Parameters for the elecNRTL Model in Aspen Plus™.

Binary Interaction Pairs	τ
Molecule-electrolyte	10
Electrolyte-molecule	-2
Water-electrolyte	8
Electrolyte-water	-4

The energy parameters are adjusted to provide the best fit to the data. The binary interaction parameters were assumed to be temperature dependent and were fitted to the following function of temperature:

$$\tau_{m,ca} = A_{m,ca} + \frac{B_{m,ca}}{T} \qquad 15\text{-}52$$

$$\tau_{ca,m} = A_{ca,m} + \frac{B_{ca,m}}{T} \qquad 15\text{-}53$$

where electrolyte-electrolyte interactions follow a similar form as given above. A list of the aqueous electrolyte data sets that were examined in this work is given in Table 15.4-2. The column labels σ_T , σ_{PCO2} , σ_{PPZ} , σ_{x_i} , σ_{y_i} , σ_{Cp} , $\sigma_{\Delta H}$, give relative (i.e. 2.0 %) or absolute (i.e. 0.01) standard error associated with the temperature, partial pressure of CO_2, partial pressure of PZ, liquid mole fraction, vapor mole fraction, the specific heat capacity, and the enthalpy of CO_2 absorption, respectively, with each data set. DRS suggested standard error default values were assigned unless otherwise stated by the author.

In this work, we assumed an error in loading equal to ~2 percent unless otherwise stated by the author. Skoog et al. (1996) reported that the relative standard deviation of a product or quotient is determined by the relative standard deviations of the numbers forming the computed result as illustrated by the following expressions.

$$y = \frac{a \times b}{c} \qquad 15\text{-}54$$

$$\frac{\sigma_y}{y} = \sqrt{\left(\frac{\sigma_a}{a}\right)^2 + \left(\frac{\sigma_b}{b}\right)^2 + \left(\frac{\sigma_c}{c}\right)^2} \qquad 15\text{-}55$$

Where
σ_i is the relative standard deviation for number i.

In Aspen Plus^{TM} the user can specify the standard deviation for a data point or a data set either in relative (i.e. percent error) or absolute terms.

Table 15.4-2. Experimental data used for regression of the H_2O-K_2CO_3-PZ-CO_2 systems.

	Obs.	T (^{o}C)	σ_T	σ_{PCO2}	σ_x	σ_{CO2}	σ_y	Source
P^{CO2}	136	40.0 – 120.0	0.01	2.0%	0.1%	0.22%	0	This work

	Obs.	T (^{o}C)	σ_T	σ_{PPZ}	σ_x	σ_{CO2}	σ_y	Source
P^{PZ}	83	40.0 – 60.0	0.01	2.0%	0.1%	0.22%	0	This work

	Obs.	T (^{o}C)	σ_T	σ_x	σ_{CO2}	σ_{Cp}	Source
Cp	136	40.0 – 120.0	0.1	0.1%	0.22%	2.0%	This work

	Obs.	T (^{o}C)	σ_T	σ_x	σ_{CO2}	$\sigma_{\Delta H}$	Source
ΔH_{abs}	97	40.0 – 120.0	0.01	0.1%	0.22%	2.0%	Kim(2007)

	Obs.	T (^{o}C)	σ_T	σ_x	σ_{CO2}	Source
NMR	54	27.0 – 60.0	0.01	1.0%	1.0%	Cullinane (2005)

Overall, 506 experimental data points were included in the model regression. Over the course of the model regression, four attempts were made to determine an optimum set of model parameters to adequately describe the H_2O-K_2CO_3-PZ-CO_2 system. The following discussion outlines each regression case.

In Case I, coefficients regressed in Chapter XIV for the H_2O-PZ-CO_2 system were fixed and not adjusted. Only molecule-electrolyte and electrolyte-molecule binary interaction parameters were regressed to the experimental database outlined in Table 15.4-2. Electrolyte-electrolyte binary interaction parameters were set to zero. In this case, we found that by only adjusting binary interaction parameters, experimental predictions did not adequately describe systematic trends presented in the experimental database.

In Case II, we expanded the regression to include data regressed in Chapter XIV for the H_2O-PZ-CO_2 system in addition to the experimental database outlined in Table 15.4-2. Coefficients for binary interaction parameters, the infinite dilution aqueous phase free energy of formation, the infinite dilution aqueous phase enthalpy of formation, and the infinite dilution aqueous phase heat capacity polynomial for piperazine carbamate, piperazine dicarbamate, and protonated piperazine carbamate were regressed. In Case II, we found the model was able to adequately describe a limited number of data sets but did not produce an overall model with the ability to describe systematic trends presented in both data sets. In addition, the model was unable to predict the correct solid solubility for the precipitation of $KHCO_3$ and $K_2PZ(COO)_2$ as described in Chapter V. This suggested that coefficients for the linear temperature dependent chemical equilibrium constants for the two precipitation reactions should be included within the overall data regression.

In Case III, we expanded the regression to include data regressed in Chapters XII and XIV for the H_2O-K_2CO_3-CO_2 and H_2O-PZ-CO_2 system in addition to the experimental database outlined in Table 15.4-2 and solid solubility for the precipitation of $KHCO_3$ and $K_2PZ(COO)_2$ as described in Chapter V. In Case III, we were limited by the number of adjustable parameters where we could include in the regression. All of the parameters regressed in Chapters XII and XIV plus binary interaction parameters identified to adequately describe systematic trends presented in the H_2O-K_2CO_3-PZ-CO_2 system would not fit in the DRS input form. As a result an overall global regression of the three systems was not possible and precipitation of $KHCO_3$ would not reflect the visual observations presented in Chapter V.

In our "last" and successful attempt, Case IV, coefficients for the binary interaction parameters regressed in Chapters XII and XIV for the H_2O-K_2CO_3-CO_2 and H_2O-PZ-CO_2 systems were fixed and not adjusted. Only binary interaction parameters associated with the H_2O-K_2CO_3-PZ-CO_2 system and coefficients for the infinite dilution aqueous phase free energy of formation, the infinite dilution aqueous phase enthalpy of formation, and the infinite dilution aqueous phase heat capacity polynomial for piperazine carbamate, piperazine dicarbamate, and protonated piperazine carbamate were regressed to the experimental database outlined in Table 15.4-2. This resulted in a very reasonable description of the experimental data except for the description of the specific heat capacity data. Efforts in all four cases were unsuccessful in predicting systematic trends presented within the experimental specific heat capacity data. When DRS was forced to fit the experimental data, systematic trends presented in CO_2 solubility, amine volatility, enthalpy of CO_2 absorption, and NMR speciation became skewed to unrealistic predictions. This would suggest that the experimental specific heat capacity may not be consistent with the experimental database presented in Table 15.4-2, but an analysis of the average experimental specific heat capacity as compared to model predictions will help to justify the validity of the experimental data.

Table 15.4-3 shows the regression summary statistics output for estimates of the adjustable binary parameter coefficients, the infinite dilution aqueous phase free energy of formation, the infinite dilution aqueous phase enthalpy of formation, and the infinite dilution aqueous phase heat capacity polynomial for piperazine carbamate, piperazine dicarbamate, and protonated piperazine carbamate after performing a nonlinear regression for the full model using DRS in Aspen Plus^{TM}.

Table 15.4-3. DRS Regression Output for Full H_2O-K_2CO_3-PZ-CO_2 System Model.

	i	j	k	Estimate	σ wrt Estimate
1	ΔG_{PZCOO}			-219798175	14861456
2	ΔH_{PZCOO}			-480595349	107218242
3-CP-A	$PZCOO^{-1}$			-10934868	23749467
4-CP-B	$PZCOO^{-1}$			32868	113126
5-CP-C	$PZCOO^{-1}$			5.08	149
6	ΔG_{PZCOO2}			-568456411	3038877
7	ΔH_{PZCOO2}			-844124384	51078182
8-CP-A	$PZ(COO^{-1})_2$			-661253	13076923
9-CP-B	$PZ(COO^{-1})_2$			-1993	48432
10-CP-C	$PZ(COO^{-1})_2$			-2.04	57.9
11	ΔG_{HPZCOO}			-278352287	127392
12	ΔH_{HPZCOO}			-521810729	12090721
13-CP-A	H^+PZCOO^{-1}			420610	8694248
14-CP-B	H^+PZCOO^{-1}			-2298	51210
15-CP-C	H^+PZCOO^{-1}			6.72	81
16-$A_{m,ca}$	H_2O	K^+	$PZCOO^{-1}$	16.2	28.1
17-$B_{m,ca}$	H_2O	K^+	$PZCOO^{-1}$	-343	9143
18-$A_{ca,m}$	K^+	$PZCOO^{-1}$	H_2O	-6.21	3.50
19-$B_{ca,m}$	K^+	$PZCOO^{-1}$	H_2O	-288	1267
20-$A_{m,ca}$	H_2O	K^+	$PZ(COO^{-1})_2$	-3.31	36.3
21-$B_{m,ca}$	H_2O	K^+	$PZ(COO^{-1})_2$	-35.1	2152
22-$A_{ca,m}$	K^+	$PZ(COO^{-1})_2$	H_2O	14.8	28.8
23-$B_{ca,m}$	K^+	$PZ(COO^{-1})_2$	H_2O	4.11	87.6
24-$A_{m,ca}$	H_2O	PZH^+	$PZ(COO^{-1})_2$	11.0	3.28
25-$B_{m,ca}$	H_2O	PZH^+	$PZ(COO^{-1})_2$	20.4	366
26-$A_{ca,m}$	PZH^+	$PZ(COO^{-1})_2$	H_2O	-0.244	2.67
27-$B_{ca,m}$	PZH^+	$PZ(COO^{-1})_2$	H_2O	-2.34	210
28-$A_{m,ca}$	PZ	K^+	HCO_3^{-1}	18.7	178
29-$B_{m,ca}$	K^+	HCO_3^{-1}	PZ	2.08	108
30-$A_{ca,m}$	PZ	K^+	$PZCOO^{-1}$	4.16	3.51
31-$B_{ca,m}$	K^+	$PZCOO^{-1}$	PZ	-4.85	13.8
32-$A_{m,ca}$	PZ	K^+	$PZ(COO^{-1})_2$	5.61	42.2
33-$B_{m,ca}$	K^+	$PZ(COO^{-1})_2$	PZ	3.53	40.8

Residual Sum of Squares:	141,532
Residual Root Mean Square:	23.7460
Degree of Freedom:	473

Recall that the standard error of an estimate is the estimated standard deviation of that statistic. Notice that eighteen of the estimates are smaller relative to their standard errors. Table 15.4-4 gives a complete description of the variability of the coefficient estimates which requires examining the correlations between the estimates.

Table 15.4-4 shows 18 highly negative and positive correlations out of a possible 561. The highly correlated parameters are between the temperature dependent coefficients and the respective constant for the each energy parameter estimate, but the correlation between other coefficients is relatively small, suggesting that a number of temperature dependent parameters might be usefully removed from the model without significant loss of information.

Table 15.4-4. Correlation Matrix of the Coefficient Estimates for the Full H_2O-K_2CO_3-PZ-CO_2 System Model

Parameter	1	2	3	4	5	6	7	8	9	10	11	12	13	14	15	16	17	18	19	20	21	22	23	24	25	26	27	28	29	30	31	32	33
1	1																																
2	0.46	1.00																															
3	-0.27	-0.54	1.00																														
4	0.30	0.48	-0.95	1.00																													
5	-0.29	-0.33	0.76	-0.92	1.00																												
6	0.00	-0.20	0.15	-0.05	-0.09	1.00																											
7	0.01	-0.22	0.25	-0.06	-0.18	0.68	1.00																										
8	0.09	0.34	-0.44	0.27	-0.02	-0.44	-0.76	1.00																									
9	-0.12	-0.34	0.40	-0.29	0.12	0.22	0.47	-0.92	1.00																								
10	0.10	0.19	-0.14	0.19	-0.23	0.25	0.23	0.36	-0.70	1.00																							
11	0.07	0.11	-0.11	0.06	0.00	-0.09	-0.11	0.11	-0.07	-0.03	1.00																						
12	-0.15	0.23	-0.44	0.26	0.01	-0.17	-0.49	0.46	-0.28	-0.16	0.26	1.00																					
13	0.06	0.12	-0.03	0.04	-0.05	0.13	0.09	0.16	-0.32	0.46	-0.06	-0.21	1.00																				
14	-0.06	-0.19	0.18	-0.13	0.05	-0.08	0.02	-0.31	0.42	-0.43	-0.01	-0.02	-0.96	1.00																			
15	0.06	0.24	-0.29	0.20	-0.05	0.03	-0.13	0.42	-0.49	0.38	0.06	0.23	0.85	-0.97	1.00																		
16	-0.41	-0.76	0.24	-0.35	0.44	-0.04	-0.17	-0.01	0.13	-0.28	-0.04	0.15	-0.13	0.10	-0.07	1.00																	
17	0.54	0.74	-0.26	0.38	-0.47	0.06	0.18	0.02	-0.14	0.28	0.04	-0.17	0.13	-0.10	0.07	-0.99	1.00																
18	-0.05	-0.37	0.24	-0.08	-0.15	0.16	0.20	-0.14	0.05	0.13	-0.01	-0.28	0.11	-0.02	-0.06	-0.12	0.16	1.00															
19	-0.01	0.36	-0.17	0.02	0.19	-0.19	-0.19	0.11	-0.03	-0.13	0.00	0.25	-0.10	0.03	0.05	0.11	-0.17	-0.98	1.00														
20	-0.27	-0.10	0.21	-0.26	0.28	0.26	-0.03	-0.10	0.10	-0.03	-0.02	0.07	0.03	-0.02	0.00	0.26	-0.31	-0.23	0.29	1.00													
21	-0.06	0.23	-0.39	0.31	-0.17	-0.06	-0.27	0.23	-0.14	-0.09	0.00	0.49	0.01	-0.10	0.18	0.02	-0.03	-0.25	0.18	0.10	1.00												
22	-0.26	0.05	0.08	-0.13	0.17	-0.23	-0.06	-0.09	0.11	-0.07	0.00	0.07	-0.13	0.13	-0.12	0.14	-0.22	-0.35	0.44	0.74	0.10	1.00											
23	0.00	-0.28	0.11	-0.01	-0.12	0.38	0.18	-0.15	0.06	0.12	-0.05	-0.08	0.29	-0.22	0.15	0.15	-0.11	0.27	-0.28	0.06	-0.12	-0.29	1.00										
24	0.21	-0.12	-0.14	0.13	-0.10	0.40	-0.09	0.20	-0.18	0.06	-0.01	0.23	0.09	-0.14	0.17	0.10	-0.01	0.21	-0.33	-0.30	0.23	-0.77	0.45	1.00									
25	-0.08	0.17	0.06	-0.05	0.02	-0.21	0.07	-0.10	0.08	-0.01	0.00	-0.18	-0.06	0.10	-0.12	-0.21	0.16	-0.08	0.14	0.04	-0.16	0.30	-0.51	-0.67	1.00								
26	0.08	0.10	-0.18	0.10	0.02	-0.03	-0.20	0.21	-0.17	0.02	0.00	0.23	0.04	-0.10	0.15	0.16	-0.15	-0.22	0.20	0.23	0.50	0.16	-0.16	0.05	-0.07	1.00							
27	-0.05	-0.27	0.42	-0.39	0.30	-0.02	0.11	-0.16	0.15	-0.06	-0.03	-0.30	-0.04	0.11	-0.17	0.16	-0.16	0.17	-0.09	0.07	-0.78	-0.02	0.20	-0.15	0.05	-0.27	1.00						
28	0.14	0.26	-0.42	0.38	-0.26	-0.15	-0.13	0.24	-0.20	0.02	0.05	0.11	-0.12	0.05	0.02	-0.22	0.24	-0.14	0.06	-0.30	0.25	-0.10	-0.48	0.08	-0.03	-0.10	-0.50	1.00					
29	0.15	0.23	-0.27	0.28	-0.24	0.05	0.02	0.10	-0.16	0.18	0.05	0.04	0.00	-0.04	0.07	-0.25	0.27	-0.05	0.00	-0.20	0.29	-0.06	-0.34	0.02	0.09	0.01	-0.80	0.60	1.00				
30	-0.31	-0.13	0.36	-0.36	0.30	0.15	0.15	-0.17	0.10	0.09	-0.03	-0.24	0.10	-0.02	-0.06	0.12	-0.19	-0.11	0.19	0.34	-0.22	0.22	0.10	-0.30	0.23	-0.09	0.24	-0.26	-0.10	1.00			
31	-0.03	0.20	-0.26	0.26	-0.23	-0.34	-0.17	0.26	-0.21	0.02	0.01	0.17	0.04	-0.09	0.12	-0.24	0.21	0.13	-0.12	-0.28	0.13	-0.09	-0.23	-0.01	0.03	0.00	0.03	0.20	-0.14	-0.57	1.00		
32	0.04	-0.06	0.04	-0.01	-0.03	0.20	0.04	0.07	-0.15	0.24	0.00	0.17	0.18	-0.18	0.15	0.03	-0.01	0.22	-0.23	0.29	0.11	0.06	0.24	0.11	-0.03	0.33	-0.06	-0.33	0.04	0.15	-0.01	1.00	
33	0.08	-0.03	0.04	0.07	-0.20	0.12	0.26	-0.27	0.19	0.04	0.01	-0.29	-0.06	0.10	-0.13	-0.20	0.21	0.21	-0.18	-0.06	-0.53	0.00	0.10	-0.21	0.12	-0.19	0.23	-0.18	0.02	-0.29	-0.08	-0.11	1.00

After performing backward elimination using DRS, the following "optimum" model regression summary statistics output for estimates of the adjustable binary parameter coefficients is shown in Table 15.4-5.

Table 15.4-5. DRS Regression Output for Optimum H_2O-K_2CO_3-PZ-CO_2 System Model.

	i	j	k	Estimate	σ wrt Estimate
1	ΔG_{PZCOO}			-218137150	2143552
2	ΔH_{PZCOO}			-481386606	80811382
3-CP-A	$PZCOO^{-1}$			-6828489	54832038
4-CP-B	$PZCOO^{-1}$			19071	170318
5-CP-C	$PZCOO^{-1}$			1.80	35.4
6	ΔG_{PZCOO2}			-579217142	1560262
7	ΔH_{PZCOO2}			-861319029	67212986
8-CP-A	$PZ(COO^{-1})_2$			-1197496	36207783
9-CP-B	$PZ(COO^{-1})_2$			-33117	530381
10-CP-C	$PZ(COO^{-1})_2$			107	1586
11	ΔG_{HPZCOO}			-273664898	916512
12	ΔH_{HPZCOO}			-521907884	36257838
13-CP-A	H^+PZCOO^{-1}			4501454	30891169
14-CP-B	H^+PZCOO^{-1}			-13231	94782
15-CP-C	H^+PZCOO^{-1}			-0.00512	0.449
16-$A_{m,ca}$	H_2O	K^+	$PZCOO^{-1}$	8.25	29.1
17-$A_{ca,m}$	K^+	$PZCOO^{-1}$	H_2O	-0.415	11.1
18-$A_{m,ca}$	H_2O	K^+	$PZ(COO^{-1})_2$	-3.31	36.3
19-$A_{ca,m}$	K^+	$PZ(COO^{-1})_2$	H_2O	14.8	28.8
20-$A_{m,ca}$	H_2O	PZH^+	$PZ(COO^{-1})_2$	8.2	29.1
21-$B_{m,ca}$	H_2O	PZH^+	$PZ(COO^{-1})_2$	4445	8926
22-$A_{ca,m}$	PZH^+	$PZ(COO^{-1})_2$	H_2O	-114	601
23-$B_{ca,m}$	PZH^+	$PZ(COO^{-1})_2$	H_2O	44926	194761
24-$A_{m,ca}$	PZ	K^+	HCO_3^{-1}	7.27	0.913
25-$B_{m,ca}$	K^+	HCO_3^{-1}	PZ	-7.85	7.84
26-$A_{ca,m}$	PZ	K^+	$PZCOO^{-1}$	6.49	7.51
27-$B_{ca,m}$	K^+	$PZCOO^{-1}$	PZ	7.81	73.1
28-$A_{m,ca}$	PZ	K^+	$PZ(COO^{-1})_2$	7.51	9.21
29-$B_{m,ca}$	K^+	$PZ(COO^{-1})_2$	PZ	7.99	12.3

Residual Sum of Squares:	138,147
Residual Root Mean Square:	22.1066
Degree of Freedom:	477

Notice that nine of the estimates are smaller relative to their standard errors. In comparing the estimates from the full model to the "optimum" model, there was relatively little difference between the estimated values. With the elimination of two parameters from the full model, the optimum model was unable to provide adequate predictions to the experimental data even though the sum of squares decreased by 2.45 percent.

Furthermore, none of the other possible submodels proposed by backward elimination were able to provide adequate predictions and capture systematic trends with the data sets. This may suggest that the full model may not be a physically significant thermodynamic model due to the number of parameters required to capture systematic trends presented in the experimental database. **In this work, we chose the full model to describe the interactions in the H_2O-K_2CO_3-PZ-CO_2 system**. We would recommend that future work limit the number of solvents included in the regression to improve the statistical fit for the binary interaction parameters listed in Table 15.4-3.

Estimated Binary Interaction Parameters

With the determination of the estimates for the binary interaction parameters known for the full model, we can use Equation 15-52 and Equation 15-53 to illustrate the temperature dependence of the molecule-electrolyte ($\tau_{m,ca}$), electrolyte-molecule ($\tau_{ca,m}$), water-electrolyte ($\tau_{m,ca}$), and electrolyte-water ($\tau_{ca,m}$) energy parameters as shown in Figure 15.4-1 through Figure 15.4-6.

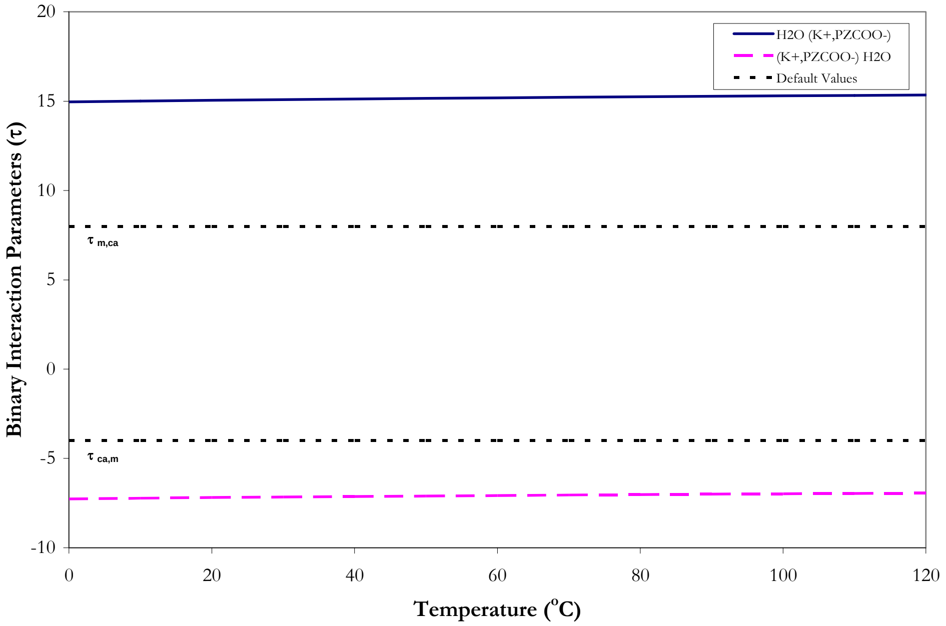

Figure 15.4-1. Binary Interaction Parameters for H_2O, K^+/$PZCOO^{-1}$.

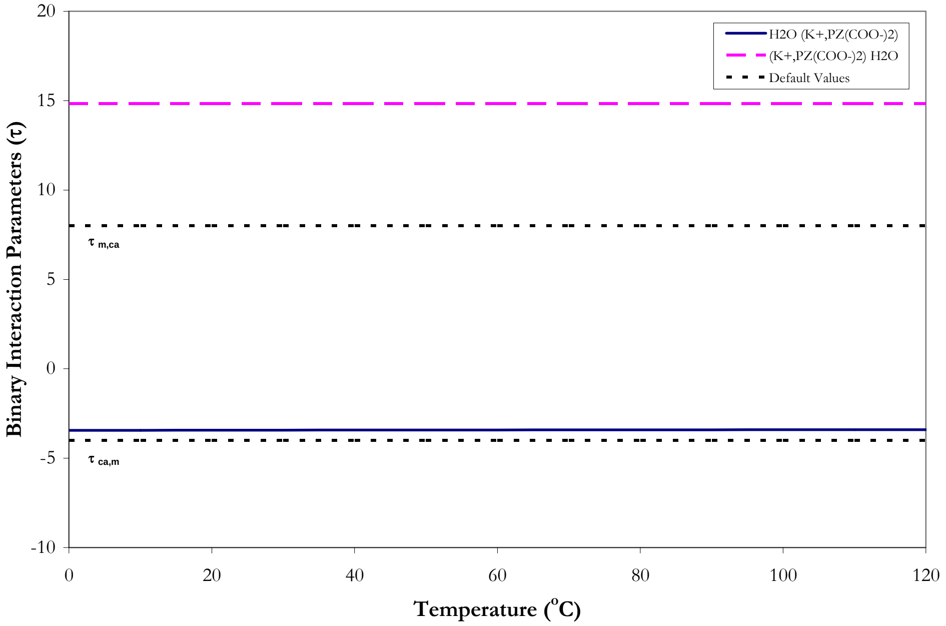

Figure 15.4-2. Binary Interaction Parameters for H_2O, $K^+/PZ(COO^{-1})_2$.

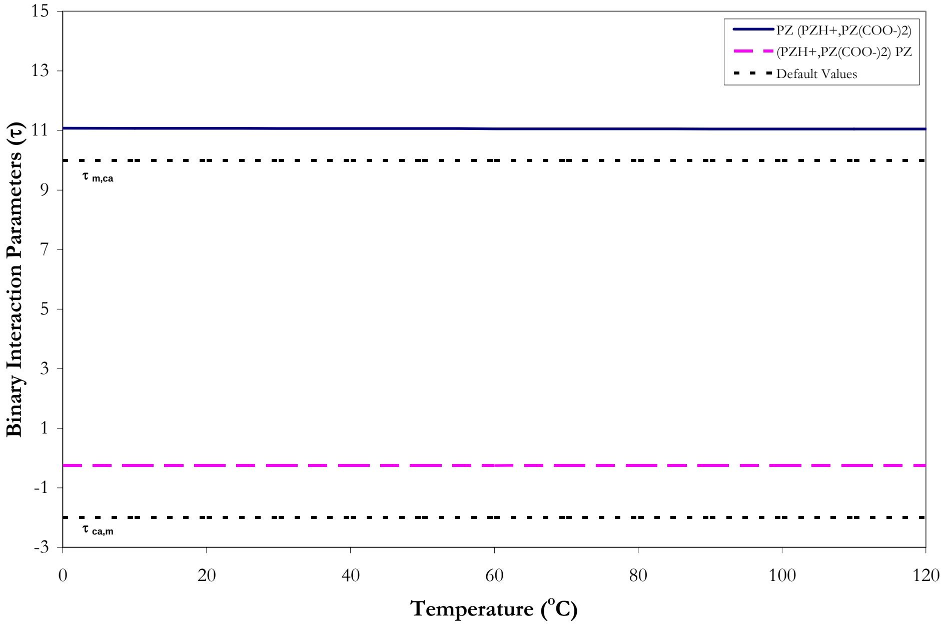

Figure 15.4-3. Binary Interaction Parameters for PZ, $K^+/PZ(COO^{-1})_2$.

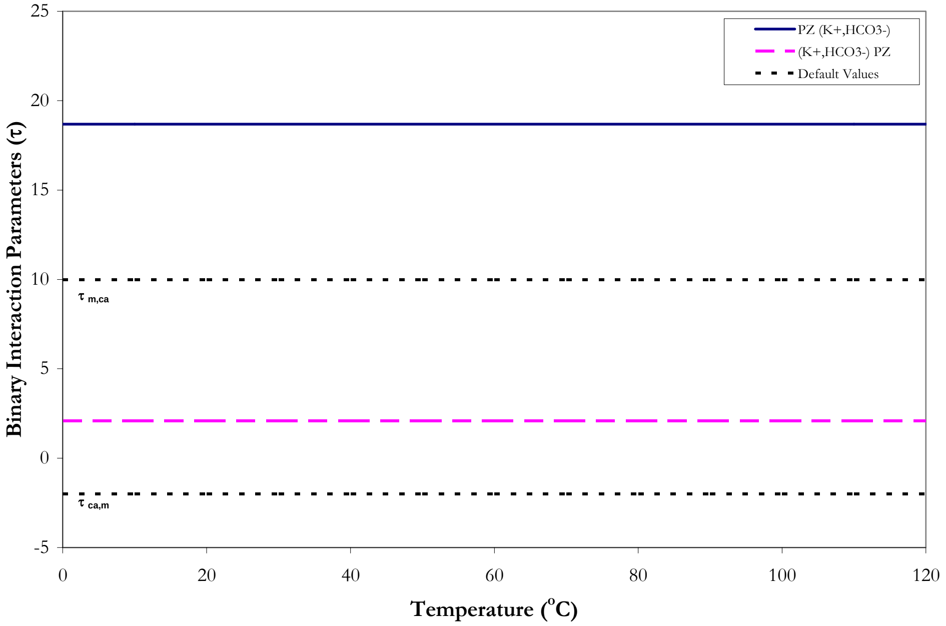

Figure 15.4-4. Binary Interaction Parameters for PZ, K^+/HCO_3^{-1}.

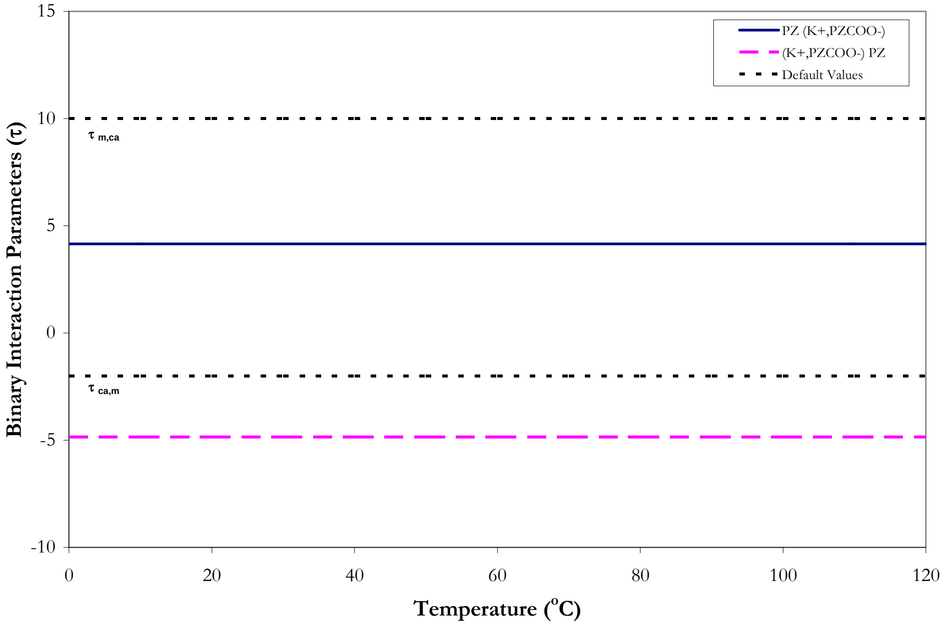

Figure 15.4-5. Binary Interaction Parameters for PZ, $K^+/PZCOO^{-1}$.

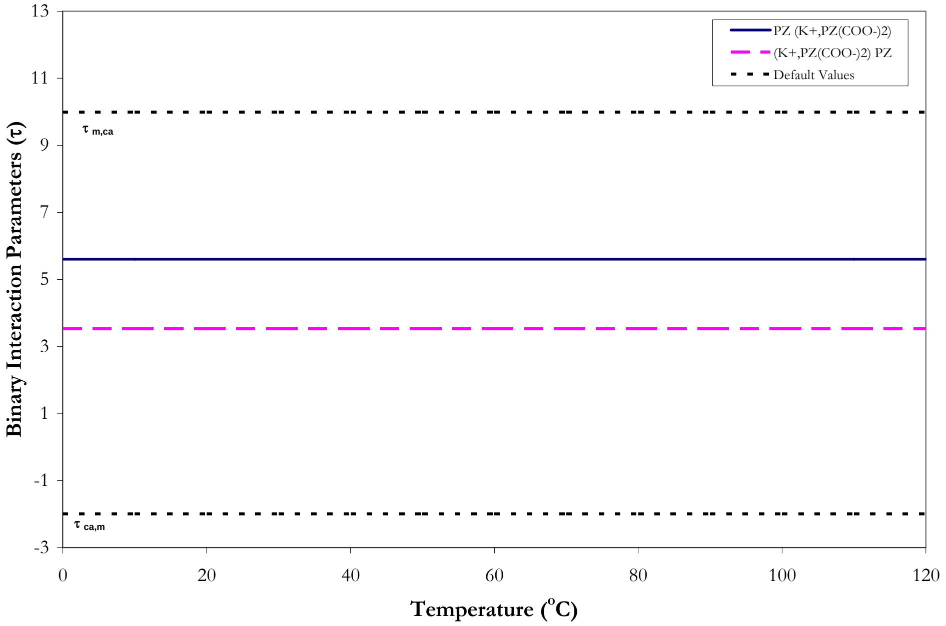

Figure 15.4-6. Binary Interaction Parameters for PZ, $K^+/PZ(COO^{-1})_2$.

15.4.1 *Full Model Results*

With the determination of the estimates for the binary interaction parameters known for the full model, a simple Aspen PlusTM Flash model was used to test the predictive capability of the H_2O-K_2CO_3-PZ-CO_2 model against literature data. For each data point, the deviation between the experimental and estimated values is expressed in terms of the average absolute relative deviation (AARD) given in Table 15.4-6 and Table 15.4-7. Overall, the model adequately described the H_2O-K_2CO_3-PZ-CO_2 property data listed above within an average absolute relative error of ± 15.48 percent, with the exception of a few outliers.

Table 15.4-6. Absolute Percent Relative Error for the H_2O-K_2CO_3-PZ-CO_2 Full Model.

CO_2 Solubility	**P^{CO2} AARD**	**Loading AARD**
This work	22.74	0.62
PZ Solubility	**P^{PZ}**	**Loading**
This work	57.78	1.44
Enthalpy of CO_2 Abs.	**ΔH_{ABS}**	**Loading**
Kim (2007)	4.46	1.76
Specific Heat Capacity	**Cp**	**Loading**
This work	16.48	0.2
Overall	**15.48**	**4.31**

Table 15.4-7. Absolute Percent Relative Error for the H_2O-K_2CO_3-PZ-CO_2 Full Model Speciation.

NMR Speciation	**$PZ+PZH^+$ AARD**	**$H^+PZCOO^-+PZCOO^-$ AARD**	**$PZ(COO^-)_2$ AARD**	**Loading AARD**
Cullinane (2005)	2.40	3.46	1.02	17.52

15.5 Full Model Predictions

In this work, we have compiled a large database of consistently high quality data needed to obtain a unique set of binary interaction parameters to describe the H_2O-K_2CO_3-PZ-CO_2 system. The remainder of this chapter will be devoted to using our model as a predictive tool as described in the subsequent sections.

Since coefficients for the precipitation of $KHCO_3$ were not included in Case IV, visual observations described in Chapter V are not consistent with model predictions in this chapter because the full model is predicting the precipitation of $PZ{\cdot}6H_2O$ which conflicts with results presented in Chapter V for the precipitation of $KHCO_3$ in mixtures of H_2O-K_2CO_3-PZ-CO_2. Experimental unit cell x-ray diffraction analysis of mixtures of H_2O-K_2CO_3-PZ-CO_2 by Lynch (2007) were based on the collection of a single crystal from the solid phase precipitation. There may have been a mixture of two solid phases at low loading within the submitted samples. Since the description of solid solubility was never a major research objective of this work; we would recommend that in future work powder x-ray diffraction would need to be completed on similar solution compositions to verify the results of the unit cell x-ray diffraction and model predictions. For these reasons, we regressed coefficients for the linear temperature dependent chemical equilibrium constant of $K_2PZ(COO)_2$ as described in section 15.5.5, but we chose not to include this precipitation reaction within the overall full model.

15.5.1 *CO_2 Solubility and Amine Volatility*

Figure 15.5-1 through Figure 15.5-9 give the results of fit for the experimental CO_2 solubility from this work to full model predictions over a temperature range from 20 to 120 °C. Predictions from Hilliard (2005) were not included due to discrepancies between the Cullinane (2005) data set and results presented in this work as described previously. Overall, the full model adequately describes systematic trends presented in the H_2O-K_2CO_3-PZ-CO_2 experimental database except for 2.5 m K^+ + 3.6 m PZ where model predictions tend to break down at low loading over the temperature range from 40 – 80 °C.

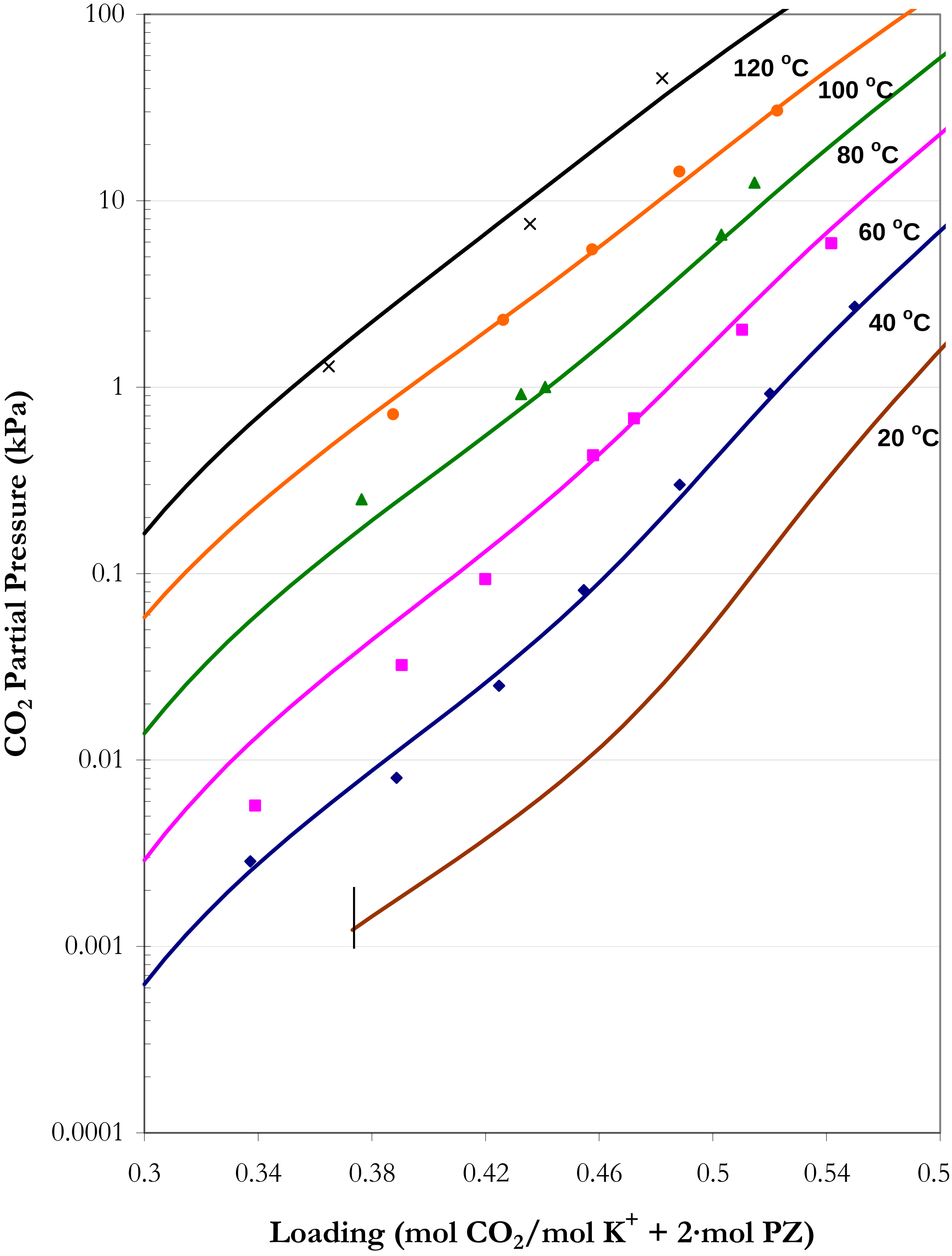

Figure 15.5-1. CO_2 Solubility in 5 m K^+ + 2.5 m PZ from 20 – 120 °C. Points: ♦, 40 °C, ■, 60 °C, ▲, 80 °C, ●, 100 °C, ×, 120 °C. Lines: elecNRTL Model Predictions. Vertical Line: Solid Solubility Boundary.

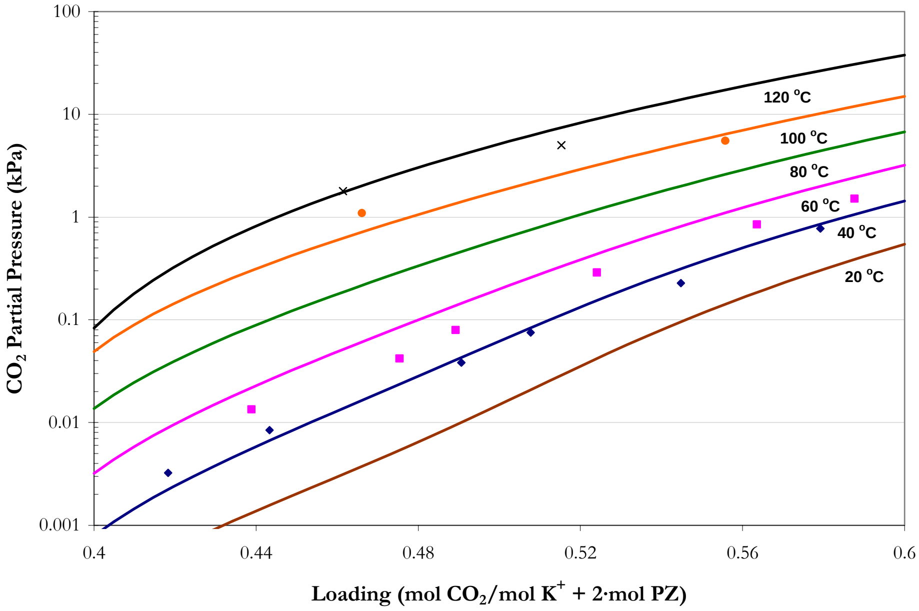

Figure 15.5-2. CO_2 Solubility in 3.6 m K^+ + 0.6 m PZ from 20 – 120 °C. Points: ♦, 40 °C, ■, 60 °C, ●, 100 °C, ×, 120 °C. Lines: elecNRTL Model Predictions.

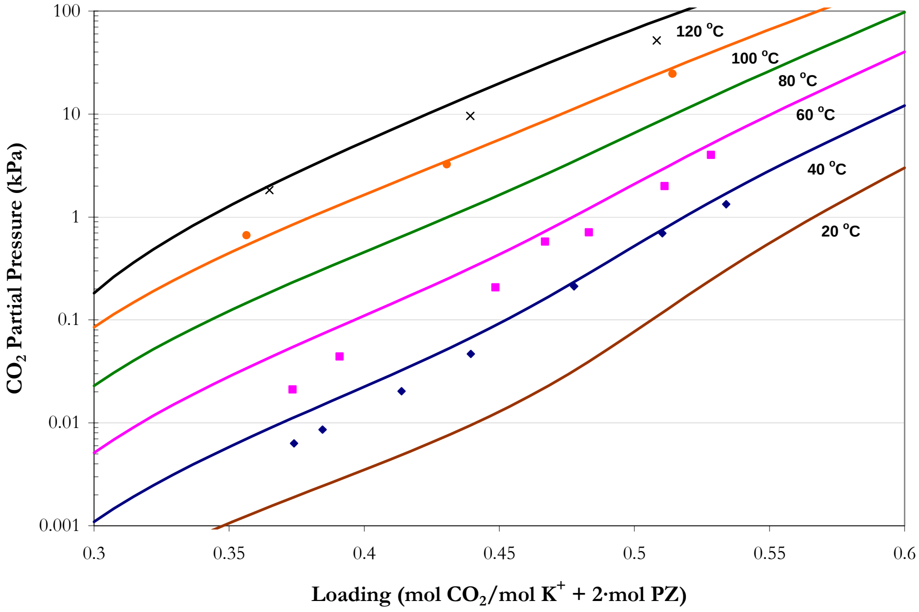

Figure 15.5-3. CO_2 Solubility in 3.6 m K^+ + 1.8 m PZ from 20 – 120 °C. Points: ♦, 40 °C, ■, 60 °C, ▲, 80 °C, ●, 100 °C, ×, 120 °C. Lines: elecNRTL Model Predictions.

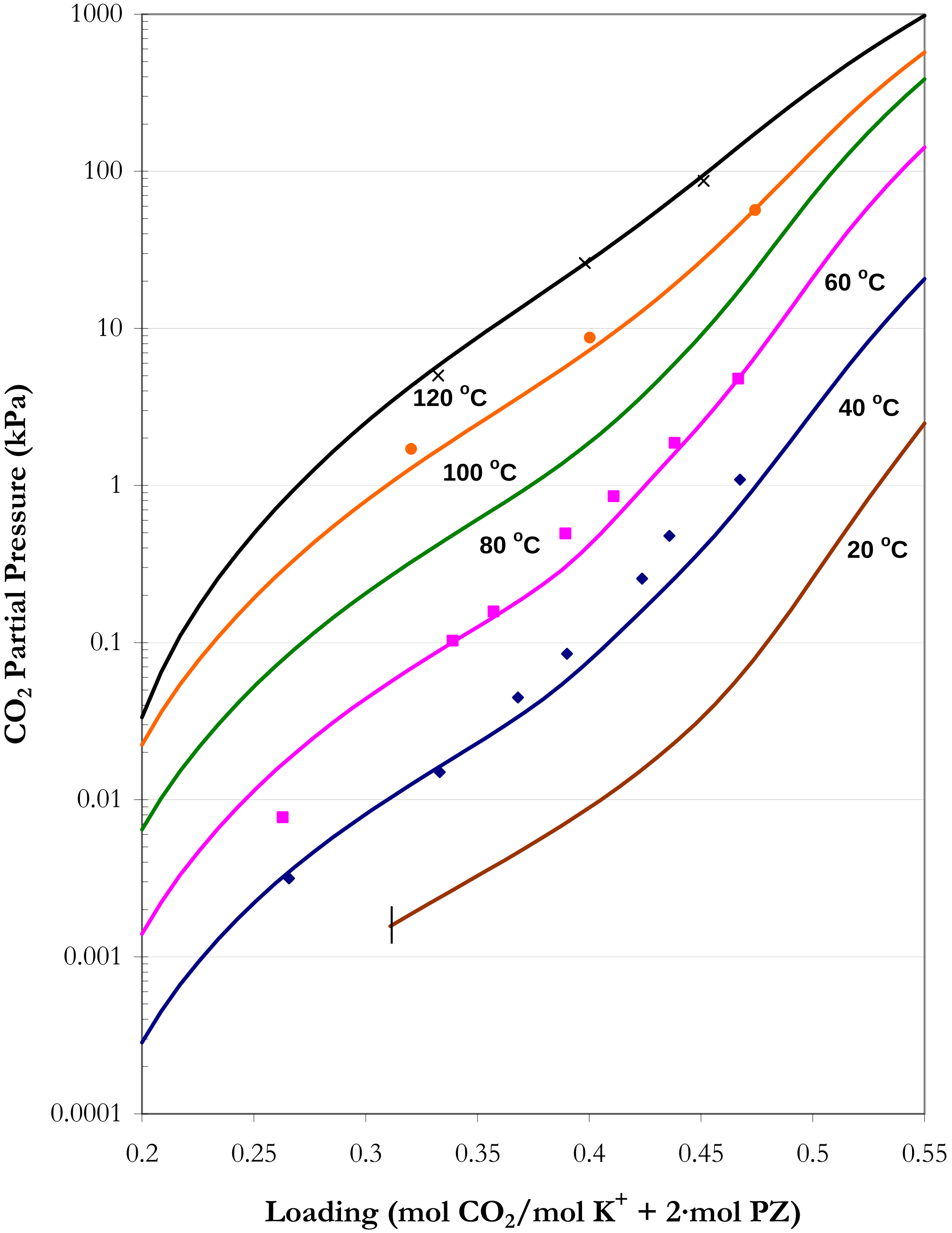

Figure 15.5-4. **CO_2 Solubility in 3.6 m K^+ + 3.6 m PZ from 20 – 120 °C. Points: ◆, 40 °C, ■, 60 °C, ▲, 80 °C, ●, 100 °C, ×, 120 °C. Lines: elecNRTL Model Predictions. Vertical Line: Solid Solubility Boundary.**

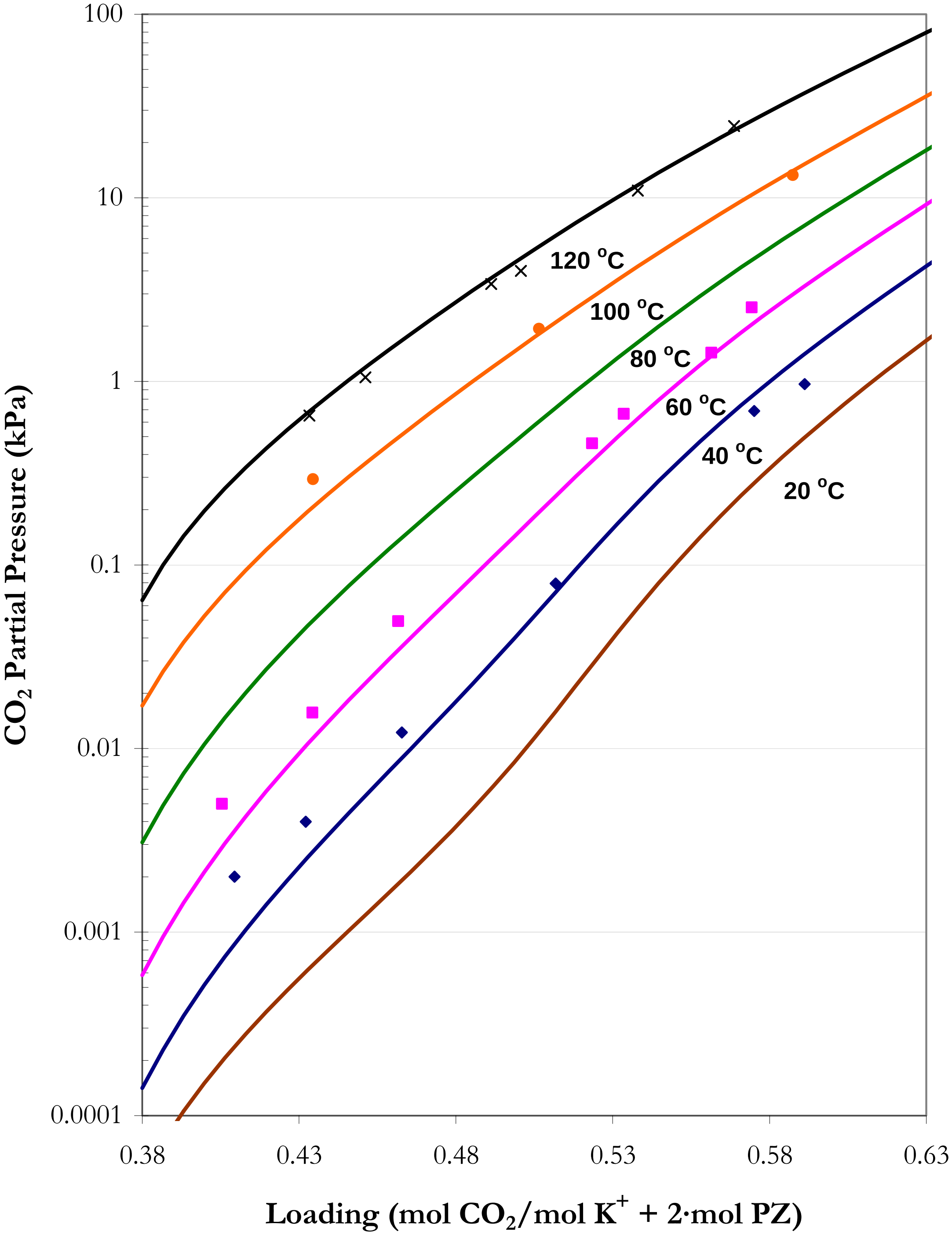

Figure 15.5-5. CO$_2$ Solubility in 6 m K$^+$ + 1.2 m PZ from 20 – 120 °C. Points: ◆, 40 °C, ■, 60 °C, ▲, 80 °C, ●, 100 °C, ×, 120 °C. Lines: elecNRTL Model Predictions.

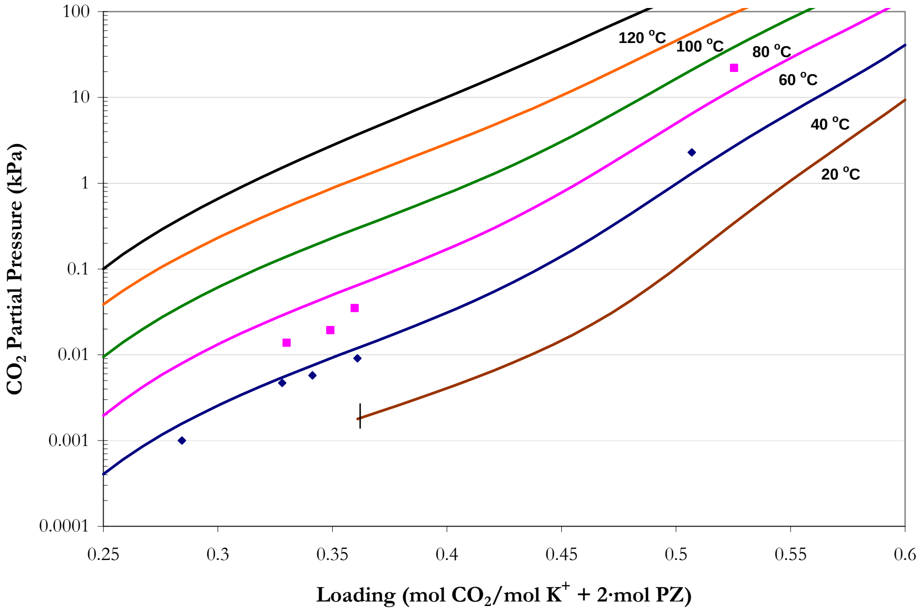

Figure 15.5-6. CO$_2$ Solubility in 5 m K$^+$ + 3.6 m PZ from 20 – 120 °C. Points: ♦, 40 °C, ■, 60 °C. Lines: elecNRTL Model Predictions. Vertical Line: Solid Solubility Boundary.

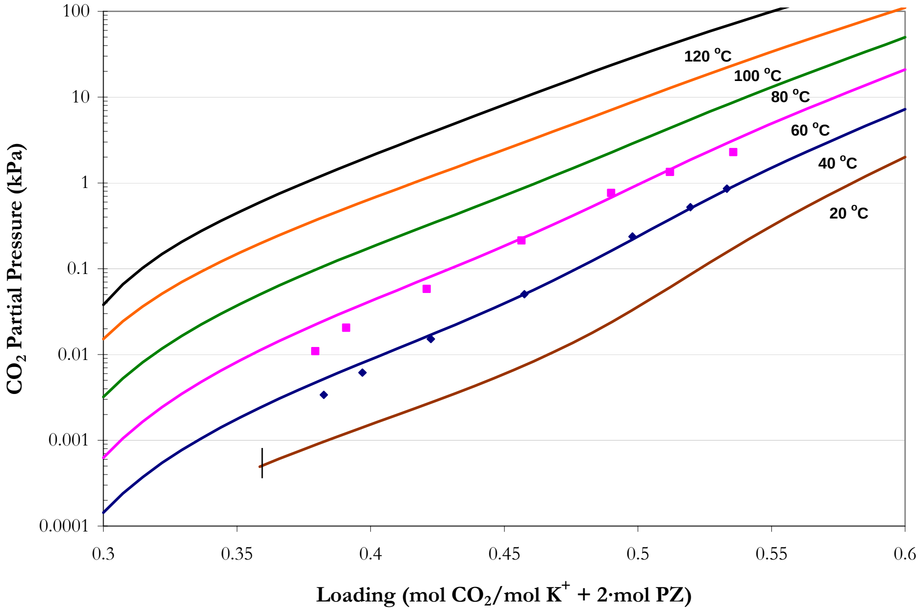

Figure 15.5-7. CO$_2$ Solubility in 5 m K$^+$ + 2 m PZ from 20 – 120 °C. Points: ♦, 40 °C, ■, 60 °C. Lines: elecNRTL Model Predictions. Vertical Line: Solid Solubility Boundary.

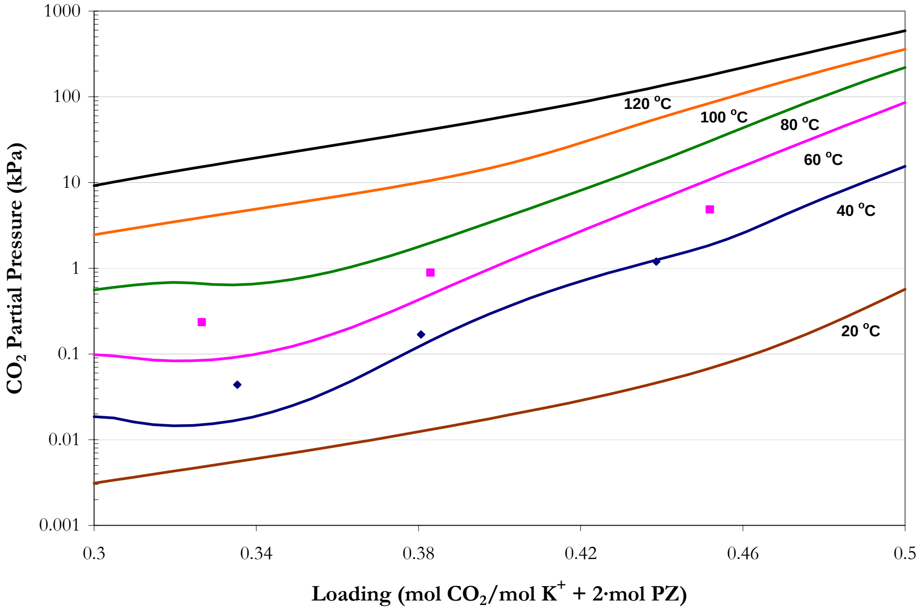

Figure 15.5-8. **CO_2 Solubility in 2.5 m K^+ + 3.6 m PZ from 20 – 120 °C. Points: ♦, 40 °C, ■, 60 °C. Lines: elecNRTL Model Predictions.**

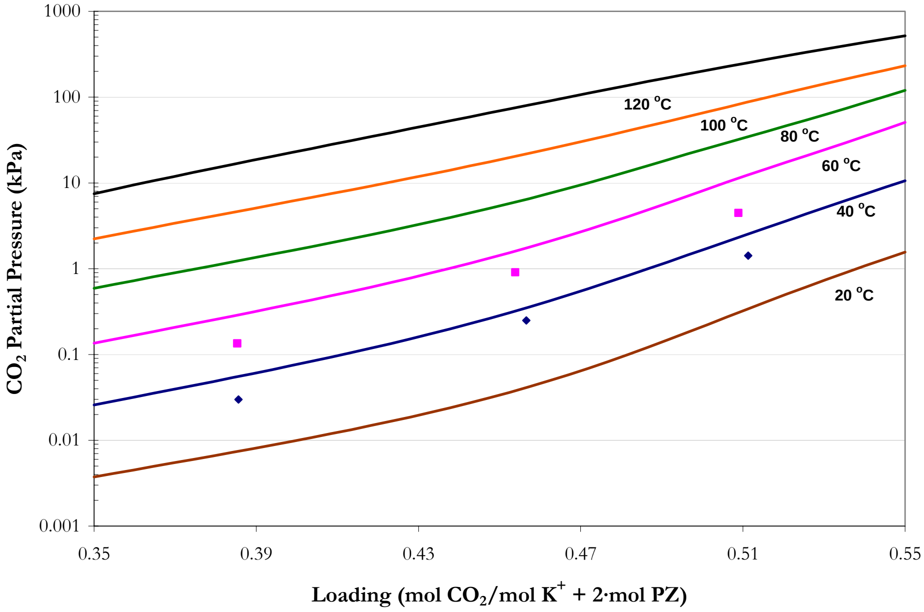

Figure 15.5-9. **CO_2 Solubility in 2.5 m K^+ + 2 m PZ from 20 – 120 °C. Points: ♦, 40 °C, ■, 60 °C. Lines: elecNRTL Model Predictions.**

CO_2 Solubility Differential Capacity

We can quantify the effects of CO_2 solubility in the above systems by illustrating trends in CO_2 solubility at 60 °C based on the differential capacity of the solvent between the range of 0.01 and 1.0 kPa as shown in Table 15.5-1.

Table 15.5-1 illustrates that 7 m MEA demonstrates a greater differential capacity as compared to piperazine or other mixed salt-amine systems. For mixed salt-amine systems, only systems composed of salt concentrations less than 5 m K^+ exhibited an increase in the differential capacity as compared to similar systems containing 5 m K^+. Overall, 2.5 m K^+ + 3.6 m PZ exhibited the largest differential capacity equal to 0.19 out of nine solvents studied as part of this work.

Table 15.5-1. Comparison of Differential Solvent Capacity Between CO_2 Partial Pressures of 0.01 and 1.0 kPa at 60 °C.

	Differential Capacity		
System	α	β	γ
7 m MEA	0.34	2.38	-
2 m PZ	0.23	0.90	0.23
5 m K^+ + 2.5 m PZ	0.13	1.32	0.26
3.6 m K^+ + 0.6 m PZ	0.15	0.71	0.59
3.6 m K^+ + 1.8 m PZ	0.14	1.02	0.28
3.6 m K^+ + 3.6 m PZ	0.15	1.58	0.22
6 m K^+ + 1.2 m PZ	0.13	1.06	0.44
5 m K^+ + 3.6 m PZ	0.12	1.43	0.20
5 m K^+ + 2 m PZ	0.13	1.18	0.29
2.5 m K^+ + 3.6 m PZ	0.19	1.83	0.25
2.5 m K^+ + 2 m PZ	0.16	1.06	0.27

α: mole CO_2/Total Alkalinity, β: mole CO_2/kg-H_2O,
γ: mole CO_2/2·mol PZ

PZ Volatility Predictions

Figure 15.5-10 through Figure 15.5-18 give the results of fit for the experimental PZ volatility from this work to full model predictions over a temperature range from 40 to 80 °C. Overall, the full model had a hard time fitting experimental PZ volatility for the H_2O-K_2CO_3-PZ-CO_2 system. This may be due to a PZ interaction parameter that was fixed within the H_2O-PZ-CO_2 regression, but efforts at adjusting parameters described in Chapter XIV did not result in substantial improvements in PZ volatility and were consequently left at their original regressed values.

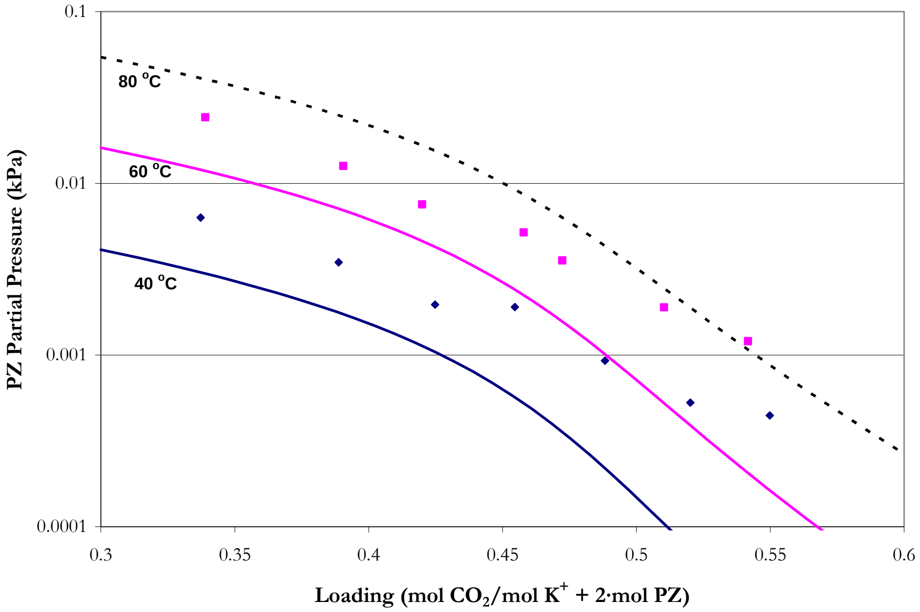

Figure 15.5-10. PZ Volatility in 5 m K^+ + 2.5 m PZ from 40 – 80 °C. Points: ♦, 40 °C and ■, 60 °C. Lines: elecNRTL Model Predictions.

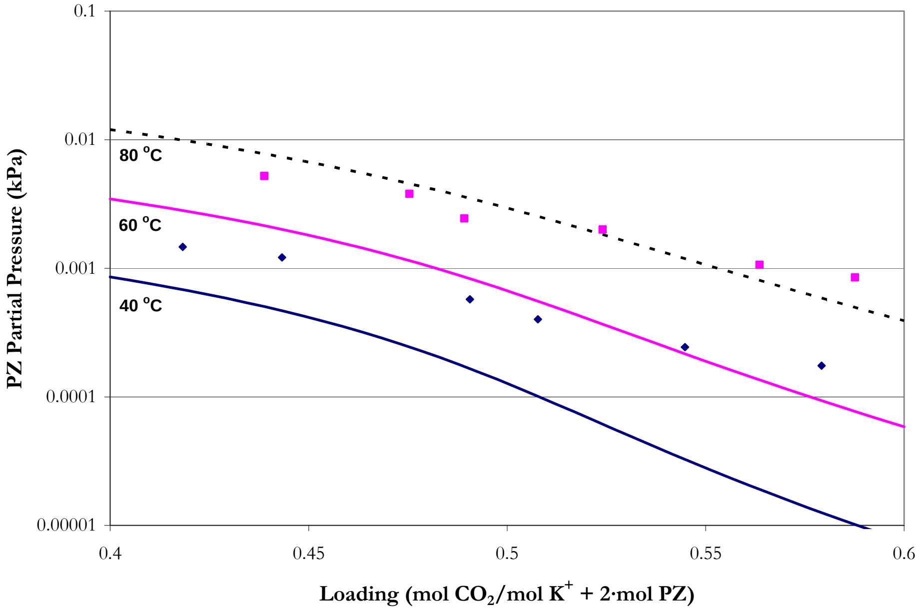

Figure 15.5-11. PZ Volatility in 3.6 m K^+ + 0.6 m PZ from 40 – 80 ^oC. Points: ♦, 40 ^oC and ■, 60 ^oC. Lines: elecNRTL Model Predictions.

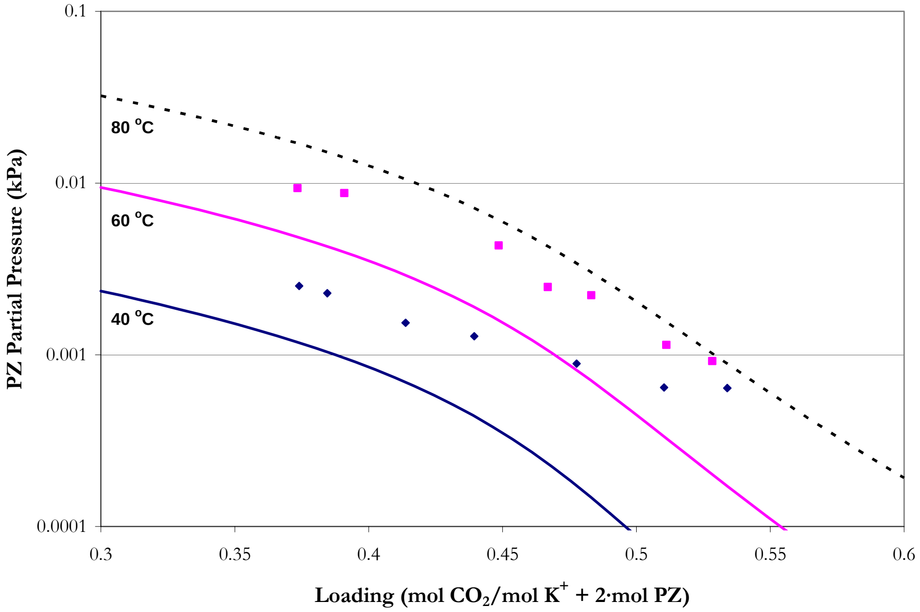

Figure 15.5-12. PZ Volatility in 3.6 m K^+ + 1.8 m PZ from 40 – 80 ^oC. Points: ♦, 40 ^oC and ■, 60 ^oC. Lines: elecNRTL Model Predictions.

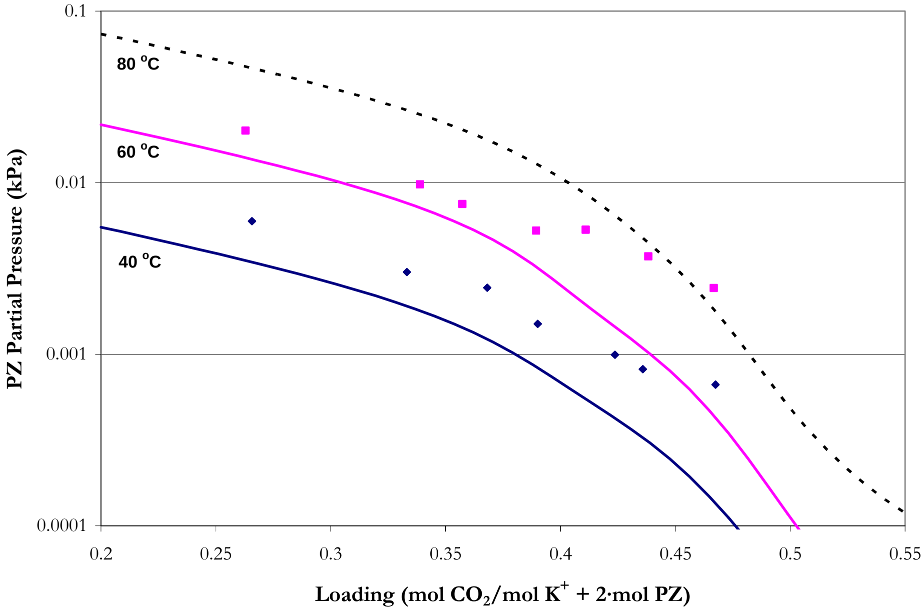

Figure 15.5-13. PZ Volatility in 3.6 m K^+ + 3.6 m PZ from 40 – 80 °C. Points: ♦, 40 °C and ■, 60 °C. Lines: elecNRTL Model Predictions.

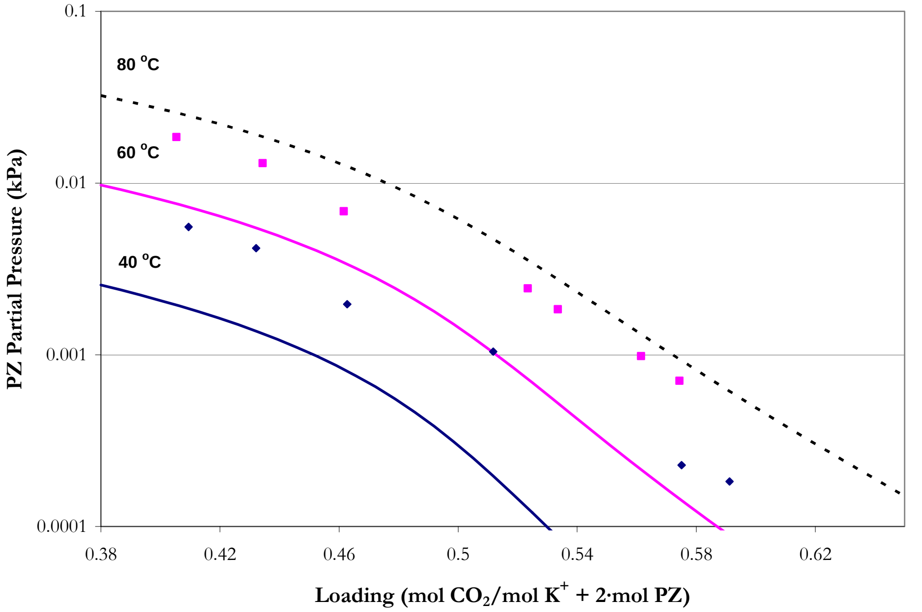

Figure 15.5-14. PZ Volatility in 6 m K^+ + 1.2 m PZ from 40 – 80 °C. Points: ♦, 40 °C and ■, 60 °C. Lines: elecNRTL Model Predictions.

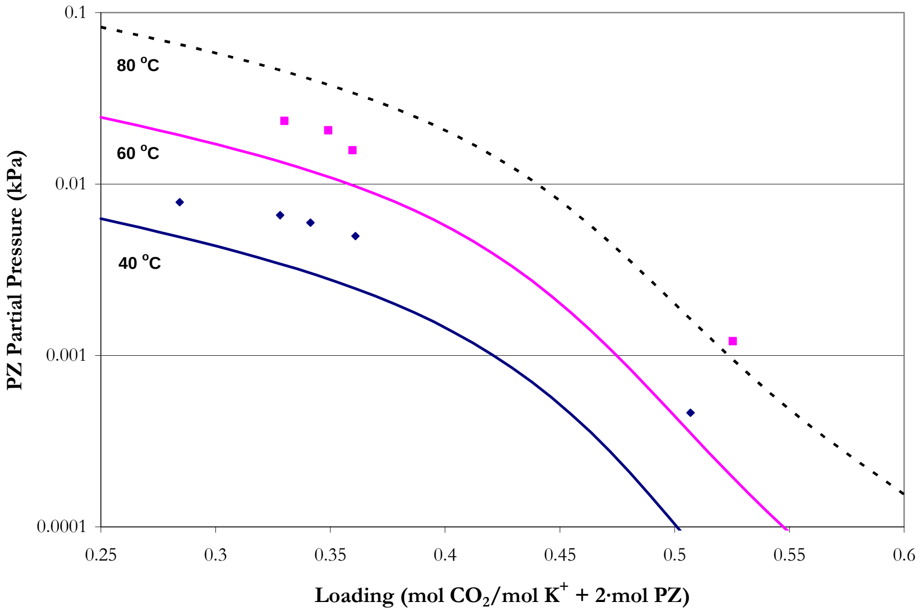

Figure 15.5-15. PZ Volatility in 5 m K⁺ + 3.6 m PZ from 40 – 80 °C. Points: ♦, 40 °C and ■, 60 °C. Lines: elecNRTL Model Predictions.

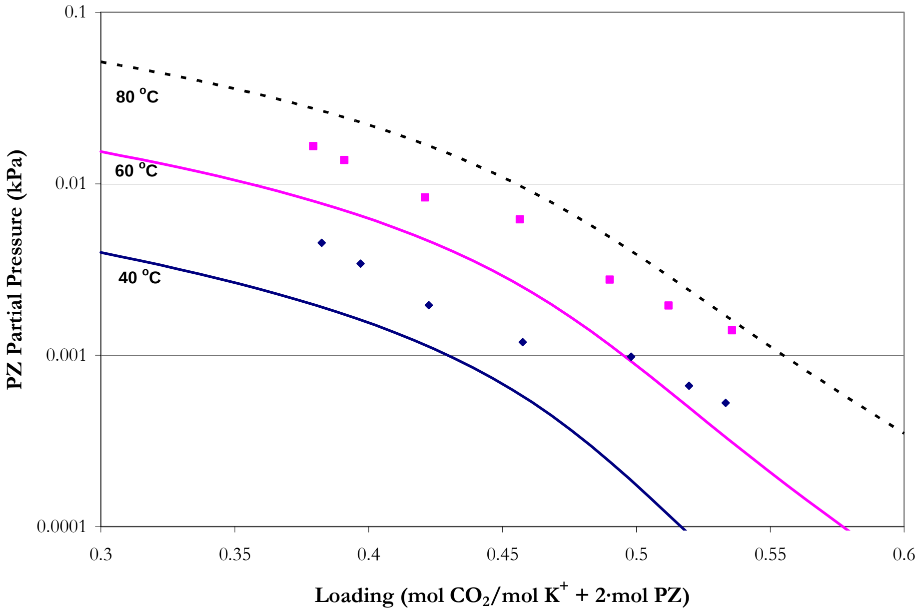

Figure 15.5-16. PZ Volatility in 5 m K⁺ + 2 m PZ from 40 – 80 °C. Points: ♦, 40 °C and ■, 60 °C. Lines: elecNRTL Model Predictions.

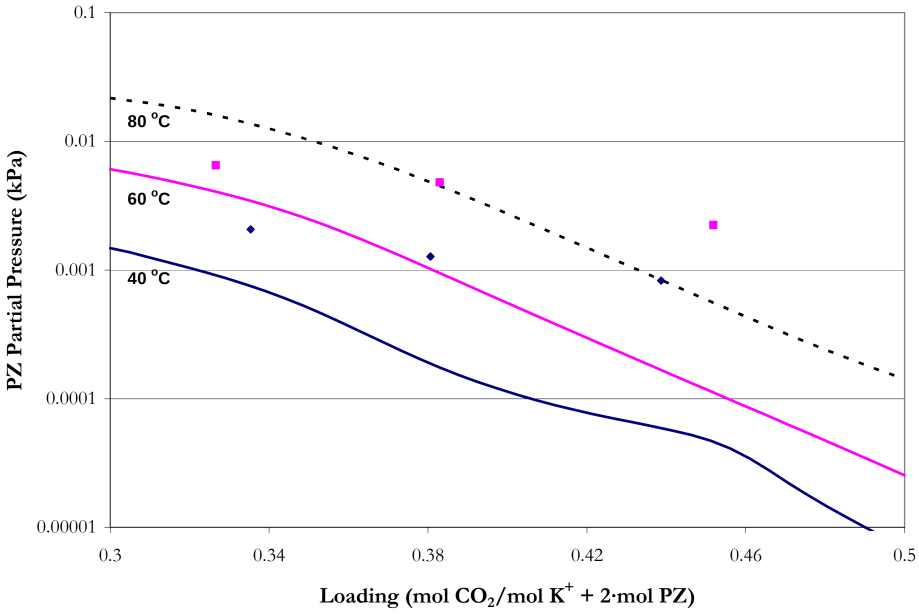

Figure 15.5-17. PZ Volatility in 2.5 m K^+ + 3.6 m PZ from 40 – 80 °C. Points: ♦, 40 °C and ■, 60 °C. Lines: elecNRTL Model Predictions.

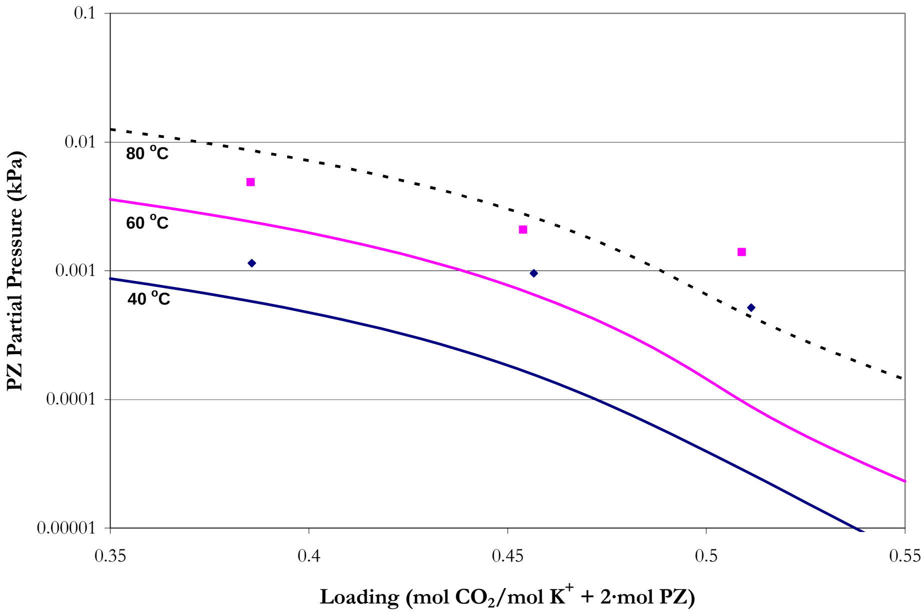

Figure 15.5-18. PZ Volatility in 2.5 m K^+ + 2 m PZ from 40 – 80 °C. Points: ♦, 40 °C and ■, 60 °C. Lines: elecNRTL Model Predictions.

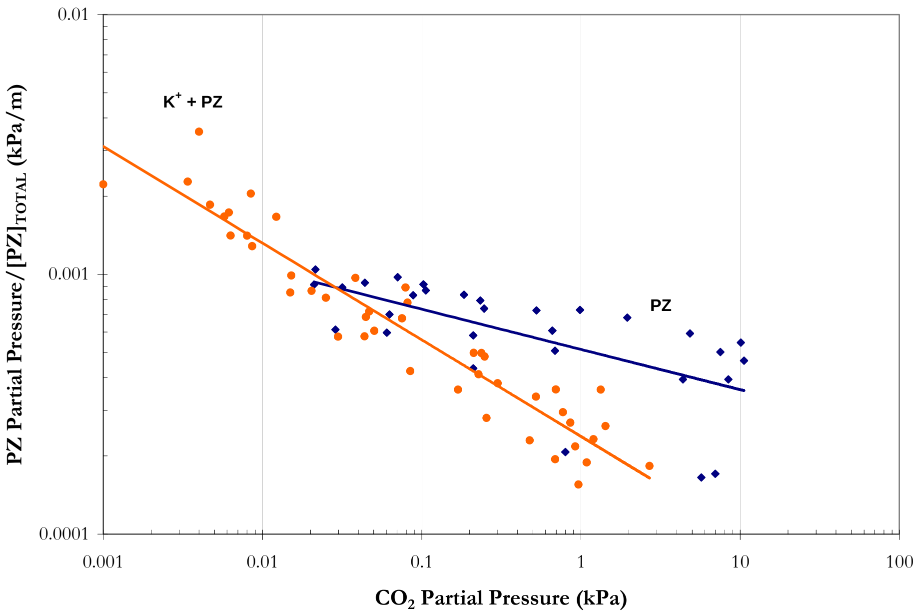

Figure 15.5-19. Comparison of the Experimental PZ Volatility Database versus CO_2 Solubility at 40 °C from this work. Points: ♦, H_2O-PZ-CO_2 System Data, ●, H_2O-K_2CO_3-PZ-CO_2 System Data.

Amine volatility at 40 °C for each solvent can then be compared based on a CO_2 partial pressure from 0.01 to 0.1 kPa as illustrated in Figure 15.5-19 based on experimental PZ volatility from this work. Table 15.5-2 compares the amine volatility of the nine mixed salt-amine systems in this work to the base sub-component systems of 7 m MEA and 2 m PZ at 40 °C.

As shown in Table 15.5-2, 7 m MEA demonstrates a greater volatility at 40 °C compared to piperazine or other mixed salt-amine systems. For different combinations of potassium + piperazine, the volatility of PZ varied between 54 to 4 ppm_v over a CO_2 partial pressure from 0.01 to 0.1 kPa at 40 °C and is consistent with effects exhibited in the H_2O-

PZ-CO_2 system (37 to 8 ppm$_v$) where large changes in the solution alkalinity may not have a large effect on the volatility of PZ.

Table 15.5-2. Comparison of Experimental Amine Volatility Evaluated at a CO_2 Partial Pressure from 0.01 to 0.1 kPa at 40 °C.

System	P^i (ppm$_v$)
7 m MEA	62-35
2 m PZ	21-18
5 m K^+ + 2.5 m PZ	32-13
3.6 m K^+ + 0.6 m PZ	10-4
3.6 m K^+ + 1.8 m PZ	22-12
3.6 m K^+ + 3.6 m PZ	36-15
6 m K^+ + 1.2 m PZ	22-6
5 m K^+ + 3.6 m PZ	54-39
5 m K^+ + 2 m PZ	27-11
2.5 m K^+ + 3.6 m PZ	29-16
2.5 m K^+ + 2 m PZ	15-9

15.5.2 *Enthalpy of CO_2 Absorption*

Figure 15.5-20 through Figure 15.5-28 compares experimental differential enthalpy of CO_2 absorption measurements from Kim (2007) to predictions based on Equation 15-39 (Gibbs-Helmholtz) from this work.

Model predictions from Hilliard (2005) were not included due to previously mentioned reasons: the Hilliard (2005) model predicts the wrong temperature dependence (Temperature ↓ with ↑ ΔHabs) of the enthalpy of CO_2 absorption as compared to experimental measurements from Kim (2007). On the other hand, the Hilliard (2005) model did not include calometric measurements as part of his original regression analysis.

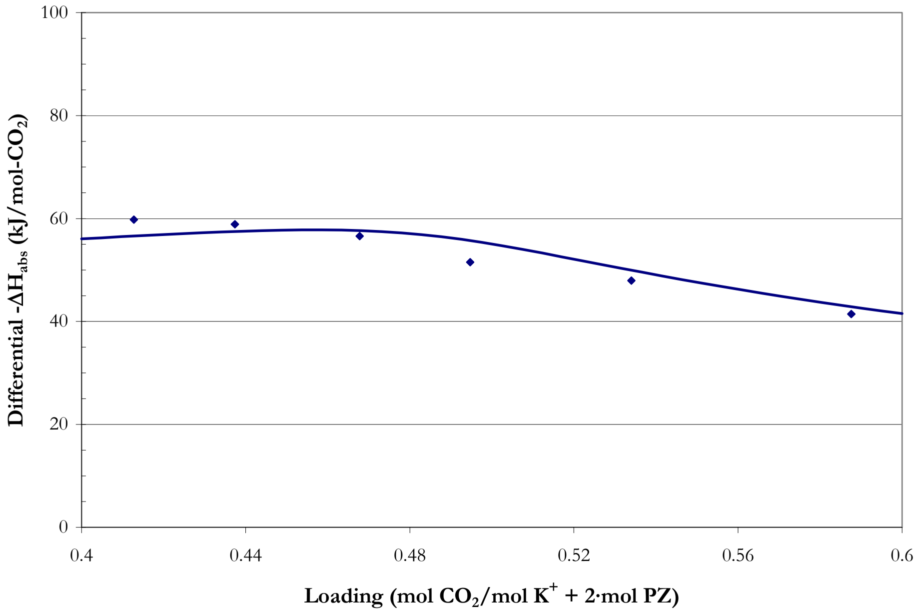

Figure 15.5-20. Comparison of the Enthalpy of CO_2 Absorption in 5 m K^+ + 2.5 m PZ at 40 °C from Kim (2007) to Predictions from this work.

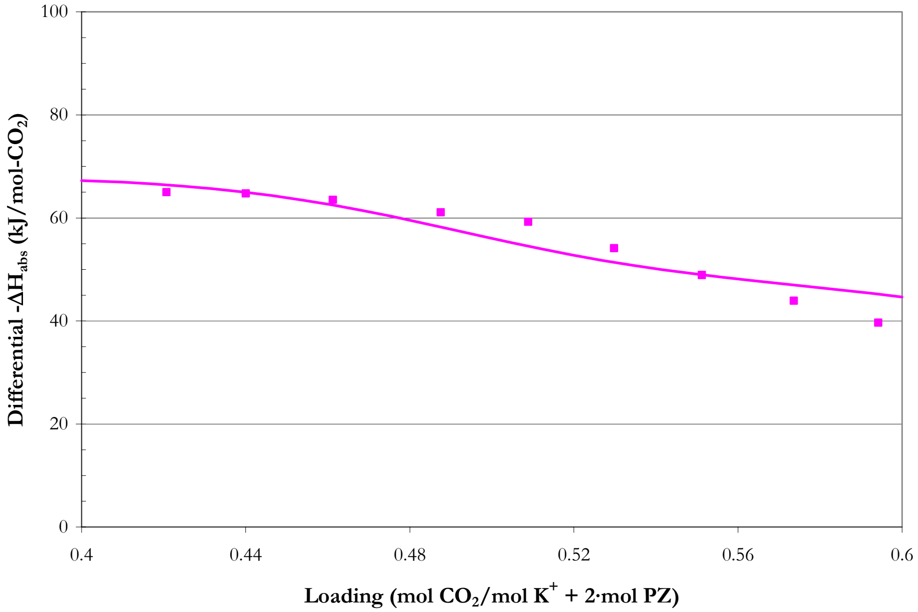

Figure 15.5-21. Comparison of the Enthalpy of CO_2 Absorption in 5 m K^+ + 2.5 m PZ at 60 °C from Kim (2007) to Predictions from this work.

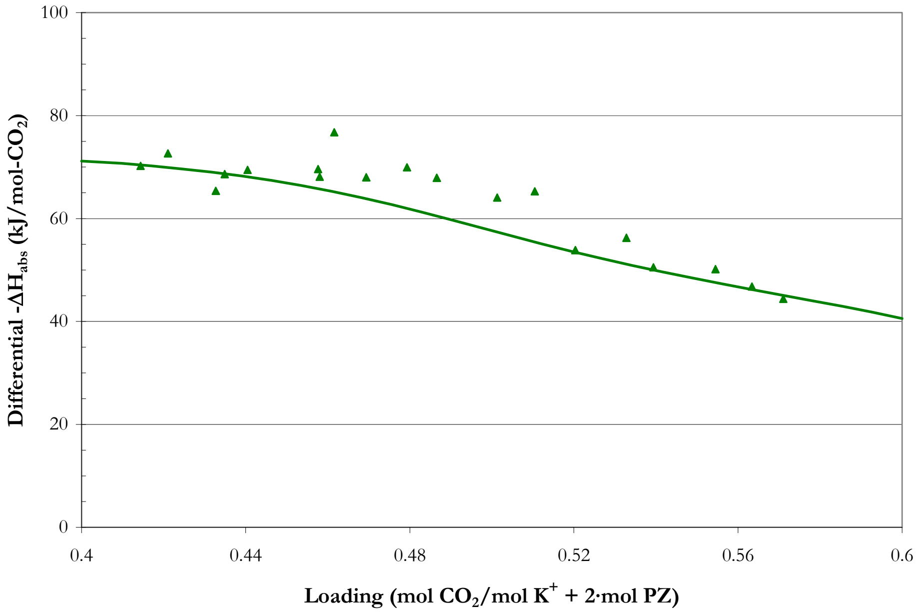

Figure 15.5-22. Comparison of the Enthalpy of CO_2 Absorption in 5 m K^+ + 2.5 m PZ at 80 °C from Kim (2007) to Predictions from this work.

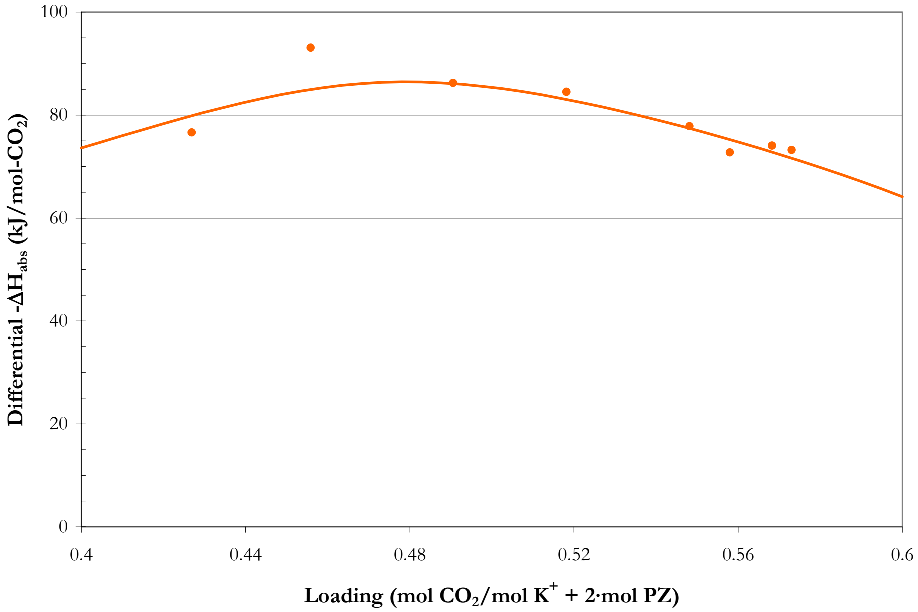

Figure 15.5-23. Comparison of the Enthalpy of CO_2 Absorption in 5 m K^+ + 2.5 m PZ at 120 °C from Kim (2007) to Predictions from this work.

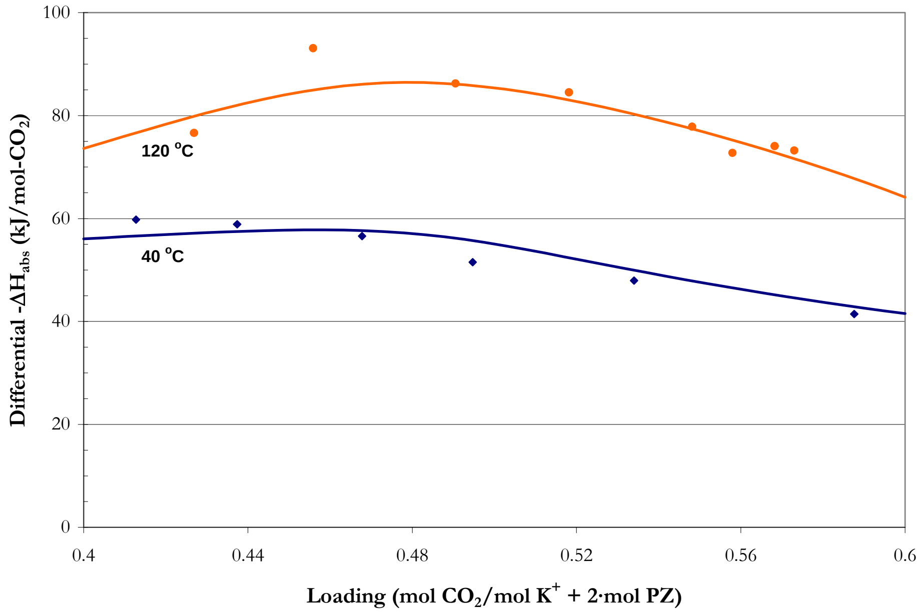

Figure 15.5-24. Comparison of the Enthalpy of CO$_2$ Absorption in 5 m K$^+$ + 2.5 m PZ at 40 and 120 °C from Kim (2007) to Predictions from this work.

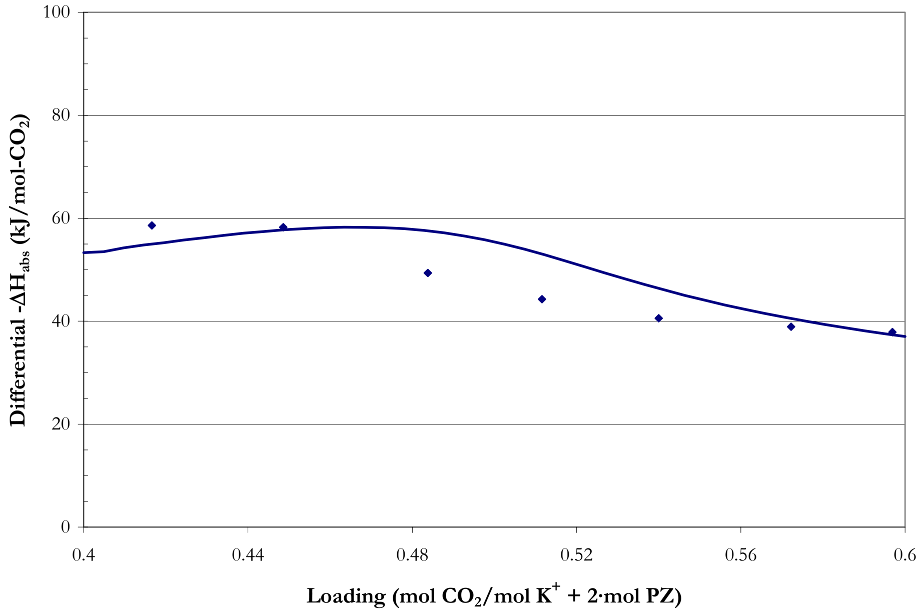

Figure 15.5-25. Comparison of the Enthalpy of CO$_2$ Absorption in 6 m K$^+$ + 1.2 m PZ at 40 °C from Kim (2007) to Predictions from this work.

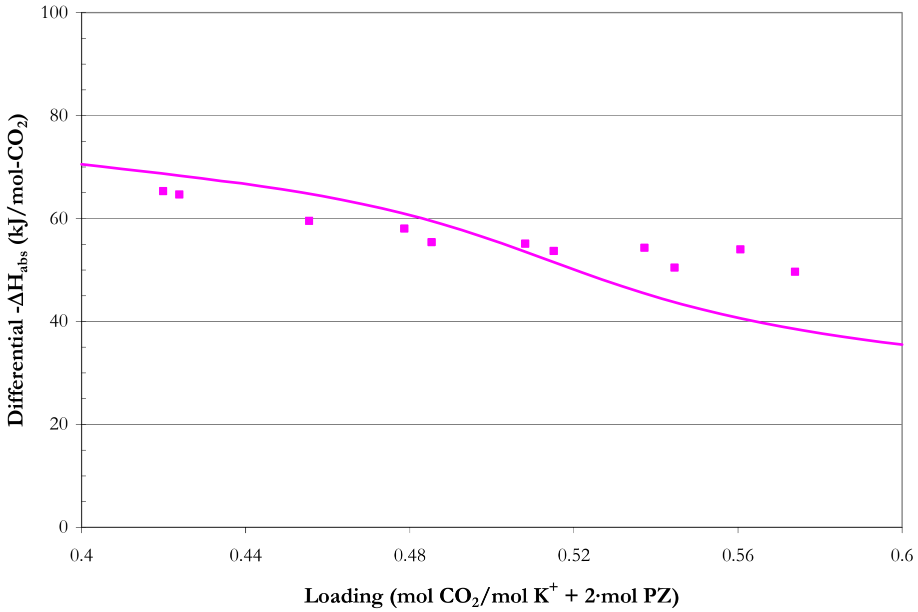

Figure 15.5-26. Comparison of the Enthalpy of CO$_2$ Absorption in 6 m K$^+$ + 1.2 m PZ at 60 °C from Kim (2007) to Predictions from this work.

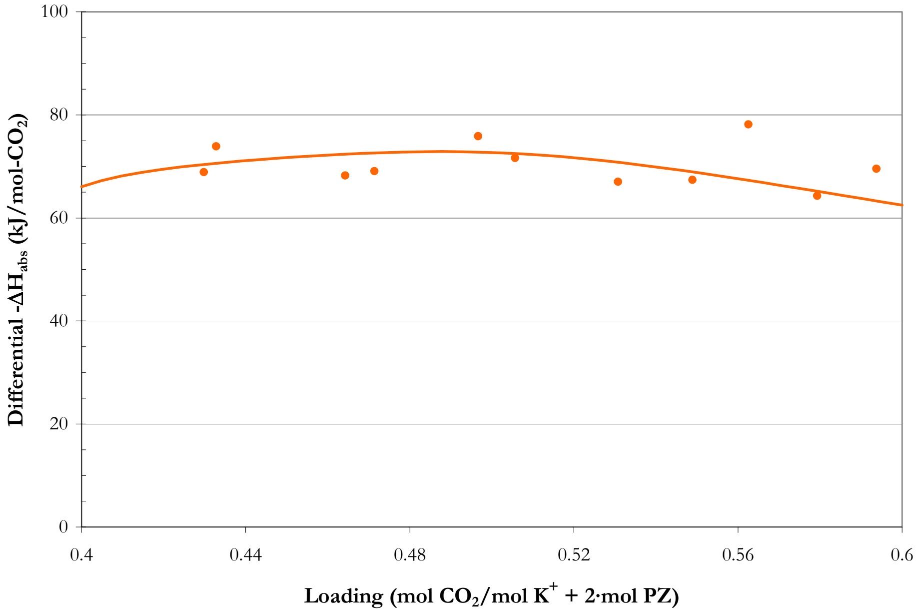

Figure 15.5-27. Comparison of the Enthalpy of CO$_2$ Absorption in 6 m K$^+$ + 1.2 m PZ at 120 °C from Kim (2007) to Predictions from this work.

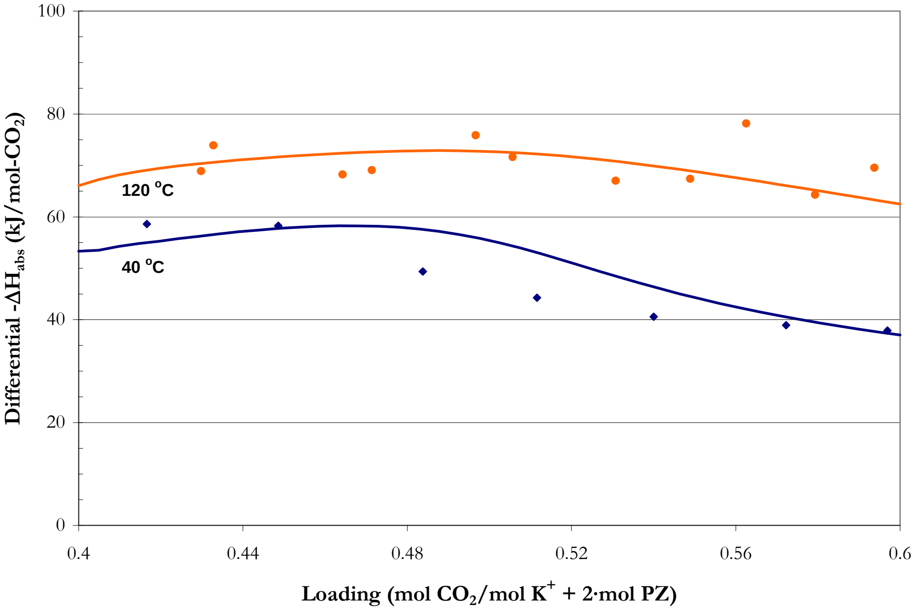

Figure 15.5-28. Comparison of the Enthalpy of CO_2 Absorption in 6 m K^+ + 1.2 m PZ at 40 and 120 °C from Kim (2007) to Predictions from this work.

The above results illustrate that the full model adequately describes the enthalpy of CO_2 absorption in mixtures of 5 m K^+ + 2.5 m PZ and 6 m K^+ + 1.2 m PZ. We can now compare model predictions for 5 m K^+ + 2.5 m PZ and 6 m K^+ + 1.2 m PZ at 40 and 120 °C to predictions for 7 m MEA verses predictions for the partial pressure of CO_2 as shown in Figure 15.5-29.

Figure 15.5-29 illustrates an approximate 30 kJ/mol-CO_2 decrease in the enthalpy of CO_2 absorption at 40 °C as compared to 7 m MEA. At 120 °C, only 6 m K^+ + 1.2 m PZ also demonstrates an approximate 30 kJ/mol-CO_2 decrease as compared to 5 m K^+ + 2.5 m PZ which exhibits only an approximate 10 kJ/mol-CO_2 decrease in the enthalpy of CO_2 absorption.

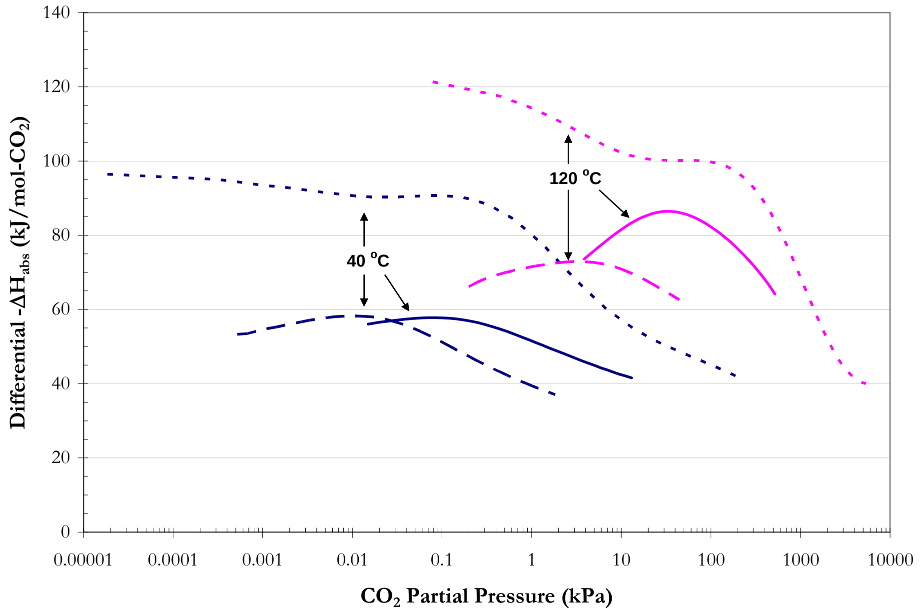

Figure 15.5-29. Comparison of the Enthalpy of CO_2 Absorption Model Predictions from this work in Mixtures of H_2O-MEA-CO_2 and H_2O-K_2CO_3-PZ-CO_2 at 40 and 120 °C. Lines: ▬, 5 m K^+ + 2.5 m PZ, — —, 6 m K^+ + 1.2 m PZ, - - -, 7 m MEA.

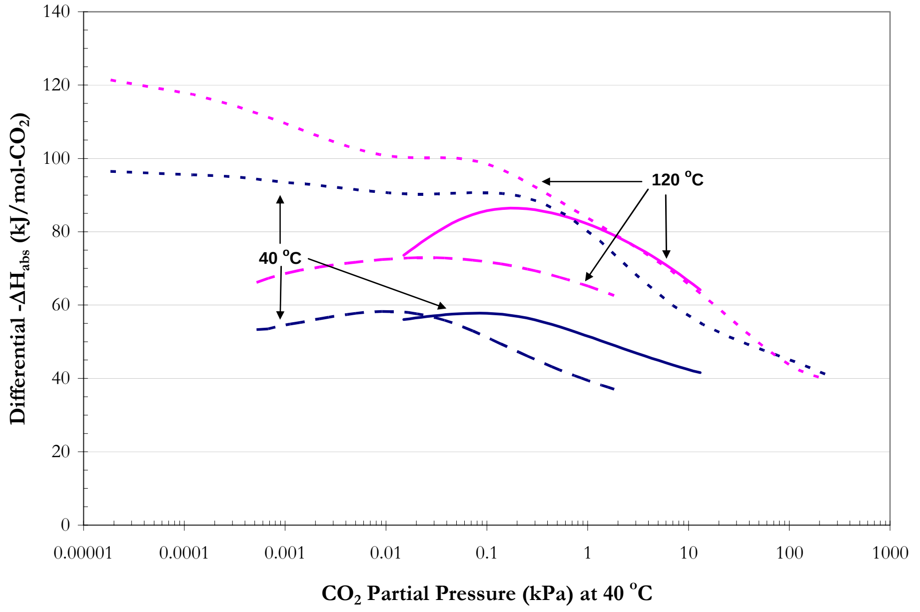

Figure 15.5-30. Comparison of the Enthalpy of CO_2 Absorption Model Predictions from this work in Mixtures of H_2O-MEA-CO_2 and H_2O-K_2CO_3-PZ-CO_2 at 40 and 120 °C versus CO_2 Partial Pressures at 40 °C. Lines: ▬, 5 m K^+ + 2.5 m PZ, — —, 6 m K^+ + 1.2 m PZ, - - -, 7 m MEA.

15.5.3 *Specific Heat Capacity*

Figure 15.5-31 through Figure 15.5-32 compares experimental specific heat capacity measurements from this work to predictions from this work. Predictions from this work do capture the correct trends in the specific heat capacity as a function of temperature but did fall short in predicting the correct specific heat capacity on the order of ± 10 percent.

One possibility for this discrepancy may result from an inconsistency between the enthalpy of CO_2 absorption measurements from Kim (2007) and specific heat capacity measurements from this work.

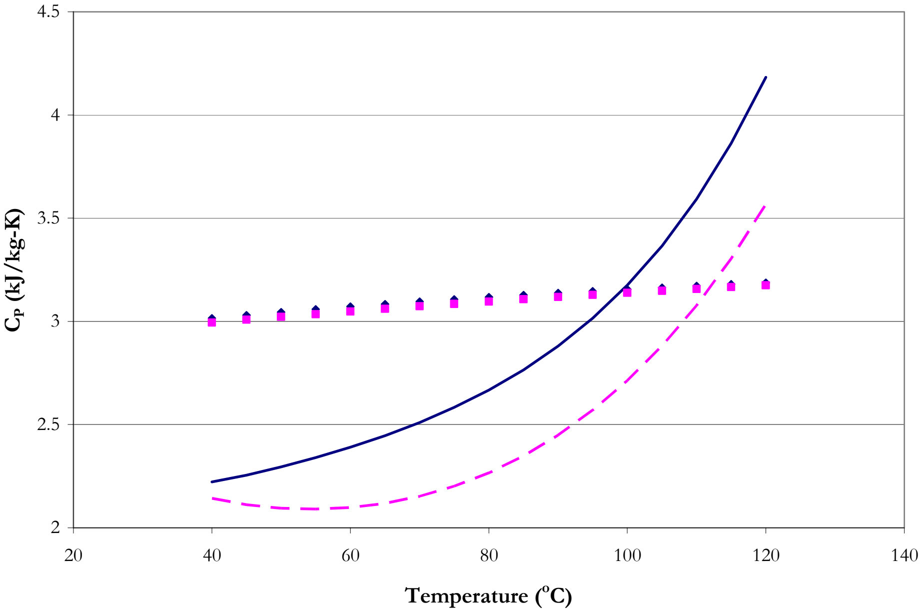

Figure 15.5-31. Comparison of Experimental Specific Heat Capacity in Loaded 5 m K^+ + 2.5 m PZ Mixtures from 40 to 120 °C. Points: ♦, Ldg = 0.39, ■, Ldg = 0.55. Lines: —, Ldg = 0.39, – –, Ldg = 0.55.

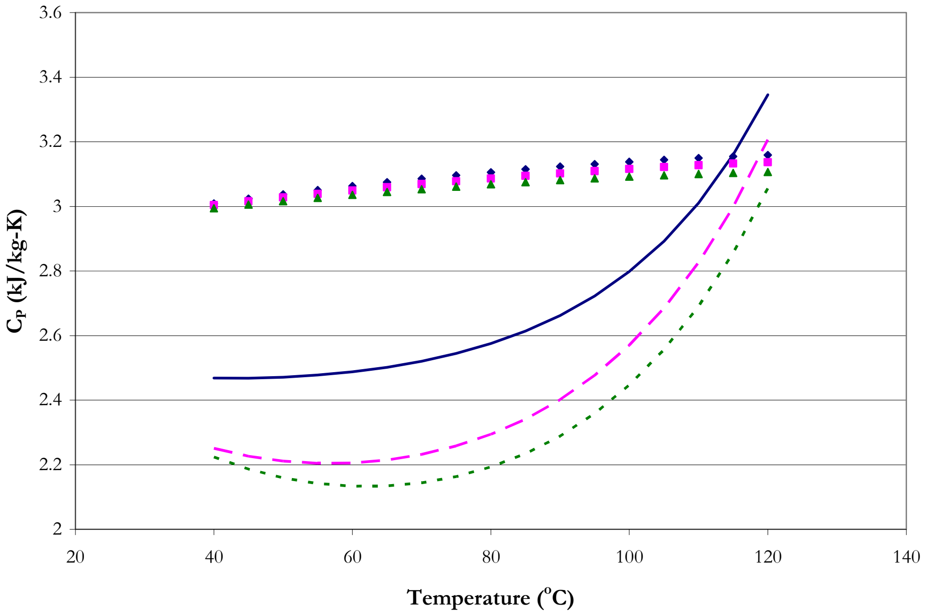

Figure 15.5-32. Comparison of Experimental Specific Heat Capacity in Loaded 6 m K$^+$ + 1.2 m PZ Mixtures from 40 – 120 °C. Points: ♦, Ldg = 0.43, ■, Ldg = 0.53, ▲, Ldg = 0.57. Lines: ▬, Ldg = 0.43, – –, Ldg = 0.53, - - - , Ldg = 0.57.

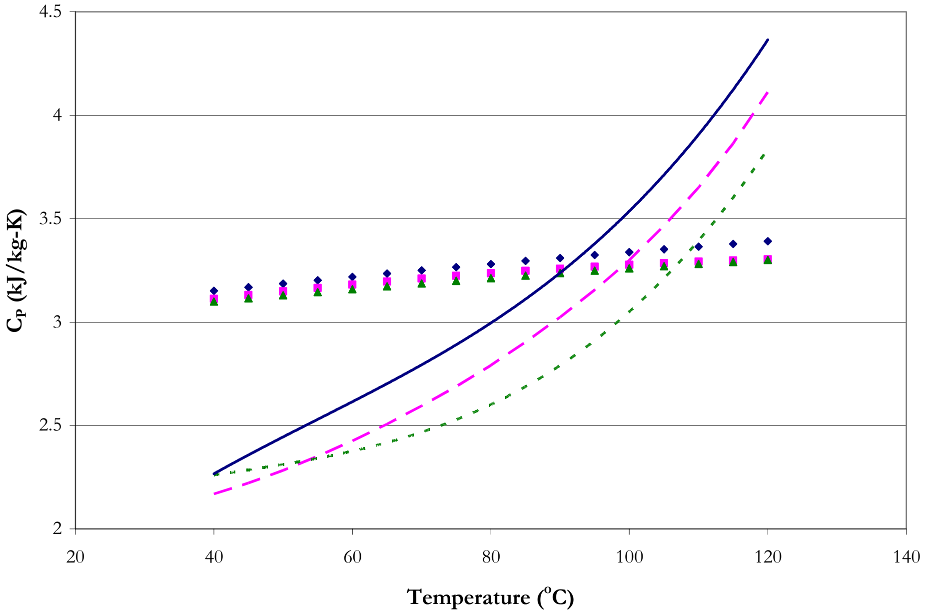

Figure 15.5-33. Comparison of Experimental Specific Heat Capacity in Loaded 3.6 m K$^+$ + 3.6 m PZ Mixtures from 40 – 120 °C. Points: ♦, Ldg = 0.33, ■, Ldg = 0.42, ▲, Ldg = 0.47. Lines: ▬, Ldg = 0.33, – –, Ldg = 0.42, - - - , Ldg = 0.47.

We can relate the liquid phase specific heat capacity measurements to the sensible liquid phase enthalpy of solution from 40 to 120 °C by comparing the average experimental specific heat capacity to predictions based on the full model as shown in Table 15.5-3.

Table 15.5-3. Comparison of Average Specific Heat Capacity (kJ/kg-K) from 40 – 120 °C.

System	Loading	Experimental	Full Model	AARD (%)
5 m K^+ + 2.5 m PZ	0.39	3.1114	2.8559	8.20
	0.55	3.0919	2.4814	19.8
6 m K^+ + 1.2 m PZ	0.43	3.0976	2.6893	13.2
	0.53	3.0806	2.4471	20.6
	0.57	3.0616	2.3510	23.2
3.6 m K^+ + 3.6 m PZ	0.33	3.2771	3.2222	1.67
	0.42	3.2258	3.0414	5.72
	0.47	3.2076	2.9269	8.75

The average absolute relative error presented in Table 15.5-3 illustrates that the experimental specific heat capacity is not consistent with predictions from the full model for the sensible liquid phase enthalpy within the experimental accuracy of ± 2.0 percent error. For all other amine systems studied in this work, the temperature ramp rate was set to 5 °C/min which produced acceptable results, but *a priori* to the completion of experimental work, we found that Thomsen et al. (1999) mentioned that for salt systems a rate of 1 °C/min should be used to improve the sample response resolution and allow the sample to achieve equilibrium at a desired temperature. We would recommend that future work verify specific heat capacity measurements gathered in this work utilizing a similar procedure outlined in Chapter IV but instead use a temperature ramp rate of 1 °C/min. In addition, in this work we did not adjust the infinite dilution aqueous phase heat capacity for the potassium ion because it did not show an additional benefit to the overall regression. If the scope of the work was limited to a specific solvent concentration, the adjustment of the potassium ion infinite dilution aqueous phase heat capacity may improve the overall statistical fit for the experimental specific heat capacity data.

Even though the model did not adequately describe systematic trends presented in the experimental specific heat capacity data, we can use the model to describe the possible departure from an ideal solution behavior. Figures 15.5-34 and 15.5-35 illustrate the proposed molar infinite dilution aqueous phase heat capacity for ionic and molecule solute species in the H_2O-K_2CO_3-PZ-CO_2 system where the molar infinite dilution aqueous phase heat capacity for K^{+1}, CO_3^{-2}, and HCO_3^{-1}, and PZH^{+1} were described in Chapters XII and IX, respectively.

By differentiating Equation 15-36 with respect to temperature, the molar infinite dilution aqueous phase heat capacity for CO_2 can be determined as shown in Figure 15.5-34. From Table 15.4-3, coefficients for the molar infinite dilution aqueous phase heat capacity of $PZCOO^{-1}$, $PZ(COO^{-1})_2$, and $H^{+1}PZCOO^{-1}$, were determined through simultaneous regression as described in Section 15.4.

Figure 15.5-36 separates the molar heat capacity in 5 m K^+ + 2.5 m PZ at a loading of 0.39 (mol CO_2/mol K^+ + 2·mol PZ) into the weighted molar heat capacity of each contributing species with respect to the components reference state (i.e. Solvents: pure liquid, Ionic and Molecular Solutes: infinite dilution in water). By describing the molar heat capacity of the solution by the following equation:

$$\begin{aligned} C_p = {} & x_{H_2O} C_p^{*,l} + x_{PZ} C_p^{*,l} + x_{CO_2} C_p^{\infty,aq} + x_{CO_3^{-2}} C_p^{\infty,aq} + x_{HCO_3^{-1}} C_p^{\infty,aq} + x_{PZH^{+1}} C_p^{\infty,aq} \\ & + x_{PZCOO^{-1}} C_p^{\infty,aq} + x_{PZ\left(COO^{-1}\right)_2} C_p^{\infty,aq} + x_{H^{+}PZCOO^{-1}} C_p^{\infty,aq} + x_{K^{+1}} C_p^{\infty,aq} + C_p^{Ex} \end{aligned} \qquad 15\text{-}56$$

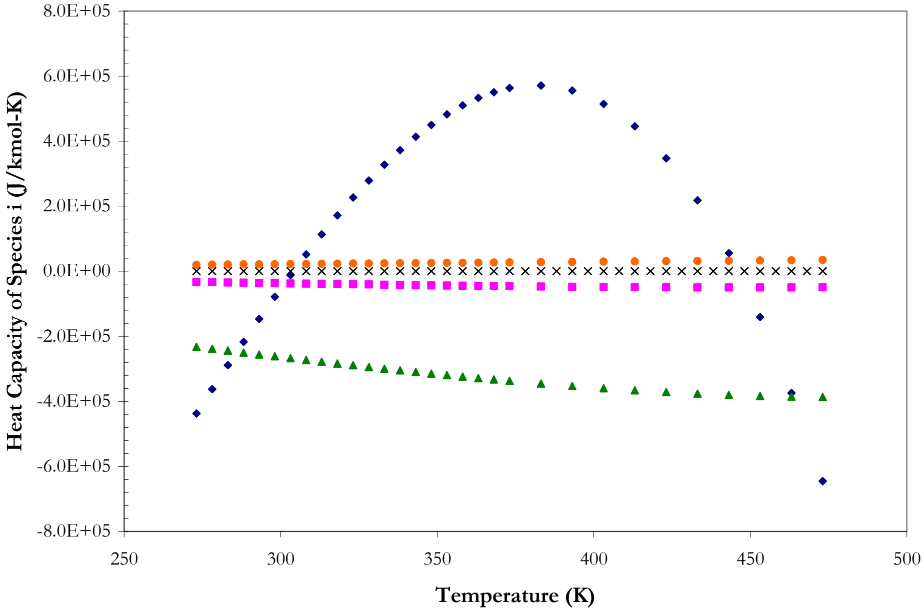

Figure 15.5-34. Molar Infinite Dilution Aqueous Phase Heat Capacity for Ionic and Molecular Solute Species in the H_2O-K_2CO_3-PZ-CO_2 System. Points: ♦, CO_2, ■, HCO_3^{-1}, ▲, CO_3^{-2}, ●, K^{+1}, ×, H_2O.

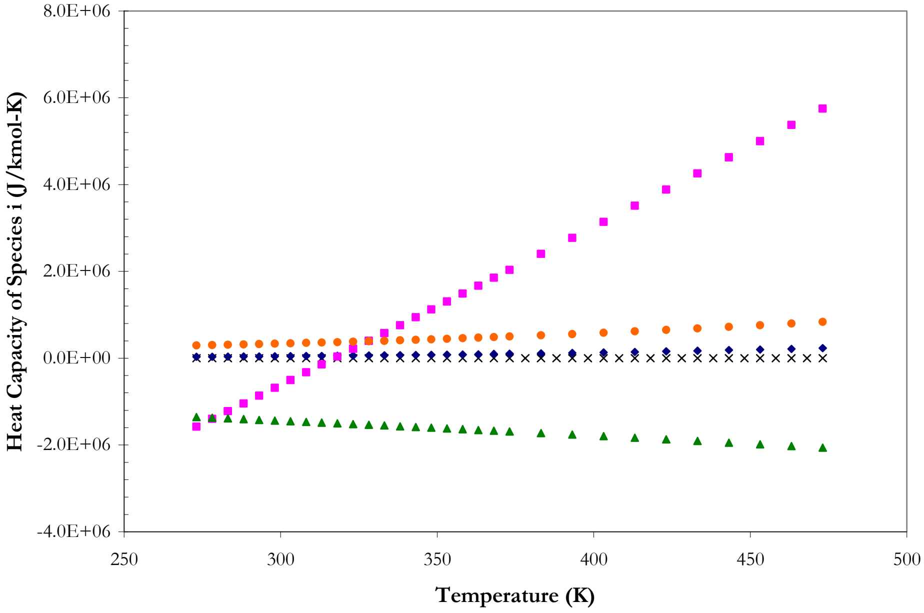

Figure 15.5-35. Molar Infinite Dilution Aqueous Phase Heat Capacity for Ionic and Molecular Solute Species in the H_2O-K_2CO_3-PZ-CO_2 System. Points: ♦, PZH^{+1}, ■, $PZCOO^{-1}$, ▲, $PZ(COO^{-1})_2$, ●, $H^{+1}PZCOO^{-1}$, ×, PZ.

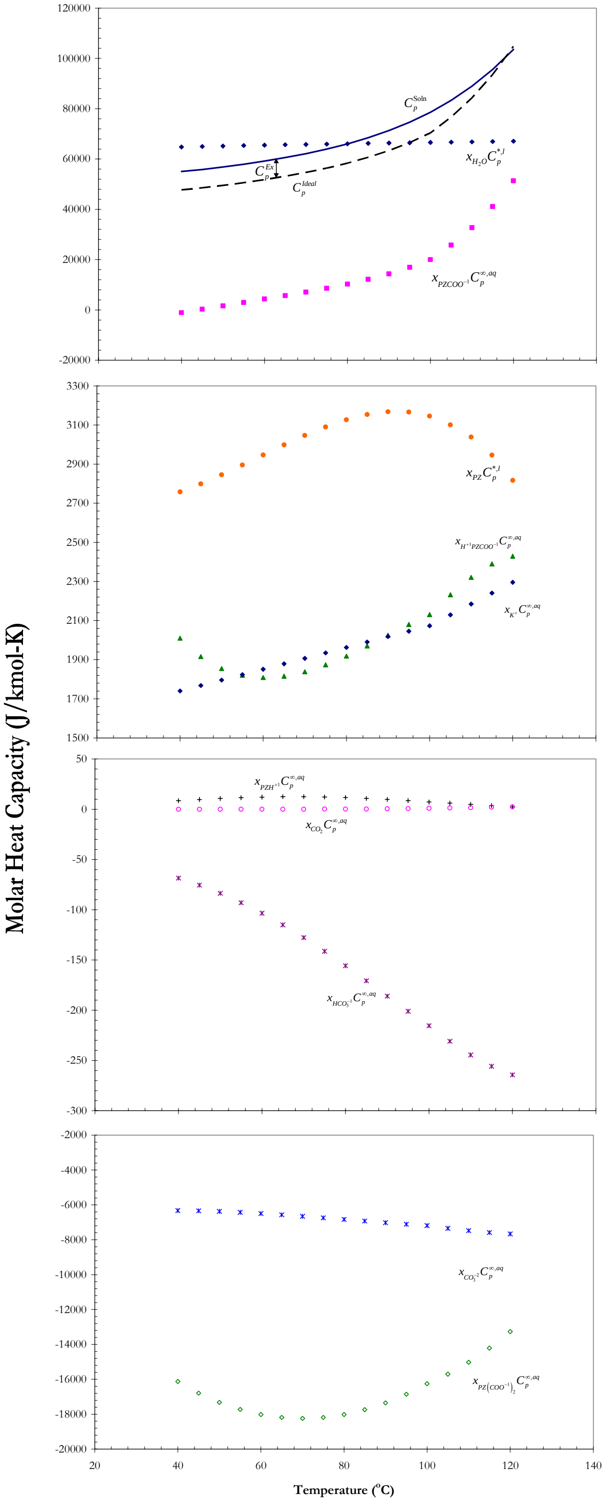

Figure 15.5-36. Comparison of the Molar Heat Capacity for 5 m K^++2.5 m PZ at Ldg = 0.39.

where deviations between the molar heat capacity of the solution from the ideal molar heat capacity are accounted for by the excess molar heat capacity. The excess molar heat capacity also accounts for the heat of reaction associated with any change in speciation with temperature.

To investigate the effect of CO_2 loading on the liquid phase specific heat capacity, we can normalize the specific heat capacity by the kilograms of H_2O in the experimental solution as shown in Figure 15.5-37.

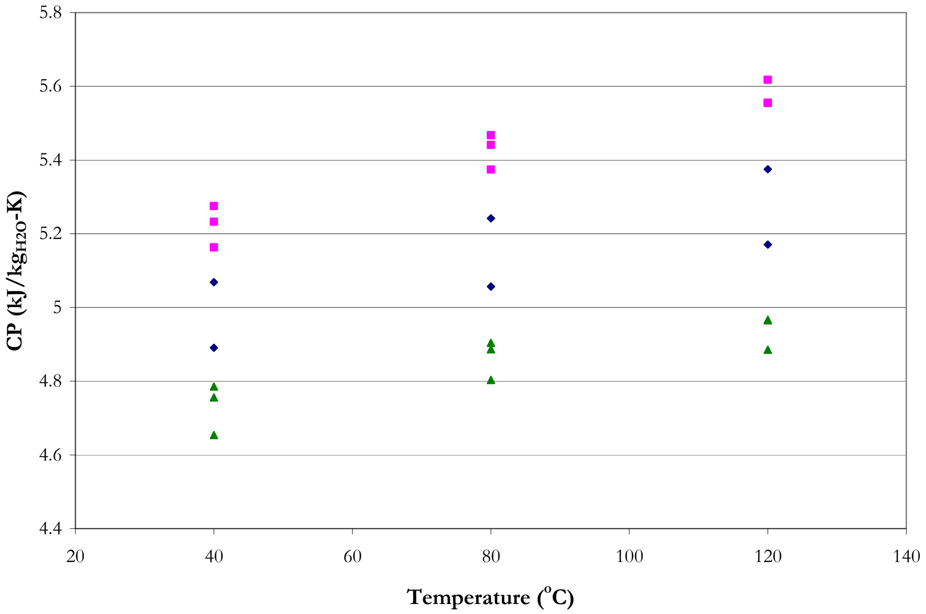

Figure 15.5-37. Apparent Partial Specific Heat Capacity for Mixtures of Potassium Carbonate + Piperazine. Points: ♦, 5 m K^+ + 2.5 m PZ, ■, 3.6 m K^+ + 3.6 m PZ, ▲, 6 m K^+ + 1.2 m PZ.

By cross-plotting Figure 15.5-37 with respect to the total moles of CO_2 per mole of H_2O, we can infer the apparent specific heat capacity of CO_2 based on the slope of the ordinary least squares approximation as show in Figure 15.5-38 through Figure 15.5-40.

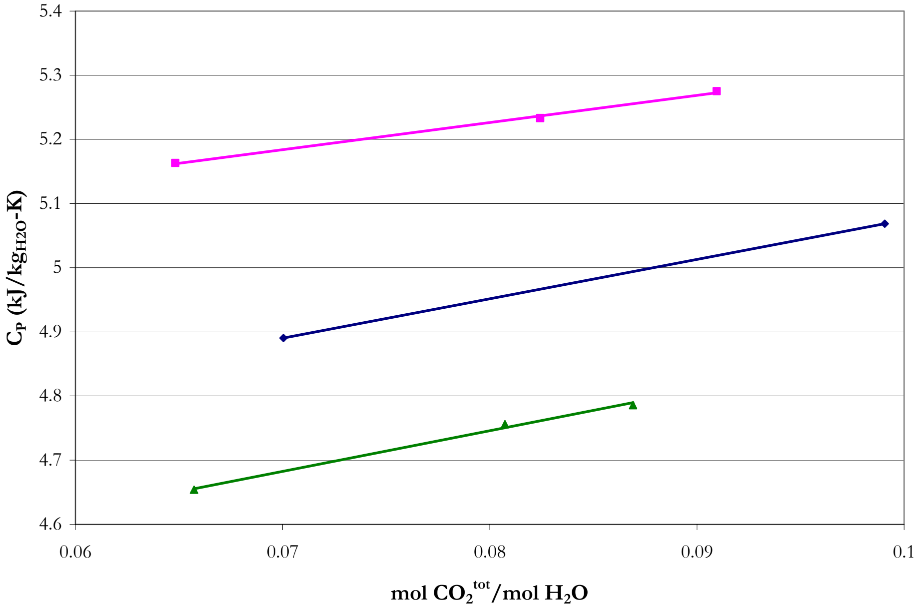

Figure 15.5-38. Apparent Partial Specific Heat Capacity for Mixtures of Potassium Carbonate + Piperazine at 40 °C. Points: ♦, 5 m K^+ + 2.5 m PZ, ■, 3.6 m K^+ + 3.6 m PZ, ▲, 6 m K^+ + 1.2 m PZ. Lines: OLS Approximations.

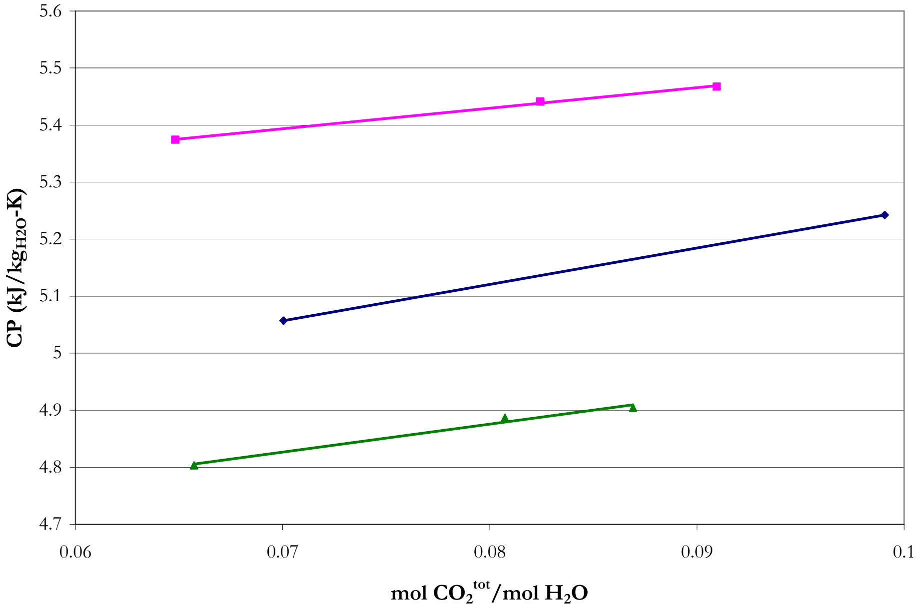

Figure 15.5-39. Apparent Partial Specific Heat Capacity for Mixtures of Potassium Carbonate + Piperazine at 80 °C. Points: ♦, 5 m K^+ + 2.5 m PZ, ■, 3.6 m K^+ + 3.6 m PZ, ▲, 6 m K^+ + 1.2 m PZ. Lines: OLS Approximations.

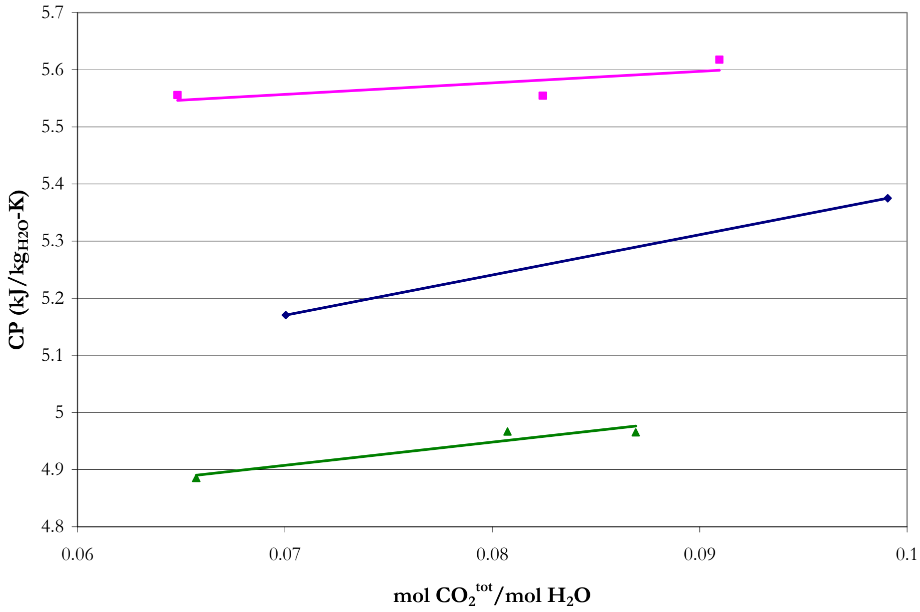

Figure 15.5-40. Apparent Partial Specific Heat Capacity for Mixtures of Potassium Carbonate + Piperazine at 120 °C. Points: ♦, 5 m K^+ + 2.5 m PZ, ■, 3.6 m K^+ + 3.6 m PZ, ▲, 6 m K^+ + 1.2 m PZ. Lines: OLS Approximations.

Based on the above analysis, we can infer the apparent partial specific heat capacity of CO_2 (Table 15.5-4) and compare to the molar infinite dilution aqueous phase heat capacity of CO_2 as shown in Figure 15.5-34.

Table 15.5-4. Apparent Partial Specific Heat Capacity of CO_2 in Mixtures of Potassium Carbonate + Piperazine.

	System (kJ/kg$_i$-K)			
Temp. (°C)	6 m K^++1.2 m PZ	5 m K^++2.5 m PZ	3.6 m K^++3.6 m PZ	H_2O(l)
40	6.3254	6.1366	4.2359	4.1772
80	4.9154	6.3863	3.0673	4.2624
120	4.0717	7.0466	2.0075	4.3340
Average	5.1042	6.5232	3.1036	4.2579

Table 15.5-4 illustrates how the experimental apparent partial heat capacity of CO_2 may have an average value of 4.9103 kJ/kg$_{CO2}$-K over the temperature range from 40 to 120 °C in aqueous mixtures of potassium carbonate plus piperazine and is comparable to the

specific heat capacity of H_2O. This may suggest that contributions of the apparent partial heat capacity of CO_2 may not be considered small aqueous mixtures of potassium carbonate plus piperazine.

15.5.4 *NMR Speciation*

Figure 15.5-41 through Figure 15.5-115 compare experimental liquid phase NMR speciation measurements from Cullinane (2005) to predictions from this work. As metioned previously, Cullinane (2005) reported proton (H^1) NMR speciation for H_2O-K_2CO_3-PZ-CO_2 system where the main drawback with an H^1 NMR speciation analysis is not having the ability to measure the loading of the solution as compared to carbon C^{13} NMR speciation as described in Chapter XIII. In the H^1 NMR analysis the loading of the solution has to be determined *a prori* which may result in a discrepancy between the loading at the time of the NMR experiment and at the time of the CO_2 analysis since the loading for NMR solutions reported by Cullinane (2005) were completed in a similar manner as CO_2 solubility measurements. The uncertainty in loading for experimental NMR speciation data reported by Cullinane (2005) were assigned a standard deviation of ± 10 % to account for the discrepancy in the loading analysis as compared to this work. This in effect allowed DRS to adjust the loading of the solution to be consistent with experimental CO_2 solubility, amine volatility, and enthalpy of CO_2 absorption data but allowed DRS to use information provided within the speciation to adjust liquid phase activity coefficients for the present reactive species. Overall, the full model was able to adequately predict the experimental liquid phase speciation concentrations (vertical axis) within an average relative error of ± 2.29 percent.

Liquid Phase Speciation for 5 m K^+ + 2.5 m PZ at 27 °C

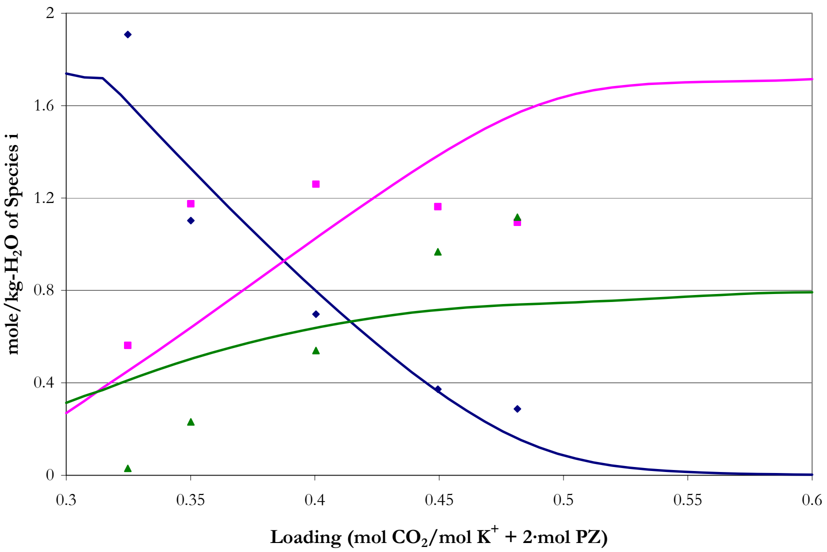

Figure 15.5-41. Comparison of Liquid Phase NMR Speciation in 5 m K^+ + 2.5 m PZ at 27 °C to Model Predictions. Points: ♦, $PZ+PZH^{+1}$, ■, $PZCOO^{-1}+H^+PZCOO^{-1}$, ▲, $PZ(COO^{-1})_2$ from Cullinane (2005). Lines: —, this work.

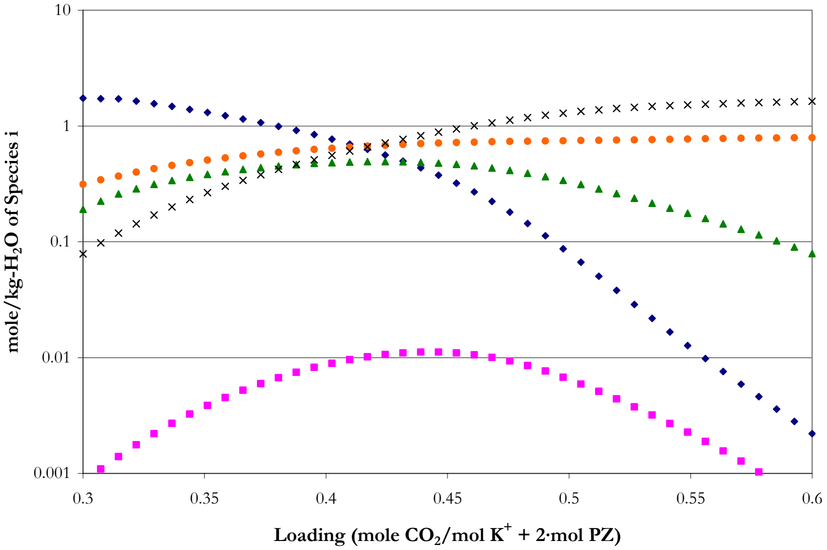

Figure 15.5-42. Predictions for the Liquid Phase Speciation in 5 m K^+ + 2.5 m PZ at 27 °C from this work. Points: ♦, PZ, ■, PZH^{+1}, ▲, $PZCOO^{-1}$, ●, $PZ(COO^{-1})_2$, ×, H^+PZCOO^{-1}.

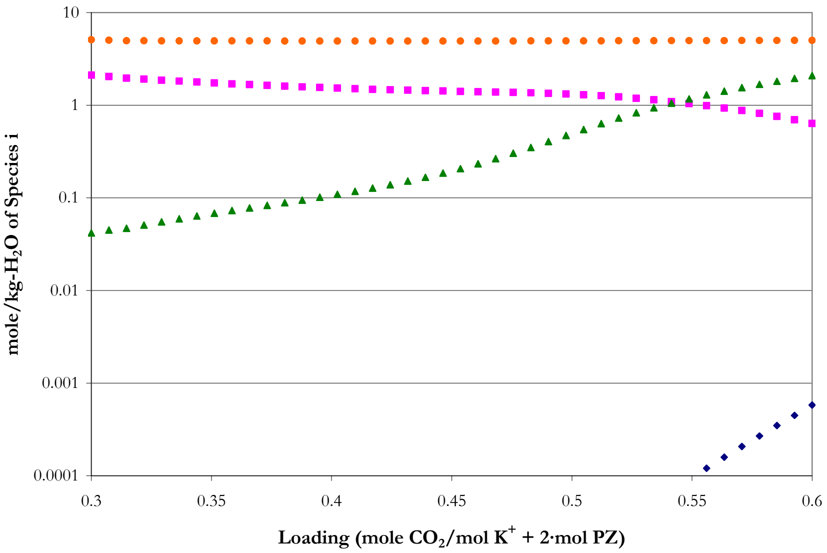

Figure 15.5-43. Predictions for the Liquid Phase Speciation in 5 m K^+ + 2.5 m PZ at 27 °C from this work. Points: ♦, CO_2, ■, CO_3^{-2}, ▲, HCO_3^{-1}, ●, K^+.

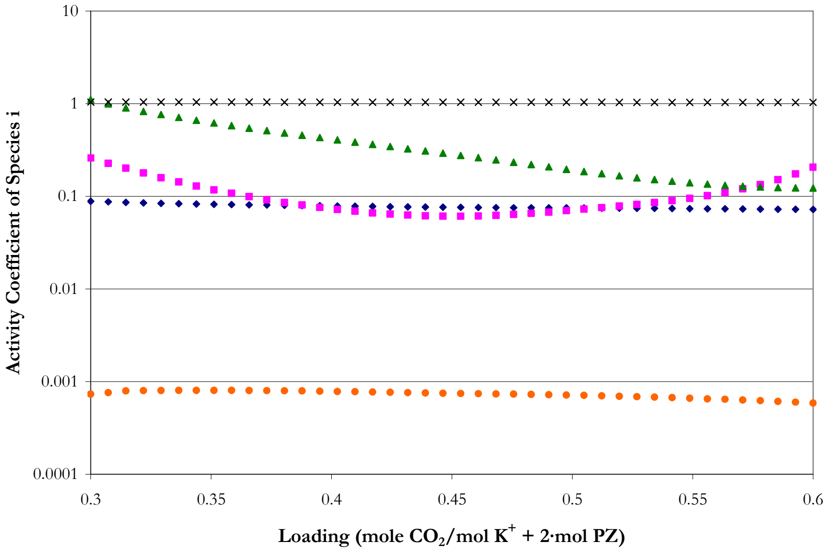

Figure 15.5-44. Predictions for the Liquid Phase Activity Coefficients in 5 m K^+ + 2.5 m PZ at 27 °C from this work. Points: ♦, PZ, ■, PZH^{+1}, ▲, $PZCOO^{-1}$, ●, $PZ(COO^{-1})_2$, ×, H^+PZCOO^{-1}.

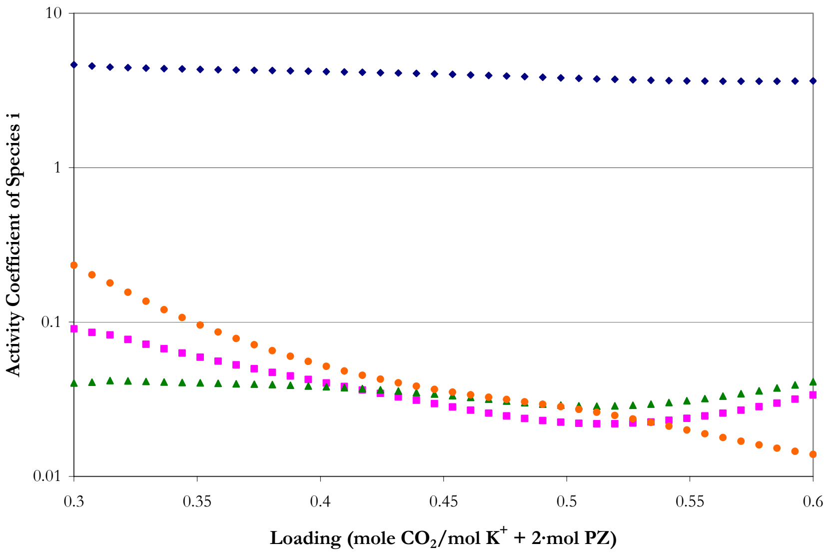

Figure 15.5-45. Predictions for the Liquid Phase Activity Coefficients in 5 m K^+ + 2.5 m PZ at 27 °C from this work. Points: ♦, CO_2, ■, CO_3^{-2}, ▲, HCO_3^{-1}, ●, K^+.

Liquid Phase Speciation for 5 m K^+ + 2.5 m PZ at 40 °C

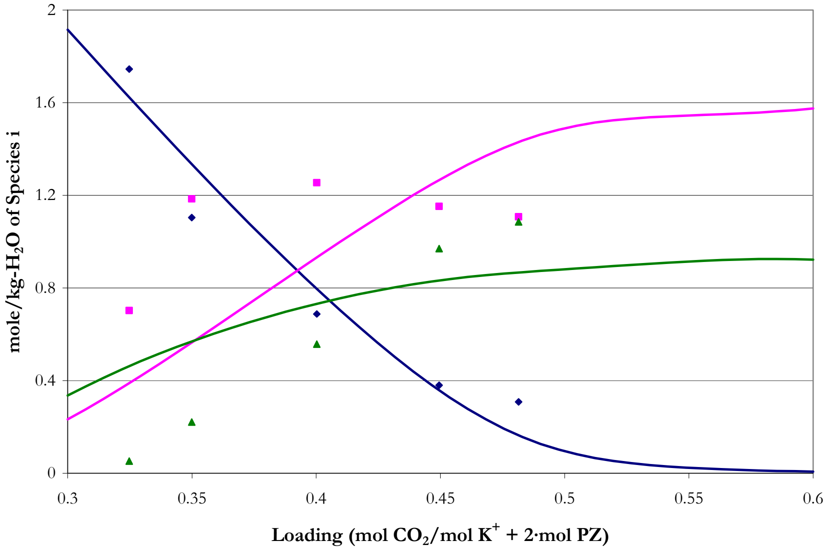

Figure 15.5-46. Comparison of Liquid Phase NMR Speciation in 5 m K^+ + 2.5 m PZ at 40 °C to Model Predictions. Points: ♦, PZ+PZH^{+1}, ■, $PZCOO^{-1}$+H^+PZCOO^{-1}, ▲, $PZ(COO^{-1})_2$ from Cullinane (2005). Lines: ▬, this work.

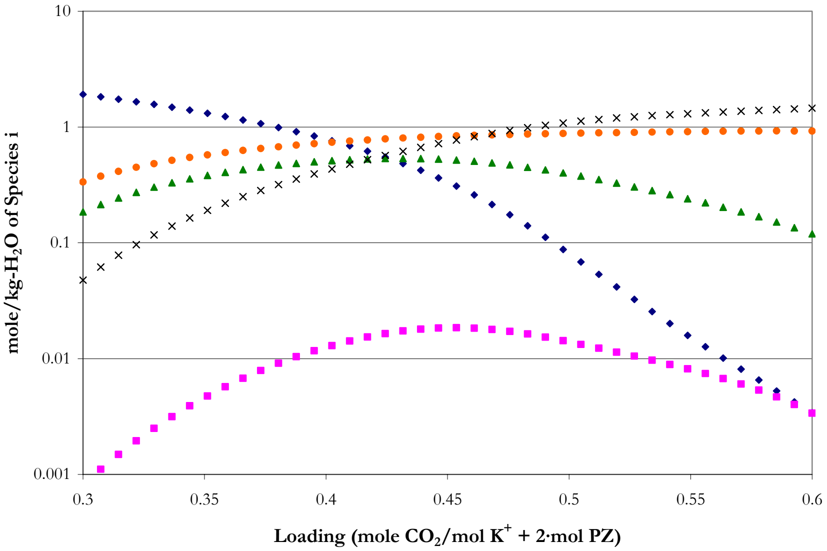

Figure 15.5-47. **Predictions for the Liquid Phase Speciation in 5 m K^+ + 2.5 m PZ at 40 °C from this work. Points: ♦, PZ, ■, PZH^{+1}, ▲, $PZCOO^{-1}$, ●, $PZ(COO^{-1})_2$, ×, H^+PZCOO^{-1}.**

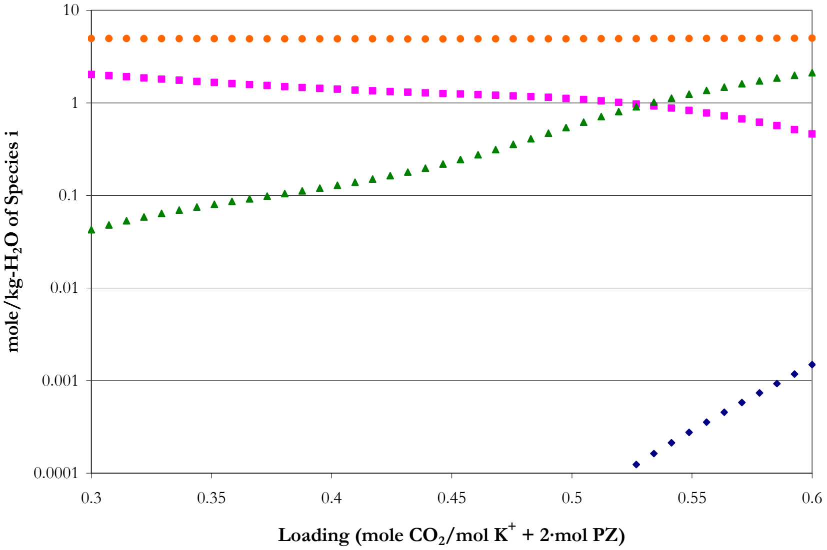

Figure 15.5-48. **Predictions for the Liquid Phase Speciation in 5 m K^+ + 2.5 m PZ at 27 °C from this work. Points: ♦, CO_2, ■, CO_3^{-2}, ▲, HCO_3^{-1}, ●, K^+.**

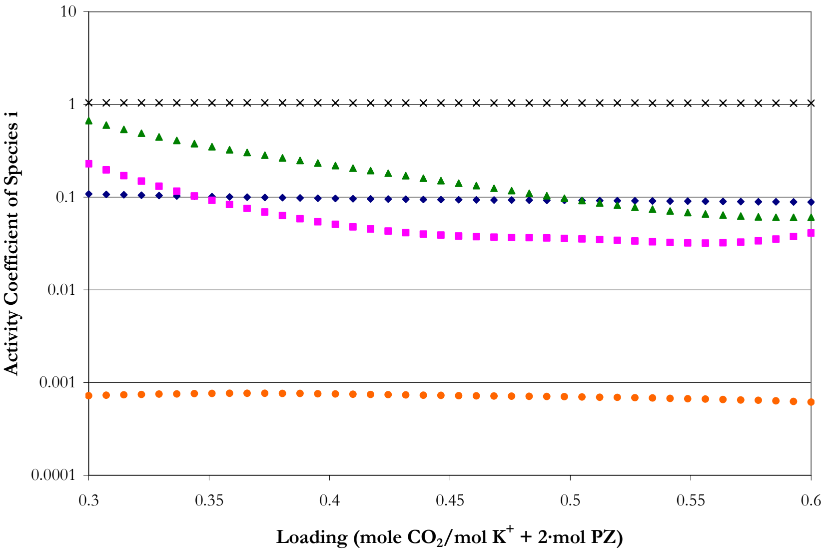

Figure 15.5-49. Predictions for the Liquid Phase Activity Coefficients in 5 m K$^+$ + 2.5 m PZ at 27 ^{o}C from this work. Points: ♦, PZ, ■, PZH^{+1}, ▲, PZCOO^{-1}, ●, PZ(COO^{-1})$_2$, ×, H$^+$PZCOO^{-1}.

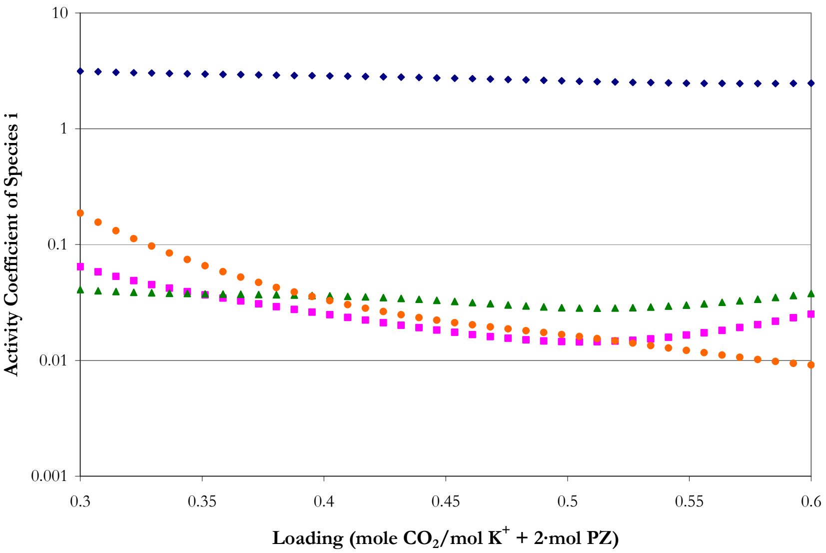

Figure 15.5-50. Predictions for the Liquid Phase Activity Coefficients in 5 m K$^+$ + 2.5 m PZ at 27 ^{o}C from this work. Points: ♦, CO$_2$, ■, CO$_3$$^{-2}$, ▲, HCO$_3$$^{-1}$, ●, K$^+$.

Liquid Phase Speciation for 5 m K^+ + 2.5 m PZ at 60 °C

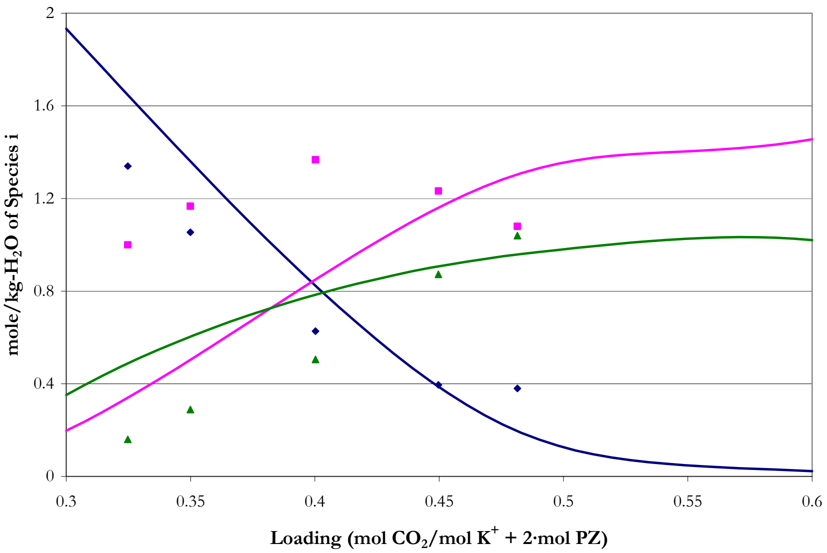

Figure 15.5-51. Comparison of Liquid Phase NMR Speciation in 5 m K^+ + 2.5 m PZ at 60 °C to Model Predictions. Points: ♦, PZ+PZH^{+1}, ■, $PZCOO^{-1}$+H^+PZCOO^{-1}, ▲, $PZ(COO^{-1})_2$ from Cullinane (2005). Lines: —, this work.

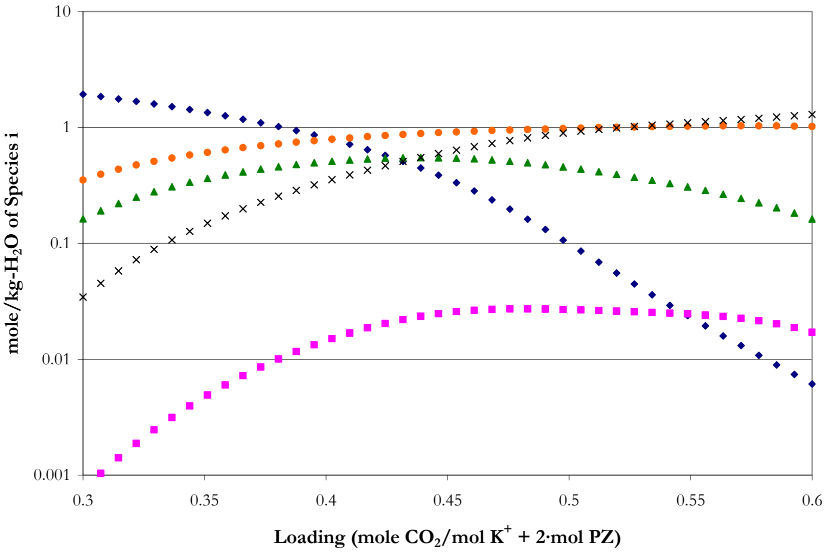

Figure 15.5-52. Predictions for the Liquid Phase Speciation in 5 m K^+ + 2.5 m PZ at 60 °C from this work. Points: ♦, PZ, ■, PZH^{+1}, ▲, $PZCOO^{-1}$, ●, $PZ(COO^{-1})_2$, ×, H^+PZCOO^{-1}.

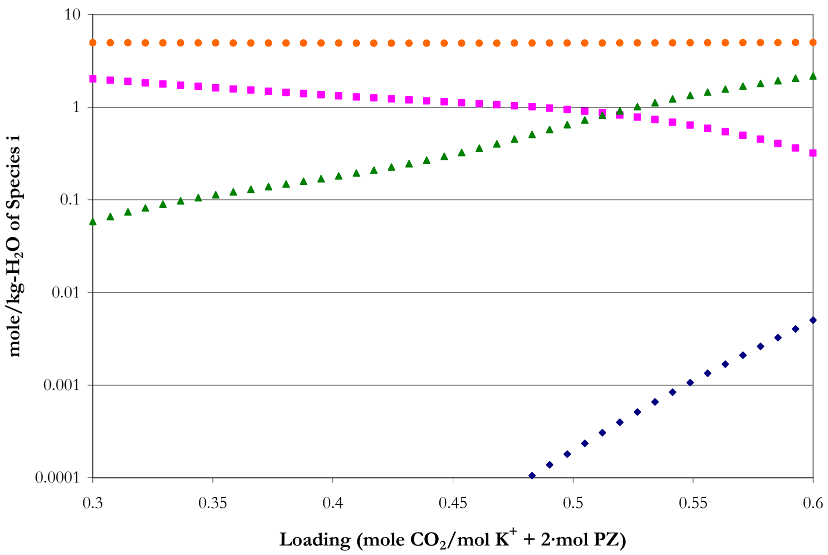

Figure 15.5-53. Predictions for the Liquid Phase Speciation in 5 m K^+ + 2.5 m PZ at 60 °C from this work. Points: ♦, CO_2, ■, CO_3^{-2}, ▲, HCO_3^{-1}, ●, K^+.

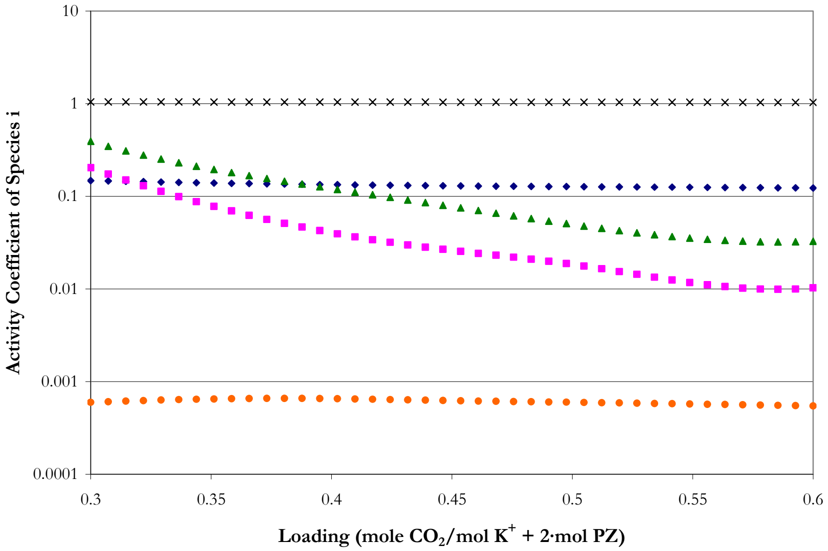

Figure 15.5-54. Predictions for the Liquid Phase Activity Coefficients in 5 m K^+ + 2.5 m PZ at 60 °C from this work. Points: ♦, PZ, ■, PZH^{+1}, ▲, $PZCOO^{-1}$, ●, $PZ(COO^{-1})_2$, ×, H^+PZCOO^{-1}.

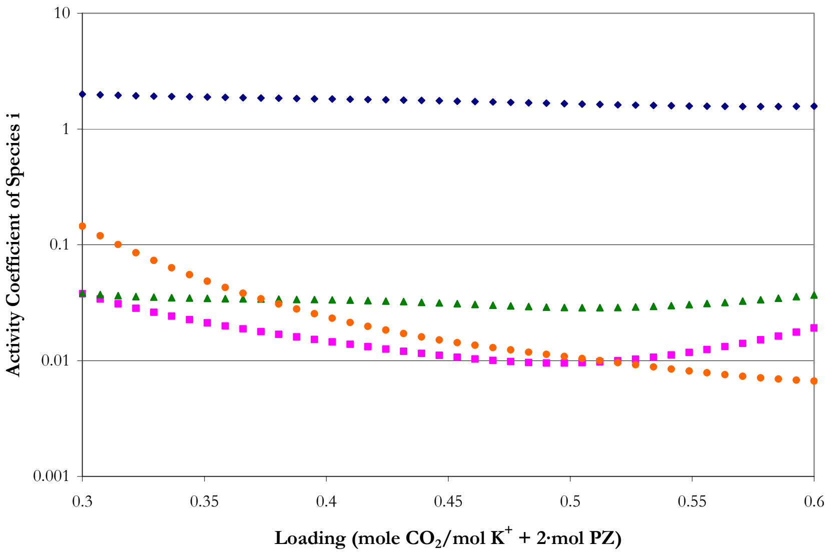

Figure 15.5-55. Predictions for the Liquid Phase Activity Coefficients in 5 m K^+ + 2.5 m PZ at 60 °C from this work. Points: ♦, CO_2, ■, CO_3^{-2}, ▲, HCO_3^{-1}, ●, K^+.

Liquid Phase Speciation for 3.6 m K^+ + 3.6 m PZ at 27 °C

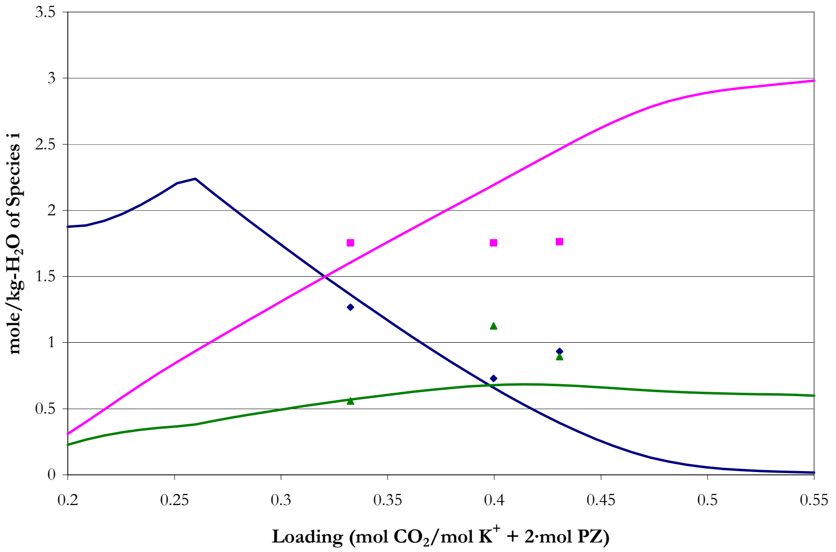

Figure 15.5-56. Comparison of Liquid Phase NMR Speciation in 3.6 m K^+ + 3.6 m PZ at 27 °C to Model Predictions. Points: ♦, PZ+PZH^{+1}, ■, $PZCOO^{-1}$+H^+PZCOO^{-1}, ▲, $PZ(COO^{-1})_2$ from Cullinane (2005). Lines: —, this work.

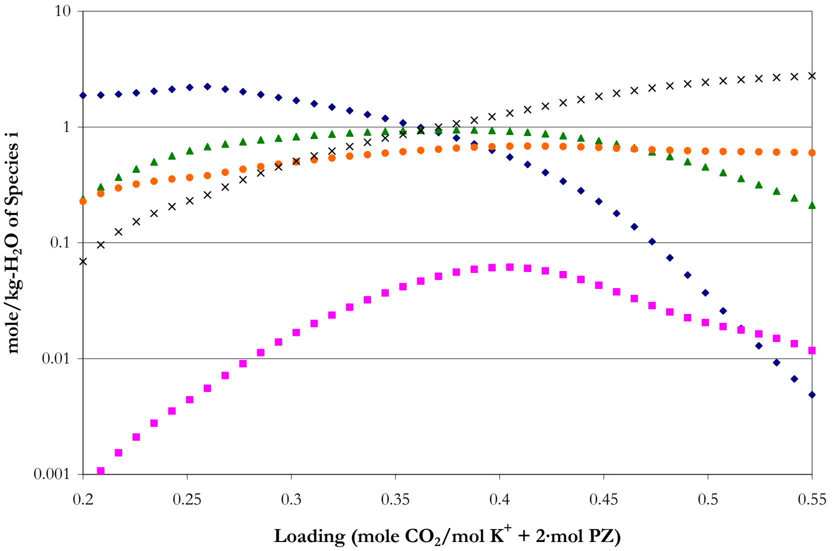

Figure 15.5-57. Predictions for the Liquid Phase Speciation in 3.6 m K^+ + 3.6 m PZ at 27 °C from this work. Points: ♦, PZ, ■, PZH^{+1}, ▲, $PZCOO^{-1}$, ●, $PZ(COO^{-1})_2$, ×, H^+PZCOO^{-1}.

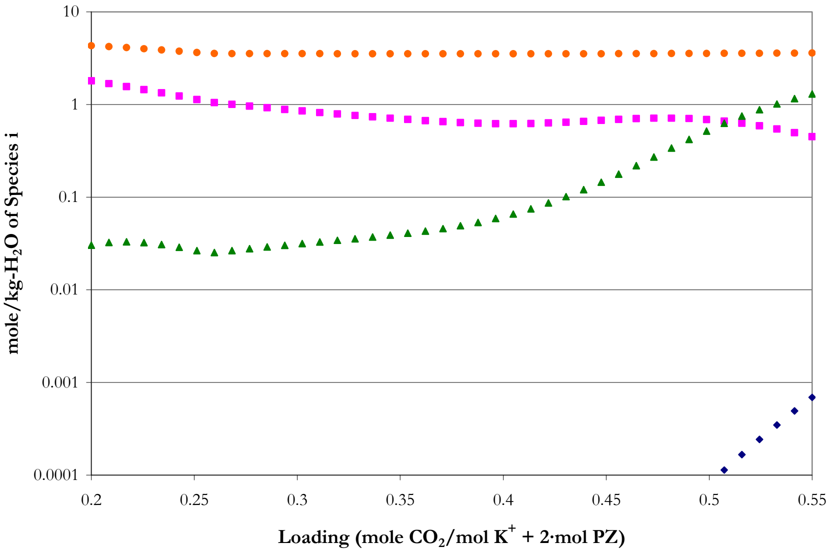

Figure 15.5-58. Predictions for the Liquid Phase Speciation in 3.6 m K^+ + 3.6 m PZ at 27 °C from this work. Points: ♦, CO_2, ■, CO_3^{-2}, ▲, HCO_3^{-1}, ●, K^+.

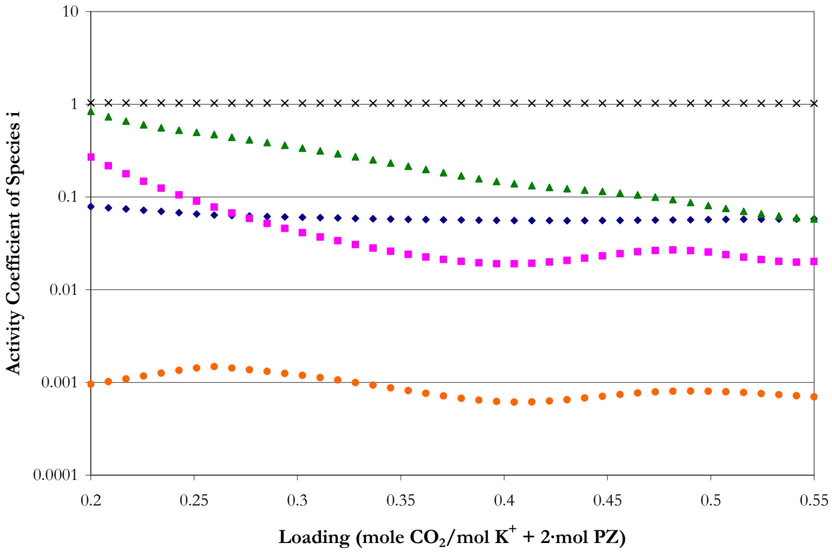

Figure 15.5-59. Predictions for the Liquid Phase Activity Coefficients in 3.6 m K^+ + 3.6 m PZ at 27 °C from this work. Points: ♦, PZ, ■, PZH^{+1}, ▲, $PZCOO^{-1}$, ●, $PZ(COO^{-1})_2$, ×, H^+PZCOO^{-1}.

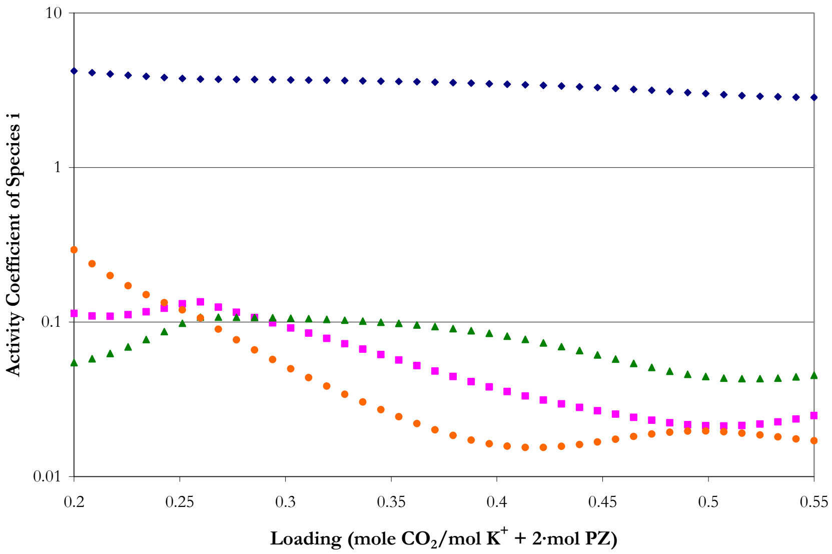

Figure 15.5-60. Predictions for the Liquid Phase Activity Coefficients in 3.6 m K^+ + 3.6 m PZ at 27 °C from this work. Points: ♦, CO_2, ■, CO_3^{-2}, ▲, HCO_3^{-1}, ●, K^+.

Liquid Phase Speciation for 3.6 m K^+ + 3.6 m PZ at 40 °C

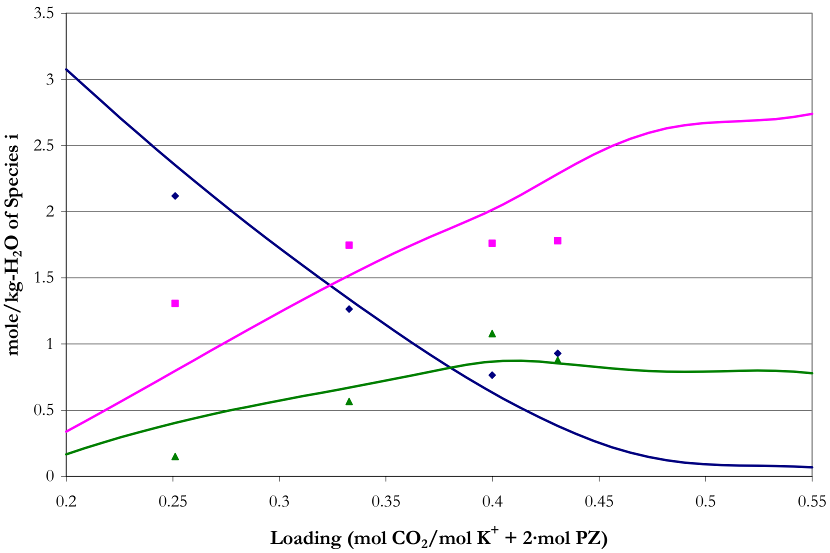

Figure 15.5-61. Comparison of Liquid Phase NMR Speciation in 3.6 m K^+ + 3.6 m PZ at 40 °C to Model Predictions. Points: ♦, PZ+PZH^{+1}, ■, $PZCOO^{-1}$+H^+PZCOO^{-1}, ▲, $PZ(COO^{-1})_2$ from Cullinane (2005). Lines: ▬, this work.

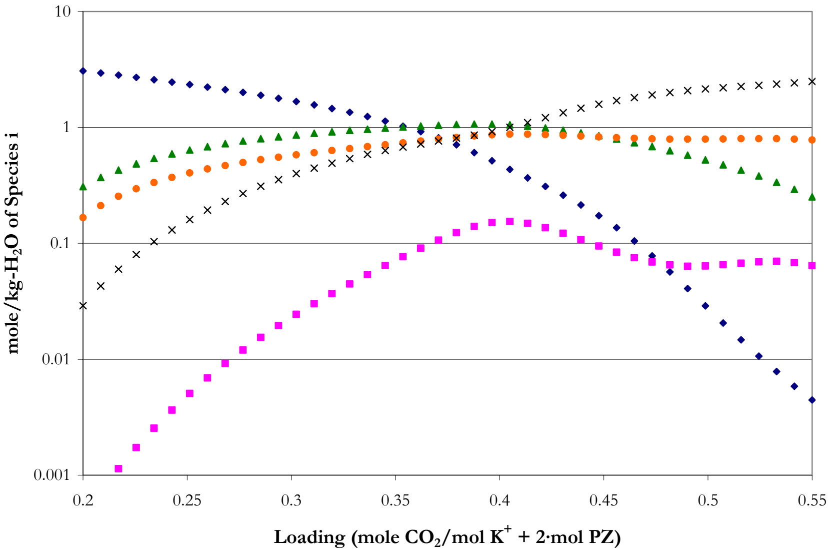

Figure 15.5-62. Predictions for the Liquid Phase Speciation in 3.6 m K^+ + 3.6 m PZ at 40 °C from this work. Points: ♦, PZ, ■, PZH^{+1}, ▲, $PZCOO^{-1}$, ●, $PZ(COO^{-1})_2$, ×, H^+PZCOO^{-1}.

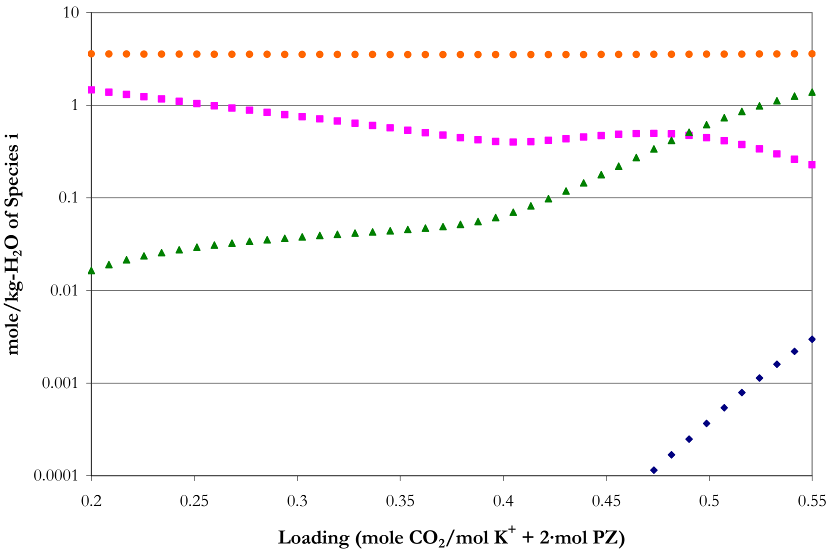

Figure 15.5-63. Predictions for the Liquid Phase Speciation in 3.6 m K^+ + 3.6 m PZ at 40 °C from this work. Points: ♦, CO_2, ■, CO_3^{-2}, ▲, HCO_3^{-1}, ●, K^+.

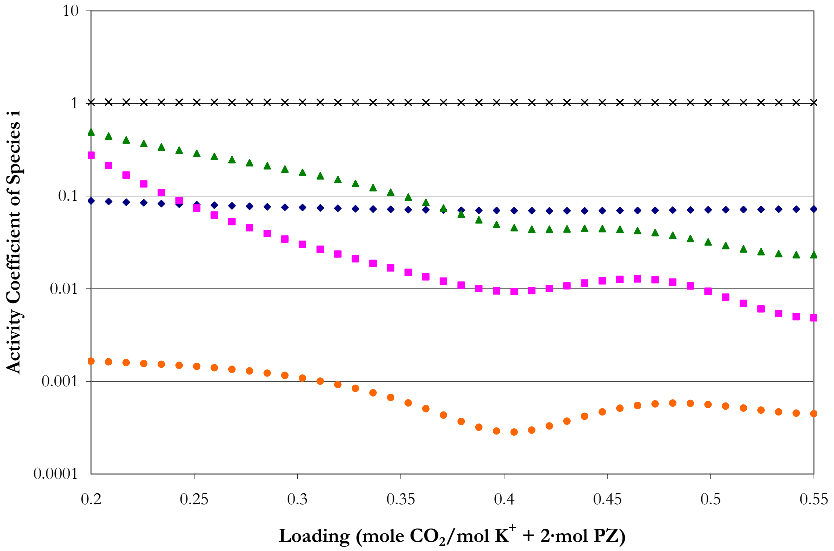

Figure 15.5-64. Predictions for the Liquid Phase Activity Coefficients in 3.6 m K^+ + 3.6 m PZ at 40 °C from this work. Points: ♦, PZ, ■, PZH^{+1}, ▲, $PZCOO^{-1}$, ●, $PZ(COO^{-1})_2$, ×, H^+PZCOO^{-1}.

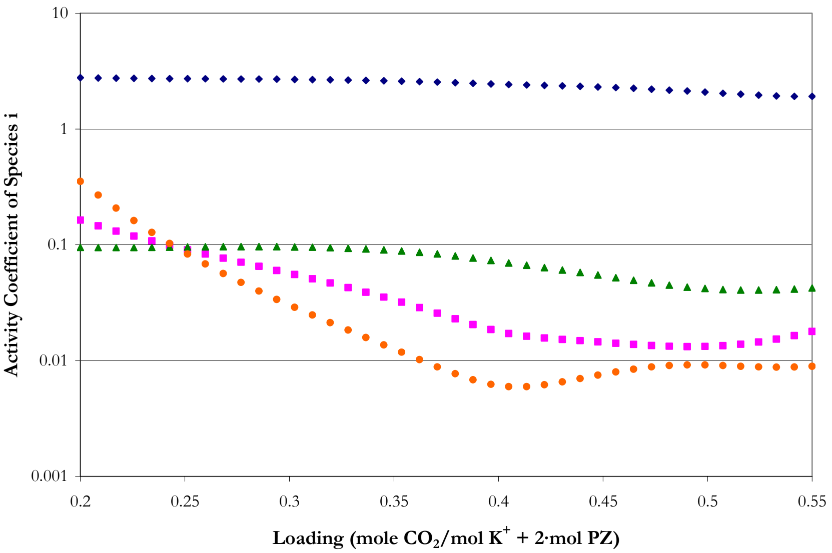

Figure 15.5-65. Predictions for the Liquid Phase Activity Coefficients in 3.6 m K^+ + 3.6 m PZ at 40 °C from this work. Points: ♦, CO_2, ■, CO_3^{-2}, ▲, HCO_3^{-1}, ●, K^+.

Liquid Phase Speciation for 3.6 m K^+ + 3.6 m PZ at 60 °C

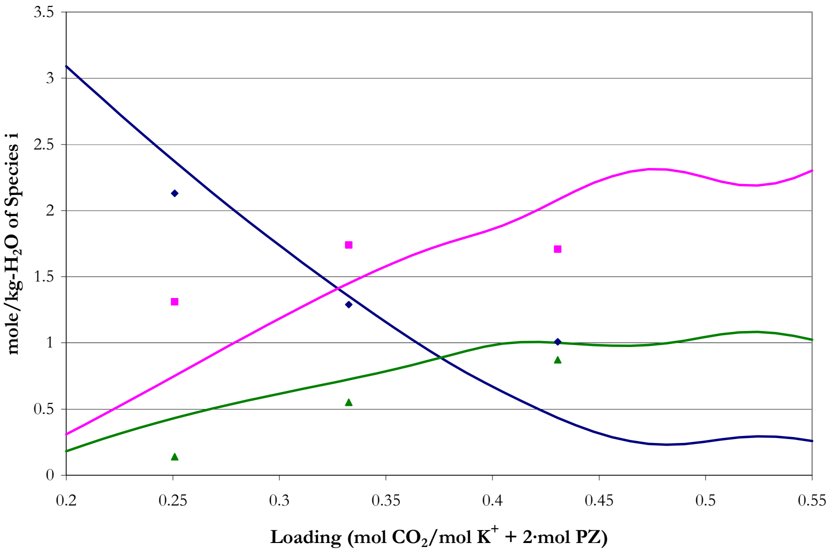

Figure 15.5-66. Comparison of Liquid Phase NMR Speciation in 3.6 m K^+ + 3.6 m PZ at 60 °C to Model Predictions. Points: ♦, PZ+PZH^{+1}, ■, $PZCOO^{-1}$+H^+PZCOO^{-1}, ▲, $PZ(COO^{-1})_2$ from Cullinane (2005). Lines: —, this work.

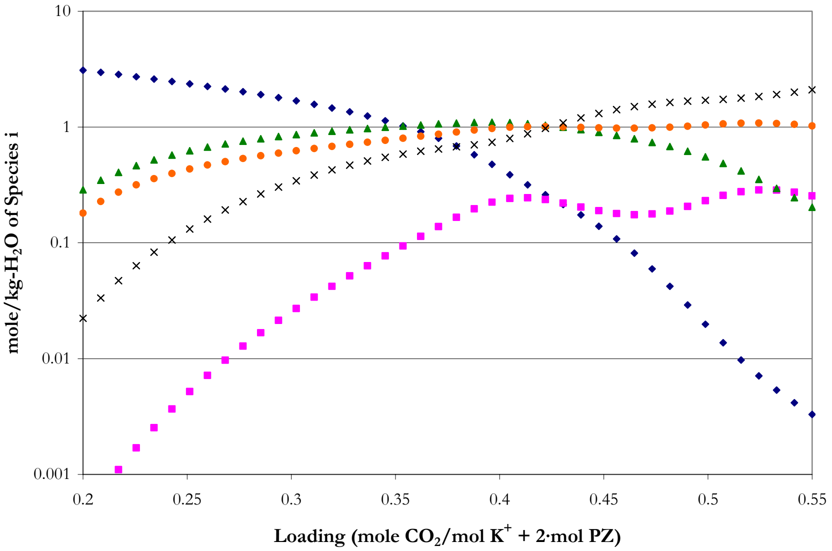

Figure 15.5-67. Predictions for the Liquid Phase Speciation in 3.6 m K^+ + 3.6 m PZ at 60 °C from this work. Points: ♦, PZ, ■, PZH^{+1}, ▲, $PZCOO^{-1}$, ●, $PZ(COO^{-1})_2$, ×, H^+PZCOO^{-1}.

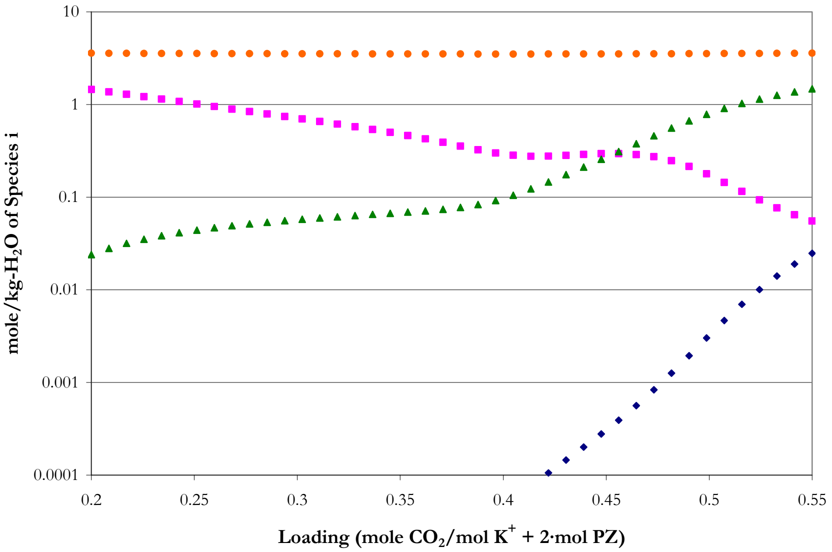

Figure 15.5-68. Predictions for the Liquid Phase Speciation in 3.6 m K^+ + 3.6 m PZ at 60 °C from this work. Points: ♦, CO_2, ■, CO_3^{-2}, ▲, HCO_3^{-1}, ●, K^+.

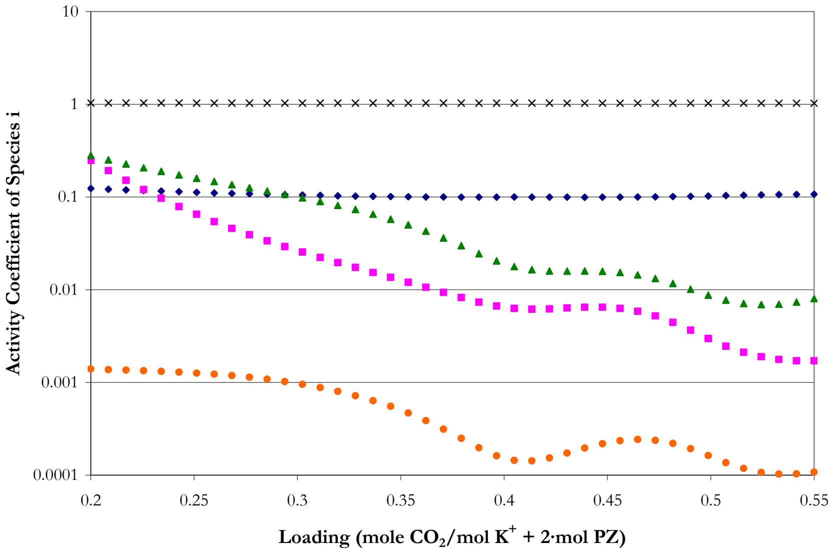

Figure 15.5-69. Predictions for the Liquid Phase Activity Coefficients in 3.6 m K^+ + 3.6 m PZ at 60 °C from this work. Points: ♦, PZ, ■, PZH^{+1}, ▲, $PZCOO^{-1}$, ●, $PZ(COO^{-1})_2$, ×, H^+PZCOO^{-1}.

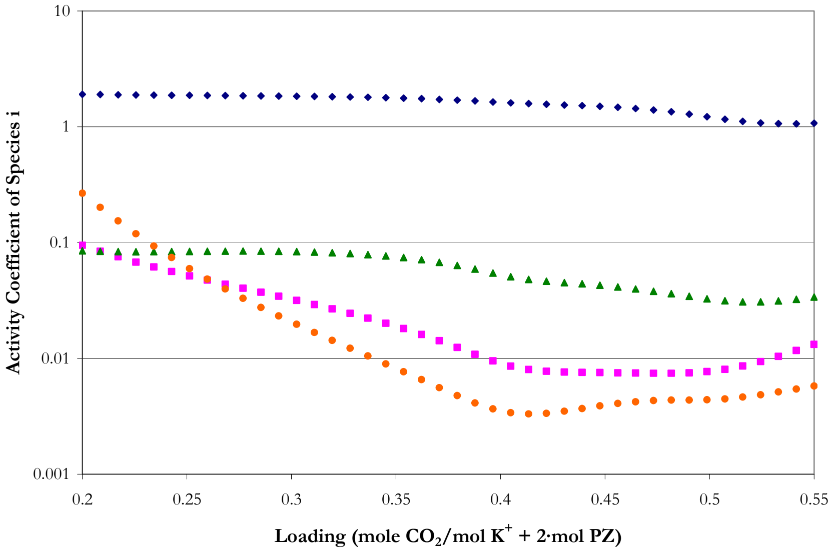

Figure 15.5-70. Predictions for the Liquid Phase Activity Coefficients in 3.6 m K^+ + 3.6 m PZ at 60 °C from this work. Points: ♦, CO_2, ■, CO_3^{-2}, ▲, HCO_3^{-1}, ●, K^+.

Liquid Phase Speciation for 6 m K^+ + 1.2 m PZ at 27 °C

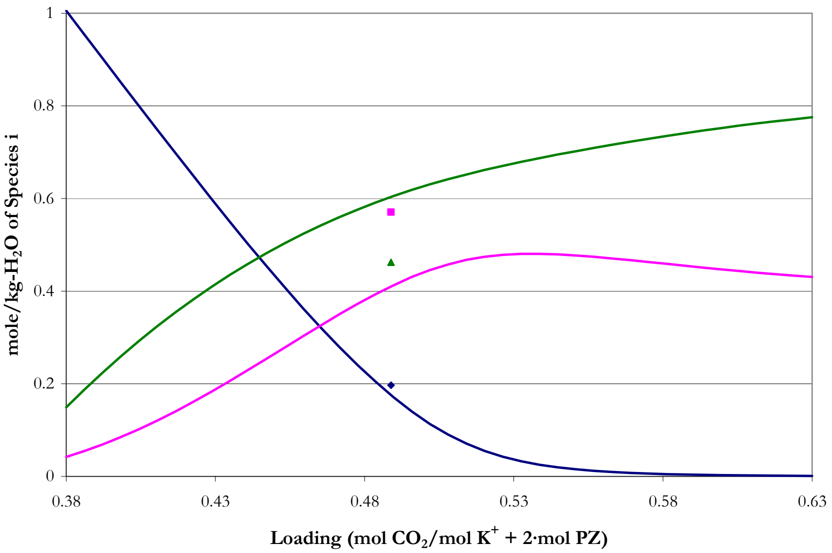

Figure 15.5-71. Comparison of Liquid Phase NMR Speciation in 6 m K^+ + 1.2 m PZ at 27 °C to Model Predictions. Points: ♦, PZ+PZH^{+1}, ■, $PZCOO^{-1}$+H^+PZCOO^{-1}, ▲, $PZ(COO^{-1})_2$ from Cullinane (2005). Lines: ▬, this work.

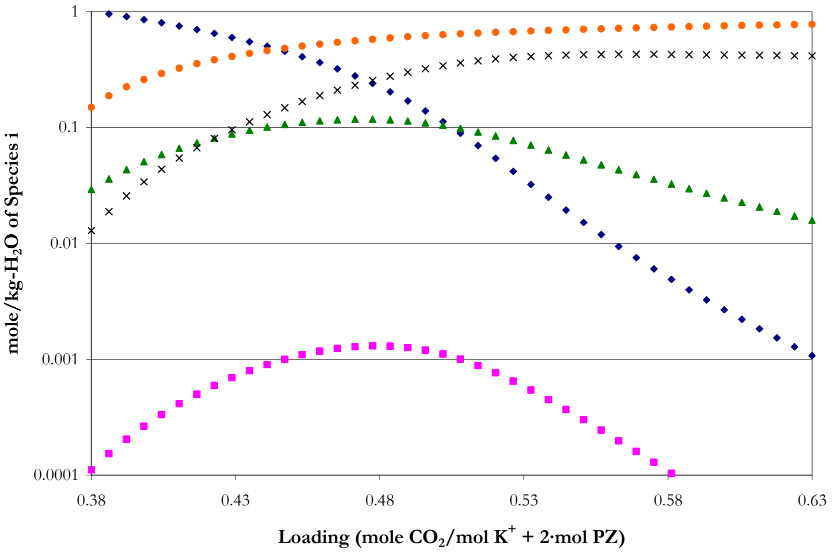

Figure 15.5-72. Predictions for the Liquid Phase Speciation in 6 m K^+ + 1.2 m PZ at 27 °C from this work. Points: ♦, PZ, ■, PZH^{+1}, ▲, $PZCOO^{-1}$, ●, $PZ(COO^{-1})_2$, ×, H^+PZCOO^{-1}.

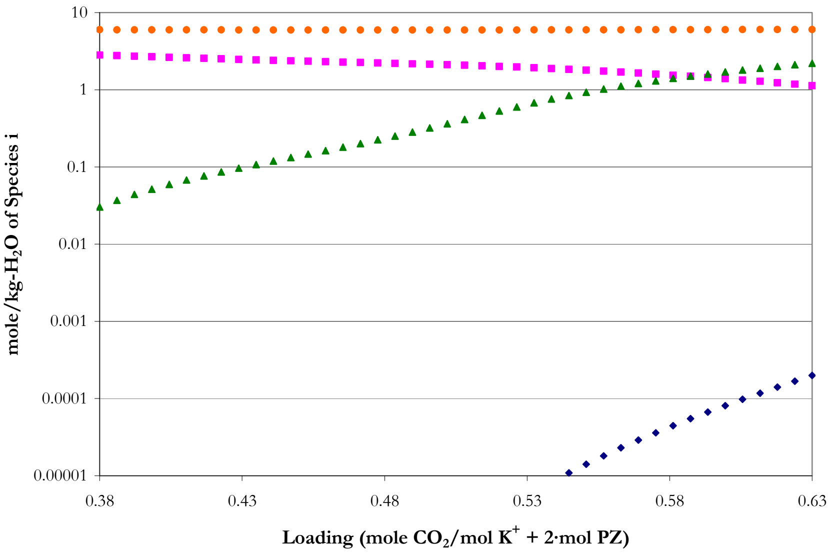

Figure 15.5-73. Predictions for the Liquid Phase Speciation in 6 m K^+ + 1.2 m PZ at 27 °C from this work. Points: ♦, CO_2, ■, CO_3^{-2}, ▲, HCO_3^{-1}, ●, K^+.

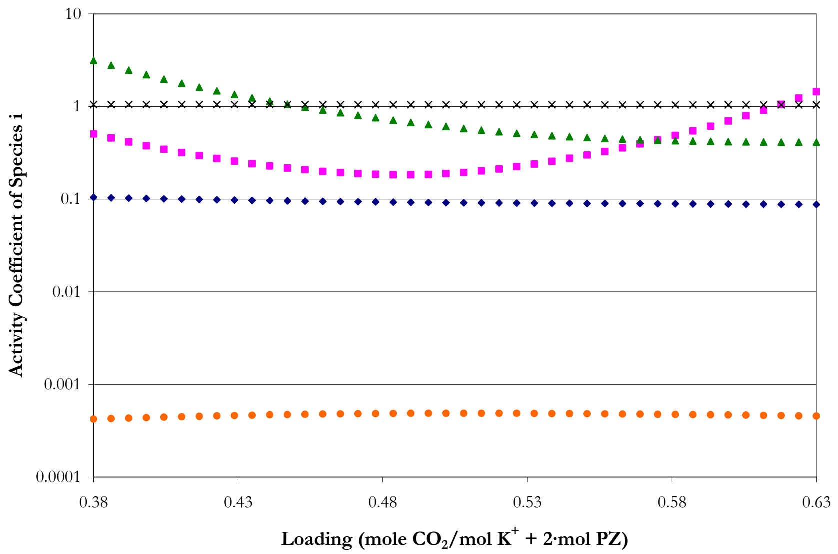

Figure 15.5-74. Predictions for the Liquid Phase Activity Coefficients in 6 m K^+ + 1.2 m PZ at 27 °C from this work. Points: ♦, PZ, ■, PZH^{+1}, ▲, $PZCOO^{-1}$, ●, $PZ(COO^{-1})_2$, ×, H^+PZCOO^{-1}.

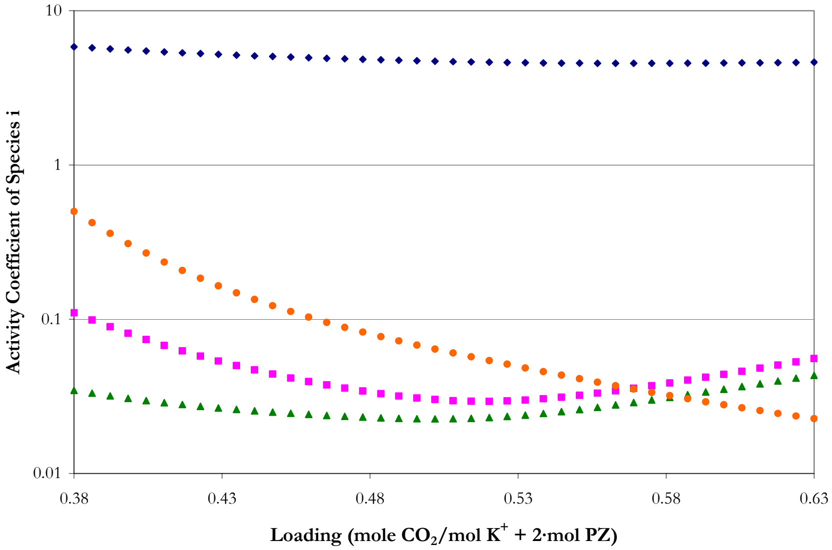

Figure 15.5-75. Predictions for the Liquid Phase Activity Coefficients in 6 m K$^+$ + 1.2 m PZ at 27 ^{o}C from this work. Points: ♦, CO$_2$, ■, CO$_3^{-2}$, ▲, HCO$_3^{-1}$, ●, K$^+$.

Liquid Phase Speciation for 6 m K$^+$ + 1.2 m PZ at 40 ^{o}C

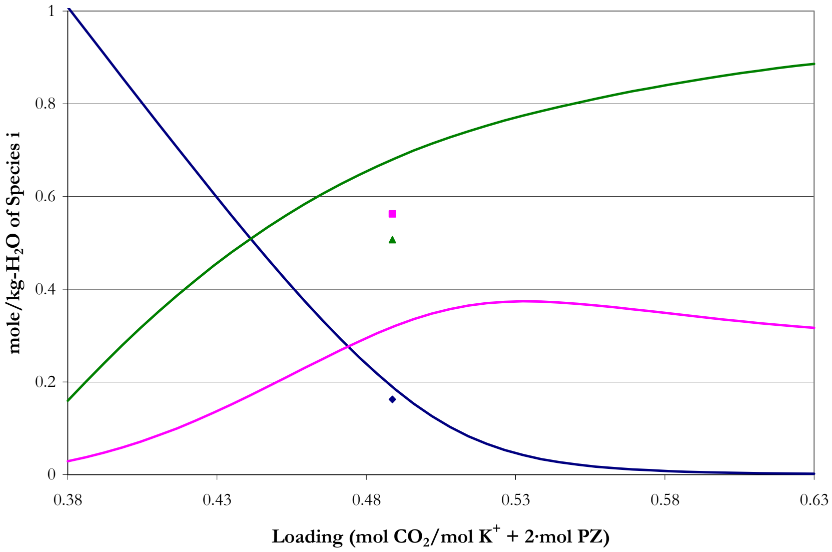

Figure 15.5-76. Comparison of Liquid Phase NMR Speciation in 6 m K$^+$ + 1.2 m PZ at 40 ^{o}C to Model Predictions. Points: ♦, PZ+PZH^{+1}, ■, PZCOO^{-1}+H$^+$PZCOO^{-1}, ▲, PZ(COO^{-1})$_2$ from Cullinane (2005). Lines: —, this work.

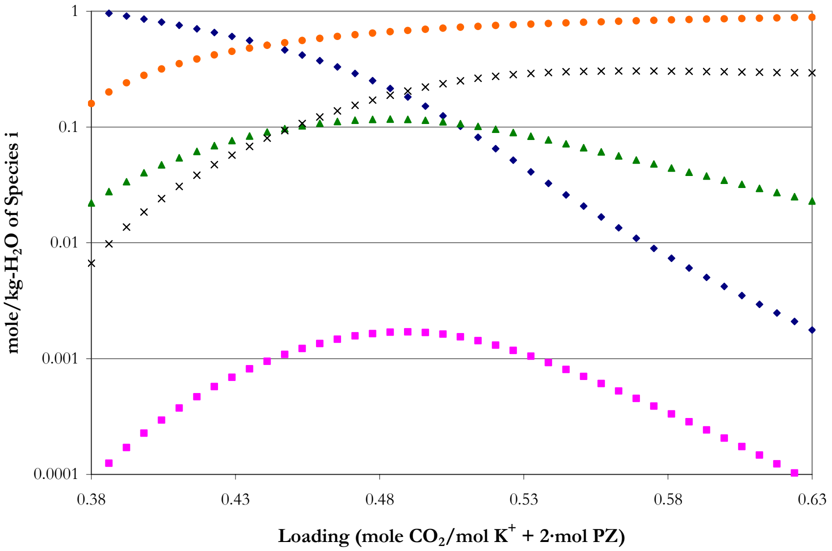

Figure 15.5-77. Predictions for the Liquid Phase Speciation in 6 m K^+ + 1.2 m PZ at 40 °C from this work. Points: ◆, PZ, ■, PZH^{+1}, ▲, $PZCOO^{-1}$, ●, $PZ(COO^{-1})_2$, ×, H^+PZCOO^{-1}.

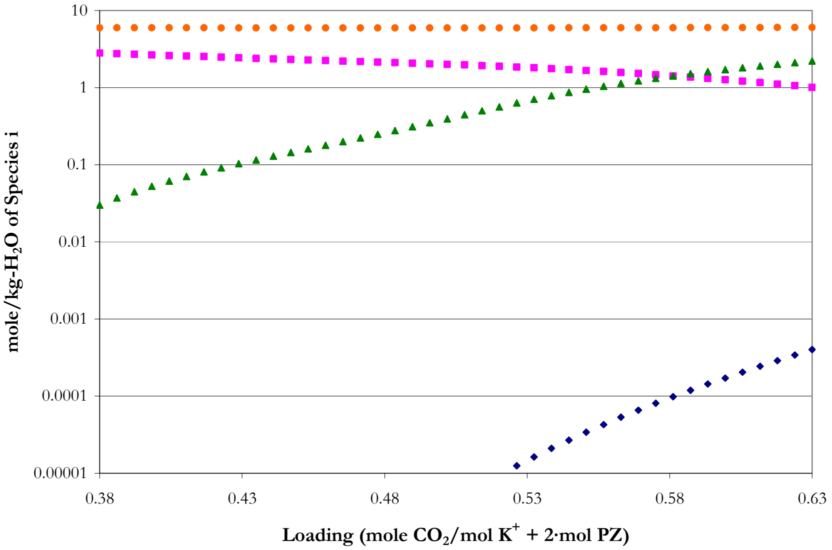

Figure 15.5-78. Predictions for the Liquid Phase Speciation in 6 m K^+ + 1.2 m PZ at 40 °C from this work. Points: ◆, CO_2, ■, CO_3^{-2}, ▲, HCO_3^{-1}, ●, K^+.

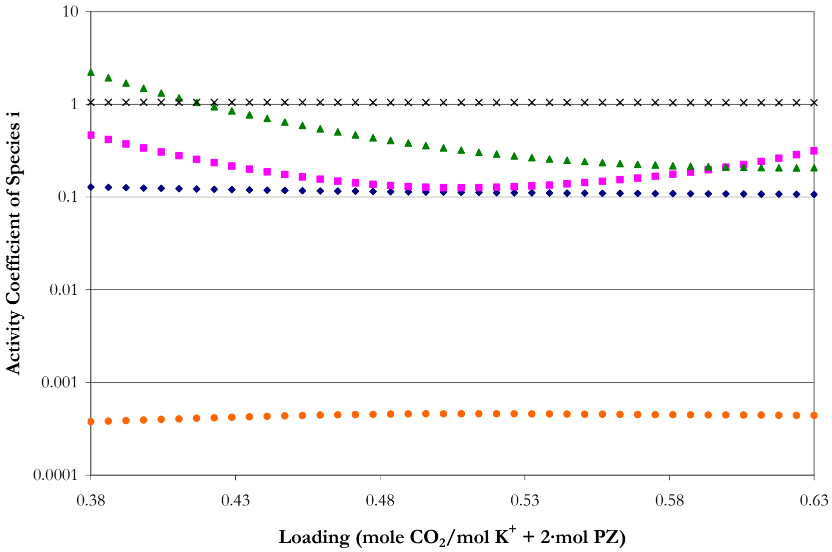

Figure 15.5-79. Predictions for the Liquid Phase Activity Coefficients in 6 m K^+ + 1.2 m PZ at 40 °C from this work. Points: ♦, PZ, ■, PZH^{+1}, ▲, $PZCOO^{-1}$, ●, $PZ(COO^{-1})_2$, ×, H^+PZCOO^{-1}.

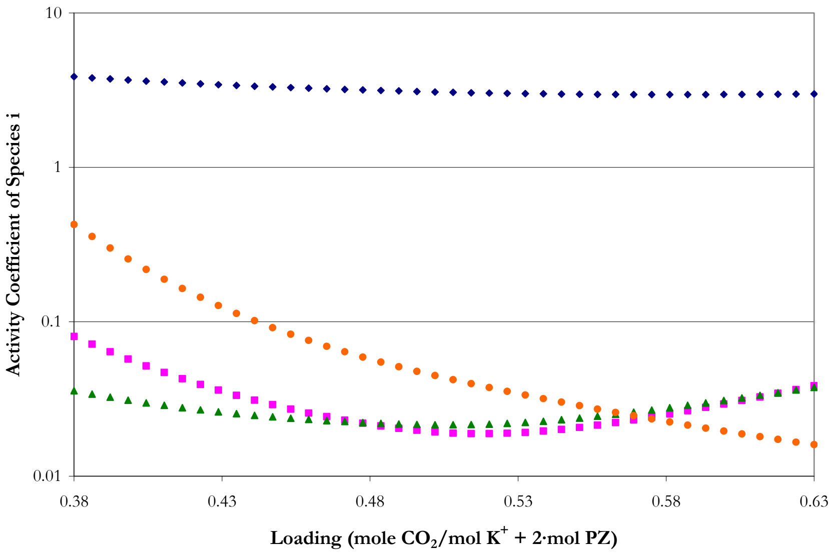

Figure 15.5-80. Predictions for the Liquid Phase Activity Coefficients in 6 m K^+ + 1.2 m PZ at 40 °C from this work. Points: ♦, CO_2, ■, CO_3^{-2}, ▲, HCO_3^{-1}, ●, K^+.

Liquid Phase Speciation for 6 m K^+ + 1.2 m PZ at 60 °C

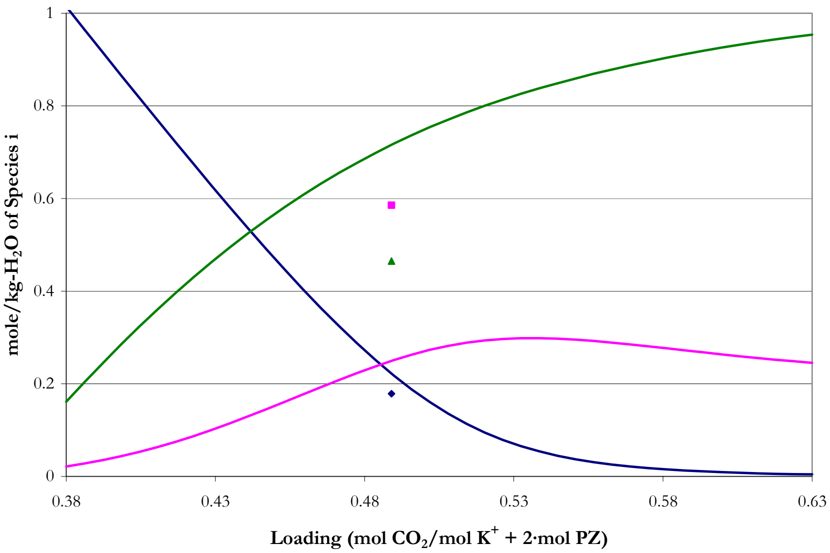

Figure 15.5-81. Comparison of Liquid Phase NMR Speciation in 6 m K^+ + 1.2 m PZ at 60 °C to Model Predictions. Points: ♦, PZ+PZH^{+1}, ■, PZCOO^{-1}+H$^+$PZCOO^{-1}, ▲, PZ(COO^{-1})$_2$ from Cullinane (2005). Lines: ▬, this work.

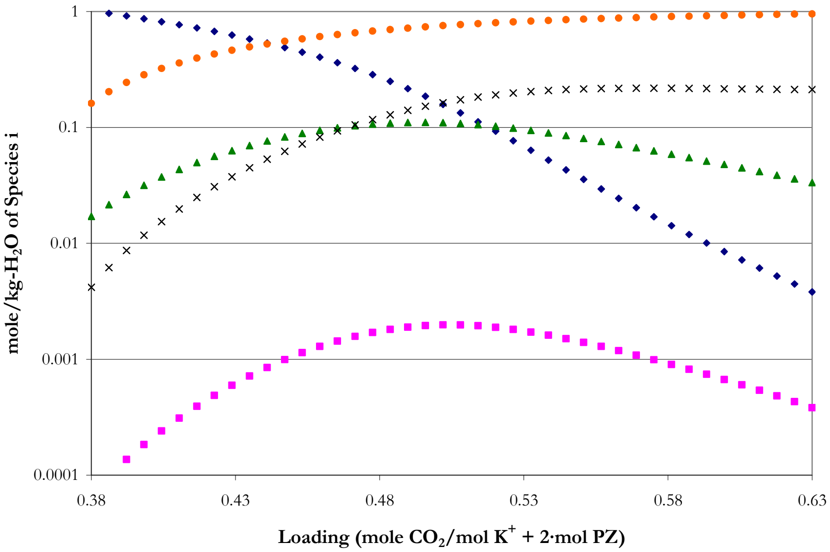

Figure 15.5-82. Predictions for the Liquid Phase Speciation in 6 m K^+ + 1.2 m PZ at 60 °C from this work. Points: ♦, PZ, ■, PZH^{+1}, ▲, PZCOO^{-1}, ●, PZ(COO^{-1})$_2$, ×, H$^+$PZCOO^{-1}.

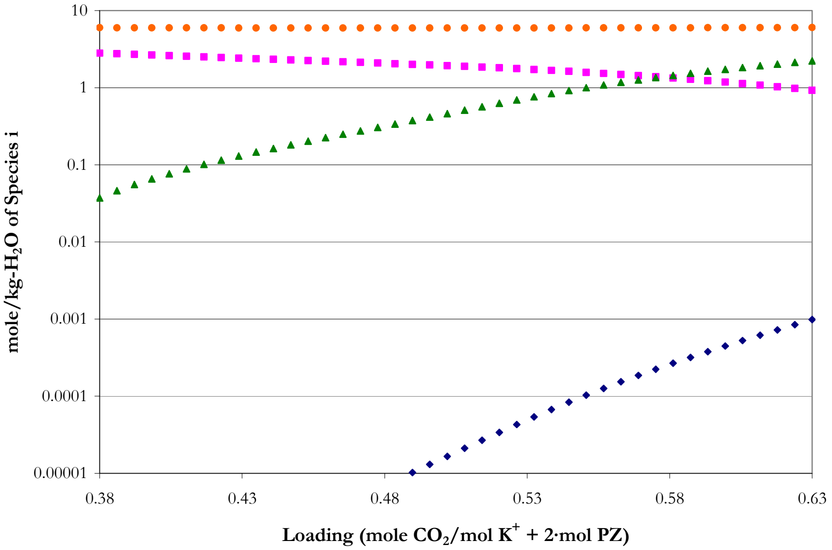

Figure 15.5-83. Predictions for the Liquid Phase Speciation in 6 m K^+ + 1.2 m PZ at 60 °C from this work. Points: ♦, CO_2, ■, CO_3^{-2}, ▲, HCO_3^{-1}, ●, K^+.

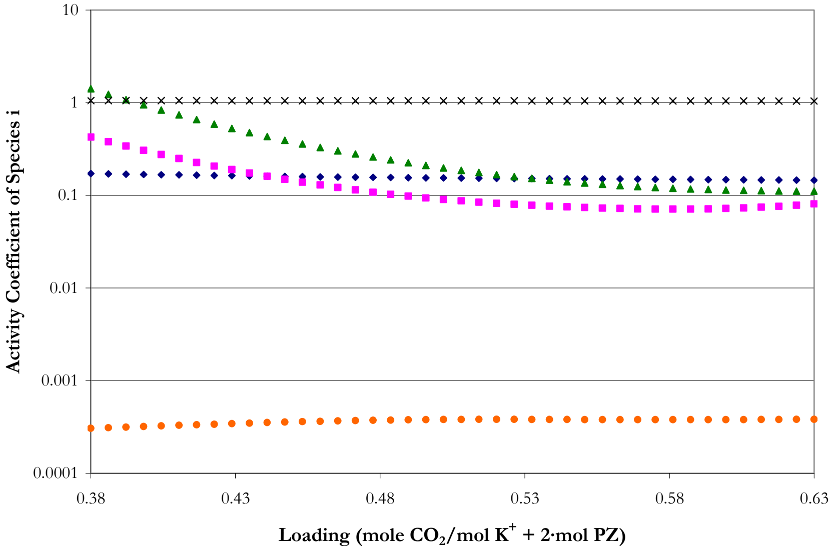

Figure 15.5-84. Predictions for the Liquid Phase Activity Coefficients in 6 m K^+ + 1.2 m PZ at 60 °C from this work. Points: ♦, PZ, ■, PZH^{+1}, ▲, $PZCOO^{-1}$, ●, $PZ(COO^{-1})_2$, ×, H^+PZCOO^{-1}.

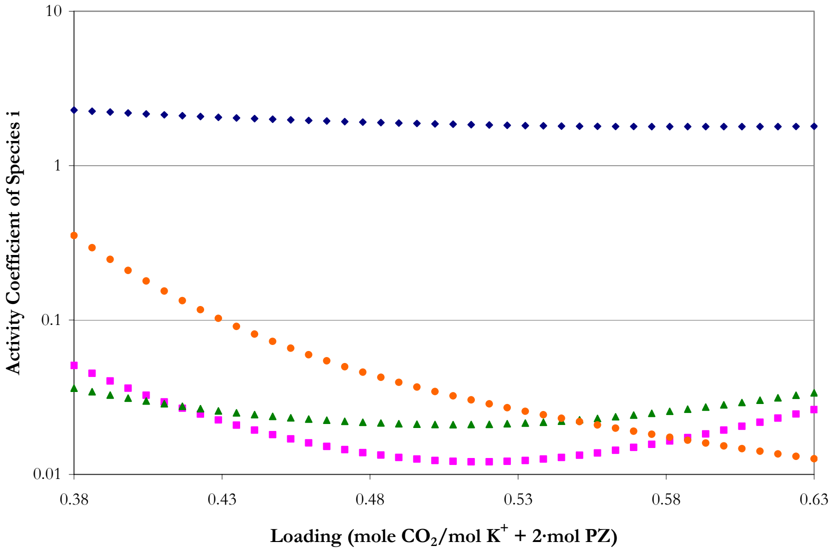

Figure 15.5-85. Predictions for the Liquid Phase Activity Coefficients in 6 m K^+ + 1.2 m PZ at 60 °C from this work. Points: ♦, CO_2, ■, CO_3^{-2}, ▲, HCO_3^{-1}, ●, K^+.

Liquid Phase Speciation for 3.6 m K^+ + 0.6 m PZ at 27 °C

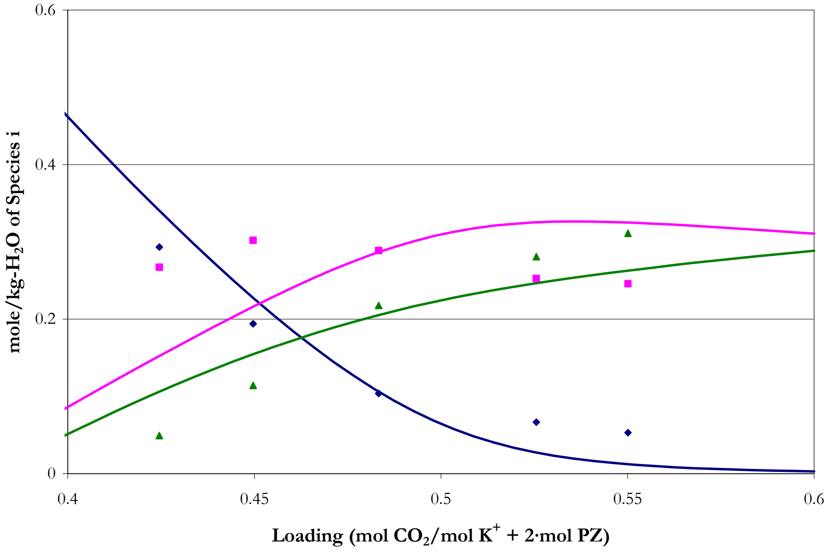

Figure 15.5-86. Comparison of Liquid Phase NMR Speciation in 3.6 m K^+ + 0.6 m PZ at 27 °C to Model Predictions. Points: ♦, $PZ+PZH^{+1}$, ■, $PZCOO^{-1}+H^+PZCOO^{-1}$, ▲, $PZ(COO^{-1})_2$ from Cullinane (2005). Lines: —, this work.

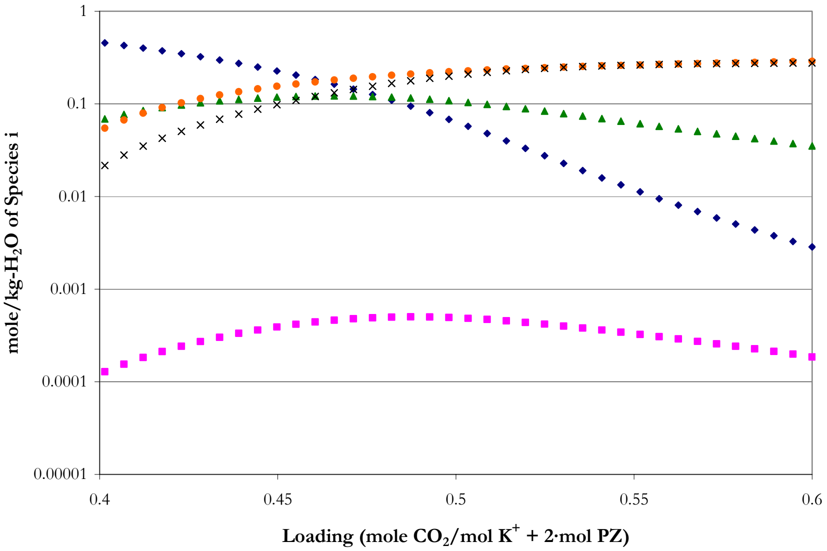

Figure 15.5-87. Predictions for the Liquid Phase Speciation in 3.6 m K^+ + 0.6 m PZ at 27 °C from this work. Points: ♦, PZ, ■, PZH^{+1}, ▲, $PZCOO^{-1}$, ●, $PZ(COO^{-1})_2$, ×, H^+PZCOO^{-1}.

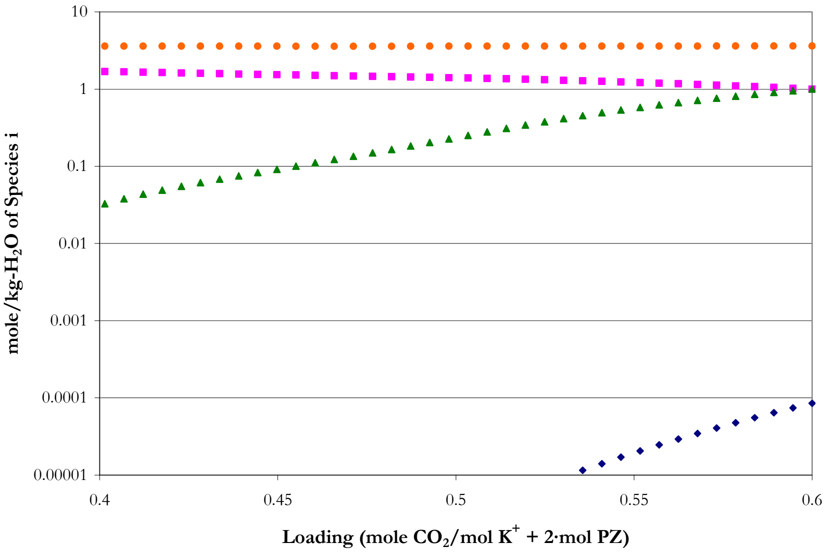

Figure 15.5-88. Predictions for the Liquid Phase Speciation in 3.6 m K^+ + 0.6 m PZ at 27 °C from this work. Points: ♦, CO_2, ■, CO_3^{-2}, ▲, HCO_3^{-1}, ●, K^+.

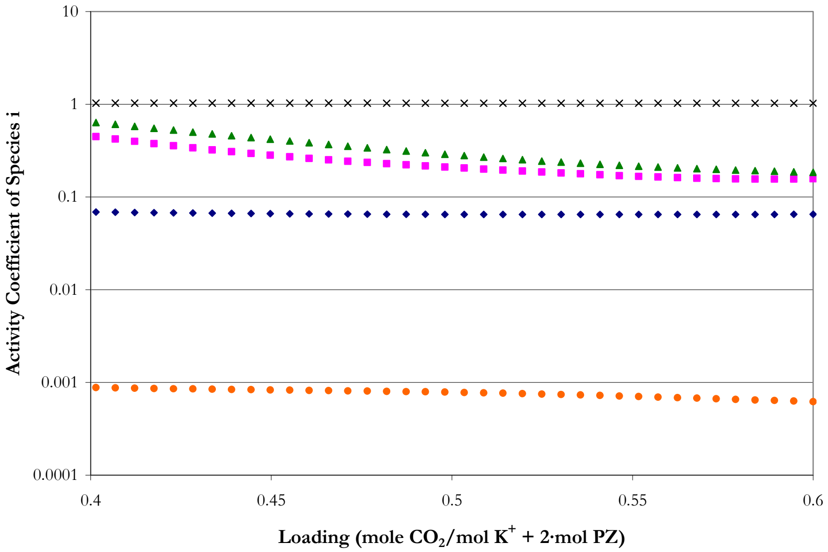

Figure 15.5-89. Predictions for the Liquid Phase Activity Coefficients in 3.6 m K^+ + 0.6 m PZ at 27 °C from this work. Points: ♦, PZ, ■, PZH^{+1}, ▲, $PZCOO^{-1}$, ●, $PZ(COO^{-1})_2$, ×, H^+PZCOO^{-1}.

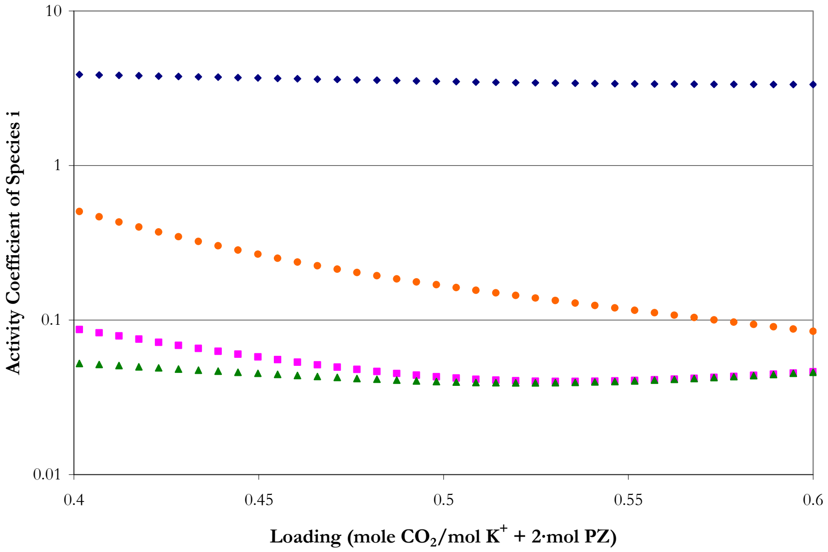

Figure 15.5-90. Predictions for the Liquid Phase Activity Coefficients in 3.6 m K^+ + 0.6 m PZ at 27 °C from this work. Points: ♦, CO_2, ■, CO_3^{-2}, ▲, HCO_3^{-1}, ●, K^+.

Liquid Phase Speciation for 3.6 m K^+ + 0.6 m PZ at 40 °C

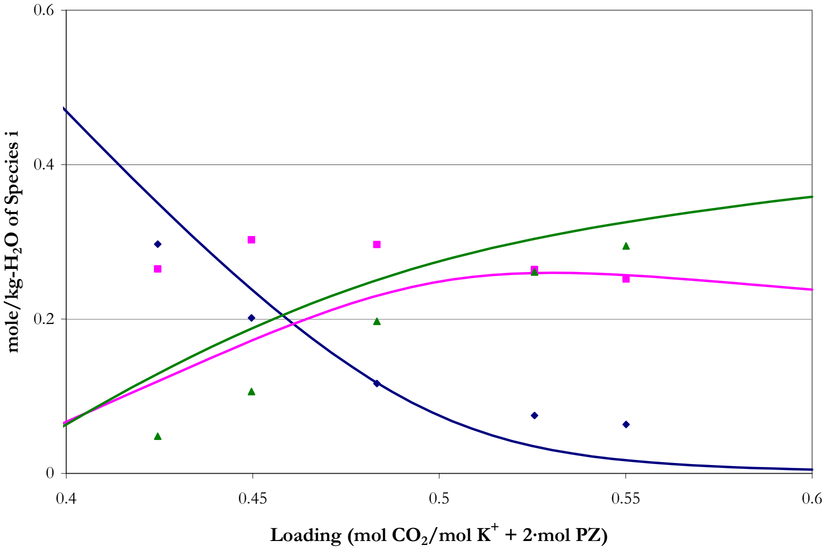

Figure 15.5-91. Comparison of Liquid Phase NMR Speciation in 3.6 m K^+ + 0.6 m PZ at 40 °C to Model Predictions. Points: ♦, PZ+PZH^{+1}, ■, $PZCOO^{-1}$+H^+PZCOO^{-1}, ▲, $PZ(COO^{-1})_2$ from Cullinane (2005). Lines: ▬, this work.

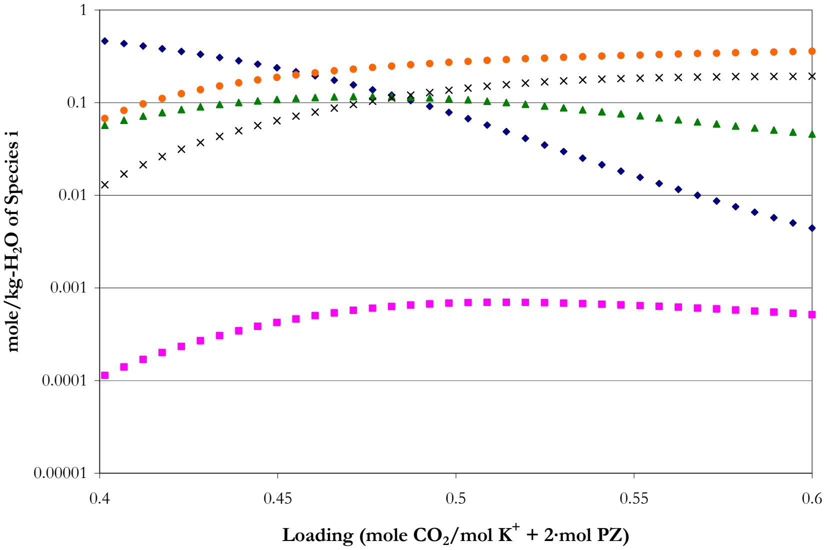

Figure 15.5-92. Predictions for the Liquid Phase Speciation in 3.6 m K^+ + 0.6 m PZ at 40 °C from this work. Points: ♦, PZ, ■, PZH^{+1}, ▲, $PZCOO^{-1}$, ●, $PZ(COO^{-1})_2$, ×, H^+PZCOO^{-1}.

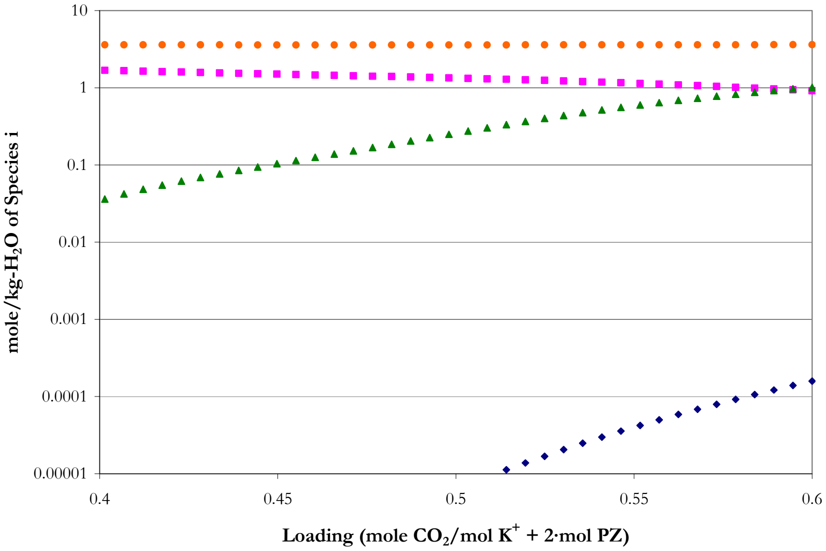

Figure 15.5-93. Predictions for the Liquid Phase Speciation in 3.6 m K^+ + 0.6 m PZ at 40 °C from this work. Points: ♦, CO_2, ■, CO_3^{-2}, ▲, HCO_3^{-1}, ●, K^+.

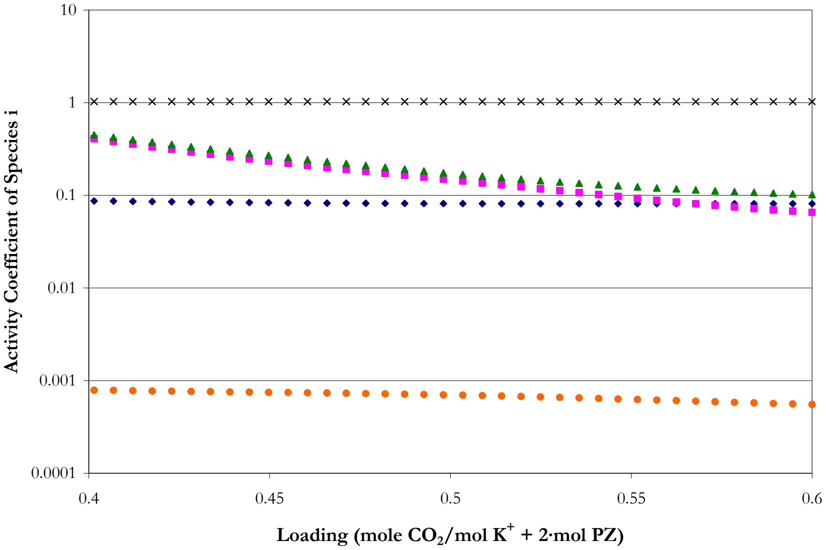

Figure 15.5-94. Predictions for the Liquid Phase Activity Coefficients in 3.6 m K^+ + 0.6 m PZ at 40 °C from this work. Points: ♦, PZ, ■, PZH^{+1}, ▲, $PZCOO^{-1}$, ●, $PZ(COO^{-1})_2$, ×, H^+PZCOO^{-1}.

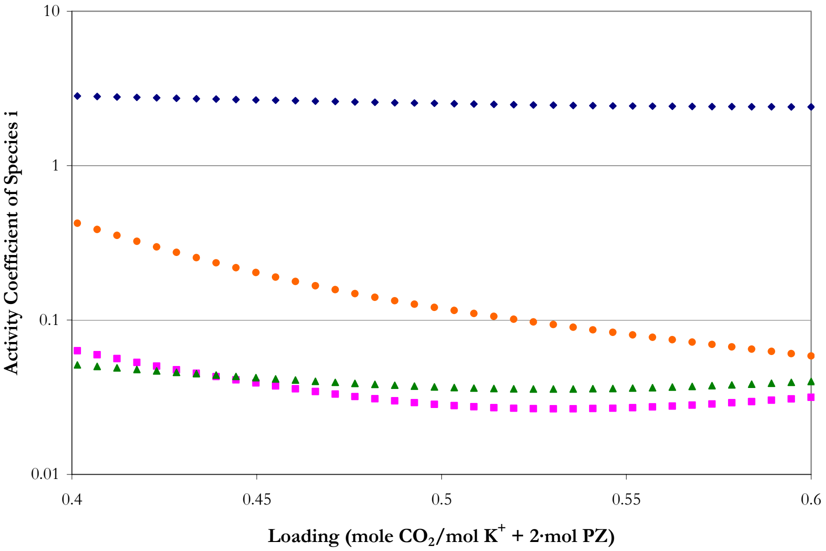

Figure 15.5-95. Predictions for the Liquid Phase Activity Coefficients in 3.6 m K^+ + 0.6 m PZ at 40 °C from this work. Points: ♦, CO_2, ■, CO_3^{-2}, ▲, HCO_3^{-1}, ●, K^+.

Liquid Phase Speciation for 3.6 m K^+ + 0.6 m PZ at 60 °C

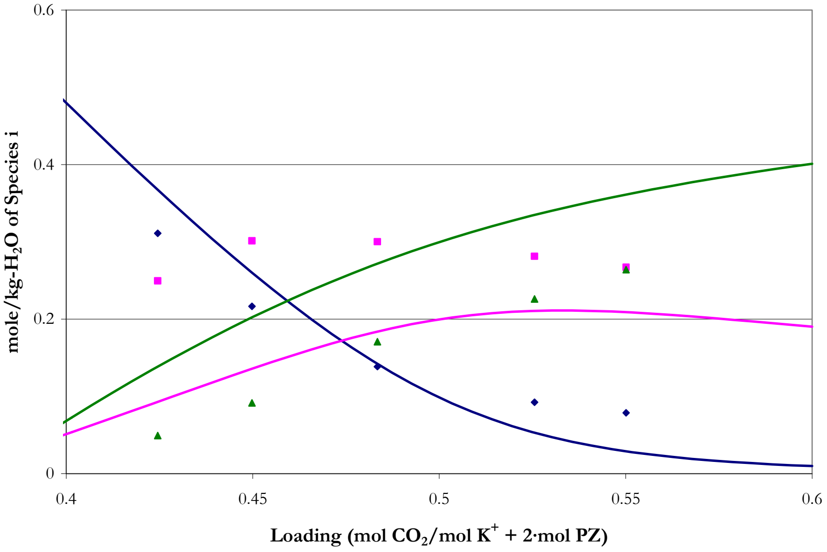

Figure 15.5-96. Comparison of Liquid Phase NMR Speciation in 3.6 m K^+ + 0.6 m PZ at 60 °C to Model Predictions. Points: ♦, PZ+PZH^{+1}, ■, $PZCOO^{-1}$+H^+PZCOO^{-1}, ▲, $PZ(COO^{-1})_2$ from Cullinane (2005). Lines: —, this work.

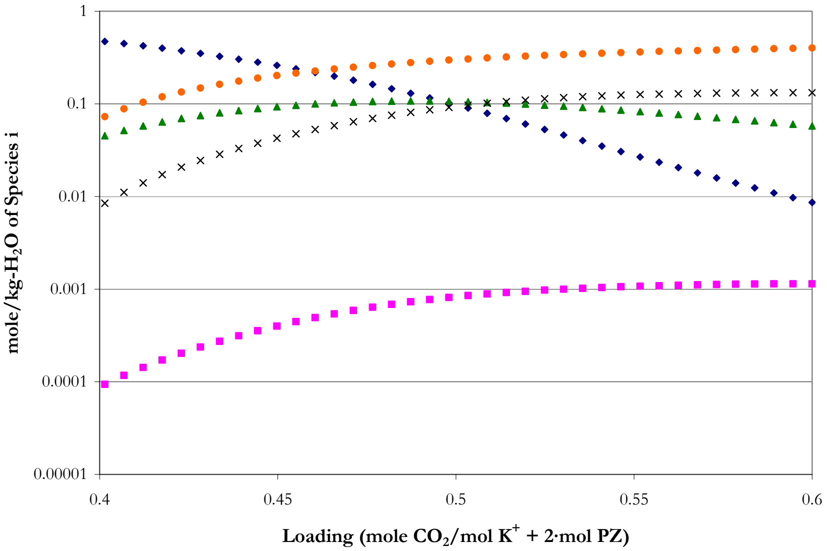

Figure 15.5-97. Predictions for the Liquid Phase Speciation in 3.6 m K^+ + 0.6 m PZ at 60 °C from this work. Points: ♦, PZ, ■, PZH^{+1}, ▲, $PZCOO^{-1}$, ●, $PZ(COO^{-1})_2$, ×, H^+PZCOO^{-1}.

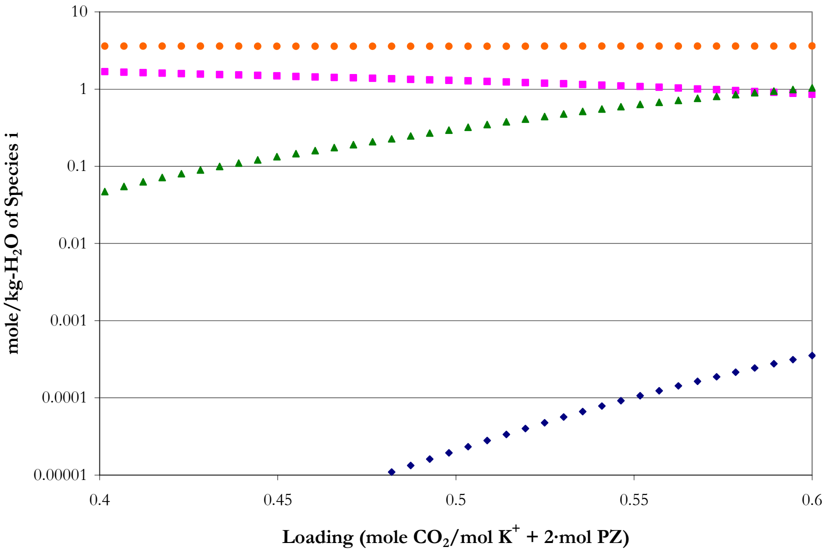

Figure 15.5-98. Predictions for the Liquid Phase Speciation in 3.6 m K^+ + 0.6 m PZ at 60 °C from this work. Points: ♦, CO_2, ■, CO_3^{-2}, ▲, HCO_3^{-1}, ●, K^+.

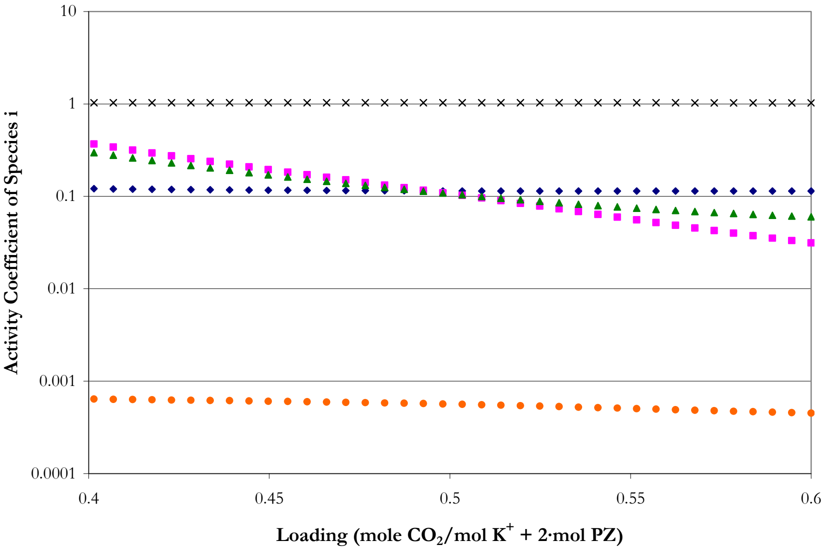

Figure 15.5-99. Predictions for the Liquid Phase Activity Coefficients in 3.6 m K+ + 0.6 m PZ at 60 °C from this work. Points: ♦, PZ, ■, PZH^{+1}, ▲, $PZCOO^{-1}$, ●, $PZ(COO^{-1})_2$, ×, H^+PZCOO^{-1}.

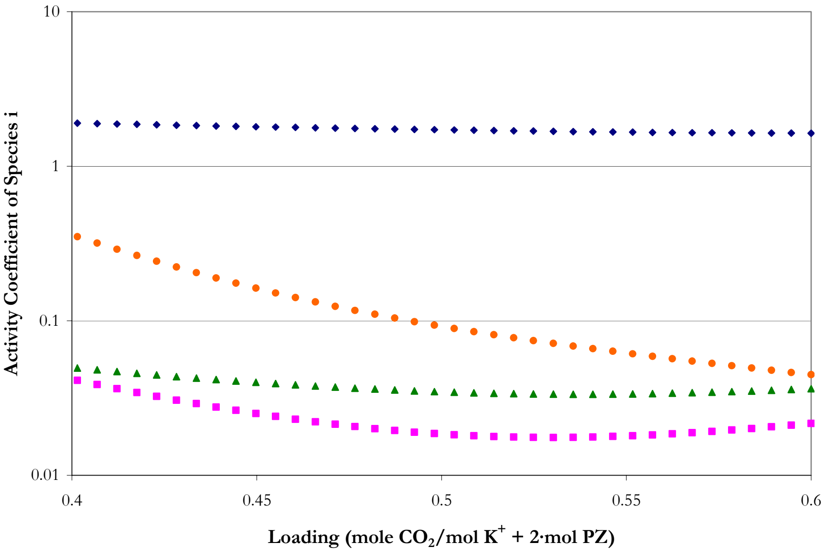

Figure 15.5-100. Predictions for the Liquid Phase Activity Coefficients in 3.6 m K+ + 0.6 m PZ at 60 °C from this work. Points: ♦, CO_2, ■, CO_3^{-2}, ▲, HCO_3^{-1}, ●, K^+.

Liquid Phase Speciation for 3.6 m K$^+$ + 1.8 m PZ at 27 ^{o}C

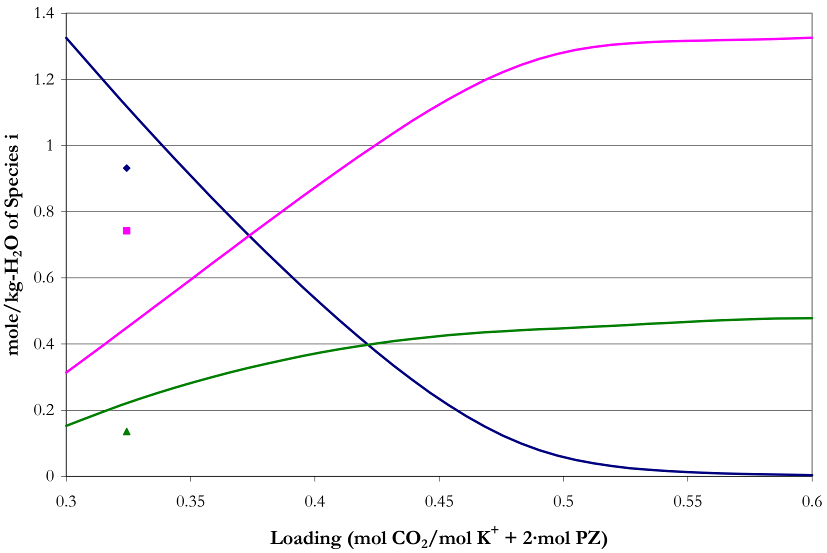

Figure 15.5-101. Comparison of Liquid Phase NMR Speciation in 3.6 m K$^+$ + 1.8 m PZ at 27 ^{o}C to Model Predictions. Points: ♦, PZ+PZH^{+1}, ■, PZCOO^{-1}+H$^+$PZCOO^{-1}, ▲, PZ(COO^{-1})$_2$ from Cullinane (2005). Lines: —, this work.

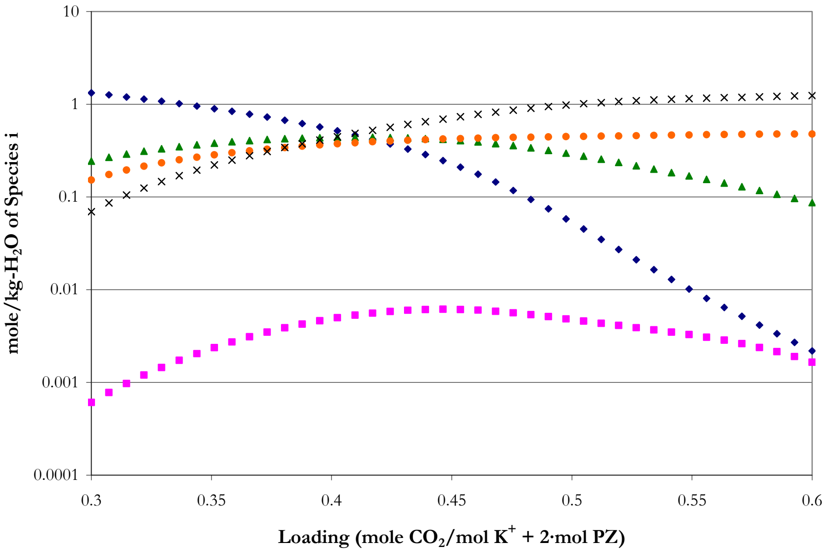

Figure 15.5-102. Predictions for the Liquid Phase Speciation in 3.6 m K$^+$ + 1.8 m PZ at 27 ^{o}C from this work. Points: ♦, PZ, ■, PZH^{+1}, ▲, PZCOO^{-1}, ●, PZ(COO^{-1})$_2$, ×, H$^+$PZCOO^{-1}.

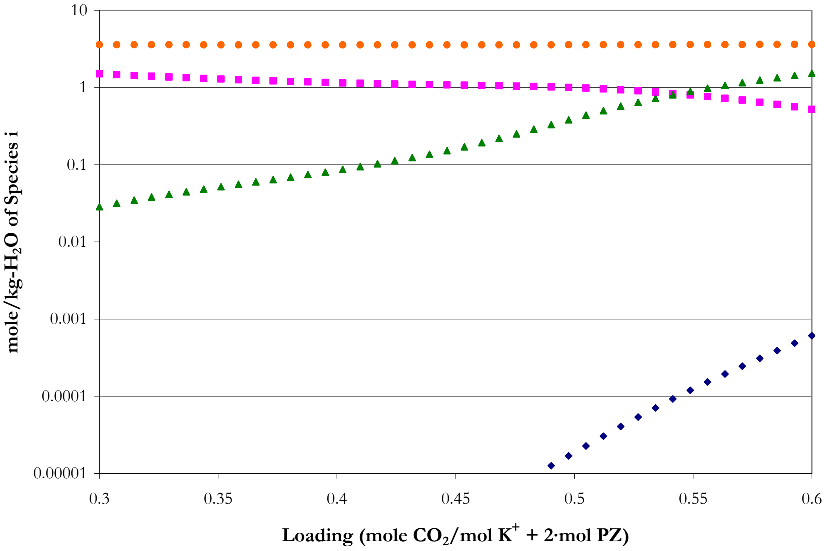

Figure 15.5-103. **Predictions for the Liquid Phase Speciation in 3.6 m K^+ + 1.8 m PZ at 27 °C from this work. Points: ♦, CO_2, ■, CO_3^{-2}, ▲, HCO_3^{-1}, ●, K^+.**

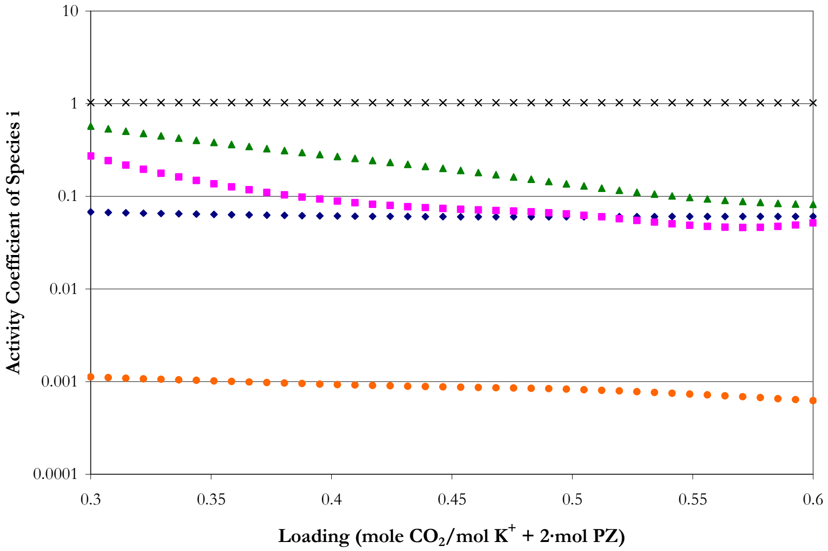

Figure 15.5-104. **Predictions for the Liquid Phase Activity Coefficients in 3.6 m K^+ + 1.8 m PZ at 27 °C from this work. Points: ♦, PZ, ■, PZH^{+1}, ▲, $PZCOO^{-1}$, ●, $PZ(COO^{-1})_2$, ×, H^+PZCOO^{-1}.**

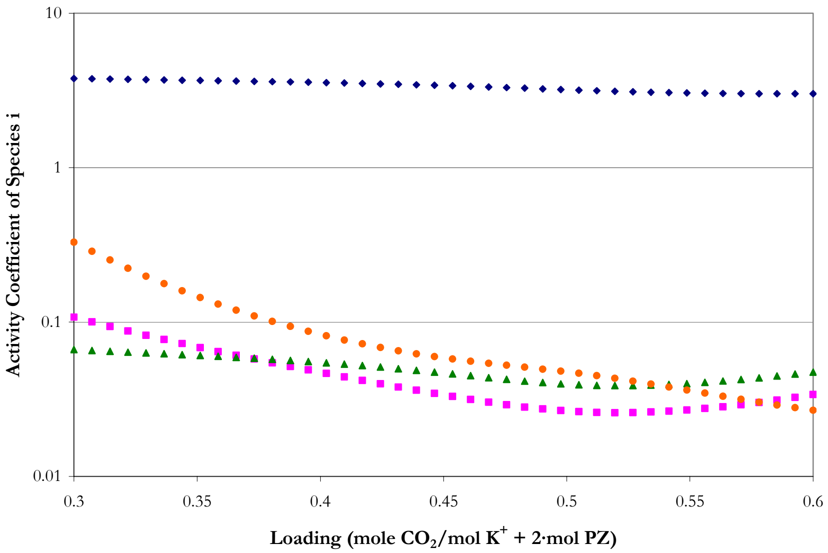

Figure 15.5-105. Predictions for the Liquid Phase Activity Coefficients in 3.6 m K^+ + 1.8 m PZ at 27 °C from this work. Points: ♦, CO_2, ■, CO_3^{-2}, ▲, HCO_3^{-1}, ●, K^+.

Liquid Phase Speciation for 3.6 m K^+ + 1.8 m PZ at 40 °C

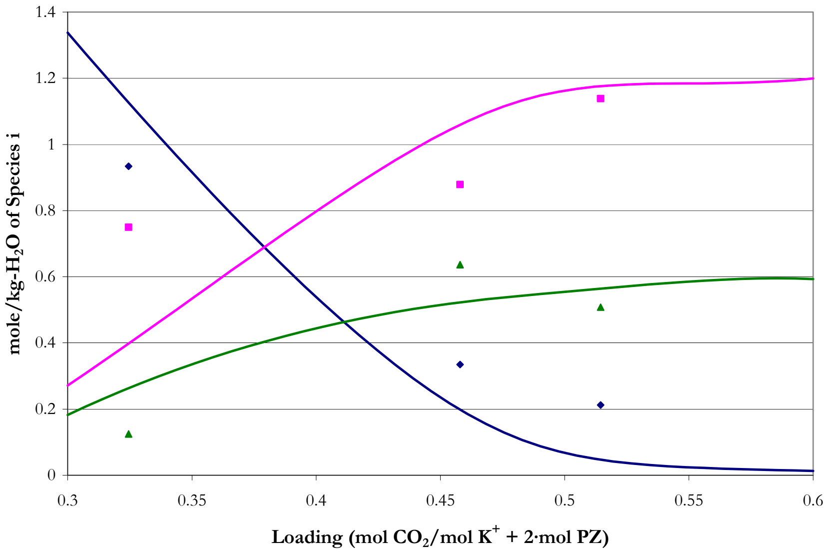

Figure 15.5-106. Comparison of Liquid Phase NMR Speciation in 3.6 m K^+ + 1.8 m PZ at 40 °C to Model Predictions. Points: ♦, PZ+PZH^{+1}, ■, $PZCOO^{-1}$+H^+PZCOO^{-1}, ▲, $PZ(COO^{-1})_2$ from Cullinane (2005). Lines: —, this work.

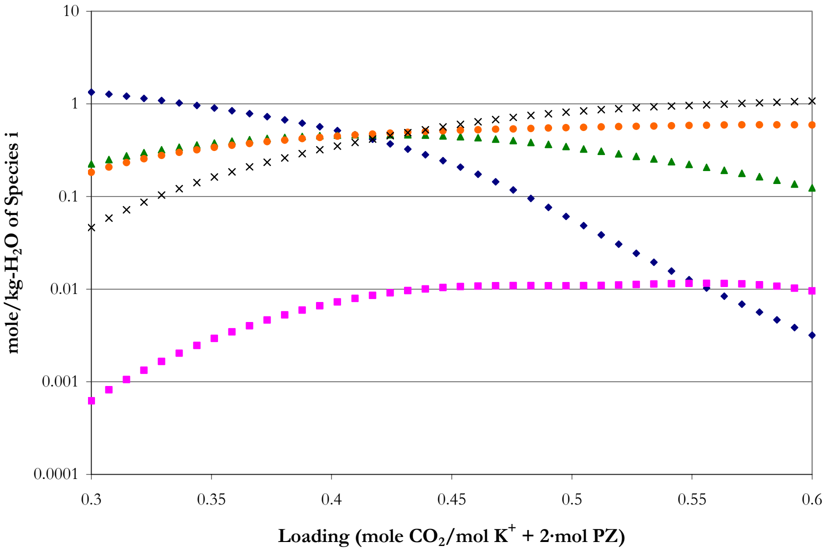

Figure 15.5-107. Predictions for the Liquid Phase Speciation in 3.6 m K^+ + 1.8 m PZ at 40 °C from this work. Points: ♦, PZ, ■, PZH^{+1}, ▲, $PZCOO^{-1}$, ●, $PZ(COO^{-1})_2$, ×, H^+PZCOO^{-1}.

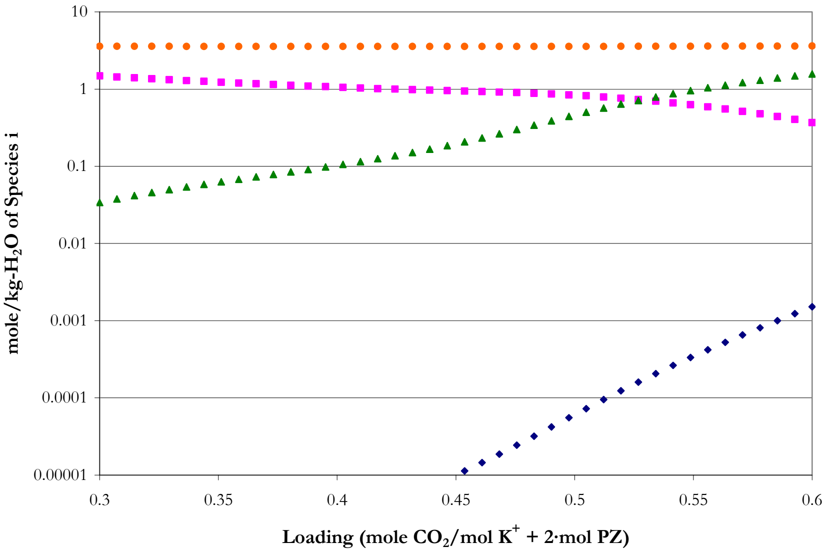

Figure 15.5-108. Predictions for the Liquid Phase Speciation in 3.6 m K^+ + 1.8 m PZ at 40 °C from this work. Points: ♦, CO_2, ■, CO_3^{-2}, ▲, HCO_3^{-1}, ●, K^+.

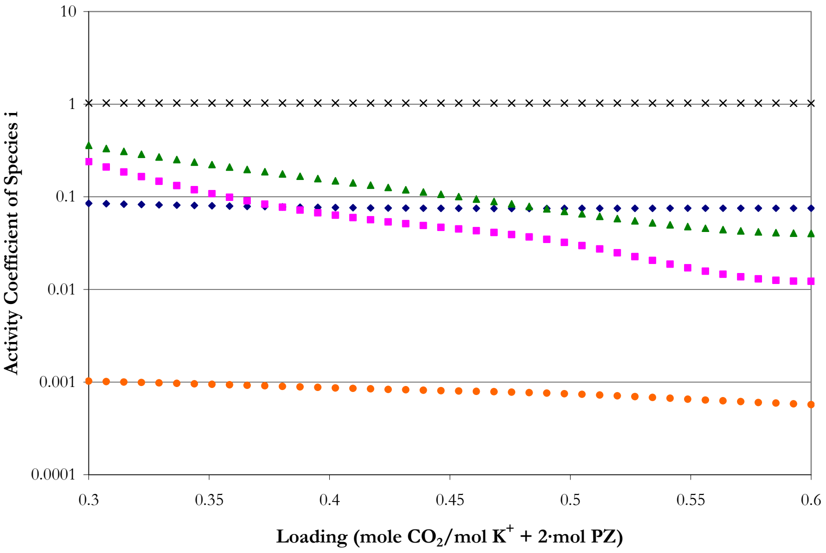

Figure 15.5-109. Predictions for the Liquid Phase Activity Coefficients in 3.6 m K^+ + 1.8 m PZ at 40 °C from this work. Points: ◆, PZ, ■, PZH^{+1}, ▲, $PZCOO^{-1}$, ●, $PZ(COO^{-1})_2$, ×, H^+PZCOO^{-1}.

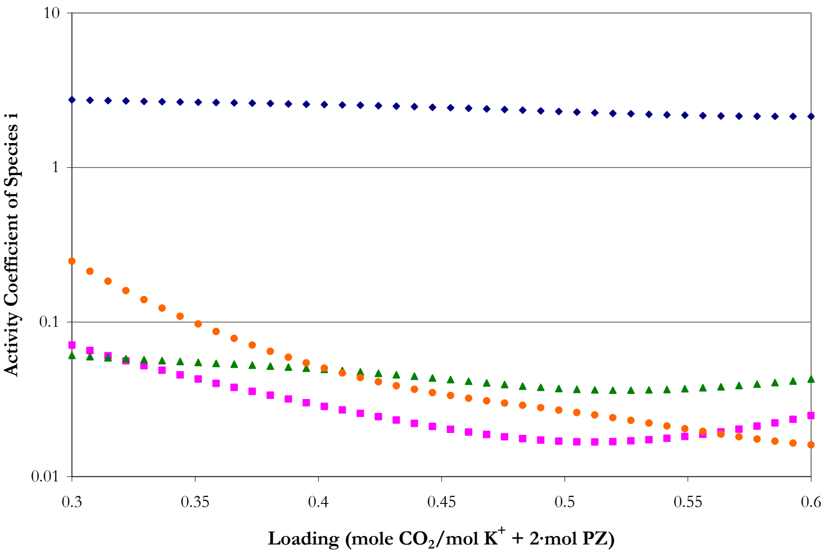

Figure 15.5-110. Predictions for the Liquid Phase Activity Coefficients in 3.6 m K^+ + 1.8 m PZ at 40 °C from this work. Points: ◆, CO_2, ■, CO_3^{-2}, ▲, HCO_3^{-1}, ●, K^+.

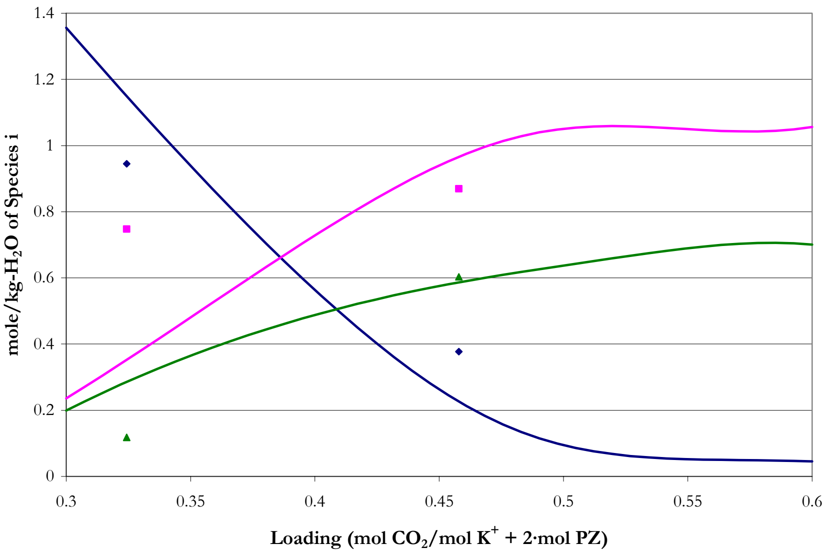

Figure 15.5-111. Comparison of Liquid Phase NMR Speciation in 3.6 m K$^+$ + 1.8 m PZ at 60 °C to Model Predictions. Points: ♦, PZ+PZH^{+1}, ■, PZCOO^{-1}+H$^+$PZCOO^{-1}, ▲, PZ(COO^{-1})$_2$ from Cullinane (2005). Lines: ▬, this work.

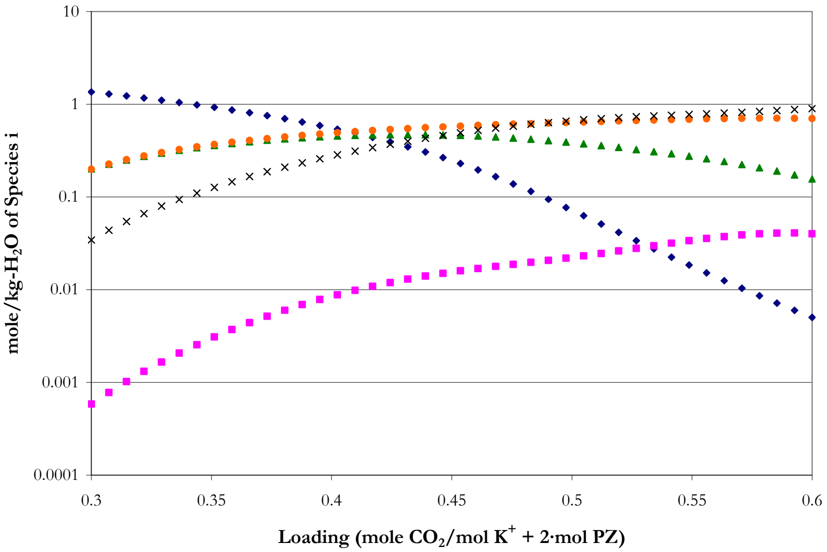

Figure 15.5-112. Predictions for the Liquid Phase Speciation in 3.6 m K$^+$ + 1.8 m PZ at 60 °C from this work. Points: ♦, PZ, ■, PZH^{+1}, ▲, PZCOO^{-1}, ●, PZ(COO^{-1})$_2$, ×, H$^+$PZCOO^{-1}.

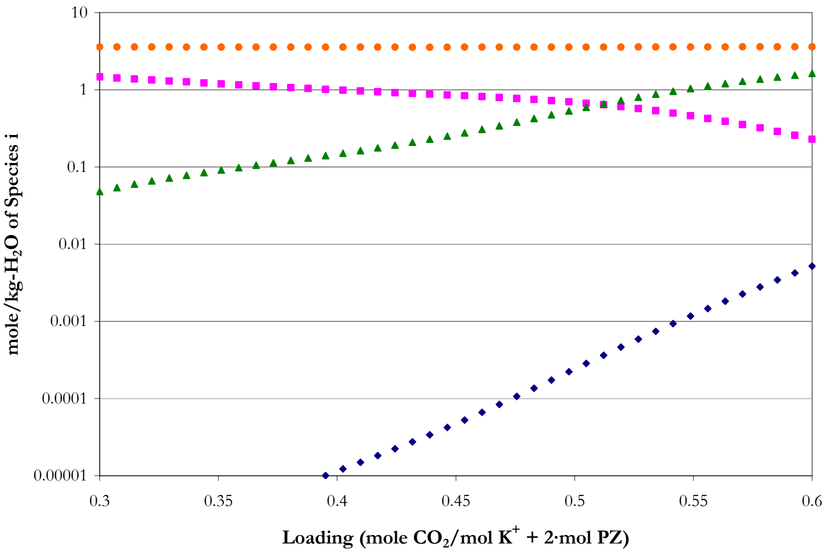

Figure 15.5-113. Predictions for the Liquid Phase Speciation in 3.6 m K^+ + 1.8 m PZ at 60 °C from this work. Points: ♦, CO_2, ■, CO_3^{-2}, ▲, HCO_3^{-1}, ●, K^+.

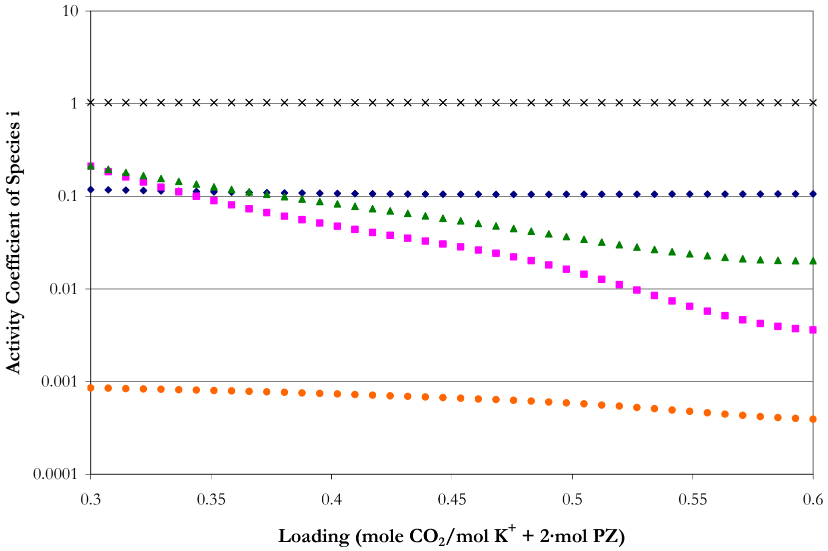

Figure 15.5-114. Predictions for the Liquid Phase Activity Coefficients in 3.6 m K^+ + 1.8 m PZ at 60 °C from this work. Points: ♦, PZ, ■, PZH^{+1}, ▲, $PZCOO^{-1}$, ●, $PZ(COO^{-1})_2$, ×, H^+PZCOO^{-1}.

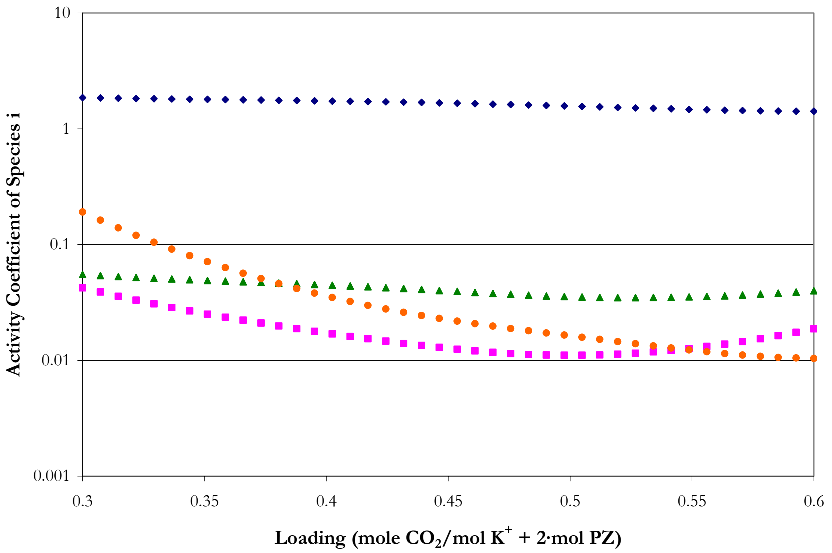

Figure 15.5-115. Predictions for the Liquid Phase Activity Coefficients in 3.6 m K^+ + 1.8 m PZ at 60 ^oC from this work. Points: ♦, CO_2, ■, CO_3^{-2}, ▲, HCO_3^{-1}, ●, K^+.

Predictions for the activity coefficient of $PZ(COO^{-1})_2$ may not represent a behavior that is physically significant as compared to other reactive PZ species as illustrated above. Due to the large number of parameters that were required to adequately fit the experimental database; the above results suggest that the full model represents the experimental database mathematically, but may not be a physically realistic representation of the system.

15.5.5 *Solid Solubility*

In this work, we observed the precipitation of dipotassium piperazine dicarbamate ($K_2PZ(COO)_2$) as described in Chapter V, and using the full model as a predictive tool we were able to regress coefficients (Table 15.5-5) for the salt precipitation equilibrium reaction, Equation 15-51, based on solid solubility predictions from this work. We chose not to include the salt precipitation reaction in the full model due to a limited amount of solid solubility data and for reasons previously stated.

Table 15.5-5. Chemical Equilibrium Coefficients for the Salt Precipitation of $K_2PZ(COO)_2$ Based on Equation 15-51 (mole fraction basis).

Equation #	A	σ_A	B	σ_B	C	σ_C	D	σ_D
15-51	-1709	210	0.0	-	355	44.3	-1.13	0.143

$\ln K = A + B/T(K) + C \cdot \ln T(K) + D \cdot T(K)$

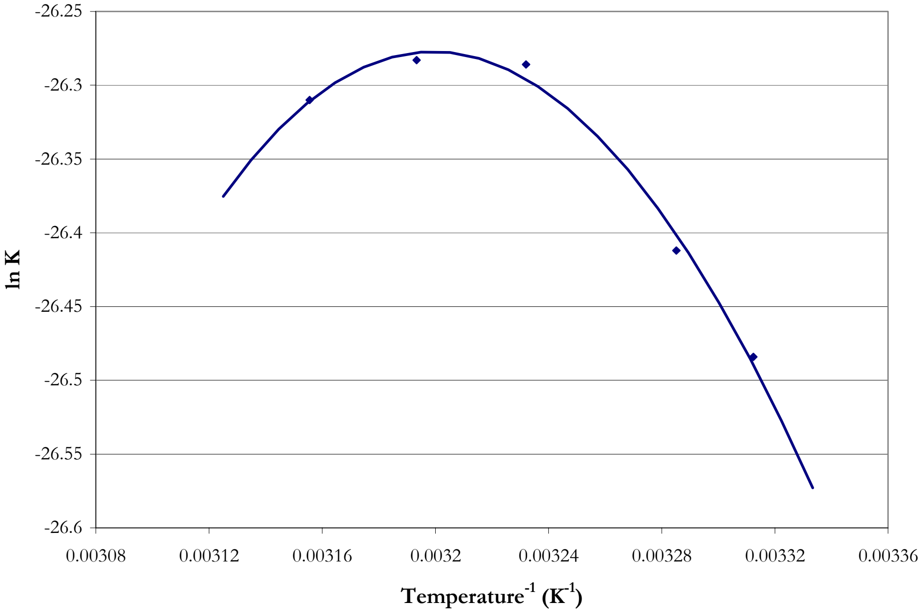

Figure 15.5-116. Comparison of the Chemical Equilibrium Salt Precipitation reaction for $K_2PZ(COO)_2$. Points: Chapter V from this work. Line: Predictions Using Table 15.5-4.

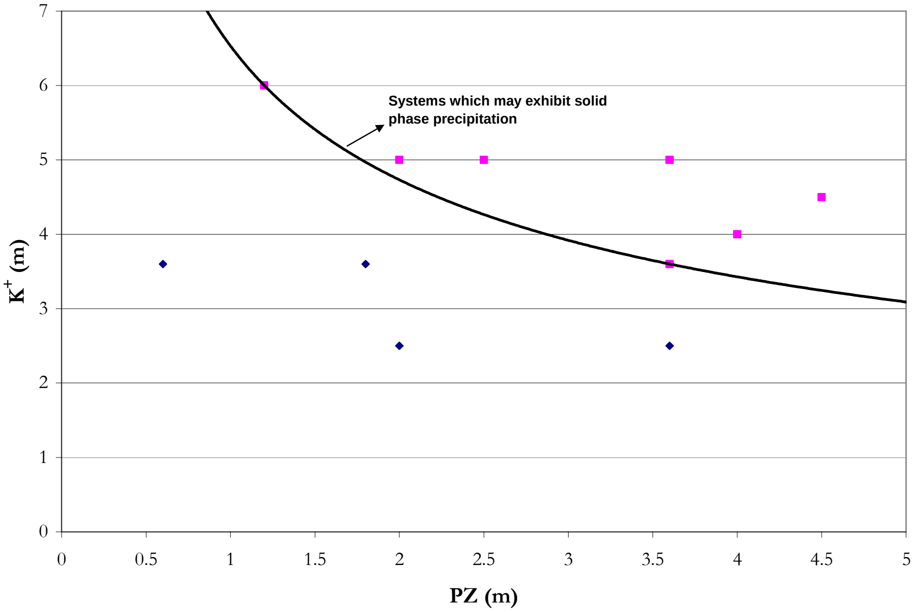

Figure 15.5-117. Proposed Solution Compositions Which May Exhibit Solid Phase Precipitation Based On Experimental Observations from this work.

Figure 15.5-117 illustrate a possible potassium + piperazine solid phase boundary where systems were observed to have precipitated a solid phase during the course of experimental work.

15.5.6 *Carbamate Stability Constant*

Using Equation 15-25 and estimates for the infinite dilution aqueous phase free energy of formation, the infinite dilution aqueous phase enthalpy of formation, and the infinite dilution aqueous phase heat capacity polynomial for piperazine carbamate, piperazine dicarbamate, and protonated piperazine carbamate, we can then analytically determine the chemical equilibrium constants as shown in Figure 15.5-118 through Figure 15.5-121 (molality infinite dilution in water basis) for the formation of $PZCOO^{-1}$, $PZ(COO^{-1})_2$ and

H^+PZCOO^{-1} given by Equations 15-57 through 15-59. The chemical equilibrium constants for Equations 15-11, 15-12, and 15-13 are regressed into linear temperature dependent functions given in Table 15.5-6 on a mole fraction, infinite dilution in water basis.

Table 15.5-6. Chemical Equilibrium Coefficients for the H_2O-K_2CO_3-PZ-CO_2 System on a Mole Fraction, Infinite Dilution in Water Basis.

Equation #	A	σ_A	B	σ_B	C	σ_C	D	σ_D
15-11	1025	0.49	0.0	-	-214	0.085	0.657	0.001
15-12	192	44.6	0.0	-	-44.7	7.69	0.200	0.012
15-13	668	1.96	0.0	-	-156	0.338	0.594	0.001

ln K = A + B/T(K) + C·lnT(K) + D·T(K)

$$\mathrm{PZ} + CO_2 \leftrightarrow \mathrm{PZCOO}^{-1} + H^+ \tag{15-57}$$

$$\mathrm{PZCOO}^{-1} + CO_2 \leftrightarrow \mathrm{PZ}\left(\mathrm{COO}^{-1}\right)_2 + H^+ \tag{15-58}$$

$$H^+PZCOO^{-1} \leftrightarrow \mathrm{PZCOO}^{-1} + H^+ \tag{15-59}$$

Figure 15.5-118 through Figure 14.5-121 illustrate a comparison between chemical equilibrium constants regressed as part of the H_2O-K_2CO_3-PZ-CO_2 system to activity based equilibrium constants described in Chapter XIV for the H_2O-PZ-CO_2 system. With the addition of a salt to the H_2O-PZ-CO_2 system, the above figures illustrate that the chemical equilibrium constant is slightly shifted for $PZCOO^{-1}$ and $H+PZCOO^{-1}$, but for $PZ(COO^{-1})_2$ figure 15.5-10 illustrates a dramatic shift due to increased concentrations of $PZ(COO^{-1})_2$ present in H_2O-K_2CO_3-PZ-CO_2 system. The main discrepancy between the cited literature may be due to the thermodynamic foundations of each model framework. Each model would describe the activity coefficients differently based on the regression methodology it employed, the type of thermodynamic model used, and the types of thermodynamic data that were used in the model regression. In addition, the behavior for the activity coefficient of PZ as a function of temperature and concentration might also have the possibility of affecting the description of the chemical equilibrium environment. Overall, predictions for the chemical equilibrium constants appear to be consistent with previous work given the range of scatter of the reported values.

Figure 15.5-121 compare the carbamate chemical equilibrium constants from this work to carbamate chemical equilibrium constants associated with the H_2O-MEA-CO_2 and H_2O-PZ-CO_2 systems based on the formation of the carbamate from the aqueous amine reacting with aqueous carbon dioxide (Equation 15-57).

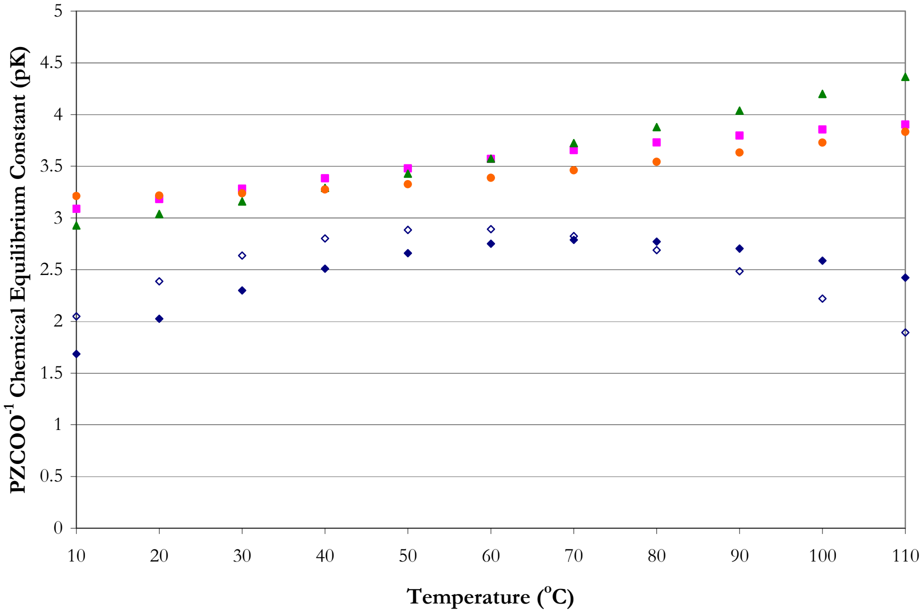

Figure 15.5-118. Comparison of the Chemical Equilibrium Constant of PZCOO^{-1}. Points: ●, Ermatchkov et al. (2003, ■, Cullinane (2005), ▲, Derks et al. (2005), ♦, this work, ◊, Chapter XIV.

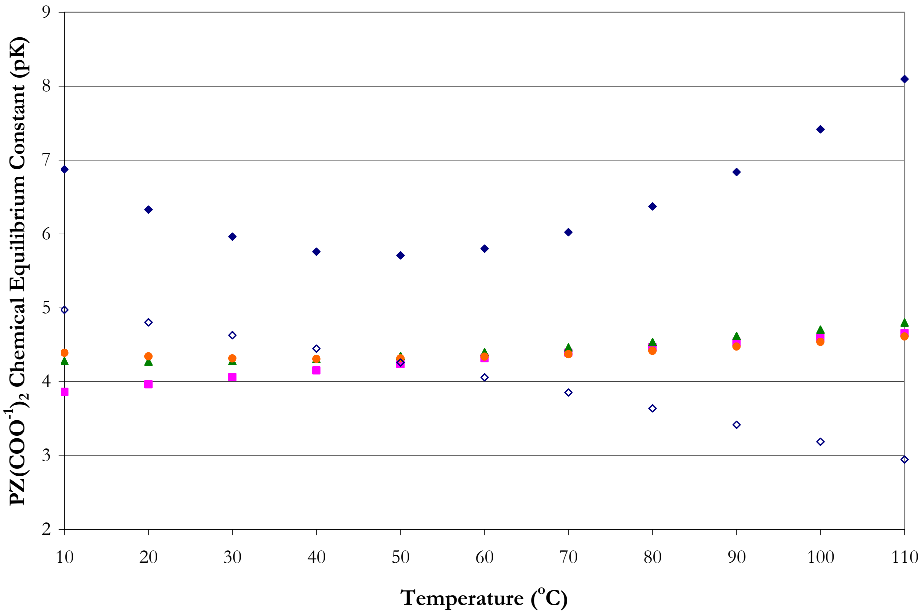

Figure 15.5-119. Comparison of the Chemical Equilibrium Constant of $PZ(COO^{-1})_2$. Points: ●, Ermatchkov et al. (2003, ■, Cullinane (2005), ▲, Derks et al. (2005), ♦, this work, ◊, Chapter XIV.

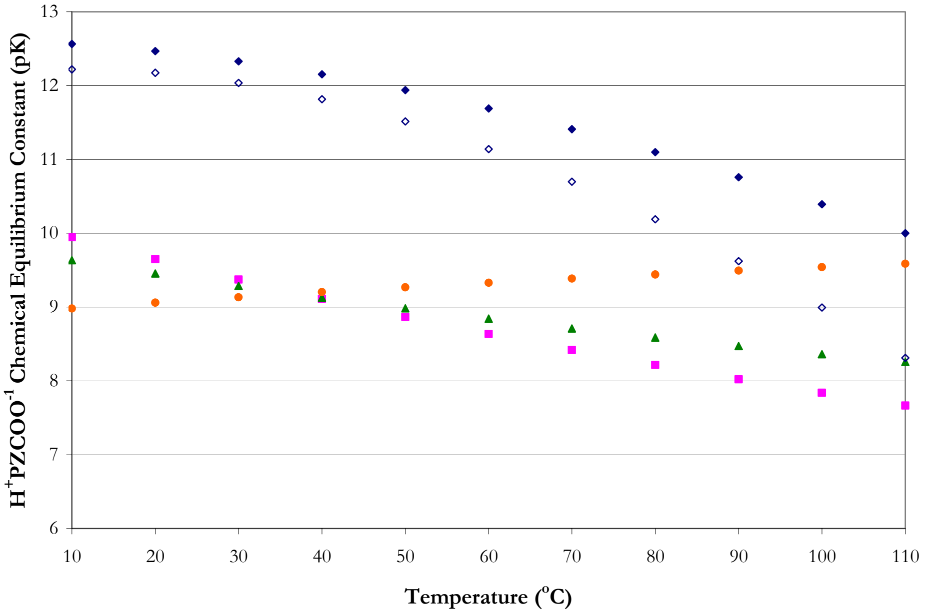

Figure 15.5-120. Comparison of the Chemical Equilibrium Constant of $H^{+}PZCOO^{-1}$. Points: ●, Ermatchkov et al. (2003, ■, Cullinane (2005), ▲, Derks et al. (2005), ♦, this work, ◊, Chapter XIV.

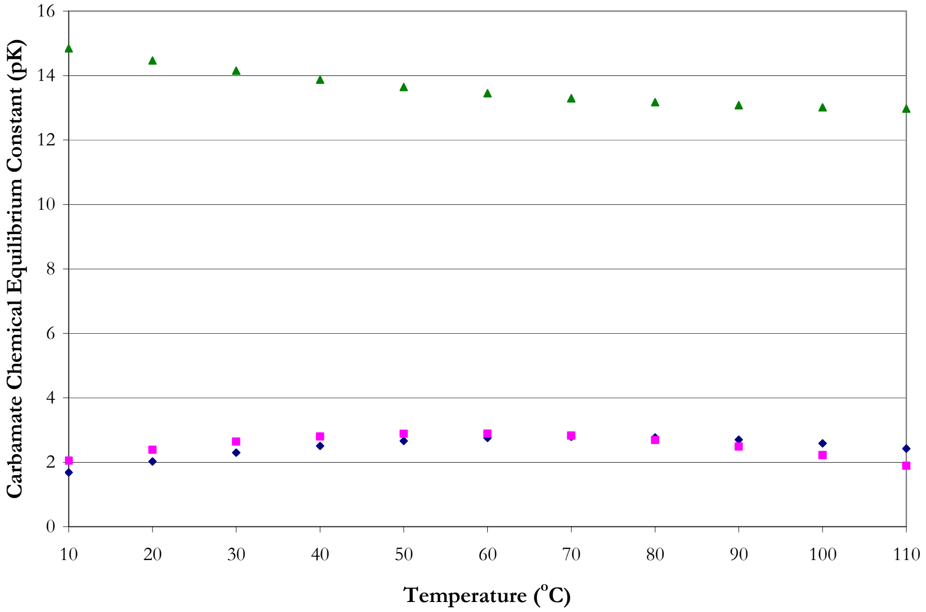

Figure 15.5-121. Comparison of the MEA and PZ Carbamate Based Chemical Equilibrium Constants from this work. Points: ♦, this work, ■, Chapter XIV, ▲,Chapter XIII.

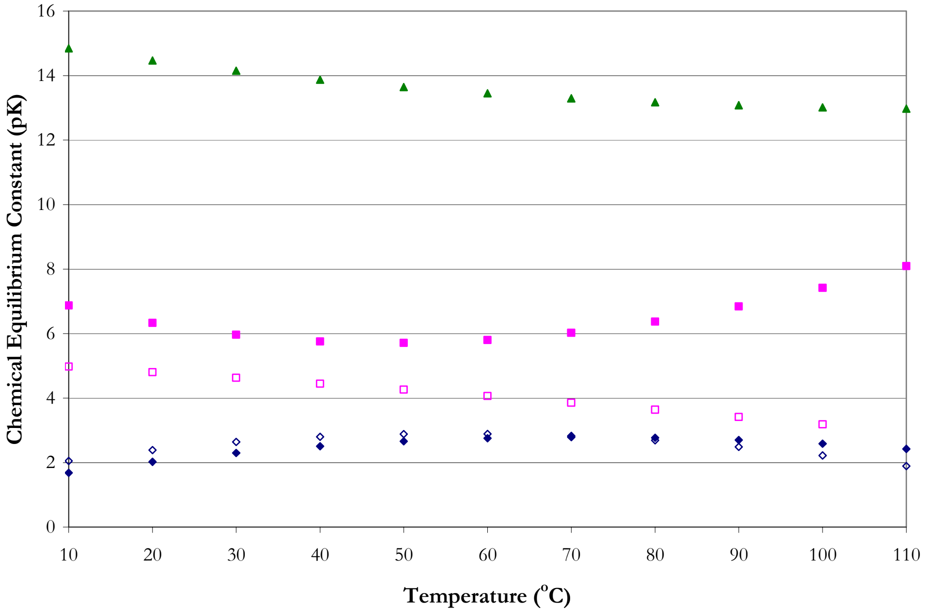

Figure 15.5-122. Comparison of the MEA and PZ Carbamate and Bicarbamate Based Chemical Equilibrium Constants from this work. Points: $PZCOO^{-1}$: ♦, this work, ◊, Chapter XIV, $PZ(COO^{-1})_2$: ■, this work, □, Chapter XIV, $MEACOO^{-1}$: ▲,Chapter XIII.

The chemical equilibrium constants for the three systems, in Figure 15.5-121, illustrate that with the addition of potassium to a solution of loaded piperazine, the behavior of the piperazine carbamate chemical equilibrium constant is not very different from the H_2O-PZ-CO_2 system.

Figure 15.5-122 illustrates that the chemical equilibrium constants associated with the formation of carbamate and bicarbamate are consistent with trends observed for the rates of reaction and suggests that monoethanolamine carbamate may be less stable than piperazine carbamate or piperazine dicarbamate.

15.6 Conclusions

In conclusion, one of the main goals in this work was to verify experimental CO_2 solubility measurements reported by Cullinane (2005). Figure 15.3-2 illustrated a loading discrepancy for the solubility of CO_2 in mixtures of 5 m K^+ + 2.5 m PZ. Comparing experimental results from this work for other solvent combinations, similar trends were exhibited between the two data sets. During the liquid phase CO_2 analysis Cullinane (2005) chose not to integrate the response single but instead correlate the peak height to the response of known Na_2CO_3 standards by assuming that the peak height was proportional to the peak area. This alternative method was illustrated in Figure 15.3-4 as compared to the same calibration curve based on the integral of the peak area. Acidic evolution based on the response of the peak height as compared to the integrated response peak area may yield an average absolute relative error of ± 7.30 percent and would seem to agree with the experimental uncertainty reported by Cullinane (2005) for reported loading measurements based on peak height. This result may explain the discrepancy between reported CO_2 solubility measurements from Cullinane (2005) and from this work. In addition, Cullinane (2005) chose not to analyze the total alkalinity of the experimental solution and may pose an addition error within the reported experimental loading. Based on the above analysis, we chose to exclude reported CO_2 solubility from Cullinane (2005) due to an error in the loading analysis.

Furthermore, Cullinane (2005) observed that solvent concentrations with the same potassium to piperazine ratio may exhibit the same CO_2 solubility. Figure 15.3-5 illustrated that the salt to amine ratio effect for 5 m K^+ + 2.5 m PZ and 3.6 m K^+ + 1.8 m PZ at 40 and 60 °C exhibited a similar experimental CO_2 solubility for the two solvents based on measurements from this work. On the other hand, experimental results from Cullinane (2005) demonstrated that systematic trends in the experimental data are not internally consistent. We would conclude that the Cullinane (2005) CO_2 solubility data set are not consistent with reported observations by Cullinane (2005) and should be treated with caution in future work.

In terms of PZ volatility, Figure 15.3-8 illustrated that with the decrease in the salt concentration the relative volatility of piperazine decreased by a factor of 2.3 even though the concentration of piperazine was increased by a factor of 1.5.

For NMR Speciation, Cullinane (2005) measured the proton peak areas or intensities for the corresponding protons associated with each molecule(s). The main drawback with the proton NMR speciation analysis is not having the ability to measure the loading of the solution as compared to carbon C^{13} NMR speciation described in Chapter XIII. The loading of the solution has to be determined a *priori* which may result in a discrepancy between the loading at the time of the NMR experiment and at the time of the CO_2 analysis. We would recommend that future work should concentrate on validating the reported NMR speciation reported from Cullinane (2005) using carbon C^{13} NMR speciation for loaded potassium plus piperazine solutions due to the possible error in the liquid phase loading analysis as previously stated.

Table 15.5-1 illustrated that 7 m MEA demonstrated a greater differential capacity as compared to piperazine or other mixed salt-amine systems. For mixed salt-amine systems, only systems composed of salt concentrations less than 5 m K^+ exhibited an increase in the differential capacity as compared to similar systems containing 5 m K^+. Overall, 2.5 m K^+ + 3.6 m PZ exhibited the largest differential capacity equal to 0.19 out of nine solvents studied as part of this work.

Table 15.5-2 illustrated that 7 m MEA demonstrated a greater range of volatility at 40 °C as compared to piperazine or other mixed salt-amine systems. For different combinations of potassium + piperazine the volatility of PZ varied between 54 to 4 ppm_v over a CO_2 partial pressure from 0.01 to 0.1 kPa at 40 °C and is consistent with effects exhibited in the H_2O-PZ-CO_2 system (37 to 8 ppm_v) where large changes in the solution alkalinity may not have a large effect on the volatility of PZ.

In terms of the enthalpy of CO_2 absorption, Figure 15.5-29 illustrated an approximately 30 kJ/mol-CO_2 decrease in the enthalpy of CO_2 absorption at 40 °C as compared to 7 m MEA; 6 m K^+ + 1.2 m PZ also demonstrated a 30 kJ/mol-CO_2 decrease in the enthalpy of CO_2 absorption at 120 °C as compared to 7 m MEA where a mixture of 5 m

K^+ + 2.5 m PZ at 120 °C exhibited only a 10 kJ/mol-CO_2 decrease in the enthalpy of CO_2 absorption.

In terms of specific heat capacity, predictions from this work were unable to capture the correct trends presented in the experimental specific heat capacity data as a function of temperature. Overall, the full model did fall short in predicting the correct specific heat capacity on the order of ± 10 percent. One possibility for this discrepancy may result from an inconsistency between the enthalpy of CO_2 absorption measurements from Kim (2007) and specific heat capacity measurements from this work.

Based on the average absolute relative error presented in Table 15.5-3, the experimental specific heat capacity from this work are not consistent with predictions from the full model in terms of the sensible liquid phase enthalpy within the experimental accuracy of ± 2.0 percent error. For all other amine systems studied in this work, the temperature ramp rate was set to 5 °C/min which produced acceptable results, but a *priori* to the completion of experimental work, we found that Thomsen et al. (1999) mentioned that for salt systems a rate of 1 °C/min should be used to improve the sample response resolution and allow the sample to achieve equilibrium at a desired temperature. We would recommend that future work verify specific heat capacity measurements gathered in this work utilizing a similar procedure outlined in Chapter IV but instead use a temperature ramp rate of 1 °C/min.

To investigate the effect of CO_2 loading on the liquid phase specific heat capacity, we normalized the specific heat capacity by the kilograms of H_2O in the experimental solution to generate a cross-plot with respect to the total moles of CO_2 per mole of H_2O. We then inferred the apparent partial specific heat capacity of CO_2, based on ordinary least squares approximations of the transformed experimental data, to have an average value of 4.9103 kJ/kg$_{CO2}$-K over the temperature range from 40 to 120 °C in aqueous mixtures of potassium carbonate plus piperazine and is comparable to the specific heat capacity of H_2O. This may suggest that contributions of the apparent partial heat capacity of CO_2 may not be considered small aqueous mixtures of potassium carbonate plus piperazine.

Predictions for the activity coefficient of $PZ(COO^{-1})_2$ may not represent a behavior that is physically significant as compared to other reactive PZ species as illustrated above. Due to the large number of parameters that were required to adequately fit the experimental database; the above results suggest that the full model represents the experimental database mathematically, but may not be a physically realistic representation of the system.

Figure 15.5-118 through Figure 14.5-121 illustrated a comparison between chemical equilibrium constants regressed as part of the H_2O-K_2CO_3-PZ-CO_2 system to activity based equilibrium constants described in Chapter XIV for the H_2O-PZ-CO_2 system. Comparing the formation of the piperazine carbamate to the formation of monoethanolamine carbamate, there is a dramatically different behavior associated with the chemical equilibrium constant. Figure 15.5-122 illustrated that the chemical equilibrium constants associated with the formation of carbamate and bicarbamate are consistent with trends observed for the rates of reaction and suggests that monoethanolamine carbamate may be less stable than piperazine carbamate or piperazine dicarbamate.

Overall, the results presented above indicated that the elecNRTL model, through simultaneous regression, gave a set of unique parameters for the H_2O-K_2CO_3-PZ-CO_2

system where the full model adequately represents the literature data for loaded potassium plus piperazine solutions.

PART IV

Quaternary and Quinary

System Predictions

CHAPTER XVI

Quaternary System Predictions: H_2O-MEA-PZ-CO_2

16.1 Introduction

The thermodynamic models describing each sub-system have been established and the combined model can now be used as a predictive tool for the quaternary system. This chapter compares experimental CO_2 solubility from Dang (2003) and Okoye (2005) in addition to CO_2 solubility, amine volatility, NMR speciation, enthalpy of CO_2 absorption, and specific heat capacity data from this work for the H_2O-MEA-PZ-CO_2 system to model predictions based on the combined H_2O-MEA-CO_2 and H_2O-PZ-CO_2 system models. The combined predictive model represents the experimental data with an average absolute relative error of ± 37.9 %, with the exception of a few outliers.

16.2 H_2O-MEA-PZ-CO_2 System

Up to this point for the H_2O-MEA-PZ-CO_2 system, we have been able to describe the molecule-molecule and molecule-electrolyte interactions between H_2O-MEA, H_2O-PZ, H_2O-MEA-PZ, H_2O-MEA-CO_2, and H_2O-PZ-CO_2 given in Chapters VIII, IX, X, XIII, and XIV respectively, as shown in Table 16.2-1.

Table 16.2-1. Binary Interaction Parameters for the H_2O-MEA-PZ-CO_2 system.

	Interaction Species		
System	i	j	k
H_2O-MEA	H_2O	MEA	
	MEA	H_2O	
H_2O-PZ	H_2O	PZ	
	PZ	H_2O	
H_2O-MEA-CO_2	H_2O	$MEAH^{+1}$	HCO_3^{-1}
	$MEAH^{+1}$	HCO_3^{-1}	H_2O
	H_2O	$MEAH^{+1}$	$MEACOO^{-1}$
	$MEAH^{+1}$	$MEACOO^{-1}$	H_2O
	MEA	$MEAH^{+1}$	HCO_3^{-1}
	$MEAH^{+1}$	HCO_3^{-1}	MEA
	MEA	$MEAH^{+1}$	$MEACOO^{-1}$
	$MEAH^{+1}$	$MEACOO^{-1}$	MEA
	CO_2	$MEAH^{+1}$	HCO_3^{-1}
	$MEAH^{+1}$	HCO_3^{-1}	CO_2
H_2O-PZ-CO_2	H_2O	PZH^{+1}	HCO_3^{-1}
	PZH^{+1}	HCO_3^{-1}	H_2O
	H_2O	PZH^{+1}	$PZCOO^{-1}$
	PZH^{+1}	$PZCOO^{-1}$	H_2O
	PZ	PZH^{+1}	HCO_3^{-1}
	PZH^{+1}	HCO_3^{-1}	PZ
	PZ	PZH^{+1}	$PZCOO^{-1}$
	PZH^{+1}	$PZCOO^{-1}$	PZ
	CO_2	PZH^{+1}	HCO_3^{-1}
	PZH^{+1}	HCO_3^{-1}	CO_2

For the mixed amine system, Posey (1996) suggested a general method for parameter determination by examining the mixed amine parameters to form an adequate model. Posey

(1996) also reported that many of the mixed system interaction parameters appeared to be independent of the amine interaction and could be assigned the default values of 10 and -2. Mixed systems parameters involving H_2O and a carbamate species were assigned an average value consistent between the two systems. Posey (1996) did not optimize the parameters to fit the experimental data, but was interested in the ability of the model to predict the mixed system.

In this work, we have followed a similar approach to the method developed by Posey (1996), in terms of choosing values for the mixed system binary interaction parameters to examine the predictive ability of our model. Table 16.2-2 lists binary interaction parameters associated with the mixed amine system which were not included as part of the original model regressions.

Table 16.2-2. Mixed Salt/Amine Binary Interaction Parameters.

Interaction Species			Binary Interaction Coefficients		
i	j	k	A	B	C
H_2O	$MEAH^{+1}$	$PZCOO^{-1}$	8.42	-43.0	-51.1
$MEAH^{+1}$	$PZCOO^{-1}$	H_2O	-2.78	413	-27.9
H_2O	$MEAH^{+1}$	$PZ(COO^{-1})_2$	8.13	4.55	-0.595
$MEAH^{+1}$	$PZ(COO^{-1})_2$	H_2O	-4.14	-12.7	0.190
H_2O	PZH^{+1}	$MEACOO^{-1}$	9.12	122	-31.4
PZH^{+1}	$MEACOO^{-1}$	H_2O	-3.45	186	-6.43
MEA	PZH^{+1}	$MEACOO^{-1}$	79.7	0.0	0.0
PZH^{+1}	$MEACOO^{-1}$	MEA	-2.62	0.0	0.0
MEA	PZH^{+1}	HCO_3^{-1}	28.0	0.0	0.0
PZH^{+1}	HCO_3^{-1}	MEA	-7.44	0.0	0.0
PZ	$MEAH^{+1}$	$PZCOO^{-1}$	0.388	0.0	0.0
$MEAH^{+1}$	$PZCOO^{-1}$	PZ	-11.4	0.0	0.0
PZ	$MEAH^{+1}$	HCO_3^{-1}	3.64	0.0	0.0
$MEAH^{+1}$	HCO_3^{-1}	PZ	-10.2	0.0	0.0

Binary interaction parameters for MEA and PZ did exhibit similar properties as reported by Posey (1996). Interactions associated with each amine, given in Table 16.2-2, which were assigned to similar interaction values involving the alternative protonated amine, did benefit the quality of the model predictions as compared to the experimental data. Binary interaction parameters for H_2O, given in Table 16.2-2, were based on the average value between H_2O $MEAH^+/MEACOO^{-1}$ and H_2O, $PZH^{+1}/PZCOO^{-1}$ as given in Chapters XIII and XIV. This assumption did exhibit a small benefit to the prediction of CO_2 solubility data, but varying the parameter from the default values to the average values had a minimal effect on the overall predictive outcome at high loading.

We would recommend that future work to adequately predict the experimental CO_2 solubility, amine volatility, NMR speciation, enthalpy of CO_2 absorption, and specific heat capacity data for the H_2O-MEA-PZ-CO_2 system, an overall regression of the binary interaction parameters associated with the original and mixed amine systems in addition to the chemical equilibrium constant for $MEACOO^{-1}$,$PZCOO^{-1}$, $PZ(COO^{-1})_2$, and $H^{+1}PZCOO^{-1}$ would need to be regressed simultaneously to adequately fit the experimental data. This would need to be completed due to the thermodynamic framework adopted in this work utilizing Aspen Plus^{TM} 2006.5.

The following section describes the different data types gathered in this work for the H_2O-MEA-PZ-CO_2 system as compared to the predictive ability of the combined model.

16.2.1 *CO_2 Solubility and Amine Volatility*

Data in the form of CO_2 solubility, which measures the partial pressure of CO_2 over aqueous MEA plus PZ solutions, as a function of loading (mole of CO_2 per mole of MEA plus two times the moles of PZ) and temperature were compared to predictions based on the combined model for the H_2O-MEA-PZ-CO_2 system.

For our quaternary system (H_2O, MEA, PZ, and CO_2), the following equation may be used to represent the equilibrium for CO_2 solubility data.

$$Py_{CO_2} = x_{CO_2}\gamma^*_{CO_2}H_{CO_2,H_2O} \qquad 16\text{-}1$$

Where
y_{CO_2} is the vapor mole fraction of CO_2,
$\gamma^*_{CO_2}$ is the unsymmetric activity coefficient of CO_2,
H_{CO_2,H_2O} is the Henry's Constant for CO_2 in H_2O.

In this work, we used a unique Fourier-transform infrared (FT-IR) technique to measure the vapor phase speciation in aqueous alkanolamine systems as described in Chapter II. Using this technique, we have been able to measure the vapor phase partial pressure of MEA and PZ over aqueous mixed amine solutions, P_{amine}, as a function of loading (mole CO_2 per mole MEA + 2·mole PZ) and temperature.

For our quaternary system (H_2O, MEA, PZ, and CO_2), the following equation may be used to represent the equilibrium for amine volatility data.

$$Py_{\text{Amine}} = x_{\text{Amine}}\gamma_{\text{Amine}}P^o_{\text{Amine}} \qquad 16\text{-}2$$

Where
y_{Amine} is the vapor mole fraction of the amine,
γ_{Amine} is the asymmetric activity coefficient of the amine,
P^o_{Amine} is the extended Antoine vapor pressure correlation for the amine given in Chapter VI.

Experimental CO_2 solubility and amine volatility data collected in this work for mixtures of MEA plus PZ from 40 and 120 °C are illustrated in Figure 16.2-1 through Figure 16.2-10. CO_2 solubility from Dang (2003) and Okoye (2005) at 40 and 60 °C were also included. Ordinary least squares (OLS) approximations were included to clarify systematic trends within the data set.

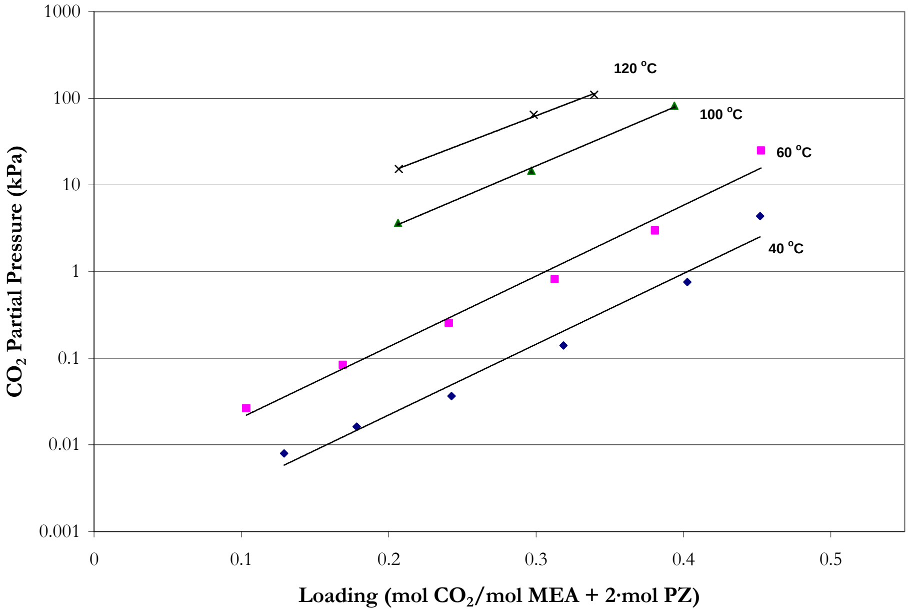

Figure 16.2-1. Experimental CO_2 Solubility in Mixtures of 3.5 m MEA Plus 2 m PZ from 40 to 120 °C from this work. Points: ♦ (40 °C). ■ (60 °C), ▲ (100 °C), and × (120 °C). Lines: OLS Approximations.

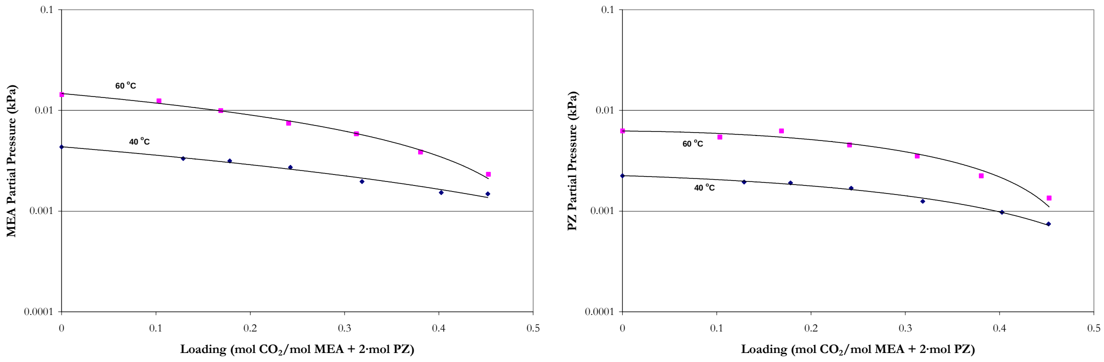

Figure 16.2-2. Experimental MEA and PZ Volatility in Mixtures of 3.5 m MEA Plus 2 m PZ at 40 and 60 °C from this work. Points: ♦ (40 °C) and ■ (60 °C). Lines: OLS Approximations.

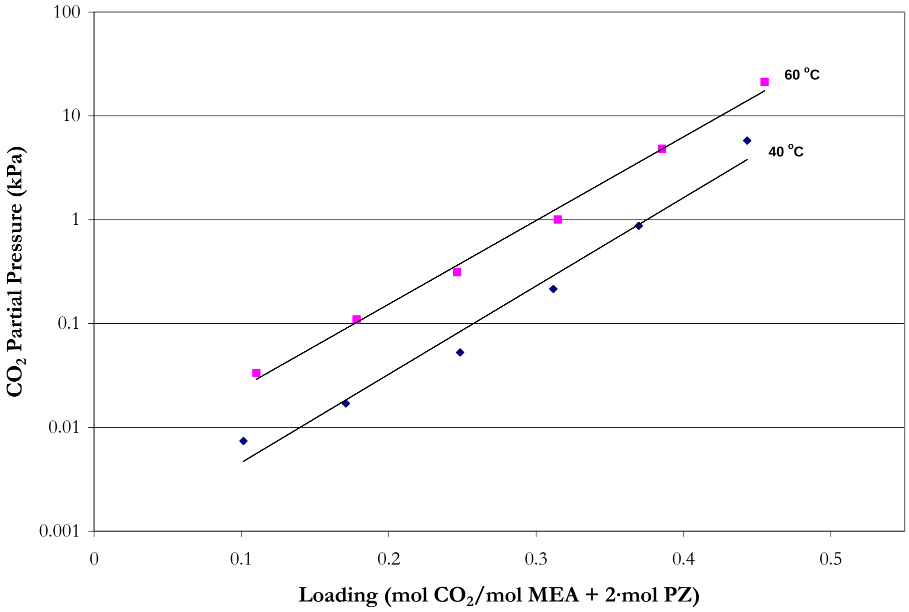

Figure 16.2-3. Experimental CO_2 Solubility in Mixtures of 3.5 m MEA Plus 3.6 m PZ at 40 and 60 °C from this work. Points: ♦ (40 °C) and ■ (60 °C). Lines: OLS Approximations.

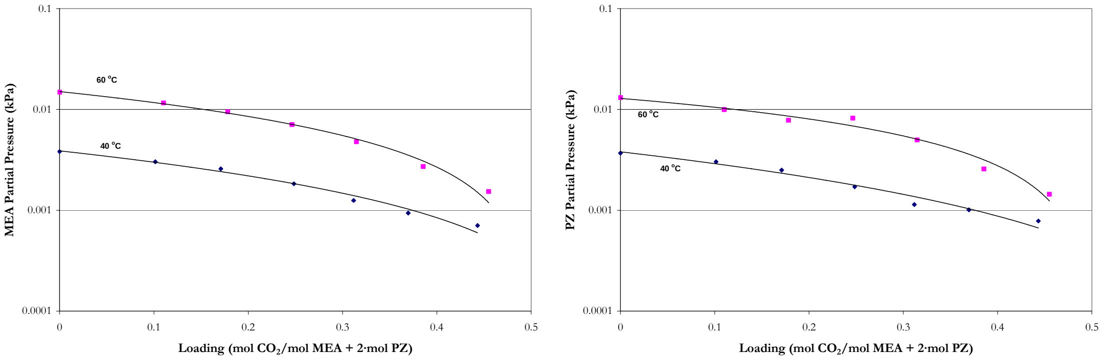

Figure 16.2-4. Experimental MEA and PZ Volatility in Mixtures of 3.5 m MEA Plus 3.6 m PZ at 40 and 60 °C from this work. Points: ♦ (40 °C) and ■ (60 °C). Lines: OLS Approximations.

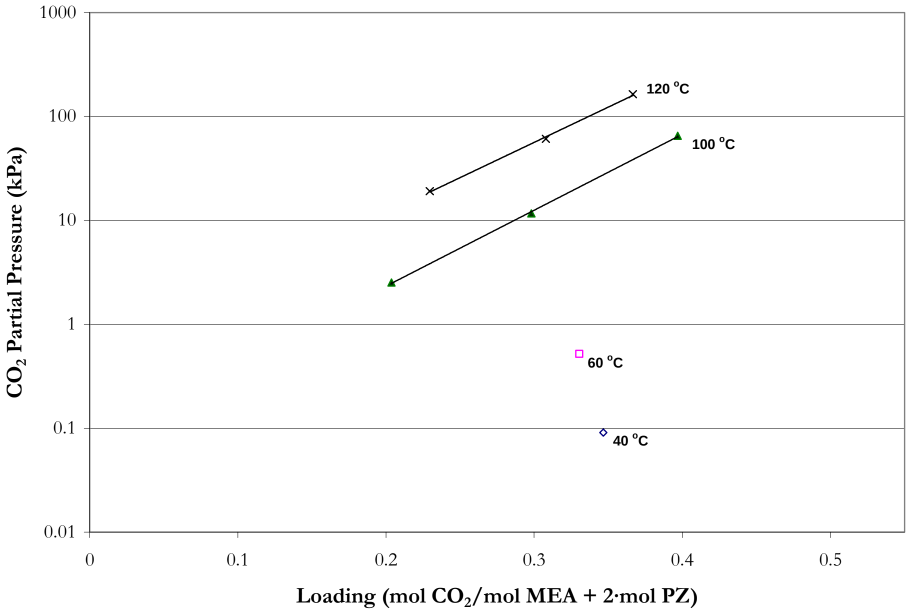

Figure 16.2-5. Experimental CO$_2$ Solubility in Mixtures of 5.6 m MEA Plus 1.8 m PZ from 40 to 120 °C from Dang (2003) and from this work. Points: ◊ (40 °C)and □ (60 °C), Dang (2003), ▲ (100 °C) and × (120 °C), this work. Lines: OLS Approximations.

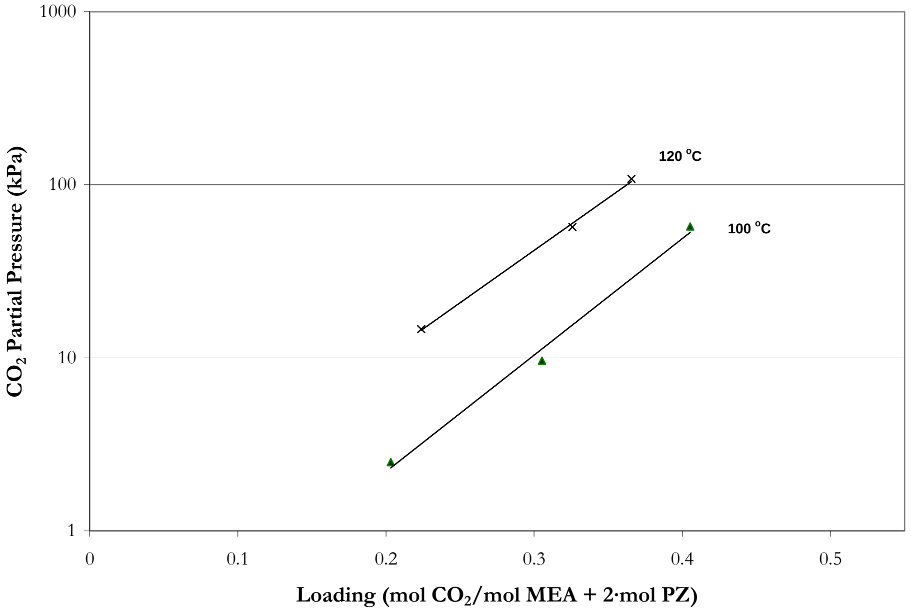

Figure 16.2-6. Experimental CO$_2$ Solubility in Mixtures of 7 m MEA Plus 1 m PZ at 100 and 120 °C from this work. Points: ▲ (100 °C) and × (120 °C). Lines: OLS Approximations.

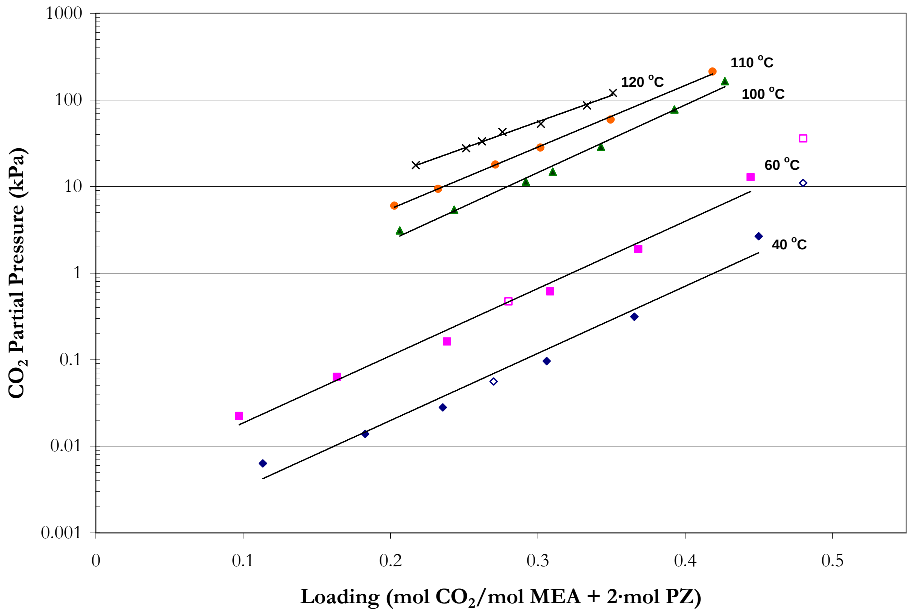

Figure 16.2-7. Experimental CO_2 Solubility in Mixtures of 7 m MEA Plus 2 m PZ from 40 to 120 °C from Okoye (2005) and from this work. Points: ◊ (40 °C)and □ (60 °C), Okoye (2005), ♦ (40 °C), ■ (60 °C), ▲ (100 °C) ● (110 °C), and × (120 °C), this work. Lines: OLS Approximations.

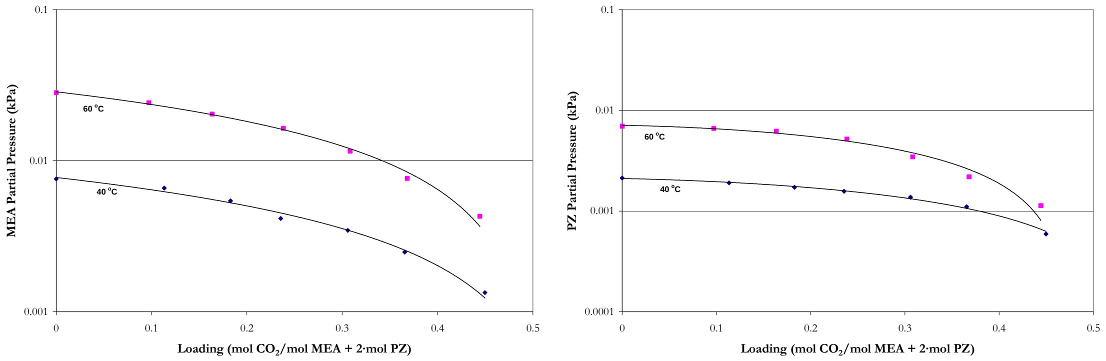

Figure 16.2-8. Experimental MEA and PZ Volatility in Mixtures of 7 m MEA Plus 2 m PZ at 40 and 60 °C from this work. Points: ♦ (40 °C) and ■ (60 °C). Lines: OLS Approximations.

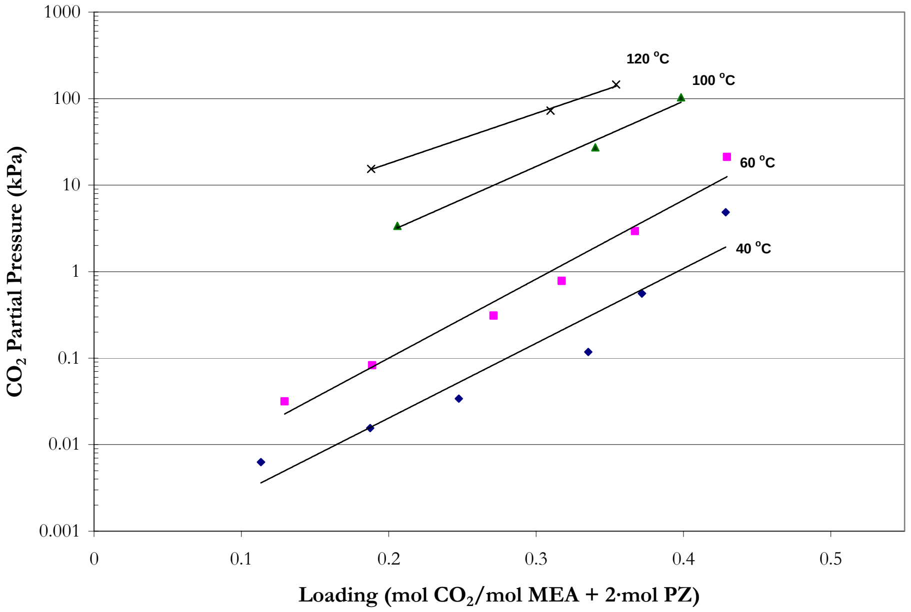

Figure 16.2-9. Experimental CO$_2$ Solubility in Mixtures of 7 m MEA Plus 3.6 m PZ from 40 to 120 °C from this work. Points: ♦ (40 °C). ■ (60 °C), ▲ (100 °C), and × (120 °C). Lines: OLS Approximations.

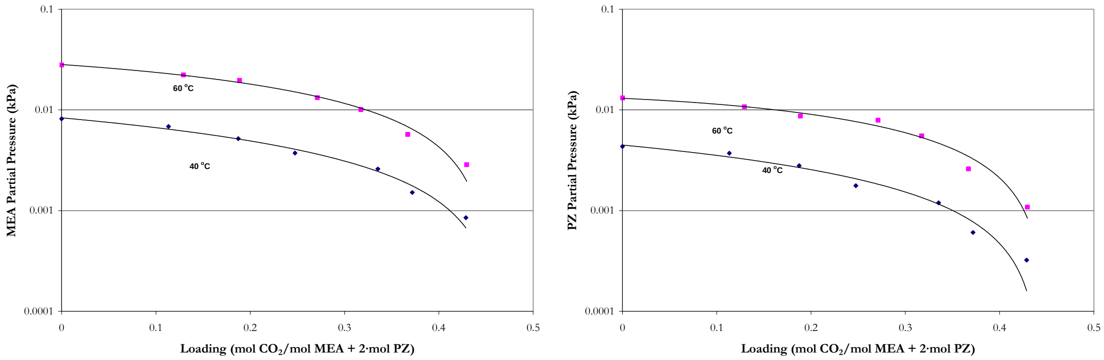

Figure 16.2-10. Experimental MEA and PZ Volatility in Mixtures of 7 m MEA Plus 3.6 m PZ at 40 and 60 °C from this work. Points: ♦ (40 °C) and ■ (60 °C). Lines: OLS Approximations.

We can quantify the effects of CO_2 solubility and amine volatility in the above systems by illustrating trends in the CO_2 solubility based on the differential capacity of the solvent between 0.01 and 1.0 kPa at 60 °C. Amine volatility at 40 °C for each solvent at a loading equal to 0.2 (mol CO_2/mol MEA + 2·mol PZ) as compared to the base sub-component systems of 7 m MEA and 2 m PZ is shown in Table 16.2-3.

Table 16.2-3. Comparison of Differential Solvent Capacity Between a CO_2 Partial Pressures of 0.01 and 1.0 kPa at 60 °C and Amine Volatility (ppm_v) at 40 °C at a loading = 0.2 (mol CO_2/mol MEA + 2·mol PZ).

	Differential Capacity	P^{MEA}	P^{PZ}
System	mol CO_2/mol MEA + 2·mol PZ	ppm_v	ppm_v
7 m MEA	0.31	61	-
2 m PZ	0.23	-	19
7 m MEA + 2 m PZ	0.26	49	17
3.5 m MEA + 2 m PZ	0.24	29	17
7 m MEA + 3.6 m PZ	0.22	48	26
3.5 m MEA + 3.6 m PZ	0.25	22	21

As shown in Table 16.2-3, 7 m MEA has a greater differential capacity as compared to piperazine or other mixed amine systems. On the other hand, 7 m MEA has demonstrated to be more volatile as compared to the other mixed amine systems. With the combination of 7 m MEA + 2 m PZ, the relative volatility decreased as compared to the base sub-component systems by a factor of ~ 1.2. When the MEA concentration decreased from 7 m to 3.5 m, differential capacity and MEA volatility decreased due to the decrease in the total alkalinity of the solvent and is reflected in the MEA volatility deceasing by a factor of 2. However, PZ volatility remained approximately constant and is consistent with effects exhibited in the H_2O-MEA-PZ systems where large changes in the solution alkalinity may not have an effect on the volatility of PZ.

16.2.2 *Specific Heat Capacity*

As stated in Chapter VI, Aspen Plus™ calculates the liquid phase heat capacity of a *mixture* (CPMX) by taking the derivative of the liquid enthalpy at constant pressure:

$$H_m^l\left(T+\Delta T\right)-H_m^l\left(T\right)=\int\limits_T^{T+\Delta T} C_{p,m}^l dT \qquad 16\text{-}3$$

where the liquid enthalpy of a mixture is calculated by the following equation:

$$H_m^l\left(T\right)=\sum_i x_i H_i+\sum_k x_k H_k^\infty+H_m^E \qquad 16\text{-}4$$

for solvents:

$$H_i\left(T\right)=\Delta H_f^{ig}\left(T^{ref}\right)+\int\limits_{T^{ref}}^{T} C_p^{ig} dT+\left[H_i\left(T,p\right)-H_i^{ig}\left(T,p\right)\right] \qquad 16\text{-}5$$

for molecular solutes (CO_2):

$$H_i\left(T\right)=H_i^{ig}\left(T\right)+RT\ln\left(\frac{H_{i,H_2O}}{P^{ref}}\right) \qquad 16\text{-}6$$

for cations or anions:

$$H_k^\infty\left(T\right)=\Delta H_{f,k}^\infty\left(T^{ref}\right)+\int\limits_{T^{ref}}^{T} C_{p,k}^\infty dT \qquad 16\text{-}7$$

Where
ΔT is the perturbation in temperature from *T*,
H_m^E is the excess enthalpy of the mixture,
$\Delta H_f^{ig}\left(T^{ref}\right)$ is the standard enthalpy of formation of component i at T^{ref} ,
T^{ref} is the reference temperature, 25.0 °C,
C_p^{ig} is the ideal gas heat capacity of component i,
H_i^{ig} is the ideal gas enthalpy of component i,
H_k^∞ is the infinite dilution aqueous enthalpy of component k,

$\Delta H_{f,k}^{\infty}\left(T^{ref}\right)$ is the infinite dilution aqueous phase standard enthalpy of formation of component k at T^{ref},
$C_{p,k}^{\infty}$ is the infinite dilution aqueous phase heat capacity polynomial of component k.

Data in the form of specific heat capacity as a function of loading, molality, and temperature were measured in this work for 3.5 m MEA + 2 m PZ and in 7 m MEA + 2 m PZ. Examples of the experimental specific heat capacity from this work from 40 to 120 °C are shown in Figure 16.2-11 and Figure 16.2-12, respectively. Points corresponding to a loading of zero were regressed as part of Chapter X. Please refer to Chapter X for more information.

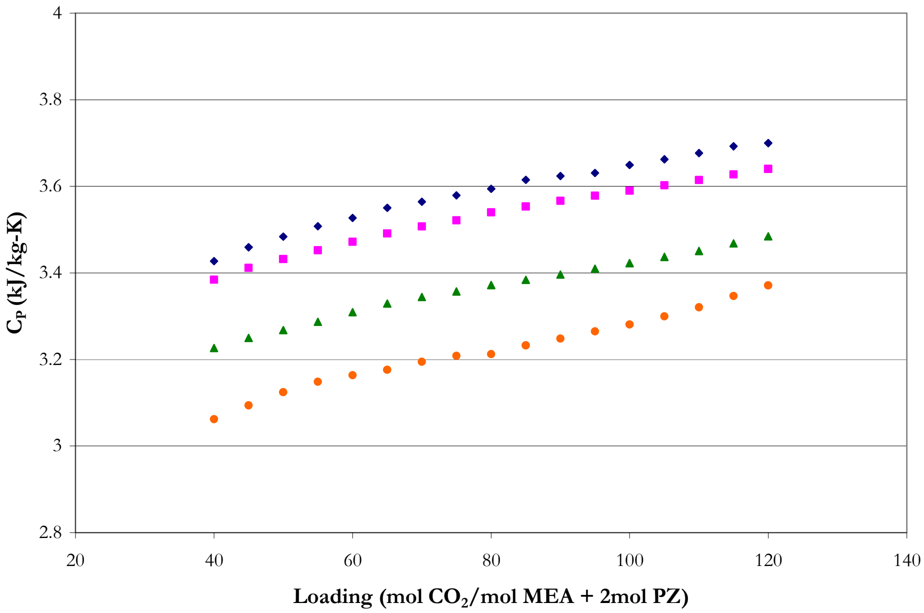

Figure 16.2-11. Specific Heat Capacity in Loaded 7 m MEA + 2 m PZ Solutions from this work. Points: ♦, Ldg = 0.00, ■, Ldg = 0.10, ▲, Ldg = 0.25, ●, Ldg = 0.43.

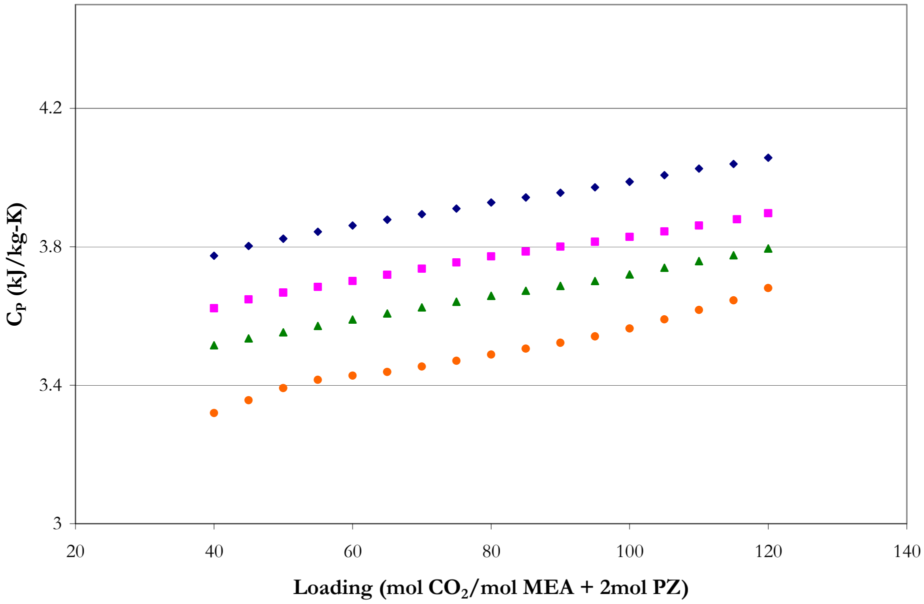

Figure 16.2-12. Specific Heat Capacity in Loaded 3.5 m MEA + 2 m PZ Solutions from this work. Points: ♦, Ldg = 0.00, ■, Ldg = 0.11, ▲, Ldg = 0.24, ●, Ldg = 0.43.

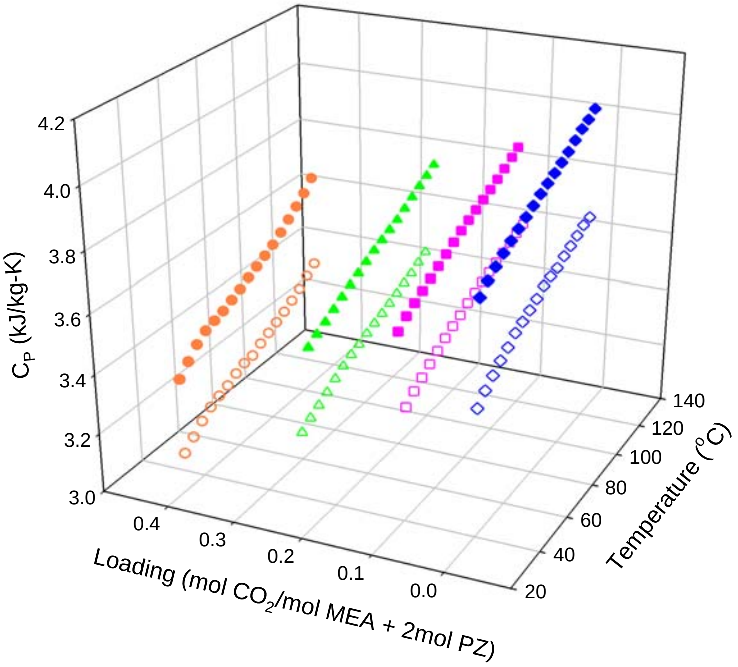

Figure 16.2-13. Specific Heat Capacity in Loaded 7 and 3.5 m MEA plus 2 m PZ Solutions from this work. Points: 3.5 m MEA + 2 m PZ, ♦, Ldg = 0.00, ■, Ldg = 0.11, ▲, Ldg = 0.24, ●, Ldg = 0.43, 7 m MEA + 2 m PZ, ◊, Ldg = 0.00, □, Ldg = 0.10, Δ, Ldg = 0.25, ○, Ldg = 0.43.

Figure 16.2-6 illustrates that the specific heat capacity from this work is internally consistent. Increasing the concentration of MEA would require the specific heat capacity to decrease by a factor of 2 and does exhibit this concentration based trend as compared to vapor-liquid equilibrium experimental results.

16.2.3 *Enthalpy of CO_2 Absorption*

Data in the form of the enthalpy of CO_2 absorption for aqueous monoethanolamine plus piperazine solutions as a function of loading and temperature were measured by Kim (2007) as part of an international collaboration between The University of Texas and the Norwegian University of Science and Technology. Kim (2007) determined the differential enthalpy of CO_2 absorption for 7 m MEA + 2 m PZ and 7 m MEA + 3.5 m PZ, based on a consistent experimental method developed for monoethanolamine [Kim et al. (2007)], at 40, 80, and 120 °C and over the range of loading from 0 – 0.55 mol CO_2/mol MEA + 2·mol PZ for use in this work.

For our true component quaternary system (H_2O, MEA, PZ, and CO_2), the Gibbs-Helmholtz equation can be used to represent the differential enthalpy of CO_2 absorption:

$$-\frac{\Delta H_{abs}}{R} = \left(\frac{d\, f_{CO_2}^{v}}{d\left(1/T\right)} \right)_{x_{CO_2}} \tag{16-8}$$

The heat released can be measured by direct calorimetry or estimated from CO_2 solubility data. The later has been shown to have a high degree of uncertainty on the order of ± 20 to 30 % as reported by Lee et al. (1974). However, if the loading span within one CO_2 addition can be kept rather low, the measurements gave enthalpy data close to differential values in loading rather than integral as shown by Kim et al. (2007) with respect to the total amount of heat released from zero loading to the experimental loading data point as shown by the following expression:

$$-\Delta H_{\text{int}} = -\int_{0}^{\alpha} \Delta H_{diff}\, \mathrm{d}\alpha \qquad 16\text{-}9$$

Where
α is the loading of the solution, mole CO_2/mole MEA.

An example of the experimental differential enthalpy of CO_2 absorption used in this work from Kim et al. (2007) at 40, 80, and 120 °C for 30 wt% monoethanolamine as compared to the mixed amine solutions are shown in Figure 16.2-14 through Figure 16.2-19.

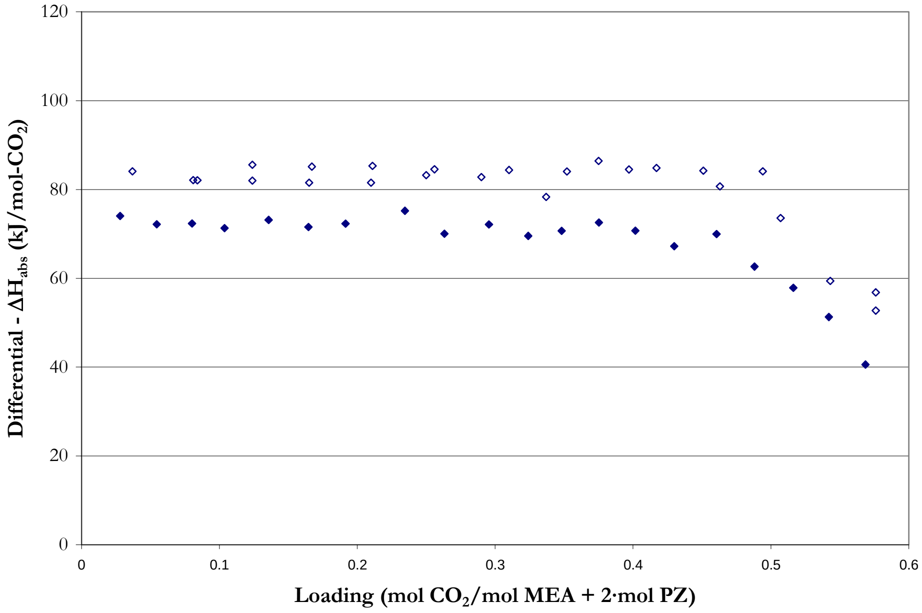

Figure 16.2-14. Negative Differential Enthalpy of CO_2 Absorption for 7 MEA and 7 m MEA + 2 m PZ at 40 °C. Points: ◊, Kim et al. (2007), ♦, Kim (2007).

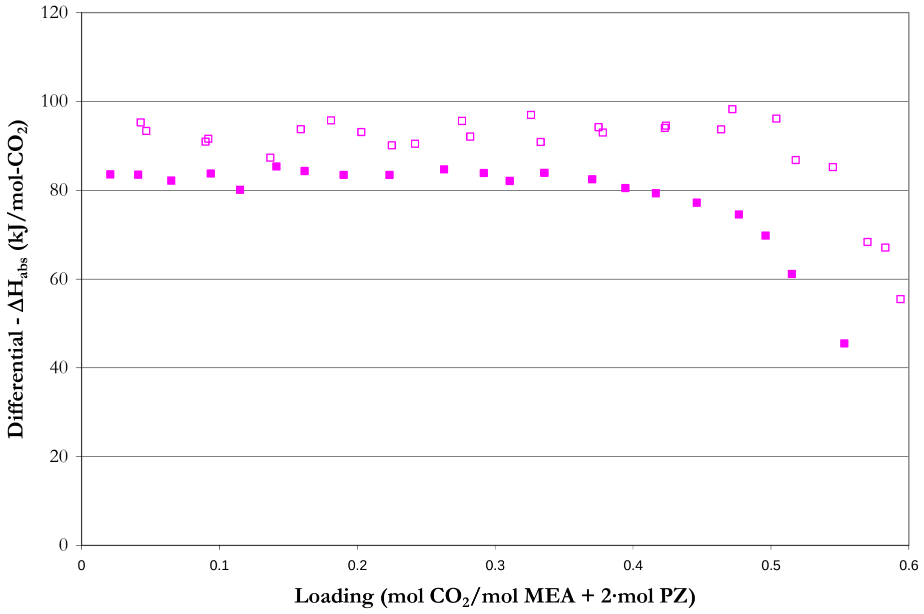

Figure 16.2-15. Negative Differential Enthalpy of CO_2 Absorption for 7 MEA and 7 m MEA + 2 m PZ at 80 °C. Points: □, Kim et al. (2007), ■, Kim (2007).

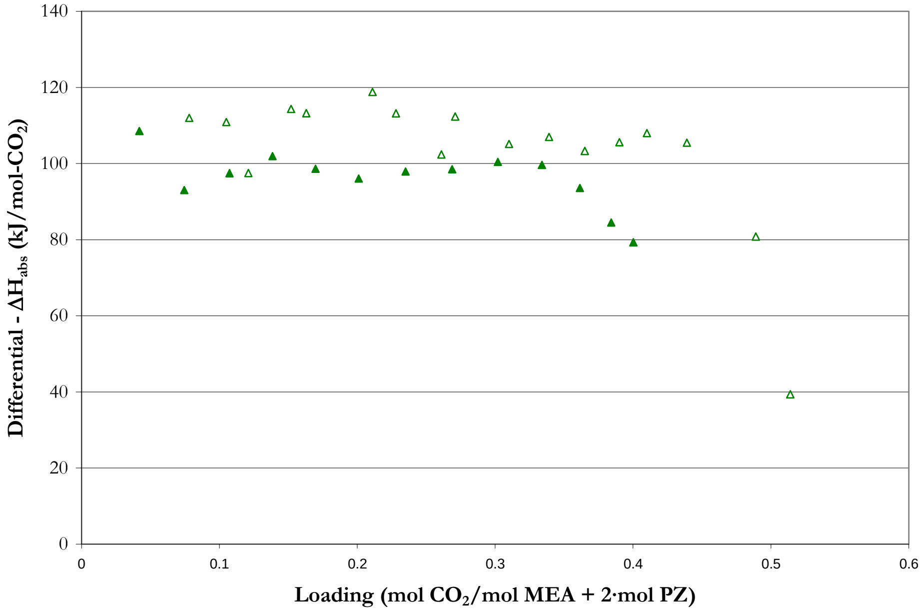

Figure 16.2-16. Negative Differential Enthalpy of CO_2 Absorption for 7 MEA and 7 m MEA + 2 m PZ at 120 °C. Points: △, Kim et al. (2007), ▲, Kim (2007).

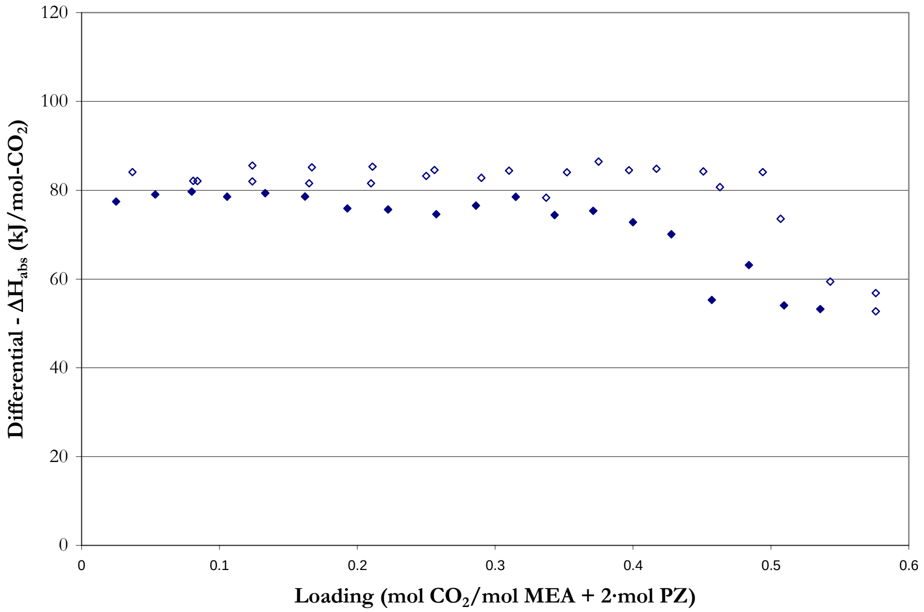

Figure 16.2-17. Negative Differential Enthalpy of CO_2 Absorption for 7 MEA and 7 m MEA + 3.5 m PZ at 40 °C. Points: ◊, Kim et al. (2007), ♦, Kim (2007).

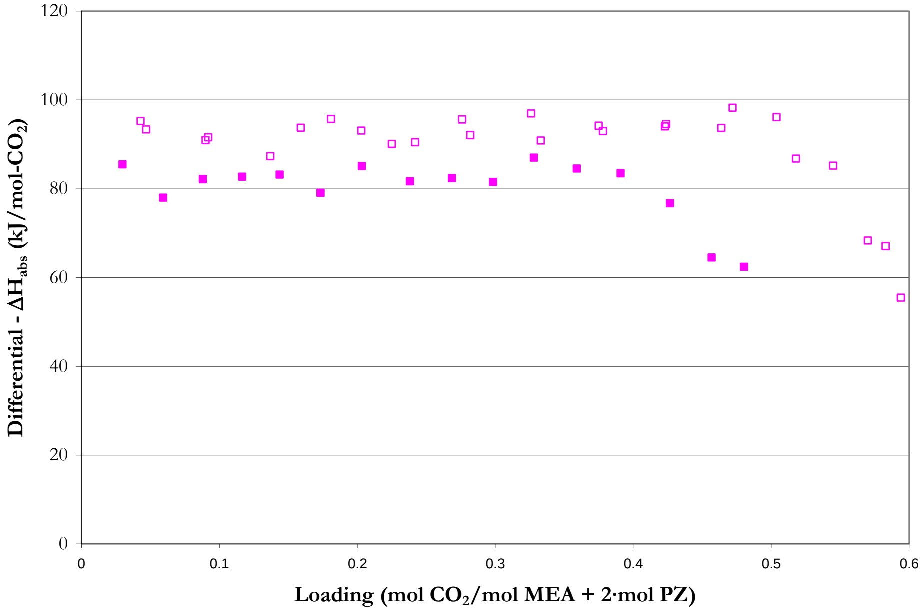

Figure 16.2-18. Negative Differential Enthalpy of CO_2 Absorption for 7 MEA and 7 m MEA + 3.5 m PZ at 80 °C. Points: □, Kim et al. (2007), ■, Kim (2007).

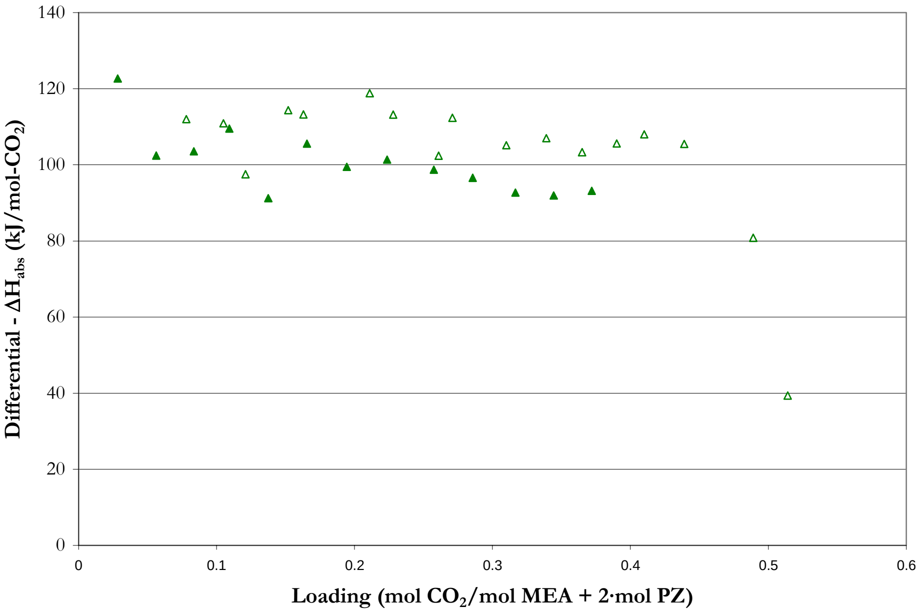

Figure 16.2-19. Negative Differential Enthalpy of CO_2 Absorption for 7 MEA and 7 m MEA + 3.5 m PZ at 120 °C. Points: △, Kim et al. (2007), ▲, Kim (2007).

With the addition of PZ to a 7 m MEA solution, the enthalpy of CO_2 absorption decreased over the range in temperature on the order of approximately 10 kJ per mole of CO_2. In addition, the enthalpy of CO_2 absorption for the mixed amine solutions illustrates a shift in speciation. Over the range in loading between 0 and 0.5 mol CO_2/mol MEA, the main reaction mechanism is the protonation of MEA where beyond a loading of 0.5 the main reaction mechanism is the reaction of MEA with bicarbonate to form MEA carbamate as indicated by the steep drop in the enthalpy of CO_2 absorption. With the addition of PZ to the system, the reaction mechanism for the protonation of MEA has been shifted to 0.4 mol CO_2/mol MEA + 2·mol PZ due to a change in the total alkalinity of the system.

16.2.4 *NMR Speciation*

Data in the form of carbon13 NMR speciation for aqueous monoethanolamine plus piperazine solutions as a function of loading, concentration, and temperature were measured for the H_2O-MEA-PZ-CO_2 system in 7 m MEA + 3.6 m PZ.

For our true component quaternary system (H_2O, MEA, PZ, and CO_2), the following equations can be used to represent the liquid phase equilibrium for the NMR speciation data from this work.

$$n^*_{MEA} = n_{MEA} + n_{MEAH^+} \qquad 16\text{-}10$$

$$n^*_{MEACOO^{-1}} = n_{MEACOO^{-1}} \qquad 16\text{-}11$$

$$n^*_{PZ} = n_{PZ} + n_{PZH^+} + n_{PZH^{+2}} \qquad 16\text{-}12$$

$$n^*_{PZ(COO)_2^{-2}} = n_{PZ(COO)_2^{-2}} \qquad 16\text{-}13$$

$$n^*_{H^+/PZCOO^{-1}} = n_{H^+PZCOO^{-1}} + n_{PZCOO^{-1}} \qquad 16\text{-}14$$

$$n^*_{CO_2} = n_{CO_2} + n_{CO_3^{-2}} + n_{HCO_3^{-1}} \qquad 16\text{-}15$$

Where
n_i is the true number of moles for each component per kilogram of water corresponding to the relative proton/carbon NMR peak areas,
ni* is the pseudo-component quantity based on experimental NMR data.

An example of the experimental NMR speciation used in this work for 7 m MEA + 3.6 m PZ solutions at 27, 40, and 60 °C is shown in Figure 15.3-14, Figure 15.3-15, and Figure 15.3-16, respectively. We were unable to gather speciation for 7 m MEA + 2 m PZ due to the sensitivity of the NMR analysis for the detection of low concentration species.

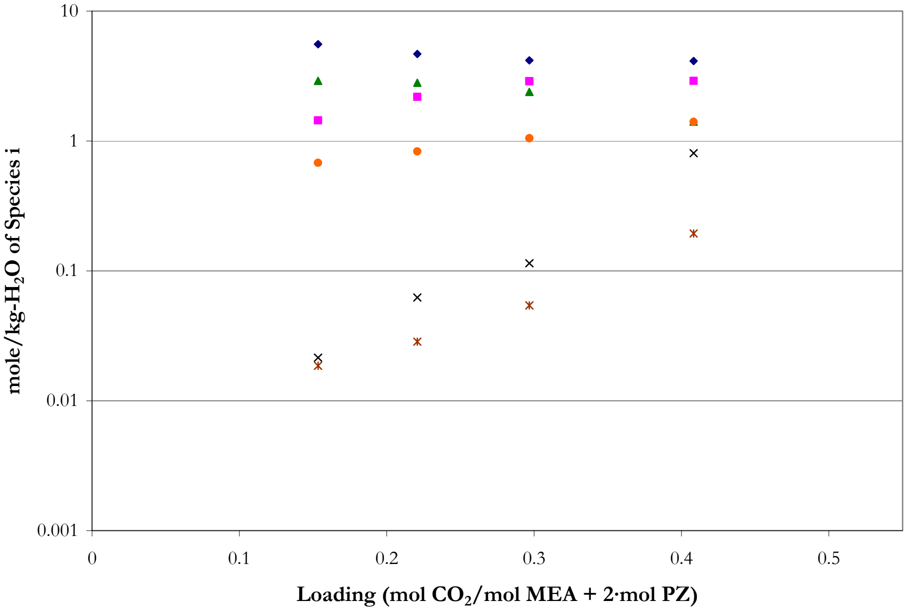

Figure 16.2-20. Liquid Phase Speciation from C^{13} NMR at 27 °C. Points: ♦, MEA + $MEAH^{+1}$, ■, $MEACOO^{-1}$, ▲, PZ + PZH^{+1}, ●, $H^{+1}PZCOO^{-1}$ + $PZCOO^{-1}$, ×, $PZ(COO^{-1})_2$, *, CO_3^{-2}+HCO_3^{-1}.

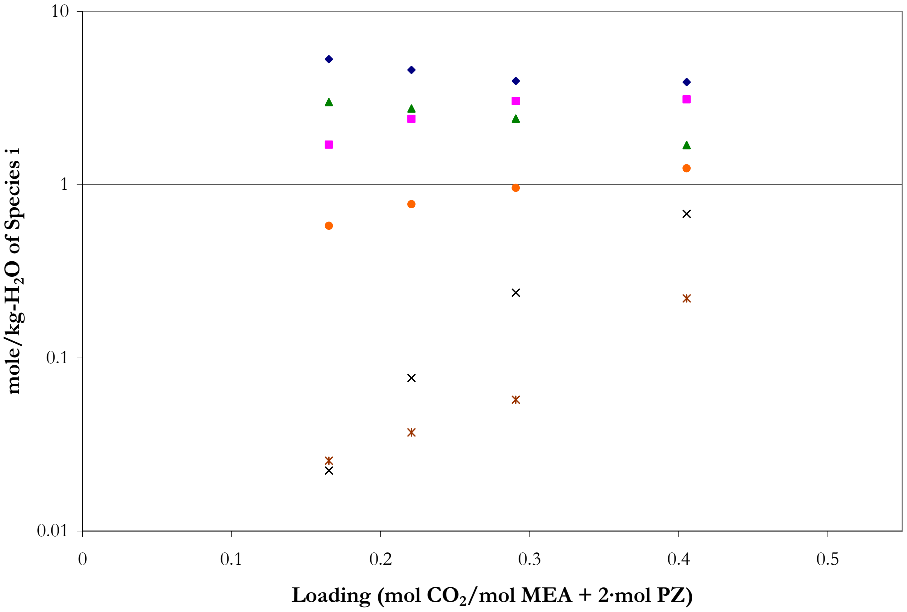

Figure 16.2-21. Liquid Phase Speciation from C^{13} NMR at 40 °C. Points: ♦, MEA + $MEAH^{+1}$, ■, $MEACOO^{-1}$, ▲, PZ + PZH^{+1}, ●, $H^{+1}PZCOO^{-1}$ + $PZCOO^{-1}$, ×, $PZ(COO^{-1})_2$, *, CO_3^{-2}+HCO_3^{-1}.

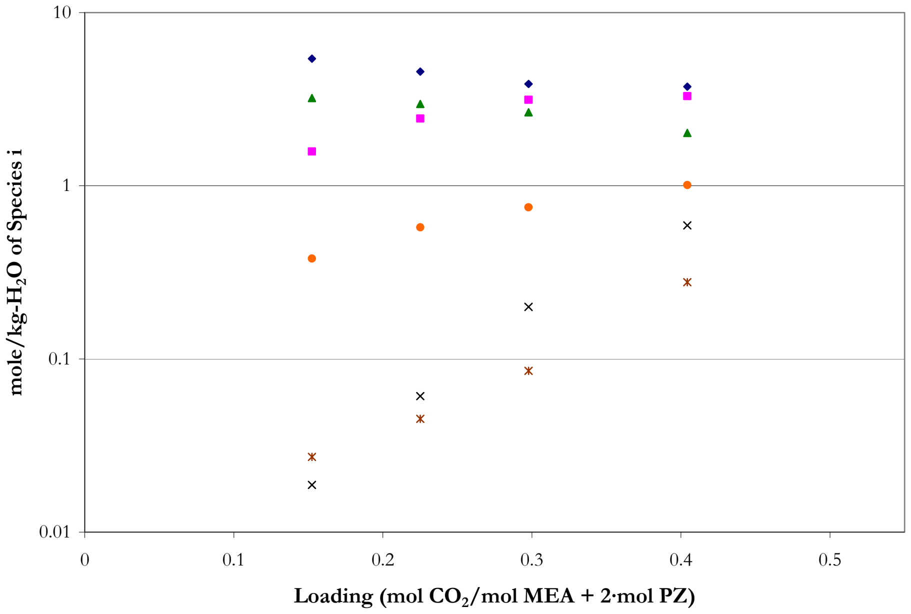

Figure 16.2-22. Liquid Phase Speciation from C^{13} NMR at 60 °C. Points: ♦, MEA + $MEAH^{+1}$, ■, $MEACOO^{-1}$, ▲, PZ + PZH^{+1}, ●, $H^{+1}PZCOO^{-1}$ + $PZCOO^{-1}$, ×, $PZ(COO^{-1})_2$, *, CO_3^{-2}+HCO_3^{-1}.

16.3 Combined Model Predictions

A simple Aspen Plus™ Flash model was used to test the predictive capability of the H_2O-MEA-PZ-CO_2 model against experimental data from using in this work. For each data point, the deviation between the experimental and estimated values is expressed in terms of the average absolute relative deviation (AARD) given in Table 16.3-1.

Table 16.3-1. Absolute Percent Relative Error for the H_2O-MEA-PZ-CO_2 System.

Data Type	Source	AARD (%)
P^{CO2}	Dang (2003)	21.2
	Okoye (2005)	55.3
	This work.	27.4
P^{MEA}	This work	40.7
P^{PZ}	This work	76.3
ΔH_{abs}	Kim (2007)	15.8
C_P	This work	5.1
NMR Speciation	This work	61.5

Overall, the combined model did not adequately describe the H_2O-MEA-PZ-CO_2 property data listed above as shown by an average absolute relative error of ± 37.9 percent with the exception of a few outliers. This would suggest that there may be a need for parameter optimization to improve the statistical fit of the experimental data as described by the combined model.

One of the goals of this work was to be able to build a consistent and rigorous thermodynamic model to describe the base systems, then to combine the two models and test the predictive behavior of the combined model. Table 16.3-1 illustrates that a simple exchange between binary interaction parameters based on the separate systems to create analogous interactions for the combined model did not result in an adequate fit of the experimental data. We would recommend that future work interested in the H_2O-MEA-PZ-CO_2 system should optimize the binary interaction parameters to capture systematic trends presented within the experimental data. The rest of this chapter will illustrate the combined model predictions for the H_2O-MEA-PZ-CO_2 system.

16.3.1 *CO_2 Solubility and Amine Volatility*

Figure 16.3-1 through Figure 16.3-22 gives the results of fit for the experimental CO_2 solubility and amine volatility for amine mixtures of MEA plus PZ versus loading from 40 to 120 °C. Overall, the combined model moderately described the experimental data within an average absolute relative error of ± 44.2 percent.

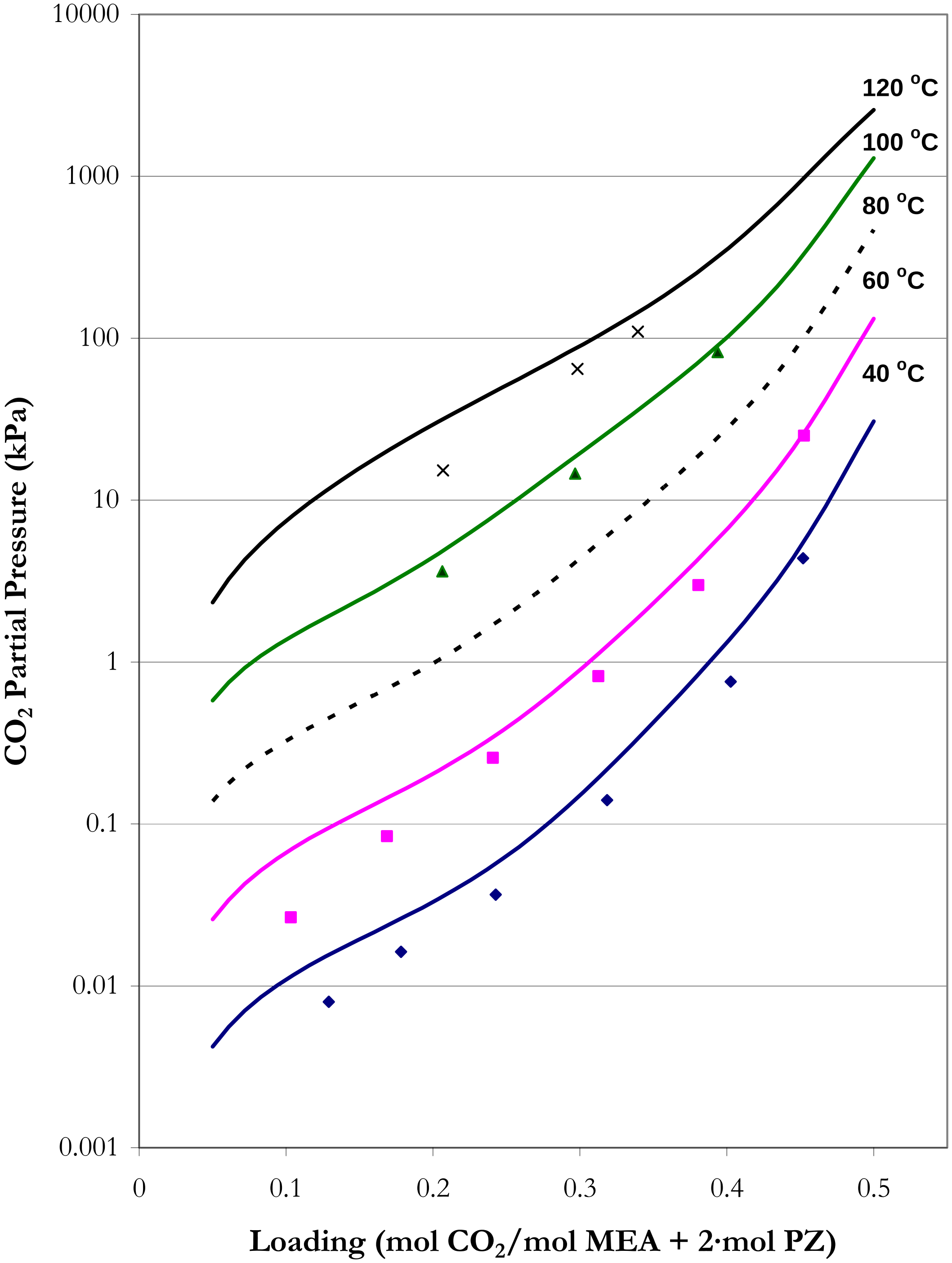

Figure 16.3-1. Experimental CO_2 Solubility in Mixtures of 3.5 m MEA Plus 2 m PZ from 40 to 120 °C from this work. Points: ♦ (40 °C). ■ (60 °C), ▲ (100 °C), and × (120 °C). Lines: elecNRTL Predictions.

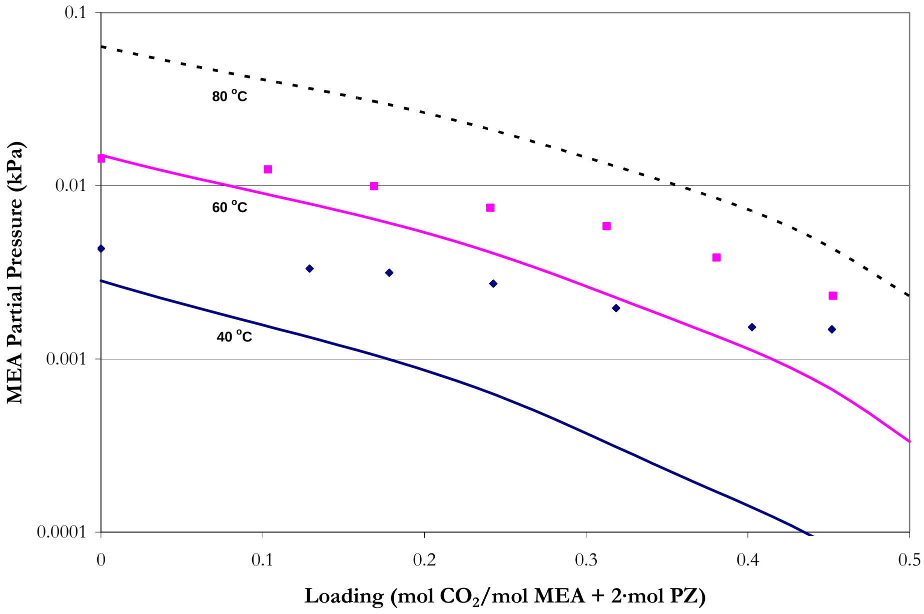

Figure 16.3-2. Experimental MEA Volatility in Mixtures of 3.5 m MEA Plus 2 m PZ at 40 and 60 °C from this work. Points: ♦ (40 °C) and ■ (60 °C). Lines: elecNRTL Predictions.

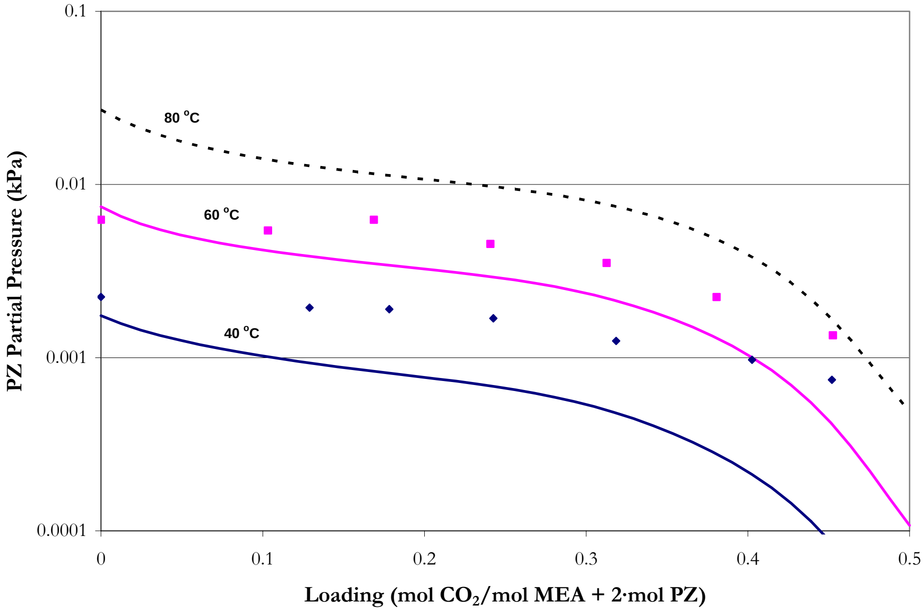

Figure 16.3-3. Experimental PZ Volatility in Mixtures of 3.5 m MEA Plus 2 m PZ at 40 and 60 °C from this work. Points: ♦ (40 °C) and ■ (60 °C). Lines: elecNRTL Predictions.

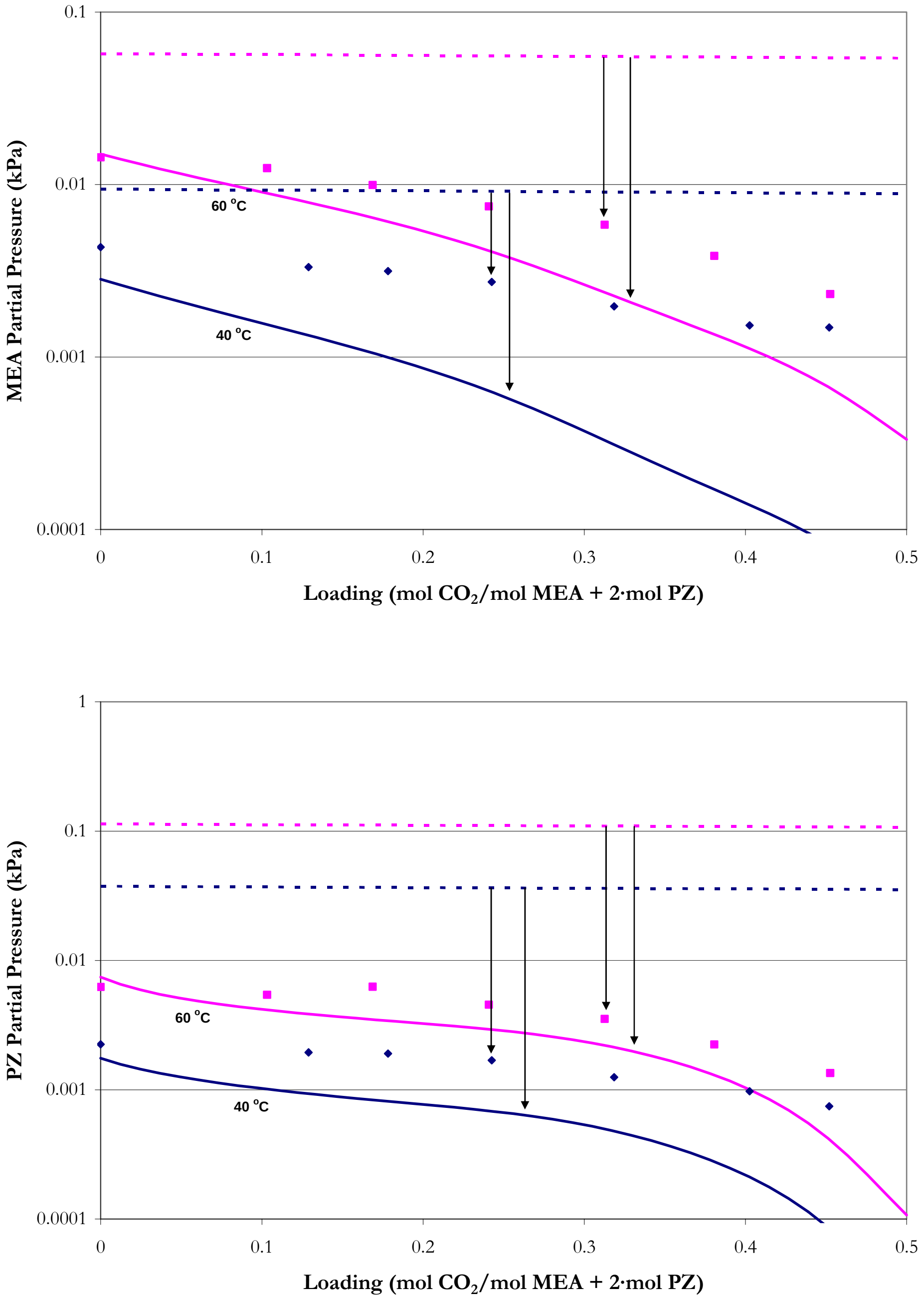

Figure 16.3-4. Experimental MEA and PZ Volatility in Mixtures of 3.5 m MEA Plus 2 m PZ at 40 and 60 °C from this work. Points: ♦ (40 °C) and ■ (60 °C). Solid lines: elecNRTL Predictions, Dash lines: Raoult's Law Approximations.

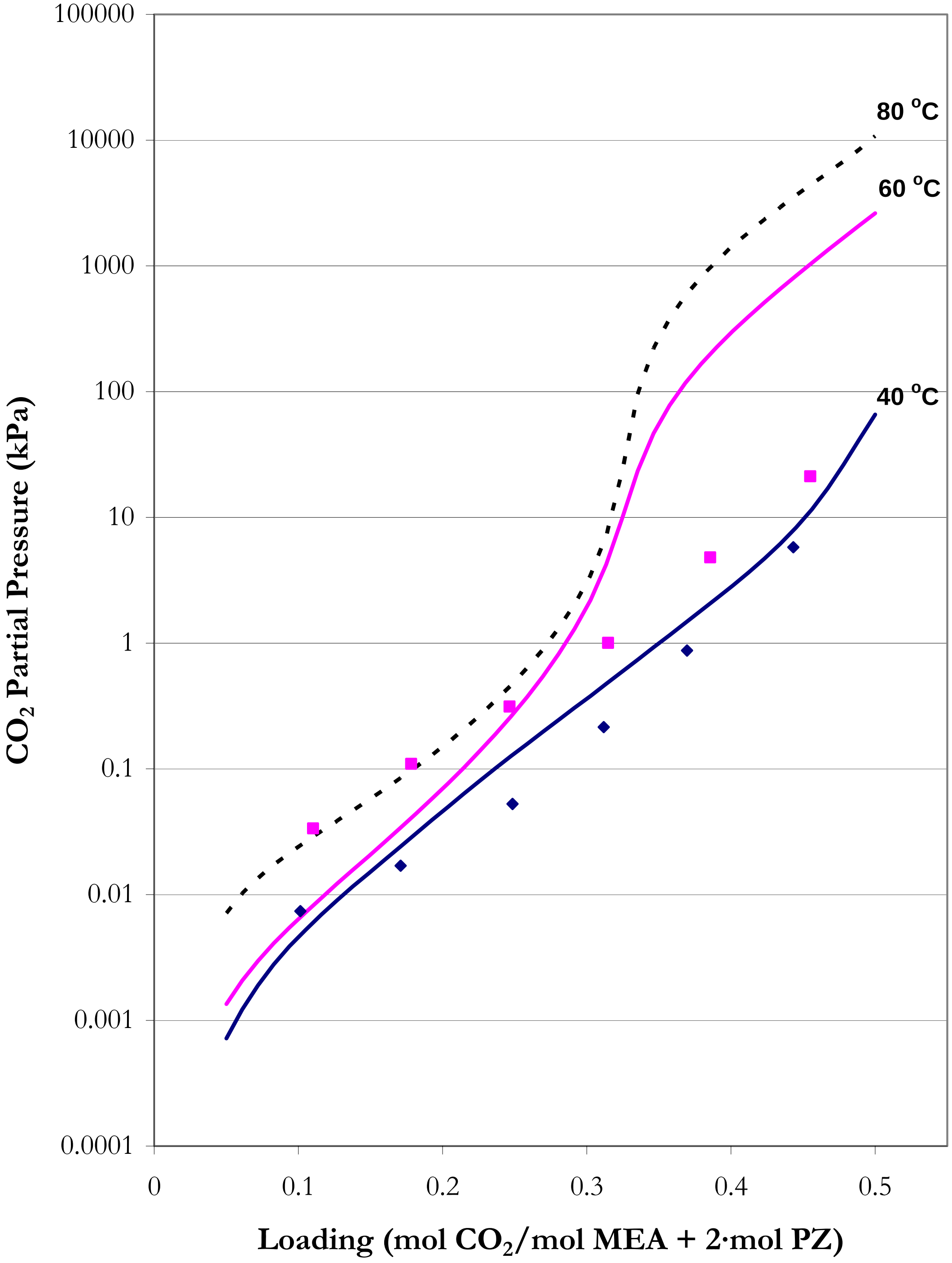

Figure 16.3-5. **Experimental CO_2 Solubility in Mixtures of 3.5 m MEA Plus 3.6 m PZ from 40 and 60 °C from this work. Points: ◆ (40 °C) and ■ (60 °C). Lines: elecNRTL Predictions.**

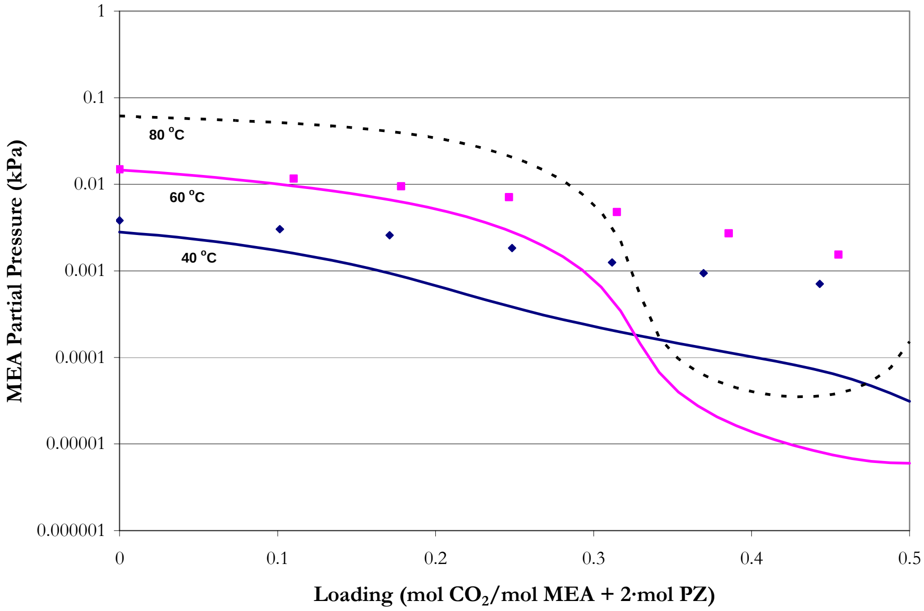

Figure 16.3-6. Experimental MEA Volatility in Mixtures of 3.5 m MEA Plus 3.6 m PZ at 40 and 60 °C from this work. Points: ♦ (40 °C) and ■ (60 °C). Lines: elecNRTL Predictions.

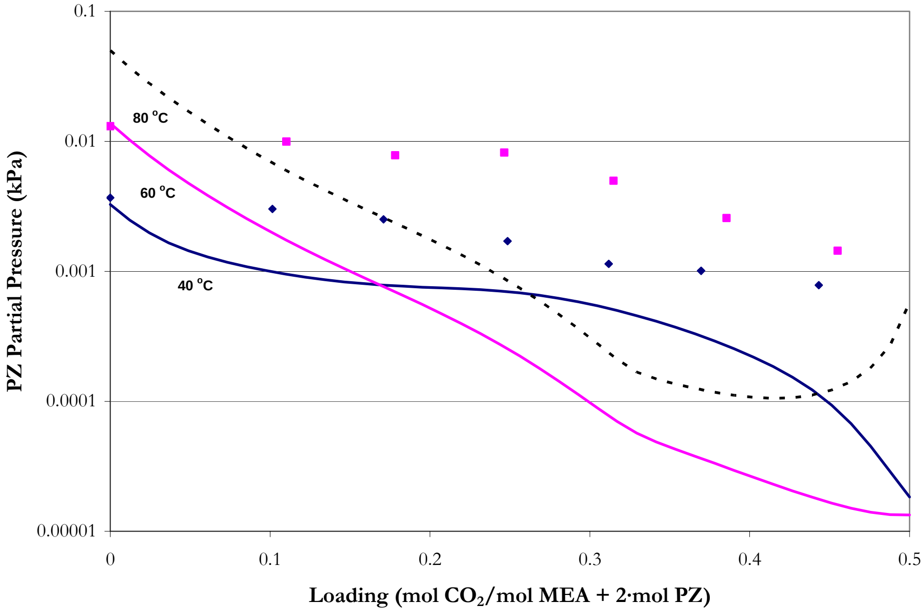

Figure 16.3-7. Experimental PZ Volatility in Mixtures of 3.5 m MEA Plus 3.6 m PZ at 40 and 60 °C from this work. Points: ♦ (40 °C) and ■ (60 °C). Lines: elecNRTL Predictions.

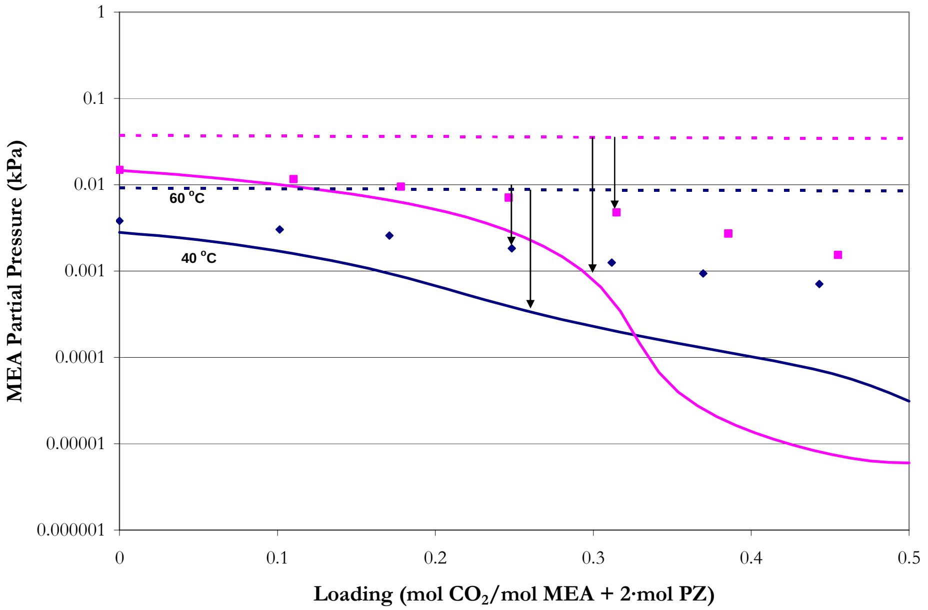

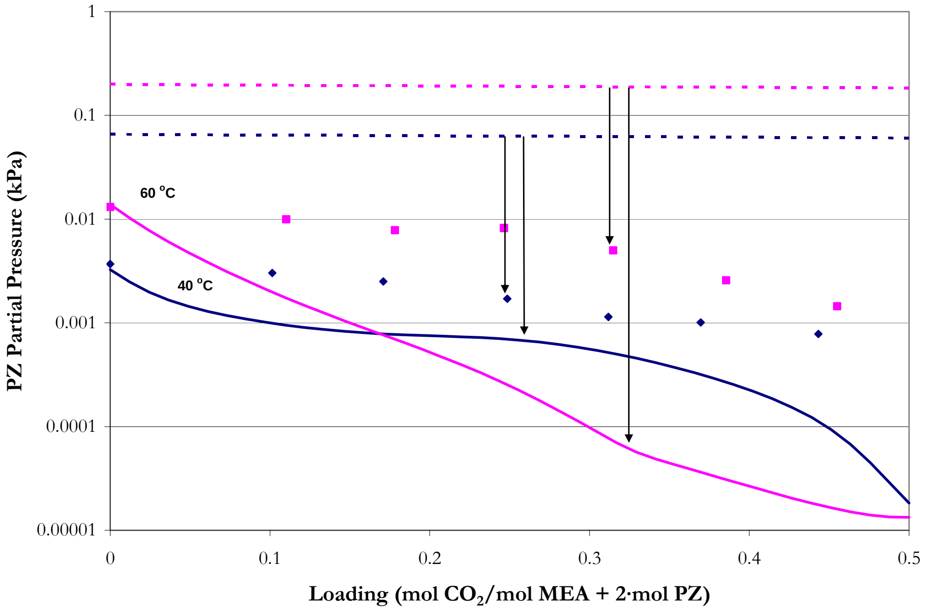

Figure 16.3-8. Experimental MEA and PZ Volatility in Mixtures of 3.5 m MEA Plus 3.6 m PZ at 40 and 60 °C from this work. Points: ◆ (40 °C) and ■ (60 °C). Solid lines: elecNRTL Predictions, Dash lines: Raoult's Law Approximations.

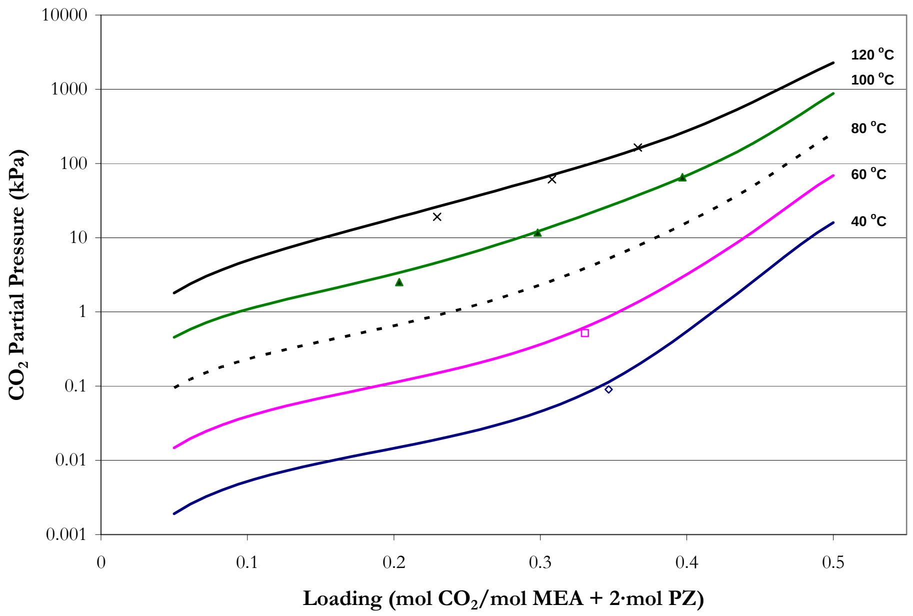

Figure 16.3-9. Experimental CO_2 Solubility in Mixtures of 5.6 m MEA Plus 1.8 m PZ from 40 to 120 °C from Dang (2003) and from this work. Points: ◊ (40 °C)and □ (60 °C), Dang (2003), ▲ (100 °C) and × (120 °C), this work. Lines: elecNRTL Predictions.

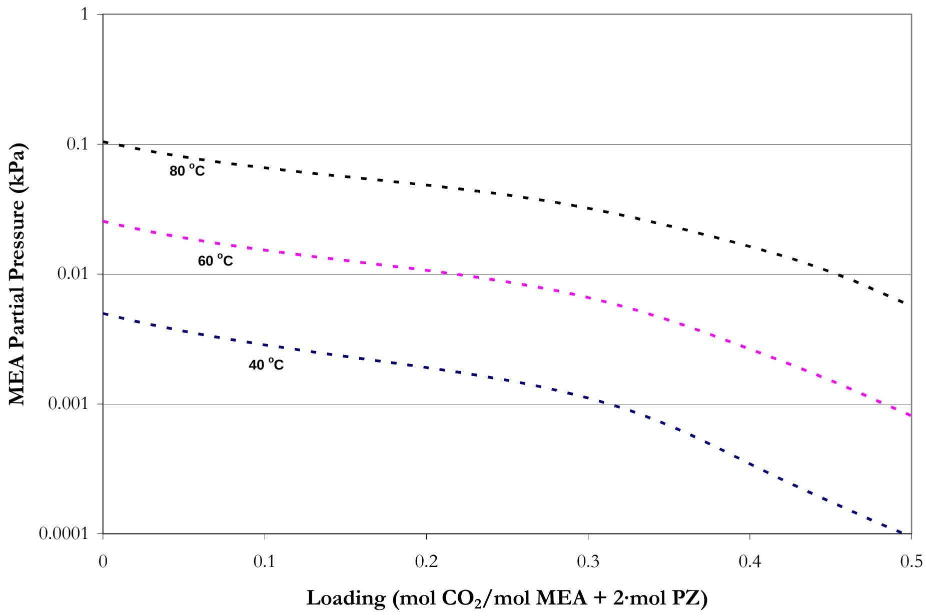

Figure 16.3-10. Experimental MEA Volatility in Mixtures of 5.6 m MEA Plus 1.8 m PZ from 40 to 80 °C. Lines: elecNRTL Predictions.

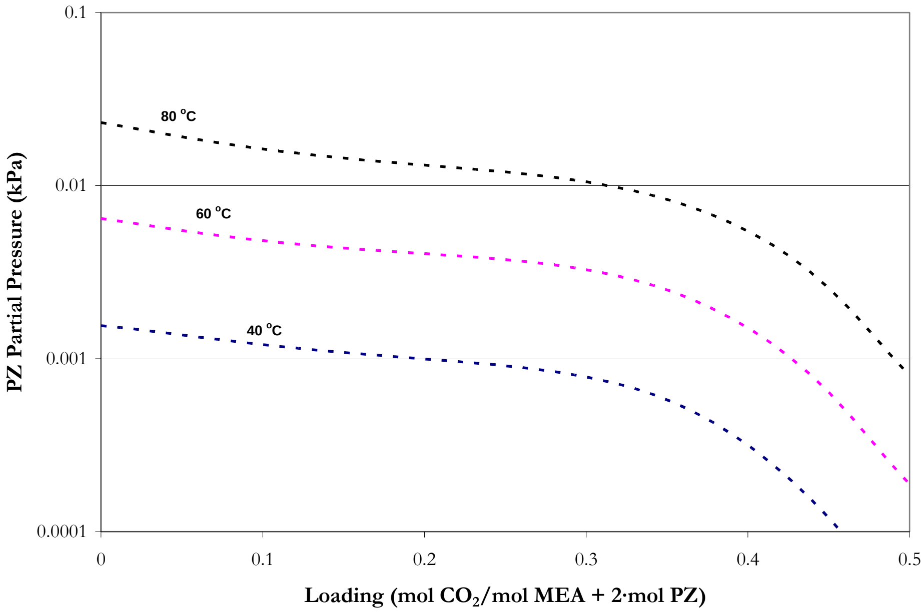

Figure 16.3-11. Experimental PZ Volatility in Mixtures of 5.6 m MEA Plus 1.8 m PZ from 40 to 80 °C. Lines: elecNRTL Predictions.

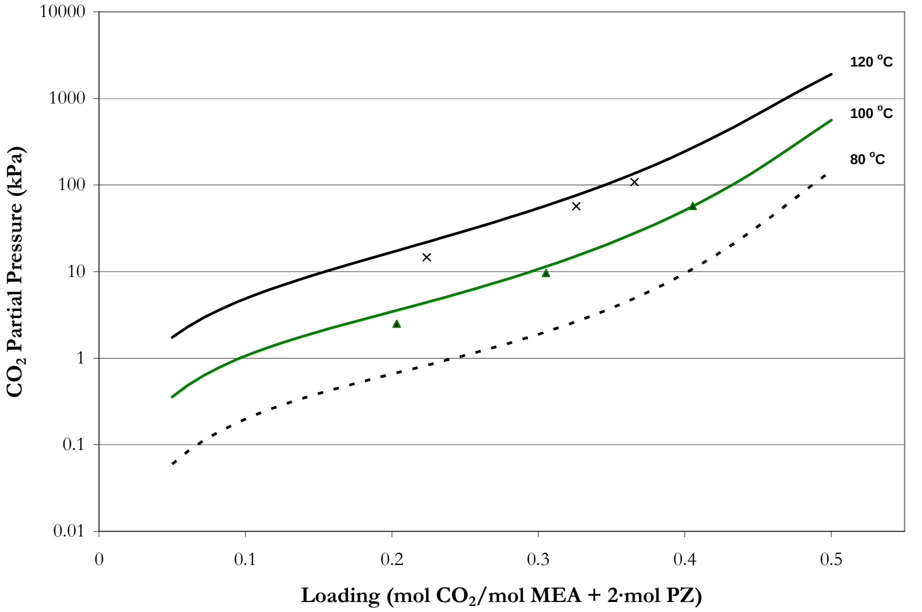

Figure 16.3-12. Experimental CO_2 Solubility in Mixtures of 7 m MEA Plus 1 m PZ at 100 and 120 °C from this work. Points: ▲ (100 °C) and × (120 °C). Lines: elecNRTL Perdictions.

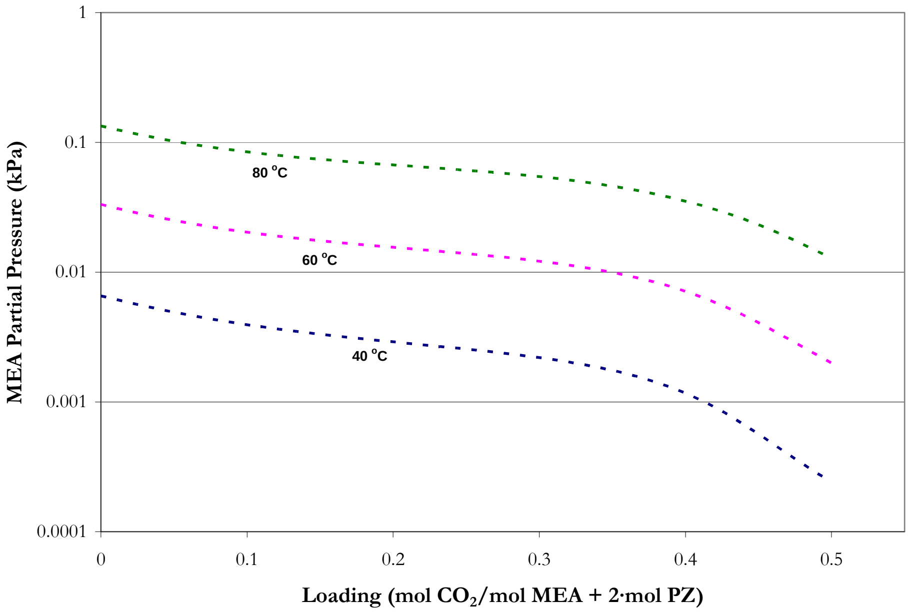

Figure 16.3-13. Experimental MEA Volatility in Mixtures of 7 m MEA Plus 1 m PZ from 40 to 80 °C. Lines: elecNRTL Predictions.

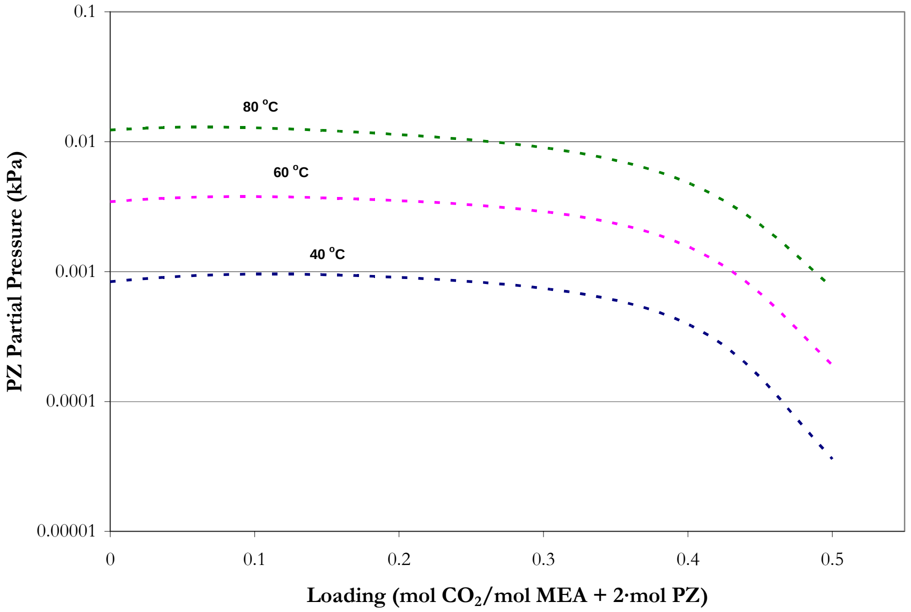

Figure 16.3-14. Experimental PZ Volatility in Mixtures of 7 m MEA Plus 1 m PZ from 40 to 80 °C. Lines: elecNRTL Predictions.

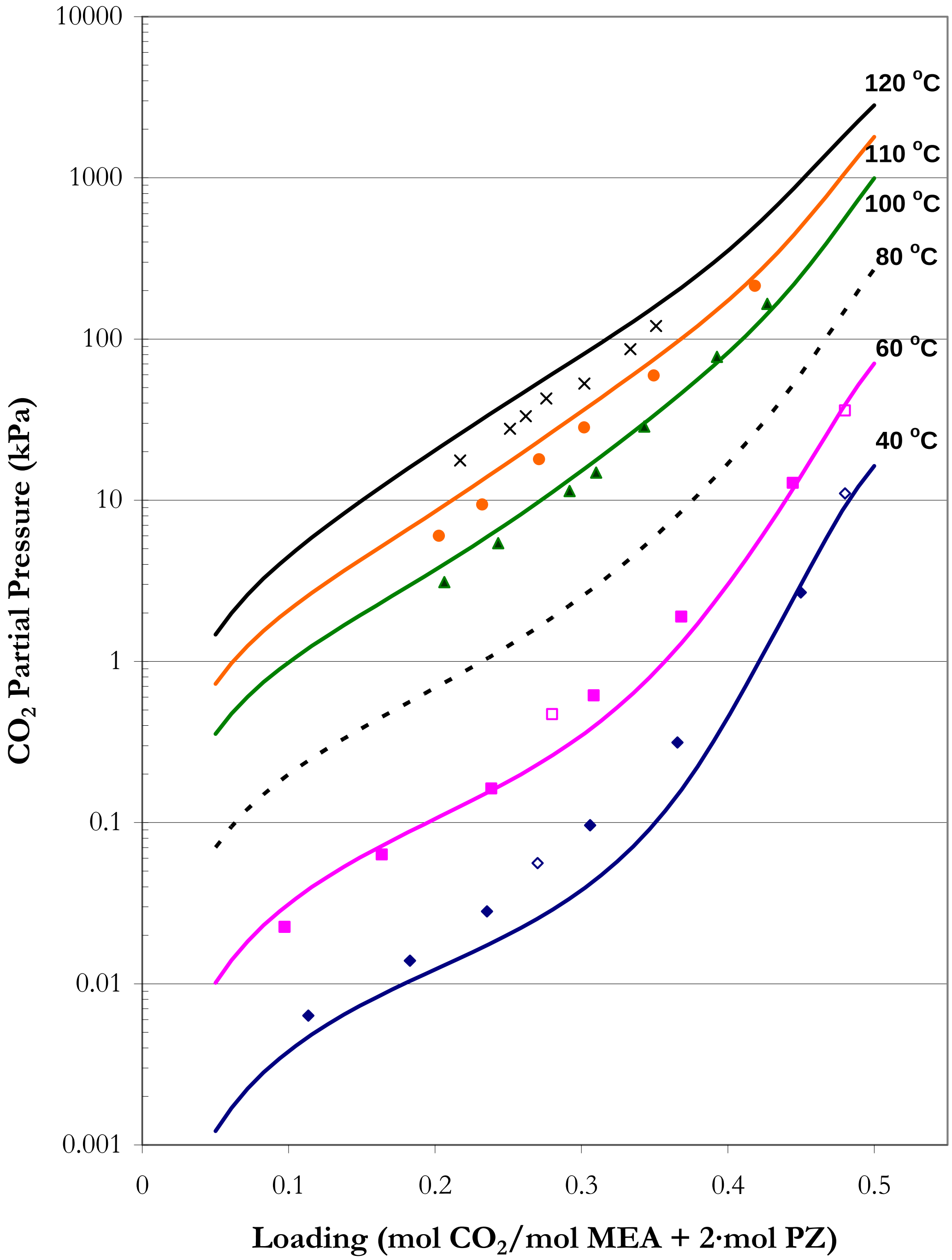

Figure 16.3-15. Experimental CO_2 Solubility in Mixtures of 7 m MEA Plus 2 m PZ from 40 to 120 °C from Okoye (2005) and from this work. Points: ◊ (40 °C)and □ (60 °C), Okoye (2005), ♦ (40 °C), ■ (60 °C), ▲ (100 °C) ● (110 °C), and × (120 °C), this work. Lines: elecNRTL Perdictions.

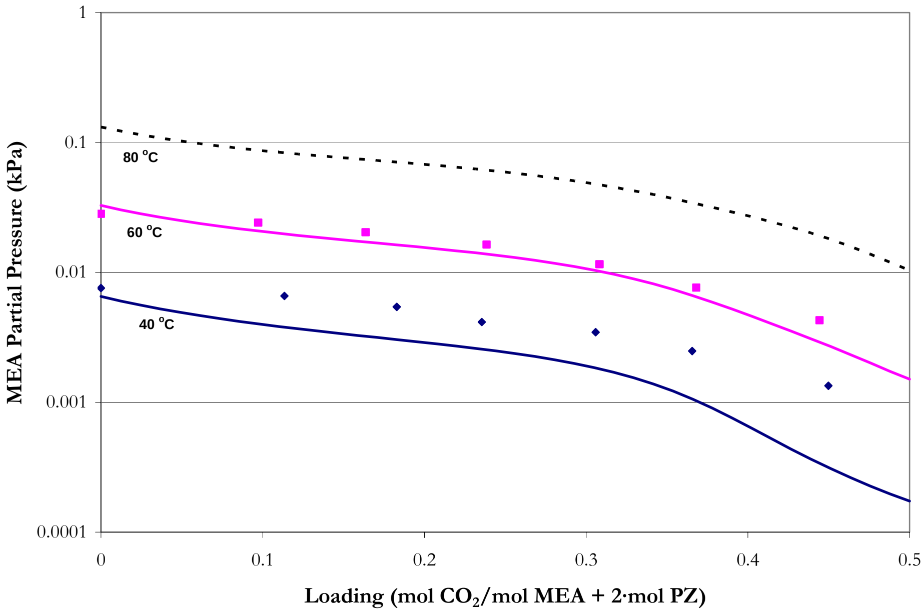

Figure 16.3-16. Experimental MEA Volatility in Mixtures of 7 m MEA Plus 2 m PZ from 40 to 80 °C from this work. Points: ♦ (40 °C) and ■ (60 °C). Lines: elecNRTL Predictions.

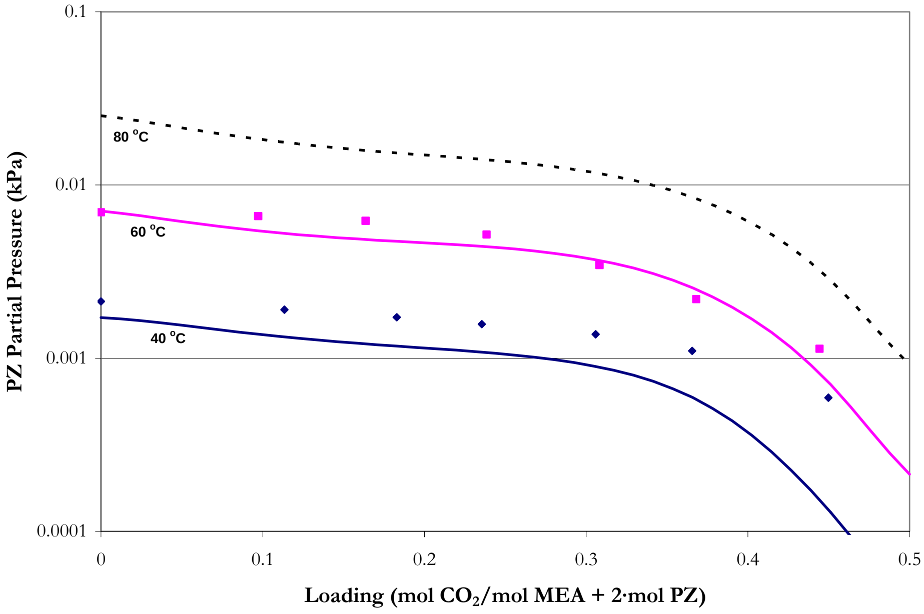

Figure 16.3-17. Experimental MEA Volatility in Mixtures of 7 m MEA Plus 2 m PZ from 40 to 80 °C from this work. Points: ♦ (40 °C) and ■ (60 °C). Lines: elecNRTL Predictions.

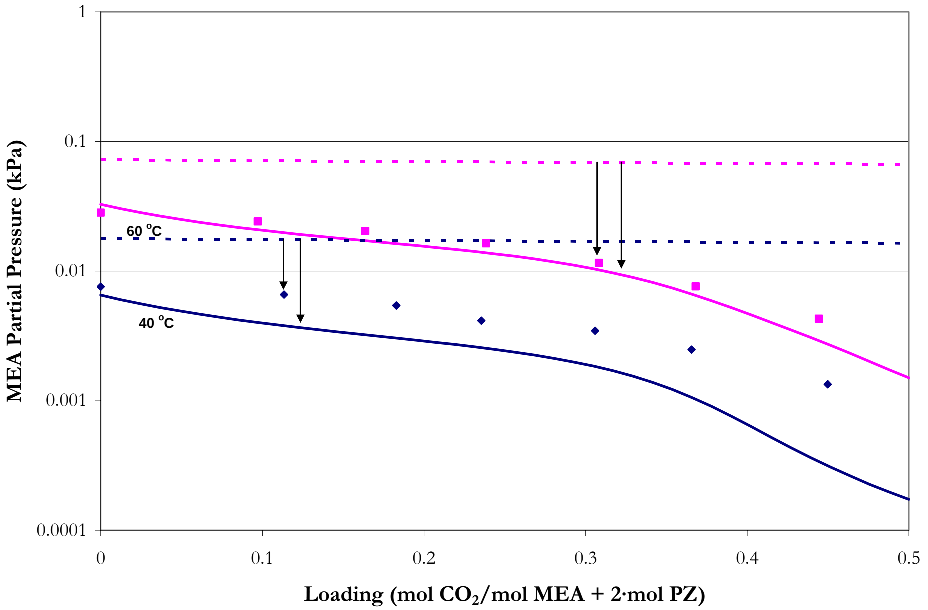

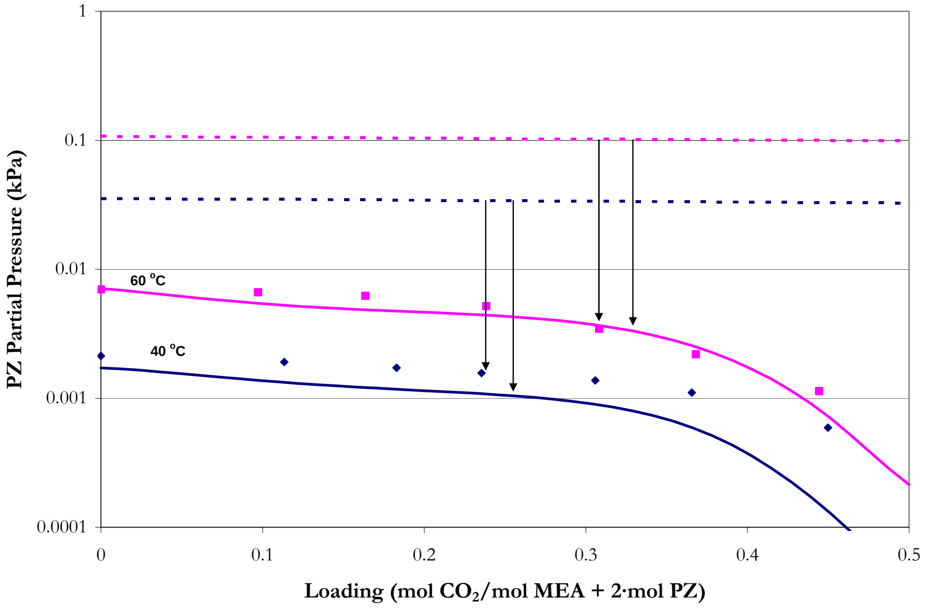

Figure 16.3-18. Experimental MEA and PZ Volatility in Mixtures of 7 m MEA Plus 2 m PZ from 40 to 80 °C from this work. Points: ♦ (40 °C) and ■ (60 °C). Solid lines: elecNRTL Predictions, Dash lines: Raoult's Law Approximations.

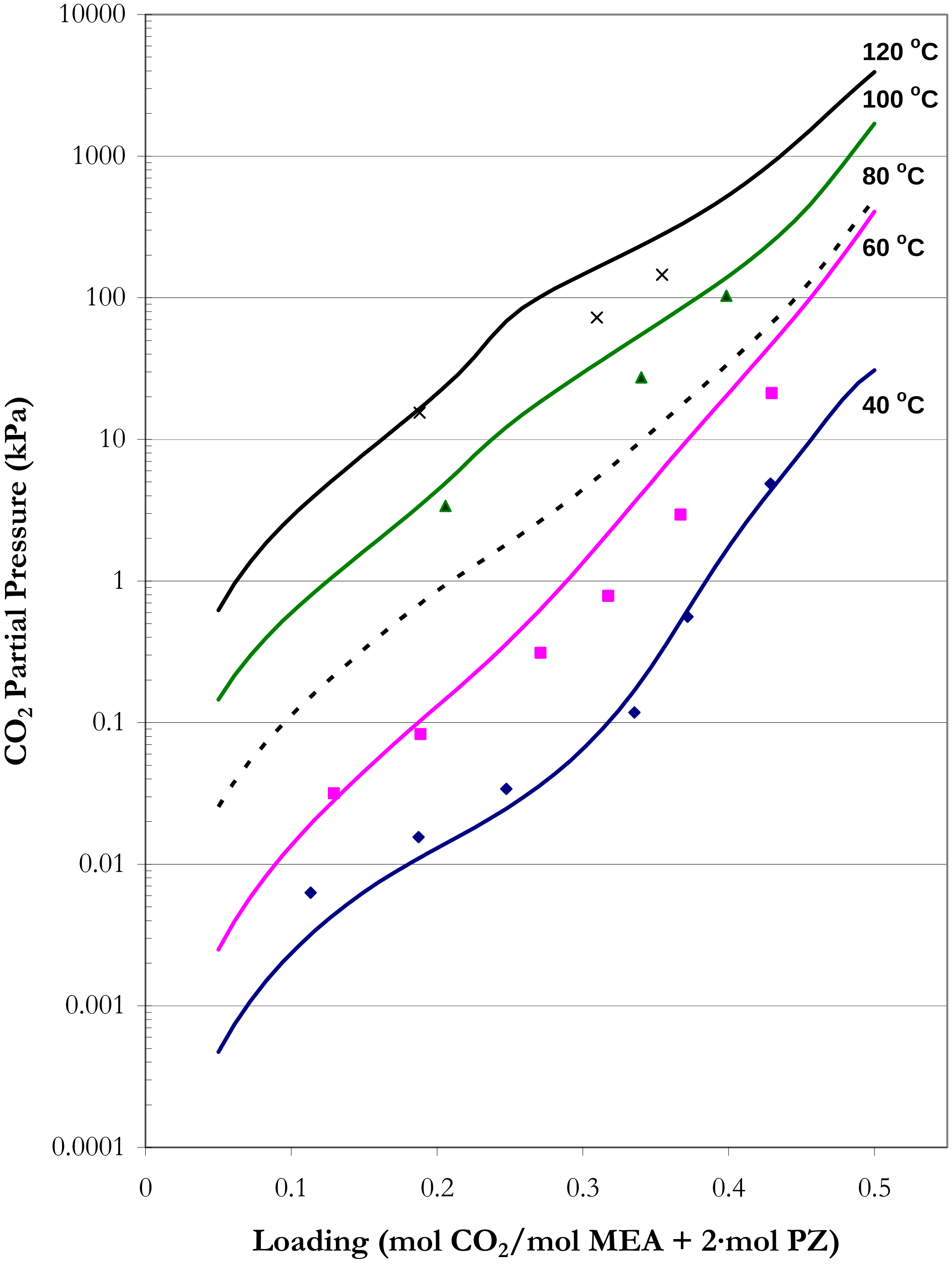

Figure 16.3-19. Experimental CO_2 Solubility in Mixtures of 7 m MEA Plus 3.6 m PZ from 40 to 120 °C from this work. Points: ♦ (40 °C). ■ (60 °C), ▲ (100 °C), and × (120 °C). Lines: elecNRTL Predictions.

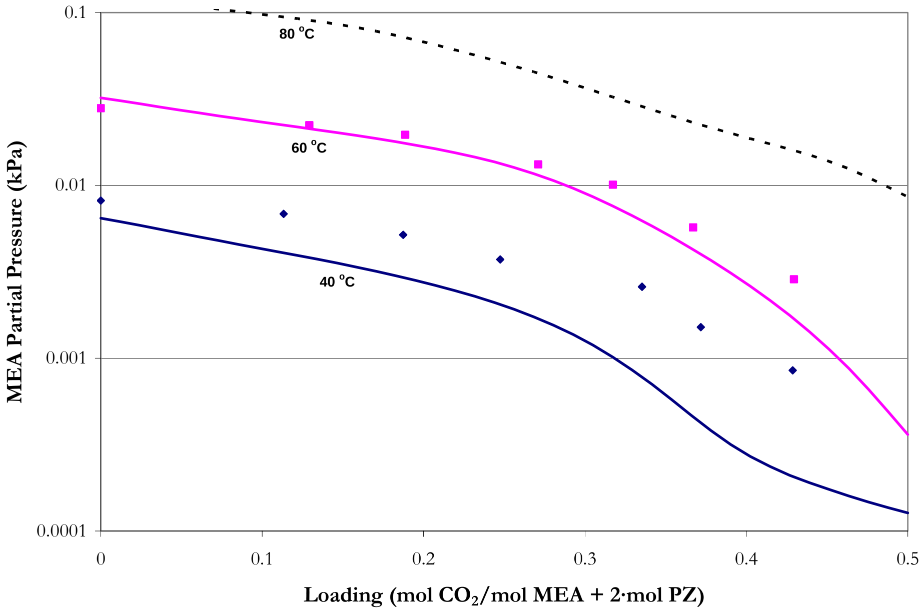

Figure 16.3-20. Experimental MEA Volatility in Mixtures of 7 m MEA Plus 3.6 m PZ from 40 to 80 °C from this work. Points: ♦ (40 °C) and ■ (60 °C). Lines: elecNRTL Predictions.

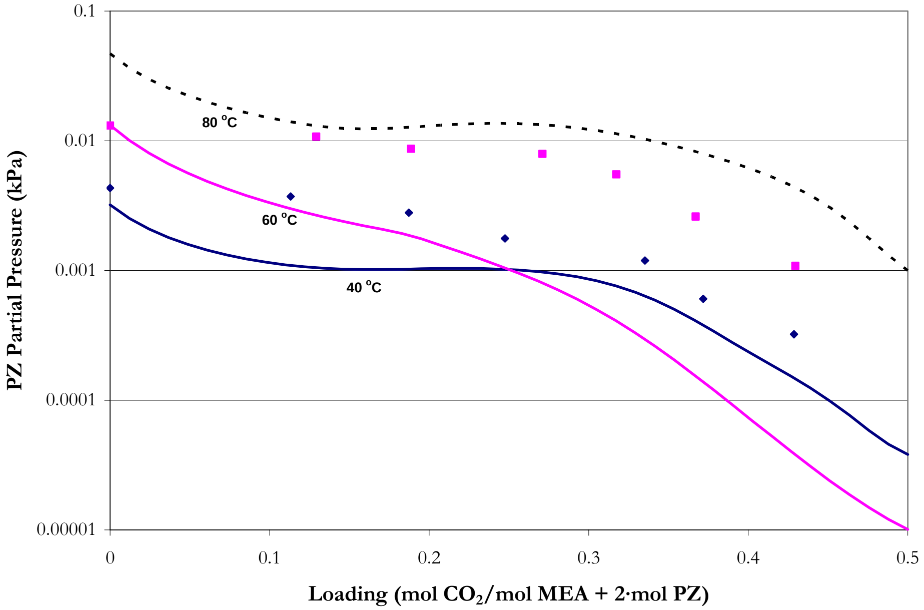

Figure 16.3-21. Experimental PZ Volatility in Mixtures of 7 m MEA Plus 3.6 m PZ from 40 to 80 °C from this work. Points: ♦ (40 °C) and ■ (60 °C). Lines: elecNRTL Predictions.

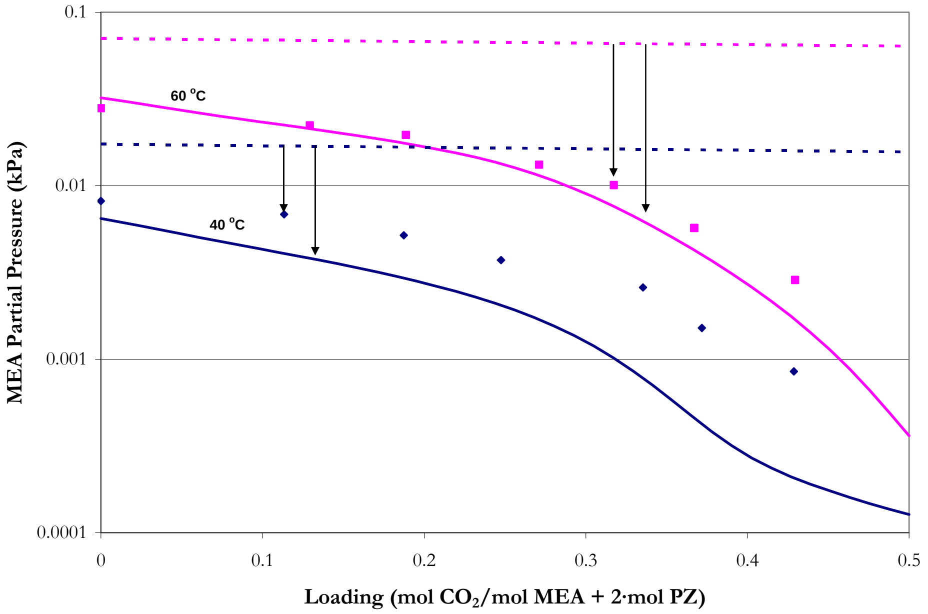

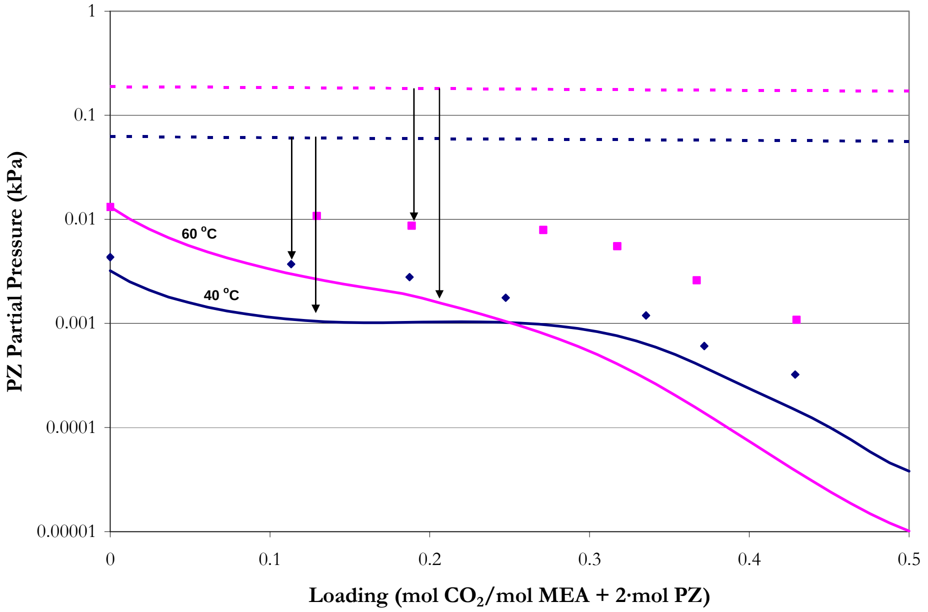

Figure 16.3-22. Experimental MEA and PZ Volatility in Mixtures of 7 m MEA Plus 3.6 m PZ at 40 and 60 °C from this work. Points: ◆ (40 °C) and ■ (60 °C). Solid lines: elecNRTL Predictions, Dash lines: Raoult's Law Approximations.

As shown in the above figures, the combined model adequately predicts CO_2 solubility and amine volatility for 7 m MEA + 2 m PZ and 3.5 m MEA + 2 m PZ. For other systems, 7 m MEA + 3.6 m PZ, the combined model moderately predicts CO_2 solubility and MEA volatility, but the combined model does not adequately predict PZ volatility. For 3.5 m MEA + 3.6 m PZ, the combined model fails to predict CO_2 solubility and amine volatility over the entire range of loading and temperature. Deviations from an ideal solution behavior vis-à-vis Raoult's Law as compared to predictions from the combined elecNRTL model for MEA and PZ volatility illustrates that for the H_2O-MEA-PZ-CO_2 system Raoult's does not adequately describe the vapor pressure of MEA and PZ over the entire range of temperature, concentration, and loading. Raoult's Law predictions do illustrate a considerable effect on the activity coefficient of MEA and PZ in terms of predictions for the amine vapor pressure. Discrepancies in the PZ volatility might be explained due to an error in the effect of speciation for the free amine concentration. If the combined model is unable to predict the correct liquid phase speciation in terms of the free amine concentration, this would affect the vapor pressure of PZ negatively.

16.3.2 *Specific Heat Capacity*

Figure 16.3-23 and Figure 16.3-25 compare experimental specific heat capacity measurements from this work to predictions from the combined model. Predictions from this work do capture the correct trends in the specific heat capacity as a function of temperature but fall short in predicting the correct specific heat capacity on the order of ± 40 percent in some cases. On the other hand, the combined model does adequately predict the specific heat capacity below 80 °C in most cases.

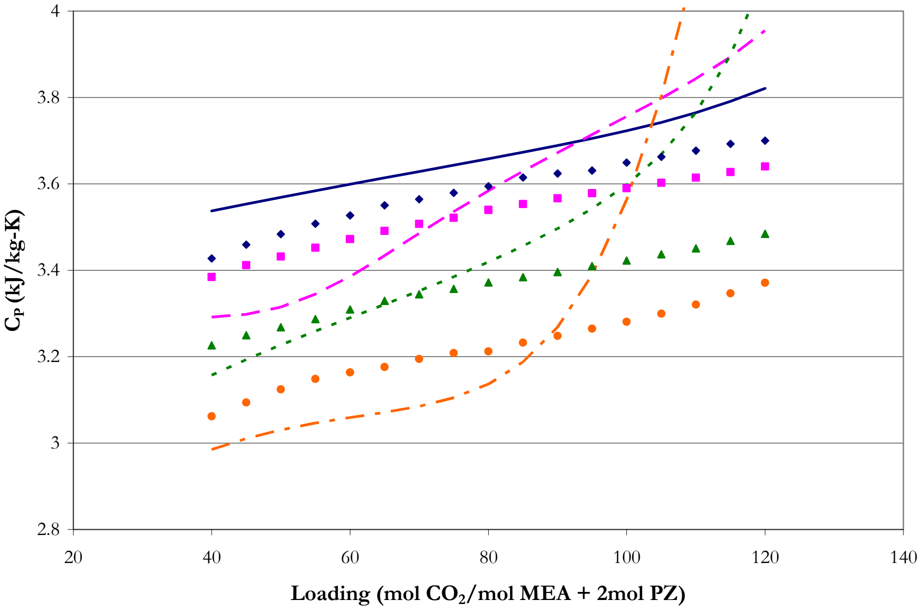

Figure 16.3-23. Specific Heat Capacity in Loaded 7 m MEA + 2 m PZ Solutions from this work. Points: ♦, Ldg = 0.00, ■, Ldg = 0.10, ▲, Ldg = 0.25, ●, Ldg = 0.43. Lines: —, Ldg = 0.00, — —, Ldg = 0.10, - - -, Ldg = 0.25, — - —, Ldg = 0.43.

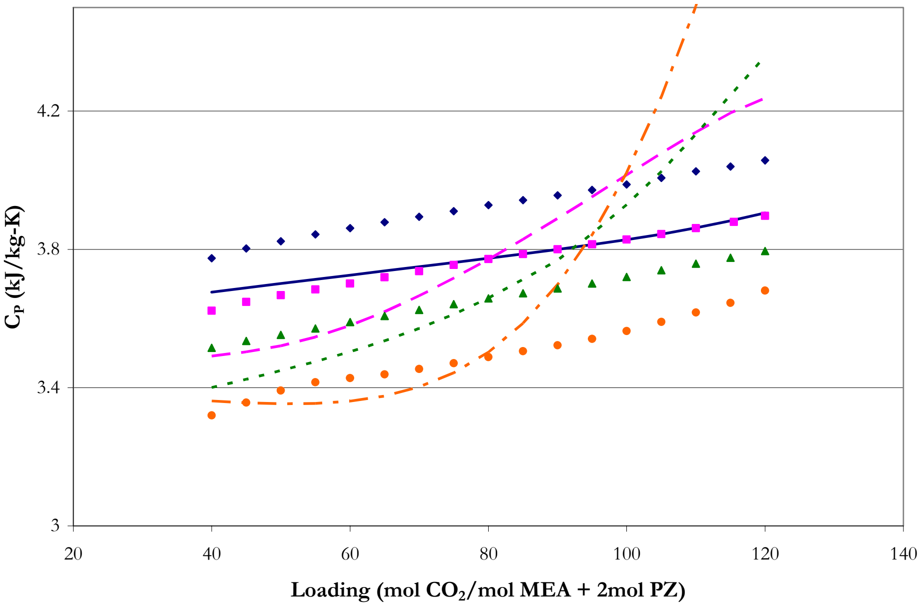

Figure 16.3-24. Specific Heat Capacity in Loaded 3.5 m MEA + 2 m PZ Solutions from this work. Points: ♦, Ldg = 0.00, ■, Ldg = 0.11, ▲, Ldg = 0.24, ●, Ldg = 0.43. Lines: —, Ldg = 0.00, — —, Ldg = 0.11, - - -, Ldg = 0.24, — - —, Ldg = 0.43.

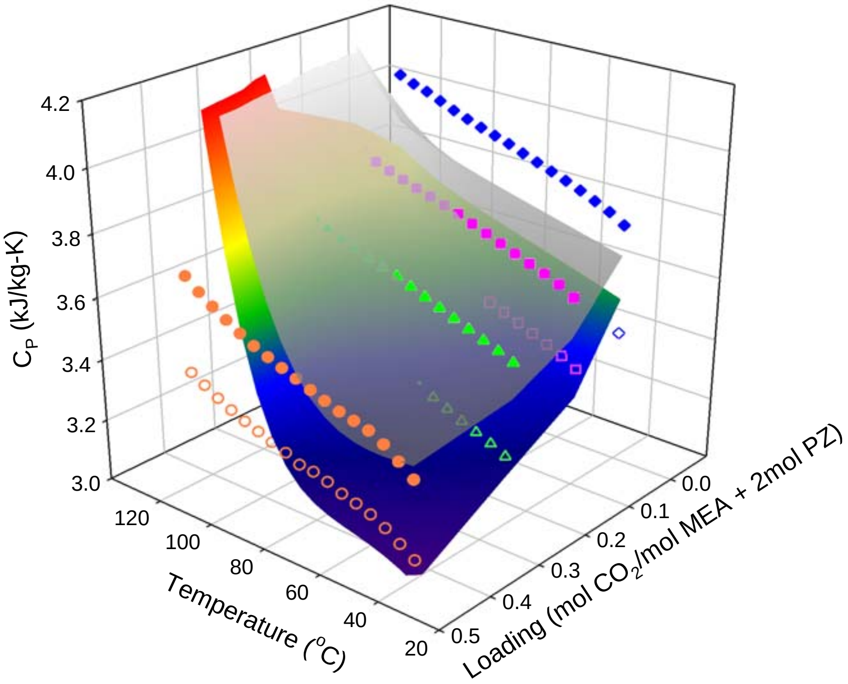

Figure 16.3-25. Specific Heat Capacity in Loaded 7 and 3.5 m MEA plus 2 m PZ Solutions from this work. Points: 3.5 m MEA + 2 m PZ, ♦, Ldg = 0.00, ■, Ldg = 0.11, ▲, Ldg = 0.24, ●, Ldg = 0.43, 7 m MEA + 2 m PZ, ◊, Ldg = 0.00, □, Ldg = 0.10, Δ, Ldg = 0.25, ○, Ldg = 0.43. Surface: 3.5 m MEA + 2 m PZ, Gray Intensities, 7 m MEA + 2 m PZ, Spectrium Intensities.

To investigate the effect of CO_2 loading on the liquid phase specific heat capacity, we can normalize the specific heat capacity by the kilograms of H_2O+MEA+PZ in the experimental solution as shown in Figure 16.3-26.

Figure 16.3-27 illustrates how the experimental apparent partial heat capacity of CO_2 may have an average value of 1.0987 kJ/kg$_{CO2}$-K over the temperature range from 40 to 120 °C in aqueous mixtures of monoethanolamine plus piperazine. This may suggest that contributions of the apparent partial heat capacity of CO_2 may be considered small.

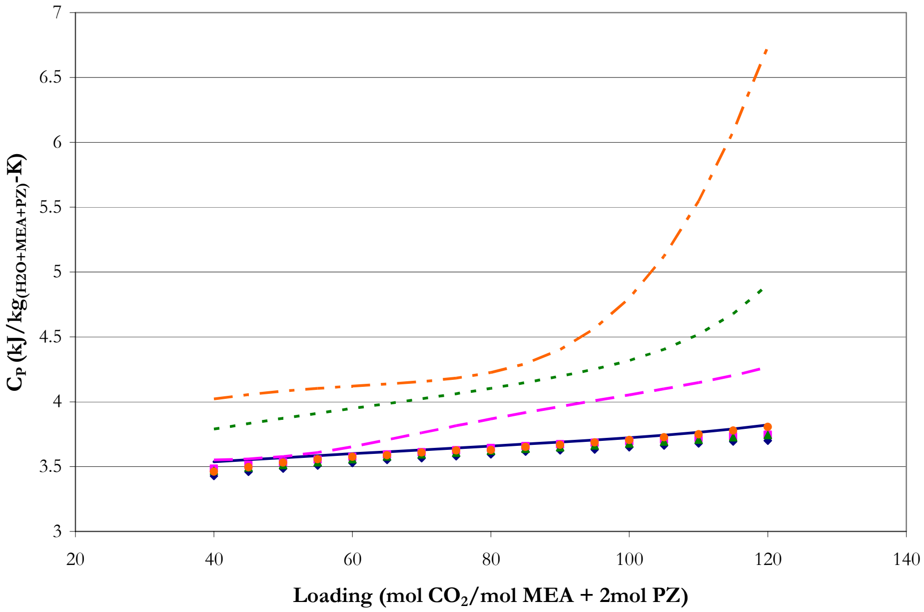

Figure 16.3-26. Apparent Partial Specific Heat Capacity in Loaded 7 m MEA + 2 m PZ Solutions from this work. Points: ♦, Ldg = 0.00, ■, Ldg = 0.10, ▲, Ldg = 0.25, ●, Ldg = 0.43. Lines: —, Ldg = 0.00, – –, Ldg = 0.10, - - -, Ldg = 0.25, — - —, Ldg = 0.43.

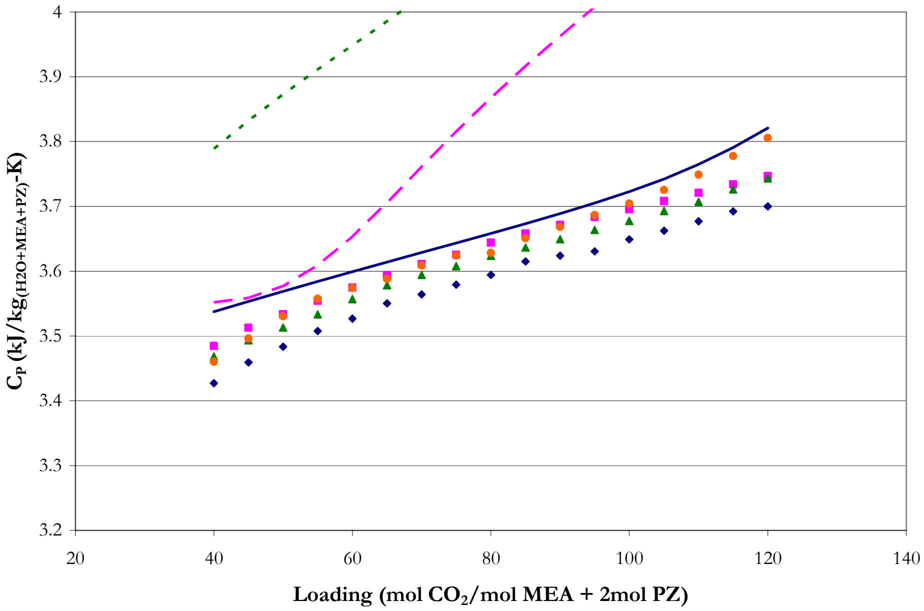

Figure 16.3-27. Enlarged Apparent Partial Specific Heat Capacity in Loaded 7 m MEA + 2 m PZ Solutions from this work. Points: ♦, Ldg = 0.00, ■, Ldg = 0.10, ▲, Ldg = 0.25, ●, Ldg = 0.43. Lines: —, Ldg = 0.00, – –, Ldg = 0.10, - - -, Ldg = 0.25.

16.3.3 *Enthalpy of CO_2 Absorption*

Figure 16.3-26 through Figure 16.3-31 compare experimental differential enthalpy of CO_2 absorption measurements from Kim (2007) to predictions based on Equation 16-8 (Gibbs-Helmholtz) from this work.

Combined model predictions do not adequately describe systematic trends presented in the enthalpy of CO_2 absorption data even though each separate sub-component model was able to adequately describe the enthalpy of CO_2 absorption for 7 m MEA and 2.4 m PZ over the range of loading and temperature. This error may be due to a possible convergence issue within Aspen Plus^{TM} for the H_2O-MEA-PZ-CO_2 system; since the enthalpy of CO_2 absorption was adequately described within the two base sub-component systems.

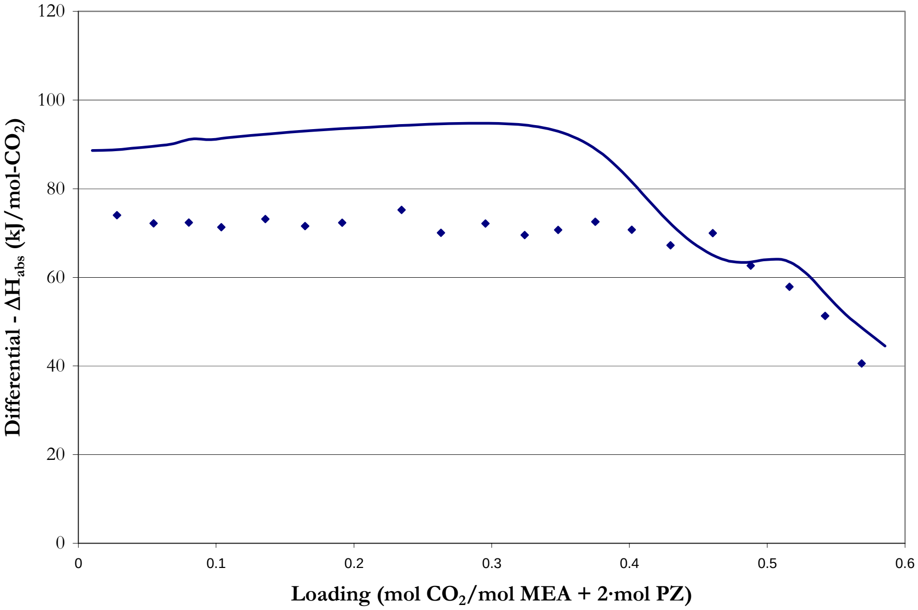

Figure 16.3-28. Negative Differential Enthalpy of CO_2 Absorption for 7 m MEA + 2 m PZ at 40 °C. Points: ♦, Kim (2007). Lines: elecNRTL model.

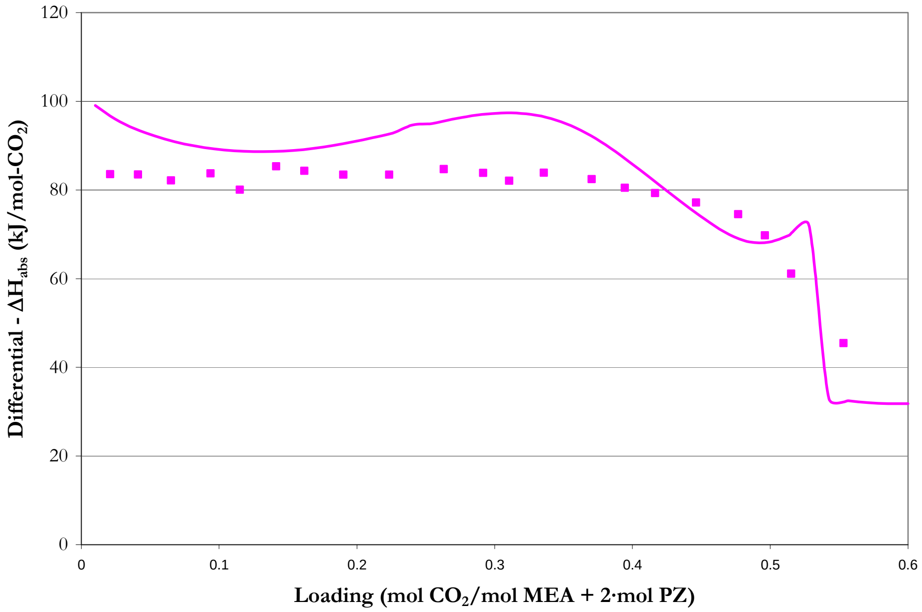

Figure 16.3-29. Negative Differential Enthalpy of CO_2 Absorption for 7 m MEA + 2 m PZ at 80 °C. Points: ■, Kim (2007).

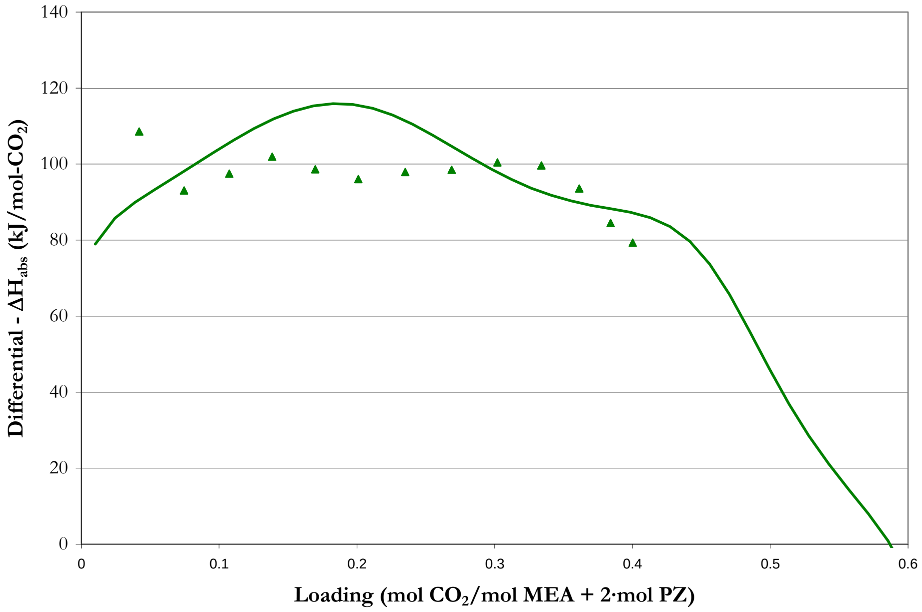

Figure 16.3-30. Negative Differential Enthalpy of CO_2 Absorption for 7 m MEA + 2 m PZ at 120 °C. Points: ▲, Kim (2007).

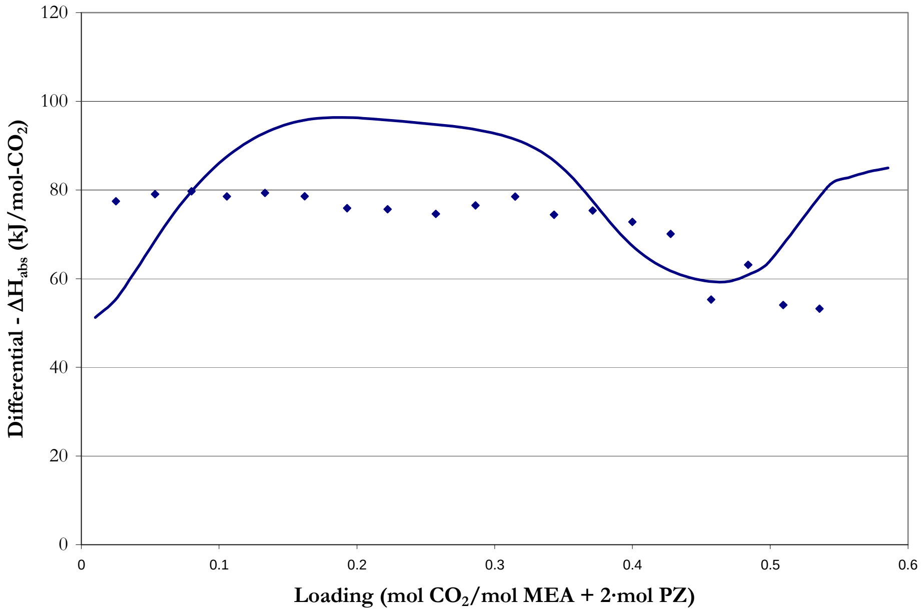

Figure 16.3-31. Negative Differential Enthalpy of CO_2 Absorption for 7 m MEA + 3.5 m PZ at 40 °C. Points: ♦, Kim (2007).

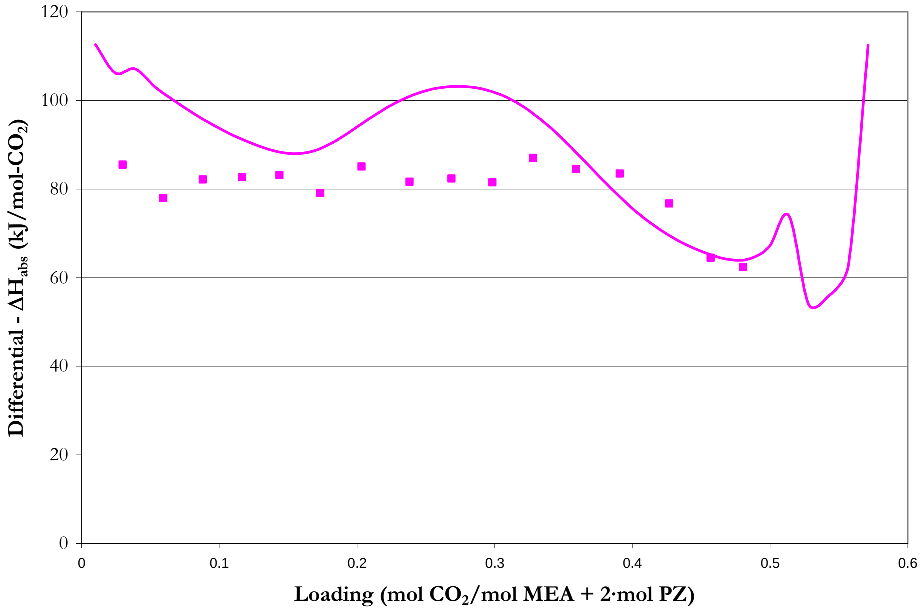

Figure 16.3-32. Negative Differential Enthalpy of CO_2 Absorption for 7 m MEA + 3.5 m PZ at 80 °C. Points: ■, Kim (2007).

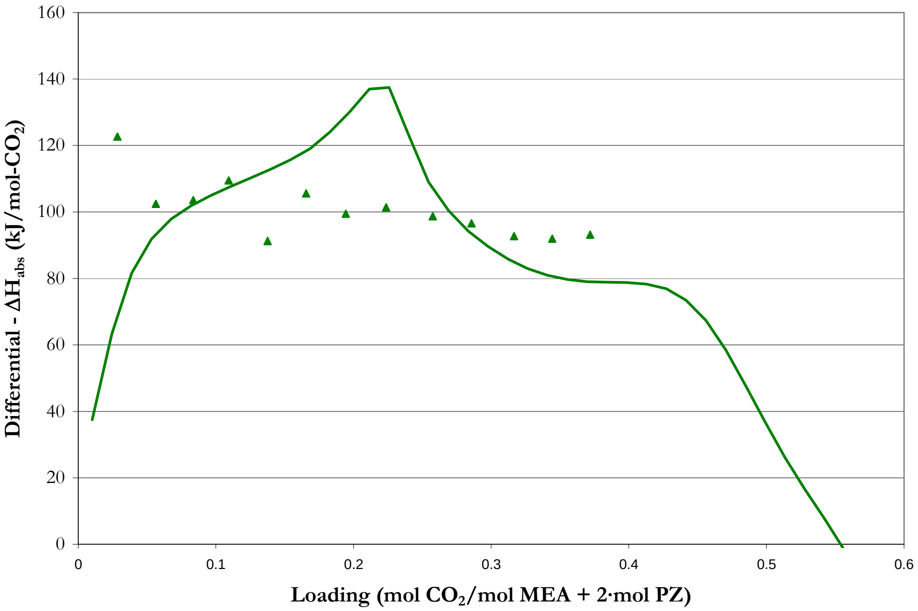

Figure 16.3-33. Negative Differential Enthalpy of CO_2 Absorption for 7 m MEA + 3.5 m PZ at 120 °C. Points: ▲, Kim (2007).

16.3.4 *NMR Speciation*

Figure 16.3-32 through Figure 16.3-34 compare experimental liquid phase NMR speciation measurements from this work to combined model predictions for 7 m MEA + 3.6 m PZ at 27, 40, and 60 °C. Figure 16.3-32 and 16.3-33 illustrate that the combined model adequately describes the speciation for the major concentration species, but does fall short in prediction the correct speciation for CO_3^{-2}+HCO_3^{-1} and PZ(COO^{-1})$_2$. Trends in the carbonate and bicarbonate are due to the speciation of bicarbonate as illustrated in Figure 16.3-35, since bicarbonate could be considered one of the dominant CO_2 reactive species in the H_2O-MEA-PZ-CO_2 system.

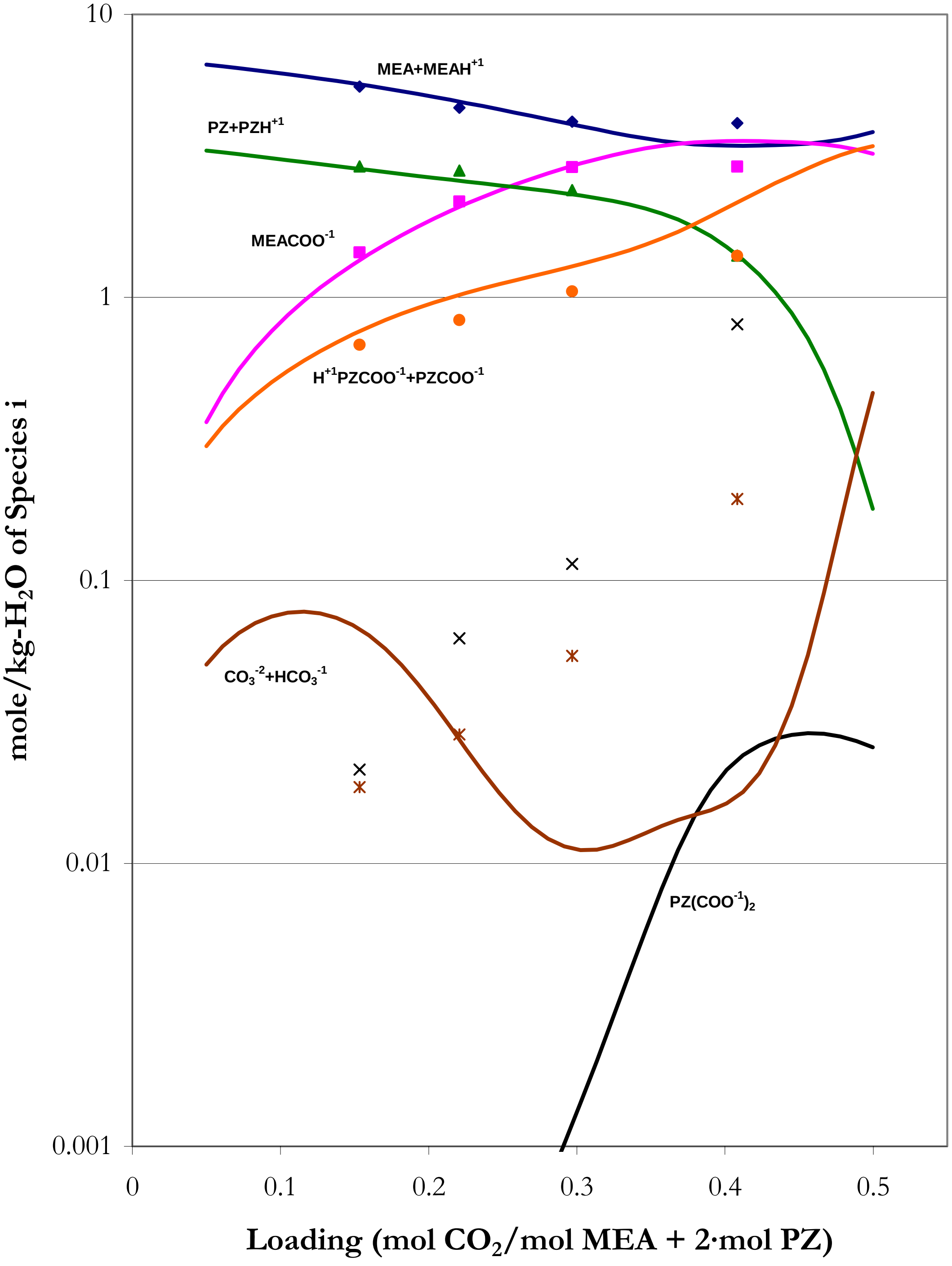

Figure 16.3-34. Liquid Phase Speciation from C^{13} NMR in 7 m MEA + 3.6 m PZ at 27 °C. Points: ♦, MEA + MEAH^{+1}, ■, MEACOO^{-1}, ▲, PZ + PZH^{+1}, ●, H^{+1}PZCOO^{-1} + PZCOO^{-1}, ×, PZ(COO^{-1})$_2$, *, CO_3^{-2}+HCO_3^{-1}. Lines: elecNRTL Predictions.

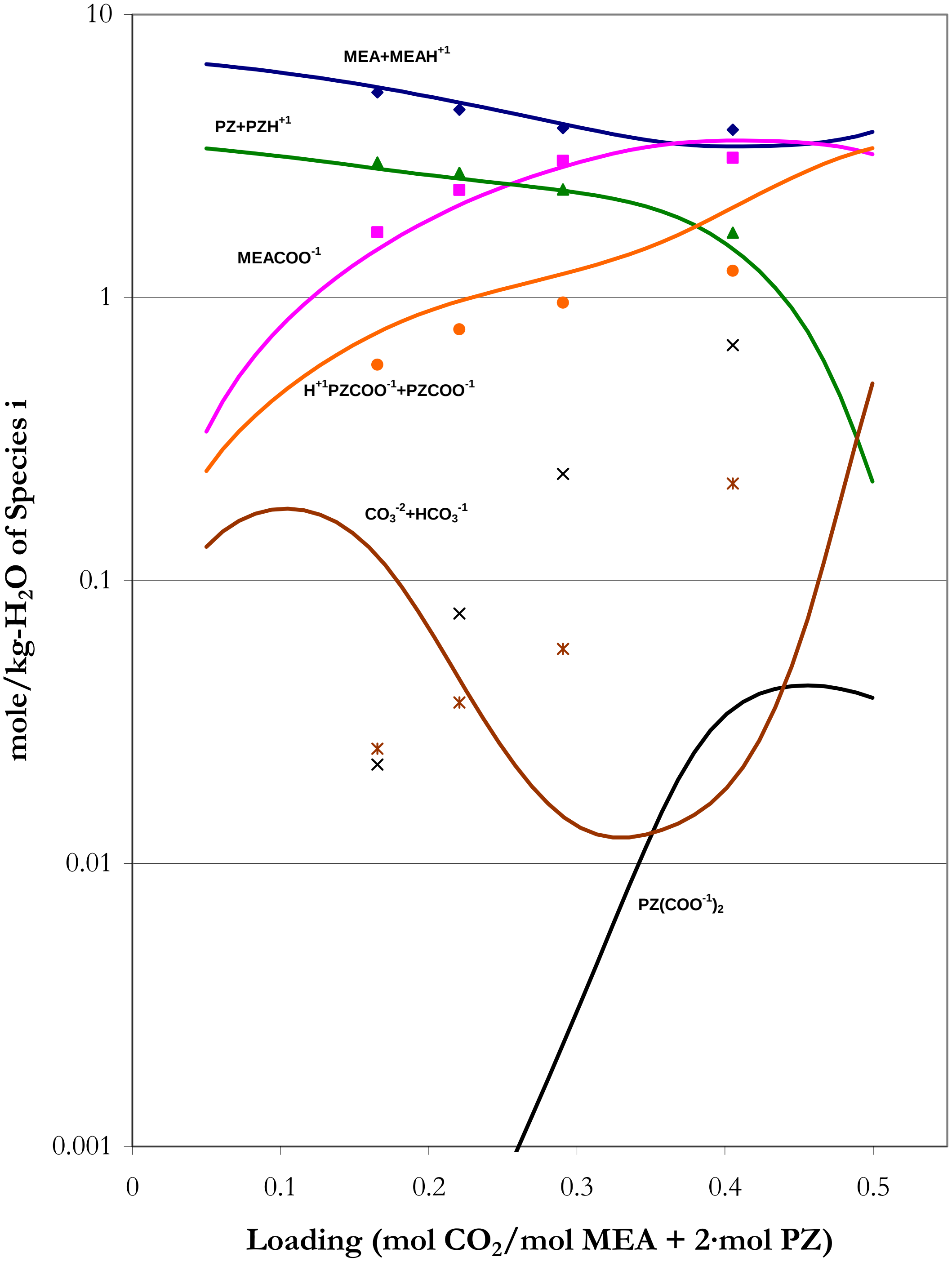

Figure 16.3-35. Liquid Phase Speciation from C^{13} NMR in 7 m MEA + 3.6 m PZ at 40 °C. Points: ♦, MEA + $MEAH^{+1}$, ■, $MEACOO^{-1}$, ▲, PZ + PZH^{+1}, ●, $H^{+1}PZCOO^{-1}$ + $PZCOO^{-1}$, ×, $PZ(COO^{-1})_2$, *, CO_3^{-2}+HCO_3^{-1}. Lines: elecNRTL Predictions.

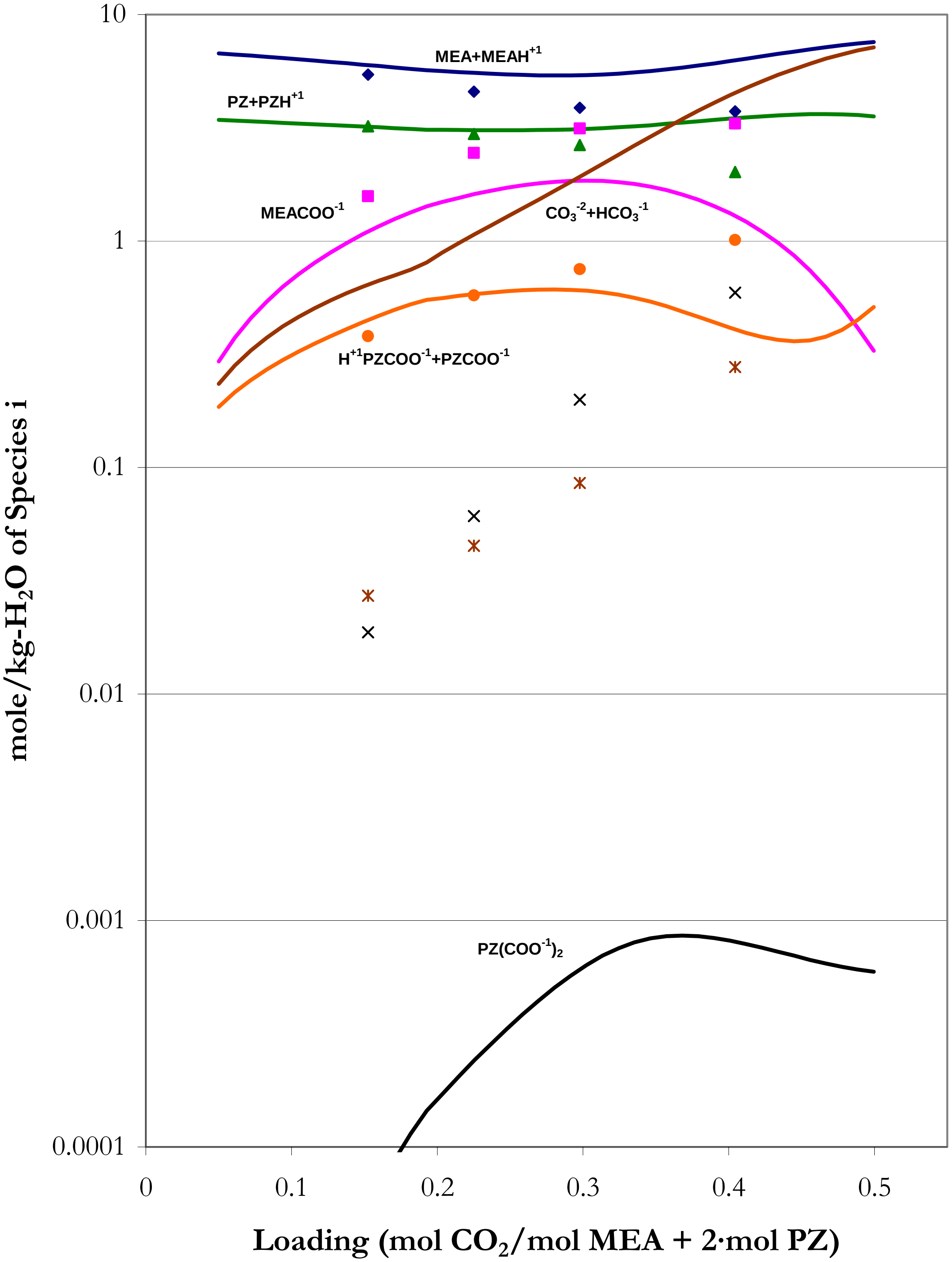

Figure 16.3-36. Liquid Phase Speciation from C^{13} NMR in 7 m MEA + 3.6 m PZ at 60 °C. Points: ♦, MEA + MEAH^{+1}, ■, MEACOO^{-1}, ▲, PZ + PZH^{+1}, ●, H^{+1}PZCOO^{-1} + PZCOO^{-1}, ×, PZ(COO^{-1})$_2$, *, CO_3^{-2}+HCO_3^{-1}. Lines: elecNRTL Predictions.

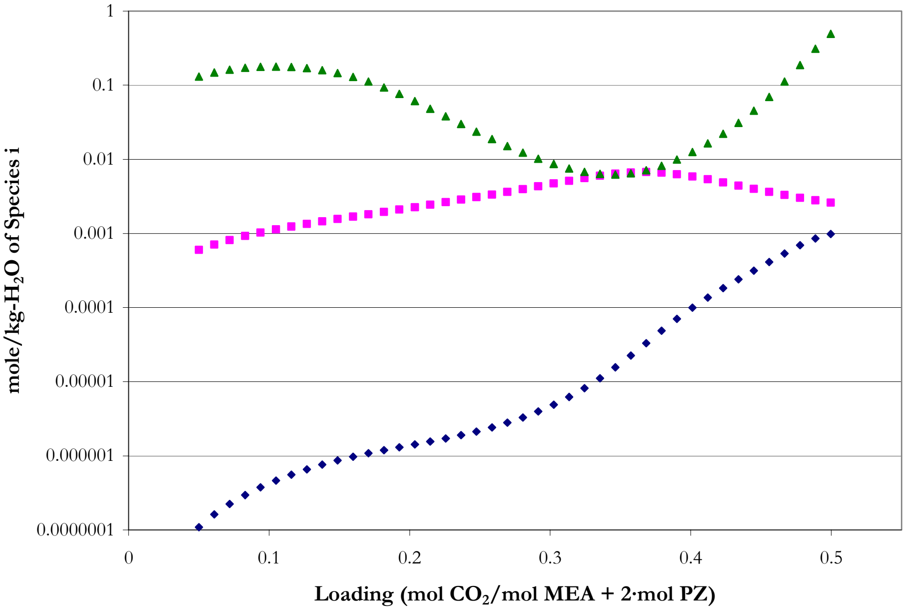

Figure 16.3-37. Predictions for Liquid Phase Speciation in 7 m MEA + 3.6 m PZ at 40 °C from this work. Points: ♦, CO_2, ■, CO_3^{-2}, ▲, HCO_3^{-1}.

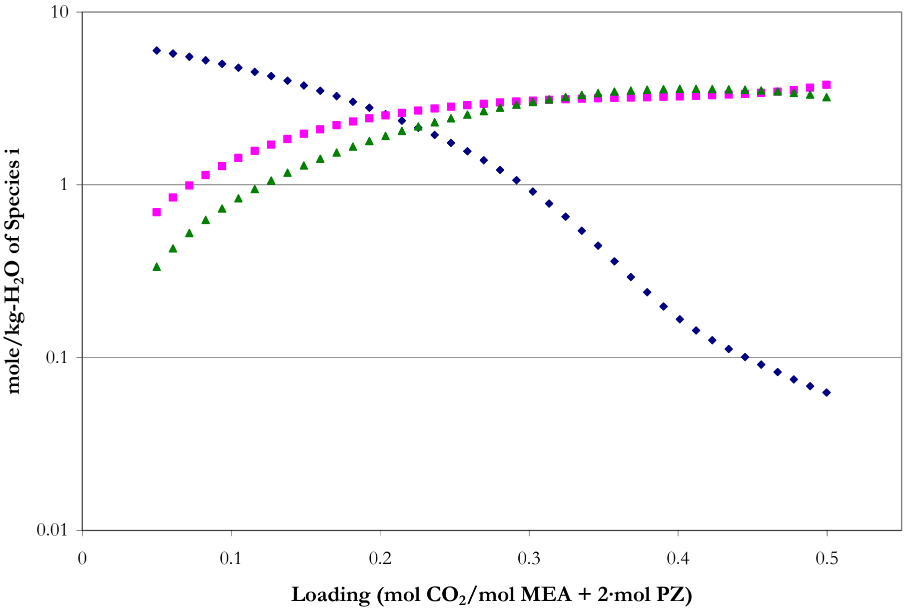

Figure 16.3-38. Predictions for Liquid Phase Speciation in 7 m MEA + 3.6 m PZ at 40 °C from this work. Points: ♦, MEA, ■, $MEAH^{+1}$, ▲, $MEACOO^{-1}$.

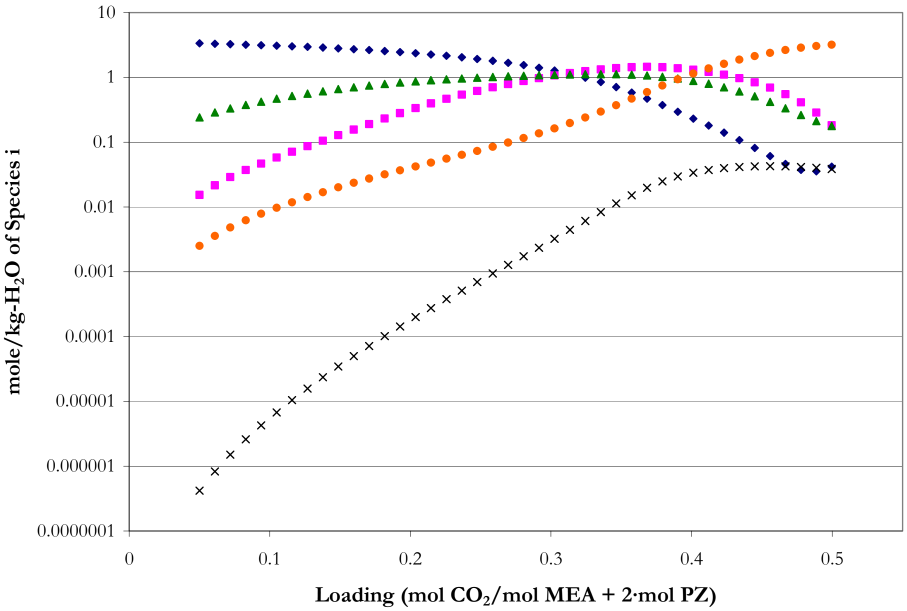

Figure 16.3-39. Predictions for Liquid Phase Speciation in 7 m MEA + 3.6 m PZ at 40 °C from this work. Points: ♦, PZ, ■, PZH^{+1}, ▲, $PZCOO^{-1}$, ●, $H^{+1}PZCOO^{-1}$, ×, $PZ(COO^{-1})_2$.

Piperazine speciation presented in Figure 16.3-37 does not explain the behavior of the amine vapor pressure prediction previously shown. The behavior exhibited in the PZ volatility might be a result of the predictive activity coefficient of PZ from the combined model, thereby adversely affecting the loading and temperature dependence of the amine volatility.

16.4 Conclusions

In conclusion, we have followed in this work a similar approach to the method developed by Posey (1996) in terms of choosing values for the mixed system binary interaction parameters to examine the predictive ability of our model. Table 16.2-2 gave binary interaction parameters associated with the mixed amine system which were not included as part of the original model regressions.

We found that binary interaction parameters for MEA and PZ exhibited similar properties as reported by Posey (1996) where interactions associated with each amine, given in Table 16.2-2, which were assigned to similar interactions values involving the alternative protonated amine, did benefit the quality of the model predictions as compared to the experimental data. Binary interaction parameters for H_2O, given in Table 16.2-2, were based on the average value between H_2O $MEAH^{+1}/MEACOO^{-1}$ and H_2O, $PZH^{+1}/PZCOO^{-1}$ as given in Chapters XIII and XIV. This assumption did exhibit a small benefit to the prediction of CO_2 solubility data but by varying the parameter from the default values to the average values had a minimal effect on the overall predictive outcome at high loading.

We would recommend that future work to adequately predict the experimental CO_2 solubility, amine volatility, NMR speciation, enthalpy of CO_2 absorption, and specific heat capacity data for the H_2O-MEA-PZ-CO_2 system complete an overall simultaneous regression of the binary interaction parameters associated with the original and mixed amine systems in addition to the chemical equilibrium constant for $MEACOO^{-1}$,$PZCOO^{-1}$, $PZ(COO^{-1})_2$, and $H^{+1}PZCOO^{-1}$ to adequately fit the experimental data. This would need to be completed due to the thermodynamic framework adopted in this work utilizing Aspen Plus™ 2006.5.

As shown in Table 16.2-3, 7 m MEA exhibited a greater differential capacity but exhibited a greater volatility as compared to piperazine or other mixed amine systems. With the combination of 7 m MEA + 2 m PZ, the relative volatility decreased as compared to the base sub-component systems by a factor of ~ 1.2. When the concentration of MEA decreased from 7 m to 3.5 m; the differential capacity and MEA volatility also decreased due to the decease in the total alkalinity of the solvent as reflected in the MEA volatility deceasing by a factor of 2. However, PZ volatility remained approximately constant which would be consistent with effects exhibited in the H_2O-MEA-PZ systems where large changes in the solution alkalinity may not have an effect on the volatility of PZ.

Figure 16.2-6 illustrated that the specific heat capacity from this work may be considered internally consistent since increasing the concentration of MEA would require the specific heat capacity to decrease by a factor of 2 as compared to trends exhibited in vapor-liquid equilibrium experimental results.

Figure 16.3-27 illustrated how the experimental apparent partial heat capacity of CO_2 may have an average value of 1.0987 kJ/kg_{CO2}-K over the temperature range from 40 to 120 ^oC in aqueous mixtures of monoethanolamine plus piperazine. This may suggest that contributions of the apparent partial heat capacity of CO_2 may be considered small.

With the addition of PZ to a solution of 7 m MEA, the enthalpy of CO_2 absorption decreased over the range in temperature on the order of approximately 10 kJ per mole of CO_2. In addition, the enthalpy of CO_2 absorption for the mixed amine solutions illustrated a shift in speciation. Over the range in loading between 0 and 0.5 mol CO_2/mol MEA, the main reaction mechanism could be considered the protonation of MEA where beyond a loading of 0.5, the main reaction mechanism may be considered the reaction of MEA with bicarbonate to form MEA carbamate as indicated by the steep drop in the enthalpy of CO_2 absorption. With the addition of PZ to the system, the reaction mechanism for the protonation of MEA has been shifted to 0.4 mol CO_2/mol MEA + 2·mol PZ mainly due to a change in the total alkalinity of the system.

Overall, the combined model **did not** adequately describe the H_2O-MEA-PZ-CO_2 property data listed above as shown by an average absolute relative error of ± 37.9 percent, with the exception of a few outliers. This would suggest that there may be a need for parameter optimization to improve the statistical fit of the experimental data as described by the combined model.

One of the goals of this work was to be able to build a consistent and rigorous thermodynamic model to describe the base systems, then to combine the two models and test the predictive behavior of the combine model. Table 16.3-1 illustrated that a simple exchange between binary interaction parameters based on the separate systems to create analogous interactions for the combined model did not result in an adequate fit of the experimental data. We would recommend that future work interested in the H_2O-MEA-PZ-CO_2 system should optimize the binary interaction parameters to capture systematic trends presented within the experimental data.

CHAPTER XVII

Quaternary System Predictions: H_2O-K_2CO_3-MEA-CO_2

17.1 Introduction

The thermodynamic models describing each sub-system have been established and the combined model can now be used as a predictive tool for the quaternary system. This chapter compares experimental CO_2 solubility and amine volatility data from this work for the H_2O-K_2CO_3-MEA-CO_2 system to model predictions based on the combined H_2O-MEA-CO_2 and H_2O-K2CO_3-CO_2 system models. The combined predictive model represents the experimental data with an average absolute relative error of ± 41.9 %, with the exception of a few outliers.

17.2 H_2O-K_2CO_3-MEA-CO_2 System

Up to this point for the H_2O-K_2CO_3-MEA-CO_2 system, we have been able to describe the molecule-molecule and molecule-electrolyte interactions between H_2O-K_2CO_3, H_2O-$KHCO_3$, H_2O-MEA, H_2O-K_2CO_3-CO_2 and H_2O-MEA-CO_2 given in Chapters XII, VIII, XII, and XIII, respectively, as shown in Table 17.2-1.

Table 17.2-1. Binary Interaction Parameters for the H_2O-K_2CO_3-MEA-CO_2 system.

	Interaction Species		
System	i	j	k
H_2O-K_2CO_3-CO_2	H_2O	K^+	CO_3^{-2}
	K^+	CO_3^{-2}	H_2O
	H_2O	K^+	HCO_3^{-1}
	K^+	HCO_3^{-1}	H_2O
	K^+/CO_3^{-2}	K^+/HCO_3^{-1}	
H_2O-MEA	H_2O	MEA	
	MEA	H_2O	
H_2O-MEA-CO_2	H_2O	$MEAH^{+1}$	HCO_3^{-1}
	$MEAH^{+1}$	HCO_3^{-1}	H_2O
	H_2O	$MEAH^{+1}$	$MEACOO^{-1}$
	$MEAH^{+1}$	$MEACOO^{-1}$	H_2O
	MEA	$MEAH^{+1}$	HCO_3^{-1}
	$MEAH^{+1}$	HCO_3^{-1}	MEA
	MEA	$MEAH^{+1}$	$MEACOO^{-1}$
	$MEAH^{+1}$	$MEACOO^{-1}$	MEA
	CO_2	$MEAH^{+1}$	HCO_3^{-1}
	$MEAH^{+1}$	HCO_3^{-1}	CO_2

For the mixed salt/amine system, Posey (1996) suggested a general method for parameter determination by examining the mixed salt/amine parameters to form an adequate model. Posey (1996) also reported that many of the mixed system interaction parameters appeared to be independent of the amine interaction and could be assigned to a default value. Mixed systems parameters involving H_2O and a carbamate species were assigned an average value consistent between the two systems. Posey (1996) did not optimize the parameters to fit the experimental data, but was interested in the ability of the model to predict the mixed system.

In this work, we have followed a similar approach to the method developed by Posey (1996), in terms of choosing values for the mixed system binary interaction parameters to examine the predictive ability of our model. Table 17.2-2 lists binary interaction parameters associated with the mixed salt/amine system which were not included as part of the original model regressions.

Table 17.2-2. Mixed Salt/Amine Binary Interaction Parameters.

Interaction Species			Binary Interaction Coefficients		
i	j	k	A	B	C
H_2O	K^+	$MEACOO^{-1}$	-3234	999981	40484
K^+	$MEACOO^{-1}$	H_2O	-2469	761540	30650
MEA	K^+	CO_3^{-2}	10	0.0	0.0
K^+	CO_3^{-2}	MEA	-2	0.0	0.0
MEA	K^+	HCO_3^{-1}	10	0.0	0.0
K^+	HCO_3^{-1}	MEA	-2	0.0	0.0
MEA	K^+	$MEACOO^{-1}$	10	0.0	0.0
K^+	$MEACOO^{-1}$	MEA	-2	0.0	0.0

Binary interaction parameters for MEA did exhibit similar properties as reported by Posey (1996). Interactions associated with MEA, given in Table 17.2-2, which were assigned to similar interaction values involving $MEAH^{+1}$, did not benefit the quality of the model predictions as compared to the experimental data. Therefore, default binary interaction parameters were assigned. Binary interaction parameters for H_2O, given in Table 17.2-2, were based on the average value between H_2O, K^+/HCO_3^{-1} and H_2O, $MEAH^{+1}/MEACOO^{-1}$ as given in Chapters XII and XIII. This assumption did exhibit a small benefit to the prediction of CO_2 solubility data but varying the parameter from the default values to the average values had a minimal effect on the overall predictive outcome.

To adequately predict the experimental CO_2 solubility and amine volatility data from this work for the H_2O-K_2CO_3-MEA-CO_2 system, an overall regression of the binary interaction parameters associated with the original and mixed salt/amine systems in addition to the chemical equilibrium constant for $MEACOO^{-1}$ would need to be regressed simultaneously to adequately fit the experimental data.

The following section describes the different data types gathered in this work for the H_2O-K_2CO_3-MEA-CO_2 system as compared to the predictive ability of the combined model.

17.2.1 *CO_2 Solubility and Amine Volatility*

Data in the form of CO_2 solubility, which measures the partial pressure of CO_2 over aqueous K_2CO_3 plus MEA solutions as a function of loading (mole CO_2 per mole K^+ plus mole MEA) and temperature were compared to predictions based on the combined model for the H_2O-K_2CO_3-MEA-CO_2 system.

For our quaternary system (H_2O, K_2CO_3, MEA, and CO_2), the following equation may be used to represent the equilibrium for CO_2 solubility data.

$$Py_{CO_2} = x_{CO_2}\gamma^*_{CO_2}H_{CO_2,H_2O} \qquad 17\text{-}1$$

Where

y_{CO_2} is the vapor mole fraction of CO_2,

$\gamma^*_{CO_2}$ is the unsymmetric activity coefficient of CO_2,

H_{CO_2,H_2O} is the Henry's Constant for CO_2 in H_2O.

In this work, we used a unique Fourier-transform infrared (FT-IR) technique to measure the vapor phase speciation in aqueous alkanolamine systems as described in Chapter II. Using this technique, we have been able to measure the vapor phase partial pressure of MEA over aqueous MEA solutions, P_{MEA}, as a function of loading (mole CO_2 per mole K^+ plus mole MEA) and temperature.

For our quaternary system (H_2O, K_2CO_3, MEA, and CO_2), the following equation may be used to represent the equilibrium for MEA volatility data.

$$Py_{MEA} = x_{MEA}\gamma_{MEA}P^o_{MEA} \tag{17-2}$$

Where

y_{MEA} is the vapor mole fraction of MEA,

γ_{MEA} is the asymmetric activity coefficient of MEA,

P^o_{MEA} is the extended Antoine vapor pressure correlation for MEA given in Chapter VI.

Experimental CO_2 solubility and amine volatility data collected in this work for mixtures of 2.5 and 5.0 m (mole/kg-H2O) K^+ plus 3.5 and 7.0 m MEA at 40 and 60 °C are illustrated in Figure 17.2-1 through Figure 17.2-4. Ordinary least squares (OLS) approximations were included to clarify systematic trends within the data set.

Figure 17.2-1 through Figure 17.2-4 illustrates the effect of K^+ on CO_2 solubility and amine volatility in 3.5 and 7.0 m MEA solutions. As the ionic strength of the solution increased, from 2.5 m K^+ to 5.0 m K^+, CO_2 solubility increased by a factor of 6 whereas the MEA partial pressure moderately decreased. We could also infer, based on the OLS approximations, a decease in the differential capacity of the solvent from 0.12 to 0.15 over a CO_2 partial pressure range from 0.01 to 1.0 kPa at 60 °C.

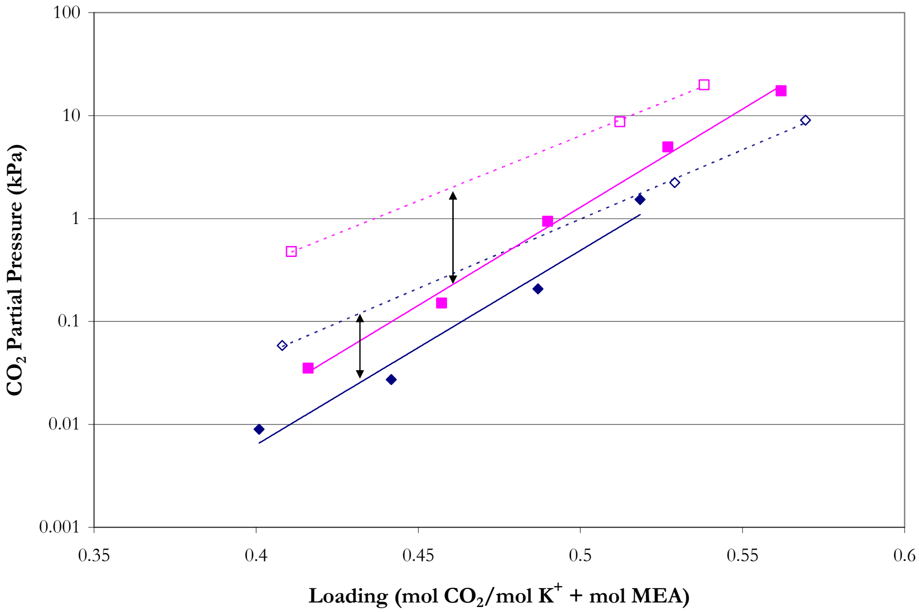

Figure 17.2-1. Experimental CO_2 Solubility in Mixtures of 2.5 and 5.0 m K^+ Plus 7 m MEA at 40 and 60 °C from this work. Points: ◆ (40 °C) and ■ (60 °C) for 5.0 m K^+ Plus 7 m MEA, ◊ (40 °C) and □ (60 °C) for 2.5 m K^+ Plus 7 m MEA. Lines: OLS Approximations.

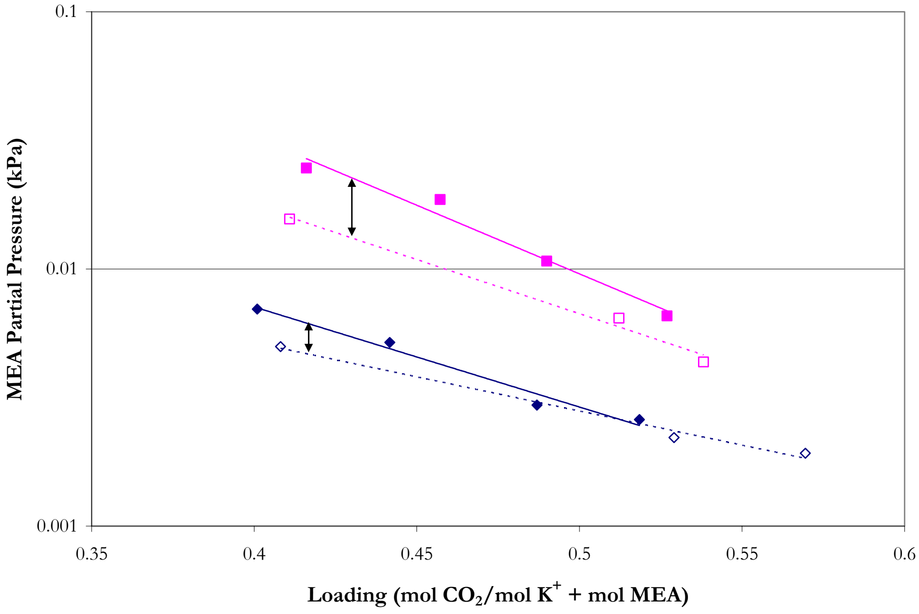

Figure 17.2-2. Experimental MEA Volatility in Mixtures of 2.5 and 5.0 m K^+ Plus 7 m MEA at 40 and 60 °C from this work. Points: ◆ (40 °C) and ■ (60 °C) for 5.0 m K^+ Plus 7 m MEA, ◊ (40 °C) and □ (60 °C) for 2.5 m K^+ Plus 7 m MEA. Lines: OLS Approximations.

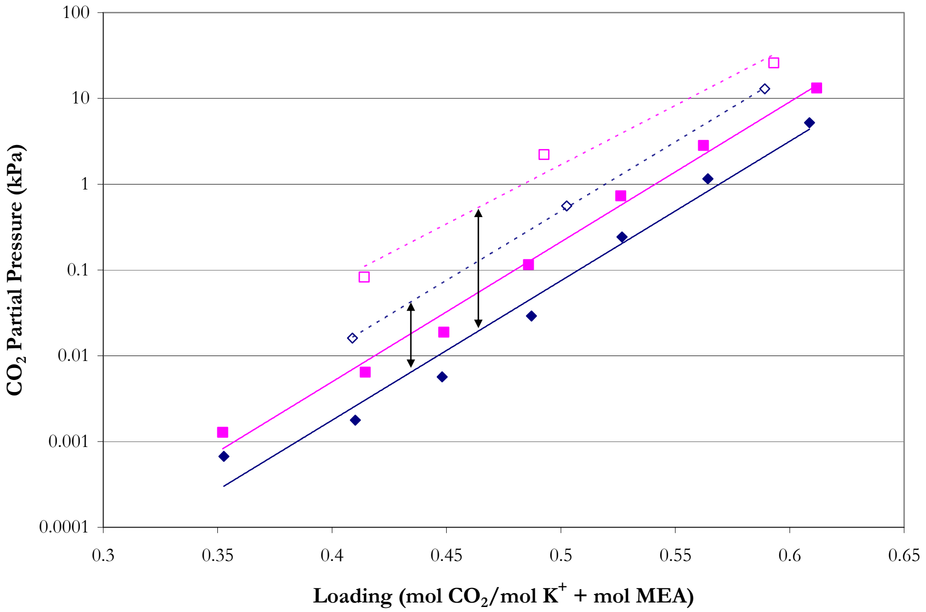

Figure 17.2-3. Experimental CO_2 Solubility in Mixtures of 2.5 and 5.0 m K^+ Plus 3.5 m MEA at 40 and 60 °C from this work. Points: ♦ (40 °C) and ■ (60 °C) for 5.0 m K^+ Plus 3.5 m MEA, ◊ (40 °C) and □ (60 °C) for 2.5 m K^+ Plus 3.5 m MEA. Lines: OLS Approximations.

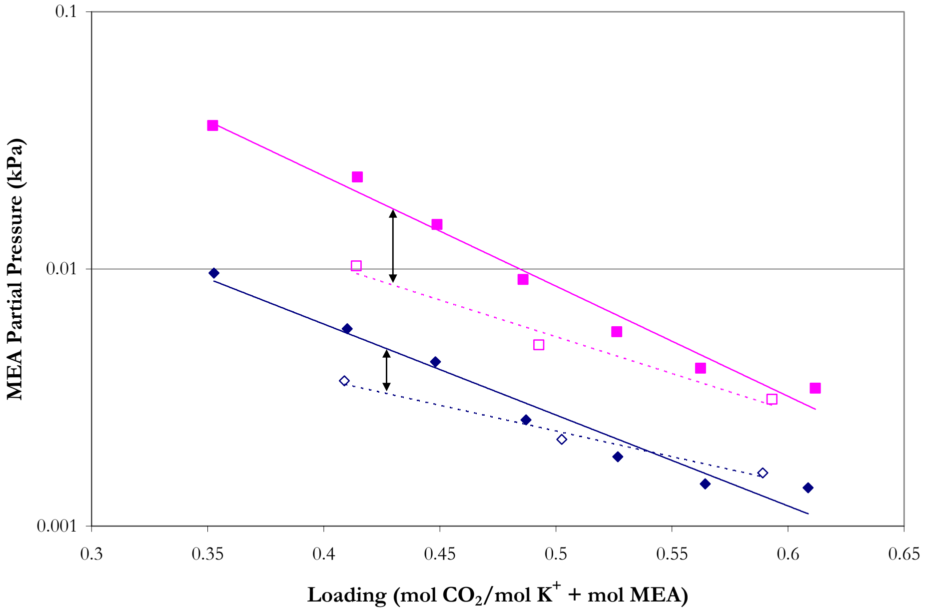

Figure 17.2-4. Experimental MEA Volatility in Mixtures of 2.5 and 5.0 m K^+ Plus 3.5 m MEA at 40 and 60 °C from this work. Points: ♦ (40 °C) and ■ (60 °C) for 5.0 m K^+ Plus 3.5 m MEA, ◊ (40 °C) and □ (60 °C) for 2.5 m K^+ Plus 3.5 m MEA. Lines: OLS Approximations.

A simple Aspen Plus™ Flash model was then used to test the predictive capability of the H_2O-K_2CO_3-MEA-CO_2 model against experimental data from this work. For each data point, the deviation between the experimental and estimated values is expressed in terms of the average absolute relative deviation (AARD) given in Table 17.2-3.

Table 17.2-3. Absolute Percent Relative Error for the H_2O-K_2CO_3-MEA-CO_2 System.

	AARD (%)		
System	P^{CO2}	P^{MEA}	Loading
5 m K^+ + 3.5 m MEA	58.05	30.82	0.67
2.5 m K^+ + 3.5 m MEA	40.88	45.05	0.95
5 m K^+ + 7.0 m MEA	37.10	35.47	1.33
2.5 m K^+ + 7.0 m MEA	39.20	48.98	3.57
Overall	46.08	37.71	1.37

Overall, the combined model **did not** adequately describe the H_2O-K_2CO_3-MEA-CO_2 property data listed above as shown by an average absolute relative error of ± 41.9 percent, with the exception of a few outliers. This would suggest that there may be a need for parameter optimization to improve the statistical fit of the experimental data as described by the combined model.

One of the goals of this work was to be able to build a consistent and rigorous thermodynamic model to describe the base systems, then to combine the two models and test the predictive behavior of the combine model. Table 17.2-3 illustrates that a simple exchange between binary interaction parameters base on the separate systems to create analogous interactions for the combined model did not result in an adequate fit of the experimental data. We would recommend that future work interested in the H_2O-K_2CO_3-MEA-CO_2 system should optimize the binary interaction parameters to capture systematic trends presented within the experimental data. The rest of this chapter will illustrate VLE predictions based on the combined model for the H_2O-K_2CO_3-MEA-CO_2 system.

Figure 17.2-5 through Figure 17.2-8 compares experimental CO_2 solubility from this work to predictions from the combined elecNRTL model. Figure 17.2-5 and Figure 17.2-7 illustrates that the combined model adequately predicts CO_2 solubility even though the temperature and loading dependence does not reflect the systematic trends presented within the experimental data. Figure 17.2-6 represents the least adequate representation for all of the mixed salt/amine system compared in this work. The concentration of 2.5 m K^+ was a part of the original concentration range of K_2CO_3 in the H_2O-K_2CO_3-CO_2 model regression. Since this mixture is a part of the concentration boundary for the overall system, this error may be due to an extrapolation error of the combined model given the fact that the combined model was not optimized to the experimental data.

Figure 17.2-9 through Figure 17.2-12 compares experimental MEA volatility from this work to predictions from the combined elecNRTL model. Figure 17.2-9 through 17.2-12 illustrates the departure from an ideal solution behavior vis-à-vis Raoult's Law as compared to prediction from the combined elecNRTL model. For the H_2O-K_2CO_3-MEA-CO_2 system, Raoult's Law does not adequately describe the vapor pressure of MEA over the entire range of temperature, concentration, and loading dependence. Raoult's Law predictions do illustrate a considerable effect of the activity coefficient of MEA on the prediction for the vapor pressure of MEA. In addition, the effect of speciation on the free amine concentration also plays an important role in predicting the correct vapor pressure of MEA.

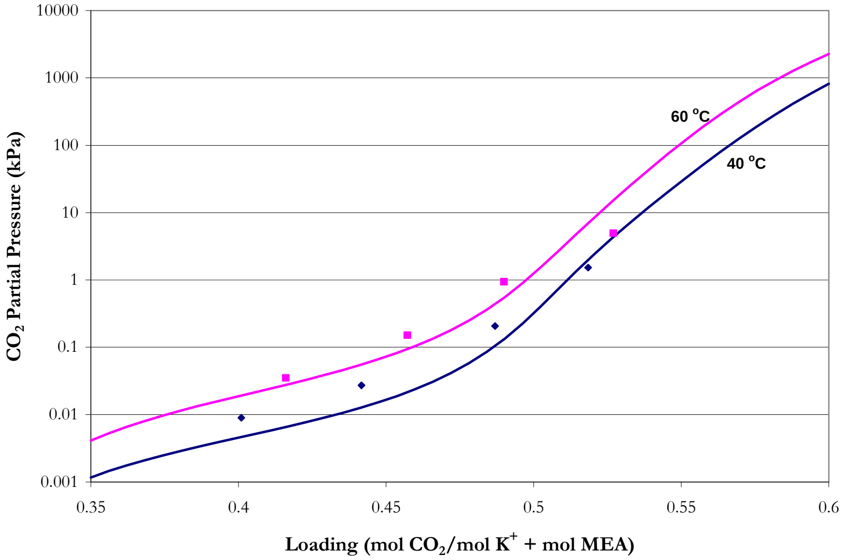

Figure 17.2-5. Comparison of Experimental CO_2 Solubility to Combined Model Predictions for 5 m K^+ + 7 m MEA at 40 and 60 °C. Points: ♦, 40 °C, ■, 60 °C. Lines: Combined elecNRTL Model Predictions.

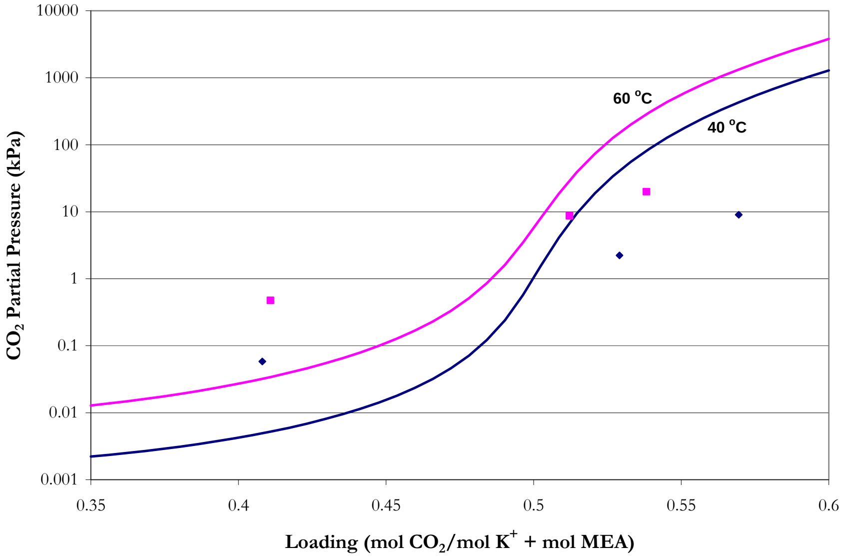

Figure 17.2-6. Comparison of Experimental CO_2 Solubility to Combined Model Predictions for 2.5 m K^+ + 7 m MEA at 40 and 60 °C. Points: ♦, 40 °C, ■, 60 °C. Lines: Combined elecNRTL Model Predictions.

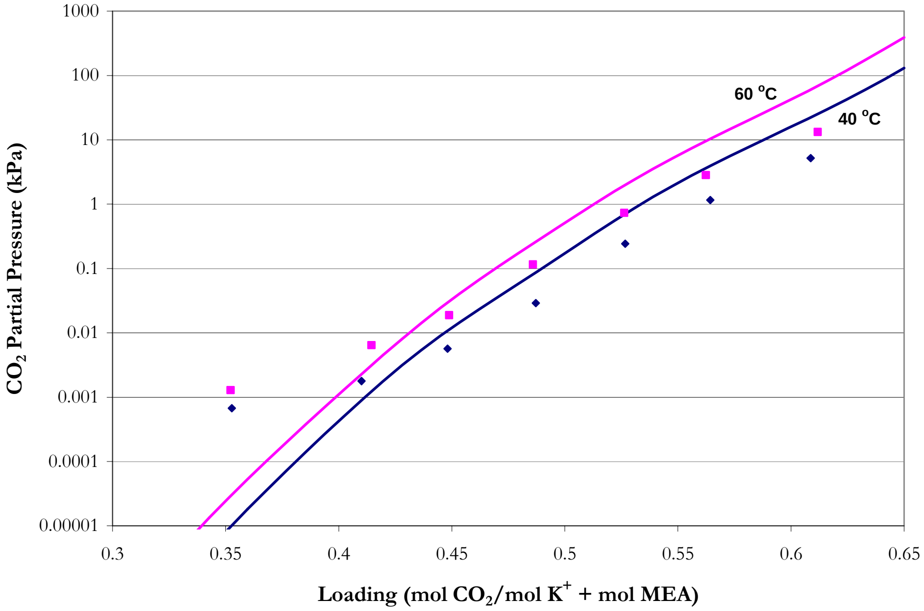

Figure 17.2-7. Comparison of Experimental CO_2 Solubility to Combined Model Predictions for 5 m K^+ + 3.5 m MEA at 40 and 60 ^{o}C. Points: ♦, 40 ^{o}C, ■, 60 ^{o}C. Lines: Combined elecNRTL Model Predictions.

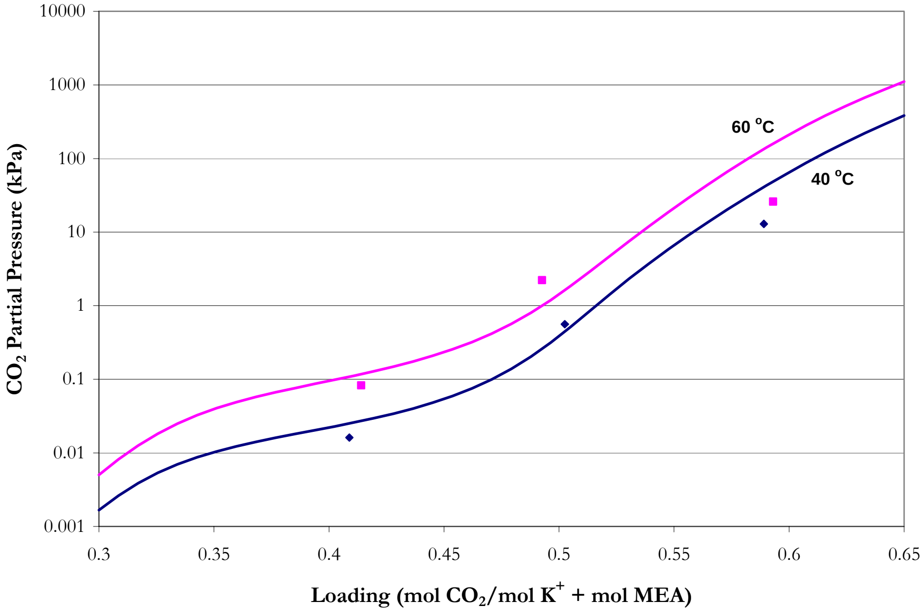

Figure 17.2-8. Comparison of Experimental CO_2 Solubility to Combined Model Predictions for 2.5 m K^+ + 3.5 m MEA at 40 and 60 ^{o}C. Points: ♦, 40 ^{o}C, ■, 60 ^{o}C. Lines: Combined elecNRTL Model Predictions.

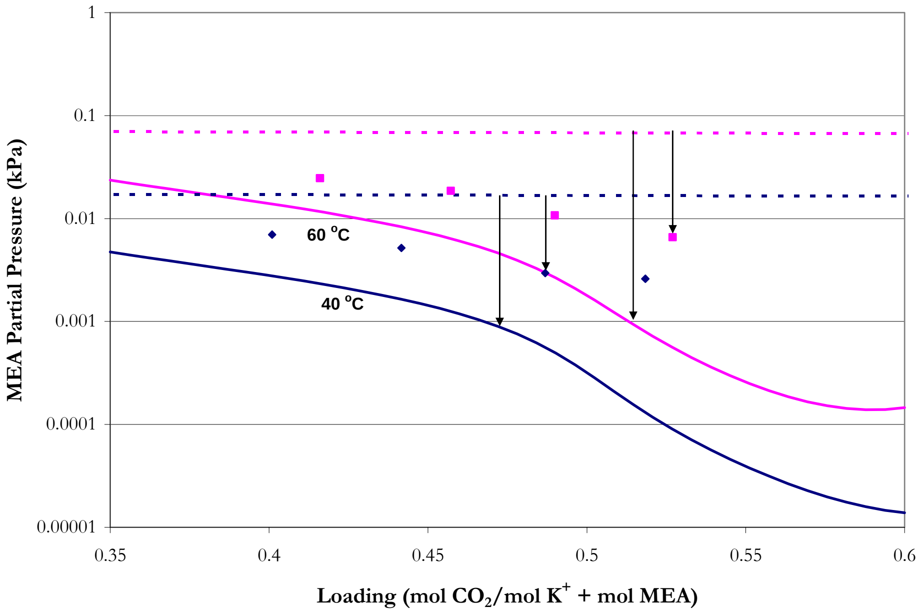

Figure 17.2-9. Comparison of Experimental Amine Volatility to Combined Model Predictions for 5 m K⁺ + 7 m MEA at 40 and 60 °C. Points: ♦, 40 °C, ■, 60 °C. Lines: —, Combined elecNRTL Model Predictions, - - -, Raoult's Law Predictions.

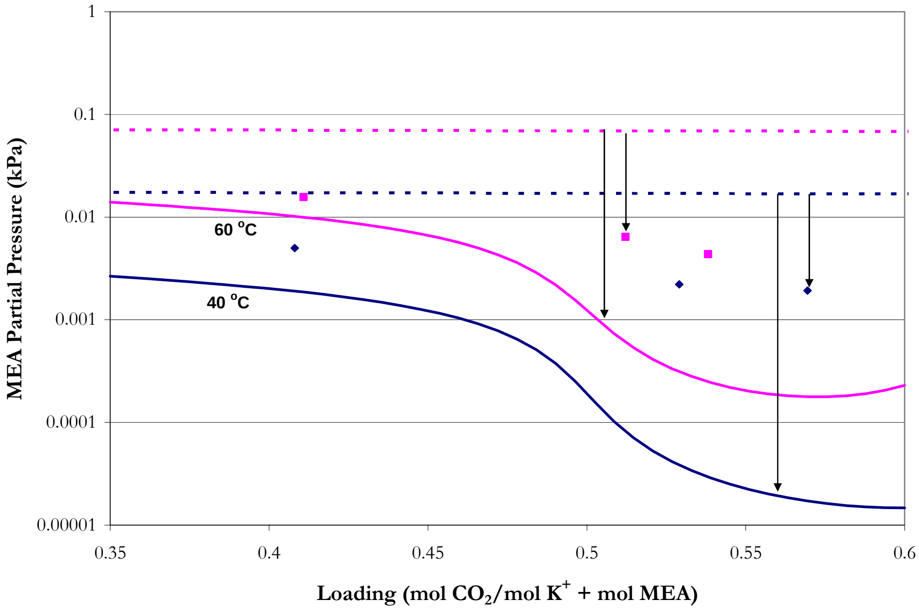

Figure 17.2-10. Comparison of Experimental Amine Volatility to Combined Model Predictions for 2.5 m K⁺ + 7 m MEA at 40 and 60 °C. Points: ♦, 40 °C, ■, 60 °C. Lines: —, Combined elecNRTL Model Predictions, - - -, Raoult's Law Predictions.

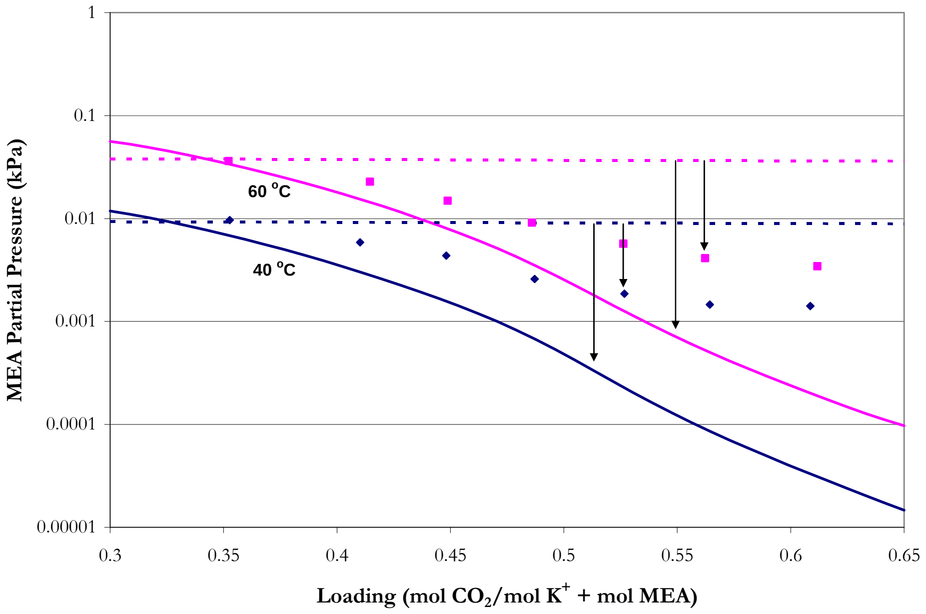

Figure 17.2-11. Comparison of Experimental Amine Volatility to Combined Model Predictions for 5 m K^+ + 3.5 m MEA at 40 and 60 °C. Points: ♦, 40 °C, ■, 60 °C. Lines: —, Combined elecNRTL Model Predictions, - - -, Raoult's Law Predictions.

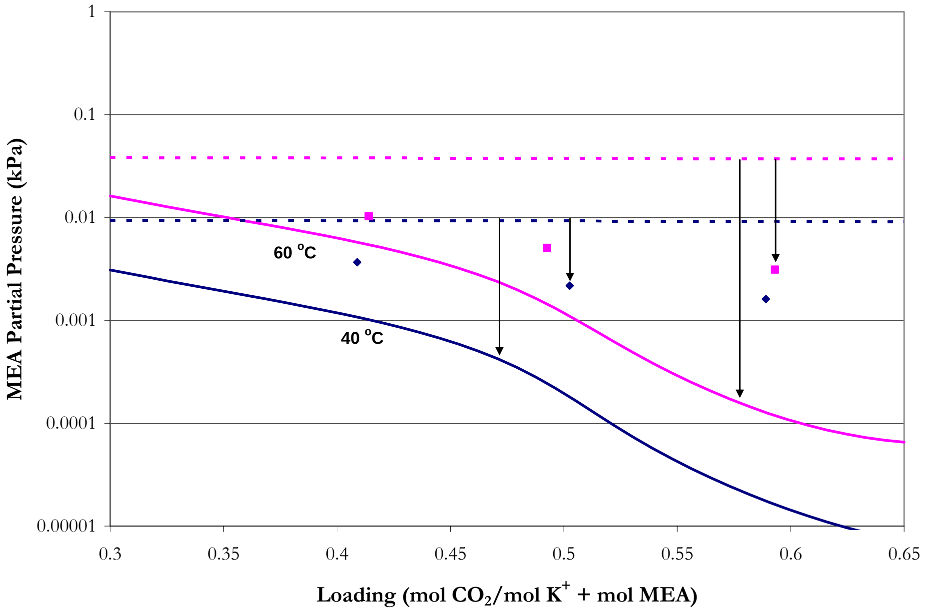

Figure 17.2-12. Comparison of Experimental Amine Volatility to Combined Model Predictions for 2.5 m K^+ + 3.5 m MEA at 40 and 60 °C. Points: ♦, 40 °C, ■, 60 °C. Lines: —, Combined elecNRTL Model Predictions, - - -, Raoult's Law Predictions.

17.3 Conclusions

In conclusion, in this work we have followed a similar approach to the method developed by Posey (1996) in terms of choosing values for the mixed system binary interaction parameters to examine the predictive ability of our model. Table 17.2-2 gave binary interaction parameters associated with the mixed salt/amine system which were not included as part of the original model regressions.

We found that binary interaction parameters for MEA exhibit similar properties as reported by Posey (1996) where interactions associated with MEA, given in Table 17.2-2, which were assigned to similar interactions values involving $MEAH^{+1}$, did not benefit the quality of the model predictions as compared to the experimental data. Therefore, default binary interaction parameters were then assigned. Binary interaction parameters for H_2O, given in Table 17.2-2, were based on the average value between H_2O, K^+/HCO_3^{-1} and H_2O, $MEAH^{+1}/MEACOO^{-1}$ given in Chapters XII and XIII. This assumption did exhibit a small benefit to the prediction of CO_2 solubility data, but varying the parameter from the default value to the average value had a minimal effect on the overall predictive outcome.

We found that to adequately predict the experimental CO_2 solubility and amine volatility data from this work for the H_2O-K_2CO_3-MEA-CO_2 system, an overall regression of the binary interaction parameters associated with the original and mixed salt/amine systems in addition to the chemical equilibrium constant for $MEACOO^{-1}$ would need to be regressed simultaneously to adequately fit the experimental data.

Figure 17.2-1 through Figure 17.2-4 illustrated the effect of K^+ on CO_2 solubility and amine volatility in 3.5 and 7.0 m MEA solutions. As the ionic strength of the solution increased from 2.5 m K^+ to 5.0 m K^+, CO_2 solubility increased by a factor of 6 whereas the MEA partial pressure moderately decreased. We also inferred, based on an ordinary least squares approximation, a decrease in the differential capacity of the solvent from 0.12 to 0.15 over a CO_2 partial pressure range from 0.01 to 1.0 kPa at 60 °C.

Figure 17.2-5 through Figure 17.2-8 compared experimental CO_2 solubility from this work to predictions from the combined elecNRTL model. Figure 17.2-5 and Figure 17.2-7 illustrated that the combined model adequately predicts CO_2 solubility even though the temperature and loading dependence does not reflect the systematic trends presented within the experimental data. Figure 17.2-6 represented the least adequate representation for all of the mixed salt/amine system compared in this work. This discrepancy may be due to a concentration boundary for the overall system. A concentration of 2.5 m K^+ was within the original concentration range for the H_2O-K_2CO_3-CO_2 regression, but this error may be an extrapolation error of the combined model given the fact that the combined model was not optimized to the experimental data.

Figure 17.2-9 through Figure 17.2-12 compared experimental MEA volatility from this work to predictions from the combined elecNRTL model. Figure 17.2-9 through 17.2-12 illustrated the departure from an ideal solution behavior vis-à-vis Raoult's Law as compared to prediction from the combined elecNRTL model. For the H_2O-K_2CO_3-MEA-CO_2 system, Raoult's Law did not adequately describe the vapor pressure of MEA over the entire range of temperature, concentration, and loading dependence. Raoult's Law predictions did illustrate a considerable effect of the activity coefficient of MEA on the prediction for the vapor pressure of MEA. In addition, the effect of speciation on the free amine concentration also played an important role in predicting the correct vapor pressure of MEA.

One of the goals of this work was to be able to build a consistent and rigorous thermodynamic model to describe the base systems, then to combine the two models and test the predictive behavior of the combined model. Table 17.2-3 illustrated that a simple exchange between binary interaction parameters based on the separate systems to create analogous interactions for the combined model did not result in an adequate fit of the experimental data. We would recommend that future work interested in the H_2O-K_2CO_3-MEA-CO_2 system should optimize the binary interaction parameters to capture the systematic trends presented within the experimental data from this work.

CHAPTER XVIII

Quinary System Predictions: H_2O-K_2CO_3-MEA-PZ-CO_2

18.1 Introduction

In our efforts to describe the thermodynamics in mixed salt/amine electrolyte solutions, we have arrived at the final system involving mixtures of water (H_2O), potassium carbonate (K_2CO_3), potassium bicarbonate ($KHCO_3$), monoethanolamine (MEA), piperazine (PZ), and carbon dioxide (CO_2). This chapter compares experimental CO_2 solubility and amine volatility data from this work for the H_2O-K_2CO_3-MEA-PZ-CO_2 system to model predictions based on the combined model for each sub-system. The combined predictive model represents the experimental data with an average absolute relative error of ± 163 %, with the exception of a few outliers.

18.2 H_2O-K_2CO_3-MEA-PZ-CO_2 System

At this point, the thermodynamic model is complete. For each sub-system, we have utilized techniques to fit experimental data from the literature and based on this work. In each ternary system, we were very successful in describing the experimental data but using the model as a predictive tool for quaternary systems, the combined model illustrated that to adequately fit the experimental data an overall parameter optimization was required. For the H_2O-K_2CO_3-MEA-PZ-CO_2 system, all of the practical binary interaction parameters and state properties used to describe interactions between molecule-molecule, molecule-electrolyte, and electrolyte-electrolyte already have been assigned in previous chapters. Thus, the H_2O-K_2CO_3-MEA-PZ-CO_2 system illustrates the final test for the predictive capabilities of the combined model. As a result, the following section describes the different data types gathered in this work for the H_2O-K_2CO_3-MEA-PZ-CO_2 system as compared to the predictive ability of the combined model.

18.2.1 ***CO_2 Solubility and Amine Volatility***

Data in the form of CO_2 solubility, which measures the partial pressure of CO_2 over aqueous K_2CO_3 plus MEA plus PZ solutions, as a function of loading (mole CO_2 per mole K^+ plus mole MEA plus 2 moles PZ) and temperature were compared to predictions based on the combined model for the H_2O-K_2CO_3-MEA-PZ-CO_2 system.

For our quinary system (H_2O, K_2CO_3, MEA, PZ, and CO_2), the following equation may be used to represent the equilibrium for CO_2 solubility data.

$$Py_{CO_2} = x_{CO_2}\gamma^*_{CO_2}H_{CO_2,H_2O} \qquad 18\text{-}1$$

Where

y_{CO_2} is the vapor mole fraction of CO_2,

$\gamma^*_{CO_2}$ is the unsymmetric activity coefficient of CO_2,

H_{CO_2,H_2O} is the Henry's Constant for CO_2 in H_2O.

In this work, we used a unique Fourier-transform infrared (FT-IR) technique to measure the vapor phase speciation in aqueous alkanolamine systems as described in Chapter II Using this technique, we have been able to measure the vapor phase partial pressure of each amine over aqueous solutions, P_{Amine}, as a function of loading (mole CO_2 per mole K^+ plus mole MEA plus 2 mole PZ) and temperature.

For our quaternary system (H_2O, K_2CO_3, MEA, and CO_2), the following equation may be used to represent the equilibrium for amine volatility data.

$$Py_{\text{Amine}} = x_{\text{Amine}}\gamma_{\text{Amine}}P^o_{\text{Amine}} \qquad 18\text{-}2$$

Where

y_{Amine} is the vapor mole fraction of the amine,

γ_{Amine} is the asymmetric activity coefficient of the amine,

P^o_{Amine} is the extended Antoine vapor pressure correlation for the amine given in Chapter VI.

Experimental CO_2 solubility and amine volatility data collected in this work for mixtures presented in Table 18.2-1 at 40 and 60 °C are illustrated in Figure 18.2-1 through Figure 18.2-9. Ordinary least squares (OLS) approximations were included to clarify systematic trends within the data set.

Table 18.2-1. Experimental Mixtures for the H_2O-K_2CO_3-MEA-PZ-CO_2 system.

5 m K^++3.5 m MEA+2 m PZ	2.5 m K^++7 m MEA+2 m PZ	2.5 m K^++3.5 m MEA+1.8 m PZ
2.5 m K^++3.5 m MEA+2 m PZ	2.5 m K^++7 m MEA+3.6 m PZ	5 m K^++3.5 m MEA+3.6 m PZ
5 m K^++7 m MEA+2 m PZ	5 m K^++7 m MEA+3.6 m PZ	2.5 m K^++3.5 m MEA+3.6 m PZ

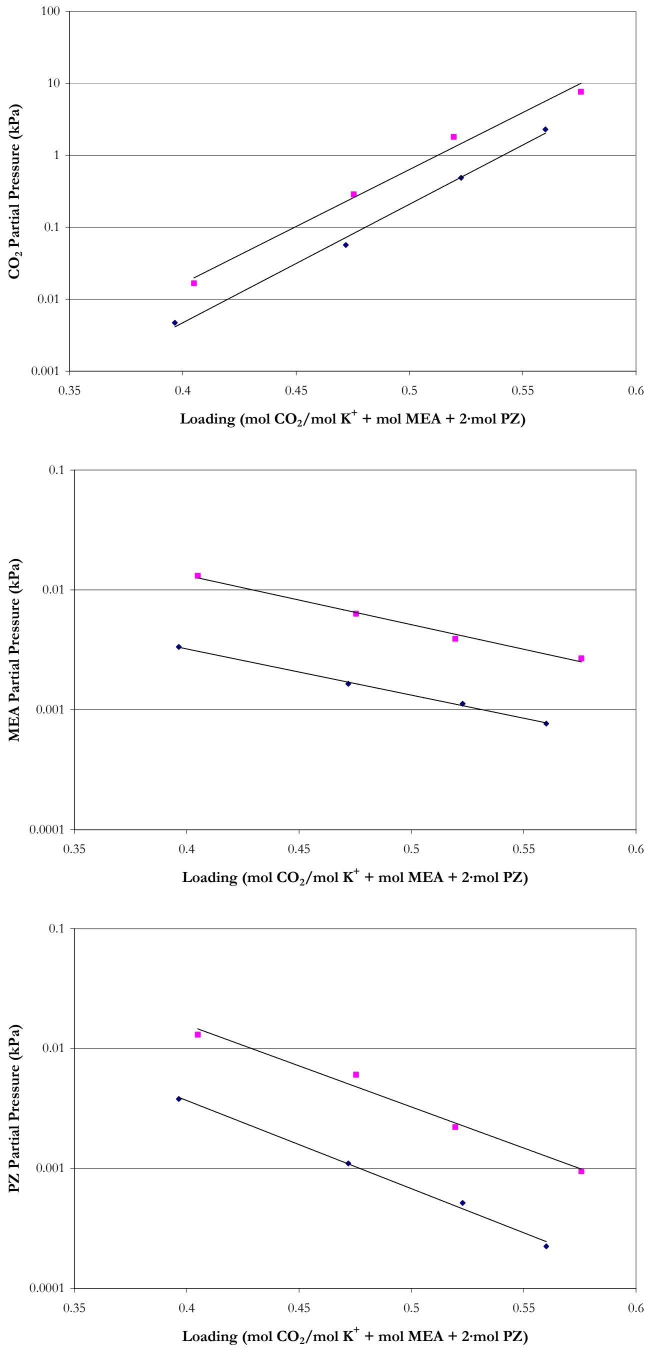

Figure 18.2-1. Experimental Data in Mixtures of 5 m K^+ + 3.5 m MEA + 2 m PZ at 40 and 60 °C from this work. Points: ◆ (40 °C) and ■ (60 °C). Lines: OLS Approximations.

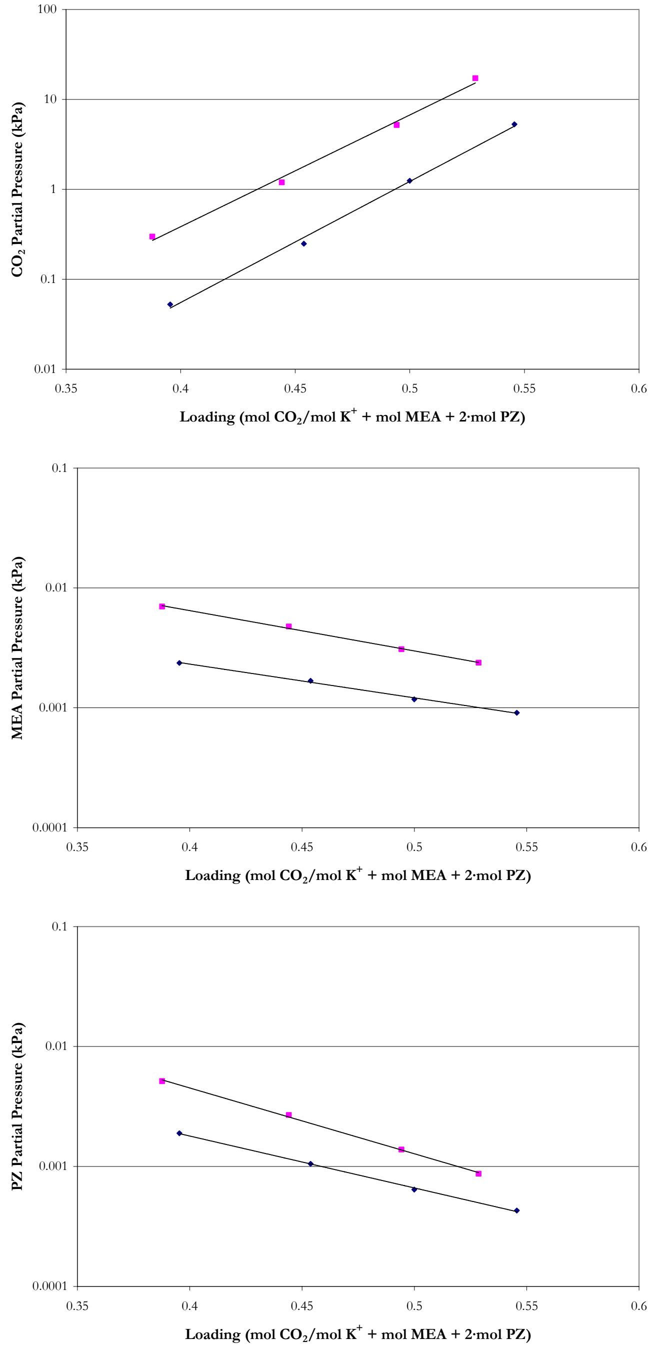

Figure 18.2-2. Experimental Data in Mixtures of 2.5 m K^+ + 3.5 m MEA + 2 m PZ at 40 and 60 ^{o}C from this work. Points: ♦ (40 ^{o}C) and ■ (60 ^{o}C). Lines: OLS Approximations.

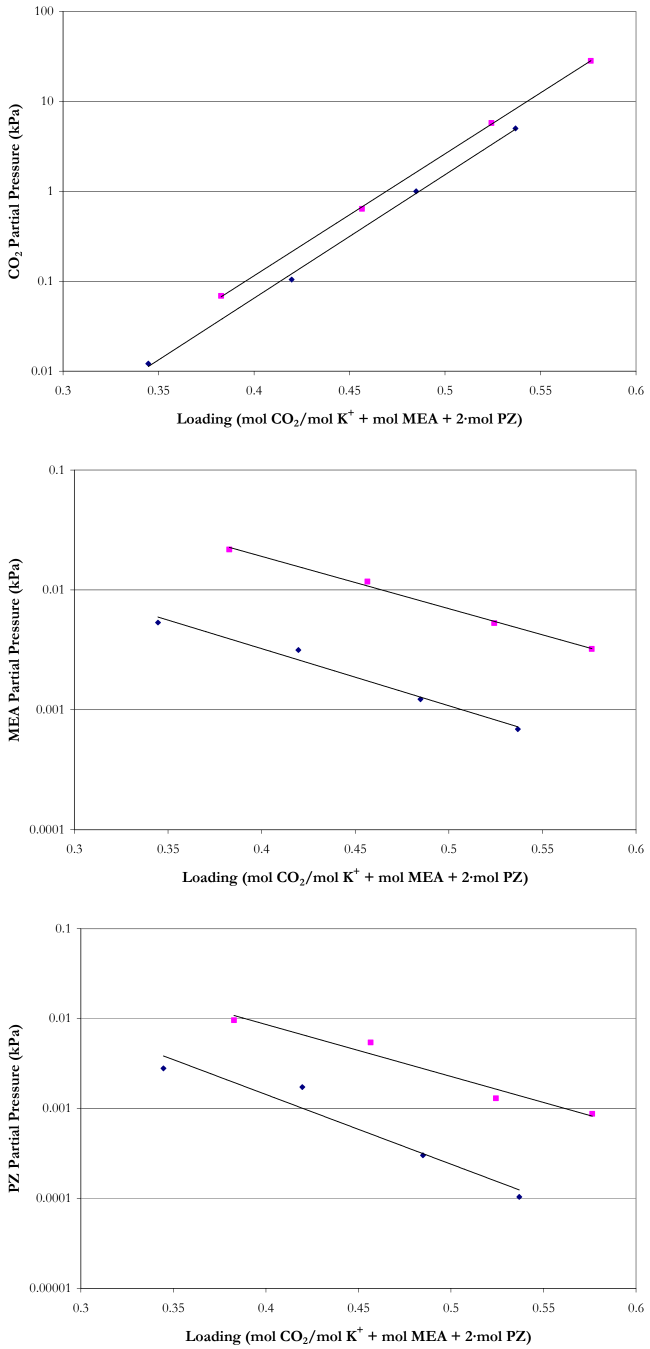

Figure 18.2-3. Experimental Data in Mixtures of 5 m K^+ + 7 m MEA + 2 m PZ at 40 and 60 °C from this work. Points: ♦ (40 °C) and ■ (60 °C). Lines: OLS Approximations.

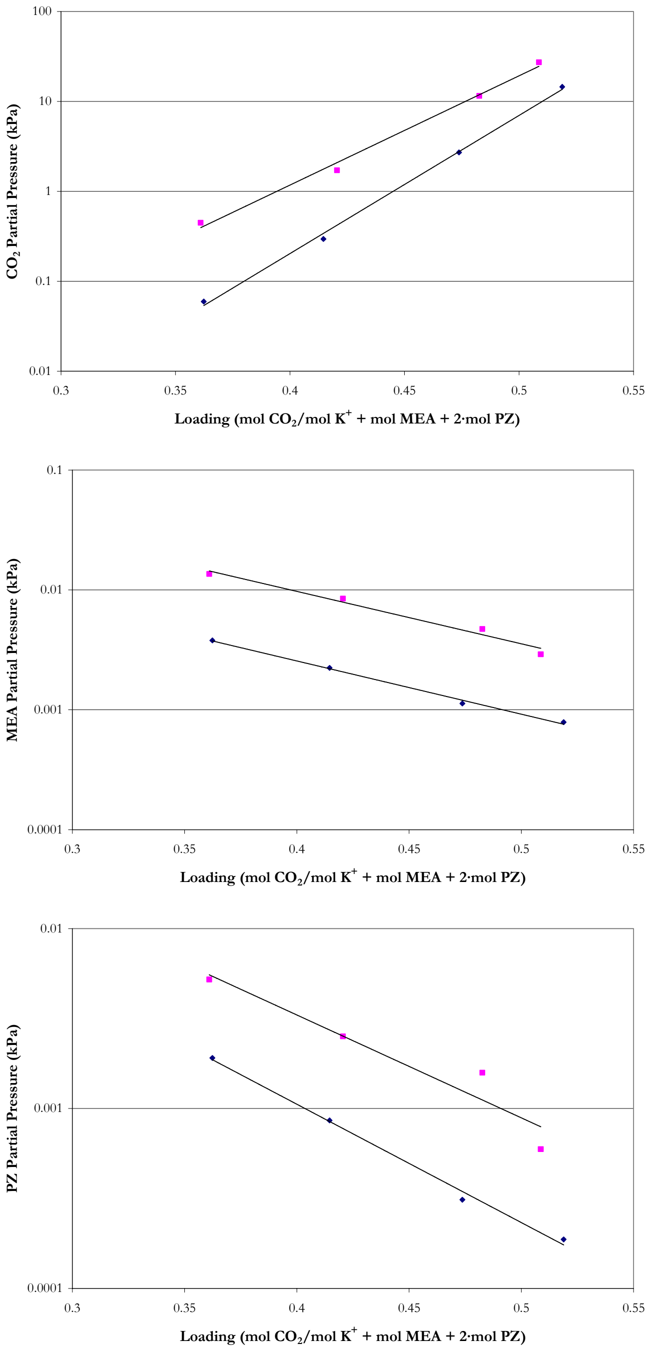

Figure 18.2-4. Experimental Data in Mixtures of 2.5 m K^+ + 7 m MEA + 2 m PZ at 40 and 60 °C from this work. Points: ♦ (40 °C) and ■ (60 °C). Lines: OLS Approximations.

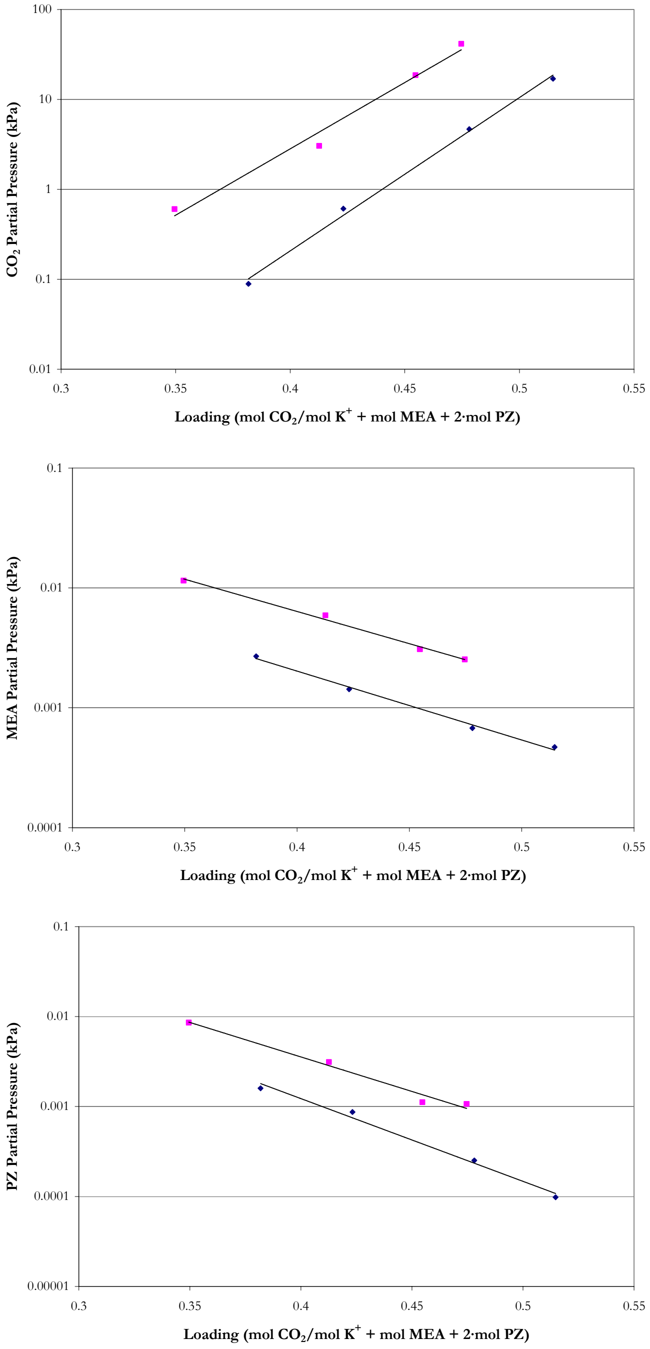

Figure 18.2-5. Experimental Data in Mixtures of 2.5 m K$^+$ + 7 m MEA + 3.6 m PZ at 40 and 60 ^{o}C from this work. Points: ♦ (40 ^{o}C) and ■ (60 ^{o}C). Lines: OLS Approximations.

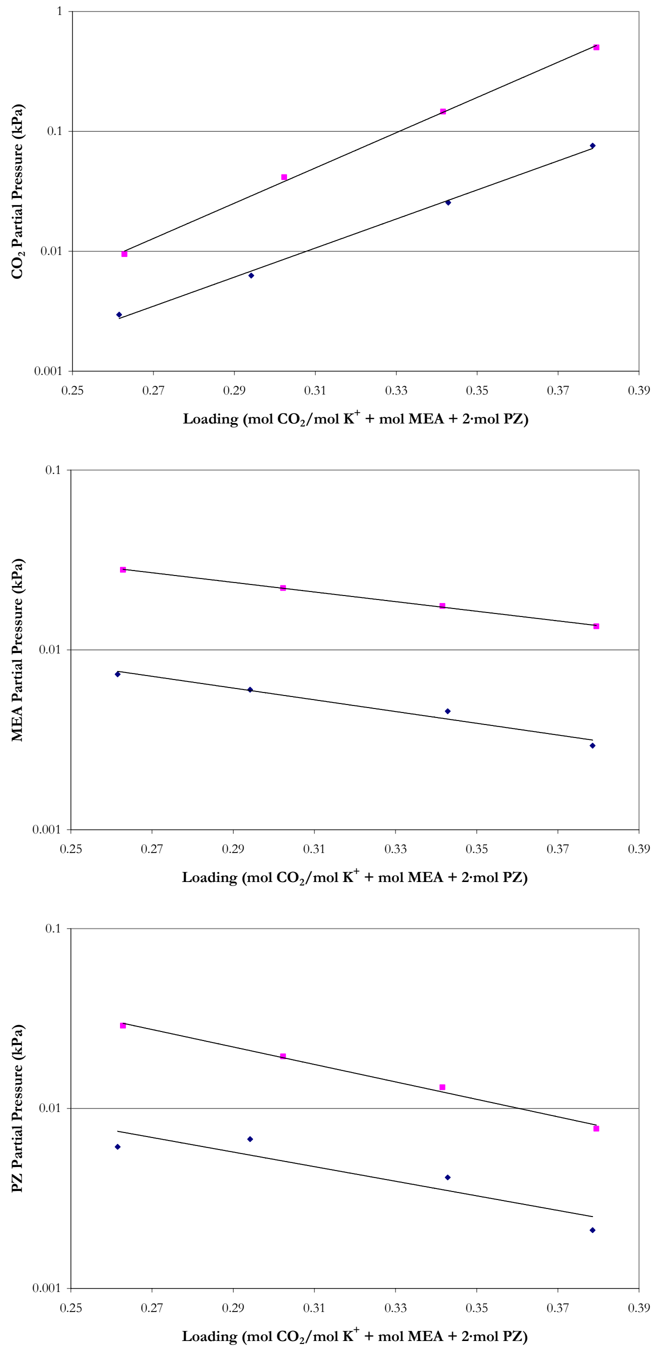

Figure 18.2-6. Experimental Data in Mixtures of 5 m K^+ + 7 m MEA + 3.6 m PZ at 40 and 60 ^oC from this work. Points: ♦ (40 ^oC) and ■ (60 ^oC). Lines: OLS Approximations.

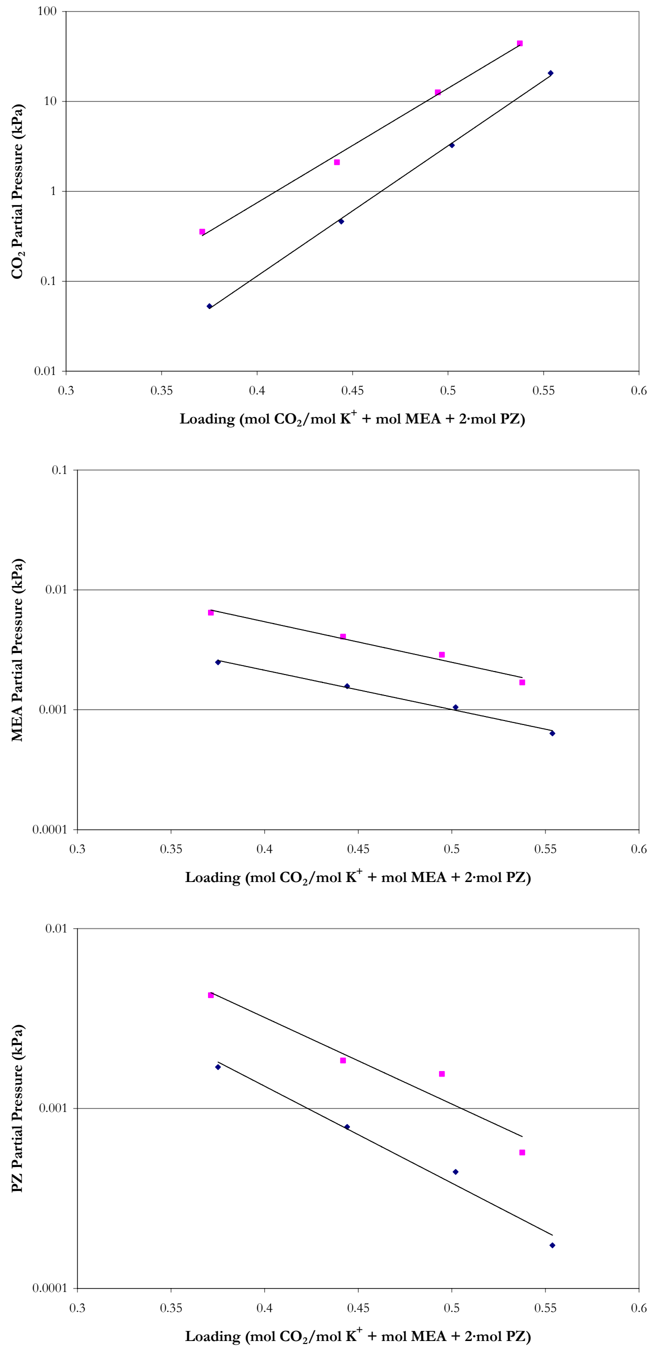

Figure 18.2-7. Experimental Data in Mixtures of 2.5 m K⁺ + 3.5 m MEA + 1.8 m PZ at 40 and 60 °C from this work. Points: ◆ (40 °C) and ■ (60 °C). Lines: OLS Approximations.

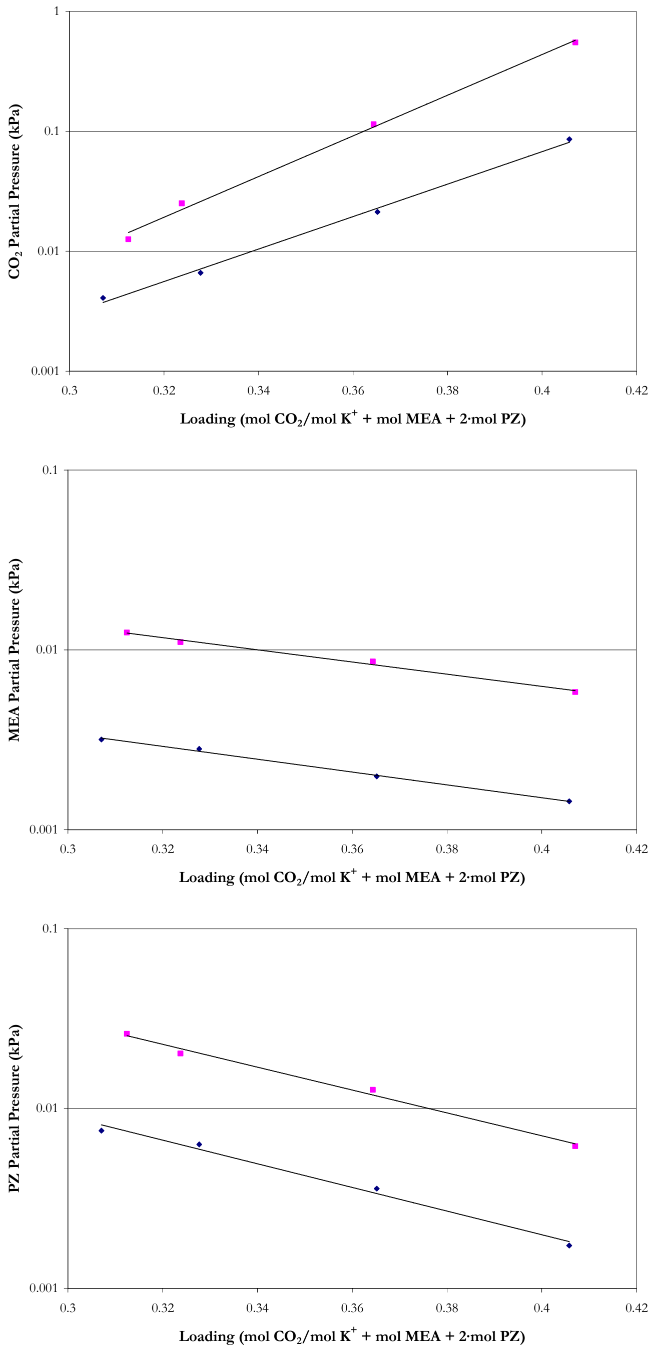

Figure 18.2-8. Experimental Data in Mixtures of 5 m K^+ + 3.5 m MEA + 3.6 m PZ at 40 and 60 ^{o}C from this work. Points: ♦ (40 ^{o}C) and ■ (60 ^{o}C). Lines: OLS Approximations.

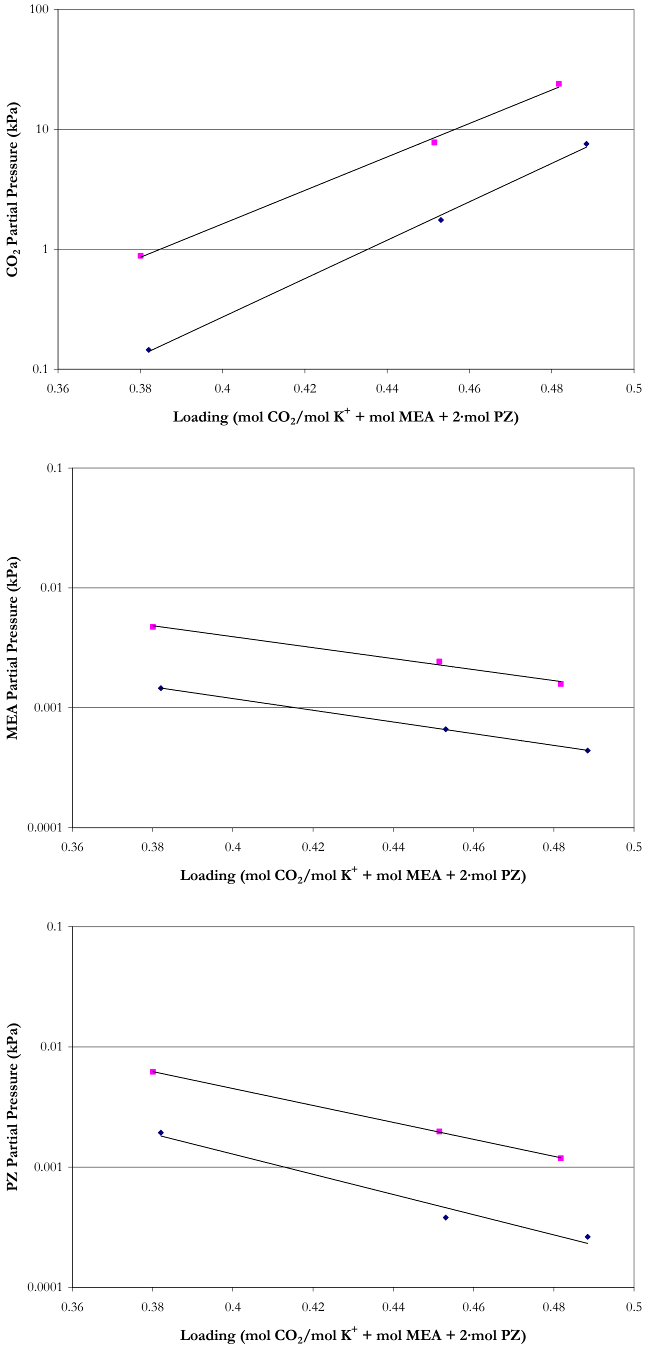

Figure 18.2-9. Experimental Data in Mixtures of 2.5 m K$^+$ + 3.5 m MEA + 3.6 m PZ at 40 and 60 ^{o}C from this work. Points: ♦ (40 ^{o}C) and ■ (60 ^{o}C). Lines: OLS Approximations.

We can quantify the effects of CO_2 solubility in the above systems by illustrating trends in CO_2 solubility at 60 °C based on the differential capacity of the solvent between the range of 0.01 and 1.0 kPa as shown in Table 18.2-2.

Table 18.2-2. Comparison of Differential Solvent Capacity Between CO_2 Partial Pressures of 0.01 and 1.0 kPa at 60 °C.

System	Differential Capacity mol CO_2/mol K^+ + mol MEA + 2·mol PZ
7 m MEA	0.31
2 m PZ	0.23
5 m K^++3.5 m MEA+2 m PZ	0.13
2.5 m K^++3.5 m MEA+2 m PZ	0.16
5 m K^++7 m MEA+2 m PZ	0.15
2.5 m K^++7 m MEA+2 m PZ	0.17
2.5 m K^++7 m MEA+3.6 m PZ	0.13
5 m K^++7 m MEA+3.6 m PZ	0.14
2.5 m K^++3.5 m MEA+1.8 m PZ	0.16
5 m K^++3.5 m MEA+3.6 m PZ	0.12
2.5 m K^++3.5 m MEA+3.6 m PZ	0.14

As shown in Table 18.2-2, 7 m MEA demonstrated a greater differential capacity as compared to piperazine or other mixed salt-amine systems. For mixed salt-amine systems, only systems composed of 2.5 m K^+ exhibited an increase in the differential capacity as compared to similar systems containing 5 m K^+. Overall, 2.5 m K^++7 m MEA+2 m PZ exhibited the largest differential capacity equal to 0.17 out of nine solvents studied as part of this work.

Amine volatility at 40 °C for each solvent can then be compared based on a CO_2 partial pressure from 0.01 to 0.1 kPa as illustrated in Figure 18.2-10 based on experimental MEA volatility and in Figure 18.2-11 based on experimental PZ volatility. Table 18.2-3 compares the amine volatility of the nine mixed salt-amine systems in this work to the base sub-component systems of 7 m MEA and 2 m PZ at 40 °C.

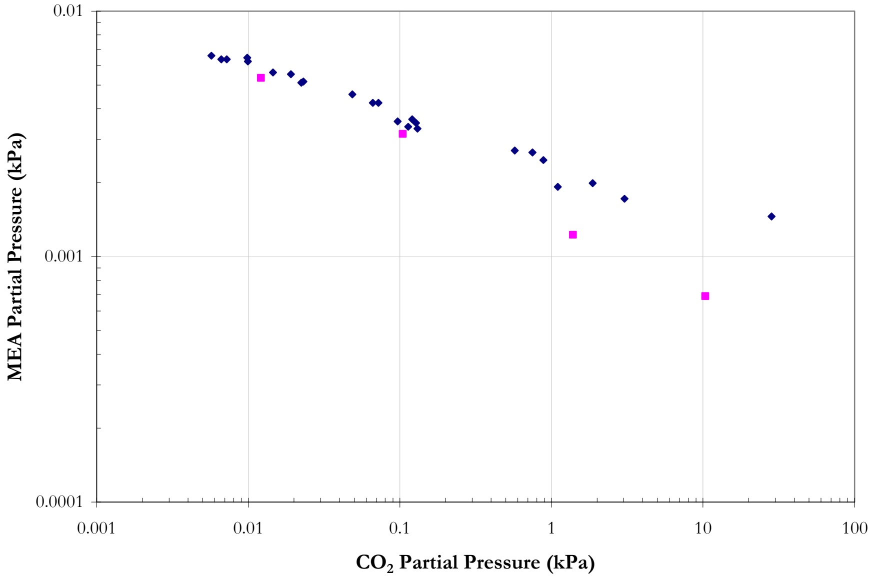

Figure 18.2-10. Comparison of Experimental MEA Volatility versus CO_2 Solubility at 40 °C from this work. Points: ♦, 7 m MEA, ■, 5 m K^+ + 7 m MEA + 2 m PZ.

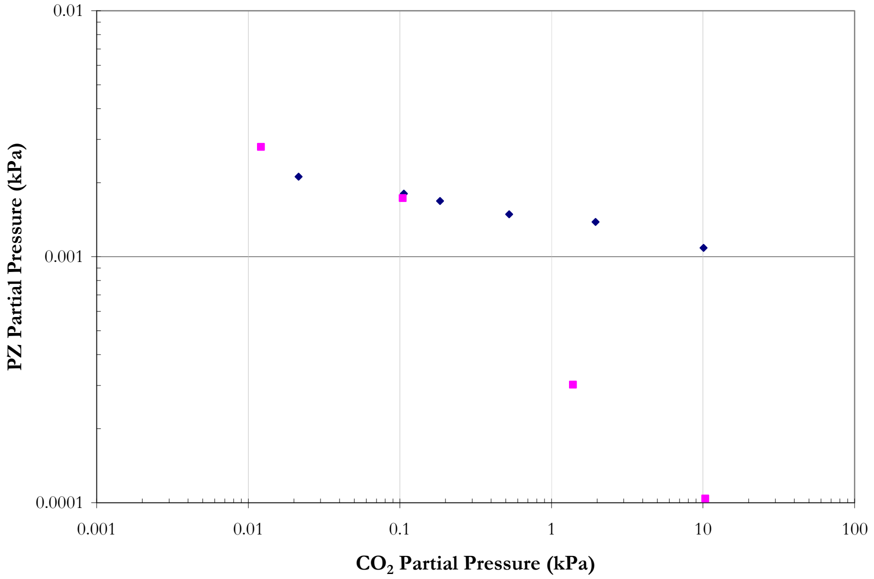

Figure 18.2-11. Comparison of Experimental PZ Volatility versus CO_2 Solubility at 40 °C from this work. Points: ♦, 2 m PZ, ■, 5 m K^+ + 7 m MEA + 2 m PZ.

We can quantify the effects of amine volatility for each solvent at a given CO_2 partial pressure from 0.01 to 0.1 kPa at 40 °C as compared to the base sub-component systems of 7 m MEA and 2 m PZ as shown in Table 18.2-3.

Table 18.2-3. Comparison of Experimental Amine Volatility Evaluated at a CO_2 Partial Pressure from 0.01 to 0.1 kPa at 40 °C.

System	P^{MEA} (ppm_v)	P^{PZ} (ppm_v)
7 m MEA	62-35	-
2 m PZ	-	21-18
5 m K^++3.5 m MEA+2 m PZ	25-15	24-9
2.5 m K^++3.5 m MEA+2 m PZ	32-20	29-14
5 m K^++7 m MEA+2 m PZ	60-27	39-11
2.5 m K^++7 m MEA+2 m PZ	54-28	32-12
2.5 m K^++7 m MEA+3.6 m PZ	54-25	60-17
5 m K^++7 m MEA+3.6 m PZ	54-29	49-23
2.5 m K^++3.5 m MEA+1.8 m PZ	37-22	33-14
5 m K^++3.5 m MEA+3.6 m PZ	25-14	52-17
2.5 m K^++3.5 m MEA+3.6 m PZ	31-16	68-21

As shown in Table 18.2-3, 7 m MEA demonstrates a greater range of volatility at 40 °C as compared to piperazine or other mixed salt-amine systems. For different combinations of potassium + 7 m MEA + piperazine; the relative volatility of MEA remained between 55 and 27 ppm_v over the range of CO_2 partial pressures. When the MEA concentration decreased from 7 m to 3.5 m, the volatility of MEA volatility decreased due to the decease in the total alkalinity of the solvent and is reflected in the MEA volatility deceasing by a factor of 2. However, PZ volatility remained approximately constant and is consistent with effects exhibited in the H_2O-MEA-PZ systems, where large changes in the solution alkalinity may not have an effect on the volatility of PZ.

Figure 18.2-12 through Figure 18.2-20 illustrates the effects exhibited in CO_2 solubility and amine volatility due to an increase in the concentration of potassium, monoethanolamine, and piperazine, respectively, Table 18.2-4 documents systematic trends presented within the experimental data.

Table 18.2-4. Systematic Trends For Effects Exhibited in CO_2 Solubility and Amine Volatility Due to an Increase in the Concentration of K^+, MEA, or PZ.

Effect of	Relative Change		
K^+/MEA/PZ	P^{CO2}	P^{MEA}	P^{PZ}
2.5-5/7/2	↑	↓	↓
5/3.5-7/2	↓	-	↑
5/7/2-3.6	↑	↓	↓

Potassium Effect

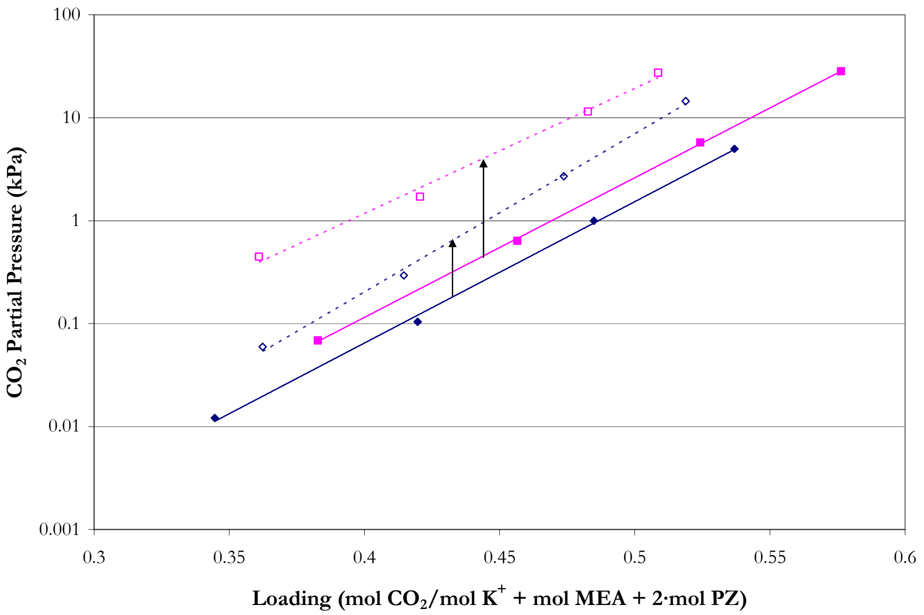

Figure 18.2-12. Effect of Increasing K^+ Concentration on CO_2 Solubility from 2.5 to 5 m in a 7 m MEA + 2 m PZ Solution at 40 and 60 °C. Points: ♦ (40 °C) and ■ (60 °C) for 5 m K^+ + 7 m MEA+ 2 m PZ, ◊ (40 °C) and □ (60 °C) for 2.5 m K^+ + 7 m MEA+ 2 m PZ. Lines: OLS Approximations.

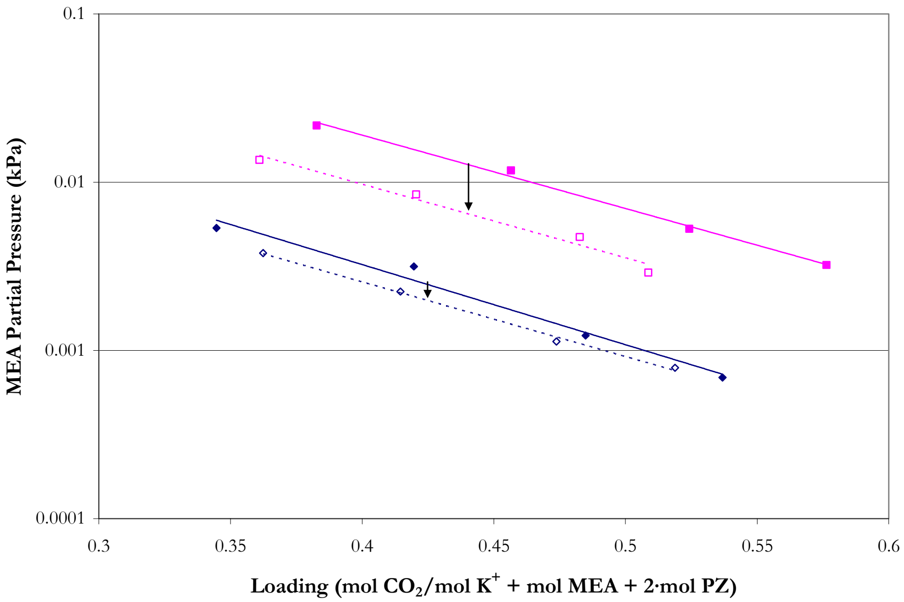

Figure 18.2-13. Effect of Increasing K^+ Concentration on MEA Volatility from 2.5 to 5 m in a 7 m MEA + 2 m PZ Solution at 40 and 60 °C. Points: ◆ (40 °C) and ■ (60 °C) for 5 m K^+ + 7 m MEA+ 2 m PZ, ◊ (40 °C) and □ (60 °C) for 2.5 m K^+ + 7 m MEA+ 2 m PZ. Lines: OLS Approximations.

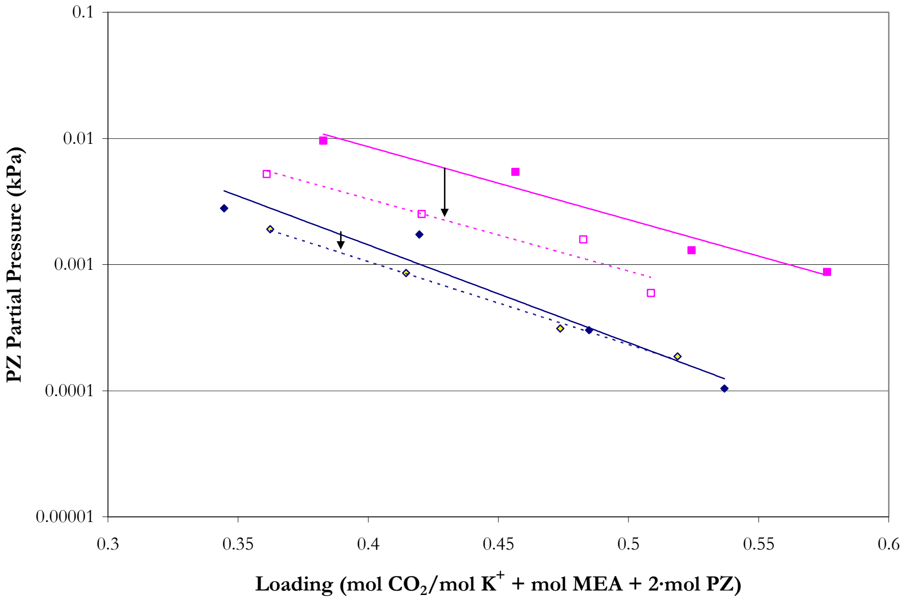

Figure 18.2-14. Effect of Increasing K^+ Concentration on PZ Volatility from 2.5 to 5 m in a 7 m MEA + 2 m PZ Solution at 40 and 60 °C. Points: ◆ (40 °C) and ■ (60 °C) for 5 m K^+ + 7 m MEA+ 2 m PZ, ◊ (40 °C) and □ (60 °C) for 2.5 m K^+ + 7 m MEA+ 2 m PZ. Lines: OLS Approximations.

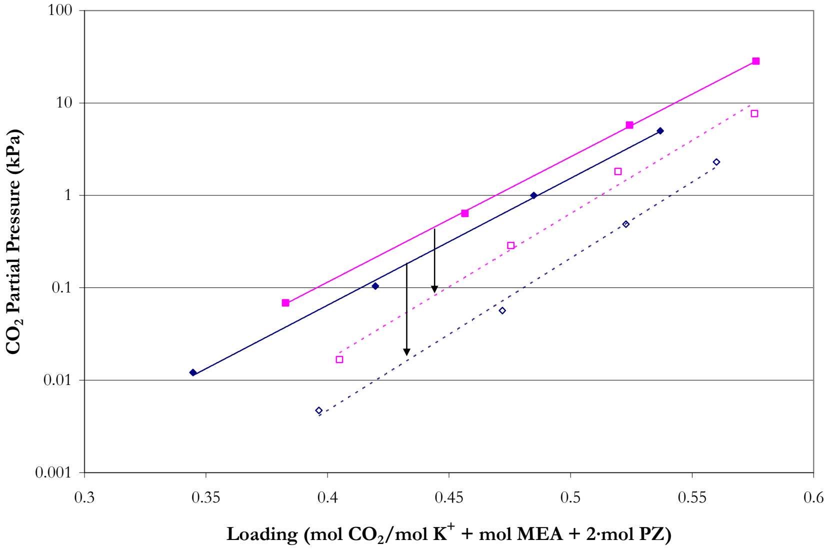

Figure 18.2-15. Effect of Increasing MEA Concentration on CO_2 Solubility from 3.5 to 7 m in a 5 m K^+ + 2 m PZ Solution at 40 and 60 °C. Points: ♦ (40 °C) and ■ (60 °C) for 5 m K^+ + 7 m MEA+ 2 m PZ, ◊ (40 °C) and □ (60 °C) for 5 m K^+ + 3.5 m MEA+ 2 m PZ. Lines: OLS Approximations.

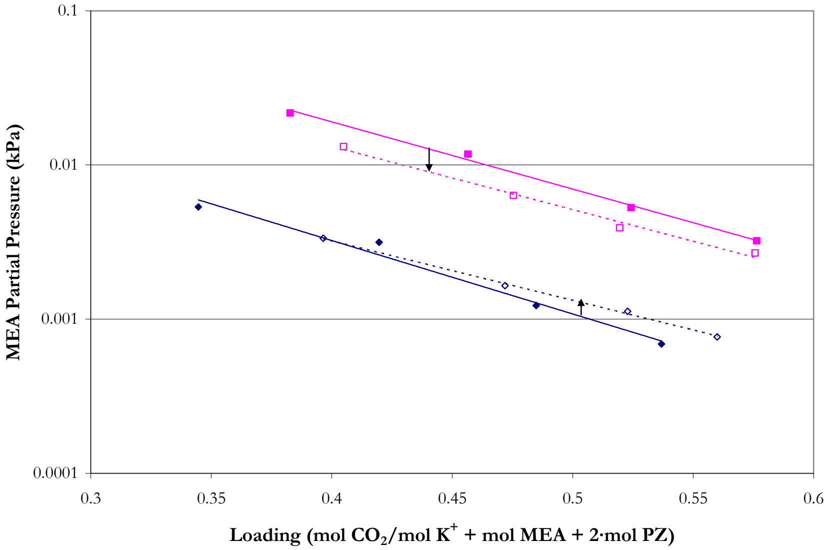

Figure 18.2-16. Effect of Increasing MEA Concentration on MEA Volatility from 3.5 to 7 m in a 5 m K^+ + 2 m PZ Solution at 40 and 60 °C. Points: ♦ (40 °C) and ■ (60 °C) for 5 m K^+ + 7 m MEA+ 2 m PZ, ◊ (40 °C) and □ (60 °C) for 5 m K^+ + 3.5 m MEA+ 2 m PZ. Lines: OLS Approximations.

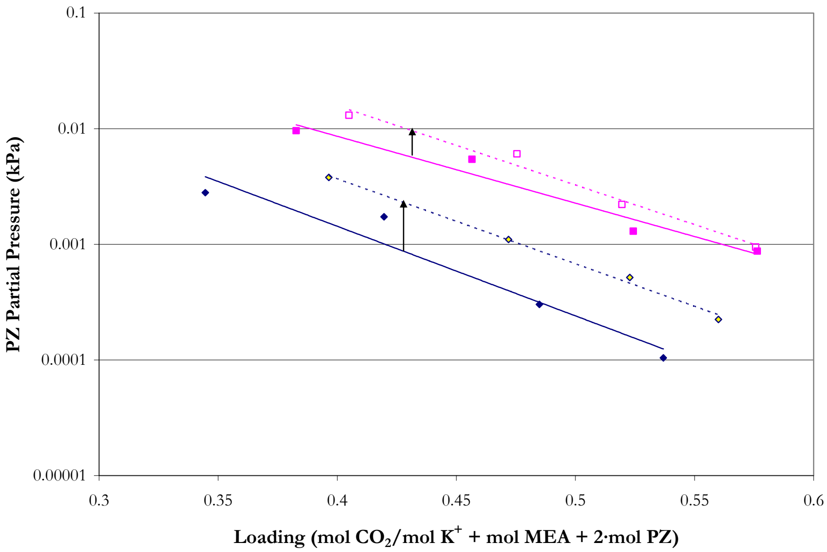

Figure 18.2-17. Effect of Increasing MEA Concentration on PZ Volatility from 3.5 to 7 m in a 5 m K^+ + 2 m PZ Solution at 40 and 60 ^{o}C. Points: ♦ (40 ^{o}C) and ■ (60 ^{o}C) for 5 m K^+ + 7 m MEA+ 2 m PZ, ◊ (40 ^{o}C) and □ (60 ^{o}C) for 5 m K^+ + 3.5 m MEA+ 2 m PZ. Lines: OLS Approximations.

Piperazine Effect

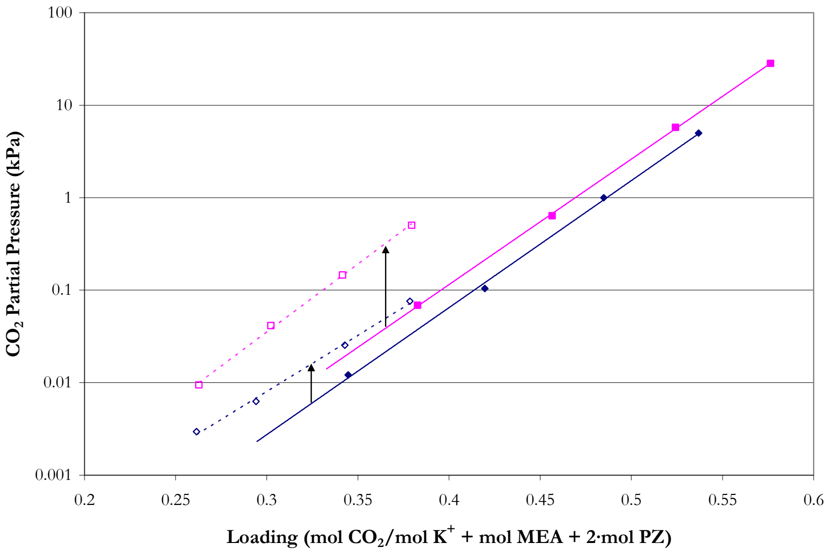

Figure 18.2-18. Effect of Increasing PZ Concentration on CO_2 Solubility from 2 to 3.6 m in a 5 m K^+ + 7 m MEA Solution at 40 and 60 ^{o}C. Points: ♦ (40 ^{o}C) and ■ (60 ^{o}C) for 5 m K^+ + 7 m MEA+ 2 m PZ, ◊ (40 ^{o}C) and □ (60 ^{o}C) for 5 m K^+ + 7 m MEA+ 3.6 m PZ. Lines: OLS Approximations.

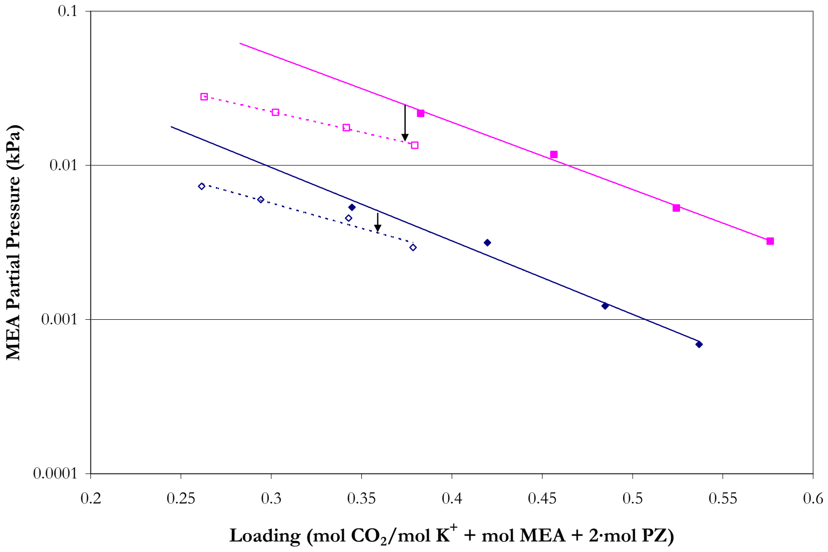

Figure 18.2-19. Effect of Increasing PZ Concentration on MEA Volatility from 2 to 3.6 m in a 5 m K^+ + 7 m MEA Solution at 40 and 60 °C. Points: ♦ (40 °C) and ■ (60 °C) for 5 m K^+ + 7 m MEA+ 2 m PZ, ◊ (40 °C) and □ (60 °C) for 5 m K^+ + 7 m MEA+ 3.6 m PZ. Lines: OLS Approximations.

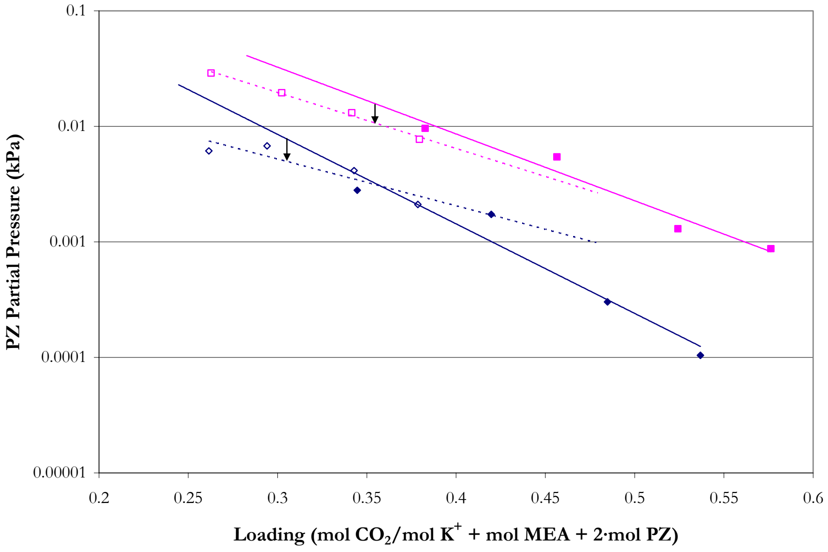

Figure 18.2-20. Effect of Increasing PZ Concentration on PZ Volatility from 2 to 3.6 m in a 5 m K^+ + 7 m MEA Solution at 40 and 60 °C. Points: ♦ (40 °C) and ■ (60 °C) for 5 m K^+ + 7 m MEA+ 2 m PZ, ◊ (40 °C) and □ (60 °C) for 5 m K^+ + 7 m MEA+ 3.6 m PZ. Lines: OLS Approximations.

18.3 Combined Model Predictions

A simple Aspen PlusTM Flash model was used to test the predictive capability of the H_2O-K_2CO_3-MEA-PZ-CO_2 combined model against experimental data from this work. For each data point, the deviation between the experimental and estimated values is expressed in terms of the average absolute relative deviation (AARD) given in Table 18.3-1.

Table 18.3-1. Absolute Percent Relative Error for the H_2O-K_2CO_3-MEA-PZ-CO_2 System.

	AARD (%)		
System	P^{CO2}	P^{MEA}	P^{PZ}
5 m K^++3.5 m MEA+2 m PZ	1071	54	73
2.5 m K^++3.5 m MEA+2 m PZ	168	64	47
5 m K^++7 m MEA+2 m PZ	402	58	43
2.5 m K^++7 m MEA+2 m PZ	26	56	37
2.5 m K^++7 m MEA+3.6 m PZ	26	49	21
5 m K^++7 m MEA+3.6 m PZ	20	44	23
2.5 m K^++3.5 m MEA+1.8 m PZ	79	62	45
5 m K^++3.5 m MEA+3.6 m PZ	254	24	32
2.5 m K^++3.5 m MEA+3.6 m PZ	38	43	17
Overall	**237**	**51**	**38**

Overall, the combined model moderately described most of the H_2O-K_2CO_3-MEA-PZ-CO_2 property data list above. Even though, the combined model did fall short in describing the CO_2 solubility in 5 m K^++3.5 m MEA+2 m PZ, 2.5 m K^++3.5 m MEA+2 m PZ, 5 m K^++7 m MEA+2 m PZ, and 5 m K^++3.5 m MEA+3.6 m PZ, the combined model did an moderate job at predicting the amine volatility for all of the solvents studied in this work. The above results would suggest that there may be a need for parameter optimization to improve the statistical fit of the experimental data as described by the combined model.

One of the goals of this work was to be able to build a consistent and rigorous thermodynamic model to describe the base systems. The three models where then merged to test the combined model's predictive behavior. Table 18.3-1 illustrates that a simple exchange between binary interaction parameters, as utilized in previous chapters, to create a combined model for the H_2O-K_2CO_3-MEA-PZ-CO_2 system **did not** result in an adequate fit of the experimental data. We would recommend that future work interested in the H_2O-K_2CO_3-MEA-PZ-CO_2 system to optimize the binary interaction parameters to capture systematic trends presented within the experimental data. The rest of this chapter will illustrate VLE predictions based on the combined model for the H_2O-K_2CO_3-MEA-PZ-CO_2 system.

Figure 18.3-1 through Figure 18.3-27 compares experimental CO_2 solubility and amine volatility from this work to predictions from the combined elecNRTL model. As illustrated in Table 18.3-1 the combined model moderately describes most of the experimental H_2O-K_2CO_3-MEA-PZ-CO_2 system data, but does fall short for the previously mentioned compositions. In addition, the combined model does not predict the precipitation of $KHCO_3$ and $K_2PZ(COO)_2$ as illustrated in Chapter V. Figure 18.3-10 through Figure 18.3-27 illustrates the combined model predictions to experimental amine volatility from this work. Raoult's Law approximations have also been included to described the departure from an ideal solution behavior as compared to predictions from the combined elecNRTL model. Even though, Raoult's Law **does not** adequately describe the amine volatility, the comparison does illustrate a considerable effect of the activity coefficient on the prediction of the amine vapor pressure.

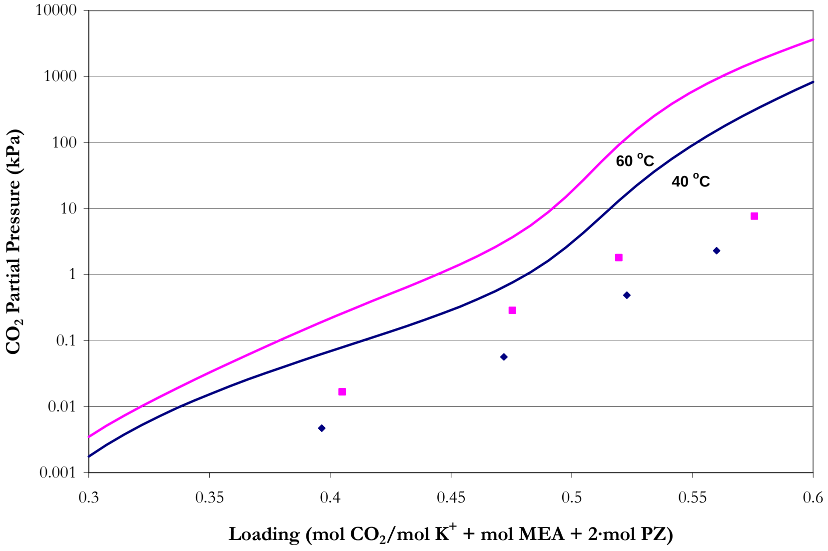

Figure 18.3-1. Comparison of Experimental CO_2 Solubility to Combined Model Predictions for 5 m K^+ + 3.5 m MEA + 2 m PZ at 40 and 60 °C. Points: ♦, 40 °C, ■, 60 °C. Lines: Combined elecNRTL Model Predictions.

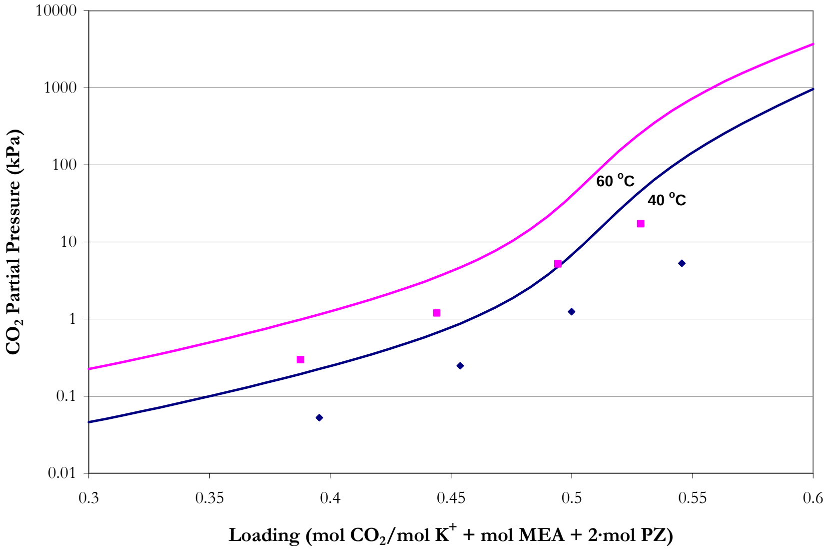

Figure 18.3-2. Comparison of Experimental CO_2 Solubility to Combined Model Predictions for 2.5 m K^+ + 3.5 m MEA + 2 m PZ at 40 and 60 °C. Points: ♦, 40 °C, ■, 60 °C. Lines: Combined elecNRTL Model Predictions.

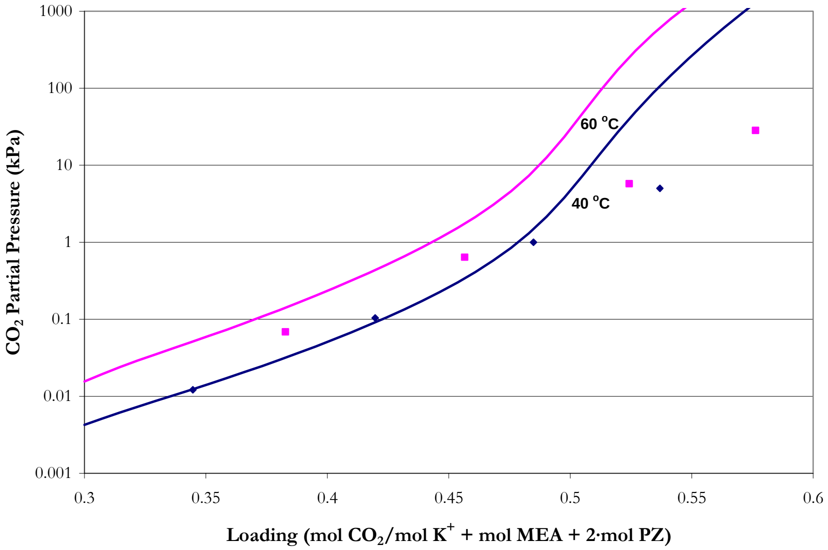

Figure 18.3-3. Comparison of Experimental CO_2 Solubility to Combined Model Predictions for 5 m K^+ + 7 m MEA + 2 m PZ at 40 and 60 °C. Points: ♦, 40 °C, ■, 60 °C. Lines: Combined elecNRTL Model Predictions.

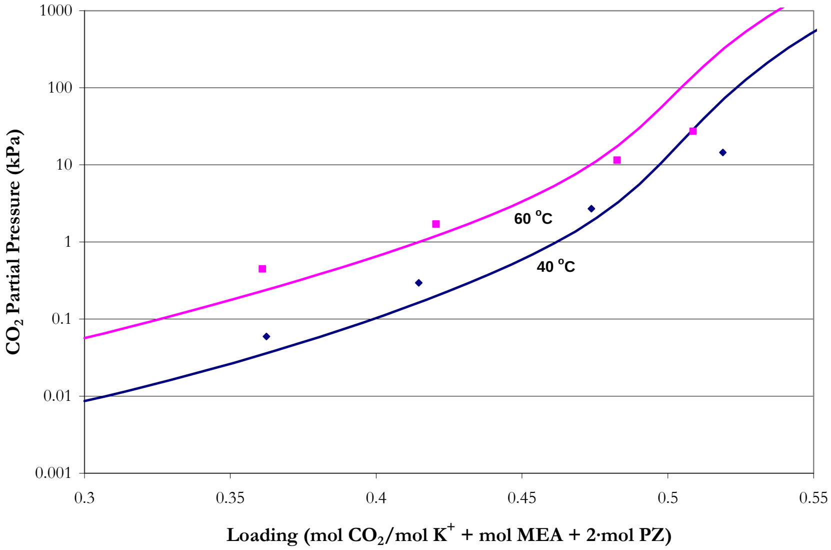

Figure 18.3-4. Comparison of Experimental CO_2 Solubility to Combined Model Predictions for 2.5 m K^+ + 7 m MEA + 2 m PZ at 40 and 60 °C. Points: ♦, 40 °C, ■, 60 °C. Lines: Combined elecNRTL Model Predictions.

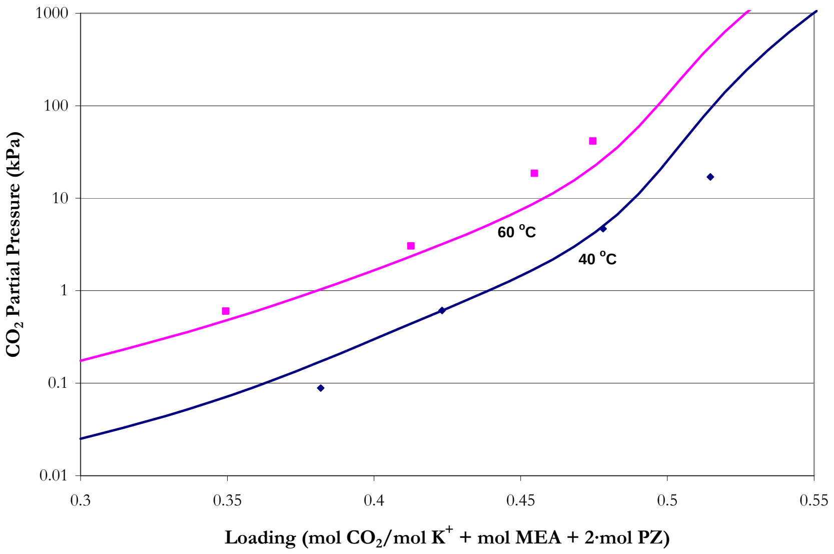

Figure 18.3-5. Comparison of Experimental CO$_2$ Solubility to Combined Model Predictions for 2.5 m K^+ + 7 m MEA + 3.6 m PZ at 40 and 60 °C. Points: ♦, 40 °C, ■, 60 °C. Lines: Combined elecNRTL Model Predictions.

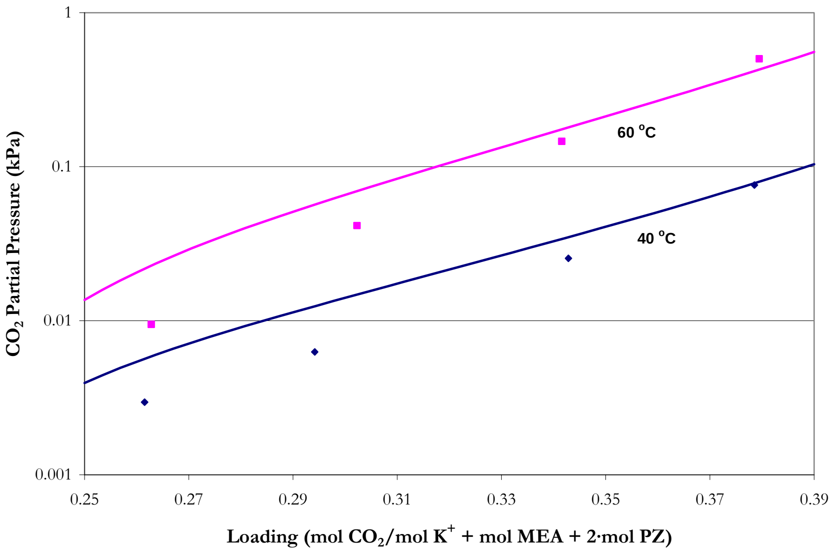

Figure 18.3-6. Comparison of Experimental CO$_2$ Solubility to Combined Model Predictions for 5 m K^+ + 7 m MEA + 3.6 m PZ at 40 and 60 °C. Points: ♦, 40 °C, ■, 60 °C. Lines: Combined elecNRTL Model Predictions.

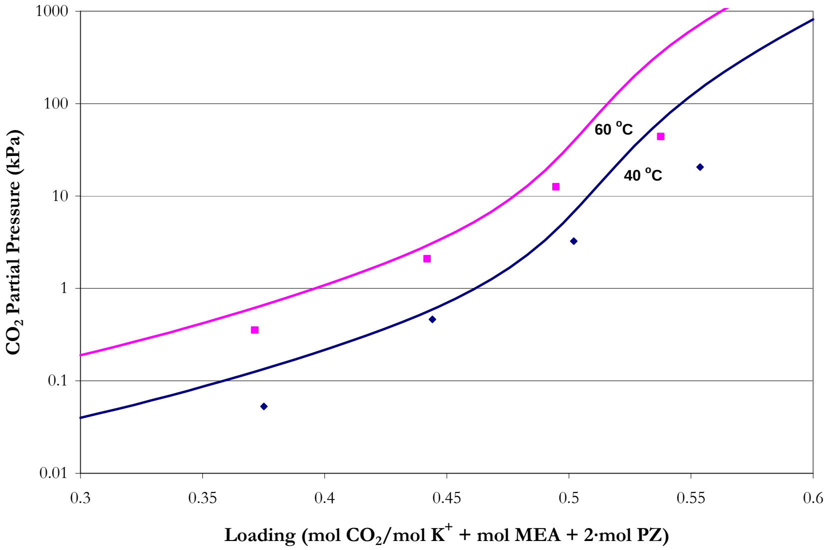

Figure 18.3-7. Comparison of Experimental CO_2 Solubility to Combined Model Predictions for 2.5 m K^+ + 3.5 m MEA + 1.8 m PZ at 40 and 60 °C. Points: ♦, 40 °C, ■, 60 °C. Lines: Combined elecNRTL Model Predictions.

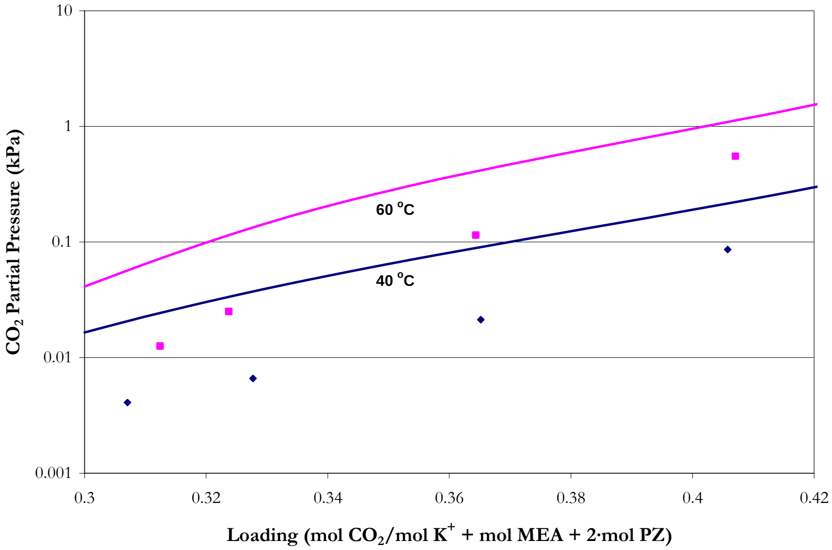

Figure 18.3-8. Comparison of Experimental CO_2 Solubility to Combined Model Predictions for 5 m K^+ + 3.5 m MEA + 3.6 m PZ at 40 and 60 °C. Points: ♦, 40 °C, ■, 60 °C. Lines: Combined elecNRTL Model Predictions.

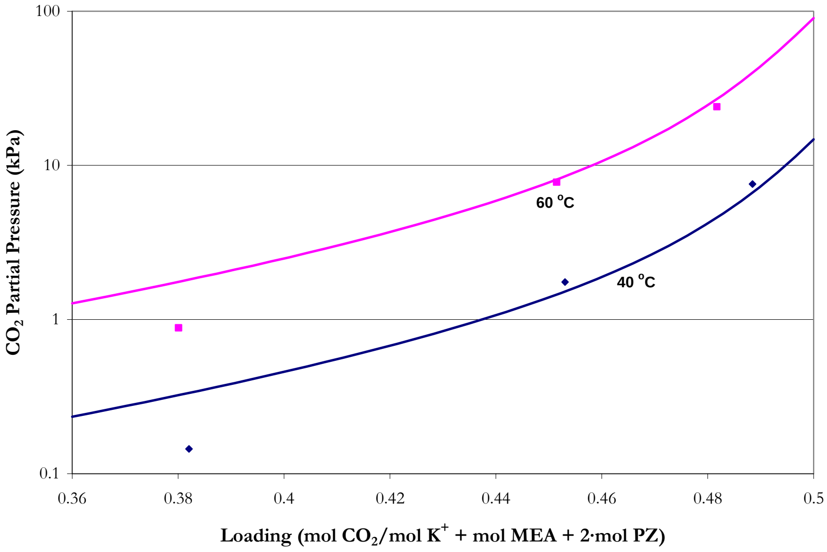

Figure 18.3-9. Comparison of Experimental CO_2 Solubility to Combined Model Predictions for 2.5 m K^+ + 3.5 m MEA + 3.6 m PZ at 40 and 60 ^{o}C. Points: ♦, 40 ^{o}C, ■, 60 ^{o}C. Lines: Combined elecNRTL Model Predictions.

MEA Volatility

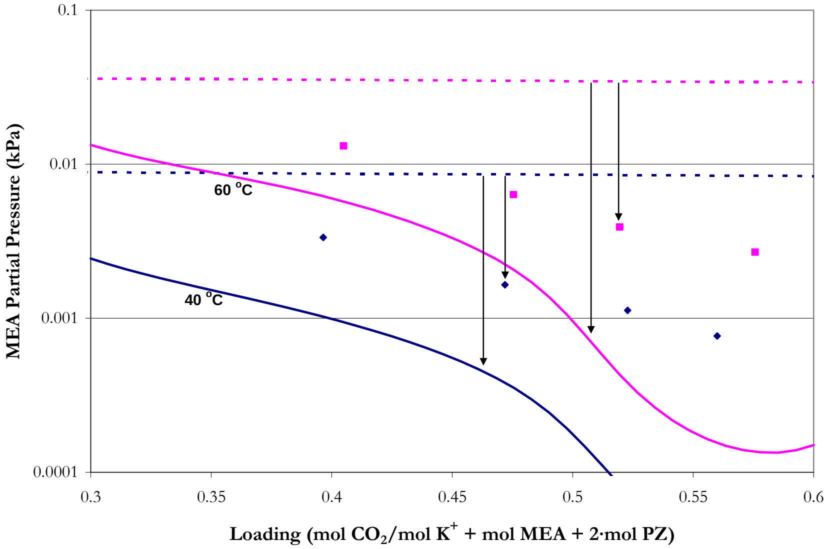

Figure 18.3-10. Comparison of Experimental MEA Volatility to Combined Model Predictions for 5 m K^+ + 3.5 m MEA + 2 m PZ at 40 and 60 ^{o}C. Points: ♦, 40 ^{o}C, ■, 60 ^{o}C. Solid Lines: Combined elecNRTL Model Predictions. Dash Lines: Raoult's Law Approximations.

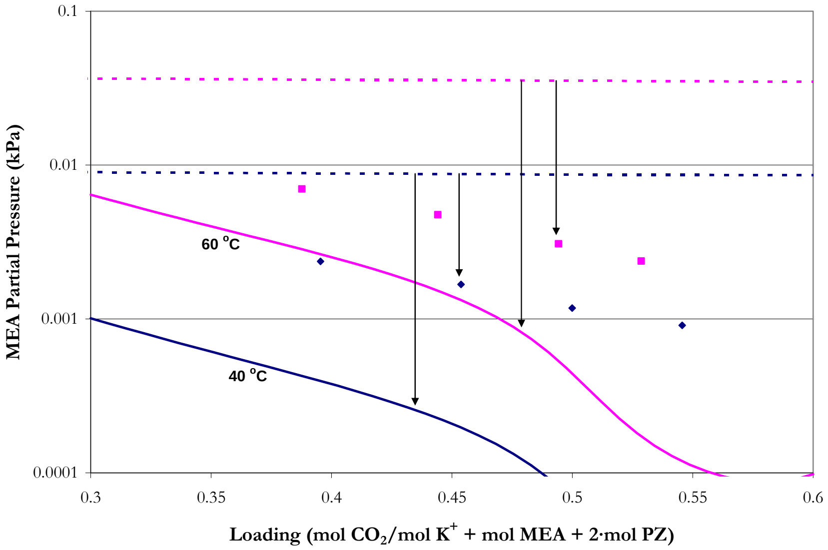

Figure 18.3-11. **Comparison of Experimental MEA Volatility to Combined Model Predictions for 2.5 m K+ + 3.5 m MEA + 2 m PZ at 40 and 60 °C. Points: ♦, 40 °C, ■, 60 °C. Solid Lines: Combined elecNRTL Model Predictions. Dash Lines: Raoult's Law Approximations.**

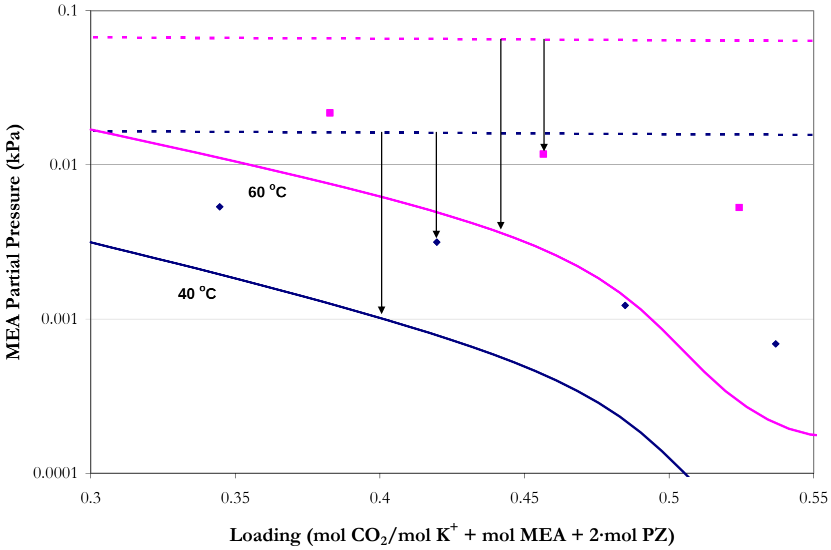

Figure 18.3-12. **Comparison of Experimental MEA Volatility to Combined Model Predictions for 5 m K+ + 7 m MEA + 2 m PZ at 40 and 60 °C. Points: ♦, 40 °C, ■, 60 °C. Solid Lines: Combined elecNRTL Model Predictions. Dash Lines: Raoult's Law Approximations.**

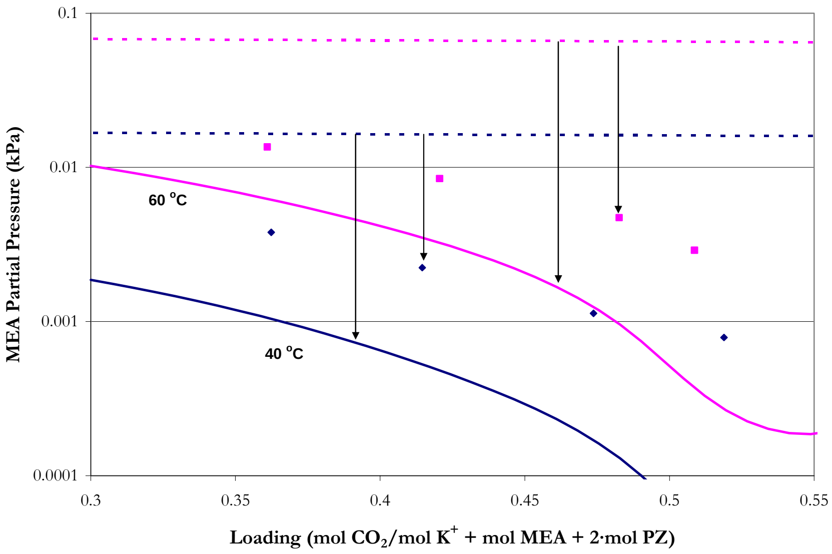

Figure 18.3-13. Comparison of Experimental MEA Volatility to Combined Model Predictions for 2.5 m K^+ + 7 m MEA + 2 m PZ at 40 and 60 °C. Points: ♦, 40 °C, ■, 60 °C. Solid Lines: Combined elecNRTL Model Predictions. Dash Lines: Raoult's Law Approximations.

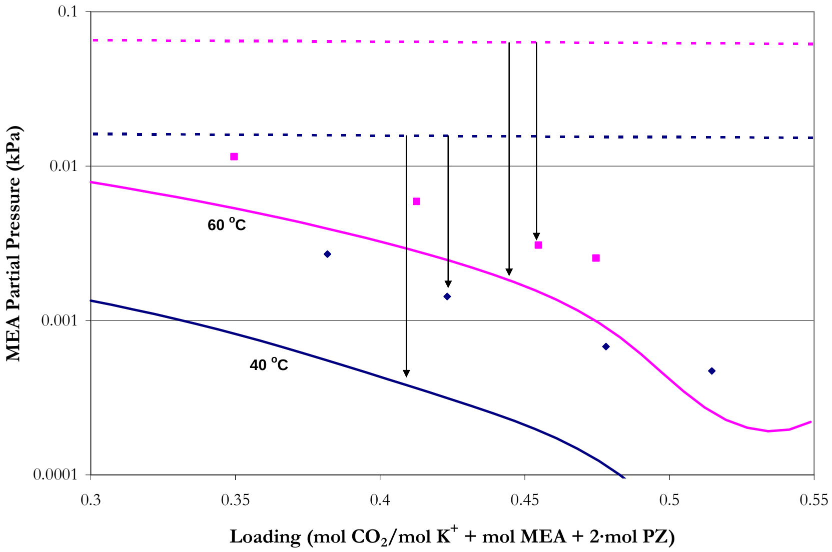

Figure 18.3-14. Comparison of Experimental MEA Volatility to Combined Model Predictions for 2.5 m K^+ + 7 m MEA + 3.6 m PZ at 40 and 60 °C. Points: ♦, 40 °C, ■, 60 °C. Solid Lines: Combined elecNRTL Model Predictions. Dash Lines: Raoult's Law Approximations.

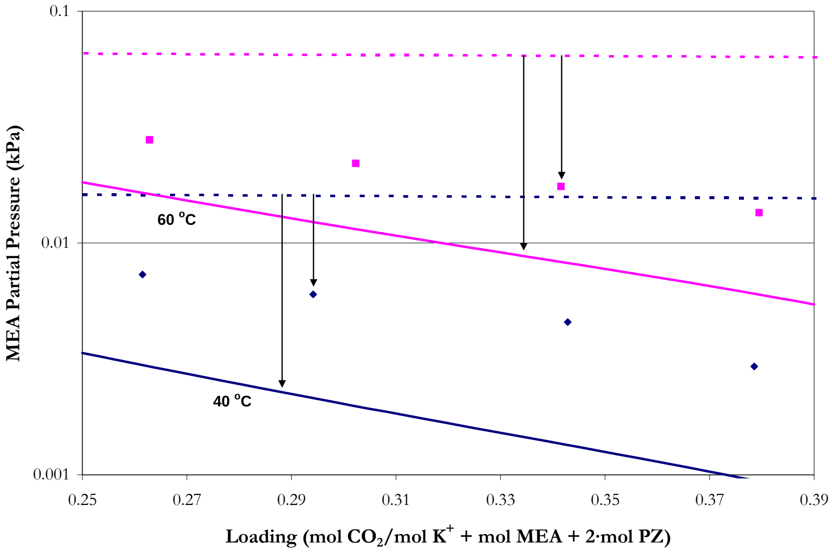

Figure 18.3-15. **Comparison of Experimental MEA Volatility to Combined Model Predictions for 5 m K+ + 7 m MEA + 3.6 m PZ at 40 and 60 °C. Points: ♦, 40 °C, ■, 60 °C. Solid Lines: Combined elecNRTL Model Predictions. Dash Lines: Raoult's Law Approximations.**

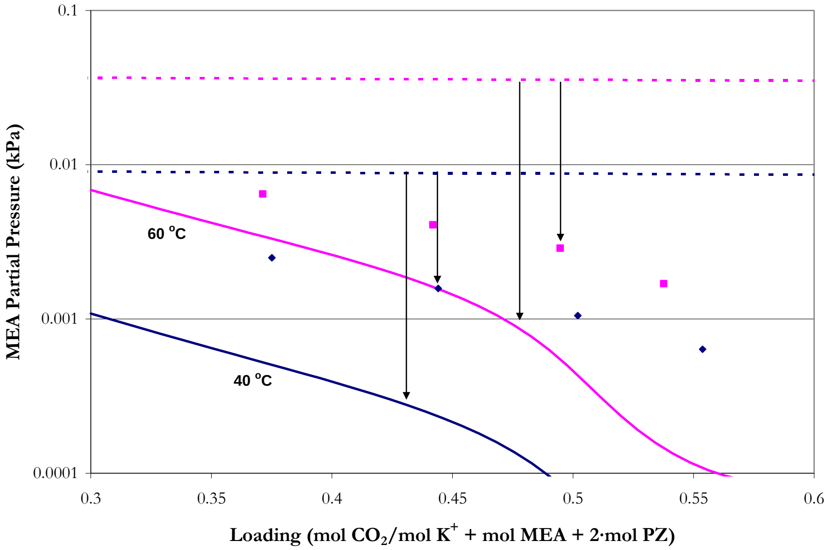

Figure 18.3-16. **Comparison of Experimental MEA Volatility to Combined Model Predictions for 2.5 m K+ + 3.5 m MEA + 1.8 m PZ at 40 and 60 °C. Points: ♦, 40 °C, ■, 60 °C. Solid Lines: Combined elecNRTL Model Predictions. Dash Lines: Raoult's Law Approximations.**

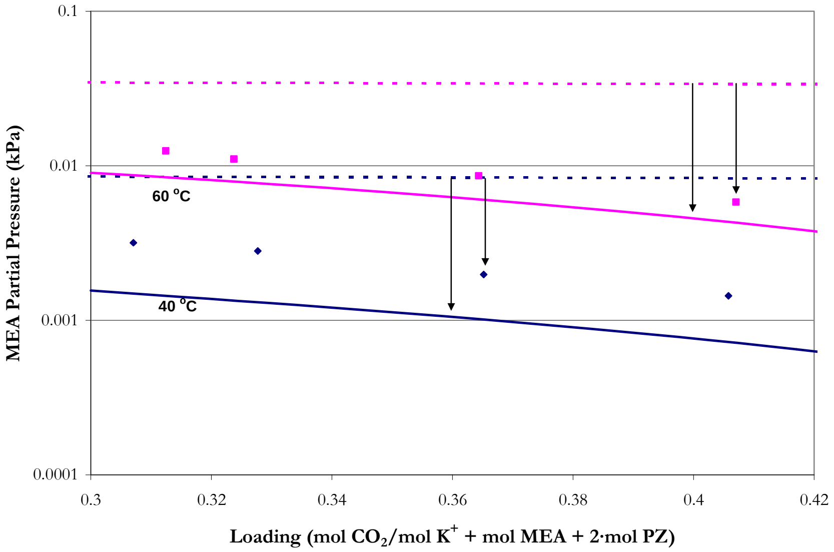

Figure 18.3-17. Comparison of Experimental MEA Volatility to Combined Model Predictions for 5 m K^+ + 3.5 m MEA + 3.6 m PZ at 40 and 60 °C. Points: ♦, 40 °C, ■, 60 °C. Solid Lines: Combined elecNRTL Model Predictions. Dash Lines: Raoult's Law Approximations.

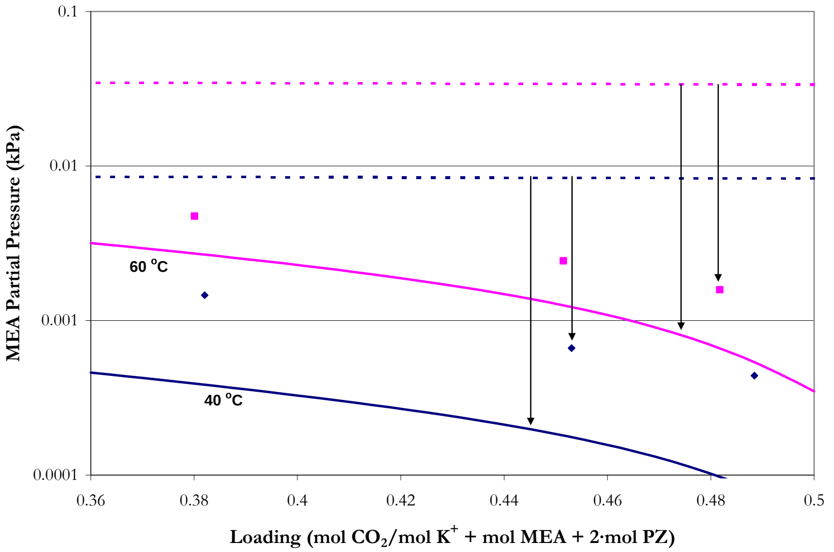

Figure 18.3-18. Comparison of Experimental MEA Volatility to Combined Model Predictions for 2.5 m K^+ + 3.5 m MEA + 3.6 m PZ at 40 and 60 °C. Points: ♦, 40 °C, ■, 60 °C. Solid Lines: Combined elecNRTL Model Predictions. Dash Lines: Raoult's Law Approximations.

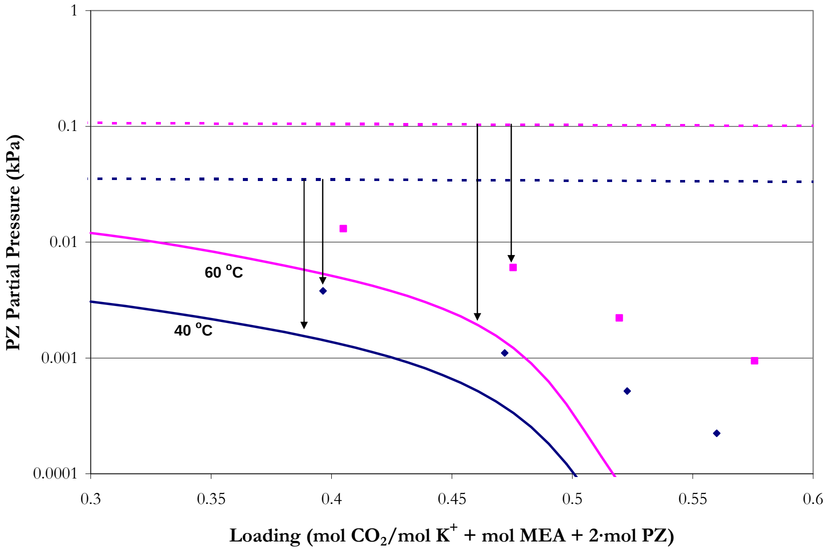

Figure 18.3-19. Comparison of Experimental PZ Volatility to Combined Model Predictions for 5 m K⁺ + 3.5 m MEA + 2 m PZ at 40 and 60 °C. Points: ♦, 40 °C, ■, 60 °C. Solid Lines: Combined elecNRTL Model Predictions. Dash Lines: Raoult's Law Approximations.

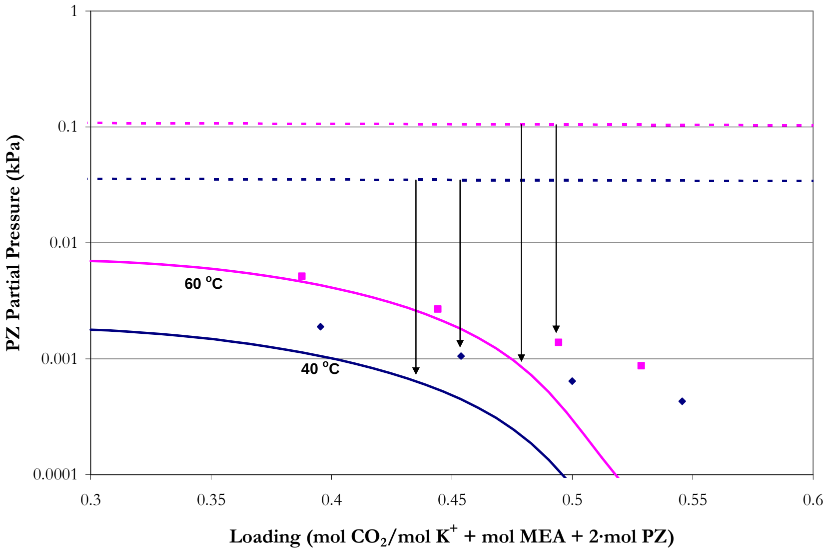

Figure 18.3-20. Comparison of Experimental PZ Volatility to Combined Model Predictions for 2.5 m K⁺ + 3.5 m MEA + 2 m PZ at 40 and 60 °C. Points: ♦, 40 °C, ■, 60 °C. Solid Lines: Combined elecNRTL Model Predictions. Dash Lines: Raoult's Law Approximations.

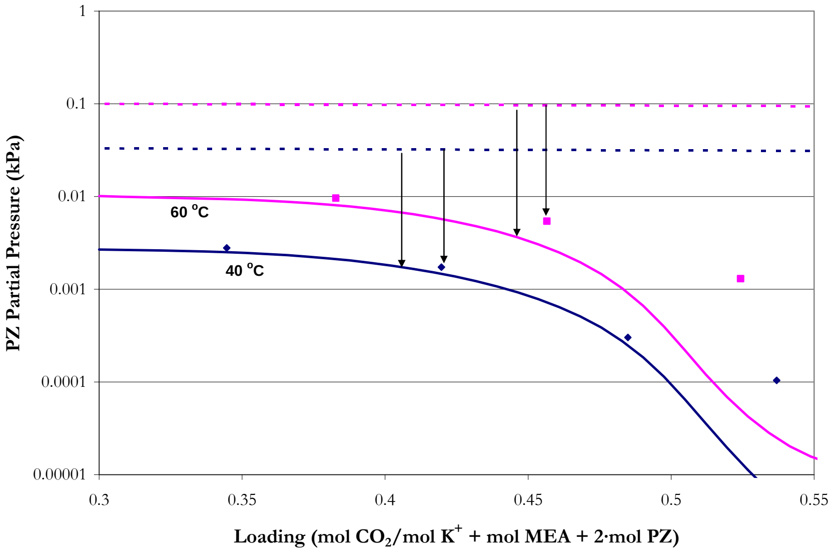

Figure 18.3-21. Comparison of Experimental PZ Volatility to Combined Model Predictions for 5 m K^+ + 7 m MEA + 2 m PZ at 40 and 60 °C. Points: ♦, 40 °C, ■, 60 °C. Solid Lines: Combined elecNRTL Model Predictions. Dash Lines: Raoult's Law Approximations.

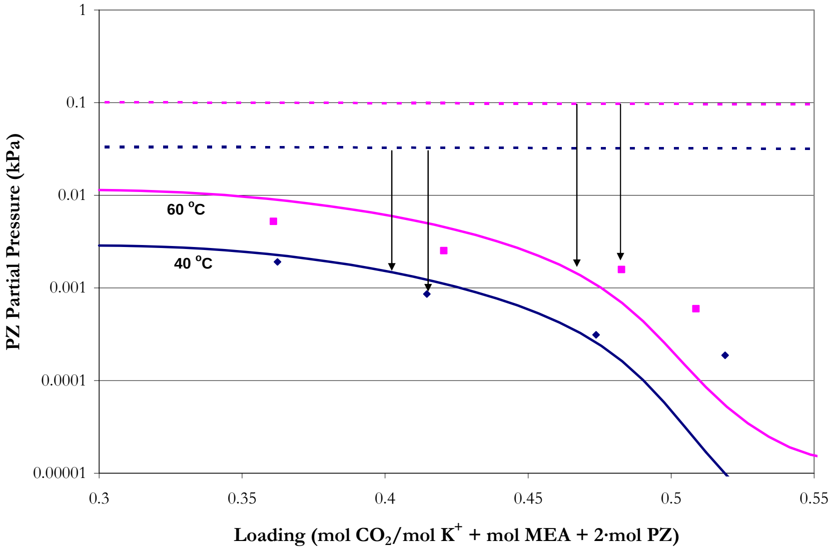

Figure 18.3-22. Comparison of Experimental PZ Volatility to Combined Model Predictions for 2.5 m K^+ + 7 m MEA + 2 m PZ at 40 and 60 °C. Points: ♦, 40 °C, ■, 60 °C. Solid Lines: Combined elecNRTL Model Predictions. Dash Lines: Raoult's Law Approximations.

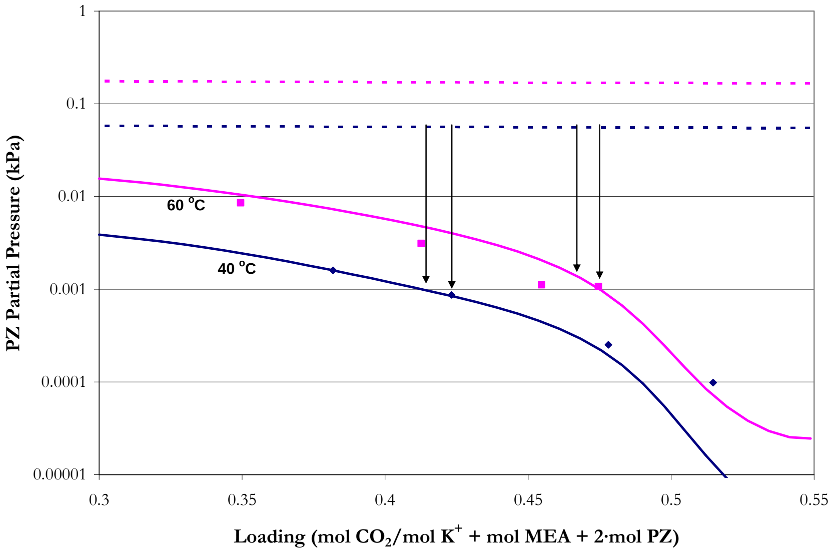

Figure 18.3-23. Comparison of Experimental PZ Volatility to Combined Model Predictions for 2.5 m K^+ + 7 m MEA + 3.6 m PZ at 40 and 60 °C. Points: ♦, 40 °C, ■, 60 °C. Solid Lines: Combined elecNRTL Model Predictions. Dash Lines: Raoult's Law Approximations.

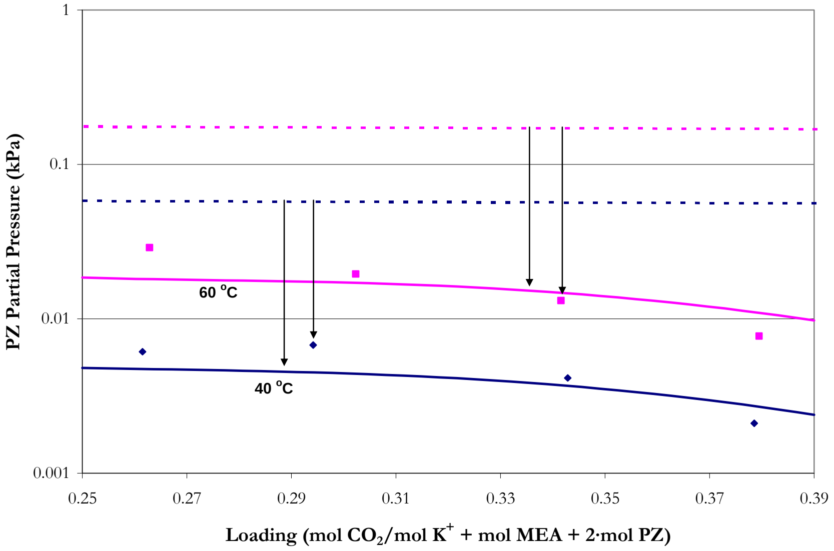

Figure 18.3-24. Comparison of Experimental PZ Volatility to Combined Model Predictions for 5 m K^+ + 7 m MEA + 3.6 m PZ at 40 and 60 °C. Points: ♦, 40 °C, ■, 60 °C. Solid Lines: Combined elecNRTL Model Predictions. Dash Lines: Raoult's Law Approximations.

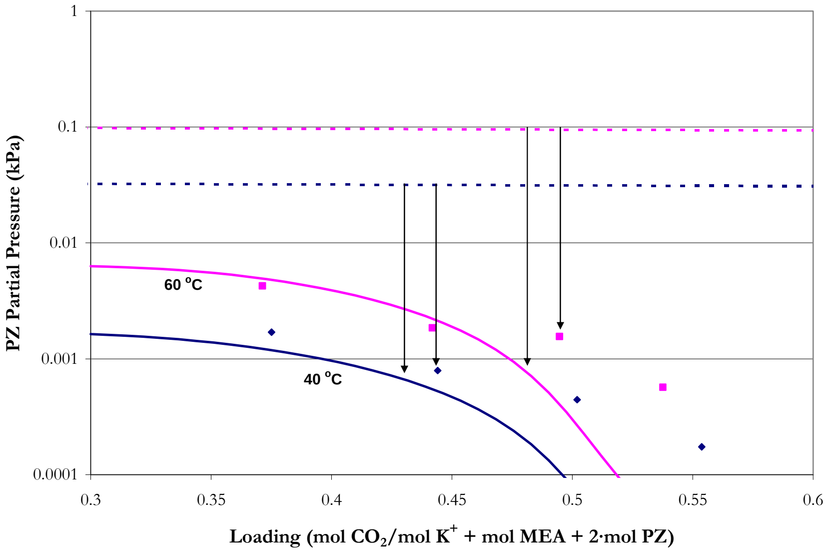

Figure 18.3-25. Comparison of Experimental PZ Volatility to Combined Model Predictions for 2.5 m K^+ + 3.5 m MEA + 1.8 m PZ at 40 and 60 °C. Points: ♦, 40 °C, ■, 60 °C. Solid Lines: Combined elecNRTL Model Predictions. Dash Lines: Raoult's Law Approximations.

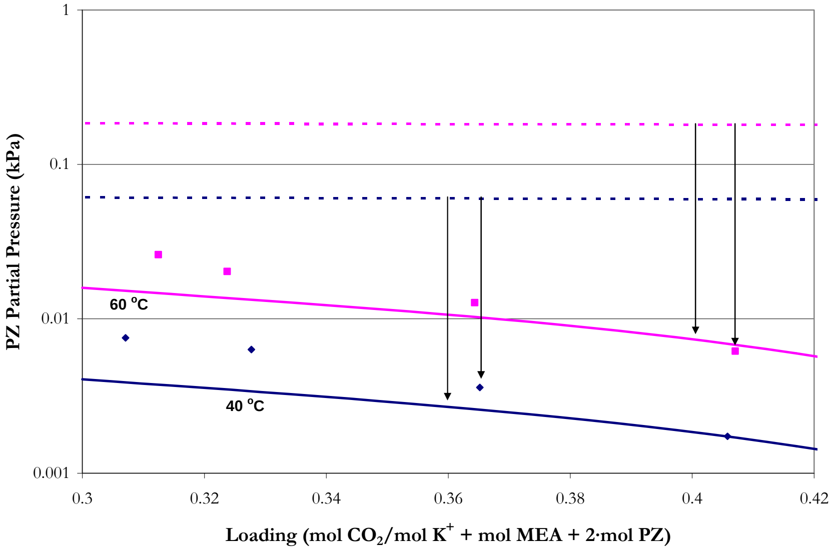

Figure 18.3-26. Comparison of Experimental PZ Volatility to Combined Model Predictions for 5 m K^+ + 3.5 m MEA + 3.6 m PZ at 40 and 60 °C. Points: ♦, 40 °C, ■, 60 °C. Solid Lines: Combined elecNRTL Model Predictions. Dash Lines: Raoult's Law Approximations.

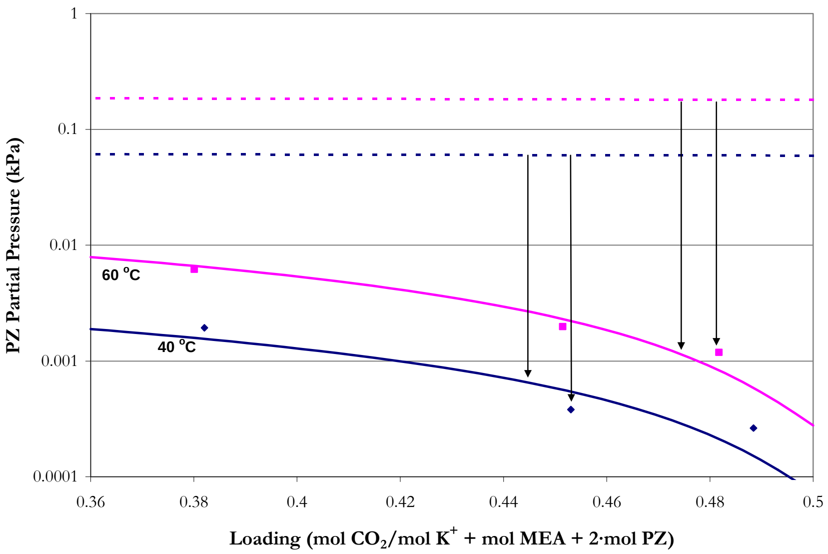

Figure 18.3-27. Comparison of Experimental PZ Volatility to Combined Model Predictions for 2.5 m K^+ + 3.5 m MEA + 3.6 m PZ at 40 and 60 °C. Points: ♦, 40 °C, ■, 60 °C. Solid Lines: Combined elecNRTL Model Predictions. Dash Lines: Raoult's Law Approximations.

18.4 Conclusions

In conclusion, in this work we have illustrated an approach to predicting the vapor phase behavior of CO_2, MEA and PZ associated with the H2O-K_2CO_3-MEA-PZ-CO_2 system. For the H_2O-K_2CO_3-MEA-PZ-CO_2 system, all of the practical binary interaction parameters and state properties used to describe interactions between molecule-molecule, molecule-electrolyte, and electrolyte-electrolyte already were assigned in previous chapters. Thus, the H_2O-K_2CO_3-MEA-PZ-CO_2 system illustrated the final test for the predictive capabilities of the combined model. As a result, the combined model moderately described most of the H_2O-K_2CO_3-MEA-PZ-CO_2 property even though, the combined model did fall short in describing the CO_2 solubility in 5 m K^++3.5 m MEA+2 m PZ, 2.5 m K^++3.5 m MEA+2 m PZ, 5 m K^++7 m MEA+2 m PZ, and 5 m K^++3.5 m MEA+3.6 m PZ. The combined model did do an moderate job in predicting the amine volatility for all of the solvents studied in this work. Results presented in this work would suggest that there may be a need for parameter optimization to improve the statistical fit of the experimental data as described by the combined model.

In terms of differential capacity, 7 m MEA demonstrated a greater differential capacity as compared to piperazine or other mixed salt-amine systems. For mixed salt-amine systems composed of 2.5 m K^+ did exhibited an increase in the differential capacity as compared to similar systems containing 5 m K^+. Overall, 2.5 m K^++7 m MEA+2 m PZ exhibited the largest differential capacity equal to 0.17 out of nine solvents studied as part of this work. In addition, Table 18.2-3 illustrated that 7 m MEA demonstrated a greater range of volatility at 40 °C as compared to piperazine or other mixed salt-amine systems. For different combinations of potassium + 7 m MEA + piperazine; the relative volatility of MEA remained between 55 and 27 ppm_v over the range of CO_2 partial pressures. When the MEA concentration decreased from 7 m to 3.5 m, the volatility of MEA volatility decreased due to the decease in the total alkalinity of the solvent and is reflected in the MEA volatility deceasing by a factor of 2. However, PZ volatility remained approximately constant and is consistent with effects exhibited in the H_2O-MEA-PZ systems, where large changes in the solution alkalinity may not have an effect on the volatility of PZ.

One of the goals of this work was to be able to build a consistent and rigorous thermodynamic model to describe the base systems. Then combine the three models and test the predictive behavior of the combined model. Table 18.3-1 illustrated that a simple exchange between binary interaction parameters, as utilized in previous chapters, to create a combined model for the H_2O-K_2CO_3-MEA-PZ-CO_2 system **did not** result in an adequate fit of the experimental data. We would recommend that future work interested in the H_2O-K_2CO_3-MEA-PZ-CO_2 system to optimize the binary interaction parameters to capture systematic trends presented within the experimental data.

CHAPTER XIX

Overall Differential Capacity and Amine Volatility

19.1 Introduction

In this work, we have completed a comprehensive review of experimental data collected and have created a rigorous and consistent thermodynamic model to describe the sub-component systems for the H_2O-K_2CO_3-MEA-PZ-CO_2 system. Some parts of the model adequately described systematic trends better than others, but on the whole we are satisfied with the overall result. At this point, we can use the experimental data collected in this work and illustrate systematic trends for the differential capacity and amine volatility associated with each solvent.

19.2 Differential Capacity

We can quantify the effects of CO_2 solubility in the systems studied in this work by illustrating trends in experimental CO_2 solubility at 60 °C based on the differential capacity of the solvent between the range of 0.01 and 1.0 kPa as shown in Table 19.2-1.

Table 19.2-1. Differential Capacity Based on Experimental CO_2 Solubility at 60 °C Between the Range of 0.01 and 1.0 kPa from this work.

				Differential Capacity			
K+ (m)	MEA (m)	PZ (m)	TA	α	β	γ	δ
-	7	-	7	0.34	2.38	-	0.34
-	3.5	-	3.5	0.32	1.11	-	0.32
-	11	-	11	0.32	3.50	-	0.32
-	-	0.9	1.8	0.21	0.38	0.21	-
-	-	2	4	0.23	0.90	0.23	-
-	-	2.5	5	0.24	1.19	0.24	-
-	-	3.6	7.2	0.22	1.60	0.22	-
-	-	5	10	0.20	1.96	0.20	-
-	3.5	2	7.5	0.24	1.82	0.46	0.52
-	3.5	3.6	10.7	0.24	2.60	0.36	0.74
-	7	2	11	0.26	2.82	0.71	0.40
-	7	3.6	14.2	0.22	3.08	0.43	0.44
2.5	3.5	-	6	0.15	0.87	-	0.25
2.5	7	-	9.5	0.16	1.50	-	0.21
5	3.5	-	8.5	0.12	1.06	-	0.30
5	7	-	12	0.11	1.27	-	0.18
5	-	2.5	10	0.13	1.32	0.26	-
3.6	-	0.6	4.8	0.15	0.71	0.59	-
3.6	-	1.8	7.2	0.14	1.02	0.28	-
3.6	-	3.6	10.8	0.15	1.58	0.22	-
6	-	1.2	8.4	0.13	1.06	0.44	-
5	-	3.6	12.2	0.12	1.43	0.20	-
5	-	2	9	0.13	1.18	0.29	-
2.5	-	3.6	9.7	0.19	1.83	0.25	-
2.5	-	2	6.5	0.16	1.06	0.27	-
5	3.5	2	12.5	0.13	1.57	0.39	0.45
2.5	3.5	2	10	0.16	1.60	0.40	0.46
5	7	2	16	0.15	2.34	0.59	0.33
2.5	7	2	13.5	0.16	2.21	0.55	0.32
2.5	7	3.6	16.7	0.13	2.25	0.31	0.32
5	7	3.6	19.2	0.14	2.60	0.36	0.37
2.5	3.5	1.8	9.6	0.16	1.50	0.42	0.43
5	3.5	3.6	15.7	0.12	1.84	0.26	0.52
2.5	3.5	3.6	13.2	0.14	1.88	0.26	0.54

TA: Total Alkalinity, α: mol CO_2/Total Alkalinity, β: mol CO_2/kg-H_2O, γ: mol CO_2/mol MEA, δ: mol CO_2/2·mol PZ.

We can illustrate trends presented in Table 19.2-1 for the differential capacity of each solvent normalized by the kilograms of H_2O within the solvent as shown in Figure 19.2-1. Ordinary least squared (OLS) approximations were added for clarification.

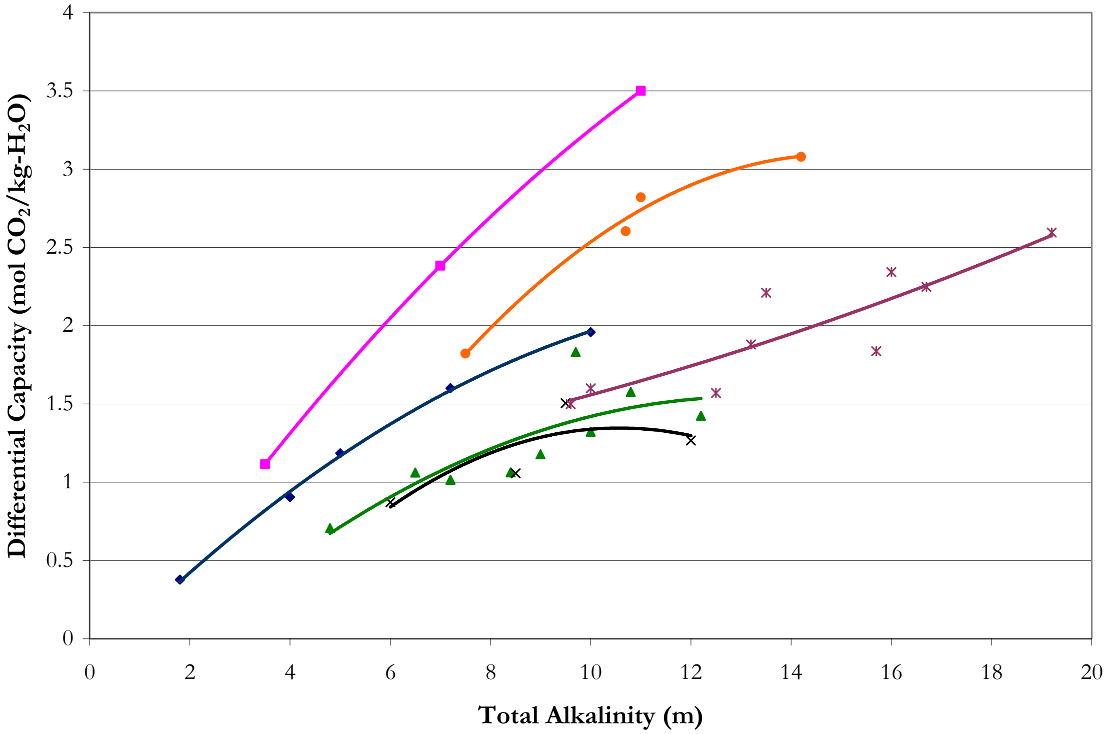

Figure 19.2-1. Differential Capacity of Each Solvent Normalized by the Kilograms of Water. Points: ■, H_2O-MEA-CO_2, ♦, H_2O-PZ-CO_2, ●, H_2O-MEA-PZ-CO_2, ▲, H_2O-K_2CO_3-PZ-CO_2, ×, H_2O-K_2CO_3-MEA-CO_2, *, H_2O-K_2CO_3-MEA-PZ-CO_2. Lines: OLS Approximations.

Figure 19.2-1, vis-à-vis Table 19.2-1, illustrates that very few solvent compositions have a greater differential capacity than 7 m MEA; specifically only five solvents (11 m MEA, 3.5 m MEA + 3.6 m MEA, 7 m MEA + 2 m PZ, 7 m MEA + 3.6 m PZ, and 5 m K^+ + 7 m MEA + 3.6 m PZ) demonstrate a greater differential capacity as compared to 7 m MEA. Piperazine may exhibit a possible maximum differential capacity of 2.21 at a piperazine concentration of 7.3 m based on a forward extrapolation of the OLS curve. For the two mixed salt-amine systems, only systems composed of piperazine exhibit an increase in the differential capacity as compared to similar systems containing monoethanolamine.

19.3 Amine Volatility

Experimental amine volatility at 40 °C for each solvent can then be compared based on a CO_2 partial pressure from 0.01 to 0.1 kPa as illustrated in Figure 19.3-1 and Figure 19.3-2 based on experimental MEA and PZ volatility. Table 19.3-1 compares the amine volatility for the 37 mixed salt and or amine systems in this work at 40 °C.

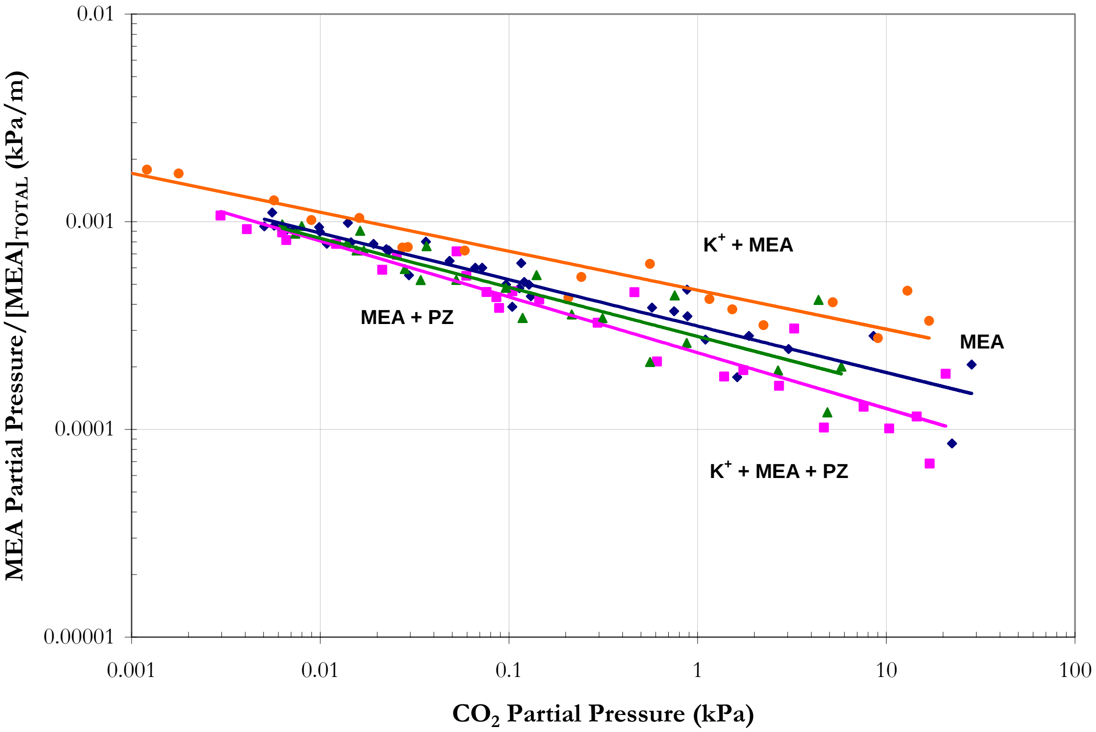

Figure 19.3-1. Comparison of Normalized MEA Volatility versus CO_2 Solubility at 40 °C from this work. Points: ♦, H_2O-MEA-CO_2, ▲, H_2O-MEA-PZ-CO_2, ●, H_2O-K_2CO_3-MEA-CO_2, ■, H_2O-K_2CO_3-MEA-PZ-CO_2. Lines: OLS Approximations.

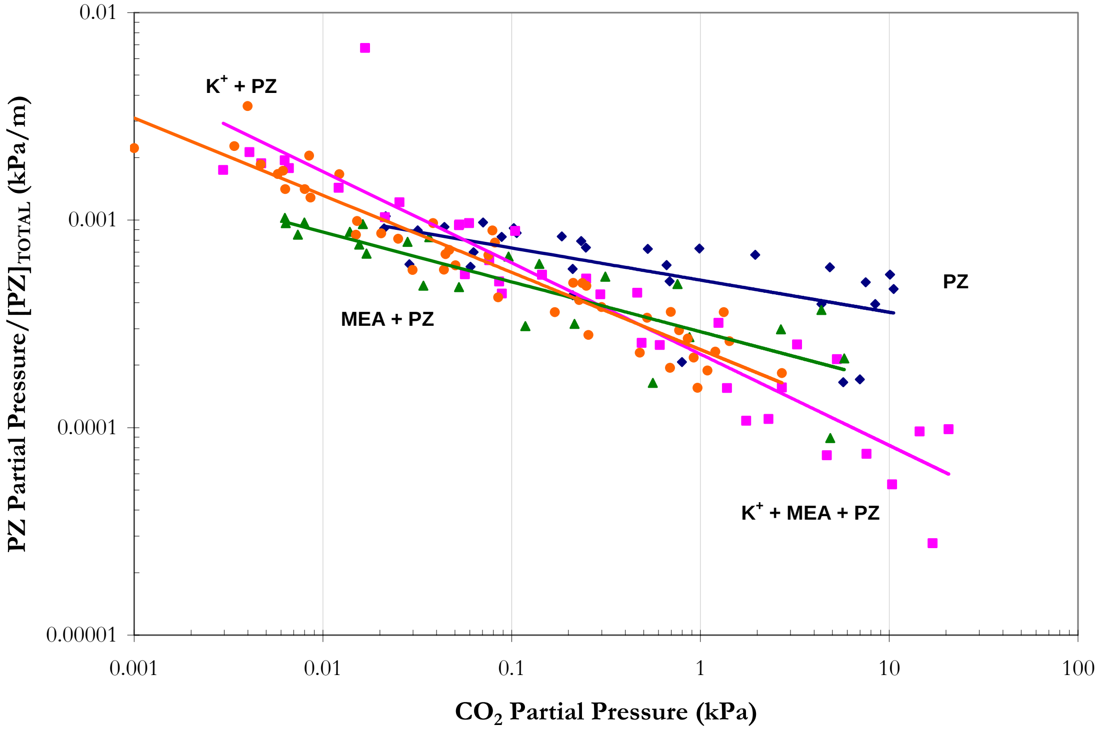

Figure 19.3-2. Comparison of Normalized PZ Volatility versus CO_2 Solubility at 40 °C from this work. Points: ♦, H_2O-PZ-CO_2, ▲, H_2O-MEA-PZ-CO_2, ●, H_2O-K_2CO_3-PZ-CO_2, ■, H_2O-K_2CO_3-MEA-PZ-CO_2. Lines: OLS Approximations.

Table 19.3-1. Comparison of Experimental Amine Volatility Evaluated at a CO_2 Partial Pressure from 0.01 to 0.1 kPa at 40 °C.

K+ (m)	MEA (m)	PZ (m)	TA	P^{MEA} (ppm$_v$)	P^{PZ} (ppm$_v$)
-	7	-	7	58 - 38	
-	3.5	-	3.5	39 - 31	
-	11	-	11	84 - 49	
-	-	0.9	1.8		10 - 8
-	-	2	4		22 - 18
-	-	2.5	5		25 - 20
-	-	3.6	7.2		34 - 24
-	-	5	10		37 - 24
-	3.5	2	7.5	32 - 24	18 - 14
-	3.5	3.6	10.7	26 - 17	25 - 17
-	7	2	11	56 - 37	18 - 14
-	7	3.6	14.2	55 - 34	30 - 18
2.5	3.5	-	6	41 - 29	
2.5	7	-	9.5	74 - 44	
5	3.5	-	8.5	43 - 25	
5	7	-	12	59 - 41	

K+ (m)	MEA (m)	PZ (m)	TA	P^{MEA} (ppm$_v$)	P^{PZ} (ppm$_v$)
5	-	2.5	10		32 - 13
3.6	-	0.6	4.8		10 - 4
3.6	-	1.8	7.2		22 - 12
3.6	-	3.6	10.8		36 - 15
6	-	1.2	8.4		22 - 6
5	-	3.6	12.2		54 - 39
5	-	2	9		27 - 11
2.5	-	3.6	9.7		29 - 16
2.5	-	2	6.5		15 - 9
5	3.5	2	12.5	25 - 15	24 - 9
2.5	3.5	2	10	32 - 20	29 - 14
5	7	2	16	60 - 27	39 - 11
2.5	7	2	13.5	54 - 28	32 - 12
2.5	7	3.6	16.7	54 - 25	60 - 17
5	7	3.6	19.2	54 - 29	49 - 23
2.5	3.5	1.8	9.6	37 - 22	33 - 14
5	3.5	3.6	15.7	25 - 14	52 - 17
2.5	3.5	3.6	13.2	31 - 16	68 - 21

TA: Total Alkalinity

Figure 19.3-1, vis-à-vis Table 19.3-1, illustrates that with the addition of potassium to a ternary mixture of H_2O-MEA-CO_2, the volatility of MEA increases whereas with the addition of piperazine and or potassium the volatility of MEA decreased. Over the CO_2 partial pressure range of 0.01 to 0.1 kPa, the volatility of MEA can be approximated to be 50 ppm$_v$ at 40 °C for any solvent composition studied in this work within an absolute error of approximately ± 15 percent. In terms of PZ volatility, with the addition of potassium and potassium + MEA to a ternary mixture of H_2O-PZ-CO_2, the volatility of PZ increases at low CO_2 partial pressures and has the opposite effect at high CO_2 partial pressures. On the other hand, with the addition of MEA, the volatility of PZ decreases by a factor of approximately 1.5. Over the CO_2 partial pressure range of 0.01 to 0.1 kPa the volatility of PZ can be approximated to be approximately 20 ppm$_v$ at 40 °C for any solvent composition studied in this work within an absolute error of approximately ± 30 percent.

19.4 Conclusions

In this work, we have illustrated trends associated with differential capacity and amine volatility for each solvent concentration studied. We have been able to generalize systematic trends associated with the experimental data where very few solvent compositions exhibited a greater differential capacity as compared to 7 m MEA at 60 °C. Piperazine was shown to have the possibility to exhibit a maximum differential capacity of 2.21 at a piperazine concentration of 7.3 m based on a forward extrapolation of the OLS curve, but this would need to be validated through additional experimentation. We would recommend that additional CO_2 solubility and PZ volatility measurements be carried out for piperazine concentrations greater than 5 m but less than 10 m. Concentrations greater than 10 m PZ would be exponentially difficult to handle in terms of avoiding salt precipitation in the low temperature atmospheric pressures reactor used in this work to determine the CO_2 solubility and amine volatility at 40 and 60 °C. Generally, over the CO_2 partial pressure range of 0.01 to 0.1 kPa, the volatility of MEA and PZ can be approximated to be 50 ppm_v and 20 ppm_v at 40 °C for any solvent composition studied within an absolute error of approximately ± 15 and 30 percent, respectively.

CHAPTER XX

Summary and Recommendations

At the end of each chapter, we gave detailed conclusions and recommendations on each topic covered in this work. This chapter provides a summary based on previous chapters and offers suggestions for future work.

In this work we developed a new vapor-liquid equilibrium apparatus to measure carbon dioxide, amine, and water vapor pressures at 40 and 60 °C for aqueous combinations of potassium carbonate (K_2CO_3), potassium bicarbonate ($KHCO_3$), monoethanolamine (MEA), piperazine (PZ), and carbon dioxide (CO_2). We found that the volatility of MEA and PZ can be approximated at 50 ppm_v and 20 ppm_v at 40 °C for any solvent composition studied in this work, within an absolute error of approximately ± 15 and 30 percent, respectively, over the CO_2 partial pressure range of 0.01 to 0.1 kPa. We have also generalized systematic trends associated with the experimental data; very few solvent compositions exhibited a greater differential capacity than 7 m MEA at 60 °C. Piperazine exhibited a possible maximum differential capacity of 2.21 mole CO_2/kg-H_2O at a concentration of 7.3 m, but this would need to be validated through addition experimentation. We recommend that additional CO_2 solubility and PZ volatility measurements be carried out for piperazine concentrations greater than 5 m but less than 10 m. Concentrations greater than 10 m PZ would be exponentially difficult to handle in terms of avoiding salt precipitation in the low temperature atmospheric pressure reactor used in this work to determine the CO_2 solubility and amine volatility at 40 and 60 °C.

As in international collaboration between The University of Texas and the Norwegian University of Science and Technology, Kim (2007) determined the differential enthalpy of CO_2 absorption for aqueous combinations of potassium carbonate, potassium bicarbonate, monoethanolamine, piperazine, and carbon dioxide, based on a consistent experimental method she developed for monoethanolamine [Kim et al. (2007)], from 40 to 120 °C for use in this work. In addition, we developed a consistent method, based on the ASTM standard, to measure the specific heat capacity for a number of similar solvent combinations. We found that the enthalpy of CO_2 absorption increased in temperature because the apparent partial heat capacity of CO_2 is small due to the heat capacities of the amine carbamate and the hydrated amine are approximately equal over a given temperature interval.

By using a differential scanning calorimeter, we determined the dissolution temperature for aqueous mixtures of unloaded piperazine. When this data was modeled, we found that piperazine hexahydrate ($PZ \cdot 6H_2O$) would not precipitate from solutions of concentrated piperazine, greater than 5 m PZ, over a loading range between 0.25 to 0.45 mole CO_2/2·mol PZ. In addition, we were able to identify and characterize the presence of three solid phases, in aqueous mixture combinations of potassium carbonate, potassium bicarbonate, piperazine, and carbon dioxide, in the H_2O-PZ system as piperazine hexahydrate and in the H_2O-K_2CO_3-PZ-CO_2 system as potassium bicarbonate ($KHCO_3$) and dipotassium piperazine dicarbamate ($K_2PZ(COO)_2$) through a unit cell x-ray diffraction analysis performed by Lynch (2007).

Finally, we developed a rigorous and consistent thermodynamic model in Aspen Plus^{TM} 2006.5 which adequately predicts CO_2 solubility, amine volatility, enthalpy of CO_2 absorption, and specific heat capacity for the base sub-component systems in aqueous mixture combinations of potassium carbonate, potassium bicarbonate, monoethanolamine, piperazine, and carbon dioxide. Due to the broad scope of this work, the model does not represent a comprehensive thermodynamic model for all systems studied in this work and therefore should not be relied upon for extrapolation outside the bounds of this work.

APPENDIX A

CO_2 Analysis via Titration

A.1 Experimental Method

The CO_2 loading analysis was preformed by using two parallel liquid samples each titrated for CO_2 and total alkalinity using barium chloride ($BaCl_2$) precipitation and sulfuric acid (H_2SO_4), respectively, using a Metrohm 720 SM Titrino automatic titrator. The relative standard uncertainty in the loadings was estimated to be ± 2 %.

A.2 CO_2 Analysis Procedure

Sample Preparation

1. Take a 250 ml Erlenmeyer flask and dispense 25 ml of 0.5 M $BaCl_2$ and 50 ml of 0.1 M NaOH from the automatic dispensers.
2. Weigh the flask and tare the scale.
3. Use an automatic pipette and dispense 0.25 ml of sample into the Erlenmeyer flask and weight.
4. Record the weight of the sample.
5. Seal the flask with a stopper with vapor tube.
6. Place the flask on the warming plate and bring to a boil.
7. Boil for ~4 minutes.
    a. $BaCO_3$ will precipitate out of solution by the given reaction:

$$Ba^{2+} + CO_2 + 2OH^- = BaCO_3(s) + H_2O$$

8. After 4 minutes, transfer the flask to the cooling tray and wait 5 minutes.
9. After 5 minutes replace the stopper with a square of paraffin wax and seal the flask.
10. After 5 minutes the flask should be at room temperature and can then be transported to the vacuum filtration apparatus.

CO$_2$ Filtration

1. Take a silicone filter and place it in the center the vacuum filter.
    a. The thickness of filter is 0.6 micrometer with a diameter of 47 millimeters.
2. Start the vacuum filter.
3. Wet the filter with a little bit of DI water.
4. Place the top of the filter and clap the apparatus together.
5. Pour your cooled solution into the middle of filter.
6. Use DI water to get the last drop of solution from the flask rim.
7. Go through 3 - 100 ml washings of the flask.
8. Carefully take off the top of the vacuum filter and place it onto the work bench.
9. Remove the filter and place it into a 100 ml beaker.
10. Place the top of the vacuum filter on top of the 100 beaker and rinse the top with 50 ml of DI water.
11. Turn off the suction.

CO$_2$ Titration

1. Weigh the flask and tare the scale.
2. For Sample A and B, dispense 40 ml of a 0.1 N HCl solution using the automatic dispenser.
3. For the Blank, dispense 10 ml of a 0.1 N HCl solution using the automatic dispenser.
4. Barium carbonate will then react with the hydrochloric acid liberating CO_2 into the solution by the following reaction:

$$BaCO_3 + 2HCl = BaCl_2 + CO_2 + H_2O$$

5. Record the weight of the acid.
6. Place on the magnetic stirrer and allow the $BaCO_3$ to dissolve completely.
7. After the $BaCO_3$ has completely dissolved, place the flask on the autotitrator.
8. We are going to titrate the solution with 0.1 M NaOH until we get a pH=5.2
    b. A method has been programmed into the autotitrator to stops automatically after measuring a pH = 5.2 for a given period of time.
9. Rinse the electrode and the NaOH dispenser with DI water.

10. Tap dry with a paper towel.
11. Push the dose button twice to clear the line.
12. Push the fill button to fill the reservoir.
13. Place the flask on the magnetic stirrer and lower the electrode into the solution.
14. Be careful not to allow the electrode to touch the magnetic stirrer.
15. Push start.
16. After the titration is complete, record the final amount of NaOH.
17. Use the following equation to calculate the CO_2 concentration:

$$CO_2\left(\text{mole/kg-soln}\right)=\frac{1}{20}\cdot\frac{HCl\left(gm\right)-NaOH\left(ml\right)-\left[\text{Blank }HCl\left(gm\right)-\text{Blank NaOH}\left(ml\right)\right]}{Sample\left(gm\right)}$$

A.3 Total Alkalinity Analysis Procedure

Sample Preparation

1. Take a 100 ml beaker and dispense 60 ml of DI water from the automatic dispenser.
2. Weigh the beaker and tare the scale.
3. Use an automatic pipette and dispense 0.5 ml of sample into the beaker and weight.
4. Record the weight of the sample.
5. Place the beaker on the autotitrator with a magnetic stir rode in the bottom of the beaker.
6. We are going to titrate the solution with 0.1 M H_2SO_4 until we get a pH~2.00
    c. A method has not been programmed into the autotitrator to stop automatically, so you will have to monitor the titration results.
7. Rinse the electrode and the H_2SO_4 dispenser with DI water.
8. Tap dry with a paper towel.
9. Push the dose button twice to clear the line.
10. Push the fill button to fill the reservoir.
11. Place the flask on the magnetic stirrer and lower the electrode into the solution.
12. Be careful not to allow the electrode to touch the magnetic stir rode.
13. Push start.
14. After the titration is complete, record the amount of H_2SO_4 and the measured pH at each equivalence point. An example of a typical titration curve for a loaded amine solution is shown in Figure A.3-1.

Please note: Since CO_2 species are present in the titration; at point "A" CO_2 species are reacting with the acid to form bicarbonate. On the other side of point "A" the bicarbonate reacts with more acid to form CO_2 (g). With increasing amounts of acid, more of amine species are protanated where beyond point "B" most of the amine species are converted to the ionic form.

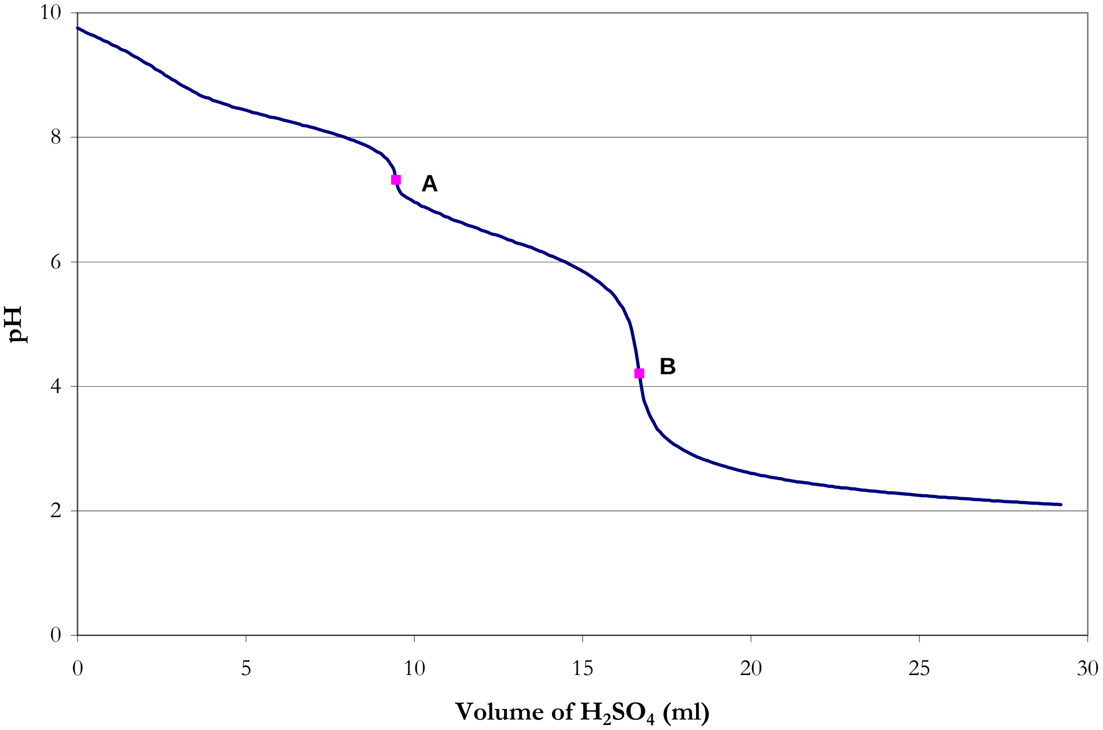

Figure A.3-1. Example Titration Curve for a Loaded Amine Solution.

15. Use the following equation to calculate the total alkalinity at Point B:

$$\text{Total Alkalinity}\left(\text{mole/kg-soln}\right)=\frac{H_2SO_4\left(ml\right)\cdot 0.2}{Sample\left(gm\right)}$$

Please note: For samples containing a primary and a secondary amine, the total alkalinity will be equal to the primary amine plus two times the secondary amine (i.e. MEA + 2PZ).

A.4 Total Piperazine Analysis Procedure

Sample Preparation

1. Take the Total Alkalinity 100 ml beaker and place the flask on the warming plate and bring to a boil.
2. Boil for ~2 minutes.
3. After 2 minutes, transfer the beaker to the cooling tray and wait 5 minutes until the beaker returns to room temperature.

4. We are going to titrate the solution with 0.1 M NaOH until we get a pH=10.0
    d. A method has not been programmed into the autotitrator to stop automatically, so you will have to monitor the titration results.
5. Rinse the electrode and the NaOH dispenser with DI water.
6. Tap dry with a paper towel.
7. Push the dose button twice to clear the line.
8. Push the fill button to fill the reservoir.
9. Place the flask on the magnetic stirrer and lower the electrode into the solution.
10. Be careful not to allow the electrode to touch the magnetic stir rode.
11. Push start.
16. After the titration is complete, record the amount of NaOH and the measured pH at each equivalence point. An example of a typical back titration curve for a loaded amine solution is shown in Figure A.4-1.

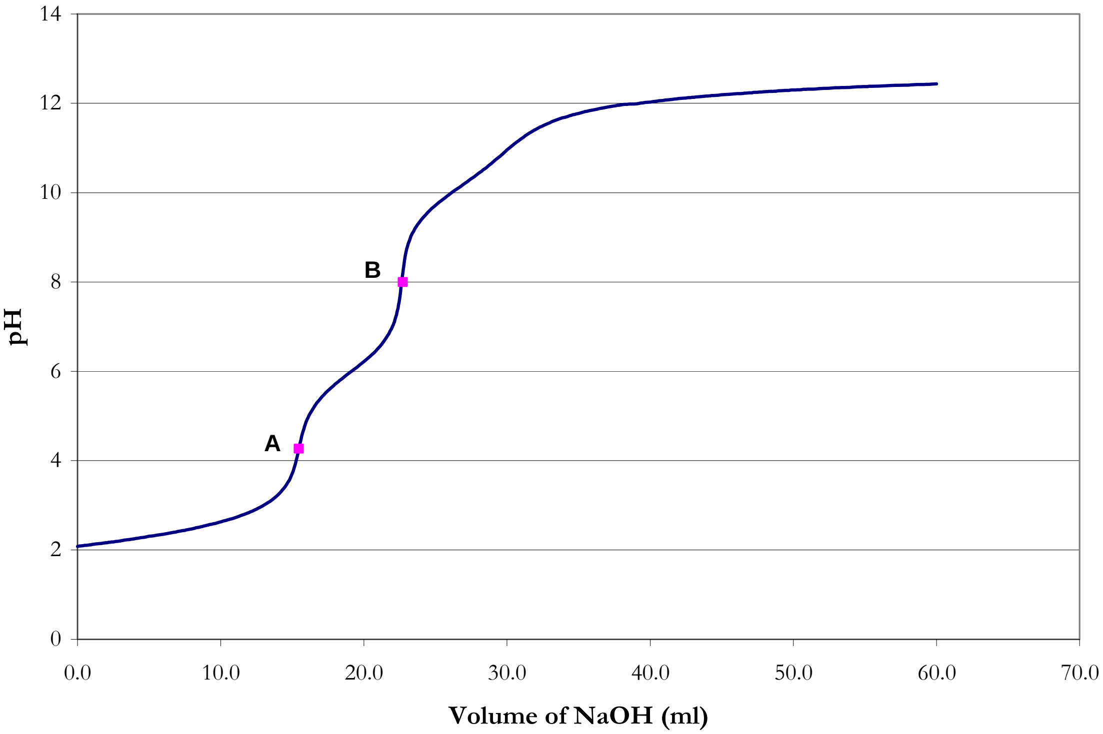

Figure A.4-1. Example Back Titration Curve for a Loaded Amine Solution.

Please note: A back titration is only required when your sample contains two different amines (i.e. MEA and PZ) or salt plus amine. In Figure A.4-1, the measured pH to the left of point "A" represents a buffer between $H^+ \rightarrow H_2O$. Between points "A" and "B" represents another buffer region between $PZH^{+2} \rightarrow PZH^+$ and the region to the right of point "B" represent a buffer between $PZH^+ \rightarrow PZ$. By taking the difference between points

"B" and "A" we can represent the total amount of piperazine that has been converted from PZH^{+2}.

12. Use the following equation to calculate the total piperazine concentration:

$$\text{Total Piperazine}\left(\text{mole/kg-soln}\right)=\frac{\left[NaOH^{pH=7}\left(ml\right)-NaOH^{pH=4}\left(ml\right)\right]\cdot 0.1}{Sample\left(gm\right)}$$

We can now use both equations to solve for the amount of primary amine (i.e. MEA) in our sample by the following equation:

$$MEA\left(\text{mole/kg-soln}\right)=TA-2\cdot TPZ$$

APPENDIX B

CO_2 Analysis via Acidic Evolution

B.1 Reagents

Solution standards were made from sodium carbonate (Na_2CO_3) obtained from Acros Organics, 99.5 % pure, without further purification. Nitrogen (N2) gas was obtained from the Cryogenics Laboratory at The University of Texas at Austin at a purity of 99.0 mol%.

B.2 Experimental Method

CO_2 loading analysis was determined by analyzing for total inorganic carbon by acidic evolution, 30 wt% phosphoric acid (H_2PO_4), into a Horiba PIR 2000 carbon dioxide analyzer shown in Figure B.2-1.

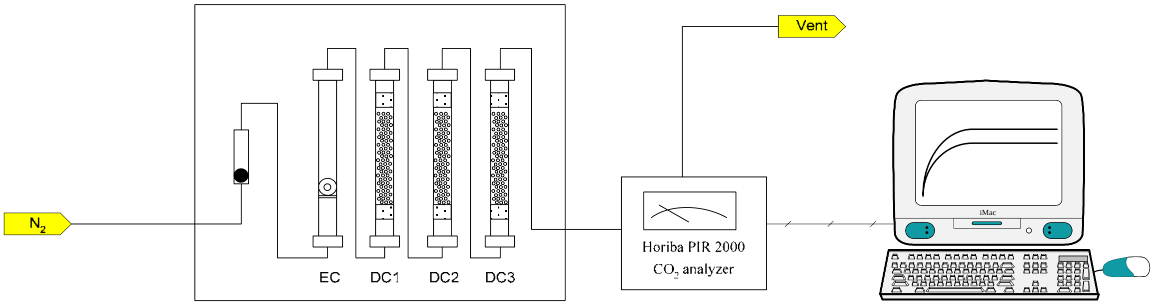

Figure B.2-1. Process Flow Diagram for CO_2 Analysis.

During the analysis, N_2 gas flows through a evolution column (EC) containing ~1 cm^3 of H_2PO_4. When a standard (1000 ppmv Na_2CO_3) or unknown sample is injected into the EC, CO_2 is released through the following chemical reactions:

$$2H_2O \leftrightarrow H_3O^+ + OH^- \qquad Kw = \left[H_3O^+\right]\left[OH^-\right] \tag{1}$$

For the polyfunctional acid:

$$H_3PO_4 + H_2O \leftrightarrow H_2PO_4^- + H_3O^+ \qquad \mathrm{K}_{a1}^{a} = \frac{\left[H_3O^+\right]\left[H_2PO_4^-\right]}{\left[H_3PO_4\right]} \tag{2}$$

$$H_2PO_4^- + H_2O \leftrightarrow HPO_4^{2-} + H_3O^+ \qquad \mathrm{K}_{a2}^{a} = \frac{\left[H_3O^+\right]\left[HPO_4^{2-}\right]}{\left[H_2PO_4^-\right]} \tag{3}$$

$$HPO_4^{2-} + H_2O \leftrightarrow PO_4^{3-} + H_3O^+ \qquad \mathrm{K}_{a3}^{a} = \frac{\left[H_3O^+\right]\left[PO_4^{3-}\right]}{\left[HPO_4^{2-}\right]} \tag{4}$$

For the polyfunctional base:

$$HCO_3^- + H_2O \leftrightarrow H_3O^+ + CO_3^{2-} \qquad \mathrm{K}_{a1}^{b} = \frac{\left[H_3O^+\right]\left[CO_3^{2-}\right]}{\left[HCO_3^-\right]} \tag{5}$$

$$CO_2\left(aq\right) + 2H_2O \leftrightarrow H_3O^+ + HCO_3^- \qquad \mathrm{K}_{a2}^{b} = \frac{\left[H_3O^+\right]\left[HCO_3^-\right]}{\left[CO_2\right]} \tag{6}$$

B.3 Sample Preparation

For each sample to be analyzed, the total dissolved CO_2 concentration in each sample should be within the range of 15 – 150 ppm_v of total carbon. If the sample has a high total CO_2 concentration, the sample should be diluted in order for the analyzer response to stay within the calibration range.

Sample Dilution

1. Weigh a dry 25 ml volumetric flask and tare the scale.
2. Record the weight of the flask.
3. Use a glass pipette and dispense ~25 ml of Ultra pure DI-water so that the meniscus or the curved upper surface of the liquid is just touching the 25 ml calibration line.
4. Record the weight of the sample.
5. Use an automatic pipette; dispense 100 μl of your sample into the volumetric flask.

6. Record the weight of the sample.
7. Seal the volumetric flask with a yellow stopper.

Now we can determine the dilution factor for your unknown sample using the following equation:

$$F = \frac{m_{H_2O}}{m_{Sample}}$$

B.4 Equipment Preparation

Drying bed(s)

There are 3 magnesium perchlorate drying beds on the carbonate analyzer. The first bed must be changed each day before analyzing samples. It may also need to be changed again if many samples are to be analyzed. The second drying bed may be changed occasionally if the analyzer continues giving erratic results after changing the first bed. The third drying bed should rarely need to be changed.

To change any of the drying beds:

1. Remove the drying bed by pulling up on the glass tube. Be careful not to break the glass.
2. Discard the glass wool and the old bed.
3. Wash out the glass tube and then dry thoroughly.
4. Cut a small piece of glass wool and insert it into one end of the glass tube.
5. Through the other end, fill the tube with large magnesium perchlorate crystals.
6. Cut another small piece of glass wool and insert it into the open end of the tube.
7. Place the drying bed back in the carbonate analyzer.

Gas flow

1. Verify that the nitrogen (N_2) cylinder is open and the pressure regulator is set at a minimum pressure of 40 psi.
2. Open the nitrogen needle valve by the hood.
3. Adjust the rotameter so that the middle of the ball float is at 12.
4. Check that the gas is flowing all the way through the analyzer and is not obstructed.
5. Allow N_2 to flow through the analyzer for ~5 minutes before starting your analysis.

Acid bath

1. Obtain 30 wt% phosphoric acid (H_3PO_4) solution.
2. Check that the septum on the analyzer for wear. If necessary, turn off gas and replace septum.
3. Using a 3 mL syringe, inject approximately 1 mL of acid into the analyzer.
4. Wait for the background CO_2 to be stripped out of solution and allow the analyzer response to stabilize/return back to "zero."

Data Logger

1. Turn on the computer and log-in using the Rochelle Group password.
2. The data logger software can be found by going to START>Programs>Pico Technology>PicoLog Recorder
3. The data logger will record the voltage, in 1 second increments, from the CO_2 analyzer and display the values graphically and in a tabular spreadsheet format.
4. Create a new file for your calibration/sample data points by pressing the New File button on the control panel.
5. Save your data under My Documents and then the appropriate subfolder.
6. When you are ready to start collecting data, BEFORE you inject a solution into the CO_2 analyzer, press the Start Recording button on the control panel.
7. When you are finished collecting data for sample, press the Stop Recording button on the control panel.
8. You can transfer your tabular data to Excel by pressing Select button and then by pressing Copy to clipboard button on the control panel.
9. Open Excel and select cell A1 and press Ctrl V to paste your data into the spreadsheet.
10. Make sure that the average area deviation for each group of calibration points is < 2 % error. Please refer to the Data Analysis Section for more information about calculating the area for each curve.

B.5 Calibration

The calibration solutions and procedure will depend on the expected concentrations of the samples to be analyzed.

Standard solutions

For our standard, we will be using a 15, 25, 50, 75, 100, 125, and 150 ppm_v of carbon solutions prepared from sodium carbonate (Na_2CO_3). Make sure that you follow proper laboratory procedures when handling this standards. Please replace and tighten the cap after each use.

Calibration procedure

Calibrate the total carbonate analyzer by injecting different amounts of a known concentration.

1. Adjust the range on the analyzer. (For spray experiments, the analyzer should be on the 0.05% range.)
2. Flush a 250 μL syringe with Ultra-pure DI-H_2O and discard into a waste container.
3. Repeat Step 2 three times to clean the syringe.
4. Record the weight of the syringe.
5. Draw 100 μL of standard solution into a 100 μL syringe and then discard it.
6. Draw 100 μL of standard solution into the 100 μL syringe.
7. Press Start Recording on the Data Logger control panel.
8. Inject the 100 μL of standard solution into the analyzer.
9. Watch for the peak on the data logger and wait for the analyzer output to return to zero.
10. Repeat steps 2, 3, 5-7, 9-10 until you have three peaks in close agreement (similar peak heights).
11. Press Stop Recording when you are finished collecting data for a particular data point.
12. Press Re-Record and then create a new file to store your new data.
13. Repeat with other volumes of the standard solutions to create a calibration curve.

Sample Analysis

1. Flush a 100 μL syringe with Ultra-pure DI-H_2O and discard into a waste container.
2. Repeat Step 2 three times to clean the syringe.
3. Draw 100 μL of the dilute sample into the 100 μL syringe and then discard it.
4. Draw 100 μL of the dilute sample into the 100 μL syringe.
5. Press Start Recording on the Data Logger control panel.
6. Inject the 100 μL of sample into the analyzer.
7. Watch for the peak on the data logger and wait for the analyzer output to return to zero.
8. Repeat steps 1-9 until you have three peaks in close agreement (similar peak heights).
9. Press Stop Recording when you are finished collecting data for a particular data point.

B.6 Data Analysis

Once you have collected your data, integrate the peak area using the trapezoid rule.

$$A = \sum_{i=1}^{n} a_i = \frac{h}{2} \sum_{i=1}^{n} (f_i + f_{i+1})$$

where,

n is the number of data points in your curve,

h is the length of the interval, 1 sec,

f_i is the voltage of data point i.

In Excel, your data should look something like this.

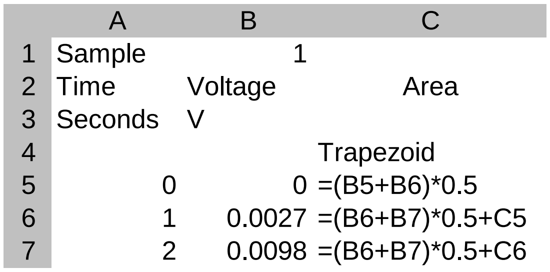

	A	B	C
1	Sample	1	
2	Time	Voltage	Area
3	Seconds	V	
4			Trapezoid
5	0	0	=(B5+B6)*0.5
6	1	0.0027	=(B6+B7)*0.5+C5
7	2	0.0098	=(B6+B7)*0.5+C6

Drag the formula in cell C7 until the analyzer output (voltage) returns to zero. At this point, the value will correspond to the area under the curve as shown below in Figure B.6-1.

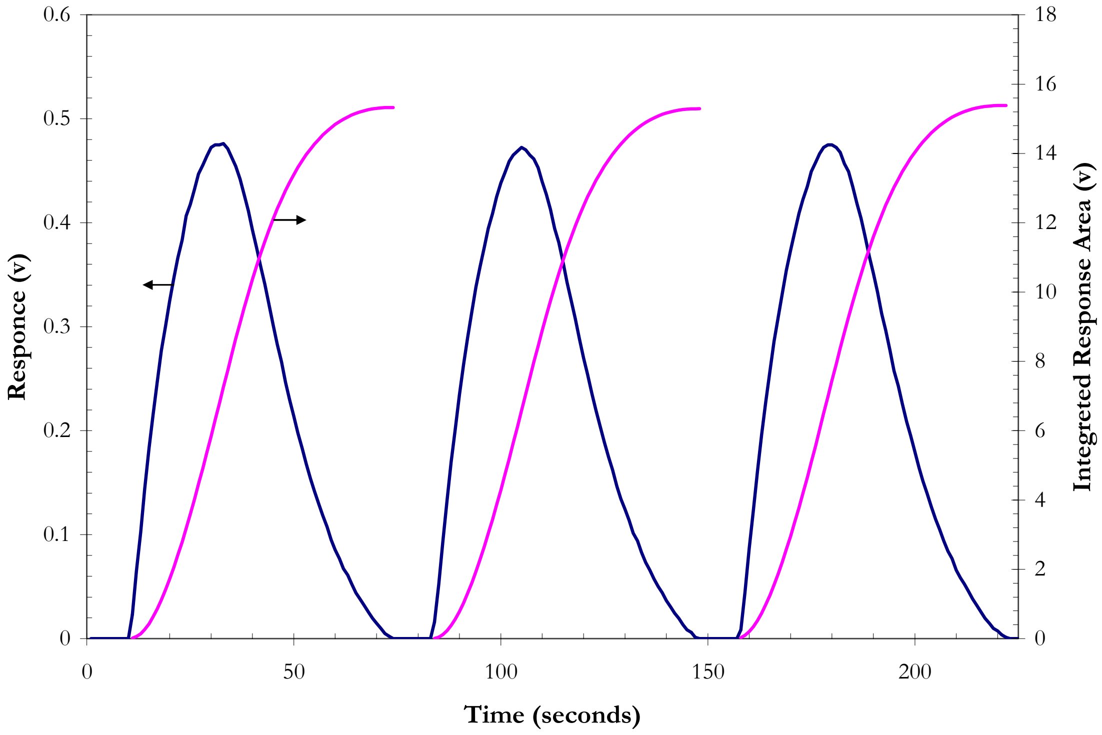

Figure B.6-1. Response Signal for 100 ppm$_v$ of Carbon Standard of Na_2CO_3 Solution.

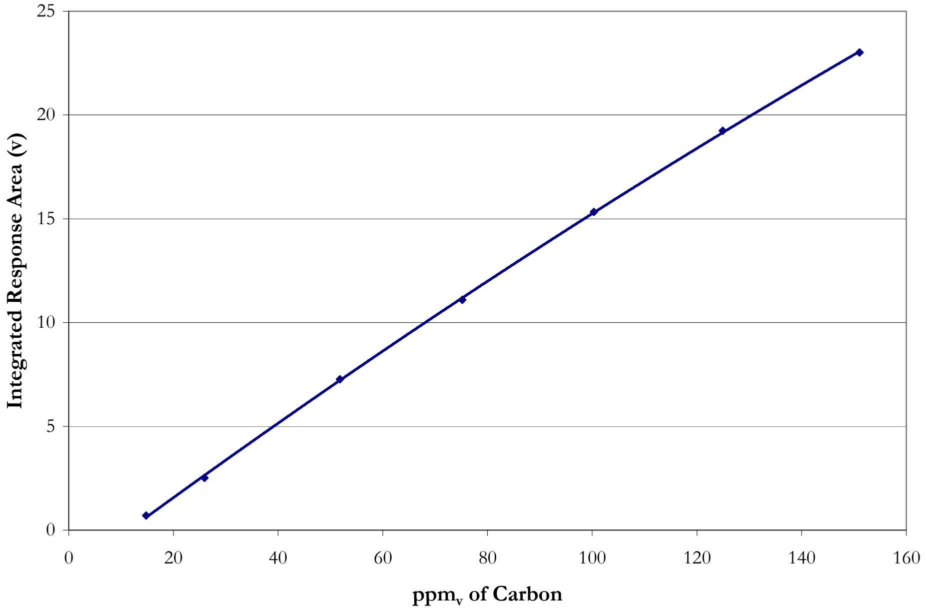

Figure B.6-2. Acidic Evolution Calibration Curve Based on Na_2CO_3 Standards.

1. Calculate the area for the other data points you have collected.
2. Calculate the average area for each set of data points.
3. Make sure that the average area deviation for each group of calibration points is < 2 % error.

Your calibration curve will look something like Figure B.6-2. From this you will be able to determine the total CO_2 concentration of your dilute unknown sample.

Use the calibration curve to determine the concentration of your unknown sample based on the integrated area of the response peaks in ppm$_v$ of carbon.

Then convert ppm$_v$ of carbon to mol CO_2/kg-soln using the following equation:

$$n_{CO_2}\left(\frac{\text{mol CO}_2}{\text{kg-soln}}\right)=\frac{\text{ppm}_\text{v}\text{ of Carbon}}{12.0107*1000}$$

Then you can calculate the concentration of total CO_2 in your concentrated sample using the dilution factor of your unknown sample.

$$N_{CO_2}\left(\frac{\text{mol CO}_2}{\text{kg-soln}}\right)=n_{CO_2}*F$$

B.7 Troubleshooting

From time to time, check that the rotameter is still at 12 and inject 100 μL of the 100 ppm_v standard solution to check the calibration.

Sample cell gets full

1. Remove the acid bath/sample solution from the analyzer with the 3 mL syringe.
2. Flush a 100 μL syringe with Ultra-pure DI-H_2O and discard into a waste container.
3. Using a 3 mL syringe, inject approximately 1mL of acid into the analyzer.
4. Wait for the background CO_2 to be stripped out of solution. Allow the analyzer response to stabilize/return back to "zero."
5. Inject 100 μL of standard solution to check the calibration.

Sudden drop in gas flow

1. Check gas flow through analyzer.
2. May need to change the drying bed. Turn off the gas flow, empty the acid bath, and replace the drying bed(s).

No response from analyzer

1. Check gas flow through analyzer.
2. Inspect tubing inside and outside of analyzer.

Shutdown

1. Reduce the gas flow by turning the rotameter down to about 3.
2. Remove the acid bath/sample solution from the analyzer with the 3mL syringe.
3. Turn the rotameter down to zero. Close the nitrogen needle valve by the hood.
4. If no one else is using the nitrogen, close the cylinder.
5. Rinse the syringes with distilled water.
6. Close the PicoLog Recorder and shut down the computer.

B.8 Total Alkalinity Analysis Procedure

Please refer to Appendix A, Section A.3 for more information. The same method was used in this work.

B.9 Total Piperazine Analysis Procedure

Please refer to Appendix A, Section A.4 for more information. The same method was used in this work.

APPENDIX C

FT-IR Analysis Methods

C.1 Introduction

This appendix documents the CALCMET^{TM} analysis method used in this work for low CO_2 concentration analysis, medium CO_2 concentration analysis, and high CO_2 concentration analysis as described in Chapter II.

C.2 Low CO_2 Concentration Analysis Method

```
LibraryPath = C:\Pickle Piperazine Method\
ComponentNumber = 1
ComponentName = Water vapor H2O
ConcentrationUnit = vol-%
ActiveLines = All
AutoAnalyze = 1 (1=Yes)
OutputChannel = 0
ViewResults = 1 (1=Yes)
AllowNegative = 0 (1=Yes)
ConversionMultiplier = 1
ResultSmoothing = 0
RangeSetting = 0
Range1 = 0 15
Range2 = 0 30
AlarmLimits = 0 30
AlarmSound = 0
```

```
Compensations = 1 1 1 0 -11
Calibrations = 0 0 4 2
ResidualWarningLimit = 0.01
ResidualErrorLimit = 0.02
UseDoubleReferences = 1 (1=Yes)
AutoInterferenceUpdate = 1 0.001
DefaultReference = 11
BaselineCorrections = 1 0
MethodNumber = 0 (1=Yes)
AnalysisArea = 1 1096 1304 1
AnalysisArea = 1 1923 2223 1
AnalysisArea = 1 2559 3319 0.5
Interference = 00111111010001000000001100111111
CrossInterferences = 0 0 0 0 0
ReferenceFile = H2O_03.ref
ReferenceFile = H2O_01.ref
ReferenceFile = H2O_02.ref
ReferenceFile = C:\Pickle Piperazine Method\Water Ref - 20050802\H2O_04.ref
ReferenceFile = C:\Pickle Piperazine Method\Water Ref - 20050802\H2O_06.ref
ReferenceFile = C:\Pickle Piperazine Method\Water Ref - 20050802\H2O_08.ref
ReferenceFile = C:\Pickle Piperazine Method\Water Ref - 20050802\H2O_10.ref
ReferenceFile = C:\Pickle Piperazine Method\Water Ref - 20050802\H2O_12.ref
ReferenceFile = C:\Pickle Piperazine Method\Water Ref - 20050802\H2O_24.ref
ReferenceFile = C:\Pickle Piperazine Method\Water Ref - 20050802\H2O_26.ref
ReferenceFile = C:\Pickle Piperazine Method\Water Ref - 20050802\H2O_28.ref
ReferenceFile = C:\Library 01253\Water Ref - 20040616\H2O_30.ref
ReferenceFile = C:\Library 01253\Water Ref - 20040616\H2O_22.ref
ReferenceFile = C:\Library 01253\Water Ref - 20040616\H2O_14.ref
ReferenceFile = C:\Library 01253\Water Ref - 20040616\H2O_16.ref
ReferenceFile = C:\Library 01253\Water Ref - 20040616\H2O_18.ref
ReferenceFile = C:\Library 01253\Water Ref - 20040616\H2O_20.ref
ComponentNumber = 2
ComponentName = Carbon dioxide CO2 (vol%)
ConcentrationUnit = vol-%
ActiveLines = All
AutoAnalyze = 0 (1=Yes)
OutputChannel = 0
ViewResults = 1 (1=Yes)
AllowNegative = 0 (1=Yes)
ConversionMultiplier = 1
ResultSmoothing = 0
RangeSetting = 2
Range1 = 0 5
Range2 = 0 50
AlarmLimits = 0 60
AlarmSound = 0
Compensations = 1 1 1 0 -11
Calibrations = 0 4 0 2
ResidualWarningLimit = 0.01
ResidualErrorLimit = 0.02
UseDoubleReferences = 0 (1=Yes)
AutoInterferenceUpdate = 0 0.001
DefaultReference = 0
BaselineCorrections = 1 0
MethodNumber = 0 (1=Yes)
AnalysisArea = 1 910 1019 1
AnalysisArea = 0 2450 2650 0.5
AnalysisArea = 1 1984 2169 0.5
Interference = 10101110100000000000000100111001
CrossInterferences = 0 0 0 0 0
ComponentNumber = 3
ComponentName = Carbon monoxide CO
ConcentrationUnit = ppm
ActiveLines = All
AutoAnalyze = 1 (1=Yes)
OutputChannel = 0
ViewResults = 1 (1=Yes)
```

```
AllowNegative = 1 (1=Yes)
ConversionMultiplier = 1
ResultSmoothing = 0
RangeSetting = 0
Range1 = 0 10
Range2 = 0 500
AlarmLimits = 0 5000
AlarmSound = 0
Compensations = 1 1 1 0 -11
Calibrations = 0 0 4 2
ResidualWarningLimit = 0.01
ResidualErrorLimit = 0.02
UseDoubleReferences = 0 (1=Yes)
AutoInterferenceUpdate = 1 0.001
DefaultReference = 1
BaselineCorrections = 1 0
MethodNumber = 0 (1=Yes)
AnalysisArea = 1 2007 2207 0.5
AnalysisArea = 1 2624 2750 1
AnalysisArea = 0 2550 2600 1
Interference = 100011101000000000001100111101
CrossInterferences = 0 0 0 0 0
ReferenceFile = CO_998.ref
ReferenceFile = CO_11.ref
ReferenceFile = CO_51.ref
ReferenceFile = CO_100.ref
ReferenceFile = CO_200.ref
ReferenceFile = CO_402.ref
ReferenceFile = CO_602.ref
ReferenceFile = CO_805.ref
ComponentNumber = 4
ComponentName = Methane CH4
ConcentrationUnit = ppm
ActiveLines = All
AutoAnalyze = 1 (1=Yes)
OutputChannel = 0
ViewResults = 1 (1=Yes)
AllowNegative = 1 (1=Yes)
ConversionMultiplier = 1
ResultSmoothing = 0
RangeSetting = 0
Range1 = 0 10
Range2 = 0 100
AlarmLimits = 0 500
AlarmSound = 0
Compensations = 1 1 1 0 -11
Calibrations = 0 0 4 2
ResidualWarningLimit = 0.01
ResidualErrorLimit = 0.02
UseDoubleReferences = 0 (1=Yes)
AutoInterferenceUpdate = 1 0.001
DefaultReference = 2
BaselineCorrections = 1 0
MethodNumber = 0 (1=Yes)
AnalysisArea = 0 1292 1412 0.5
AnalysisArea = 1 2833 3203 0.5
AnalysisArea = 1 3018 3203 0.5
Interference = 100010101000100000001100111011
CrossInterferences = 0 0 0 0 0
ReferenceFile = C:\Library180\Methane CH4 0050 ppm.ref
ReferenceFile = C:\Library180\Methane CH4 0101 ppm.ref
ComponentNumber = 5
ComponentName = Nitrous oxide N2O
ConcentrationUnit = ppm
ActiveLines = All
AutoAnalyze = 1 (1=Yes)
OutputChannel = 0
```

```
ViewResults = 1 (1=Yes)
AllowNegative = 1 (1=Yes)
ConversionMultiplier = 1
ResultSmoothing = 0
RangeSetting = 0
Range1 = 0 100
Range2 = 0 500
AlarmLimits = 0 100000
AlarmSound = 1
Compensations = 1 1 1 0 -11
Calibrations = 0 0 0 2
ResidualWarningLimit = 0.01
ResidualErrorLimit = 0.02
UseDoubleReferences = 0 (1=Yes)
AutoInterferenceUpdate = 1 0.001
DefaultReference = 2
BaselineCorrections = 1 0
MethodNumber = 0 (1=Yes)
AnalysisArea = 1 2107 2246 0.5
AnalysisArea = 1 2647 2900 1
AnalysisArea = 0 2400 2700 1
Interference = 101101101000000000001100111111
CrossInterferences = 0 0 0 0 0
ReferenceFile = Nitrous oxide N2O 0122 ppm.ref
ReferenceFile = Nitrous oxide N2O 0050 ppm.ref
ComponentNumber = 6
ComponentName = Nitrogen monoxide NO
ConcentrationUnit = ppm
ActiveLines = All
AutoAnalyze = 1 (1=Yes)
OutputChannel = 0
ViewResults = 1 (1=Yes)
AllowNegative = 1 (1=Yes)
ConversionMultiplier = 1
ResultSmoothing = 0
RangeSetting = 0
Range1 = 0 20
Range2 = 0 150
AlarmLimits = 0 1000
AlarmSound = 0
Compensations = 1 1 1 0 -11
Calibrations = 0 0 4 2
ResidualWarningLimit = 0.01
ResidualErrorLimit = 0.02
UseDoubleReferences = 0 (1=Yes)
AutoInterferenceUpdate = 0 0.001
DefaultReference = 1
BaselineCorrections = 1 0
MethodNumber = 0 (1=Yes)
AnalysisArea = 0 1760 1868 0.8
AnalysisArea = 1 1883 2099 0.8
AnalysisArea = 1 2450 2700 1
Interference = 1010100010000000000001001001
CrossInterferences = 0 0 0 0 0
ReferenceFile = NO_194.ref
ReferenceFile = NO_10.ref
ReferenceFile = NO_50.ref
ReferenceFile = NO_99.ref
ComponentNumber = 7
ComponentName = Nitrogen dioxide NO2
ConcentrationUnit = ppm
ActiveLines = All
AutoAnalyze = 1 (1=Yes)
OutputChannel = 0
ViewResults = 1 (1=Yes)
AllowNegative = 1 (1=Yes)
ConversionMultiplier = 1
```

```
ResultSmoothing = 0
RangeSetting = 0
Range1 = 0 20
Range2 = 0 1000
AlarmLimits = 0 1000
AlarmSound = 0
Compensations = 1 1 1 0 -11
Calibrations = 0 0 4 2
ResidualWarningLimit = 0.01
ResidualErrorLimit = 0.02
UseDoubleReferences = 0 (1=Yes)
AutoInterferenceUpdate = 1 0.001
DefaultReference = 1
BaselineCorrections = 1 0
MethodNumber = 0 (1=Yes)
AnalysisArea = 0 941 1397 1
AnalysisArea = 0 1497 1706 1.8
AnalysisArea = 1 2550 2933 0.5
Interference = 1001100010001000000001100111011
CrossInterferences = 0 0 0 0 0
ReferenceFile = Nitrogen dioxide NO2 0050 ppm.ref
ReferenceFile = NO2_194.ref
ReferenceFile = Nitrogen dioxide NO2 0005 ppm.ref
ComponentNumber = 8
ComponentName = Sulfur dioxide SO2
ConcentrationUnit = ppm
ActiveLines = All
AutoAnalyze = 0 (1=Yes)
OutputChannel = 0
ViewResults = 1 (1=Yes)
AllowNegative = 1 (1=Yes)
ConversionMultiplier = 1
ResultSmoothing = 0
RangeSetting = 0
Range1 = 0 500
Range2 = 0 3000
AlarmLimits = 0 5000
AlarmSound = 0
Compensations = 1 1 1 0 -11
Calibrations = 0 4 0 2
ResidualWarningLimit = 0.01
ResidualErrorLimit = 0.02
UseDoubleReferences = 0 (1=Yes)
AutoInterferenceUpdate = 1 0.001
DefaultReference = 1
BaselineCorrections = 1 0
MethodNumber = 0 (1=Yes)
AnalysisArea = 1 1042 1250 1
AnalysisArea = 0 1190 1250 1
AnalysisArea = 1 2485 2600 1
Interference = 11001000100000000000011001
CrossInterferences = 0 0 0 0 0
ReferenceFile = SO2_810.ref
ReferenceFile = SO2_1012.ref
ReferenceFile = SO2_202.ref
ReferenceFile = SO2_408.ref
ReferenceFile = SO2_50.ref
ReferenceFile = SO2_602.ref
ReferenceFile = SO2_10.ref
ComponentNumber = 9
ComponentName = Ammonia NH3
ConcentrationUnit = ppm
ActiveLines = All
AutoAnalyze = 1 (1=Yes)
OutputChannel = 0
ViewResults = 1 (1=Yes)
AllowNegative = 1 (1=Yes)
```

```
ConversionMultiplier = 1
ResultSmoothing = 0
RangeSetting = 0
Range1 = 0 250
Range2 = 0 1000
AlarmLimits = 0 1000
AlarmSound = 0
Compensations = 1 1 1 0 -11
Calibrations = 0 4 0 2
ResidualWarningLimit = 0.01
ResidualErrorLimit = 0.02
UseDoubleReferences = 0 (1=Yes)
AutoInterferenceUpdate = 1 0.001
DefaultReference = 6
BaselineCorrections = 1 0
MethodNumber = 0 (1=Yes)
AnalysisArea = 1 910 980 0.5
AnalysisArea = 0 1096 1250 0.5
AnalysisArea = 1 3196 3396 0.5
Interference = 1000101000000100000001100111101
CrossInterferences = 0 0 0 0 0
ReferenceFile = NH3_1000ppm.ref
ReferenceFile = NH3_51ppm.ref
ReferenceFile = NH3_100ppm.ref
ReferenceFile = NH3_249ppm.ref
ReferenceFile = NH3_498ppm.ref
ReferenceFile = NH3_742ppm.ref
ComponentNumber = 10
ComponentName = Hydrogen chloride HCl
ConcentrationUnit = ppm
ActiveLines = All
AutoAnalyze = 0 (1=Yes)
OutputChannel = 0
ViewResults = 1 (1=Yes)
AllowNegative = 0 (1=Yes)
ConversionMultiplier = 1
ResultSmoothing = 0
RangeSetting = 0
Range1 = 0 20
Range2 = 0 1000
AlarmLimits = 0 1000
AlarmSound = 0
Compensations = 1 1 1 0 -11
Calibrations = 0 0 4 2
ResidualWarningLimit = 0.01
ResidualErrorLimit = 0.02
UseDoubleReferences = 0 (1=Yes)
AutoInterferenceUpdate = 1 0.001
DefaultReference = 1
BaselineCorrections = 0 0
MethodNumber = 0 (1=Yes)
AnalysisArea = 0 2550 2990 1
AnalysisArea = 0 2550 3200 1
AnalysisArea = 1 2609 2888 0.5
Interference = 00000001000000000000001
CrossInterferences = 0 0 0 0 0
ReferenceFile = HCl_983.ref
ReferenceFile = HCL_801.ref
ReferenceFile = HCL_100.ref
ReferenceFile = HCL_19.ref
ReferenceFile = HCL_200.ref
ReferenceFile = HCL_403.ref
ReferenceFile = HCL_49.ref
ReferenceFile = HCL_51.ref
ReferenceFile = HCL_599.ref
ReferenceFile = HCL_10.ref
ComponentNumber = 11
```

```
ComponentName = Hydrogen fluoride HF
ConcentrationUnit = ppm
ActiveLines = All
AutoAnalyze = 0 (1=Yes)
OutputChannel = 0
ViewResults = 0 (1=Yes)
AllowNegative = 0 (1=Yes)
ConversionMultiplier = 1
ResultSmoothing = 0
RangeSetting = 1
Range1 = 0 10
Range2 = 0 1000
AlarmLimits = 0 500
AlarmSound = 0
Compensations = 1 1 1 0 -11
Calibrations = 0 0 4 2
ResidualWarningLimit = 0.01
ResidualErrorLimit = 0.02
UseDoubleReferences = 0 (1=Yes)
AutoInterferenceUpdate = 0 0.001
DefaultReference = 1
BaselineCorrections = 1 0
MethodNumber = 0 (1=Yes)
AnalysisArea = 0 910 1397 1
AnalysisArea = 0 1798 2246 1
AnalysisArea = 1 4010 4230 1
Interference = 100000000100001
CrossInterferences = 0 0 0 0 0
ReferenceFile = C:\Temet\library180\HF_100.ref
ComponentNumber = 12
ComponentName = MEK C4H80
ConcentrationUnit = ppm
ActiveLines = All
AutoAnalyze = 0 (1=Yes)
OutputChannel = 0
ViewResults = 1 (1=Yes)
AllowNegative = 0 (1=Yes)
ConversionMultiplier = 1
ResultSmoothing = 0
RangeSetting = 0
Range1 = 0 10
Range2 = 0 100
AlarmLimits = 0 100
AlarmSound = 0
Compensations = 1 1 1 0 -11
Calibrations = 0 0 4 2
ResidualWarningLimit = 0.01
ResidualErrorLimit = 0.02
UseDoubleReferences = 0 (1=Yes)
AutoInterferenceUpdate = 1 0.001
DefaultReference = 2
BaselineCorrections = 1 0
MethodNumber = 0 (1=Yes)
AnalysisArea = 1 950 1230 0.5
AnalysisArea = 1 1644 1837 0.5
AnalysisArea = 0 2871 3064 0.5
Interference = 1111111110101110111111
CrossInterferences = 0 0 0 0 0
ReferenceFile = C:\Temet\library\Methyl ethyl ketone C4H8O 0021 ppm.ref
ReferenceFile = C:\Temet\library\Methyl ethyl ketone C4H8O 0058 ppm.ref
ComponentNumber = 13
ComponentName = Ethylene C2H4
ConcentrationUnit = ppm
ActiveLines = All
AutoAnalyze = 1 (1=Yes)
OutputChannel = 0
ViewResults = 1 (1=Yes)
```

```
AllowNegative = 1 (1=Yes)
ConversionMultiplier = 1
ResultSmoothing = 0
RangeSetting = 1
Range1 = 0 500
Range2 = 0 1000
AlarmLimits = 0 500
AlarmSound = 0
Compensations = 1 1 1 0 -11
Calibrations = 0 0 4 2
ResidualWarningLimit = 0.01
ResidualErrorLimit = 0.02
UseDoubleReferences = 0 (1=Yes)
AutoInterferenceUpdate = 1 0.001
DefaultReference = 1
BaselineCorrections = 0 0
MethodNumber = 0 (1=Yes)
AnalysisArea = 1 918 995 1
AnalysisArea = 0 1800 2250 1
AnalysisArea = 0 2925 3234 1
Interference = 100010001000000000001100011101
CrossInterferences = 0 0 0 0 0
ReferenceFile = C:\Library180\Ethylene C2H4 0093 ppm.ref
ComponentNumber = 14
ComponentName = Acetone C3H60
ConcentrationUnit = ppm
ActiveLines = All
AutoAnalyze = 0 (1=Yes)
OutputChannel = 0
ViewResults = 1 (1=Yes)
AllowNegative = 0 (1=Yes)
ConversionMultiplier = 1
ResultSmoothing = 0
RangeSetting = 0
Range1 = 0 10
Range2 = 0 100
AlarmLimits = 0 100
AlarmSound = 0
Compensations = 1 1 1 0 -11
Calibrations = 0 0 4 2
ResidualWarningLimit = 0.01
ResidualErrorLimit = 0.02
UseDoubleReferences = 0 (1=Yes)
AutoInterferenceUpdate = 1 0.001
DefaultReference = 1
BaselineCorrections = 1 0
MethodNumber = 0 (1=Yes)
AnalysisArea = 1 1142 1320 0.5
AnalysisArea = 0 1798 2238 1
AnalysisArea = 0 2825 3450 1
Interference = 1001110010110000111111
CrossInterferences = 0 0 0 0 0
ReferenceFile = C:\Temet\library\Acetone C3H6O 0084 ppm.ref
ReferenceFile = C:\Temet\library\Acetone C3H6O 0490 ppm.ref
ComponentNumber = 15
ComponentName = Sulfur Hexafluoride
ConcentrationUnit = ppm
ActiveLines = All
AutoAnalyze = 0 (1=Yes)
OutputChannel = 0
ViewResults = 1 (1=Yes)
AllowNegative = 0 (1=Yes)
ConversionMultiplier = 1
ResultSmoothing = 0
RangeSetting = 1
Range1 = 0 20
Range2 = 0 1000
```

```
AlarmLimits = 0 100
AlarmSound = 0
Compensations = 1 1 1 0 -11
Calibrations = 0 0 4 2
ResidualWarningLimit = 0.01
ResidualErrorLimit = 0.02
UseDoubleReferences = 0 (1=Yes)
AutoInterferenceUpdate = 1 0.001
DefaultReference = 1
BaselineCorrections = 1 0
MethodNumber = 0 (1=Yes)
AnalysisArea = 1 895 1032 1
AnalysisArea = 0 1800 2250 1
AnalysisArea = 0 2550 3450 1
Interference = 1101010111111100110111
CrossInterferences = 0 0 0 0 0
ReferenceFile = C:\EMS Library\SF6-10.ref
ComponentNumber = 16
ComponentName = Hexane C6H14
ConcentrationUnit = ppm
ActiveLines = All
AutoAnalyze = 0 (1=Yes)
OutputChannel = 0
ViewResults = 0 (1=Yes)
AllowNegative = 0 (1=Yes)
ConversionMultiplier = 1
ResultSmoothing = 0
RangeSetting = 0
Range1 = 0 100
Range2 = 0 1000
AlarmLimits = 0 100
AlarmSound = 0
Compensations = 1 1 1 0 -11
Calibrations = 0 0 4 2
ResidualWarningLimit = 0.01
ResidualErrorLimit = 0.02
UseDoubleReferences = 0 (1=Yes)
AutoInterferenceUpdate = 1 0.001
DefaultReference = 1
BaselineCorrections = 1 0
MethodNumber = 0 (1=Yes)
AnalysisArea = 0 900 1400 1
AnalysisArea = 0 1800 2250 1
AnalysisArea = 1 2825 3003 0.5
Interference = 11010011010101001111111
CrossInterferences = 0 0 0 0 0
ReferenceFile = C:\Temet\library\Hexane C6H14 0024 ppm.ref
ReferenceFile = C:\Temet\library\Hexane C6H14 0045 ppm.ref
ComponentNumber = 17
ComponentName = Propane
ConcentrationUnit = ppm
ActiveLines = All
AutoAnalyze = 0 (1=Yes)
OutputChannel = 0
ViewResults = 1 (1=Yes)
AllowNegative = 0 (1=Yes)
ConversionMultiplier = 1
ResultSmoothing = 0
RangeSetting = 1
Range1 = 0 100
Range2 = 0 1000
AlarmLimits = 0 100
AlarmSound = 0
Compensations = 1 1 1 0 -11
Calibrations = 0 4 0 2
ResidualWarningLimit = 0.01
ResidualErrorLimit = 0.02
```

```
UseDoubleReferences = 0 (1=Yes)
AutoInterferenceUpdate = 1 0.001
DefaultReference = 1
BaselineCorrections = 1 0
MethodNumber = 0 (1=Yes)
AnalysisArea = 1 1296 1558 0.5
AnalysisArea = 0 1800 2250 1
AnalysisArea = 1 2918 3100 1
Interference = 11011011111101010111111
CrossInterferences = 0 0 0 0 0
ReferenceFile = C:\Temet\library\Propane C3H8 0147 ppm.ref
ComponentNumber = 18
ComponentName = Butane
ConcentrationUnit = ppm
ActiveLines = All
AutoAnalyze = 0 (1=Yes)
OutputChannel = 0
ViewResults = 1 (1=Yes)
AllowNegative = 0 (1=Yes)
ConversionMultiplier = 1
ResultSmoothing = 0
RangeSetting = 1
Range1 = 0 100
Range2 = 0 1000
AlarmLimits = 0 100
AlarmSound = 0
Compensations = 1 1 1 0 -11
Calibrations = 0 4 0 2
ResidualWarningLimit = 0.01
ResidualErrorLimit = 0.02
UseDoubleReferences = 0 (1=Yes)
AutoInterferenceUpdate = 1 0.001
DefaultReference = 1
BaselineCorrections = 1 0
MethodNumber = 0 (1=Yes)
AnalysisArea = 0 895 1380 0.8
AnalysisArea = 0 1810 2223 0.8
AnalysisArea = 1 2550 2910 0.5
Interference = 10011011010101011011111
CrossInterferences = 0 0 0 0 0
ReferenceFile = C:\Temet\library\Butane C4H10 0097 ppm.ref
ComponentNumber = 19
ComponentName = Octane
ConcentrationUnit = ppm
ActiveLines = All
AutoAnalyze = 0 (1=Yes)
OutputChannel = 0
ViewResults = 1 (1=Yes)
AllowNegative = 0 (1=Yes)
ConversionMultiplier = 1
ResultSmoothing = 0
RangeSetting = 1
Range1 = 0 100
Range2 = 0 1000
AlarmLimits = 0 100
AlarmSound = 0
Compensations = 1 1 1 0 -11
Calibrations = 0 4 0 2
ResidualWarningLimit = 0.01
ResidualErrorLimit = 0.02
UseDoubleReferences = 0 (1=Yes)
AutoInterferenceUpdate = 1 0.001
DefaultReference = 1
BaselineCorrections = 1 0
MethodNumber = 0 (1=Yes)
AnalysisArea = 0 895 1380 0.8
AnalysisArea = 0 1810 2223 0.8
```

```
AnalysisArea = 1 2800 2965 0.8
Interference = 1101001101010101011101111
CrossInterferences = 0 0 0 0 0
ReferenceFile = C:\Temet\library\n-Octane C8H18 0036 ppm.ref
ComponentNumber = 20
ComponentName = Benzene C2H6
ConcentrationUnit = ppm
ActiveLines = All
AutoAnalyze = 0 (1=Yes)
OutputChannel = 0
ViewResults = 0 (1=Yes)
AllowNegative = 0 (1=Yes)
ConversionMultiplier = 1
ResultSmoothing = 0
RangeSetting = 1
Range1 = 0 100
Range2 = 0 1000
AlarmLimits = 0 100
AlarmSound = 0
Compensations = 1 1 1 0 -11
Calibrations = 0 0 4 2
ResidualWarningLimit = 0.01
ResidualErrorLimit = 0.02
UseDoubleReferences = 0 (1=Yes)
AutoInterferenceUpdate = 1 0.001
DefaultReference = 1
BaselineCorrections = 1 0
MethodNumber = 0 (1=Yes)
AnalysisArea = 0 910 1397 1
AnalysisArea = 0 1798 2238 1
AnalysisArea = 1 3000 3130 0.5
Interference = 101100001001111111101
CrossInterferences = 0 0 0 0 0
ReferenceFile = C:\Temet\library\Benzene C6H6 0066 ppm.ref
ComponentNumber = 21
ComponentName = Formaldehyde
ConcentrationUnit = ppm
ActiveLines = All
AutoAnalyze = 1 (1=Yes)
OutputChannel = 0
ViewResults = 1 (1=Yes)
AllowNegative = 1 (1=Yes)
ConversionMultiplier = 1
ResultSmoothing = 0
RangeSetting = 0
Range1 = 0 10
Range2 = 0 100
AlarmLimits = 0 100
AlarmSound = 0
Compensations = 1 1 1 0 -11
Calibrations = 0 0 4 2
ResidualWarningLimit = 0.01
ResidualErrorLimit = 0.02
UseDoubleReferences = 0 (1=Yes)
AutoInterferenceUpdate = 1 0.001
DefaultReference = 1
BaselineCorrections = 1 0
MethodNumber = 0 (1=Yes)
AnalysisArea = 0 995 1250 1
AnalysisArea = 1 2450 2600 0.6
AnalysisArea = 1 2650 3211 0.5
Interference = 10011010101000100000000100111111
CrossInterferences = 0 0 0 0 0
ReferenceFile = HCHO_50.ref
ReferenceFile = Formaldehyde CH2O.ref
ReferenceFile = HCHO_10.ref
ComponentNumber = 22
```

```
ComponentName = Acetaldehyde
ConcentrationUnit = ppm
ActiveLines = All
AutoAnalyze = 1 (1=Yes)
OutputChannel = 0
ViewResults = 1 (1=Yes)
AllowNegative = 1 (1=Yes)
ConversionMultiplier = 1
ResultSmoothing = 0
RangeSetting = 0
Range1 = 0 10
Range2 = 0 100
AlarmLimits = 0 100
AlarmSound = 0
Compensations = 1 1 1 0 -11
Calibrations = 0 4 0 2
ResidualWarningLimit = 0.01
ResidualErrorLimit = 0.02
UseDoubleReferences = 0 (1=Yes)
AutoInterferenceUpdate = 1 0.001
DefaultReference = 1
BaselineCorrections = 1 0
MethodNumber = 0 (1=Yes)
AnalysisArea = 1 3200 3350 1
AnalysisArea = 1 2925 3200 1
AnalysisArea = 1 2638 2916 1
Interference = 100110101000100000001000111011
CrossInterferences = 0 0 0 0 0
ReferenceFile = Acetaldehyde C2H4O_05.ref
ReferenceFile = Acetaldehyde C2H4O 0100 ppm.ref
ReferenceFile = Acetaldehyde C2H4O 0500 ppm.ref
ComponentNumber = 23
ComponentName = Ozone O3
ConcentrationUnit = ppm
ActiveLines = All
AutoAnalyze = 0 (1=Yes)
OutputChannel = 0
ViewResults = 1 (1=Yes)
AllowNegative = 0 (1=Yes)
ConversionMultiplier = 1
ResultSmoothing = 0
RangeSetting = 1
Range1 = 0 100
Range2 = 0 1000
AlarmLimits = 0 100
AlarmSound = 0
Compensations = 1 1 1 0 -11
Calibrations = 0 4 0 2
ResidualWarningLimit = 0.01
ResidualErrorLimit = 0.02
UseDoubleReferences = 0 (1=Yes)
AutoInterferenceUpdate = 1 0.001
DefaultReference = 1
BaselineCorrections = 1 0
MethodNumber = 0 (1=Yes)
AnalysisArea = 1 926 1127 1
AnalysisArea = 0 1798 2246 1
AnalysisArea = 0 2550 3450 1
Interference = 1101010110110110111111
CrossInterferences = 0 0 0 0 0
ReferenceFile = O3_785.ref
ReferenceFile = O3_560.ref
ReferenceFile = O3_190.ref
ComponentNumber = 24
ComponentName = SO3
ConcentrationUnit = ppm
ActiveLines = All
```

```
AutoAnalyze = 0 (1=Yes)
OutputChannel = 0
ViewResults = 1 (1=Yes)
AllowNegative = 0 (1=Yes)
ConversionMultiplier = 1
ResultSmoothing = 0
RangeSetting = 1
Range1 = 0 100
Range2 = 0 1000
AlarmLimits = 0 100
AlarmSound = 0
Compensations = 1 1 1 0 -11
Calibrations = 0 4 0 2
ResidualWarningLimit = 0.01
ResidualErrorLimit = 0.02
UseDoubleReferences = 0 (1=Yes)
AutoInterferenceUpdate = 0 0.001
DefaultReference = 1
BaselineCorrections = 1 0
MethodNumber = 0 (1=Yes)
AnalysisArea = 1 1196 1397 1
AnalysisArea = 0 1800 2250 1
AnalysisArea = 0 2550 3450 1
Interference = 110000011
CrossInterferences = 0 0 0 0 0
ReferenceFile = C:\DemoLibrary\Sulfur trioxide SO3 50ppm (cemdemo).ref
ComponentNumber = 25
ComponentName = MEA
ConcentrationUnit = ppm
ActiveLines = All
AutoAnalyze = 1 (1=Yes)
OutputChannel = 0
ViewResults = 1 (1=Yes)
AllowNegative = 0 (1=Yes)
ConversionMultiplier = 1
ResultSmoothing = 0
RangeSetting = 0
Range1 = 0 300
Range2 = 0 700
AlarmLimits = 0 15000
AlarmSound = 1
Compensations = 1 1 1 0 -11
Calibrations = 0 0 0 2
ResidualWarningLimit = 0.01
ResidualErrorLimit = 0.02
UseDoubleReferences = 0 (1=Yes)
AutoInterferenceUpdate = 1 0.005
DefaultReference = 1
BaselineCorrections = 1 0
MethodNumber = 0 (1=Yes)
AnalysisArea = 1 2624 3150 1
AnalysisArea = 1 2416 2601 1
AnalysisArea = 0 995 1119 1
Interference = 100110100000100000001100011011
CrossInterferences = 0 0 0 0 0
ReferenceFile = MEA_500.ref
ReferenceFile = MEA_100.ref
ReferenceFile = C:\Pickle References\MEA_15000.ref
ReferenceFile = C:\Pickle References\MEA_1000.ref
ReferenceFile = C:\Pickle References\MEA_2000.ref
ReferenceFile = C:\Pickle References\MEA_5000.ref
ReferenceFile = C:\Pickle References\MEA_10000.ref
ComponentNumber = 26
ComponentName = Methanol
ConcentrationUnit = Auto
ActiveLines = All
AutoAnalyze = 1 (1=Yes)
```

```
OutputChannel = 0
ViewResults = 1 (1=Yes)
AllowNegative = 1 (1=Yes)
ConversionMultiplier = 1
ResultSmoothing = 0
RangeSetting = 0
Range1 = 0 25
Range2 = 0 500
AlarmLimits = 0 1000
AlarmSound = 0
Compensations = 1 1 1 0 -11
Calibrations = 0 0 4 2
ResidualWarningLimit = 0.01
ResidualErrorLimit = 0.02
UseDoubleReferences = 0 (1=Yes)
AutoInterferenceUpdate = 1 0.005
DefaultReference = 1
BaselineCorrections = 1 0
MethodNumber = 0 (1=Yes)
AnalysisArea = 1 995 1073 1
AnalysisArea = 1 1095 1150 1
AnalysisArea = 1 2450 3180 1
Interference = 1001101010001000000001100101111
CrossInterferences = 0 0 0 0 0
ReferenceFile = C:\Library180\Methanol_100.ref
ComponentNumber = 27
ComponentName = Methylamine
ConcentrationUnit = Auto
ActiveLines = All
AutoAnalyze = 1 (1=Yes)
OutputChannel = 0
ViewResults = 1 (1=Yes)
AllowNegative = 1 (1=Yes)
ConversionMultiplier = 1
ResultSmoothing = 0
RangeSetting = 0
Range1 = 0 10
Range2 = 0 100
AlarmLimits = 0 100
AlarmSound = 0
Compensations = 1 1 1 0 -11
Calibrations = 0 0 4 2
ResidualWarningLimit = 0.01
ResidualErrorLimit = 0.02
UseDoubleReferences = 0 (1=Yes)
AutoInterferenceUpdate = 1 0.001
DefaultReference = 1
BaselineCorrections = 1 0
MethodNumber = 0 (1=Yes)
AnalysisArea = 1 2022 2223 1
AnalysisArea = 1 2450 2650 1
AnalysisArea = 1 2800 3203 1
Interference = 1011111010001000000001100110111
CrossInterferences = 0 0 0 0 0
ReferenceFile = Methylamine CH5N 0100 ppm.ref
ReferenceFile = Methylamine CH5N 0500 ppm.ref
ReferenceFile = Methylamine CH5N 0894 ppm.ref
ComponentNumber = 28
ComponentName = Carbon Dioxide CO2 (ppm)
ConcentrationUnit = Auto
ActiveLines = All
AutoAnalyze = 1 (1=Yes)
OutputChannel = 0
ViewResults = 1 (1=Yes)
AllowNegative = 0 (1=Yes)
ConversionMultiplier = 1
ResultSmoothing = 0
```

```
RangeSetting = 0
Range1 = 0 1000
Range2 = 0 7000
AlarmLimits = 0 6000
AlarmSound = 0
Compensations = 1 1 1 0 -11
Calibrations = 0 4 0 2
ResidualWarningLimit = 0.01
ResidualErrorLimit = 0.02
UseDoubleReferences = 0 (1=Yes)
AutoInterferenceUpdate = 1 0.001
DefaultReference = 1
BaselineCorrections = 1 0
MethodNumber = 0 (1=Yes)
AnalysisArea = 1 2207 2501 1
AnalysisArea = 1 1984 2169 1
AnalysisArea = 0 910 1019 1
Interference = 1010111010001000000001100111001
CrossInterferences = 0 0 0 0 0
ReferenceFile = CO2_1000ppm.ref
ReferenceFile = CO2_5000ppm.ref
ReferenceFile = CO2_100ppm.ref
ReferenceFile = CO2_15000ppm.ref
ReferenceFile = CO2_50ppm.ref
ReferenceFile = CO2_250ppm.ref
ReferenceFile = CO2_750ppm.ref
ReferenceFile = CO2_2500ppm.ref
ReferenceFile = CO2_500ppm.ref
ComponentNumber = 29
ComponentName = Methane CH4
ConcentrationUnit = Auto
ActiveLines = All
AutoAnalyze = 0 (1=Yes)
OutputChannel = 0
ViewResults = 1 (1=Yes)
AllowNegative = 1 (1=Yes)
ConversionMultiplier = 1
ResultSmoothing = 0
RangeSetting = 0
Range1 = 0 10
Range2 = 0 100
AlarmLimits = 0 100
AlarmSound = 0
Compensations = 1 1 1 0 -11
Calibrations = 0 0 4 2
ResidualWarningLimit = 0.01
ResidualErrorLimit = 0.02
UseDoubleReferences = 0 (1=Yes)
AutoInterferenceUpdate = 1 0.001
DefaultReference = 1
BaselineCorrections = 1 0
MethodNumber = 0 (1=Yes)
AnalysisArea = 0 1292 1412 0.5
AnalysisArea = 1 2833 3203 0.5
AnalysisArea = 1 3018 3203 0.5
Interference = 1001101010000000000001100101001
CrossInterferences = 0 0 0 0 0
ReferenceFile = Methane CH4 0101 ppm.ref
ReferenceFile = Methane CH4 0050 ppm.ref
ComponentNumber = 30
ComponentName = Piperazine
ConcentrationUnit = Auto
ActiveLines = All
AutoAnalyze = 1 (1=Yes)
OutputChannel = 0
ViewResults = 1 (1=Yes)
AllowNegative = 1 (1=Yes)
```

```
ConversionMultiplier = 1
ResultSmoothing = 0
RangeSetting = 0
Range1 = 0 250
Range2 = 0 500
AlarmLimits = 0 500
AlarmSound = 1
Compensations = 1 1 1 0 -11
Calibrations = 0 0 4 2
ResidualWarningLimit = 0.01
ResidualErrorLimit = 0.02
UseDoubleReferences = 0 (1=Yes)
AutoInterferenceUpdate = 1 0.001
DefaultReference = 4
BaselineCorrections = 1 0
MethodNumber = 0 (1=Yes)
AnalysisArea = 0 1096 1380 1
AnalysisArea = 0 1810 2223 1
AnalysisArea = 1 2550 3095 1
Interference = 100110101000100000000110011101
CrossInterferences = 0 0 0 0 0
ReferenceFile = Piperazine_2ppm_180C.ref
ReferenceFile = Piperazine_105ppm_180C.ref
ReferenceFile = Piperazine_188ppm_180C.ref
ReferenceFile = Piperazine_407ppm_180C.ref
ReferenceFile = Piperazine_471ppm_180C.ref
ReferenceFile = Piperazine_40ppm_180C.ref
ComponentNumber = 201
ComponentName = NOx
ConcentrationUnit = ppm
ActiveLines = All
AutoAnalyze = 0 (1=Yes)
OutputChannel = 0
ViewResults = 1 (1=Yes)
AllowNegative = 1 (1=Yes)
ConversionMultiplier = 1
ResultSmoothing = 0
RangeSetting = 0
Range1 = 0 20
Range2 = 0 250
AlarmLimits = 0 500
AlarmSound = 0
Compensations = 1 1 1 0 -11
Calibrations = 0 0 4 2
Interference = 0000111
CrossInterferences = 0 0 0 0 0
ComponentNumber = 202
ComponentName = THC
ConcentrationUnit = ppm
ActiveLines = All
AutoAnalyze = 0 (1=Yes)
OutputChannel = 0
ViewResults = 1 (1=Yes)
AllowNegative = 1 (1=Yes)
ConversionMultiplier = 1
ResultSmoothing = 0
RangeSetting = 1
Range1 = 0 500
Range2 = 0 1000
AlarmLimits = 0 500
AlarmSound = 0
Compensations = 1 1 1 0 -11
Calibrations = 0 0 4 2
Interference = 0001000000011
CrossInterferences = 0 0 0 0 0
ComponentNumber = 211
ComponentName = Input1
```

```
ConcentrationUnit = %
ActiveLines = All
AutoAnalyze = 0 (1=Yes)
OutputChannel = 0
ViewResults = 1 (1=Yes)
AllowNegative = 1 (1=Yes)
ConversionMultiplier = 1
ResultSmoothing = 0
RangeSetting = 1
Range1 = 0 100
Range2 = 0 1000
AlarmLimits = 0 100
AlarmSound = 0
Compensations = 1 1 1 0 -11
Calibrations = 0 0 4 2
Interference = 0
CrossInterferences = 0 0 0 0 0
ComponentNumber = 212
ComponentName = Input2
ConcentrationUnit = %
ActiveLines = All
AutoAnalyze = 0 (1=Yes)
OutputChannel = 0
ViewResults = 1 (1=Yes)
AllowNegative = 1 (1=Yes)
ConversionMultiplier = 1
ResultSmoothing = 0
RangeSetting = 1
Range1 = 0 100
Range2 = 0 1000
AlarmLimits = 0 100
AlarmSound = 0
Compensations = 1 1 1 0 -11
Calibrations = 0 0 4 2
Interference = 0
CrossInterferences = 0 0 0 0 0
ComponentNumber = 213
ComponentName = Input3
ConcentrationUnit = %
ActiveLines = All
AutoAnalyze = 0 (1=Yes)
OutputChannel = 0
ViewResults = 1 (1=Yes)
AllowNegative = 1 (1=Yes)
ConversionMultiplier = 1
ResultSmoothing = 0
RangeSetting = 1
Range1 = 0 100
Range2 = 0 1000
AlarmLimits = 0 100
AlarmSound = 0
Compensations = 1 1 1 0 -11
Calibrations = 0 0 4 2
Interference = 0
CrossInterferences = 0 0 0 0 0
ComponentNumber = 214
ComponentName = Input4
ConcentrationUnit = %
ActiveLines = All
AutoAnalyze = 0 (1=Yes)
OutputChannel = 0
ViewResults = 1 (1=Yes)
AllowNegative = 1 (1=Yes)
ConversionMultiplier = 1
ResultSmoothing = 0
RangeSetting = 1
Range1 = 0 100
```

```
Range2 = 0 1000
AlarmLimits = 0 100
AlarmSound = 0
Compensations = 1 1 1 0 -11
Calibrations = 0 0 4 2
Interference = 0
CrossInterferences = 0 0 0 0 0
ComponentNumber = 215
ComponentName = Input5
ConcentrationUnit = %
ActiveLines = All
AutoAnalyze = 0 (1=Yes)
OutputChannel = 0
ViewResults = 1 (1=Yes)
AllowNegative = 1 (1=Yes)
ConversionMultiplier = 1
ResultSmoothing = 0
RangeSetting = 1
Range1 = 0 100
Range2 = 0 1000
AlarmLimits = 0 100
AlarmSound = 0
Compensations = 1 1 1 0 -11
Calibrations = 0 0 4 2
Interference = 0
CrossInterferences = 0 0 0 0 0
ComponentNumber = 216
ComponentName = Input6
ConcentrationUnit = %
ActiveLines = All
AutoAnalyze = 0 (1=Yes)
OutputChannel = 0
ViewResults = 1 (1=Yes)
AllowNegative = 1 (1=Yes)
ConversionMultiplier = 1
ResultSmoothing = 0
RangeSetting = 1
Range1 = 0 100
Range2 = 0 1000
AlarmLimits = 0 100
AlarmSound = 0
Compensations = 1 1 1 0 -11
Calibrations = 0 0 4 2
Interference = 0
CrossInterferences = 0 0 0 0 0
ComponentNumber = 217
ComponentName = Input7
ConcentrationUnit = %
ActiveLines = All
AutoAnalyze = 0 (1=Yes)
OutputChannel = 0
ViewResults = 1 (1=Yes)
AllowNegative = 1 (1=Yes)
ConversionMultiplier = 1
ResultSmoothing = 0
RangeSetting = 1
Range1 = 0 100
Range2 = 0 1000
AlarmLimits = 0 100
AlarmSound = 0
Compensations = 1 1 1 0 -11
Calibrations = 0 0 4 2
Interference = 0
CrossInterferences = 0 0 0 0 0
ComponentNumber = 218
ComponentName = Input8
ConcentrationUnit = %
```

```
ActiveLines = All
AutoAnalyze = 0 (1=Yes)
OutputChannel = 0
ViewResults = 1 (1=Yes)
AllowNegative = 1 (1=Yes)
ConversionMultiplier = 1
ResultSmoothing = 0
RangeSetting = 1
Range1 = 0 100
Range2 = 0 1000
AlarmLimits = 0 100
AlarmSound = 0
Compensations = 1 1 1 0 -11
Calibrations = 0 0 4 2
Interference = 0
CrossInterferences = 0 0 0 0 0
ComponentNumber = 219
ComponentName = Pressure
ConcentrationUnit = mbar
ActiveLines = All
AutoAnalyze = 1 (1=Yes)
OutputChannel = 0
ViewResults = 1 (1=Yes)
AllowNegative = 1 (1=Yes)
ConversionMultiplier = 1
ResultSmoothing = 0
RangeSetting = 1
Range1 = 0 2000
Range2 = 0 2000
AlarmLimits = 900 2000
AlarmSound = 0
Compensations = 1 1 1 0 -11
Calibrations = 0 0 4 2
Interference = 0
CrossInterferences = 0 0 0 0 0
ComponentNumber = 220
ComponentName = Oxygen (O2)
ConcentrationUnit = vol-%
ActiveLines = All
AutoAnalyze = 0 (1=Yes)
OutputChannel = 0
ViewResults = 1 (1=Yes)
AllowNegative = 1 (1=Yes)
ConversionMultiplier = 1
ResultSmoothing = 0
RangeSetting = 1
Range1 = 0 100
Range2 = 0 1000
AlarmLimits = 0 100
AlarmSound = 0
Compensations = 1 1 1 0 -11
Calibrations = 0 0 4 2
Interference = 0
CrossInterferences = 0 0 0 0 0
ComponentNumber = 221
ComponentName = AUX
ConcentrationUnit = %
ActiveLines = All
AutoAnalyze = 0 (1=Yes)
OutputChannel = 0
ViewResults = 1 (1=Yes)
AllowNegative = 1 (1=Yes)
ConversionMultiplier = 1
ResultSmoothing = 0
RangeSetting = 1
Range1 = 0 100
Range2 = 0 1000
```

```
AlarmLimits = 0 100
AlarmSound = 0
Compensations = 1 1 1 0 -11
Calibrations = 0 0 4 2
Interference = 0
CrossInterferences = 0 0 0 0 0
```

C.3 Medium CO_2 Concentration Analysis Method

```
LibraryPath = C:\Pickle Piperazine Method\
ComponentNumber = 1
ComponentName = Water vapor H2O
ConcentrationUnit = vol-%
ActiveLines = All
AutoAnalyze = 1 (1=Yes)
OutputChannel = 0
ViewResults = 1 (1=Yes)
AllowNegative = 0 (1=Yes)
ConversionMultiplier = 1
ResultSmoothing = 0
RangeSetting = 0
Range1 = 0 15
Range2 = 0 30
AlarmLimits = 0 30
AlarmSound = 0
Compensations = 1 1 1 0 -11
Calibrations = 0 0 4 2
ResidualWarningLimit = 0.01
ResidualErrorLimit = 0.02
UseDoubleReferences = 1 (1=Yes)
AutoInterferenceUpdate = 1 0.001
DefaultReference = 11
BaselineCorrections = 1 0
MethodNumber = 0 (1=Yes)
AnalysisArea = 1 1096 1304 1
AnalysisArea = 1 1923 2223 1
AnalysisArea = 1 2559 3319 0.5
Interference = 001111101000100000001100111111
CrossInterferences = 0 0 0 0 0
ReferenceFile = H2O_03.ref
ReferenceFile = H2O_01.ref
ReferenceFile = H2O_02.ref
ReferenceFile = C:\Pickle Piperazine Method\Water Ref - 20050802\H2O_04.ref
ReferenceFile = C:\Pickle Piperazine Method\Water Ref - 20050802\H2O_06.ref
ReferenceFile = C:\Pickle Piperazine Method\Water Ref - 20050802\H2O_08.ref
ReferenceFile = C:\Pickle Piperazine Method\Water Ref - 20050802\H2O_10.ref
ReferenceFile = C:\Pickle Piperazine Method\Water Ref - 20050802\H2O_12.ref
ReferenceFile = C:\Pickle Piperazine Method\Water Ref - 20050802\H2O_24.ref
ReferenceFile = C:\Pickle Piperazine Method\Water Ref - 20050802\H2O_26.ref
ReferenceFile = C:\Pickle Piperazine Method\Water Ref - 20050802\H2O_28.ref
ReferenceFile = C:\Library 01253\Water Ref - 20040616\H2O_30.ref
ReferenceFile = C:\Library 01253\Water Ref - 20040616\H2O_14.ref
ReferenceFile = C:\Library 01253\Water Ref - 20040616\H2O_16.ref
ReferenceFile = C:\Library 01253\Water Ref - 20040616\H2O_18.ref
ReferenceFile = C:\Library 01253\Water Ref - 20040616\H2O_20.ref
ReferenceFile = C:\Library 01253\Water Ref - 20040616\H2O_22.ref
ComponentNumber = 2
ComponentName = Carbon dioxide CO2 (vol%)
ConcentrationUnit = vol-%
ActiveLines = All
AutoAnalyze = 0 (1=Yes)
OutputChannel = 0
ViewResults = 1 (1=Yes)
AllowNegative = 0 (1=Yes)
```

```
ConversionMultiplier = 1
ResultSmoothing = 0
RangeSetting = 2
Range1 = 0 5
Range2 = 0 50
AlarmLimits = 0 60
AlarmSound = 0
Compensations = 1 1 1 0 -11
Calibrations = 0 4 0 2
ResidualWarningLimit = 0.01
ResidualErrorLimit = 0.02
UseDoubleReferences = 0 (1=Yes)
AutoInterferenceUpdate = 0 0.001
DefaultReference = 0
BaselineCorrections = 1 0
MethodNumber = 0 (1=Yes)
AnalysisArea = 1 910 1019 1
AnalysisArea = 0 2450 2650 0.5
AnalysisArea = 1 1984 2169 0.5
Interference = 101011101000000000000100111001
CrossInterferences = 0 0 0 0 0
ComponentNumber = 3
ComponentName = Carbon monoxide CO
ConcentrationUnit = ppm
ActiveLines = All
AutoAnalyze = 1 (1=Yes)
OutputChannel = 0
ViewResults = 1 (1=Yes)
AllowNegative = 1 (1=Yes)
ConversionMultiplier = 1
ResultSmoothing = 0
RangeSetting = 0
Range1 = 0 10
Range2 = 0 500
AlarmLimits = 0 5000
AlarmSound = 0
Compensations = 1 1 1 0 -11
Calibrations = 0 0 4 2
ResidualWarningLimit = 0.01
ResidualErrorLimit = 0.02
UseDoubleReferences = 0 (1=Yes)
AutoInterferenceUpdate = 1 0.001
DefaultReference = 1
BaselineCorrections = 1 0
MethodNumber = 0 (1=Yes)
AnalysisArea = 1 2007 2207 0.5
AnalysisArea = 1 2624 2750 1
AnalysisArea = 0 2550 2600 1
Interference = 100011101000000000001100111101
CrossInterferences = 0 0 0 0 0
ReferenceFile = CO_998.ref
ReferenceFile = CO_11.ref
ReferenceFile = CO_51.ref
ReferenceFile = CO_100.ref
ReferenceFile = CO_200.ref
ReferenceFile = CO_402.ref
ReferenceFile = CO_602.ref
ReferenceFile = CO_805.ref
ComponentNumber = 4
ComponentName = Methane CH4
ConcentrationUnit = ppm
ActiveLines = All
AutoAnalyze = 1 (1=Yes)
OutputChannel = 0
ViewResults = 1 (1=Yes)
AllowNegative = 1 (1=Yes)
ConversionMultiplier = 1
```

```
ResultSmoothing = 0
RangeSetting = 0
Range1 = 0 10
Range2 = 0 100
AlarmLimits = 0 500
AlarmSound = 0
Compensations = 1 1 1 0 -11
Calibrations = 0 0 4 2
ResidualWarningLimit = 0.01
ResidualErrorLimit = 0.02
UseDoubleReferences = 0 (1=Yes)
AutoInterferenceUpdate = 1 0.001
DefaultReference = 2
BaselineCorrections = 1 0
MethodNumber = 0 (1=Yes)
AnalysisArea = 0 1292 1412 0.5
AnalysisArea = 1 2833 3203 0.5
AnalysisArea = 1 3018 3203 0.5
Interference = 100010101000100000001100111011
CrossInterferences = 0 0 0 0 0
ReferenceFile = C:\Library180\Methane CH4 0050 ppm.ref
ReferenceFile = C:\Library180\Methane CH4 0101 ppm.ref
ComponentNumber = 5
ComponentName = Nitrous oxide N2O
ConcentrationUnit = ppm
ActiveLines = All
AutoAnalyze = 1 (1=Yes)
OutputChannel = 0
ViewResults = 1 (1=Yes)
AllowNegative = 1 (1=Yes)
ConversionMultiplier = 1
ResultSmoothing = 0
RangeSetting = 0
Range1 = 0 100
Range2 = 0 500
AlarmLimits = 0 100000
AlarmSound = 1
Compensations = 1 1 1 0 -11
Calibrations = 0 0 0 2
ResidualWarningLimit = 0.01
ResidualErrorLimit = 0.02
UseDoubleReferences = 0 (1=Yes)
AutoInterferenceUpdate = 1 0.001
DefaultReference = 2
BaselineCorrections = 1 0
MethodNumber = 0 (1=Yes)
AnalysisArea = 1 2107 2246 0.5
AnalysisArea = 1 2647 2900 1
AnalysisArea = 0 2400 2700 1
Interference = 101101101000000000001100111111
CrossInterferences = 0 0 0 0 0
ReferenceFile = Nitrous oxide N2O 0122 ppm.ref
ReferenceFile = Nitrous oxide N2O 0050 ppm.ref
ComponentNumber = 6
ComponentName = Nitrogen monoxide NO
ConcentrationUnit = ppm
ActiveLines = All
AutoAnalyze = 1 (1=Yes)
OutputChannel = 0
ViewResults = 1 (1=Yes)
AllowNegative = 1 (1=Yes)
ConversionMultiplier = 1
ResultSmoothing = 0
RangeSetting = 0
Range1 = 0 20
Range2 = 0 150
AlarmLimits = 0 1000
```

```
AlarmSound = 0
Compensations = 1 1 1 0 -11
Calibrations = 0 0 4 2
ResidualWarningLimit = 0.01
ResidualErrorLimit = 0.02
UseDoubleReferences = 0 (1=Yes)
AutoInterferenceUpdate = 0 0.001
DefaultReference = 1
BaselineCorrections = 1 0
MethodNumber = 0 (1=Yes)
AnalysisArea = 0 1760 1868 0.8
AnalysisArea = 1 1883 2099 0.8
AnalysisArea = 1 2450 2700 1
Interference = 1010100010000000000001001001
CrossInterferences = 0 0 0 0 0
ReferenceFile = NO_194.ref
ReferenceFile = NO_10.ref
ReferenceFile = NO_50.ref
ReferenceFile = NO_99.ref
ComponentNumber = 7
ComponentName = Nitrogen dioxide NO2
ConcentrationUnit = ppm
ActiveLines = All
AutoAnalyze = 1 (1=Yes)
OutputChannel = 0
ViewResults = 1 (1=Yes)
AllowNegative = 1 (1=Yes)
ConversionMultiplier = 1
ResultSmoothing = 0
RangeSetting = 0
Range1 = 0 20
Range2 = 0 1000
AlarmLimits = 0 1000
AlarmSound = 0
Compensations = 1 1 1 0 -11
Calibrations = 0 0 4 2
ResidualWarningLimit = 0.01
ResidualErrorLimit = 0.02
UseDoubleReferences = 0 (1=Yes)
AutoInterferenceUpdate = 1 0.001
DefaultReference = 1
BaselineCorrections = 1 0
MethodNumber = 0 (1=Yes)
AnalysisArea = 0 941 1397 1
AnalysisArea = 0 1497 1706 1.8
AnalysisArea = 1 2550 2933 0.5
Interference = 100110001000100000001100111011
CrossInterferences = 0 0 0 0 0
ReferenceFile = Nitrogen dioxide NO2 0050 ppm.ref
ReferenceFile = NO2_194.ref
ReferenceFile = Nitrogen dioxide NO2 0005 ppm.ref
ComponentNumber = 8
ComponentName = Sulfur dioxide SO2
ConcentrationUnit = ppm
ActiveLines = All
AutoAnalyze = 0 (1=Yes)
OutputChannel = 0
ViewResults = 1 (1=Yes)
AllowNegative = 1 (1=Yes)
ConversionMultiplier = 1
ResultSmoothing = 0
RangeSetting = 0
Range1 = 0 500
Range2 = 0 3000
AlarmLimits = 0 5000
AlarmSound = 0
Compensations = 1 1 1 0 -11
```

```
Calibrations = 0 4 0 2
ResidualWarningLimit = 0.01
ResidualErrorLimit = 0.02
UseDoubleReferences = 0 (1=Yes)
AutoInterferenceUpdate = 1 0.001
DefaultReference = 1
BaselineCorrections = 1 0
MethodNumber = 0 (1=Yes)
AnalysisArea = 1 1042 1250 1
AnalysisArea = 0 1190 1250 1
AnalysisArea = 1 2485 2600 1
Interference = 11001000100000000000011001
CrossInterferences = 0 0 0 0 0
ReferenceFile = SO2_810.ref
ReferenceFile = SO2_1012.ref
ReferenceFile = SO2_202.ref
ReferenceFile = SO2_408.ref
ReferenceFile = SO2_50.ref
ReferenceFile = SO2_602.ref
ReferenceFile = SO2_10.ref
ComponentNumber = 9
ComponentName = Ammonia NH3
ConcentrationUnit = ppm
ActiveLines = All
AutoAnalyze = 1 (1=Yes)
OutputChannel = 0
ViewResults = 1 (1=Yes)
AllowNegative = 1 (1=Yes)
ConversionMultiplier = 1
ResultSmoothing = 0
RangeSetting = 0
Range1 = 0 250
Range2 = 0 1000
AlarmLimits = 0 1000
AlarmSound = 0
Compensations = 1 1 1 0 -11
Calibrations = 0 4 0 2
ResidualWarningLimit = 0.01
ResidualErrorLimit = 0.02
UseDoubleReferences = 0 (1=Yes)
AutoInterferenceUpdate = 1 0.001
DefaultReference = 6
BaselineCorrections = 1 0
MethodNumber = 0 (1=Yes)
AnalysisArea = 1 910 980 0.5
AnalysisArea = 0 1096 1250 0.5
AnalysisArea = 1 3196 3396 0.5
Interference = 1000101000001000000001100111101
CrossInterferences = 0 0 0 0 0
ReferenceFile = NH3_1000ppm.ref
ReferenceFile = NH3_51ppm.ref
ReferenceFile = NH3_100ppm.ref
ReferenceFile = NH3_249ppm.ref
ReferenceFile = NH3_498ppm.ref
ReferenceFile = NH3_742ppm.ref
ComponentNumber = 10
ComponentName = Hydrogen chloride HCl
ConcentrationUnit = ppm
ActiveLines = All
AutoAnalyze = 0 (1=Yes)
OutputChannel = 0
ViewResults = 1 (1=Yes)
AllowNegative = 0 (1=Yes)
ConversionMultiplier = 1
ResultSmoothing = 0
RangeSetting = 0
Range1 = 0 20
```

```
Range2 = 0 1000
AlarmLimits = 0 1000
AlarmSound = 0
Compensations = 1 1 1 0 -11
Calibrations = 0 0 4 2
ResidualWarningLimit = 0.01
ResidualErrorLimit = 0.02
UseDoubleReferences = 0 (1=Yes)
AutoInterferenceUpdate = 1 0.001
DefaultReference = 1
BaselineCorrections = 0 0
MethodNumber = 0 (1=Yes)
AnalysisArea = 0 2550 2990 1
AnalysisArea = 0 2550 3200 1
AnalysisArea = 1 2609 2888 0.5
Interference = 00000001000000000000001
CrossInterferences = 0 0 0 0 0
ReferenceFile = HCl_983.ref
ReferenceFile = HCL_801.ref
ReferenceFile = HCL_100.ref
ReferenceFile = HCL_19.ref
ReferenceFile = HCL_200.ref
ReferenceFile = HCL_403.ref
ReferenceFile = HCL_49.ref
ReferenceFile = HCL_51.ref
ReferenceFile = HCL_599.ref
ReferenceFile = HCL_10.ref
ComponentNumber = 11
ComponentName = Hydrogen fluoride HF
ConcentrationUnit = ppm
ActiveLines = All
AutoAnalyze = 0 (1=Yes)
OutputChannel = 0
ViewResults = 0 (1=Yes)
AllowNegative = 0 (1=Yes)
ConversionMultiplier = 1
ResultSmoothing = 0
RangeSetting = 1
Range1 = 0 10
Range2 = 0 1000
AlarmLimits = 0 500
AlarmSound = 0
Compensations = 1 1 1 0 -11
Calibrations = 0 0 4 2
ResidualWarningLimit = 0.01
ResidualErrorLimit = 0.02
UseDoubleReferences = 0 (1=Yes)
AutoInterferenceUpdate = 0 0.001
DefaultReference = 1
BaselineCorrections = 1 0
MethodNumber = 0 (1=Yes)
AnalysisArea = 0 910 1397 1
AnalysisArea = 0 1798 2246 1
AnalysisArea = 1 4010 4230 1
Interference = 100000000100001
CrossInterferences = 0 0 0 0 0
ReferenceFile = C:\Temet\library180\HF_100.ref
ComponentNumber = 12
ComponentName = MEK C4H80
ConcentrationUnit = ppm
ActiveLines = All
AutoAnalyze = 0 (1=Yes)
OutputChannel = 0
ViewResults = 1 (1=Yes)
AllowNegative = 0 (1=Yes)
ConversionMultiplier = 1
ResultSmoothing = 0
```

```
RangeSetting = 0
Range1 = 0 10
Range2 = 0 100
AlarmLimits = 0 100
AlarmSound = 0
Compensations = 1 1 1 0 -11
Calibrations = 0 0 4 2
ResidualWarningLimit = 0.01
ResidualErrorLimit = 0.02
UseDoubleReferences = 0 (1=Yes)
AutoInterferenceUpdate = 1 0.001
DefaultReference = 2
BaselineCorrections = 1 0
MethodNumber = 0 (1=Yes)
AnalysisArea = 1 950 1230 0.5
AnalysisArea = 1 1644 1837 0.5
AnalysisArea = 0 2871 3064 0.5
Interference = 1111111110101110111111
CrossInterferences = 0 0 0 0 0
ReferenceFile = C:\Temet\library\Methyl ethyl ketone C4H8O 0021 ppm.ref
ReferenceFile = C:\Temet\library\Methyl ethyl ketone C4H8O 0058 ppm.ref
ComponentNumber = 13
ComponentName = Ethylene C2H4
ConcentrationUnit = ppm
ActiveLines = All
AutoAnalyze = 1 (1=Yes)
OutputChannel = 0
ViewResults = 1 (1=Yes)
AllowNegative = 1 (1=Yes)
ConversionMultiplier = 1
ResultSmoothing = 0
RangeSetting = 1
Range1 = 0 500
Range2 = 0 1000
AlarmLimits = 0 500
AlarmSound = 0
Compensations = 1 1 1 0 -11
Calibrations = 0 0 4 2
ResidualWarningLimit = 0.01
ResidualErrorLimit = 0.02
UseDoubleReferences = 0 (1=Yes)
AutoInterferenceUpdate = 1 0.001
DefaultReference = 1
BaselineCorrections = 0 0
MethodNumber = 0 (1=Yes)
AnalysisArea = 1 918 995 1
AnalysisArea = 0 1800 2250 1
AnalysisArea = 0 2925 3234 1
Interference = 100010001000000000001100011101
CrossInterferences = 0 0 0 0 0
ReferenceFile = C:\Library180\Ethylene C2H4 0093 ppm.ref
ComponentNumber = 14
ComponentName = Acetone C3H60
ConcentrationUnit = ppm
ActiveLines = All
AutoAnalyze = 0 (1=Yes)
OutputChannel = 0
ViewResults = 1 (1=Yes)
AllowNegative = 0 (1=Yes)
ConversionMultiplier = 1
ResultSmoothing = 0
RangeSetting = 0
Range1 = 0 10
Range2 = 0 100
AlarmLimits = 0 100
AlarmSound = 0
Compensations = 1 1 1 0 -11
```

```
Calibrations = 0 0 4 2
ResidualWarningLimit = 0.01
ResidualErrorLimit = 0.02
UseDoubleReferences = 0 (1=Yes)
AutoInterferenceUpdate = 1 0.001
DefaultReference = 1
BaselineCorrections = 1 0
MethodNumber = 0 (1=Yes)
AnalysisArea = 1 1142 1320 0.5
AnalysisArea = 0 1798 2238 1
AnalysisArea = 0 2825 3450 1
Interference = 1001110010110000111111
CrossInterferences = 0 0 0 0 0
ReferenceFile = C:\Temet\library\Acetone C3H6O 0084 ppm.ref
ReferenceFile = C:\Temet\library\Acetone C3H6O 0490 ppm.ref
ComponentNumber = 15
ComponentName = Sulfur Hexafluoride
ConcentrationUnit = ppm
ActiveLines = All
AutoAnalyze = 0 (1=Yes)
OutputChannel = 0
ViewResults = 1 (1=Yes)
AllowNegative = 0 (1=Yes)
ConversionMultiplier = 1
ResultSmoothing = 0
RangeSetting = 1
Range1 = 0 20
Range2 = 0 1000
AlarmLimits = 0 100
AlarmSound = 0
Compensations = 1 1 1 0 -11
Calibrations = 0 0 4 2
ResidualWarningLimit = 0.01
ResidualErrorLimit = 0.02
UseDoubleReferences = 0 (1=Yes)
AutoInterferenceUpdate = 1 0.001
DefaultReference = 1
BaselineCorrections = 1 0
MethodNumber = 0 (1=Yes)
AnalysisArea = 1 895 1032 1
AnalysisArea = 0 1800 2250 1
AnalysisArea = 0 2550 3450 1
Interference = 1101010111111100110111
CrossInterferences = 0 0 0 0 0
ReferenceFile = C:\EMS Library\SF6-10.ref
ComponentNumber = 16
ComponentName = Hexane C6H14
ConcentrationUnit = ppm
ActiveLines = All
AutoAnalyze = 0 (1=Yes)
OutputChannel = 0
ViewResults = 0 (1=Yes)
AllowNegative = 0 (1=Yes)
ConversionMultiplier = 1
ResultSmoothing = 0
RangeSetting = 0
Range1 = 0 100
Range2 = 0 1000
AlarmLimits = 0 100
AlarmSound = 0
Compensations = 1 1 1 0 -11
Calibrations = 0 0 4 2
ResidualWarningLimit = 0.01
ResidualErrorLimit = 0.02
UseDoubleReferences = 0 (1=Yes)
AutoInterferenceUpdate = 1 0.001
DefaultReference = 1
```

```
BaselineCorrections = 1 0
MethodNumber = 0 (1=Yes)
AnalysisArea = 0 900 1400 1
AnalysisArea = 0 1800 2250 1
AnalysisArea = 1 2825 3003 0.5
Interference = 11010011010101001111111
CrossInterferences = 0 0 0 0 0
ReferenceFile = C:\Temet\library\Hexane C6H14 0024 ppm.ref
ReferenceFile = C:\Temet\library\Hexane C6H14 0045 ppm.ref
ComponentNumber = 17
ComponentName = Propane
ConcentrationUnit = ppm
ActiveLines = All
AutoAnalyze = 0 (1=Yes)
OutputChannel = 0
ViewResults = 1 (1=Yes)
AllowNegative = 0 (1=Yes)
ConversionMultiplier = 1
ResultSmoothing = 0
RangeSetting = 1
Range1 = 0 100
Range2 = 0 1000
AlarmLimits = 0 100
AlarmSound = 0
Compensations = 1 1 1 0 -11
Calibrations = 0 4 0 2
ResidualWarningLimit = 0.01
ResidualErrorLimit = 0.02
UseDoubleReferences = 0 (1=Yes)
AutoInterferenceUpdate = 1 0.001
DefaultReference = 1
BaselineCorrections = 1 0
MethodNumber = 0 (1=Yes)
AnalysisArea = 1 1296 1558 0.5
AnalysisArea = 0 1800 2250 1
AnalysisArea = 1 2918 3100 1
Interference = 11011011111101010111111
CrossInterferences = 0 0 0 0 0
ReferenceFile = C:\Temet\library\Propane C3H8 0147 ppm.ref
ComponentNumber = 18
ComponentName = Butane
ConcentrationUnit = ppm
ActiveLines = All
AutoAnalyze = 0 (1=Yes)
OutputChannel = 0
ViewResults = 1 (1=Yes)
AllowNegative = 0 (1=Yes)
ConversionMultiplier = 1
ResultSmoothing = 0
RangeSetting = 1
Range1 = 0 100
Range2 = 0 1000
AlarmLimits = 0 100
AlarmSound = 0
Compensations = 1 1 1 0 -11
Calibrations = 0 4 0 2
ResidualWarningLimit = 0.01
ResidualErrorLimit = 0.02
UseDoubleReferences = 0 (1=Yes)
AutoInterferenceUpdate = 1 0.001
DefaultReference = 1
BaselineCorrections = 1 0
MethodNumber = 0 (1=Yes)
AnalysisArea = 0 895 1380 0.8
AnalysisArea = 0 1810 2223 0.8
AnalysisArea = 1 2550 2910 0.5
Interference = 10011011010101011011111
```

```
CrossInterferences = 0 0 0 0 0
ReferenceFile = C:\Temet\library\Butane C4H10 0097 ppm.ref
ComponentNumber = 19
ComponentName = Octane
ConcentrationUnit = ppm
ActiveLines = All
AutoAnalyze = 0 (1=Yes)
OutputChannel = 0
ViewResults = 1 (1=Yes)
AllowNegative = 0 (1=Yes)
ConversionMultiplier = 1
ResultSmoothing = 0
RangeSetting = 1
Range1 = 0 100
Range2 = 0 1000
AlarmLimits = 0 100
AlarmSound = 0
Compensations = 1 1 1 0 -11
Calibrations = 0 4 0 2
ResidualWarningLimit = 0.01
ResidualErrorLimit = 0.02
UseDoubleReferences = 0 (1=Yes)
AutoInterferenceUpdate = 1 0.001
DefaultReference = 1
BaselineCorrections = 1 0
MethodNumber = 0 (1=Yes)
AnalysisArea = 0 895 1380 0.8
AnalysisArea = 0 1810 2223 0.8
AnalysisArea = 1 2800 2965 0.8
Interference = 1101001101010101011101111
CrossInterferences = 0 0 0 0 0
ReferenceFile = C:\Temet\library\n-Octane C8H18 0036 ppm.ref
ComponentNumber = 20
ComponentName = Benzene C2H6
ConcentrationUnit = ppm
ActiveLines = All
AutoAnalyze = 0 (1=Yes)
OutputChannel = 0
ViewResults = 0 (1=Yes)
AllowNegative = 0 (1=Yes)
ConversionMultiplier = 1
ResultSmoothing = 0
RangeSetting = 1
Range1 = 0 100
Range2 = 0 1000
AlarmLimits = 0 100
AlarmSound = 0
Compensations = 1 1 1 0 -11
Calibrations = 0 0 4 2
ResidualWarningLimit = 0.01
ResidualErrorLimit = 0.02
UseDoubleReferences = 0 (1=Yes)
AutoInterferenceUpdate = 1 0.001
DefaultReference = 1
BaselineCorrections = 1 0
MethodNumber = 0 (1=Yes)
AnalysisArea = 0 910 1397 1
AnalysisArea = 0 1798 2238 1
AnalysisArea = 1 3000 3130 0.5
Interference = 1011000010011111111101
CrossInterferences = 0 0 0 0 0
ReferenceFile = C:\Temet\library\Benzene C6H6 0066 ppm.ref
ComponentNumber = 21
ComponentName = Formaldehyde
ConcentrationUnit = ppm
ActiveLines = All
AutoAnalyze = 1 (1=Yes)
```

```
OutputChannel = 0
ViewResults = 1 (1=Yes)
AllowNegative = 1 (1=Yes)
ConversionMultiplier = 1
ResultSmoothing = 0
RangeSetting = 0
Range1 = 0 10
Range2 = 0 100
AlarmLimits = 0 100
AlarmSound = 0
Compensations = 1 1 1 0 -11
Calibrations = 0 0 4 2
ResidualWarningLimit = 0.01
ResidualErrorLimit = 0.02
UseDoubleReferences = 0 (1=Yes)
AutoInterferenceUpdate = 1 0.001
DefaultReference = 1
BaselineCorrections = 1 0
MethodNumber = 0 (1=Yes)
AnalysisArea = 0 995 1250 1
AnalysisArea = 1 2450 2600 0.6
AnalysisArea = 1 2650 3211 0.5
Interference = 100110101000100000000100111111
CrossInterferences = 0 0 0 0 0
ReferenceFile = HCHO_50.ref
ReferenceFile = Formaldehyde CH2O.ref
ReferenceFile = HCHO_10.ref
ComponentNumber = 22
ComponentName = Acetaldehyde
ConcentrationUnit = ppm
ActiveLines = All
AutoAnalyze = 1 (1=Yes)
OutputChannel = 0
ViewResults = 1 (1=Yes)
AllowNegative = 1 (1=Yes)
ConversionMultiplier = 1
ResultSmoothing = 0
RangeSetting = 0
Range1 = 0 10
Range2 = 0 100
AlarmLimits = 0 100
AlarmSound = 0
Compensations = 1 1 1 0 -11
Calibrations = 0 4 0 2
ResidualWarningLimit = 0.01
ResidualErrorLimit = 0.02
UseDoubleReferences = 0 (1=Yes)
AutoInterferenceUpdate = 1 0.001
DefaultReference = 1
BaselineCorrections = 1 0
MethodNumber = 0 (1=Yes)
AnalysisArea = 1 3200 3350 1
AnalysisArea = 1 2925 3200 1
AnalysisArea = 1 2638 2916 1
Interference = 100110101000100000001000111011
CrossInterferences = 0 0 0 0 0
ReferenceFile = Acetaldehyde C2H4O_05.ref
ReferenceFile = Acetaldehyde C2H4O 0100 ppm.ref
ReferenceFile = Acetaldehyde C2H4O 0500 ppm.ref
ComponentNumber = 23
ComponentName = Ozone O3
ConcentrationUnit = ppm
ActiveLines = All
AutoAnalyze = 0 (1=Yes)
OutputChannel = 0
ViewResults = 1 (1=Yes)
AllowNegative = 0 (1=Yes)
```

```
ConversionMultiplier = 1
ResultSmoothing = 0
RangeSetting = 1
Range1 = 0 100
Range2 = 0 1000
AlarmLimits = 0 100
AlarmSound = 0
Compensations = 1 1 1 0 -11
Calibrations = 0 4 0 2
ResidualWarningLimit = 0.01
ResidualErrorLimit = 0.02
UseDoubleReferences = 0 (1=Yes)
AutoInterferenceUpdate = 1 0.001
DefaultReference = 1
BaselineCorrections = 1 0
MethodNumber = 0 (1=Yes)
AnalysisArea = 1 926 1127 1
AnalysisArea = 0 1798 2246 1
AnalysisArea = 0 2550 3450 1
Interference = 1101010110110110111111
CrossInterferences = 0 0 0 0 0
ReferenceFile = O3_785.ref
ReferenceFile = O3_560.ref
ReferenceFile = O3_190.ref
ComponentNumber = 24
ComponentName = SO3
ConcentrationUnit = ppm
ActiveLines = All
AutoAnalyze = 0 (1=Yes)
OutputChannel = 0
ViewResults = 1 (1=Yes)
AllowNegative = 0 (1=Yes)
ConversionMultiplier = 1
ResultSmoothing = 0
RangeSetting = 1
Range1 = 0 100
Range2 = 0 1000
AlarmLimits = 0 100
AlarmSound = 0
Compensations = 1 1 1 0 -11
Calibrations = 0 4 0 2
ResidualWarningLimit = 0.01
ResidualErrorLimit = 0.02
UseDoubleReferences = 0 (1=Yes)
AutoInterferenceUpdate = 0 0.001
DefaultReference = 1
BaselineCorrections = 1 0
MethodNumber = 0 (1=Yes)
AnalysisArea = 1 1196 1397 1
AnalysisArea = 0 1800 2250 1
AnalysisArea = 0 2550 3450 1
Interference = 110000011
CrossInterferences = 0 0 0 0 0
ReferenceFile = C:\DemoLibrary\Sulfur trioxide SO3 50ppm (cemdemo).ref
ComponentNumber = 25
ComponentName = MEA
ConcentrationUnit = ppm
ActiveLines = All
AutoAnalyze = 1 (1=Yes)
OutputChannel = 0
ViewResults = 1 (1=Yes)
AllowNegative = 0 (1=Yes)
ConversionMultiplier = 1
ResultSmoothing = 0
RangeSetting = 0
Range1 = 0 300
Range2 = 0 500
```

```
AlarmLimits = 0 15000
AlarmSound = 0
Compensations = 1 1 1 0 -11
Calibrations = 0 0 0 2
ResidualWarningLimit = 0.01
ResidualErrorLimit = 0.02
UseDoubleReferences = 0 (1=Yes)
AutoInterferenceUpdate = 1 0.005
DefaultReference = 1
BaselineCorrections = 1 0
MethodNumber = 0 (1=Yes)
AnalysisArea = 1 2624 3150 1
AnalysisArea = 1 2416 2601 1
AnalysisArea = 0 995 1119 1
Interference = 1001101000001000000001100011011
CrossInterferences = 0 0 0 0 0
ReferenceFile = MEA_500.ref
ReferenceFile = MEA_100.ref
ReferenceFile = C:\Pickle References\MEA_15000.ref
ReferenceFile = C:\Pickle References\MEA_1000.ref
ReferenceFile = C:\Pickle References\MEA_2000.ref
ReferenceFile = C:\Pickle References\MEA_5000.ref
ReferenceFile = C:\Pickle References\MEA_10000.ref
ComponentNumber = 26
ComponentName = Methanol
ConcentrationUnit = Auto
ActiveLines = All
AutoAnalyze = 1 (1=Yes)
OutputChannel = 0
ViewResults = 1 (1=Yes)
AllowNegative = 1 (1=Yes)
ConversionMultiplier = 1
ResultSmoothing = 0
RangeSetting = 0
Range1 = 0 25
Range2 = 0 500
AlarmLimits = 0 1000
AlarmSound = 0
Compensations = 1 1 1 0 -11
Calibrations = 0 0 4 2
ResidualWarningLimit = 0.01
ResidualErrorLimit = 0.02
UseDoubleReferences = 0 (1=Yes)
AutoInterferenceUpdate = 1 0.005
DefaultReference = 1
BaselineCorrections = 1 0
MethodNumber = 0 (1=Yes)
AnalysisArea = 1 995 1073 1
AnalysisArea = 1 1095 1150 1
AnalysisArea = 1 2450 3180 1
Interference = 1001101010001000000001100101111
CrossInterferences = 0 0 0 0 0
ReferenceFile = C:\Library180\Methanol_100.ref
ComponentNumber = 27
ComponentName = Methylamine
ConcentrationUnit = Auto
ActiveLines = All
AutoAnalyze = 1 (1=Yes)
OutputChannel = 0
ViewResults = 1 (1=Yes)
AllowNegative = 1 (1=Yes)
ConversionMultiplier = 1
ResultSmoothing = 0
RangeSetting = 0
Range1 = 0 10
Range2 = 0 100
AlarmLimits = 0 100
```

```
AlarmSound = 0
Compensations = 1 1 1 0 -11
Calibrations = 0 0 4 2
ResidualWarningLimit = 0.01
ResidualErrorLimit = 0.02
UseDoubleReferences = 0 (1=Yes)
AutoInterferenceUpdate = 1 0.001
DefaultReference = 1
BaselineCorrections = 1 0
MethodNumber = 0 (1=Yes)
AnalysisArea = 1 2022 2223 1
AnalysisArea = 1 2450 2650 1
AnalysisArea = 1 2800 3203 1
Interference = 1011111010001000000001100110111
CrossInterferences = 0 0 0 0 0
ReferenceFile = Methylamine CH5N 0100 ppm.ref
ReferenceFile = Methylamine CH5N 0500 ppm.ref
ReferenceFile = Methylamine CH5N 0894 ppm.ref
ComponentNumber = 28
ComponentName = Carbon Dioxide CO2 (ppm)
ConcentrationUnit = Auto
ActiveLines = All
AutoAnalyze = 1 (1=Yes)
OutputChannel = 0
ViewResults = 1 (1=Yes)
AllowNegative = 0 (1=Yes)
ConversionMultiplier = 1
ResultSmoothing = 0
RangeSetting = 0
Range1 = 0 5000
Range2 = 0 25000
AlarmLimits = 0 25000
AlarmSound = 0
Compensations = 1 1 1 0 -11
Calibrations = 0 4 0 2
ResidualWarningLimit = 0.01
ResidualErrorLimit = 0.02
UseDoubleReferences = 0 (1=Yes)
AutoInterferenceUpdate = 1 0.001
DefaultReference = 6
BaselineCorrections = 1 0
MethodNumber = 0 (1=Yes)
AnalysisArea = 0 2207 2501 1.2
AnalysisArea = 1 1984 2169 1
AnalysisArea = 1 910 1019 1
Interference = 1010101010001000000001100111001
CrossInterferences = 0 0 0 0 0
ReferenceFile = CO2_500ppm.ref
ReferenceFile = CO2_1000ppm.ref
ReferenceFile = CO2_5000ppm.ref
ReferenceFile = CO2_100ppm.ref
ReferenceFile = CO2_15000ppm.ref
ReferenceFile = CO2_50ppm.ref
ReferenceFile = CO2_250ppm.ref
ReferenceFile = CO2_750ppm.ref
ReferenceFile = CO2_2500ppm.ref
ComponentNumber = 29
ComponentName = Methane CH4
ConcentrationUnit = Auto
ActiveLines = All
AutoAnalyze = 0 (1=Yes)
OutputChannel = 0
ViewResults = 1 (1=Yes)
AllowNegative = 1 (1=Yes)
ConversionMultiplier = 1
ResultSmoothing = 0
RangeSetting = 0
```

```
Range1 = 0 10
Range2 = 0 100
AlarmLimits = 0 100
AlarmSound = 0
Compensations = 1 1 1 0 -11
Calibrations = 0 0 4 2
ResidualWarningLimit = 0.01
ResidualErrorLimit = 0.02
UseDoubleReferences = 0 (1=Yes)
AutoInterferenceUpdate = 1 0.001
DefaultReference = 1
BaselineCorrections = 1 0
MethodNumber = 0 (1=Yes)
AnalysisArea = 0 1292 1412 0.5
AnalysisArea = 1 2833 3203 0.5
AnalysisArea = 1 3018 3203 0.5
Interference = 100110101000000000001100101001
CrossInterferences = 0 0 0 0 0
ReferenceFile = Methane CH4 0101 ppm.ref
ReferenceFile = Methane CH4 0050 ppm.ref
ComponentNumber = 30
ComponentName = Piperazine
ConcentrationUnit = Auto
ActiveLines = All
AutoAnalyze = 1 (1=Yes)
OutputChannel = 0
ViewResults = 1 (1=Yes)
AllowNegative = 1 (1=Yes)
ConversionMultiplier = 1
ResultSmoothing = 0
RangeSetting = 0
Range1 = 0 250
Range2 = 0 500
AlarmLimits = 0 500
AlarmSound = 1
Compensations = 1 1 1 0 -11
Calibrations = 0 0 4 2
ResidualWarningLimit = 0.01
ResidualErrorLimit = 0.02
UseDoubleReferences = 0 (1=Yes)
AutoInterferenceUpdate = 1 0.001
DefaultReference = 4
BaselineCorrections = 1 0
MethodNumber = 0 (1=Yes)
AnalysisArea = 0 1096 1380 1
AnalysisArea = 0 1810 2223 1
AnalysisArea = 1 2550 3095 1
Interference = 10011010100010000000110011101
CrossInterferences = 0 0 0 0 0
ReferenceFile = Piperazine_2ppm_180C.ref
ReferenceFile = Piperazine_105ppm_180C.ref
ReferenceFile = Piperazine_188ppm_180C.ref
ReferenceFile = Piperazine_407ppm_180C.ref
ReferenceFile = Piperazine_471ppm_180C.ref
ReferenceFile = Piperazine_40ppm_180C.ref
ComponentNumber = 201
ComponentName = NOx
ConcentrationUnit = ppm
ActiveLines = All
AutoAnalyze = 0 (1=Yes)
OutputChannel = 0
ViewResults = 1 (1=Yes)
AllowNegative = 1 (1=Yes)
ConversionMultiplier = 1
ResultSmoothing = 0
RangeSetting = 0
Range1 = 0 20
```

```
Range2 = 0 250
AlarmLimits = 0 500
AlarmSound = 0
Compensations = 1 1 1 0 -11
Calibrations = 0 0 4 2
Interference = 0000111
CrossInterferences = 0 0 0 0 0
ComponentNumber = 202
ComponentName = THC
ConcentrationUnit = ppm
ActiveLines = All
AutoAnalyze = 0 (1=Yes)
OutputChannel = 0
ViewResults = 1 (1=Yes)
AllowNegative = 1 (1=Yes)
ConversionMultiplier = 1
ResultSmoothing = 0
RangeSetting = 1
Range1 = 0 500
Range2 = 0 1000
AlarmLimits = 0 500
AlarmSound = 0
Compensations = 1 1 1 0 -11
Calibrations = 0 0 4 2
Interference = 0001000000011
CrossInterferences = 0 0 0 0 0
ComponentNumber = 211
ComponentName = Input1
ConcentrationUnit = %
ActiveLines = All
AutoAnalyze = 0 (1=Yes)
OutputChannel = 0
ViewResults = 1 (1=Yes)
AllowNegative = 1 (1=Yes)
ConversionMultiplier = 1
ResultSmoothing = 0
RangeSetting = 1
Range1 = 0 100
Range2 = 0 1000
AlarmLimits = 0 100
AlarmSound = 0
Compensations = 1 1 1 0 -11
Calibrations = 0 0 4 2
Interference = 0
CrossInterferences = 0 0 0 0 0
ComponentNumber = 212
ComponentName = Input2
ConcentrationUnit = %
ActiveLines = All
AutoAnalyze = 0 (1=Yes)
OutputChannel = 0
ViewResults = 1 (1=Yes)
AllowNegative = 1 (1=Yes)
ConversionMultiplier = 1
ResultSmoothing = 0
RangeSetting = 1
Range1 = 0 100
Range2 = 0 1000
AlarmLimits = 0 100
AlarmSound = 0
Compensations = 1 1 1 0 -11
Calibrations = 0 0 4 2
Interference = 0
CrossInterferences = 0 0 0 0 0
ComponentNumber = 213
ComponentName = Input3
ConcentrationUnit = %
```

```
ActiveLines = All
AutoAnalyze = 0 (1=Yes)
OutputChannel = 0
ViewResults = 1 (1=Yes)
AllowNegative = 1 (1=Yes)
ConversionMultiplier = 1
ResultSmoothing = 0
RangeSetting = 1
Range1 = 0 100
Range2 = 0 1000
AlarmLimits = 0 100
AlarmSound = 0
Compensations = 1 1 1 0 -11
Calibrations = 0 0 4 2
Interference = 0
CrossInterferences = 0 0 0 0 0
ComponentNumber = 214
ComponentName = Input4
ConcentrationUnit = %
ActiveLines = All
AutoAnalyze = 0 (1=Yes)
OutputChannel = 0
ViewResults = 1 (1=Yes)
AllowNegative = 1 (1=Yes)
ConversionMultiplier = 1
ResultSmoothing = 0
RangeSetting = 1
Range1 = 0 100
Range2 = 0 1000
AlarmLimits = 0 100
AlarmSound = 0
Compensations = 1 1 1 0 -11
Calibrations = 0 0 4 2
Interference = 0
CrossInterferences = 0 0 0 0 0
ComponentNumber = 215
ComponentName = Input5
ConcentrationUnit = %
ActiveLines = All
AutoAnalyze = 0 (1=Yes)
OutputChannel = 0
ViewResults = 1 (1=Yes)
AllowNegative = 1 (1=Yes)
ConversionMultiplier = 1
ResultSmoothing = 0
RangeSetting = 1
Range1 = 0 100
Range2 = 0 1000
AlarmLimits = 0 100
AlarmSound = 0
Compensations = 1 1 1 0 -11
Calibrations = 0 0 4 2
Interference = 0
CrossInterferences = 0 0 0 0 0
ComponentNumber = 216
ComponentName = Input6
ConcentrationUnit = %
ActiveLines = All
AutoAnalyze = 0 (1=Yes)
OutputChannel = 0
ViewResults = 1 (1=Yes)
AllowNegative = 1 (1=Yes)
ConversionMultiplier = 1
ResultSmoothing = 0
RangeSetting = 1
Range1 = 0 100
Range2 = 0 1000
```

```
AlarmLimits = 0 100
AlarmSound = 0
Compensations = 1 1 1 0 -11
Calibrations = 0 0 4 2
Interference = 0
CrossInterferences = 0 0 0 0 0
ComponentNumber = 217
ComponentName = Input7
ConcentrationUnit = %
ActiveLines = All
AutoAnalyze = 0 (1=Yes)
OutputChannel = 0
ViewResults = 1 (1=Yes)
AllowNegative = 1 (1=Yes)
ConversionMultiplier = 1
ResultSmoothing = 0
RangeSetting = 1
Range1 = 0 100
Range2 = 0 1000
AlarmLimits = 0 100
AlarmSound = 0
Compensations = 1 1 1 0 -11
Calibrations = 0 0 4 2
Interference = 0
CrossInterferences = 0 0 0 0 0
ComponentNumber = 218
ComponentName = Input8
ConcentrationUnit = %
ActiveLines = All
AutoAnalyze = 0 (1=Yes)
OutputChannel = 0
ViewResults = 1 (1=Yes)
AllowNegative = 1 (1=Yes)
ConversionMultiplier = 1
ResultSmoothing = 0
RangeSetting = 1
Range1 = 0 100
Range2 = 0 1000
AlarmLimits = 0 100
AlarmSound = 0
Compensations = 1 1 1 0 -11
Calibrations = 0 0 4 2
Interference = 0
CrossInterferences = 0 0 0 0 0
ComponentNumber = 219
ComponentName = Pressure
ConcentrationUnit = mbar
ActiveLines = All
AutoAnalyze = 1 (1=Yes)
OutputChannel = 0
ViewResults = 1 (1=Yes)
AllowNegative = 1 (1=Yes)
ConversionMultiplier = 1
ResultSmoothing = 0
RangeSetting = 1
Range1 = 0 2000
Range2 = 0 2000
AlarmLimits = 900 2000
AlarmSound = 0
Compensations = 1 1 1 0 -11
Calibrations = 0 0 4 2
Interference = 0
CrossInterferences = 0 0 0 0 0
ComponentNumber = 220
ComponentName = Oxygen (O2)
ConcentrationUnit = vol-%
ActiveLines = All
```

```
AutoAnalyze = 0 (1=Yes)
OutputChannel = 0
ViewResults = 1 (1=Yes)
AllowNegative = 1 (1=Yes)
ConversionMultiplier = 1
ResultSmoothing = 0
RangeSetting = 1
Range1 = 0 100
Range2 = 0 1000
AlarmLimits = 0 100
AlarmSound = 0
Compensations = 1 1 1 0 -11
Calibrations = 0 0 4 2
Interference = 0
CrossInterferences = 0 0 0 0 0
ComponentNumber = 221
ComponentName = AUX
ConcentrationUnit = %
ActiveLines = All
AutoAnalyze = 0 (1=Yes)
OutputChannel = 0
ViewResults = 1 (1=Yes)
AllowNegative = 1 (1=Yes)
ConversionMultiplier = 1
ResultSmoothing = 0
RangeSetting = 1
Range1 = 0 100
Range2 = 0 1000
AlarmLimits = 0 100
AlarmSound = 0
Compensations = 1 1 1 0 -11
Calibrations = 0 0 4 2
Interference = 0
CrossInterferences = 0 0 0 0 0
```

C.4 High CO_2 Concentration Analysis Method

```
LibraryPath = C:\Pickle Piperazine Method\
ComponentNumber = 1
ComponentName = Water vapor H2O
ConcentrationUnit = vol-%
ActiveLines = All
AutoAnalyze = 1 (1=Yes)
OutputChannel = 0
ViewResults = 1 (1=Yes)
AllowNegative = 0 (1=Yes)
ConversionMultiplier = 1
ResultSmoothing = 0
RangeSetting = 0
Range1 = 0 15
Range2 = 0 30
AlarmLimits = 0 30
AlarmSound = 0
Compensations = 1 1 1 0 -11
Calibrations = 0 0 4 2
ResidualWarningLimit = 0.01
ResidualErrorLimit = 0.02
UseDoubleReferences = 1 (1=Yes)
AutoInterferenceUpdate = 1 0.001
DefaultReference = 12
BaselineCorrections = 1 0
MethodNumber = 0 (1=Yes)
AnalysisArea = 1 1093 1304 1
AnalysisArea = 1 1923 2223 1
AnalysisArea = 1 2550 3319 0.5
```

```
Interference = 0111111010001000000001100111011
CrossInterferences = 0 0 0 0 0
ReferenceFile = H2O_03.ref
ReferenceFile = H2O_01.ref
ReferenceFile = H2O_02.ref
ReferenceFile = C:\Pickle Piperazine Method\Water Ref - 20050802\H2O_04.ref
ReferenceFile = C:\Pickle Piperazine Method\Water Ref - 20050802\H2O_06.ref
ReferenceFile = C:\Pickle Piperazine Method\Water Ref - 20050802\H2O_08.ref
ReferenceFile = C:\Pickle Piperazine Method\Water Ref - 20050802\H2O_10.ref
ReferenceFile = C:\Pickle Piperazine Method\Water Ref - 20050802\H2O_12.ref
ReferenceFile = C:\Pickle Piperazine Method\Water Ref - 20050802\H2O_24.ref
ReferenceFile = C:\Pickle Piperazine Method\Water Ref - 20050802\H2O_26.ref
ReferenceFile = C:\Pickle Piperazine Method\Water Ref - 20050802\H2O_28.ref
ReferenceFile = C:\Library 01253\Water Ref - 20040616\H2O_30.ref
ReferenceFile = C:\Library 01253\Water Ref - 20040616\H2O_14.ref
ReferenceFile = C:\Library 01253\Water Ref - 20040616\H2O_16.ref
ReferenceFile = C:\Library 01253\Water Ref - 20040616\H2O_18.ref
ReferenceFile = C:\Library 01253\Water Ref - 20040616\H2O_20.ref
ReferenceFile = C:\Library 01253\Water Ref - 20040616\H2O_22.ref
ComponentNumber = 2
ComponentName = Carbon dioxide CO2 (vol%)
ConcentrationUnit = vol-%
ActiveLines = All
AutoAnalyze = 1 (1=Yes)
OutputChannel = 0
ViewResults = 1 (1=Yes)
AllowNegative = 0 (1=Yes)
ConversionMultiplier = 1
ResultSmoothing = 0
RangeSetting = 0
Range1 = 0 15
Range2 = 0 60
AlarmLimits = 0 50
AlarmSound = 0
Compensations = 1 1 1 0 -11
Calibrations = 0 4 0 2
ResidualWarningLimit = 0.01
ResidualErrorLimit = 0.02
UseDoubleReferences = 0 (1=Yes)
AutoInterferenceUpdate = 1 0.001
DefaultReference = 3
BaselineCorrections = 1 0
MethodNumber = 0 (1=Yes)
AnalysisArea = 1 910 1019 1
AnalysisArea = 0 2450 2650 0.5
AnalysisArea = 1 1984 2169 0.5
Interference = 1010101010001000000001100111001
CrossInterferences = 0 0 0 0 0
ReferenceFile = CO2_30vol.ref
ReferenceFile = CO2_06vol.ref
ReferenceFile = CO2_03vol.ref
ReferenceFile = CO2_27vol.ref
ReferenceFile = CO2_24vol.ref
ReferenceFile = CO2_21vol.ref
ReferenceFile = CO2_09vol.ref
ReferenceFile = CO2_12vol.ref
ReferenceFile = CO2_15vol.ref
ReferenceFile = CO2_50vol.ref
ComponentNumber = 3
ComponentName = Carbon monoxide CO
ConcentrationUnit = ppm
ActiveLines = All
AutoAnalyze = 1 (1=Yes)
OutputChannel = 0
ViewResults = 1 (1=Yes)
AllowNegative = 1 (1=Yes)
ConversionMultiplier = 1
```

```
ResultSmoothing = 0
RangeSetting = 0
Range1 = 0 10
Range2 = 0 500
AlarmLimits = 0 5000
AlarmSound = 0
Compensations = 1 1 1 0 -11
Calibrations = 0 0 4 2
ResidualWarningLimit = 0.01
ResidualErrorLimit = 0.02
UseDoubleReferences = 0 (1=Yes)
AutoInterferenceUpdate = 1 0.001
DefaultReference = 1
BaselineCorrections = 1 0
MethodNumber = 0 (1=Yes)
AnalysisArea = 1 2007 2207 0.5
AnalysisArea = 1 2624 2750 1
AnalysisArea = 0 2550 2600 1
Interference = 11001110100000000000001100111001
CrossInterferences = 0 0 0 0 0
ReferenceFile = CO_998.ref
ReferenceFile = CO_11.ref
ReferenceFile = CO_51.ref
ReferenceFile = CO_100.ref
ReferenceFile = CO_200.ref
ReferenceFile = CO_402.ref
ReferenceFile = CO_602.ref
ReferenceFile = CO_805.ref
ComponentNumber = 4
ComponentName = Methane CH4
ConcentrationUnit = ppm
ActiveLines = All
AutoAnalyze = 1 (1=Yes)
OutputChannel = 0
ViewResults = 1 (1=Yes)
AllowNegative = 1 (1=Yes)
ConversionMultiplier = 1
ResultSmoothing = 0
RangeSetting = 0
Range1 = 0 10
Range2 = 0 100
AlarmLimits = 0 500
AlarmSound = 0
Compensations = 1 1 1 0 -11
Calibrations = 0 0 4 2
ResidualWarningLimit = 0.01
ResidualErrorLimit = 0.02
UseDoubleReferences = 0 (1=Yes)
AutoInterferenceUpdate = 1 0.001
DefaultReference = 2
BaselineCorrections = 1 0
MethodNumber = 0 (1=Yes)
AnalysisArea = 0 1292 1412 0.5
AnalysisArea = 1 2833 3203 0.5
AnalysisArea = 1 3018 3203 0.5
Interference = 10001010100010000000001100111011
CrossInterferences = 0 0 0 0 0
ReferenceFile = C:\Library180\Methane CH4 0050 ppm.ref
ReferenceFile = C:\Library180\Methane CH4 0101 ppm.ref
ComponentNumber = 5
ComponentName = Nitrous oxide N2O
ConcentrationUnit = ppm
ActiveLines = All
AutoAnalyze = 1 (1=Yes)
OutputChannel = 0
ViewResults = 1 (1=Yes)
AllowNegative = 1 (1=Yes)
```

```
ConversionMultiplier = 1
ResultSmoothing = 0
RangeSetting = 0
Range1 = 0 100
Range2 = 0 500
AlarmLimits = 0 100000
AlarmSound = 1
Compensations = 1 1 1 0 -11
Calibrations = 0 0 0 2
ResidualWarningLimit = 0.01
ResidualErrorLimit = 0.02
UseDoubleReferences = 0 (1=Yes)
AutoInterferenceUpdate = 1 0.001
DefaultReference = 2
BaselineCorrections = 1 0
MethodNumber = 0 (1=Yes)
AnalysisArea = 1 2107 2246 0.5
AnalysisArea = 1 2647 2900 1
AnalysisArea = 0 2400 2700 1
Interference = 111101101000000000001100111011
CrossInterferences = 0 0 0 0 0
ReferenceFile = Nitrous oxide N2O 0122 ppm.ref
ReferenceFile = Nitrous oxide N2O 0050 ppm.ref
ComponentNumber = 6
ComponentName = Nitrogen monoxide NO
ConcentrationUnit = ppm
ActiveLines = All
AutoAnalyze = 1 (1=Yes)
OutputChannel = 0
ViewResults = 1 (1=Yes)
AllowNegative = 1 (1=Yes)
ConversionMultiplier = 1
ResultSmoothing = 0
RangeSetting = 0
Range1 = 0 20
Range2 = 0 150
AlarmLimits = 0 1000
AlarmSound = 0
Compensations = 1 1 1 0 -11
Calibrations = 0 0 4 2
ResidualWarningLimit = 0.01
ResidualErrorLimit = 0.02
UseDoubleReferences = 0 (1=Yes)
AutoInterferenceUpdate = 0 0.001
DefaultReference = 1
BaselineCorrections = 1 0
MethodNumber = 0 (1=Yes)
AnalysisArea = 0 1760 1868 0.8
AnalysisArea = 1 1883 2099 0.8
AnalysisArea = 1 2450 2700 1
Interference = 1110100010000000000001001001
CrossInterferences = 0 0 0 0 0
ReferenceFile = NO_194.ref
ReferenceFile = NO_10.ref
ReferenceFile = NO_50.ref
ReferenceFile = NO_99.ref
ComponentNumber = 7
ComponentName = Nitrogen dioxide NO2
ConcentrationUnit = ppm
ActiveLines = All
AutoAnalyze = 1 (1=Yes)
OutputChannel = 0
ViewResults = 1 (1=Yes)
AllowNegative = 1 (1=Yes)
ConversionMultiplier = 1
ResultSmoothing = 0
RangeSetting = 0
```

```
Range1 = 0 20
Range2 = 0 1000
AlarmLimits = 0 1000
AlarmSound = 0
Compensations = 1 1 1 0 -11
Calibrations = 0 0 4 2
ResidualWarningLimit = 0.01
ResidualErrorLimit = 0.02
UseDoubleReferences = 0 (1=Yes)
AutoInterferenceUpdate = 1 0.001
DefaultReference = 1
BaselineCorrections = 1 0
MethodNumber = 0 (1=Yes)
AnalysisArea = 0 941 1397 1
AnalysisArea = 0 1497 1706 1.8
AnalysisArea = 1 2550 2933 0.5
Interference = 10011000100010000000001100111011
CrossInterferences = 0 0 0 0 0
ReferenceFile = Nitrogen dioxide NO2 0050 ppm.ref
ReferenceFile = NO2_194.ref
ReferenceFile = Nitrogen dioxide NO2 0005 ppm.ref
ComponentNumber = 8
ComponentName = Sulfur dioxide SO2
ConcentrationUnit = ppm
ActiveLines = All
AutoAnalyze = 0 (1=Yes)
OutputChannel = 0
ViewResults = 1 (1=Yes)
AllowNegative = 1 (1=Yes)
ConversionMultiplier = 1
ResultSmoothing = 0
RangeSetting = 0
Range1 = 0 500
Range2 = 0 3000
AlarmLimits = 0 5000
AlarmSound = 0
Compensations = 1 1 1 0 -11
Calibrations = 0 4 0 2
ResidualWarningLimit = 0.01
ResidualErrorLimit = 0.02
UseDoubleReferences = 0 (1=Yes)
AutoInterferenceUpdate = 1 0.001
DefaultReference = 1
BaselineCorrections = 1 0
MethodNumber = 0 (1=Yes)
AnalysisArea = 1 1042 1250 1
AnalysisArea = 0 1190 1250 1
AnalysisArea = 1 2485 2600 1
Interference = 11001000100000000000011001
CrossInterferences = 0 0 0 0 0
ReferenceFile = SO2_810.ref
ReferenceFile = SO2_1012.ref
ReferenceFile = SO2_202.ref
ReferenceFile = SO2_408.ref
ReferenceFile = SO2_50.ref
ReferenceFile = SO2_602.ref
ReferenceFile = SO2_10.ref
ComponentNumber = 9
ComponentName = Ammonia NH3
ConcentrationUnit = ppm
ActiveLines = All
AutoAnalyze = 1 (1=Yes)
OutputChannel = 0
ViewResults = 1 (1=Yes)
AllowNegative = 1 (1=Yes)
ConversionMultiplier = 1
ResultSmoothing = 0
```

```
RangeSetting = 0
Range1 = 0 250
Range2 = 0 1000
AlarmLimits = 0 1000
AlarmSound = 0
Compensations = 1 1 1 0 -11
Calibrations = 0 4 0 2
ResidualWarningLimit = 0.01
ResidualErrorLimit = 0.02
UseDoubleReferences = 0 (1=Yes)
AutoInterferenceUpdate = 1 0.001
DefaultReference = 6
BaselineCorrections = 1 0
MethodNumber = 0 (1=Yes)
AnalysisArea = 1 910 980 0.5
AnalysisArea = 0 1096 1250 0.5
AnalysisArea = 1 3196 3396 0.5
Interference = 11001010000001000000001100111001
CrossInterferences = 0 0 0 0 0
ReferenceFile = NH3_1000ppm.ref
ReferenceFile = NH3_51ppm.ref
ReferenceFile = NH3_100ppm.ref
ReferenceFile = NH3_249ppm.ref
ReferenceFile = NH3_498ppm.ref
ReferenceFile = NH3_742ppm.ref
ComponentNumber = 10
ComponentName = Hydrogen chloride HCl
ConcentrationUnit = ppm
ActiveLines = All
AutoAnalyze = 0 (1=Yes)
OutputChannel = 0
ViewResults = 1 (1=Yes)
AllowNegative = 0 (1=Yes)
ConversionMultiplier = 1
ResultSmoothing = 0
RangeSetting = 0
Range1 = 0 20
Range2 = 0 1000
AlarmLimits = 0 1000
AlarmSound = 0
Compensations = 1 1 1 0 -11
Calibrations = 0 0 4 2
ResidualWarningLimit = 0.01
ResidualErrorLimit = 0.02
UseDoubleReferences = 0 (1=Yes)
AutoInterferenceUpdate = 1 0.001
DefaultReference = 1
BaselineCorrections = 0 0
MethodNumber = 0 (1=Yes)
AnalysisArea = 0 2550 2990 1
AnalysisArea = 0 2550 3200 1
AnalysisArea = 1 2609 2888 0.5
Interference = 00000001000000000000001
CrossInterferences = 0 0 0 0 0
ReferenceFile = HCl_983.ref
ReferenceFile = HCL_801.ref
ReferenceFile = HCL_100.ref
ReferenceFile = HCL_19.ref
ReferenceFile = HCL_200.ref
ReferenceFile = HCL_403.ref
ReferenceFile = HCL_49.ref
ReferenceFile = HCL_51.ref
ReferenceFile = HCL_599.ref
ReferenceFile = HCL_10.ref
ComponentNumber = 11
ComponentName = Hydrogen fluoride HF
ConcentrationUnit = ppm
```

```
ActiveLines = All
AutoAnalyze = 0 (1=Yes)
OutputChannel = 0
ViewResults = 0 (1=Yes)
AllowNegative = 0 (1=Yes)
ConversionMultiplier = 1
ResultSmoothing = 0
RangeSetting = 1
Range1 = 0 10
Range2 = 0 1000
AlarmLimits = 0 500
AlarmSound = 0
Compensations = 1 1 1 0 -11
Calibrations = 0 0 4 2
ResidualWarningLimit = 0.01
ResidualErrorLimit = 0.02
UseDoubleReferences = 0 (1=Yes)
AutoInterferenceUpdate = 0 0.001
DefaultReference = 1
BaselineCorrections = 1 0
MethodNumber = 0 (1=Yes)
AnalysisArea = 0 910 1397 1
AnalysisArea = 0 1798 2246 1
AnalysisArea = 1 4010 4230 1
Interference = 100000000100001
CrossInterferences = 0 0 0 0 0
ReferenceFile = C:\Temet\library180\HF_100.ref
ComponentNumber = 12
ComponentName = MEK C4H80
ConcentrationUnit = ppm
ActiveLines = All
AutoAnalyze = 0 (1=Yes)
OutputChannel = 0
ViewResults = 1 (1=Yes)
AllowNegative = 0 (1=Yes)
ConversionMultiplier = 1
ResultSmoothing = 0
RangeSetting = 0
Range1 = 0 10
Range2 = 0 100
AlarmLimits = 0 100
AlarmSound = 0
Compensations = 1 1 1 0 -11
Calibrations = 0 0 4 2
ResidualWarningLimit = 0.01
ResidualErrorLimit = 0.02
UseDoubleReferences = 0 (1=Yes)
AutoInterferenceUpdate = 1 0.001
DefaultReference = 2
BaselineCorrections = 1 0
MethodNumber = 0 (1=Yes)
AnalysisArea = 1 950 1230 0.5
AnalysisArea = 1 1644 1837 0.5
AnalysisArea = 0 2871 3064 0.5
Interference = 111111110101110111111
CrossInterferences = 0 0 0 0 0
ReferenceFile = C:\Temet\library\Methyl ethyl ketone C4H8O 0021 ppm.ref
ReferenceFile = C:\Temet\library\Methyl ethyl ketone C4H8O 0058 ppm.ref
ComponentNumber = 13
ComponentName = Ethylene C2H4
ConcentrationUnit = ppm
ActiveLines = All
AutoAnalyze = 1 (1=Yes)
OutputChannel = 0
ViewResults = 1 (1=Yes)
AllowNegative = 1 (1=Yes)
ConversionMultiplier = 1
```

```
ResultSmoothing = 0
RangeSetting = 1
Range1 = 0 500
Range2 = 0 1000
AlarmLimits = 0 500
AlarmSound = 0
Compensations = 1 1 1 0 -11
Calibrations = 0 0 4 2
ResidualWarningLimit = 0.01
ResidualErrorLimit = 0.02
UseDoubleReferences = 0 (1=Yes)
AutoInterferenceUpdate = 1 0.001
DefaultReference = 1
BaselineCorrections = 0 0
MethodNumber = 0 (1=Yes)
AnalysisArea = 1 918 995 1
AnalysisArea = 0 1800 2250 1
AnalysisArea = 0 2925 3234 1
Interference = 110010001000000000001100011001
CrossInterferences = 0 0 0 0 0
ReferenceFile = C:\Library180\Ethylene C2H4 0093 ppm.ref
ComponentNumber = 14
ComponentName = Acetone C3H60
ConcentrationUnit = ppm
ActiveLines = All
AutoAnalyze = 0 (1=Yes)
OutputChannel = 0
ViewResults = 1 (1=Yes)
AllowNegative = 0 (1=Yes)
ConversionMultiplier = 1
ResultSmoothing = 0
RangeSetting = 0
Range1 = 0 10
Range2 = 0 100
AlarmLimits = 0 100
AlarmSound = 0
Compensations = 1 1 1 0 -11
Calibrations = 0 0 4 2
ResidualWarningLimit = 0.01
ResidualErrorLimit = 0.02
UseDoubleReferences = 0 (1=Yes)
AutoInterferenceUpdate = 1 0.001
DefaultReference = 1
BaselineCorrections = 1 0
MethodNumber = 0 (1=Yes)
AnalysisArea = 1 1142 1320 0.5
AnalysisArea = 0 1798 2238 1
AnalysisArea = 0 2825 3450 1
Interference = 1001110010110000111111
CrossInterferences = 0 0 0 0 0
ReferenceFile = C:\Temet\library\Acetone C3H6O 0084 ppm.ref
ReferenceFile = C:\Temet\library\Acetone C3H6O 0490 ppm.ref
ComponentNumber = 15
ComponentName = Sulfur Hexafluoride
ConcentrationUnit = ppm
ActiveLines = All
AutoAnalyze = 0 (1=Yes)
OutputChannel = 0
ViewResults = 1 (1=Yes)
AllowNegative = 0 (1=Yes)
ConversionMultiplier = 1
ResultSmoothing = 0
RangeSetting = 1
Range1 = 0 20
Range2 = 0 1000
AlarmLimits = 0 100
AlarmSound = 0
```

```
Compensations = 1 1 1 0 -11
Calibrations = 0 0 4 2
ResidualWarningLimit = 0.01
ResidualErrorLimit = 0.02
UseDoubleReferences = 0 (1=Yes)
AutoInterferenceUpdate = 1 0.001
DefaultReference = 1
BaselineCorrections = 1 0
MethodNumber = 0 (1=Yes)
AnalysisArea = 1 895 1032 1
AnalysisArea = 0 1800 2250 1
AnalysisArea = 0 2550 3450 1
Interference = 1101010111111100110111
CrossInterferences = 0 0 0 0 0
ReferenceFile = C:\EMS Library\SF6-10.ref
ComponentNumber = 16
ComponentName = Hexane C6H14
ConcentrationUnit = ppm
ActiveLines = All
AutoAnalyze = 0 (1=Yes)
OutputChannel = 0
ViewResults = 0 (1=Yes)
AllowNegative = 0 (1=Yes)
ConversionMultiplier = 1
ResultSmoothing = 0
RangeSetting = 0
Range1 = 0 100
Range2 = 0 1000
AlarmLimits = 0 100
AlarmSound = 0
Compensations = 1 1 1 0 -11
Calibrations = 0 0 4 2
ResidualWarningLimit = 0.01
ResidualErrorLimit = 0.02
UseDoubleReferences = 0 (1=Yes)
AutoInterferenceUpdate = 1 0.001
DefaultReference = 1
BaselineCorrections = 1 0
MethodNumber = 0 (1=Yes)
AnalysisArea = 0 900 1400 1
AnalysisArea = 0 1800 2250 1
AnalysisArea = 1 2825 3003 0.5
Interference = 11010011010101001111111
CrossInterferences = 0 0 0 0 0
ReferenceFile = C:\Temet\library\Hexane C6H14 0024 ppm.ref
ReferenceFile = C:\Temet\library\Hexane C6H14 0045 ppm.ref
ComponentNumber = 17
ComponentName = Propane
ConcentrationUnit = ppm
ActiveLines = All
AutoAnalyze = 0 (1=Yes)
OutputChannel = 0
ViewResults = 1 (1=Yes)
AllowNegative = 0 (1=Yes)
ConversionMultiplier = 1
ResultSmoothing = 0
RangeSetting = 1
Range1 = 0 100
Range2 = 0 1000
AlarmLimits = 0 100
AlarmSound = 0
Compensations = 1 1 1 0 -11
Calibrations = 0 4 0 2
ResidualWarningLimit = 0.01
ResidualErrorLimit = 0.02
UseDoubleReferences = 0 (1=Yes)
AutoInterferenceUpdate = 1 0.001
```

```
DefaultReference = 1
BaselineCorrections = 1 0
MethodNumber = 0 (1=Yes)
AnalysisArea = 1 1296 1558 0.5
AnalysisArea = 0 1800 2250 1
AnalysisArea = 1 2918 3100 1
Interference = 11011011111101010111111
CrossInterferences = 0 0 0 0 0
ReferenceFile = C:\Temet\library\Propane C3H8 0147 ppm.ref
ComponentNumber = 18
ComponentName = Butane
ConcentrationUnit = ppm
ActiveLines = All
AutoAnalyze = 0 (1=Yes)
OutputChannel = 0
ViewResults = 1 (1=Yes)
AllowNegative = 0 (1=Yes)
ConversionMultiplier = 1
ResultSmoothing = 0
RangeSetting = 1
Range1 = 0 100
Range2 = 0 1000
AlarmLimits = 0 100
AlarmSound = 0
Compensations = 1 1 1 0 -11
Calibrations = 0 4 0 2
ResidualWarningLimit = 0.01
ResidualErrorLimit = 0.02
UseDoubleReferences = 0 (1=Yes)
AutoInterferenceUpdate = 1 0.001
DefaultReference = 1
BaselineCorrections = 1 0
MethodNumber = 0 (1=Yes)
AnalysisArea = 0 895 1380 0.8
AnalysisArea = 0 1810 2223 0.8
AnalysisArea = 1 2550 2910 0.5
Interference = 10011011010101011011111
CrossInterferences = 0 0 0 0 0
ReferenceFile = C:\Temet\library\Butane C4H10 0097 ppm.ref
ComponentNumber = 19
ComponentName = Octane
ConcentrationUnit = ppm
ActiveLines = All
AutoAnalyze = 0 (1=Yes)
OutputChannel = 0
ViewResults = 1 (1=Yes)
AllowNegative = 0 (1=Yes)
ConversionMultiplier = 1
ResultSmoothing = 0
RangeSetting = 1
Range1 = 0 100
Range2 = 0 1000
AlarmLimits = 0 100
AlarmSound = 0
Compensations = 1 1 1 0 -11
Calibrations = 0 4 0 2
ResidualWarningLimit = 0.01
ResidualErrorLimit = 0.02
UseDoubleReferences = 0 (1=Yes)
AutoInterferenceUpdate = 1 0.001
DefaultReference = 1
BaselineCorrections = 1 0
MethodNumber = 0 (1=Yes)
AnalysisArea = 0 895 1380 0.8
AnalysisArea = 0 1810 2223 0.8
AnalysisArea = 1 2800 2965 0.8
Interference = 11010011010101011101111
```

```
CrossInterferences = 0 0 0 0 0
ReferenceFile = C:\Temet\library\n-Octane C8H18 0036 ppm.ref
ComponentNumber = 20
ComponentName = Benzene C2H6
ConcentrationUnit = ppm
ActiveLines = All
AutoAnalyze = 0 (1=Yes)
OutputChannel = 0
ViewResults = 0 (1=Yes)
AllowNegative = 0 (1=Yes)
ConversionMultiplier = 1
ResultSmoothing = 0
RangeSetting = 1
Range1 = 0 100
Range2 = 0 1000
AlarmLimits = 0 100
AlarmSound = 0
Compensations = 1 1 1 0 -11
Calibrations = 0 0 4 2
ResidualWarningLimit = 0.01
ResidualErrorLimit = 0.02
UseDoubleReferences = 0 (1=Yes)
AutoInterferenceUpdate = 1 0.001
DefaultReference = 1
BaselineCorrections = 1 0
MethodNumber = 0 (1=Yes)
AnalysisArea = 0 910 1397 1
AnalysisArea = 0 1798 2238 1
AnalysisArea = 1 3000 3130 0.5
Interference = 10110000100111111111101
CrossInterferences = 0 0 0 0 0
ReferenceFile = C:\Temet\library\Benzene C6H6 0066 ppm.ref
ComponentNumber = 21
ComponentName = Formaldehyde
ConcentrationUnit = ppm
ActiveLines = All
AutoAnalyze = 1 (1=Yes)
OutputChannel = 0
ViewResults = 1 (1=Yes)
AllowNegative = 1 (1=Yes)
ConversionMultiplier = 1
ResultSmoothing = 0
RangeSetting = 0
Range1 = 0 10
Range2 = 0 100
AlarmLimits = 0 100
AlarmSound = 0
Compensations = 1 1 1 0 -11
Calibrations = 0 0 4 2
ResidualWarningLimit = 0.01
ResidualErrorLimit = 0.02
UseDoubleReferences = 0 (1=Yes)
AutoInterferenceUpdate = 1 0.001
DefaultReference = 1
BaselineCorrections = 1 0
MethodNumber = 0 (1=Yes)
AnalysisArea = 0 995 1250 1
AnalysisArea = 1 2450 2600 0.6
AnalysisArea = 1 2650 3211 0.5
Interference = 110110101000100000000100111011
CrossInterferences = 0 0 0 0 0
ReferenceFile = HCHO_50.ref
ReferenceFile = Formaldehyde CH2O.ref
ReferenceFile = HCHO_10.ref
ComponentNumber = 22
ComponentName = Acetaldehyde
ConcentrationUnit = ppm
```

```
ActiveLines = All
AutoAnalyze = 1 (1=Yes)
OutputChannel = 0
ViewResults = 1 (1=Yes)
AllowNegative = 1 (1=Yes)
ConversionMultiplier = 1
ResultSmoothing = 0
RangeSetting = 0
Range1 = 0 10
Range2 = 0 100
AlarmLimits = 0 100
AlarmSound = 0
Compensations = 1 1 1 0 -11
Calibrations = 0 4 0 2
ResidualWarningLimit = 0.01
ResidualErrorLimit = 0.02
UseDoubleReferences = 0 (1=Yes)
AutoInterferenceUpdate = 1 0.001
DefaultReference = 1
BaselineCorrections = 1 0
MethodNumber = 0 (1=Yes)
AnalysisArea = 1 3200 3350 1
AnalysisArea = 1 2925 3200 1
AnalysisArea = 1 2638 2916 1
Interference = 1101101010001000000001000111011
CrossInterferences = 0 0 0 0 0
ReferenceFile = Acetaldehyde C2H4O_05.ref
ReferenceFile = Acetaldehyde C2H4O 0100 ppm.ref
ReferenceFile = Acetaldehyde C2H4O 0500 ppm.ref
ComponentNumber = 23
ComponentName = Ozone O3
ConcentrationUnit = ppm
ActiveLines = All
AutoAnalyze = 0 (1=Yes)
OutputChannel = 0
ViewResults = 1 (1=Yes)
AllowNegative = 0 (1=Yes)
ConversionMultiplier = 1
ResultSmoothing = 0
RangeSetting = 1
Range1 = 0 100
Range2 = 0 1000
AlarmLimits = 0 100
AlarmSound = 0
Compensations = 1 1 1 0 -11
Calibrations = 0 4 0 2
ResidualWarningLimit = 0.01
ResidualErrorLimit = 0.02
UseDoubleReferences = 0 (1=Yes)
AutoInterferenceUpdate = 1 0.001
DefaultReference = 1
BaselineCorrections = 1 0
MethodNumber = 0 (1=Yes)
AnalysisArea = 1 926 1127 1
AnalysisArea = 0 1798 2246 1
AnalysisArea = 0 2550 3450 1
Interference = 1101010110110110111111
CrossInterferences = 0 0 0 0 0
ReferenceFile = O3_785.ref
ReferenceFile = O3_560.ref
ReferenceFile = O3_190.ref
ComponentNumber = 24
ComponentName = SO3
ConcentrationUnit = ppm
ActiveLines = All
AutoAnalyze = 0 (1=Yes)
OutputChannel = 0
```

```
ViewResults = 1 (1=Yes)
AllowNegative = 0 (1=Yes)
ConversionMultiplier = 1
ResultSmoothing = 0
RangeSetting = 1
Range1 = 0 100
Range2 = 0 1000
AlarmLimits = 0 100
AlarmSound = 0
Compensations = 1 1 1 0 -11
Calibrations = 0 4 0 2
ResidualWarningLimit = 0.01
ResidualErrorLimit = 0.02
UseDoubleReferences = 0 (1=Yes)
AutoInterferenceUpdate = 0 0.001
DefaultReference = 1
BaselineCorrections = 1 0
MethodNumber = 0 (1=Yes)
AnalysisArea = 1 1196 1397 1
AnalysisArea = 0 1800 2250 1
AnalysisArea = 0 2550 3450 1
Interference = 110000011
CrossInterferences = 0 0 0 0 0
ReferenceFile = C:\DemoLibrary\Sulfur trioxide SO3 50ppm (cemdemo).ref
ComponentNumber = 25
ComponentName = MEA
ConcentrationUnit = ppm
ActiveLines = All
AutoAnalyze = 1 (1=Yes)
OutputChannel = 0
ViewResults = 1 (1=Yes)
AllowNegative = 0 (1=Yes)
ConversionMultiplier = 1
ResultSmoothing = 0
RangeSetting = 0
Range1 = 0 300
Range2 = 0 500
AlarmLimits = 0 15000
AlarmSound = 0
Compensations = 1 1 1 0 -11
Calibrations = 0 0 0 2
ResidualWarningLimit = 0.01
ResidualErrorLimit = 0.02
UseDoubleReferences = 0 (1=Yes)
AutoInterferenceUpdate = 1 0.005
DefaultReference = 1
BaselineCorrections = 1 0
MethodNumber = 0 (1=Yes)
AnalysisArea = 1 2624 3150 1
AnalysisArea = 1 2416 2601 1
AnalysisArea = 0 995 1119 1
Interference = 1101101000001000000001100011011
CrossInterferences = 0 0 0 0 0
ReferenceFile = MEA_500.ref
ReferenceFile = MEA_100.ref
ReferenceFile = C:\Pickle References\MEA_15000.ref
ReferenceFile = C:\Pickle References\MEA_1000.ref
ReferenceFile = C:\Pickle References\MEA_2000.ref
ReferenceFile = C:\Pickle References\MEA_5000.ref
ReferenceFile = C:\Pickle References\MEA_10000.ref
ComponentNumber = 26
ComponentName = Methanol
ConcentrationUnit = Auto
ActiveLines = All
AutoAnalyze = 1 (1=Yes)
OutputChannel = 0
ViewResults = 1 (1=Yes)
```

```
AllowNegative = 1 (1=Yes)
ConversionMultiplier = 1
ResultSmoothing = 0
RangeSetting = 0
Range1 = 0 25
Range2 = 0 500
AlarmLimits = 0 1000
AlarmSound = 0
Compensations = 1 1 1 0 -11
Calibrations = 0 0 4 2
ResidualWarningLimit = 0.01
ResidualErrorLimit = 0.02
UseDoubleReferences = 0 (1=Yes)
AutoInterferenceUpdate = 1 0.005
DefaultReference = 1
BaselineCorrections = 1 0
MethodNumber = 0 (1=Yes)
AnalysisArea = 1 995 1073 1
AnalysisArea = 1 1095 1150 1
AnalysisArea = 1 2450 3180 1
Interference = 1101101010001000000001100101011
CrossInterferences = 0 0 0 0 0
ReferenceFile = C:\Library180\Methanol_100.ref
ComponentNumber = 27
ComponentName = Methylamine
ConcentrationUnit = Auto
ActiveLines = All
AutoAnalyze = 1 (1=Yes)
OutputChannel = 0
ViewResults = 1 (1=Yes)
AllowNegative = 1 (1=Yes)
ConversionMultiplier = 1
ResultSmoothing = 0
RangeSetting = 0
Range1 = 0 10
Range2 = 0 100
AlarmLimits = 0 100
AlarmSound = 0
Compensations = 1 1 1 0 -11
Calibrations = 0 0 4 2
ResidualWarningLimit = 0.01
ResidualErrorLimit = 0.02
UseDoubleReferences = 0 (1=Yes)
AutoInterferenceUpdate = 1 0.001
DefaultReference = 1
BaselineCorrections = 1 0
MethodNumber = 0 (1=Yes)
AnalysisArea = 1 2022 2223 1
AnalysisArea = 1 2450 2650 1
AnalysisArea = 1 2800 3203 1
Interference = 1111111010001000000001100110011
CrossInterferences = 0 0 0 0 0
ReferenceFile = Methylamine CH5N 0100 ppm.ref
ReferenceFile = Methylamine CH5N 0500 ppm.ref
ReferenceFile = Methylamine CH5N 0894 ppm.ref
ComponentNumber = 28
ComponentName = Carbon Diocide- CO2 (ppm)
ConcentrationUnit = Auto
ActiveLines = All
AutoAnalyze = 0 (1=Yes)
OutputChannel = 0
ViewResults = 1 (1=Yes)
AllowNegative = 0 (1=Yes)
ConversionMultiplier = 1
ResultSmoothing = 0
RangeSetting = 2
Range1 = 0 20000
```

```
Range2 = 0 100000
AlarmLimits = 0 100000
AlarmSound = 0
Compensations = 1 1 1 0 -11
Calibrations = 0 4 0 2
ResidualWarningLimit = 0.01
ResidualErrorLimit = 0.02
UseDoubleReferences = 0 (1=Yes)
AutoInterferenceUpdate = 0 0.005
DefaultReference = 0
BaselineCorrections = 1 0
MethodNumber = 0 (1=Yes)
AnalysisArea = 1 3273 3666 0.5
AnalysisArea = 1 1984 2554 0.5
AnalysisArea = 1 910 1019 0.5
Interference = 101010101000100000000100111001
CrossInterferences = 0 0 0 0 0
ComponentNumber = 29
ComponentName = Methane CH4
ConcentrationUnit = Auto
ActiveLines = All
AutoAnalyze = 0 (1=Yes)
OutputChannel = 0
ViewResults = 1 (1=Yes)
AllowNegative = 1 (1=Yes)
ConversionMultiplier = 1
ResultSmoothing = 0
RangeSetting = 0
Range1 = 0 10
Range2 = 0 100
AlarmLimits = 0 100
AlarmSound = 0
Compensations = 1 1 1 0 -11
Calibrations = 0 0 4 2
ResidualWarningLimit = 0.01
ResidualErrorLimit = 0.02
UseDoubleReferences = 0 (1=Yes)
AutoInterferenceUpdate = 1 0.001
DefaultReference = 1
BaselineCorrections = 1 0
MethodNumber = 0 (1=Yes)
AnalysisArea = 0 1292 1412 0.5
AnalysisArea = 1 2833 3203 0.5
AnalysisArea = 1 3018 3203 0.5
Interference = 100110101000000000001100101001
CrossInterferences = 0 0 0 0 0
ReferenceFile = Methane CH4 0101 ppm.ref
ReferenceFile = Methane CH4 0050 ppm.ref
ComponentNumber = 30
ComponentName = Piperazine
ConcentrationUnit = Auto
ActiveLines = All
AutoAnalyze = 1 (1=Yes)
OutputChannel = 0
ViewResults = 1 (1=Yes)
AllowNegative = 1 (1=Yes)
ConversionMultiplier = 1
ResultSmoothing = 0
RangeSetting = 0
Range1 = 0 250
Range2 = 0 500
AlarmLimits = 0 500
AlarmSound = 1
Compensations = 1 1 1 0 -11
Calibrations = 0 0 4 2
ResidualWarningLimit = 0.01
ResidualErrorLimit = 0.02
```

```
UseDoubleReferences = 0 (1=Yes)
AutoInterferenceUpdate = 1 0.001
DefaultReference = 2
BaselineCorrections = 1 0
MethodNumber = 0 (1=Yes)
AnalysisArea = 0 1096 1380 1
AnalysisArea = 0 1810 2223 1
AnalysisArea = 1 2550 3095 1
Interference = 10011010100010000000110011101
CrossInterferences = 0 0 0 0 0
ReferenceFile = Piperazine_2ppm_180C.ref
ReferenceFile = Piperazine_105ppm_180C.ref
ReferenceFile = Piperazine_188ppm_180C.ref
ReferenceFile = Piperazine_407ppm_180C.ref
ReferenceFile = Piperazine_471ppm_180C.ref
ReferenceFile = Piperazine_40ppm_180C.ref
ComponentNumber = 201
ComponentName = NOx
ConcentrationUnit = ppm
ActiveLines = All
AutoAnalyze = 0 (1=Yes)
OutputChannel = 0
ViewResults = 1 (1=Yes)
AllowNegative = 1 (1=Yes)
ConversionMultiplier = 1
ResultSmoothing = 0
RangeSetting = 0
Range1 = 0 20
Range2 = 0 250
AlarmLimits = 0 500
AlarmSound = 0
Compensations = 1 1 1 0 -11
Calibrations = 0 0 4 2
Interference = 0000111
CrossInterferences = 0 0 0 0 0
ComponentNumber = 202
ComponentName = THC
ConcentrationUnit = ppm
ActiveLines = All
AutoAnalyze = 0 (1=Yes)
OutputChannel = 0
ViewResults = 1 (1=Yes)
AllowNegative = 1 (1=Yes)
ConversionMultiplier = 1
ResultSmoothing = 0
RangeSetting = 1
Range1 = 0 500
Range2 = 0 1000
AlarmLimits = 0 500
AlarmSound = 0
Compensations = 1 1 1 0 -11
Calibrations = 0 0 4 2
Interference = 0001000000011
CrossInterferences = 0 0 0 0 0
ComponentNumber = 211
ComponentName = Input1
ConcentrationUnit = %
ActiveLines = All
AutoAnalyze = 0 (1=Yes)
OutputChannel = 0
ViewResults = 1 (1=Yes)
AllowNegative = 1 (1=Yes)
ConversionMultiplier = 1
ResultSmoothing = 0
RangeSetting = 1
Range1 = 0 100
Range2 = 0 1000
```

```
AlarmLimits = 0 100
AlarmSound = 0
Compensations = 1 1 1 0 -11
Calibrations = 0 0 4 2
Interference = 0
CrossInterferences = 0 0 0 0 0
ComponentNumber = 212
ComponentName = Input2
ConcentrationUnit = %
ActiveLines = All
AutoAnalyze = 0 (1=Yes)
OutputChannel = 0
ViewResults = 1 (1=Yes)
AllowNegative = 1 (1=Yes)
ConversionMultiplier = 1
ResultSmoothing = 0
RangeSetting = 1
Range1 = 0 100
Range2 = 0 1000
AlarmLimits = 0 100
AlarmSound = 0
Compensations = 1 1 1 0 -11
Calibrations = 0 0 4 2
Interference = 0
CrossInterferences = 0 0 0 0 0
ComponentNumber = 213
ComponentName = Input3
ConcentrationUnit = %
ActiveLines = All
AutoAnalyze = 0 (1=Yes)
OutputChannel = 0
ViewResults = 1 (1=Yes)
AllowNegative = 1 (1=Yes)
ConversionMultiplier = 1
ResultSmoothing = 0
RangeSetting = 1
Range1 = 0 100
Range2 = 0 1000
AlarmLimits = 0 100
AlarmSound = 0
Compensations = 1 1 1 0 -11
Calibrations = 0 0 4 2
Interference = 0
CrossInterferences = 0 0 0 0 0
ComponentNumber = 214
ComponentName = Input4
ConcentrationUnit = %
ActiveLines = All
AutoAnalyze = 0 (1=Yes)
OutputChannel = 0
ViewResults = 1 (1=Yes)
AllowNegative = 1 (1=Yes)
ConversionMultiplier = 1
ResultSmoothing = 0
RangeSetting = 1
Range1 = 0 100
Range2 = 0 1000
AlarmLimits = 0 100
AlarmSound = 0
Compensations = 1 1 1 0 -11
Calibrations = 0 0 4 2
Interference = 0
CrossInterferences = 0 0 0 0 0
ComponentNumber = 215
ComponentName = Input5
ConcentrationUnit = %
ActiveLines = All
```

```
AutoAnalyze = 0 (1=Yes)
OutputChannel = 0
ViewResults = 1 (1=Yes)
AllowNegative = 1 (1=Yes)
ConversionMultiplier = 1
ResultSmoothing = 0
RangeSetting = 1
Range1 = 0 100
Range2 = 0 1000
AlarmLimits = 0 100
AlarmSound = 0
Compensations = 1 1 1 0 -11
Calibrations = 0 0 4 2
Interference = 0
CrossInterferences = 0 0 0 0 0
ComponentNumber = 216
ComponentName = Input6
ConcentrationUnit = %
ActiveLines = All
AutoAnalyze = 0 (1=Yes)
OutputChannel = 0
ViewResults = 1 (1=Yes)
AllowNegative = 1 (1=Yes)
ConversionMultiplier = 1
ResultSmoothing = 0
RangeSetting = 1
Range1 = 0 100
Range2 = 0 1000
AlarmLimits = 0 100
AlarmSound = 0
Compensations = 1 1 1 0 -11
Calibrations = 0 0 4 2
Interference = 0
CrossInterferences = 0 0 0 0 0
ComponentNumber = 217
ComponentName = Input7
ConcentrationUnit = %
ActiveLines = All
AutoAnalyze = 0 (1=Yes)
OutputChannel = 0
ViewResults = 1 (1=Yes)
AllowNegative = 1 (1=Yes)
ConversionMultiplier = 1
ResultSmoothing = 0
RangeSetting = 1
Range1 = 0 100
Range2 = 0 1000
AlarmLimits = 0 100
AlarmSound = 0
Compensations = 1 1 1 0 -11
Calibrations = 0 0 4 2
Interference = 0
CrossInterferences = 0 0 0 0 0
ComponentNumber = 218
ComponentName = Input8
ConcentrationUnit = %
ActiveLines = All
AutoAnalyze = 0 (1=Yes)
OutputChannel = 0
ViewResults = 1 (1=Yes)
AllowNegative = 1 (1=Yes)
ConversionMultiplier = 1
ResultSmoothing = 0
RangeSetting = 1
Range1 = 0 100
Range2 = 0 1000
AlarmLimits = 0 100
```

```
AlarmSound = 0
Compensations = 1 1 1 0 -11
Calibrations = 0 0 4 2
Interference = 0
CrossInterferences = 0 0 0 0 0
ComponentNumber = 219
ComponentName = Pressure
ConcentrationUnit = mbar
ActiveLines = All
AutoAnalyze = 1 (1=Yes)
OutputChannel = 0
ViewResults = 1 (1=Yes)
AllowNegative = 1 (1=Yes)
ConversionMultiplier = 1
ResultSmoothing = 0
RangeSetting = 1
Range1 = 0 2000
Range2 = 0 2000
AlarmLimits = 900 2000
AlarmSound = 0
Compensations = 1 1 1 0 -11
Calibrations = 0 0 4 2
Interference = 0
CrossInterferences = 0 0 0 0 0
ComponentNumber = 220
ComponentName = Oxygen (O2)
ConcentrationUnit = vol-%
ActiveLines = All
AutoAnalyze = 0 (1=Yes)
OutputChannel = 0
ViewResults = 1 (1=Yes)
AllowNegative = 1 (1=Yes)
ConversionMultiplier = 1
ResultSmoothing = 0
RangeSetting = 1
Range1 = 0 100
Range2 = 0 1000
AlarmLimits = 0 100
AlarmSound = 0
Compensations = 1 1 1 0 -11
Calibrations = 0 0 4 2
Interference = 0
CrossInterferences = 0 0 0 0 0
ComponentNumber = 221
ComponentName = AUX
ConcentrationUnit = %
ActiveLines = All
AutoAnalyze = 0 (1=Yes)
OutputChannel = 0
ViewResults = 1 (1=Yes)
AllowNegative = 1 (1=Yes)
ConversionMultiplier = 1
ResultSmoothing = 0
RangeSetting = 1
Range1 = 0 100
Range2 = 0 1000
AlarmLimits = 0 100
AlarmSound = 0
Compensations = 1 1 1 0 -11
Calibrations = 0 0 4 2
Interference = 0
CrossInterferences = 0 0 0 0 0
```

APPENDIX D Tabulated VLE Data (UT)

D.1 Tabulated Data for H_2O-MEA

MEA/m	Date	T/°C	Soln	P_{MEA}/kPa	P_{H2O}/kPa
3.50	03/15/06	45.952	1-1	0.00588	8.69
3.50	03/15/06	51.210	1-2	0.00800	11.8
3.50	03/15/06	58.875	1-3	0.0135	16.6
3.50	03/15/06	65.294	1-4	0.0190	21.0
3.50	03/21/06	42.698	2-1	0.00451	6.85
3.50	03/21/06	49.400	2-2	0.00729	9.76
3.50	03/21/06	56.312	2-3	0.0112	13.6
3.50	03/21/06	65.471	2-4	0.0182	19.9
3.50	10/31/06	59.950	1[a]	0.0132	17.1
3.50	11/06/06	39.969	3[a]	0.00419	6.94

a: Sample part of MEA-CO_2-H_2O data set

MEA/m	Date	T/°C	Soln	P_{MEA}/kPa	P_{H2O}/kPa
7.00	03/10/06	72.656	3-5	0.0790	29.1
7.00	03/14/06	64.734	4-5	0.0336	20.6
7.00	03/22/06	42.114	5-1	0.0106	6.60
7.00	03/22/06	49.250	5-2	0.0156	9.29
7.00	03/22/06	52.797	5-3	0.0205	11.0
7.00	03/22/06	56.752	5-4	0.0210	13.1
7.00	03/22/06	61.433	5-5	0.0283	15.4
7.00	09/22/06	39.800	10[a]	0.0100	7.50
7.00	10/02/06	59.945	12[a]	0.0271	18.3
11.00	10/03/06	60.026	3[a]	0.0402	15.3
11.00	10/09/06	39.993	2[a]	0.0120	6.17
23.80	03/23/06	42.768	2-1	0.0243	4.86
23.80	03/23/06	49.948	2-2	0.0447	6.70
23.80	03/23/06	53.872	2-3	0.0611	8.26
23.80	03/23/06	61.686	2-4	0.141	12.1

a: Sample part of MEA-CO_2-H_2O data set

D.2 Tabulated Data for H_2O-PZ

PZ/m	Date	T/°C	Soln	P_{PZ}/kPa	P_{H2O}/kPa
0.90	04/03/06	35.949	1-1	0.00049	6.06
0.90	04/03/06	44.290	1-2	0.00129	9.51
0.90	04/03/06	52.768	1-3	0.00216	14.0
0.90	04/03/06	63.411	1-4	0.00544	22.2
0.89	05/01/06	35.467	2-1	0.00056	6.01
0.89	05/01/06	44.040	2-2	0.00125	9.37
0.89	05/01/06	52.474	2-3	0.00267	13.7
0.89	05/01/06	61.592	2-4	0.00517	19.7
0.90	11/08/06	40.012	1[a]	0.00104	7.23
0.90	11/14/06	59.994	3[a]	0.00375	18.1
1.80	04/05/06	36.180	1-1	0.00150	5.93
1.80	04/05/06	44.427	1-2	0.00211	9.08
1.80	04/05/06	52.833	1-3	0.00434	13.6
1.80	04/05/06	60.405	1-4	0.00759	19.4

a: Sample part of PZ-CO_2-H_2O data set

PZ/m	Date	T/°C	Soln	P_{PZ}/kPa	P_{H2O}/kPa
1.80	05/02/06	35.553	2-1	0.00149	5.87
1.80	05/02/06	43.857	2-2	0.00208	9.16
1.80	05/02/06	52.210	2-3	0.00458	13.6
1.80	05/02/06	60.725	2-4	0.00680	19.4
2.00	11/17/06	60.026	1[a]	0.00678	17.6
2.00	11/29/06	40.019	4[a]	0.00217	7.06
2.49	04/06/06	32.722	2-1	0.00160	6.17
2.49	04/06/06	39.704	2-2	0.00299	9.13
2.49	04/06/06	52.920	2-3	0.00720	16.6
2.49	04/06/06	61.006	2-4	0.0124	23.1
2.50	05/03/06	35.610	3-1	0.00140	5.78
2.50	05/03/06	44.035	3-2	0.00302	9.03
2.50	05/03/06	52.255	3-3	0.00526	13.4
2.50	05/03/06	60.393	3-4	0.0101	19.2
2.50	12/04/06	40.006	1[a]	0.00267	7.15
2.50	12/07/06	59.976	3[a]	0.00763	17.9
3.60	04/07/06	34.655	1-1	0.00194	5.70
3.60	04/07/06	45.083	1-2	0.00471	9.97
3.60	04/07/06	53.218	1-3	0.00885	14.6
3.60	04/07/06	61.156	1-4	0.0156	20.8
3.60	05/04/06	35.122	2-1	0.00201	5.66
3.60	05/04/06	43.804	2-2	0.00422	8.73
3.60	05/04/06	52.513	2-3	0.00685	13.1
3.60	05/04/06	60.376	2-4	0.0114	18.6
3.60	12/13/06	39.995	3[a]	0.00374	6.99
3.60	12/11/06	60.001	1[a]	0.0116	17.7
5.00	05/05/06	40.558	1-1	0.00430	6.70
5.00	05/05/06	44.713	1-2	0.00540	8.45
5.00	05/05/06	53.317	1-3	0.0108	12.8
5.00	05/05/06	60.970	1-4	0.0238	18.3
5.00	02/06/07	40.013	1[a]	0.00512	6.77
5.00	02/08/07	60.006	3[a]	0.0172	17.1

[a] Sample part of PZ-CO_2-H_2O data set

D.3 Tabulated Data for H_2O-MEA-PZ

MEA/m	PZ/m	Date	T/°C	Soln	P_{MEA}/kPa	P_{PZ}/kPa	P_{H2O}/kPa
3.50	1.80	04/10/06	37.317	1-1	0.00248	0.00142	5.58
3.50	1.80	04/10/06	44.934	1-2	0.00462	0.00202	8.63
3.50	1.80	04/10/06	52.647	1-3	0.00899	0.00438	12.9
3.50	1.80	04/10/06	60.362	1-4	0.0161	0.00702	18.5
3.50	1.80	05/08/06	37.084	2-1	0.00275	0.00119	5.45
3.50	1.80	05/08/06	44.144	2-2	0.00450	0.00175	8.45
3.50	1.80	05/08/06	53.072	2-3	0.00857	0.00394	12.8
3.50	1.80	05/08/06	60.900	2-4	0.0162	0.00701	18.3
3.50	2.00	01/03/07	40.018	1[a]	0.00433	0.00224	6.77
3.50	2.00	01/05/07	59.994	3[a]	0.0144	0.00624	17.3
3.50	3.60	04/11/06	37.241	1-1	0.00265	0.00219	5.34
3.50	3.60	04/11/06	44.776	1-2	0.00498	0.00485	8.11
3.50	3.60	04/11/06	53.438	1-3	0.00982	0.00746	12.4
3.50	3.60	04/11/06	60.325	1-4	0.0190	0.0154	17.9
3.50	3.60	05/09/06	34.478	2-1	0.00235	0.00154	5.17
3.50	3.60	05/09/06	42.772	2-2	0.00415	0.00346	7.97
3.50	3.60	05/09/06	51.325	2-3	0.00793	0.00652	12.3
3.50	3.60	05/09/06	60.226	2-4	0.0152	0.0124	17.6
3.50	3.60	01/23/07	40.004	1[a]	0.00382	0.00368	6.54
3.50	3.60	01/26/07	60.007	3[a]	0.0148	0.0131	17.1
7.00	1.80	04/12/06	36.820	1-1	0.00498	0.00106	5.23
7.00	1.80	04/12/06	44.473	1-2	0.00991	0.00238	7.99
7.00	1.80	04/12/06	53.726	1-3	0.0181	0.00483	12.1
7.00	1.80	04/12/06	61.446	1-4	0.0337	0.00719	17.6
7.00	1.80	05/10/06	34.463	2-1	0.00451	0.00074	5.02
7.00	1.80	05/10/06	43.141	2-2	0.00812	0.00162	7.71
7.00	1.80	05/10/06	43.273	2-3	0.00809	0.00164	7.71
7.00	1.80	05/10/06	60.504	2-4	0.0262	0.00591	17.1
7.00	2.00	12/15/06	39.957	1[a]	0.00758	0.00213	6.38
7.00	2.00	12/19/06	59.998	3[a]	0.0282	0.00697	16.5
7.00	3.60	04/13/06	35.783	1-1	0.00502	0.00216	4.96
7.00	3.60	04/13/06	44.522	1-2	0.0108	0.00472	7.55

a: Sample part of MEA-PZ-CO_2-H_2O data set

MEA/m	PZ/m	Date	T/°C	Soln	P_{MEA}/kPa	P_{PZ}/kPa	P_{H2O}/kPa
7.00	3.60	04/13/06	53.036	1-3	0.0197	0.00873	11.5
7.00	3.60	04/13/06	60.688	1-4	0.0366	0.0169	16.7
7.00	3.60	05/11/06	36.676	2-1	0.00517	0.00188	4.87
7.00	3.60	05/11/06	44.822	2-2	0.00871	0.00397	7.40
7.00	3.60	05/11/06	52.846	2-3	0.0158	0.00698	11.5
7.00	3.60	05/11/06	60.513	2-4	0.0281	0.0130	16.7
7.00	3.60	01/30/07	40.016	1[a]	0.00817	0.00433	6.11
7.00	3.60	02/02/07	60.012	3[a]	0.0279	0.0131	15.9

a: Sample part of MEA-PZ-CO_2-H_2O data set

D.4 Tabulated H_2O-MEA-CO_2 Data

MEA/m	Date	T/°C	Soln	α[a]	P_{CO2}/kPa	P_{MEA}/kPa	P_{H2O}/kPa
3.57	11/01/06	59.948	2-1	0.159	0.0212	0.0110	17.57
3.63	11/01/06	60.057	2-2	0.219	0.0780	0.00926	17.63
3.53	11/01/06	60.039	2-3	0.307	0.244	0.00720	17.64
3.57	11/01/06	60.018	2-4	0.380	0.794	0.00508	17.62
3.55	11/02/06	59.944	2-5	0.477	4.32	0.00323	17.70
3.54	11/02/06	60.005	2-6	0.504	14.8	0.00219	18.01
3.53	11/06/06	39.979	4-1	0.121	0.00555	0.00391	6.880
3.46	11/06/06	40.023	4-2	0.212	0.0140	0.00341	6.971
3.51	11/07/06	39.938	4-3	0.300	0.0362	0.00281	6.980
3.54	11/07/06	40.079	4-4	0.369	0.116	0.00224	7.024
3.57	11/07/06	40.003	4-5	0.467	0.879	0.00168	7.058
3.49	11/08/06	39.969	4-6	0.552	8.56	0.00098	7.128
6.88	09/05/06	39.987	6-1	0.153	0.00570	0.00658	6.60
6.98	09/05/06	39.985	6-2	0.170	0.00721	0.00636	6.65
6.95	09/05/06	40.058	6-3	0.163	0.00664	0.00636	6.69
6.85	09/07/06	40.034	6-4	0.194	0.00985	0.00645	6.71
6.97	09/07/06	40.144	6-5	0.191	0.00995	0.00623	6.61
6.93	09/07/06	40.353	6-6	0.272	0.0224	0.00511	6.65
7.06	09/11/06	40.034	7-1	0.232	0.0146	0.00563	6.63
7.08	09/11/06	40.120	7-2	0.246	0.0191	0.00553	6.65
7.10	09/11/06	39.968	7-3	0.269	0.0231	0.00516	6.63

a: α = loading = mole CO_2/mol MEA

MEA/m	Date	T/°C	Soln	α^a	P_{CO2}/kPa	P_{MEA}/kPa	P_{H2O}/kPa
7.12	09/12/06	39.870	7-4	0.360	0.0966	0.00355	6.75
7.05	09/12/06	39.990	7-5	0.350	0.0721	0.00423	6.75
7.06	09/12/06	39.880	7-6	0.386	0.120	0.00362	6.66
7.05	09/18/06	39.850	8-1	0.389	0.113	0.00338	6.59
7.05	09/18/06	40.000	8-2	0.400	0.128	0.00350	6.71
7.58	09/19/06	40.050	8-3	0.382	0.131	0.00332	6.72
7.00	09/19/06	39.930	8-4	0.466	0.574	0.00270	6.75
7.11	09/19/06	40.000	8-5	0.591	28.3	0.00146	6.72
7.06	09/19/06	39.990	8-6	0.481	0.883	0.00247	6.73
7.17	09/22/06	40.019	9-1	0.464	0.750	0.00266	6.67
7.06	09/22/06	40.018	9-2	0.501	1.87	0.00199	6.80
7.11	09/25/06	39.878	9-3	0.491	1.10	0.00193	6.68
7.06	09/25/06	39.997	9-4	0.518	3.03	0.00172	6.80
7.06	09/25/06	39.866	9-5	0.326	0.0485	0.00458	6.60
7.04	09/26/06	39.879	9-6	0.348	0.0662	0.00423	6.60
7.00	10/03/06	59.868	11-1	0.114	0.0194	0.0215	16.6
7.08	10/03/06	59.964	11-2	0.191	0.0589	0.0186	16.7
7.07	10/03/06	59.960	11-3	0.291	0.209	0.0141	16.6
7.03	10/04/06	59.884	11-4	0.386	0.763	0.0100	16.7
7.14	10/04/06	59.771	11-5	0.485	4.86	0.00494	16.8
7.17	10/04/06	60.106	11-6	0.544	25.8	0.00316	16.8
7.38	10/31/06	59.945	13	0.565	50.2	0.00288	18.0
11.00	10/09/06	39.989	1-1	0.115	0.00505	0.0104	6.09
10.75	10/11/06	40.021	1-2	0.201	0.0108	0.00842	6.12
10.90	10/12/06	39.938	1-3	0.298	0.0295	0.00603	6.14
11.28	10/12/06	40.108	1-4	0.373	0.104	0.00439	6.18
11.06	10/13/06	39.996	1-5	0.485	1.62	0.00198	6.29
11.12	10/13/06	39.967	1-6	0.545	22.3	0.00095	6.59
11.21	10/03/06	59.996	4-1	0.136	0.0155	0.03609	15.4
11.17	10/03/06	60.043	4-2	0.225	0.0731	0.02838	15.5
11.12	10/04/06	59.986	4-3	0.291	0.199	0.02252	15.5
11.36	10/04/06	60.041	4-4	0.415	0.847	0.0143	15.5
11.32	10/04/06	59.931	4-5	0.464	6.98	0.00655	15.8
10.98	10/02/06	60.003	4-6	0.502	26.5	0.00416	16.3

a: α = loading = mole CO_2/mol MEA

D.5 Tabulated H_2O-PZ-CO_2 Data

PZ/m	Date	T/°C	Soln	α[a]	P_{CO_2}/kPa	P_{PZ}/kPa	P_{H_2O}/kPa
0.89	11/09/06	39.977	2-1	0.208	0.0440	0.00083	7.29
0.91	11/09/06	40.089	2-2	0.217	0.0705	0.00089	7.33
0.93	11/09/06	39.987	2-3	0.241	0.103	0.00085	7.37
0.91	11/13/06	40.000	2-4	0.284	0.234	0.00072	7.22
0.91	11/13/06	40.012	2-5	0.344	0.987	0.00066	7.39
0.90	11/13/06	40.024	2-6	0.418	4.85	0.00053	7.46
0.91	11/14/06	60.051	4-1	0.111	0.0290	0.00325	18.5
0.91	11/14/06	60.001	4-2	0.217	0.299	0.00197	18.6
0.91	11/14/06	60.016	4-3	0.242	0.841	0.00157	18.6
0.89	11/15/06	60.003	4-4	0.325	1.93	0.00108	18.3
0.89	11/15/06	60.032	4-5	0.370	8.29	0.00085	18.5
0.91	11/16/06	59.948	4-6	0.383	14.7	0.00080	18.6
2.03	11/17/06	60.058	2-1	0.132	0.0924	0.00555	18.0
2.02	11/17/06	60.039	2-2	0.193	0.296	0.00480	18.1
2.03	11/18/06	59.999	2-3	0.275	1.40	0.00293	17.9
2.02	11/18/06	59.998	2-4	0.330	3.95	0.00224	18.1
2.02	11/18/06	60.037	2-5	0.370	9.91	0.00177	18.2
2.00	11/19/06	59.951	2-6	0.412	24.7	0.00128	18.5
1.90	11/28/06	59.945	3-1	0.169	0.142	0.00513	17.9
2.07	11/28/06	59.965	3-2	0.383	13.7	0.00187	18.3
2.03	11/29/06	40.050	5-1	0.146	0.0215	0.00212	7.13
2.08	11/29/06	40.013	5-2	0.227	0.106	0.00180	7.21
2.02	11/29/06	40.072	5-3	0.257	0.184	0.00168	7.20
2.05	11/30/06	40.007	5-4	0.309	0.526	0.00149	7.07
2.03	11/30/06	40.090	5-5	0.372	1.95	0.00138	7.18
1.99	11/30/06	40.058	5-6	0.431	10.1	0.00109	7.51
2.57	12/04/06	40.007	2-1	0.166	0.0317	0.00229	7.16
2.50	12/05/06	39.969	2-2	0.228	0.0884	0.00208	7.13
2.49	12/05/06	39.975	2-3	0.278	0.247	0.00184	7.23
2.50	12/06/06	39.966	2-4	0.328	0.662	0.00152	7.27
2.49	12/06/06	40.014	2-5	0.423	7.51	0.00125	7.53
2.48	12/06/06	40.011	2-6	0.437	10.6	0.00115	7.57
2.51	12/07/06	59.974	4-1	0.164	0.141	0.00618	18.1

[a]: α = loading = mole CO_2/mol 2·PZ

PZ/m	Date	T/°C	Soln	α[a]	P_{CO_2}/kPa	P_{PZ}/kPa	P_{H_2O}/kPa
2.50	12/07/06	60.029	4-2	0.196	0.263	0.00527	18.0
2.53	12/08/06	59.980	4-3	0.251	0.725	0.00456	18.0
2.52	12/08/06	60.018	4-4	0.341	3.96	0.00311	18.2
2.53	12/08/06	60.028	4-5	0.400	16.9	0.00245	18.5
2.45	12/08/06	60.021	4-6	0.443	27.4	0.00224	18.6
3.63	12/11/06	59.991	2-1	0.158	0.129	0.00747	17.7
3.58	12/11/06	60.016	2-2	0.217	0.431	0.00642	17.7
3.58	12/11/06	60.013	2-3	0.277	1.05	0.00493	17.8
3.60	12/12/06	60.009	2-4	0.338	3.49	0.00382	17.8
3.67	12/12/06	60.006	2-5	0.385	13.6	0.00309	17.9
3.66	12/12/06	60.128	2-6	0.400	19.3	0.00277	18.1
3.63	12/13/06	40.031	4-1	0.146	0.0211	0.00331	7.10
3.59	12/13/06	40.017	4-2	0.217	0.0628	0.00251	7.02
3.65	12/13/06	40.009	4-3	0.272	0.211	0.00212	7.08
3.61	12/14/06	39.995	4-4	0.318	0.687	0.00183	7.02
3.65	12/14/06	40.043	4-5	0.384	4.37	0.00144	7.11
3.58	12/14/06	40.024	4-6	0.412	8.42	0.00141	7.27
5.09	02/06/07	40.028	2-1	0.172	0.0287	0.00312	6.83
4.83	02/06/07	40.049	2-2	0.220	0.0605	0.00288	6.92
5.07	02/06/07	40.029	2-3	0.274	0.211	0.00220	6.86
4.97	02/06/07	39.997	2-4	0.339	0.798	0.00103	6.83
4.96	02/06/07	40.029	2-5	0.409	5.71	0.00082	6.94
5.02	02/06/07	40.051	2-6	0.413	6.99	0.00086	6.99
5.18	02/08/07	60.023	4-1	0.164	0.137	0.0102	17.3
5.05	02/08/07	60.020	4-2	0.226	0.365	0.00745	17.3
5.08	02/08/07	60.042	4-3	0.296	1.29	0.00559	17.6
5.05	02/08/07	60.075	4-4	0.330	3.31	0.00486	17.4
5.02	02/08/07	60.046	4-5	0.386	18.3	0.00286	17.6
4.96	02/08/07	60.061	4-6	0.417	51.4	0.00223	18.5

a: α = loading = mole CO_2/mol 2·PZ

D.6 Tabulated H_2O-K_2CO_3-PZ-CO_2 Data

K_2CO_3 m	$KHCO_3$ m	K^{+a} m	PZ m	Date	T °C	Soln	α^b	P_{CO2} kPa	P_{PZ} kPa	P_{H2O} kPa
1.63	1.75	5.00	2.50	02/10/07	39.996	1	0.337	0.00286	0.00632	6.16
1.60	1.72	4.92	2.46	02/10/07	39.995	2-1	0.389	0.00802	0.00347	6.22
1.57	1.70	4.85	2.42	02/10/07	39.981	2-2	0.425	0.0250	0.00197	6.29
1.59	1.71	4.90	2.45	02/10/07	40.005	2-3	0.455	0.0815	0.00191	6.31
1.58	1.71	4.88	2.44	02/10/07	39.992	2-4	0.488	0.300	0.00093	6.36
1.58	1.70	4.86	2.43	02/10/07	39.974	2-5	0.520	0.922	0.00053	6.31
1.58	1.70	4.86	2.43	02/10/07	40.002	2-6	0.550	2.70	0.00045	6.41
1.63	1.75	5.00	2.50	02/12/07	59.994	4-0	0.339	0.00569	0.0243	15.7
1.61	1.73	4.95	2.48	02/12/07	59.988	4-1	0.391	0.0323	0.0126	15.9
1.60	1.73	4.93	2.47	02/12/07	60.022	4-2	0.420	0.0935	0.00754	16.1
1.60	1.72	4.91	2.46	02/12/07	60.013	4-3	0.458	0.431	0.00518	16.5
1.60	1.72	4.91	2.46	02/12/07	60.007	4-4	0.472	0.680	0.00356	16.5
1.59	1.71	4.90	2.45	02/12/07	60.090	4-5	0.510	2.03	0.00190	16.6
1.60	1.72	4.91	2.46	02/12/07	60.003	4-6	0.542	5.91	0.00120	16.6
0.71	2.14	3.56	3.56	02/15/07	40.006	1	0.266	0.00315	0.00597	6.21
0.71	2.13	3.54	3.54	02/15/07	39.994	2-1	0.333	0.0150	0.00301	6.36
0.71	2.14	3.57	3.57	02/15/07	40.003	2-2	0.368	0.0447	0.00245	6.42
0.71	2.13	3.54	3.54	02/15/07	40.001	2-3	0.390	0.0848	0.00150	6.42
0.71	2.13	3.55	3.55	02/15/07	40.009	2-4	0.424	0.255	0.00099	6.43
0.72	2.15	3.58	3.58	02/15/07	40.006	2-5	0.436	0.477	0.00082	6.43
0.71	2.12	3.53	3.53	02/15/07	40.012	2-6	0.467	1.09	0.00067	6.48
0.71	2.14	3.57	3.57	02/16/07	60.007	3	0.263	0.00771	0.0201	16.4
0.71	2.12	3.53	3.53	02/16/07	60.002	4-1	0.339	0.103	0.00977	16.4
0.71	2.12	3.54	3.54	02/16/07	60.026	4-2	0.357	0.158	0.00751	16.4
0.71	2.13	3.54	3.54	02/16/07	60.038	4-3	0.389	0.496	0.00526	16.5
0.72	2.15	3.58	3.58	02/16/07	59.998	4-4	0.411	0.852	0.00532	16.5
0.72	2.15	3.58	3.58	02/16/07	60.032	4-5	0.438	1.87	0.00372	16.6
0.71	2.14	3.57	3.57	02/16/07	60.041	4-6	0.467	4.78	0.00243	16.7

a: mol K^+ = mol $2\cdot K_2CO_3$ + mol $KHCO_3$

b: α = loading = mole CO_2^{tot}/mol K^+ + mol 2·PZ

K_2CO_3 m	$KHCO_3$ m	K^{+a} m	PZ m	Date	T °C	Soln	α^b	P_{CO2} kPa	P_{PZ} kPa	P_{H2O} kPa
0.86	3.22	4.95	3.57	03/11/07	40.010	2-0	0.341	0.00577	0.00595	5.93
0.84	3.14	4.83	3.48	03/11/07	40.002	2-1^c	0.361	0.00909	0.00497	6.05
0.81	3.03	4.66	3.36	03/11/07	39.898	2-6^c	0.507	2.28	0.00046	6.27
1.53	1.84	4.90	3.53	03/12/07	40.003	5-1	0.284	0.00100	0.00784	5.89
1.54	1.85	4.93	3.55	03/12/07	40.005	5-4A	0.328	0.00469	0.00658	5.91
0.82	3.06	4.70	3.38	03/11/07	59.998	4-0	0.349	0.0194	0.0206	15.3
0.85	3.16	4.86	3.50	03/11/07	60.022	4-1	0.360	0.0350	0.0157	15.6
0.82	3.07	4.71	3.39	03/11/07	60.014	4-6	0.525	22.1	0.00121	16.6
1.54	1.85	4.92	3.54	03/12/07	59.996	5-4B	0.330	0.0138	0.0234	15.5
1.63	1.71	4.96	1.99	03/08/07	40.017	2-0	0.382	0.0034	0.00452	6.28
1.62	1.70	4.95	1.98	03/08/07	40.007	2-1	0.397	0.0062	0.00343	6.30
1.62	1.70	4.94	1.98	03/08/07	40.001	2-2	0.423	0.0152	0.00196	6.45
1.61	1.69	4.92	1.97	03/08/07	40.039	2-3	0.458	0.0504	0.00119	6.34
1.62	1.69	4.93	1.97	03/08/07	40.015	2-4	0.498	0.237	0.00098	6.47
1.61	1.69	4.91	1.97	03/08/07	40.030	2-5	0.520	0.522	0.00066	6.52
1.61	1.69	4.91	1.97	03/08/07	40.016	2-6	0.533	0.858	0.00053	6.50
1.63	1.71	4.96	1.98	03/09/07	60.009	4-0	0.379	0.0109	0.0166	16.0
1.62	1.70	4.95	1.98	03/09/07	60.058	4-1	0.391	0.0205	0.0138	16.3
1.63	1.71	4.96	1.98	03/09/07	60.044	4-2	0.421	0.0581	0.00833	16.4
1.62	1.70	4.95	1.98	03/09/07	60.000	4-3	0.456	0.214	0.00621	16.4
1.63	1.71	4.97	1.99	03/09/07	60.035	4-4	0.490	0.764	0.00276	16.5
1.62	1.70	4.95	1.98	03/09/07	60.042	4-5	0.512	1.34	0.00195	16.5
1.62	1.70	4.95	1.98	03/09/07	59.989	4-6	0.536	2.29	0.00140	16.4
2.53	0.91	5.97	1.19	02/20/07	40.004	1	0.409	0.00200	0.00556	6.16
2.50	0.90	5.90	1.18	02/20/07	40.024	2-1	0.432	0.00399	0.00418	6.16
2.51	0.90	5.92	1.18	02/20/07	40.022	2-2	0.463	0.0122	0.00197	6.28
2.49	0.89	5.87	1.17	02/20/07	39.999	2-3	0.512	0.0792	0.00104	6.33
2.49	0.89	5.87	1.17	02/20/07	40.012	2-4	0.575	0.689	0.000228	6.39

a: mol K^+ = mol $2 \cdot K_2CO_3$ + mol $KHCO_3$

b: α = loading = mole CO_2^{tot}/mol K^+ + mol $2 \cdot PZ$

c: solid phase present

K_2CO_3 m	$KHCO_3$ m	K^{+a} m	PZ m	Date	T °C	Soln	α^b	P_{CO2} kPa	P_{PZ} kPa	P_{H2O} kPa
2.47	0.89	5.83	1.17	02/21/07	60.003	3	0.405	0.00499	0.0185	15.9
2.50	0.90	5.89	1.18	02/21/07	59.972	4-1	0.434	0.0157	0.0131	16.0
2.49	0.89	5.87	1.17	02/21/07	60.030	4-2	0.462	0.0494	0.00686	16.3
2.49	0.89	5.88	1.18	02/21/07	60.023	4-3	0.523	0.459	0.00244	16.3
2.50	0.90	5.90	1.18	02/21/07	60.026	4-4	0.534	0.664	0.00184	16.3
2.51	0.90	5.91	1.18	02/21/07	60.038	4-5	0.561	1.43	0.000981	16.4
2.43	0.87	5.74	1.15	02/21/07	60.020	4-6	0.574	2.53	0.000705	16.4
1.58	0.43	3.59	0.60	02/27/07	40.008	2-0	0.418	0.00324	0.00147	6.78
1.57	0.43	3.56	0.59	02/27/07	40.024	2-1	0.443	0.00846	0.00121	6.87
1.56	0.43	3.55	0.59	02/27/07	40.027	2-2	0.491	0.0384	0.00057	6.93
1.56	0.43	3.55	0.59	02/27/07	40.025	2-3	0.508	0.0753	0.000401	6.91
1.56	0.43	3.55	0.59	02/27/07	40.043	2-4	0.545	0.228	0.000244	6.96
1.57	0.43	3.56	0.59	02/27/07	40.016	2-5	0.579	0.771	0.000175	6.94
1.58	0.43	3.60	0.60	02/28/07	60.025	4-0	0.439	0.0134	0.00522	17.3
1.59	0.43	3.61	0.60	02/28/07	60.041	4-1	0.475	0.0421	0.00379	17.5
1.58	0.43	3.59	0.60	02/28/07	59.991	4-2	0.489	0.0796	0.00244	17.3
1.58	0.43	3.60	0.60	02/28/07	60.055	4-3	0.524	0.289	0.00200	17.4
1.58	0.43	3.60	0.60	02/28/07	60.078	4-4	0.564	0.848	0.00107	17.4
1.58	0.43	3.59	0.60	02/28/07	60.008	4-5	0.588	1.51	0.000849	17.4
1.58	0.43	3.58	0.60	02/28/07	60.029	4-6	0.630	5.98	0.000608	17.5
1.00	1.57	3.57	1.79	03/02/07	40.013	2-0	0.374	0.00631	0.00252	6.57
1.00	1.57	3.56	1.78	03/02/07	40.017	2-1	0.385	0.00861	0.00228	6.60
1.00	1.57	3.56	1.78	03/02/07	40.035	2-2	0.414	0.0204	0.00154	6.64
1.00	1.57	3.57	1.78	03/02/07	40.018	2-3	0.439	0.0467	0.00128	6.65
1.00	1.57	3.57	1.78	03/02/07	39.994	2-4	0.478	0.212	0.000889	6.75
1.00	1.57	3.57	1.79	03/02/07	40.001	2-5	0.510	0.696	0.000644	6.77
1.00	1.57	3.56	1.78	03/02/07	40.003	2-6	0.534	1.33	0.000641	6.81

a: mol K^+ = mol $2 \cdot K_2CO_3$ + mol $KHCO_3$

b: α = loading = mole CO_2^{tot}/mol K^+ + mol $2 \cdot PZ$

K_2CO_3 m	$KHCO_3$ m	K^{+a} m	PZ m	Date	T °C	Soln	α^b	P_{CO2} kPa	P_{PZ} kPa	P_{H2O} kPa
1.02	1.60	3.64	1.82	03/03/07	60.005	4-0	0.373	0.0211	0.00935	16.9
1.01	1.58	3.59	1.80	03/03/07	60.005	4-1	0.391	0.0442	0.00875	17.2
1.01	1.58	3.59	1.80	03/03/07	60.073	4-2	0.449	0.208	0.00433	17.3
1.00	1.57	3.58	1.79	03/03/07	60.011	4-3	0.467	0.575	0.00248	17.3
1.01	1.58	3.60	1.80	03/03/07	60.075	4-4	0.483	0.708	0.00222	17.3
1.00	1.58	3.59	1.79	03/03/07	60.078	4-5	0.511	2.00	0.00114	17.3
1.01	1.58	3.60	1.80	03/03/07	60.075	4-6	0.528	4.01	0.000920	17.4
0.36	1.76	2.49	3.58	04/07/07	40.032	2-0	0.335	0.0438	0.00207	6.66
0.36	1.74	2.46	3.54	04/07/07	39.996	2-1	0.381	0.169	0.00127	6.69
0.36	1.75	2.47	3.56	04/07/07	40.025	2-2	0.439	1.20	0.000826	6.72
0.36	1.75	2.47	3.56	04/07/07	60.037	4-0	0.327	0.235	0.00651	17.1
0.36	1.75	2.47	3.56	04/07/07	60.042	4-1	0.383	0.889	0.00480	17.2
0.36	1.76	2.48	3.57	04/07/07	60.031	4-2	0.452	4.85	0.00224	17.3
0.34	1.81	2.49	1.99	04/09/07	40.014	2-0	0.386	0.0299	0.00114	6.92
0.34	1.80	2.48	1.98	04/09/07	40.021	2-1	0.457	0.249	0.000956	7.01
0.34	1.80	2.48	1.98	04/09/07	40.002	2-2	0.511	1.43	0.000516	7.11
0.34	1.82	2.49	2.00	04/09/07	60.016	4-0	0.385	0.135	0.00488	17.6
0.34	1.82	2.50	2.00	04/09/07	59.990	4-1	0.454	0.909	0.00208	17.6
0.34	1.81	2.49	1.99	04/09/07	60.004	4-2	0.509	4.47	0.00140	17.5

a: mol K^+ = mol $2\cdot K_2CO_3$ + mol $KHCO_3$

b: α = loading = mole CO_2^{tot}/mol K^+ + mol 2·PZ

D.7 Tabulated H_2O-MEA-PZ-CO_2 Data

MEA/m	PZ/m	Date	T/°C	Soln	α^a	P_{CO2}/kPa	P_{MEA}/kPa	P_{PZ}/kPa	P_{H2O}/kPa
7.00	2.00	12/15/06	39.957	1	0.000	-	0.00758	0.00213	6.38
6.90	1.97	12/15/06	40.023	2-1	0.113	0.00635	0.00659	0.00191	6.40
6.86	1.96	12/15/06	39.997	2-2	0.183	0.0139	0.00542	0.00172	6.43
6.99	2.00	12/18/06	39.981	2-3	0.235	0.0281	0.00414	0.00157	6.43
7.20	2.06	12/18/06	40.010	2-4	0.306	0.0962	0.00346	0.00137	6.50
7.23	2.07	12/18/06	40.007	2-5	0.366	0.313	0.00248	0.00110	6.51
6.95	1.99	12/18/06	39.968	2-6	0.450	2.67	0.00134	0.000592	6.50

a: Loading = mol CO_2/mol MEA + 2·mol PZ)

MEA/m	PZ/m	Date	T/°C	Soln	α^a	P_{CO2}/kPa	P_{MEA}/kPa	P_{PZ}/kPa	P_{H2O}/kPa
7.00	2.00	12/19/06	59.998	3	0.000	-	0.0282	0.00697	16.5
7.13	2.04	12/19/06	60.004	4-1	0.097	0.0225	0.0242	0.00662	16.5
7.13	2.04	12/19/06	60.013	4-2	0.164	0.0633	0.0204	0.00621	16.6
7.01	2.00	12/19/06	60.005	4-3	0.238	0.162	0.0164	0.00518	16.7
7.01	2.00	12/20/06	59.992	4-4	0.308	0.615	0.0116	0.00345	16.6
7.16	2.04	12/20/06	60.013	4-5	0.368	1.90	0.00763	0.00219	16.6
7.09	2.03	12/20/06	60.003	4-6	0.444	12.8	0.00428	0.00113	16.9
3.50	2.00	01/03/07	40.018	1	0.000	-	0.00433	0.00224	6.77
3.49	2.00	01/04/07	40.076	2-1	0.129	0.00797	0.00333	0.00194	6.86
3.48	1.99	01/04/07	40.018	2-2	0.178	0.0163	0.00315	0.00191	6.89
3.57	2.04	01/04/07	40.020	2-3	0.243	0.0365	0.00272	0.00169	6.90
3.55	2.03	01/04/07	40.009	2-4	0.318	0.140	0.00197	0.00125	6.89
3.45	1.98	01/04/07	40.005	2-5	0.403	0.756	0.00153	0.000972	6.90
3.52	2.02	01/04/07	40.022	2-6	0.452	4.37	0.00148	0.000745	6.95
3.50	2.00	01/05/07	59.994	3	0.000	-	0.0144	0.00624	17.3
3.52	2.01	01/05/07	60.005	4-1	0.103	0.0265	0.0124	0.00542	17.3
3.53	2.02	01/05/07	60.006	4-2	0.169	0.0840	0.00994	0.00626	17.3
3.53	2.02	01/08/07	60.020	4-3	0.241	0.256	0.00746	0.00454	17.4
3.54	2.02	01/08/07	60.005	4-4	0.313	0.817	0.00585	0.00352	17.5
3.62	2.07	01/08/07	60.003	4-5	0.381	2.98	0.00385	0.00224	17.5
3.56	2.04	01/08/07	60.046	4-6	0.453	25.0	0.00232	0.00135	17.9
7.00	3.60	01/30/07	40.016	1	0.000	-	0.00817	0.00433	6.11
7.04	3.62	01/30/07	40.028	2-1	0.113	0.00628	0.00684	0.00371	6.11
7.11	3.65	01/30/07	40.025	2-2	0.187	0.0156	0.00518	0.00279	6.14
7.11	3.66	01/31/07	40.005	2-3	0.248	0.0341	0.00372	0.00177	6.14
7.53	3.87	01/31/07	40.018	2-4	0.335	0.118	0.00259	0.00119	6.20
7.16	3.68	01/31/07	40.055	2-5	0.372	0.559	0.00151	0.000606	6.18
7.03	3.62	01/31/07	39.999	2-6	0.429	4.87	0.000850	0.000323	6.24
7.00	3.60	02/02/07	60.012	3	0.000	-	0.0279	0.0131	15.9
6.91	3.56	02/02/07	60.011	4-1	0.129	0.0316	0.0223	0.0108	15.9
6.95	3.57	02/02/07	60.012	4-2	0.189	0.0827	0.0196	0.00869	15.8
6.95	3.57	02/02/07	60.000	4-3	0.271	0.310	0.0132	0.00790	15.8
6.97	3.59	02/05/07	60.004	4-4	0.317	0.783	0.0101	0.00551	15.9

a: Loading = mol CO_2/mol MEA + 2·mol PZ)

MEA/m	PZ/m	Date	T/°C	Soln	α^a	P_{CO2}/kPa	P_{MEA}/kPa	P_{PZ}/kPa	P_{H2O}/kPa
7.15	3.68	02/05/07	60.033	4-5	0.367	2.95	0.00571	0.00260	16.0
6.87	3.54	02/05/07	59.999	4-6	0.430	21.2	0.00286	0.00108	16.4
3.50	3.60	01/23/07	40.004	1	0.000	-	0.00382	0.00368	6.54
3.45	3.55	01/24/07	39.995	2-1	0.101	0.0	0.00302	0.00303	6.52
3.53	3.63	01/24/07	40.072	2-2	0.171	0.0	0.00257	0.00251	6.62
3.49	3.59	01/24/07	40.002	2-3	0.248	0.1	0.00183	0.00171	6.60
3.50	3.60	01/24/07	40.115	2-4	0.312	0.2	0.00125	0.00114	6.65
3.60	3.71	01/25/07	39.996	2-5	0.370	0.9	0.00094	0.00101	6.68
3.53	3.63	01/25/07	39.995	2-6	0.443	5.8	0.00071	0.00078	6.74
3.50	3.60	01/26/07	60.007	3	0.000	-	0.01483	0.01307	17.1
3.49	3.59	01/26/07	60.062	4-1	0.110	0.0	0.01161	0.00996	16.9
3.47	3.57	01/26/07	60.049	4-2	0.178	0.1	0.00949	0.00781	16.9
3.44	3.54	01/26/07	60.015	4-3	0.246	0.3	0.00708	0.00821	16.9
3.51	3.61	01/29/07	59.991	4-4	0.315	1.0	0.00479	0.00498	16.9
3.52	3.62	01/29/07	60.020	4-5	0.386	4.8	0.00272	0.00257	17.0
3.56	3.66	01/29/07	60.024	4-6	0.455	21.2	0.00153	0.00144	17.3

a: Loading = mol CO_2/mol MEA + 2·mol PZ)

D.8 Tabulated H_2O-K_2CO_3-MEA-CO_2 Data

MEA m	K^+ m	K_2CO_3 m	$KHCO_3$ m	Date	T °C	Soln	α^a	P_{CO2} kPa	P_{MEA} kPa	P_{H2O} kPa
3.47	4.96	2.01	0.94	03/16/07	40.001	2-0	0.353	0.000672	0.00964	6.05
3.44	4.91	1.99	0.93	03/16/07	40.012	2-1	0.410	0.00178	0.00586	6.18
3.43	4.91	1.99	0.93	03/16/07	40.039	2-2	0.448	0.00568	0.00435	6.25
3.43	4.90	1.99	0.93	03/16/07	40.042	2-3	0.487	0.0291	0.00259	6.31
3.44	4.91	1.99	0.93	03/16/07	40.033	2-4	0.527	0.242	0.00186	6.36
3.44	4.91	1.99	0.93	03/16/07	40.021	2-5	0.564	1.16	0.00146	6.38
3.45	4.92	1.99	0.94	03/16/07	40.016	2-6	0.609	5.21	0.00141	6.48
3.47	4.96	2.01	0.94	03/17/07	60.008	4-0	0.352	0.00128	0.0361	16.0
3.45	4.93	2.00	0.94	03/17/07	60.003	4-1	0.415	0.00643	0.0228	16.3
3.46	4.95	2.00	0.94	03/17/07	60.010	4-2	0.449	0.0188	0.0149	16.3
3.48	4.97	2.01	0.94	03/17/07	60.008	4-3	0.486	0.115	0.00910	16.4
3.46	4.95	2.00	0.94	03/17/07	60.051	4-4	0.526	0.732	0.00570	16.4
3.47	4.96	2.01	0.94	03/17/07	60.021	4-5	0.562	2.83	0.00411	16.5

a: α = loading = mole CO_2/mol K^+ + mol MEA

MEA m	K^+ m	K_2CO_3 m	$KHCO_3$ m	Date	T °C	Soln	α^a	P_{CO2} kPa	P_{MEA} kPa	P_{H2O} kPa
3.43	4.89	1.98	0.93	03/17/07	60.027	4-6	0.612	13.2	0.00344	16.7
3.48	2.48	0.81	0.85	03/19/07	40.042	2-0	0.285	0.00121	0.00620	6.29
3.52	2.52	0.83	0.87	03/19/07	40.024	2-1	0.409	0.0161	0.00367	6.82
3.47	2.48	0.81	0.85	03/19/07	40.000	2-2	0.503	0.559	0.00217	6.86
3.46	2.47	0.81	0.85	03/19/07	40.051	2-3	0.589	13.0	0.00161	6.97
3.44	2.46	0.81	0.85	03/19/07	60.051	4-1	0.414	0.0827	0.0103	17.2
3.57	2.55	0.84	0.88	03/19/07	60.023	4-2	0.493	2.21	0.00506	17.3
3.50	2.50	0.82	0.86	03/19/07	60.011	4-3	0.593	26.0	0.00312	17.6
6.90	4.93	1.62	1.70	03/22/07	40.049	2-0	0.269	0.000786	0.0150	5.64
6.86	4.90	1.61	1.69	03/22/07	40.046	2-1	0.401	0.00898	0.00699	5.89
6.89	4.92	1.62	1.69	03/22/07	40.036	2-2	0.442	0.0273	0.00518	5.99
6.87	4.90	1.61	1.69	03/22/07	40.031	2-3	0.487	0.207	0.00296	6.01
6.87	4.91	1.61	1.69	03/22/07	40.015	2-4	0.518	1.53	0.00260	6.03
6.87	4.91	1.61	1.69	03/22/07	39.996	2-6	0.599	16.9	0.00229	6.11
7.09	5.07	1.66	1.74	03/23/07	60.044	4-0	0.279	0.00182	0.0552	14.3
7.01	5.01	1.64	1.72	03/23/07	60.011	4-1	0.416	0.0352	0.0247	15.2
7.03	5.02	1.65	1.73	03/23/07	60.046	4-2	0.457	0.151	0.0186	15.0
6.99	5.00	1.64	1.72	03/23/07	60.090	4-3	0.490	0.939	0.0107	15.2
7.08	5.06	1.66	1.74	03/23/07	60.047	4-4	0.527	4.95	0.00657	15.3
7.02	5.02	1.65	1.73	03/23/07	60.047	4-5	0.562	17.4	0.00489	15.5
6.93	2.47	0.81	0.85	03/23/07	40.025	2-0	0.172	0.00112	0.01270	6.23
6.88	2.46	0.81	0.85	03/23/07	40.031	2-1	0.408	0.0583	0.00499	6.43
6.96	2.49	0.81	0.86	03/23/07	40.032	2-2	0.529	2.23	0.00221	6.49
6.98	2.49	0.82	0.86	03/23/07	40.041	2-3	0.569	9.04	0.00192	6.55
6.94	2.48	0.81	0.85	03/24/07	60.044	4-0	0.173	0.00297	0.03910	16.1
6.92	2.47	0.81	0.85	03/24/07	60.010	4-1	0.411	0.477	0.01563	16.6
6.98	2.49	0.82	0.86	03/24/07	60.063	4-2	0.512	8.71	0.00643	16.8
7.03	2.51	0.82	0.87	03/24/07	60.082	4-3	0.538	19.9	0.00435	16.7

a: α = loading = mole CO_2/mol K^+ + mol MEA

D.9 Tabulated H_2O-K_2CO_3-MEA-PZ-CO_2 Data

K_2CO_3/m	$KHCO_3$/m	K^{+a}/m	MEA/m	PZ/m	Date	T/°C	Soln	α^b	P_{CO2}/kPa	P_{MEA}/kPa	P_{PZ}/kPa	P_{H2O}/kPa
1.52	2.02	5.05	3.54	2.02	03/26/07	40.020	2-0	0.396	0.00471	0.00335	0.00380	5.86
1.51	2.01	5.03	3.52	2.01	03/26/07	40.008	2-1	0.472	0.0567	0.00165	0.00110	6.05
1.51	2.02	5.05	3.53	2.02	03/26/07	40.025	2-2	0.523	0.488	0.00112	0.000517	6.10
1.53	2.04	5.09	3.56	2.04	03/26/07	40.056	2-3	0.560	2.30	0.000768	0.000224	6.20
1.45	1.94	4.84	3.39	1.94	03/26/07	60.027	4-0	0.405	0.0167	0.0131	0.0131	15.0
1.52	2.03	5.07	3.55	2.03	03/26/07	60.061	4-1	0.475	0.287	0.00634	0.00605	15.3
1.52	2.02	5.05	3.54	2.02	03/26/07	60.049	4-2	0.520	1.81	0.00391	0.00221	15.8
1.54	2.05	5.12	3.59	2.05	03/26/07	60.040	4-3	0.576	7.68	0.00269	0.00095	15.7
0.75	1.00	2.50	3.51	2.00	03/27/07	40.019	2-0	0.395	0.0525	0.00237	0.00189	6.52
0.76	1.01	2.52	3.53	2.02	03/27/07	40.021	2-1	0.454	0.248	0.00168	0.00105	6.53
0.75	1.00	2.51	3.51	2.01	03/27/07	40.026	2-2	0.500	1.25	0.00118	0.000641	6.55
0.75	1.00	2.51	3.51	2.01	03/27/07	39.989	2-3	0.546	5.29	0.000910	0.000429	6.59
0.76	1.01	2.52	3.53	2.01	03/27/07	60.025	4-0	0.388	0.298	0.00699	0.00515	16.6
0.75	1.01	2.52	3.52	2.01	03/27/07	59.992	4-1	0.444	1.20	0.00476	0.00269	16.6
0.75	1.01	2.51	3.52	2.01	03/27/07	60.029	4-2	0.494	5.19	0.00308	0.00138	16.70
0.76	1.01	2.52	3.53	2.02	03/27/07	60.052	4-3	0.529	17.2	0.00238	0.000870	17.01
0.59	3.70	4.89	6.84	1.95	03/29/07	40.038	2-0	0.345	0.0121	0.00535	0.00280	5.62
0.59	3.69	4.87	6.82	1.95	03/29/07	40.075	2-1	0.420	0.104	0.00316	0.00173	5.77
0.59	3.69	4.87	6.82	1.95	03/29/07	40.000	2-2	0.485	1.38	0.00123	0.000302	5.75
0.59	3.70	4.88	6.83	1.95	03/29/07	40.020	2-3	0.537	10.4	0.000690	0.000104	5.76
0.61	3.78	4.99	6.99	2.00	03/29/07	60.033	4-0	0.383	0.0688	0.0217	0.00961	14.2
0.61	3.82	5.04	7.06	2.02	03/29/07	60.028	4-1	0.457	0.638	0.0117	0.00542	14.6
0.61	3.84	5.07	7.10	2.03	03/29/07	60.004	4-2	0.524	5.75	0.00528	0.00130	14.6
0.61	3.84	5.07	7.09	2.03	03/29/07	60.032	4-3	0.576	28.2	0.00322	0.000873	14.8

a: mol K^+ = mol $2{\cdot}K_2CO_3$ + mol $KHCO_3$

b: α = loading = mole CO_2^{tot}/mol K^+ + mol MEA + mol 2·PZ

K_2CO_3/m	$KHCO_3$/m	K^{+a}/m	MEA/m	PZ/m	Date	T/°C	Soln	α^b	P_{CO2}/kPa	P_{MEA}/kPa	P_{PZ}/kPa	P_{H2O}/kPa
0.74	0.99	2.47	6.90	1.97	03/30/07	39.996	2-0	0.362	0.0594	0.00379	0.00191	6.11
0.73	0.98	2.45	6.85	1.96	03/30/07	40.047	2-1	0.415	0.295	0.00224	0.000858	6.15
0.75	1.00	2.49	6.98	1.99	03/30/07	40.001	2-2	0.474	2.70	0.00113	0.000311	6.14
0.73	0.98	2.44	6.84	1.95	03/30/07	40.035	2-3	0.519	14.5	0.000789	0.000187	6.28
0.73	0.98	2.44	6.84	1.95	03/30/07	60.018	4-0	0.361	0.447	0.01357	0.00521	15.6
0.74	0.98	2.46	6.88	1.97	03/30/07	60.044	4-1	0.421	1.71	0.00846	0.00252	15.9
0.74	0.99	2.47	6.92	1.98	03/30/07	60.013	4-2	0.483	11.5	0.00472	0.00158	16.0
0.75	0.99	2.48	6.95	1.99	03/30/07	60.008	4-3	0.509	27.3	0.00290	0.000595	16.2
0.29	1.93	2.50	7.01	3.61	04/03/07	40.045	2-0	0.382	0.0887	0.00269	0.00160	5.81
0.28	1.85	2.41	6.75	3.47	04/03/07	40.015	2-1	0.423	0.610	0.00143	0.000867	5.91
0.27	1.83	2.37	6.65	3.42	04/03/07	40.003	2-2	0.478	4.67	0.000678	0.000251	5.90
0.28	1.89	2.45	6.88	3.54	04/03/07	40.048	2-3	0.515	17.0	0.000470	0.0000981	6.04
0.28	1.87	2.43	6.80	3.50	04/03/07	60.052	4-0	0.350	0.602	0.0115	0.00855	14.8
0.28	1.88	2.45	6.85	3.52	04/03/07	60.044	4-1	0.413	3.04	0.00590	0.00312	15.1
0.28	1.87	2.43	6.80	3.50	04/03/07	60.016	4-2	0.455	18.6	0.00308	0.00112	15.1
0.28	1.85	2.41	6.75	3.47	04/03/07	60.088	4-3	0.475	41.6	0.00253	0.00107	15.7
0.56	3.75	4.88	6.83	3.51	04/04/07	40.039	2-0	0.262	0.00296	0.00732	0.00613	5.2
0.56	3.71	4.83	6.76	3.47	04/04/07	40.009	2-1	0.294	0.00627	0.00600	0.00676	5.3
0.54	3.62	4.71	6.60	3.39	04/04/07	39.996	2-2	0.343	0.0255	0.00456	0.00414	5.4
0.53	3.51	4.57	6.39	3.29	04/04/07	40.016	2-3	0.379	0.0761	0.00293	0.00211	5.5
0.57	3.77	4.90	6.86	3.53	04/04/07	60.076	4-0	0.263	0.00946	0.0279	0.0289	13.4
0.55	3.66	4.76	6.67	3.43	04/04/07	60.088	4-1	0.302	0.0415	0.0221	0.0195	13.8
0.54	3.62	4.71	6.59	3.39	04/04/07	59.989	4-2	0.342	0.146	0.0176	0.0131	13.8
0.53	3.54	4.60	6.43	3.31	04/04/07	60.005	4-3	0.379	0.502	0.0135	0.00773	14.0

a: mol K^+ = mol $2{\cdot}K_2CO_3$ + mol $KHCO_3$

b: α = loading = mole CO_2^{tot}/mol K^+ + mol MEA + mol 2·PZ

K_2CO_3/m	$KHCO_3$/m	K^{+a}/m	MEA/m	PZ/m	Date	T/°C	Soln	α^b	P_{CO2}/kPa	P_{MEA}/kPa	P_{PZ}/kPa	P_{H2O}/kPa
0.35	1.77	2.48	3.47	1.78	04/05/07	40.017	2-0	0.375	0.0529	0.00250	0.00170	6.58
0.35	1.75	2.46	3.44	1.77	04/05/07	40.002	2-1	0.444	0.462	0.00157	0.000790	6.59
0.35	1.75	2.45	3.44	1.77	04/05/07	40.007	2-2	0.502	3.25	0.00105	0.000444	6.62
0.35	1.75	2.46	3.44	1.77	04/05/07	40.011	2-3	0.554	20.6	0.000636	0.000174	6.84
0.35	1.77	2.47	3.46	1.78	04/05/07	60.069	4-0	0.371	0.355	0.00647	0.00426	16.8
0.35	1.77	2.47	3.46	1.78	04/05/07	59.998	4-1	0.442	2.10	0.00408	0.00185	16.8
0.35	1.76	2.47	3.46	1.78	04/05/07	60.020	4-2	0.495	12.6	0.00287	0.00156	17.0
0.35	1.77	2.48	3.47	1.79	04/05/07	60.099	4-3	0.538	44.2	0.00169	0.000569	17.5
0.60	3.73	4.92	3.45	3.54	04/06/07	40.037	2-0	0.307	0.00409	0.00317	0.00753	5.56
0.60	3.73	4.92	3.45	3.55	04/06/07	40.032	2-1	0.328	0.00660	0.00281	0.00632	5.65
0.58	3.65	4.82	3.38	3.47	04/06/07	39.997	2-2	0.365	0.0213	0.00198	0.003586	5.82
0.58	3.60	4.75	3.33	3.42	04/06/07	40.010	2-3	0.406	0.0859	0.00144	0.00173	5.85
0.60	3.74	4.94	3.46	3.55	04/06/07	60.050	4-0	0.312	0.0126	0.0125	0.0260	14.4
0.60	3.74	4.94	3.46	3.56	04/06/07	60.014	4-1	0.324	0.0251	0.0111	0.0202	14.7
0.58	3.63	4.79	3.35	3.45	04/06/07	60.059	4-2	0.364	0.114	0.00861	0.0127	14.8
0.57	3.58	4.73	3.31	3.40	04/06/07	59.994	4-3	0.407	0.552	0.00582	0.00618	15.0
0.30	1.87	2.47	3.45	3.55	04/07/07	40.015	2-0	0.382	0.145	0.00146	0.00193	6.31
0.30	1.86	2.45	3.44	3.53	04/07/07	40.026	2-1	0.453	1.75	0.000662	0.000381	6.37
0.30	1.85	2.45	3.42	3.52	04/07/07	40.018	2-2	0.488	7.58	0.000440	0.000263	6.37
0.30	1.87	2.47	3.45	3.55	04/07/07	60.075	4-0	0.380	0.882	0.00474	0.00620	16.0
0.30	1.87	2.46	3.45	3.55	04/07/07	60.028	4-1	0.451	7.78	0.00243	0.00198	16.3
0.30	1.87	2.46	3.45	3.55	04/07/07	60.012	4-2	0.482	24.0	0.00158	0.00118	16.5

a: mol K^+ = mol $2{\cdot}K_2CO_3$ + mol $KHCO_3$

b: α = loading = mole CO_2^{tot}/mol K^+ + mol MEA + mol 2·PZ

APPENDIX E

Tabulated VLE Data (NTNU)

E.1 Tabulated H_2O-K_2CO_3-PZ-CO_2 Data

K^+/m	K_2CO_3/m	PZ/m	T/°C	CO_2 Loading[a]	CO_2 Loading[b]	P_{CO2}^{Exp}/kPa	P_{CO2}^{Corr}/kPa
3.6	1.8	0.6	100	0.533	0.466	0.895	1.09
3.6	1.8	0.6	100	0.635	0.556	5.43	5.53
3.6	1.8	0.6	100	0.735	0.643	24.5	24.3
3.6	1.8	0.6	120	0.527	0.461	1.15	1.79
3.6	1.8	0.6	120	0.589	0.515	4.53	5.01
3.6	1.8	0.6	120	0.728	0.637	48.2	48.7
3.6	1.8	1.8	100	0.475	0.356	0.316	0.664
3.6	1.8	1.8	100	0.574	0.431	2.94	3.24
3.6	1.8	1.8	100	0.685	0.514	25.1	24.6

a: Loading = mol CO_2/(mol K^+ + mol PZ)

b: Loading = mole CO_2/mol K^+ + 2·mol PZ

K^+/m	K_2CO_3/m	PZ/m	T/°C	CO_2 Loading[a]	CO_2 Loading[b]	P_{CO2}^{Exp}/kPa	P_{CO2}^{Corr}/kPa
3.6	1.8	1.8	120	0.487	0.365	0.717	1.82
3.6	1.8	1.8	120	0.586	0.439	8.63	9.59
3.6	1.8	1.8	120	0.678	0.508	52.8	51.9
3.6	1.8	3.6	100	0.481	0.320	1.26	1.71
3.6	1.8	3.6	100	0.600	0.400	8.45	8.73
3.6	1.8	3.6	100	0.711	0.474	63.6	56.6
3.6	1.8	3.6	120	0.499	0.332	3.60	5.02
3.6	1.8	3.6	120	0.597	0.398	26.7	26.1
3.6	1.8	3.6	120	0.677	0.451	106.0	87.0
5	2.5	2.5	80	0.502	0.376	0.0508	0.251
5	2.5	2.5	80	0.577	0.433	12.4	0.918
5	2.5	2.5	80	0.588	0.441	0.141	1.00
5	2.5	2.5	80	0.671	0.503	0.841	6.58
5	2.5	2.5	80	0.686	0.515	7.51	12.5
5	2.5	2.5	100	0.517	0.388	0.369	0.715
5	2.5	2.5	100	0.568	0.426	1.94	2.29
5	2.5	2.5	100	0.610	0.458	5.14	5.48
5	2.5	2.5	100	0.651	0.488	14.1	14.3
5	2.5	2.5	100	0.697	0.523	31.4	30.4
5	2.5	2.5	120	0.487	0.365	0.216	1.29
5	2.5	2.5	120	0.581	0.436	6.41	7.51
5	2.5	2.5	120	0.643	0.482	43.5	45.4
6	3	1.2	100	0.507	0.434	0.0817	0.293
6	3	1.2	100	0.591	0.506	1.75	1.94
6	3	1.2	100	0.685	0.587	13.0	13.3
6	3	1.2	120	0.505	0.433	0.0866	0.650
6	3	1.2	120	0.526	0.451	0.442	1.05
6	3	1.2	120	0.573	0.491	2.70	3.40
6	3	1.2	120	0.584	0.501	3.30	4.00
6	3	1.2	120	0.628	0.538	9.82	10.9
6	3	1.2	120	0.663	0.569	22.0	24.6

a: Loading = mol CO_2/(mol K^+ + mol PZ)

b: Loading = mole CO_2/mol K^+ + 2·mol PZ

E.2 Tabulated H_2O-MEA-PZ-CO_2 Data

MEA/m	PZ/m	T/°C	Soln	α^a	P_{CO2}/kPa
7.00	3.50	100.01	8-1	0.206	3.39
7.00	3.50	100.04	15-1	0.340	27.4
7.00	3.50	100.03	8-3	0.398	103
7.00	3.50	120.31	8-4	0.188	15.4
7.00	3.50	120.17	9-1	0.310	72.5
7.00	3.50	120.01	8-6	0.354	145.3
7.00	2.00	120.73	3-1	0.217	17.6
7.00	2.00	120.02	3-2	0.251	27.7
7.00	2.00	120.82	3-3	0.262	33.2
7.00	2.00	120.98	3-4	0.276	42.8
7.00	2.00	120.17	7-1	0.302	52.8
7.00	2.00	120.08	7-2	0.333	86.5
7.00	2.00	120.17	7-3	0.351	121
7.00	2.00	110.17	4-4	0.203	6.00
7.00	2.00	110.24	4-5	0.232	9.40
7.00	2.00	110.17	5-1	0.271	17.9
7.00	2.00	110.02	5-2	0.302	28.3
7.00	2.00	110.03	7-4	0.349	59.3
7.00	2.00	110.04	7-5	0.418	213
7.00	2.00	100.63	3-5	0.206	3.10
7.00	2.00	100.71	4-1	0.243	5.40
7.00	2.00	100.24	4-2	0.292	11.4
7.00	2.00	100.10	4-3	0.310	14.8
7.00	2.00	100.17	5-3	0.343	28.7
7.00	2.00	100.44	5-4	0.393	77.6
7.00	2.00	100.40	5-5	0.427	165

a: Loading = mol CO_2/mol MEA + 2mol PZ)

MEA/m	PZ/m	T/°C	Soln	α^a	P_{CO2}/kPa
7.00	1.00	100.00	10-1	0.203	2.50
7.00	1.00	100.03	10-2	0.305	9.64
7.00	1.00	100.05	10-3	0.405	57.46
7.00	1.00	120.04	10-4	0.224	14.64
7.00	1.00	120.04	10-5	0.326	57.01
7.00	1.00	120.04	10-6	0.366	108
5.60	1.80	100.03	11-1	0.204	2.52
5.60	1.80	100.04	12-1	0.298	11.7
5.60	1.80	100.02	12-2	0.397	65.2
5.60	1.80	120.00	12-3	0.230	19.1
5.60	1.80	120.02	12-4	0.308	60.9
5.60	1.80	120.08	12-5	0.367	164
3.50	1.75	100.02	13-1	0.206	3.63
3.50	1.75	100.05	14-1	0.297	14.6
3.50	1.75	100.05	14-2	0.394	82.0
3.50	1.75	120.08	14-3	0.207	15.3
3.50	1.75	120.00	14-4	0.298	64.5
3.50	1.75	120.08	14-5	0.339	110

a: Loading = mol CO_2/mol MEA + 2mol PZ)

APPENDIX F

Tabulated NMR Data (UT)

F.1 Tabulated 3.5 m MEA Data

Solution	T (°C)	α^a	mole/kg-H_2O $MEA/MEAH^+$	$MEACOO^{-1}$	HCO_3^{-1}/CO_3^{-2}
1-2	27	0.1738	2.9049	0.5977	0.0111
1-4	27	0.3387	2.4217	1.2095	0.0203
1-5	27	0.4046	2.2038	1.3994	0.0586
1-6	27	0.4330	2.0307	1.4022	0.0842
1-7	27	0.4574	2.0334	1.4525	0.1418
1-2	40	0.1763	3.1312	0.6564	0.0115
1-4	40	0.3556	2.3211	1.2346	0.0297
1-5	40	0.4067	2.1256	1.3798	0.0459
1-6	40	0.4353	2.1731	1.5363	0.0783
1-7	40	0.4505	2.0781	1.4580	0.1349
1-2	60	0.1728	3.1507	0.6452	0.0107
1-4	60	0.3447	2.4133	1.2039	0.0432
1-5	60	0.3982	2.2094	1.3212	0.0846
1-6	60	0.4341	2.1619	1.4245	0.1324
1-7	60	0.4466	2.2457	1.4636	0.1931

a: Loading = mole CO_2/mole MEA

F.2 Tabulated 7 m MEA Data

Solution	T (^oC)	α^a	mole/kg-H_2O $MEA/MEAH^+$	 $MEACOO^{-1}$	 HCO_3^{-1}/CO_3^{-2}
12-1	27	0.1012	6.4223	0.6859	0.0024
12-2	27	0.2622	5.2108	1.6689	0.0108
12-3	27	0.4046	4.2466	2.8087	0.0382
12-4	27	0.4542	3.8610	3.0386	0.0950
13-1	27	0.0861	6.5884	0.5717	0.0031
13-2	27	0.3179	4.6827	2.1535	0.0199
13-3	27	0.4565	4.0565	3.2187	0.1027
13-4	27	0.4630	3.7045	2.8442	0.1879
18-1	27	0.1445	6.1159	1.0250	0.0071
18-2	27	0.1714	5.7571	1.1788	0.0099
18-4	27	0.3431	4.6126	2.3917	0.0117
18-5	27	0.4181	4.2196	2.9042	0.0745
18-6	27	0.4228	4.0659	3.0689	0.1979
12-1	40	0.1112	6.3907	0.5873	0.0045
12-2	40	0.2604	5.1628	1.8179	0.0253
12-3	40	0.3800	4.7634	2.8458	0.0461
12-4	40	0.4609	4.3537	3.7264	0.1977
12-5	40	0.5171	4.2513	3.5219	0.9180
12-1	60	0.1024	6.5781	0.7451	0.0047
12-2	60	0.2616	5.9469	2.0765	0.0226
12-3	60	0.4647	4.6812	3.9251	0.0738
12-4	60	0.4613	4.6668	3.9102	0.1691
12-5	60	0.4751	4.6002	4.0205	0.2128

a: Loading = mole CO_2/mole MEA

F.3 Tabulated 11 m MEA Data

			mole/kg-H_2O		
Solution	T (^oC)	α^a	$MEA/MEAH^+$	$MEACOO^{-1}$	HCO_3^{-1}/CO_3^{-2}
1-2	27	0.1623	9.4515	1.8166	0.0121
1-4	27	0.3431	8.0036	4.0863	0.0615
1-5	27	0.4305	7.0704	5.1386	0.1173
1-6	27	0.4456	6.8476	5.2500	0.1403
1-7	27	0.4739	6.6863	5.2577	0.4027
1-2	40	0.1849	9.6704	2.1814	0.0098
1-4	40	0.3538	7.4890	4.0249	0.0492
1-5	40	0.4341	7.0857	5.2538	0.1030
1-6	40	0.4488	6.6825	5.6763	0.1702
1-7	40	0.4759	6.6720	5.7761	0.4653
1-2	60	0.1876	9.4806	2.2736	0.0205
1-4	60	0.3563	7.4275	4.0057	0.0685
1-5	60	0.4267	7.2278	5.0848	0.1690
1-6	60	0.4423	7.1470	5.2853	0.2236
1-7	60	0.4696	7.1933	5.4305	0.4981

a: Loading = mole CO_2/mole MEA

F.4 Tabulated 1 m PZ Data

			mole/kg-H_2O			
Solution	T (^oC)	α^a	PZ/PZH^{+1}	$PZCOO^{-1}/H^{+1}$	$PZ(COO^{-1})_2$	HCO_3^{-1}/CO_3^{-2}
1-1	27	0.1554	0.8682	0.1396	0.0055	0.0069
1-2	27	0.3136	0.7725	0.2273	0.0158	0.0235
1-3	27	0.4106	0.9897	0.4098	0.0495	0.0862

a: Loading = mol CO_2/2·mol PZ

F.5 Tabulated 2 m PZ Data

			mole/kg-H_2O			
Solution	T (^oC)	α^a	PZ/PZH^{+1}	$PZCOO^{-1}/H^{+1}$	$PZ(COO^{-1})_2$	HCO_3^{-1}/CO_3^{-2}
3-3	27	0.315	1.6173	0.5697	0.0389	0.0526
3-4	27	0.398	1.4365	0.6603	0.0635	0.0717
3-5	27	0.650	0.9912	0.9114	0.1701	0.0952
3-2	27	0.670	0.9021	0.9070	0.1629	0.0882
3-6	27	0.803	0.5908	1.3189	0.0211	0.1891

a: Loading = mol CO_2/2·mol PZ

F.6 Tabulated 7 m MEA + 3.6 m PZ Data

			mole/kg-H_2O					
Solution	T (C)	α^a	$MEA/MEAH^+$	$MEACOO^{-1}$	PZ/PZH^{+1}	$PZCOO^{-1}/H^{+1}$	$PZ(COO^{-1})_2$	HCO_3^{-1}/CO_3^{-2}
1-1	27	0.1534	5.5609	1.4423	2.9025	0.6796	0.0215	0.0186
1-2	27	0.2207	4.6808	2.1844	2.8085	0.8321	0.0624	0.0285
1-3	27	0.2968	4.1815	2.8848	2.3924	1.0506	0.1144	0.0541
1-4	27	0.4282	4.1270	2.8982	1.4065	1.4022	0.8043	0.1939
1-1	40	0.1654	5.3034	1.7007	3.0010	0.5786	0.0224	0.0255
1-2	40	0.2207	4.6091	2.3977	2.7550	0.7719	0.0765	0.0371
1-3	40	0.2907	3.9714	3.0404	2.4097	0.9584	0.2379	0.0573
1-4	40	0.4252	3.9147	3.1138	1.6928	1.2426	0.6792	0.2203
1-1	60	0.1524	5.4266	1.5777	3.2096	0.3797	0.0187	0.0272
1-2	60	0.2251	4.5601	2.4477	2.9675	0.5754	0.0610	0.0451
1-3	60	0.2978	3.8769	3.1372	2.6561	0.7515	0.1995	0.0855
1-4	60	0.4243	3.7368	3.2988	2.0162	1.0106	0.5914	0.2777

a: Loading = mol CO_2/mol MEA + 2·mol PZ

APPENDIX G

Tabulated Cp Data (UT)

G.1 Tabulated 3.5 m MEA (kJ/kg-K) Data

Temperature (°C)	Ldg = 0.000	Ldg = 0.097	Ldg = 0.375	Ldg = 0.583
40	3.9059	3.7996	3.6327	3.5168
45	3.9227	3.8186	3.6552	3.5421
50	3.9384	3.8347	3.6755	3.5666
55	3.9552	3.8388	3.6929	3.5809
60	3.9700	3.8619	3.7107	3.5904
65	3.9810	3.8726	3.7291	3.6012
70	3.9918	3.8742	3.7437	3.6135
75	4.0034	3.8777	3.7517	3.6235
80	4.0165	3.8870	3.7636	3.6348
85	4.0285	3.8988	3.7805	3.6504
90	4.0415	3.9203	3.7990	3.6688
95	4.0535	3.9385	3.8156	3.6882
100	4.0693	3.9572	3.8346	3.7107
105	4.0826	3.9750	3.8546	3.7336
110	4.0962	3.9933	3.8759	3.7567
115	4.1100	4.0088	3.8985	3.7788
120	4.1241	4.0255	3.9245	3.8050

LDG: Loading = mol CO_2/mol MEA

G.2 Tabulated 7 m MEA (kJ/kg-K) Data

Temperature (°C)	Ldg = 0.000	Ldg = 0.139	Ldg = 0.358	Ldg = 0.541
40	3.6968	3.4910	3.3482	3.2491
45	3.7195	3.5151	3.3675	3.2750
50	3.7416	3.5330	3.3848	3.2941
55	3.7647	3.5479	3.4011	3.3044
60	3.7862	3.5594	3.4145	3.3119
65	3.8054	3.5717	3.4288	3.3221
70	3.8219	3.5836	3.4415	3.3332
75	3.8397	3.5980	3.4553	3.3451
80	3.8566	3.6107	3.4707	3.3580
85	3.8755	3.6220	3.4916	3.3694
90	3.8916	3.6362	3.5177	3.3843
95	3.9061	3.6499	3.5270	3.4007
100	3.9207	3.6625	3.5409	3.4166
105	3.9349	3.6749	3.5534	3.4346
110	3.9485	3.6873	3.5677	3.4498
115	3.9615	3.6989	3.5840	3.4731
120	3.9739	3.7119	3.6020	3.4981

LDG: Loading = mol CO_2/mol MEA

G.3 Tabulated 2 m PZ (kJ/kg-K) Data

Temperature (°C)	Ldg = 0.000	Ldg = 0.157	Ldg = 0.269	Ldg = 0.401
40	3.8677	3.7462	3.6365	3.5811
45	3.8815	3.7610	3.6535	3.6179
50	3.8939	3.7748	3.6748	3.6527
55	3.9053	3.7869	3.6949	3.6660
60	3.9160	3.7996	3.7126	3.6688
65	3.9258	3.8118	3.7249	3.6741
70	3.9368	3.8232	3.7368	3.6861
75	3.9452	3.8317	3.7472	3.6958
80	3.9591	3.8451	3.7621	3.7107
85	3.9820	3.8655	3.7848	3.7324
90	3.9996	3.8841	3.8031	3.7516
95	4.0155	3.9026	3.8231	3.7746
100	4.0300	3.9174	3.8402	3.7916
105	4.0454	3.9307	3.8557	3.8110
110	4.0587	3.9420	3.8692	3.8311
115	4.0721	3.9542	3.8860	3.8517
120	4.0830	3.9680	3.9033	3.8736

LDG: Loading = mol CO_2/2·mol PZ

G.4 Tabulated 3.6 m PZ (kJ/kg-K) Data

Temperature (°C)	Ldg = 0.000	Ldg = 0.159	Ldg = 0.375
40	3.7194	3.4987	3.2943
45	3.7304	3.5261	3.3427
50	3.7414	3.5474	3.3826
55	3.7524	3.5666	3.4111
60	3.7634	3.5849	3.4187
65	3.7744	3.6041	3.4333
70	3.7854	3.6188	3.4478
75	3.7964	3.6336	3.4650
80	3.8074	3.6497	3.4854
85	3.8184	3.6646	3.5044
90	3.8294	3.6790	3.5226
95	3.8404	3.6919	3.5425
100	3.8514	3.7095	3.5670
105	3.8624	3.7309	3.5929
110	3.8734	3.7493	3.6211
115	3.8844	3.7646	3.6461
120	3.8954	3.7821	3.6845

LDG: Loading = mol CO_2/2·mol PZ

G.5 Tabulated 5 m K^+ + 2.5 m PZ (kJ/kg-K) Data

Temperature (°C)	Ldg = 0.389	Ldg = 0.550
40	3.0150	2.9939
45	3.0303	3.0080
50	3.0448	3.0218
55	3.0585	3.0351
60	3.0716	3.0481
65	3.0840	3.0608
70	3.0957	3.0730
75	3.1068	3.0849
80	3.1175	3.0964
85	3.1276	3.1075
90	3.1372	3.1182
95	3.1464	3.1286
100	3.1552	3.1386
105	3.1637	3.1482
110	3.1719	3.1575
115	3.1799	3.1664
120	3.1876	3.1749

LDG: Loading = mol CO_2/mol K^+ + 2·mol PZ

G.6 Tabulated 3.6 m K^+ + 3.6 m PZ (kJ/kg-K) Data

Temperature (^{o}C)	Ldg = 0.333	Ldg = 0.424	Ldg = 0.467
40	3.1516	3.1126	3.0992
45	3.1687	3.1311	3.1147
50	3.1855	3.1488	3.1298
55	3.2021	3.1656	3.1445
60	3.2183	3.1815	3.1589
65	3.2343	3.1965	3.1728
70	3.2499	3.2107	3.1863
75	3.2653	3.2239	3.1995
80	3.2805	3.2363	3.2123
85	3.2953	3.2478	3.2246
90	3.3098	3.2585	3.2366
95	3.3241	3.2682	3.2482
100	3.3381	3.2771	3.2594
105	3.3518	3.2851	3.2703
110	3.3652	3.2922	3.2807
115	3.3783	3.2984	3.2907
120	3.3911	3.3038	3.3004

LDG: Loading = mol CO_2/mol K^+ + 2·mol PZ

G.7 Tabulated 6 m K^+ + 1.2 m PZ (kJ/kg-K) Data

Temperature (^{o}C)	Ldg = 0.434	Ldg = 0.534	Ldg = 0.574
40	3.0092	3.0040	2.9941
45	3.0236	3.0161	3.0054
50	3.0374	3.0277	3.0161
55	3.0505	3.0387	3.0262
60	3.0629	3.0493	3.0358
65	3.0746	3.0593	3.0448
70	3.0857	3.0689	3.0532
75	3.0960	3.0780	3.0611
80	3.1057	3.0866	3.0684
85	3.1148	3.0946	3.0751
90	3.1231	3.1022	3.0813
95	3.1308	3.1093	3.0869
100	3.1377	3.1158	3.0919
105	3.1440	3.1219	3.0964
110	3.1497	3.1275	3.1003
115	3.1546	3.1325	3.1037
120	3.1589	3.1371	3.1064

LDG: Loading = mol CO_2/mol K^+ + 2·mol PZ

G.8 Tabulated 7 m MEA + 2 m PZ (kJ/kg-K) Data

Temperature (°C)	Ldg = 0.000	Ldg = 0.098	Ldg = 0.248	Ldg = 0.430
40	3.4272	3.3844	3.2264	3.0621
45	3.4594	3.4116	3.2496	3.0938
50	3.4836	3.4320	3.2682	3.1244
55	3.5077	3.4522	3.2871	3.1485
60	3.5268	3.4720	3.3092	3.1637
65	3.5505	3.4909	3.3291	3.1760
70	3.5641	3.5076	3.3443	3.1948
75	3.5792	3.5214	3.3571	3.2085
80	3.5942	3.5398	3.3718	3.2125
85	3.6151	3.5533	3.3841	3.2327
90	3.6239	3.5666	3.3961	3.2482
95	3.6307	3.5782	3.4096	3.2648
100	3.6491	3.5899	3.4227	3.2808
105	3.6625	3.6023	3.4371	3.2995
110	3.6770	3.6146	3.4505	3.3207
115	3.6924	3.6274	3.4682	3.3465
120	3.6998	3.6400	3.4843	3.3713

LDG: Loading = mol CO_2/mol MEA + 2·mol PZ

G.9 Tabulated 3.5 m MEA + 2 m PZ (kJ/kg-K) Data

Temperature (°C)	Ldg = 0.000	Ldg = 0.109	Ldg = 0.236	Ldg = 0.432
40	3.7742	3.6225	3.5154	3.3199
45	3.8024	3.6484	3.5353	3.3566
50	3.8233	3.6677	3.5528	3.3916
55	3.8436	3.6842	3.5713	3.4159
60	3.8616	3.7016	3.5898	3.4279
65	3.8783	3.7193	3.6075	3.4386
70	3.8944	3.7370	3.6249	3.4542
75	3.9106	3.7547	3.6415	3.4706
80	3.9283	3.7722	3.6587	3.4887
85	3.9427	3.7865	3.6731	3.5055
90	3.9566	3.8006	3.6873	3.5228
95	3.9718	3.8146	3.7016	3.5411
100	3.9881	3.8291	3.7203	3.5642
105	4.0071	3.8446	3.7399	3.5904
110	4.0258	3.8612	3.7587	3.6174
115	4.0395	3.8794	3.7760	3.6453
120	4.0578	3.8972	3.7953	3.6808

LDG: Loading = mol CO_2/mol MEA + 2·mol PZ

APPENDIX H

Tabulated Differential ΔHabs Data (NTNU)

H.1 Tabulated 2.4 m PZ Data

T (^{o}C)	a[a]	ΔHabs/kJ/mol-CO_2
40	0.034	74.602
40	0.053	74.590
40	0.069	72.786
40	0.103	78.846
40	0.140	77.654
40	0.178	70.564
40	0.223	71.423
40	0.257	66.198
40	0.284	67.170
40	0.297	64.383
40	0.335	64.171
40	0.369	58.440
40	0.383	59.575
40	0.418	50.910
40	0.434	51.397
40	0.483	46.936

a: Loading = mol CO_2/2·mol PZ

T (^{o}C)	a[a]	ΔHabs/kJ/mol-CO_2
40	0.498	42.620
80	0.041	82.194
80	0.068	75.252
80	0.085	88.922
80	0.127	82.496
80	0.157	78.398
80	0.168	82.676
80	0.214	77.922
80	0.241	70.847
80	0.263	72.400
80	0.311	78.017
80	0.338	70.305
80	0.360	69.834
80	0.421	69.435
80	0.431	66.357
80	0.469	44.256
80	0.487	46.210
120	0.049	93.099
120	0.063	102.415
120	0.098	96.216
120	0.139	94.593
120	0.147	94.264
120	0.194	92.843
120	0.195	98.922
120	0.256	103.227
120	0.257	103.900
120	0.292	100.869
120	0.306	98.033
120	0.344	91.766
120	0.358	99.508
120	0.403	99.834

a: Loading = mol CO_2/2·mol PZ

H.2 Tabulated 5 m K^+ + 2.5 m PZ Data

T (^oC)	α^a	ΔHabs/kJ/mol-CO_2
40	0.390	59.689
40	0.413	59.798
40	0.437	58.883
40	0.468	56.588
40	0.495	51.508
40	0.534	47.938
40	0.588	41.453
40	0.610	35.605
40	0.643	60.072
40	0.671	48.164
40	0.698	48.548
40	0.724	32.327
40	0.743	45.851
40	0.761	30.683
40	0.773	17.311
60	0.370	69.394
60	0.392	70.159
60	0.421	64.995
60	0.440	64.764
60	0.461	63.518
60	0.488	61.084
60	0.509	59.263
60	0.530	54.131
60	0.551	48.933
60	0.574	43.950
60	0.594	39.671
60	0.614	37.070
60	0.633	32.560
60	0.651	31.312
60	0.676	26.327

a: Loading = mol CO_2/mol K^+ + 2·mol PZ

T (^oC)	α^a	ΔHabs/kJ/mol-CO_2
80	0.399	67.647
80	0.399	68.679
80	0.433	65.378
80	0.440	69.457
80	0.458	68.115
80	0.469	68.004
80	0.414	70.246
80	0.421	72.652
80	0.435	68.635
80	0.458	69.611
80	0.462	76.748
80	0.479	69.951
80	0.487	67.920
80	0.501	64.079
80	0.510	65.291
80	0.520	53.864
80	0.533	56.250
80	0.539	50.508
80	0.555	50.167
80	0.563	46.789
80	0.571	44.416
80	0.595	30.656
120	0.399	69.219
120	0.427	76.620
120	0.456	93.104
120	0.491	86.238
120	0.518	84.506
120	0.548	77.821
120	0.558	72.759
120	0.568	74.078
120	0.573	73.204

a: Loading = mol CO_2/mol K^+ + 2·mol PZ

H.3 Tabulated 6 m K^+ + 1.2 m PZ Data

T (^oC)	α^a	ΔHabs/kJ/mol-CO_2
40	0.417	58.616
40	0.449	58.253
40	0.484	49.380
40	0.512	44.256
40	0.540	40.566
40	0.572	38.943
40	0.597	37.873
40	0.622	36.872
40	0.646	57.394
40	0.670	57.721
40	0.699	50.189
40	0.751	40.101
40	0.774	43.089
40	0.797	42.464
40	0.819	41.898
40	0.844	36.363
40	0.871	21.266
60	0.420	65.322
60	0.424	64.655
60	0.455	59.539
60	0.479	58.055
60	0.485	55.412
60	0.508	55.098
60	0.515	53.702
60	0.537	54.315
60	0.545	50.455
60	0.561	53.992
60	0.574	49.651
60	0.601	54.833
60	0.602	47.040

a: Loading = mol CO_2/mol K^+ + 2·mol PZ

T (^{o}C)	α[a]	ΔHabs/kJ/mol-CO_2
60	0.626	52.458
60	0.633	48.229
60	0.652	48.338
60	0.664	51.385
60	0.677	42.676
60	0.694	47.635
60	0.702	41.551
60	0.720	72.285
60	0.726	36.024
60	0.744	68.954
60	0.749	66.496
60	0.761	68.186
60	0.789	48.961
60	0.818	38.352
120	0.430	68.906
120	0.433	73.901
120	0.464	68.248
120	0.471	69.082
120	0.497	75.870
120	0.506	71.645
120	0.531	67.034
120	0.549	67.395
120	0.563	78.166
120	0.579	64.307
120	0.594	69.546
120	0.616	65.488
120	0.624	66.958
120	0.644	67.627
120	0.663	67.860

a: Loading = mol CO_2/mol K^+ + 2·mol PZ

H.4 Tabulated 7 m MEA + 2 m PZ Data

T (^{o}C)	α^a	ΔHabs/kJ/mol-CO_2
40	0.028	74.041
40	0.055	72.166
40	0.080	72.354
40	0.104	71.308
40	0.136	73.138
40	0.165	71.561
40	0.191	72.318
40	0.235	75.202
40	0.263	70.034
40	0.295	72.130
40	0.324	69.533
40	0.348	70.680
40	0.375	72.553
40	0.402	70.732
40	0.430	67.214
40	0.460	69.969
40	0.488	62.641
40	0.516	57.858
40	0.542	51.269
40	0.569	40.592
40	0.613	35.185
80	0.021	83.557
80	0.041	83.462
80	0.065	82.162
80	0.094	83.747
80	0.115	80.066
80	0.141	85.338
80	0.162	84.318
80	0.190	83.459

a: Loading = mol CO_2/mol MEA + 2·mol PZ

T (^oC)	α^a	ΔHabs/kJ/mol-CO_2
80	0.223	83.428
80	0.263	84.686
80	0.292	83.875
80	0.311	82.071
80	0.336	83.898
80	0.370	82.445
80	0.394	80.476
80	0.416	79.305
80	0.446	77.176
80	0.477	74.535
80	0.496	69.762
80	0.515	61.126
80	0.553	45.470
120	0.042	108.570
120	0.075	93.066
120	0.107	97.486
120	0.138	101.934
120	0.170	98.643
120	0.201	96.051
120	0.235	97.920
120	0.269	98.519
120	0.302	100.436
120	0.334	99.665
120	0.361	93.591
120	0.384	84.500
120	0.400	79.338

a: Loading = mol CO_2/mol MEA + 2·mol PZ

H.5 Tabulate 7 m MEA + 3.5 m PZ Data

T (^oC)	α^a	ΔHabs/kJ/mol-CO_2
40	0.025	77.443
40	0.053	79.023
40	0.080	79.677
40	0.106	78.533
40	0.133	79.342
40	0.162	78.578
40	0.193	75.901
40	0.222	75.659
40	0.257	74.595
40	0.286	76.519
40	0.315	78.510
40	0.343	74.399
40	0.371	75.352
40	0.400	72.798
40	0.428	70.083
40	0.457	55.288
40	0.484	63.117
40	0.509	54.048
40	0.536	53.217
80	0.030	85.503
80	0.059	77.988
80	0.088	82.154
80	0.117	82.719
80	0.144	83.163
80	0.173	79.095
80	0.203	85.075
80	0.238	81.674
80	0.269	82.393
80	0.298	81.512

a: Loading = mol CO_2/mol MEA + 2·mol PZ

T (^{o}C)	α^{a}	ΔHabs/kJ/mol-CO_2
80	0.328	87.006
80	0.359	84.531
80	0.391	83.482
80	0.427	76.715
80	0.457	64.504
80	0.480	62.429
120	0.028	122.685
120	0.056	102.449
120	0.084	103.564
120	0.109	109.509
120	0.138	91.248
120	0.166	105.609
120	0.194	99.480
120	0.224	101.375
120	0.258	98.708
120	0.286	96.581
120	0.317	92.718
120	0.344	91.964
120	0.372	93.167

a: Loading = mol CO_2/mol MEA + 2·mol PZ

APPENDIX I

Tabulated SLE Data (UT)

I.1 Tabulated H_2O-PZ Dissolution Data

Solution	PZ wt frac	Date	Temperature (°C) Solidus	Temperature (°C) Liquidius
0	0.0000	4/24/2007	-0.32	4.14
0.5A	0.0425	4/24/2007	-0.47	5.51
0.5B	0.0425	4/24/2007	-0.53	5.64
1A	0.0789	4/10/2007	-0.61	7.60
1B	0.0789	4/10/2007	-0.66	7.68
2A	0.1466	4/10/2007	-0.73	24.95
2B	0.1466	4/10/2007	-0.86	24.75
3A	0.2046	4/10/2007	-1.02	32.30
3B	0.2046	4/10/2007	-1.04	32.10
4A	0.2534	4/10/2007	-0.95	38.07
4B	0.2534	4/10/2007	-0.96	37.54
5A	0.3002	4/10/2007	-0.98	41.35
5B	0.3002	4/10/2007	-0.82	42.10
6A	0.3380	4/24/2007	-0.97	44.57
6B	0.3380	4/24/2007	-0.21	44.73

Solution	PZ wt frac	Date	Temperature (°C)	
			Solidus	Liquidius
7A	0.3711	4/24/2007	-0.91	46.76
7B	0.3711	4/24/2007	-1.16	47.38
8A	0.4055	4/24/2007	-1.29	48.82
8B	0.4055	4/24/2007	-1.42	48.22
9A	0.4324	4/24/2007	-1.65	49.84
9B	0.4324	4/24/2007	-2.54	50.14
10A	0.4590	4/10/2007	32.84	50.94
10B	0.4590	4/10/2007	32.42	50.69
11A	0.4821	4/26/2007	31.82	48.35
11B	0.4821	4/26/2007	31.85	47.89
12A	0.5026	4/26/2007	31.14	45.44
12B	0.5026	4/26/2007	30.92	44.55
13A	0.5243	4/26/2007	31.19	42.99
13B	0.5243	4/26/2007	30.99	42.81
14A	0.5366	4/26/2007	31.08	41.34
14B	0.5366	4/26/2007	31.01	40.98
15A	0.5589	4/12/2007	30.88	39.54
15B	0.5589	4/12/2007	31.18	40.19
17.5A	0.5952	4/26/2007	31.03	37.97
17.5B	0.5952	4/26/2007	30.98	37.72
20A	0.6250	4/12/2007	31.04	39.21
20B	0.6250	4/12/2007	30.93	38.90
25A	0.6805	4/12/2007	30.77	46.77
25B	0.6805	4/12/2007	30.85	45.98
30A	0.7163	4/12/2007	30.84	53.56
30B	0.7163	4/12/2007	30.77	53.73
35A	0.7464	4/12/2007	30.92	63.30
35B	0.7464	4/12/2007	30.89	63.73
40A	0.7713	4/12/2007	30.58	70.65
40B	0.7713	4/12/2007	29.53	69.73

I.2 Tabulated H_2O-K_2CO_3-PZ-CO_2 Dissolution Data

K^+/m	PZ/m	α^a	T (^oC)	Salt Phase
5	2.5	0.542	28.75	$K_2PZ(COO)_2$
5	2.5	0.550	31.25	$K_2PZ(COO)_2$
5	3.6	0.33	38.75	$KHCO_3$
5	3.6	0.341	38.75	$KHCO_3$
5	3.6	0.349	41.25	$KHCO_3$
5	3.6	0.360	51.25	$KHCO_3$
5	3.6	0.361	51.25	$KHCO_3$
5	3.6	0.507	36.25	$K_2PZ(COO)_2$
5	3.6	0.525	43.75	$K_2PZ(COO)_2$
6	1.2	0.591	31.25	$K_2PZ(COO)_2$

a: Loading = mol CO_2/mol K + 2·mol PZ)

APPENDIX J Aspen Plus™ Input File

J.1 Overall Input File for the H_2O-K_2CO_3-MEA-PZ-CO_2 System

```
;IN-UNITS SI MASS-FLOW='kg/hr' MOLE-FLOW='mol/hr' PRESSURE=kPa  &
        TEMPERATURE=C MASS-HEAT-CA='kJ/kg-K' PDROP='N/sqm'

DEF-STREAMS CONVEN ALL

SIM-OPTIONS
    IN-UNITS MET VOLUME-FLOW='cum/hr' ENTHALPY-FLO='Gcal/hr'  &
        HEAT-TRANS-C='kcal/hr-sqm-K' PRESSURE=bar TEMPERATURE=C  &
        VOLUME=cum DELTA-T=C HEAD=meter MOLE-DENSITY='kmol/cum'  &
        MASS-DENSITY='kg/cum' MOLE-ENTHALP='kcal/mol'  &
        MASS-ENTHALP='kcal/kg' HEAT=Gcal MOLE-CONC='mol/l'  &
        PDROP=bar
    SIM-OPTIONS GAMUS-BASIS=AQUEOUS

RUN-CONTROL MAX-TIME=10800.

DESCRIPTION "
    Electrolytes Simulation with Metric Units :
    C, bar, kg/hr, kmol/hr, Gcal/hr, cum/hr.

    Property Method: ELECNRTL

    Flow basis for input: Mass
```

```
    Stream report composition: Mass flow
    "

DATABANKS ASPENPCD  / AQUEOUS  / SOLIDS  / INORGANIC  /  &
        PURE20

PROP-SOURCES ASPENPCD  / AQUEOUS  / SOLIDS  / INORGANIC  /  &
        PURE20

COMPONENTS
    H2O H2O /
    CO2 CO2 /
    MEA C2H7NO /
    MEA+ C2H8NO+ /
    MEACOO- C3H6NO3- /
    HCO3- HCO3- /
    CO3-- CO3-2 /
    H+ H+ /
    OH- OH- /
    "MEA/H" C2H8NO+ /
    "CO3/HCO3" CO3-2 /
    K2CO3 K2CO3 /
    KHCO3 KHCO3 /
    K+ K+ /
    "K2CO3(S)" K2CO3 /
    "KHCO3(S)" KHCO3 /
    PZ C4H10N2 /
    PZCOO-2 C6H8N2O4 /
    PZCOO- C5H9N2O2 /
    PZH+ C4H11N2 /
    PZH+2 C4H12N2 /
    HPZCOO C5H10N2O /
    "PZ/H" /
    "H/PZCOO" /
    "PZ/H2" /
    PZ6H2O C4H10N2

FORMULA PZCOO-2 C6H8N2O4 / PZCOO- C5H9N2O2 / PZH+ C4H11N2 /  &
        PZH+2 C4H12N2 / HPZCOO C5H10N2O

HENRY-COMPS HC-1 CO2

CHEMISTRY GLOBAL
    PARAM
    DISS K2CO3 K+ 2. / CO3-- 1.
    DISS KHCO3 K+ 1. / HCO3- 1.
    STOIC 1 H2O -1. / H+ 1. / OH- 1.
    STOIC 2 CO2 -1. / H2O -1. / H+ 1. / HCO3- 1.
    STOIC 3 HCO3- -1. / H+ 1. / CO3-- 1.
    STOIC 4 MEA+ -1. / MEA 1. / H+ 1.
    STOIC 5 MEACOO- -1. / H2O -1. / MEA 1. / HCO3- 1.
    STOIC 6 PZH+ -1. / PZ 1. / H+ 1.
    STOIC 8 PZ -1. / HCO3- -1. / PZCOO- 1. / H2O 1.
```

```
    STOIC 9 PZCOO- -1. / HCO3- -1. / PZCOO-2 1. / H2O 1.
    STOIC 10 HPZCOO -1. / PZCOO- 1. / H+ 1.
    SALT "K2CO3(S)" K+ 2. / CO3-- 1. / H2O 1.5
    SALT "KHCO3(S)" K+ 1. / HCO3- 1.
    SALT PZ6H2O PZ 1. / H2O 6.
    K-SALT "K2CO3(S)" A=-70.329741 B=1361.48182 C=13.508799  &
        D=-0.0581808
    K-SALT "KHCO3(S)" A=-1420.7517 B=40190.9436 C=240.615458  &
        D=-0.3144982
    K-SALT PZ6H2O A=-291.03967 B=0. C=56.5058062 D=-0.1275574

FLOWSHEET
    BLOCK B1 IN=1 OUT=2 3

PROPERTIES ELECNRTL HENRY-COMPS=HC-1 CHEMISTRY=GLOBAL

STRUCTURES
    STRUCTURES PZCOO- C1 N2 S / N2 C3 S / N2 C4 S / C3  &
        C5 S / C5 N6 S / C1 C7 S / C7 N6 S / C4 O8  &
        D / C4 O9 S

PROP-DATA
    PROP-LIST ATOMNO / NOATOM
    PVAL PZCOO- 6 8 7 1 / 5. 2. 2. 9.

STRUCTURES
    STRUCTURES PZCOO-2 C1 N2 S / N2 C3 S / C3 C4 S / C4  &
        N5 S / C1 C6 S / C6 N5 S / N5 C7 S / C7 O8  &
        D / C7 O9 S / N2 C10 S / C10 O11 D / C10 O12  &
        S

PROP-DATA
    PROP-LIST ATOMNO / NOATOM
    PVAL PZCOO-2 6 8 7 1 / 6. 4. 2. 8.

STRUCTURES
    STRUCTURES PZH+ C1 N2 S / N2 C3 S / C3 C4 S / C4  &
        N5 S / C1 C6 S / C6 N5 S

PROP-DATA
    PROP-LIST ATOMNO / NOATOM
    PVAL PZH+ 6 7 1 / 4. 2. 11.

PROP-DATA MDH
    IN-UNITS SI MASS-FLOW='kg/hr' MOLE-FLOW='mol/hr' PRESSURE=kPa  &
        TEMPERATURE=C MASS-HEAT-CA='kJ/kg-K' PDROP='N/sqm'
    PROP-LIST DGAQFM / DHAQFM
    PVAL MEA+ -171023632 / -336961728.8
    PVAL MEACOO- -492922520 / -707209080

PROP-DATA REVIEW-1
    IN-UNITS MET VOLUME-FLOW='cum/hr' ENTHALPY-FLO='Gcal/hr'  &
        HEAT-TRANS-C='kcal/hr-sqm-K' PRESSURE=bar TEMPERATURE=C  &
```

```
        VOLUME=cum DELTA-T=C HEAD=meter MOLE-DENSITY='kmol/cum'  &
        MASS-DENSITY='kg/cum' MOLE-ENTHALP='kcal/mol'  &
        MASS-ENTHALP='kcal/kg' HEAT=Gcal MOLE-CONC='mol/l'  &
        PDROP=bar
    PROP-LIST API / DGFORM / DGSFRM / DHFORM / DHSFRM /  &
        DHVLB / FREEZEPT / HCOM / MUP / MW / OMEGA / PC /  &
        RKTZRA / SG / TB / TC / VB / VC / VLSTD / ZC
    PVAL H2O 10.0 / -54.6343 / -56.5492 / -57.7949 /  &
        -69.9627 / 9.744507 / 0.0 / 0.0 / 1.84972 /  &
        18.01528 / 0.344861 / 220.64 / 0.243172 / 1.0 /  &
        100.0 / 373.946 / 18.8311 / 55.9472 / 18.0691 /  &
        0.229
    PROP-LIST API / DGFORM / DHFORM / DHVLB / FREEZEPT /  &
        HCOM / MUP / MW / OMEGA / PC / RKTZRA / SG / TB / &
        TC / VB / VC / VLSTD / ZC
    PVAL MEA 7.5 / -24.6893 / -49.4025 / 11.88812 / 10.5 /  &
        -325.765 / 0.77646 / 61.08308 / 0.446737 / 71.24 /  &
        0.24764 / 1.0179 / 170 / 405.05 / 68.6673 / 225 /  &
        60.3415 / 0.284
    PROP-LIST API / DGFORM / DHFORM / DHVLB / FREEZEPT /  &
        HCOM / MUP / MW / OMEGA / PC / SG / TB / TC /  &
        VB / VC / VLSTD / ZC
    PVAL PZ 80.4899 / 40.6310 / 3.91969 / 9.999355 / 106 /  &
        -654.398 / 1.47000 / 86.1356 / 0.41376 / 55.3 /  &
        0.667485 / 146 / 364.85 / 134.772 / 310 / 129.371 /  &
        0.323
    PROP-LIST DHFORM / FREEZEPT / MW / PC / VC / VLSTD /  &
        ZC / RGYR
    PVAL CO2 -94.05110000 / -56.57 / 44.0095 / 73.83 / 94 /  &
        61.6782 / 0.274 / 1.04000E-10
    PROP-LIST FREEZEPT / MW
    PVAL PZ6H2O 44.0000000 / 194.22728
    PROP-LIST MW
    PVAL "K2CO3(S)" 165.22872

PROP-DATA REVIEW-1
    IN-UNITS MET VOLUME-FLOW='cum/hr' ENTHALPY-FLO='Gcal/hr'  &
        HEAT-TRANS-C='kcal/hr-sqm-K' PRESSURE=bar TEMPERATURE=C  &
        VOLUME=cum DELTA-T=C HEAD=meter MOLE-DENSITY='kmol/cum'  &
        MASS-DENSITY='kg/cum' MOLE-ENTHALP='J/kmol'  &
        MASS-ENTHALP='kcal/kg' MOLE-ENTROPY='J/kmol-K' HEAT=Gcal  &
        MOLE-CONC='mol/l' PDROP=bar
    PROP-LIST DGAQFM / DHAQFM
    PVAL HCO3- -587370182.1 / -690767961
    PVAL CO3-- -538355662.9 / -677140000
    PVAL "MEA/H" -171023632 / -336961728.8
    PVAL "CO3/HCO3" -538355662.9 / -677140000

PROP-DATA USRDEF
    IN-UNITS SI MASS-FLOW='kg/hr' MOLE-FLOW='mol/hr' PRESSURE=kPa  &
        TEMPERATURE=C MASS-HEAT-CA='kJ/kg-K' PDROP='N/sqm'
    PROP-LIST MW / DGAQFM / DHAQFM / CHARGE
    PVAL PZCOO-2 172.14 / -576616170 / -860671110 / -2
```

```
    PVAL PZCOO- 129.13771 / -216402690 / -482028620 / -1
    PVAL PZH+ 87.14299 / 102408575 / -91542774.38 / 1
    PVAL PZH+2 88.1504 / 91897612.25 / -122665214.9 / 2
    PVAL HPZCOO 130.145 / -273454210 / -522383060 / 1E-5
    PVAL "PZ/H" 87.14299 / 102408575 / -91542774.38 / 1
    PVAL "H/PZCOO" 129.13771 / -199884924.9 / -451987161.7 /  &
        -1
    PVAL "PZ/H2" 87.14299 / 102408575 / -91542774.38 / 1

PROP-DATA CPAQ0-1
    IN-UNITS SI MASS-FLOW='kg/hr' MOLE-FLOW='mol/hr' PRESSURE=kPa  &
        MASS-HEAT-CA='kJ/kg-K' PDROP='N/sqm'
    PROP-LIST CPAQ0
    PVAL CO3-- 1334017.129 -5564.838795 5.192267274  &
        -118575111.1 0.0 0.0 0.0 2000.000000
    PVAL HCO3- 211386.984 -881.7986241 0.874689511 -18789290.32  &
        0.0 0.0 0.0 2000.000000
    PVAL MEA+ -1700442.83 7093.368695 -8.487374579 151145133.9  &
        0.0 0.0 0.0 2000.000
    PVAL MEACOO- -2408071.1 17268.3153 -26.0389963 0.0 0.0  &
        0.0 0.0 2000.000
    PVAL "MEA/H" -1700442.83 7093.368695 -8.487374579  &
        151145133.9 0.0 0.0 0.0 2000.000
    PVAL PZCOO-2 -881653.81 -18936.0286 80.1449288 0.0 0.0  &
        0.0 0.0 2000.000000
    PVAL PZCOO- -6853708.7 23208.6029 4.90072448 0.0 0.0 0.0  &
        0.0 2000.000000
    PVAL PZH+ 603662.8765 -2518.16458 4.16532815 -53657026.67  &
        0.0 0.0 0.0 2000.000000
    PVAL PZH+2 1228464.475 -5124.516124 7.090651102  &
        -109192984.4 0.0 0.0 0.0 2000.000000
    PVAL HPZCOO 4189849.52 -13613.5878 5.18822841 0.0 0.0 0.0  &
        0.0 2000.000000
    PVAL "PZ/H" 603662.8765 -2518.16458 4.16532815 -53657026.67  &
        0.0 0.0 0.0 2000.000000
    PVAL "H/PZCOO" 196731.375 -1647.062505 3.392069397 0.0 0.0  &
        0.0 0.0 2000.000000
    PVAL "PZ/H2" 603662.8765 -2518.16458 4.16532815  &
        -53657026.67 0.0 0.0 0.0 2000.000000

PROP-DATA CPDIEC-1
    IN-UNITS MET VOLUME-FLOW='cum/hr' ENTHALPY-FLO='Gcal/hr'  &
        HEAT-TRANS-C='kcal/hr-sqm-K' PRESSURE=bar TEMPERATURE=C  &
        VOLUME=cum DELTA-T=C HEAD=meter MOLE-DENSITY='kmol/cum'  &
        MASS-DENSITY='kg/cum' MOLE-ENTHALP='kcal/mol'  &
        MASS-ENTHALP='kcal/kg' HEAT=Gcal MOLE-CONC='mol/l'  &
        PDROP=bar
    PROP-LIST CPDIEC
    PVAL H2O 78.24662286 32730.85746 298.15
    PVAL MEA 31.06961991 15128.19841 298.15
    PVAL PZ 4.253042941 1532.198738 298.15

PROP-DATA CPSPO1-1
```

```
    IN-UNITS SI MASS-FLOW='kg/hr' MOLE-FLOW='mol/hr' PRESSURE=kPa  &
        TEMPERATURE=C MASS-HEAT-CA='kJ/kg-K' PDROP='N/sqm'
    PROP-LIST CPSPO1
    PVAL K2CO3 139225.2346 79.85942112 0.00509505 1159199.446  &
        -3154750.005 -340154.0227 6.85 900.85
    PVAL "K2CO3(S)" 139225.2346 79.85942112 0.00509505  &
        1159199.446 -3154750.005 -340154.0227 6.85 900.85
    PVAL KHCO3 139225.2346 79.85942112 0.00509505 1159199.446  &
        -3154750.005 -340154.0227 6.85 900.85
    PVAL "KHCO3(S)" 139225.2346 79.85942112 0.00509505  &
        1159199.446 -3154750.005 -340154.0227 6.85 900.85

PROP-DATA DHVLDP-1
    IN-UNITS MET VOLUME-FLOW='cum/hr' ENTHALPY-FLO='Gcal/hr'  &
        HEAT-TRANS-C='kcal/hr-sqm-K' PRESSURE=bar TEMPERATURE=C  &
        VOLUME=cum DELTA-T=C HEAD=meter MOLE-DENSITY='kmol/cum'  &
        MASS-DENSITY='kg/cum' MOLE-ENTHALP='J/kmol'  &
        MASS-ENTHALP='kcal/kg' HEAT=Gcal MOLE-CONC='mol/l'  &
        PDROP=bar
    PROP-LIST DHVLDP
    PVAL PZ 64355423.1 0.38570286 0.02568786 0.0 0.0 106.00  &
        364.85
    PVAL PZ6H2O 64355423.1 0.38570286 0.02568786 0.0 0.0  &
        106.00 364.85

PROP-DATA DHVLWT-1
    IN-UNITS MET VOLUME-FLOW='cum/hr' ENTHALPY-FLO='Gcal/hr'  &
        HEAT-TRANS-C='kcal/hr-sqm-K' PRESSURE=bar TEMPERATURE=C  &
        VOLUME=cum DELTA-T=C HEAD=meter MOLE-DENSITY='kmol/cum'  &
        MASS-DENSITY='kg/cum' MOLE-ENTHALP='J/kmol'  &
        MASS-ENTHALP='kcal/kg' HEAT=Gcal MOLE-CONC='mol/l'  &
        PDROP=bar
    PROP-LIST DHVLWT
    PVAL H2O 40655000 100.00 0.26623503 0.09110321 0.01
    PVAL MEA 54835800 126.67 0.4041153 0.11011257 -27.37

PROP-DATA PLXANT-1
    IN-UNITS SI MASS-FLOW='kg/hr' MOLE-FLOW='mol/hr' PRESSURE=kPa  &
        TEMPERATURE=C MASS-HEAT-CA='kJ/kg-K' PDROP='N/sqm'
    PROP-LIST PLXANT
    PVAL PZCOO-2 -1.000000E+20 0.0 0.0 0.0 0.0 0.0 0.0  &
        -273.1500000 1726.850000
    PVAL PZCOO- -1.000000E+20 0.0 0.0 0.0 0.0 0.0 0.0  &
        -273.1500000 1726.850000
    PVAL PZH+ -1.000000E+20 0.0 0.0 0.0 0.0 0.0 0.0  &
        -273.1500000 1726.850000
    PVAL PZH+2 -1.000000E+20 0.0 0.0 0.0 0.0 0.0 0.0  &
        -273.1500000 1726.850000
    PVAL HPZCOO -1.000000E+20 0.0 0.0 0.0 0.0 0.0 0.0  &
        -273.1500000 1726.850000
    PVAL "PZ/H" -1.000000E+20 0.0 0.0 0.0 0.0 0.0 0.0  &
        -273.1500000 1726.850000
    PVAL "H/PZCOO" -1.000000E+20 0.0 0.0 0.0 0.0 0.0 0.0  &
```

```
      -273.1500000 1726.850000
   PVAL "PZ/H2" -1.000000E+20 0.0 0.0 0.0 0.0 0.0 0.0  &
      -273.1500000 1726.850000

PROP-DATA HENRY-1
   IN-UNITS MET VOLUME-FLOW='cum/hr' ENTHALPY-FLO='Gcal/hr'  &
      HEAT-TRANS-C='kcal/hr-sqm-K' PRESSURE=Pa TEMPERATURE=K  &
      VOLUME=cum DELTA-T=C HEAD=meter MOLE-DENSITY='kmol/cum'  &
      MASS-DENSITY='kg/cum' MOLE-ENTHALP='kcal/mol'  &
      MASS-ENTHALP='kcal/kg' HEAT=Gcal MOLE-CONC='mol/l'  &
      PDROP=bar
   PROP-LIST HENRY
   BPVAL CO2 H2O 170.7126000 -8477.711000 -21.95743000  &
      5.78074800E-3 273.0000000 500.0000000 0.0
   BPVAL CO2 MEA 89.452 -2934.6 -11.592 0.01644 273.0000000  &
      500.0000000 0.0

PROP-DATA NRTL-1
   IN-UNITS MET VOLUME-FLOW='cum/hr' ENTHALPY-FLO='Gcal/hr'  &
      HEAT-TRANS-C='kcal/hr-sqm-K' PRESSURE=bar TEMPERATURE=C  &
      VOLUME=cum DELTA-T=C HEAD=meter MOLE-DENSITY='kmol/cum'  &
      MASS-DENSITY='kg/cum' MOLE-ENTHALP='kcal/mol'  &
      MASS-ENTHALP='kcal/kg' HEAT=Gcal MOLE-CONC='mol/l'  &
      PDROP=bar
   PROP-LIST NRTL
   BPVAL H2O MEA -123.323712 2575.16998 0.2 0.0 22.061396  &
      -0.029745916 0.0 1000
   BPVAL MEA H2O -1.71338728 -214.123176 0.2 0.0 0.0 0.0  &
      0.0 1000
   BPVAL H2O CO2 10.06400000 -3268.135000 .2000000000 0.0 0.0  &
      0.0 0.0 200.0000000
   BPVAL CO2 H2O 10.06400000 -3268.135000 .2000000000 0.0 0.0  &
      0.0 0.0 200.0000000
   BPVAL H2O PZ -4.771449207 0 0.2 0 0 0.010652211 0 1000
   BPVAL PZ H2O 0.378443544 0 0.2 0 0 0.024904765 0 1000
   BPVAL MEA PZ 24.12346614 0 0.2 0 0.0 -0.138066091 0  &
      1000
   BPVAL PZ MEA 1.64418205 0 0.2 0 0.0 0 0 1000

PROP-DATA VLCLK-1
   IN-UNITS MET VOLUME-FLOW='cum/hr' ENTHALPY-FLO='Gcal/hr'  &
      HEAT-TRANS-C='kcal/hr-sqm-K' PRESSURE=bar TEMPERATURE=C  &
      VOLUME=cum DELTA-T=C HEAD=meter MOLE-DENSITY='kmol/cum'  &
      MASS-DENSITY='kg/cum' MOLE-ENTHALP='kcal/mol'  &
      MASS-ENTHALP='kcal/kg' HEAT=Gcal MOLE-CONC='mol/l'  &
      PDROP=bar
   PROP-LIST VLCLK
   BPVAL K+ HCO3- 35.23311000 21.81205000
   BPVAL K+ CO3-- 19.73097000 74.55601000
   BPVAL K+ OH- 1.373720000 52.13633000
   BPVAL MEA+ OH- -390.9954000 1000.000000
   BPVAL "MEA/H" OH- -390.9954000 1000.000000
   BPVAL K+ "CO3/HCO3" 19.73097000 74.55601000
```

```
PROP-DATA GMELCC-1
    IN-UNITS MET VOLUME-FLOW='cum/hr' ENTHALPY-FLO='Gcal/hr'  &
        HEAT-TRANS-C='kcal/hr-sqm-K' PRESSURE=bar TEMPERATURE=C  &
        VOLUME=cum DELTA-T=C HEAD=meter MOLE-DENSITY='kmol/cum'  &
        MASS-DENSITY='kg/cum' MOLE-ENTHALP='kcal/mol'  &
        MASS-ENTHALP='kcal/kg' HEAT=Gcal MOLE-CONC='mol/l'  &
        PDROP=bar
    PROP-LIST GMELCC
    PPVAL H2O ( K+ HCO3- ) 11.11228480
    PPVAL ( K+ HCO3- ) H2O -4.94142428
    PPVAL H2O ( K+ CO3-- ) 10.44069660
    PPVAL ( K+ CO3-- ) H2O -4.41820292
    PPVAL H2O ( K+ OH- ) 7.84067300
    PPVAL ( K+ OH- ) H2O -4.25869600
    PPVAL H2O ( H+ HCO3- ) 8.04500000
    PPVAL ( H+ HCO3- ) H2O -4.07200000
    PPVAL H2O ( H+ CO3-- ) 8.04500000
    PPVAL ( H+ CO3-- ) H2O -4.07200000
    PPVAL H2O ( H+ OH- ) 8.04500000
    PPVAL ( H+ OH- ) H2O -4.07200000
    PPVAL ( K+ CO3-- ) ( K+ HCO3- ) 11.29371830
    PPVAL ( K+ HCO3- ) ( K+ CO3-- ) 0.49023478
    PPVAL H2O ( MEA+ HCO3- ) 12.77005390
    PPVAL ( MEA+ HCO3- ) H2O -3.80956870
    PPVAL CO2 ( MEA+ HCO3- ) 49.15747970
    PPVAL ( MEA+ HCO3- ) CO2 -5.89256106
    PPVAL CO2 ( MEA+ CO3-- ) 15.00000000
    PPVAL ( MEA+ CO3-- ) CO2 -8.00000000
    PPVAL CO2 ( MEA+ OH- ) 15.00000000
    PPVAL ( MEA+ OH- ) CO2 -8.00000000
    PPVAL MEA ( MEA+ HCO3- ) 1.78726059
    PPVAL ( MEA+ HCO3- ) MEA -30.84763770
    PPVAL MEA ( MEA+ CO3-- ) 15.00000000
    PPVAL ( MEA+ CO3-- ) MEA -8.00000000
    PPVAL MEA ( MEA+ OH- ) 15.00000000
    PPVAL ( MEA+ OH- ) MEA -8.00000000
    PPVAL H2O ( MEA+ MEACOO- ) 19.03188830
    PPVAL ( MEA+ MEACOO- ) H2O -7.38531897
    PPVAL CO2 ( MEA+ MEACOO- ) 15.00000000
    PPVAL ( MEA+ MEACOO- ) CO2 -8.00000000
    PPVAL MEA ( MEA+ MEACOO- ) 16.87100390
    PPVAL ( MEA+ MEACOO- ) MEA -13.62627530
    PPVAL H2O ( PZH+ PZCOO- ) -1.04735906
    PPVAL ( PZH+ PZCOO- ) H2O -103.954042
    PPVAL H2O ( PZH+ HCO3- ) 4.43651036
    PPVAL ( PZH+ HCO3- ) H2O -0.7872577
    PPVAL PZ ( PZH+ HCO3- ) 7.03927214
    PPVAL ( PZH+ HCO3- ) PZ -5.75420279
    PPVAL PZ ( PZH+ PZCOO- ) 6.91492088
    PPVAL ( PZH+ PZCOO- ) PZ 1.72226212
    PPVAL CO2 ( PZH+ HCO3- ) 10.4764239
    PPVAL ( PZH+ HCO3- ) CO2 11.8017499
```

```
    PPVAL H2O ( MEA+ PZCOO- ) 8.415954480
    PPVAL ( MEA+ PZCOO- ) H2O -2.775938700
    PPVAL H2O ( PZH+ MEACOO- ) 9.120664520
    PPVAL ( PZH+ MEACOO- ) H2O -3.451708430
    PPVAL H2O ( MEA+ PZCOO-2 ) 8.128572400
    PPVAL ( MEA+ PZCOO-2 ) H2O -4.138965770
    PPVAL MEA ( PZH+ HCO3- ) 27.963687800
    PPVAL ( PZH+ HCO3- ) MEA 7.439322480
    PPVAL MEA ( PZH+ MEACOO- ) 79.735467500
    PPVAL ( PZH+ MEACOO- ) MEA -2.617294680
    PPVAL PZ ( MEA+ HCO3- ) -0.387925294
    PPVAL ( MEA+ HCO3- ) PZ -11.373957500
    PPVAL PZ ( MEA+ PZCOO- ) -3.640482320
    PPVAL ( MEA+ PZCOO- ) PZ -10.217645500
    PPVAL H2O ( K+ MEACOO- ) -3234.36057
    PPVAL ( K+ MEACOO- ) H2O -2468.65674

PROP-DATA GMELCD-1
    IN-UNITS MET VOLUME-FLOW='cum/hr' ENTHALPY-FLO='Gcal/hr'  &
        HEAT-TRANS-C='kcal/hr-sqm-K' PRESSURE=bar TEMPERATURE=C  &
        VOLUME=cum DELTA-T=C HEAD=meter MOLE-DENSITY='kmol/cum'  &
        MASS-DENSITY='kg/cum' MOLE-ENTHALP='kcal/mol'  &
        MASS-ENTHALP='kcal/kg' HEAT=Gcal MOLE-CONC='mol/l'  &
        PDROP=bar
    PROP-LIST GMELCD
    PPVAL H2O ( K+ HCO3- ) 0.0
    PPVAL ( K+ HCO3- ) H2O 0.0
    PPVAL H2O ( K+ CO3-- ) -364.55635300
    PPVAL ( K+ CO3-- ) H2O -54.24351940
    PPVAL H2O ( K+ OH- ) 773.36010000
    PPVAL ( K+ OH- ) H2O -305.65090000
    PPVAL ( K+ CO3-- ) ( K+ HCO3- ) -2907.57314000
    PPVAL ( K+ HCO3- ) ( K+ CO3-- ) -725.82256800
    PPVAL H2O ( MEA+ HCO3- ) 156.09046700
    PPVAL ( MEA+ HCO3- ) H2O -214.82514800
    PPVAL CO2 ( MEA+ HCO3- ) 430.10816000
    PPVAL ( MEA+ HCO3- ) CO2 14444.83540000
    PPVAL CO2 ( MEA+ CO3-- ) 0.0
    PPVAL ( MEA+ CO3-- ) CO2 0.0
    PPVAL CO2 ( MEA+ OH- ) 0.0
    PPVAL ( MEA+ OH- ) CO2 0.0
    PPVAL MEA ( MEA+ HCO3- ) 3128.53045000
    PPVAL ( MEA+ HCO3- ) MEA 6981.73393000
    PPVAL MEA ( MEA+ CO3-- ) 0.0
    PPVAL ( MEA+ CO3-- ) MEA 0.0
    PPVAL MEA ( MEA+ OH- ) 0.0
    PPVAL ( MEA+ OH- ) MEA 0.0
    PPVAL H2O ( MEA+ MEACOO- ) -789.61025500
    PPVAL ( MEA+ MEACOO- ) H2O 432.17895100
    PPVAL CO2 ( MEA+ MEACOO- ) 0.0
    PPVAL ( MEA+ MEACOO- ) CO2 0.0
    PPVAL MEA ( MEA+ MEACOO- ) -2809.73880000
    PPVAL ( MEA+ MEACOO- ) MEA 1864.65113000
```

```
    PPVAL H2O ( PZH+ PZCOO- ) 3578.20122000
    PPVAL ( PZH+ PZCOO- ) H2O 40581.19910000
    PPVAL H2O ( PZH+ HCO3- ) 5972.56733000
    PPVAL ( PZH+ HCO3- ) H2O -3071.15767000
    PPVAL PZ ( PZH+ HCO3- ) 0.0212558000
    PPVAL ( PZH+ HCO3- ) PZ 0.0216480850
    PPVAL PZ ( PZH+ PZCOO- ) -0.0127269080
    PPVAL ( PZH+ PZCOO- ) PZ -0.0507645074
    PPVAL CO2 ( PZH+ HCO3- ) 0.0139118385
    PPVAL ( PZH+ HCO3- ) CO2 -0.0132888524
    PPVAL H2O ( MEA+ PZCOO- ) -43.00920930
    PPVAL ( MEA+ PZCOO- ) H2O 413.21151100
    PPVAL H2O ( PZH+ MEACOO- ) 122.09758500
    PPVAL ( PZH+ MEACOO- ) H2O 186.21597900
    PPVAL H2O ( MEA+ PZCOO-2 ) 4.54763774
    PPVAL ( MEA+ PZCOO-2 ) H2O -12.66545670
    PPVAL H2O ( K+ MEACOO- ) 999981.356
    PPVAL ( K+ MEACOO- ) H2O 761539.522

PROP-DATA GMELCE-1
    IN-UNITS MET VOLUME-FLOW='cum/hr' ENTHALPY-FLO='Gcal/hr'  &
        HEAT-TRANS-C='kcal/hr-sqm-K' PRESSURE=bar TEMPERATURE=C  &
        VOLUME=cum DELTA-T=C HEAD=meter MOLE-DENSITY='kmol/cum'  &
        MASS-DENSITY='kg/cum' MOLE-ENTHALP='kcal/mol'  &
        MASS-ENTHALP='kcal/kg' HEAT=Gcal MOLE-CONC='mol/l'  &
        PDROP=bar
    PROP-LIST GMELCE
    PPVAL H2O ( K+ HCO3- ) -5.22878174
    PPVAL ( K+ HCO3- ) H2O 2.47425900
    PPVAL H2O ( K+ CO3-- ) 5.01426411
    PPVAL ( K+ CO3-- ) H2O 0.0
    PPVAL H2O ( K+ OH- ) -5.85238200
    PPVAL ( K+ OH- ) H2O 4.75413000
    PPVAL ( K+ CO3-- ) ( K+ HCO3- ) -35.46904460
    PPVAL ( K+ HCO3- ) ( K+ CO3-- ) -9.69354360
    PPVAL H2O ( MEA+ HCO3- ) 24.60156680
    PPVAL ( MEA+ HCO3- ) H2O -5.89393435
    PPVAL CO2 ( MEA+ HCO3- ) 2262.77769000
    PPVAL ( MEA+ HCO3- ) CO2 659.23135400
    PPVAL CO2 ( MEA+ CO3-- ) 0.0
    PPVAL ( MEA+ CO3-- ) CO2 0.0
    PPVAL CO2 ( MEA+ OH- ) 0.0
    PPVAL ( MEA+ OH- ) CO2 0.0
    PPVAL MEA ( MEA+ HCO3- ) 66.01464320
    PPVAL ( MEA+ HCO3- ) MEA 440.40354300
    PPVAL MEA ( MEA+ CO3-- ) 0.0
    PPVAL ( MEA+ CO3-- ) MEA 0.0
    PPVAL MEA ( MEA+ OH- ) 0.0
    PPVAL ( MEA+ OH- ) MEA 0.0
    PPVAL H2O ( MEA+ MEACOO- ) -19.69365630
    PPVAL ( MEA+ MEACOO- ) H2O 1.75887248
    PPVAL CO2 ( MEA+ MEACOO- ) 0.0
    PPVAL ( MEA+ MEACOO- ) CO2 0.0
```

```
    PPVAL MEA ( MEA+ MEACOO- ) 22.41433100
    PPVAL ( MEA+ MEACOO- ) MEA 16.45050280
    PPVAL CO2 ( MEA+ MEACOO- ) 0.0
    PPVAL ( MEA+ MEACOO- ) CO2 0.0
    PPVAL CO2 ( "MEA/H" MEACOO- ) 0.0
    PPVAL ( "MEA/H" MEACOO- ) CO2 0.0
    PPVAL H2O ( PZH+ PZCOO- ) 0.0
    PPVAL ( PZH+ PZCOO- ) H2O 0.0
    PPVAL H2O ( PZH+ HCO3- ) 0.0
    PPVAL ( PZH+ HCO3- ) H2O 0.0
    PPVAL PZ ( PZH+ HCO3- ) 0.0
    PPVAL ( PZH+ HCO3- ) PZ 0.0
    PPVAL PZ ( PZH+ PZCOO- ) 0.0
    PPVAL ( PZH+ PZCOO- ) PZ 0.0
    PPVAL CO2 ( PZH+ HCO3- ) 0.0
    PPVAL ( PZH+ HCO3- ) CO2 0.0
    PPVAL H2O ( MEA+ PZCOO- ) -51.077677500
    PPVAL ( MEA+ PZCOO- ) H2O -27.881532000
    PPVAL H2O ( PZH+ MEACOO- ) -31.416637500
    PPVAL ( PZH+ MEACOO- ) H2O -6.431454760
    PPVAL H2O ( MEA+ PZCOO-2 ) -0.595441887
    PPVAL ( MEA+ PZCOO-2 ) H2O 0.190244883
    PPVAL H2O ( K+ MEACOO- ) 40483.8452
    PPVAL ( K+ MEACOO- ) H2O 30649.658

PROP-DATA GMELCN-1
    IN-UNITS MET VOLUME-FLOW='cum/hr' ENTHALPY-FLO='Gcal/hr'  &
        HEAT-TRANS-C='kcal/hr-sqm-K' PRESSURE=bar TEMPERATURE=C  &
        VOLUME=cum DELTA-T=C HEAD=meter MOLE-DENSITY='kmol/cum'  &
        MASS-DENSITY='kg/cum' MOLE-ENTHALP='kcal/mol'  &
        MASS-ENTHALP='kcal/kg' HEAT=Gcal MOLE-CONC='mol/l'  &
        PDROP=bar
    PROP-LIST GMELCN
    PPVAL H2O ( K+ OH- ) 0.2
    PPVAL H2O ( K+ HCO3- ) 0.2
    PPVAL H2O ( K+ CO3-- ) 0.2
    PPVAL CO2 ( MEA+ HCO3- ) .1000000000
    PPVAL CO2 ( MEA+ CO3-- ) .1000000000
    PPVAL CO2 ( MEA+ OH- ) .1000000000
    PPVAL MEA ( MEA+ HCO3- ) .1000000000
    PPVAL MEA ( MEA+ CO3-- ) .1000000000
    PPVAL MEA ( MEA+ OH- ) .1000000000
    PPVAL CO2 ( MEA+ MEACOO- ) .1000000000
    PPVAL MEA ( MEA+ MEACOO- ) .1000000000

PROP-SET MOL-P6H MOLEFRAC SUBSTREAM=MIXED COMPS=PZ6H2O PHASE=S

PROP-SET PPCO2-KP PPMX UNITS='kPa' SUBSTREAM=MIXED COMPS=CO2  &
        PHASE=V

PROP-SET PPMEA PPMX UNITS='kPa' SUBSTREAM=MIXED COMPS=MEA  &
        PHASE=V
```

```
PROP-SET PPPZ PPMX UNITS='kPa' SUBSTREAM=MIXED COMPS=PZ  &
      PHASE=V

STREAM 1
   SUBSTREAM MIXED TEMP=25. PRES=101.325
   MASS-FLOW H2O 1.

BLOCK B1 FLASH2
   PARAM TEMP=40. VFRAC=0.0001
   PROPERTIES ELECNRTL HENRY-COMPS=HC-1 CHEMISTRY=GLOBAL  &
      TRUE-COMPS=YES

EO-CONV-OPTI

STREAM-REPOR NOMOLEFLOW MASSFLOW PROPERTIES=PPCO2-KP MOL-P6H

PROPERTY-REP NOPCES PROP-DATA DFMS NOPARAM-PLUS

PROP-TABLE 7-2 FLASHCURVE
   MASS-FLOW H2O 1.
   STATE VFRAC=0.0001
   VARY TEMP
   RANGE LIST=40. 60.
   VARY MOLE-FLOW COMP=K2CO3
   RANGE LIST=1.25
   VARY MOLE-FLOW COMP=MEA
   RANGE LIST=3.5
   VARY MOLE-FLOW COMP=PZ
   RANGE LIST=3.6
   VARY MOLE-FLOW COMP=CO2
   RANGE LOWER=3.502 UPPER=5.35 NPOINT=41
   TABULATE PROPERTIES=PPCO2-KP PPMEA PPPZ
;
```

J.2 Overall Input File for the H_2O-K_2CO_3-PZ-CO_2 System

```
IN-UNITS SI MASS-FLOW='kg/hr' MOLE-FLOW='mol/hr' PRESSURE=kPa  &
      TEMPERATURE=C MASS-HEAT-CA='kJ/kg-K' PDROP='N/sqm'

DEF-STREAMS CONVEN ALL

SIM-OPTIONS
   IN-UNITS MET VOLUME-FLOW='cum/hr' ENTHALPY-FLO='Gcal/hr'  &
      HEAT-TRANS-C='kcal/hr-sqm-K' PRESSURE=bar TEMPERATURE=C  &
      VOLUME=cum DELTA-T=C HEAD=meter MOLE-DENSITY='kmol/cum'  &
      MASS-DENSITY='kg/cum' MOLE-ENTHALP='kcal/mol'  &
      MASS-ENTHALP='kcal/kg' HEAT=Gcal MOLE-CONC='mol/l'  &
      PDROP=bar
   SIM-OPTIONS GAMUS-BASIS=AQUEOUS
```

```
RUN-CONTROL MAX-TIME=10800.

DESCRIPTION "
   Electrolytes Simulation with Metric Units :
   C, bar, kg/hr, kmol/hr, Gcal/hr, cum/hr.

   Property Method: ELECNRTL

   Flow basis for input: Mass

   Stream report composition: Mass flow
   "

DATABANKS ASPENPCD  / AQUEOUS  / SOLIDS  / INORGANIC  /  &
      PURE20

PROP-SOURCES ASPENPCD  / AQUEOUS  / SOLIDS  / INORGANIC  /  &
      PURE20

COMPONENTS
   H2O H2O /
   CO2 CO2 /
   MEA C2H7NO /
   MEA+ C2H8NO+ /
   MEACOO- C3H6NO3- /
   HCO3- HCO3- /
   CO3-- CO3-2 /
   H+ H+ /
   OH- OH- /
   "MEA/H" C2H8NO+ /
   "CO3/HCO3" CO3-2 /
   K2CO3 K2CO3 /
   KHCO3 KHCO3 /
   K+ K+ /
   "K2CO3(S)" K2CO3 /
   "KHCO3(S)" KHCO3 /
   PZ C4H10N2 /
   PZCOO-2 C6H8N2O4 /
   PZCOO- C5H9N2O2 /
   PZH+ C4H11N2 /
   PZH+2 C4H12N2 /
   HPZCOO C5H10N2O /
   "PZ/H" /
   "H/PZCOO" /
   "PZ/H2" /
   PZ6H2O C4H10N2 /
   K2PZCOO2 C4H10N2

FORMULA PZCOO-2 C6H8N2O4 / PZCOO- C5H9N2O2 / PZH+ C4H11N2 /  &
      PZH+2 C4H12N2 / HPZCOO C5H10N2O

HENRY-COMPS HC-1 CO2
```

```
CHEMISTRY GLOBAL
    PARAM
    DISS K2CO3 K+ 2. / CO3-- 1.
    DISS KHCO3 K+ 1. / HCO3- 1.
    STOIC 1 H2O -1. / H+ 1. / OH- 1.
    STOIC 2 CO2 -1. / H2O -1. / H+ 1. / HCO3- 1.
    STOIC 3 HCO3- -1. / H+ 1. / CO3-- 1.
    STOIC 4 MEA+ -1. / MEA 1. / H+ 1.
    STOIC 5 MEACOO- -1. / H2O -1. / MEA 1. / HCO3- 1.
    STOIC 6 PZH+ -1. / PZ 1. / H+ 1.
    STOIC 8 PZ -1. / HCO3- -1. / PZCOO- 1. / H2O 1.
    STOIC 9 PZCOO- -1. / HCO3- -1. / PZCOO-2 1. / H2O 1.
    STOIC 10 HPZCOO -1. / PZCOO- 1. / H+ 1.
    SALT "K2CO3(S)" K+ 2. / CO3-- 1. / H2O 1.5
    SALT "KHCO3(S)" K+ 1. / HCO3- 1.
    SALT PZ6H2O PZ 1. / H2O 6.
    K-SALT "K2CO3(S)" A=-70.329741 B=1361.48182 C=13.508799  &
        D=-0.0581808
    K-SALT "KHCO3(S)" A=-1420.7517 B=40190.9436 C=240.615458  &
        D=-0.3144982
    K-SALT PZ6H2O A=-291.0396675 B=0. C=56.5058062  &
        D=-0.127557356

FLOWSHEET
    BLOCK B1 IN=1 OUT=2 3

PROPERTIES ELECNRTL HENRY-COMPS=HC-1 CHEMISTRY=GLOBAL

STRUCTURES
    STRUCTURES PZCOO- C1 N2 S / N2 C3 S / N2 C4 S / C3  &
        C5 S / C5 N6 S / C1 C7 S / C7 N6 S / C4 O8  &
        D / C4 O9 S

PROP-DATA
    PROP-LIST ATOMNO / NOATOM
    PVAL PZCOO- 6 8 7 1 / 5. 2. 2. 9.

STRUCTURES
    STRUCTURES PZCOO-2 C1 N2 S / N2 C3 S / C3 C4 S / C4  &
        N5 S / C1 C6 S / C6 N5 S / N5 C7 S / C7 O8  &
        D / C7 O9 S / N2 C10 S / C10 O11 D / C10 O12  &
        S

PROP-DATA
    PROP-LIST ATOMNO / NOATOM
    PVAL PZCOO-2 6 8 7 1 / 6. 4. 2. 8.

STRUCTURES
    STRUCTURES PZH+ C1 N2 S / N2 C3 S / C3 C4 S / C4  &
        N5 S / C1 C6 S / C6 N5 S

PROP-DATA
    PROP-LIST ATOMNO / NOATOM
```

```
   PVAL PZH+ 6 7 1 / 4. 2. 11.

PROP-DATA MDH
   IN-UNITS SI MASS-FLOW='kg/hr' MOLE-FLOW='mol/hr' PRESSURE=kPa  &
      TEMPERATURE=C MASS-HEAT-CA='kJ/kg-K' PDROP='N/sqm'
   PROP-LIST DGAQFM / DHAQFM
   PVAL MEA+ -171023632 / -336961728.8
   PVAL MEACOO- -492922520 / -707209080

PROP-DATA REVIEW-1
   IN-UNITS MET VOLUME-FLOW='cum/hr' ENTHALPY-FLO='Gcal/hr'  &
      HEAT-TRANS-C='kcal/hr-sqm-K' PRESSURE=bar TEMPERATURE=C  &
      VOLUME=cum DELTA-T=C HEAD=meter MOLE-DENSITY='kmol/cum'  &
      MASS-DENSITY='kg/cum' MOLE-ENTHALP='kcal/mol'  &
      MASS-ENTHALP='kcal/kg' HEAT=Gcal MOLE-CONC='mol/l'  &
      PDROP=bar
   PROP-LIST API / DGFORM / DGSFRM / DHFORM / DHSFRM /  &
      DHVLB / FREEZEPT / HCOM / MUP / MW / OMEGA / PC /  &
      RKTZRA / SG / TB / TC / VB / VC / VLSTD / ZC
   PVAL H2O 10.0 / -54.6343 / -56.5492 / -57.7949 /  &
      -69.9627 / 9.744507 / 0.0 / 0.0 / 1.84972 /  &
      18.01528 / 0.344861 / 220.64 / 0.243172 / 1.0 /  &
      100.0 / 373.946 / 18.8311 / 55.9472 / 18.0691 /  &
      0.229
   PROP-LIST API / DGFORM / DHFORM / DHVLB / FREEZEPT /  &
      HCOM / MUP / MW / OMEGA / PC / RKTZRA / SG / TB / &
      TC / VB / VC / VLSTD / ZC
   PVAL MEA 7.5 / -24.6893 / -49.4025 / 11.88812 / 10.5 /  &
      -325.765 / 0.77646 / 61.08308 / 0.446737 / 71.24 /  &
      0.24764 / 1.0179 / 170 / 405.05 / 68.6673 / 225 /  &
      60.3415 / 0.284
   PROP-LIST API / DGFORM / DHFORM / DHVLB / FREEZEPT /  &
      HCOM / MUP / MW / OMEGA / PC / SG / TB / TC /  &
      VB / VC / VLSTD / ZC
   PVAL PZ 80.4899 / 40.6310 / 3.91969 / 9.999355 / 106 /  &
      -654.398 / 1.47000 / 86.1356 / 0.41376 / 55.3 /  &
      0.667485 / 146 / 364.85 / 134.772 / 310 / 129.371 /  &
      0.323
   PROP-LIST DHFORM / FREEZEPT / MW / PC / VC / VLSTD /  &
      ZC / RGYR
   PVAL CO2 -94.05110000 / -56.57 / 44.0095 / 73.83 / 94 /  &
      61.6782 / 0.274 / 1.04000E-10
   PROP-LIST FREEZEPT / MW
   PVAL PZ6H2O 44.0000000 / 194.22728
   PROP-LIST MW
   PVAL "K2CO3(S)" 165.22872
   PVAL K2PZCOO2 250.3355

PROP-DATA REVIEW-1
   IN-UNITS MET VOLUME-FLOW='cum/hr' ENTHALPY-FLO='Gcal/hr'  &
      HEAT-TRANS-C='kcal/hr-sqm-K' PRESSURE=bar TEMPERATURE=C  &
      VOLUME=cum DELTA-T=C HEAD=meter MOLE-DENSITY='kmol/cum'  &
      MASS-DENSITY='kg/cum' MOLE-ENTHALP='J/kmol'  &
```

```
        MASS-ENTHALP='kcal/kg' MOLE-ENTROPY='J/kmol-K' HEAT=Gcal  &
        MOLE-CONC='mol/l' PDROP=bar
    PROP-LIST DGAQFM / DHAQFM
    PVAL HCO3- -587370182.1 / -690767961
    PVAL CO3-- -538355662.9 / -677140000
    PVAL "MEA/H" -171023632 / -336961728.8
    PVAL "CO3/HCO3" -538355662.9 / -677140000

PROP-DATA USRDEF
    IN-UNITS SI MASS-FLOW='kg/hr' MOLE-FLOW='mol/hr' PRESSURE=kPa  &
        TEMPERATURE=C MASS-HEAT-CA='kJ/kg-K' PDROP='N/sqm'
    PROP-LIST MW / DGAQFM / DHAQFM / CHARGE
    PVAL PZCOO-2 172.14 / -568456410 / -844124380 / -2
    PVAL PZCOO- 129.13771 / -219798180 / -480595350 / -1
    PVAL PZH+ 87.14299 / 102408575 / -91542774.38 / 1
    PVAL PZH+2 88.1504 / 91897612.25 / -122665214.9 / 2
    PVAL HPZCOO 130.145 / -278352290 / -521810730 / 1E-5
    PVAL "PZ/H" 87.14299 / 102408575 / -91542774.38 / 1
    PVAL "H/PZCOO" 129.13771 / -219798180 / -480595350 / -1
    PVAL "PZ/H2" 87.14299 / 102408575 / -91542774.38 / 1

PROP-DATA CPAQ0-1
    IN-UNITS SI MASS-FLOW='kg/hr' MOLE-FLOW='mol/hr' PRESSURE=kPa  &
        MASS-HEAT-CA='kJ/kg-K' PDROP='N/sqm'
    PROP-LIST CPAQ0
    PVAL CO3-- 1334017.129 -5564.838795 5.192267274  &
        -118575111.1 0.0 0.0 0.0 2000.000000
    PVAL HCO3- 211386.984 -881.7986241 0.874689511 -18789290.32  &
        0.0 0.0 0.0 2000.000000
    PVAL MEA+ -1700442.83 7093.368695 -8.487374579 151145133.9  &
        0.0 0.0 0.0 2000.000
    PVAL MEACOO- -2408071.1 17268.3153 -26.0389963 0.0 0.0  &
        0.0 0.0 2000.000
    PVAL "MEA/H" -1700442.83 7093.368695 -8.487374579  &
        151145133.9 0.0 0.0 0.0 2000.000
    PVAL PZCOO-2 -661253.42 -1993.11459 -2.03752889 0.0 0.0  &
        0.0 0.0 2000
    PVAL PZCOO- -10934868 32867.9873 5.07597874 0.0 0.0 0.0  &
        0.0 2000
    PVAL PZH+ 603662.8765 -2518.16458 4.16532815 -53657026.67  &
        0.0 0.0 0.0 2000
    PVAL PZH+2 1228464.475 -5124.516124 7.090651102  &
        -109192984.4 0.0 0.0 0.0 2000
    PVAL HPZCOO 420609.773 -2297.97759 6.72200937 0.0 0.0 0.0  &
        0.0 2000
    PVAL "PZ/H" 603662.8765 -2518.16458 4.16532815 -53657026.67  &
        0.0 0.0 0.0 2000
    PVAL "H/PZCOO" -10934868 32867.9873 5.07597874 0.0 0.0  &
        0.0 0.0 2000
    PVAL "PZ/H2" 603662.8765 -2518.16458 4.16532815  &
        -53657026.67 0.0 0.0 0.0 2000

PROP-DATA CPDIEC-1
```

```
    IN-UNITS MET VOLUME-FLOW='cum/hr' ENTHALPY-FLO='Gcal/hr'  &
        HEAT-TRANS-C='kcal/hr-sqm-K' PRESSURE=bar TEMPERATURE=C  &
        VOLUME=cum DELTA-T=C HEAD=meter MOLE-DENSITY='kmol/cum'  &
        MASS-DENSITY='kg/cum' MOLE-ENTHALP='kcal/mol'  &
        MASS-ENTHALP='kcal/kg' HEAT=Gcal MOLE-CONC='mol/l'  &
        PDROP=bar
    PROP-LIST CPDIEC
    PVAL H2O 78.24662286 32730.85746 298.15
    PVAL MEA 31.06961991 15128.19841 298.15
    PVAL PZ 4.253042941 1532.198738 298.15

PROP-DATA CPIGDP-1
    IN-UNITS SI MASS-FLOW='kg/hr' MOLE-FLOW='mol/hr' PRESSURE=kPa  &
        TEMPERATURE=C MASS-HEAT-CA='kJ/kg-K' PDROP='N/sqm'
    PROP-LIST CPIGDP
    PVAL PZ6H2O 81930.00000 2.36600000E+5 1269.800000  &
        1.74500000E+5 695.0000000 26.85000000 1226.850000
    PVAL K2PZCOO2 81930.00000 2.36600000E+5 1269.800000  &
        1.74500000E+5 695.0000000 26.85000000 1226.850000

PROP-DATA CPSPO1-1
    IN-UNITS SI MASS-FLOW='kg/hr' MOLE-FLOW='mol/hr' PRESSURE=kPa  &
        TEMPERATURE=C MASS-HEAT-CA='kJ/kg-K' PDROP='N/sqm'
    PROP-LIST CPSPO1
    PVAL K2CO3 139225.2346 79.85942112 0.00509505 1159199.446  &
        -3154750.005 -340154.0227 6.85 900.85
    PVAL "K2CO3(S)" 139225.2346 79.85942112 0.00509505  &
        1159199.446 -3154750.005 -340154.0227 6.85 900.85
    PVAL KHCO3 139225.2346 79.85942112 0.00509505 1159199.446  &
        -3154750.005 -340154.0227 6.85 900.85
    PVAL "KHCO3(S)" 139225.2346 79.85942112 0.00509505  &
        1159199.446 -3154750.005 -340154.0227 6.85 900.85

PROP-DATA DHVLDP-1
    IN-UNITS MET VOLUME-FLOW='cum/hr' ENTHALPY-FLO='Gcal/hr'  &
        HEAT-TRANS-C='kcal/hr-sqm-K' PRESSURE=bar TEMPERATURE=C  &
        VOLUME=cum DELTA-T=C HEAD=meter MOLE-DENSITY='kmol/cum'  &
        MASS-DENSITY='kg/cum' MOLE-ENTHALP='J/kmol'  &
        MASS-ENTHALP='kcal/kg' HEAT=Gcal MOLE-CONC='mol/l'  &
        PDROP=bar
    PROP-LIST DHVLDP
    PVAL PZ 64355423.1 0.38570286 0.02568786 0.0 0.0 106.00  &
        364.85
    PVAL PZ6H2O 64355423.1 0.38570286 0.02568786 0.0 0.0  &
        106.00 364.85
    PVAL K2PZCOO2 64355423.1 0.38570286 0.02568786 0.0 0.0  &
        106.00 364.85

PROP-DATA DHVLWT-1
    IN-UNITS MET VOLUME-FLOW='cum/hr' ENTHALPY-FLO='Gcal/hr'  &
        HEAT-TRANS-C='kcal/hr-sqm-K' PRESSURE=bar TEMPERATURE=C  &
        VOLUME=cum DELTA-T=C HEAD=meter MOLE-DENSITY='kmol/cum'  &
        MASS-DENSITY='kg/cum' MOLE-ENTHALP='J/kmol'  &
```

```
      MASS-ENTHALP='kcal/kg' HEAT=Gcal MOLE-CONC='mol/l'  &
      PDROP=bar
   PROP-LIST DHVLWT
   PVAL H2O 40655000 100.00 0.26623503 0.09110321 0.01
   PVAL MEA 54835800 126.67 0.4041153 0.11011257 -27.37

PROP-DATA PLXANT-1
   IN-UNITS SI MASS-FLOW='kg/hr' MOLE-FLOW='mol/hr' PRESSURE=kPa  &
      TEMPERATURE=C MASS-HEAT-CA='kJ/kg-K' PDROP='N/sqm'
   PROP-LIST PLXANT
   PVAL PZCOO-2 -1.000000E+20 0.0 0.0 0.0 0.0 0.0 0.0  &
      -273.1500000 1726.850000
   PVAL PZCOO- -1.000000E+20 0.0 0.0 0.0 0.0 0.0 0.0  &
      -273.1500000 1726.850000
   PVAL PZH+ -1.000000E+20 0.0 0.0 0.0 0.0 0.0 0.0  &
      -273.1500000 1726.850000
   PVAL PZH+2 -1.000000E+20 0.0 0.0 0.0 0.0 0.0 0.0  &
      -273.1500000 1726.850000
   PVAL HPZCOO -1.000000E+20 0.0 0.0 0.0 0.0 0.0 0.0  &
      -273.1500000 1726.850000
   PVAL "PZ/H" -1.000000E+20 0.0 0.0 0.0 0.0 0.0 0.0  &
      -273.1500000 1726.850000
   PVAL "H/PZCOO" -1.000000E+20 0.0 0.0 0.0 0.0 0.0 0.0  &
      -273.1500000 1726.850000
   PVAL "PZ/H2" -1.000000E+20 0.0 0.0 0.0 0.0 0.0 0.0  &
      -273.1500000 1726.850000

PROP-DATA HENRY-1
   IN-UNITS MET VOLUME-FLOW='cum/hr' ENTHALPY-FLO='Gcal/hr'  &
      HEAT-TRANS-C='kcal/hr-sqm-K' PRESSURE=Pa TEMPERATURE=K  &
      VOLUME=cum DELTA-T=C HEAD=meter MOLE-DENSITY='kmol/cum'  &
      MASS-DENSITY='kg/cum' MOLE-ENTHALP='kcal/mol'  &
      MASS-ENTHALP='kcal/kg' HEAT=Gcal MOLE-CONC='mol/l'  &
      PDROP=bar
   PROP-LIST HENRY
   BPVAL CO2 H2O 170.7126000 -8477.711000 -21.95743000  &
      5.78074800E-3 273.0000000 500.0000000 0.0
   BPVAL CO2 MEA 89.452 -2934.6 -11.592 0.01644 273.0000000  &
      500.0000000 0.0

PROP-DATA NRTL-1
   IN-UNITS MET VOLUME-FLOW='cum/hr' ENTHALPY-FLO='Gcal/hr'  &
      HEAT-TRANS-C='kcal/hr-sqm-K' PRESSURE=bar TEMPERATURE=C  &
      VOLUME=cum DELTA-T=C HEAD=meter MOLE-DENSITY='kmol/cum'  &
      MASS-DENSITY='kg/cum' MOLE-ENTHALP='kcal/mol'  &
      MASS-ENTHALP='kcal/kg' HEAT=Gcal MOLE-CONC='mol/l'  &
      PDROP=bar
   PROP-LIST NRTL
   BPVAL H2O MEA -123.323712 2575.16998 0.2 0.0 22.061396  &
      -0.029745916 0.0 1000
   BPVAL MEA H2O -1.71338728 -214.123176 0.2 0.0 0.0 0.0  &
      0.0 1000
   BPVAL H2O CO2 10.06400000 -3268.135000 .2000000000 0.0 0.0  &
```

```
        0.0 0.0 200.0000000
    BPVAL CO2 H2O 10.06400000 -3268.135000 .2000000000 0.0 0.0  &
        0.0 0.0 200.0000000
    BPVAL H2O PZ -4.771449207 0 0.2 0 0 0.010652211 0 1000
    BPVAL PZ H2O 0.378443544 0 0.2 0 0 0.024904765 0 1000

PROP-DATA VLCLK-1
    IN-UNITS MET VOLUME-FLOW='cum/hr' ENTHALPY-FLO='Gcal/hr'  &
        HEAT-TRANS-C='kcal/hr-sqm-K' PRESSURE=bar TEMPERATURE=C  &
        VOLUME=cum DELTA-T=C HEAD=meter MOLE-DENSITY='kmol/cum'  &
        MASS-DENSITY='kg/cum' MOLE-ENTHALP='kcal/mol'  &
        MASS-ENTHALP='kcal/kg' HEAT=Gcal MOLE-CONC='mol/l'  &
        PDROP=bar
    PROP-LIST VLCLK
    BPVAL K+ HCO3- 35.23311000 21.81205000
    BPVAL K+ CO3-- 19.73097000 74.55601000
    BPVAL K+ OH- 1.373720000 52.13633000
    BPVAL MEA+ OH- -390.9954000 1000.000000
    BPVAL "MEA/H" OH- -390.9954000 1000.000000
    BPVAL K+ "CO3/HCO3" 19.73097000 74.55601000

PROP-DATA GMELCC-1
    IN-UNITS MET VOLUME-FLOW='cum/hr' ENTHALPY-FLO='Gcal/hr'  &
        HEAT-TRANS-C='kcal/hr-sqm-K' PRESSURE=bar TEMPERATURE=C  &
        VOLUME=cum DELTA-T=C HEAD=meter MOLE-DENSITY='kmol/cum'  &
        MASS-DENSITY='kg/cum' MOLE-ENTHALP='kcal/mol'  &
        MASS-ENTHALP='kcal/kg' HEAT=Gcal MOLE-CONC='mol/l'  &
        PDROP=bar
    PROP-LIST GMELCC
    PPVAL H2O ( K+ HCO3- ) 11.11228480
    PPVAL ( K+ HCO3- ) H2O -4.94142428
    PPVAL H2O ( K+ CO3-- ) 10.44069660
    PPVAL ( K+ CO3-- ) H2O -4.41820292
    PPVAL H2O ( K+ OH- ) 7.84067300
    PPVAL ( K+ OH- ) H2O -4.25869600
    PPVAL H2O ( H+ HCO3- ) 8.04500000
    PPVAL ( H+ HCO3- ) H2O -4.07200000
    PPVAL H2O ( H+ CO3-- ) 8.04500000
    PPVAL ( H+ CO3-- ) H2O -4.07200000
    PPVAL H2O ( H+ OH- ) 8.04500000
    PPVAL ( H+ OH- ) H2O -4.07200000
    PPVAL ( K+ CO3-- ) ( K+ HCO3- ) 11.29371830
    PPVAL ( K+ HCO3- ) ( K+ CO3-- ) 0.49023478
    PPVAL H2O ( MEA+ HCO3- ) 12.77005390
    PPVAL ( MEA+ HCO3- ) H2O -3.80956870
    PPVAL CO2 ( MEA+ HCO3- ) 49.15747970
    PPVAL ( MEA+ HCO3- ) CO2 -5.89256106
    PPVAL CO2 ( MEA+ CO3-- ) 15.00000000
    PPVAL ( MEA+ CO3-- ) CO2 -8.00000000
    PPVAL CO2 ( MEA+ OH- ) 15.00000000
    PPVAL ( MEA+ OH- ) CO2 -8.00000000
    PPVAL MEA ( MEA+ HCO3- ) 1.78726059
    PPVAL ( MEA+ HCO3- ) MEA -30.84763770
```

```
    PPVAL MEA ( MEA+ CO3-- ) 15.00000000
    PPVAL ( MEA+ CO3-- ) MEA -8.00000000
    PPVAL MEA ( MEA+ OH- ) 15.00000000
    PPVAL ( MEA+ OH- ) MEA -8.00000000
    PPVAL H2O ( MEA+ MEACOO- ) 19.03188830
    PPVAL ( MEA+ MEACOO- ) H2O -7.38531897
    PPVAL CO2 ( MEA+ MEACOO- ) 15.00000000
    PPVAL ( MEA+ MEACOO- ) CO2 -8.00000000
    PPVAL MEA ( MEA+ MEACOO- ) 16.87100390
    PPVAL ( MEA+ MEACOO- ) MEA -13.62627530
    PPVAL H2O ( PZH+ PZCOO- ) -1.04735906
    PPVAL ( PZH+ PZCOO- ) H2O -103.954042
    PPVAL H2O ( PZH+ HCO3- ) 4.43651036
    PPVAL ( PZH+ HCO3- ) H2O -0.7872577
    PPVAL PZ ( PZH+ HCO3- ) 7.03927214
    PPVAL ( PZH+ HCO3- ) PZ -5.75420279
    PPVAL PZ ( PZH+ PZCOO- ) 6.91492088
    PPVAL ( PZH+ PZCOO- ) PZ 1.72226212
    PPVAL CO2 ( PZH+ HCO3- ) 10.4764239
    PPVAL ( PZH+ HCO3- ) CO2 11.8017499
    PPVAL H2O ( K+ PZCOO- ) 16.215816
    PPVAL ( K+ PZCOO- ) H2O -6.21116267
    PPVAL H2O ( K+ PZCOO-2 ) -3.31378754
    PPVAL ( K+ PZCOO-2 ) H2O 14.8343291
    PPVAL H2O ( PZH+ PZCOO-2 ) 10.999002
    PPVAL ( PZH+ PZCOO-2 ) H2O -0.244146518
    PPVAL PZ ( K+ HCO3- ) 18.6888553
    PPVAL ( K+ HCO3- ) PZ 2.07609342
    PPVAL PZ ( K+ PZCOO- ) 4.15766326
    PPVAL ( K+ PZCOO- ) PZ -4.84686271
    PPVAL PZ ( K+ PZCOO-2 ) 5.60790154
    PPVAL ( K+ PZCOO-2 ) PZ 3.52882395

PROP-DATA GMELCD-1
    IN-UNITS MET VOLUME-FLOW='cum/hr' ENTHALPY-FLO='Gcal/hr'  &
        HEAT-TRANS-C='kcal/hr-sqm-K' PRESSURE=bar TEMPERATURE=C  &
        VOLUME=cum DELTA-T=C HEAD=meter MOLE-DENSITY='kmol/cum'  &
        MASS-DENSITY='kg/cum' MOLE-ENTHALP='kcal/mol'  &
        MASS-ENTHALP='kcal/kg' HEAT=Gcal MOLE-CONC='mol/l'  &
        PDROP=bar
    PROP-LIST GMELCD
    PPVAL H2O ( K+ HCO3- ) 0.0
    PPVAL ( K+ HCO3- ) H2O 0.0
    PPVAL H2O ( K+ CO3-- ) -364.55635300
    PPVAL ( K+ CO3-- ) H2O -54.24351940
    PPVAL H2O ( K+ OH- ) 773.36010000
    PPVAL ( K+ OH- ) H2O -305.65090000
    PPVAL ( K+ CO3-- ) ( K+ HCO3- ) -2907.57314000
    PPVAL ( K+ HCO3- ) ( K+ CO3-- ) -725.82256800
    PPVAL H2O ( MEA+ HCO3- ) 156.09046700
    PPVAL ( MEA+ HCO3- ) H2O -214.82514800
    PPVAL CO2 ( MEA+ HCO3- ) 430.10816000
    PPVAL ( MEA+ HCO3- ) CO2 14444.83540000
```

```
    PPVAL CO2 ( MEA+ CO3-- ) 0.0
    PPVAL ( MEA+ CO3-- ) CO2 0.0
    PPVAL CO2 ( MEA+ OH- ) 0.0
    PPVAL ( MEA+ OH- ) CO2 0.0
    PPVAL MEA ( MEA+ HCO3- ) 3128.53045000
    PPVAL ( MEA+ HCO3- ) MEA 6981.73393000
    PPVAL MEA ( MEA+ CO3-- ) 0.0
    PPVAL ( MEA+ CO3-- ) MEA 0.0
    PPVAL MEA ( MEA+ OH- ) 0.0
    PPVAL ( MEA+ OH- ) MEA 0.0
    PPVAL H2O ( MEA+ MEACOO- ) -789.61025500
    PPVAL ( MEA+ MEACOO- ) H2O 432.17895100
    PPVAL CO2 ( MEA+ MEACOO- ) 0.0
    PPVAL ( MEA+ MEACOO- ) CO2 0.0
    PPVAL MEA ( MEA+ MEACOO- ) -2809.73880000
    PPVAL ( MEA+ MEACOO- ) MEA 1864.65113000
    PPVAL H2O ( PZH+ PZCOO- ) 3578.20122000
    PPVAL ( PZH+ PZCOO- ) H2O 40581.19910000
    PPVAL H2O ( PZH+ HCO3- ) 5972.56733000
    PPVAL ( PZH+ HCO3- ) H2O -3071.15767000
    PPVAL PZ ( PZH+ HCO3- ) 0.0
    PPVAL ( PZH+ HCO3- ) PZ 0.0
    PPVAL PZ ( PZH+ PZCOO- ) 0.0
    PPVAL ( PZH+ PZCOO- ) PZ 0.0
    PPVAL CO2 ( PZH+ HCO3- ) 0.0
    PPVAL ( PZH+ HCO3- ) CO2 0.0
    PPVAL H2O ( K+ PZCOO- ) -342.763486
    PPVAL ( K+ PZCOO- ) H2O -287.67483
    PPVAL H2O ( K+ PZCOO-2 ) -35.081338
    PPVAL ( K+ PZCOO-2 ) H2O 4.1098466
    PPVAL H2O ( PZH+ PZCOO-2 ) 20.3527407
    PPVAL ( PZH+ PZCOO-2 ) H2O -2.33941249

PROP-DATA GMELCE-1
    IN-UNITS MET VOLUME-FLOW='cum/hr' ENTHALPY-FLO='Gcal/hr'  &
        HEAT-TRANS-C='kcal/hr-sqm-K' PRESSURE=bar TEMPERATURE=C  &
        VOLUME=cum DELTA-T=C HEAD=meter MOLE-DENSITY='kmol/cum'  &
        MASS-DENSITY='kg/cum' MOLE-ENTHALP='kcal/mol'  &
        MASS-ENTHALP='kcal/kg' HEAT=Gcal MOLE-CONC='mol/l'  &
        PDROP=bar
    PROP-LIST GMELCE
    PPVAL H2O ( K+ HCO3- ) -5.22878174
    PPVAL ( K+ HCO3- ) H2O 2.47425900
    PPVAL H2O ( K+ CO3-- ) 5.01426411
    PPVAL ( K+ CO3-- ) H2O 0.0
    PPVAL H2O ( K+ OH- ) -5.85238200
    PPVAL ( K+ OH- ) H2O 4.75413000
    PPVAL ( K+ CO3-- ) ( K+ HCO3- ) -35.46904460
    PPVAL ( K+ HCO3- ) ( K+ CO3-- ) -9.69354360
    PPVAL H2O ( MEA+ HCO3- ) 24.60156680
    PPVAL ( MEA+ HCO3- ) H2O -5.89393435
    PPVAL CO2 ( MEA+ HCO3- ) 2262.77769000
    PPVAL ( MEA+ HCO3- ) CO2 659.23135400
```

```
    PPVAL CO2 ( MEA+ CO3-- ) 0.0
    PPVAL ( MEA+ CO3-- ) CO2 0.0
    PPVAL CO2 ( MEA+ OH- ) 0.0
    PPVAL ( MEA+ OH- ) CO2 0.0
    PPVAL MEA ( MEA+ HCO3- ) 66.01464320
    PPVAL ( MEA+ HCO3- ) MEA 440.40354300
    PPVAL MEA ( MEA+ CO3-- ) 0.0
    PPVAL ( MEA+ CO3-- ) MEA 0.0
    PPVAL MEA ( MEA+ OH- ) 0.0
    PPVAL ( MEA+ OH- ) MEA 0.0
    PPVAL H2O ( MEA+ MEACOO- ) -19.69365630
    PPVAL ( MEA+ MEACOO- ) H2O 1.75887248
    PPVAL CO2 ( MEA+ MEACOO- ) 0.0
    PPVAL ( MEA+ MEACOO- ) CO2 0.0
    PPVAL MEA ( MEA+ MEACOO- ) 22.41433100
    PPVAL ( MEA+ MEACOO- ) MEA 16.45050280
    PPVAL CO2 ( MEA+ MEACOO- ) 0.0
    PPVAL ( MEA+ MEACOO- ) CO2 0.0
    PPVAL CO2 ( "MEA/H" MEACOO- ) 0.0
    PPVAL ( "MEA/H" MEACOO- ) CO2 0.0
    PPVAL H2O ( PZH+ PZCOO- ) 0.0
    PPVAL ( PZH+ PZCOO- ) H2O 0.0
    PPVAL H2O ( PZH+ HCO3- ) 0.0
    PPVAL ( PZH+ HCO3- ) H2O 0.0
    PPVAL PZ ( PZH+ HCO3- ) 0.0
    PPVAL ( PZH+ HCO3- ) PZ 0.0
    PPVAL PZ ( PZH+ PZCOO- ) 0.0
    PPVAL ( PZH+ PZCOO- ) PZ 0.0
    PPVAL CO2 ( PZH+ HCO3- ) 0.0
    PPVAL ( PZH+ HCO3- ) CO2 0.0
    PPVAL H2O ( K+ PZCOO- ) 0.0
    PPVAL ( K+ PZCOO- ) H2O 0.0

PROP-DATA GMELCN-1
    IN-UNITS MET VOLUME-FLOW='cum/hr' ENTHALPY-FLO='Gcal/hr'  &
        HEAT-TRANS-C='kcal/hr-sqm-K' PRESSURE=bar TEMPERATURE=C  &
        VOLUME=cum DELTA-T=C HEAD=meter MOLE-DENSITY='kmol/cum'  &
        MASS-DENSITY='kg/cum' MOLE-ENTHALP='kcal/mol'  &
        MASS-ENTHALP='kcal/kg' HEAT=Gcal MOLE-CONC='mol/l'  &
        PDROP=bar
    PROP-LIST GMELCN
    PPVAL H2O ( K+ OH- ) 0.2
    PPVAL H2O ( K+ HCO3- ) 0.2
    PPVAL H2O ( K+ CO3-- ) 0.2
    PPVAL CO2 ( MEA+ HCO3- ) .1000000000
    PPVAL CO2 ( MEA+ CO3-- ) .1000000000
    PPVAL CO2 ( MEA+ OH- ) .1000000000
    PPVAL MEA ( MEA+ HCO3- ) .1000000000
    PPVAL MEA ( MEA+ CO3-- ) .1000000000
    PPVAL MEA ( MEA+ OH- ) .1000000000
    PPVAL CO2 ( MEA+ MEACOO- ) .1000000000
    PPVAL MEA ( MEA+ MEACOO- ) .1000000000
```

```
STREAM 1
    SUBSTREAM MIXED TEMP=25. PRES=101.325
    MASS-FLOW H2O 1.

BLOCK B1 FLASH2
    PARAM TEMP=40. VFRAC=0.0001
    PROPERTIES ELECNRTL HENRY-COMPS=HC-1 CHEMISTRY=GLOBAL  &
        TRUE-COMPS=YES

EO-CONV-OPTI

STREAM-REPOR NOMOLEFLOW MASSFLOW

PROPERTY-REP NOPCES PROP-DATA DFMS NOPARAM-PLUS
;
```

APPENDIX K

Aspen Plus^{TM} User Fortran Subroutine

K.1 Fortran Subroutine Code for NMR and Enthalpy of CO_2 Absorption

```
      SUBROUTINE DRUSR0 (T, P, X, Y, NCP, IDX, NBOPST, KDIAG,
     1                 ITYPE, PROP, KER)
C
C----------------------------------------------------------------------
C        COPYRIGHT (C) 2008
C         THE UNIVERISYT OF TEXAS AT AUSTIN
C         AUSTIN, TEXAS, USA
C----------------------------------------------------------------------
C
C     MODULE TITLE: GENERIC USER PROPERTY VS. STATE VARIABLES
C
C     VARIABLES USED:
C
C      VARIABLES IN ARGUMENT LIST - NONE
C
C      IMPORTANT INTERNAL VARIABLES
C
C       VARIABLE  I/O   TYPE     DIMENSION     DESCRIPTION AND RANGE
C
C          T      I     R*8        -          TEMPERATURE, K
C
C          P      I     R*8        -          PRESSURE, PASCAL
C
C          X      I     R*8       NCP         LIQUID MOLE FRAC VECTOR
```

```
C
C          Y      I     R*8        NCP        VAPOR MOLE FRAC VECTOR
C
C          NCP    I     I          -          NO. OF COMPONENT PRESENT
C
C          IDX    I     I          NCP        COMPONENT INDEX VECTOR
C
C          NBOPST I     I          6          OPTION SET BEAD
C
C          KDIAG  I     I          -          PROPERTY DIAGNOSTIC CODE
C
C          ITYPE  I     I          -          TYPE OF PROPERTY
C                                             (SEE ABOVE)
C
C          PROP   O     R*8        1          CALCULATED PURE COMP
C                                             PROPERTY
C                                  NCP        CALCULATED PARTIAL PROP
C                                  1          CALCULATED MIXTURE PROP
C
C          KER    O     I          -          ERROR RETURN CODE
C
C     ERROR CONDITIONS: NONE
C
C     SUBROUTINES CALLED:
C
C     FILES:
C
C        SPECIFICATIONS, DECLARATIONS, DATA STATEMENTS, ETC.
C
      IMPLICIT NONE
C
#include "dms_global.cmn"
#include "dms_rglob.cmn"
#include "dms_ncomp.cmn"
C
#include "shs_stwork.cmn"
#include "dms_stwkwk.cmn"
      EQUIVALENCE (NCPM, STWKWK_NCPMOO)
      EQUIVALENCE (PCALC, STWKWK_PCALC)
C
#include "dms_plex.cmn"

      EQUIVALENCE (IB(1), B(1))
C
C     DECLARE ARGUMENTS
C
      INTEGER IDX(1),NBOPST(1),    NCP,   KDIAG, ITYPE,
     +        KER,   I
      REAL*8 X(1),  Y(1),  PROP(1), T, P, MEATOT, CO2TOT,
     +        MEAH, MEACOO, CO3HCO3, OBJFUN, AA, BB, CC
C
C     DECLARE LOCAL VARIABLES
C
```

```
      INTEGER IPROG(2), LDRU1, LDRU2, addValue, caseValue, idValue
      REAL*8 B(1), SVEC(20), TOL, SPEC1,
     +          SPEC2, GUESS, RETN(1000), total
      INTEGER NSUBS, IXTYPE, KODE, NPKODE, MAXIT,
     +        IRETN(6), JRES,KRESLT, lcflag, lmsg, lpmsg,
     +                    kphase, idxsub(1)
C
      REAL*8 XT, XL, XS, S2TL, TL2AL, HMX, DHMX
      INTEGER IDXT, IDXL ,IDXS, KH, N, KBASE,
     1        NL, NS, NT
      DIMENSION XT(20), IDXT(20), XL(20), IDXL(20),
     1          XS(20), IDXS(20)
      INTEGER KPPMON(4), KENTHL(5), IFPTR
C
      INTEGER IOLI, NPHASE, MXIT, LODIAG, NV, IDXV(1),
     1        NBOPSTS
              REAL*8  HDUM, XV(1), SF, VF, LF, T2A
              REAL*8 XMEA, XMEAH, XTEMP(20), XMEACOO, XCO2, XCO3, XHCO3, XH2O
C
C    DECLARE LOCAL VARIABLES
C      IMEA STORES THE ALIAS OF MEA (8 CHARACTERS)
C      IMEAH STORES THE ALIAS OF MEAH+ (8 CHARACTERS)
C      AND SO ON...
C
      INTEGER NCPM, J, II, FRMULA, LFRMULA, IMEA(2), IMEAH(2),
     .        IMEACOO(2), ICO2(2), ICO3(2), IHCO3(2), Z, IH2O(2)
C
      REAL*8 PCALC, YTEMP(20), PRES, PPTEMP(20), ZTEMP(20), RecT

#include "dms_initv.cmn"
#include "dms_ipoff1.cmn"
#include "dms_ipoff4.cmn"
#include "ppexec_user.cmn"
C
C     DATA STATEMENTS
C
      DATA IPROG/4HDRUS, 4HR0  /
      DATA KPPMON / 4HPPMO, 4HN    ,2*4H    /
      DATA KENTHL / 4HPPMO, 4HN_EN, 4HTHL , 2*4H    /
C
      DATA IMEA   /4HC2H7, 4HNO  /,
     .    IH2O   /4HH2O , 4HH   /,
     .    IMEAH  /4HC2H8, 4HNO+ /,
     .    IMEACOO/4HC3H6, 4HNO3-/,
     .    ICO2   /4HCO2 , 4H    /,
     .    ICO3   /4HCO3-, 4H2   /,
     .    IHCO3  /4HHCO3, 4H-   /

C
C  STATEMENT FUNCTIONS FOLLOW
C
      FRMULA(I,J) = LFRMULA + 3*(J - 1) + I
C
```

```
C    BEGIN EXECUTABLE CODE
C
C  SET PLEX OFFSETS
C
     LDRU1 = IPOFF1_IPOFF1(102)
     LDRU2 = IPOFF1_IPOFF1(103)
     LFRMULA = IPOFF4_IPOFF4(1)
C
C    Case Value for NMR or DHabs code Based on Component Index Vectors
C
     addValue = 1D0
     caseValue = 0D0
     idValue = 0D0

     DO I=1,NCP

           IF (IDX(I).ne.0) THEN
           caseValue = caseValue + addValue
           idValue = IDX(I) + idValue
     ENDIF

           addValue = addValue*2

           END DO
C          write (user_nhstry,*) ' '
C      write(user_nhstry,*) 'Final idValue ' ,idValue
C      write (user_nhstry,*) ' '
 ==============================================================
C
     IF (idValue.EQ.27) THEN
C
C          MEA Only NMR Data
C    Convert Mole fractions to total mole fractions
C
     MEATOT = X(1)+ X(2)
     CO2TOT = X(2)+ X(3)
C
C    Dummy Variable for use later
C
     MEAH = X(1)
     MEACOO = X(2)
     CO3HCO3 = X(3)
C
C    Convert to SVEC components according to the SPECIES list
C
     XTEMP(1)=1D0-MEATOT-CO2TOT
     XTEMP(2)=CO2TOT
     XTEMP(3)=MEATOT
     XTEMP(4)=0D0
C
C    The following code calls the FLash subroutine.
C
```

```
                 TOTAL = 0D0
                 DO 299 I=1, NCOMP_NCC+9
                         SVEC(I) = 0D0
 299        CONTINUE
C
      DO 300 I = 1, NCP
                  SVEC(I) = XTEMP(I)
                  TOTAL = SVEC(I) + TOTAL
C
 300    CONTINUE
C
C       write (user_nhstry,*) ' '
C       write (user_nhstry,*) 'total ',total
          SVEC(NCOMP_NCC+1) = TOTAL
          svec(ncomp_ncc+2) = t
          svec(ncomp_ncc+3) = P
C
C                 do 98 i = 1, ncomp_ncc+9
C           write(user_nhstry,*) 'svec(ncomp_ncc) ' ,svec(i),i
C   98      continue

                 NSUBS = 1
                 IXTYPE = 1
                 KODE = 5
                 NPKODE = 2
                 MAXIT = 30
                 TOL = 1E-4
                 SPEC1 = T
                 SPEC2= 0.0001
                 GUESS = P
                 JRES= 0
                 KRESLT = 1
      KPHASE = 2
      idxsub(1) = 1
C
C
          CALL FLSH_FLASH (SVEC, NSUBS, IDXSUB, IXTYPE, NBOPST, KODE,
    +     NPKODE, KPHASE, MAXIT, TOL, SPEC1,SPEC2, GUESS, LMSG, LPMSG,
    +     JRES, KRESLT, RETN, IRETN, LCFLAG)

C
C
C       write (user_nhstry,*) ' '
C          write(user_nhstry,*) 'lcflag ',lcflag
C
C          do 99 i = 1, ncomp_ncc+9
C            write(user_nhstry,*) 'svec(ncomp_ncc) ' ,svec(i)
C 99       continue

C
C     GET CALCULATED PRESSURE
C
     PRES = PCALC
```

```
C      write (user_nhstry,*) 'PCALC, [Pa]', PCALC
C
C     GET VAPOR MOLE FRACTIONS
C
      DO I = 1, NCP
        YTEMP(I) = 0D0
      END DO

C      write (user_nhstry,*) ' '
      DO I = 1, NCPM
       YTEMP(i) = B(STWKWK_LRSTW+(STWORK_MY+I-1))
C
C       FIND CO2
C
       IF (IB(FRMULA(1,I)).EQ.ICO2(1) .AND.
     .     IB(FRMULA(2,I)).EQ.ICO2(2)) THEN
         PPTEMP(I) = PRES*YTEMP(i)
C          write (user_nhstry,*) 'YTEMP-CO2, i', YTEMP(i), i
C          write (user_nhstry,*) 'PPTEMP-CO2,[Pa] ',PPTEMP(i), i
       ENDIF
      END DO
C
C     The following code is to get true species.
C
      CALL PPSTUB_GETTRU ( NT, IDXT, XT, NL, IDXL, XL, NS, IDXS, XS,
     1              S2TL, TL2AL )
C
C      write (user_nhstry,*) ' '
C      do 101 I = 1, NL
C             write(user_nhstry,*) 'XL ' ,XL(I), I, IDXL(I)
C 101      continue

C
C    The Following Code retrieves the liquid phase mole fractions
C
      XMEA = 0D0
      XH2O = 0D0
      XMEAH = 0D0
      XMEACOO = 0D0
      XCO2 = 0D0
      XCO3 = 0D0
      XHCO3 = 0D0

C      write (user_nhstry,*) 'XH2O TRUE ',XH2O
C
C      write (user_nhstry,*) ' '
      DO I = 1, NL
        IF (IB(FRMULA(1,IDXL(I))) .EQ. IMEA(1). AND.
     .      IB(FRMULA(2,IDXL(I))).EQ.IMEA(2)) THEN
          XMEA = XL(I)
          write (user_nhstry,*) 'XMEA TRUE ',XMEA
        ELSE IF (IB(FRMULA(1,IDXL(I))) .EQ. IH2O(1). AND.
```

```
 .      IB(FRMULA(2,IDXL(I))).EQ.IH2O(2)) THEN
        XH2O = XL(I)
        write (user_nhstry,*) 'XH2O TRUE ',XH2O
      ELSE IF (IB(FRMULA(1,IDXL(I))) .EQ. IMEAH(1). AND.
 .          IB(FRMULA(2,IDXL(I))).EQ.IMEAH(2)) THEN
        XMEAH = XL(I)
        write (user_nhstry,*) 'XMEAH TRUE ', XMEAH
      ELSE IF (IB(FRMULA(1,IDXL(I))) .EQ. IMEACOO(1). AND.
 .          IB(FRMULA(2,IDXL(I))).EQ.IMEACOO(2)) THEN
        XMEACOO = XL(I)
        write (user_nhstry,*) 'XMEACOO TRUE ', XMEACOO
      ELSE IF (IB(FRMULA(1,IDXL(I))) .EQ. ICO2(1). AND.
 .          IB(FRMULA(2,IDXL(I))).EQ.ICO2(2)) THEN
        XCO2 = XL(I)
        write (user_nhstry,*) 'XCO2 TRUE ', XCO2
      ELSE IF (IB(FRMULA(1,IDXL(I))) .EQ. ICO3(1). AND.
 .          IB(FRMULA(2,IDXL(I))).EQ.ICO3(2)) THEN
        XCO3 = XL(I)
        write (user_nhstry,*) 'XCO3 TRUE ', XCO3
      ELSE IF (IB(FRMULA(1,IDXL(I))) .EQ. IHCO3(1). AND.
 .          IB(FRMULA(2,IDXL(I))).EQ.IHCO3(2)) THEN
        XHCO3 = XL(I)
        write (user_nhstry,*) 'XHCO3 TRUE ', XHCO3
      ENDIF
    END DO
C
C    Sum up the true species from the subroutene program corresponding to the following
C
    AA = XMEA + XMEAH
    BB = XMEACOO
    CC = XCO2 + XCO3 + XHCO3
C
C    Objective Function
C
    OBJFUN = (MEAH - AA)**2 + (MEACOO - BB)**2 + (CO3HCO3 - CC)**2
C
    PROP(1) = 1D0 - OBJFUN
C
C
C     write (user_nhstry,*) ' '
C          write (user_nhstry,*) 'prop(1) ',prop(1)
C          write (user_nhstry,*) ' '

          ENDIF
C
C
==============================================================
C
          IF (idValue.EQ.6) THEN
C
C         DHabs Only Data
C
C    Convert to SVEC components according to the SPECIES list
```

```
C
C     X(1) = MEA
C     X(2) = CO2
C     X(3) = H2O
C
     XTEMP(1)=X(3)
     XTEMP(2)=X(2)
     XTEMP(3)=X(1)
C
C     The following code calls the FLash subroutine.
C
                    TOTAL = 0D0
                    DO 296 I=1, NCOMP_NCC+9
                              SVEC(I) = 0D0
 296         CONTINUE
C
       DO 340 I = 1, NCP
                     SVEC(I) = XTEMP(I)
                     TOTAL = SVEC(I) + TOTAL
C
 340    CONTINUE
C
C        write (user_nhstry,*) ' '
C        write (user_nhstry,*) 'total ',total
          SVEC(NCOMP_NCC+1) = TOTAL
          svec(ncomp_ncc+2) = t
          svec(ncomp_ncc+3) = P
C
C                   do 92 i = 1, ncomp_ncc+9
C             write(user_nhstry,*) 'svec(ncomp_ncc) ' ,svec(i),i
C  92        continue
C
C       THE FOLLOWING DO LOOP FLASHES THE SAME STREAM TWICE AT T AND T+1
C       TO GET THE PARTIAL PRESSURE OF CO2 FOR DHABS CALCULATION.
C
      DO 230 z = 1,2
C
                    NSUBS = 1
                    IXTYPE = 1
                    KODE = 5
                    NPKODE = 2
                    MAXIT = 30
                    TOL = 1E-4
                    SPEC1 = T
                    SPEC2= 0.0001
                    GUESS = P
                    JRES= 0
                    KRESLT = 1
      KPHASE = 2
      idxsub(1) = 1
C
C
          CALL FLSH_FLASH (SVEC, NSUBS, IDXSUB, IXTYPE, NBOPST, KODE,
```

```
   +      NPKODE, KPHASE, MAXIT, TOL, SPEC1,SPEC2, GUESS, LMSG, LPMSG,
   +      JRES, KRESLT, RETN, IRETN, LCFLAG)

C
C
C      write (user_nhstry,*) ' '
C         write(user_nhstry,*) 'lcflag ',lcflag
C
C         do 97 i = 1, ncomp_ncc+9
C           write(user_nhstry,*) 'svec(ncomp_ncc) ' ,svec(i)
C 97      continue

C
C    GET CALCULATED PRESSURE
C
     PRES = PCALC

C     write (user_nhstry,*) 'PCALC, [Pa]', PCALC
C
C    GET VAPOR MOLE FRACTIONS
C
     DO I = 1, NCP
       YTEMP(I) = 0D0
     END DO

C     write (user_nhstry,*) ' '
     DO I = 1, NCPM
      YTEMP(i) = B(STWKWK_LRSTW+(STWORK_MY+I-1))
C
C      FIND CO2
C
      IF (IB(FRMULA(1,I)).EQ.ICO2(1) .AND.
   .     IB(FRMULA(2,I)).EQ.ICO2(2)) THEN
        PPTEMP(I) = PRES*YTEMP(i)
        ZTEMP(Z) = PPTEMP(I)
C         write (user_nhstry,*) 'YTEMP-CO2, i', YTEMP(i), i
C         write (user_nhstry,*) 'PPTEMP-CO2,[Pa] ',PPTEMP(i), i
C         write (user_nhstry,*) 'ZTEMP-CO2,[Pa] ',ZTEMP(Z), Z
      ENDIF
     END DO
C
     t = t + 1D0
C
 230 END DO
C
C    PUT T BACK TO WHERE IT WAS T-1

     t = t - 1D0
c
c    CALCULATE RECIPICAL TEMPERATURE DIFFERENCE

     RecT = (1/(T+1D0))-(1/(T))
C     write (user_nhstry,*) 'RecT ',RecT
```

```
C
C     CALCULATE -DHABS IN kJ/mol
C
      PROP(1) = -0.008314*(log(ZTEMP(2)/ZTEMP(1))/RecT)
C
C     PROP(1) = 1D0
C
C
C      write (user_nhstry,*) ' '
C            write (user_nhstry,*) 'prop(1) ',prop(1)
C            write (user_nhstry,*) ' '

            ENDIF

      RETURN
#undef P_NPOFF1
      END
```

APPENDIX L

Aspen Plus^{TM} Data Regression Procedures

L.1 Introduction

The following discussion documents the data regression procedures for literature data entered into the Aspen Plus^{TM} Data Regression System (DRS) for aqueous mixture combinations of K_2CO_3, $KHCO_3$, MEA, PZ, and CO_2.

L.2 Overall Regression Procedure

Adjustable binary interaction parameters were determined by DRS within Aspen Plus^{TM} utilizing the maximum likelihood principle of Britt and Luecke (1973) through the minimization of the objective function as given in Chapter VI. The following procedure outlines the steps to determine the optimum set of binary interaction parameters used in this work.

1. Start with the Aspen Plus^{TM} Default Parameters as the initial values given in Chapter VI.
2. Run the DRS regression package to regress the full model.
    a. If the ratio of the predicted and experimental data point is greater than 2.0 or less than 0.5 the data point was marked as a possible outlier.
    b. Run the DRS regression without the possible outlier to determine the effect on the remaining experimental database to decide if the point should be excluded.
3. Document the full model regression case results as "Full."
4. Start with the results from the full model as the initial values.
5. Fix or exclude a parameter to the default value starting with coefficients associated with the C term.
    a. If all coefficients associated with the C term are set to the default value, then fix or exclude a parameter to the default value starting with coefficients associated with the B term.
    b. If all coefficients associated with the B term are set to the default value, then fix or exclude a parameter to the default value starting with coefficients associated with the A term. This action will then fix the selected tau parameter to the appropriate default value.
6. Select which coefficient gave the smallest change between the sum of squares of the fixed regression case and the full model.
7. Delete or fixed to the default value the coefficient with the smallest change.
8. Repeat steps 5 through 7 until all coefficients/parameters are fixed to the default parameters.
9. Sort (ascending) the regression cases by the sum of squares.
10. Perform a logic test on each regression case by determining if the standard error with respect to the estimate of the coefficient is less than the value for the estimate of the coefficient.
    a. If the standard error is less than the estimate of the coefficient then add one to the count for each regression case.
    b. Tabulate the total count for each regression case and sort (ascending) the results.
11. Determine for each regression case how many parameters are highly positively or negatively correlated.
    a. If the correlation coefficient between two parameters is greater than 0.9 or less than -0.9 add one to the count for each regression case.
    b. Tabulate the total count for each regression case and sort (ascending) the results.
12. Select cases with the lowest value associated with the sum of squares, logic test, and the total number of correlated parameters. Label each possible optimum case.
13. Test each optimum case to see which case gives the lowest absolute average relative deviation (AARD) for each data set.
14. Label the case with the lowest AARD for each data set as the Optimum Model.

APPENDIX M

Nomenclature

M.1 Aspen Plus^{TM} Scalar Parameter Nomenclature

API	Standard API gravity
CHARGE	Ionic Charge number (positive for cations, negative for anions)
CHI	Stiel polar factor
DGAQFM	Aqueous phase free energy of formation at infinite dilution and 25 deg C. For ionic species and molecular solutes in electrolyte systems
DGAQHG	Helgeson infinite dilution Gibbs energy of formation
DGFORM	Standard free energy of formation for ideal gas at 25 deg C
DGFVK	Parameter for the Gibbs free energy of formation. Used by the van Krevelen models
DGSFRM	Solid free energy of formation at 25 deg C
DHAQFM	Aqueous phase heat of formation at infinite dilution and 25 deg C. For ionic species and molecular splutes in electrolyte systems
DHAQHG	Helgeson infinite dilution enthalpy of formation
DHFORM	Standard enthalpy of formation for ideal gas at 25 deg C
DHFVK	Parameter for the enthalpy of formation. Used by the van Krevelen models
DHSFRM	Solid enthalpy of formation at 25 deg C
DHVLB	Enthalpy of vaporization at TB
DLWC	Vector indication diffusing or non-diffusing components for Wilke-Chang Model. Enter 1 for diffusing component or 0 or non-diffusing component.

DVBLNC	Vector indication diffusing or non-diffusing components for Chapman-Enskog-Wike-Lee Model. Enter 1 for diffusing component or 0 or non-diffusing component
HCOM	Standard enthalpy of combustion at 298.2 K
IONRDL	Riedel ionic coefficient for correction to the liquid mixture thermal conductivity of a mixture due to the presence of electrolytes
IONTYP	Ion type for the Criss-Cobble aqueous infinite dilution ionic heat capacity equation (1=cations; 2=simple anions, OH-; 3=oxy anions; 4=acid oxy anions; 5=H+)
MUP	Dipole moment
MW	Molecular weight
OMEGA	Pitzer acentric factor
OMEGHG	Helgeson Omega heat capacity coefficient
PC	Critical Pressure
RADIUS	Born radius of ionic species
RHOM	Mass density
RKTZRA	Parameter for the Rackett liquid molar volume model
S25HG	Helgeson entropy at 25 deg C
S025C	Absolute entropy at 25 deg C used in the Criss-Cobble equation for estimation of aqueous infinite dilution ionic heat capacity
S025E	Sum of element entropies at 25 deg C
SG	Standard specific gravity at 60 deg F
TB	Normal boiling point
TC	Critical temperature
TFP	Freezing point temperature
TREFHS	Reference temperature when solid reference state is used (RSTATE = 3). TREFHS is used together with DHSFRM and DGSFRM
VB	Liquid molar volume at TB
VC	Critical volume
VCRKT	Critical volume for the Rackett liquid model; defaults to VC
VLSTD	Standard liquid volume at 60 deg F
ZC	Critical compressibility factor

M.2 Aspen Plus^{TM} Temperature Dependent Nomenclature

AHGPAR	Helgeson Equation of state coefficients (for ions in the chemical reactions)
ATOMNO	Vector containing the atom types (atomic numbers) for a given molecule (e.g., H=1, C=6, O=8). Must use the vector NOATOM to define the number of occurrences of each atom.
CHGPAR	Helgeson C Heat Capacity coefficient (for ions in the chemical reactions)
CPAQ0	Aqueous phase heat capacity at infinite dilution polynomial. If no values are given then uses Criss-Cobble equation to calculate heat capacity.
CPDIEC	Pure component dielectric constant coefficients of nonaqueous solvents

CPIG	Ideal gas heat capacity
CPIGDP	DIPPR ideal gas heat capacity equation is used for most pure components
CPLXP1	Barin liquid phase heat capacity for the first temperature range
CPLXP2	Barin liquid phase heat capacity for the second temperature range
CPSDIP	Coefficients for the DIPPR solid heat capacity equation
CPSPO1	Solids heat capacity polynomial
DHVLDP	Pure component heat of vaporization coefficients for the DIPPR heat of vaporization equation
DHVLWT	Watson Heat of Vaporization equation for pure components
DNLDIP	DIPPR liquid density equation for pure components if DNLDIP is available (pure component liquid molar volume)
DNSDIP	DIPPR solid density equation
IONMOB	Coefficients for the Jones-Dole correction to liquid mixture viscosity due to the presence of electrolytes (moles)
IONMUB	Coefficients for the Jones-Dole correction to liquid mixture viscosity due to the presence of electrolytes (volume/mole)
KLDIP	Pure component liquid thermal conductivity coefficients for the DIPPR liquid thermal conductivity equation
KSPOLY	Solid Thermal conductivity
KVDIP	Pure component vapor thermal conductivity for low pressure gasses coefficients for the DIPPR vapor thermal conductivity equation
MULAND	Pure component liquid viscosity coefficients for the Andrade Liquid Viscosity equation
MULDIP	Pure component liquid viscosity coefficients for the DIPPR Liquid Viscosity equation
MUVDIP	Pure component low pressure vapor viscosity coefficients for the DIPPR Liquid Viscosity equation
NOATOM	Vector containing the number of each type of element in the component. Must be used with ATOMNO.
PCES	Parameters Estimation by the Aspen Physical Property System
PLXANT	Coefficients for the Extended Antoine vapor pressure equation for a liquid
PSANT	Pure component Coefficients for Solid Antoine vapor pressure equation
SIGDIP	Pure component liquid surface tension coefficients for the DIPPR liquid surface tension equation
VLBROC	Brelvi-O-Connell Volume Parameter
VLPO	IK-CAPE liquid density equation for pure components if VLPO is available (pure component liquid molar volume)
VSPOLY	Pure component coefficients for the solid molar volume equation
WATSOL	Coefficients for the water solubility equation model that calculates solubility of water in a hydrocarbon-rich liquid phase. This model is used automatically when you model a hydrocarbon-water system with free-water option.

REFERENCES

1. *Vapor Pressures and Critical Points of Liquids XIV: Aliphatic Oxygen-Nitrogen Compounds. Item 79030*. Engineering Sciences Data: London, England, 1979.

2. The Alkanolamines Handbook. In 3rd ed.; The Dow Chemical Company: Midland, Michigan, 1981.

3. *International Tables for X-ray Crystallography, Vol. C, Tables 4.2.6.8 and 6.1.1.4*. Kluwer Academic Press: Boston, MA, 1992.

4. *Arc Version 1.06*, http://www.stat.umn.edu/arc/: 2004.

5. Abbott, M. M.; O'Connell, J. P., *Chemical Engineering Education* **1994,** 28, 18-23 and 77.

6. Altomare, A.; Burla, M. C.; Camalli, M.; Cascarano, G. L.; Giacovazzo, C.; Guagliardi, A.; Moliterni, A. G. G.; Polidori, G.; Spagna, R., SIR97: A program for crystal structure solution. *J. Appl. Cryst.* **1999,** 32, 115-119.

7. Apelblat, A., The Vapor Pressures of Water Over Saturated Aqueous Solutions of Barium Chloride, Magnesium Nitrate, Calcium Nitrate, Potassium Carbonate, and Zinc Sulfate, at Temperatures from 283 K to 313 K. *Journal of Chemical Thermodynamics* **1982,** 24, 619-626.

8. Archer, D. G., *Journal of Physical Chemistry Ref. Data* **1993,** 22, (6), 1441-1453.

9. Aroua, M. K.; Mohd, S. R., Solubility of CO_2 in Aqueous Piperazine and its Modelling Using the Kent–Eisenberg Approach. *Chemical Engineering Technology* **2003,** 27, 65-70.

10. Aseyev, G. G., *Electrolytes: Equilibria in Solutions and Phase Equilibria. Calculation of Multicomponent Systems and Experimental Data on the Activities of Water, Vapor Pressures, and Osmotic Coefficients*. Begell House: New York, 1999.

11. Aseyev, G. G.; Zaytsev, I. D., *Volumetric Properties of Electrolyte Solutions: Estimation Methods and Experimental Data*. Begell House: New York, 1996.

12. Atkins, P.; de Paula, J., *Physical Chemistry*. Seventh ed.; W. H. Freeman and Company: New York, 2002.

13. Austgen, D. M.; Rochelle, G. T.; Chen, C. C., Model of Vapor-Liquid Equilibria for Aqueous Acid Gas-Alkanolamine Systems. 2. Representation of H_2S and CO_2 Solubility in Aqueous MDEA and CO_2 Solubility in Aqueous Mixtures of MDEA with MEA or DEA. *Ind. Eng. Chem. Res.* **1991,** 30, (3), 543-555.

14. Austgen, D. M.; Rochelle, G. T.; Peng, X.; Chen, C. C., Model of Vapor-Liquid Equilibria for Aqueous Acid Gas-Alkanolamine Systems Using the Electrolyte-NRTL Equation. *Ind. Eng. Chem. Res.* **1989,** 28, 1060-1073.

15. Barth, D.; Rubini, P.; Delpuech, J. J., Determination des parametres thermodynamiques de l'equilibre de formation de carbamates d'amino-alcools en solution aqueuse par resonance magnetique nucleaire du carbone-13. *Bulletin de la societe chemique de france* **1984,** 7, (8).

16. Bates, R. G.; Pinching, G. D., Acidic Dissociation Constant and Related Thermodynamic Quantities for Monoethanolammonium Ion in Water From 0 to 50 °C. *Journal of Research of the National Bureau of Standards* **1951,** 46, (5), 349352.

17. Ben-Naim, A.; Baer, S., Method for Measuring Solubilities of Slightly Soluble Gasas in Liquids. *Trans. Faraday Soc.* **1963,** 59, 2735-2738.

18. Benson, B. B.; Krause, D.; Peterson, M. A., The Solubility and Fractionation of Gases in Dilute Aqueous Solution. *Journal of Solution Chemistry* **1979,** 8, 655-690.

19. Bishnoi, S.; Rochelle, G. T., Absorption of Carbon Dioxide into Aqueous Piperazine: Reaction Kinetics, Mass Transfer, and Solubility. *Chemical Engineering Science* **1999,** 55, 5531-5543.

20. Bishnoi, S.; Rochelle, G. T., Absorption of Carbon Dioxide into Aqueous Piperazine: Reaction Kinetics, Mass Transfer, and Solubility. *Chemical Engineering Science* **2000,** 55, 5531-5543.

21. Bishnoi, S.; Rochelle, G. T., Thermodynamics of Piperazine/Methyldiethanolamine/Water/Carbon Dioxide. *Ind. Eng. Chem. Res.* **2002,** 41, 604-612.

22. Cai, Z.; Xie, R.; Wu, Z., Binary Isobaric Vapor-Liquid Equilibria of Ethanolamines + Water. *Journal of Chemical and Engineering Data* **1996,** 41, (5), 1101-1103.

23. Carson, J. K.; Marsh, K. N.; Mather, A. E., Enthalpy of Solution of Carbon Dioxide in (Water + Ethanolamine, or Diethanolamine, or N-Methyldiethanolamine) at T = 298.15 K. *Journal of Chemical Thermodynamics* **2000,** 32.

24. Chang, H. T.; Posey, M.; Rochelle, G. T., Thermodynamics of Alkanolamine-Water Solutions from Freezing Point Measurements. *Ind. Eng. Chem. Res.* **1993,** 32, (10), 2324-2335.

25. Chen, C. C.; Britt, H. I.; Boston, J. F.; Evans, L. B., Extensiion and Application of the Pitzer Equation for Vapor-Liquid Equilibrium of Aqueous Electrolyte Systems with Molecular Solutes. *AICHE J.* **1979,** 25, 820-831.

26. Chen, C. C.; Britt, H. I.; Boston, J. F.; Evans, L. B., Local Composition Model for Excess Gibbs Energy of Electrolyte Solutions. Part 1: Single Solvent, Single Completely Dissociated Electrolyte Systems. *AICHE J.* **1982,** 28, (4), 588-596.

27. Chen, C. C.; Evans, L. B., A Local Composition Model for the Excess Gibbs Energy of Aqueous Electrolyte Systems. *AICHE J.* **1986,** 32, (3), 444-454.

28. Chiu, L. F.; Li, M. H., Heat Capacity of Alkanolamine Aqueous Solutions. *Journal of Chemical and Engineering Data* **1999,** 44, (6), 1396-1401.

29. Chiu, L. F.; Liu, H. F.; Li, M. H., Heat Capacity of Alkanolamines by Differential Scanning Calorimetry. *Journal of Chemical and Engineering Data* **1999,** 44, (4), 631-636.

30. Clapeyron, E. J., Memoirs on the Motive Power of Heat. *L'ecole Polytechnique* **1834,** 14, (23), 153.

31. Clarke, J. K., Kinetics of Absorption of Carbon Dioxide in Monoethanolamine Solutions at Short Contact Times. *Industral and Engineering Chemistry Fundamentals* **1964,** 3, (3), 239-245.

32. Cullinane, J. T. Thermodynamics and Kinetics of Aqueous Piperazine with Potassium Carbonate for Carbon Dioxide Absorption. The University of Texas at Austin, Austin, Texas, 2005.

33. Dang, H. Absorption Rate and Solubility in MEA/PZ/H_20. The University of Texas at Austin, Austin, TX, 2000.

34. Dang, H.; Rochelle, G. T., CO_2 Absorption Rate and Solubility in Monoethanolamine/Piperazine/Water. *Sep. Sci. Tech* **2003,** 38, (2), 337-357.

35. Derks, P. W. J.; Dijkstra, H. B. S.; Hogendoorn, J. A.; Versteeg, G. F., Solubility of Carbon Dioxide in Aqueous Piperazine Solutions. *AICHE Journal* **2005,** 51, (8), 2311-2327.

36. Deshmukh, R. D.; Mather, A. E., A Mathematical Model for Equilibrium Solubility of Hydrogen Sulfide and Carbon Dioxide in Aqueous Alkanolamine Solutions. *Chemical Engineering Science* **1981,** 36, 355-362.

37. Ditmars, D. A.; Plint, C. A.; Shukla, R. C., *Int. J. Thermophys* **1985,** 6, 499-515.

38. Dobrosavlijevic, A. S.; Maglic, K. D., Measurements of Specific Heat and Electrical Resistivity of Austenitic Stainless Steel (St. 1.4970) in the Range 300-1500 K by Pulse Calorimetry. *Int. J. Thermophys* **1992,** 13, (1), 57-64.

39. Edwards, T. J.; Maurer, G.; Newman, J.; Prausnitz, J. M., Vapor-Liquid Equilibria in Multicomponent Aqueous Solution of Valatile Weak Electrolytes. *AICHE J.* **1978,** 24, (6), 966-976.

40. Edwards, T. J.; Newman, J.; Prausnitz, J. M., Thermodynamics of aqueous solutions containing volatile weak electrolytes. *AICHE J.* **1975,** 21, 248-259.

41. Ellis, A. J.; Golding, R. M., The Solubility of Carbon Dioxide above 100 ^{o}C in Water and in Sodium Chloride Solutions. *American Journal of Science* **1963,** 261, 47-60.

42. Enea, O.; Berthton, G., Heats of Dissolution and Protonation of Piperazine and Its Derivatives in Different Water-Ethanol Mixtures. *Electrochim* **1973,** 18, (8), 579-582.

43. Ermatchkov, V.; Kamps, A. P.-S.; Speyer, D.; Maurer, G., Solubility of Carbon Dioxide in Aqueous Solutions of Piperazine in the Low Gas Loading Region. *Journal of Chemical and Engineering Data* **2006,** 51, (5), 1788-1796.

44. Ermatchkov, V.; Perez-Salado Kamps, A.; Maurer, G., Chemical equilibrium constants for the formation of carbamates in (carbon dioxide + piperazine + water) from ^{1}H NMR-spectroscopy. *Journal of Chemical Thermodynamics* **2003,** 35, 1277-1289.

45. Farrugia, L. J., WinGX 1.64: An Integrated System of Windows Programs for the Solution, Refinement and Analysis of Single Crystal X-ray Diffraction Data. *J. Appl. Cryst.* **1999,** 32, 837-838.

46. Ferguia, S. Modeling of CO_2 Removal from Flue Gasses with Monoethanolamine. The University of Texas at Austin, Austin, TX, 2002.

47. Gmehling, J.; Li, J.; Schiller, M., A Modified UNIFAC Model. 2. Present Parameter Matrix and Result for Different Thermodynamic Properties. *Ind. Eng. Chem. Res.* **1993,** 32, (1), 178-193.

48. Goff, G. S. Oxidative Degradation of Aqueous Monoethanolamine in CO_2 Capture Processes: Iron and Copper Catalysis, Inhibition, and O_2 Mass Transfer. The University of Texas at Austin, Austin, Texas, 2005.

49. Goldman, A. M.; Leibush, A. G., Study of the Equilibrium of Carbon Dioxide Desorption of Monoethanolamine Solutions in The Temperature Rage 75-140 ^oC. *Tr. Gos. Nauchno-Issled. Proektn. Inst. Azotn. Promsti.* **1959,** 10, 54-82.

50. Hala, E.; Fried, V.; Boublik, T., *The Vapour Pressures of Pure Substances.* Elsevier: New York, New York, 1973.

51. Harned, H. S.; Owen, B. B., *The Physical Chemistry of Electrolyte Solutions.* 3rd ed.; Reinhold: New York, 1958.

52. Hefter, G. T.; Tomkins, R. P. T., *The Experimental Determination of Solubilities.* John Wiley & Sons, Ltd.: West Sussex, England, 2003.

53. Hetzer, H. B.; Robinson, R. G.; Bates, J., Dissociation Constants of Piperazinium Ion and Related Thermodynamic Quantities from 0 to 50^o. *Journal of Physical Chemistry* **1968,** 72, 2081-2086.

54. Hill, A. E.; Hill, D. G., Ternary Systems. V. Potassium Bicarbonate, Potassium Carbonate and Water. *Journal of American Chemical Society* **1927,** 49, 968-969.

55. Hilliard, M. D. Thermodynamics of Aqueous Piperazine/Potassium Carbonate/Carbon Dioxide Characterized by the Electrolyte NRTL Model within Aspen Plus. The University of Texas at Austin, Austin, 2005.

56. Houghton, G.; McLean, A. M.; Ritchie, P. D., Compressibility, Fugacity and Water Solubility of Carbon Dioxide in The Region 0-36 atm and 0-100 ^oC. *Chemical Engineering Science* **1957,** 6, 132.

57. Hsu, C. H.; Li, M. H., Densities of Aqueous Blended Amines. *Journal of Chemical and Engineering Data* **1997,** 42, (3), 502-507.

58. Huang, S. S. S.; Leu, A. D.; Ng, H. J.; Robinson, D. B., The Phase Behavior of Two Mixtures of Methane, Carbon Dioxide, Hydrogen Sulfide, and Water. *Fluid Phase Equilibria* **1985,** 19, 21-32.

59. Jou, F.-Y.; Mather, A. E.; Otto, F. D., The Solubility of CO_2 in a 30 Mass Percent Monoethanolamine Solution. *The Canadian Journal of Chemical Engineering* **1995,** 73, 140-146.

60. Kaewsichan, L.; Al-Bofersen, O.; Yesavage, V. F.; Selim, M. S., Predictions of The Solubility of Acid Gases in Monoethanolamine (MEA) and Methyldiethanolamine (MDEA) Solutions Using the Electrolyte-UNIQAC Model. *Fluid Phase Equilibria* **2001,** 183-184, 159-171.

61. Kell, G. S.; Haar, L.; Gallagher, J. S., *NBS/NRC Steam Tables. Thermodynamic and Transport Properties and Computer Programs for Vapor and Liquid States of Water in SI Units.* Hemisphere Publishing Corporation: Washington, 1984.

62. Kennan, R. P.; Pollack, G. L., Pressure Dependence of the Solubility of Nitrogen, Argon, Krypton, and Xenon in Water. *Journal of Chemical Physics* **1990,** 93, 2724-2735.

63. Kent, R.; Eisenberg, B., Better data for amine treating. *Hydrocarbon Proc.* **1976,** 55, 87-90.

64. Kim, I. Personal Communication. The Norwegian University of Science and Technology, Trondheim, Norway, 2007.

65. Kim, I.; Svendsen, H. F., Heat of Absorption of Carbond Dioxide (CO_2) in Monoethanolamine (MEA) and 2-(Aminoethyl)ethanolamine (AEEA) Solutions. *Ind. Eng. Chem. Res.* **2007,** 46, 5803-5809.

66. Kim, J. H.; Dobrogowska, C.; Hepler, L. G., Thermodynamics of Ionization of Aqueous Alkanolamines. *Canadian Journal of Chemistry* **1987,** 65, 1726-1728.

67. Lawson, J. D.; Garst, A. W., Gas Sweetening Data: Equilibrium Solubility of Hydrogen Sulfide and Carbon Dioxide in Aqueous Monoethanolamine and Aqueous Diethanolamine Solutions. *Journal of Chemical and Engineering Data* **1976,** 21, (1), 20-30.

68. Lee, J. I.; Otto, F. D.; Mather, A. E., The Solubility of H_2S and CO_2 in Aqueous Monoethanolamine Solutions. *Canadian Journal of Chemical Engineering* **1974,** 52, 803-805.

69. Lee, J. I.; Otto, F. D.; Mather, A. E., Equilibrium Between Carbon Dioxide and Aqueous Monoethanolamine Solutions. *Journal of Applied Chemistry and Biotechnology* **1976,** 26, 541-549.

70. Lee, L. J. B. A Vapor-Liquid Equilibrium Model for Natural Gas Sweetening Process. The University of Oklahoma, Norman, Oklahoma, 1996.

71. Li, M. H.; Lai, M. D., Solubility and Diffusivity of N_2O and CO_2 in (monoethanolamine + N+Methyldiethanolamine + Water) and in (Monoethanolamine + 2-Amino-2-methyl-1-propanol + Water). *Journal of Chemical and Engineering Data* **1995,** 40, 486-492.

72. Li, Y. G.; Mather, A. E., Correlation and Prediction of The Solubility of CO_2 in a Mixed Alkanolamine Solution. *Ind. Eng. Chem. Res.* **1994,** 33, 2006-2015.

73. Lide, D. R., *CRC Handbook of Chemistry and Physics*. 81 ed.; CRC Press: 2004.

74. Linke, W. F.; Seidell, A., *Solubility of Inorganic and Metal Organic Compounds*. American Chemical Society: Washington, D.C., 1965; Vol. 2, p 81, 85, and 102.

75. Littel, R. J.; Versteeg, G. F.; van Swaaij, W. P. M., Solubility and Diffusivity Data for the Absorption of COS, CO_2, and N_2O in Amine Solutions. *Journal of Chemical and Engineering Data* **1992,** 37, 49-55.

76. Lynch, V. Perconal Communication. The University of Texas at Austin, Austin, Texas, USA, 2007.

77. Lyudkovskaya, M. A.; Fridman, S. D.; Klevke, V. A., Purification of Gases from CO_2 by a "Hot" Solution of K_2CO_3. Phase Equilibriums in the System K_2CO_3-$KHCO_3$-H_2O. *Khimicheskaia Promyghlennost* **1965,** 41, 339-343.

78. Malinin, S. D., The System H_2O-CO_2 at high Temperatures and Pressures. *Geokhimiya* **1959,** 3, 235.

79. Malinin, S. D., Thermodynamics of the H_2O-CO_2 System. *Geochemical International* **1975,** 11, 1060.

80. Ma'mun, S.; Nilsen, R.; Svendsen, H. F., Solubility of Carbon Dioxide in 30 mass % Monoethanolamine and 50 mass % Methyldiethanolamine Solutions. *Journal of Chemical and Engineering Data* **2005,** 50, (2), 630-634.

81. Mandal, B. P.; Biswas, A. K.; Bandyopadhyay, S. S., Absorptioni of carbon dioxide into aqueous blends of 2-amino-2-methyl-1-propanol and diethanolamine. *Journal of Chemical Engineering Science* **2003,** 58, 4137-4144.

82. Mandal, B. P.; Kundu, M.; Bandyopadhyay, S. S., Physical Solubility and Diffusivity of N_2O and CO_2 into Aqueous Solutions of (2-Amino-2-methyl-1-propanol + Monoethanolamine) and (N-Methyldiethanolamine + Monoethanolamine). *Journal of Chemical and Engineering Data* **2005,** 50, (2), 352-358.

83. Mathonat, C. Calorimetrie de Melange, a Ecoulement, a Temperatures et Pressions Elevees. Application a l'Etude de l'Elimination du Dioxide de Carbone a l'Aide de Solutions Aqueuses d'Alecanolamines. Universitat Blaise Pascal, Clermont-Ferrand, France, 1995.

84. Mathonat, C.; Majer, V.; Mather, A. E., Use of Flow Calorimetry for Determining Enthalpies of Absorption and the Solubility of CO2 in Aqueous Monoethanolamine Solutions. *Ind. Eng. Chem. Res.* **1998,** 37.

85. Matthews, E.; Fried, V.; Boublik, T., *The Vapour Pressures of Pure Substances*. Elsevier: New York, NY, 1973.

86. Matthews, J. B.; Sumner, J. F.; Moelwyn-Huges, E. A., The vapor pressure of certian liquids. *Trans. Faraday Soc.* **1950,** 46, 797-803.

87. Mock, B.; Evans, L. B.; Chen, C. C., Thermodynamic Representation of Phase Equilibria of Mixed-Solvent Electrolyte Systems. *AICHE J.* **1986,** 32, (10), 1655-1664.

88. Moore, J. G.; Keyes, F. G.; Keenan, J. H.; Hill, P. G., *Steam Tables. Thermodynamic Properties of Water Including Vapor, Liquid, and Solid Phases.* John Wiley & Sons, Inc.: New York, 1969.

89. Moore, R. C.; Mesmer, R. E.; Simonson, J. M., Solubility of Potassium Carbonate in Water between 384 and 529 K Measured Using the Synthetic Method. *Journal of Chemical and Engineering Data* **1997,** 42, (6), 1078-1081.

90. Mshewa, M. M. Carbon Dioxide Desorption/Absorption with Aqueous Mixtures of Methyldiethanolamine and Diethanolamine at 40 to 120 °C. The University of Texas at Austin, Austin, Texas, 1995.

91. Nath, A.; Bender, E., Isothermal Vapor-Liquid Equilibrium of Binary and Ternary Mixtures Containing Alcohol, Alkanolamine, and Water with a New Static Device. *Journal of Chemical and Engineering Data* **1983,** 28, (4), 370-375.

92. Okoye, C. Carbon DIoxide Solubility and Absorption Rate in Monoethanolamine/Piperazine/H_2O. The University of Texas at Austin, Austin, TX, 2005.

93. Osborne, N. S.; Stimson, H. F.; Ginnings, D. C., Measurements of Heat Capacity and Heat of Vaporization of Water in the Range 0 °C to 100 °C. *Journal of Research of the National Bureau of Standards* **1939,** 23, 197-260.

94. Ostwald, W., *Manual of Physico-Chemical Measurements*. Macmillan: London, England, 1894; p 172-175.

95. Otwinowski, Z.; Minor, W., *Methods in Enzymology (DENZO-SMN)*. Academic Press: 1997.

96. Page, M.; Huot, J. Y.; Jolicoeur, C., A Comprehensive Thermodynamic Investigation of Water-Ethanolamine Mixtures at 10, 25, and 40 ºC. *Canadian Journal of Chemistry* **1993,** 71, (7), 1064-1072.

97. Park, S. B.; Lee, H., Vapor-Liquid Equilibria For the Binary Monoethanolamine + Water and Monoethanolamine + Ethanol Systems. *Korean Journal of Chemical Engineering* **1997,** 14, (2), 146-148.

98. Perez-Salado Kamps, A.; Meyer, E.; Runpf, B.; Maurer, G., Solubility of CO_2 in Aqueous Solutions of KCL and in Aqueous Solutions of K_2CO_3. *Journal of Chemical and Engineering Data* **2007,** 52, (3), 817-832.

99. Perez-Salado Kamps, A.; Xia, R.; Maurer, G., Solubility of CO_2 in (H_2O + Piperazine) and in (H_2O + MDEA + Piperazine). *AICHE J.* **2003,** 49, 2662-2670.

100. Picker, P.; Jolicoeur, C.; Desnoyers, J. E., *Journal of Chemical Thermodynamics* **1969,** 1, 469.

101. Picker, P.; Leduc, P. A.; P.R., P.; Desnoyers, J. E., *Journal of Chemical Thermodynamics* **1971,** 3, 631.

102. Poplsteinova, J. Absorption of Carbon Dioxide - Modeling and Experimental Characterization. Norwegian University of Science and Technology, Trondheim, Norway, 2004.

103. Poplsteinova, J.; Krane, J.; Svendsen, H. F., Liquid-Phase Composition Determination in CO_2-H_2O-Alkanolamine Systems: An NMR Study. *Ind. Eng. Chem. Res.* **2005,** 44, 9894-9903.

104. Posey, M. L. Thermodynamic Model for Acid Gas Loaded Aqueous Alkanolamine Solutions. The University of Texas at Austin, Austin, 1996.

105. Prausnitz, J. M.; Lichtenthaler, R. N.; de Azevedo, E. G., *Molecular Thermodynamics of Fluid Phase Equilibria*. 3rd ed.; Prentice Hall PTR: New York, 1999.

106. Puchkov, L. V.; Kurochkina, V. V., Saturated Vapor Pressure Over Aqueous Solutions of Potassium Carboonate. *Zhur. Prikland. Khim.* **1970,** 43, (1), 181-183.

107. Redlich, O.; Kwong, J. N. S., On the Thermodynamics of Solutions. V. An Equation of State. Fugacities of Gaseous Solutions V. An Equation of State. Fugacities of Gaseous Solutions. *Chem. Rev* **1949,** 44, (1), 233-244.

108. Renon, H.; Prausnitz, J. M., Local Compositiions in Thermodynamic Excess Functions for Liquid Mixtures. *AICHE J.* **1968,** 14, (1), 135-44.

109. Riddick, J. A.; Bunger, W. B., *Organic Solvents: Physical Properties and Methods of Purification.* 3rd ed.; Wiley Interscience: New York, 1970.

110. Ronalter, M. Personal Communication. The University of Texas at Austin, Austin, Texas, USA, 2007.

111. Rowley, R. L.; Wilding, W. V.; Oscarson, J. L.; Yang, Y.; Zundel, N. A., DIPPR® Data Compilation of Pure Chemicals Properties, Design Institute for Physical Properties. In Brigham Young University. Provo, Utah.: 2004.

112. Saarinen, P.; Kauppinen, J., Multicomponent Anaylsis of FT-IR Spectra. *Applied Spectroscopy* **1991,** 45, (6), 953-963.

113. Sada, E.; Kito, S., Solubilities of Gases in Aqueous Monoethanolamine Solutions. *Kagaku Kogaku* **1972,** 36, (2), 218-220.

114. Sarbar, M.; Covington, A. K.; Nuttall, R. L.; Goldberg, R. N., Activity and Osmotic Coefficients of Aqueous Potassium Carboonate. *Journal of Chemical Thermodynamics* **1982,** 14, 695-702.

115. Sheldrick, G. M. SHELXL97: Program for the Refinement of Crystal Structures. University of Gottingen, Gottingen, Germany, 1994.

116. Sheldrick, G. M., *SHELXTL/PC (Version 5.03).* Siemens Analytical X-ray Instruments, Inc.: Madison, Wisconsin, USA, 1994.

117. Smith, J. M.; Van Ness, H. C.; Abbott, M. M., *Introduction to Chemical Engineering Thermodynamics.* McGraw-Hill: New York, 1996.

118. Soave, G., Equilibrium Constants for Modified Redlich Kwong Equation of State. *Chemical Engineering Science* **1972,** 27, 1196-1203.

119. Spek, A. L. PLATON: A Multipurpose Crystallographic Tool. Utrecht University, The Netherlands, 1998.

120. Steele, W. V.; Smith, N. K.; Nguyen, A.; Knipmeyer, S. E.; Chirico, R. D., Thermodynamic Properties and Ideal-Gas Enthalpies of Formation for Dicyclohexyl Sulfide, Diethylenetriamine, Di-n-octyl Sulfide, Dimethyl Carbonate, Piperazine, Hexachloroprop-1-ene, Tetrakis(dimethylamino)ethylene, N,N'-Bis-(2-hydroxyethyl)ethylene. *Journal of Chemical and Engineering Data* **1997,** 42, 1037-1052.

121. Stewart, P. B.; Munjal, P., Solubility of Carbon Dioxide in Pure Water, Synthetic Sea Water, and Synthetic Sea Water Concentrates at -5 °C to 25 °C and 10- to 45-atm Pressure. *Journal of Chemical and Engineering Data* **1970,** 115, 67.

122. Suda, T.; Iwaki, T.; Mimura, T., Facile Determination of Dissolved SPecises in CO_2-Amine-H_2O System by NMR Spectroscopy. *Chemistry Letters* **1996**.
123. Swanson, A. C.; Chueh, C. F., Estimating Liquid Heat Capacity. *Chemical Engineering Progress* **1973,** 69, 83.

124. Tochigi, K.; Akimoto, K.; Ochi, K.; Liu, F.; Rawase, Y., Isothermal Vapor-Liquid Equilibria for Water + 2-Aminoethanol + Dimethyl Sulfoxide and Its Constituent Three Binary Systems. *Journal of Chemical and Engineering Data* **1999,** 44, (3), 588-590.

125. Tosh, J. S.; Field, J. H.; Benson, H. E.; Haynes, W. P. *Equilibrium Study of the System Potassium Carbonate, Potassium Bicarbonate, Carbon Dioxide, and Water*; 1959; p 23.

126. Touhara, H.; Okazaki, S.; Okino, F.; Tanaka, H.; Ikari, K.; Nakanishi, K., Thermodynamic Properties of Aqueous Mixtures of Hydrophilic Compounds 2. Aminoethanol and its Methyl Derivatives. *Journal of Chemical Thermodynamics* **1982,** 14, 145-156.

127. Tsai, T. C.; Ko, J. J.; Wang, H. M.; Lin, C. Y.; Li, M. H., Solubility of Nitrous Oxide in Alkanolamine Aqueous Solutions. *Journal of Chemical and Engineering Data* **2000,** 45, (2), 341-347.

128. Versteeg, G. F.; van Swaaij, W. P. M., Solubility and Diffusivity of Acid Gases (CO_2, H_2S) in Aqueous Alkanolamine Solutions. *Journal of Chemical and Engineering Data* **1988,** 33, (1), 29-34.

129. Wang, D. Equilibrium Constant Study for Carbamate Formation in Alkanolamine Solutions from NMR Measurements. University of Canterbury, Christchurch, New Zealand, 2001.

130. Wang, Y. W.; Xu, S.; Otto, F. D.; Mather, A. E., Solubility of N_2O in Alkanolamines and in Mixed Solvents. *The Chemical Engineering Journal* **1992,** 48, 31-40.

131. Weidlich, U.; Gmehling, J., A Modified UNIFAC Model. 1. Prediction of VLE, Excess Enthalpy, and Infinite Dilution Activity Coefficients. *Ind. Eng. Chem. Res.* **1987,** 26, 1372-1381.

132. Weiland, R. H.; Chakravarty, T.; Mather, A. E., Solubility of Carbon Dioxide and Hydrogen Sulfide in Aqueous Alkanolamines. *Ind. Eng. Res.* **1993,** 32, 1419-1430.

133. Weiland, R. H.; Digman, J. C.; Cronin, D. B., Heat Capacity of Aqueous Monoethanolamine, Diethanolamine, *N*-Methyldiethanolamine, and *N*-Methyldiethanolamine-Based Blends with Carbon Dioxide. *Journal of Chemical and Engineering Data* **1997,** 42, (5), 1004-1006.

134. Willian, J.; Sorey, S. Personal Communication. The University of Texas at Austin, Austin, Texas, USA, 2007.

135. Wilson, H. L.; Wilding, W. V., *Vapor Liquid and Liquid-Liquid Equilibrium Measurements on Twenty Two Binary Mixtures*. Experimental Results for Dippr 1990 91 Projects on Phase Equilibria and Pure Component Properties: 1994; p 63-115.

136. Xia, J.; Perez-Salado Kamps, A.; Maurer, G., Solubility of H_2S in (H_2O + piperazine) and in (H_2O + MDEA + piperazine). *Fluid Phase Equilibria* **2003,** 207, 23-34.

VITA

Marcus Douglas Hilliard was born in El Paso, Texas USA, on January 31, 1977, the son of Mary Elizabeth and Gregg Hannah. In the fall of 1996, he entered Texas Tech University in Lubbock, Texas USA. From 1998 to 2000, he worked for the Dow Chemical Company as part of the school's cooperative education program. At the completion of his studies at Texas Tech University, he received the degree of Bachelor of Science in Chemical Engineering with a Minor in Chemistry in 2001. In August, 2001, he entered The Graduate School at The University of Texas at Austin as a PhD student working under Dr. Gary T. Rochelle. In January, 2005, he traveled to Trondheim, Norway, as an exchange researcher at the Norges Teknish-Naturvitenshapelige Universitet (The Norwegian University of Science and Technology) working under Dr. Hallvard F. Svendsen. In May, 2005, he received the degree of Master of Science in Engineering from The University of Texas at Austin, for his work entitled, "Thermodynamics of Aqueous Piperazine/Potassium Carbonate/Carbon Dioxide Characterized by the Electrolyte NRTL Model within Aspen Plus". In terms of future endeavors, Marcus has accepted a full-time employment offer with The Dow Chemical Company in Freeport, Texas, USA.

Permanent Address: 101 Cluck Creek Trail
Cedar Park, Texas 78613
USA

This dissertation was typed by the author.